Guan-Yuan Wu · Kuang-Chung Tsai ·
W. K. Chow   *Editors*

The Proceedings of 11th Asia-Oceania Symposium on Fire Science and Technology

Springer

The Proceedings of 11th Asia-Oceania Symposium on Fire Science and Technology

Guan-Yuan Wu · Kuang-Chung Tsai ·
W. K. Chow

Editors

The Proceedings of 11th Asia-Oceania Symposium on Fire Science and Technology

Editors
Guan-Yuan Wu
Department of Fire Science
Central Police University
Taoyuan City, Taiwan

Kuang-Chung Tsai
National Kaohsiung University
of Science and Technology
Kaohsiung City, Taiwan

W. K. Chow
Hong Kong Polytechnic University
Hong Kong, China

Contents

Fire and Smoke Modeling and Experiment

Human Behavior in Fire

Fire Safety Design and Codes

Structural Behavior in Fire

Fire Properties and Testing Methods of Materials

Fire Physics and Chemistry

Numerical Investigation on Temperature Profile of Horizontally Oriented Subsonic Jet Fires with Square Fuel Source

Youbo Huang, Yanfeng Li and Bingyan Dong

Abstract The temperature profile of horizontally oriented jet flame with square fuel source has rarely been investigated in past years; especially, the effect of fuel portal geometry aspect ratio on temperature distribution of horizontally oriented jet flame has little appeared in the previous literature. In order to study the temperature profile of horizontal jet fire, a numerical simulated code was carried out to simulate horizontal jet fire with square fire source and natural gas as fuel. The fuel jet velocity was varied from 27.5 to 205.8 m/s. The temperature distribution features on horizontal and vertical directions were investigated, and the temperature prediction model was amended. The results show that the temperature is influenced by fuel jet velocity heavily. The heat release rate increases linearly with fuel jet velocity, and the slope is 29.1. The horizontal maximum temperature on orifice centerline direction rises from 304.5 to 614.8 °C with fuel jet velocity increase. The predicted model is modified to apply to horizontal jet fire, and the predictions by amended model agree well with simulated data.

Keywords Jet flame · Temperature distribution · Square fuel source · Fire safety · Heat release rate

Nomenclature

b Flame width (m)
C_p Constant pressure specific heat, J/(kg·K)

Y. Huang · Y. Li (✉)
College of Architecture and Civil Engineering, Beijing University of Technology,
100124 Beijing, China
e-mail: liyanfeng@bjut.edu.cn

Y. Huang
e-mail: huangyoubo6@163.com

B. Dong
School of Energy and Environmental Engineering, Hebei University of Technology, 300401
Tianjin, China

C_T, C_1 Constants
$D*$ Characteristic fire diameter
f External force vector (kg/s^2/m)
g Gravitational acceleration (ms^{-2})
h Sensible enthalpy (kJ/kg)
p Pressure (Pa)
Q Theoretical heat release rate (kW/m^2)
q Conductive and radiate heat fluxes (kW/m^2)
R Universal gas constant (J/(mol K))
t Time (s)
T Ambient temperature (K)
$\triangle T$ Temperature rise above ambient (K)
v Velocity (m/s)
W Molecular weight of the gas mixture (kg/mol)
y Width (m)
Z Height (m)

Greek symbols

β Constant
ρ Density (kg/m^3)
τ_{ij} Viscous stress tensor (kg/s^2/m)
κ Coefficient
η Coefficient
Φ Dissipation rate (kW/m^3)

Subscripts

0   Ambient
1   Per unit length
m   Centerline
int   Intermittent flame region
plu   Plume region

1 Introduction

The pipeline transportation becomes main ways for natural gas because of its high efficiency and low cost. But with the increasing natural gas pipeline, the probability

of jet fire which is caused by pipeline aging and third-party damage increases. On the basis of API581 [1], the jet fire accident is major damage for gas pipeline transportation. A historical survey shows that 50% of jet fire accidents will undergo at least one additional event with much more severe effects and consequences [2]. It is necessary to research jet fire behavior and mechanism.

The temperature is one of the important parameter of jet fire, and a lot of researchers studied it and proposed some semiempirical model. Quintiere and Grove [3] proposed the theoretical model to predict the vertical flame plume temperature. Zhang [4] found that the temperature prediction model conducted by Quintiere and Grove cannot be applied to subatmosphere and amended it based on a series of small-scale experiments in reduced atmospheric pressure condition. Lowesmith et al. [5] conducted a series of large-scale high pressure jet fires using natural gas and natural gas/hydrogen mixtures to investigate flame features and found the total heat loading to the pipe target was 15% higher for mixed gas. But all of above temperature studies are about vertical jet fire. As horizontal jet fire, Zhang [6] conducted propane horizontally oriented rectangular nozzles jet fire with aspect ratio n varied from 1:1 to 71:1 to investigate the flame projection distance. Gopalaswami [7] and Laboureur [8] conducted propane horizontal jet fire experiments with nozzle diameter 19 mm to analyze the effect of fuel exit velocity on flame geometry and compared with empirical function data. Johnson et al. [9] proposed a model to predict the thermal radiation of large-scale horizontally released natural gas jet fires. However, few researches were available for horizontal jet fire temperature in the literature. Tao et al. [10] conducted a series of experiments to investigate the temperature rise along flame trajectories near a bounded wall with different nozzle inclined angle between horizontal direction and fuel orifice direction. The empirical equation has been developed in his study. When the inclined angle equal to zero in Tao's temperature model, which means the jet flame is horizontally oriented jet flame. The corresponding correlation could be applied to predict the temperature profile of horizontally oriented jet flame, theoretically. But his model is in the basic of flame bounded wall, and the feasibility for free horizontally oriented jet flame needs affirming.

The temperature profile of horizontally oriented jet fire with square fuel source of different jet velocities is investigated in this paper by using numerical simulator. And the temperature prediction model taking jet velocity into account which is applied for horizontal temperature was proposed.

2   Theoretical Models

The temperature prediction model of vertical flame plume was proposed by Yuan based on a series of experiments and dimension analysis [11]. The predicted model includes two parts which are vertical and horizontal temperatures, respectively. The equations are as follows:

$$\frac{\Delta T_m}{T_0} = C_T \left(\frac{Q_1}{\rho_0 C_P T_0 \sqrt{g}} \right)^{2/3} Z^{-1} \tag{1}$$

$$\frac{\Delta T}{\Delta T_m} = \exp(-\beta y^2 / b^2) \tag{2}$$

Tao's model [10] to predict the temperature profile along flame trajectories is shown in Eq. (3). When the inclined angle equal to zero in Tao's temperature model, which means the jet flame is horizontally oriented jet flame. The corresponding correlation could be applied to predict the temperature profile of horizontally oriented jet flame, theoretically.

$$\Delta T = \left(\frac{\kappa}{0.9\sqrt{2g}} \right)^2 \left(\frac{Z}{Q^{2/5}} \right)^\eta . T_0 \tag{3}$$

$$\kappa_{\text{int}} = 2.47 - 0.21 \cos^2 \theta, \kappa_{plu} = 1.87 - 0.65 \cos^2 \theta \tag{4}$$

where κ and η are the coefficients, κ_{int} is the coefficient for intermittent flame region, κ_{plu} is the coefficient for plume region, and η is equal to 0, −1, and −5/3 for continuous flame region, intermittent flame region, and plume region.

3 CFD Numerical Modeling

The numerical simulations are performed using the fire dynamic simulator (FDS) developed by National Institute of Standards and Technology, USA (NIST). The large eddy simulation (LES) which is built on a good approximation of equations for the low Mach number was carried out to simulate jet fire. The model defines a subgrid turbulent viscosity using the subgrid model of Smagorinsky type in the reference [12], and the Smagorinsky model is adopted to deal with the turbulence. The heat conductivity and mass diffusion coefficients for Smagorinsky model are described in Eqs. (5) and (6). The physical equations of FDS solver include Navier–Stokes equations for flow analysis and other scalar conservation equations including conservation of mass, momentum, energy, species, and so on [12].

$$k_{\text{LES}} = \frac{\mu_{\text{LES}} G_P}{P_r} (\rho D)_{\text{LES}} = \frac{\mu_{\text{LES}}}{Sc} \tag{5}$$

$$\mu_{ijk} = \rho_{ijk} (C_s \Delta)^2 |S| \tag{6}$$

where C_s is Smagorinsky constant (LES); Δ is LES filter width; D is diffusion coefficient; Pr is Prandtl number; Sc is Schmidt number; and μ is dynamic viscosity, N s/m^2.
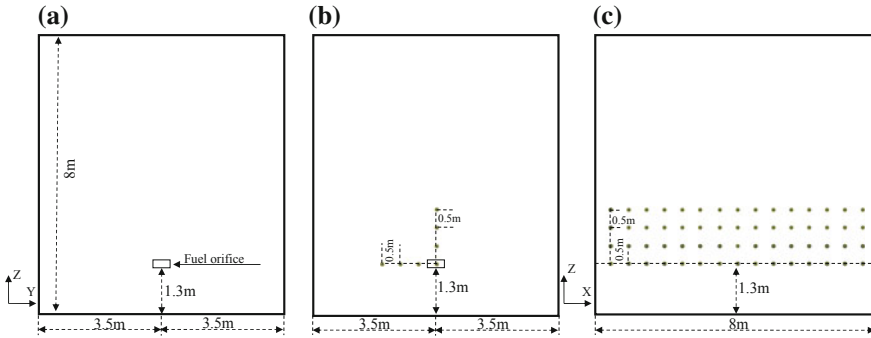
Fig. 1 A schematic of the simulation, **a** fuel source, **b** thermocouples at transverse plane, and **c** thermocouples along jet direction

3.1 Physical Model

The leaked natural gas with high pressure will be jetted out as a jet flow from the split; if the leaked gas is lit at the split, then the jet fire is happened. The fuel orifice was established horizontally to discharge natural gas, and ignition source was below the orifice to supply low ignition energy. When gas jetted out could be ignited. In order to detect jet fire characteristics, the ignition source disappeared after 3 s. The simulation area is 8 m length and high and 7 m width (8 m × 7 m × 8 m). The area of fuel orifice is 400 mm² (20 mm × 20 mm), the distance between orifice and ground is 1.3 m, and the details are shown in Fig. 1a. Those 13 kinds of fuel jet velocity varied from 27.5 to 205.8 m/s were simulated as given in Table 1.

Temperature measurements were made at 105 points in two stations at different distances from the fuel orifice, including horizontal and vertical station. Horizontal station had 60 thermocouples (15 longitudinal, 4 transverse) distributed along the X-axis and Y-axis which were fixed 0.5 m front of the fuel orifice to measure temperatures, and the longitudinal and transverse interval of every thermocouple was 0.5 m. All the thermocouples of horizontal were on the right of fuel orifice. And the vertical station had 45 thermocouples (15 longitudinal, 3 vertical) where interval of every thermocouples was 0.5 m, and all the vertical thermocouples were made along the orifice centerline, as shown in Fig. 1b, c.

3.2 Grid Sensitivity Analyses

The measured result is more accurate with refining grid size, but that would increase mesh quantity and consume more computation time. The grid dimension is always determined by the characteristic fire diameter D*. It is suggested that the ratio of fire characteristic diameter D* to grid size ranges from 4 to 16 for the validation

Table 1 Summary of test cases

Test no	1	2	3	4	5	6	7	8	9	10	11	12	13
Exit velocity(m/s)	27.5	30.5	46.5	74.2	78.2	87.4	101	125	171.2	173.1	188.1	203.4	205.8

study [12]. The multi-grid system was carried out, the cell size near fire source 3-m-diameter domain is 20 mm, and the other domain is 40 mm.

4 Results and Discussion

4.1 Horizontal Temperature

The temperature near the orifice was not too high. There were some distance between the maximum temperature of horizontal centerline and orifice shown in Fig. 2. The maximum temperatures of horizontal centerline were 304.5 and 614.8 °C when the jet velocities were 27.5 and 205.8 m/s, respectively. The horizontal centerline maximum temperature increased with the jet velocity increased, and the distance between orifice and maximum temperature location also increased. The fuel gas cannot entrain much fresh air to combust due to high jet velocity, so the temperature near orifice is lower. The heat of per unit fuel is constant, and the total heat increases with the increasing fuel jet velocity due to the larger fuel mass. Because of this reason, the temperature increases with the increasing jet velocity. The temperature along orifice centerline increases to peak value and then decreases to ambient temperature. The fuel spreads horizontally to entrain the air to supply combustion, the flame gets closer to the completely combustion away from orifice. And at the highest temperature position, the combustion is most close to complete combustion, and then, the temperature decreases due to recessionary combustion with less fuel.
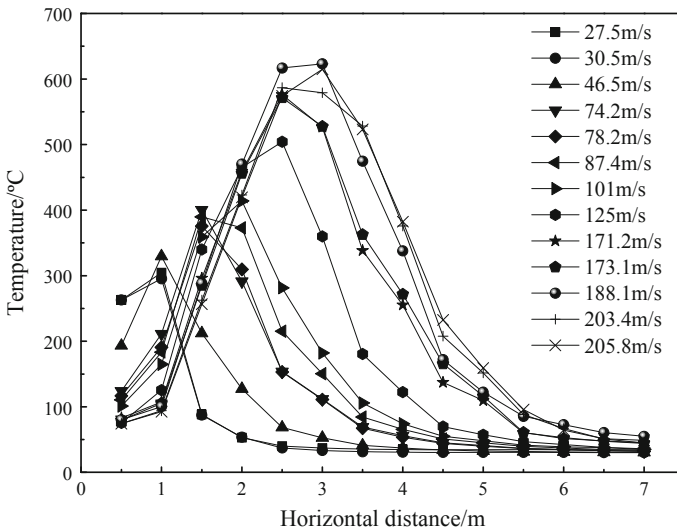
Fig. 2 Horizontal temperature distribution
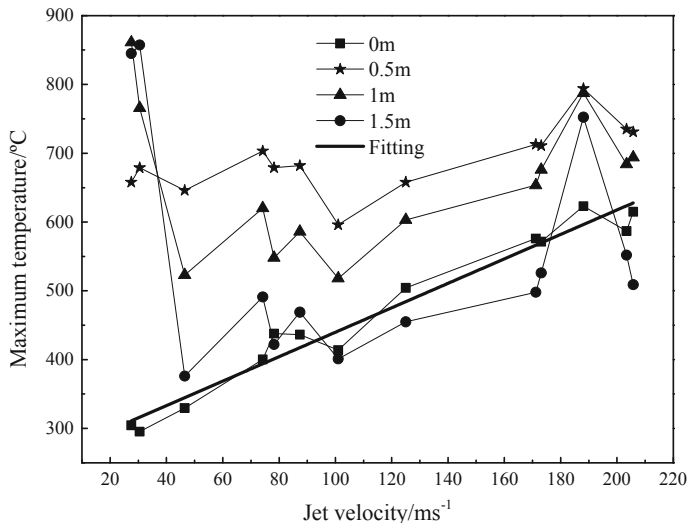
Fig. 3 Horizontal maximum temperature

The horizontal temperature above orifice centerline also detected interval of 0.5 m, and the maximum temperature of every horizontal location is shown in Fig. 3. The temperature over orifice 0.5 m is larger than that at orifice height, and then, temperature decreases along vertical distance. The flame entrains air in vertical direction to supply combustion; thus, the flame exits some width. The position is closer to the flame vertical edge, and the higher temperature is due to full burning. But away from flame edge, the temperature decrease because of the convection heat transfer and radiation with ambient atmosphere. The horizontal maximum temperature at orifice height along the orifice centerline increased linearly with jet velocity, and the linear fitting was conducted. The relationship between horizontal maximum temperature at orifice height along orifice centerline and jet velocity is shown in Eq. (7), where v is fuel jet velocity in m/s.

$$\Delta T_{\max} = 262 + 1.78v \tag{7}$$

The above equation of predicted horizontal maximum temperature is a simple one. The horizontal maximum temperature at orifice height also can be deducted using dimensionless analysis. From Yuan's studies, the maximum temperature at any height can be predicted by defining the height Z. His model can be referenced to propose the maximum temperature formula at orifice height along horizontal direction. The temperature is closed to dimensionless value Φ as shown in Eq. (8), and the formula of Φ is shown in Eq. (9), where Q is total heat release rate (kW) and correlated with jet velocity. The relationship between heat release rate and jet velocity is shown in Fig. 4, and the fitting can be expressed as Eq. (10). The predicted equation of horizontal maximum temperature at orifice height along orifice centerline is shown
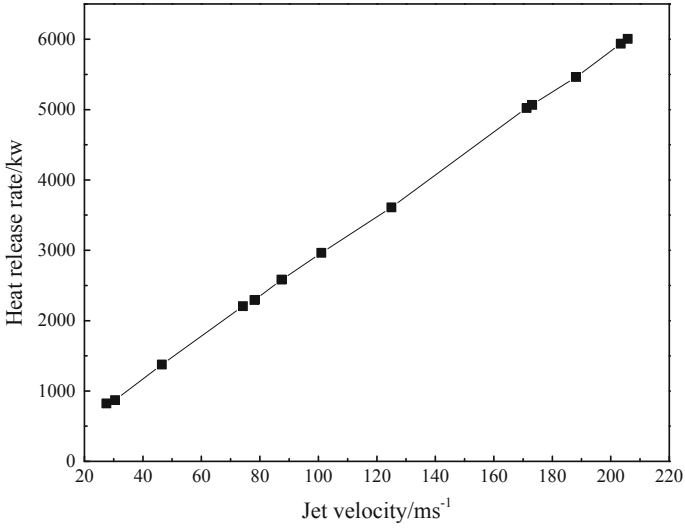
Fig. 4 Correlation of heat release rate and jet velocity

in Eq. (11) after liner fitting. And the comparison of predictions by Eq. (11) with measured values is shown in Fig. 5, they agree well, and the degree of fitting is more than 0.97.

$$\Delta T_m \propto \Phi y \tag{8}$$
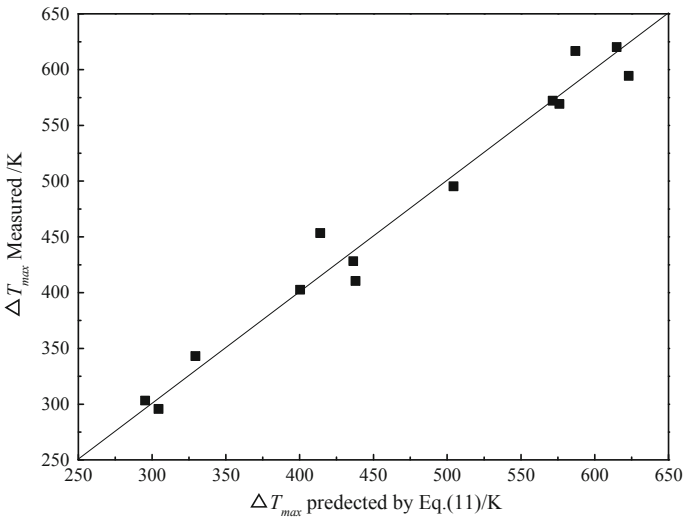
Fig. 5 Horizontal maximum temperature of orifice centerline

$$\Phi = T_0 C_T \left(\frac{Q}{\rho_0 C_P T_0 \sqrt{g}} \right)^{2/\beta} \tag{9}$$

$$Q = 18.61 + 29.1v \cdots \tag{10}$$

$$\Delta T_m = 0.187 T_0 C_T \left(\frac{Q}{\rho_0 C_P T_0 \sqrt{g}} \right)^{2/3} + 179 \tag{11}$$

4.2 Vertical Temperature

The temperature of jet fire reaches the maximum value far from orifice 0.5 m at vertical direction for most jet velocity. And then, the temperature decreases with the vertical distance increase. The vertical temperature has been measured, and the horizontal distance between measured point and orifice is 3.5 m, shown in Fig. 6. The vertical temperature increases firstly, reaching the maximum value, and then decreases with vertical distance increase. The maximum vertical temperature is located at 1 m from orifice when jet velocity is equal and less than 125 m/s, but when jet velocity is more than 125 m/s, the maximum temperature is located at 0.5 m from orifice. The reason for this phenomenon is that when jet velocity is relatively small, the flame spreads less distance at horizontal direction and then spreads vertically. So the flame begins vertical spreading away from orifice 3.5 m. The position of vertical maximum tem-
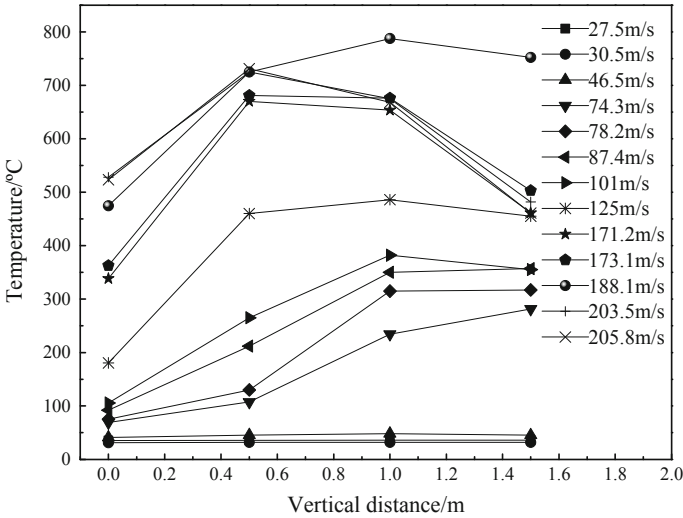
Fig. 6 Temperature vertical distribution at 3.5 m
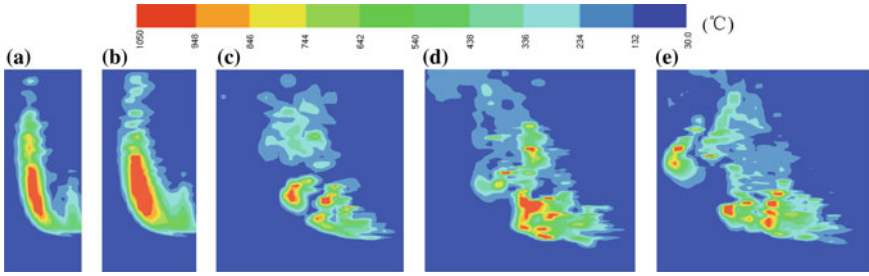
Fig. 7 Temperature vertical distribution at centerline plane with different jet velocity **a** 27.5 m/s, **b** 30.5 m/s, **c** 101.0 m/s, **d** 171.2 m/s, and **e** 205.8 m/s

perature is far from orifice 1 m. But when jet velocity is relatively large, the flame spreads far distance horizontally and then spreads vertically derived by buoyancy and air entrainment. From orifice 3.5 m in horizontal direction, the flame is at the horizontal spread stage when jet velocity is more than 125 m/s, so the flame width in vertical direction is small and the maximum vertical temperature point is far from orifice 0.5 m.

The temperature vertical distribution at centerline plane is shown in Fig. 7. It is can be found that the liftoff distance increases with the increase in fuel jet velocity. The liftoff distance is 0 m when jet velocity is 27.5 m/s, but when jet velocity is 205.8 m/s, the liftoff distance is more than 0.5 m. It is obvious that the temperature profile is stable when jet velocity is relatively small, and when jet velocity is relatively large, the temperature profile is more turbulent which reflects that when jet velocity is relatively small, the jet flame is stable, and when jet velocity is larger, the jet flame is more turbulent. When jet velocity increases, the temperature area over 100 °C along horizontal direction increases that means the hazard area along horizontal direction increases and the flame length increases with jet velocity.

5 Conclusions

The numerical simulations have been carried out to investigate the horizontal jet fires with square fuel source. These have provided data for different fuel jet velocities, and the temperature distribution has been analyzed.

(1) The maximum horizontal temperature along orifice centerline is larger with larger fuel jet velocity, and the distance between maximum temperature point and orifice is farther.

(2) The heat release rate is linear with jet velocity, and the horizontal maximum temperature based on heat release rate can be predicted by Eq. (11) after dimensionless analysis. The horizontal temperature increases and then decreases along horizontal direction.

(3) The vertical temperature increases and then decreases along vertical direction. When fuel jet velocity is relatively small, the flame spreads less distance at horizontal direction and then vertical direction, but when fuel jet velocity is relatively large, the flame spreads farther at horizontal direction.

References

1. API581. (2008). *Risk based inspection technology.* American Petroleum Institute.
2. Gómez-Mares, M., Zárate, L., & Casal, J. (2008). Jet fires and the domino effect. *Fire Safety Journal, 43,* 583–588.
3. Quintiere, J. G., & Grove, B. S. (1998). A unified analysis for fire plumes. *Proceedings of the Combustion Institute, 27,* 2757–2766.
4. Zhang, X. C., Hu, L. H., Zhu, W., & Yang, L. (2014). Axial temperature profile in buoyant plume of square fuel source jet fire in normal and a sub atmospheric pressure. *Fuel, 134,* 455–459.
5. Lowesmith, B. J., & Hankinson, G. (2012). Large scale high pressure jet fires involving natural gas and natural gas hydrogen mixtures. *Process Safety and Environmental Protection, 90,* 108–120.
6. Zhang, X. L., Hu, L. H., Zhang, X. C., Tang, F., Jiang, Y., & Lin, Y. J. (2017). Flame projection distance of horizontally oriented buoyant turbulent rectangular jet fires. *Combustion and Flame, 176,* 370–376.
7. Gopalaswami, N., Liu, Y., Laboureur, D. M., Zhang, B., & Mannan, M. S. (2016). Experimental study on propane jet fire hazards comparison of main geometrical features with empirical models. *Journal of Loss Prevention in the Process Industries, 41,* 365–375.
8. Laboureur, D. M., Gopalaswami, N., Zhang, B., Liu, Y., & Mannan, M. S. (2016). Experimental study on propane jet fire hazards: Assessment of the main geometrical features of horizontal jet flames. *Journal of Loss Prevention in the Process Industries, 41,* 355–364.
9. Johnson, A. D., Brightwell, H. M., & Carsley, A. J. (1994). A model for predicting the thermal radiation hazards from large-scale horizontally released natural gas jet fires. *Transactions of the Institution of Chemical Engineers, 72*(B), 157–166.
10. Tao, C. F., Qian, Y. J., Tang, F., & Wang, Q. (2017). Experimental investigations on temperature profile and air entrainment of buoyancy-controlled jet flame from inclined nozzle bounded the wall. *Applied Thermal Engineering, 111,* 510–515.
11. Yuan, L. M., & Cox, G. (1996). An experimental study of some fire lines. *Fire Safety Journal, 27,* 123–139.
12. McGrattan, K., Hostikka, S., Floyd, J., Baum, H., Rehm, R., Mell, W., & McDermott, R. (2010). *Fire dynamics simulator (version 5): Technical reference guide.* NIST Special Publication.

Fire Dynamics in Informal Settlement "Shacks": Lessons Learnt and Appraisal of Fire Behavior Based on Full-Scale Testing

Richard Walls, Charles Kahanji, Antonio Cicione and Mariska Jansen van Vuuren

Abstract This paper presents discussions regarding informal settlement (also known as slums, shantytowns, favelas, etc.) fire dynamics and lessons learnt from full-scale tests on dwellings, typically referred to as "shacks" in South Africa. Smoldering and flaming fire setups are considered, and both timber and representative household contents are used as fuel sources. It is shown that due to the small size of shacks, flashover can be obtained within minutes. Maximum temperatures recorded are typically around, or in excess of, 1000 °C, depending on the fuel and structural configurations. Due to the poor construction methods used for such structures, they can collapse, or walls can open up, meaning that ventilation conditions continuously change and are difficult to accurately define. The presence of flammable wall finishes or drapes has a significant effect on the rate of fire spread and fire behavior, and such flammable finishes are often present in dwellings. Computational fluid dynamic (CFD) software [Fire Dynamics Simulator (FDS)] is utilized to analyze certain tests, which generally shows good correlation. However, due to significant variations in fuel contents, ventilation conditions, structural configurations, and wall finishes, there is a high degree of uncertainty inherent in developing models for such environments. From the work, a greater understanding of fire dynamics in low income, temporary structures (comparable with some refugee camps) can be obtained through which better solutions and interventions can be developed. Recommendations are provided for how to simulate shack fire scenarios in experimental testing more effectively.

Keywords Informal settlement · Fire engineering · Full-scale test · Shack · South Africa · Slum · Timber structure

R. Walls (✉) · C. Kahanji · A. Cicione · M. J. van Vuuren
Department of Civil Engineering, Stellenbosch University, c/o Banhoek & Joubert Roads, Matieland 7602, South Africa
e-mail: rwalls@sun.ac.za

15

1 Introduction

With the world's population expected to increase to 11.2 billion people by 2100 [1], cities around the world, but especially in the developing/third world, will continue to see large informal settlements growing on their peripheries. Along with the social and economic problems these settlements experience, there are also regular fire disasters [2]. Large fire disasters can cause loss of life, major financial burdens to municipalities, and those living in poverty being drastically affected by losing everything they own. In 2015, in South Africa, 219 fire-related deaths occurred at the scene of a fire in settlements [3], with a significant number of additional deaths occurring in hospital afterward (current this number statistically unquantified but hypothesized to large). In just the Western Cape Province of South Africa, around 1200–1300 informal settlement fires occur every year [4]. Informal settlement dwellings, often referred to as shacks (or shanties, hokkies, etc.), are typically highly combustible as they are built from any readily available material, such as old steel sheets, timber planks, plastic layers, boards of various kinds, and many other materials. In denser settlements, where there is negligible space between dwellings, and limited access paths, fires can propagate rapidly.

As an example of a large informal settlement fire, Fig. 1 presents the area of Imizamo Yethu which experienced a devastating fire in March 2017 where around 2200 structures were destroyed (2000 in the first fire and an additional 200 in another fire shortly thereafter), leaving approximately 10,000 people homeless [5]. The settlement is located on steep terrain adjacent to the wealthy suburb of Hout Bay in Cape Town, South Africa. Once the fire had become fully developed, it became extremely difficult for firefighters to access the fire and put it out. In addition, a lack of adequate water reticulation infrastructure, community interactions, and difficult terrain hampered firefighting activities. It should be understood that with this fire burning for approximately 13.5 h, it meant that on average, approximately 2.5–3.0 homes were consumed per minute throughout the entire period, highlighting the rapid rate of spread. Further details of the incident are provided in [6].

Fig. 1 Imizamo Yethu informal settlement after (left) and during (right) a large fire which left approximately 10,000 people homeless. The dashed red line shows the outline of the area that was burnt down. (Pictures courtesy of: Left—Bruce Sutherland of City of Cape Town, Right—Ryan Heydenrych of Vulcan Wildfire Services)

Due to the frequent occurrence of fires in settlements, product developers in South Africa, and other countries, are regularly proposing new "solutions" to improve fire safety [7]. However, often such interventions lack a solid basis in fire science. Hence, this paper seeks to outline results from various full-scale tests that have been conducted to understand the shack fire dynamics and how such results may influence solutions. The current work has focused on single- and double-shack experiments. However, future work will focus on multi-shack setups, fire spread through entire areas, and large-scale tests.

In traditional performance-based fire design scenarios, engineers and researchers must typically consider what *portion* of a building is on fire [8], whereas for informal settlement fires researchers must rather consider *how many* structures may be on fire. Furthermore, a change in objectives is required in that the goal of informal settlement fire safety engineering is the determination of how to most effectively utilize the minimal resources available, rather than how to effectively apply building codes in a controlled environment, as typically done.

2   Full-Scale Shack Fire Tests

The details below summarize (a) smoldering tests, (b) fire tests with timber and "representative" fuel loads, (c) a double-shack setup, and (d) two shacks with timber frames. Ultimately, the question to be answered through this work is: If a fire was to occur in the dwellings shown in Fig. 2, how would it behave and how can that best be captured in full-scale tests? Furthermore, what fuel configuration and load, ventilation conditions, walling system, and setup size are most suitable? Further community surveys are required to define many parameters, but the testing conducted provides good guidance in terms of developing suitable testing methodologies.

Fig. 2 Multiple shacks adjacent to each other (Left and middle). Note the timber pile, variation in construction types and materials of dwellings, and use of old and new materials, etc. Right-hand photograph shows a picture inside a dwelling where highly flammable materials are placed on walls for insulation, electrical appliances are present, and floors are carpeted or have a linoleum finish (such details vary from dwelling to dwelling)

It should be noted that with the inherent variability surrounding informal settlement dwellings, it is not possible to be highly accurate; however, representative scenarios are required. In the fire engineering fraternity, it is debated whether standard fire tests (ISO 834 [9]) are suitable in the formal construction environment, and there is a drive toward full-scale testing [10] and performance-based design. Such discussions are even more relevant in the informal arena where codes cannot be enforced. Hence, decision-making linked to the suitability of interventions must be pragmatically based on realistic testing scenarios.

2.1 Smoldering Test and CFD Analysis

Smoldering tests using a smoke generator setup based upon [11] were carried out, as reported on in [12]. Additional computational fluid dynamic (CFD) modeling has now been carried out based on the experimental data, and to consider various parameters. Figure 3 presents the smoke generator employed in the work, along with the CFD model developed in PyroSim [13] (based on FDS v.6.5.3), with the figure showing the predicted velocities in the shack.

Rather than considering the magnitude of the velocities (which will change depending on the reaction heat release rate specified), consider the air movement through the dwelling. Variations encountered in the quality of the construction of shack dwellings are large, meaning that boundary and ventilation conditions are not easy to define for a "typical" shack. When walls intersect the roof, there are often open spaces. However, for thermal insulation, and to prevent drafts, residents may close these using newspaper or any deformable materials. For a heat release rate of between 23 and 100 W, and using a polyurethane reaction (as per the original experiment), it was found from FDS analyses that in the $2.4 \times 3.0 \times 2.1$ m high experimental shack utilized that a 30-mm gap around the top leads to smoke only building up in approximately the upper third of the shack. However, if these openings
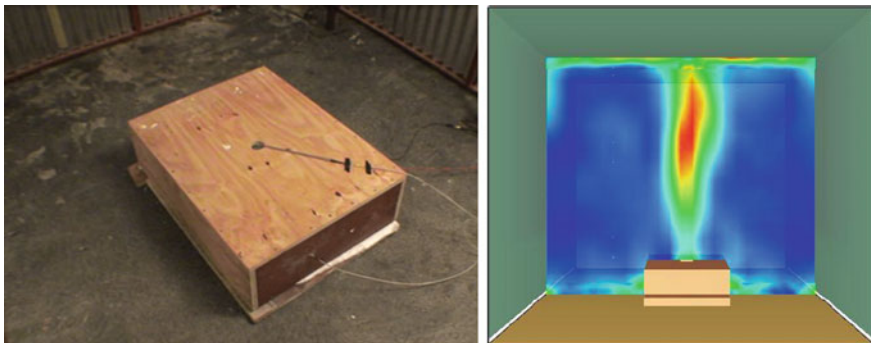
Fig. 3 Smoke generator and CFD model of smoke behavior in the smoldering shack experiment

are closed, the smoke layer rapidly descends and can fill the shack in less than 15 min from the start of the experiment (considering that there is an initial heating phase). Figure 3 also shows the leakages occurring at the bottom of walls. If shack walls are placed onto hard surfaces, there may be openings. For insulation, residents use materials such as soil, plastic sheets, or newspaper to close these bottom openings. Hence, when considering the design of smoke detection systems, multiple ventilation configurations need to be considered as large leakages may be a reality, even when doors and windows are closed.

2.2 Corrugated Steel Shack with Timber and "Representative" Fuel Loads

Full-scale fire experiments were carried out on the same $2.4 \times 3.0 \times 2.1$ m high shack discussed in Sect. 2.1 above, as reported in [12]. The structure had a door measuring 0.75×1.8 m and a window measuring 0.6×0.8 m. In the first test, a timber fuel load of 25 kg/m^2 was utilized, whereas in the second, a "representative" fuel load consisting of a bed, table, clothing, cardboard cladding on walls, and a bottle of paraffin (kerosene) were all placed in the dwelling (all these items are commonly found in informal settlements). For the timber test, $25 \times 25 \times 700$ SA pine sections were used, and the fire was ignited using a gas burner adjacent to the door. For the latter test, the resultant fuel load was calculated to be equivalent to approximately 16.9 kg/m^2 of timber, or 321 MJ/m^2. For this test, the sheet on the bed was ignited by bringing in a traditional "galley bin" burner (25 L paint tin with holes) used to keep inhabitants warm in winter, and the sheet was draped onto it. Roof thermocouples were located 150 mm below the roof level, while the middle zone readings were taken at the mid-height of the side and back walls. Figure 4 presents a picture of the experimental setup, along with images of the shack after the timber fuel load test, and the "representative" fuel load test.

Figure 5 shows the maximum roof and middle zone temperatures recorded in the two tests, along with predicted temperatures from a FDS model and an Ozone

Fig. 4 Experimental shack setup (left), setup after the timber fuel load test (middle), and during the "representative" fire test (right)
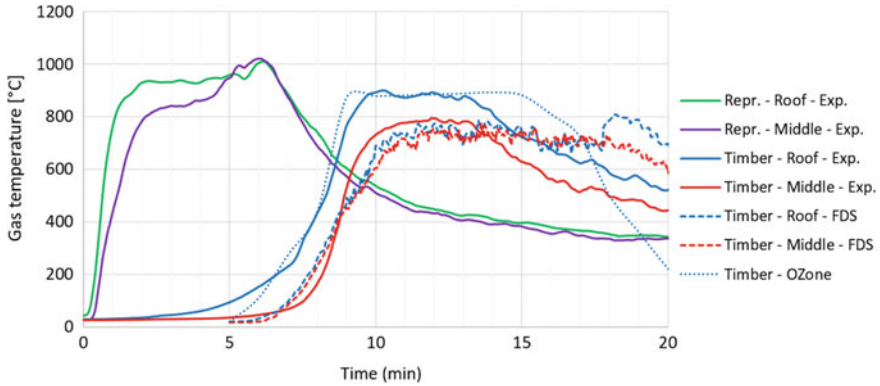
Fig. 5 Time–temperature graphs of the representative shack test (Repr.) and timber fuel load test (Timber) showing experimental (Exp.) and theoretical (FDS or Ozone) temperatures at the roof and middle zones

model [14] (a simple one-/two-zonal model), with input parameters based upon the experimental results (in terms of ventilation and associated factors). For the Ozone model a "fast" fire growth rate was specified. For the development of the FDS model, a timber reaction was specified, and a t^2 fire reaction with a maximum heat release rate of 675 kW/m^2, based on [15]. The window pane and sheeting sections which fell off during the test were modeled using panels that were removed at specific times (which would be extremely difficult to capture in a priori modeling). A sheeting panel of 2.1 × 0.8 m adjacent to the window came loose, with the upper section (20%) of it dislodging at 11min06, while the entire panel fell off at 17min49. The window cracked and fell out at 8min53. A leakage equivalent to an opening 30 mm high was specified at the top and bottom of walls to account for the gaps between walls and side panels, and the profile of the sheeting.

From Fig. 5 an important factor to note is that even though the "representative" test had a lower fuel load (16.9 kg/m^2 equivalent vs. 25 kg/m^2), the rate of fire development was significantly different, and higher temperatures were obtained. Both the presence of the 750 mL paraffin bottle and the cardboard cladding caused flashover to occur much more rapidly, at approximately 1 min after ignition. The total energy released from the timber test was higher, but presents a less severe scenario for fire safety interventions.

Figure 6 presents images from the CFD model used to determine the predicted temperatures in Fig. 5 and also shows the flame behavior and air velocity in the vicinity of the door. With panels falling off the shack, the typical airflow pattern at the door, of cool air entrainment at the bottom and hot gases escaping at the top [16], has been disturbed. From Fig. 5, it is interesting to note that the CFD results show a more homogenous hot layer with top and middle temperatures being approximately the same, whereas the experimental results show a larger difference of up to 273 °C at 8:15 in the timber setup, and 327 °C in the representative test at 1:05. This points toward a hot and cool zone still in existence at these times [17].
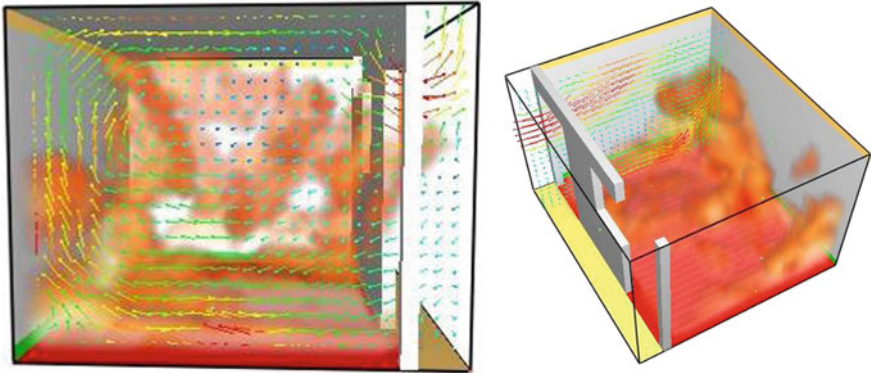
Fig. 6 Fire behavior predicted by FDS during the timber fuel load test showing flames and air velocity

Also, from Fig. 5, it is interesting to the extent to which a simple Ozone model has captured the behavior, although the inclusion of changing ventilation conditions was done based upon experimental results. This shows that traditional fire dynamics principles do capture the hot layer behavior in informal dwellings relatively well.

Additional modeling is required to fully understand the aforementioned behavior, and to consider the representative test. When carrying out CFD modeling, it can be observed that models are sensitive to the ventilation conditions specified, as can easily be observed even when considering temperatures predicted by simple parametric fire curves [18]. However, as discussed above, the poor quality of materials used in shack construction, and the fact that walls and roof panels open during experiments, results in challenges when trying to accurately capture behavior. In Fig. 6, the openings in the wall on the bottom-right-hand picture were modeled as wall sections which disappeared to account for panels of steel sheeting falling off during the test, as also shown in the middle photograph in Fig. 4. Also, corrugated steel sheeting used in dwellings ranges in thickness and quality, so the amount of time that passes before wall distortion occurs will vary. From Fig. 4, the right-hand image shows flames emerging from the gaps between the wall and side sheeting. Even if residents initially had closed up such openings with paper it would rapidly burn away during the course of a fire.

2.3 Double Corrugated Steel Shack Test

An additional test was conducted using two of the steel framed shacks, as utilized in Sects. 2.1 and 2.2 above. The two shacks were only separated from each other by a single 0.5-mm-thick, corrugated, steel sheet. Sheets were pop riveted to the steel frame. In both shacks, a fuel load of 25 kg/m^2 of timber was used. No cladding was placed on walls. The fire was started in the first compartment (on the left of Fig. 7,
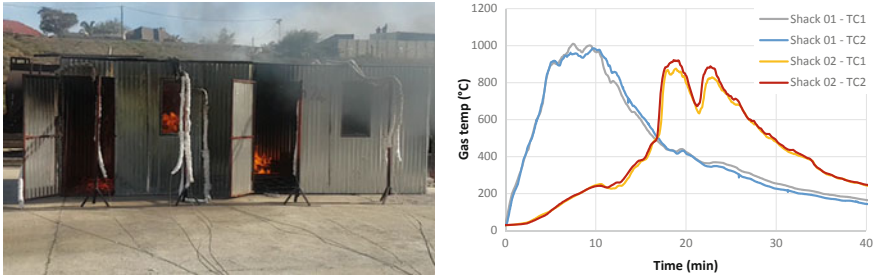
Fig. 7 Full-scale test on two steel framed, corrugated steel clad shacks with 25 kg/m^2 timber fuel load. The right-hand figure provides the roof gas temperatures from two thermocouples (TC) in each shack (Shack 01 being the left-hand side, and 02 being the right-hand side)

called Shack 01). The primary objective of the test was to study the fire spread from the shack or origin to the adjacent dwelling (Shack 02). Flashover in the first shack was attained after approximately 2–4 min. However, the fire only spread to the next shack after approximately 12 min, with flashover occurring at around 17 min. Roof temperatures, measured by thermocouples 150 mm from the roof, are shown in Fig. 7.

The wood cribs burnt relatively slowly, and it took a considerable amount of time for flashover to be attained in both dwellings. Despite being separated only by a thin steel sheeting, the fire was generally expected to spread easily to the next compartment but struggled to do so until the sheeting between the units had warped to a sufficient degree to allow flames to pass through and cause piloted ignition, and this took longer than initially anticipated. Furthermore, with the wood being positioned within the lower 400 mm of the second shack the radiation from the internal steel sheet had only a limited effect and failed to emit a sufficient heat flux to cause spontaneous combustion. Had the walls been lined with more combustible materials the rate of spread would have increased significantly (consistent with firefighter observations in real fires). Furthermore, the use of thinner sheeting, less fixings to the steel frame, or a more combustible fuel source would have increased the rate of spread.

Figure 7 also displays the roof temperatures recorded during the experiment. Roof temperatures in the first dwelling reached a maximum of 1010 °C, whereas the temperatures in the second dwelling reached a maximum of 922 °C. The fluctuation in temperatures at 20–23 min in the second dwelling was caused by the door initially being sucked closed and ventilation being reduced, following by a sheeting panel falling off leading to increased ventilation and an increased heat release rate. It is interesting to note the development of a hot layer in Shack 02 from 0–15 min due to heat transferred through the wall, and any leakages around the sides of the wall. However, it appears that had piloted ignition of the wood samples not occurred spread and flashover would not have resulted, due to the fuel configuration.

In interviews conducted in November 2017 with the Breede Valley Fire Department (i.e., after the tests discussed in Sect. 2.4 below), it was confirmed that newer structures in their area are being constructed with 0.3-mm-thick sheeting (significantly weaker than the 0.5 mm sheeting used in tests to date). Such thinner sheeting

results in openings forming more quickly. In a priori CFD modeling scenarios, it would be almost impossible to model the time at which openings form, and assumptions would need to be based upon tests from similar structural configurations or very approximate estimates.

Consideration of test results

For the shacks tests in Sects. 2.1–2.3, a steel frame was utilized, and it was observed that this influences fire behavior in that full structural collapse is prevented. However, the use of a steel frame is beneficial in that ventilation and geometric conditions can be controlled more accurately, simplifying the validation of numerical models after experiments.

During the experiments, a maximum gas temperature of approximately 1000 °C was recorded and the observed flames reached an approximate height of 3–4 m. In June–July 2016, and throughout 2017, the authors have interviewed firefighters who have shared their firefighting experience in informal settlements. During firefighting operations, the firefighters are not in a position to accurately record the rate at which structures burn. However, based on feedback the observed experimental results from the representative shack test above appear to corroborate better with the firefighters' accounts, vis-à-vis intensity and early attainment of flashover. Hence, in such small dwellings, it has been found that using only timber planks for fuel results a rate of fire spread *within* dwellings significantly less than that which would be encountered when typical shack contents are considered, and the use of only timber is especially insufficient when considering spread *between* dwellings. Based on such findings, it is necessary to augment tests using items such as cardboard cladding on the walls, accelerants, or more flammable fuel sources (e.g., polyurethane). This is discussed further in Sect. 2.4.

2.4 Timber and Corrugated Steel Clad Shacks with Wall Lining and Timber Fuel Load

Based on the tests discussed above, it was identified that to consider behavior such as shack collapse and the influence of flammable wall finishes additional testing was required. The details below present preliminary data from recent tests designed to investigate such phenomena, with a detailed analysis of the data provided in [19, 20]. Two full-scale fire tests, as shown in Fig. 8, were performed on structures with timber frames consisting of 50×50 mm sections. Both shacks measured 3×3 m and were 2.3 m high. One shack had 0.5-mm steel sheeting cladding on all four sides and the roof. The other had timber cladding all four sides, while its roof was still covered by a steel sheeting. The inner walls and the floor of both shacks were lined using corrugated cardboard to increase the rate of flame spread. The fuel source was timber cribs ($40 \times 60 \times 900$ mm) with a fuel load of 45 kg/m^2, and these were stacked uniformly across the floor. The increased fuel load was specified to also investigate the influence of higher fuel loads, and to ensure that a more severe fire was created.

Fig. 8 Full-scale fire experiment on a timber clad shack (left) and corrugated steel (right)

The Breede Valley Fire Brigade has identified that in their region there is a prominent use of "Wendy Houses" for homes, along with the use of wooden walls for shacks, due to the materials available locally. Hence, the wooden shack was included both to investigate the influence of the walling system and to better understand what may happen in small timber shacks when they burn.

For the wooden shack test, a 900-mL tin can with 750 mL of paraffin was placed below the crib nearest to the door, and two timber pieces of 125 mm above the can were dipped in paraffin, to prevent the very slow initial growth observed in the steel shack test. 8.2 min after the paraffin source was ignited the flames spread and had grown high enough to just reach the roof. At this point the cardboard on the side walls caught fire and flashover ensued approximately 10 s later. This is consistent with the steel shack test in that approximately 10 s after the cardboard lining in the steel shack ignited flashover occurred.

The maximum gas temperature recorded in the timber shack was 1102 °C, while in the corrugated steel shack the maximum temperature reached was 1083 °C. The timber framing that supported both shacks burnt through leading to the total collapse of the shacks. The timber cladding, which consisted of thin strips of wood, provided additional fuel that enhanced the flammability and heat release rate, due to the large exposed area of combustible material. In the timber clad shack, numerous openings formed in the wall as the structure burnt away, especially between timber strips. This continuously altered the ventilation conditions. The corrugated sheets of the steel clad shack also distorted leading to openings forming between walls and the roof, and between sheeting panels.

There is an interesting contrast in behavior between the two shacks when considering fire behavior. The timber shack had a much larger exposed area of timber releasing energy; hence, overall there was a higher heat release rate for the second test. However, the ventilation also rapidly increased as the walls burnt through. Thus, in this specific scenario, it appears the increase in heat release rate was approximately offset by an increase in ventilation when it is considered that maximum temperatures between the structures were approximately equal.

In these tests, the cribs were augmented using $40 \times 60 \times 900$ pieces of polystyrene, with 4 pieces per crib. This was done based on personal advice received from other

researchers who had conducted full-scale experiments. However, it was generally observed the polystyrene melted and only had a negligible effect on the behavior, so its inclusion in future tests is not recommended. Before the test commenced, it was debated whether the cardboard should be lighted directly, but this was not done due to concerns of flashover occurring too rapidly and useful information regarding fire development not being obtained.

Further analyses and CFD analyses of these tests will be forthcoming in the near future. However, from the tests, it was observed that based on the flame heights of 3–5 m emitted from dwellings, and the fact that flashover rapidly ensued once the side cladding was alight, spread between such dwellings would readily occur. Hence, even though the initial mechanism to start the fire needs refinement, the setup appears more in terms of replicating real shack behavior. The fuel load to be used needs further research as average fuel load values for informal dwellings have not been defined in the literature. It is acknowledged that it is likely that 45 kg/m^2 of timber will represent a conservative fuel load.

3   Conclusions

From the details of the full-scale experimental shack fire tests discussed in this paper, researchers can obtain a greater appreciation for shack fire dynamics, and how to develop experimental setups that more accurately represent the behavior of real informal settlement dwellings. However, it is acknowledged that setups still need further refinement, and based on the high level of uncertainty inherent in informal settlements results will only serve as approximate indications of real-world behavior. Nevertheless, these tests represent a significant advance relative to existing knowledge. Temperature data obtained can be used for understanding temperatures that any proposed intervention may be exposed to, along with allowing the calibration of numerical analyses. Specific aspects to consider in relation to shack fire dynamics and testing are:

- Because of their smaller size and the presence of highly flammable materials, shack dwellings may experience flashover in as little as 1 min, depending on the contents and the method of ignition. There will always be a scatter in results, and the time from ignition to flashover will vary considerably depending on how the shack is ignited.
- When only timber cribs are used, the fuel source did not provide the expected rate of spread and fire intensity that is usually associated with real shack fires.
- Lining the inner walls with corrugated cardboard improved the combustibility and rate of fire spread in shack dwellings, and it is proposed that this more closely provides a realistic behavior, although further testing is required.
- There was an observable difference in the burning behavior between the timber clad and the steel clad shacks and understandably so. However, an increased heat release rate was partially offset by a much increased ventilation rate resulting in maximum

temperatures between the steel and timber clad shack being approximately the same. However, the rate of spread between dwellings and measured heat fluxes adjacent to structures are typically higher when combustible walling systems are used.

It is shown that CFD models can be used for modeling the behavior of informal settlement structures. A good understanding of fire behavior and spread can be obtained using such tools. However, with the high level of uncertainty inherent in settlements they only provide a good indication of what may happen for specific configurations, understanding that in real scenarios there will be an extensive scatter in results obtained—in excess of that even observed in traditional structures. The inclusion of steel frames makes tests more easily reproducible in modeling software, but prevents structural collapse, which does occur.

Future work will focus on large-scale testing to understand fire spread between multiple dwellings. Surveys will be conducted to more accurately define parameters such as ventilation conditions, fuel loads, structural configurations, and building materials.

References

1. Melorose, J. Perroy, R., & Careas, S. (2015*). World population prospects: The 2015 revision, key findings and advance tables*. Working Paper No. ESA/P/WP.241. United Nations, Department of Economic and Social Affairs Population Division (Vol. 1, pp. 1–59).
2. Walls, R. S., & Zweig, P. (2017). Towards sustainable slums: Understanding fire engineering in informal settlements. In *Advanced Technologies for Sustainable Systems* (pp. 93–98).
3. FPASA. (2017). *Fire Stats 2015. Fire Protection*, June (pp. 23–36).
4. DMFRS. (2015). Western Cape strategic framework for fire and burn injury prevention. *Western Cape Disaster Management and Fire Rescue Services*.
5. Pluke, M. (2017). Case study—Imizamo Yethu fire disaster 11 March 2017. In *Western Cape Disaster Management Risk Symposium*, March, 2017.
6. Kahanji, C., Walls, R. S., & Cicione, A. (2019). Fire spread analysis for the 2017 Imizamo Yethu informal settlement conflagration in South Africa. *International Journal of Disaster Risk Reduction*, 101146.
7. Mike, H. (2012). *Right of response: Cape town spends hundreds of millions of rand on informal settlement sanitation*.
8. Hurley, M. J., & Rosenbaum, E. (2017). *Performance-based fire safety design*. Boca Raton: CRC Press.
9. ISO. (1999). *ISO 834 Fire-resistance tests—Elements of building construction. Parts 1–12*. Geneva: International Organization for Standardization.

10. Bisby, L., Gales, J., & Maluk, C. (2013). A contemporary review of large-scale non-standard structural fire testing. *Fire Science Review, 2*(1), 1–27.
11. Sesseng, C., & Reitan, K. N. (2016). Experimental investigation of using CO sensors to detect smouldering fires in dwellings. In *Suppression, Detection and Signaling Research and Applications Symposium*.
12. Walls, R., Olivier, G., & Eksteen, R. (2017). Informal settlement fires in South Africa: Fire engineering overview and full-scale tests on 'shacks'. *Fire Safety Journal, 91,* 997–1006.
13. Thunderhead Engineering. (2017). *PyroSim*. Manhattan, KS.
14. Cadorin, J.-F., & Franssen, J.-M. (2003). A tool to design steel elements submitted to compartment fires—OZone V2. Part 1: Pre- and post-flashover compartment fire model. *Fire Safety Journal, 38,* 395–427.
15. Rinne, T., Hietaniemi, J., & Hostikka, S. (2007). *Experimental validation of the FDS simulations of smoke and toxic gas concentrations*.
16. Drysdale, D. D. (2011). *An introduction to fire dynamics* (3rd ed.). Chichester: Wiley.
17. Quintiere, J. (2016). *Principles of fire behavior*. Boca Raton: CRC Press.
18. BSI. (2002). *BS EN 1991-1-2: Eurocode 1—Actions on structures part 1—basis of design*. London: British Standards Institute.
19. Cicione, A., Walls, R. S., & Kahanji, C. (2019). Experimental study of fire spread between multiple full scale informal settlement dwellings. *Fire Safety Journal*, *105*, 19–27.
20. Cicione, A., Beshir, M., Walls, R. S., & Rush, D. Full-scale informal settlement dwelling fire experiments and development of numerical models. *Fire Technology*.

Investigation of the Effect of DMMP Addition on the Methane–Air Premixed Flame Thickness

Wei Li, Yong Jiang and Rujia Fan

Abstract Flame thickness is an important parameter in both laminar and turbulent flame studies. To provide some basic understanding of the effect of the fire inhibitor on the laminar flame thickness, numerical calculations of methane–air premixed flames doped by dimethyl methyl phosphonate (DMMP) were conducted. The results show that the flame speed depends highly on the reactions: $HOPO_2 + H_2 = PO_2 + H_2O$; $PO_2 + H + M = HOPO + M$; $HOPO + OH = PO_2 + H2O$; and $HOPO + OH = PO_2 + H_2O$ The laminar flame thickness increases with the increase of the DMMP addition. The preheat sub-zone in the flame front is more vulnerable to the inhibition effect of DMMP. Based on the opposed-flow flame calculations with different outlet velocities, the results indicate that the preheat sub-zone is more dependent on the local stretch rate than the reaction sub-zone. To figure out the reason why the flames become thicker after DMMP addition, the flames' chemical structures are extracted and discussed. It is found that the chemical reactions in the flame zone are retarded and the upstream gas flow velocity is artificially reduced to make the flame surface stay in a certain area in the calculation. Accordingly, the residence time of the reactant mixture increases, and the CH_2O and OH diffuse and distribute in a wide area. Therefore, the radical-based flame thickness increases with DMMP addition.

Keywords Fire inhibitor · Flame thickness · Flame structure · DMMP

1 Introduction

The utility of Halon 1301 (CF_3Br), which used to be an efficient fire inhibitor, has been banned by the Montreal Protocol due to its high depletion of ozone in the stratosphere [1]. To meet the needs of aircraft fire protection, tremendous efforts have been made to explore the replacements [2–4]. So far, the halogen-containing compounds are used as the replacements temporarily. However, the burning products of these halogen-containing compounds are recognized to be potential ozone-depleting substances

W. Li · Y. Jiang (✉) · R. Fan
State Key Laboratory of Fire Science, University of Science and Technology of China, Hefei 230000, China
e-mail: yjjiang@ustc.edu.cn

[5, 6]. Besides, the burning products of these compounds contain some strongly acidic substances (HF, HCl, and HBr), and these substances are harmful to the human beings and the apparatus which are exposed to the fire smoke. Therefore, a kind of organic fire inhibitor, phosphorus-containing compounds (PCCs), arouses growing interests. PCCs have been widely used as the fire retardants in polymers, where they can act in either condensed phase or gas phase during the fire process [7, 8]. Meanwhile, PCCs are also considered as a kind of efficient fire inhibitor [9–12]. The present work focuses on the inhibition effect on the flame thickness of PCCs in the gas phase.

When talking about the methods to evaluate the effectiveness of fire inhibitors, the usual practices are to measure the laminar flame speed [9, 10, 13] and minimal extinguishing concentration (MEC) [11, 12]. Although they can characterize the global effectiveness of the inhibitors, these methods are limited in the laminar regime, and the fires in actual fire scenes are in the turbulent regime. It is interesting to investigate the efficiency of fire inhibitors in a turbulent fire. When studying the turbulent combustions through numerical simulations, the first thing to know is which regime the studied fire falls into in the turbulent premixed combustion regime diagram proposed by Borghi [14] and Peters [15]. Only if the combustion regime is properly derived, a correct choice of the turbulent combustion model can be made. To do this judgment, the laminar flame reaction sub-zone thickness (σ_{RZ}) and the preheat sub-zone thickness (σ_{PH}) need to be known. These two parameters are important for choosing the calculation models in turbulent combustion simulation. Besides, the flame thickness has a relationship with the quenching distance. Considering the importance of the flame thickness, the main purpose of this paper is to investigate the effect of dimethyl methyl phosphonate (DMMP, a typical kind of the PCCs) addition on the methane–air premixed flame thickness.

There are several definitions of the flame thickness. Zeldovich [16] proposed the first definition of the flame thickness which was known as "characteristic flame thickness" $\sigma = \lambda/(c_p \rho_u u_L)$ where λ is the thermal conductivity, c_p is the specific heat at constant pressure, ρ_u is the density of the unburned mixture, and u_L is the laminar flame speed. Based on the temperature curve through the flame, Spalding [17] defined the thermal flame thickness as the ratio of the maximum temperature difference and the maximum temperature gradient. Both the "characteristic flame thickness" and the "thermal flame thickness" recognized the flame zone as a homogeneous zone, without identifying the preheat sub-zone and the reaction sub-zone. Both of these two definitions fail to distinguish the reaction sub-zone and the preheat sub-zone in the flame front. Recent studies [18, 19] defined the flame thickness based on the radical distributions. According to radical-based definition, the reaction sub-zone thickness is defined to be the width of the CH_2O–OH overlap layer at 50% of its maximum value (FWHM), and the preheat sub-zone thickness is defined as the width of the CH_2O signal from its 30% point on the reactant side to the leading edge of the reaction sub-zone. This definition of the flame thickness meets the needs of dividing the flame zone into two sub-zones, and the structure of the flame zone can be measured experimentally; thus, this definition of the flame thickness is chosen in the present study. A schematic diagram of both of the thermal flame thickness (σ_{Temp}) and the

Fig. 1 Schematic diagram of an unstretched laminar flame structure (σ_{Temp}: thermal flame thickness, σ_{PH}: preheat sub-zone thickness, σ_{RZ}: reaction sub-zone thickness)
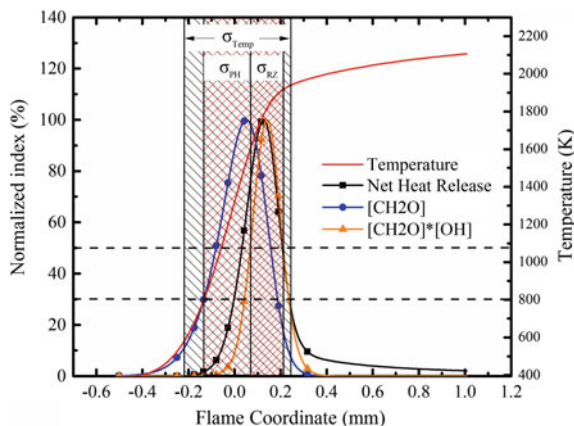
radical-based flame thickness ($\sigma_{PH} + \sigma_{RZ}$) of a typical premixed flame, calculated by CHEMKIN-PRO, is provided in Fig. 1. The thermal flame thickness centered at the maximum temperature gradient point. The thermal flame thickness is wider than the main heat release zone. The radical-based flame thickness gives a good reference of the preheat sub-zone thickness and the reaction sub-zone thickness, because the reaction sub-zone envelops the main heat release region and the preheat sub-zone envelops the temperature from 800 to 1600 K.

2 Numerical Approach

The freely propagating flame reactor and the opposed-flow flame reactor embedded in the CHEMKIN-PRO package were utilized to calculate the laminar flame speed (S_L) and the flame thickness. The calculation domain was set to 10 cm long, and both the GRAD and CURV grid parameters were set to 0.05. In the opposed-flow flame calculation, the distance between the two nozzle outlets was 2 cm and the GRAD and CURV grid parameters were also set to 0.05. Both of the calculation domains contain more than 420 grids and further refining the grids leads to less than 4% discrepancy in flame speeds. For the sake of more accurately capturing the distribution of small radicals in the flames, Soret effect (thermal diffusion) was included in the simulations.

In the present study, the comprehensive chemical kinetic mechanism for the reactions of DMMP in hydrocarbon flames was proposed by Jayaweera et al. [10]. To validate the simulations in the present work, the calculated flame speeds of methane–air mixtures over a range of equivalence ratios without DMMP addition are compared to measured data in the literature [20, 21]. As shown in Fig. 2, a good agreement between the computational and experimental results is found, which indicates that the simulations in this work provide reasonable predictions about the burning process.

Fig. 2 Unstretched laminar flame speeds for CH_4–air premixed flames over a range of equivalence ratios without DMMP addition (initial temperature of 373 K, and initial pressure of 1 atm)
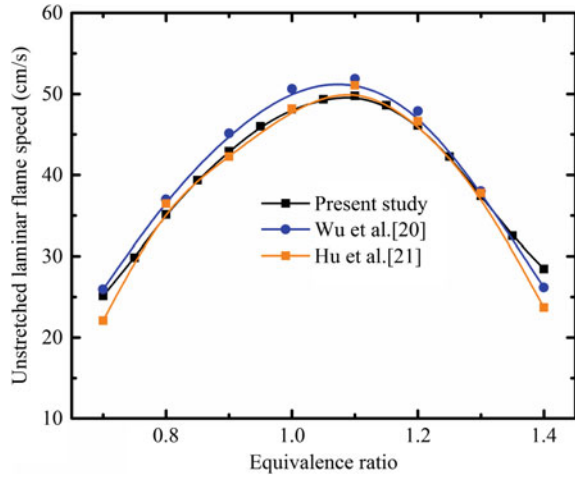
Table 1 Summary of the calculation conditions

Calculation	Reactor	Equivalence ratio	DMMP concentration (ppm)
Flame speed and thickness	Freely propagating flame reactor	0.8	0–3000
Flame speed and thickness		1.0	0–3000
Flame speed and thickness		1.2	0–3000
Flame thickness	Opposed-flame reactor	1.0	0–1500

The calculation conditions studied are summarized in Table 1. All of the calculations were run at an initial temperature of 373 K and pressure of 1 atm. The choice of these initial conditions is based on experimental concerning. During the PLIF experiments (not shown here), the DMMP was gasified at 373 K with a high saturated vapor pressure (6.34 kPa) [22].

3   Results and Discussion

3.1   Laminar Flame Speed and Temperature

Unstretched laminar flame speed is an inherent property of the combustible premixed gas mixture. High flame speed means high burning intensity and high fuel consumption rate. In other words, the heat release rate is much high and the flame is more thriving and more difficult to be put out. Therefore, the flame speeds of methane–air

mixtures with DMMP addition are discussed first. As shown in Fig. 3a, the flame speeds of all the three mixtures at different equivalence ratios decrease with the addition of DMMP. Moreover, the degree of declining for rich flames is higher than that for lean flames. On the contrary, the flame temperature of the lean mixture increases with the addition of DMMP, while the temperature of the rich mixture decreases with the addition of DMMP. For the stoichiometric mixture, the temperature keeps almost the same with the increase of DMMP addition (0.18% temperature rise at 0.09% DMMP addition). Although the temperature of the lean mixtures rises with the DMMP addition, the laminar flame speed decreases monotonically. According to the study of Babushok et al. [23], the temperature rise is aroused by the fuel effect of the hydrocarbon moiety in the DMMP molecule. As a supplement to the previous work, the present work explores the fuel effect from a new perspective. The fuel effect is more intuitive by calculating the integral heat release over the calculation domain for each elementary reaction in the mechanism. Figure 3b shows the top 20 heat release reactions for the undoped and 3000 ppm doped flames at an equivalence ratio of 0.8. The heat release for each reaction is normalized by the total heat release of the burning process. The orders are arranged by the absolute value of heat release rate. These two top 20 sets of reactions account for 80.97 and 76.90% of the total heat release for the undoped and 3000 ppm doped flame, respectively. The numbering of the elementary reactions can be found in Appendix 1. In the pure flame, R8, R24, and R108 are the top three heat source with an order of R108 > R8 > R24. While in the doped flame, the R8 ($H_2O + M = H + OH + M$) is out of the top 20 reactions, and R24, R108, and R493 become the top three heat source with an order of R108 > R493 > R24. The R493 ($PO_2 + H + M = HOPO + M$) and R506 ($PO_2 + O + M = PO_3 + M$) account for 16 and 9.7% of the total heat release, respectively. Therefore, the temperature rise of the lean flames with DMMP addition can be attributed to the heat release of the reactions concerning phosphorus oxides.
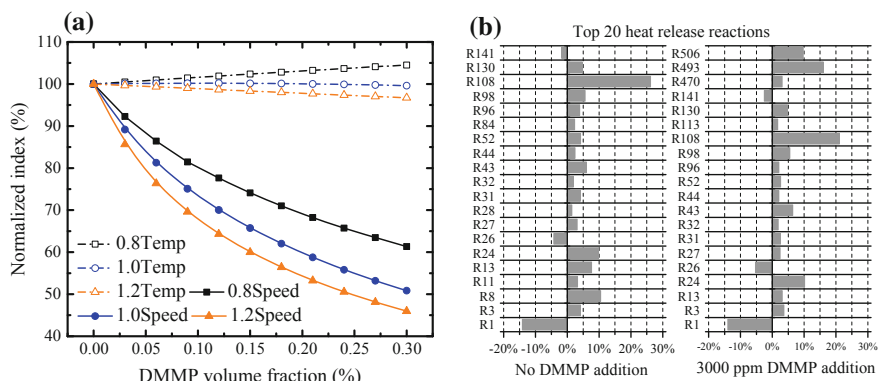
Fig. 3 Illustration of **a** flame temperature and unstretched laminar flame speeds for CH_4–air flames with DMMP addition at equivalence ratios of 0.8, 1.0, and 1.2 and, **b** the top 20 heat release reactions in the flames at an equivalence ratio of 0.8

3.2 Sensitivity Analysis of Laminar Flame Speed

It is confirmed that the flame thickness increases with the decrease of the laminar flame speed [15], and the laminar flame speed is always used as an indicator of the reaction rate. Therefore, it is valuable to perform sensitivity analysis for the flame speed to illustrate the effect of phosphorus-containing elementary reactions on the reaction rate. The sensitivity coefficients of the major influential reactions are calculated by the ratio of the amount of change in speed and that in the pre-exponential factor of the Arrhenius rate expression [24]. The incensement of the pre-exponential factor is set to 10% [25]. Figure 4 shows the sensitivity coefficients of the flame speed for flames with 3000 ppm DMMP addition at different equivalence ratio ($\varphi = 0.8$, 1.0, and 1.2). The coefficients of reaction 1, reduced by five times, are used as a reference. Obviously, reaction 1 is less effective in the rich flame than in the lean and stoichiometric flames, as the coefficient decreases about a half. The flame speed shows a high dependency on $HOPO_2 + H = PO_2 + H_2O$ (R476), $PO_2 + H + M = HOPO + M$ (R493), $HOPO + OH = PO_2 + H_2O$ (R497), and $HOPO + OH = PO_2 + H_2O$ (R506). Especially, R476, R493, and R506 have higher coefficients in lean flames than in the rich flames, which is opposite of R497 with higher coefficient in the rich flame. It is unexpected that increasing the reaction rate of an exothermic reaction (R493 as shown in Fig. 3b) decreases the flame speed (a negative sensitivity coefficient). R486 shows a significantly different effect on the flame speed of the lean-stoichiometric and the rich flame. This is because in the rich flames, oxygen is in shortage for full combustion, and the reaction rate is dominated by the concentration of oxygen free radical in the flame. Increasing the reaction rate of R486 will decrease the concentration of oxygen free radical; thus, it will reduce the flame speed of the rich flame.

Fig. 4 Sensitivity coefficients of the laminar burning velocity for flames with 3000 ppm DMMP addition at three different equivalence ratios ($\varphi = 0.8$, 1.0, and 1.2)
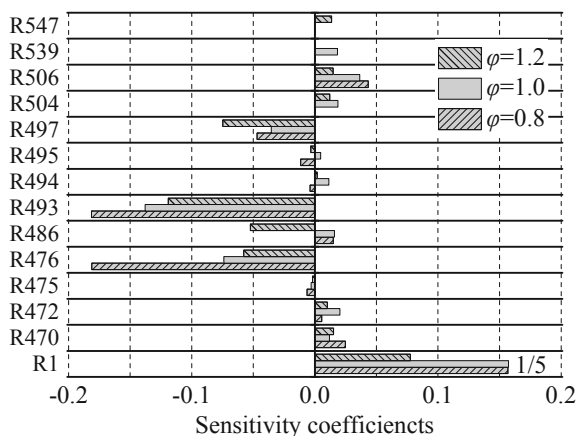
3.3 Unstretched Flame Thickness Discussion

Figure 5 shows the unstretched flame thickness for methane–air premixed flames at different equivalence ratios ($\varphi = 0.8, 1.0, 1.2$) and the preheat/reaction sub-zone thickness of the stoichiometric flames. As indicated in Fig. 5a, the flame thickness of the rich flames is larger than that of the stoichiometric and lean flames after the addition of DMMP. The flame thickness of the stoichiometric flames is the thinnest. The flame thickness increases with the addition of DMMP for all the mixtures at three equivalence ratios. The difference is that the effect of DMMP on the lean flame thickness is smaller than that on the others as the rising rate of the flame thickness for the lean flame is smaller than that of the other two flames. This may be attributed to the temperature rising with the addition of DMMP into the lean flames. Since the temperature rises, the burning rate is strengthened. As shown in Fig. 5b, with the addition of DMMP from 0 to 3000 ppm, the preheat sub-zone thickness increases from 0.2 to 0.45 mm and the reaction sub-zone thickness increases from 0.14 to 0.25 mm, increasing by 2.25 times and 1.78 times, respectively. The preheat sub-zone is more vulnerable to the inhibition effect of DMMP. As mentioned in [26], the inhibition effect of DMMP on the laminar flame speed is mainly attributed to the reduction of the OH concentration. However, the OH radical in preheat sub-zone is much lower than that in the reaction sub-zone. The reaction sub-zone should be more vulnerable to the inhibition effect of DMMP than the preheat sub-zone logically. As the DMMP is introduced to the flame, the peak concentration of active radicals becomes low. The gradient of the temperature decreases, leading to the chemical reactions taking place in a relatively wider region. The curve of the concentration of CH_2O becomes flatter. Therefore, according to the definition of the flame thickness, the preheat sub-zone is more vulnerable to the inhibition effect of DMMP.

Fig. 5 Flame thickness as a function of DMMP volume fraction: a total flame thickness (σ_T) of flames at different equivalence ratios, b the preheat sub-zone thickness (σ_{PH}), and the reaction sub-zone thickness (σ_{RZ}) at an equivalence ratio of 1.0
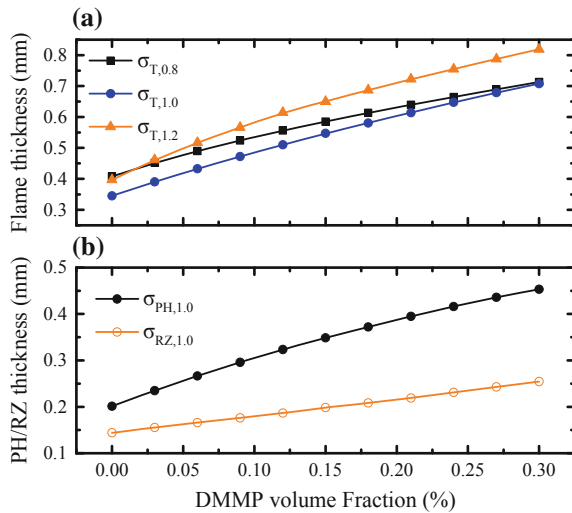
3.4 Stretched Flame Thickness Discussion

The local stretch rate (K_l) of the opposed-flow flame was defined as the maximum axial velocity gradient before the minimum velocity point. In the opposed-flow flame, the reference flame speed is depended on the K_l, and the unstretched laminar flame speeds are deduced by non-linear extrapolations based on the reference flame speeds and the stretch rate [2]. It is unknown whether the flame thickness has the same dependency on the local stretch rate. Figure 6 shows the dependency of the flame thickness on the stretch rate. The solid symbols represent the flames with no DMMP addition, while the open symbols represent the flames with 1500 ppm DMMP addition. As shown in Fig. 6, both the preheat sub-zone and the reaction sub-zone of the undoped flames keep almost unchanged but rise a little with the stretch rate. However, the DMMP doped flames show a little different trend. The reaction sub-zone thickness of the doped flames still keep almost unchanged but rise a little with the stretch rate, but the preheat sub-zone thickness decreases a little with the increase of the stretch rate, leading to thinning flame structure. According to the definition of the local stretch rate in the opposed-flow flames, the stretched effect is caused by the flow velocity gradient. If there is no flame in the opposed-flow configuration, the velocity in the center line decreases monotonically to zero. But if there exists a flame in the configuration, the velocity firstly decreases to a minimum value and then increases to a maximum value because of the expansion caused by the heat release of the flame, and finally, it decreases to zero due to the opposed gas flow configuration. The gas flow velocity in the flame reaction sub-zone is much higher than the minimum value. Because of the existence of the minimum point of velocity before the flame zone, the gas flow velocity in the reaction sub-zone (the main heat release zone) is weakly affected by the initial velocity of the gas flow; thus, the reaction sub-zone thickness (σ_{RZ}) is weakly affected by the local stretch rate. But for the preheat sub-zone, the

Fig. 6 Flame thickness as a function of the stretch rate for stoichiometric flames with/without DMMP addition
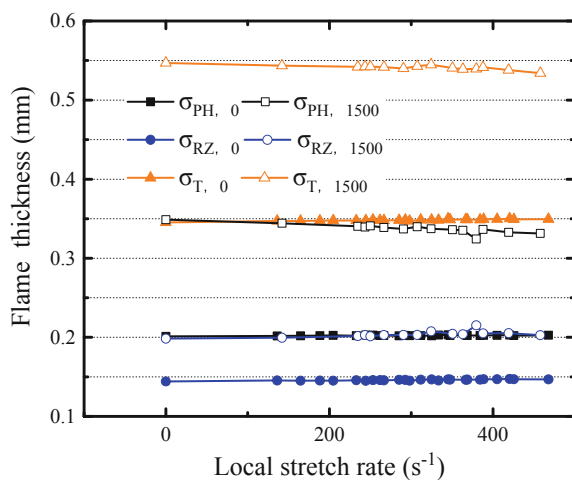
expansion ratio is relatively small and the main cause of the expansion is the heat transferred from the reaction sub-zone, therefore, the gas flow velocity at the leading edge of the preheat sub-zone is more vulnerable to the stretch effect than the reaction sub-zone.

3.5 Flame Chemical Kinetic Structures

Since the flame thickness discussed in the present work is based on the OH and CH_2O radical concentration, Fig. 7 depicts the generating rate and the concentration of CH_2O and OH along the axis for two 1-D freely propagated flames at an equivalence ratio of 1.0. The solid and open symbols represent the flames doped with 0 and 3000 ppm DMMP, respectively. As shown in Fig. 7a, the peak generating rate of CH_2O is reduced to two-fifths of the original by the addition of 3000 ppm DMMP. But the concentration of CH_2O gets some increase rather than decrease. This unexpected growth of the concentration of CH_2O is attributed to the increase of hydrocarbon content after 3000 ppm DMMP addition because each molecular of DMMP contains three methyl groups. In addition, the relatively moderate consumption rate of CH_2O with DMMP addition is also considered to cause the increase of CH_2O concentration. The reduced peak generating and consuming rate of CH_2O indicate that the reactions are retarded, and it needs more time to decompose the fuel. To make the flame surface stay at a certain point in the calculation, the fuel feed rate should be reduced. Since the equivalence ratio is unchanged, the initial gas velocity, which is equal to the laminar burning velocity in the CHEMKIN-PRO calculation, is reduced artificially after DMMP addition. As the feeding velocity is reduced, the residence time, which is defined as the time a mass point needs to pass a certain distance in the flame, increases. Moreover, the mass diffusion of CH_2O in the negative direction is strengthened due to the increase in peak CH_2O concentration. The net effect of the two factor makes the CH_2O distribute in a wide area. Because the preheat sub-zone thickness
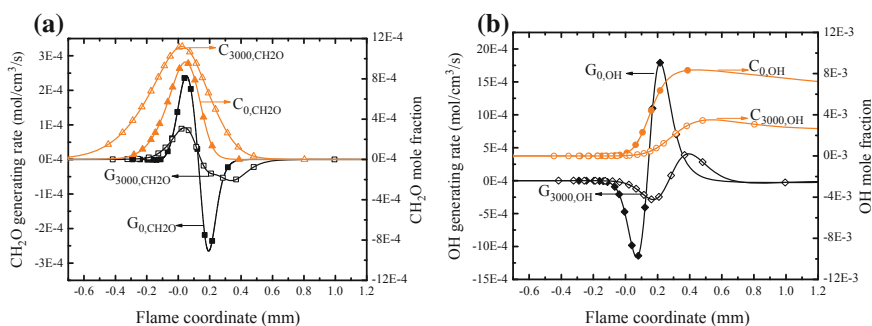
Fig. 7 Active **a** CH_2O, **b** OH radical generating rate and concentration along the axis for flames at an equivalence ratio of 1.0 (G_x: generating rate; C_x: mole fraction)

is defined based on the CH_2O distribution, the preheat sub-zone thickness increases with DMMP addition.

In Fig. 7b, the peak concentration and the peak generating rate of OH show a consistent trend, and both of these two peak values decrease after DMMP addition. The peak generating rate of OH is reduced to one-fifth of the original by the addition of 3000 ppm DMMP. Like the condition of the preheat sub-zone, the same explanation can be applied to the reaction sub-zone. The chemical reactions in reaction sub-zone are retarded and the gas flow velocity in this zone needs to be reduced to make this zone stay in a certain area. Then, the residence time increases, leading to the distribution of OH in a wide area. Therefore, the thickness of the reaction sub-zone increases with DMMP addition.

4   Conclusions

In order to provide some basic understanding of the effect of DMMP on the laminar flame thickness, numerical calculations were conducted based on the CHEMKIN-PRO package. By comparing the computational laminar flame speeds of methane–air flames with the experimental results in the literature, the simulation results provide a reasonable prediction about the burning process. The flame speed shows a high dependency on R476, R493, R497, and R506. The flame thickness increases with the increasing of DMMP addition for flames at equivalence ratios of 0.8, 1.0, and 1.2. The fuel-like characteristic of DMMP is found since the flame temperature of the lean flames increases as the DMMP concentration increasing. However, for the stoichiometric and rich flames, the fuel-like effect is negligible. Moreover, the DMMP decreases the flame temperature of the rich flames. The fuel effect in lean flames is considered to be caused by the phosphorous oxidation/reduction reactions. The preheat sub-zone of the laminar flame is more vulnerable to the inhibition effect of DMMP. Finally, the flame chemical kinetic structures are discussed. It is found that the chemical reactions in the flame area are retarded and the gas flow velocity in this zone needs to be reduced to make the flame surface stay in a certain area. Then, the residence time increases, leading to the distribution of CH_2O and OH in a wide area. Therefore, the flame thickness increases with DMMP addition.

Appendix 1: Digital Coding of the Elementary Reactions Mentioned in Fig. 3b

R1	$H + O_2 = O + OH$
R3	$OH + H_2 = H + H_2O$
R8	$H_2O + M = H + OH + M$
R11	$HO_2 + H = 2OH$
R13	$HO_2 + OH = H_2O + O_2$
R24	$CO + OC = CO_2 + H$
R26	$HCO + M = H + CO + M$
R27	$HCO + O_2 = CO + HO_2$
R28	$HCO + H = CO + H_2$
R31	$HCO + OH = CO + H_2O$
R32	$HCO + CH_3 = CH_4 + CO$
R43	$CH_2O + OH = HCO + H_2O$
R44	$CH_2O + H = HCO + H_2$
R52	$HOCHO = HCO + OH$
R84	$CH_3OH(+M) = CH_3 + OH(+M)$
R96	$CH_3 + H(+M) = CH_4(+M)$
R98	$CH_4 + OH = CH_3 + H_2O$
R108	$CH_3 + O = CH_2O + H$
R113	$CH_2[S] + O_2 \Longrightarrow CO + OH + H$
R130	$2CH_3(+M) = C_2H_6(+M)$
R141	$C_2H_4 + H(+M) = C_2H_5(+M)$
R470	$PO_2 + OH + M = HOPO_2 + M$
R472	$HOPO + O + M = HOPO_2 + M$
R475	$HOPO_2 + H = PO(OH)_2$
R476	$HOPO_2 + H = PO_2 + H_2O$
R486	$HOPO_2 + O = O_2 + HOPO$
R493	$PO_2 + H + M = HOPO + M$
R494	$HOPO + H = H_2 + PO_2$
R495	$HOPO + O = OH + PO_2$
R497	$HOPO + OH = PO_2 + H_2O$
R504	$PO + O_2 = PO_2 + O$
R506	$HOPO + OH = PO_2 + H_2O$
R539	$HPO_2 = HOPO$
R547	$HPO_2 + CH_3 = CH_4 + PO_2$

References

1. The Montreal Protocol on Substances that Deplete the Ozone Layer, in U. Nations (5th ed.), 1999.
2. Xu, W., Jiang, Y., Qiu, R., & Ren, X. (2017). Influence of Halon replacements on laminar flame speeds and extinction limits of hydrocarbon flames. *Combustion and Flame, 182,* 1–13.
3. Ren, X., Jiang, Y., & Xu, W. (2016). Numerical investigation of the chemical and physical effects of halogenated fire suppressants addition on methane–air mixtures. *Journal of Fire Sciences, 34,* 416–430.
4. Babushok, V. I., Linteris, G. T., Meier, O. C., & Pagliaro, J. L. (2014). Flame inhibition by CF3CHCl2(HCFC-123). *Combustion Science and Technology, 186,* 792–814.
5. Simpson, W. R., Glasow, R. V., Riedel, K., Anderson, P., & Ariya, P. (2007). Halogens and their role in polar boundary-layer ozone depletion. *European Geosciences Union, 16,* 4375–4418.
6. Solomon, S. (1999). Stratospheric ozone depletion: A review of concepts and history. *Reviews of Geophysics, 37,* 275–316.
7. Fontaine, G., Bourbigot, S., & Duquesne, S. (2008). Neutralized flame retardant phosphorus agent: Facile synthesis, reaction to fire in PP and synergy with zinc borate. *Polymer Degradation and Stability, 93,* 68–76.
8. Bourbigot, S., & Duquesne, S. (2007). Fire retardant polymers: Recent developments and opportunities. *Journal of Materials Chemistry, 17,* 2283.
9. Korobeinichev, O. P., Shvartsberg, V. M., Shmakov, A. G., Bolshova, T. A., Jayaweera, T. M., Melius, C. F., et al. (2005). Flame inhibition by phosphorus-containing compounds in lean and rich propane flames. *Proceedings of the Combustion Institute, 30,* 2353–2360.
10. Jayaweera, T. M., Melius, C. F., Pitz, W. J., Westbrook, C. K., Korobeinichev, O. P., Shvartsberg, V. M., et al. (2005). Flame inhibition by phosphorus-containing compounds over a range of equivalence ratios. *Combustion and Flame, 140,* 103–115.
11. Macdonald, M. A., Jayaweera, T. M., Fisher, E. M., & Gouldin, F. C. (1999). Inhibition of non-premixed flames by phosphorus-containing compounds. *Combustion and Flame, 116,* 166–176.
12. Bouvet, N., Linteris, G. T., Babushok, V. I., Takahashi, F., Katta, V. R., & Krämer, R. (2016). A comparison of the gas-phase fire retardant action of DMMP and Br 2 in co-flow diffusion flame extinguishment. *Combustion and Flame, 169,* 340–348.
13. Pagliaro, J. L., Linteris, G. T., & Babushok, V. I. (2016). Premixed flame inhibition by $C_2HF_3Cl_2$ and C_2HF_5. *Combustion and Flame, 163,* 54–65.
14. Borghi, R. (1988). Turbulent combustion modelling. *Progress in Energy and Combustion Science, 14,* 245–292.
15. Peters, N. (2000). *Turbulent combustion*. Cambridge: Cambridge University Press.
16. Zeldovich, Y. B. (1944). *The theory of combustion and detonation*. Publ. Academy of Sciences.
17. Spalding, D. B. (1955). *Some fundamentals of combustion*, Butterworth Scientific.
18. Li, Z., Li, B., Sun, Z., Bai, X. S., & Aldén, M. (2010). Turbulence and combustion interaction: High resolution local flame front structure visualization using simultaneous single-shot PLIF imaging of CH, OH, and CH_2O in a piloted premixed jet flame. *Combustion and Flame, 157,* 1087–1096.
19. Temme, J., Wabel, T. M., Skiba, A. W., Driscoll, J. F. (2015). Measurements of premixed turbulent combustion regimes of high reynolds number flames. In *AIAA Aerospace Sciences Meeting*. https://doi.org/10.2514/6.2015-0168.
20. Wu, Y., Modica, V., Rossow, B., & Grisch, F. (2016). Effects of pressure and preheating temperature on the laminar flame speed of methane/air and acetone/air mixtures. *Fuel, 185,* 577–588.
21. Hu, E., Li, X., Meng, X., Chen, Y., Cheng, Y., Xie, Y., et al. (2015). Laminar flame speeds and ignition delay times of methane–air mixtures at elevated temperatures and pressures. *Fuel, 158,* 1–10.
22. Fan, C. L., & Wang, L. S. (2010). Vapor pressure of dimethyl phosphite and dimethyl methylphosphonate. *Journal of Chemical and Engineering Data, 55,* 479–481.

23. Babushok, V. I., Linteris, G. T., Katta, V. R., & Takahashi, F. (2016). Influence of hydrocarbon moiety of DMMP on flame propagation in lean mixtures. *Combustion and Flame, 171,* 168–172.
24. Luo, C., Dlugogorski, B. Z., & Kennedy, E. M. (2008). Influence of CF_3I and CBr_3 on methanol-air and methane-air premixed flames. *Fire Technology, 44,* 221–237.
25. Babushok, V., & Tsang, W. (2000). Inhibitor rankings for alkane combustion. *Combustion and Flame, 123,* 488–506.
26. Bouvet, N., Linteris, G., Babushok, V., Takahashi, F., Katta, V., & Krämer, R. (2016). Experimental and numerical investigation of the gas-phase effectiveness of phosphorus compounds. *Fire and Materials, 40,* 683–696.

Influence of Initial Humidity on the Flame Propagation Rate of LPG/Air and LPG/O$_2$/N$_2$ Mixtures

Tomohiko Imamura, Masaya Ohtsuki, Shota Kumata, Yuki Furuya, Reito Ohno, Akira Tanaka and Akira Kawaguchi

Abstract   We examined the influence of the initial humidity to the flame propagation rate of LPG/air and LPG/O$_2$/N$_2$ mixtures to contribute to the risk assessment of the alternative energies. The ignition chamber was 1.36 L of volume, made by SUS316 steel. The moisture was added to the chamber by introducing air or inert gas which was passed through the bubbler. The ignition was initiated by the electric spark which was generated at the gap of needle electrode. First, we found that the ignition probability of LPG decreased with adding the moisture. On the other hand, we also found that the following three effects simultaneously appeared in the LPG combustion under the presence of moisture; (1) combustion-promoting effect that the unreacted LPG reacts to the O and/or OH radicals which were decomposed from the moisture, (2) combustion-suppressing effect by cooling due to the latent heat and the sensible heat of moisture, and (3) combustion-suppressing effect due to the oxygen insufficient which was caused by adding the moisture. The present experimental results could be explained by the above three effects. Furthermore, we confirmed that the results of chemical equilibrium analysis using CHEMKIN-PRO support the above hypothesis.

Keywords LPG · Initial humidity · Flame propagation rate · Chemical equilibrium analysis

Nomenclature

C_{st} Stoichiometric concentration (vol%)
P Pressure (Pa)
T Temperature (K)
t Time (s)
S Flame propagation rate (m/s)

T. Imamura (✉) · M. Ohtsuki · S. Kumata · Y. Furuya · R. Ohno · A. Tanaka · A. Kawaguchi
Faculty of Engineering, Suwa University of Science, 5000-1 Toyohira, Chino, Nagano 391-0292, Japan
e-mail: imamura@rs.sus.ac.jp

Subscripts

dry   Dry condition (relative humidity is zero)
wet   Wet condition

1   Introduction

In the viewpoint of controlling the promotion of the global warming, to spread the alternative energies like hydrogen, dimethyl ether, methane, to products and social infrastructures has been expected. To spread these alternative energies for products and infrastructures, to ensure safety based on the risk assessment assuming various handling situations of these alternative situations is indispensable. Fundamental characteristics of ignition and flame propagation of these gases, like the flammable limit, the ignition energy, the quenching distance, and the burning velocity, have been clarified by the previous theoretical and/or experimental studies [1]. Influences of ambient conditions, like the initial temperature, the initial pressure, have also been investigated [2–7]. For example, the burning velocity generally increases with the increase of initial temperature, and the dependence of burning velocity on the initial pressure is varied with the range of the value of burning velocity. Umezawa and Kawakami [8] examined influences of moisture on the flame propagation rate under the fuel-lean condition in the low oxygen concentration (less than 21 vol%). However, influences of moisture to the combustion behavior under the various compositions of flammable mixtures, from the range from fuel-lean to fuel-rich composition, have not been clarified. Furthermore, the influence of the initial humidity on the combustion behavior has not been completely clarified, too.

In this paper, we focused on the influence of initial humidity to the flame propagation rate of LPG/air and LPG/O_2/N_2 mixtures based on the laboratory-scale experiment using a combustion chamber and simulation for the chemical equilibrium analysis.

2   Experiment

2.1   Experimental Setup

The experimental setup consisted of a combustion chamber, a schlieren optical system, a high-speed camera, a bubbler to supply moisture, an ignition system, and pipes to connect these items, as shown in Fig. 1.

The cylinder-type combustion chamber was made by SUS304 steel, its dimension was 120 mm diameter and 120 mm height, its volume was 1.36 L, and its resistant

Fig. 1 Schematic diagram of experimental apparatus

①: combustion chamber ②: lens ③: knife edge ④: light source
⑤: high–speed camera ⑥: Neon transformer ⑦: relay
⑧: electrodes ⑨: bubbler ⑩: pressure transmitter ⑪: dew point sensor
⑫: ion probe ⑭: thermocouple ⑮: oscilloscope ⑯: pulse generator
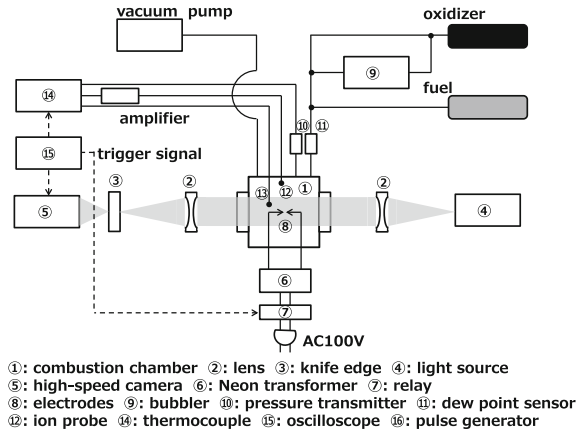
pressure was 2 MPa. The diameter of observation windows, made by quartz glass, was ϕ30 mm. A sheathed thermocouple (K-type, outer diameter of protection tube: ϕ1.6 mm) was fixed at the center of the chamber, an ion probe to detect the flame reaching was fixed at the ceiling of the chamber inside, and a pressure transmitter (KH15-L34, Nagano Keiki Co., Ltd.) was fixed to measure the pressure rise. Outputs from the thermocouple, the pressure transmitter, and the ion probe were recorded by a chart recorder (8860-50, HIOKI).

The flame propagation behavior was observed from the schlieren images of flame taken by a high-speed camera (Photron, SA-X). The schlieren optical system (Kato Koken Co., Ltd.) consisted of a xenon light source (75 W), a pair of schlieren lens, and a knife-edge.

The moisture was supplied by passing oxidizer and/or inert gas through the bubbler. The initial humidity was arranged by controlling the introducing amount of air or inert gas which was passed through the bubbler. Both the chamber and the bubbler were covered with jacket heaters to maintain temperatures between the chamber and the bubbler uniformly. The relative humidity in the chamber was calculated from the vapor pressure of the target mixture, which was estimated by the dew point and the saturated vapor pressure at the initial temperature which was estimated by Tetens's equation, as shown in Eq. 1. The dew point in the chamber was measured by a dew point sensor (SF72, MICHELL).

$$P = 6.11 \times 10^{\frac{7.5T}{237.3+T}} \tag{1}$$

The air-actuated valves (Swagelok, SS-4BK-1C) were fixed in the piping and to supply air to operate these valves was controlled using the solenoid valves (AG31-02-2, CKD).

The ignition system consisted of a pair of needle electrodes (tungsten, diameter: ϕ2.0 mm, tip angle: 30°) and a Neon transformer (15 kV, 20 mA, L2204840, LECIP). A solid-state relay was inserted to the power supply line to the Neon transformer, and

this solid relay was activated by single pulse signal of 5 Vp-p which was generated by a pulse generator (33500B, Agilent). The timings of the spark generation, the activation of the chart recorder, and the activation of a high-speed camera were synchronized by this single pulse signal.

2.2   Experimental Conditions

The mixtures of LPG/air and LPG/O_2/N_2 were focused as the test flammable mixture. For the test of LPG/air mixture, the concentration of LPG was varied in the range from 2.9 to 7.0 vol %. On the other hand, for the test of LPG/O_2/N_2 mixture, the concentration of LPG was varied in the range from 3.0 to 8.0 vol%, and the concentration of O_2 in the mixture was fixed at 21.0 vol% regardless of LPG concentration.

The ignition experiment was conducted under two moist conditions; the "dry condition" which there was no moisture in the mixture, and the "wet condition" which there was several amounts of moistures. In the "wet condition", the initial relative humidity was varied in the range from 0 to 50%. The duration time of ignition spark was fixed 100 ms, and the gap of the electrode was varied in the range from 0.05 to 2.0 mm.

3   Conditions of Chemical Equilibrium Analysis

The chemical equilibrium analysis for the combustion of LPG/O_2/N_2 mixture was conducted using CHEMIKN-PRO. The detailed conditions of chemical equilibrium analysis were shown below.

(a) Combustion model
    The "closed homogeneous model" was selected as the combustion model.
(b) Reaction model
    The reaction model which means a series of datasets of elementary reactions was simulated by GRI-Mech3.0 [9].
(c) Initial conditions
    The initial pressure was regarded as the atmospheric pressure. Since the spark ignition with initial temperature could not be reproduced by CHEMKIN-PRO, the initial temperature of the mixture was set as 1000 K, which is much more than the auto-ignition temperature of propane (470 °C) [10].
    The mole fraction of LPG was varied in the range from 3.0 to 10.0 vol%, and it of O_2 was maintained at 21.0 vol%. These conditions were the same as the experimental conditions. The mole fraction of H_2O was varied in the range from 0 to 10 vol% with the interval of 1.0 vol%. Nitrogen was added as the balance gas.

4   Experimental Results

4.1   Influence of Moisture to the Qualitative Flame Propagation

Figure 2 show the sequence photographs of high-speed schlieren images of flame propagation under the dry and wet condition. The gap between the electrodes was fixed 0.05 mm which was much narrower than the quenching distance. In the below paragraph, we describe the qualitative ignition behavior observed for each of the three compositions of LPG/air mixture.

(a)   Fuel-lean condition (LPG: 2.9–3.0 vol%, Fig. 2a)
      In the dry condition, ignition was initiated at the gap between the electrodes, and the flame propagated to the entire the chamber. On the other hand, in the wet condition, although the flame originated by the spark could be confirmed in the initial stage of ignition, the flame could not propagate to the entire of the chamber.
(b)   Stoichiometric condition (LPG: 4.0 vol%, Fig. 2b)
      Under both the dry and the wet condition, the flame propagated to the entire the chamber. The flame propagation rate in the wet condition was slightly smaller than that in the dry condition.
(c)   Fuel-rich condition (LPG: 6.0 vol%, Fig. 2c)
      In the dry condition, flame propagated to the entire the chamber. On the other hand, in the wet condition, flame quenched in the middle of propagation. The
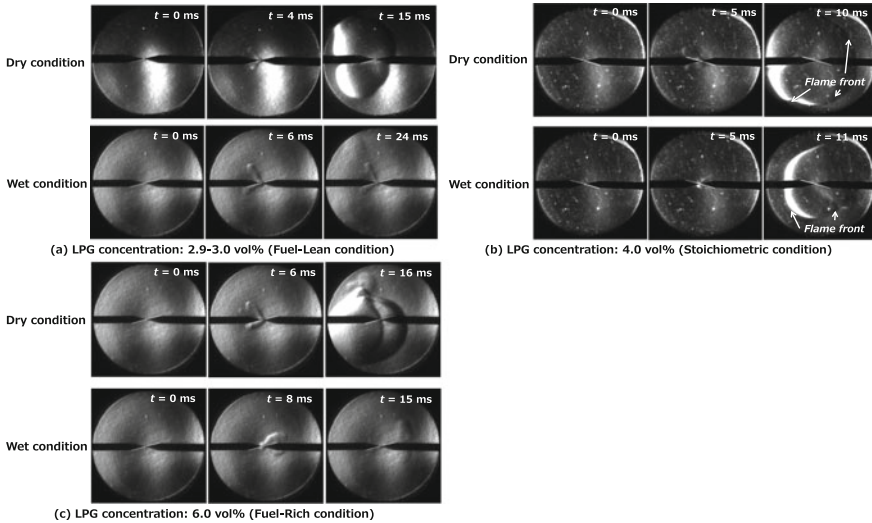
Fig. 2   High-speed schlieren images of flame propagation of LPG/air mixture. The gap of electrode: 0.05 mm

flame propagation rate which could be read from Fig. 2c was much smaller than that in the case of stoichiometric concentration as shown in Fig. 2b, and it was as fast as that in the case of the fuel-lean condition.

Based on these experimental results, the following brief summaries about the qualitative behavior of flame propagation of LPG/air mixture in the presence of moisture were found.

(1) LPG/air mixture could be ignited even if the gap between the needle electrode was much smaller than the quenching distance. Generally, a pair of the electrode with glass circular flange which is designated in ASTM E582-07 [11] is often used for the measurement of quenching distance, so the heat loss from the core of flame in the initial stage of ignition when a pair of needle electrode was used was very small.

(2) LPG/air mixture under the wet condition was harder to ignite than the dry condition.

(3) For the fuel-lean and the fuel-rich conditions, the influence of moisture to the flame propagation behavior appeared easier than that in the stoichiometric condition.

(4) For the stoichiometric condition, the influence of moisture to the flame propagation behavior hardly appeared.

4.2 Characteristics of Flame Propagation Rate in the Presence of Moisture

Figure 3 shows the relation between the flame propagation rate and the LPG concentration. The gap of electrode was fixed 2.0 mm. This gap length was approximately coincided to the quenching distance of propane/air mixture.

(a) LPG/air mixture (Fig. 3a)
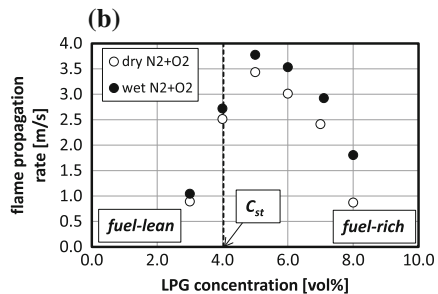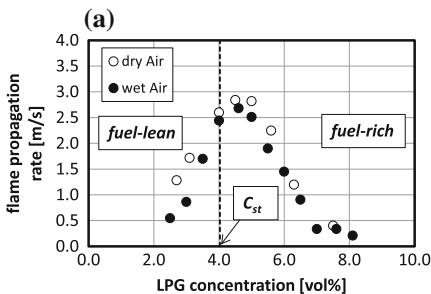
Fig. 3 Dependence of the flame propagation rate on the LPG concentration. The gap between the electrodes: 2.0 mm. **a** LPG/air mixture. **b** LPG/O_2/N_2 mixture

Fig. 4 Relation between the ratio of flame propagation rate in the wet condition to it in the dry condition and the propane concentration
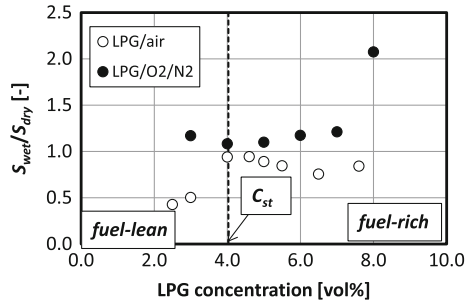
Both the dry and the wet conditions, the flame propagation rate increased with the increase of LPG concentration up to the concentration which was slightly larger than C_{st}. After that, it decreased with the increase of LPG concentration. The flame propagation rate under the wet condition was smaller than that of the dry condition for all ranges of LPG concentration in the present experiment. On the other hand, the difference between the flame propagation rate in the wet condition and the dry condition was hardly confirmed, especially in the fuel-rich condition ($>C_{st}$).

Figure 4 shows the relation between the ratio of flame propagation rate under the wet condition against it under the dry condition, S_{wet}/S_{dry}, and the LPG concentration. In the fuel-lean condition ($<C_{st}$), the value of S_{wet} was less than half of S_{dry}. However, the value of S_{wet}/S_{dry} increased with the increase of LPG concentration, at the C_{st}, the value of S_{wet}/S_{dry} became almost 1. In the fuel-rich condition ($>C_{st}$), although the value of S_{wet}/S_{dry} slightly decreased from the value which was shown near C_{st}, it maintained approximately 0.85 uniformly whole the range of the fuel-rich condition. It was larger than that which was obtained in the fuel-lean condition.

(b) LPG/O_2/N_2 mixture (Fig. 3b)

As with the case of LPG/air mixture, both the dry and the wet conditions, the relation between the flame propagation rate and the LPG concentration showed upward convex curve. Especially the vertex of the upward convex curve which implies the LPG concentration that the flame propagation rate shows the maximum value shifted to larger concentration (approximately 5 vol%). Furthermore, in contrast to the case of LPG/air mixture, the value of S_{wet} was larger than the value of S_{dry} in whole the range of LPG concentration. Especially in the fuel-rich condition, the value of S_{wet}/S_{dry} became larger than that in the fuel-lean condition as shown in Fig. 4, it showed over 2 when the LPG concentration was 8.0 vol%.

4.3 Dependence of the Initial Humidity on the Flame Propagation Rate

Figure 5a shows the relation between the flame propagation rate and the initial relative humidity under the fuel-rich condition. These data were obtained under approximately 27 °C of initial temperature. Figure 5b shows the relation between the values of the increasing rate of the flame propagation rate against the initial relative humidity, which was estimated as the slope of the Fig. 5a, and the initial relative humidity.

The relation between the flame propagation rate and the initial relative humidity showed upward convex curves. For the flame propagation rate as shown in Fig. 5a, when the LPG concentration was 5 vol%, the flame propagation rate showed maximum value at the approximately 10% of the relative humidity, and then it slowly decreased with the increase of the relative humidity. The relative humidity which the flame propagation rate showed the maximum value monotonously shifted to the large side with the increase of LPG concentration; approximately 20%R.H. under 6 vol% of LPG concentration, approximately 30%R.H. under 7 vol% of LPG, approximately 40%R.H. under 8 vol% of LPG. Furthermore, the magnitude of the increasing rate of the flame propagation rate in the cases of 6 and 7 vol% of LPG concentration was significantly larger than that in the cases of 5 and 8 vol% of LPG concentration, as shown in Fig. 5b. In other words, the influence of moisture to the flame propagation rate in the cases of 6 and 7 vol% of LPG appeared comparatively more significant than that of other cases of LPG concentrations.
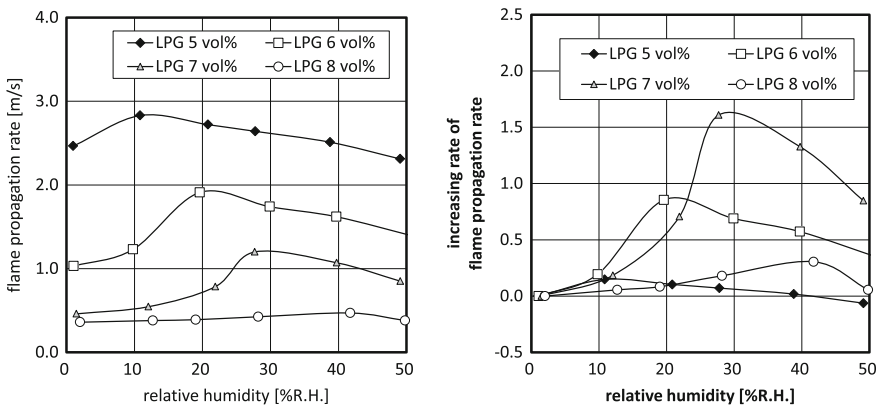
Fig. 5 Dependence of flame propagation rate on the initial relative humidity, **a** flame propagation rate, **b** increasing rate of flame propagation rate

5 Discussion of the Influence of Moisture and Relative Humidity to the Combustion Behavior

Based on the experimental results about the influence of moisture and the initial humidity to the combustion behavior which were described in the above section, we considered a simple hypothesis about the mechanism of the combustion of LPG under the presence of moisture. Figure 6 shows the schematic image of the considered hypothesis.

In the first place, the combustion of LPG is caused by the reaction between LPG and oxygen contained in the initial flammable mixture. When there is enough amount of oxygen to react to the LPG in the initial flammable mixture, namely fuel-lean condition, as shown in Fig. 6a, all amount of LPG in the initial flammable mixture reacts to the oxygen; therefore, H_2O molecular in the initial flammable mixture does not contribute to promote the combustion reaction. On the other hand, when there is excess LPG against the oxygen in the initial flammable mixture as shown in Fig. 6b, namely fuel-rich condition, some amount of LPG remained unreacted with oxygen. This unreacted LPG reacts to the O radical and/or OH radical which is decomposed from the moisture in the initial flammable mixture. So in the case of fuel-rich condition, the combustion reaction promotes with the increase of the initial humidity up to the condition that the all amount of remained unreacted LPG reacts to the oxygen which is decomposed from the moisture in the initial flammable mixture.

On the other hand, there are combustion-suppressing effects by adding the moisture to the initial flammable mixture. First, there is a cooling effect on the combustion by the latent heat and the sensible heat of H_2O molecular. Besides, for example, the LPG/air mixture, the concentration of oxygen in the initial flammable mixture relatively decreases with the addition of moisture if the LPG concentration in the initial flammable mixture is maintained. In this case, combustion strength becomes weak due to the oxygen insufficient.

From the above, the influence of moisture on the combustion of LPG is summarized into the following three effects;
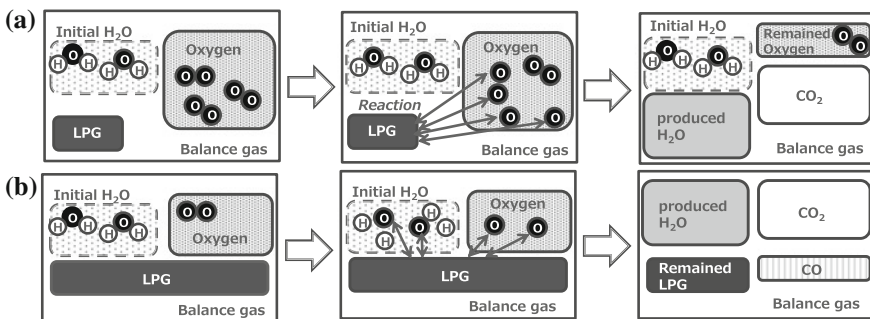
Fig. 6 Schematic images of mechanisms of moisture on the LPG combustion, **a** mechanism in the fuel-lean condition, **b** mechanism in fuel-rich condition

(1) Combustion-promoting effect that the unreacted fuel reacts to the O radical and/or OH radical which is decomposed from the moisture;
(2) Combustion-suppressing effect by cooling due to the latent heat and sensible heat of moisture;
(3) Combustion-suppressing effect due to the oxygen insufficient which is caused by adding the moisture.

In the combustion under the presence of moisture, above three conflicting effects simultaneously appear. In the fuel-lean condition, combustion-promoting effect which is mentioned in the above (1) was not appeared because no fuel remains after the reaction, so the flame propagation rate became weak in comparison with it in the dry condition. On the other hand, in the fuel-rich condition, the combustion-promoting effect mentioned in (1) appeared in addition to the combustion-suppressing effect which implied above (2) and (3). Of course, in the condition that there is much moisture, combustion-suppressing effect becomes dominant, but the combustion-promoting effect becomes dominant when there is suitable moisture for reaction with LPG, and then the combustion strength becomes large. Since this effect should be more strongly appeared as more amount of LPG was remained, the initial relative humidity which the flame propagation rate showed the maximum value monotonously increased with the increase of the LPG concentration, as confirmed in Fig. 5.

In the case of LPG/O_2/N_2 mixture, since the O_2 concentration was maintained 21 vol% regardless of the LPG concentration and the initial relative humidity, the combustion-suppressing effect which was described in above (3) did not appear. Therefore, in the case of LPG/O_2/N_2 mixture, amount of LPG more than the case of LPG/air mixture could be burned even if the concentration of LPG in the mixture was the same as the case of LPG/air mixture. So the LPG concentration which the flame propagation rate showed the maximum value shifted to more rich side, and the flame propagation rate under the wet condition and the fuel-rich condition became larger than that in the case of LPG/air mixture.

As mentioned above, based on the above hypothesis of the mechanism of LPG combustion under the presence of moisture, we could explain the present experimental results clearly.

6   Validation of the Hypothesis by the Chemical Equilibrium Analysis

Figure 7 shows the molecular increasing rate in the fuel-rich condition. Figure 7a shows the relation between the CO increasing rate and the relative humidity in the after-burnt mixture, and Fig. 7b shows it of CO_2. CO molecular is generated by the incomplete combustion, and CO_2 molecular is generated by the complete combustion. The increasing rate of CO_2 increased and it of CO decreased with the initial relative humidity. It implies that the combustion reaction promoted by the reaction
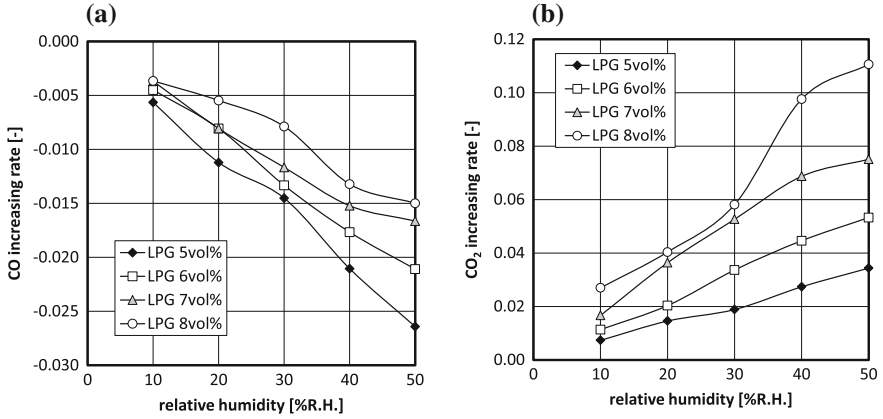
Fig. 7 Dependences of increasing rate of CO and CO_2 on the initial relative humidity, **a** for CO, **b** for CO_2

between remained unreacted LPG and the OH radical which was decomposed from the added moisture, so the amount of CO_2 increased and CO decreased.

Furthermore, the magnitude of the increasing rate of CO and CO_2 was in order of LPG concentration. This is because the amount of remained unreacted LPG increased with the increase of LPG concentration, so the combustion-promoting effect which is implied by above (1) was appeared in dominant. Therefore, the combustion improvement effect which could be read from the chemical equilibrium analysis could be explained by the hypothesis developed by the experimental results which were mentioned in the above section. In other words, the validation of the mechanism of influence of moisture and initial humidity to the combustion strength which was suggested in the above section developed by the present experimental results was supported by the chemical equilibrium analysis.

7   Conclusions

A series of experiments and chemical equilibrium analysis were conducted to clarify the influence of moisture and initial relative humidity to the flame propagation rate of LPG/air and LPG/O_2/N_2 mixtures. We found the following new knowledge.

(1) The ignition probability of LPG decreased with adding the moisture.
(2) The following three effects appeared simultaneously in the LPG combustion under the presence of moisture; (1) combustion-promoting effect that the unreacted LPG reacts to the O radical and/or OH radical which is decomposed from the moisture, (2) combustion-suppressing effect by cooling due to the latent heat and sensible heat of moisture, and (3) combustion-suppressing effect due to the oxygen insufficient which is caused by adding the moisture. The present exper-

imental results, influence of initial relative humidity to the flame propagation rate, difference of combustion behavior between in the wet and dry condition, could be explained as the interaction of the above three effects.

(3) We checked the above hypothesis of mechanism of the LPG combustion under the presence of moisture by the chemical equilibrium analysis. The generation of CO_2 in the wet condition, which was generated in complete combustion, was more than that of dry condition, and it of CO which was generated in the incomplete condition was less than that of dry condition. These results supported the above hypothesis.

References

1. Lewis, B., & von Elbe, G. (1961). *Combustion, flames and explosions of gases* (2nd ed.). Cambridge: Academic Press.
2. Japan Society for Safety Engineering (JSSE). (1999). *Handbook of safety engineering* (p. 156). Corona Publishing (in Japanese).
3. Kuo, K. K. (2005). *Principles of combustions* (2nd ed., pp. 500–501). Hoboken: Wiley.
4. Egolfopous, F. N., & Law, C. K. (1990). An experimental and computational study of the burning rates of ultra-lean to moderately-rich $H_2/O_2/N_2$ laminar flames with pressure variation. In *23rd Symposium on Combustion* (pp. 333–340).
5. Metghalchi, M., & Keck, J. C. (1982). Burning velocities of mixtures of air with methanol, isooctane, and indolene at high pressure and temperature. *Combustion and Flame, 48,* 191–210.
6. Dugger, G. L., Heimel, S., & Weast, R. C. (1955). Flame velocity and preflame reaction in heated propane-air mixtures. *Industrial and Engineering Chemistry, 47,* 114–116.
7. Lewis, B. (1954). *Discussion*: *Selected combustion problems* (p. 177), AGARD, Butterworths, London.
8. Umezawa, S., & Kawakami, T. (2005). Combustion characteristics near the flame propagation limit in high humidity and low oxygen concentration. In *Proceedings of Annual Meeting of Japan Society of Mechanical Engineers (JSME) Kanto Branch* (pp. 217–218) (in Japanese).
9. Website about GRI-Mech 3.0. (2017). http://combustion.berkeley.edu/gri-mech/ (Last accessed December 15, 2017).
10. Lewis, D. J. (1980). Autoignition temperature determinations and their relationship to other types of potential ignition sources and their application to practical situations. In *IchemE Symposium Series No. 58* (pp. 257–273).
11. ASTM E582-07. (2013). *Standard test method for minimum ignition energy and quenching distance in gaseous mixtures*.

The Influence of Compartment Temperature on Backdraught Dynamics

Chia Lung Wu and Ricky Carvel

Abstract Backdraught is an unpredictable and dangerous fire phenomenon, particularly for firefighters during search, rescue and firefighting activities. Most previous research into backdraught has used methane as fuel, leaving many questions unanswered. A series of reduced-scale backdraught experiments have been carried out using solid polypropylene as a fuel source, and conclusions have been drawn correlating the compartment temperatures to the onset of backdraught. It is found that when the maximum temperature in the compartment is above 350 °C when the door is opened, a backdraught can occur by auto-ignition, and no ignition source is required. However, no correlations could be identified with temperatures near the door or near the floor. It was also found that there is a correlation between compartment temperature and backdraught delay time, with cooler compartment temperatures leading to longer delays.

Keywords Backdraught · Temperature distribution · Firefighting

1 Introduction

In a fire scene, flashover and backdraught are perhaps the top two fire conditions that firefighters do not want to encounter. The former generally creating a rapid temperature increase due to most of the materials being ignited at the same time, this is a fuel-dependent phenomenon; if there is not enough fuel, then flashover cannot occur. Many research studies have quantified and explored indicators for the onset of flashover, such as heat flux, temperature, and external flaming. In [1], firefighters are routinely trained to look for the signs of an impending flashover. However, backdraught has only been sporadically researched even though identifying the conditions leading up to the onset of this fire phenomenon is equally necessary to ensure the safety of fire-rescuers.

In theory, a backdraught can only occur when there is a hot, fuel-rich fire compartment with a limited air supply, and this shortage of oxygen supply will constrain the fire to become smouldering or extinguished. If a sudden opening occurs, such as a window breaking by the fire or a door being opened by firefighters, the mixing of the hot gases from inside fire compartment with cooler fresh air from outside may create a flammable gas mixture. If an ignition source is present, the gas ignites, typically resulting in an explosive fireball projected through the opening, a potentially fatal occurrence if fire fighters are near the opening.

Unlike most fire phenomena, the majority of backdraught casualties are firefighters because backdraught usually occurs late in the fire timeline and is triggered when doors or windows are opened, which firefighters need to do as part of their search and rescue activities. Twenty years ago, Fleischmann et al. [2–4] started their pioneering backdraught research, using a laboratory-scale chamber ($2.4 \times 1.2 \times 1.2$ m). This research established a fundamental understanding of this phenomenon and concluded that a critical amount of "unburned gases" is the main factor controlling the onset of backdraught. Later on, Weng and Fan [5–7] conducted similar experiments at half the scale of Fleischmann's to investigate how the opening geometry influences the critical gas concentrations and made some conclusions regarding water mist as a mitigating tactic. All the above studies were based on experiments using methane as fuel. Methane is not a typical fuel in compartment fires.

Basic fire chemistry tells us that a fire requires three things: heat, fuel and oxygen, the classic fire triangle. Fires involving most fuels cannot occur if one of the elements is missing. It is expected that variations in temperature will influence the onset of backdraught, but such variations cannot be observed in tests using methane, a fuel that is readily ignited at room temperature. The research described here seeks to investigate the dependence on temperature, using fuels other than methane; solid fuels are much more realistic.

Backdraught, when it occurs, does not occur at the instant the door is opened. There is a delay during which the gases within the compartment mix with the inflowing air. Due to buoyancy, the cooler air flows under the hot compartment gases, in the so-called gravity current/gravity wave. This has been studied in some depth [8–10], but the conclusions regarding the backdraught delay time are still lacking. Also, previous research has generally focused on piloted ignition of backdraught, using an electric spark to initiate the backdraught. In reality, particularly when temperatures are elevated, backdraught may occur spontaneously by auto-ignition. This has not been widely studied before, so this study investigated backdraught without any ignition source apart from the hot fire compartment.

This research aims to identify the thermal conditions crucial to the occurrence of backdraught using solid fuels and also investigate the factors influencing the delay time of backdraught. Once such factors are understood, a strategic firefighting tactic approach can be developed.

2 Experimental Set-up and Procedure

2.1 Experimental Set-up

A small-scale fire compartment (0.8 × 0.4 × 0.4 m, see Fig. 1) was designed for this project, the same size ratio as Fleischmann's, but one third the size. The size of compartment does not affect if backdraught will occur or not [11]. It is instrumented with 7 thermocouple trees (24 type K thermocouples). TCT 5-2 and 5-1 are positioned on the centreline of the compartment, at 0.4 and 0.6 m from the back wall of the compartment. On these trees, there are TCs fixed at 0.0, 0.1, 0.2, 0.3 and 0.4 m below the ceiling. TCT 3-3 and 3-4 are positioned on either side of TCT 5-2, halfway between the centreline of the compartment and the wall. Similarly, TCT 3-1 and 3-2 are positioned on either side of TCT 5-1. Trees 3-1, 3-2, 3-3 & 3-4 have TCs at 0.1, 0.2 and 0.3 m below the ceiling. TCT 2 is positioned in line with TCT 3-4 and 3-2, as this is the location of the fire, and it only has TCs at 0.1 and 0.3 m. The fuel bed is contained in a steel tray, which is 20 × 20 × 5 cm, and is positioned 10 cm from the rear wall. The compartment is constructed of two layers of expanded insulating vermiculate boards, stable up to 1100 °C.

There are three removable baffles which may be positioned across the opening of the compartment, to investigate the effects of opening size. In all the experiments described here, the upper two baffles were kept in place such that the opening was fixed at 0.13 m × 0.4 m wide. Other door opening sizes and configurations will be tested in the future, and the findings will be published in due course. A sliding outer door is used to seal and open the compartment; this ensures that the experimenter is safely to the side of the compartment when the door is opened.
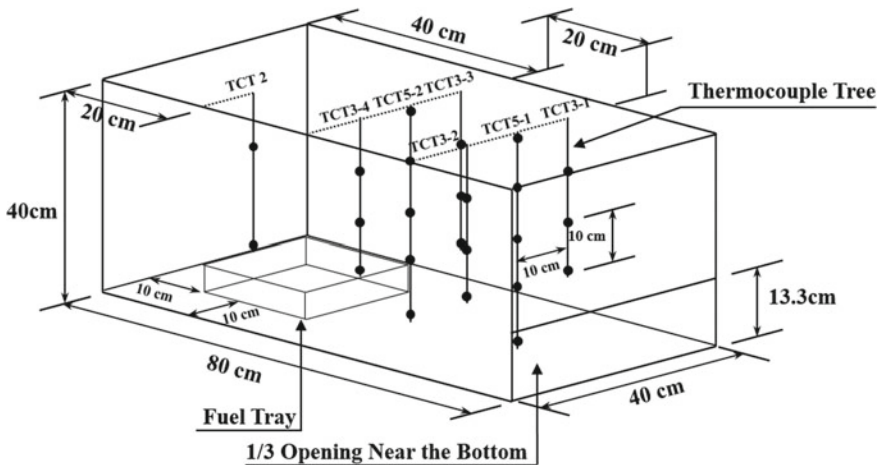
Fig. 1 Diagram showing the locations and dimensions of the thermocouples, fuel tray and door opening

2.2   Experimental Procedure

In this research, backdraught events were investigated based on different preburning times, before door closure, this experimental protocol provides a range of different thermal distributions in the fire compartment, hence enables the experimental comparison in various fire conditions. In each test, 300 g of polypropylene (PP) pellets was used as fuel, with 150 ml of n-heptane (C_6H_{16}) used as an accelerant. It was found that this quantity of n-heptane was consumed thoroughly in the first 5 min of burning, so it is assumed that the quantity of heptane is negligible at the time of door closure in all tests. In the tests where backdraught did not occur, it was always found that there was still unburned fuel in the fuel tray at the end of the test, which means the lack of backdraught was not due to insufficient fuel in the test.

Figure 2 shows that backdraught is typically observed to start (by auto-ignition) at a location above the fuel container. Backdraught, as can be seen, initiated at the intersection or near of the clean air and hot smoke.

A typical temperature history profile is shown in Fig. 3. Here, the door was closed at 14 min. After closure, it is clear that the fire was rapidly smothered and all locations within the compartment tended towards similar values, indicating that the compartment gases are quite well mixed, and not particularly stratified, with only about 50 °C variation between the hottest and coolest locations. During the period of door closure, the compartment cools down slowly. In this instance, after waiting approximately 240 s, the door was opened. After a few seconds of delay, backdraught occurred.

Fig. 2   Auto-ignition of backdraught (3 consecutive video stills at 0.034 s intervals)

Fig. 3   Typical temperature history in backdraught testing
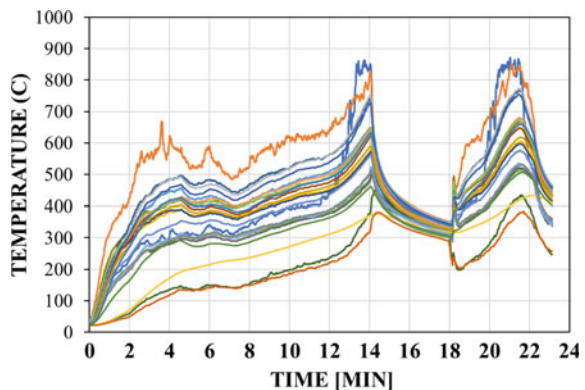
Backdraught experiments were tested with different preburning times, ranging from 7 min after ignition to just after flashover (at about 14 min), and for different door closure times. The opening time in each test was established on the basis of the compartment temperature at the time of opening. Initial experiments showed that fire growth to flashover before door closure is not necessary to attain backdraught conditions [12]. The conditions inside the chamber when the door is closed, at different stages of the fire, have a considerable influence over the properties of the resulting backdraught; see Fig. 4.

It can be observed that the earlier the door is closed, the less fierce the fireball will be. From observation, when the door was closed earlier than 12 min, the neutral plan of the smoke was stable, staying at the same height. After 12 min, the temperature dramatically increased, and the smoke layer became thicker at the same time, which corresponding to the previous research [12], is found that the neutral plane changes dramatically after 12 min burning time in the design fire. This can be observed from the temperature data at different heights in various preburning conditions; see Fig. 5.

Figure 5 shows that the temperature variation increases steadily from 6 to 12 min, for TCs at different heights. The highest temperature is the TC installed at 30 cm from the bottom of the compartment, with an approximately 20 °C increase every 2 min. It is not surprising that the temperature accelerated after 12 min, and at this

12 mins   13 mins   14 mins   After flashover
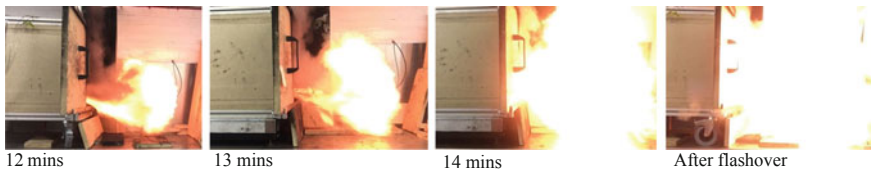
Fig. 4 Backdraught tests with different preburning times before the door was closed

Fig. 5 Temperature in the compartment at different heights, for various times of burning
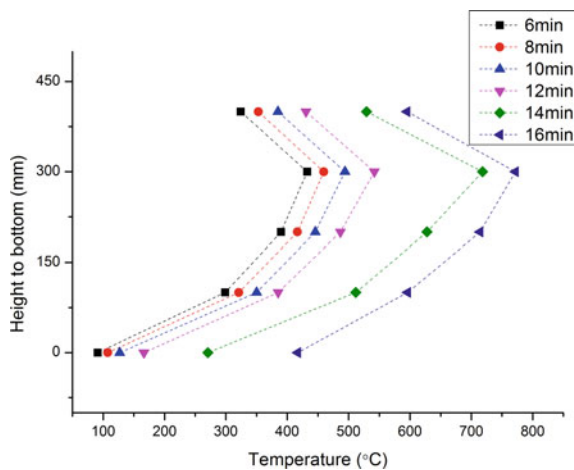
time, it was observed the smoke layer gradually decreased owing to the fire transited to ventilation-controlled.

3   Result and Discussion

3.1   Temperature Distribution

A series of 64 experiments was carried, with 35 of the tests leading to backdraught. The temperature data for the time of door opening are presented in Figs. 6, 7 and 8. These tests had various burning times before door closing, ranging from 7 min after ignition to after flashover. In tests 1–34 (indicated using triangle markers), the door was closed, while the fire was in the steady growth phase, between 7 and 12 min after ignition. Here, the smoke layer height remained approximately constant and the temperature increased in a steady manner. Tests 35 and 36 (square markers) were just before the onset of flashover. In the rest of tests (diamond markers), the door was closed after the fire had transitioned to flashover. From these results, we can identify the thermal conditions required, at the time of door opening, for backdraught to occur.

Instead of comparing all the 24 TCs in the compartment, 3 TCs were chosen for analysis: the TC with the highest temperature (TC-1003, TC-1003, the one with 10 cm to the top of TCT 2), one near the floor near the opening (TC-1031, the bottom one of TCT 5-1) and one near the top of the compartment (TC-1025, the top one of TCT 5-2).

In Fig. 6, it can be seen that the temperature near the opening has no clear correlation with the onset of backdraught. It can be seen that all tests above 300 °C at
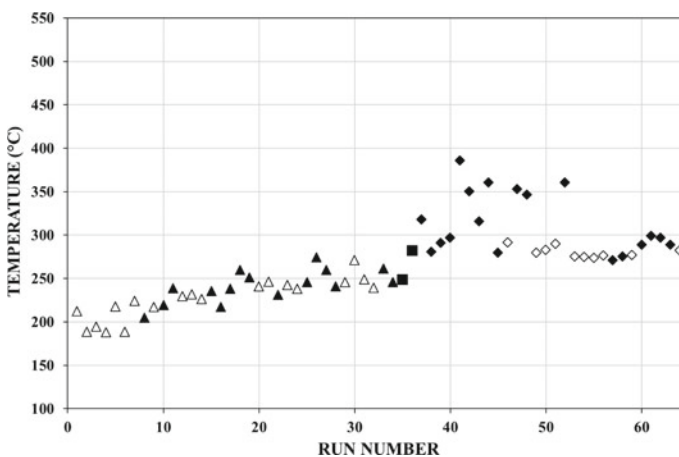
Fig. 6 Temperature (near the floor, near the door) with or w/o backdraught
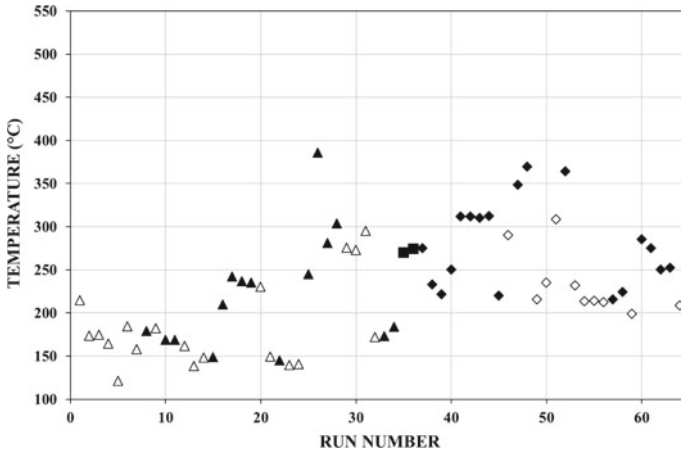
Fig. 7 Temperature (near the ceiling, in the middle of the compartment) with or w/o backdraught
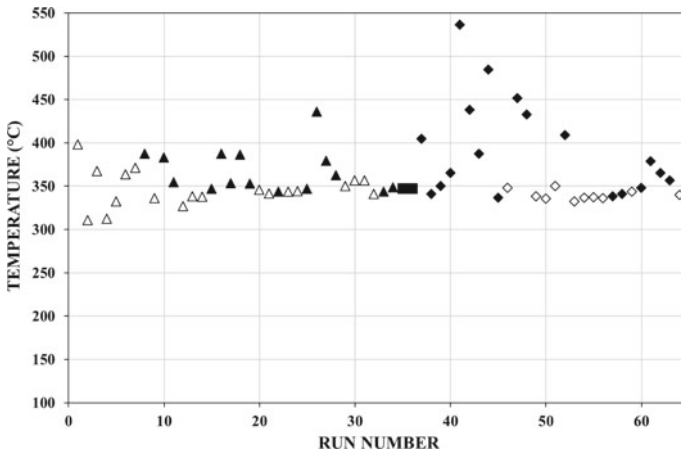
Fig. 8 Temperature (maximum) with or w/o backdraught

this location lead to backdraught, but this is only evident in tests where the door was closed after flashover. At lower temperatures, no correlation is apparent; for example, in test 8 the temperature was only 200 °C, yet backdraught was observed; however, in test 30 the temperature was 270 °C and no backdraught was observed.

Figure 7 shows the observed temperature at the time of door opening at TC (TC-1025) near the ceiling, in the middle of the fire compartment. Once again there is no clear correlation between temperature and the onset of backdraughts. Backdraught occurred at temperatures ranging between 150 and 390°C, yet other tests exhibited no backdraught at temperatures ranging from 120 to over 300 °C.

However, there appears to be more of a correlation between temperature and onset of backdraught when TC-1003 is used. In all tests, this TC showed the highest temperatures, both as the fire grew and during the period of door closure; it is located 30 cm above the edge of fuel tray. Figure 8 shows that, except for tests 1 to 7, where the door was closed very early and the period of door closure was very short, there appears to be a critical temperature of about 350 °C determining whether backdraught would occur or not. In the first 7 tests, it appears likely that the shorter preburning time meant that the box was relatively cool, so pyrolysis may have been slow or not occurring, and the relatively short closure times meant that there was insufficient time to accumulate a critical quantity of flammable gases.

In summary, it has been observed that the temperature at some locations in the compartment has no apparent correlation with the onset of backdraught. However, for the tested scenario at least, it is possible to use the compartment maximum temperature at the time of door opening to predict whether or not backdraught will occur. On the basis of these observations, a "critical temperature of 350 °C" is required for backdraught to occur.

3.2 Delay Time of Backdraught with the Relationship to Temperature

When a firefighter opens a door during search and rescue operations, they do not know if a backdraught will occur. When "nothing" happens after the door is opened, there is still a great uncertainty as to whether backdraught will occur or not, as there is always a delay before a backdraught. In our study, we compared backdraught delay times, measured using video cameras, giving an accuracy of 1/29th of a second, with compartment temperatures. Figure 9 shows the data for backdraught delay time
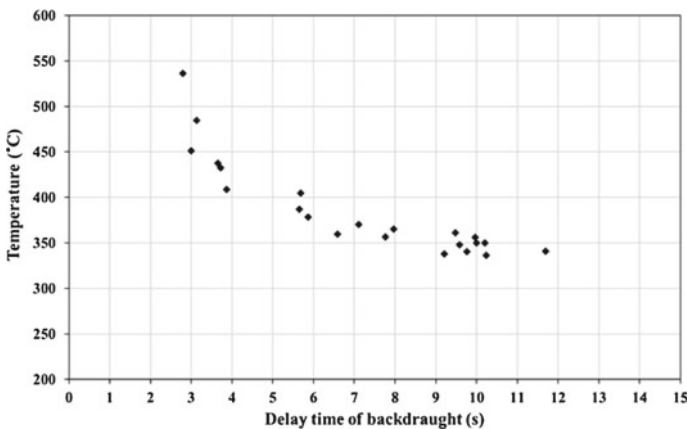
Fig. 9 Delay time of backdraught after door opening

versus compartment maximum temperature, for fires which grew to flashover before door closure. In these tests, the backdraught delay time varied between 3 and 12 s, and there is an observable trend in the data, with hotter temperatures leading to faster backdraughts. It should be noted that backdraught delay times in real compartments will be considerably longer due to scale [12]. Previous research suggested that the backdraught delay time was linked to the time taken by the gravity current to reach the back of the compartment [13]; however, this observation was made from experiments using a spark igniter at the back of the compartment. In our apparatus, the gravity current only requires 2–3 s to reach the back wall, so it is clear that other factors must be contributing to the delay time.

When the temperature was close to the critical temperature for backdraught, 350 °C in these tests, the delay time was consistently about 9–10 s. In these tests with the long delay times, the compartment door had been closed for more than four minutes. In general, the longer the time of closure, the lower the temperature will be and the longer the delay time will be. Thus, if we know the highest temperature inside the compartment and have information about the duration of door closure, we should be able to approximately predict the delay time for backdraught. However, it should be noted that the compartment used for this project was small and a detailed analysis correlating this to a full sized room has yet to be carried out.

4 Conclusion and Future Work

In this research, a series of reduced-scale compartment fire tests has been carried out to investigate the driving force governing the occurrence of backdraught, using solid PP fuel. It has been demonstrated that the temperature distribution in the compartment is not correlated with the onset of backdraught, but a critical maximum temperature of about 350 °C, at the time of door opening, has been observed to determine the onset of backdraught. This, perhaps, would be useful information for firefighters with infrared thermographers (infrared cameras), who may be able to assess temperatures and predict (with some uncertainty) whether backdraught is likely or unlikely.

If the fire has longer development before the door is closed, a more violent fireball will be generated because of accumulated unburned flammable gases. While flashover is not required to bring a compartment to backdraught conditions, fires which have transitioned to flashover before door closure have an increased possibility of backdraught due to a hotter compartment. It has been shown that if the compartment door is closed before the neutral plane of the fire begins to drop (that is, well before flashover), backdraught still can be triggered.

A range of delay times for backdraught was obtained. The observed trend is that a longer door closure time and a lower compartment temperature leads to a longer delay time. Infrared cameras may be used by firefighters to predict whether backdraught is likely to occur, although there is considerable uncertainty here.

References

1. Drysdale, D. (2011). *An introduction to fire dynamics* (3rd ed.). Wiley, Hoboken. https://doi.org/10.1002/9781119975465.
2. Fleischmann, C. M., Pagni, P. J., & Williamson, R. B. (1992). Preliminary backdraft experiments. In *12th Joint Panel Meeting of the UJNR Panel on Fire Research and Safety* (pp. 208–215).
3. Fleischmann, C. M., Pagni, P. J., & Williamson, R. B. (1993). Exploratory backdraft experiments. *Fire Technology, 29*(4), 298–316.
4. Fleischmann, C. M., Pagni, P. J., & Williamson, R. B. (1992) Quantitative backdraft experiments. In *4th International Symposium on Fire Safety Science* (pp. 337–348).
5. Weng, W. G., & Fan, W. C. (2002). Experimental study on the mitigation of backdraft in compartment fires with water mist. *Journal of Fire Sciences, 20*(4), 259–278.
6. Weng, W. G., & Fan, W. C. (2003). Critical condition of backdraft in compartment fires: A reduced-scale experimental study. *Journal of Loss Prevention in the Process Industries, 16*(1), 19–26.
7. Weng, W. G., Fan, W. C., Yang, L. Z., Song, H., Deng, Z. H., & Qin, J. (2003). Experimental study of back-draft in a compartment with openings of different geometries. *Combustion and Flame, 132*(4), 709–714.
8. Fleischmann, C. M., & McGrattan, K. B. (1999). Numerical and experimental gravity currents related to backdrafts. *Fire Safety Journal, 33*(1), 21–34.
9. Yang, R., Weng, W. G., Fan, W. C., & Wang, Y. S. (2005). Subgrid scale laminar flamelet model for partially premixed combustion and its application to backdraft simulation. *Fire Safety Journal, 40*(2), 81–98.
10. Weng, W. G., Fan, W. C., & Hasemi, Y. (2005). Prediction of the formation of backdraft in a compartment based on large eddy simulation. *Engineering Computations, 22*(4), 376–392.
11. Bolliger, I. (1995). *Full residential-scale backdraft*. Christchurch: University of Canterbury.
12. Wu, L., & Carvel, R. (2017). An experimental study on backdraught: The dependence on temperature. *Fire Safety Journal, 91,* 320–326.
13. Fleischmann, C. M., Pagni, P. J., & Williamson, R. B. (1993). Exploratory backdraft experiments. *Fire Technology, 29*(4), 298–316.

Shape and Oscillation of Ethylene and Propane Laminar Diffusion Flames in Micro- and Normal Gravities

Luyao Zhao, Dan Zhang, Jingwu Wang, Jun Fang, Kaiyuan Li, Jinfu Guan, Jinjun Wang and Yongming Zhang

Abstract In this study, a set of experiments were carried out in micro- and normal gravities to study the flame shape and oscillation of co-flow laminar diffusion ethylene and propane flames. The experimental results show that in microgravity, the flame length and width are larger than those under normal gravity, and the ratio of flame length to width is lower than that in normal gravity. The flame length and width decrease seriously with the increasing co-flow air velocity in microgravity, while they are almost unaffected by the co-flow air velocity in normal gravity. The flame oscillation is not experimentally noticeable in microgravity. In normal gravity, it is found that the flame oscillation frequency increases linearly with the volume flow rate of co-flow air. The flame oscillation is fully suppressed when the air co-flow velocity exceeds the critical velocity. And, the critical air co-flow velocity increases with the initial fuel flow velocity.

Keywords Microgravity · Shape · Oscillation · Diffusion flame

1 Introduction

Flame shape and oscillation are crucial parameters for diffusion flames. They were found to vary with the gravity level and influence the airflow fields [1–3]. Hence, the developed theories in normal gravity cannot be directly used to solve the problems

L. Zhao · J. Wang · J. Fang (✉) · J. Wang · Y. Zhang
State Key Laboratory of Fire Science, University of Science and Technology of China, Hefei 230026, China
e-mail: fangjun@ustc.edu.cn

D. Zhang
School of Building Environment Engineering, Zhengzhou University of Light Industry, Zhengzhou 450002, China

K. Li
Department of Civil and Structural Engineering, Aalto University, Espoo 02150, Finland

J. Guan
Hefei Institute for Public Safety Research, Tsinghua University, Hefei, Anhui 230601, China

of microgravity flames. Besides, it is also very important to study the differences between flames under still and co-flowing air conditions.

Flame shapes of laminar diffusion flames in microgravity were mostly studied numerically due to the experimental limitation [4–6]. Some experimental studies obtained non-buoyant laminar-jet diffusion flame by reducing the ambient pressure [7, 8]. Previous studies showed that flame shape in microgravity are different from that in normal gravity and the combustion in microgravity is more violent [7, 9]. This study tries to reveal the effects of air co-flow velocity on flame shape in microgravity.

It is well known that the flickering or oscillation of laminar diffusion flames is caused mainly by the interaction of the flame and the vortices both inside and outside the flame. Many researchers studied the influences of gravity on flame oscillation, which considered hydrocarbon-fueled flames burning in still air. Katta et al. [10] found that the flame oscillation frequency and gravity level can be correlated as $f \propto g^{1/2}$ by numerical study. Durox et al. [8] conducted experimental studies and found that the flame oscillation frequency depends on the gravity by a power between 1/2 and 2/3. Sato et al. [11] found that there are two different modes of oscillation: tip flickering and bulk flickering. It has been shown in many literatures that the type of fuel and the fuel jet velocity have a little effect on the low frequency oscillation of flame [12, 13]. However, the co-flow air velocity has a large effect on the dynamics and stability of a laminar non-lifted diffusion flame. But much less studies have been performed considering the effects of co-flow air velocity on the flame oscillation. Darabkhani et al. [14] conducted experimental study on the effects of co-flow air velocity on the oscillation behavior of laminar non-lifted methane diffusion flames and found that the dominant oscillation frequency, f, increases linearly with the air volume flow rate (slpm), $U_{a,0}$, as $f = 0.33\,U_{a,0} + 11$.

In this study, a set of experiments were carried out to study the effects of gravity and air co-flow on the shape and oscillation of ethylene and propane laminar diffusion flames. The relationships between the air co-flow velocity, fuel flow velocity, and the flame oscillation frequency were studied in depth.

2 Experimental Methods

Experimental methods will be described only briefly (see Ref. [15] for more details). The microgravity experiments were performed using a drop tower facility in national microgravity laboratory of China, as shown in Fig. 1a, which can provide a gravity level of 10^{-3} g with a duration time up to 3.5 s. The experimental rig packed in the drop cabin is shown in Fig. 1b, which includes the combustion chamber, fuel supply and ignition system, and measurement system. Mass-flow-rate controllers (Alicat-KM7100) were used to control the flow rates of fuel and air with an accuracy of 0.8%. The flame behaviors were recorded by a CCD camera at 30 fps and a high-speed camera (FASTCAM SA5) at 250 fps. The ignition was achieved by a hot wire which was placed at the nozzle exit and was moved away once the ignition was successful. Variation of the gravity level with time in one experiment run is shown in Fig. 1c.
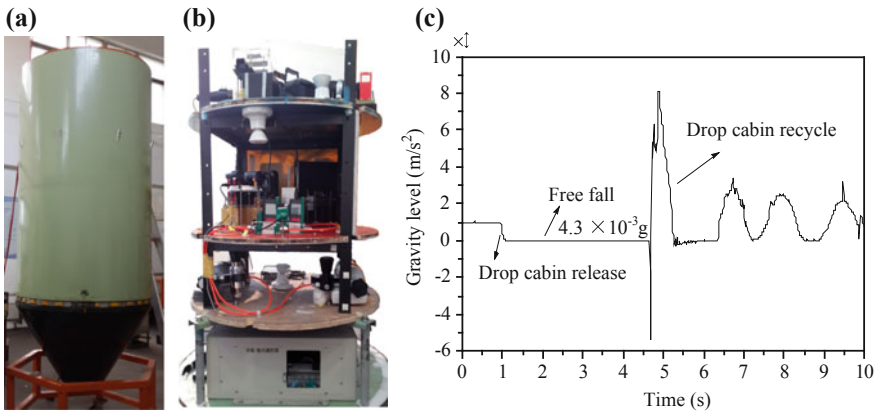
Fig. 1 **a** Drop cabin, **b** experimental rig, **c** variation of the gravity level with time during one experiment

The schematic diagram and image of co-flow jet nozzle are shown in Fig. 2. The fuel and air nozzle diameters are given in Table 1, where d_f is the fuel jet nozzle
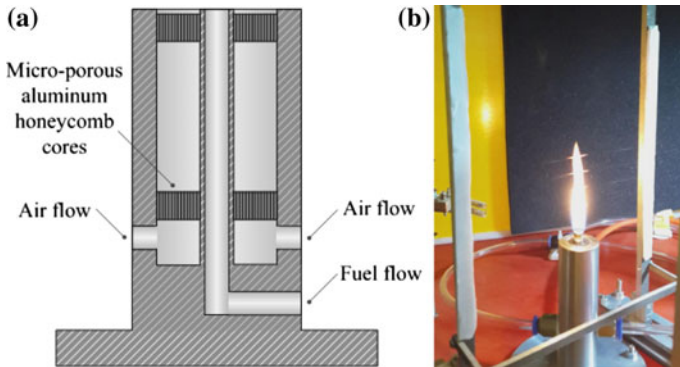
Fig. 2 Co-flow jet nozzle: **a** schematic diagram and, **b** image

Table 1 Co-flow jet nozzle diameters

	d_f (mm)	$d_{a,i}$ (mm)	$d_{a,o}$ (mm)
1	3	6	15
2	4	8	20
3	8	12	30
4	10	14	30
5	12	16	30
6	14	18	30

Table 2 Properties of fuel and air at standard conditions

Fuel	ρ (kgm^{-3})	Heating value (kJmol^{-1})	Ignition temperature (°C)	μ (10^{-5} Pa)
Ethylene (C_2H_4)	1.255	1411.0	425	0.912
Propane (C_3H_8)	2.004	2217.8	450	0.774
Air	1.289	–	–	1.73

diameter, $d_{a,i}$ and $d_{a,o}$ are the inner and outer diameter of air jet nozzle, respectively. The effect of fuel type was considered by using ethylene and propane as fuels in the experiments. Ethylene diffusion flame produces soot easily. Propane produces less soot and is widely used in industry. The properties of fuel and air at standard conditions are given in Table 2. The fuel flow velocities of ethylene were 0–0.24 m/s and the fuel flow velocity of propane was 0–0.23 m/s, while the air co-flow velocities were 0–0.06 m/s. The exit Reynolds numbers were determined to be 50–230.

3 Results and Discussion

3.1 Flame Shapes

This part mainly focuses on the flame length, flame width, and ratio of flame length to flame width. To study the effects of low co-flow air velocities ($u_{a,0}/u_{f,0} = 0$–1, where $u_{a,0}$ is the initial air co-flow velocity, and $u_{f,0}$ is the initial fuel flow velocity) on the flame shapes, definitions of flame scale parameters are established in Fig. 3. For a flickering flame, the flame length refers to the length of continuous flame, and 50% intermittency flame length is used hereinafter as flame length (L_f). The oscillation amplitude (A_f) is defined as the vertical distance between the lowest (H-min) and highest (H-max) flame lengths. For a non-flickering flame, the flame length is defined
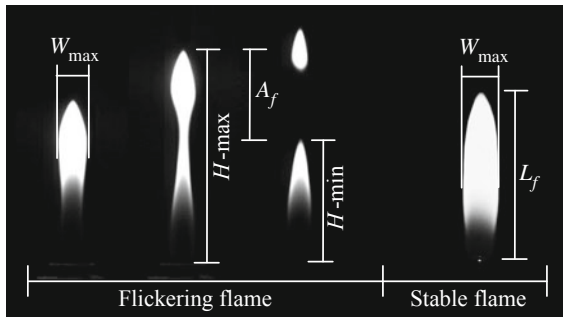
Fig. 3 Definitions of flame scale parameters

as the vertical distance between the burner exit and the tip of the luminous region of the flame. The flame width ($W_{\max}$) is defined as the maximum diameter of the flame.

The captured color images of ethylene flames with increasing co-flow velocity in normal and microgravities are shown in Fig. 4, where the initial fuel flow velocity ($u_{f,0}$) is 0.24 m/s and the fuel nozzle diameter is 3 mm. It is obvious that the flame shapes in normal and microgravities are different. For ethylene diffusion flames in microgravity, the flame length and width decrease with increasing air co-flow velocity, and there are no flame oscillation, of which the reason will be addressed in detail in the next section.

The dimensionless flame length is defined as the ratio of flame length to fuel jet nozzle diameter, L_f/d_f. Likewise, the dimensionless flame width is defined as the ratio of flame width to fuel jet nozzle diameter, $W_{\max}/d_f$. And, the dimensionless airflow velocity is defined as the ratio of initial airflow velocity to fuel flow velocity, $u_{a,0}/u_{f,0}$. Figure 5 gives the variations of the dimensionless flame length and flame width with the dimensionless airflow velocity. Data of ethylene flame in this study are taken with $d_f = 3$ mm and $u_{f,0} = 0.24$ m/s. Data of methane flame are taken with $d_f = 3$ mm and $u_{f,0} = 0.71$ m/s [15]. And, data of acetylene are taken with $d_f = 1.6$ and 4.8 mm [16]. It shows that the flame shape is associated with the type of fuel at low co-flow velocities. The dimensionless flame length and flame width exhibit the same variation trends. Both of them decrease seriously with the increasing dimensionless air co-flow velocity in microgravity, while they are almost unaffected by the dimensionless airflow velocity in normal gravity. The dimensionless flame length and width are larger in microgravity. As we know, the combustion of diffusion flames is primarily controlled by the mixing process of fuel and oxidant when the chemical reaction rate is large enough [17]. In microgravity, the mixing of fuel and
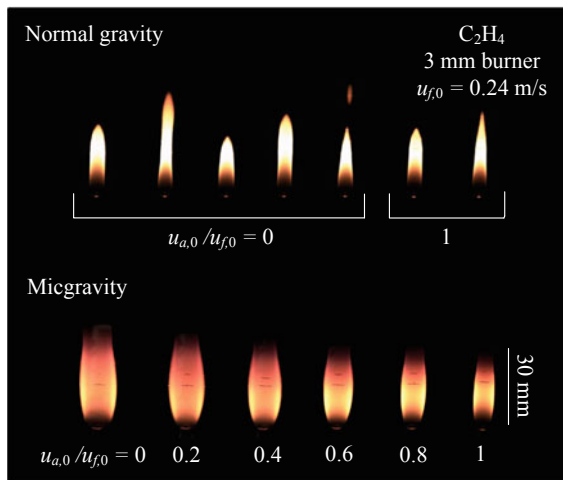
Fig. 4 Color images of C_2H_4 flames with increasing air co-flow velocity in normal and microgravity conditions
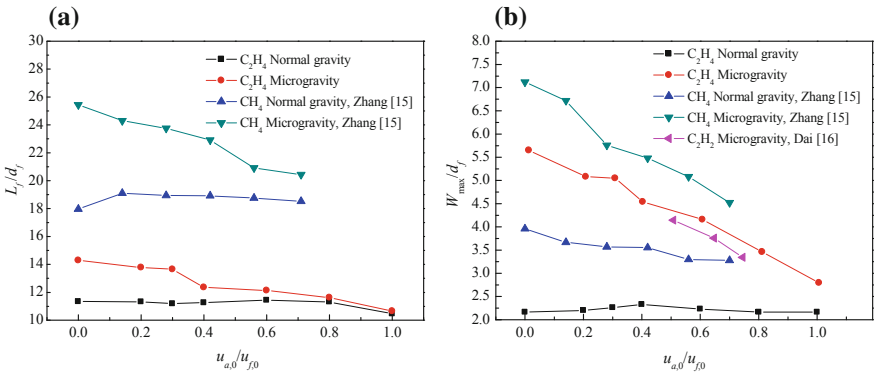
Fig. 5 **a** Dimensionless flame length and, **b** dimensionless flame width versus dimensionless air co-flow velocity

surrounding oxidant is weakened for the absence of buoyancy effect, thus the flame sheet expands to gain more oxidant gas, resulting in a longer and wider flame than in normal gravity. Similarly, the larger air co-flow velocity enhances the mixing of fuel and oxidant and leads to a shorter and narrower flame.

Figure 6 shows the ratio of flame length to flame width against the dimensionless air co-flow velocity. The ratio in normal gravity is larger than that in microgravity, which is attributed to the fact that the buoyancy effect in the axial direction in normal gravity leads to a slender flame.
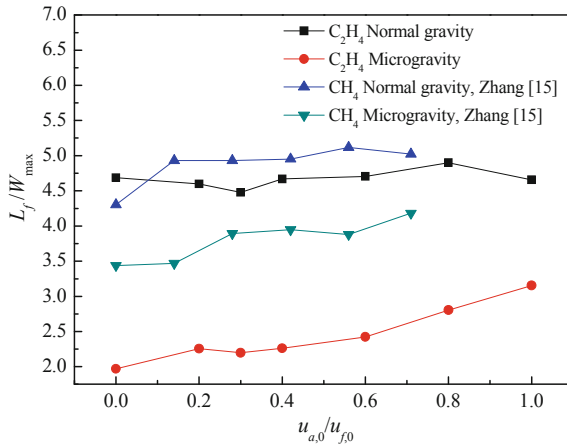
Fig. 6 Ratio of flame length to flame width versus dimensionless air co-flow velocity

3.2 Flame Oscillation

The flame vortex structure is controlled by the Kelvin–Helmholtz and buoyancy instabilities [18, 19], which means that the flame oscillation frequency will be affected by buoyancy and flow field. In this part, the oscillation frequency is determined by fast Fourier transform (FFT) analysis of the flame length images obtained by the high-speed camera.

Sequential images of ethylene flames in normal and microgravities are shown in Fig. 7. The initial fuel flow velocity is 0.1 L/min (0.24 m/s) and the fuel nozzle diameter is 3 mm. It can be seen that the flames in microgravity are stable and the flame oscillation amplitude is almost equal to 0. In normal gravity, the flame oscillation frequency of ethylene flames versus the dimensionless air co-flow velocity is presented in Fig. 8, which shows that the oscillation frequency increases with increasing dimensionless air co-flow velocity in normal gravity.

Figure 9 shows the oscillation frequency of propane flames versus $u_{a,0}$ in normal gravity, where the fuel nozzle diameters are 4, 10, and 12 mm. The oscillation frequency of propane flame presents the similar trend as that of ethylene flame, i.e., the oscillation frequency increases with the increasing co-flow velocity. It can also be found that the effects of fuel flow velocity and fuel nozzle diameter on flame oscillation frequency can be neglected compared to the air co-flow velocity (for the range of tested flow rates). Data of the flame oscillation frequency are summarized in Fig. 10, which shows a linear relationship between the flame oscillation frequency and the volume flow rate of co-flow air ($U_{a,0}$) as: $f = 0.50\,U_{a,0} + 12.4$. By comparing the result with that of Darabkhani et al. [14] $f = 0.33\,U_{a,0} + 11$ in methane flames, we can see that the type of fuel has an effect on the flame oscillation frequency.

Figure 11 plots the propane flame length against the air co-flow velocity, where H-ave presents the average flame length calculated as the mean value of H-max and H-min. As the air co-flow velocity increases, H-min increases while H-max decreases, and H-ave maintains relatively stable.

Figure 12 plots the variation of the flame oscillation amplitude with the air co-flow velocity in normal gravity. It shows that the flame oscillation amplitude decreases with the increasing air co-flow velocity while increasing with the fuel flow velocity. When the air co-flow velocity is large enough (exceeding a critical air co-flow velocity), the flame oscillation is fully suppressed and the oscillation amplitude is 0.

The critical air co-flow velocity of propane flames in normal gravity is plotted in Fig. 13, where the fuel nozzle diameter is 8–14 mm and the fuel flow velocity is 0.015–0.085 m/s. The critical air co-flow velocity increases with the fuel flow velocity and the nozzle diameter.

(a) Normal gravity (left) and microgravity flames (right), $u_{a,0} / u_{f,0} = 0$.

(b) Normal gravity (left) and microgravity flames (right), $u_{a,0} / u_{f,0} = 0.2$.

(c) Normal gravity (left) and microgravity flames (right), $u_{a,0} / u_{f,0} = 0.3$

(d) Normal gravity (left) and microgravity flames (right), $u_{a,0} / u_{f,0} = 0.4$.

(e) Normal gravity (left) and microgravity flames (right), $u_{a,0} / u_{f,0} = 0.6$

(f) Normal gravity (left) and microgravity flames (right), $u_{a,0} / u_{f,0} = 0.8$

(g) Normal gravity (left) and microgravity flames (right), $u_{a,0} / u_{f,0} = 1$

Fig. 7 Sequential images of ethylene flames in normal and microgravities, $u_{f,0} = 0.1$ L/min (0.24 m/s)
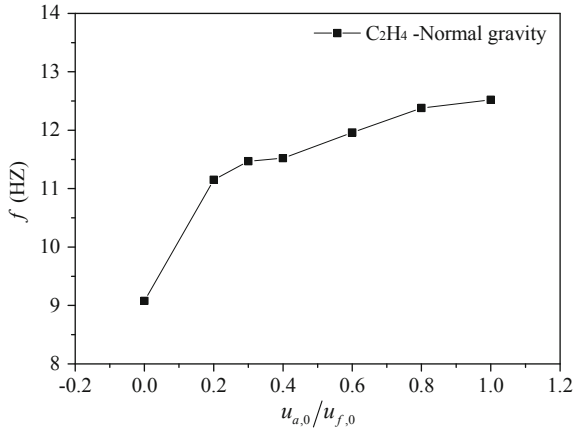
Fig. 8 Oscillation frequency of ethylene flames versus $u_{a,0}/u_{f,0}$ in normal gravity
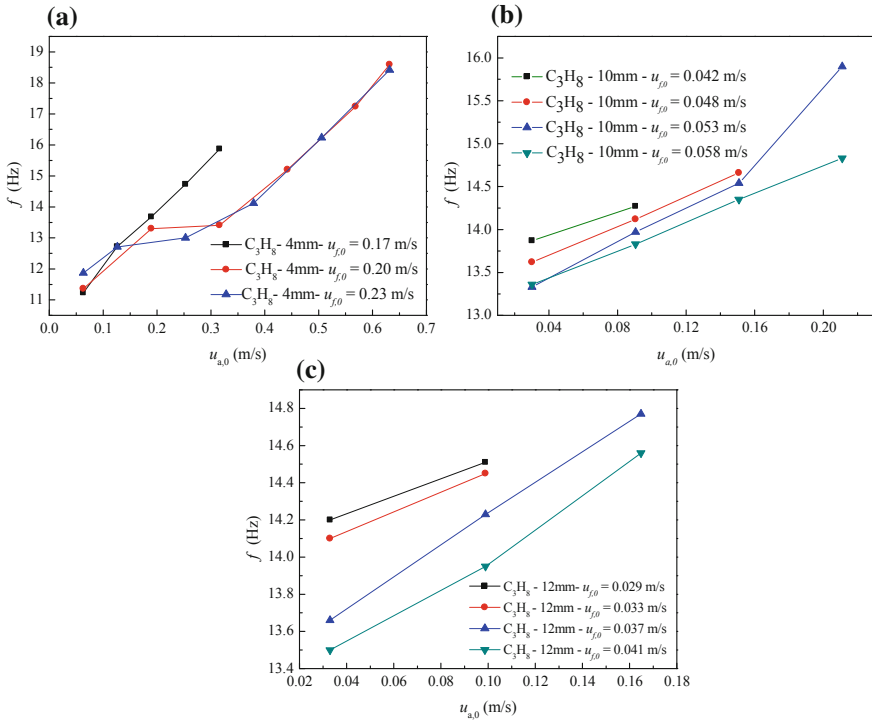
Fig. 9 Oscillation frequency of propane flames versus $u_{a,0}$ in normal gravity with fuel nozzle diameters: **a** 4 mm, **b** 10 mm, and **c** 12 mm

Fig. 10 Experimental and
fitting results of the
oscillation frequency of
propane flame versus $U_{a,0}$ in
normal gravity
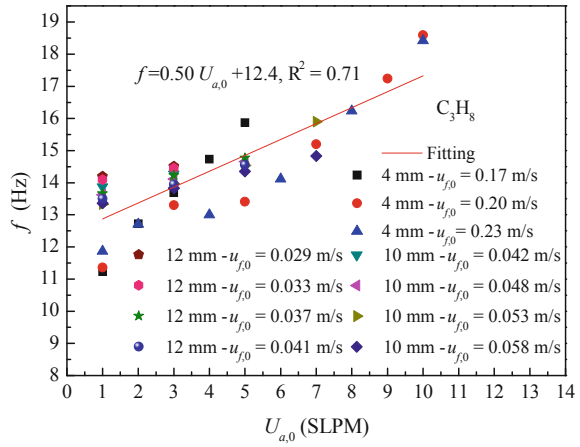
Fig. 11 Flame length of
propane versus $u_{a,0}$ in
normal gravity
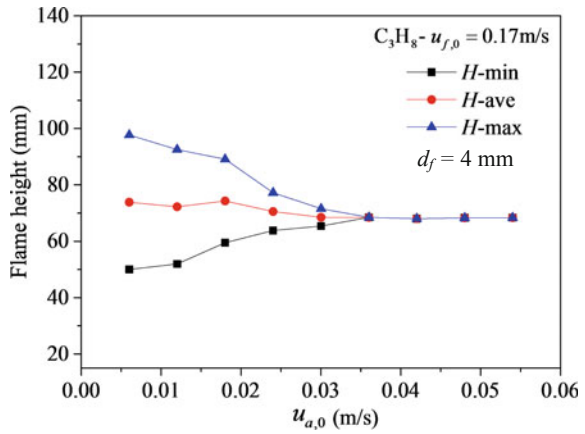
Fig. 12 Flame oscillation
amplitude of propane flames
versus $u_{a,0}$ in normal gravity
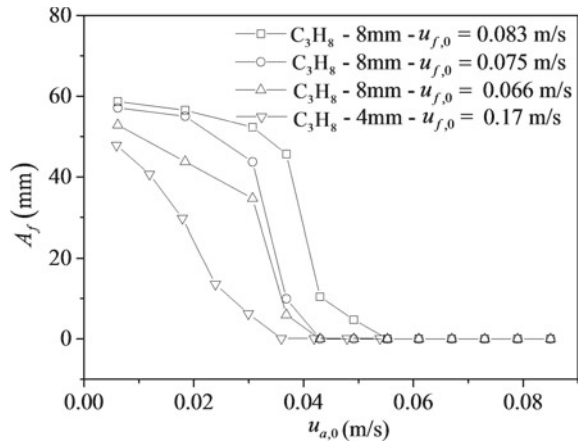
Fig. 13 Critical air co-flow velocity of propane flames in normal gravity
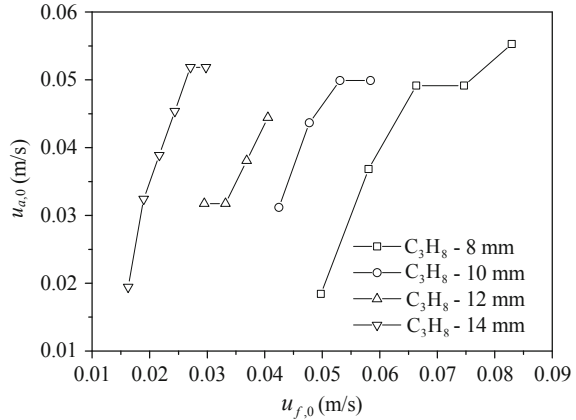
4 Conclusion

The flame shape and oscillation characteristics of laminar-jet co-flow diffusion flames in microgravity and earth gravity were measured under various fuel flow velocities, jet nozzle diameters, and air co-flow velocities. The conclusions are as follows:

(1) The dimensionless flame length and width decrease seriously with the increasing dimensionless air co-flow velocity in microgravity, while they are almost unaffected by the dimensionless air co-flow velocity in normal gravity. The flame length and width are larger in microgravity.

(2) There was no oscillation for ethylene-fueled diffusion flames in microgravity. In normal gravity, the flame oscillation frequency increases while the flame oscillation amplitude decreases with the increasing air co-flow velocity for ethylene and propane flames. The flame oscillation frequency was found to have a linear relationship with the volume flow rate of airflow.

(3) In normal gravity, when the air co-flow velocity is large enough (exceeding the critical value), the flame oscillation of diffusion flames will be suppressed, and the flame oscillation amplitude approaches to 0. The critical air co-flow velocity increases with increasing fuel flow velocity, and a larger critical air co-flow velocity is needed to suppress the flame oscillation for propane diffusion flames with a larger nozzle diameter.

References

1. Sato, H., Amagai, K., & Arai, M. (2000). Diffusion flames and their flickering motions related with Froude numbers under various gravity levels. *Combustion and Flame, 123,* 107–118.
2. Won, S. H., Kim, J., Shin, M. K., Chung, S. H., Fujita, O., Mori, T., et al. (2002). Normal and microgravity experiment of oscillating lifted flames in coflow. *Proceedings of the Combustion Institute, 29,* 37–44.
3. Contreras, J., Consalvi, J.-L., & Fuentes, A. (2017). Oxygen index effect on the structure of a laminar boundary layer diffusion flame in a reduced gravity environment. *Proceedings of the Combustion Institute, 36,* 3237–3245.
4. Nakamura, Y., Yamashita, H., & Saito, K. (2006). A numerical study on extinction behaviour of laminar micro-diffusion flames. *Combustion Theory and Modelling, 10,* 927–938.
5. Bhowal, A. J., & Mandal, B. K. (2017). Numerical simulation of transient development of flame, temperature and velocity under reduced gravity in a methane air diffusion flame. *Microgravity Science and Technology, 29,* 151–175.
6. Charest, M. R. J., Groth, C. P. T., & Gülder, Ö. L. (2011). A numerical study on the effects of pressure and gravity in laminar ethylene diffusion flames. *Combustion and Flame, 158,* 1933–1945.
7. Aalburg, C., Diez, F. J., Faeth, G. M., Sunderland, P. B., Urban, D. L., & Yuan, Z. G. (2005). Shapes of nonbuoyant round hydrocarbon-fueled laminar-jet diffusion flames in still air. *Combustion and Flame, 142,* 1–16.
8. Durox, D., Yuan, T., & Villermaux, E. (1997). The effect of buoyancy on flickering in diffusion flames. *Combustion Science and Technology, 124,* 277–294.
9. Sunderland, P. B., Krishnan, S. S., & Gore, J. P. (2004). Effects of oxygen enhancement and gravity on normal and inverse laminar jet diffusion flames. *Combustion and Flame, 136,* 254–256.
10. Katta, V. R., Goss, L. P., & Roquemore, W. M. (1992). Numerical investigations on the dynamic behavior of a H2-N2 diffusion flame under the influence of gravitational force. In *30th Aerospace Sciences Meeting and Exhibit* (p. 335). Reno, NV, USA.
11. Sato, H., Amagai, K., & Arai, M. (2000). Flickering frequencies of diffusion flames observed under various gravity fields. *Proceedings of the Combustion Institute, 28,* 1981–1987.
12. Lingens, A., Neemann, K., Meyer, J., & Schreiber, M. (1996). Instability of diffusion flames. *Proceedings of the Combustion Institute, 26,* 1053–1061.
13. Kimura, I. (1965). Stability of laminar-jet flames. *Proceedings of the Combustion Institute, 10,* 1295–1300.
14. Darabkhani, H. G., Wang, Q., Chen, L., & Zhang, Y. (2011). Impact of co-flow air on buoyant diffusion flames flicker. *Energy Conversion and Management, 52,* 2996–3003.
15. Zhang, D., Fang, J., Guan, J. F., Wang, J. W., Zeng, Y., Wang, J. J., et al. (2014). Laminar jet methane/air diffusion flame shapes and radiation of low air velocity coflow in microgravity. *Fuel, 130,* 25–33.
16. Dai, Z., Xu F., & Faeth, G. (2001). Shapes of soot-free laminar coflowing jet diffusion flames. In *39th Aerospace Sciences Meeting and Exhibit* (p. 1078).
17. Kuo, K. K. (2005). *Principles of combustion* (2nd ed.). Hoboken, NJ, United States: Wiley.
18. Chen, M., Herrmann, M., & Peters, N. (2000). Flamelet modeling of lifted turbulent methane/air and propane/air jet diffusion flames. *Proceedings of the Combustion Institute, 28,* 167–174.
19. Darabkhani, H. G., & Zhang, Y. (2010). Stabilisation mechanism of a flickering methane diffusion flame with co-flow of air. *Engineering Letters, 18,* 369.

Importance of Intersystem Crossing on Flammability Properties of Carbon Disulphide (CS$_2$)

Zhe Zeng, Bogdan Z. Dlugogorski, Ibukun Oluwoye and Mohammednoor Altarawneh

Abstract Carbon disulphide (CS$_2$) represents an important chemical commodity, unfortunately, found responsible for several factory, laboratory and transportation fires. This contribution examines the high flammability of CS$_2$ by exploring the fire chemistry of the intersystem crossing (ISC) process that occurs within the two key elementary reactions. By expanding the potential enthalpy surfaces of CS + O$_2$ reaction into three-dimensional space, we reveal the unusual changeover from the triplet surface onto the singlet surface through the ISC point. We calculate the minimum energy crossing point to locate the ISC structure, resulting in a lowered activation energy for the CS$_2$ + O$_2$ and CS + O$_2$ reactions. This enables us to explain the low ignition temperature and high flammability of CS$_2$, a common compound in the chemical industry.

Keywords Flammability · Potential enthalpy surface (PES) · Intersystem crossing (ISC) · Minimum energy crossing point (MECP)

1 Introduction

Carbon disulphide (CS$_2$) has found numerous applications in chemical industries and, as a non-polar solvent, in laboratories. However, it displays extreme flammability that identifies CS$_2$ as a hazardous material [1]. As an important feedstock in the manufacturing of fibres [2] and fertilisers [3], CS$_2$ initiated several factory [4] and transportation [5] fires. Fire accidents of flammable chemicals usually involve significant human and material losses, such as those in chemical warehouses or in haulage. These fires tend to induce explosions and contaminate local communities

Z. Zeng · I. Oluwoye · M. Altarawneh (✉)
Discipline of Chemistry and Physics, College of Science, Health, Engineering and Education (SHEE), Murdoch University, 90 South Street, Murdoch, Perth, WA 6150, Australia
e-mail: M.Altarawneh@murdoch.edu.au

B. Z. Dlugogorski
Office of Deputy Vice Chancellor Research & Innovation, Charles Darwin University, Darwin, NT 0909, Australia

Table 1 Comparison of flammability between CS_2 and other flammable species

Fuel type	Flash point (°C)	Auto-ignition temperature (°C)
White phosphorous (P)		34
Carbon disulphide (CS_2)	**−43**	**90**
Ethanol (C_2H_5OH)	17	365
Gasoline	−43	280

with toxic products of combustion. As a widely employed non-polar solvent, CS_2 also causes fires in laboratories, often resulting in significant economic losses [6].

Pure CS_2 exists as a colourless volatile liquid at room temperature (25 °C) with a boiling point of 46 °C. The low flash point of CS_2 of −43 °C signifies its prominent flammability, as does its auto-ignition temperature that is as low as 90 °C [7]. Mixtures of CS_2–O_2, initially present between 190 and 300 °C and under ambient pressure, explode spontaneously [8], indicating high explosion propensity of CS_2. Table 1 compares the flash point and the auto-ignition temperature of CS_2 with other flammable chemicals. The flash point of CS_2 matches that of gasoline, while its auto-ignition temperature does not even exceed that of white phosphorous by 60 °C.

Although CS_2 exhibits dangerous flammability, detailed understanding of its oxidation chemistry remains elusive. For a flammable species, the reaction rate of the initiation steps defines its ignition temperature, while its explosion propensity depends on the rate of chain-branching and propagation reactions. Based on the accurate theoretical calculations of the triplet (ground state) reaction surface, Glarborg et al. have developed a detailed mechanism of the CS_2 oxidation, with $CS_2 + O_2 \rightarrow COS + SO$ ($E_a = 251$ kJ/mol) as the main initiation reaction and $CS + O_2 \rightarrow CO + SO$ ($E_a = 117$ kJ/mol) as an important chain propagation step [9]. However, this mechanism over-predicts the ignition temperature of CS_2 in a tubular-flow reactor by as much as 260 °C [10], failing to explain the extreme flammability of CS_2. Clearly, the activation energies of the chain initiation step as well as those of the chain propagation corridors are too high to account for the observed ignition temperature of CS_2.

We have recently investigated the oxidation of CS_2 in a tubular-flow reactor, validating its high flammability as a result of low ignition temperature [11]. We introduced the intersystem crossing (ISC) process into the key elementary reactions. The occurrence of ISC reduces the activation barrier of sensitive chain initiation and chain propagation steps. ISC represents the transition between two electronic states with different spin multiplicities at the same energy level. In the case of CS_2, triplet oxygen ($CS_2 + {}^3O_2$ and $CS + {}^3O_2$) initiates the oxidation process. The reaction soon enters the singlet pathway through the ISC points located on the potential energy surface (PES), offering an alternative reaction corridor with much lower activation barriers. Figure 1 demonstrates the calculated potential enthalpy surface (PES) for the chain initiation $CS_2 + {}^3O_2$ and chain propagation $CS + {}^3O_2$. Although the figure illustrates the crossover between the triplet and the singlet reaction channels, we
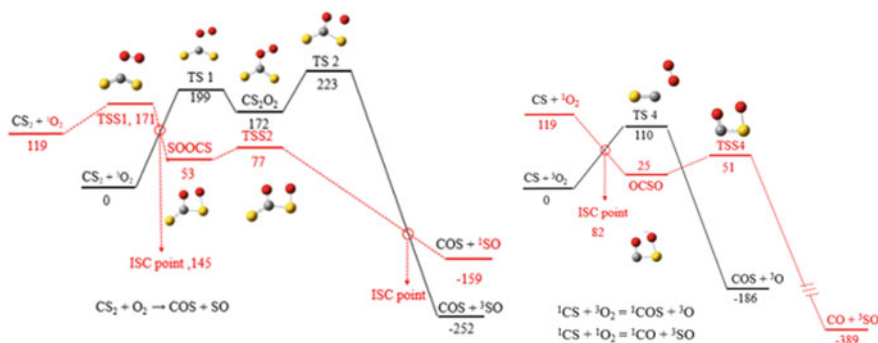
Fig. 1 Potential enthalpy surface of $CS_2 + O_2$ and $CS + O_2$ for both singlet and triplet reaction pathway in our previous work [11]. All enthalpy values are in reference to the separate reactants ($CS_2 + {}^3O_2$) and ($CS + {}^3O_2$), respectively, in kJ/mol at 298.15 K

neither validate the occurrence of the ISC process nor capture the precise geometry of ISC structures. The relative enthalpies of the ISC points were simply estimated by considering the upper and lower limits in the PES.

The present study employed quantum chemistry calculations to further investigate the ISC processes of the elementary $CS + O_2$ and $CS_2 + O_2$ reactions. We expanded the PES mapping of $CS + O_2$ into the three-dimensional space in search for the crossing-over point between the initial triplet surface and excited singlet reaction surface. A series of ISC points have been located, featured with identical geometries and energy levels, but different in electronic states. Finally, we applied the minimum energy crossing point (MECP) calculation to pinpoint the transition structure. We confirmed that a series of ISC points provide alternative reaction pathways, which lowers the reaction barrier of chain initiation and chain propagation process to explain the fire hazard of CS_2.

2 Methodology

We employed density functional theory (DFT) calculations to develop an improved understanding of ISC in $CS + O_2$ and $CS_2 + O_2$ reactions. Gaussian 09 software package [12] facilitated all structural optimisations and energy calculations by deploying the meta-hybrid M062X density function with 6–311++G(3df, 3pd) basis set [13]. Previous work on 267 different molecules verified the limit of accuracy of the M062X method to be 3.15 kJ/mol [14]. We applied the intrinsic reaction coordinate (IRC) calculation [15] to confirm the reaction pathways. By preparing the adjacent structures of the calculated transition state, we constructed the three-dimensional PES of both singlet and triplet reaction pathways to locate a series of ISC points. Finally, we determined the minimum energy crossing point by following the algorithm proposed by Chachiyo and Rodriguez [16], as implemented by the Siam Quantum (SQ)

software packages [17]. The Chemkin Pro [18] enabled the kinetic modelling to validate the flammability of CS_2 by comparing its ignition temperature with those of H_2 and CH_4.

3 Results and Discussion

3.1 *Location of ISC Points of CS + O₂ Reaction*

In order to locate the crossover points between the singlet and triplet reaction surfaces of CS_2 oxidation, we begin with $CS + O_2$ reaction to reduce the geometrical complexity. The idea here is to find the structures for which singlet and triplet states share the same energy level. Another premise to follow remains that the reaction has to initiate on the triplet pathway (ground state, $CS + {}^3O_2$) and transit into the singlet corridor. The $CS + O_2$ system has four atoms being fitted to a plane to minimise the degree of freedom (DOF). As demonstrated in Fig. 2, the S atom has one DOF, while the two O atoms individually have two DOF, relatively to the carbon backbone. Conducting an exhaustive search with a grid of 10 for each DOF, i.e. listing all the possible structures and calculating their respective enthalpies at both singlet and triplet electronic states yields $10 \times 10 \times 10 \times 10 \times 10 \times 2 = 2 \times 10^5$ files. In $CS_2 + O_2$ reaction, the extra sulphur atom results in an additional two DOF and 2×10^7 files for the Gaussian package to execute. Although this could be a comprehensive method to find all ISC structures, it seems computational too costly even with the aid of a supercomputer.

Considering the fact that the reaction starts with reactants in their ground state $CS + {}^3O_2$, and then crosses into the singlet pathway before encountering the triplet transition state, we investigated the potential crossover between $CS + {}^3O_2$ and TS4,

Fig. 2 Degree of freedom of CSOO system and selection of variables in the structure
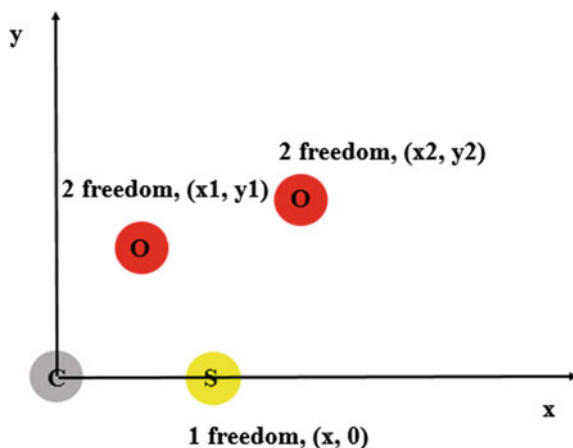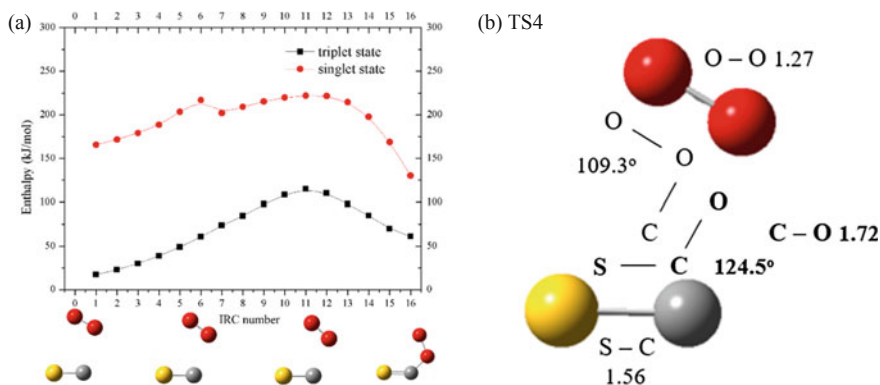
Fig. 3 **a** Triplet and singlet relative enthalpy of the structures along the intrinsic reaction coordinate (IRC) of triplet TS4; **b** Structure variables in CSOO system: angle S–C–O, angle C–O–O, distance C–S, distance C–O, distance O–O. In this case, we fix the angle C–O–O at 109.3°, distance C–S at 1.56 Å, distance O–O at 1.27 Å, and vary only the **angle S–C–O** and **distance C–O** (in bold) nearby the geometry of TS4 structure

as shown in Fig. 1. The intrinsic reaction coordinate (IRC) calculation of TS4 (in triplet state) provided the geometries of the structures along the reaction pathway. Subsequently, we performed separate calculations to estimate the relative enthalpies of these structures in singlet state. Figure 3a compares the relative enthalpies on triplet and singlet surface along the reaction pathway linking $CS + {}^3O_2$ to TS4. No crossover point exists between the two PESs. The relative enthalpies of singlet states are all higher than those of triplet states with the same geometries. Therefore, it seems that two-dimensional reaction surfaces cannot locate the crossing-over point.

We propose that the ISC may not necessarily go through the reaction coordinate of triplet pathway. Therefore, we broaden our searching area just around the triplet transition state. By varying the angle S–C–O and distance C–O (Fig. 3b), we intended to map the three-dimensional PES for both singlet and triplet states. This included the geometry of triplet TS4 and singlet OCSO as similar as possible. We then compared the relative enthalpies of the resulting singlet and triplet structures to locate the ISC points.

Figure 4 demonstrates the structures of CSOO system prepared to map the PES of $CS + O_2$ reaction. We based all the structures on the geometry of TS4 shown in Fig. 3b. We fixed the angle C–O–O, and the distances C–S and O–O to be identical to TS4, varying the angle S–C–O and distance C–O to represent other important structures in PES, such as initial reactant (similar to O15), singlet OCSO (similar to A1) and the final product (similar to A15). In Fig. 4, The C–S bond length increases from 1.2 to 2.32 Å (A–O), and the angle S–C–O changes from 80° to 178° (1–15) to achieve the 15 × 15 geometry matrix.

The meta-hybrid M062X density functional along with the basis set of 6–311++G(3df, 3pd) afforded the quantum chemistry calculation for the structures prepared in Fig. 4. We compared the performance of M062X in the CS_2–O_2 system with the complete basis set CBS-QB3 method [11], resulting in a difference

singlet			1	2	3	4	5	6	7	8	9	10	11	12	13	14	15
			S-C-O	S-C-O	S-C-O	S-C-O	S-C-O	S-C-O	S-C-O	S-C-O	S-C-O	S-C-O	S-C-O	S-C-O	S-C-O	S-C-O	S-C-O
			80	87	94	101	108	115	122	129	136	143	150	157	164	171	178
A	C-S	1.2															
B	C-S	1.28															
C	C-S	1.36															
D	C-S	1.44															
E	C-S	1.52															
F	C-S	1.6															
G	C-S	1.68						Relative enthalpy									
H	C-S	1.76															
I	C-S	1.84															
J	C-S	1.92															
K	C-S	2															
L	C-S	2.08															
M	C-S	2.16															
N	C-S	2.24															
O	C-S	2.32															
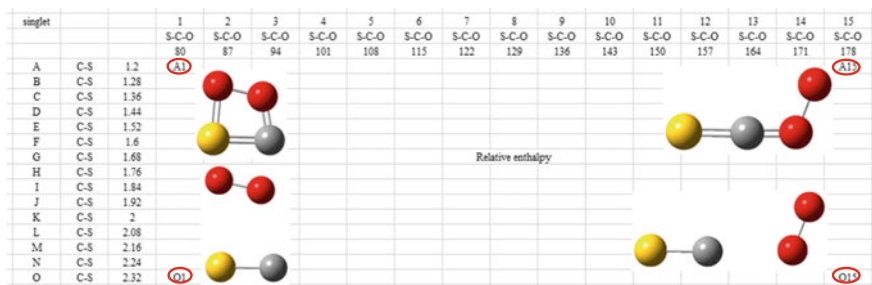
Fig. 4 Geometries prepared for the three-dimensional potential enthalpy surfaces of the $CS + {}^3O_2$ reaction. For the five DOF, we fixed the angle C–O–O at 109.3°, distance C–S at 1.56 Å, distance O–O and vary only angle S–C–O and distance C–O nearby the geometry of the TS4 structure, as shown in Fig. 3b

of 9.8 kJ/mol. Figure 5 illustrates the calculated three-dimensional PES of both triplet and singlet channels. The three-dimensional PES (Fig. 5) also depicts the two-dimensional reaction process in Fig. 1. Only one saddle point (at TS4) exists on the triplet reaction surface. Meanwhile, on the singlet reaction surface, the reactants initially form the singlet OCSO adduct via a barrier less step that subsequently undergoes the singlet TSS4 to form the respective products. The increasing trend of triplet reaction surface and the descending pattern on singlet reaction surface will intersect somewhere to give the ISC points.

Furthermore, we have compared the two PESs in Fig. 5 to extract the ISC points. Figure 6a demonstrates the crossover between the triplet reaction surface and that of the singlet reaction for $CS + {}^3O_2$. We observed the intersection between the increasing trend of triplet surface and the descending trend of singlet surface. Figure 6b locates the ISC points between triplet state and singlet state. It is remarkable to obtain these ISC points as they share the same geometry and relative enthalpy level, but different electron spin state. The relative enthalpies of ISC points vary from 84 to
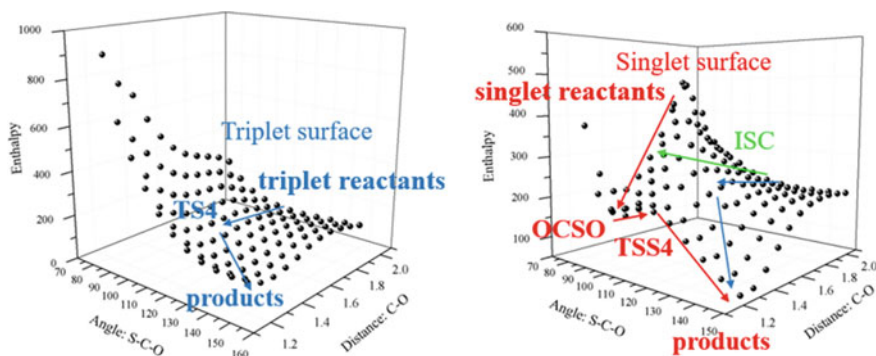
Fig. 5 Three-dimensional potential enthalpy surface calculated for fixed geometry with different electronic state (triplet and singlet), unit in kJ/mol
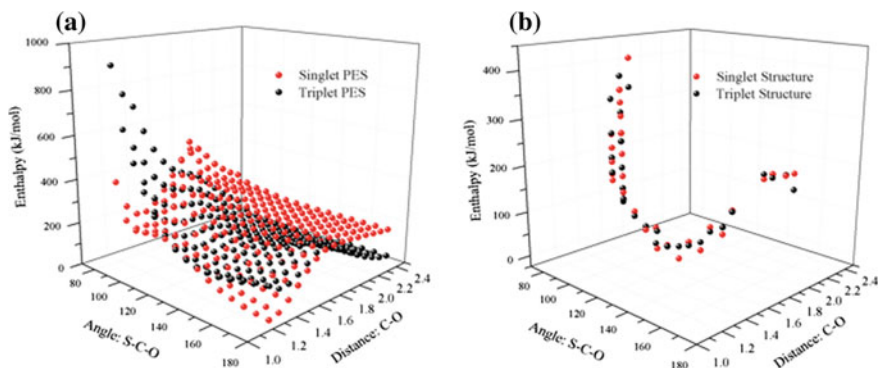
Fig. 6 **a** Crossover between singlet reaction surface and triplet reaction surface for $CS + {}^3O_2$ reaction; **b** Crossing-over points located for $CS + {}^3O_2$ reaction

374 kJ/mol. Considering the activation barrier (110 kJ/mol) on triplet reaction pathway, the ISC points indeed provide an alternative channel for $CS + {}^3O_2$ reaction. As shown in Fig. 7, we propose the most plausible reaction pathway for the ISC process of reaction $CS + {}^3O_2$. The ISC point occurs prior to the singlet TSS4, agreeing well with the results in Fig. 1.

Although we have found a series of ISC points for $CS + {}^3O_2$ reaction, they appear to be a small portion of numerous plausible structures. In this case, we have fixed the angle C–O–O, the distance C–S and the distance O–O at a specific value.
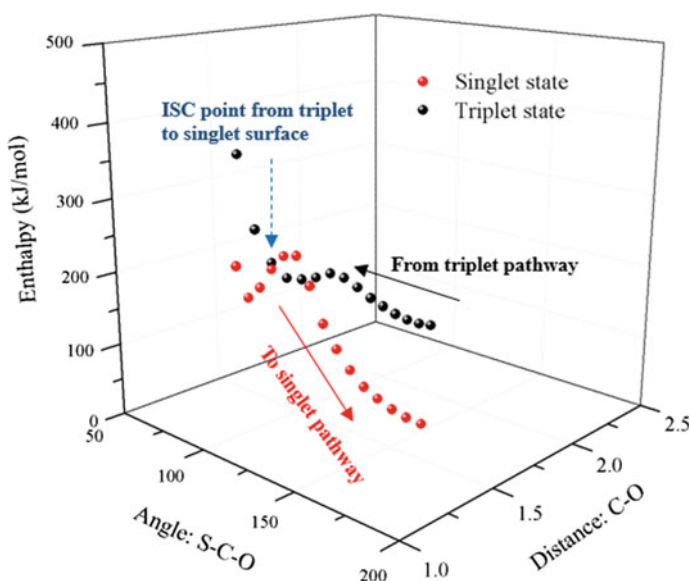
Fig. 7 The most plausible reaction pathway for ISC process of reaction $CS + {}^3O_2$

If we consider the relaxation of these geometries, we could achieve lower relative enthalpy of the CSOO system, which means ISC points with lower barriers. In the next section, we search the minimum energy crossing point (MECP) between two reaction surfaces to obtain the ISC with the lowest activation barrier.

3.2 Minimum Energy Crossing Point (MECP) Calculation for $CS + O_2$ and $CS_2 + O_2$

We obtained a visual understanding of the ISC process by calculating the potential enthalpy surface of $CS + O_2$ reaction. The reaction initiates from triplet-state reactants, proceed through the ISC point (i.e. OCSO) before the TSS4 and then into singlet reaction surface. However, due to the fixed parameters (such as the angle C–O–O, the distance C–S and the distance O–O) comparatively to the geometry of triplet TS4, the relative enthalpies of the singlet OCSO and TSS4 in Fig. 5 reside at 151 and 198 kJ/mol. These appear relatively high compared to the enthalpy values of the optimised structure in Fig. 1. However, expanding our calculation by varying the three fixed parameters will increase the cost of computation by at least a factor of 10^3.

In order to obtain the most feasible ISC points, we adopt the minimum energy crossing point (MECP) algorithm developed by Chachiyo and Rodriguez [16] in Siam Quantum software [17]. The algorithm searches for the minimum energy crossing point (MECP) between the two reaction surfaces after optimising the initial guesses (i.e. the pseudo input files) in both singlet and triplet states. For $CS + {}^3O_2$ reaction, the optimised triplet structure falls into the products of triplet pathway $COS + {}^3O$, while the fully relaxed singlet structure yields reactants on the singlet pathway $CS + O_2$. We obtained the MECP structure linking the two reaction pathways as shown in Fig. 8. Also, we calculated the energy level of the MECP structure for CSOO system in both singlet and triplet states, employing the Hartree–Fock (HF) approximation. Although the singlet state and triplet state of MECP structure have different electron spin states (as shown in Fig. 8b), the difference in energy level is 2.25 kJ/mol only, residing within the error range of HF method of 60 kJ/mol (Fig. 9).

$$\text{HF energy}|\text{tri\_MECP\_CSOO} - \text{sin\_MECP\_CSOO}| = 2.25 \, \text{kJ/mol}.$$

It is also worthwhile to mention that the HF method features a considerably large error limit as compared to relatively higher level of theory, such as Møller-Plesset perturbation theory (MP2) and DFT. We have conducted the MECP calculation for $CS_2 + {}^3O_2$ reaction, resulting in the MECP structure between $({}^3CS_2O + {}^3O)$ and singlet SOOCS. The relative enthalpy of MECP structure locates 42 kJ/mol above that of singlet SOOCS. We also calculated the energy level of the MECP structure for the CS_2O_2 system on both singlet and triplet state, returning a difference 0.03 kJ/mol in term of energy level.

$$\text{HF energy}|\text{tri\_MECP\_CS}_2\text{O}_2 - \text{sin\_MECP\_CS}_2\text{O}_2| = 0.03\,\text{kJ/mol}$$

By comparing the energy level of MECP points with the relevant structures on the PES, we now have an estimation of the energy level of ISC points for both $CS + O_2$ and $CS_2 + O_2$. Figure 10 updates the relative enthalpy of the estimated ISC points with MECP structures. For $CS_2 + O_2$ reaction, the ISC process offers an alternative reaction route by reducing the activation enthalpy from 199 to 95 kJ/mol. For $CS + O_2$ reaction, the activation barrier drops from 119 to 90 kJ/mol. This unusual process explains the high flammability and fire hazard of CS_2 in the chemical industry.

Heretofore, we have illustrated the transition pathway from triplet surface to singlet surface through the ISC points. By adopting the algorithm of Chachiyo and Rodriguez [16] to calculate the minimum energy of crossing points (MECP), we have located the relative enthalpy level of the ISC points for $CS + O_2$ and $CS_2 + O_2$. However, as pointed out by Harvey [19], the probability of hopping from one surface to the other in the vicinity of the crossing region is still unknown and open to speculation. Here we used the relative enthalpy value of the ISC points as the activation energy of the reaction, and adopted the pre-exponential factor proposed in our previous results [11] to update the rate parameter of $CS + O_2$ and $CS_2 + O_2$ as:

$$k_{CS+O_2} = 8.1 \times 10^{12} \times e^{-90/RT}$$
$$k_{CS_2+O_2} = 4.1 \times 10^{12} \times e^{-95/RT}$$
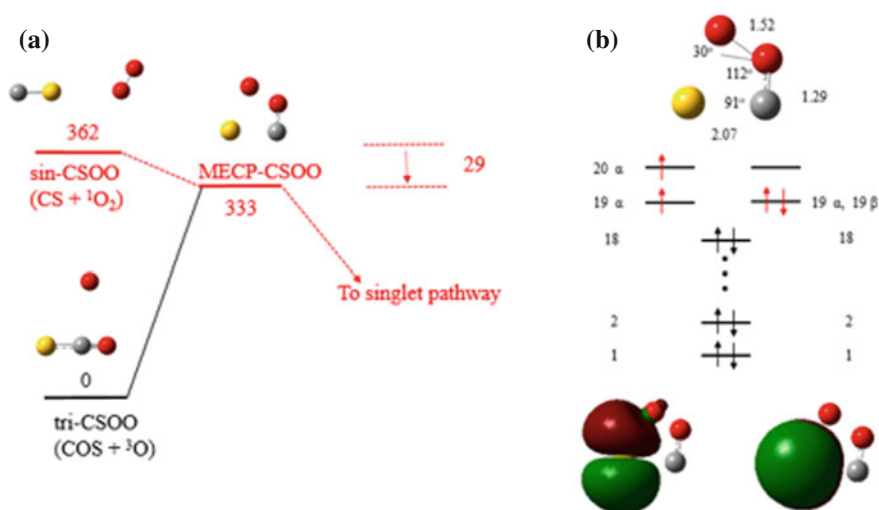
Fig. 8 a MECP calculation for $CS + O_2$ reaction with HF level of theory, the relative enthalpy (kJ/mol) is in comparison with the tri-CSOO; **b** The geometry and electron distribution for the MECP structure, geometry units in Å and degree
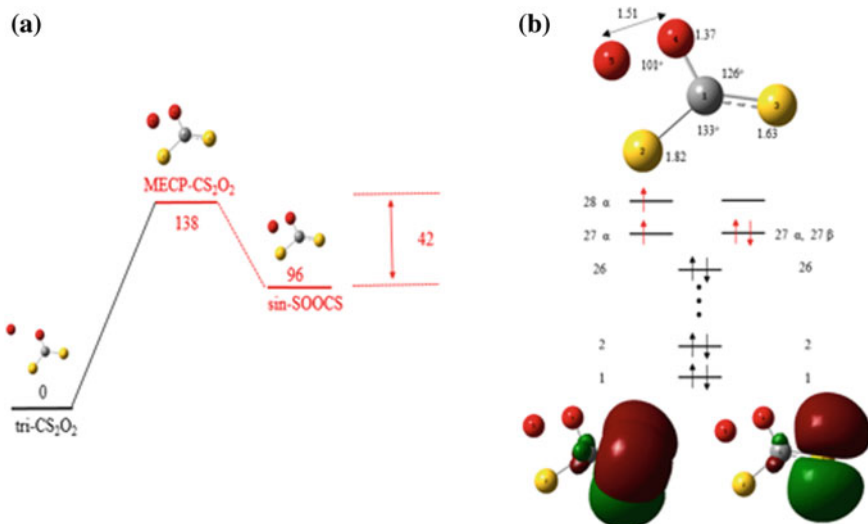
Fig. 9 a MECP calculation for $CS_2 + O_2$ reaction with HF level of theory, the relative enthalpy (kJ/mol) is in comparison with the tri-CS_2O_2; **b** The geometry and electron distribution for the MECP structure, geometry units in Å and degree
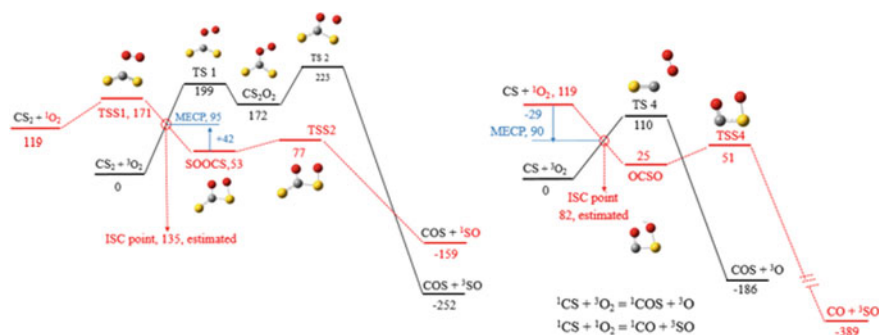
Fig. 10 Potential enthalpy surface updated with MECP calculation for $CS_2 + O_2$ and $CS + O_2$ under both singlet and triplet reaction pathway. All enthalpy values are in reference to the initial reactants ($CS_2 + {}^3O_2$) and ($CS + {}^3O_2$), respectively, in kJ/mol at 298.15 K

The updated mechanism of CS_2 oxidation enabled us to conduct the kinetic modelling within tubular-flow reactor to validate against the experimental results from our previous work [11]. Our updated mechanism captures well the low ignition temperature of CS_2 as depicted in Fig. 11. Out of curiosity, we also calculated the ignition temperature of H_2 [20] and CH_4 [21] under equivalent condition within the tubular-flow reactor. As expected, the ignition temperature of CS_2 is much lower than that of H_2 and CH_4, confirming the high flammability and fire hazard of CS_2 as discussed in this study.
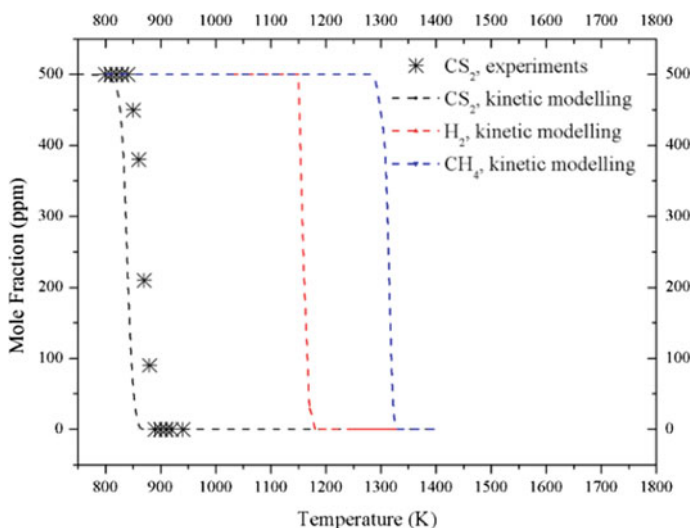
Fig. 11 Comparison of ignition temperature of CS_2 with that of H_2 and CH_4 under stoichiometric condition in tubular-flow reactor at 0.3 s residence time ([CS_2]: [O_2] = 500 ppm: 1250 ppm; [H_2]: [O_2] = 500 ppm: 250 ppm; [CH_4]: [O_2] = 500 ppm: 1000 ppm). The experimental results for CS_2 oxidation originate from our previous work [11], and the mechanism for CS_2 oxidation is updated with the rate parameter of $CS_2 + {}^3O_2$ and $CS + {}^3O_2$ proposed in this work. We adopt the AramcoMech 2.0 [21] for kinetic modelling of CH_4 oxidation and O'Conaire et al.'s mechanism [20] for modelling of H_2 oxidation

4   Conclusion

The paper inspects the fire chemistry and the flammability of CS_2. By examining the three-dimensional potential enthalpy surfaces of $CS + O_2$ reaction, we manage to visualise the unusual ISC process from triplet surface to singlet surface. Further minimum energy crossing point (MECP) calculation facilitates precise selection of the crossing point with the lowest activation barrier, offering an alternative pathway compared to the traditional triplet reaction pathway with high activation energy. This unusual process within $CS_2 + O_2$ and $CS + O_2$ reactions lowers the activation barrier from 223 and 110 kJ/mol to 95 and 90 kJ/mol, respectively. This explains the low ignition temperature CS_2, affording a new perspective to study the flammability of CS_2 as widely used in the chemical industry.

References

1. Bodner, G. M. (1985). Lecture demonstration accidents from which we can learn. *Journal of Chemistry Education, 62,* 1105.
2. Sherwood, P. W. (1963). Raw materials for man-made fibers. *Industrial and Engineering Chemistry, 55,* 37–42.
3. Zhao, F., Hawkesford, M., & McGrath, S. (1999). Sulphur assimilation and effects on yield and quality of wheat. *Journal of Cereal Science, 30,* 1–17.
4. Chittora, S., & Dwivedi, A. K. Recent trends in safety management system in carbon disulphide plant: A research.
5. Praveen, M. P. Safety takes a back seat in transportation of chemicals. http://www.thehindu.com/news/cities/Kochi/Safety-takes-a-back-seat-in-transportation-of-chemicals/article16091178.ece.
6. Lab Safety Fire Incidents—Chemical-based. https://www.aiha.org/get-involved/VolunteerGroups/LabHSCommittee/Incident%20Pages/Lab-Safety-Fire-Incidents—Chemical-based.aspx. Accessed 04/01/2018.
7. Wikipedia. http://en.wikipedia.org/wiki/Carbon_disulfide.
8. Hanst, P. L., & Myerson, A. L. (1954). Absorption spectroscopy of explosions. *Review of Scientific Instrument, 25,* 469–470.
9. Glarborg, P., Halaburt, B., Marshall, P., Guillory, A., Troe, J., Thellefsen, M., et al. (2014). Oxidation of reduced sulfur species: Carbon disulfide. *The Journal of Physical Chemistry A, 118,* 6798–6809.
10. Abián, M., Cebrián, M., Millera, Á., Bilbao, R., & Alzueta, M. U. (2015). CS_2 and COS conversion under different combustion conditions. *Combustion and Flame, 162,* 2119–2127.
11. Zeng, Z., Dlugogorski, B. Z., & Altarawneh, M. (2017). Flammability of CS_2 and other reduced sulfur species. *Fire Safety Journal, 91,* 226–234.
12. Frisch, M. J., Trucks, G. W., Schlegel, H. B., Scuseria, G. E., Robb, M. A., Cheesema, J. R., et al. (2009). Gaussian 09, Revision B.01, Wallingford CT.
13. Zhao, Y., & Truhlar, D. (2008). The M06 suite of density functionals for main group thermochemistry, thermochemical kinetics, noncovalent interactions, excited states, and transition elements: Two new functionals and systematic testing of four M06-class functionals and 12 other functionals. *Theoretical Chemistry Accounts, 120,* 215–241.
14. Zhao, Y., & Truhlar, D. G. (2008). Exploring the limit of accuracy of the global hybrid meta density functional for main-group thermochemistry, kinetics, and noncovalent interactions. *Journal of Chemical Theory and Computation, 4,* 1849–1868.
15. Fukui, K. (1981). The path of chemical reactions-the IRC approach. *Accounts of Chemical Research, 14,* 363–368.
16. Chachiyo, T., & Rodriguez, J. H. (2005). A direct method for locating minimum-energy crossing points (MECPs) in spin-forbidden transitions and nonadiabatic reactions. *The Journal of Chemical Physics, 123,* 094711.
17. Chachiyo, T., et al. (2016). Siam quantum: A compact open-source quantum simulation software for molecules, Thailand.
18. Reaction Design, San Diego, CHEMKIN-PRO (2013).
19. Harvey, J. N. (2007). Understanding the kinetics of spin-forbidden chemical reactions. *Physical Chemistry Chemical Physics, 9,* 331–343.
20. Conaire, M. Ó., Curran, H. J., Simmie, J. M., Pitz, W. J., & Westbrook, C. K. (2004). A comprehensive modeling study of hydrogen oxidation. *International Journal of Chemical Kinetics, 36,* 603–622.
21. Metcalfe, W. K., Burke, S. M., Ahmed, S. S., & Curran, H. J. (2013). A hierarchical and comparative kinetic modeling study of C1 – C2 hydrocarbon and oxygenated fuels. *International Journal of Chemical Kinetics, 45,* 638–675.

Fire and Smoke Modeling and Experiment

Unsteady Three-Layer Fluid Model for Smoke Movement Prediction

Keichi Suzuki

Abstract This paper describes a new method for modeling smoke movement within large rooms. The model includes horizontally two-dimensional and three laminar flows including the ceiling jet, reversed flow, and airflow. This model is practical because it can predict three-dimensional temperature distributions of any points in the volume simulations in a short time. For simple validation, predictions delivered by the model are compared to the measurements from fire experiments in a large building. The predicted gas temperature profiles agree qualitatively with the measurement, and then the performance of the model is generally acceptable.

Keywords Modeling · Compartment fires · Ceiling jet · Reversed flow · 3-layer

Nomenclature

c_p	Specific heat of air (kJ/kg K)
g	Gravitation acceleration (m^2/s)
h	Depth of layer (m)
H	Ceiling height from fire source (m)
P	Pressure (Pa)
q''	Heat loss to ceiling (kW/m^2)
t	Time (s)
ΔT	Gas temperature rise (K)
u	Velocity of the x-axis (m/s)
v	Velocity of the y-axis (m/s)
v_0	Horizontal velocity at edge of plume near ceiling (m/s)
w	Vertical velocity in fire plume (m/s)
x	Horizontal coordinate (m)
y	Horizontal coordinate (m)
z	Vertical coordinate (m)

K. Suzuki (✉)

Institute of Technology Shimizu Corporation, 3-4-17 Etchujima, Koto-Ku, Tokyo 1358530, Japan
e-mail: keichi@shimz.co.jp

Greek Symbols

β Buoyancy factor ($=1/T_\infty$)
γ Ceiling jet profile factor ($=1.16$)
τ_w Wall shear stress (kgf/m^2)
ρ Gas density (kg/m^3)

Subscripts

max   Maximum value in vertical profile
u   Ceiling jet
m   Reversed flow
l   Air layer
∞ Ambient
0   Initial value of ceiling jet
p   Plume

1 Introduction

In the practical fire safety design for buildings, two-layer zone models are more often used than computational fluid dynamics (CFD) simulations because of the short computation times. In this model, the domains are divided into only two layers in which the gas properties are assumed to be uniform and the heat and gas productions are assumed to diffuse instantaneously. The image of the model is shown in Fig. 1a. For a small room, these assumptions are acceptable; however, they are not appropriate for a large room because the temperatures and the smoke depths are not uniform owing to the heat lost to the ceiling and the smoke spreading in the transitional step, as shown in Fig. 1b. An analytical approach that works successively along the flow is then necessary for detailed simulations of smoke properties.

In a similar manner, the ceiling jet, which is the layered flow below the ceiling that stems from the vertical floating flow above the fire plume, has been studied since its initial formulation in the 1950s by Alpert [1, 2]. Alpert generalized the theory of ceiling jet and indicated that the velocities, temperatures, and thicknesses of it in steady fires under unconfined ceilings can be clearly predicted by analytical methods if the horizontal distance from the fire is less than twice the ceiling height [1]. However, prediction of the temperature distribution in a large space is difficult with the theory. Thus, I have previously developed the ceiling jet model for predicting the unsteady smoke flows in large spaces [3]. This model is also more advantageous than two-layer zone models because the velocities, gas temperatures, and depths of the ceiling jet can be computed at any distance from the fire. However, this ceiling jet
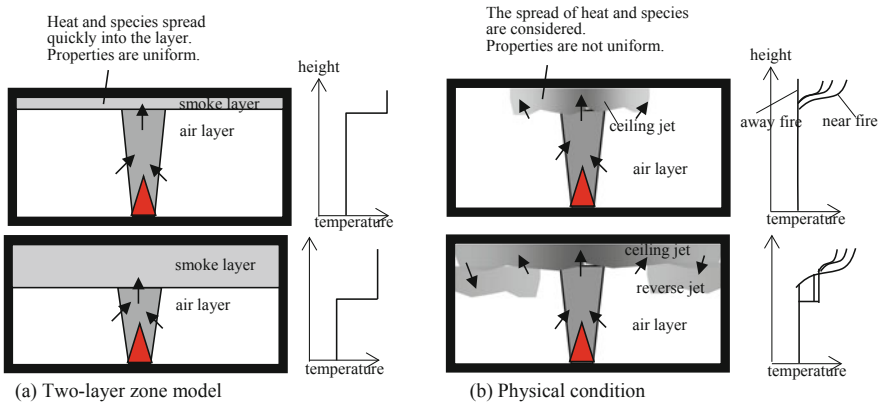
Fig. 1 Comparison of the two-layer zone model and physical condition

model did not model the smoke flow returning from the walls, so it is only appropriate for predictions in the early stage of a fire before smoke flows return from the walls. The present study extends the new model includes horizontal two-dimensional and three vertical laminar flows, which included the returning flow from the walls. This model is more practical because it can predict three-dimensional temperature distributions in a large room. I compared predictions delivered by the model to measurements from fire experiments in a large room. Compared with CFDs simulations, the model is not as precise because it adopts a simple function for interlamellar mixtures based on waterway experiments and introduces assumptions for the flow behavior after collisions with the ceiling and walls instead of detailed turbulence models like LES. However, the model characterizes the smoke flows measured in the experiment and consumed much less time than CFD simulations. This lightness is made possible mainly by assuming three vertical layers of smoke and simplifying the horizontal pressure calculations.

2 Modeling

2.1 Computation Domain

In the previous model, cylindrical polar coordinates were used for the computational domain and it was divided vertically into ceiling jet and air layer. In this new model, the domain is divided horizontally into small lattice-like volumes and the following three layers: ceiling jet, "reversed jet," and air layer, as shown in Figs. 2 and 3. Similar to the two-layer zone models, the heights of the boundaries between layers changed over time. The distributions of temperatures and velocities in the vertical direction of the ceiling and reversed jets were assumed to be Gaussian. To simplify

Fig. 2 Schematic of ceiling
jet and heat transfer
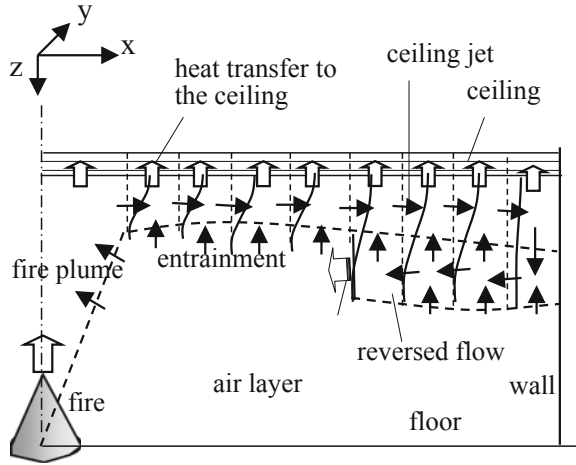
Fig. 3 Schematic of flows
and heat transports
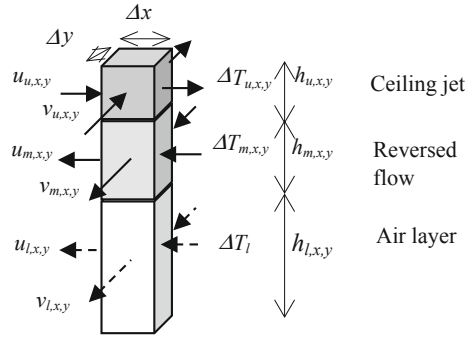
the calculations, these Gaussian distributions were transformed to uniform values
Ellison's method [4]. The air entrainments were considered between the air layer
or reversed jet and the ceiling jet. In the air layer, heat transfer was ignored. The
ceiling was also divided into a lattice at the same pitch as the ceiling jet. Each
lattice cell of the internal domain of the ceiling was divided into thin layers because
the temperatures inside the ceiling are calculated by unsteady one-dimensional heat
conduction equations. Additionally, the previously reported model only applies to
indoor spaces without surrounding walls, and the flow returning from the walls was
not considered.

2.2 Governing Equations

The governing equations that model the horizontal two-dimensional ceiling jet are equation of state, continuity, conservation of momentum, and conservation of energy. The conservation of momentum is as follows:

$$\frac{d}{dt}\int_0^{h_u} u_u dz + \frac{d}{dx}\int_0^{h_u} u_u^2 dz + \frac{d}{dy}\int_0^{h_u} u_u v_u dz = -\frac{\tau_w}{\rho_\infty} - \frac{d}{dx}\int_0^{h_u} g\beta\Delta T_u z dz - \frac{d}{dx}\int_0^{h_u} \frac{P}{\rho_\infty} dz \quad (1)$$

The conservation of energy is as follows:

$$\frac{d}{dt}\int_0^{h_u} c_p \rho_u \Delta T_u dz + \frac{d}{dx}\int_0^{h_u} c_p \rho_u u_u \Delta T_u dz + \frac{d}{dy}\int_0^{h_u} c_p \rho_u v_u \Delta T_u dz = -q'' \quad (2)$$

Following the method of Ellison and Turner [4], the values with distributions, u_u and ΔT_u, were modeled in terms of the average values, $\bar{u}_u$ and $\Delta \bar{T}_u$ and the depth of the ceiling jet, h_u. These definitions are described as

$$\bar{u}_u h_u \equiv \int_0^{h_u} u_u dy, \ \bar{u}_u^2 h_u \equiv \int_0^{h_u} u_u^2 dy, \ \bar{u}_u h_u \Delta \bar{T}_u = C \int_0^{h_u} \bar{u}_u g \Delta T_u dx,$$

$$C = \sqrt{(\gamma^2 + 1)/2\gamma^2} \quad (3)$$

These equations follow from the assumption that the temperatures and velocities have Gaussian distributions because the average values are then $1/\sqrt{2}$ times as much as the maximum values near the ceiling, u_{max} and ΔT_{max}. Figure 4 shows a schematic of the flow and the heat transports among the areas of the ceiling jet after rearranging the model in terms of the average values and dividing into radial segments. Equations of the same form were used to model the reversed flows and the air layers.

The present model used an unsteady two-dimensional SIMPLE algorithm [5] for semi-implicitly calculating the pressure gradient term and solving the momentum equations for the velocity field. In the finite volume method, flows through all faces

Fig. 4 The schematic of flows and heat transports
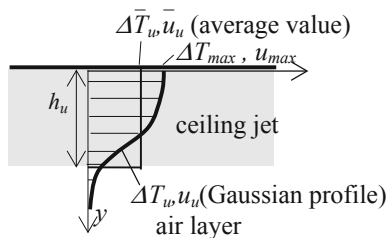
of the control volumes, which were thin cuboids from the floor to the ceiling as shown in Fig. 3, were summed in the pressure correction calculation.

2.3   Other Submodels

The temperature of the fire plume near the ceiling, the velocity at the edge of the jet, and the depth at the edge were used as boundary conditions in this simulation. Figure 5 illustrates these boundary conditions. The mass flow of the fire plume near the ceiling (at the height H) was calculated the equation from Cetegen et al. [6]. The average vertical velocity of the fire plume near the ceiling was calculated by dividing the mass flow of the fire plume by the area of the fire plume at the edge near the ceiling. The radius is assumed as $0.13H$. The average horizontal velocity at the edge of the plume follows from the moment balance at the boundary of the fire plume. The depth of the ceiling jet at the edge of the fire plume can be calculated from the mass flow balance at the boundary of the plume and the jet. The average gas temperature above the fire source and near the ceiling (the turning region) and the average gas temperature out of the plume edge were calculated with the equation of conservation energy at the boundary.

The ceiling jet stops and reverses to flow under itself after reaching the walls. The depth of the returning flow from the wall was assumed to be the same as the depth of the ceiling jet that flows over it. However, the initial velocity of the returned flow was assumed to be 80% of the ceiling jet's velocity just before it reaches the wall.

The temperature distribution in the ceiling material was calculated by one-dimensional heat conduction equations. The convective heat transfer rate on the surface of the ceiling is given from Yao and Marshall [7].

The friction of ceiling jet to the ceiling could be obtained in the turbulent region which white gained by using Coles' law of the wall wake in the turbulent boundary layer [8].

The function describing the entrainment between the ceiling jet and the reversed flow or air layer depends on the number density of the fluid. In a study by Suga and Takahashi, it was defined with data from a series of saltwater experiments [9].

Fig. 5 The boundary with the fire plume
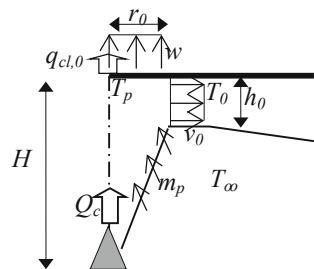
3 Comparison with Full-Scale Experimental Data

For a simple validation of this model, data from a number of full-scale smoke experiments in large office-building spaces are compared with the modeled results for the distribution of the gas temperature.

3.1 Overview of Experiments

As shown in Fig. 6, the area of the fire experiments was "L" shape with 2550 m^2 of floor area. As the boundary's materials, the upper and left side of the figure are mostly glass belong the outside and other sides are plaster. In the area, all doors and windows to the outdoors and to the central core were closed. The most part of the ceiling height was 2.8 m high however for fire resistance of the experiment a drop ceiling covered rockwool fiberboard was installed within 3 m from the fire. Methanol was used as the fuel, and then it poured in one (case 1) or two (case 2) steel pans (0.5 m × 0.5 m) and ignited in two different cases. The weight losses of the fuel were measured by load cells under the pans, and the convective heat release rates were estimated by the net calorific value of methanol (19.94 MJ/kg), and a convection fraction of 0.9 as shown in Fig. 7. The peak values of the convective heat release rates were about 150 kW (case 1) and 300 kW (case 2). The outside temperatures were between 21 °C and 27 °C.

For measuring the gas temperature profiles, *K*-type thermocouples were set at distances of 1.4, 1.8, 2.2, 2.5, and 2.7 m from the floor, the last of which was 0.1 m below the ceiling. The gas temperature was measured at five points ((a) 3.6 m, (b) 7.2 m, (c) 21.6 m, (d) 39.6 m, and (e) 57.6 m from the fire) to the left of the fire, as shown in Fig. 6. These data were compared with the calculations from the model.

Fig. 6 Top-down view of the experimental domain and measured points
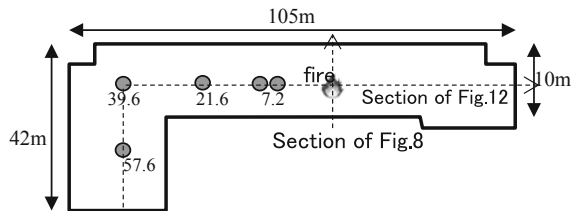
Fig. 7 Heat release rates in the experiment
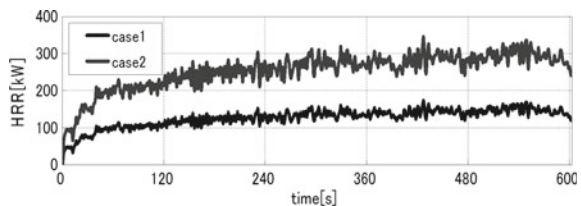
3.2 Calculation Setting

The dimensions of the calculation domain were matched to the dimensions of the experiment space. The domain was divided 0.25 m pitch horizontally. The time interval was set to 0.05 s. The initial temperatures of the gas and the ceiling were assumed to be 22 °C (case 1) and 23 °C (case 2), respectively, from measurements taken before the experiment. The heat release rates were set as the values measured from the experiment given in Fig. 7, and the convection ratio of the heat release rate was set to 0.9. The density, capacity, conductivity, and depth of the rock fiberboard ceiling were set to 300 kg/m^3, 1.63 kJ/kg K, 0.04 W/m K, and 0.015 m, respectively.

3.3 Vertical Section of Contour Graphs

In the simulation, the averaged values $\Delta \overline{T}_u$ and $\Delta \overline{T}_m$ were used for simplifying the calculation as described above. Figures 8, 9, 10, 11, 12, 13 and 14 plot the two-dimensional temperature distributions, ΔT_z, into contour lines every 5 K (the lowest

(a) 20 second   (b) 80 second

(c) 180 second
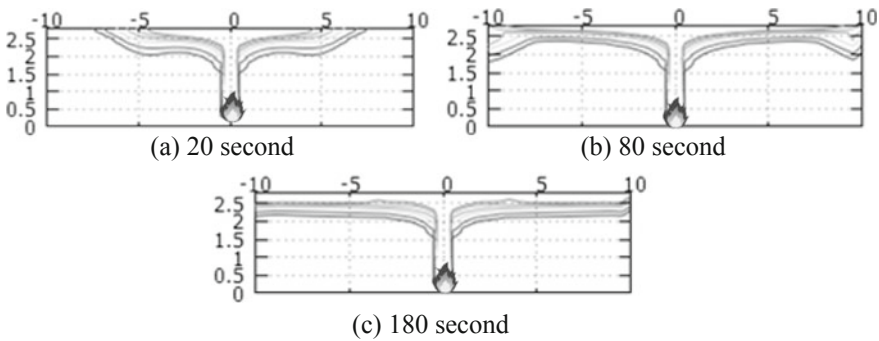
Fig. 8 These contours of temperature with 2.5 K intervals show transition of vertical smoke spreading of case 1: **a** is the time of spreading of the ceiling jet (20 s), **b** is the time of veering ceiling jet at the wall (80 s) and **c** is the time of returning of the reversed flow (180 s)

(a) 2 min   (b) 6 min
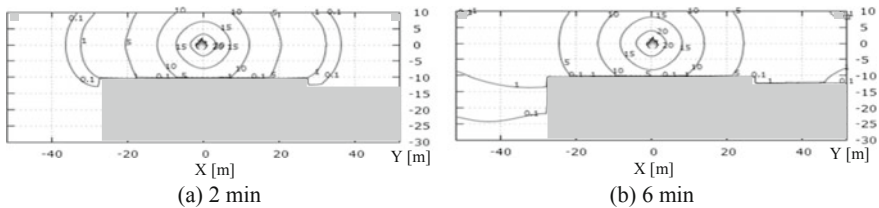
Fig. 9 These contours show horizontal distributions of the ceiling jet temperature rise (K) with 5 K intervals of case 1: **a** is at 2 min and **b** is at 6 min

(a) 2 min   (b) 6 min
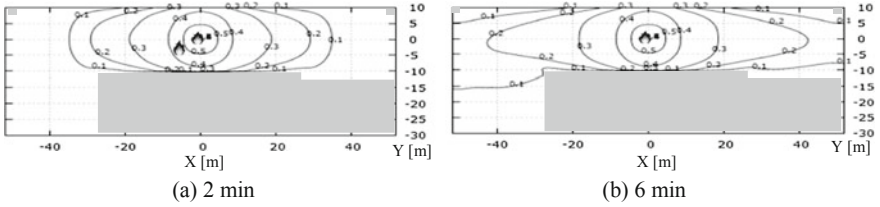
Fig. 10 These contours show horizontal distributions of the velocity (m/s) with 0.1 m/s intervals of case 1: **a** is at 2 min and **b** is at 6 min

(a) 2 min   (b) 6 min
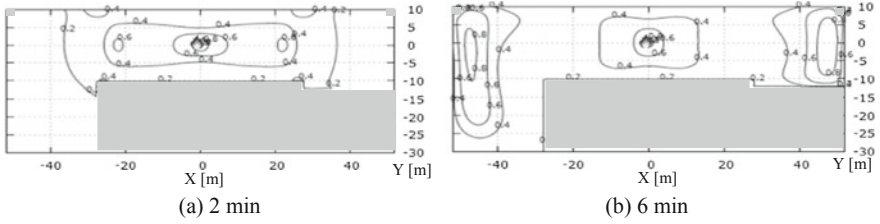
Fig. 11 These contours show horizontal distributions of the smoke depth (ceiling jet + reversed flow) (m) with 0.2 m intervals of case 1: **a** is at 2 min and **b** is at 6 min

(a) 2 min   (b) 6 min
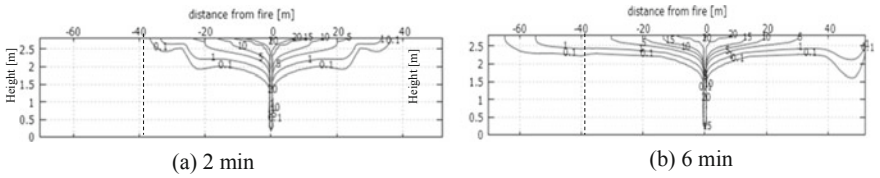
Fig. 12 These contours of temperature with 1 K intervals of case 1 show ceiling jet spreading in a large room: **a** is at 2 min and **b** is at 6 min

(a) -3.6 m   (b) -7.2 m   (c) -21.6 m   (d) -39.6 m   (e) -57.6 m
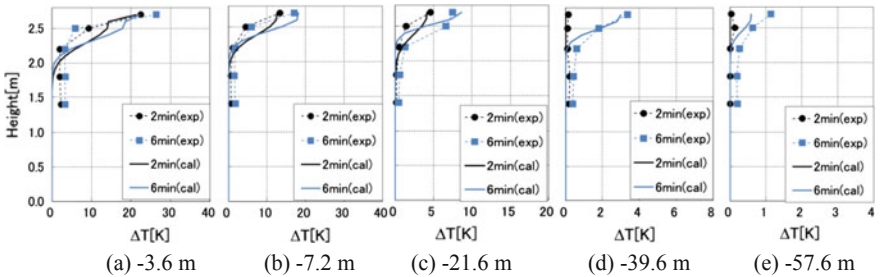
Fig. 13 Comparisons of the vertical temperature distributions (case 1)
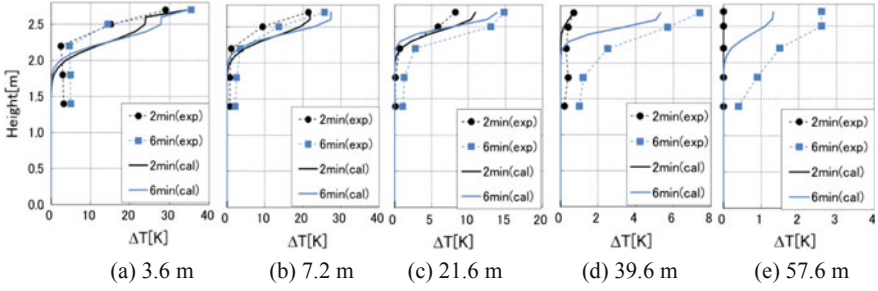
Fig. 14 Comparisons of the vertical temperature distributions (case 2)

line is 0.1 °C) which were calculated by Eq. (4) from the results for $\Delta\overline{T}_u$, $\Delta\overline{T}_m$, h_m, and h_1. The vertical axis is the height from the floor, z, the horizontal axis, x, is the distance from the fire, and (a)–(e) correspond to the measurement points marked in Fig. 6.

$$\Delta T_z = \begin{cases} \sqrt{2}\Delta\overline{T}_u \exp\left\{-\pi(z-h_m-h_1)^2/2h_u^2\right\} & (z > h_m + h_1) \\ \sqrt{2}\Delta\overline{T}_m \exp\left\{-\pi(z-h_1)^2/2h_m^2\right\} & (h_m + h_1 \geq z > h_1) \\ 0 & (z \leq h_1) \end{cases} \quad (4)$$

4 Result

4.1 Outline of the Smoke Spreading Transition

These following three stages of smoke movement were confirmed by the experimental observations and also reproduced by the simulation of case 1, and the sectional distributions of the temperature are shown in Fig. 8. First, the tip of the ceiling jet spreads radially from the fire source and is slightly thick because the ambient air is entrained by large eddies in the jet. The depth is almost constant beyond the tip and less air is entrained by smaller eddies, as shown in Fig. 8a. The ceiling jet descends a little and slowly turns back toward the fire when it reaches a wall. The flow near the wall becomes thick (nearly reaches the floors if the temperature is low), as shown in Fig. 8b. A reversed flow returns under the ceiling jet toward the fire after reaching wall, as shown in Fig. 8c. Some amount of the reversed flow is entrained into the upper ceiling jet, and the remainder is absorbed back into the fire plume.

Figure 9 shows the contour of the horizontal distribution of the temperature increase of the ceiling jet spreading concentrically from the fire source at 2 and 6 min as calculated in the simulation. The calculation reproduced the turning and bending of the ceiling jet at the left corner well, as shown in Fig. 9b.

Figure 10 shows the contour of the concentrically spreading horizontal distribution of the velocity of the ceiling jet which resembles Fig. 9. Temperature and velocity of the ceiling jet are to decrease in a similar ratio by the heat loss to the ceiling and the friction with it each.

Figure 11 shows the contour of the horizontal distribution of the smoke depth that was added up the ceiling jet depth, h_j, and the reversed flow depth, h_m. Under the influence of the reversed reflected from the upper and the lower parts of the wall, the distribution flattened slightly from its concentric shape at 2 min, as shown in Fig. 11a. Because the velocity decreased due to friction and the loss of the buoyancy near the wall on the right and left sides, the depth became thick at 6 min, as shown in Fig. 11b.

Figure 12 plots the vertical distributions of the temperature increase at 2 and 6 min given by the calculations along the cross-sectional lines marked in Fig. 6. The smoke depth changed drastically at −28 m and +28 m at 2 min because the depth began to include the reverse flows from the upper and the lower wall. The smoke layers thickened near the right wall, and the smoke spread smoothly to the left beyond the corner at −39.6 m.

4.2   Comparison with the Experiment

The profiles of the simulated temperature increase at 2 and 6 min were compared with measurements taken during the experiments. They agreed qualitatively, as shown in Figs. 13 and 14. However, the predicted values were lower than the values measured in the experiment at distances far from the fire source, as shown particularly in Figs. 13e and 14e. The reason for this divergence is not clear because various factors could have an influence, such as friction, entrainment, diffusion, heat loss to the ceiling, and the flow reversing at the corners of the room. In addition, the properties of the ceiling material may have an influence on the temperature distribution that was not captured in the simulation.

5   Summary and Conclusions

In this study, a simulation method that models smoke flows as horizontally two-dimensional and three laminar flows including the ceiling jet, reversed flow and airflow was developed, and its predictions were compared with experimental data from fire tests conducted in a large room. The predicted profiles of the gas temperature agreed qualitatively with the measurements. The model still offers distinct advantages over conventional approaches and CFD simulations. The present model is comprehensive; therefore, it should be divided into each modeled element and validated with detailed experimental data. As described above, the model is useful because it can deliver pseudo-three-dimensional temperature distributions in the

same manner as CFD simulations in much shorter time. The short computation time makes the present model an improvement on typical fire safety design practices for large buildings.

References

1. Alpert, R. L. (1975). Turbulent ceiling-jet induced by large-scale fires. *Combustion Science and Technology, 11,* 197–213. https://doi.org/10.1080/00102207508946699.
2. Alpert, R. L. (1972). Calculation of response time of ceiling-mounted fire detectors. *Fire Technology, 8,* 181–195. https://doi.org/10.1007/BF02590543.
3. Suzki, K. (2013). Unsteady ceiling jet model for large building spaces. *Fire Safety Journal, 61,* 83–91.
4. Ellison, T. H., & Turner, J. S. (1959). Turbulent entrainment in stratified flows. *Journal of Fluid Mechanics, 6,* 423–448. https://doi.org/10.1017/S0022112059000738.
5. Patankar, S. (1980). *Numerical heat transfer and fluid flow*. *Hemisphere series on computational methods in mechanics and thermal science* (Vol. 126). CRC Press.
6. Cetegen, B. M., Zukoski, E. E, & Kubota, T. (1982). Entrainment in the near and far field of fire plumes. *Combustion Science and Technology, 39*. http://dx.doi.org/10.1080/00102208408923794.
7. Yao, X., & Marshall, A. W. (2006). Quantitative salt-water modeling of fire-induced flow. *Fire Safety Journal, 41,* 497–508.
8. Coles, D. (1956). The law of the wake in the turbulent boundary layer. *Journal Fluid Mechanics, 1*, 191–226.
9. Suga, K., & Takahashi, A. (1976). Entrainment coefficient of the two layers flow with low density salt water (Japanese). *Fire Safety Journal, 61,* 83–91.

Side Wind Effect on the Flow Behavior of the Window Plume

Junmei Li, Yuhang Zhao, W. K. Chow and T. K. Yue

Abstract Wind action on the flow behavior of the window plume along the exterior wall of a building was studied by analytical and numerical methods. Heat release rate of fire and outside wind speed were varied in the study. It was found that the window plume would flow downward under side wind. Fire might spread to the room above the window when the wind speed was low. With the wind speed increasing, the plume would be blown to downward direction, giving hazardous conditions to rooms at downstream of the wind. The tilted angle of the window plume was derived by theoretical analysis.

Keywords Side wind · Window plume · Fire

Nomenclature

b	Width of the window flame (m)
v	Speed (m/s)
C	Coefficient
F	Force (N)
L	Flame length (m)
T	Temperature (K)
W	Length of the window plume (m)

J. Li · Y. Zhao
Beijing Key Laboratory of Green Built Environment and Energy Efficient Technology, Beijing 100124, China

College of Architecture and Civil Engineering, Beijing University of Technology, Beijing 100024, China

W. K. Chow (✉) · T. K. Yue
Department of Building Services Engineering, Research Centre for Fire Engineering, The Hong Kong Polytechnic University, Hong Kong, China
e-mail: bewkchow@polyu.edu.hk; beelize@polyu.edu.hk

Greek Symbols

θ Angle (°)
ρ Density (kg/m^3)

Subscripts

a   Ambient
g   Gas
w   Wind

1   Introduction

With the rapid urbanization in China, the rapid growth of urban population and the shortage of land resources in large cities made high-rise buildings an effective way to solve this problem. Fire safety in high-rise buildings is always a main concern and getting more and more attention with many fire tragedies in high-rise buildings occurring over the world each year. Following the relative statistics, 60% of the fire accidents occur in buildings every year, and 80% of the building fires are high-rise building fires. Casualties and property losses are more serious in these kinds of fires.

Having various ignition sources, a lot of spread ways, fast spread speed, difficulties in evacuating the occupants, and extinguishing the fire are the main characteristics of high-rise building fires. Early research and fire accident survey show that most of the fire spreads in high-rise buildings are from the opening in the exterior wall. When the fire develops to a certain scale in a fire room, high pressures and thermal radiation due to the hot smoke will lead to the breaking of the window. High-temperature gas with flame ejects from the broken window and forms the window flame. Heat flux transferred from the window flames might ignite combustibles stored in rooms at upper floors and cause vertical fire spread. Window flame is generally recognized as one of the most important contributors of fire spread beyond the room of fire origin. Therefore, a good understanding of the flow behavior of the window flame is the key to fire protection design in high-rise buildings.

Window flame behavior was studied extensively in the past decades. Based on the reduced-scale tests and theoretical analysis, Yokoi [1] established the theoretical model of the window plume. Empirical models on temperature and velocity along the trajectory of external flames were obtained. Oleszkiewicz [2, 3] experimentally investigated the effect of window geometry on the window flame behavior. Results showed that a very low-height and wide window provided the most flame exposure to the wall above, while a relatively square window provided the least flame exposure. The hot gases passing through the low wide opening had lower velocities and the

flames attached to the wall more easily than with a tall narrow window opening. Yamaguchi and Tanaka [4] investigated the window geometry and arrangement of eaves on temperature distributions of the window flame through the small-scale model experiments. Himoto et al. [5] also conducted a series of reduced-scale experiments to investigate the thermal behavior of window flame, and expressions for temperature rise and flame width along the trajectory were derived. Lee et al. [6] proposed to use two new length scales to describe the thermal behavior of the ejected window plume. Tang et al. [7–9] studied the thermal behavior of the window plume under different external boundary and pressure conditions.

Behavior of the window plume, to a large extent, is affected by the heat release rate of the fire, the geometry of the fire room, and shape and size of the opening. However, in windy environments, the flow behavior of the window plume would be affected by the outside wind. Although some results were reported [10–12], further studies are needed to better understand wind action on window plume under different fire sizes.

2 Theoretical Analysis of the Window Plume Tilted Angle Under the Effect of Side Wind

Under the action of the side wind, the window plume would be inclined downward (as shown in Fig. 1). With the action of the inertial force due to the side wind and the buoyancy due to the hot gas, tilted angle of the window plume can be predicted by

$$\tan\theta \propto \frac{F_b}{F_f} \tag{1}$$

where F_f is the buoyancy force, N; and F_b is the inertial force, N.

Assuming that the height of the window flame is L_f, and the window plume can be taken as a plume rising up from a rectangle fire source, F_f can be evaluated by

$$F_f \propto g(\rho_a - \rho_g)L_f bW \tag{2}$$

Fig. 1 Sketch of the tilted window plume under the side wind
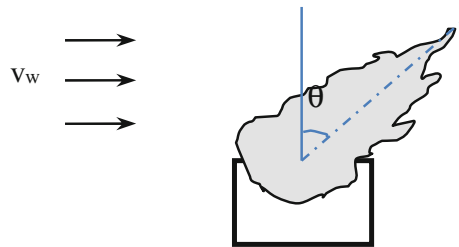
where g is the acceleration due to gravity, m/s^2; ρ_a is the ambient air density, kg/m^3; ρ_g is the density of the hot gas, kg/m^3; W is the length of the window plume, m; L_f is the height of the window plume, m; and b is the width of the window plume at height z, m.

The inertial force F_b due to the wind can be estimated by

$$F_b \propto C_f \frac{\rho_a v_w^2}{2} \cdot \frac{L_f b}{2} \tag{3}$$

where v_w is the side wind speed, m/s; and C_f is a coefficient.

Substituting Eqs. (2) and (3) into Eq. (1),

$$\tan \theta = \frac{F_b}{F_f} \propto \frac{C_f \rho_a v_w^2}{4(\rho_a - \rho_g)g W} \tag{4}$$

Using the ideal gas law,

$$\rho_g T_g = \rho_a T_a$$

$$\tan \theta = \frac{C_{f1} T_g v_w^2}{(T_g - T_a)g W} \tag{5}$$

Tilted angle θ of the window plume can be calculated by

$$\theta = \arctan \left[\frac{C_{f1} T_g v_w^2}{(T_g - T_a)g W} \right] \tag{6}$$

where T_g is the temperature of the hot gas, K; and T_a is the ambient temperature, K.

3   Numerical Simulations

FDS 6.0 [13] was developed by the Building and Fire Research Laboratory at the National Institute of Standards and Technology based on large eddy simulation theory. Accuracy of Computational Fluid Dynamics has been discussed on fire simulations and sprinklers before [14–20].

Taking a typical standard hotel room as an example, since at the initial stage of the fire, fire spread can only limit to two or three levels, and in order to save the computational time, building studied would only have three levels. Fire room is in the middle of the first floor, and it is 5 m long, 4 m wide, and 3.3 m high. There is a window of 1.5 m long, 1.2 m high in the front wall, and 1 m above the ground floor. Fire source is put at 0.5 m from the window, and its size is 2 m × 1 m. Wind flow direction is from right to left. To reduce the boundary effect, the computational

domain is extended in both horizontal and vertical directions. The total computational domain size is 14 m × 5 m × 15 m ($L \times W \times H$), as shown in Fig. 2. Temperature measurement points in simulations are also shown in Fig. 2.

In order to study the impacts of the fire size and wind speed on the flow behavior of the window plume, different fire power and wind speed would be investigated. The design fire commonly used in this kind of building [21–23] is about 5 MW, and three fire sizes of 1 MW, 2 MW, and higher fire power of 6 MW would be used in the simulations. The side wind speed would be 1, 3, and 5 m/s, respectively, in each scenario.

Grid size in this study is set as 0.1 m × 0.1 m × 0.1 m. The boundary of wind flow is set as the inlet boundary; others are set as free boundaries. The ambient temperature in the simulation is set to 20 °C.

Temperature contours at the vertical plan 0.1 m away from the exterior wall under different conditions are shown in Figs. 3 and 4. It is observed that, with no outside wind, flame and hot smoke eject from the window and after that rise by buoyancy vertically, and high-temperature zones are found at the upper floor above the fire room. This might be dangerous to the upper floor. Under windy conditions, the window plume will be blown to the downward direction. Tilted angles of the wind plume are found to be depended on the fire power and wind speed. The tilted angle would increase with the wind speed increasing. However, for the small fire power, the tilted angle would be greatly affected by the wind speed, and a relatively large wind speed can give a large tilted angle. For the large fire size, the tilted angle would be dominated by buoyancy.

(a) Front view   (b) side view
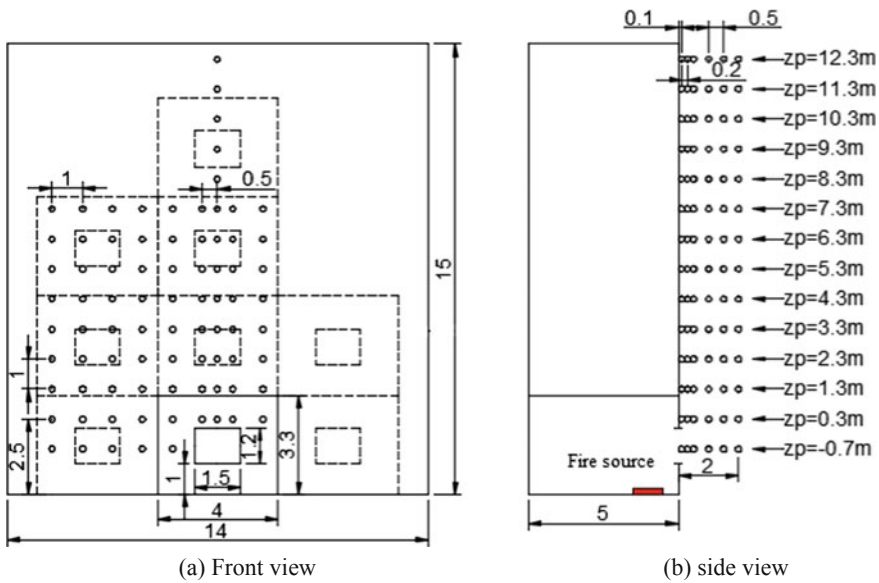
Fig. 2 Computational domain
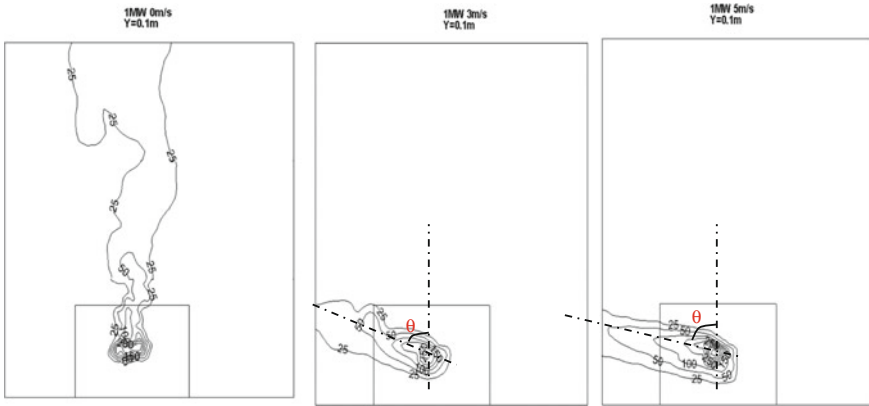
Fig. 3 Temperature contours at 0.1 m away from the front wall ($Q = 1$ MW)
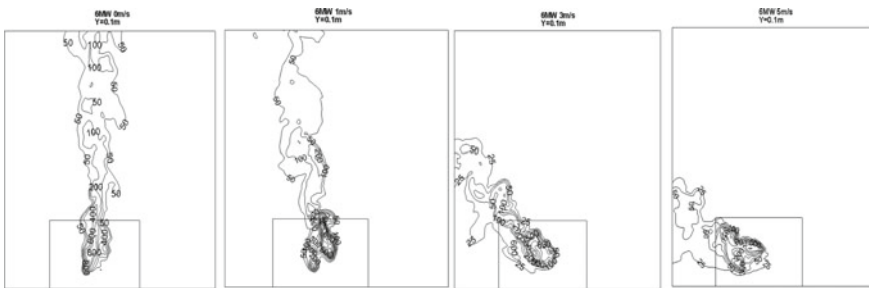
Fig. 4 Temperature contours at 0.1 m away from the front wall ($Q = 6$ MW)

Variations of window plume tilted angle under different fire conditions with different wind speed are shown in Fig. 5. Comparisons of the numerical results with those predicted by the empirical equation are also shown in the figure. Tilted angles are found to increase with the increase of wind speed and decrease with the increase of fire power. Numerical tilted angles are found to agree well with those calculated by empirical equation under higher and lower wind speeds.

Large differences are found between the numerical results and those predicted by the theoretical model. This may be because the value of the coefficient C_{f1} might not be suitable under this condition; more experiments need to be carried out to obtain this coefficient.
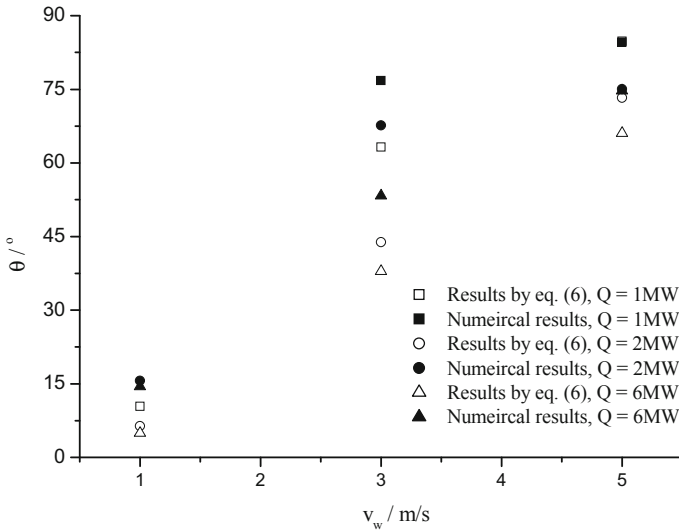
Fig. 5 Variation of the plume tilted angle with side wind speed under different fire conditions

4 Conclusions

Effects of side wind and heat release rate of fire on the window plume were studied analytically with numerical simulations in this paper. Tilted angle of the window plume resulted under different fires with different side wind speed is a key factor. The following conclusions can be drawn:

- Window plume would be blown toward the downward direction. Tilted angle depends on the fire power and side wind speed and can be predicted by Eq. (6);
- External wind would affect the fire spread to levels above the fire room. However, fire would spread to the upper floor at the downwind direction. Much higher wind speed would reduce the temperature of the plume and prevent the hot gas from spilling out from the fire room. This might reduce the risk of vertical fire spread to some extent.
- Further studies should be carried out to fully understand the behavior of the window plume under windy conditions.

References

1. Yokoi, S. (1960). *Study on the prevention of fire-spread caused by hot upward current*. Report of the Building Research Institute, Japan.
2. Oleszkiewicz, I. (1991). Vertical separation of windows using spandrel walls and horizontal projections. *Fire Technology, 11,* 334–340.
3. Oleszkiewicz, I. (1990). Fire and combustible cladding. *Construct Canada, 32*(4), 16-8, 20-1.
4. Yamaguchi, J., & Tanaka, T. (2004). Temperature profiles of window jet plume. In *Fire Safety Science Digital Archive, 6th Asia-Oceania Symposium of fire Science and Technology*.
5. Himoto, K., Tsuchihashi, T., Tanaka, Y., & Tanaka, Y. (2009). Modelling thermal behaviours of window flame ejected from a compartment. *Fire Safety Journal, 44,* 230–240.
6. Lee, Y. P., Delichatsios, M. A., & Ohmiya, Y. (2012). The physics of the outflow from the opening of an enclosure fire and re-examination of Yokoi's correlation. *Fire Safety Journal, 49,* 82–88.
7. Tang, F. (2013). Study on the characteristics of fire plume behavior of building facade under different external boundary and pressure conditions. China University of Science and Technology (in Chinese).
8. Tang, F., Hu, L. H., Delichatsios, M. A., Lu, K. H., Zhu, W., et al. (2012). Experimental study on flame height and temperature profile of window spill thermal plume for compartment fires. *International Journal of Heat and Mass Transfer, 52,* 93–101.
9. Tang, F. (2013). A mathematical model on lateral temperature profile of buoyant window pill plume from a compartment fire. *International Journal of Heat and Mass Transfer, 56,* 447–453.
10. Sugawa, O., Momita, D., & Takahashi, W. (1997). Flow behaviour of ejected fire flame/plume from an opening effected by external side wind. In: *Proceedings of the 5th International Symposium on Fire Safety Science*, Melbourne, Australia, pp. 249–260.
11. Chow, C. L., Chow, W. K., Han, S. S., & So, A. K. W. (2007–2008). Vertical air temperature profiles in a single skin glass façade with a 'jumping fire' scenario. *Journal of Applied Fire Science, 17*(2), 107–130.
12. Miao, L., & Chow, C. L. (2018). A study on window plume from a room fire to the cavity of a double-skin façade. *Applied Thermal Engineering, 129,* 230–241.
13. McGrattan, K., Hostikka, S., McDermott, R., Floyd, J., Weinschenk, C., & Overholt, K. (2013). *Fire dynamics simulator (version 6.0) use's guide*. NIST Special Publication 1019. Maryland: National Institute of Standards and Technology.
14. Chow, W. K., & Fong, N. K. (1993). Application of field modelling technique to simulate interaction of sprinkler and fire-induced smoke layer. *Combustion Science and Technology, 89,* 101–151.
15. Chow, W. K. (1995). Use of computational fluid dynamics for simulating enclosure fires. *Journal of Fire Sciences, 13*(4), 300–334.
16. Chow, W. K. (1995). A comparison of the use of fire zone and field models for simulating atrium smoke-filling processes. *Fire Safety Journal, 25*(4), 337–353.
17. Chow, W. K. (1998). Numerical studies on recent large high-rise building fire. *Journal of Architectural Engineering, 4*(2), 65–74.
18. Chow, W. K., Li, S. S., Gao, Y., & Chow, C. L. (2009). Numerical studies on atrium smoke movement and control with validation by field tests. *Building and Environment, 44*(6), 1150–1155.
19. Chow, W. K., & Zou, G. W. (2009). Numerical simulation of pressure changes in closed chamber fires. *Building and Environment, 44*(6), 1261–1275.
20. Chow, C. L., & Chow, W. K. (2009). Fire safety aspects of refuge floors in supertall buildings with computational fluid dynamics. *Journal of Civil Engineering and Management, 15*(3), 225–236.
21. Chow, W. K. (2003). Fire safety in green or sustainable buildings: Application of the fire engineering approach in Hong Kong. *Architectural Science Review, 46*(3), 297–303.

22. The Chartered Institution of Building Services Engineers. (2010). *CIBSE guide E—Fire engineering*. Dorchester, UK: The Dorset Press.
23. Chow, W. K. (2015). Performance-based approach to determining fire safety provisions for buildings in the Asia-Oceania regions. *Building and Environment—Fifty Year Anniversary for Building and Environment, 91,* 127–137.

Assessment of Radiation Solvers for Fire Simulation Models Using RADNNET-ZM

Wai Cheong Tam and Walter W. Yuen

Abstract The paper presents a neural-network-based zonal method (RADNNET-ZM) for the analysis of radiative heat transfer in an arbitrary Cartesian enclosure with an isothermal, homogeneous, non-gray medium. The model accounts for the non-gray effect of absorbing species in a combustion environment and the geometric effect of any three-dimensional enclosures. The model is verified against benchmark solutions. Maximum local error is observed to be less than 4%. Prediction accuracy of an existing zonal radiation solver is assessed. Results demonstrate that RADNNET-ZM can provide a substantial improvement to zone fire simulation models for the prediction of radiative heat transfer without a significant increase in computation cost.

Keywords Neural network · Zonal method · Non-gray · Multi-dimensional · Fire simulation model

Nomenclature

a_λ	Local absorption coefficient
A_i	Elemental area i
D	Grid size of discretization
$e_{\lambda b}$	Planck function
f_v	Soot volume fraction
F_{ij}	View factor between A_i and A_j
$F_{ss,xx}$	Generic exchange factor (xx = pd, pp)
$L_{ij,xx}$	Center-to-center distance between A_i and A_j (xx = pd, pp)

W. C. Tam (✉)
Fire Research Division, National Institute of Standards and Technology, Gaithersburg, MD, USA
e-mail: waicheong.tam@nist.gov

W. W. Yuen
Department of Mechanical Engineering, University of California at Santa Barbara, Santa Barbara, CA, USA

$L_{pd,x}$	Mean beam length between two perpendicular elemental areas (x = soot, gas)
L_{pp}	Mean beam length between two parallel elemental areas
n_x, n_y, n_z	Dimensionless distances for A_j relative to A_i
P_{CO_2}	Partial pressure of CO_2
P_{H_2O}	Partial pressure of H_2O
P_g	Total pressure of an $N_2/H_2O/CO_2$ mixture
$\dot{q}_g''$	Incident heat flux due to emission of mixture medium
$\dot{q}_w''$	Incident heat flux due to emission of wall
ss	Surface–surface exchange factor
SS	Total surface–surface exchange factor
T_g	Gas temperature
T_w	Wall temperature
X_{CO_2}	Mole fraction of CO_2
X, Y, Z	Dimensions of an enclosure

Greek Symbols

α	Total absorptivity (sum of soot and gas absorptivity)
α_s	Soot absorptivity
$\Delta\alpha$	Gas absorptivity
β_{xx}	Normalized mean beam length (xx = pd, pp)
λ	Wavelength
ε	Emissivity of gas mixture
σ	Stefan–Boltzmann constant

Subscripts

pd	Perpendicular
pp	Parallel

1 Introduction

A significant amount of research has been conducted in both computational techniques for multi-dimensional radiation heat transfer and the understanding of spectroscopic absorption properties of different combustion gases over the past 30 years. To account for the geometric effect, there are zonal methods [1], discrete ordinate

methods [2], discrete transfer methods [3], and many others [4]. To simulate the spectral effect, there are narrowband models [5], *k*-distribution models [6], and weighted sum of gray gas models [7]. In recent years, simulation methods to simultaneously account for both the spectral and geometric effect have also been developed [8]. Despite these efforts to deal with the non-gray multi-dimensional aspects of radiative heat transfer, few have been utilized in any significant degree by the engineering design and fire safety community in the areas of combustion and fire, where in many cases the effect of radiation is known to be not only important, but dominant. The primary difficulty is the mathematical complexity.

The evaluation of radiative heat transfer with the presence of a participating medium consisting of typical combustion products (H_2O, CO_2, and soot particulate) at low pressure (i.e., one atmosphere) in a three-dimensional enclosure is numerically complex. For a one-dimensional isothermal homogeneous medium, the absorptivity is a complicated function of six independent variables (optical thickness of H_2O, CO_2, and CO, source temperature, mixture temperature, and soot volume fraction) [9]. To obtain an accurate evaluation of the spectral behavior of the gas mixture, a direct numerical integration using realistic spectral data (i.e., the narrowband model) is required to be carried out. For the evaluation of radiative heat transfer between surfaces and the gaseous medium, the geometric effect is significant and another direct numerical integration is required. In a typical calculation, such as to simulate the transient thermal environment within a fire resistance furnace, previous work [10] indicates that more than 60 million numerical evaluations are needed to determine the exchange factors. Since the condition within the furnace is continuously changing, the exchange factors are required to be re-evaluated for every time step in a simulation. This level of computational effort is clearly not feasible for practical engineering applications. For this reason, many existing zone fire models, such as CFAST (Consolidated Fire And Smoke Transport [11]), and CFD codes, including FDS (Fire Dynamics Simulator [12]) and FLUENT [13], implement approximate radiation solvers which rely on empirical charts/correlations to enhance computational efficiency.

The objective of this paper is to present a generalized radiation solver that has the capabilities to simulate accurately the realistic effect of radiation heat transfer in any arbitrary three-dimensional fire/combustion environment efficiently. The radiation solver, RADNNET-ZM (RADiation Neural NETwork–Zonal Method), is a generalization of the zonal method using the concept of the generic exchange factor (GEF) [14]. The GEFs have been demonstrated to be an efficient approach for the evaluation of radiative heat transfer in a multi-dimensional gray medium. In a recent work [15], the GEFs are expanded to account for the non-gray effect of a H_2O/CO_2/soot mixture medium by using a neural network correlation, RADNNET [9]. To improve the computational efficiency in the evaluation of the GEFs, the concept of mean beam length (MBL) is utilized. Additional neural networks are generated for the MBLs to characterize the non-gray absorptivity and emissivity of the medium bounded by the elemental surfaces. Using superposition, total exchange factors between arbitrary surfaces can be determined for the evaluation of radiative heat transfer within an enclosure accurately and efficiently.

In the following sections, the mathematical formulation of RADNNET-ZM is presented. Model verification for RADNNET-ZM is provided. Comparison with results generated from the radiation solver used in CFAST [11] is made. Note that the development of the GEFs is described with details in [14, 15]. Therefore, only the features related to the incorporation of the GEFs in the solution algorithms are addressed below.

2 Mathematical Formulation

Consider a one-zone enclosure filled with a mixture of water vapor, carbon dioxide, and soot particulate with arbitrary dimensions of X, Y, and Z as shown in Fig. 1, the analysis of radiative heat transfer to the bounding surfaces requires the evaluation of surface–surface exchange factors. Mathematically, the surface–surface exchange factors between two surfaces, $s_i s_j$, can be evaluated from the following integration [8]

$$s_i s_j = \frac{1}{\sigma T_{\mathrm{w}}^4} \int\limits_{A_i} \int\limits_{A_j} \int\limits_0^\infty \frac{e_{\lambda b}(T_{\mathrm{w}}) e^{-a_\lambda (T_{\mathrm{g}}) S} \cos\theta_i \cos\theta_j}{\pi S^2} d\lambda \, dA_j \, dA_i \qquad (1)$$

where T_{w} is the surface temperature of the source area A_i, T_{g} is the gas temperature, S is the line-of-sight distance between the two integration area elements, dA_i and dA_j, θ_i and θ_j are the angles between the line-of-sight and the unit normal vector of the two differential area elements, σ is the Stefan–Boltzmann constant, $e_{\lambda b}$ is the blackbody emissive power, and a_λ is the local absorption coefficient. To achieve good accuracy, approximately 60 million numerical evaluations of Eq. (1) are required for one time step in a typical fire simulation.
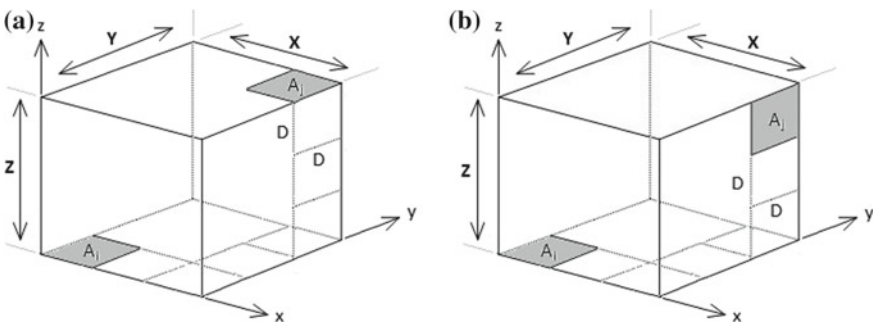
Fig. 1 Geometry for **a** parallel surface–surface GEF, $F_{\mathrm{ss,pp}}$ and **b** perpendicular surface–surface GEF, $F_{\mathrm{ss,pd}}$

Using the concept of GEF, the expression for the evaluation of the surface–surface exchange factors is reduced into a simple form and the exchange factors can be determined from existing neural network correlations such that the numerical evaluations of Eq. (1) will no longer have to be performed during the actual calculation. Specifically, the surface–surface exchange factor for two parallel elemental areas, $s_i s_{j,\text{pp}}$, as shown in Fig. 1a is

$$s_i s_{j,\text{pp}} = D^2 F_{\text{ss,pp}}\left(T_\text{w}, T_\text{g}, P_\text{g}D, X_{\text{CO}_2}, f_\text{v}D, n_x, n_y, n_z\right) \tag{2}$$

where D is the grid size for the discretization and $F_{\text{ss,pp}}$ is the GEF. For simplicity, the mathematical formulation is described under the assumption that the boundary of the enclosure can be subdivided into square elements. Additional treatment is required to handle conditions with imperfect discretization and they will be presented in future publications. ($n_x = S_x/D$, $n_y = S_y/D$, $n_z = S_z/D$) are the non-dimensionalized locations of the receiving area A_j relative to the source area A_i. S_x, S_y, and S_z are the scalar components of the vector connecting the center points of the area elements. As an example, (n_x, n_y, n_z) is (3, 3, 3) for the two parallel elemental areas being shown in Fig. 1a. Based on Eq. (2), $F_{\text{ss,pp}}$ is a function of geometry and five combustion parameters: surface temperature (T_w), gas temperature (T_g), optical thickness ($P_\text{g}D$), mole fraction of CO_2 (X_{CO_2}), and soot volume fraction (f_v). The total pressure of the gas mixture is given as

$$P_\text{g} = P_{\text{H}_2\text{O}} + P_{\text{CO}_2} \tag{3}$$

and the mole fraction of CO_2 is

$$X_{\text{CO}_2} = \frac{P_{\text{CO}_2}}{P_{\text{H}_2\text{O}} + P_{\text{CO}_2}} \tag{4}$$

Using the concept of mean beam length (MBL), the GEF can be written in a one-dimensional form

$$F_{\text{ss,pp}} = F_{ij}\left(n_x, n_y, n_z\right)\left[1 - \alpha\left(T_\text{w}, T_\text{g}, P_\text{g}L_{\text{pp}}, X_{\text{CO}_2}, f_\text{v}L_{\text{pp}}\right)\right] \tag{5}$$

where F_{ij} is the view factor between the two elemental areas, α is the total absorptivity of the sooty gas mixture, and L_{pp} is the MBL accounting for mixture absorption. The numerical evaluation for the view factor is costly when the two areas are close to each other (i.e., $n_x \leq 5$, $n_y \leq 5$, $n_z \leq 5$). For numerical efficiency, view factors are tabulated for ($n_x \leq 5$, $n_y \leq 5$, $n_z \leq 5$), and the tabulated view factors are used to obtain the generic exchange factor. When n_x, n_y, or n_z is larger than 5, the center-to-center distance between the two elemental areas is used as the MBL for the evaluation of the view factors analytically and numerical experiments show that the error associated to the approximate view factor (using the center-to-center distance) is less than 1%. α is obtained from RADNNET, a neural network correlation that predicts the one-dimensional total absorptivity for a $N_2/H_2O/CO_2$/soot mixture [9]. Given a

combustion environment which can be described by the five combustion parameters, the neural network correlation provides the corresponding total absorptivity through "lookup tables." The absorptivity data are generated using RADCAL [4] for 550 discrete values of $P_g D$, 11 discrete values of X_{CO_2}, 10 discrete value of $f_v D$, and 18 discrete values of T_w and T_g, respectively, corresponding to a set of over 19 million data points. The ranges of input variables are

$$0 \leq P_g D \leq 1000 \text{ kPa m}$$
$$0 \leq X_{CO_2} \leq 1$$
$$0 \leq f_v D \leq 10^{-6} \text{ m}$$
$$300 \leq T_w, \ T_g \leq 2000 \text{ K} \tag{6}$$

As shown in [9], the relative error associated with RADNNET is less than 5% for absorptivity or emissivity values larger than 0.01. Thus, RADNNET is expected to have the same order of accuracy as compared to RADCAL. It should be noted that the RADNNET prediction capability for the total absorptivity can continuously be improved with the inclusion of more numerical data. For the determination of the MBLs, Yuen et al. [15] demonstrate that the effect of combustion parameters is minor. For $(n_x = 1, n_y = 1, n_z = 1)$ where the effect of combustion parameters to the MBL is observed to be the largest, and the absolute values of the MBL vary about 9% as a function of the combustion parameters as shown in Eq. (6). An average MBL is shown to be sufficient to yield an accurate value for the GEF in a specific dimensionless distance. For that, L_{pp} is given as

$$L_{pp} = L_{ij,pp} \beta_{pp} \tag{7}$$

where β_{pp} is the average normalized MBL for (n_x, n_y, n_z) and $L_{ij,pp}$ is the center-to-center distance between the two parallel elemental areas. As an example, β_{pp} for two parallel areas D^2 separated by a distance D, which is being denoted as $(n_x = 1, n_y = 1, n_z = 1)$, is determined to be 1.10.

The surface–surface exchange factor for two perpendicular elemental areas, $s_i s_{j,pd}$, as shown in Fig. 1b, can be expressed in a similar form of Eq. (1)

$$s_i s_{j,pd} = D^2 F_{ss,pd}\left(T_w, T_g, P_g D, X_{CO_2}, f_v D, n_x, n_y, n_z\right) \tag{8}$$

with

$$F_{ss,pd} = F_{12}\left(n_x, n_y, n_z\right)\left[1 - \alpha_s\left(T_w, f_v L_{pd,s}\right) - \Delta\alpha\left(T_w, T_g, P_g L_{pd,g}, X_{CO_2}, f_v L_{pd,g}\right)\right] \tag{9}$$

where $F_{ss,pd}$ is the GEF for two perpendicular elemental areas and the total absorptivity, α, is separated into a soot component, α_s, and a gas component, $\Delta\alpha$. It is observed from numerical experiments conducted in [15] that the mathematical behavior of the MBL for perpendicular areas, L_{pd}, is more complex, and L_{pd} varies strongly with the

combustion parameters. For $(n_x = 1, n_y = 1, n_z = 1)$, the MBL varies more than 65% over the entire range of combustion parameters. For that, two MBLs, a soot MBL $(L_{pd,s})$ and a gas MBL $(L_{pd,g})$, are needed to account for the corresponding absorption characteristics accurately. $L_{pd,s}$ is tabulated for $(n_x \leq 4, n_y \leq 4, n_z \leq 4)$ as a function of the product of surface temperature and soot concentration. If n_x, n_y, or n_z is out of range, the center-to-center distance between the two perpendicular elemental areas can be used. For $L_{pd,g}$, a neural network, MBLG-NNET (Mean Beam Length Gas–Neural NETwork), is generated for the ranges of the five combustion parameters. Geometrically, both MBLs are proportional to the center-to-center distance between the two areas, and they are given by

$$L_{pd} = L_{ij,pd}\beta_{pd} \tag{10}$$

where β_{pd} is the corresponding normalized MBL for soot/gas mixture, and $L_{ij,pd}$ is the center-to-center distance between the two perpendicular elemental areas.

In summary, with the use of the neural network correlations (RADNNET and MBLG-NNET), the numerical evaluations for solving Eq. (1) are not needed. Furthermore, it can be demonstrated that the exchange factors for any parallel/perpendicular elemental areas can be efficiently determined for any finite surfaces at any arbitrary locations in an enclosure with an isothermal, homogeneous, non-gray medium.

Utilizing the method of superposition, the total exchange factors between finite surfaces can be determined by summing over the generic exchange factors for all elemental areas. For any finite surface A_i in an enclosure, the incident radiative heat flux consisting of emission from the surrounding walls, $\dot{q}''_{w,i}$, and emission from the sooty gas mixture, $\dot{q}''_{g,i}$, are given by

$$\dot{q}''_{w,i} = \sigma T^4_{w,j}\left(1 - \sum_{j=1}^{N} F_{ji}\alpha_{ij}\left(T_{w,j}, T_g, P_g R_x, X_{CO_2}, f_v R_x\right)\right) \tag{11}$$

$$\dot{q}''_{g,i} = \sigma T^4_g \sum_{j=1}^{N} F_{ji}\alpha_{ij}\left(T_g, T_g, P_g R_x, X_{CO_2}, f_v R_x\right) \tag{12}$$

where N is the total number of bounding surfaces, and R_x is the corresponding MBL for the different surfaces. Note that the details of the summation procedure and indexing associated with the superposition to the generic exchange factors in obtaining the total exchange factors in between two surfaces at arbitrary locations within an enclosure are demonstrated in [15]. For that, the details will not be provided in this paper. Readers can refer to the literature for detailed descriptions.

3 Results and Discussion

3.1 Verification Case: Comparison Between RADNNET-ZM and Benchmark Results

The predictive accuracy of the model described above is investigated. RADNNET-ZM is applied to a radiative heat transfer problem in a three-dimensional enclosure containing non-gray gases. Solutions for this problem were generated by Liu [16] using a statistical narrowband model (SNB) for the determination of the gas radiative properties and a ray tracing method [2] to solve for the radiative transfer equation (RTE). This benchmark problem has been used to verify newly developed/modified spectral models and/or solution methods [17]. Due to its reliable accuracy, the benchmark results will be used as the exact solutions for the verification process.

Figure 2 shows the geometry being considered in this verification study. It is a three-dimensional rectangular enclosure with the dimensions of 2 m by 2 m by 4 m. The surrounding walls are assumed to be black. Surface temperature for all walls is maintained at 300 K. The total pressure of the gas mixture is kept at 1 atm. The temperature for the gas mixture is assumed to be isothermal and is maintained at 1000 K. The composition of the gas mixture is assumed to be homogeneous and contains pure water vapor. The verification conditions are summarized in Table 1.

The verification case is calculated using uniform grids of 11 by 11 by 11 and 16 by 16 by 16. Numerical results from RADNNET-ZM are generated. The predicted incident heat flux to various locations in the x-direction at the center of the y-direction
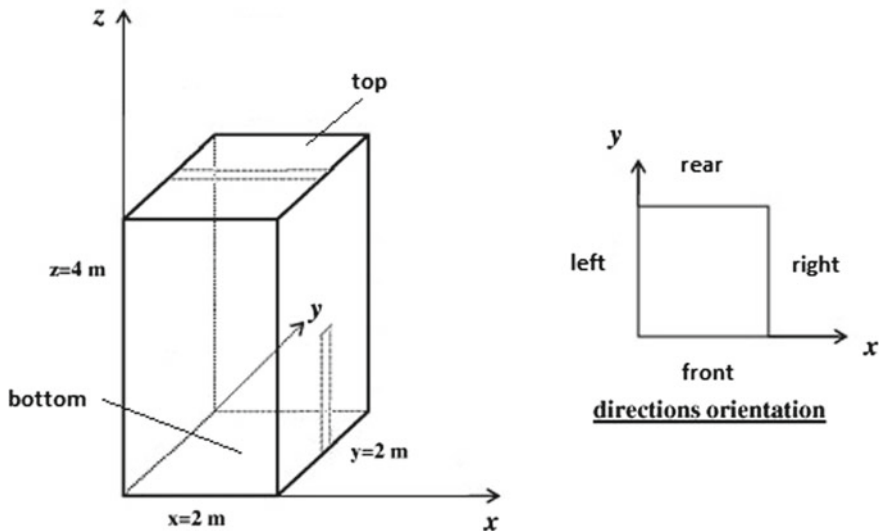
Fig. 2 Schematic of the considered geometry

Table 1 Test conditions for different test cases

Test cases	Wall conditions		Gas medium conditions		
	Temperature (K)	Emissivity	Temperature (K)	Composition	Pressure (atm)
Case 1	300	1	1000	Water vapor	1
Case 2	300/500/1000/1500	1	500	Water vapor	1

on the top surface, denoted as $(x, 1\ m, 4\ m)$, and the predicted incident heat flux at different locations in the z-direction at the center of the y-direction on the right surface, denoted as $(2\ m, 1\ m, z)$, are obtained. Comparing the benchmark results generated by Liu, relative errors associated with RADNNET-ZM are determined. Due to the symmetry condition of this problem, only half of the incident heat flux to the right surface will be presented. As shown in Fig. 3, it can be observed that the predicted results are in very good agreement with the benchmark results. The maximum local error is approximately 4%, and the large errors appeared at two ends (i.e., $x = 0\ m$ and $x = 2\ m$ as shown in Fig. 3a) are probably due to the angular discretization being used in Liu's study. For that, RADNNET-ZM solutions are possibly more accurate near the end of the wall. Overall, the results demonstrate that the RADNNET-ZM is capable to simulate both the spectral and geometric effect accurately.
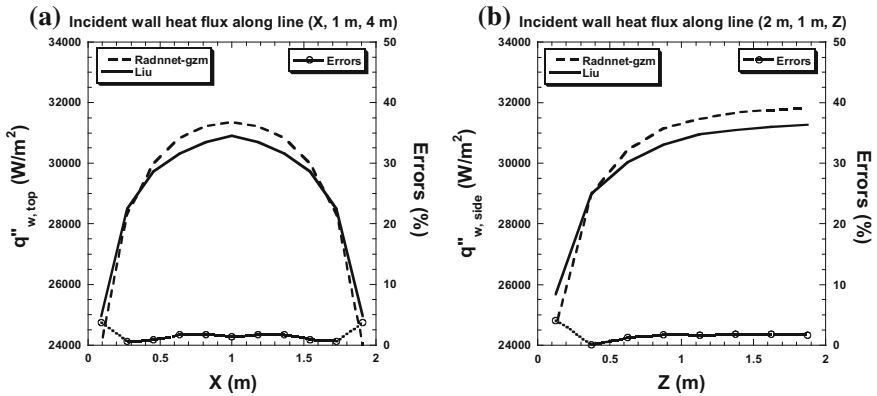
Fig. 3 Incident wall heat flux alone lines **a** $(x, 1\ m, 4\ m)$ and **b** $(2\ m, 1\ m, z)$ obtained from RADNNET-ZM and Liu [16] together with the error associated with RADNNET-ZM

3.2 Assessment of CFAST Radiation Solver Using RADNNET-ZM

CFAST [14] is a fire simulation model that divides compartments into two zones. Each zone includes a gas mixture/soot medium bounded by a ceiling or a floor and four surfaces. Thermal conditions of each zone are assumed to be uniform. When there is a fire, a hot layer will form and the medium can be divided into an upper layer and a lower layer. If the fire persists, the upper layer, consisting of combustion by-products such as H_2O, CO_2, and soot particulate, increases in depth and the upper layer temperature increases. At high temperature, thermal radiation becomes the dominant mode of heat transfer between surfaces and the medium. For that, accurate evaluation of the radiative heat transfer for a participating medium in a three-dimensional enclosure becomes crucial. However, since the absorption behavior of real gases, such as H_2O and CO_2, is a strong function of wavelength, temperature, and species concentrations, brute force numerical evaluation to account for the effect of absorption and geometry is required as discussed in Ref. [10]. Yet, this approach is not feasible for practical engineering calculations. For this reason, in many zone fire models, including CFAST, simplifications are made to their radiation solvers for the evaluation of radiative heat transfer. To account for the non-gray spectral effect of real gases, a one-dimensional empirical correlation known as the Hottel's emissivity chart [1] is typically used. To account for the geometric effect, a constant MBL, based on some ad hoc length scales without mathematical validation, is used. The application of these simplifications for the evaluation of radiative heat transfer in multi-dimensional non-gray media has not been validated. Therefore, the prediction accuracy associated with these radiation solvers is uncertain.

In the following section, the prediction accuracy of the radiation solver from CFAST is assessed. In the discussion given below, the CFAST radiation solver will be denoted as the "approximate approach." It should be noted that with the implementation of the generic exchange factor, bounding surfaces can be subdivided even in a one-zone calculation. It can also be demonstrated that RADNNET-ZM is able to capture local radiative heat transfer effect in a three-dimensional enclosure with an isothermal, homogeneous, non-gray medium accurately.

3.2.1 Test Case 1: Localized Incident Heat Flux to Surfaces (RADNNET-ZM Vs. Radiation Solver Using a Constant MBL)

This case, identical to the verification case as shown in Sect. 3.1, is simulated using the approximate approach. Target devices are specified on the top surface along (x, 1 m, 4 m) and the surface on the right along (2 m, 1 m, z) such that the corresponding incident heat flux can be obtained. Prediction generated from the approximate approach is compared to that obtained from RADNNET-ZM. Comparing RADNNET-ZM, relative errors associated with the approximate approach are also determined. As shown in Fig. 4, the approximate approach over-predicts the incident heat flux to the
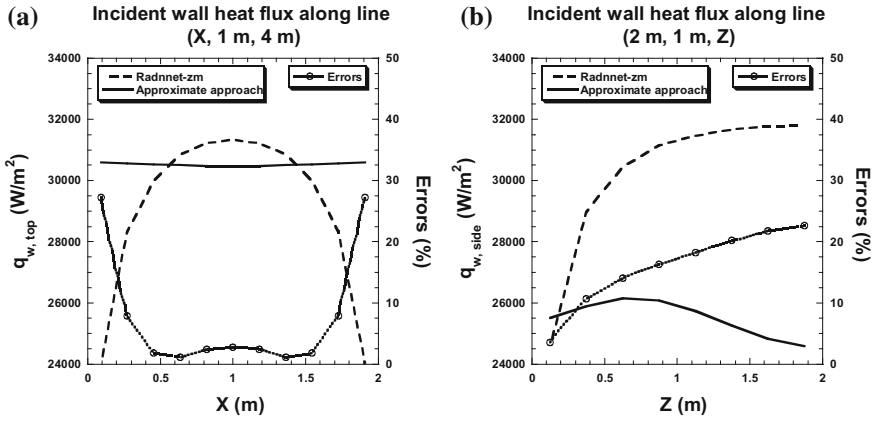
Fig. 4 Incident wall heat flux alone lines **a** (*x*, 1 m, 4 m) and **b** (2 m, 1 m, *z*) obtained from RADNNET-ZM and the approximate approach together with the error associated with the approximate approach

surface by as much as 28%. This error is caused by the simplification used in the determination of mean beam length.

3.2.2 Test Case 2: Radiative Properties of Gas Mixture (RADNNET-ZM Vs. Radiation Solver Using 1D Emissivity Expression)

For black surfaces, the emissivity of the gas mixture, radiating to surface A_i, can be obtained from the solution to the analysis of an emitting medium and non-emitting wall [10] as

$$\varepsilon_g\left(T_g, T_g\right) = \frac{Q_i}{A_i \sigma T_g^4}; \quad Q_i = \left[A_i - \sum_{j \neq i} S_i S_j\left(T_g, T_g\right)\right] \sigma T_g^4 \qquad (13)$$

where Q_i is the radiative heat flux to surface A_i due to emission from the hot medium. $S_i S_j$ is the total exchange factor, and it can be determined by summing over the generic exchange factors for all elemental areas. With identical wall temperature for all surfaces, the mixture absorptivity due to wall emission is given to be

$$\alpha_g\left(T_w, T_g\right) = \frac{1}{A_i} \sum_{j \neq i} \left[A_i F_{ij} - S_i S_j\left(T_w, T_g\right)\right] \qquad (14)$$

A series of numerical experiments is conducted to investigate the effect of wall temperature (T_w) to the radiative properties of the gas mixture. The wall temperature
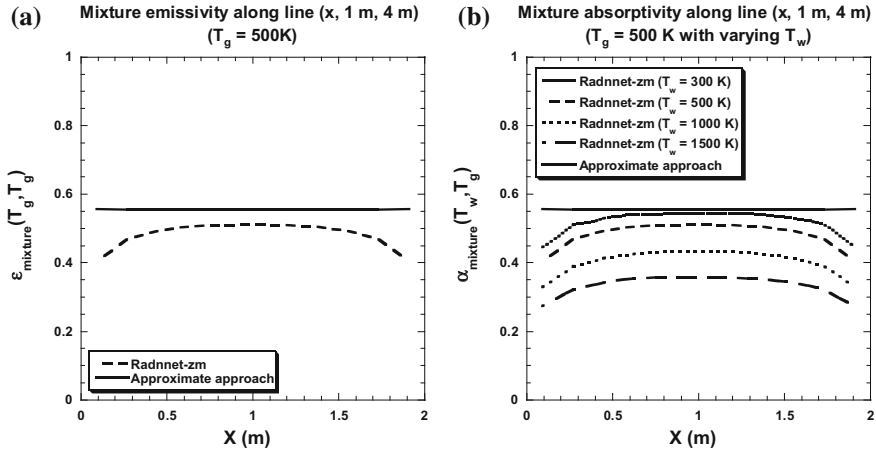
Fig. 5 a Mixture emissivity ($T_w = T_g$) and **b** mixture absorptivity ($T_w \neq T_g$) obtained from RADNNET-ZM and the approximate approach

varies from 300 to 1500 K. The gas temperature is maintained at 500 K and the remaining test conditions are identical to that used from the previous test case as shown in Sect. 3.2.2. A summary of test case 2 is provided in Table 1.

Figure 5 shows the emissivity (a) and the absorptivity (b) of the gas mixture along the line (x, 1 m, 4 m) on the top surface for different wall temperatures (300, 500, 1000, or 1500 K) with the gas temperature maintained at 500 K. For gas emission, the approximate approach over-predicts the emissivity by approximately 8–37%. For mixture absorptivity, the results show that absorptivity can vary significantly depending on the wall temperature. In Fig. 5b, it can be seen that the mixture absorptivity is decreasing with increasing wall temperature. When the wall temperature is identical to the gas temperature, the emissivity equals the absorptivity. This observation agrees well with the findings in [8, 10]. However, since the approximate approach does not account for the wall temperature in the determination of the radiative properties, the absorptivity is identical to the emissivity. As shown in Fig. 5b, the maximum discrepancy associated with the absorptivity predicted by the approximate approach can be different from that predicted by RADNNET-ZM by more than 100%.

4 Conclusions

The mathematical formulation of the neural-network-based generalized zonal method (RADNNET-ZM) is presented. Using the concept of generic exchange factor and the method of superposition, the radiative heat transfer to bounding surfaces in an arbitrary Cartesian enclosure with an isothermal, homogeneous, non-gray medium can be evaluated.

For an isothermal medium with pure water vapor emitting at 1000 K, errors associated with RADNNET-ZM predictions are within 4%. For the approximate approach that is used in CFAST, the errors associated with the predictions are within 28%.

The effect of wall temperature on the evaluation of the radiative properties has been investigated. Mixture emissivity is generally not equal to mixture absorptivity. Given a fixed gaseous concentration, it can be shown while emissivity is a strong function of the gas temperature, absorptivity varies significantly for both wall and gas (absorbing) temperature. Results show that the use of the Hottel's emissivity chart is ineffective and highly inaccurate for the determination of the radiative properties in an enclosure with non-gray gases. Comparing the results generated by RADNNET-ZM, the approximate approach over-predicts the emissivity by approximately 8–37%. For absorptivity, the discrepancy between two radiation solvers can be more than 100%.

Even though the current work focuses on isothermal homogenous media, RADNNET-ZM can be readily used to accurately simulate the radiative absorption effect for different mixtures involving other species (i.e., H_2O, CO_2, and soot particulate). Solutions generated by RADNNET-ZM can be used as benchmark results to verify other radiation solvers from other commercial/CFD codes, such as FDS. For non-isothermal and inhomogeneous conditions, the concept of mean temperatures as referenced in [18] can be implemented to expand RADNNET-ZM to account for the radiative heat transfer effect in an enclosure with non-isothermal, inhomogeneous, non-gray media. This work is currently underway and results will be presented in future publications.

References

1. Hottel, H. C., & Sarofim, A. F. (1967). *Radiative transfer*. McGraw-Hill.
2. Fiveland, W. A. (1987). Discrete ordinate methods for radiative heat transfer in isotropically and anisotropically scattering media. *Journal of Heat Transfer, 109*(3), 809–812.
3. Carvalho, M., Farias, T., & Fontes, P. (1991). Predicting radiative heat transfer in absorbing, emitting, and scattering media using the discrete transfer method. *Fundamentals of radiation heat transfer, 160*(1), 17–26.
4. Grosshandler, W. L. (1993). *RADCAL: A narrow-band model for radiation calculations in a combustion environment*. Gaithersburg, MD: National Institute of Standards and Technology.
5. Mazumder, S., & Modest, M. F. (2002). Application of the full spectrum correlated-k distribution approach to modeling non-gray radiation in combustion gases. *Combustion and Flame, 129*(4), 416–438.
6. Cumber, P. S., Fairweather, M., & Ledin, H. S. (1998). Application of wide band radiation models to non-homogeneous combustion systems. *International Journal of Heat and Mass Transfer, 41*(11), 1573–1584.
7. Choi, C. E., & Baek, S. W. (1996). Numerical analysis of a spray combustion with nongray radiation using weighted sum of gray gases model. *Combustion Science and Technology, 115*(4–6), 297–315.

8. Yuen, W. W., Tam, W. C., & Chow, W. K. (2014). Assessment of radiative heat transfer characteristics of a combustion mixture in a three-dimensional enclosure using RAD-NETT (with application to a fire resistance test furnace). *International Journal of Heat and Mass Transfer, 68,* 383–390.

9. Yuen, W. W. (2009). RAD-NNET, a neural network based correlation developed for a realistic simulation of the non-gray radiative heat transfer effect in three-dimensional gas-particle mixtures. *International Journal of Heat and Mass Transfer, 52*(13), 3159–3168.

10. Tam, W. C. (2013). *Analysis of heat transfer in a building structure accounting for the realistic effect of thermal radiation heat transfer* (Ph.D. thesis). The Hong Kong Polytechnic University, Hong Kong, China.

11. Peacock, R. D., McGrattan, K. B., Forney, G. P., & Reneke, P. A. (2015). *CFAST—Consolidated fire and smoke transport (version 7). Volume 1: Technical reference guide*. Technical Note, NIST, Gaithersburg, Maryland, 1, pp. 69–71.

12. McGrattan, K., Hostikka, S., McDermott, R., Floyd, J., Weinschenk, C., & Overholt, K. (2013). Fire dynamics simulator technical reference guide volume 1: mathematical model. NIST Special Publication, 1018(1), 175.

13. Fluent, A. N. S. Y. S. (2011). *Ansys fluent theory guide*. ANSYS Inc., USA, 15317, pp. 724–746.

14. Yuen, W. W., & Takara, E. E. (1997). The zonal method: A practical solution method for radiative transfer in nonisothermal inhomogeneous media. *Annual Review of Heat Transfer 8*(8).

15. Yuen, W. W., & Tam, W. C. (In preparation). RADNNET-ZM—The generalized zonal method for radiative transfer in multi-dimensional non-gray media.

16. Liu, F. (1999). Numerical solutions of three-dimensional non-gray gas radiative transfer using the statistical narrow-band model. *Journal of Heat Transfer, 121*(1), 200–203.

17. Coelho, P. J. (2002). Numerical simulation of radiative heat transfer from non-gray gases in three-dimensional enclosures. *Journal of Quantitative Spectroscopy and Radiative Transfer, 74*(3), 307–328.

18. Yuen, W. W. (2014). Development of the concept of mean temperatures in the analysis of radiative heat transfer in an inhomogeneous non-isothermal non-gray medium. *International Journal of Heat and Mass Transfer, 68,* 259–268.

Study on the Effect of Platform Screen Door of Different Types on Smoke Control of Platform Fire at a Subway Station

Na Meng, Xiaona Jin, Yao Wang, Wenyu Yang and Lin Xin

Abstract The effect of the platform screen door of different types on smoke control of platform fire at a subway station was investigated by numerical simulations. The results show that for ventilation mode only with over tunnel exhaust system activated, the efficiency of the smoke control system is the worst for fire scenario with full-seal platform screen door. In terms of ventilation mode only with the platform exhaust system, there is no obvious difference in the efficiency of the smoke control system for four kinds of the platform screen door, which is the same when the over tunnel exhaust system, the platform exhaust system and the lobby supply system are all activated. However, when the over tunnel exhaust system, the platform exhaust system and the lobby supply system are all activated and doors are closed, the efficiency of the smoke control system will decrease for fire scenario with full-seal platform screen door. This study might provide some referable information for the design of emergency smoke control of platform fire for various kinds of PSD installed.

Keywords Platform fire · Type of platform screen door · Smoke control · Ventilation mode

1 Introduction

Subway has become the major means of transportation in many metropolitan cities since its appearance. Due to intensive crowds and special underground space structure, fires at subway station usually lead to serious consequences. For example, the fire at London's King's Cross subway station in 1987 caused around 30 deaths and 100 injuries; the fire at Baku in 1995 was even more serious, killed more than 550 people and left around 270 people seriously injured; and the fire in Daegu Korea in 2003 caused 198 deaths [1, 2].

N. Meng (✉) · X. Jin · Y. Wang · W. Yang · L. Xin
College of Mining and Safety Engineering, Shandong University of Science and Technology, Qingdao 266590, Shandong, China
e-mail: mengna@sdust.edu.cn

In case of a fire at the subway station, the most fatal threat to passengers is smoke [3], which is usually of high temperature, contains toxic gases due to incomplete combustion, and decreases the visibility condition for the egress of people. In addition, the route of smoke propagation and the path for personnel evacuation are usually the same, which puts the evacuees at risk more easily and increases the difficulty for firefighting. Therefore, the smoke control system is urgently needed at the subway station.

Considering smoke control of fires at a subway station, a vast number of studies have been conducted [4–8]. Park et al. [4] conducted numerical analysis to evaluate the influence of a platform fire at a subway station and found that larger capacity of exhausts leads to more effective control of smoke. Rie et al. [5] used CFD technique by FDS to study the optimal vent mode for the smoke control of subway station fire and suggested an optimal mode of vent operation for the effective smoke and heat removal from the platform area. Giachetti et al. [6] experimentally investigated buoyancy-induced upward flow interaction with forced convection by mechanical ventilation in order to obtain optimal ventilation strategy in case of a fire at the subway station. They [7] also investigated the smoke spread in a subway station according to subway geometry and ventilation volumetric flow rate. However, in these studies, the types of platform screen door are usually not considered. With the development of subway, platform screen doors (PSD), which are built standing at the edge of the platform, were introduced and have been widely used in newly built subway stations as to increase passenger safety and provide more comfortable internal environment.

The widely adopted PSD at subway station can be divided into three types. The full-seal PSD is usually a glass wall standing at the edge of the platform and when the doors are closed, the platform and the tunnel rail track are completely separated, as in Fig. 1a. The full-height PSD is very much like the full-seal PSD, but with the lower standing wall, usually 3 m in height. So when the full-height PSDs are closed, the platform and the tunnel rail track are partly separated, as in Fig. 1b. As for half-height PSD, also known as the half-height safety door, the glass wall is about one half-height of the full-height PSD, usually 1.2–1.5 m above the platform floor, as in Fig. 1c. In addition, some subway stations, especially for those built at the early stage, are usually without PSD, as in Fig. 1d.

Investigations also have been conducted by considering the effect of the platform screen door on smoke control. Chen et al. [3] studied smoke control of fires in subway stations by considering the appearance of a platform edge door. Meng et al. [9] studied the effectiveness of various ventilation modes in case of a train fire stopping at a subway station and proposed an optimized smoke ventilation mode by considering two kinds of platform screen doors. However, the above studies mainly focus on train fire. As for platform fire, the influence of PSD of different types of smoke control has hardly been clarified.

In case of a platform fire at the subway station, even though the smoke control system is activated in the same mode, the efficiency of the smoke control system might be different due to the differences in PSD type. Therefore, the effect of PSD of different types on smoke control of platform fire at a subway station needs to be investigated and clarified.
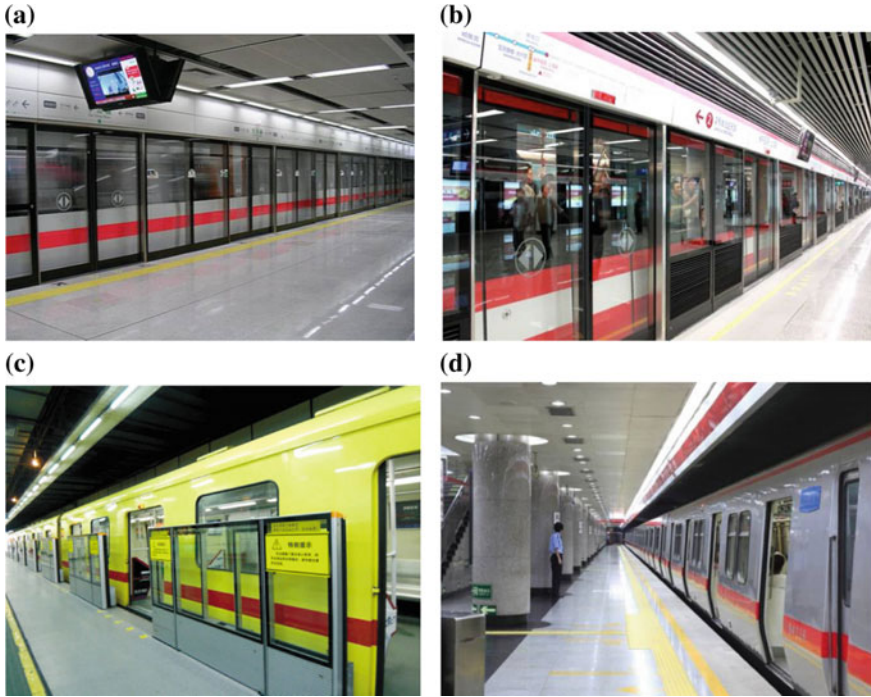
Fig. 1 Different types of PSD at subway station **a** full-seal PSD **b** full-height PSD **c** half-height PSD **d** no PSD

In this paper, numerical simulations are carried out by the Fire Dynamic Simulator (FDS) to investigate the effect of PSD of different types on smoke control of platform fire at a subway station. The visibility field, temperature field, and flow velocity field are computed for comparison. The simulation results may provide some useful referable information for the design of emergency smoke control strategy of platform fires.

2 Numerical Simulation

2.1 The Physical Model

The subway station is a typical island platform station, with tunnels located on both sides of the platform, as in Fig. 2. It is composed of two floors, the lobby floor and the platform floor. The lobby floor is the first underground floor, with dimensions of 120 m (length) × 22 m (width) × 4.5 m (height), while the platform floor is the second underground floor, with dimensions of 120 m (length) × 12 m (width) ×
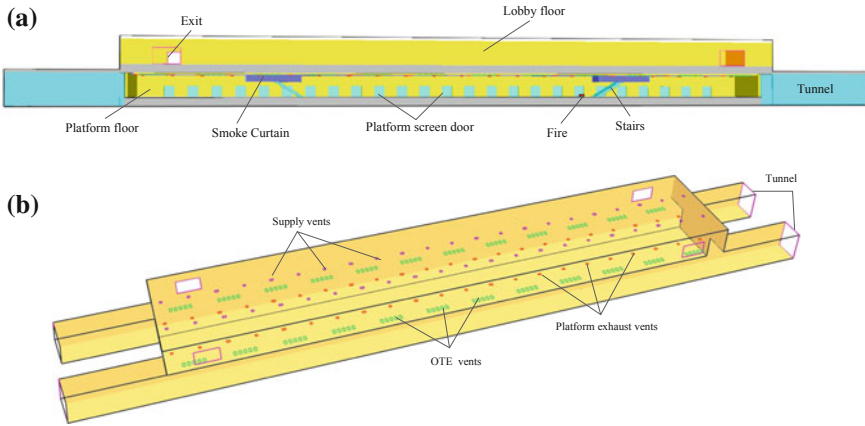
Fig. 2 Schematic of **a** inner structures of the subway station and **b** smoke control system of the subway station

4.5 m (height). The lobby floor and the platform floor are connected through stairs. There are four exits at the lobby floor. Smoke curtains are installed as an auxiliary smoke control setup.

Smoke control system considered in this model is composed of: (1) the platform exhaust system, composed of two lines of air outlets under the ceiling of the platform; (2) the over tunnel exhaust (OTE) system, exhausting smoke through the vents under the tunnel ceiling; and (3) the lobby supply system, supplying air through the air inlets below the lobby ceiling, as in Fig. 2b. The extraction rate for platform exhaust system and the supply flow rate for the lobby supply system are 2 m/s, while the extraction rate for the OTE system is 1 m/s. The capacities of the platform exhaust system, the OTE system, and the lobby supply system are 21.12, 60, and 21.12 m^3/s, respectively.

2.2 Numerical Modeling

The Fire Dynamics Simulator (FDS5) is used to carry out CFD simulations in this study. The FDS code was developed by the National Institute of Standards and Technology (NIST), USA. It solves numerically a form of the Navier–Stokes equations for low-speed, thermally driven flow [10, 11].

FDS5 includes the direct numerical simulation (DNS) and large eddy simulation (LES). LES is the default turbulence model, in which the turbulent motion can be divided into large-scale eddies and small-scale eddies. The motion of the large-scale eddies is directly computed, while the motion of the small-scale eddies is modeled by the sub-gird models [12]. In the present work, the default LES model is used.

Table 1 Grid sensitivity analysis

Grid system	Grid size near fire location (m)			Grid size in other places (m)		
	δx	δy	δz	δx	δy	δz
a	0.5	0.5	0.5	0.5	0.5	0.5
b	0.25	0.25	0.25	0.5	0.5	0.5
c	0.25	0.25	0.25	0.25	0.25	0.25
d	0.125	0.125	0.125	0.25	0.25	0.25

Fig. 3 Grid sensitivity analysis by comparing temperature under the platform ceiling for four kinds of grid sizes
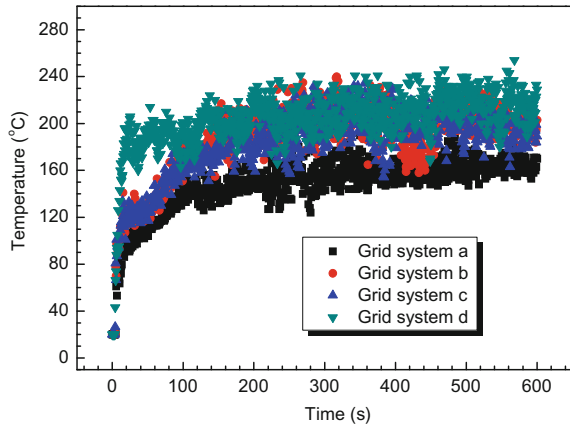
2.3 The Grid Sensitivity Analysis

Grid sensitivity analysis is conducted for the fire scenario of platform fire with closed full-seal PSD and without the smoke control system. Four kinds of grid sizes are tested as shown in Table 1. Smoke temperature under the platform ceiling is adopted for analysis, as shown in Fig. 3. It can be observed that the simulation results converge for grid system b, c, and d. As finer grids produce more accurate results, grid system d is chosen, with grid size of 0.125 m × 0.125 m × 0.125 m near the fire source, 0.25 m × 0.25 m × 0.25 m in other places of the subway station.

2.4 Fire Scenario

Combustibles at the platform mainly come from the following areas: (1) newspaper kiosk or small shops, where paper products and plastics are the main combustibles; (2) the garbage can, in which most of the wastes are burnable. Research [13] shows that the maximum heat release rate can reach 1.6 MW when newspaper kiosk or small

Table 2 Details of fire scenarios

Test No.	Type of platform screen door	State of doors	Smoke control system		
			Platform exhaust system	OTE system	Lobby supply system
1–4	Full-height	Open		✓	
5–8	Full-seal		✓		
9–12	Half-height		✓	✓	✓
13–16	No	Closed	✓	✓	✓

shops catch fire. Considering a fire scenario worse, fire source with heat release rate of 4 MW is chosen and placed near stairs on one side of the platform floor.

Four kinds of smoke control modes are considered, and for each smoke control mode, four fire scenarios are computed by considering different kinds of PSDs as in Table 2. In the present work, the standing wall is 3 m above the platform floor for full-height platform screen door and 1.5 m in height for half-height platform screen door. The simulation time is set to be 360 s and the smoke control systems are set to be activated at simulation time 60 s.

2.5 Initial and Boundary Conditions

The walls, floors, and ceilings of the subway station are considered as a thermally thick concrete blockage. The thermal property of the concrete material is available in the FDS database document [10]. The four exits at the lobby floor and four ends of the tunnels are all set to be open boundary condition. The standing wall of the platform screen door is composed of glass, and for all fire scenarios, it is assumed that the glass wall is able to withstand the smoke temperature.

3 Results and Discussion

Visibility contours, temperature contours, and flow velocity fields are computed to investigate the movement of smoke at the subway station. For the following figures, axis origin is set at the center of the platform ground. The x-axis is positioned at the longitudinal direction of the platform floor; the y-axis is set perpendicular to the x-axis and the z-axis is in the vertical direction of the subway station.

Figures 4, 5, 6, and 7 show the visibility field at the longitudinal central section of the platform floor with various kinds of smoke control modes and by considering four kinds of PSD. It can be seen that when there is only OTE system, smoke can be well controlled except for the fire scenario with full-seal PSD (Fig. 4b). Due to the existence of full-seal PSD, most of the smoke is blocked at the platform floor, which makes the OTE system does not work under such situation. The movement of smoke can be well controlled when there is only platform ventilation system irrespective of the types of the PSD (Fig. 5). When the platform exhaust system, the OTE system and the lobby supply system are all activated, and smoke can be successfully controlled at a high level for four kinds of PSD (Fig. 6). In Fig. 7, the same ventilation mode is considered as in Fig. 6 but with the PSDs closed. It can be seen that the smoke control system fails for fire scenario with full-seal PSD. As full-seal PSDs are closed, the tunnel rail track and the platform are completely separated. Smoke cannot spread to the tunnel rail track, which makes the OTE system does not work under such circumstance. Figure 7b also shows that the efficiency of the platform exhaust system will decrease when full-seal PSDs are closed. The reason might be that under such circumstance, the air is only supplied from the lobby floor.

Figure 8 shows the transient temperature contours at 2 m above the platform floor for the worst fire scenarios from Fig. 7. It shows that when there is only OTE
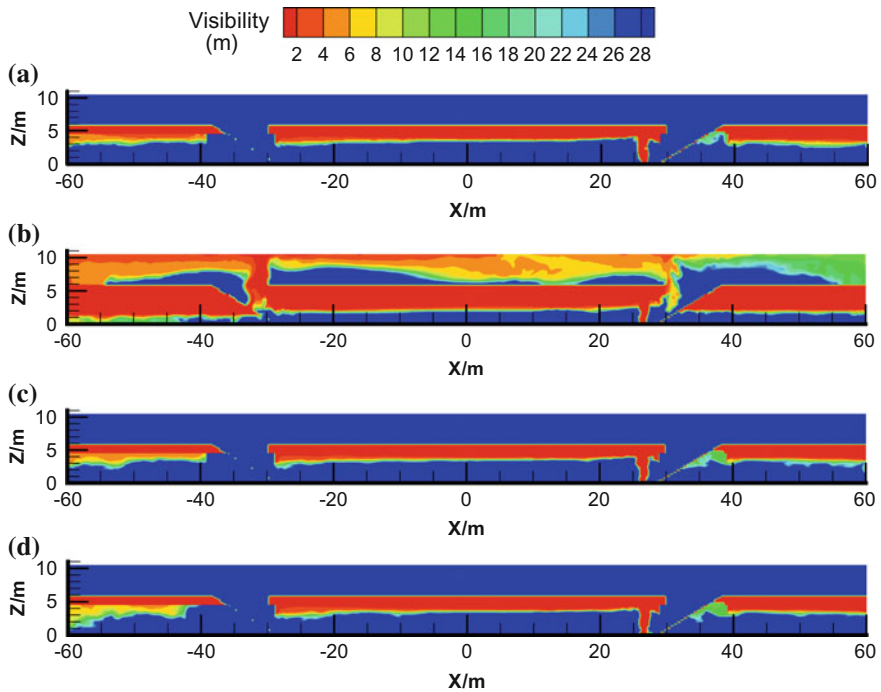
Fig. 4 Visibility contour at the longitudinal central sectional plane of the platform floor for fire scenarios only with OTE system **a** full-height PSD **b** full-seal PSD **c** half-height PSD **d** no PSD
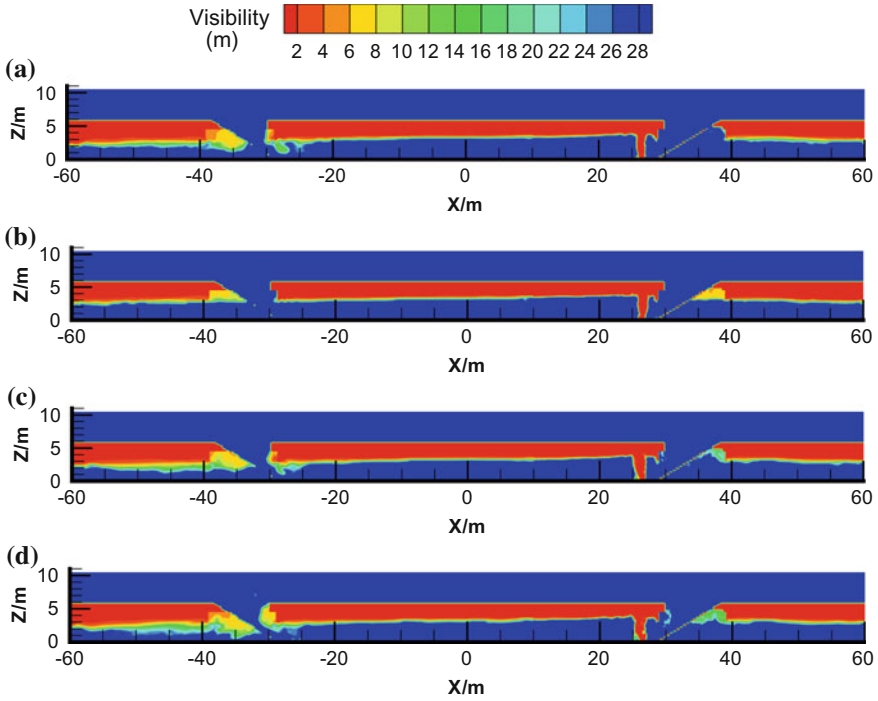
Fig. 5 Visibility contour at the longitudinal central sectional plane of the platform floor for fire scenarios only with platform exhaust system **a** full-height PSD **b** full-seal PSD **c** half-height PSD **d** no PSD

system for fire case with full-seal PSD, smoke decreases to 2 m above the tunnel floor (Fig. 8a). When there is only platform exhaust system for fire case with no PSD, the temperature at 2 m above the platform floor is almost as the environmental temperature (Fig. 8b), which is the same for fire scenario with platform exhaust system, OTE system and lobby supply system all activated and with full-seal PSD (Fig. 8c). Comparing Fig. 8c and d, it can be seen that the efficiency of the smoke control system will decrease for fire scenario with full-seal PSD when the PSDs are closed.

Figure 9 presents the flow velocity field near and in the egress stairs for fire scenarios as in Fig. 8. It can be seen that for fire scenario with only OTE system and full-seal PSD, there is upward flow through stairs. That's to say, under such circumstance, smoke propagation from the platform floor to the lobby floor cannot be controlled. As for other three fire scenarios, there is downward flow through stairs from the lobby floor to the platform floor, showing smoke propagation from the platform floor to the lobby floor well prohibited.
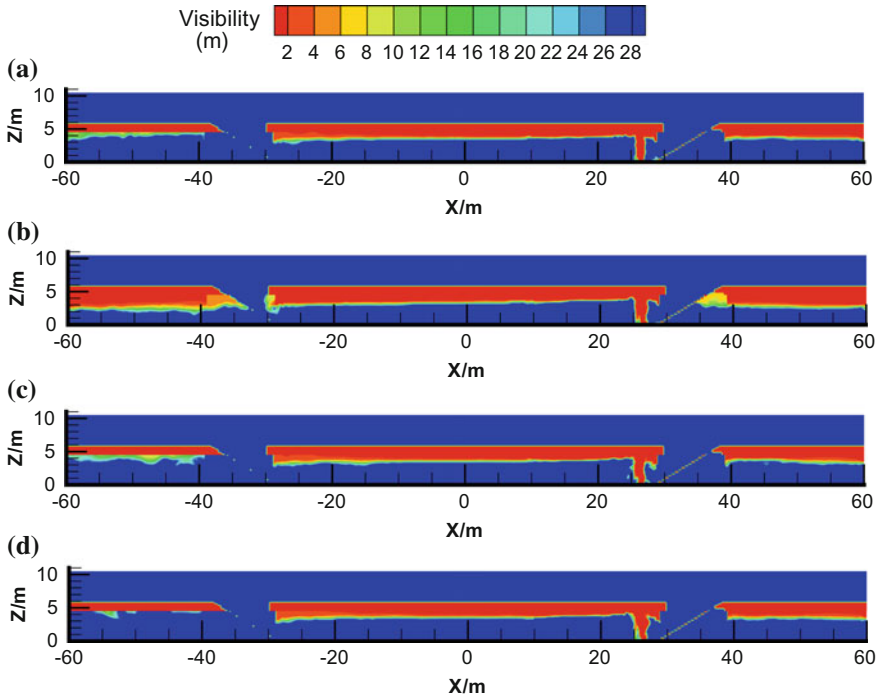
Fig. 6 Visibility contour at the longitudinal central sectional plane of the platform floor for fire scenarios with OTE system, platform exhaust system and lobby supply system all activated **a** full-height PSD **b** full-seal PSD **c** half-height PSD **d** no PSD

4 Conclusions

Effect of platform screen door of different types on smoke control of platform fire at a subway station is investigated. It can be found that in case of a platform fire, even if the mechanical smoke control system is activated in the same mode, the efficiency of the smoke control system could be different when different kinds of PSDs are adopted. Major findings include:
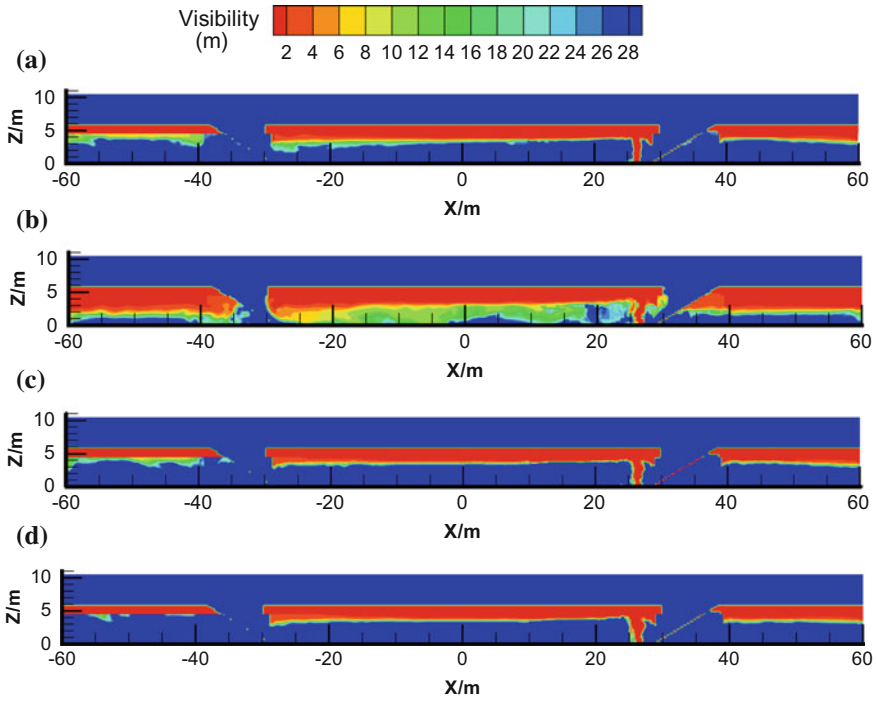
Fig. 7 Visibility contour at the longitudinal central sectional plane of the platform floor for fire scenarios with OTE system, platform exhaust system and lobby supply system all activated and doors closed **a** full-height PSD **b** full-seal PSD **c** half-height PSD **d** no PSD

(1) For ventilation mode only with OTE system activated, the efficiency of the smoke control system is the worst for fire scenario with full-seal PSD. In terms of ventilation mode only with the platform exhaust system, the efficiency of the smoke control system is almost the same for four kinds of PSD.

(2) For the ventilation system with the OTE system, the platform exhaust system and the lobby supply system all activated; smoke was well controlled for four kinds of PSDs when doors are open. However, when doors are closed, the efficiency of the smoke control system will decrease for fire scenario with full-seal PSD.
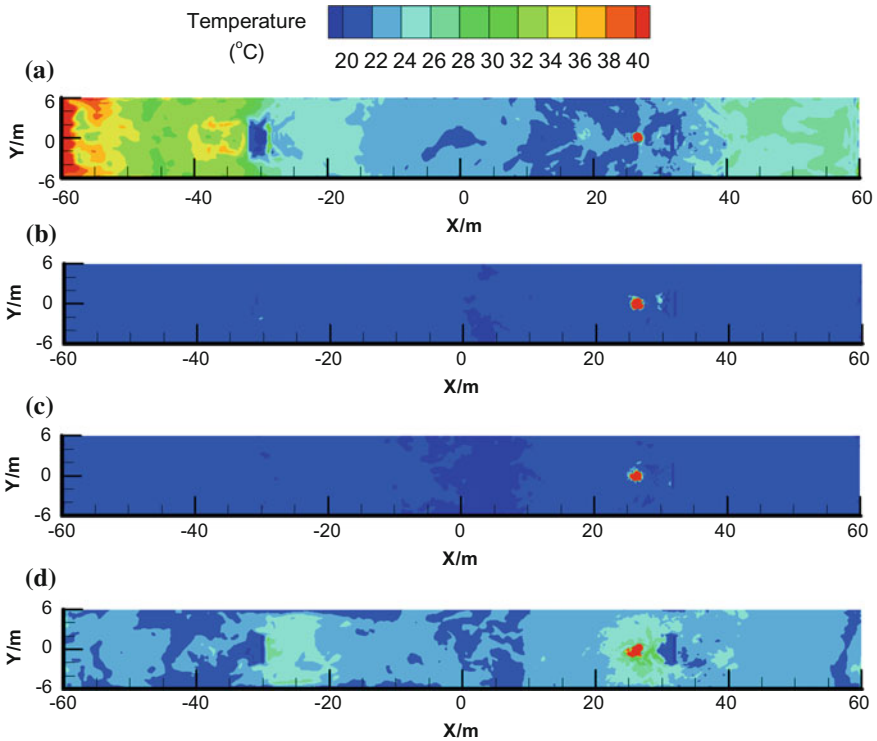
Fig. 8 Temperature contour at 2 m above the platform floor **a** fire scenario with only OTE system and full-seal PSD **b** fire scenario with only platform exhaust system and without PSD **c** fire scenario with OTE system, platform exhaust system and lobby supply system all activated and with full-seal PSD **d** fire scenario with OTE system, platform exhaust system and lobby supply system all activated and with closed full-seal PSD

In order to get better smoke control and increase the efficiency of the smoke control system in case of platform fire at a subway station, the smoke control scheme could be differently treated and carefully designed when different kinds of PSD were adopted. This study may provide some references for the smoke control of platform fire at the subway station with different kinds of PSD adopted.
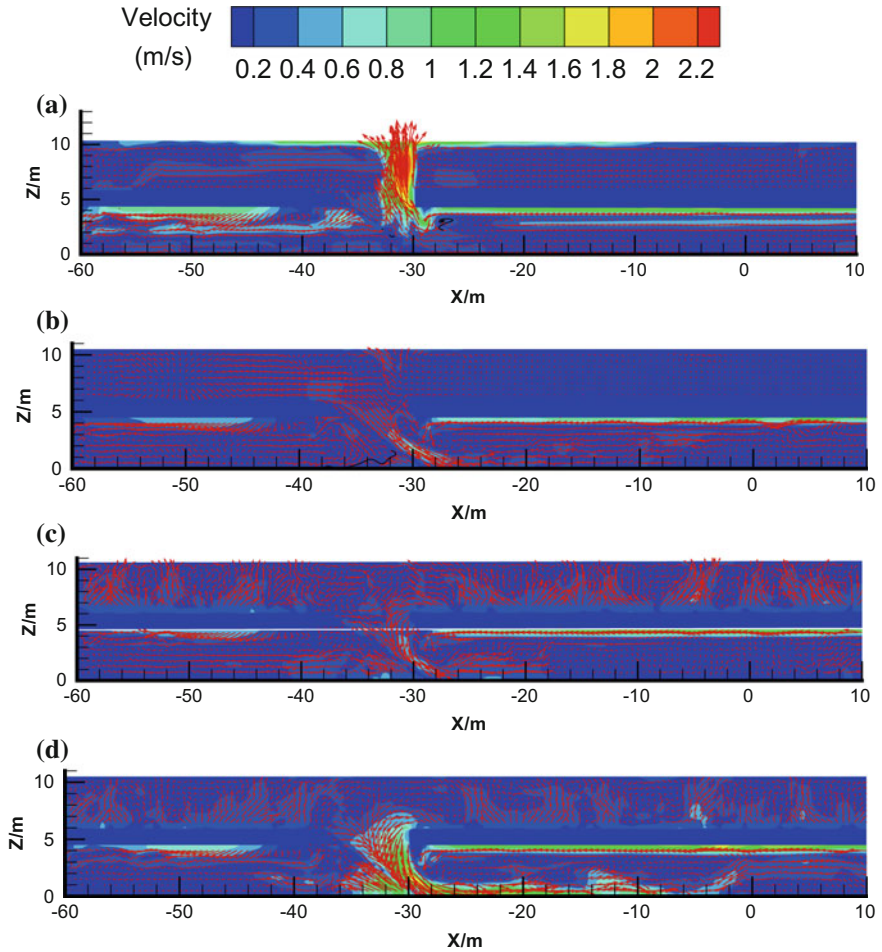
Fig. 9 Flow velocity field near and in the egress stairs **a** fire scenario with only OTE system and full-seal PSD **b** fire scenario with only platform exhaust system and without PSD **c** fire scenario with OTE system, platform exhaust system and lobby supply system all activated and with full-seal PSD **d** fire scenario with OTE system, platform exhaust system and lobby supply system all activated and with closed full-seal PSD

References

1. Park, H. J. (2004). An investigation into mysterious questions arising from the Daegu underground railway arson case through fire simulation and small-scale fire test. In *Proceedings of the 6th Asia-Oceania Symposium on Fire Science and Technology*, Daegu, Korea, pp. 16–27.
2. Hong, W. H. (2004). The progress and controlling situation of Daegu subway fire disaster. In *Proceedings of the 6th Asia-Oceania Symposium on Fire Science and Technology*, Daegu, Korea, pp. 28–46.
3. Chen, F. L., Guo, S. C., Chuay, H. Y., & Chien, S. W. (2003). Smoke control of fires in subway stations. *Theoretical and Computational Fluid Dynamics, 16*(5), 349–368.
4. Park, W. H., Kim, D. H., & Chang, H. C. (2006). Numerical predictions of smoke movement in a subway station under ventilation. *Tunnelling and Underground Space Technology, 21*(3–4), 304.
5. Rie, D. H., Hwang, M. W., Kim, S. J., Yoon, S. W., Ko, J. W., & Kim, H. Y. (2005). A study of optimal vent mode for the smoke control of subway station fire. *Tunnelling and Underground Space Technology, 21*(3–4), 300–301.
6. Giachetti, B., Couton, D., & Plourde, F. (2016). Smoke spreading analysis from an experimental subway scale model. *Fire Safety Journal, 86,* 75–82.
7. Giachetti, B., Couton, D., & Plourde, F. (2017). Smoke spreading analyses in a subway fire scale model. *Tunnelling and Underground Space Technology, 70,* 233–239.
8. Hu, L. H., Wu, L., Lu, K. H., Zhang, X. C., Liu, S., & Qiu, Z. W. (2014). Optimization of emergency ventilation mode for a train on fire stopping beside platform of a metro station. *Building Simulation, 7*(2), 137–146.
9. Meng, N., Hu, L. H., Wu, L., Yang, L. Z., Zhu, S., Chen, L. F., & Tang, W. (2014). Numerical study on the optimization of smoke ventilation mode at the conjunction area between tunnel track and platform in emergency of a train fire at subway station. *Tunnelling and Underground Space Technology, 40*, 151–159.
10. McGrattan, K., McDermott, R., Hostikka, S., & Floyd, J. (2010). *Fire dynamics simulator user's guide*. National Institute of Standards and Technology (Version 5).
11. McGrattan, K., Hostikka, S., Floyd, J., Baum, H., Rehm, R., Mell, W., & McDermott, R. (2010). *Fire dynamics simulator technical reference guide*. National Institute of Standards and Technology (Version 5).
12. Zhang, W., Hamer, A., Klassen, M., Carpenter, D., & Roby, R. (2002). Turbulence statistics in a fire room model by large eddy simulation. *Fire Safety Journal, 37*(8), 721–752.
13. Zhong, W., Huo, R., & Wang, H. B. (2006). Preliminary study on fire scenario's design of subway fires. *Journal of Safety and Environment, 6*(3), 32–34. (in Chinese).

An Experimental Study on Pressurization Smoke Control System in Staircase

Influence of a Dynamic Pressure Control System and Opening Vestibule Doors and Confirmation of Differential Pressure Adjustment Damper Performance

Hyun woo Park, Tomohiro Mitsumura, Yoshifumi Ohmiya, Masashi Kishiue and Wataru Takahashi

Abstract We conducted a full-scale experiment aimed at gathering useful knowledge for planning staircase pressurization for smoke prevention and exhaust, assuming a seven-story office building. We conducted an experimental study on dynamic pressure effects resulting from the installation of the dynamic pressure control system, confirm pressure variation in staircases resulting from opening doors to vestibules, and also confirm the performance of differential pressure adjustment dampers in staircases. The following results are obtained:

1. When the air inlet and the opened doors are on the same floor, the effect of the dynamic pressure control system is small. When a floor that opening the doors is moved away from the air supplied floor, it shows that installing a dynamic pressure control system reduces the influence of dynamic pressure near air inlet by about 54%.
2. Opening doors both staircases and vestibules did not have a large effect on pressure variation within staircases; rather, pressure conditions within staircases tended to be maintained.
3. To implementing smoke control by staircase pressurization, installing only a single differential pressure adjustment damper in staircases maintains a higher pressure than the setting for differential pressure adjustment damper (60 Pa), possibly obstructing door opening.

The original version of this chapter was revised: Subtitle has been updated in this chapter. The correction to this chapter is available at https://doi.org/10.1007/978-981-32-9139-3_79

H. Park (✉) · T. Mitsumura · Y. Ohmiya
Tokyo University of Science, 2641, Yamazaki, Noda, Chiba-Ken 278-8510, Japan
e-mail: Parkhyunwoo0402@gmail.com

M. Kishiue
Obayashi Corporation Technical Research Institute, 640, Shimokiyoto4-Chome, Kiyose-shi, Tokyo 204-8558, Japan

W. Takahashi
ING Co., Ltd., 3-1-17, Nihonbashi, Ningyo-cho, Chuo-ku, Tokyo 103-0013, Japan

This study thus provides basic information for planning staircase pressurization aimed at smoke prevention and control.

1 Introduction

Pressurization smoke control systems supply air to building staircases and vestibules on fire floors. Based on notice, this plan should consider that the pressurized space is dominant in static pressure. However, it is impossible to eliminate all the dynamic pressure and keep the static pressure in actual air supply equipment. Therefore, previous researches are conducted in the condition of relaxed dynamic pressure while pressurization of a vestibule [1]. It is reasonable to consider mitigating the influence of dynamic pressure in staircase pressurization systems. Furthermore, open and closed doors are important factors when calculating air supply. The previous study showed that when using pressurized staircases for smoke control in buildings having offices surrounded by staircases and having a staircase in the center of the rooms, the opening or closing of staircase doors alone has a small effect on pressure differentials within staircases [2]. However, these results apply to only those buildings with specific characteristics. It is difficult to apply them to the case of pressurizing only a single staircase in buildings with outside air connecting to the staircase via rooms. Furthermore, for safety considerations, the amount of air supply for staircase pressurization is often calculated under assumptions of whole-building evacuation and firefighting activities. Whole-building evacuation must consider floor evacuations of non-fire floors, and because there will be more opening and closing of doors leading to staircases than of doors between rooms and corridors, it is necessary to confirm the effectiveness of staircase pressurization for smoke control in consideration of the open/closed state of staircase and vestibule doors. Furthermore, it is necessary to plan final evacuation routes so that increased air pressure in pressurized staircases does not hinder opening staircase doors. Therefore, countermeasures such as pressure relief ports (later "differential pressure adjustment dampers") are required. However, there are no standard settings for differential pressure adjustment dampers, and it is simply necessary to maintain door-opening forces within 100 N [3]. In consideration of the above, in this study, we performed experimental research to confirm the performance of pressure control equipment, pressure differentials due to opening staircase doors leading to vestibules, and the installation of pressure differential dampers within staircases under static pressure condition.

2 Overview of the Experiment

2.1 Overview of the Real-Scale Experiment

We performed experiments in a real-scale fire disaster experiment building at the Building Research Institute, Japan, a seven-story building that is 26.3 m tall. As Fig. 1a shows, a staircase-pressurizing fan is installed on the first floor. This fan supplies air to pressurize the staircase through an air supply inlet located between an air supply shaft and the staircase. Furthermore, it is possible to change the position of the air supply inlet. We assume an office building as the target building type in this experiment, using the gray areas in Fig. 1b, c as the experimental area. As Fig. 1b, c shows, floors 1–2 and floors 3–7 have a different layout, such that corridor fire doors cannot be used to partition areas, and outside air can flow to the atrium space simply by opening the vestibule door. For this reason, floors 1 and 2 are considered as a separate experiment area from the other floors. Note that atriums are considered to be the same as the outside air.

(a) Cross sectional of the air supply shaft, staircase, rooms and atrium

(b) Plan of building used for field experiment（1F and 2F）

(c) Plan of building used for field experiment（3F–7F）
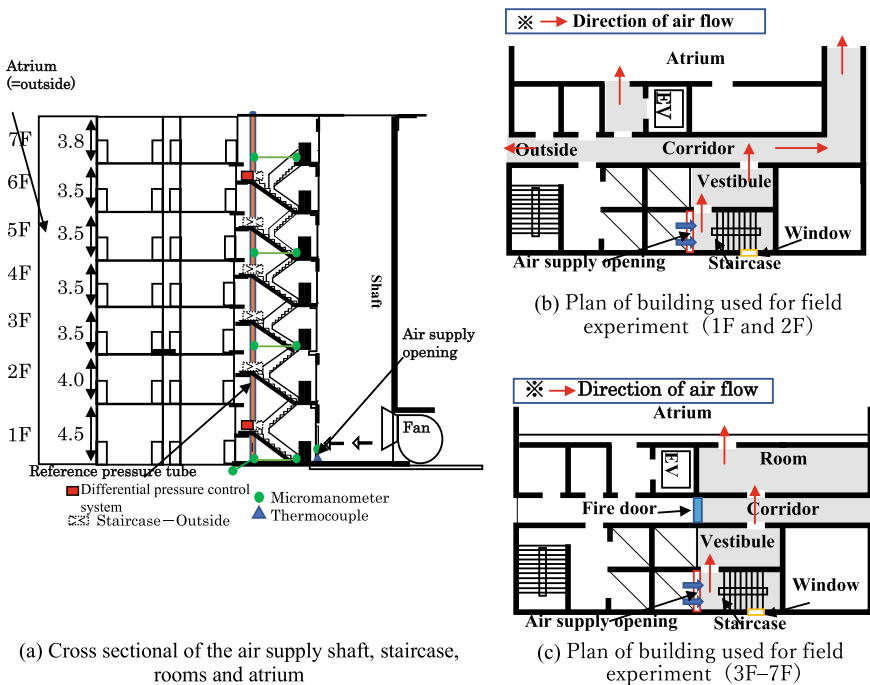
Fig. 1 Schematic diagram of experiment building

Photo 1 Dynamic pressure control system

2.2 Dynamic Pressure Control System

To minimize the effects of dynamic pressure, we used punching metal [4] to fabricate an opening ratio of approximately half the area of the air supply inlet (opening ratio: 53.6%; diameter: 1 cm; pitch: 13P) (Photo 1). We focused on the measurement of static pressure in the staircase, using a T-type [5] tube end at the measuring point of the differential pressure gauge.

2.3 Differential Pressure Adjustment Damper

We used a differential pressure adjustment damper manufactured by Nikkey Co., Ltd. (model OD-227649), which can be used for static pressures of up to 600 Pa and wind speeds of up to 10 m/s. The primary damper is airflow directional (Photo 2). We set a pressure setting of 60 Pa. Installation locations were two outside-facing windows, in staircases between floors 1 and 2 and between floors 6 and 7 (Fig. 1).

Photo 2 Differential
pressure adjustment dampers

2.4 Measurements and Methodology

2.4.1 Air Supply Amounts

We calculated the quantity of supplied air using the dynamic pressure as measured by a New Aero Eye (right angle type; Wetmaster Co., Ltd.) installed in the air inlet, and the temperature as measured by a thermocouple installed in the air supply inlet.

2.4.2 Staircase Differential Pressure

As Fig. 1 shows, the vertical pressure in the staircase is expressed as the differential pressure against a reference column (external pressure). Measurements were performed on floors 1, 3, 5, and 7. Reference column measurements were performed following the method proposed by Matsushita et al. [6], which prevents the influence of outside wind on the reference pressure required for the differential pressure measurement. The standard column is installed in the staircase, the one-way end is exposed to outside air, the inside of the reference column is made to be equal to the outside air, and the reference column is regarded as the outside air. Measurements were made according to the height of the floor level of the respective measurement floor.

2.5   Experiment Conditions

All experiments were performed at room temperature. Note that which doors were kept closed varied according to the test conditions. Tables 1, 2, and 3 show the 12 measurement conditions.

Table 1 lists the experiment conditions related to the dynamic pressure control system. Doors were opened on floors 1 and 5, and air supply was from a single location on the first floor. We performed four experiments related to the dynamic pressure control system using the presence of a dynamic pressure control device as a test condition. All doors on floors 2, 3, 4, 6, and 7 remained closed.

Table 1 Experiment conditions for dynamic pressure control through use of a dynamic pressure control system

Case	1F	5F	Air supply floor	Dynamic pressure control system	Remarks
	Door				
1	○	×	1F	Not installed	Open the doors (from staircase to outside)
2	×	○			
3	○	×		Installed	
4	×	○			

Note Doors on floors 2, 3, 4, 6, and 7 remained closed at all times
○: open, ×: closed

Table 2 Experiment conditions for pressure fluctuation in staircase by opening staircase and vestibule doors

Case	3F		5F		7F		Air supply floor	Remarks
	Door							
	Staircase	Vestibule	Staircase	Vestibule	Staircase	Vestibule		
5	○	○	×	×	×	×	1F	Open the doors (from staircase to vestibule)
6	×	×	○	○	×	×		
7	×	×	×	×	○	○		
8	×	×	○	○	×	×		Open the doors (from staircase to outside)

Note Doors on floors 1, 2, 4 and 6 remained closed at all times
○: open, ×: closed

Table 3 Experiment conditions for performance verification of differential pressure adjustment dampers installed in staircases

Case	3F	5F	Differential pressure adjustment dampers		Air supply floor	Remarks
	Door		Damper of between 1F and 2F	Damper of between 6F and 7F		
9	◯	×	◯	×	1F	Open the doors (from staircase to outside)
10	◯	◯				
11	◯	×	◯	◯		
12	◯	◯				

Note Doors on floors 1, 2, 4, 6 and 7 remained closed at all times
◯: open, ×: closed

Table 2 shows the experimental conditions on staircase pressure fluctuation resulting from opening the staircase and vestibule doors. From the staircase to vestibule doors on floors 3, 5, and 7 were opened, and in case 8, only the door from the staircase to outside air was fully opened. There was only one air inlet (on the first floor), and we measured the effects of vestibule door opening and closing under four conditions. Doors on floors 1, 2, 4, and 6 remained closed under all conditions.

Table 3 shows the experimental conditions related to performance verification of differential pressure adjustment dampers installed in staircases. Doors on floors 3 and 5 were fully opened between staircases and the outside. All doors were fully and simultaneously opened by a male adult. Pressure adjustment dampers were installed at two locations (in windows between floors 1 and 2 and between floors 6 and 7; see Fig. 1), and we tested four combinations of opening one or both dampers. Only a single air inlet was used (1F). Doors on floors 1, 2, 4, 6, and 7 remained closed at all times.

3 Measurement Results and Discussion

Experimental results were taken as the average values of stabilized values for vertical pressure within staircases (from differential pressure gauges on floors 1, 3, 5, and 7), as recorded using a measurement logger.

3.1 Control Using a Dynamic Pressure Control System

The performance of a dynamic pressure control system in the staircase on staircase pressurization is confirmed. Table 4 shows the experimental results on case 1–4 (determination of the existence of a dynamic pressure control system). When the air

Table 4 Vertical pressure distribution in staircase by the dynamic pressure control system

Condition of comparison	Case of dynamic pressure control system ◯ versus Case of dynamic pressure control system ×	
Open the doors (from staircase to outside)	1F (Case 1 and Case 3)	
Result	Figure 2	
Open the doors (from staircase to outside)	5F (Case 2 and Case 4)	
Result	Figure 3	Figure 4

inlet and the opened doors are on the same floor (case 1, 3), the effect of the dynamic pressure control system is small (Fig. 2). It is because of the supplied air flows and leaks through the opening on the same floor. When the opening doors are moved away from the air supplied floor (case 2, 4), the difference (ΔP) of measured values in 1F can be seen (Fig. 3). This influence is due to the difference in the amount of air supplied. When the dynamic pressure is generated, it is difficult to increase the pressure of close non-air supply floor (3F). Figure 4 shows that the dynamic pressure control system reduces the influence of dynamic pressure near the air inlet by about 54%. The two reasons are considered for a decay of the pressure seen from the 1F to 3F under the condition of without the dynamic pressure control system. First, this experiment focused on static pressure measurement. Second, the dynamic pressure caused by the supplied air is not converted to static pressure. Therefore, the measured value showed up lower. Also, the assumed static pressure difference (ΔP) at the relevant floor could not be secured and the smoke-preventing performance decreased. Furthermore, when the same amount of air is supplied, the pressure difference in the static pressure condition and the dynamic pressure condition is expected to increase, as it is difficult to increase the pressure of close non-air supply floor (3F).
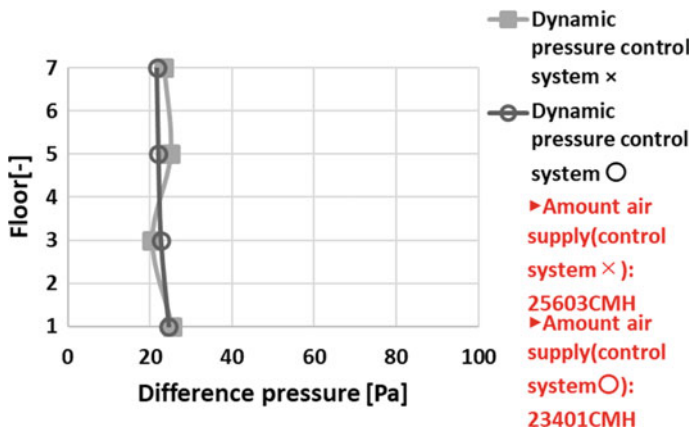
Fig. 2 Difference pressure in the staircase

Fig. 3 Difference pressure in the staircase
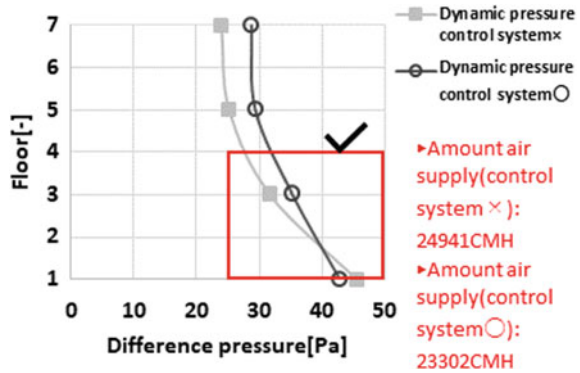
Fig. 4 Detailed description
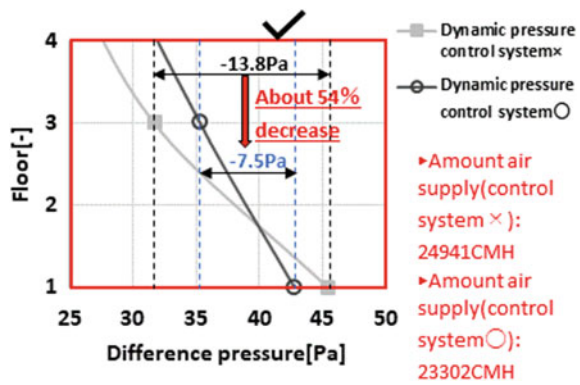
3.2 Pressure Fluctuation in Staircases by Opening Staircase and Vestibule Doors

Table 5 shows pressure fluctuations in staircases in cases 5–8, along with air supply amounts for each condition. The results show that in case 8, where the door between outside air and the staircase is fully opened, the effect of combined resistance between stairs and outside air largely influences pressure fluctuation in staircases. In cases 5–7, where only doors between staircases and vestibules were opened, there is no large

Table 5 Vertical pressure distribution in the staircase by opening the doors of staircase and vestibule

Case	Case 5–Case 8	
Condition of open the doors	Case No. 5: 3F (only staircase and vestibule)	Case No. 6: 5F (only staircase and vestibule)
	Case No. 7: 7F only staircase and vestibule)	Case No. 8: 5F (from staircase to outside)
Result	Figure 5	
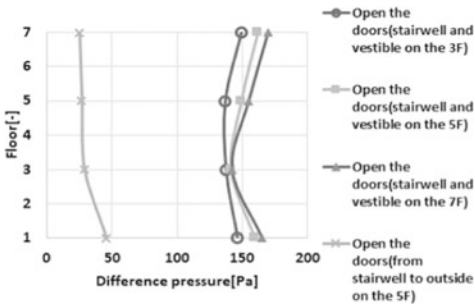
Case.	Amount air supply [CMH]
5	19152
6	18345
7	18202
8	24941

Fig. 5 Difference pressure in the staircase

effect on dynamic pressure in staircases; rather, the pressurized state in staircases was maintained. This suggests that opening doors to the vestibule for staircase smoke prevention and exhaust during an actual fire does not largely influence pressure variation in staircases. Because the vestibule in the building used for these experiments had a shaft penetrating from the first to the seventh floor (Fig. 1), these results likely can also be applied to conditions where an elevator or similar exists in the vestibule, such as for a special evacuation staircase (Fig. 5).

3.3 Confirmation of Performance of Differential Pressure Adjustment Dampers in Staircases

Table 6 shows the results for the required door-opening force when pressure differential adjustment dampers are installed (cases 9–12), along with air supply amounts for each condition. Pressure differential adjustment dampers settings were for a pressure of 60 Pa. The experimental results show that when only one damper is used, the pressure within staircases became approximately 80 Pa (Fig. 6), and using two dampers set at 60 Pa (Fig. 7). Furthermore, investigate the door-opening force based

Table 6 Performance verification testing of differential pressure control system

Case	Case 9–Case 12	
Condition of open the doors	3F (from staircase to outside) 3F and 5F at the same time (from staircase to outside)	
	Figure 6	Figure 7
Result	Figure 8	
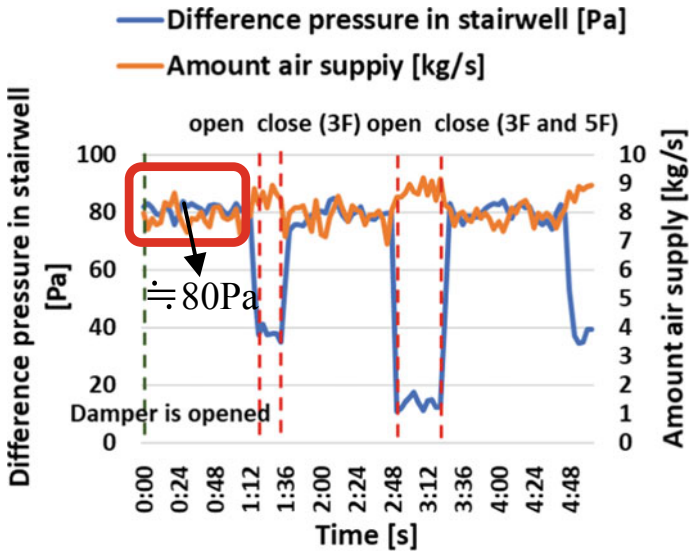
Fig. 6 Differential pressure adjustment system (one)
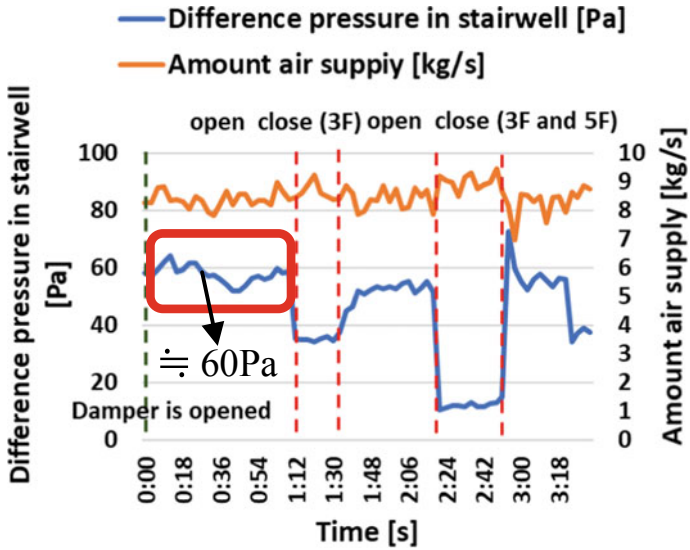
Fig. 7 Differential pressure adjustment systems (two)

Case.	Amount air supply [CMH]	Differential pressure adjustment system [The number]
9		
	23404	ONE
10		
11		
	24644	TWO
12		
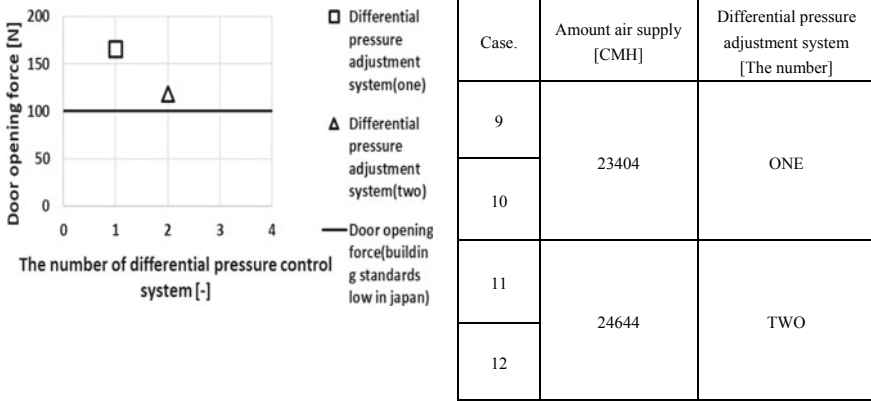
Fig. 8 Door-opening force according to the installation of the number

on Japan building standard law (required 100 N ($\triangle$P 50 Pa), when two dampers are used, the opening force of the door approaches the Japanese Building Standards Law. According to this result, when installing differential pressure adjustment dampers in staircases for staircase smoke control, operating only one damper may result in high staircase pressures that could hinder door opening (Fig. 8).

4 Conclusion

In consideration of a method for staircase pressurization for smoke control, we conducted experimental studies related to a dynamic pressure control system, pressure variation in staircases resulting from opening vestibule doors, and confirming the performance of installing differential pressure adjustment dampers in staircases. Our primary findings within the scope of this study are as follows:

- When the air inlet and the opened doors are on the same floor, the effect of the dynamic pressure control system is small. When the opening doors are moved away from the air supplied floor and show that the dynamic pressure control system reduces the influence of dynamic pressure near air inlet by about 54%.
- Opening doors both staircases and vestibules did not have a large effect on pressure variation within staircases; rather, pressure conditions within staircases tended to be maintained. Because the vestibule of the building used for these experiments had a shaft penetrating from the first to the seventh floor, these results likely can also be applied to conditions where an elevator exists in the vestibule, such as for a special evacuation staircase.
- Installing only a single-pressure differential adjustment damper for staircase pressurization for smoke control raises the pressure within staircases, possibly hindering door opening.

References

1. Kishiue, M., Yamaguchi, J., Okinaga, S., Matsuyama, K., & Matsuyama, T. (2015). Experimental study on influence of air supply system difference on smoke shielding performance in air pressure smoke control. In *Fire science and technology* (pp. 801–810).
2. Moriyama, S., & Sato, K. (2010). A practical example of verifying the performance a system for staircase pressurization for smoke prevention and exhaust (Part 2: Performance of smoke prevention without smoke exhaust—An example in a high-rise building). Summaries of Technical Papers of the Annual Meeting of the Architectural Institute of Japan (Tohoku).
3. Manual of pressurization smoke control system, 2011 (written in Japanese).
4. Kishiue, M., Yamaguchi, J., Okinaga, S., Matsuyama, K., & Matsushita, T. (2015). Performance check corresponding to dynamic pressure systems in pressurized smoke control. Part 2 Experiment of the aeration at the normal temperature using real size model. Japan Association for Fire Science and Engineering, pp. 212–213.
5. Matsuyama, K., Kishiue, M., Yamaguchi, J., Okinaga, S., & Matsushita, T. (2015). Performance check corresponding to dynamic pressure systems in pressurized smoke control. Part 1 Verification of device for measuring static pressure. Japan Association for fire Science and Engineering, pp. 210–211.
6. Matsushita, T., & Terai T. (1985). Measurement of air flow in pressurized staircase. Summaries of Technical Papers of the Annual Meeting of the Architectural Institute of Japan (Tokai).

FDS Software Simulation for Control Effect of Fire Dikes on Leakage of Cryogenic Ethylene Storage Tank

Yuanchang Liu, Xuefeng Han, Jie Ji and Juncheng Jiang

Abstract The ALOHA software was used to calculate the leak source strength of the cryogenic ethylene tank, and the calculation results were provided to the FDS software to set up the model. The study established a basic ethylene tank leakage scenario, and the diffusion process of ethylene was simulated by means of computational fluid dynamics software (FDS), which could describe a series of physical changes in the vapor cloud diffusion process. At the same time, the influence of the relevant steam control technology of setting fire dikes with different height on the downward wind direction of ethylene vapor cloud was simulated. The simulation results show that the control technique really plays a significant role in suppressing the vapor diffusion.

Keywords ALOHA software · Cryogenic ethylene · Tank leakage · Fire dike

Nomenclature

X, Y, Z Coordinates of (m)
t Time of (s)

1 Introduction

Ethylene, as an indispensable basic substance in industrial production, is widely used. Liquid ethylene is cooled from gaseous ethylene to a temperature of $-104\,°C$. Once it leaks in the liquefaction, storage, transport process, the ethylene vapor cloud formed

Y. Liu · X. Han · J. Ji · J. Jiang
College of Safety Science and Engineering, Nanjing Tech University, Nanjing, China

X. Han (✉) · J. Jiang
Fire and Fire Engineering Research Institute of Nanjing Tech University, Nanjing, China
e-mail: safety@njtech.edu.cn

by evaporating will spread rapidly. Due to the flammability and explosive properties of ethylene, the steam cloud, encountering the ignition energy in the vicinity, may be lit and even lead to an explosion, which will pose a serious threat to the surrounding staff, equipment, and environment [1]. Therefore, in order to reduce the possibility and risk of accidents, it is necessary to take appropriate preventive measures to control the spread of ethylene vapor to prevent the occurrence of accidents.

In this paper, the vapor control technology related to leakage, evaporation, and diffusion of cryogenic flammable liquefied gas was studied, low temperature ethylene storage tank as the research object. Based on the leakage model of ethylene storage tank, the source strength of ethylene storage tank was obtained by using ALOHA software. With the aid of CFD software FDS, the physical process of the downward diffusion of steam was simulated after the leakage of ethylene storage tank. The four processes of diffusion and spread of ethylene vapor were clarified. The influence of different height of fire dikes on ethylene vapor diffusion was simulated, respectively.

2 Low Temperature Ethylene Leakage Process and the Consequences of the Accident

2.1 Analysis of Ethylene Leakage and Diffusion Process

The storage condition of liquid ethylene storage tank is low temperature and atmospheric. When ethylene tank leaks due to corrosion or improper operation, there is a great temperature difference between the initial ethylene and atmospheric environment and the ground, which will cause ethylene evaporate quickly, continue to absorb heat from the atmosphere, the ground and the atmospheric environment cooling. Then, evaporation rate of ethylene decreases gradually. According to the above description of a series of changes after the ethylene leakage, ethylene tank leakage and diffusion can be simply summarized as the spread of the liquid pool on the ground surface and the diffusion of vapor cloud in the atmosphere [2].

Liquid Pool Expansion: after the leakage of tank, ethylene, under the influence of the initial leakage velocity and gravity of liquid ethylene, forms an ethylene liquid pool on the ground surface and the pool continued to expand due to gravity, buoyancy, resistance, inertial force, and its radius changes over time [3–5].

Vapor Cloud Spread: there are two main forms of vapor cloud. One is the leakage of the gas phase space above the liquid surface of low temperature ethylene tank, and the upper part of the liquid forms a vapor cloud in the gas–liquid coexistence state. The other is the leakage of the lower part of the ethylene liquid. The leaked ethylene liquid has thermal convection with the atmosphere, and heat conduction with the ground, at the same time, it will quickly flash out a lot of ethylene vapor under the heat of the sun, which gathers on the ground surface [6].

2.2 Description of Consequence of Leakage Accident

After liquid ethylene leaks from the tank, the leakage starts to gasify to form flammable vapor cloud, gather near the ground surface and spread to the downwind direction. The hazards caused by ethylene leakage are low temperature frostbite, suffocation, fire, explosion, etc. Among them, the main risk of low temperature ethylene leakage and diffusion is fire and explosion, as well as thermal radiation from fire. If the ethylene vapor is not ignited in the early stage of the leakage, the vaporized ethylene vapor will move along the atmosphere to the lower air. When the ethylene vapor concentration is not diluted to the lower combustion limit during the mixing of ethylene vapor and the atmosphere, the cloud is combustible. In case it is ignited before the vapor cloud is completely dissipated, there will be a fire accident at a distance from the ethylene storage tank. Then, this potentially dangerous area depends on many factors, including leakage rate, leakage time, evaporation rate, wind direction and wind speed, atmospheric stability, turbulence, and obstruction.

3 Low Temperature Ethylene Leakage Process and the Consequences of the Accident

3.1 Introduction to FDS Software Reliability

At present, the computational fluid dynamics (CFD) model has been the most widely used method for the calculation of the leakage and diffusion processes of cryogenic liquefied gases. FDS, one of the computational fluid dynamics software CFD, can be used not only to solve the fire smoke flow and spread but also to calculate the diffusion process of the fluid. With the help of modeling software PyroSim, it is convenient to build 3D model and import the model into FDS. The 3D flow field is analyzed accurately with appropriate mesh density and fast algorithm [7].

In this paper, the software FDS is selected to simulate the influence of different heights of fire dikes on the process of ethylene vapor diffusion, which provides guidance for the control measures of leakage and diffusion of ethylene.

3.2 Establishment of Physical Model of Ethylene Storage Tan

The model was modeled as follows:

(1) Geometric model. The ethylene storage tank is a vertical storage tank with a volume of 100 m^3, a height of 8 m, and a diameter of 4 m. The storage capacity is 80% of the volume of the tank. Assuming that the leak is located at the tank

valve, it is a rectangular crack with a size of 0.02 m × 0.1 m, which is 1 m away from the ground.

(2) Calculation of the source of leakage of ethylene storage tank. The ALOHA software is an application developed by the United States Environmental Protection Agency (USEPA) and the marine atmospheric Agency (NOAA). ALOHA contains the calculation model of the leakage rate of the medium in the case of gas leakage, liquid leakage, and two-phase flow leakage [8]. The ALOHA software was used to calculate the low temperature ethylene tank leakage rate, and the results were provided to FDS to set the leakage rate of the leakage source. The calculation process is shown in Fig. 1.

As shown in Fig. 1b, cryogenic ethylene is stored at a temperature of −104 °C in the storage tank; Fig. 1c shows that the volume of cryogenic ethylene storage tanks is 80 m³, and the quality is 45,575 kg; Fig. 1d shows the leakage size of rectangular cracks in 0.02 m × 0.1 m; Fig. 1e shows the height of the leakage from the ground is 1 m; Fig. 1f shows the leakage rate of ethylene over time in the 0–60 min leakage time, and the average rate of leakage in the early 2 min is 6 kg/s.
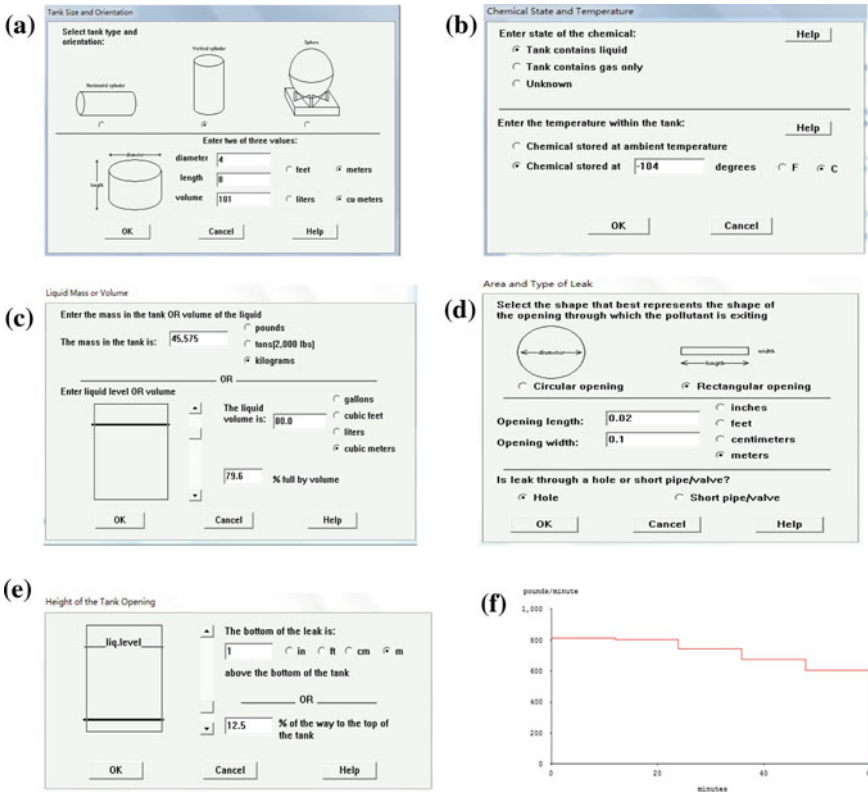
Fig. 1 Parameters of physical model for ethylene storage tank
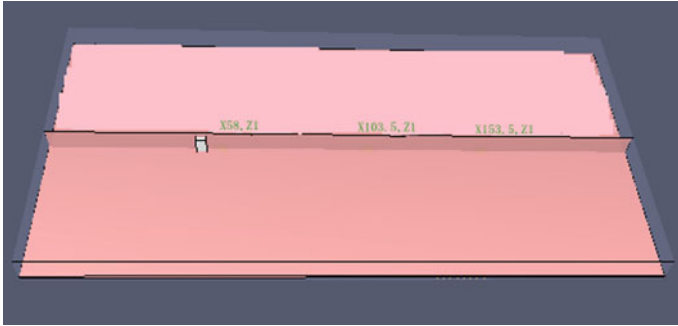
Fig. 2 Physical model of the ethylene storage tank

(3) Model simplification. To simplify the model and mesh better in FDS, the tank model was equivalent to a cubic tank with a bottom area of 3.5 m × 3.5 m and a height of 8 m, which had a rectangular leaky crack with a size of 0.02 m × 0.1 m. When the ratio of leakage area and tank wall area is less than 1:100, the leaking liquid has been completely flashing before it reaches the ground. This leakage type belongs to gas-phase leakage, just like the ethylene tank leak studied in this study [9].

The whole calculated region was 200 m × 100 m × 10 m in the open area, and the surrounding and the top of the calculation area were all open boundaries. The mesh size is 0.1 m × 0.1 m × 0.1 m, and the number of meshes is 2×10^8. The boundary conditions are that the wind speed is 2 m/s, the atmospheric temperature is 20 °C, and the leakage time is 2 min. (In accordance with the provisions of NFPA [10], it is desirable to stop the leak as soon as possible in order to effectively reduce the downwind hazard area, preferably in 2 min.) In order to observe the change of the concentration in the process of diffusion of ethylene vapor ($X = 50$–53.5 m, $Z = 8$ m), monitoring points were added at 4.5 m ($X = 58$ m), 50 m ($X = 103.5$ m), and 100 m ($X = 153.5$ m) along the centerline of the tank and 1 m high from ground. Meanwhile, in order to observe the ethylene concentration distribution in the whole calculation area after ethylene leakage, three volume fraction monitoring surfaces were set up. Since the potential source of ignition is generally located at the height of 0–2 m from the ground, the height of the monitoring surface was set as 1 m. In addition, in order to observe the variation of the thickness of the ethylene vapor cloud, the longitudinal monitoring surface was added along the centerline $Y = 50$ m of the ethylene storage tank. The model in FDS is shown in Fig. 2.

3.3 Analysis of the Prevention of Tank Fire Dike

According to the safety standard specification on low temperature flammable lique-fied gas storage site specially formulated by the USA and other western industrial
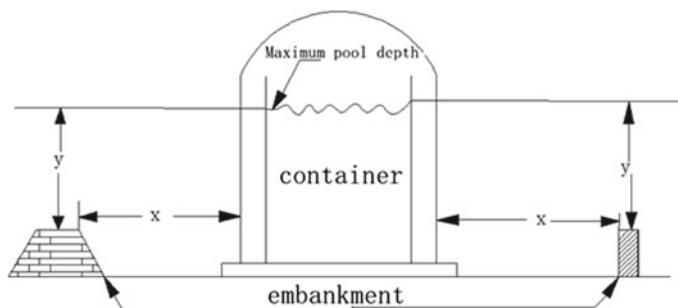
Fig. 3 Set of fire dike around the ethylene storage tank

developed countries, such as NFPA59A and 49CFR, in order to reduce the size of hazardous areas after the leakage of ethylene tanks, a fire dike shall be provided around the tank, which can prevent the spread of liquid and vaporized vapor once the low temperature ethylene leaks, as shown in Fig. 3 [11]. For a single tank, the volume of the fire dike should be able to hold between 105 and 110% of the tank volume. When the tank is accidentally leaking, the fire dike is fully drained of all the leaked liquid. The changes of the downwind spread of the vapor formed by ethylene leakage after adding fire dikes with different heights were simulated, which could further verify that the fire dike has some effect on retarding the downward wind direction.

3.3.1 Fire Dike Design Standards

According to "Code for design of fire-dike in storage tank farm" (GB 50351-2014) [12] and "Fire prevention code of petrochemical enterprise design" (GB 50160-2008) [13], the design requirements for combustible liquefied gas storage tank fire dike are as follows: (1) The fire dike should have sufficient fire performance, shock resistance, stability; (2) For vertical liquefied gas storage tanks, the height of the fire dike shall comply with the following provisions: dike height should be 0.2 higher than the design height of liquid level, but should not be less than 1.0 m (with the design of floor elevation inside dike as the standard) and should not be higher than 2.2 m (with the design of floor elevation within the range of 3 m outside the dike as the standard); (3) The capacity of the fire dike shall be able to hold the capacity of one of the largest tanks in the fire dike. (4) When the tank operating pressure is less than or equal to 100 kPa, and when the fire dike is installed separately from the tank, the distance between tank and inside vertex angle of fire dike should be greater than the difference between the maximum liquid level of storage tank and the height of fire dike wall and the sum of equivalent pressure head of gas-phase space pressure in tank. When the height of the fire dike is equal to or greater than the maximum level in the tank, the distance between tank and inside vertex angle of fire dike is not limited.

A fire dike with a ground surface size of 15 m × 15 m and a wall height of 1 m was added around the ethylene tank, and the tank was symmetrical with the fire dike center. The size of the fire dike was in accordance with "Code for design of fire-dike in storage tank farm" (GB 50351-2014) and "Fire prevention code of petrochemical enterprise design"(GB 50160-2008) and NFPA59A.

3.3.2 Analysis of Simulation Results After Adding a Fire Dike in 1 m High

A liquid diethylene tank should be provided with a fire dike at least 1 m height. Assuming that the leakage stopped (such as plugging successfully) after ethylene leaking continuously 2 min, Fig. 4 is the concentration distribution of ethylene vapor at the height of 1 m at $t = 10, 30, 60, 100$, and 200 s after adding a fire dike in 1 m high.

It shows that the ethylene vapor tends to accumulate in the interior of the fire dike at 10 s when the fire dike with a height of 1 m is added. At 30 and 60 s, the interior of the fire dike is filled with ethylene vapor, which is blocked by fire dike wall, so the ethylene vapor concentration in the fire dike is very high, and a small amount of ethylene vapor flows over the fire dike downward wind direction. At 200 s, the ethylene vapor near the storage tank dissipates slowly.
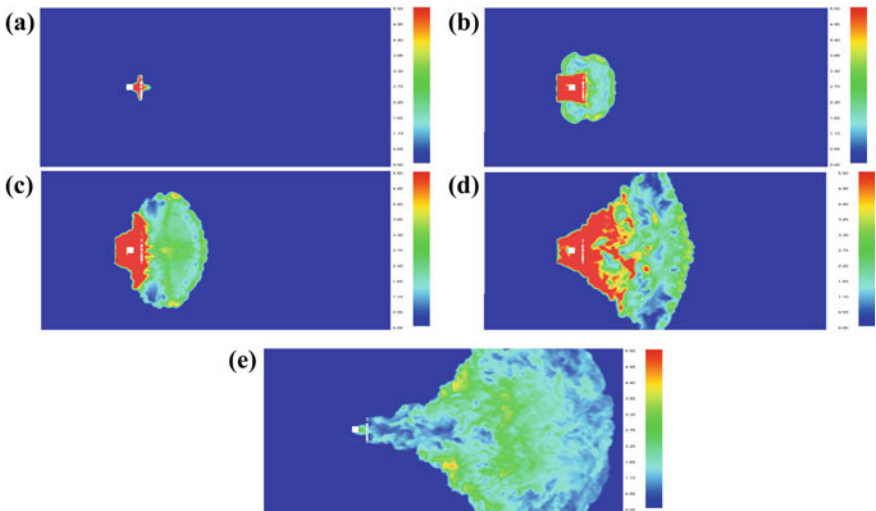
Fig. 4 Concentration distribution of ethylene vapor at a height of 1 m when time is 10, 30, 60, 100, and 200 s after setting a dike in 1 m high
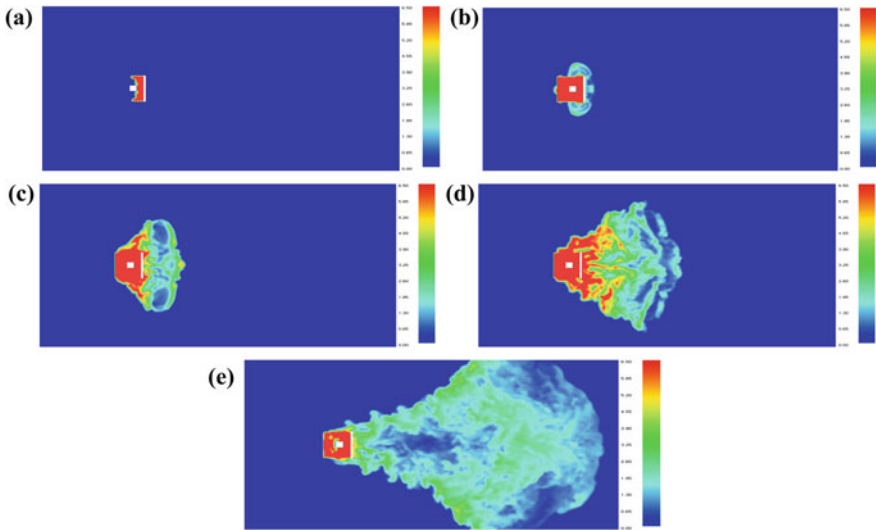
Fig. 5 Concentration distribution of ethylene vapor at a height of 1 m when time is 30, 60, 100, and 200 s after setting a 2-m-high fire dike

3.3.3 Analysis of Simulation Results After Adding a Fire Dike in 2 m High

Figure 5 is the concentration distribution of ethylene vapor at the height of 1 m at $t = 10, 30, 60, 100$, and 200 s after adding a 2-m-high fire dike.

In contrast to Fig. 4, the ethylene concentration distribution diagram of fire dike in 1 m high, it can be found that a small amount of ethylene vapor has already spread over the fire dike to leeward direction at 10 s. However, with the addition of 2 m fire dike, the ethylene vapor cloud, as Fig. 5 shows, is all blocked in the fire dike area by the baffle, and the ethylene vapor concentration in the interior of the fire dike is higher than the vapor concentration when the fire dike is 1 m high. Similarly, the ethylene vapor concentration profiles at 30, 60, and 100 s show that when the fire dike is 2 m high, the area of dangerous and harmful areas in leeward direction is smaller than that when the fire dike is 1 m high. Due to that more ethylene vapor is blocked within the fire dike, a small amount of ethylene over the fire dike spread downwind, resulting in the reduction of leeward vapor concentration.

3.3.4 Simulation Results Analysis

Figure 6 shows, respectively, the variation of the concentration in 1 m high with time, 4.5, 50, and 100 m away from the tank in case of the addition of fire dike with the height of 1 and 2 m.
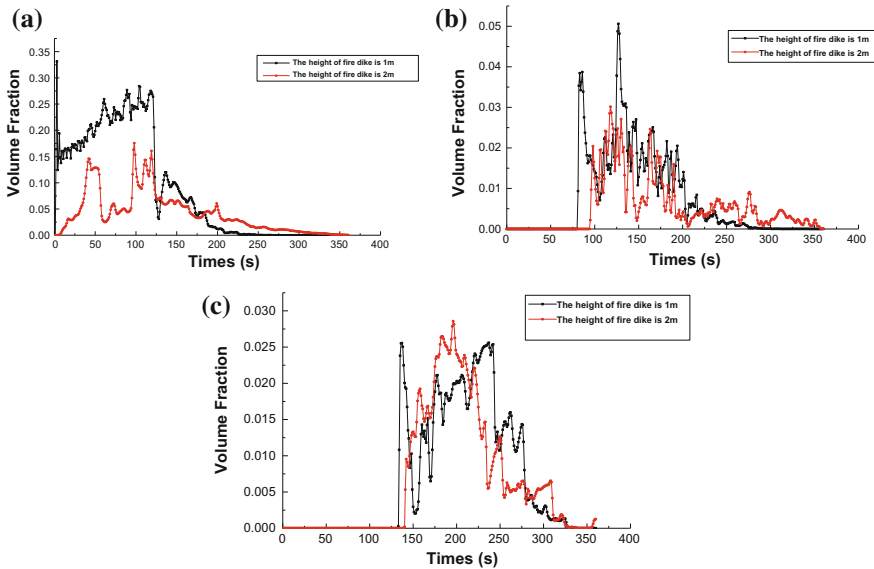
Fig. 6 Variation of the concentration in 1 m high with time, 4.5, 50, and 100 m away from the tank, in case of the addition of fire dike with the height of 1 and 2 m

It can be seen from Fig. 6 that in the 2 min of ethylene leak, with the addition of fire dike in 2 m high, the concentrations of ethylene vapor in places, where monitoring points are 4.5, 50, and 100 m away from the tank, are far less than that with fire dike in 1 m high, and their growth rates are rather slow as well. The higher the height of fire dike, the smaller the vapor concentration in the fire dike. Such as the case at 4.5 m, it can be seen from Fig. 6a that the concentration with fire dike in 1 m high is up to 15–33%, while it is 2.5–18% when the fire dike is 2 m high. This is because the height of the leak is 1 m from the ground, where the leakage of the ethylene vapor cloud is at a high level in the early time. After adding the height of fire dike, the vapor cloud spreads slowly upward along the wall in the process of diffusion. As result, partial vapor has spread to the upper part. The higher the height of the fire dike, the less ethylene vapor in the lower space. And, the ethylene vapor concentration drops sharply after the emergency stop of the leak.

4 Conclusion

In this paper, the physical model of ethylene storage tank was built, and the leakage source strength of ethylene storage tank was calculated by using ALOHA software. Then, the simulation of ethylene leakage was carried out by FDS software. Using numerical simulation method, the influence of related vapor control technology on

downward direction diffusion of ethylene vapor was studied. The main work and conclusions are as follows:

According to the standard, a fire dike at least 1 m high should be added to the ethylene storage tank, and the simulation results showed that the fire dike has a certain inhibitory effect on the movement and diffusion of the vapor cloud. A fire dike can block part of the ethylene vapor into the fire dike and delay the downwind spread of the steam to some extent. The concentration of downwind ethylene vapor was reduced, but the dissipation time of vapor cloud near the ethylene storage tank was delayed. While the dike height increased to 2 m, the simulation results showed that the vapor cloud inside spread upward along the firewall, dispersed in the longitudinal direction, a portion of which was delivered to the upper space, and that the time of ethylene spilling over the fire dike was delayed, which further reduced the distance and range of vapor diffusion downwind. When the ethylene vapor cloud spreads downwind over the fire dike, there is already a part of the vapor in the upper air. In fact, the ethylene vapor in the upper atmosphere is not very dangerous. Therefore, considering the various factors, it is better to choose the fire dike with a height of 2 m to control the diffusion of ethylene vapor.

References

1. Yuanxue, Z. (2005). Risk analysis of leakage and diffusion of ethylene cans at low temperature. *China Fire, 23,* 38–40.
2. Xue, L. (2015). *Numerical simulation of leakage and diffusion of liquefied natural gas*. Dalian: Dalian University of Technology.
3. Lin, W., Baolong, H., & Xuhai, P. (2014). Calculation of evaporation rate of LNG leakage on the ground. *Oil & Gas Storage and Transportation, 33,* 648–652.
4. Britter, R. E. (1979). The spread of a negatively buoyant plume in a calm environment. *Atmospheric Environment, 13,* 1241–1247.
5. Chowdhury, M. R., & Testik, F. Y. (2014). A review of gravity currents formed by submerged single-port discharges in inland and coastal waters. *Environmental Fluid Mechanics, 14,* 265–293.
6. Cleaver, P., Johnson, M., & Ho, B. (2007). A summary of some experimental data on LNG safety. *Journal of Hazardous Materials, 140,* 429–438.
7. Wei, X., & Guangjun, Z. (2006). FDS fire simulation and application. *Journal of Jilin Forestry Science and Technology, 6,* 367–372.
8. Lin, W., Min, W., & Baolong, H. (2015). Analysis of influencing factors on leakage risk of LNG tank. *Journal of Safety and Environment, 2,* 35–37.
9. Wei, T., Xiao, L., & Yujin, L. (2012). Advances in numerical simulation of transient leakage diffusion of hazardous liquefied gases. *Chemical Engineering, 5,* 46–49.
10. Association, National Fire Protection. (2009). *NFPA59A, Standard for the production, storage, and handling of liquefied natural gas (LNG)*. Quincy, Massachusetts: National Fire Protection Association.
11. General Administration of quality supervision, inspection and Quarantine of the People's Republic of China, China National Standardization Administration Committee. Production, storage and handling of liquefied natural gas (LNG) (GB/T20368-2012). Beijing: Standards Press of China, 2012.

12. Ministry of Housing and Urban Rural Development. (2014). *Code for design of fire-dike in storage tank farm (GB 50351-2014)*. Beijing: China Planning Press.
13. Ministry of Housing and Urban Rural Development. (2009). *Fire prevention code of petrochemical enterprise design(GB50160-2008)*. Beijing: China Planning Press.

Fire-Induced Horizontal Vent Flow Pattern in a Ceiling Vented Enclosure: Theoretical Analysis and Experimental Verification

Xiao Chen and Shouxiang Lu

Abstract The flow pattern is the one important factor to indicate the vented flow regularity, which is of great significance for understanding and preventing ceiling vented enclosure fires. In this paper, an experimental study on fire-induced flows in a ceiling vented enclosure was carried out. Five pan diameters and six horizontal opening sizes were adopted and measurements included the pressure difference in the top and temperature at the two sides of the opening. The instantaneous flow pattern was recorded by a video camera and laser technique. The purpose was to reveal the fire-induced flow pattern and make a distinguish between these flow patterns. Furthermore, the buoyancy number and the global equivalence ratio were introduced to analyze the fire-induced flow pattern in the ceiling vented enclosure. Through experimental analysis, the flow pattern across the horizontal ceiling vent induced by the real fire was revealed and summarized, which would benefit for studying the ventilation system in the fire risk assessment and firefighting.

Keywords Ceiling vented enclosure · Pool fire · Flow pattern · Buoyancy number

Nomenclature

g	Gravity acceleration (m/s^2)
t	Time (s)
v_{cb}	Characteristic buoyancy-induced velocity (m/s)
A	Area (m^2)
B	Buoyancy number (–)
D	Equivalent diameter of vent/pool (m)
Fr	Froude number (–)
Gr	Grashof number (–)
L	Vent thickness (m)

X. Chen (✉) · S. Lu
State Key Laboratory of Fire Science, University of Science and Technology of China, Hefei 230027, China
e-mail: summercx@mail.ustc.edu.cn

ΔP Pressure difference in the vent (Pa)
Re   Reynolds number (–)
T   Thermocouples (°C)
Y_{o_2} Oxygen mass fraction in the enclosure

Greek symbols

$\Delta\rho$ Density difference in the vent (kg/m^2)
$\bar{\rho}$ Average density (kg/m^2)
υ Kinematic viscosity (m^2/s)
θ Temperature ratio of ambient air and enclosure (–)
ϕ Global equivalence ratio (–)
β Constant (–)

Subscripts

fuel(f)   Fuel
vent(v)   Horizontal vent
p   Pool fire
E   Extinction

1   Introduction

The vent flow through an opening in a horizontal partition presents the instability stratification of fluid and the complexity of flow exchange, which are the major differences compared to the flow through a vertical vent, and the vent flow in the horizontal opening enclosures has been attracted a lot of attention in recent years [1–4]. As for the horizontal vent flow, different flow pattern (i.e., the direction of vent flow, the flow regime) may cause the distinct fire behavior inside the compartment. Thus, a better understanding of the flow pattern may be beneficial to study the ventilation system [5].

   Till now, much work has been focused on distinguishing the horizontal flow pattern, which could be summed up in the following several approaches. Firstly, some researchers used the ratio of vent thickness and equivalent diameter of the vent (*L/D*) to identify the flow regime. Epstein [6] proposed four different flow regimes obtained by saltwater experiment, which were identified as *L/D* and varied from 0.01 to 10: (1) oscillatory exchange flow regime; (2) Bernoulli flow regime; (3) turbulent diffusion; and (4) combined turbulent diffusion and Bernoulli flow regime. The flow

exchanges varied with *L/D* were studied by many researchers [7–9], and the frequency of oscillatory flow pattern was also investigated and was found to vary with *L/D* [10]. Secondly, the pressure difference in the vent was considered as a key factor that affects the flow pattern. Tan and Jaluria [11, 12] extended Epstein's work to cases where there may be a nonzero pressure differential across the vent. They studied the vent flow for the *L/D* range of 0.0144–6.0 to find out the critical pressure differential that distinguished the unidirectional flow regime from the bidirectional flow regime. They [12, 13] also recorded the photographs of shadowgraph images to study the transition from bidirectional to unidirectional flow (as the pressure difference increased). Gera [14] investigated the oscillatory bidirectional flow through the opening in the horizontal partition with shadowgraph. The critical (flooding) pressure difference was reported by Cooper [15] to distinguish unidirectional flow and bidirectional flow, and Cooper [16, 17] proposed the algorithms to deal with unidirectional and bidirectional flows on the basis of turbulent, large-Grashof-number flow through small *L/D* vent. Yamada [18] and Chow [4] extended Cooper's model to atrium application. Thirdly, Emmons graphically presented the flow rate with the dimensionless diameter $\Delta P/\Delta \rho g D$ and pointed out that the unidirectional flow was limited to the value $\Delta P/\Delta \rho g D$ of 0.045 and the flow occurred simultaneously in both directions in the range of $-0.45 < \Delta P/\Delta \rho g D < 0.45$ [19]. Tanaka [20] also pointed out that the actual volumetric hot gas outflow may be 2.5 times larger than the inflow when the net flow was sufficient to accommodate the fire gas expansion. At last, the buoyancy number was introduced by Tan and Jaluria [21] to infer that the induced force is buoyancy difference or pressure difference. Chow [22] proposed a new division of buoyancy number for the driving force, and the bidirectional flow was found that buoyancy number was greater than or equal to ten and the unidirectional flow happened when buoyancy number was smaller than one. These studies mentioned above were adopted with the saltwater modeling and numerical simulation, while Prétrel's group [1, 23] had conducted the smoke propagation fire tests through a horizontal opening to obtain the different flow regimes, from pure natural convection (bidirectional) to forced convection (unidirectional). They also proposed a geometrical organization of the bidirectional flow through the orifice. The ceiling vented enclosure fire has been discussed by many researchers in recent years, whereas the division of the fire-induced flow pattern needs to be paid further attention.

Relying on the small-scale experiments, this work investigates the flow pattern induced by a fire in a ceiling vented enclosure. Firstly, the experimental facilities and sets of small-scale tests are described in detail, and several parameters, such as temperature at the two sides of opening, temperature in the ceiling layer and pressure difference in the top, etc., are obtained. Then, the global equivalence ratio is adopted to analyze the flow pattern. Next, the buoyancy number was introduced to analyze the real fire to expand the application scope of the theory. Through experimental analysis, the flow pattern across the horizontal ceiling vent induced by the real fire was revealed and summarized, which would benefit for studying the ventilation system in the fire risk assessment and firefighting.

2 Experimental

Experiments were conducted in a ceiling vented enclosure at the State Key Laboratory of Fire Science (SKLFS) in Hefei (Fig. 1). The inner volume of the enclosure was 1 m³ (1 m in length, 1 m in width, and 1 m in height) as shown in Fig. 1. To enlarge the sight angle, the enclosure was constructed with 5 mm thick toughened glass. Four stainless steel columns were the support of the whole, and the other parts were 5 mm thick stainless steel. All joints were sealed with fire resistant to ensure that the compartment was fully enclosed except for a central ceiling vent. Six vent areas, 0.0025 m² (0.05 m × 0.05 m), 0.01 m² (0.1 m × 0.1 m), 0.04 m² (0.2 m × 0.2 m), 0.09 m² (0.3 m × 0.3 m), 0.16 m² (0.4 m × 0.4 m), and 0.25 m² (0.5 m × 0.5 m), were used to examine the effect of the vent size.

N-heptane (C_7H_{16}) pool fires with diameters of 7, 10, 14, 20, and 25 cm were positioned in the center of the enclosure. The initial fuel thickness was 13 mm and no further oil was added during tests. Four thermocouples named T_{v1}–T_{v4} were positioned in the ceiling vent to measure the temperature of the smoke vent flow in the horizontal opening. T_{v1} and T_{v2} were positioned in the centerline, and T_{v3} and T_{v4} were positioned at the side of the horizontal opening. A differential pressure sensor was fixed 5 cm apart from the ceiling and 5 cm apart from one sidewall to measure the pressure variation in the upper enclosure. The pressure sensor had a maximum capacity of 500 Pa with 0.05 Pa resolution.
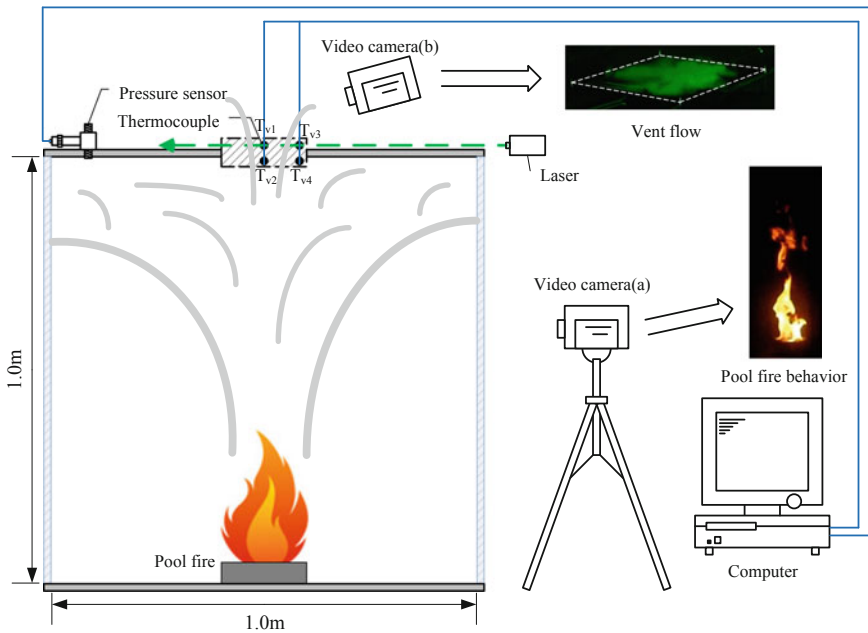
Fig. 1 Sketch of the experimental setup

The vent flow was visualized by implementing an optical technique. A green laser sheet was formed by a 2 W, 532 nm green laser, which was positioned 5 mm above the vent surface to capture visualization and scattering effect of the hot smoke and fresh air on the laser. A video camera (video camera (b) in Fig. 1) was used to record flow pattern at the vent. An additional video camera (video camera (a) in Fig. 1) was used to record the process of the fire, so as to obtain the extinction time more accurately. Twenty-fourth tests were conducted in this study, and the parameters and results are listed in Table 1.

Table 1 Summary of the small-scale tests

Test no.	Vent size L_v (m)	Pan diameter D_p (m)	A_{vent}/A_{fuel}	Extinction time t_E (s)	Flow pattern[a]
1	0.05	0.07	0.65	1490	Unidirectional
2	0.1	0.07	2.59	1427	Unidirectional
3	0.2	0.07	10.4	1224	Bidirectional
4	0.3	0.07	23.40	1087	Bidirectional
5	0.4	0.07	41.59	990	Bidirectional
6	0.5	0.07	64.99	761	Bidirectional
7	0.05	0.1	0.32	535	Unidirectional
8	0.1	0.1	1.27	637	Unidirectional
9	0.2	0.1	5.09	995	Compound
10	0.3	0.1	11.46	921	Bidirectional
11	0.4	0.1	20.38	787	Bidirectional
12	0.5	0.1	31.85	526	Bidirectional
13	0.05	0.14	0.16	237	Unidirectional
14	0.1	0.14	0.65	315	Unidirectional
15	0.2	0.14	2.6	1007	Compound
16	0.3	0.14	5.85	874	Bidirectional
17	0.4	0.14	10.39	676	Bidirectional
18	0.5	0.14	16.25	481	Bidirectional
19	0.05	0.2	0.08	110	Unidirectional
20	0.1	0.2	0.32	125	Unidirectional
21	0.2	0.2	1.28	601	Compound
22	0.05	0.25	0.05	66	Unidirectional
23	0.1	0.25	0.2	70	Unidirectional
24	0.2	0.25	0.81	63	Compound

[a]The flow pattern is the main flow regime observed during the test

3   Results and Discussions

3.1   Experimental Observation

On the basis of the different scattering effects of the hot smoke gas and fresh air on the laser, we marked the outflow and inflow through the horizontal opening as the green and black parts, respectively. In accordance with the smoke visualization results, three flow patterns could be qualitatively expressed as follows:

- Pattern I: unidirectional flow, including one-way inflow and one-way outflow; the unidirectional flow was transient and comparative stable, as schematically shown in Fig. 2a;
- Pattern II: bidirectional flow, the airflow pattern was transient and unstable, as schematically shown in Fig. 2b;
- Pattern III: compound flow, which sometimes presented both a unidirectional flow and a bidirectional flow; the compound flow was the transition flow pattern, which was more complex and unstable than patterns I and II, as shown in Fig. 2c.

Three flow patterns visualized by the video camera and laser technique in the tests are illustrated in Fig. 3. Figure 3a shows the unidirectional flow pattern (pattern I) for a diameter of 0.14 m pool fire under 0.05 m horizontal opening size in a second of the steady burning stage. In pattern I, the fire-induced expansion pressure caused the hot smoke gas to flow out through a small horizontal opening and form a stable smoke layer in the upper compartment. However, minimal fresh air poured into the compartment and mixed with the hot smoke to support the pool fire burning. In this pattern, the one-way inflow and one-way outflow did not exist simultaneously, and the transient one-way inflow and outflow accounted for the compromising value of 90% of the whole flow process according to the experimental observation.
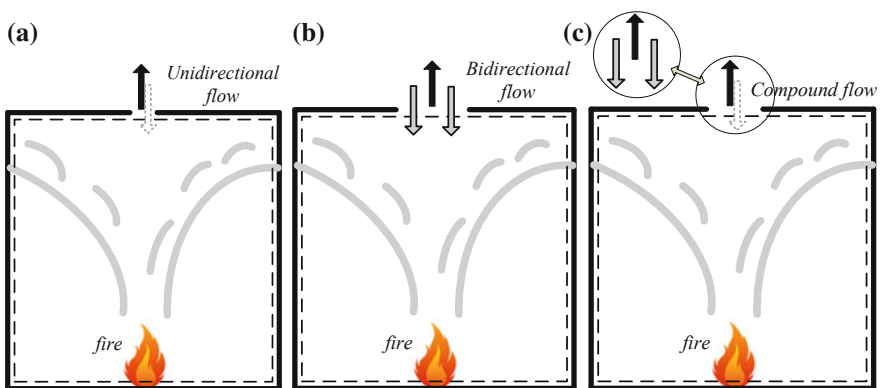
Fig. 2 Schematics of the three flow patterns, **a** flow pattern I, **b** flow pattern II, and **c** flow pattern III

(a) $D_p = 0.14$ m, $L_v = 0.05$ m, 1 s in the steady burning stage

(b) $D_p = 0.14$ m, $L_v = 0.3$ m, 1 s in the steady burning stage

(c) $D_p = 0.14$ m, $L_v = 0.2$ m, 1 s in the steady burning stage
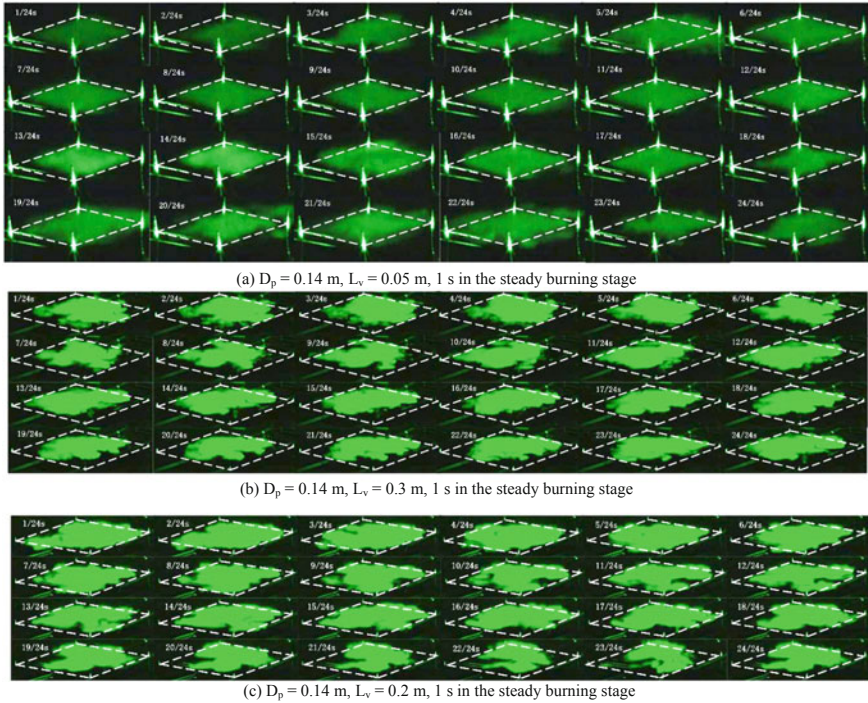
Fig. 3 Flow pattern visualized by video camera and laser technique in the tests

In pattern II, the one-way inflow and outflow occurred simultaneously for a diameter of 0.14 m pool fire under 0.3 m horizontal opening size, and the incoming and outgoing flows were transient and unstable. Given the large opening size, the mixing effect of the hot smoke gas and the fresh air was sufficient, and the fresh air flowed easily into the compartment according to the increasing displacement between the opening edge and the fire source. The transient two-way flow accounted for the compromising value of 90% of the whole flow process.

The one-way flow and two-way flows appeared alternately and not simultaneously for a diameter of 0.14 m pool fire under 0.2 m horizontal opening size in the pattern III (Fig. 3c). This situation made the outgoing hot smoke gas and incoming fresh air to exchange in a complex manner. The one-way inflow or outflow accounted for the compromising value of 50% of the whole flow process, and the two-way flow accounted for the rest of the flow process based on smoke visualization.

3.2 Theoretical Analysis

The buoyancy number is characterized by the Grashof number *Gr* and the Reynolds number *Re* [16, 21, 22] to clarify whether the buoyancy or pressure was the main driven force,

$$B = \frac{Gr}{Re^2} = \frac{g\Delta\rho D}{\Delta P} \tag{1}$$

where *B* is the buoyancy number, which was similar to Richardson number *Ri* in combined force and natural convection circumstances [16]. *Gr* and *Re* are defined by the characteristic buoyancy-induced velocity v_{cb} given by Gebbart [24] as [21, 22]

$$v_{cb} = \sqrt{\frac{g\Delta\rho D}{\bar{\rho}}}$$

$$Gr = \frac{g(\Delta\rho/\bar{\rho})D^3}{v^2} \tag{2}$$

$$Re = \sqrt{\frac{\Delta P}{\bar{\rho}}\frac{D}{v}}$$

where *g* is gravity accelerate, $\Delta\rho$ is density difference, ΔP is pressure difference, *D* is the equivalent diameter of the vent, and v is kinematic viscosity.

In general, for buoyancy-driven flow, $g\Delta\rho D \gg \Delta P$, and B approaches infinity, whereas for pressure-driven flow, $g\Delta\rho D \ll \Delta P$, and *B* approaches zero. However, Chow [22] proposed a new division to determine through numerical simulation the driving force in airflow oscillation under different vents. For pressure-driven flow, $B < 0.1$, while buoyancy-driven flow, $B > 10$, where $1 < B < 10$, the driving force is a combination of buoyancy and pressure. Chow also considered the relationship between buoyancy number and flow pattern, and he asserted that if $B \geq 10$, the flow pattern is bidirectional, but where $B \leq 1$, the flow pattern is unidirectional.

3.3 Experimental Validation and Discussion

In order to explore the flow pattern under a real fire condition, Cooper [15] also proposed a developed model to deal with the vent flow, which was suitable for the zone-type compartment fire, and the mechanism of the flow behavior through top vent was simplified to assume that the vent flow was mainly driven by pressure difference when they discussed the critical condition [15–17]. By substituting Froude number and flow coefficient, etc. obtained from experimental data, the critical pres-
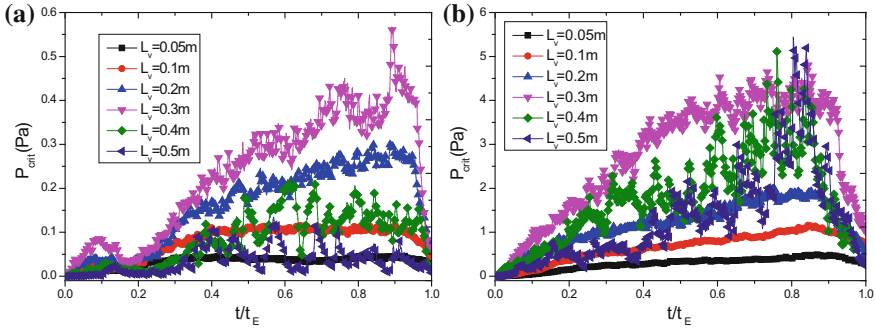
Fig. 4 Critical pressure difference under different opening sizes: **a** Dp = 0.07 m; **b** Dp = 0.14 m

sure difference under real fire conditions can be obtained. This processing method was also adopted by Wakatsuki [25].

Figure 4 illustrates the critical pressure difference under different opening sizes for 0.07 and 0.14 m pool fires. Figure 4a, b presents a similar trend for the small and medium opening sizes, where the critical pressure difference increases as the opening size increases from 0.05 m to 0.3 m, while for the larger opening sizes, i.e., 0.4 and 0.5 m, there is a marked difference between Fig. 4a, b in that the critical pressure difference of 0.14 m pool fire oscillates much more severely than that of 0.07 m pool fire. In terms of values of critical pressure difference in Fig. 4a, b, the 0.14 m pool fire is nearly ten times higher than the 0.07 m pool fire. This indicates that the critical pressure difference is affected by both opening size and pool size.

This paper tries to verify the applicability of the criteria to a real fire situation and to expand the application of the criteria. The pressure difference ratio is a ratio of pressure difference in the vent and the critical value. In this study, the ceiling layer was assumed to be a layer with uniform properties, and therefore, the pressure difference in the vent is considered to be equal to pressure difference at the top measured in the tests. Previous studies on buoyancy parameters have mainly distinguished which force is the driving force, while in the present work, we only focus on the relationship between buoyancy number and flow pattern. Figure 5a–c illustrates the buoyancy parameter under different opening sizes. There is a similar trend among 0.07, 0.1, and 0.14 m pool fires: Values of B are less than 1 for 0.05, 0.1, and 0.2 m opening sizes.

Due to the complex burning behavior, it is suitable for ceiling vent flow induced by a real fire to consider the coupling effect of the fire source and the horizontal vent; hence, the global equivalence ratio (GER) coupling the horizontal vent and fire source areas the was adopted to distinguish the flow patterns. The GER for the ceiling vented enclosure fire has been discussed in the previous study [26], which can be expressed as

(a) D_p=0.07m, B

(b) D_p=0.1m, B

(c) D_p=0.14m, B
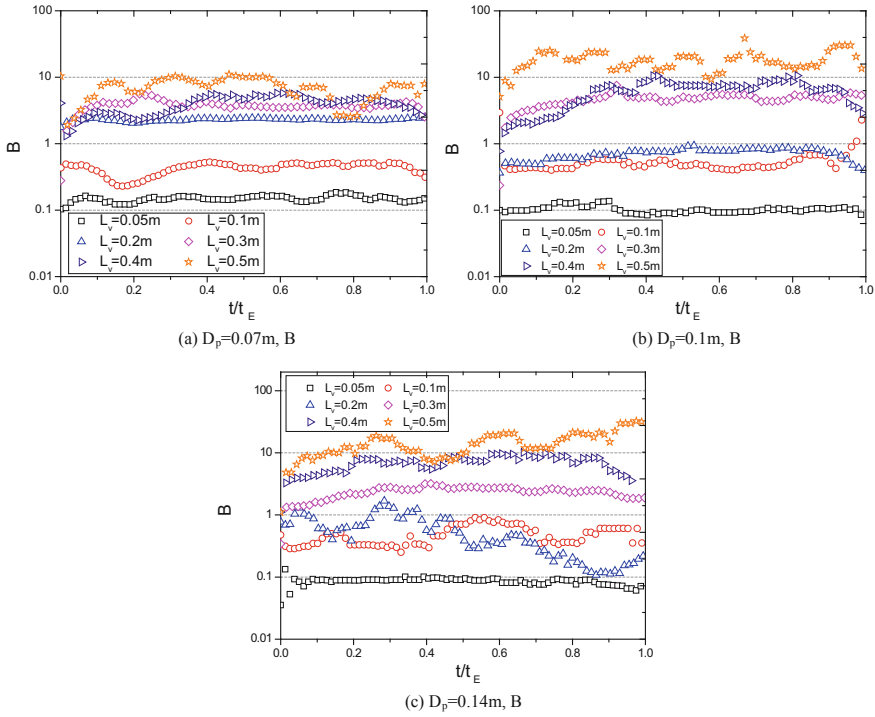
Fig. 5 Buoyancy parameter of calculated values under different opening sizes

$$\phi = \frac{\beta Y_{O_2} A_f}{A_v^{5/4} \sqrt{\frac{2(1-\theta)}{1+\theta}}} \tag{3}$$

where A_f is the fire source area, A_v is the horizontal vent area, Y_{O_2} is the oxygen mass fraction in the enclosure, θ is the temperature ratio of ambient air and enclosure, and β is a constant of 3.9 (m$^{1/2}$) only for heptanes.

To analyze the flow pattern quantitatively and determine the transition points of the flow pattern, the buoyancy number ($\Delta\rho g D/\Delta P$) was adopted in the analysis of the flow pattern with the GER (ϕ). Figure 6 illustrates the division of the flow pattern according to the variation of buoyancy number with the global equivalence ratio. In Fig. 6, hollow, solid, and half-solid symbols represent the unidirectional, bidirectional, and compound flows, respectively. The buoyancy numbers of the hollow symbols and the half-solid symbols were smaller than 1 and close to 1, respectively, whereas the buoyancy numbers of the solid numbers were larger than 1. The buoyancy number denoted the linear relationship with the global equivalence ratio. The fitting relation can be well correlated with a correlation coefficient R^2 of 0.90 as follows:
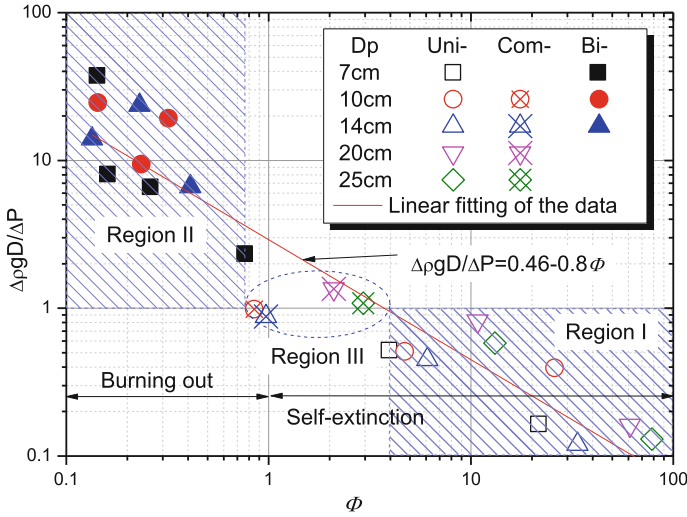
Fig. 6 Variation of the buoyancy number ($\Delta \rho g D / \Delta P$) with the global equivalence ratio (ϕ)

$$\frac{\Delta \rho g D}{\Delta P} = 0.46 - 0.8 \frac{\beta Y_{O_2} A_f}{A_v^{5/4} \sqrt{\frac{2(1-\theta)}{1+\theta}}} \qquad (4)$$

According to the intersection of the fitting line and $\Delta \rho g D / \Delta P = 1$ and the critical transition point, the three regions for the different flow patterns are shown in Fig. 6. The critical transition region for the flow pattern exchange ranged between $\phi \leq 0.76$ and $\phi \geq 3.94$. Thus, when $\phi \geq 3.94$, and the buoyancy number was less than 1 (in region I), the flow pattern is certainly unidirectional. On the contrary, when $\phi \leq 0.76$, and the buoyancy number was larger than 1 (in region II), the flow pattern is bidirectional. The compound flow was added for convenience and accurate expression, and it ranged between $0.76 < \phi < 3.94$ and the buoyancy number was near 1 (in region III). Moreover, according to the previous study [26], the bidirectional flow pattern was found in the burning out mode and the unidirectional and compound flow pattern belonged to the self-extinction mode. It is worth noting that although the transition point for the GER proposed was based on the experimental results in this research, and we need further validation to discuss the application to other enclosure dimension. It is certain that the analysis method could be used to expand in the other research.

4 Conclusions

The flow across the horizontal ceiling vent has determining impacts on fire behaviors in ceiling vented compartments. The flow pattern is the one important factor to indicate the vented flow regularity, which is of great significance for understanding

and preventing ceiling vented enclosure fires. In this paper, the results of an experimental study on fire-induced flows in a ceiling vented enclosure are presented. The vent flow pattern was observed during the tests by the video camera and laser technique. Pressure difference at the top and temperature at the two sides of the opening were obtained. The buoyancy number was induced to analyze the fire-induced flow pattern to expand the application scope of Chow's theory. Furthermore, the global equivalence ratio is proposed to distinguish the three flow patterns, namely unidirectional flow, bidirectional flow, and compound flow. Results show that the flow pattern is unidirectional flow when $\phi \geq 3.94$ and buoyancy number is less than 1, and it appears bidirectional flow when ϕ is less than 0.76 and buoyancy number is larger than 1, whereas the compound flow appears when $0.76 < \phi < 3.94$ and buoyancy number is closer to 1. Through experimental analysis, the flow pattern across the horizontal ceiling vent induced by the real fire was revealed and summarized, which would benefit for studying the ventilation system in the fire risk assessment and firefighting.

References

1. Prétrel, H., Sayada, R., Varrall, K., et al. (2017). Experimental study based on large-scale smoke propagation fire tests through a horizontal opening connecting two mechanically ventilated compartments. *Fire Safety Journal, 90,* 28–43.
2. Chen, X., Lu, S., Wang, X., et al. (2016). Pulsation behavior of pool fires in a confined compartment with a horizontal opening. *Fire Technology, 52*(2), 515–531.
3. Gera, B., Sharma, P. K., & Singh, R. K. (2014). Cfd analysis of flow through horizontal ceiling opening due to buoyancy and pressure difference. *International Journal of Modern Physics C, 25*(01), 1340022.
4. Chow, W. K., & Li, J. (2011). On the bidirectional flow across an atrium ceiling vent. *Building and Environment, 46*(12), 2598–2602.
5. NFPA 92B. (2009). *Guide for smoke management systems in malls, atria, and large areas.* Quincy, MA: National Fire Protection Association.
6. Epstein, M. (1998). Buoyancy-driven exchange flow through small openings in horizontal partitions. *Journal of Heat Transfer, 10,* 885–893.
7. Conover, T. A., Kumar, R., & Kapat, J. S. (1995). Buoyant pulsating exchange flow through a vent. *Journal of Heat Transfer, 117,* 641–648.
8. Spall, R. E., & Anderson, E. A. (1999). A numerical study of buoyant, pulsating exchange flows through a vent in a thin horizontal partition. *Numerical Heat Transfer: Part A: Applications, 36,* 263–272.
9. Harrison, R. P., & Spall, R. E. (2003). The effects of partition thickness on buoyant exchange flow through a horizontal opening. *Numerical Heat Transfer: Part A: Applications, 44,* 451–462.
10. Sleiti, A. K. (2009). Transient flow of air through rectangular vents in a horizontal partition. *HVAC and Research, 15*(6), 1145–1163.
11. Tan, Q., & Jaluria, Y. (1992). *Flow through horizontal vents as related to compartment fire environments.* NIST GCR 92-607, 105p.

12. Jaluria, Y., Lee, S. H. K., Mercier, G. P., & Tan, Q. (1993). Visualization of transport across a horizontal vent due to density and pressure differences. In: *ASME, National heat transfer conference. Visualization of Heat Transfer Processes* (HTD-Vol. 252, pp. 1–17), August 1993, Atlanta, GA, American Society of Mechanical Engineers, New York, NY.
13. Jaluria, Y., & Lee, S. H. K. (1998). Transport processes across a horizontal vent due to density and pressure differences. *Experimental Thermal and Fluid Science, 16*(3), 260–273.
14. Gera, B. (2005). *Investigation of bi-directional flow behaviour of a large opening*. M.Tech. Thesis Department of Mechanical Engineering, IIT Delhi, India.
15. Cooper, L. Y. (1996). Calculating combined buoyancy-and pressure-driven flow through a shallow, horizontal, circular vent: Application to a problem of steady burning in a ceiling-vented enclosure. *Fire Safety Journal, 27*(1), 23–35.
16. Cooper, L. Y. (1989). *Calculation of the flow through a horizontal ceiling/floor vent*. NISTIR 89–4052 (2nd ed.). Gaithersburg, MD: National Institute of Standards and Technology.
17. Cooper, L. Y. (1995). Combined buoyancy- and pressure-driven flow through a horizontal, circular vent. *Journal of Heat Transfer, 117,* 659–667.
18. Yamada, T. (1996). *Experimental study of the exchange flow through a horizontal ceiling vent in atrium fires-criteria of supply air and pressure necessary for unidirectional flow*. Paper presented at the Thirteenth Meeting of the UJNR Panel on Fire Research and Safety.
19. Emmons, H. W. (2002). Vent flows. In P. J. DiNenno, D. Drysdale, C. L. Beyler, W. D. Walton, L. P. Richard, J. R. Hall, & J. M. Watts (Eds.), *The SFPE handbook of fire protection engineering* (3rd ed.). Quincy, Massachusetts: National Fire Protection Association.
20. Tanaka, T. (1983). A model of multi-room fire spread. *Fire Science and Technology, 3*(2), 105–121.
21. Tan, Q., & Jaluria, Y. (2001). Mass flow through a horizontal vent in an enclosure due to pressure and density differences. *International Journal of Heat and Mass Transfer, 44,* 1543–1553.
22. Chow, W. K., & Gao, Y. (2011). Buoyancy and inertial force on oscillations of thermal-induced convective flow across a vent. *Building and Environment, 46*(2), 315–323.
23. Varrall, K., Pretrel, H., Vaux, S., et al. (2016). Stereoscopic particle image velocimetry investigation of the bidirectional natural convection flow through a horizontal vent. *Fire Technology, 52*(6), 2027–2041.
24. Gebbart, B., Jaluria, Y., Mahajan, R. L., & Sammakia, B. (1988). *Buoyancy induced flows and transport*. NY: Hemisphere Pub. Corp.
25. Wakatsuki, K. (2001). *Low ventilation small-scale compartment fire phenomena: Ceiling vents*. Master thesis. University of Maryland, MD.
26. Chen, X., Lu, S., & Liew, K. M. (2016). An investigation of horizontal opening effect on pool fire behavior in a confined compartment: A study based on global equivalence ratio. *Journal of Fire Sciences, 34*(1), 13–29.

Numerical Study on the Smoke Control Effect of the Air Inlet Setting in the Vestibule of Building

Hua Yang and Si-Cheng Li

Abstract The smoke control effect of mechanical pressurization system in the vestibule of the building is studied based on numerical simulation. The diversity of the actual air inlet setting of mechanical pressurization system is considered. The relative position of the air inlet and fire door opening is investigated in our research, which is divided into three cases: directly opposite, diagonally opposite, and perpendicular. The method of numerical simulation is used to study the influence of the relative position of the air inlet and door, as well as the installation heights of the air inlet of the fire-induced smoke prevention system. The smoke control effect in the case of fire and the cold state without fire is compared and analyzed; the setting position of the air inlet is optimized. The conclusion can provide technical references for smoke control design personnel, building fire protection design audit personnel, and the technical codes' creators of smoke control and fire researchers.

1 Introduction

When the building fire occurs, the trapped mainly evacuated through the corridor, vestibule, and staircase. When the smoke penetrates into an evacuation stairwell through a gap of the compartment structure or the opening of a fire door, it can cause a large number of casualties [1, 2]. As a buffer area for evacuation, the vestibule can prevent the intrusion of high temperature fire-induced smoke into the vertical shaft such as stairwell. It should ensure it is free of smoke intrusion when the fire occurred primarily. For this reason, smoke control systems are institutionalized in many countries to prevent smoke diffusion and ensure the safety of evacuation [3–5]. There are

---

H. Yang · S.-C. Li (✉)
Department of Fire Command, China People's Police University, Langfang 102800, China
e-mail: lisch@mail.ustc.edu.cn

H. Yang
Ji'Nan Municipal Fire Service Department, Fire Department of Shandong Province, Ji'Nan 250100, China

many smoke control methods. At present, among them, the method commonly used in the smoke control of the vestibule to cut off the spread of smoke is the mechanical pressurization system [6]. But there are no explicit illustrations about the specific settings in the criterion. And the location, installation heights, and format of the air inlet are dissimilar. So it is necessary to study the smoke control effect of the air supply system in different settings.

Based on the method of CFD numerical simulation, Kim et al. [7] analyzed the features of airflow through the open door in pressure differential system. By using the network model, Kim and Shin [8] analyzed the pressurization system for a model building of 20 stories. The pressurization system in their research was designed according to the standard and pressure field of compartments in whole model building induced by the pressurization system. Ryu et al. [9] conducted the study of backflow to stair-lobby at the upper vestibule. According to the simulation results, they found the gradient of supply damper's blade which leads backflow at the bottom and leads airflow steady at the upper vestibule. Based on the numerical simulation, Seo and Shin [11, 12] studied the characteristics of airflow in the multiple fire doors vestibule of an apartment building. They investigated the damper location for uniform air egress velocity in the case of two fire doors and the conditions leading to the reverse flow occurs. You et al. [13] investigated the effects of the fire door and changes of the wings of supply damper on the pressure difference in mechanical pressurization fire-induced smoke control system. In order to analyze the characteristics of the pressure evolution under different conditions in a small compartment of building, Gai and Cancelliere [14] conducted a series of numerical simulations and experimental tests. To explore and investigate the airflow profiles typical of some geometrical configurations, the pressurization and depressurization during steady-state and transient phases were studied in their research.

The focus of previous research is mainly on the distribution of the air egress velocity in the cold state without fire. In their study, the effective smoke control area is an important factor to measure the effect of the air supply in the pressure differential system on fire-induced smoke prevention. However, when the actual fire occurs, due to the existence of high temperature fire-induced smoke, the movement of airflow in the vestibule must be different from the cold state. The influence of the air inlet setting on the effect of fire-induced smoke prevention should be further studied. It is necessary to study the fire-induced smoke prevention effect of different settings of mechanical pressurization system in the vestibule of building to provide some reference for the design of building smoke control system. In this paper, aiming at the diversity of the actual air inlet setting, the relative position of it and the fire door opening is divided into three cases: directly opposite, diagonally opposite, and perpendicular. The method of numerical simulation is used to study the influence of the factors such as the relative position of the air inlet and door opening, as well as the installation heights of the air inlet vent. In order to explore the effect of fire-induced smoke on the distribution of airflow velocity in the vestibule, the cold-state simulations are performed. The smoke control effect in the case of fire and the cold state without fire is compared and analyzed; the setting position of the air inlet is optimized. The conclusion of this paper can provide some references for the

specific setting of the air supply system in the vestibule. It can provide some technical references for smoke control design personnel, building fire protection design audit personnel, fire safety management personnel, and technical codes' creators of smoke control and fire researchers.

2 Numerical Modeling

2.1 Physical Model

In order to study the effect of relative position of fire door opening and air inlet setting in the vestibule of building on the prevention of fire-induced smoke, this study established the physical model as shown in Fig. 1a. The plane diagram of the physical model is shown in Fig. 1b. In this model, the fire door position is fixed. Air inlet 1 directly opposite to the fire door opening. Air inlet 2 which has 0.4 m horizontal distance from air inlet 1 diagonally opposite to the fire door. Air inlet 3 set in the middle of the sidewall of vestibule. Different relative position between the air inlet and fire door opening is realized by different height setting of the air inlet on the vestibule walls in different directions. The fire room and the vestibule are connected by a corridor of size $16 \times 2 \times 3$ m^3. The stairwell and other areas of the building are omitted. The fire room is located at the right end of the corridor, and a fire source is set inside it. Between the fire room and corridor opened a fire door of size 1×2 m^2. The door is open when the fire occurs. At the other end of the corridor, the external airflow is set. The external airflow is open when the fire occurs which can be used for static smoke exhaust. The vestibule is of size $5 \times 3 \times 3$ m^3. The door between vestibule and corridor is 1.4 m wide and 2 m high. When the fire occurs, the door is open because of the evacuation of the trapped occupancies in the building.
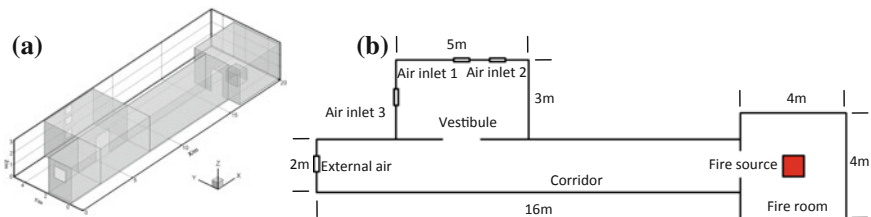
Fig. 1 a Physical model and **b** plane diagram to investigate the effect of relative position of fire door opening and air inlet in building vestibule on the prevention of fire-induced smoke

2.2 Numerical Setup

The problem studied in this paper belongs to the fire prevention and control of buildings. It is applicable to the Technical Specification for Building Smoke Control (DGJ08-88-2006). According to the clause 4.2.1 of Technical Specification for Building Smoke Control (DGJ08-88-2006) [15], the fire release rate (HRR) of fire in the room of an office building or hotel room with sprinklers should be estimated by 1.5 MW. Therefore, in our simulation study, a fire source with a power of 1.5 MW is set in the fire room. Because the focus of this paper is not the chemical reaction in the combustion process, the volume heat source (VHS) is used to set up the fire source. The fire source in the actual situation is assumed to be a source of heat and energy. The heat release rate, the type, and generation rate of the product are set up, respectively. In this simulation, the fire source is simplified to a cube of $1 \times 1 \times 1 \, m^3$. The heat release rate is 1.5 MW. It is assumed that the main components of the fire-induced smoke are CO, CO_2, and air. According to the previous research results on the composition of fire-induced smoke, it is assumed that the air accounts for 95% of the total mass and 5% for CO_2. In addition, the mass of CO is 5% of the mass of CO_2. The formation rate of fire-induced smoke is determined by the relationship with the heat release rate.

In our research, the CFD software is adopted to conduct the numerical study. In this study, the hexahedral structured grid is applied. In the fire room and the corridor, the grid size of 0.1 is adopted. In the vicinity of the vestibule and in the vestibule, the grid size of 0.05 is adopted. The computational domain contained a total of 714,000 grid cells.

Our research focuses on the effect of different air inlet setting on smoke control, so it ignores the influence of some minor factors on smoke control effect to simplify complex problems. The following assumptions are made in the numerical simulation: (1) There is no other obstacle in the vestibule, which affects the movement of the air; (2) no consideration is given to the effect of escape people on airflow during the evacuation process; (3) neglecting the possible air leakage in the elevator and the stairwell; and (4) the temperature of the air supply is consistent with the ambient temperature.

The specific boundary conditions are set as follows: (1) The flow uses a double-equation turbulence model with buoyancy correction; (2) the fire source adopts the VHS combustion model, and the size is 1.5 MW; (3) the ambient temperature is 300 K, the density is 1.225 kg/m^3, and the wall is adiabatic wall; (4) the radiation uses the discrete ordinates (DO) radiation model, which solves the radiative transfer equation (RTE) for a finite number of discrete solid angles; (5) the boundary condition of the air inlet is set to velocity inlet; (6) the external airflow is defined as outflow, and the percentage of air mass flow is 100%; and (7) the pressure correction method of SIMPLE is used to solve the discrete equation.

In the actual building, the geometry of the air inlet is rather complicated. There are many forms such as the strip air inlet vent and the louver air supply vent. If we want to simulate the geometry parameters of the air inlet accurately, we need to divide

the grid to the millimeter level, which will greatly increase the computation load. Because the focus of our research is not the influence of air supply vent structure on the effect of air supply, in order to facilitate the research, we use the traditional simplified method to simulate the air supply of the air inlet. The air inlet vent in the actual building is simplified as a rectangular shape opening in this study. The air supply volume is 10,000 m³/h. The inlet airflow velocity is defined by the velocity inlet model. The inlet airflow velocity is 11.57 m/s. The inlet airflow velocity is defined as Eq. (1):

$$V = \frac{Q}{A}$$

(1)

where Q is the air volume, and A is the air inlet area.

2.3 Simulation Scenario

This paper mainly focuses on the difference of the smoke control effect under the different setting position of the air inlet. The main variables are installation height of the air inlet in vestibule and the relative position between air inlet and fire door opening. Ten simulation scenarios are investigated in our research (shown in Table 1). Three relative positions between air inlet and fire door opening are studied for different installation height of air inlet.

Table 1 Table of simulation scenarios

Scenario	Relative position	Height of air inlet (m)
1	1: Directly opposite	0.2–0.8
2	1: Directly opposite	1.4–2.0
3	1: Directly opposite	2.3–2.9
4	2: Diagonally opposite	0.2–0.8
5	2: Diagonally opposite	1.4–2.0
6	2: Diagonally opposite	2.3–2.9
7	3: Perpendicular	0.2–0.8
8	3: Perpendicular	0.8–1.4
9	3: Perpendicular	1.4–2.0
10	3: Perpendicular	2.3–2.9

3 Results and Discussion

3.1 Directly Opposite

The contour map of temperature distribution in the fire door central section for the air inlet set at different height is shown in Fig. 2. There numerical simulation temperature result is difference with the experimental results for the following reasons: (1) numerical simulation ignores the heat transfer of building wall, which is simplified as adiabatic wall, while the main body of the experimental device is steel structure, which has good thermal conductivity and some heat will be absorbed by the steel structure; (2) although the experimental device has been sealed in the connection of components, there are still certain gaps, which lead to heat flowing through these gaps to other parts of the experimental device; and (3) liquefied petroleum gas (LPG) was used as fuel in the experiment. The firepower is determined by controlling the LPG flow. However, the actual operation of the LPG flow cannot be absolutely maintained at the set value. The actual temperature, which is influenced by room temperature, will inevitably be lower than the set value. However, the numerical simulation can avoid the above problems. This paper focuses on the comparative analysis of the advantages and disadvantages of different air inlet settings. So we ignore the detail difference between the experimental and the numerical results and directly compare, and analyze the temperature distribution under different conditions.

It can be seen from Fig. 2 that when the air inlet is set at 0.2–0.8 m, only the temperature in the lower region (in the range of inlet height) of vestibule maintains at about 320 K. In the upper space of vestibule temperature reached above 500 K, where the temperature rise is more than 200 K. It indicates that a large number of high temperature fire-induced smoke spread into the vestibule. It will jeopardize the safety of the evacuation. This result is in agreement with the conclusion of airflow velocity distribution in cold-state simulation without fire. When the installation height of the air inlet increases to 1.4–2.0 m, the smoke prevention effect in vestibule is improved. The temperature of the area below the air inlet is about 400 K, and the area above the air inlet is about 470 K. It indicates that the smoke spread in vestibule in Scenario 2 is less than it in Scenario 1. But there is still smoke spreading into the room in the area below and above the airflow. In cold-state simulation without fire,
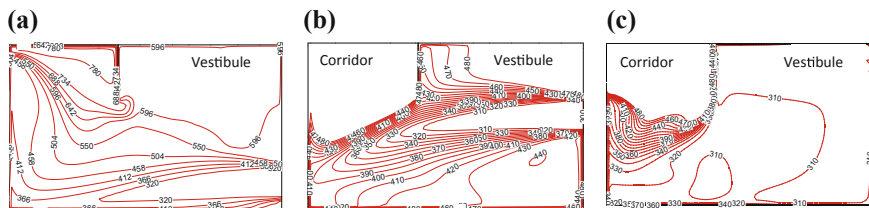
Fig. 2 Contour map of temperature distribution in the fire door central section for air inlet set at the height of **a** 0.2–0.8 m, **b** 1.4–2.0 m and **c** 2.3–2.9 m, respectively (Scenario 1–3)
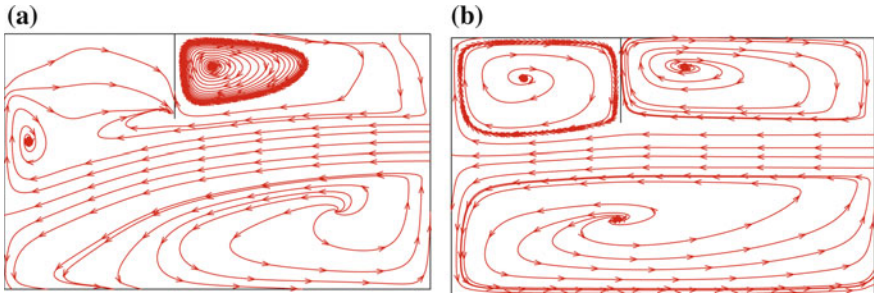
Fig. 3 Streamline diagram in the fire door central section for air inlet set at the height of 1.4–2.0 m in the condition **a** with room fire and **b** cold state without fire (Scenario 2)

the 1.4–2.0 m height is the best set height for smoke prevention, which is different from the result of Scenario 2. The main reason for this difference is that the existence of high temperature smoke in the corridor near the vestibule causes the temperature difference inside and outside the vestibule. The air inlet flow temperature is the same as the temperature of air in vestibule, which is lower than the temperature of smoke. The low temperature air inlet flow will move down under the effect of temperature difference in vestibule. As a result, the flow velocity near the upper door space is low, which leads to the spread of smoke from the upper space into vestibule. In the cold-state simulation without fire, the air inlet flow is almost horizontal flow to fire door and completely covering the upper part of the door opening. The streamline diagram in the fire door central section for air inlet set at the height of 1.4–2.0 m in Scenario 2 with room fire and cold state without fire is shown in Fig. 3.

It can be seen from Fig. 2 that when air inlet set at the height of 2.3–2.9 m (the projection of the air inlet vent is above the opening of fire door), the temperature of vestibule remained at about 310 K. The temperature rise is only about 10°. Most of the high temperature smoke is blocked outside the vestibule. In case of fire, high temperature smoke near the door will move upward, thus slowing the downward movement of the air inlet flow in vestibule. Therefore, the airflow will be concentrated in the upper part of the door opening of vestibule. As a result of a large air inlet flow, the high temperature smoke is blocked outside the vestibule, so the temperature in vestibule is not rising obviously. To summarize, according to the temperature distribution in the vestibule, it is suggested that the vent of air inlet should be set above the height of fire door opening when the air inlet directly opposite to fire door opening.

3.2 Diagonally Opposite

The focus of this paper is the protection of the positive pressure air supply to the location of the fire door. The contour map of temperature distribution in the fire
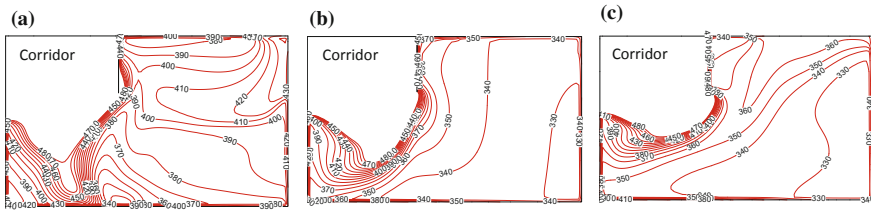
Fig. 4 Contour map of temperature distribution in the fire door central section for air inlet set at the height of **a** 0.2–0.8 m, **b** 1.4–2.0 m, and **c** 2.3–2.9 m, respectively (Scenario 4–6)

door central section can fully display the temperature distribution from the top to the bottom of the entire fire door area, thus fully reflecting the protective effect of positive pressure air supply on the door. The contour map of temperature distribution in the fire door central section for air inlet set at different heights is shown in Fig. 4. It can be seen from Fig. 4 that: (1) When the air inlet is set too low, the temperature rise of the upper part of vestibule is high. A large number of smoke flows into the vestibule endangering the evacuation; (2) when the air inlet is arranged on the upper region, the smoke control effect is improved. When the air inlet is set to 1.4–2.0 m, the overall temperature in the vestibule is in the range of 330–350 K. When the air inlet is set to 2.3–2.9 m, the overall temperature in the vestibule is in the range of 330–360 K. There is not much difference in temperature distribution between the two settings. This is consistent with the results of the cold-state simulation. Therefore, in order to get better smoke control effect, it is suggested that the vent of air inlet should be set at the upper part of vestibule when the air inlet is diagonally opposite to the fire door opening.

In order to investigate the temperature near vestibule fire door opening and analyze the effect of installation height, the 29 temperature measurement points are set in the numerical simulation scenario to measure temperature profile. The 29 temperature measurement points are with intervals of 0.05 m in the simulation. They are arranged in a vertical arrangement in the door at the 0.6 m distance from the door opening central line. Figure 5 shows the temperature comparison between the directly opposite position and the diagonally opposite position for different air inlet installation height. It can be seen that: (1) When the height is 0.2–0.8 m, the temperature rise of diagonally opposite position is less than that of directly opposite position; (2) when the height is 2.3–2.9 m, the temperature rise of diagonally opposite position is more than that of directly opposite position; (3) when the height is 1.4–2.0 m, the fire control effect of diagonally opposite position is better than that of directly opposite position.

3.3 Perpendicular

This section mainly discusses the effect of air inlet installation height on the smoke control when the air inlet perpendicular to the fire door of vestibule (this relative
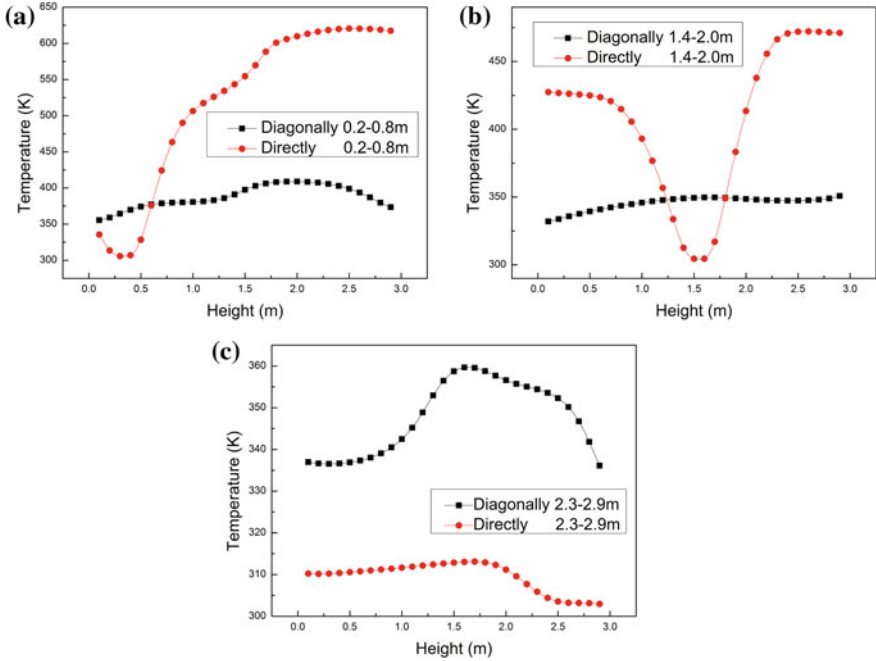
Fig. 5 Temperature comparison between the directly opposite position and the diagonally opposite position for air inlet set at the height of **a** 0.2–0.8 m, **b** 1.4–2.0 m, and **c** 2.3–2.9 m, respectively

position is the position of air inlet 3 in Fig. 1b). Figure 6 shows the temperature of the perpendicular relative position for different air inlet installation height. It can be seen that the temperature rise of vestibule increases with the increase in air inlet installation height. When the air inlet is set at 0.2–0.8 m, the temperature rise of the

Fig. 6 Temperature of the perpendicular relative position for different air inlet installation height (Scenario 7–10)
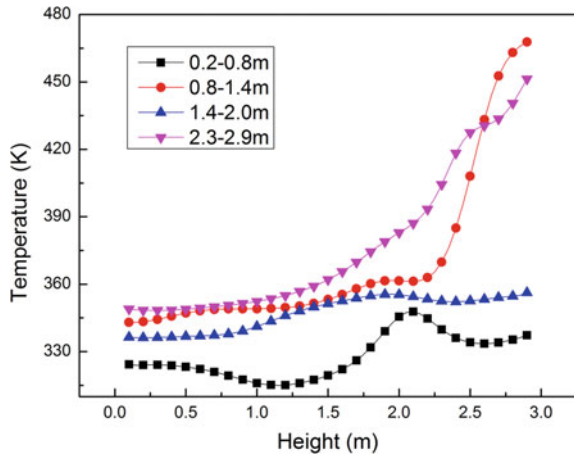
measuring point is only 40 K, and when it is set at 2.3–2.9, the temperature rise is more than 100 K.

In the cold-state numerical simulation without fire, according to the simulation results of airflow distribution, the optimal installation position of air inlet is 0.8–1.4 m when the inlet perpendicular to the fire door of vestibule. Therefore, the height of 0.8–1.4 m is added in the simulation study of the relative position 3—perpendicular relative position. The temperature comparison between different installation heights is shown in Fig. 6. It can be seen from Fig. 6 that the temperature of measuring points above 2.2 m in the Scenario 8 (0.8–1.4 m) is much higher than this temperature in the Scenario 7 (0.2–0.8 m). This is not consistent with the conclusions obtained from the cold-state experiment.

In order to analyze the reasons for the difference between the hot-smoke simulation and cold-state simulation without fire, airflow velocity distribution on the horizontal section is explored. The horizontal section distribution of airflow velocity in the height of horizontal centerline of 0.2–0.8, 0.8–1.4, and 2.3–2.9 m is shown in Fig. 7. When the air inlet is set at 0.2–0.8 m, the air inlet flow gradually shifts to the fire door side in vestibule. When the air inlet is set at 0.8–1.4 m, the effect of hot smoke near door opening on the air inlet flow is weak, so the air inlet flow can still maintain the original direction. When the air inlet is set at 2.3–2.9 m, the inlet is higher than the height of the door opening. In this height, the airflow gradually shifts away from the fire door side. However, in the cold state, the effect of high temperature smoke is ignored. No airflow shifting occurs at any air inlet installation height in the cold-state simulation. It can be seen that the shift of the supply airflow caused by the high temperature smoke has a great influence on the smoke control when the air inlet set at the upper part of the vestibule and has little influence when the air inlet set at the middle height. When the air inlet sets at the lower part of the vestibule, the shift of the supply airflow can enhance the effect of smoke control.

Although there are some differences in the optimum setting height of the air inlet, the results of the hot-smoke simulation and the cold-state simulation without fire are basically the same. When the air inlet is perpendicular to the door, the inlet should be located near the floor.
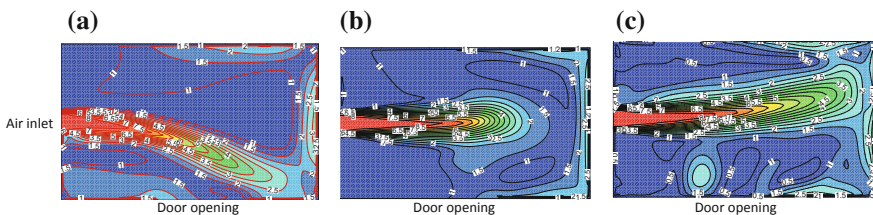
Fig. 7 Horizontal section distribution of airflow velocity in the height of horizontal centerline of **a** 0.2–0.8 m, **b** 0.8–1.4 m, and **c** 2.3–2.9 m

Fig. 8 Temperature comparison of different relative positions between air inlet opening and fire door
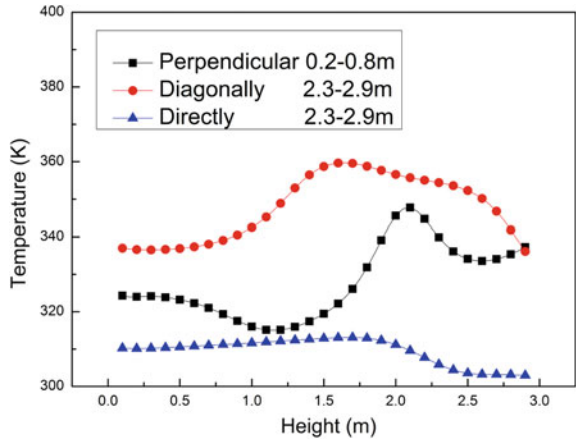
3.4 Effect of the Relative Position on Smoke Control

In order to explore the optimal setting of the air supply system in the vestibule, the optimal setting in each installation height of air inlet and relative position of air inlet and door opening is selected to comparatively analyze based on the above research.

According to the result of above three sections, the best effect of smoke control in the three different relative positions of air inlet and fire door opening, namely directly opposite, diagonally opposite, and perpendicular, is the Scenario 3, Scenario 6, and Scenario 7, respectively. Therefore, these three scenarios are compared and analyzed. The temperature comparison of different relative positions between air inlet and fire door opening of these three scenarios is shown in Fig. 8. The optimal position of air inlet is the position where directly opposite to the door and the height is greater than the height of fire door opening. The second best position is the lower part of the wall perpendicular to the fire door. The worst of the three positions is the upper region which is diagonally opposite to the fire door.

4 Conclusions

The effect of air inlet setting of the mechanical pressurization system in a vestibule of building is investigated in our research. Three relative positions between air inlet and fire door opening, namely directly opposite, diagonally opposite, and perpendicular position, and three installation height of air inlet are numerically simulated by Computational Fluid Dynamics method, in which fire and smoke effect are considered. The results of the numerical simulation are analyzed and compared with the numerical simulation results of velocity distribution in cold state without fire. In view of the current situation that the location of the air inlet in the actual building is not uniform, and the specific requirements of technical codes and standards are lacking,

the influence of different relative position and installation height of air inlet on smoke control are explored in our research. According to the research it is concluded that: In order to get good smoke control effect, (1) when the air inlet is directly opposite to fire door opening, it should be set above the height of fire door opening; (2) when the air inlet is diagonally opposite to the fire door opening, the inlet should be set at the upper part of vestibule in this case; (3) when the air inlet is perpendicular to the fire door opening, the inlet should be located near the floor. (4) The optimal position of air inlet is the position where directly opposite to the door and the height is greater than the height of fire door opening. The second best position is the lower part of the wall perpendicular to the fire door. The worst of the three positions is the upper region which is diagonally opposite to the fire door.

References

1. Huang, H., Ooka, R., Chen, H., & Kato, S. (2009). Optimum design for smoke-control system in buildings considering robustness using CFD and genetic algorithms. *Building and Environment, 44,* 2218.
2. Cheung, S. C. P., Lo, S. M., Yeoh, G. H., & Yuen, R. K. K. (2006). The influence of gaps of fire-resisting doors on the smoke spread in a building fire. *Fire Safety Journal, 41,* 539.
3. NFPA 92. (2012). *Standard for smoke control systems*. U.S.: National Fire Protection Association.
4. BS-EN 12101-6. (2005). *Smoke and heat control systems specification for pressure differential systems*. London, UK: British Standards Institution.
5. NFSC 501A of Stair Cases of Specific Fire Escape Stairs and Smoke Control Systems of Ancillary Room, Korea National Emergency Management Agency, Korea, 2008.
6. Chen, Y., Shu, Z., Li, S., & Ji, J. (2011). Application of performance-based analysis method in mechanical smoke control design. *Procedia Engineering, 11,* 27.
7. Kim J. Y., Lee D. H., & Kim H. Y. (2008). Numerical analysis on features of airflow through open door in pressure differential system. In: *Proceedings of 2008 Winter Annual Conference, The Society of Air-Conditioning and Refrigerating Engineers of Korea* (pp. 463–468).
8. Kim, J. Y., & Shin, H. J. (2010). Numerical analysis on pressurization system of smoke control in consideration of flow rate of supply and leakage. *Fire Science and Engineering, 24,* 87.
9. Ryu, S. H., Lee, S. K., Hong, D. H., & Choi, K. R. (2010). Characteristics of air egress velocity in vestibule pressurization system using the fire dynamics simulator. *Fire Science and Engineering, 24,* 153.
10. You, W. J., Ko, G. H., Sakong, S. H., Nam, J. S., & Ryou, H. S. (2013). An analysis on the major parameter and the relations of pressure difference effect of leakage area in the smoke-control zone. *Journal of Korean Institute or Fire Science & Engineering, 27,* 20.
11. Seo, C., & Shin, W. G. (2014). Numerical study on air egress velocity in vestibule pressurization system: Characteristics of air flow in the vestibule with multiple fire doors in an apartment building. *Fire Science and Engineering, 28,* 30.
12. Seo, C., & Shin, W. G. (2014). Numerical study on air egress velocity in vestibule pressurization system: Damper location for uniform air egress velocity in the case of two fire doors. *Fire Science and Engineering, 28,* 1.

13. You, W. J., Ko, G. H., & Ryou, H. S. (2014). A study on the unsteady flow characteristics in a vestibule for an injection and pressurization smoke-control system. *Fire Safety Journal, 70,* 112.
14. Gai, G., & Cancelliere, P. (2017). Design of a pressurized smoke proof enclosure: CFD analysis and experimental tests. *Safety, 3,* 13.
15. DGJ08-88-2006. (2006). *Technical specification for building smoke control*. Shanghai, China: Shanghai Municipal Construction and Transportation Committee.
16. ANSYS Fluent Theory Guide, Release 15.0. Canonsburg: ANSYS Inc., 2013.

Modeling of the Effect of Heat Release Rates on Fire Smoke Control in Multilevel Underground Parking Garage

Beline Alianto and Yulianto Sulistyo Nugroho

Abstract Smoke is the real threat in a fire in an enclosed, underground parking garage. A model of the smoke movement in a basement was simulated using Fire Dynamics Simulator (FDS) 6.0 software. In this paper, the study used a basement model of 60 m (length) × 30 m (width) × 13 m (height) and has three typical floors. Smoke ventilation shafts were provided for the basement. The required ventilation was based on the air changing ten times per hour. Smoke modeling was investigated under different fire scenarios. Well-controlled liquid pool fire with a heat release rate (HRR) of 5, 10, 15, and 20 MW was used as an input parameter. The following parameters were varied: the location of the fire, the presence or absence of sprinklers, the presence or absence of a smoke extraction system, the variation of the quantity of makeup air to be introduced to basement, and the presence or absence of a jet fan and ducting. Simulation shows that the provision of sprinklers is very important to reduce the heat release rate. The ventilation strategy through a mechanical exhaust fans and makeup air fans can be applied to make the time for smoke removal faster. When makeup air is less, the heat release rates from the design fire more than 5 MW cause high temperature in the fire compartment which may cause fatal injury when exposed to human skin. Combination of ventilation fan and jet fan shows good performance to make smoke removal time shorter.

Keywords Basement ventilation · Jet fan · Smoke exhaust · Mechanical fan · Fire

1 Introduction

Even fire in the basement is rare event and this fire may initiate in numerous ways. Recently an incident of huge fire has destroyed up to 1400 vehicles in multistory car park in Liverpool during the celebration of new year 2018. Automobile parking garages can be either enclosed or partially opened. Unlike car park which is constructed above ground, underground parking garages generally provide enclosed

B. Alianto · Y. S. Nugroho (✉)
Department of Mechanical Engineering, Faculty of Engineering, University of Indonesia, Depok 16424, Indonesia
e-mail: yulianto@eng.ui.ac.id

conditions. A large amount of smoke is generated, which leads to unpredictable smoke movement and poor conditions for evacuation.

In the previous study, Chow [1] divides underground fire protection systems into mechanical ventilation systems and fire protection systems. The study concluded that smoke movement is critical and is subject to failure because most design engineers do not have a proper understanding of what happens when a fire breaks out.

It is commonly accepted that full-scale experiments are the best way to obtain valuable information, for example, a set of various past experimental studies of single-vehicle fires which were done by [2–4]. The main objective of the study was to determine heat release rate (HRR) of vehicle fires in enclosed basement fires, which focus on smoke movement [5, 6] and fire development [7]. A reference curve of heat release rate (HRR) for one burning car and wave of burning cars is discussed in the Profil ARBED Recherches [8].

Furthermore, Horvarth et al. [9] also performed a full-scale test and a reduced-scale test of parking garages on fire using different heat release values (500–4000 kW) with different inlet air velocities (0.3–2 m/s) and derived the empirical critical velocity based on the heat rate. It can be summarized from the study that the full-scale experiments on modern cars revealed high-fire HRR values for fires, which exceed 16 MW when three cars are on fire.

Automobile parking garages can be either enclosed or partially opened. Partially open parking garages are generally above ground with open sides. Unlike natural ventilation, the air circulation to the outside is not freely available in underground. In this case, the solution comprises of vertical stacks which are designed to transport fumes and smoke being extracted to external atmosphere. ANSI/AHSRAE 62.1 [10, 11] recommended the flat rate of ventilation rate 0.0075 m^3/(s m^2) or equal to 6 ACH for enclosed parking garages. In addition, National Fire Protection Association (NFPA 88A) [12] recommended the minimum 0.005 m^3/(s m^2) and SNI 03-6572-2001 [13] proposed 6 ACH. While most of the mentioned investigations were done experimentally, Tilley et al. [14] conducted a large set (more than 350) of computational fluid dynamics (CFD) simulations have been used as "numerical experiments." A full-scale experiment on car park fires with jet fan ventilation was done by Deckers et al. [15] reveals that the impact of the exact position of the extraction fans on the smoke pattern is small when the extraction fans are not close to the fire source. Many of the studies discussed previously are using a model for a single-story underground parking garage, however, multistory basements are also important to be considered under different fire scenarios. The study here takes the different scenarios from the study which is done recently in [16].

2 Setup of the Simulation

In the configuration of simulation, as shown in Fig. 1, the underground parking garage has three floors below ground containing the fire source and an array of sprinklers. The model's size is 64 m (length) × 30 m (width) × 13 m (height).
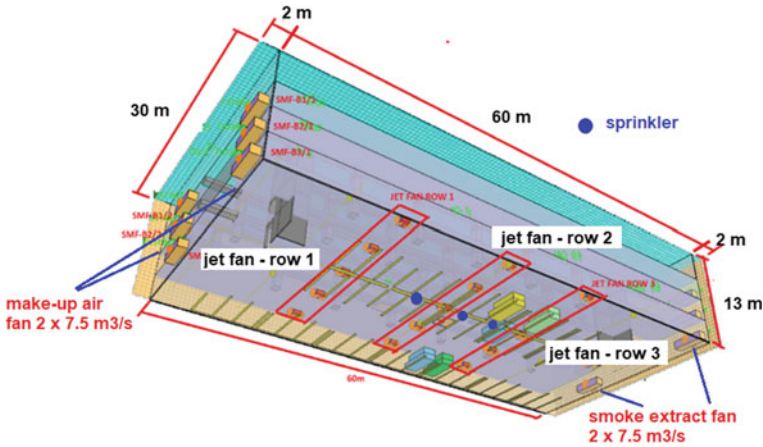
Fig. 1 Model of underground parking garage

Intake and exhaust ventilation shafts that are 2 m wide are provided at the left and right sides of the basement. For expedience of calculation, the model's domain is deliberately set to discrete meshes of size 50 cm × 50 cm × 25 cm in all simulations, which results in 199,680 cells in this case. The simulation is performed using Fire Dynamics Simulator (FDS) V.6. FDS is a computer program that solves the Large Eddy Simulation (LES) problems in Navier–Stokes equation for low-speed fluid flow, thermally driven flow in heat transfer for the growth and development of fire. Navier–Stokes equation can be expressed [17]:

$$\rho \frac{DV}{Dt} = -\nabla p + \rho g + \mu \nabla^2 V \tag{1}$$

The dimensions of the pool fire were 2 m × 2 m. Sprinklers were added above the fire source and separated to such a distance that each sprinkler covered a protection area of 12 m². Each sprinkler is also operated at 0.5 bar pressure, working temperature of 56 °C, and had a *K*-value of 80, which met the conditions for the category of ordinary hazard by NFPA 13 [18]. Three sprinklers are then separated from each other by 4 m in groups as indicated by the blue color dots in Fig. 1. Table 1 list down the different Fire Scenario (FS) to be observed. Sprinklers are located 2.5 m above the fire source. When the fires were ignited, the heat spreads into the adjacent areas, sprinkler heads are activated. In this simulation, the sprinklers are operated quickly for all intentional fire scenarios. The sizing of a fan is based on the air changing ten times per hour for the basement during the fire. A combination of smoke extract and makeup air fan is applied.

Half of the basement area is treated as an extraction zone and the other half is the makeup air zone. The position of the mechanical fans can be seen in Fig. 1. Figure 2 indicates the position of thermocouples and beam detectors as measurement devices. The provision of jet fans may result in migration of smoke faster than conventional

Table 1 List of Fire Scenario

	Sprinkler	Smoke extract fan	Makeup air fan	Jet fan	Ducting	Remark	Fire location
Fire Scenario 1	No						Center of B3
Fire Scenario 2	Yes						Center of B2
Fire Scenario 3	Yes	2×7.5 m^3/s	2×7.5 m^3/s			Supply air 100% of exhaust air	Center of B3
Fire Scenario 4	Yes	2×7.5 m^3/s	2×7.5 m^3/s	2 m^3/s/fan		3 rows at 5 unit of fan/row	Center of B3
Fire Scenario 5	Yes	2×7.5 m^3/s	2×3.75 m^3/s			Supply air 50% of exhaust air	Center of B3
Fire Scenario 6	Yes	2×7.5 m^3/s	2×9.0 m^3/s			Supply air 130% of exhaust air	Center of B3
Fire Scenario 7	Yes	2×7.5 m^3/s	–			Supply air 0% of exhaust air	Center of B3
Fire Scenario 8	Yes	2×7.5 m^3/s	–	2 m^3/s/fan		3 rows at 5 unit of fan/row	Center of B3
Fire Scenario 9	Yes	2×7.5 m^3/s	2×7.5 m^3/s	2 m^3/s/fan	Yes	1 rows at 5 unit of fan/row	Center of B3
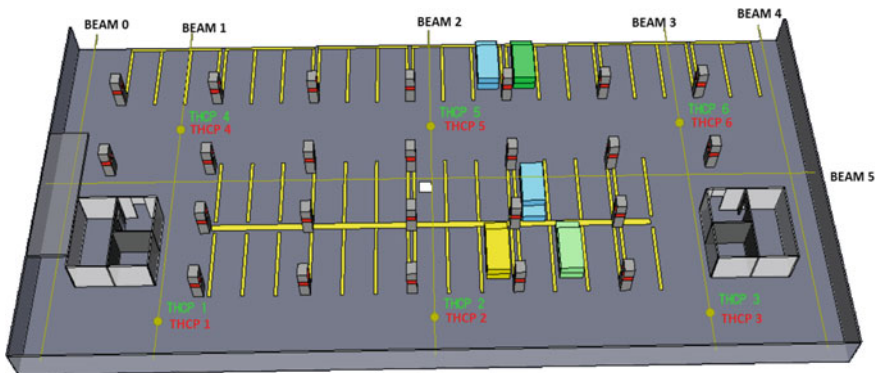
Fig. 2 Position of thermocouples and beam detectors in the simulation model
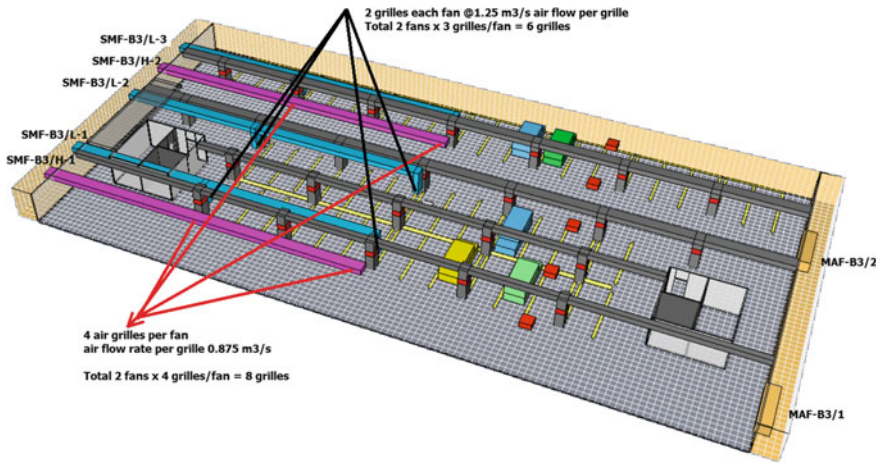
Fig. 3 Simulation setup for Fire Scenario 9 (FS 9)

ventilation without jet fans. Jet fans are necessary because of the advantages they provide through eliminating the air distribution ductwork within the parking garages. Therefore, in order to push air from air the intake side to the negative pressure smoke extract side, the parking garage models contain three rows of jet fans. Each row consists of five jet fan units, each with a capacity of 2.0 m^3/s. Ducting as the media of smoke exhaust in the extraction zone area is observed in FS 9 as shown in Fig. 3. The ducts are divided into higher and lower level extract. It is generally accepted that the system should be designed to run in two parts; commonly, each part is arranged so that 50% of the outlets are at high levels and 50% are at low levels.

The fire load is simulated as pool fire and chosen for HRR maximum of 5, 10, 15, and 20 MW in 4 m^2 fire pool. In addition, another size of fire pool is set 1 m^2 for 2 MW. Fire growth is ramped in time. The purpose of the fire ramp is to meet the actual fire growth during the experiment of car burning done by [8] at which fire reaches the peak at $T = 15$–20 min. Neither fire spread nor car fires are involved in the simulation.

3   Result and Discussion

There are neither sprinklers nor mechanical ventilation systems are provided in the Fire Scenario 1 (FS 1). The fire started at the center in basement 3. Once significant fire growth begins, these fires have the potential to spread throughout the other floors and develop into extremely large fire events beyond the capability of arriving fire departments. Opening in ramps also allows smoke to fill basement 1 and basement 2. In the period of less than 1400 s, basement 1 is fully contained with smoke and most of the basement 2 is covered as well. Furthermore, the case would be worse when the
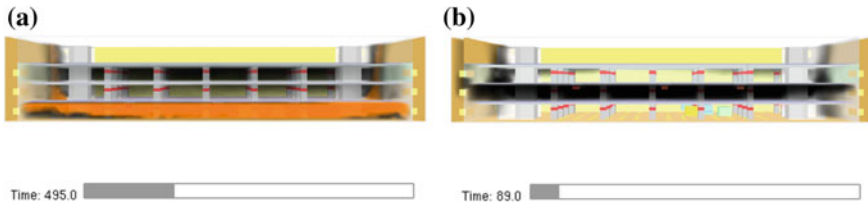
Fig. 4 Smoke movement caused by design fire load 5 MW in FS 1 (**a**) and FS 2 (**b**)

fire load is increased. When the fire load is 5, 10, 15, and 20 MW, simulation shows that basement 3 is faster totally filled with smoke in less than 500, 300, 120, and 60 s, respectively. The whole basement will be covered with smoke in 1800, 1400, 1200, and 900 s for 5, 10, 15, and 20 MW design fire, respectively.

In the Fire Scenario 2 (FS 2), fire is started in the center of basement 2. Similar to the FS 1, there is no active fire protection system is provided such as sprinkler and mechanical fan. This can be seen in Fig. 4 that smoke is naturally moved upward to leave the basement with a low possibility of smoke to travel downward.

3.1 Effect of the Variation in the Design Fire Load to the Obscuration of Beam Detector

When a fire ignites in this location and fire growth begins, the sprinkler systems are able to operate quickly as the sprinkler head is exposed to temperature at 57 °C. The fire may ignite for a moment and quickly extinguished. The fire growth is suppressed and the maximum heat release will not be achieved. Activation of sprinklers causes reduction in HRR when fire starts to decay. Figure 5 shows the extinguishing period of
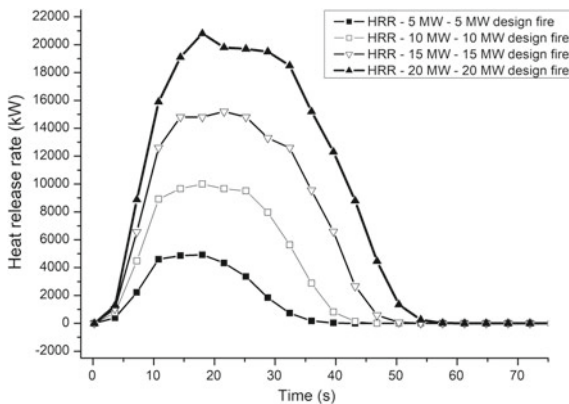
Fig. 5 Heat release rate (HRR) and extinction of fire over time for various fire load
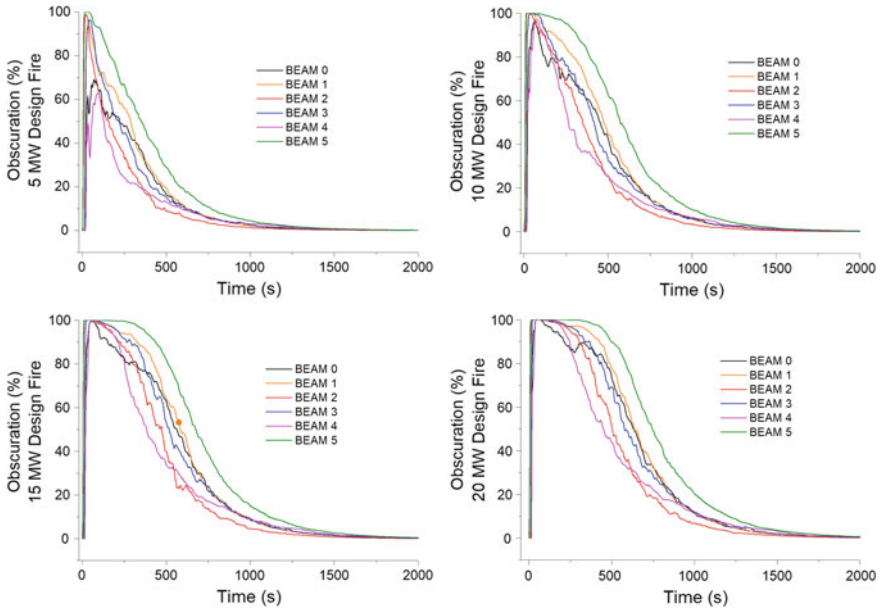
Fig. 6 Obscuration with the variation of design fire load (FS 3)

design fire load of 5, 10, 15, and 20 MW in FS 3. Fire is considered to be successfully extinguished when the fire heat release rate is zero. In addition, after the flaming fire growth, the smoke would spread to the surrounding area and then exit the basement through a ramp. The time needs to clear the basement from smoke is shown in Fig. 6 denoted by 0% obscuration. This means that when smoke filled the basement, the obscuration of beam detector is raised to 100% and reduces to 0% when smoke is cleared. Obscuration is the unit of measurement where smoke has an effect on visibility which is expressed in %/foot.

3.2 Effect of the Variation of the Quantity of Makeup Airflow Rate

In the following scenario, smoke exhaust and makeup air fans are added. Total smoke exhaust air is 15 m³/s served by two smoke extract fan at each 7.5 m³/s. The effect of variation of supply air introduced to basement is observed through FS 3 (equal capacity of smoke makeup air and smoke extract fan), FS 5 (makeup air fan is 50% of the total capacity of the exhaust fan or underventilated fire), FS 6 (capacity of the intake fan is 130% of the total capacity of extract fan/overventilated fire), and FS 7 (makeup air is turned off).
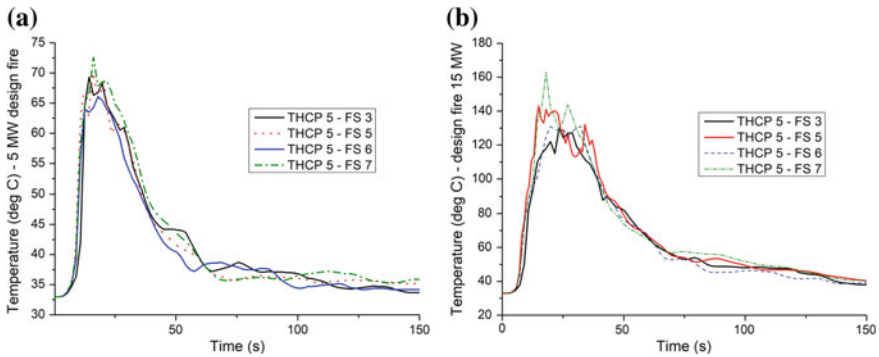
Fig. 7 Temperature profile for FS 3, FS 5, FS 6, and FS 7 for design fire load 5 MW (**a**) and 15 MW (**b**)

Figure 7 shows the effect of maximum temperature reaches in the basement over the variation of design fire load of 5 and 15 MW. The graphs show that the maximum room temperature is achieved in the case of overventilated fire compared to underventilated fire. Simulation shows that the maximum temperature is read by THCP 5. Having design fire load of 5 MW, the maximum room temperature of 73 °C is reached when the makeup air is totally turned off (FS 7) and 65 °C in case of overventilated case (FS 6). It is already the maximum temperature that human skin could be exposed without causing any harmful effect. Underventilated cases and higher fire load will result in higher room temperature. It is even worse when the fire design load is increased to 15 MW, the maximum room temperature is 160, and 130 °C in FS 7 and FS 6, respectively.

3.3   Effect of the Presence and Absence of Jet Fan Over the Smoke Clearance Time

Fire scenario 4 (FS 4) includes mechanical intake fan, exhaust fan, and series of jet fan in the simulation. Three rows of jet fans are installed in which every row consists of five unit jet fans. The airflow rate of each jet fan is 2 m^3/s. However, intake air fan is turned off during fire in FS 8. Therefore, the smoke extract system involved only jet fan and smoke exhaust fan. Sprinklers and mechanical ventilation are activated during the fire mode as in the previous scenario. Simulation shows the assistance of jet fan (FS 4) cause the smoke to be extracted faster than without jet fans (FS 3). It is also shown in Fig. 8 that smoke is extracted longer compared to the scenario when intake fans are presented (FS 3 and FS 4) than without intake air fan run (FS 8).
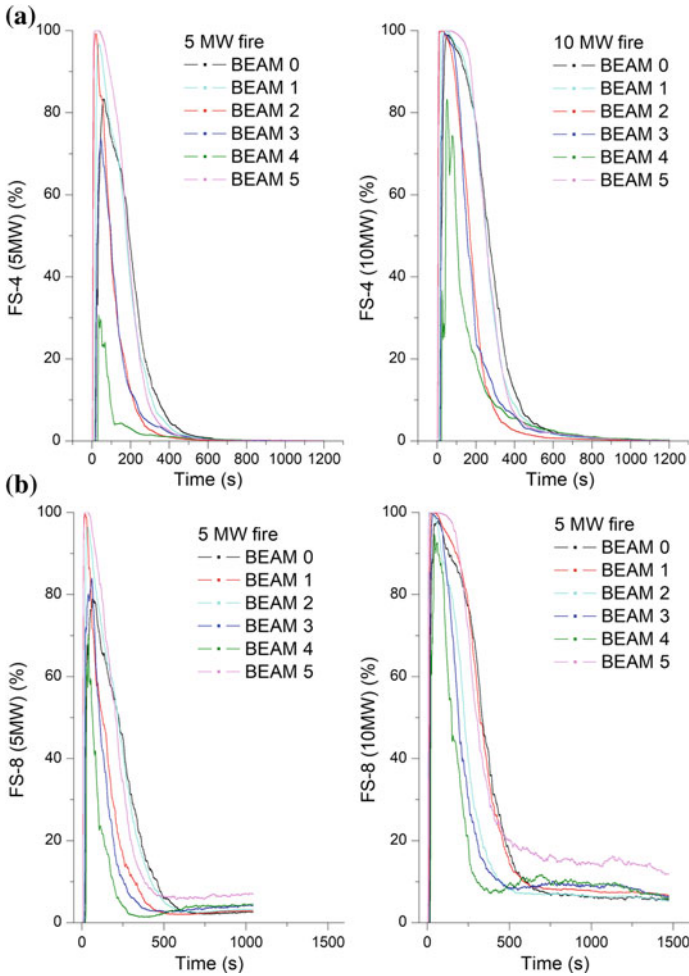
Fig. 8 Obscuration overtime in FS 4 (**a**) and FS 8 (**b**)

3.4 Smoke Extract Using Ducting and Jet Fan

The simulation setup for Fire Scenario 9 is different from previous works. This scenario is also set for fire in the center of basement 3. Unlike the previous scenario, ducting is installed in the basement. Table 2 shows the setup specification of mechanical fans system. Figure 9 shows the temperature and obscuration overtime in Fire Scenario 9 with design fire load 5 MW and 10 MW. Ducting system is apparently effective during normal ventilation mode. However, during fire mode, smoke is likely to be dispersed in uni-direction which because the smoke is extracted longer than in the FS 3 where there is no ducting introduced to the basement.

Table 2 Mechanical fan specification for scenario basement with ductworks (Scenario 10)

Mechanical fans	Fan code	Capacity per fan (m^3/s)
Makeup air fan (two units for every level of basement)	MAF-B3/1&2	7.5
Smoke exhaust fan		
– Lower exhaust fan (two units per floor)	SMF-B3/H-1&2	3.75
– Upper exhaust fan (three units per floor)	SMF-B3/L-1,2&3	2.5
Jet fan (15 units for each floor)	Three rows with five fans/row	2
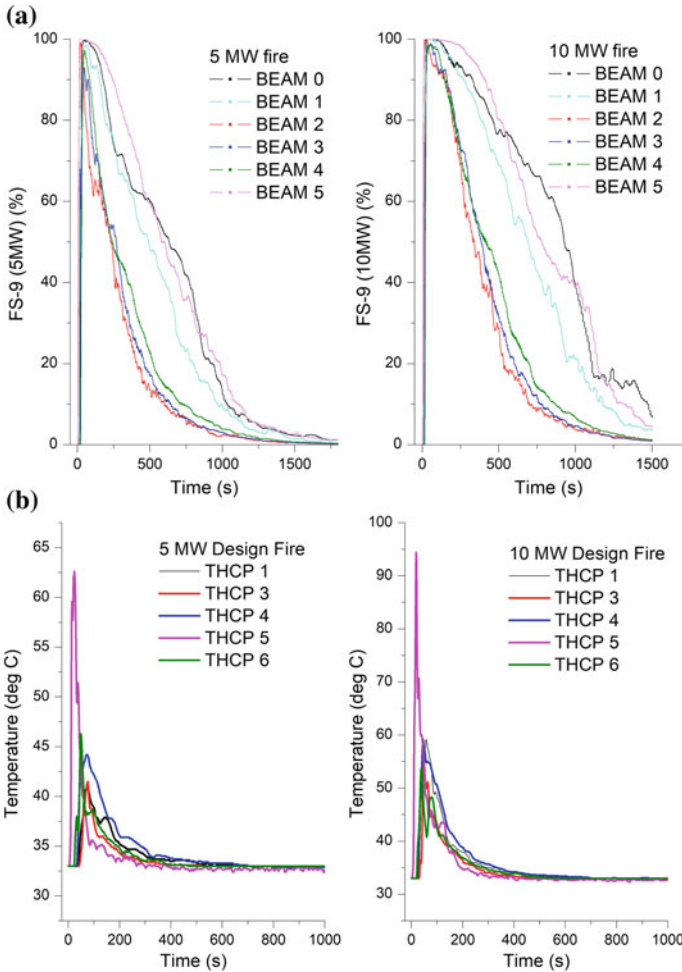
Fig. 9 Obscuration for FS 9 (**a**) and temperature profile for FS 9 (**b**)
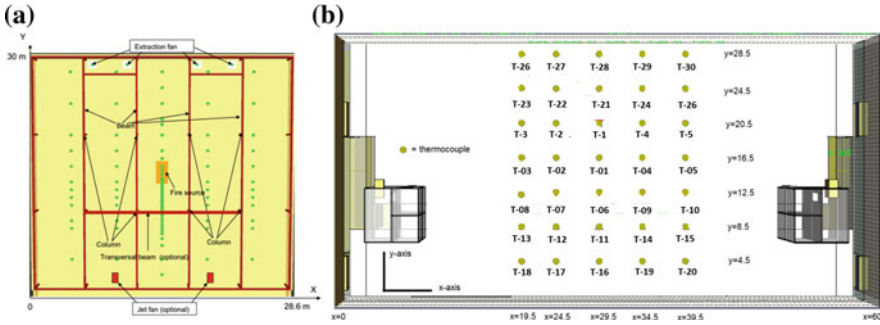
Fig. 10 Full-scale experiment model (**a**) and simulation model (**b**)

4 Comparison to Full-Scale Experiment

This paper compares the full-scale experiment done by Deckers et al. [15] as seen in Fig. 10a using an experimental car park 28.6 m (length) × 30 m (width) × 3 m (height) using fire design load 4 MW. Fire originated in the middle of the room. Ventilation rate is set 200,000 m^3/h. By plotting the car park into the plan of (x, y) coordinate system, few thermocouples are put in five rows from x-axis (as indicated by green dots in Fig. 12a in position $X = 4.3$ m; $X = 9.3$ m; $X = 14.3$ m; $X = 19.3$ m, $X = 24.3$ m. Ventilation controlled parameter is set 00000 when inlet opening is fully opened and MM0 if inlet opening is 80% obstructed and opening in the right side opened. In this paper, simulation using 00000 scenarios will be compared using design fire load 4 MW and extraction rate of 200.000 m^3/h. The position of the thermocouples of the simulation model is shown in Fig. 10b.

Temperature measurement in full-scale model is done along y-axis at $X = 4.3$ and $X = 24.3$ (10 m distance from the fire source in x-axis). This is identic to the position of thermocouple in simulation model along y-axis at $X = 19.5$ m and $X = 39.5$ m. Another temperature measurement along y-axis at $X = 9.3$ m and $X = 19.3$ m is done as well in full-scale model. This is also identic to the temperature reading from simulation model in y-axis at $X = 24.5$ and $X = 34.5$. The comparison for the reading of temperature for full-scale experiment can be seen in Fig. 11 and simulation model in Fig. 12.

5 Conclusion

When underground parking garage is not provided with active fire protection system, fire load more than 5 MW causes basement totally filled with smoke in less than 5 min. Water-based active fire protection sprinklers system is very critical to be provided for basement. It is also important to activate the mechanical fan system in another nonfire floor to avoid interfloor smoke migration. Provision of jet fans will cause
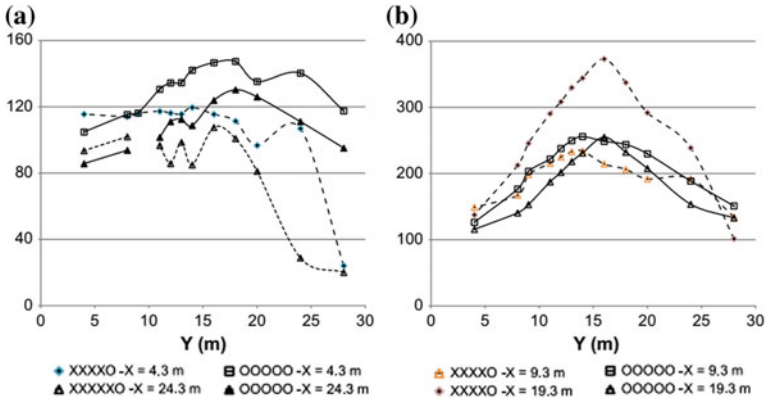
Fig. 11 Full-scale experiment temperature profile at $X = 4.3$; $X = 24.3$ (**a**) and $X = 9.3$; $X = 19.3$ (**b**) [15]
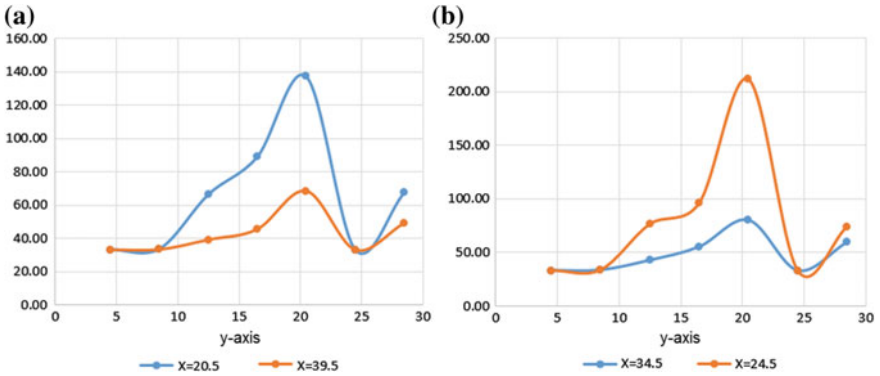
Fig. 12 Simulation model temperature profile along y-axis at $X = 20.5$; $X = 39.5$ (**a**) and $X = 34.5$; $X = 24.5$ (**b**)

smoke in the basement cleared faster. Underventilated fire because of lower quantity of makeup air introduced to the basement resulted in high temperature inside the fire compartment. The high temperature when exposed to human skin can cause severe injury for occupants in the basement.

References

1. Chow, W. K. (1998). On safety systems for underground car-parks. *Tunneling and Underground Space Technology, 13*(3), 281–287.
2. Mangs, J., & Keski-Rahkonen, O. (1994). Characterization of the fire behavior of a burning passenger car. Part II: Parameterization of measured rate of heat release rate. *Fire Safety Journal, 23,* 37–49.
3. Ship, M., & Spearpoint, M. (1995). Measurements of the severity of fire involving private vehicles. *Fire and Materials, 19,* 143–151.
4. Cheng, Y. P., & John, R. (2002). Experimental research of motorcar fire. *Journal of China University of Mining and Technology, 31*(6), 557–560.
5. Hwang, C. C., & Edwards, J. C. (2005). The critical ventilation velocity in tunnel fires—A computer simulation. *Fire Safety Journal, 40,* 213–244.
6. Vauquelin, O., & Telle, D. (2005). Definition and experimental evaluation of the smoke "confinement velocity" in tunnel fires. *Fire Safety Journal, 40,* 320–330.
7. Ingason, H., & Lonnemark, A. (2005). Heat release rates from heavy good vehicle trailer fires in tunnels. *Fire Safety Journal, 40,* 646–668.
8. Profil ARBED Researches. (1997). Development of Design Rules for Steel Structures Subjected to Natural Fires in Closed Car Parks.
9. Horvarth, I., Beeck, J. V., & Merci, B. (2013). Full-scale and reduced-scale tests on smoke movement in case of car park fire. *Fire Safety Journal, 57,* 35–43.
10. ASHRAE Handbook—Application 2015. American Standard of Heating, Ventilating and Air Conditioning Engineers, 1791—Tullie Circle NE, Atlanta, GA, 3029.
11. ANSI/ASHRAE Standard 62.1-2013 Ventilation for Acceptable Indoor Air Quality, 2013. American Standard of Heating, Ventilating and Air Conditioning Engineers, 1791—Tullie Circle NE, Atlanta, GA, 3029.
12. NFPA 88A Standard for Parking Structures. 2015, 1 Batterymarch Park, Quincy, MA, National Fire Protection Association.
13. SNI 03-6572-2001: Guidance for Ventilation and Air Conditioning Design, 2001. Standar Nasional Indonesia.
14. Tilley, N., Deckers, X., & Merci, B. (2012). CFD study of relation between ventilation velocity and smoke back-layering distance in large closed car parks. *Fire Safety Journal, 48,* 11–20.
15. Deckers, X., Haga, S., Settle, B., & Merci, B. (2013). Smoke control in case of fire in a large car park: Full-scale experiments. *Fire Safety Journal, 57,* 11–21.
16. Alianto, B., Astari, N., Nareshwara, D., & Nugroho, Y. S. (2017). Modeling of smoke control in underground parking garage. *International Journal of Technology, 8*(7), 1296–1305.
17. McGrattab, K., Hostika, S., McDermott, R., Flyod, J., Vanella, M., Weinschenk, C., & Overholt K. (2017). Fire dynamic simulator technical reference guide volume 1: Mathematical model. NIST Special Publication 1018-1, US Department of Commerce.
18. NFPA 13: Standard for the Installation of Sprinkler Systems. 2013, 1 Batterymarch Park, Quincy, MA, National Fire Protection Association.

Human Behavior in Fire

Human Behavior During an Evacuation of a Large Office Building Adjacent a Fire Site

Mineko Imanishi, Yoshikazu Deguchi, Tsutomu Nagaoka and Tomonori Sano

Abstract In 2017 in Tokyo, more than thousand occupants of a seven-story office building evacuated due to fire located at an adjacent site. Because the fire did not occur on their own site, the evacuation was spontaneous and, therefore, not performed according to a normal evacuation manual. This paper investigates the human behavior in this evacuation case, especially focusing on the decision-making process. To do this, the authors conducted face-to-face interviews with four people from the organization who made the decision to let employees evacuate and forty-one employees who evacuated. The major findings of the study are: (1) visual observation of fire through windows influences the occupants' evacuation strategy; (2) occupants tended to postpone leaving the workplace until they received an explicit evacuation cue from others; and (3) multiple occupants chose stairs by taking into consideration that the fire was not in their building. Since the fire compartments had not yet been built and there was no immediate danger to life, these results can also be applied to the evacuation of non-fire floors in a building fire.

Keywords Evacuation · Human behavior · Decision-making · Interview · Office building

1 Background

In June 2017 in Tokyo, there was a fire at a distribution center that was under demolition. Since the burned building was not in use because of the demolition, only a few people were required to evacuate from the distribution center. However, due to a large amount of black smoke from the fire carried by the wind, over a thousand employees working at an office building next to the fire site were evacuated by their company's decision. Ultimately, the fire did not spread to the surrounding buildings

M. Imanishi (✉) · Y. Deguchi · T. Nagaoka
Takenaka Research & Development Institute, Otsuka 1-5-1, Inzai, Chiba 270-1395, Japan
e-mail: imanishi.mineko@takenaka.co.jp

T. Sano
Waseda University, Mikajima 2-579-15, Tokorozawa, Saitama 359-1192, Japan

and the smoke was not toxic enough to claim victims. Despite this, the incident is suggestive as many people evacuated due to the fire in the adjacent building.

The pre-movement phase and route choice are key aspects of human behavior in fires, affecting the required egress time (RSET) [1]. Human response to fires depends a lot on the seriousness of the situation [2]. It has always been debated whether experimental conditions, such as laboratory experiments, evacuation drills, or VR case studies, can reproduce a situation of a fire accurately enough to obtain reliable human behavior data. This is especially true in those conditions that lack the influence of real flames, which provide a strong sense of urgency [3]. Hence, studying real incidents is required and important to strengthen the findings of experimental studies. However, there have only been a few studies that surveyed occupants' behaviors in real fires because of the difficulty in collecting details from rare, unexpected, and confusing disasters. Regarding office buildings, there have been two studies around 1980 in Japan [4–6], one by Brennan [7], and one by Proulx and Reid [8]. Besides these, a lot of studies have investigated evacuation behavior in the 9/11 World Trade Center (WTC) terror attack [9–11]. The High-rise Evacuation Evaluation Database project (HEED project) is the largest project that collects detailed information on evacuees' activities using questionnaires and face-to-face interviews [9]. One of the findings of the HEED project is that the occupants in WTC2, who could see the attacked WTC1 through a window, started the evacuation earlier, on average, than those in WTC1 [10]. In the pre-movement phase, occupants spend the majority of time collecting information about the incident for decision-making [11]. Although observing convincing evidence of fire is hard for occupants of a non-fire floor, occupants in an adjacent building would be able to see it better. Thus, building evacuations arising from fires in other buildings would have peculiar characteristics. However, they have not yet been studied.

In this paper, we surveyed the evacuation from the adjacent office building of which all employees evacuated, focusing on the decision-making process for evacuation. The aims of this study are: Firstly, to explore and compare the characteristics and challenges from adjacent site fire evacuations with on-site fire evacuations; and secondly, to obtain insight into evacuation planning for non-fire floors in a building fire.

2 Situation of the Evacuation

2.1 The Fire Incident

The fire site was a demolition site, a four-story distribution center, owned by a food company and located in an urban area in Tokyo. The final burned area was circa 5000 m^2 of the 9900 m^2 of total floor area. At the time, 23 workers were involved in the demolition. The fire broke out around four o'clock in the afternoon on a weekday on the first floor through the following process: A spark from a burner that one of
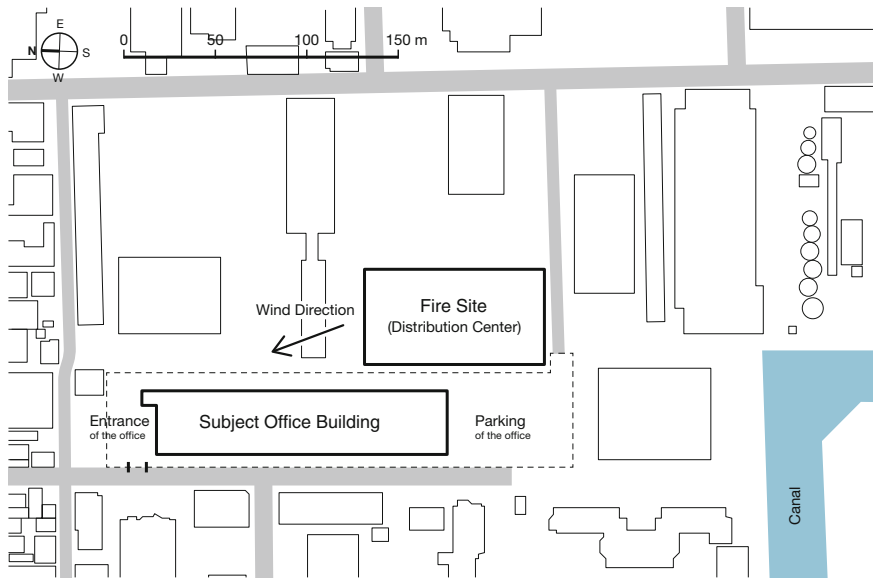
Fig. 1 Location of the subject office building and the fire site

the workers was using to cut a steel frame jumped onto a urethane wall insulation, then the fire spread rapidly with a dense cloud of black smoke. After about three and a half hours, the fire was put out by fire-fighters, which were called by an unknown individual. Since the distribution center was not in use, there were no victims except for the worker that was using the burner that ignited. He survived, but he suffered burns all over his body [12, 13].

The fire did not spread to any other building. However, since it was in a dense building area and the day was windy, an adjacent office on the leeward side, belonging to another company, decided to order a total evacuation for safety. The direction of the wind at that time was from the south-southeast [14], as illustrated in Fig. 1. The subject office building was less than 20 m away from the burned building.

2.2 The Subject Office Building

The office building that was evacuated is seven-stories in which about over thousand employees work. It is owned by a single major construction company and used as one of the head branches; thus, all the employees there belong to the same company group. It can also be said that all evacuees knew the building plan well. However, most of them have never participated to an evacuation drill there.

The second to the sixth floors are normal office spaces, while the ground and first floors are used for specific facilities like a grand entrance lobby, a cafeteria, and
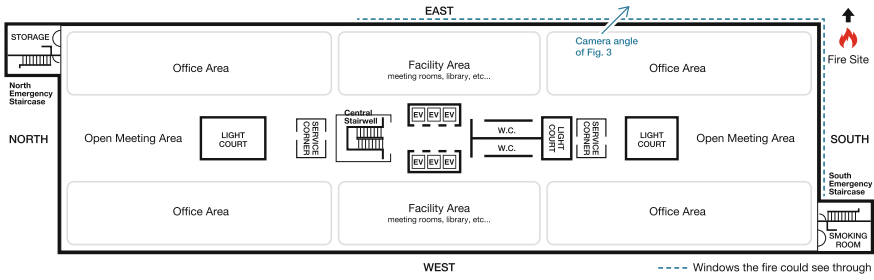
Fig. 2 General floor plan from the second to the sixth floors in the subject office building

seminar halls. Figure 2 shows the general plan of the office floors. The plan has a symmetrical pattern along the north-south and east-west axes. For vertical movement, employees usually use elevators and an open-stairwell in the center of the floor, both of which are not allowed to be used in emergency situations. Emergency staircases are on the edge of the north and south sides. Those staircases are compartmented with fire doors while the central stairwell is open and can be seen from the office area.

Since the fire site is located to the south-east of the office building, the fire could be seen only from the windows on the south-east side (Fig. 3). Nonetheless, people in the west area could also see what was going on in the east because there are neither walls nor tall partitions between west and east except for the central facility areas.

Fig. 3 A video frame of the fire shot through a window from the third floor by an employee before his evacuation

3 Methodology of the Survey

We conducted face-to-face interviews with people from the subject office about the evacuation. The interviewees can be categorized into two groups, the organization-side and the evacuee-side, as described in the following subsections.

3.1 Organization-Side Interviews

The interviewees were two people from the general affairs department of the company (hereinafter referred to as "GA department") and two people from the disaster control center, which is actually part of the company's subsidiary. The persons from the GA department included the person who took the call from the disaster control center the day of the fire. The organization-side interviews were done all at once. We asked about the situation and their roles on the day of the fire from the viewpoints of the process of information transfer and the decision-making factors of the evacuation order.

3.2 Evacuee-Side Interviews

The interviewees were employees who evacuated from the office on the day of the fire. There were 41 interviewees in total. They were sampled from each office floor, from the second to the sixth floors, and from different desk positions on the floor, distributed evenly throughout the space. Table 1 shows the distribution of the locations in the office building where the interviewees were when they recognized the fire. The distribution is partly not uniform since some of them were not at their

Table 1 Number of interviewees categorized by evacuation start position

Floor	North-East	North-West	South-East[a]	South-West	Total
Ground floor	1				1
First floor	1	1			2
Second floor	1	2	1	3	7
Third floor	3	3	1	2	9
Fourth floor	2	1		1	4
Fifth floor	3	1	1	2	7
Sixth floor	5	3	1	2	11
Total	16	11	4	10	41

[a]The direction to the fire site

desks when they observed the fire. The interviews with the evacuees took place with two or three interviewers for each interviewee.

The interviewers asked how the interviewees made decisions and acted during the evacuation by following a list of prepared questions. One of the interviewers took notes, either by laptop computer or by hand, while the interviewers were talking with an interviewee.

4 Evacuation Process

This section describes the progress of fire recognition and the evacuation of the subject building based primarily on the organization-side interviews, but partly also on the evacuee-side interviews.

4.1 Recognition of the Fire and Decision to Make the Evacuation Order

As the fire broke out around four o'clock in the evening, most employees were still working since work hours usually ended at a quarter past five. The first person who recognized the fire was a security guard at a guardhouse in the company's private parking on the fire site side. He immediately reported it via radio transceiver to the disaster control center of the office building. Receiving the report, a few people at the control center went to the parking lot to confirm the fire and then called to inform the GA department of the company. A person who took the phone call informed the manager of the GA department. At this point, people in the department could not make a final decision about whether the fire was in an adjacent building or their office building because, even though they were informed that it was the adjacent building by the control center, others said that the roof of their building was burning. There was also no information exchange between the subject office building and the fire site building during the fire.

The manager of the GA department decided to first offer the option to evacuate to all employees and then informed the company executives of the decision afterward, although it was still during office hours and there was no regulation or in-house manual that provided for the evacuation of employees due to an adjacent fire. Since the inside of the office already smelled of smoke, the manager prioritized health and safety generally rather than only responding to the risk of fire.

4.2 Delivery of the Evacuation Order

After the decision to evacuate by the manager of the GA department, employees under him scattered to different floors and conveyed the evacuation to employees verbally.

Meanwhile, a group leader in a secretaries on another floor also recognized the fire. He decided to let his employees evacuate before the evacuation order by the GA department. As he arrived at the entrance of the office building, he found that no one had yet evacuated. He waited at the entrance hall to hear whether an evacuation order would be issued by the organization; however, he did not. Therefore, he went to the disaster control center inside of the building and asked someone there to make an evacuation announcement. At that moment, there were only two or three young men in the disaster control center room because the majority of the people at the center had left to fight the fire in the parking lot to prevent the fire from spreading. Following the request of the group leader for an announcement, they broadcasted an evacuation order to every floor through the PA system. According to the organization-side interviews, the GA department also told the control center to broadcast an evacuation announcement with sentences: "There is a fire in the adjacent area. Please evacuate using the central stairwell or the north staircase." As aforementioned, the central stairwell was not designed to be used in an emergency. However, because the fire was not in the building, they decided to let evacuees use it. The south staircase was, in contrast, excluded since it was located on the fire site side.

However, the acoustic volume of those announcements was too low. Occupants could hear that they were saying something about the fire, but they were not loud enough for most to clearly understand the contents. In those evacuation announcements, the emergency alarm and the official pre-recorded evacuation instructions for fire were not used. Instead, the staff member in the disaster control center broadcasted the evacuation instructions in his own words.

4.3 Execution of the Evacuation and Issuance of the Go-Home Order

With these two evacuation orders, verbally and by broadcast, most of the employees started to evacuate. They went out from the building and assembled at the building entrance. While checking floors, members of the GA department found that some of the employees just ignored the order and continued working at their desks. They, therefore, needed to ask them directly to evacuate. After about five or ten minutes after the evacuation, at around a quarter to five, the GA department issued an announcement allowing all employees to go back to home since office hours were about to end, the fire was still not put out, and the inside of the office was filled with the smell of smoke. Some of the evacuees needed to go back to their desks to collect

their things, and such short-time returns were allowed because it seemed that there was no possibility of the fire spreading. At about six o'clock, the GA department confirmed that there was nobody left in the office building.

5 Evacuees' Behaviors

The behaviors of the evacuees were summarized through an analysis of the evacuee interview records. Remarkable factors of the evacuation were categorized and measured to clarify the decision-making process for evacuation. Some answers were classified by the location of individuals when they recognized the fire.

5.1 Fire Recognition

Table 2 shows the first factors that caused individuals to understand that something unusual was happening before they recognized the fire. At this first stage, they detected an anomaly due to non-visual factors, such as noise, smell, or the movement of others. There was no large difference between the east and west sides or the north and south sides, although the fire could be seen only from the south-east side. Multiple interviewees reported that they first thought the roof of their building was burning because they saw dark smoke coming from the light courts or realized that the inside of the office became darker due to the smoke covering the light courts. One employee answered that they detected something was unusual when he felt heat from a nearby east-facing window. He and other interviewees reported that south-east side windows became hot to the touch.

Table 3 shows the factors by which individuals realized the fire. Two-thirds of the interviewees became aware of the fire by seeing the fire or smoke themselves. While almost all of the interviewees on the south side recognized the fire by seeing

Table 2 First factors for accident perception

Factor	North-East	North-West	South-East	South-West	Total
Noisiness of surroundings	5 (31%)	6 (55%)	2 (50%)	5 (50%)	18 (44%)
Seeing smoke	4 (25%)	1 (9%)		2 (20%)	7 (17%)
Smell	3 (19%)	3 (27%)			6 (15%)
Reports by colleague	2 (13%)	1 (9%)		1 (10%)	4 (10%)
Movement of colleagues			1 (25%)	2 (20%)	3 (7%)
Evacuation announcement	1 (6%)				1 (2%)
Decrease of brightness	1 (6%)				1 (2%)

The percentages in parentheses represent the ratios among each column

Table 3 First factors of fire recognition

Factor	North-East	North-West	South-East	South-West	Total
Seeing fire or smoke	11 (69%)	4 (36%)	3 (75%)	10 (100%)	28 (68%)
Reports by colleague	4 (25%)	4 (36%)			8 (20%)
Others	1 (6%)	3 (27%)	1 (25%)		5 (12%)

the fire/smoke directly, some interviewees on the north side recognized it only by hearing a report. Thus, occupants of the west side moved to the east windows to see the fire site; however, the length of the longitudinal direction of the office plan was too far for onlookers to go to see the fire. Aside from the 24% of the interviewees who could see the fire directly from their desks, 46% of the interviewees said that they purposely moved to a window or another room to see the fire. Alternately, some of the evacuees were unclear where the fire site was even during the evacuation.

5.2 Decision-Making for the Evacuation

Table 4 shows the most important decision-making factors for beginning of the evacuation. Although most of the interviewees answered that they thought that they should evacuate, more than half only started to evacuate after a cue from others. A typical answer was: "I thought that I should. So, I turned off my computer, gathered my personal items, and then waited for an instruction to evacuate."

Common activities before beginning to evacuate were: saving current work, gathering belongings, talking to or calling colleagues, going to a window and watching the fire, or taking a photo or movie using a mobile phone. The percentage of the interviewees that took photos or videos before evacuating was 22%. One of the interviewees said that they telephoned to the disaster control center and that the center told them to wait for an announcement.

The smell of the smoke was the strongest reason cited for evacuation. As the fire progressed, the smell of the smoke inside the office became stronger and stronger. Some of the interviewees worried that the smoke could be toxic, while others thought

Table 4 Factors on decision-making to start the evacuation

Factor	Total
Evacuation announcement (including those who could not hear the content clearly)	11 (27%)
Order by the GA department	9 (22%)
Self-judgment	7 (17%)
Order by boss	6 (15%)
Conversation with colleagues	1 (2%)
Others	7 (17%)

Table 5 Whether evacuees had anxiousness or concern during the evacuation

Factor	Total
Fire could spread to the office	4 (10%)
Smoke could be toxic	3 (7%)
Some general anxiety or tension	9 (22%)
Not at all	25 (61%)

that they needed to leave the office just because the smell was too uncomfortable to work. As shown in Table 5, most of the interviewees did not believe that there was a danger to themselves.

5.3 Choice of Evacuation Route

Although the central stairwell is for non-emergency use, it was primarily used during the evacuation, as shown in Table 6. As a result, the central stairwell was very crowded during the evacuation. In contrast, most of the occupants avoided using the elevators, which were located next to the central stairwell, even though the elevators worked and were not crowded because they believed that people should not use elevators during an emergency situation. Some of the interviewees who used the central stairwell did know that the central one was not designated as an emergency exit route; nevertheless, they used it either because the fire was not inside of their building or because it was not a consideration at that moment.

The north emergency staircase was also used, especially by the evacuees who were in the north side, but was not used by anybody in the south side (Fig. 4). A large number of evacuees in the south side avoided use of the south staircase, which was located in the direction of the fire site, but they used the central stairwell and none of them went to the north staircase, which was located at the opposite side (Table 7). Multiple interviewees avoided using the emergency staircases because they thought

Table 6 Routes of vertical movement

Factor	North	South	Total
North emergency staircase	12		12
Central stairwell	11	12	23
Elevator	1		1
South emergency staircase		1	1
Lobby stairwell (only between the first and ground floors)	2		2
Multiple staircases		1	1
Not used (already at the ground floor)	1		1
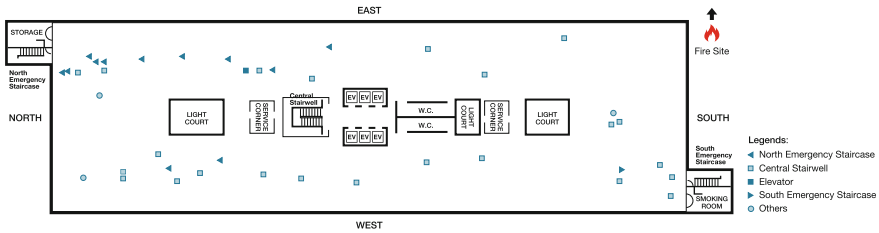
Fig. 4 Distribution of evacuation starting points on floors by classifying into staircase selection

Table 7 Reasons for the choice of the vertical movement route

Reason	North	Central	Elevator	South	Lobby	Multiple	Total
The nearest one	3 (25%)	7 (30%)			2 (100%)		12 (30%)
Followed others	2 (17%)	5 (22%)					7 (18%)
Daily used	1 (8%)	5 (22%)					6 (15%)
Far from the fire	2 (17%)	3 (13%)					5 (13%)
Not crowded	2 (17%)			1 (100%)		1 (100%)	4 (10%)
Suggestion by others	2 (17%)	1 (4%)					3 (8%)
Others		2 (9%)	1 (100%)				3 (8%)

that the exit doors of the emergency staircases might be locked for security reasons and that they would not be able to get through. They said that the door may be able to unlock during a real fire situation; however, they were not sure that it would be unlocked in this case because it was a fire just in an adjacent site.

According to multiple interviews, a significant number of the evacuees switched from the central stairwell to the north staircase on the fourth floor because of a traffic jam in the central stairwell. One occupant decided to switch, and then some others followed. The interviewee who used multiple staircases, as described in Table 6, was one of them.

6 Discussion

6.1 Decision-Making for Evacuation Under Unclear Circumstances

Today in Japan, most people are educated about how they should evacuate properly in a building fire. Building owners are also responsible for the evacuation of occupants because of a fire on their site. While evacuation plans for fire are regulated, evacuations due to a neighboring fire are not. Because of that, the occupants were not prepared for the situation.

The official fire alarm was not used during this adjacent fire. Moreover, the disaster control center did not broadcast the evacuation until pressured by an employee. An evacuation announcement is important to allow occupants to evacuate in such a situation in which it is unclear whether they should evacuate. In this incident, some occupants even waited for an announcement when they knew there was a fire. That is, they felt that they needed a definite reason to suspend their work during office hours. The announcement functions not only as a cue to evacuate or as a source of information, but also as permission to leave the position. Therefore, in order to clarify the need to evacuate, it should be considered proper to use the fire alarm during adjacent fires.

6.2 Evacuees' Assessment of the Adjacent Fire

Unlike for occupants of building fires, the state of the fire in the adjacent site could be observed by the occupants of the subject office building. Most of the occupants saw the fire directly through windows, and some of them even went to the windows just to observe it closely. Consequently, the occupants recognized the fire at an early stage and understood the positional relationship between the fire and themselves.

At the same time, the occupants belittled the necessity of the evacuation. A substantial number of evacuees understood that the evacuation as "not an actual one," and therefore, thought that the evacuation route might be different from an "actual" fire situation. The rumor of the locked emergency exits was one of the resulting consequences.

During this fire, the smoke from the adjacent fire site had actually entered the office considerably. The smoke was fortunately not toxic; however, the occupants had to evacuate since it is quite hard for ordinary people to distinguish the toxicity. Therefore, the belittling of the necessity to evacuate could be considered a kind of normalcy bias.

6.3 Use of Emergency/Non-emergency Stairs

Regarding this case, non-emergency stairs were used to make the evacuation faster. On the other hand, some evacuees avoided using emergency staircases because they believed that they might be locked. These are both effects of the evacuees' understanding that the fire was "not an actual one." In addition, a significant number of the interviewees thought that the central stairwell was emergency stairs because of the fire shutters surrounding it. The lack of knowledge may be caused by the absence of evacuation drills for every employee. The general evacuation characteristics, "following others" and "using a familiar route," spurred concentration to the central stairwell as well.

7 Conclusions

In this paper, human behaviors in a total evacuation from an office building due to a large fire at an adjacent site were surveyed by interviews with 45 occupants. Evacuations due to an adjacent fire are not commonly planned or regulated. However, for this reason, people know less about what they should do when adjacent fires occur. Regarding this incident, the announcement and evacuation routes did not conform to the proper procedures detailed in manuals for normal fire evacuations.

The remarkable characteristics of human behavior in the evacuation due to an adjacent fire are summarized below:

- No information or evacuation order was conveyed to the subject office from the fire site or other organizations.
- Occupants could observe the adjacent fire from a better angle than a fire in their own building, which allowed a better understanding of the fire state.
- Occupants had less confidence that they should evacuate, and they, therefore, did not move immediately.
- Some occupants thought that emergency staircases could not be used because it was not a real fire situation.
- Occupants took advantage of the main stairwell, which is not allowed for use in a fire.
- Occupants believed that they were safe.

The situation of this incident did not require immediate action, but indeed an evacuation. That is, the occupants' behavior had some similarities to an evacuation from a non-fire floor in a building fire. These include, for example, going to another place to confirm the state of the fire; taking photos/movies of the fire site; or psychological barriers to evacuation without an explicit order. Meanwhile, comprehensively speaking, the uncertainty of the adjacent fire caused the occupants to make individual risk assessments. They decided that fire would not spread to their building, even though the windowpanes became hot. Theoretically, people should evacuate as soon as they

have information about a fire, even if they cannot confirm it; however practically, they often postpone or dismiss the evacuation.

This study confirmed the factors influencing this phenomenon in an actual case. Taking this knowledge into consideration, professionals, such as fire safety engineers, government officials, and building managers, should develop measures to encourage evacuation at an early stage while the risks are still low. This viewpoint can be applied to evacuations, not only due to an adjacent fire, but also due to a non-fire floor evacuation in a building fire.

References

1. Bukowski, R. W., & Tubbs, J. S. (2016). *Egress concepts and design approaches: SFPE handbook* (6th ed., pp. 2012–2047). New York: Springer.
2. Saunders, W. L. (1997). Occupant decision making in office building fire emergencies: Experimental results. *Fire Safety Science, 5,* 771–782. https://doi.org/10.3801/IAFSS.FSS.5-771.
3. Proulx, G. (2003). Playing with fire: Understanding human behavior in burning buildings. *ASHRAE Journal, 45,* 33–35.
4. Kobayashi, M., & Horiuchi, S. (1979). Analysis of occupant behavior in an office building under fire: Part 1 classifications of behaviors. *Transactions of the Architectural Institute of Japan, 280,* 137–142. https://doi.org/10.3130/aijsaxx.280.0_137. (in Japanese).
5. Kobayashi, M., & Horiuchi, S. (1979). Analysis of occupant behavior in an office building under fire: Part 2 extraction of behavior patterns. *Transactions of the Architectural Institute of Japan, 284,* 11–125. https://doi.org/10.3130/aijsaxx.284.0_119. (in Japanese).
6. Abe, K. (1982). Fire and evacuation in a large office. *Yobō Jihō, 130,* 21–27. (in Japanese).
7. Brennan, P. (1997). Timing human response in real fires. *Fire Safety Science, 5,* 807–818. https://doi.org/10.3801/IAFSS.FSS.5-807.
8. Proulx, G., & Reid, I. M. A. (2006). Occupant behavior and evacuation during the Chicago cook county administration building fire. *Journal of Fire Protection Engineering, 16,* 283–309. https://doi.org/10.1177/1042391506065951.
9. Galea, E. R., Shields, T. J., Canter, D., Boyce, K., Day, R., Hulse, L., et al. (2006). Methodologies employed in the collection, retrieval and storage of human factors information derived from first hand accounts of survivors of the WTC disaster of 11 September 2001. *Journal of Applied Fire Science,* 253–276. https://doi.org/10.2190/af.15.4.b.
10. McConnell, N. C., Boyce, K., Shields, J., Galea, E. R., Day, R. C., & Hulse, L. M. (2010). The UK 9/11 evacuation study: Analysis of survivors' recognition and response phase in WTC1. *Fire Safety Journal, 45,* 21–34. https://doi.org/10.1016/j.firesaf.2009.09.001.
11. Kuligowski, E. D. (2016). *Human behavior in fire: SFPE handbook* (6th ed., pp. 2070–2114). New York: Springer.
12. Kyodo News, Fire at a distribution center, Tokyo, retrieved November 29, 2017 from https://this.kiji.is/249813469445636099. (in Japanese).
13. Jiji Press LTD., Fire at a distribution center under demolition, Tokyo, retrieved November 29, 2017 from https://www.jiji.com/jc/article?k=2017062000902. (in Japanese).
14. Japan Meteorological Agency, 10-minute resolution climate statistics at Tokyo weather station, JMA climate statistics, retrieved December 1, 2017 from http://www.data.jma.go.jp/obd/stats/etrn/. (in Japanese).

Fire Evacuation in a Large Railway Interchange Station

C. Y. Ku, W. K. Chow and T. K. Yue

Abstract Large railway interchange stations with complex geometry are common in contemporary integrated railway networks. Fire evacuation is commonly designed using the timeline analysis in comparing Available Safe Egress Time (ASET) and Required Safe Egress Time (RSET) with agreed scenarios. Smoke management systems are required to achieve longer ASET. Egress time analysis will be evaluated in this paper for a typical large railway interchange. The fire environment was simulated using fire dynamics simulator (FDS), a software based on computational fluid dynamics (CFD). Design fires of 2, 2.5, 5, 10, 25 and 50 MW were used in estimating ASET. Egress simulations by the software SIMULEX were conducted to predict the RSET under passenger loadings of 0.5, 1, 2 and 4 m^2/person. The results show that the ASET in most of the cases with higher fire size and with higher passenger loading are less than the RSET. Consequently, the passengers are unsafe in the event of fire evacuation. Therefore, a larger safety margin, defined as the difference between ASET and RSET, should be provided. In the case of low safety margin in some existing stations, fire safety management and procedures on handling fire incidents have to be reformulated properly and carefully.

Keywords Fire modeling · Evacuation · CFD · Smoke management · Performance-based design

1 Introduction

Railway networks integrated with other transport facilities are constructed to cope with the growing population in densely populated urban cities of the Asia-Oceania region. Large and complicated railway interchange stations bear heavy passenger loadings. Evacuation under fire is a concern, but there are no prescriptive fire safety codes [1, 2] specifically for railway interchanges. Consequently, performance-based design [3, 4] has to be applied as an alternative.

C. Y. Ku · W. K. Chow (✉) · T. K. Yue
Department of Building Services Engineering, Research Centre for Fire Engineering, The Hong Kong Polytechnic University, Hong Kong, China
e-mail: beelize@polyu.edu.hk; bewkchow@polyu.edu.hk

In recent years, accidental or arson fire incidents in underground railway stations, tunnels and train carriages have been reported [5]. Fire safety in large and crowded railway stations has been the concern of the general public. In addition, there are other incidents, such as signalling fault that would lead to interruption of railway services. Even under normal conditions, many passengers are often accumulated in the concourse and platform [6, 7]. The passenger loading of some railway stations [8] has reached its peak-allowable capacity.

The prescriptive building codes deal with the provision of means of escape based on the length of escape routes, width and number of exits, the time for evacuation and the evacuation path [9]. Large railway interchange stations with complicated architectural layouts and evacuation route arrangement have difficulties to comply with such code requirements. Performance-based design using the computational fluid dynamics (CFD) package fire dynamics simulator (FDS) [10] can then be used through timeline analysis. The Available Safe Egress Time (ASET) [11] could be calculated using a fire model with estimated fire load. Luggage bringing into the station by the parallel traders and people carrying trolley bags are the major contribution to the high fire load of the railway station, especially on the cross-border railway lines.

In this detailed study, the Required Safe Egress Time (RSET) for all passengers to reach a place of safety in fires [12] was calculated employing a commonly used evacuation model and the software SIMULEX [13, 14], with reference to the passenger loading under local conditions. On the other hand, the ASET was calculated using the FDS. ASET and RSET under different fire sizes and passenger loadings were then compared and used to determine the safety margin and safety index.

2   Egress Time Analysis

In planning and design of complex railway stations in particular those with passenger transport interchange, a fire and evacuation strategy report [15] is necessary to be developed with a number of important factors. Based on the station design requirements and general rules, a place with fire incident shall have sufficient time to allow passengers to leave the place before it becoming affected unduly by the smoke and fire spread; other passengers in non-incident place would be given clear and sufficient information to enable themselves to take action according to the instructions from the staff of the incident railway station concerned or broadcasting [16] with clear announcement.

Smoke management system [17] is a form of controlling the smoke generated by the fire in the railway station. The objective of the smoke control system is to keep the smoke at high levels thus facilitating the fire-fighting process and people evacuation [18]. Smoke layer height and the ASET will be estimated by FDS simulation. With sufficient data collected from the CFD simulation result, the ASET can be extended to be longer than RSET. A fire safety management plan based on the result can then be worked out to improve the railway station design.

The fundamental concept in the assessment of passenger safety in a large railway interchange station under fire condition is the determination of the time required [19, 20] for the passengers to egress [21] from the fire incident area to a place of safety before it becomes an untenable environment. In the study of fire evacuation in buildings, the timeline approach or time-based system [22] is commonly applied to large railway stations, shopping malls and public transport interchanges. The ASET refers to the time between ignition and the moment when the environment becomes untenable to evacuees [22]. It can be estimated [23, 24] by comparing the published data on tenability criteria. The RSET is commonly estimated in the Asia-Oceania region by empirical equations or evacuation software developed mainly overseas [14]. For any specific set of ASET and REST calculations [25], the safety margin (SM) is represented by the difference between ASET and RSET:

$$SM = ASET - RSET \tag{1}$$

Evacuees should reach a place of safety before the fire environment in the building exceeds the tenability limits [23]. The building design is considered to be safe if ASET is longer than RSET, whereas the safety margin should be at least 0 s or greater. It is essential to determine SM for ensuring life safety [24] so that occupants are evacuated in a safe condition without causing serious injuries or even deaths. A safety index (SI) can be derived from SM and RSET:

$$SI = \frac{SM}{RSET} \tag{2}$$

The index of SI is an indicator in numeric form to evaluate the safety level in respect of the occupants in the fire incident building. Safety index of higher values indicates increased levels of safety, in contrast, the increased risk levels are denoted by negative SI values. This fire engineering tool with the prediction of results for local buildings with high occupant loading is not justified adequately for the time being. No in-depth studies, which were supported with data by full-scale burning tests, were conducted; nor were the current studies or research data with large-scale field tests of emergency fire evacuation in buildings with high passenger loading in Hong Kong or the Asia-Oceania region. Fire models [10] with relatively small design fire size and low values on tenability limits with the ASET result were estimated [11] commonly.

To predict the flow of evacuation pattern and time, predictive evacuation simulation software [13, 14] is often used. In the current market, no single predictive fire evacuation software [26] which is applicable to the situation in Hong Kong was reported in any relevant literature. Such predictive fire evacuation software should include not only the instantaneous positions of the passengers leaving the fire incident building, but also other factors such as human behaviours due to psychological effect. So far, there have not been any systematic or research studies on human behaviours in an accidental fire in Hong Kong. Apparently, human subjects [27] with detailed research should be carefully planned together with sufficient research funding given

by the local authorities, as well as the support by the public transportation business sector such as the railway operator.

3 Methodology

3.1 Selected Interchange Railway Station

The selected interchange station has basically two major levels with mezzanine level serving as the plant room areas as shown in the sectional view in Fig. 1a–c. The approximate dimensions of the major concourse level are about 230 m (Length) × 80 m (Width) with an atrium of about 22 m (Height). There are two railway tracks on each railway line platform, consisting of the cross-border railway line of about 230 m (Length) × 18 m (Width) × 6 m (Height) and the urban railway line of about 150 m (Length) × 20 m (Width) × 4 m (Height). The platforms of the two railway lines are connected by walkways. While the urban railway line platform is a fully enclosed structure, the cross-border railway line platform is a semi-open structure without cover over the two railway tracks. The total floor area of the principal concourse level and platform level is about 18,400 and 7140 m^2, respectively.

3.2 Estimation of ASET

ASET can be estimated with fire models [28] and CFD techniques [29]. The results were used to determine whether fire safety provisions are adequate under the agreed fire scenarios for large railway stations [30]. FDS (version 5.5.3), a CFD-based software, was used [9] in this detailed study to predict the ASET in the selected interchange railway station. It solves numerically a form of the Navier–Stokes equations appropriate for low-speed, thermally driven flow with an emphasis on smoke and heat transfer from fires [31]. A baggage fire on the concourse level was considered in this detailed study based on the values in the guide book [23] and NFPA 101-2009 [22, 32].

The location of fire source on the concourse level and the isometric view of the CFD model are shown in Figs. 1d and 2, respectively. The CFD results (Zone C1) are shown in Figs. 3 and 4. The fire was initiated from $t = 0$ s and decayed when the fuel was consumed.

Based on the smoke control principle [17], tenable conditions for the railway passengers in public circulation areas of the railway stations should be maintained primarily through the use of smoke extraction system. In this detailed study, smoke extraction system is employed to minimize the evacuees' exposure to undue hazards [33, 34] as a result of smoke accumulation [35], loss of visibility or intolerable
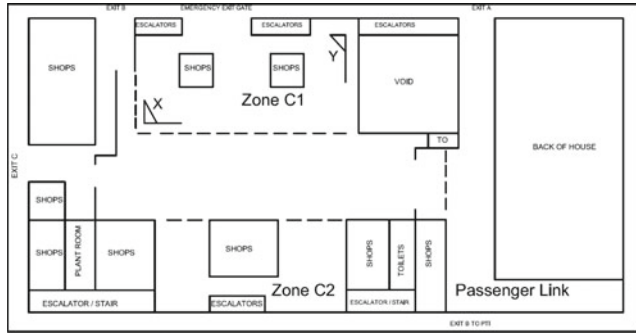
(a) Concourse layout
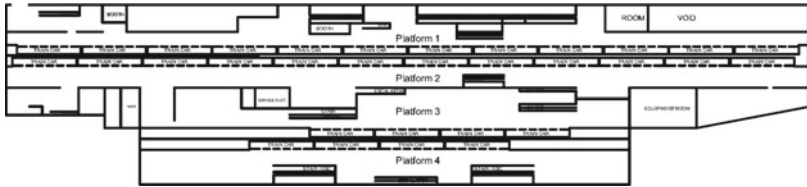
(b) Platform layout
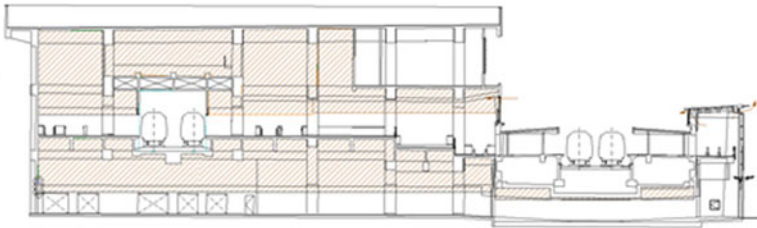
(c) Sectional view
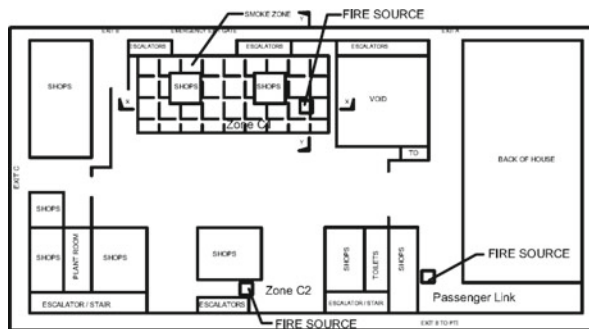
(d) Location of fire source at concourse level

Fig. 1 Selected interchange station
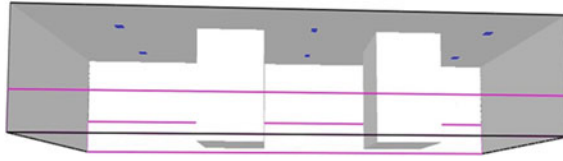
Fig. 2 FDS model for the fire at concourse level
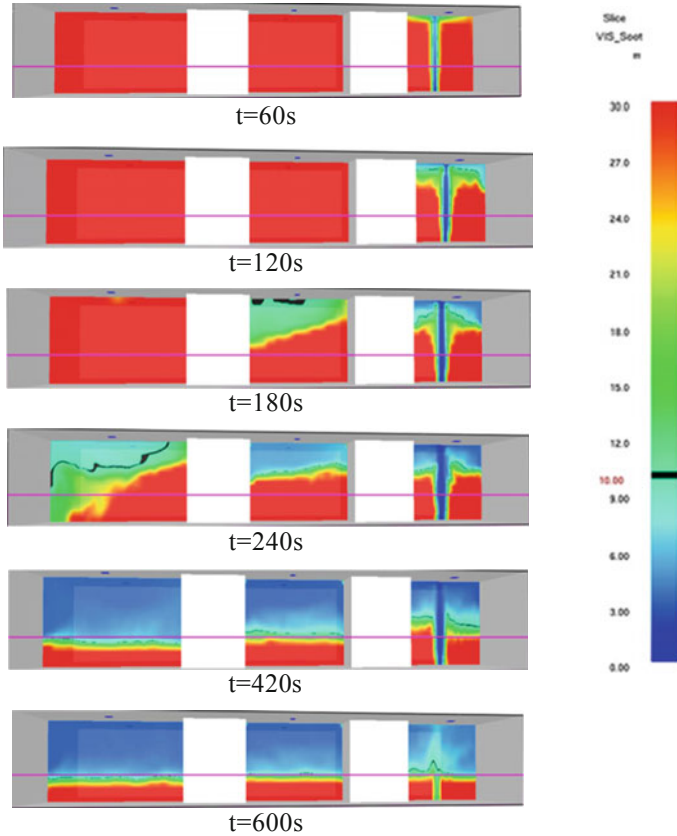
Fig. 3 Zone C1, visibility contour in *X*-direction

conditions [36] due to fire or radiation. Tenability of the station environment for evacuation takes major account of the two factors in the study.

For the purpose of smooth passenger evacuation under tenable conditions, visibility should be maintained at least 10 m. Other than the temperature and visibility limits, air velocity, radiation and carbon monoxide concentration are also important factors for the evaluation of the tenability along the evacuation path. Since the selected railway interchange station is relatively large in terms of station volume and

t=60s

t=120s

t=180s

t=240s

t=420s

t=600s
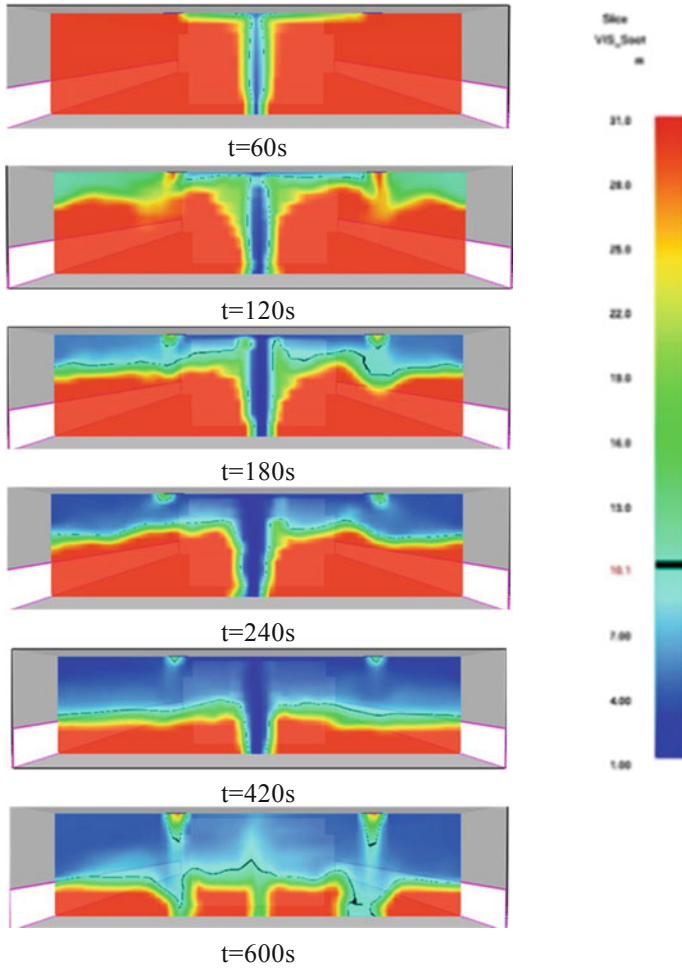
Fig. 4 Zone C1, visibility contour in *Y*-direction

floor space for circulation, evacuees can easily move away from the fire source and therefore the amount of carbon monoxide generated from the fire source will not accumulate to a high concentration to endanger the evacuees. The effect of radiation and carbon monoxide will not be the major concerns in the large railway station. As such, the assessment on the change of temperature and visibility level will be used as the basis of the formation of ASET.

Six fire sizes of 2, 2.5, 5, 10, 25 and 50 MW were chosen to assess the inter-related effect on the ASET in different types of fire sources. In the above fire scenarios, the fire source was assumed to be a baggage on fire with a peak fire heat release rate of low values used years ago (2, 2.5 and 5 MW) [28]. More reasonable values of 10, 25 and 50 MW [37, 38] were used in this study.

In this detailed study, the major parameters of the CFD input are as follows:

Simulation time duration	600 s
Ambient temperature	32 °C
Smoke extraction rate	4.2 m^3/s
Make-up air	Naturally from adjacent concourse area
Smoke soot yield	0.035 kg/kg
Peak heat release rate	2, 2.5, 5, 10, 25 and 50 MW
Heat release rate per unit area	500 kW/m^2
Visibility factor	3
Fire location	Concourse C1, concourse C2, passenger link

The above factors are the important criteria in the fire to occupants.

3.3   Prediction of RSET

SIMULEX is a computer package to simulate the escape movement of people from very large or geometrically complex buildings. SIMULEX allows the user to produce a 3D model of the building by using the CAD connected by staircases. The user can define the final external exits outside the building and SIMULEX will calculate the travel distances and routes throughout the evacuation process. The percentage distribution of passengers as defined in this study is 30% average, 30% male, 30% female and 10% child by SIMULEX. The normal unimpeded walking speed for each person is between 0.8 and 1.7 m/s. In this study, the predictive evacuation tool used to estimate the RSET was SIMULEX. The maximum allowed passenger load of transport facilities like railway stations or bus terminus is not specified clearly in the local codes of Hong Kong. However, 0.5 m^2/person is commonly used [39] in areas accessible to the public, such as places of public entertainment like cinemas and sports stadia, banking halls and viewing galleries. The number of passengers based on the 0.5 m^2/person passenger loading is shown in Table 1. The design occupancy loading in crowded railway stations in train incidents [11] is much more crowded than the maximum value of the building code with 0.5 m^2/person.

In this study, fire evacuation from the concourse level was considered. There were six fire scenarios labelled as F1, F2, F3, F4, F5 and F6 with different passenger loadings of 0.5, 1.0, 2.0 and 4.0 m^2/person, representing different operation hours of the interchange railway station.

Table 1 Summary of evacuation scenarios

Scenarios			Required safe egress time (RSET) (s)	F1	F2	F3	F4	F5	F6
Passenger loading (m²/person)	Passenger link zone	0.5	137	0.96	0.85	0.72	0.61	−0.01	−0.34
		1	124	1.16	1.05	0.9	0.78	0.1	−0.27
		2	89	2.01	1.85	1.65	1.48	0.53	0.02
		4	62	3.32	3.1	2.81	2.56	1.19	0.47
	Concourse (zone C2)	0.5	116	1.18	0.87	0.78	0.66	0.07	−0.25
		1	103	1.46	1.11	1.01	0.86	0.2	−0.16
		2	82	2.09	1.65	1.52	1.34	0.51	0.06
		4	57	3.44	2.81	2.63	2.37	1.18	0.53
	Concourse (zone C1)	0.5	225	0.03	−0.04	−0.09	−0.19	−0.59	−0.66
		1	130	0.78	0.67	0.57	0.41	−0.29	−0.42
		2	95	1.43	1.28	1.15	0.93	−0.03	−0.2
		4	65	2.55	2.34	2.14	1.82	0.42	0.17

Table 2 Details of fire simulations and ASET results

Fire scenario		F1 (2 MW)	F2 (2.5 MW)	F3 (5 MW)	F4 (10 MW)	F5 (25 MW)	F6 (50 MW)
Available safe egress time	Passenger link zone	268	254	236	221	136	91
	Concourse (zone C2)	253	217	207	192	124	87
	Concourse (zone C1)	231	217	204	183	92	76

4 Results

4.1 Simulation Results

The results of predicted ASET and RSET in the six fire scenarios and different passenger loadings are summarized in Tables 1 and 2. Under a small fire size of 2 MW, the ASET is rather long for fire evacuation. The simulation results from the predictive evacuation model can be taken as a reference by the fire engineers and fire safety management [40] to formulate the evacuation strategy.

4.2 Safety Margin

When there is uncertainty in the human factors, the safety margin [41] plays an important role in fire safety. The evaluation criteria for acceptance of the safety margin is highly simplistic [25, 42] by the fire engineers. The results on safety margin used are shown in Fig. 5a–c, respectively.

When ASET is equal to RSET, SI will become 0. The SI value lying on both positive and negative sides indicates whether the fire scenarios are safe or unsafe. As observed from the ASET/REST results, it can be seen that most of the fire scenarios under the passenger loading of 0.5 m^2/person are on the unsafe region and will pose significant fire hazards to evacuees. Results of safe egress analysis based on ASET and RSET are plotted in Figs. 6, 7 and 8 for the three fire locations under the fire size from 2 to 50 MW with the passenger loadings from 0.5 to 4 m^2/person.

5 Discussion

Apart from the quantitative variables, the evaluation of both ASET and RSET is very subjective [25] and sometimes misleading if not carefully interpreted. It is rather dangerous to use a low safety margin [27] in the ASET/RSET analysis with fire

(a) Passenger Link Zone

(b) Concourse Zone C2
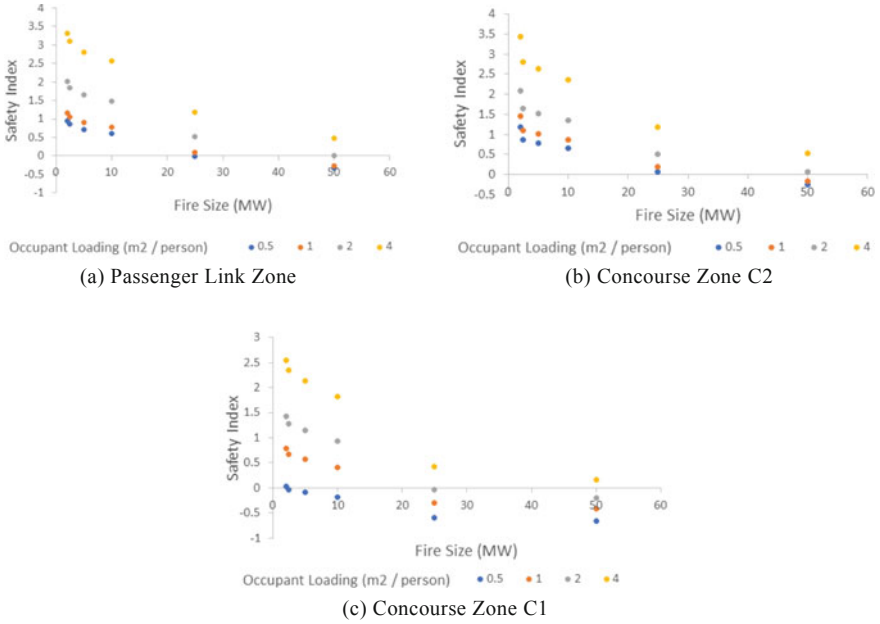
(c) Concourse Zone C1

Fig. 5 Variation of safety index
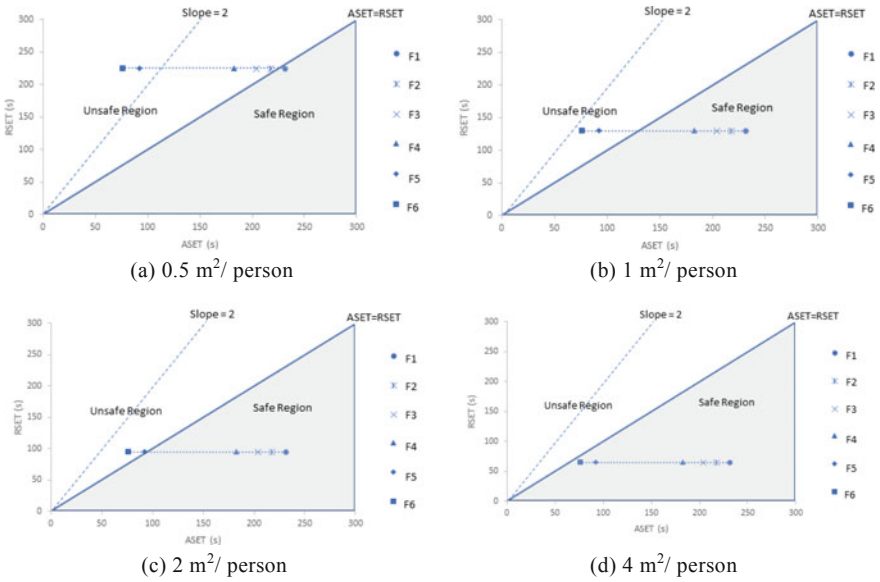
(a) 0.5 m^2/ person

(b) 1 m^2/ person

(c) 2 m^2/ person

(d) 4 m^2/ person

Fig. 6 Egress safety analysis for concourse zone C1

(a) 0.5 m^2/ person

(b) 1 m^2/ person

(c) 2 m^2/ person

(d) 4 m^2/ person

Fig. 7 Egress safety analysis for concourse zone C2

(a) 0.5 m^2/ person

(b) 1 m^2/ person

(c) 2 m^2/ person

(d) 4 m^2/ person
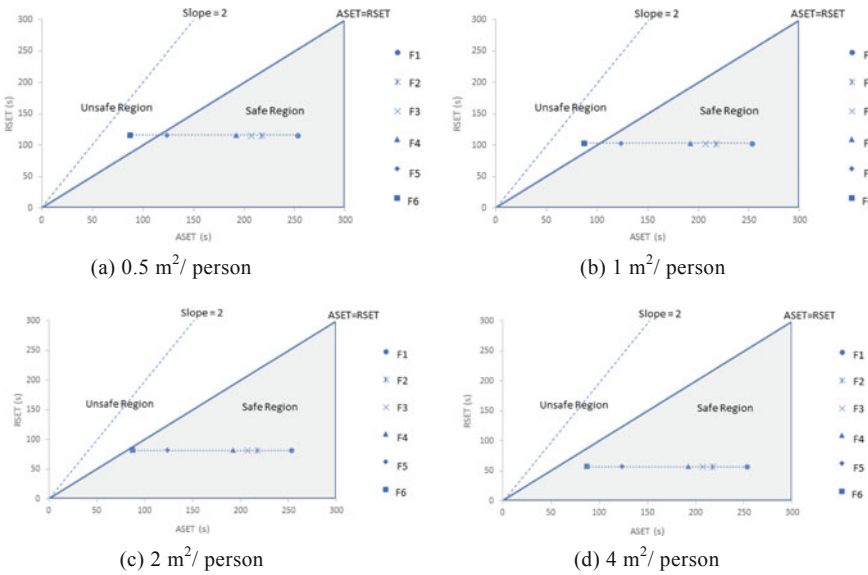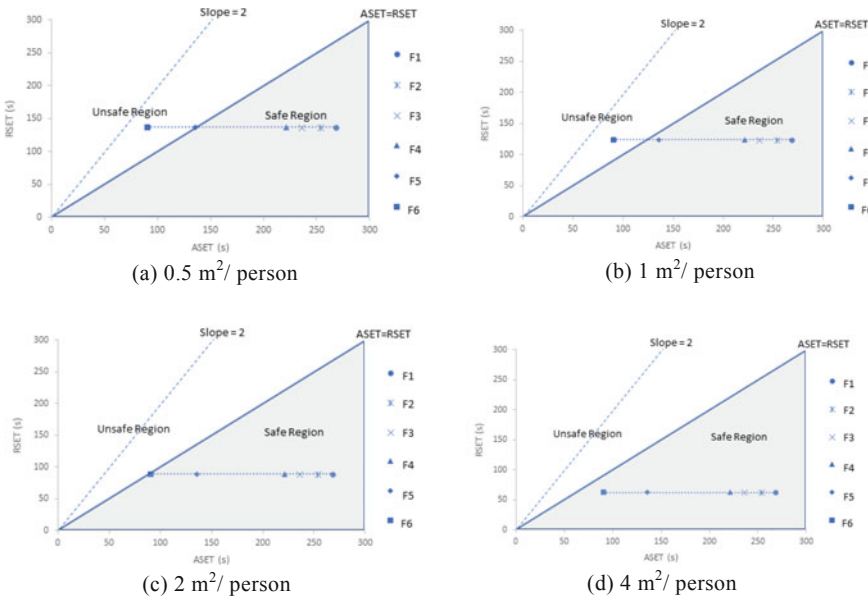
Fig. 8 Egress safety analysis for passenger link

scenarios considered in the assessment. According to a study by He [43], the safety factor or safety margin alone is only a first-order measure of risk or failure probability and is an insufficient measure to achieve a higher order estimate of failure probability.

6 Conclusion

Railway interchange station is very complex in geometry and is crowded with passengers in day-to-day operation with high passenger loading. Fire safety for the large interchange station is particularly important in terms of the integration of smoke management system, design of evacuation routes, clear directional signage, building materials used and the prediction of evacuation time. The fire risk analysis and smoke simulation with CFD with the aid of predictive fire and evacuation models will help to understand the risk hazard associated with the design of the railway stations.

The use of safety margin and then the outcome of safety index vary with environments. In this study, six fire sizes of 2, 2.5, 5, 10, 25 and 50 MW were chosen to assess the ASET. Under these six fire sizes, four different passenger loadings of 0.5, 1.0, 2.0 and 4.0 m^2/person representing loadings at different operation hours were chosen to derive the safety index based on the simulated ASET and RSET results. The safety index in most of the fire scenarios with passenger loading of 0.5 m^2/person is negative up to -0.66, representing that the passengers are unsafe in the event of fire evacuation. In other words, a safe environment can hardly be achieved with the passenger loading of 0.5 m^2/person under most of the fire scenarios. It must be pointed out that the passenger loading in the railway stations in particular those large railway station interchanges is about 0.5 m^2/person in rush hours.

References

1. Chow, W. K. (2015). Performance-based approach to determining fire safety provisions for buildings in the Asia-Oceania regions. *Building and Environment - Fifty Year Anniversary for Building and Environment, 91,* 127–137.
2. Buildings Department. (1998). *Practice note APP-87*. Hong Kong: Buildings Department.
3. Buildings Department. (2012). Code of Practice for Fire Safety in Buildings 2011, Buildings Department, Hong Kong Special Administrative Region.
4. South China Morning Post. (2017). MTR firebomb attack at height of rush hour, p. A1, 11 February 2017.
5. Chow, W. K., Qu, L., & Pang, E. C. L. (2011). Incidents on fire and ventilation provision in subway systems in Hong Kong. *International Journal on Engineering Performance-Based Fire Codes, 10*(3), 41–47.

6. Chow, W. K., & Qu, L. (2014). Fire hazard assessment for a green railway station. *Fire and Materials, 38,* 451–461.
7. Ku, C. Y., Fong, N. K., Chow, W. K. (2013). Parameters in development of the railway station evacuation strategy. In: 11th International Symposium on Building and Urban Environmental Engineering BUEE2013, December 11–14, 2013, Taipei, Taiwan.
8. Chow, W. K. (2002). Ventilation of enclosed train compartments in Hong Kong. *Applied Energy, 71*(3), 161–170.
9. McGrattan, K., Klein, B., Hostikka, S., Floyd, J. (2010). Fire Dynamics Simulator (Version 5) User's Guide. NIST Special Publication 1019-5. National Institute of Standards and Technology, USA.
10. Chow, W. K. (2011). Timeline Analysis with ASET and RSET, 9 September 2011. Department of Building Services Engineering, The Hong Kong Polytechnic University, Hong Kong. http:// www.bse.polyu.edu.hk/researchCentre/Fire_Engineering/Hot_Issues.html.
11. Fong, N. K., & Ma, C. Y. (2004). Research on evacuation design: Railway station as an example. *International Journal on Engineering Performance-Based Fire Codes, 6*(4), 188–196.
12. Lo, S. M., Fang, Z., Lin, P., & Zhi, G. S. (2004). An evacuation model: The SGEM package. *Fire Safety Journal, 39,* 169–190.
13. Integrated Environmental Solutions Limited (IES). (2015). SIMULEX user guide: Evacuation modelling software. Integrated Environmental Solutions Inc.
14. Kowloon-Canton Railway Corporation (KCRC). (2007). Fire Safety Strategy Reports, Hong Kong.
15. Ho, M. K., Ku, C. Y., Chow, W. K. (2016). Evacuation hazards in crowded subway stations. In: *4th International High Performance Buildings Conference at Purdue*, July 11–14, 2016, Illinois, USA.
16. National Fire Protection Association. (2012). NFPA 92 Standard for Smoke Control Systems, Quincy, MA, USA.
17. Ip, A. K. Y., Luo, M. C. (2005). Smoke control in pedestrian subway. In: *Proceedings of the Hubei—Hong Kong Joint Symposium 2005* (pp. 70–79), June 30–July 3, 2005, Wuhan, Hubei, China.
18. Stahl, F. I. (1982). *Time-based capabilities of occupants to escape fires in public buildings: A review of code provisions and technical literature*. Washington, DC, USA: National Bureau of Standards.
19. Ng, C. M. Y., & Chow, W. K. (2006). A brief review on the time line concept in evacuation. *International Journal on Architectural Science, 7*(1), 1–13.
20. Tubbs, J. S., & Meacham, B. J. (2007). *Egress design solutions: A guide to evacuation and crowd management planning*. USA: Wiley.
21. Hinks, A. J. (1985). Predicting danger levels to life—The deciding factors. *Fire, 77*(964), 21–24.
22. Chartered Institution of Building Services Engineers. (2010). *CIBSE Guide E: Fire Safety Engineering*. London, UK: CIBSE.
23. Shields, T. J., Silcock, G. W., & Dunlop, K. E. (1992). A methodology for the determination of code equivalency with respect to the provision of means of escape. *Fire Safety Journal, 19*(4), 267–278. https://doi.org/10.1016/0379-7112(92)90009-2.
24. International Organization for Standardization. (2009). ISO/TR 16738:2009 Fire-Safety Engineering—Technical Information on Methods for Evaluating Behaviour and Movement of People, ISO, Geneva, Switzerland.
25. Babrauskas, V., Fleming, J. M., & Russell, B. D. (2010). RSET/ASET, a flawed concept for fire safety assessment. *Fire and Materials, 34,* 341–355.
26. Chow, W. K. (2011). Six points to note in applying timeline analysis in performance-based design for fire safety provisions in the far east. *International Journal on Engineering Performance-Based Fire Codes, 10*(1), 1–5.
27. Chow, W. K. (2013). Letter to the editor: Comment on 'RSET/ASET, a flawed concept for fire safety assessment'. *Fire and Materials, 37*, 257–258. In V. Babrauskas, J. M. Fleming, & B. D. Russell (Eds.), *Fire and materials* (Vol. 34, pp. 341–355) (2010).

28. Chow, W. K. (1999). A preliminary discussion on engineering performance-based fire codes in the Hong Kong special administrative region. *International Journal on Engineering Performance-Based Fire Codes, 1*(1), 1–10.
29. Chow, W. K., Fong, N. K. (2012). Common mistakes made in using CFD in FEA Projects, CPD Lecture. 21 April 2012, Department of Building Services Engineering, The Hong Kong Polytechnic University, Hong Kong.
30. Qu, L., & Chow, W. K. (2012). Platform screen doors on emergency evacuation in underground railway stations. *Tunnelling and Underground Space Technology, 30,* 1–9. https://doi.org/10.1016/j.tust.2011.09.003.
31. Chow, W. K., & Yin, R. (2004). A new model on simulating smoke transport with computational fluid dynamics. *Building and Environment, 39*(6), 611–620.
32. Fire Services Department. (2013). Guidelines on Formulation of Fire Safety Requirements for New Railway Infrastructures. Fire Services Department, Hong Kong Special Administrative Region.
33. Milke, J. A. (2000). Evaluating the smoke hazard from fires in large spaces. *International Journal on Engineering Performance-Based Fire Codes, 2*(3), 94–103.
34. Roh, J. S., Ryou, H. S., Park, W. H., & Jang, Y. J. (2009). CFD simulation and assessment of life safety in a subway train fire. *Tunnelling and Underground Space Technology, 24*(4), 447–453. https://doi.org/10.1016/j.tust.2008.12.003.
35. Shi, S. L., Lu, W. Z., Chow, W. K., & Huo, R. (2007). An investigation on spill plume development and natural filling in large full-scale atrium under retail shop fire. *International Journal of Heat and Mass Transfer, 50*(3), 513–529.
36. Chow, W. K., & Chan, M. Y. (2003). Field measurement on transient carbon monoxide levels in vehicular tunnels. *Building and Environment, 38*(2), 227–236.
37. Thauvoye, C., Zhao, B., Klein, J., Fontana, M. (2008). Fire load survey and statistical analysis. In: *Fire Safety Science—Proceedings of the Ninth International Symposium* (pp. 991–1002).
38. Chow, W. K., Wong, K. Y., & Chung, W. Y. (2010). Longitudinal ventilation for smoke control in a tilted tunnel by scale modeling. *Tunnelling and Underground Space Technology, 25*(2), 122–128.
39. Jiang, C. S., Yuan, F., & Chow, W. K. (2010). Effect of varying two key parameters in simulating evacuation for subway stations in China. *Safety Science, 48*(4), 445–451.
40. Lui, G. C. H., & Chow, W. K. (2000). A demonstration on working out fire safety management schemes for existing karaoke establishments in Hong Kong. *International Journal on Engineering Performance-Based Fire Codes, 2*(3), 104–123.
41. Sime, J. D. (1986). Perceived time available: The margin of safety in fires. In: *Fire Safety Science—Proceedings of First International Symposium*, Hemisphere, Washington DC, USA (pp. 561–570).
42. Poon, S. L. (2014). A dynamic approach to ASET/RSET assessment in performance based design. *Procedia Engineering, 71,* 173–181.
43. He, Yaping. (2010). Linking safety factor and failure probability for fire safety engineering. *Journal of Fire Protection Engineering, 20*(3), 199–217.

Experimental Study on Single-File Movement with Different Stop Distances

Qiao Wang, Weiguo Song, Jun Zhang, Liping Lian and Siuming Lo

Abstract The single-file movement formed at exit, passageway, and stairway is a common and fundamental phenomenon in building evacuation when fire happened. In order to investigate single-file movement, the controlled experiments contained three parts: acceleration, steady state, and deceleration are effective research methods. In this paper, we conducted single-file movement experiments with two different commands in decelerating phase: (1) normal stop, (2) close stop, i.e., stop at the place as close as possible to the predecessor, in which participants move at different free moving speed. Through rescaling the speed, there is no influence for different free moving speed on speed–distance headway relationship. The linear fitting curve is executed to obtain a quantitative description of the speed–distance headway relation, and the slope in the close stop experiment is larger than that in the normal stop. It is found that there is a little difference in the decelerating phase for different participants and the average close stop distance is 0.34 m, which is a little bigger than average chest width 0.3 m. For the normal stop, the comfortable stop distance is dependent on individual proxemics. In the relation of speed–time, it was divided into two stages, which is fitted using linear regression. The value of negative acceleration in stage I is greater than stage II. Similar to the fitting result of speed–distance headway, participants in close stop experiments have bigger negative acceleration in stage I. However, in stage II, due to the uncertainty of close stop distance for different participants, the value of negative acceleration in close stop is smaller. Actually, in normal conditions, participants stopped with their comfortable stop distance when the predecessor stopped. However, in emergency or hurried conditions, the stop distance would be smaller. Therefore, it is useful to investigate the movement behavior in an emergency (such as fire and earthquake) and hurried conditions when the predecessor stopped suddenly.

Q. Wang · W. Song (✉) · J. Zhang · L. Lian
State Key Laboratory of Fire Science, University of Science and Technology of China, Hefei 230026, China
e-mail: wgsong@ustc.edu.cn

Q. Wang · L. Lian · S. Lo
Department of Civil and Architectural Engineering, City University of Hong Kong, Kowloon, Hong Kong

Nomenclature

$h_i(t)$ Distance headway of pedestrian i at time t
$x_i(t)$ X-axis coordinate of pedestrian's head at time t
$v_i(t)$ Speed of pedestrian i at time t
Δt Time interval
a Slope of linear fitting
b Intercept of linear fitting
R^2 Coefficient of determination

Subscripts

i Pedestrian

1 Introduction

In recent decades, building fire accidents happened frequently. The latest building fire accidents include 6·14 London apartment building fire accident, Philippines commercial center fire accident, and so on. In buildings, single-file movement, as the simple and fundamental phenomenon, formed at bottlenecks such as a narrow corridor, exit as well as stairway. These structures are common and play an important role on building evacuation. Furthermore, the evacuation efficiency is determined by bottlenecks when fire occurred. Therefore, the behavior of pedestrian in these areas is worth investigating, especially its decelerating phase, when the predecessor stopped suddenly. Due to the absence of pedestrian evacuation data when building fire accident occurred, the controlled experiments, one of the effective research methods, for pedestrian evacuation were conducted [1–4].

The controlled single-file movement experiments in regard to pedestrians, vehicles as well as animals have been widely studied [5–14]. As a basic movement, the density-speed and density-flow relations obtained in single-file experiments were contributed to the study of pedestrian evacuation dynamics. In addition, many researchers also focused on investigating the relationship between velocity and distance headway. Linear relation had been found in relation of velocity–distance headway (the inverse of density) [5, 8]. Rather than a piecewise linear relation, three regions (free regime, weakly constrained regime, and strongly constrained regime) were found in velocity

and distance headway relationship with the critical points of distance headway about 1.1 and 3 m [15]. However, the nonlinear curve fitted the velocity–distance headway was obtained in [7]. In single-file movement, the relation of step frequency and the distance headway which expressed as a linear relationship was studied [6, 16]. For different age pedestrians who had different mobilities, there was a significant difference in the fundamental diagram and the mixed group resulted in the heterogeneity of system [8]. Meanwhile, the difference of culture also led the difference in the fundamental diagram [17]. Different from the ground motion, the single-file movement experiments in a ship corridor simulator was performed by Sun et al. [18]. It was found that the both the density and the effect of trim and heeling had a influence on the walking speed; meanwhile, the impact of trim angles was larger than heeling angels.

The process of single-file experiment consists of three phases: acceleration, steady state, and deceleration. In the previous single-file researches, researchers focused on the steady state to study fundamental diagram [8]. However, in many cases, the decelerating phase plays an important role on behavior movement. In daily life, the decelerating phase presented in those cases as reducing velocity to avoid collision when the predecessor stopped suddenly, joining in a queued team that had been formed and braking of cars when the signal turned red. Meanwhile, in vehicle traffic field, many researchers paid attention to the decelerating phase [19–21]. As known to all, we are living in a social environment, interaction with others is one part of our life. Therefore, Edward Hall [22] proposed the proxemics, the interpersonal and spatial relationship. In proxemics theory, there were four corresponding social distances, including intimate, personal, social, and public distance. In normal circumstance, the physical contact among strangers is repulsive. However, physical contact among people happened frequently when they escaped from panics [23]. Therefore, the relationship of speed–distance, especially in the deceleration phase, also should be focused. Here, the behavior of pedestrians in decelerating phase with different stop distances in single-file experiment is studied in our work.

In this paper, the single-file pedestrian movement experiment is conducted, and we focus on the decelerating phase with different stop distances. Similar to steady state, the relations of speed–distance headway and speed–time are presented. To some degree, our work can provide a reference for the evacuation and management of crowd in emergency conditions. The rest of this paper is organized as follows. In Sects. 2 and 3, experimental process and measure and method are described briefly. The results of linear regress for speed–distance headway and speed–time are presented in Sect. 4. Finally, Sect. 5 shows the paper conclusions.

2 Experimental Setup

We conducted single-file movement experiments to study the decelerating phase with different stop distances. A video camera was mounted on the top of the room to record the whole process of experiment. The experiment was employed in the experimental

platform of pedestrian and evacuation dynamics in USTC, and all participants (11 students in total) are university students with the age ranging from 22 to 28. In order to extract trajectories of participants conveniently, red or yellow hats were worn.

The experimental scene was composed of two long horizontal channels with 4.2 m marked on the ground, which were connected by two longitudinal channels as shown in Fig. 1a. The width of the channel was 0.6 m. 2–5 participants took part in each trial, and each trial is repeated more than twice. At the beginning of each experiment procedure, participants stood at one horizontal channel randomly and then moved in this annular corridor orderly. After several laps were finished, the leader one (i.e., the first participant in one group) stopped at one end of the horizontal channel optionally (before entering the longitudinal channel); meanwhile, followers also stopped. In order to diminish the effect of the corner, the measurement region M1 is 2 m in the middle part of the horizontal channel when participants moving in the whole corridor under steady state. That means the initial data; i.e., the coordinates of each participant i moving in this region were used to calculate the individual instantaneous speed and distance headway. However, the initial date for the preceding one $i - 1$ was not limited by measure region as long as they were moving in the same channel. At the decelerating phase, the measurement region M2 is 3.1 m long which excluded the effect of one corner of one channel.

In the process of experiments, participants were asked to walk fast or normally. Both in fast walking and normal walking, there were two kinds of stop types. One is the followers stop with a comfortable distance to the preceding participant, i.e., normal stop. The other one is the followers stop as close as they can to the preceding one, i.e., close stop. That means followers stop at a place which is the shortest distance between two participants that can be accepted.
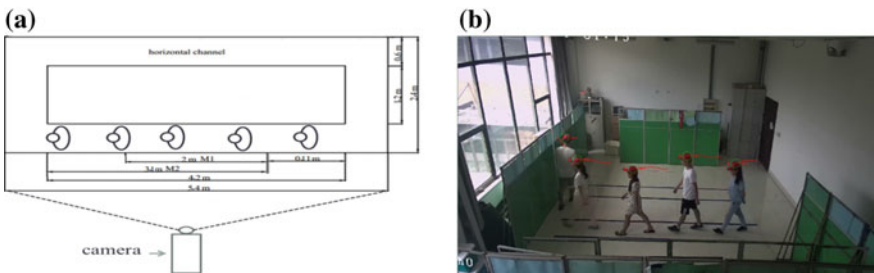
Fig. 1 Experimental scene. **a** The schematic illustration of the experimental setup. **b** A snapshot showing the trajectories of participants by using *PeTrack*

3 Ethics Statement

The study was approved by the Ethics committee of University of Science and Technology of China. All participants knew this experiment well and agreed to participate in this experiment willingly.

4 Measurement and Method

4.1 Data Extraction

The whole experimental process was recorded by means of high-resolution video camera (frame rate 25 fps). Based on the video, the trajectories of participants were extracted by using software *PeTrack* [24] (seeing Fig. 1b). The physical coordinates (x, y) of participant's head were obtained every frame. In this paper, we only pay attention to one-dimensional characteristics, namely horizontal interaction among participants. Thus, the coordinate of x-axis was used to calculate distance headway and the instantaneous speed.

4.2 Data Analysis

For any participant i, distance headway $h_i(t)$ is defined as the distance between the centers of participant i and his/her predecessor $i - 1$ at time t, which is expressed as

$$h_i(t) = x_{i-1}(t) - x_i(t) \tag{1}$$

Meanwhile, for participant i at time t, the individual instantaneous speed is calculated as

$$v_i(t) = \frac{x_i(t + \Delta t/2) - x_i(t - \Delta t/2)}{\Delta t} \tag{2}$$

where $x_i(t)$ denotes the coordinate of participant i at time t. Time interval Δt is equal to 0.4 s in this paper. For each distance headway, there is a corresponding instantaneous speed.

5 Results and Discussion

5.1 Fast and Normal Moving Speed

In the single-file movement in circle corridor, the leading participants walked with their free fast speed or free normal speed without any interference. The average free normal speed and average free fast speed are 1.22 and 1.52 m/s as shown in Table 1. Both in close stop and normal stop process, it expresses the same relation between individual instantaneous speed and distance headway as displayed in Fig. 2. In the stop process, the speed is influenced by distance headway. That is when the predecessor stopped, the speed of followers reduced with distance headway decreasing. In addition, the stop processes for fast and normal walking speed are lapped. The discrepancy between them is reflected in the value of speed walking in circle corridor, mainly. We apply scaling to normalize the speed through dividing the average free speed. The results are displayed in Fig. 3. As can be seen from Fig. 3, the free moving speed (fast speed and normal speed) has no influence on the relation of speed–distance headway both in moving and decelerating process.

Table 1 Free speed for fast and normal moving

Moving type	Average speed v (m/s)	Standard deviation	Maximum (m/s)	Minimum (m/s)
Fast moving	1.52	0.158	1.71	1.31
Normal moving	1.22	0.088	1.32	1.00
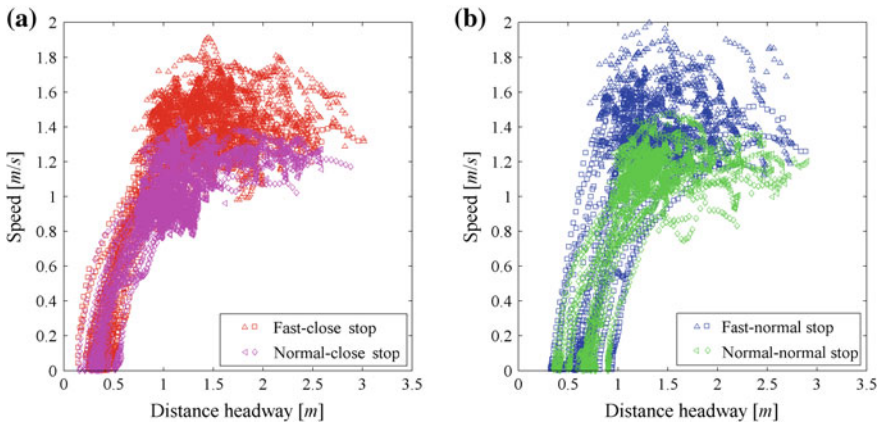
Fig. 2 Relation between instantaneous speed and distance headway for close stop (**a**) and normal stop (**b**) triangles represent data obtained in walking process and measurement area was M1. Squares represent data obtained in decelerating process and measurement area was M2. Red, magenta, blue, and green represent close stop with fast speed, close stop with normal speed, normal stop with fast speed and normal stop with normal speed, respectively
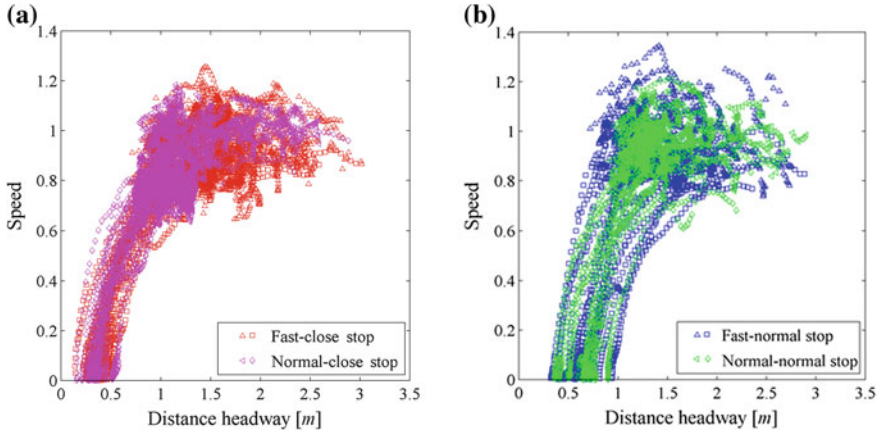
Fig. 3 Normalized relation between instantaneous speed and distance headway for close stop (**a**) and normal stop (**b**)

5.2 Close and Normal Stop

In Sect. 4.1, it reveals that relation between speed and distance headway is independent on the free moving speed. Thus, in this section, we only investigate the single-file movement in which all participants moved with fast speed. Here, we define the stop distance as the distance between adjacent participants when they stop moving. The stop distances for close stop and normal stop are separately 0.34 and 0.63 m, which are listed in Table 2. For the close stop, it has smaller stop distance and standard deviation that means participants stop moving when no space is available in front. The average stop distance is 0.34 m that is a little bigger than the average chest width 0.3 m [8]. On the contrary, the normal stop distance varies from 0.32 to 0.94 m with a large standard deviation 0.16. The normal stop distance is determined by proxemics for different participants mainly. Actually, the participants were familiar with each other; therefore, the stop distance may be smaller than that among strangers. In Table 2, the minimum of stop distance in close stop experiment is 0.14 m which is less than the average body size. The reason is that the following participant stopped, but continued to move his head ahead. Finally, he leaned his head on the predecessor's shoulder. There was a partial overlap of their heads which resulted in a small stop distance.

Table 2 Stop distance for closed and normal stop

Stop type	Average stop distance (m)	Standard deviation	Maximum (m)	Minimum (m)
Close stop	0.34	0.083	0.53	0.14
Normal stop	0.63	0.160	0.94	0.32
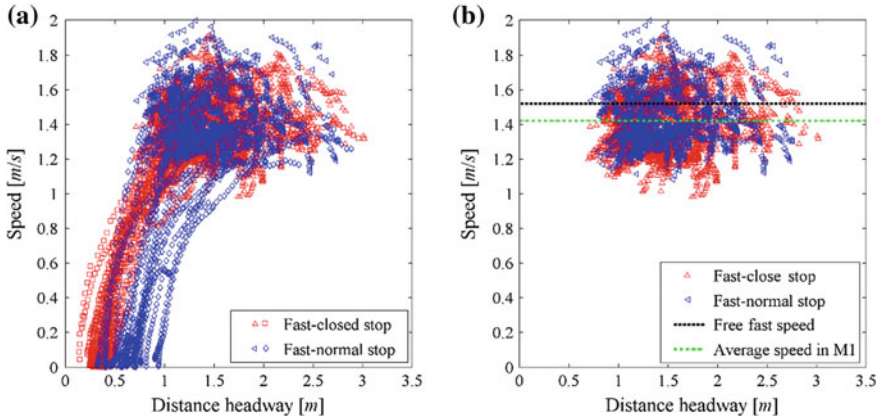
Fig. 4 Comparison of close stop and normal stop with fast speed, **a** speed–distance headway relation under steady state and decelerating processes, and **b** the individual speed in moving process

Figure 4 depicts the comparison results of close and normal stop for speed–distance headway. In the process of deceleration, the data is obtained in the observation region M2. With the decrease of distance headway, participants reduced their speed as presented in Fig. 4a. As shown in Fig. 4a, the trend of process of deceleration is approximated when they conducted close stop, while it is more discrete for normal stop process. On the other hand, intuitively, if one participant had a large stop distance, he/she started to reduce his/her speed at greater distance headway. When participants moved in circle corridor (observation region M1), they moved with fast speed 1.42 m/s in steady state which is a little less than free fast speed 1.52 m/s as illustrated in Fig. 4b. In our experiments, five participants were involved in one experiment at most, and they can see each other. By this way, participants can adjust distance headway to reach their free fast speed; however, they were also affected by the predecessors. Thus, participants are in the weak constrained regime, as proposed in [15] in this experiment.

To investigate the general rule of close and normal stop, we analyze the relationship between speed and distance headway quantitatively. The speed–distance headway diagram is plotted in Fig. 5 as using a perpendicular binning procedure [15]. In this process, first of all, the data of instantaneous speed falling into the interval period of distance headway per 0.1 m were regarded as one group. Then, the average value of speed, standard deviation, and standard error was calculated in each group. Figure 5a plots the average speed and its standard deviation varying with distance headway; meanwhile, it shows the average speed and standard error evolving with distance headway in Fig. 5b. In statistics, the standard deviation is a measure, which reflects the variation of individual observation values, while, the standard error, the other measure, reflects the variation between sample averages. Here, we used two measures to analyze the data of speed–time. In Fig. 5a, the larger standard deviation (blue shaded region) of speed is presented for normal stop experiment in the deceler-
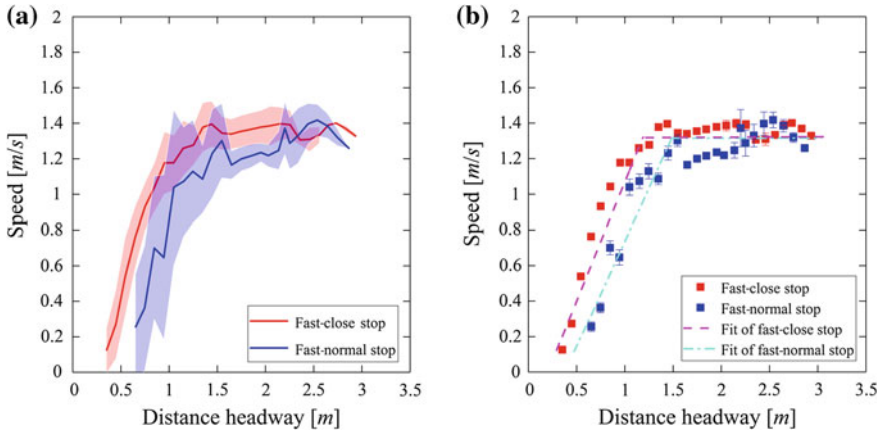
Fig. 5 Relation of speed and distance headway in process of decelerating phase for **a** the average speed and standard deviation and **b** average values of speed and the standard error

ating phase that means participants have their own proxemics for their comfortable stop distance, whereas the standard deviation (red-shaded region) of the close stop is small due to close stop distance. In Fig. 5b, the linear fit of the average speed $(y = a*x + b)$ with distance headway is depicted. Here, y and x represent average speed and distance headway, respectively. a is slope and b is intercept for fitting line. The results of fit parameters are shown in Table 3. From Table 3, the slope in the close stop experiment is 1.34, which is larger than that of normal stop 1.19. Meanwhile, both close stop and normal stop have the same speed before they reduced their speed. However, this value of speed 1.32 m/s is smaller than the free speed in steady state. The reason is the followers can know when the leader one stop and they would reduce their speed subconsciously in the deceleration phase. The greater value of a indicates the time from free walking speed to stop completely is smaller. In addition, larger a means less distance headway is needed in the close stop. On the other hand, it is clearly demonstrated that the R^2 of the estimation for close stop and normal stop are 0.93 and 0.92, which reveals a good fit for the relation of speed–distance headway.

Moreover, we investigate the evolution of speed with time in decelerating phase by using the same analytic method with speed–distance headway in observation region M2, and all participants stop at the end of region M2. The zero time is defined as the time that participants spanned the initial point of M2. Presented in Fig. 6a, the average speed in both close stop and normal stop experiments reduces with time and the curve in normal stop experiment has larger dispersion degree, i.e., larger standard

Table 3 Fit parameter value for close and normal stop with distance headway

Moving type	a	b	R^2
Close stop	1.34	−0.27	0.93
Normal stop	1.19	−0.46	0.92
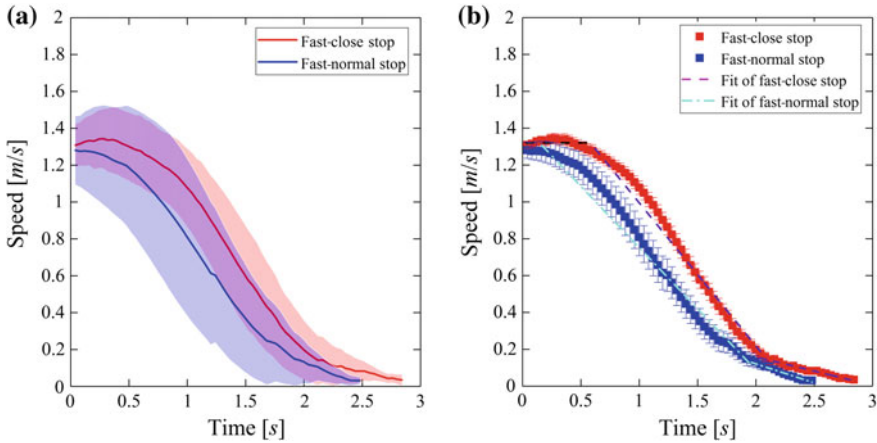
Fig. 6 Speed-time relation in decelerating phase

deviation. The reason is that, for normal stop, the stop distances of participants have large difference as mentioned above. Correspondingly, the speed in normal stop has a greater standard error as displayed in Fig. 6b. In Fig. 6b, for normal stop experiment, participants had begun to enter the phase of decelerating which expressed that the average speed at zero time is less than 1.32 m/s as obtained in above, while participants in close stop experiments started to decrease their speed after a period time (0.4 s). According to the shape of speed–time curve, the decelerating phase is divided into two sections, which is expressed as close stop-I, close stop-II, normal stop-I, and normal stop-II. In order to further investigate the deceleration process, we fit this process by using linear regression. The result of linear fit is plotted in Fig. 6b and the parameters of the fitting line are exhibited in Table 4. In the stage I of close and normal stop, the slopes are larger than those in stage II. That means in stage I, participants decreased their speed quickly; namely, they had great negative acceleration compared with stage II. In stage II, it represents the process of eventually stop, which means in final stop process, participants have smaller acceleration compared with deceleration process.

In comparison with close stop and normal stop, the negative acceleration of close stop in stage I is −0.78, which is larger than normal stop in numerical value. This result shows participants in close stop reducing their speed to a small value take less time. However, in stage II, the absolute value of slope for the normal stop is larger.

Table 4 Fit parameter value for decelerating phase

Moving type	a	b	R^2
Close stop-I	−0.78	1.77	0.98
Close stop-II	−0.15	0.467	0.97
Normal stop-I	−0.66	1.42	0.98
Normal stop-II	−0.21	0.53	0.94

It is found that participants stop at a comfortable distance on the basis of their own proxemics. For the close stop, participants stopped, but if the distance headway is not close enough, they would move ahead again. This is the uncertainty for close stop distance. Similarly, the R^2 of decelerating phase (showing in Table 4) is large enough to express a good degree of the linear fitting.

6 Conclusions

In this paper, we conducted single-file movement experiment to study the decelerating phase with different stop distances and different walking speeds. It is found that in the observation region M1 that participants moved in steady state, the value of speed in fast speed experiment is higher than that in normal speed experiment. After normalized the speed by divided the free moving speed, the curves of speed–distance headway are overlapping for fast and normal walking speed experiments. Taking fast speed experiment as an example, we found that the participants are in a weak constrained regime with the average speed 1.42 m/s in steady state, which is smaller than their free speed 1.52 m/s. In normal decelerating phase, the discrepancy of the speed reducing process is great because of different comfortable distance for different participants. However, in close stop experiment, the relation between speed and distance headway for different participants is approximate. In addition, pedestrians would like to start to reduce their speed in a shorter distance headway in close stop. By analyzing the time evolution of speed in decelerating phase, two stages were obtained. In stage I, the negative acceleration of close stop is larger than normal stop, which indicates less time is needed for pedestrian to finish the decelerating phase in close stop experiment. On the contrary, the negative acceleration of close stop is smaller due to uncertainty for close stop distance in stage II. As one part of single-file movement, the decelerating phase is also important in human behavior, especially in emergency (fire and earthquake) or hurried conditions in which the close stop is necessary. Thus, the present work is beneficial to provide a reference for evacuation, management, and modeling of the crowd in emergency conditions.

References

1. Cao, S., Song, W., Lv, W., & Fang, Z. (2015). A multi-grid model for pedestrian evacuation in a room without visibility. *Physica A: Statistical Mechanics and its Applications*, 45–61.
2. Tian, W., Song, W., Lü, W., & Fang, Z. (2011). Experiment and analysis on microscopic characteristics of pedestrian movement in building bottleneck. *Science China Technological Sciences*, 1730–1736.
3. Seyfried, A., Boltes, M., Kähler, J., Klingsch, W., Portz, A., Rupprecht, T., Schadschneider, A., Steffen, B., Winkens, A. (2010). Enhanced empirical data for the fundamental diagram and the flow through bottlenecks. In Pedestrian and Evacuation Dynamics 2008, Springer, pp. 145–156.
4. Zhang, J., Song, W., & Xu, X. (2008) Experiment and multi-grid modeling of evacuation from a classroom. *Physica A: Statistical Mechanics and its Applications*, 5901–5909.
5. Seyfried, A., Steffen, B., Klingsch, W., & Boltes, M. (2005) The fundamental diagram of pedestrian movement revisited. *Journal of Statistical Mechanics: Theory and Experiment*, P10002.
6. Fang, Z.-M., Song, W.-G., Liu, X., Lv, W., Ma, J., & Xiao, X. (2012). A continuous distance model (CDM) for the single-file pedestrian movement considering step frequency and length. *Physica A: Statistical Mechanics and its Applications*, 307–316.
7. Lv, W., Fang, Z., Wei, X., Song, W., & Liu, X. (2013). Experiment and modelling for pedestrian following behavior using velocity-headway relation. *Procedia Engineering*, 525–531.
8. Cao, S., Zhang, J., Salden, D., Ma, J., Shi, C., & Zhang, R. (2016). Pedestrian dynamics in single-file movement of crowd with different age compositions. *Physical Review E*, 012312.
9. Zhao, Y., & Zhang, H. (2017). A unified follow-the-leader model for vehicle, bicycle and pedestrian traffic. *Transportation Research Part B: Methodological*, 315–327.
10. Tadaki, S., Kikuchi, M., Fukui, M., Nakayama, A., Nishinari, K., Shibata, A., Sugiyama, Y., Yosida, T., & Yukawa, S. (2013). Phase transition in traffic jam experiment on a circuit. *New Journal of Physics*, 103034.
11. Liu, X., Song, W., & Zhang, J. (2009). Extraction and quantitative analysis of microscopic evacuation characteristics based on digital image processing. *Physica A: Statistical Mechanics and its Applications*, 2717–2726.
12. Buchin, K., Buchin, M., & Gudmundsson, J. (2008). Detecting single file movement. In *Proceedings of the 16th ACM SIGSPATIAL International Conference on Advances in Geographic Information Systems, ACM, 2008* (p. 33).
13. Chattaraj, U., Seyfried, A., Chakroborty, P., & Biswal, M. K. (2013). Modelling single file pedestrian motion across cultures. *Procedia-Social and Behavioral Sciences*, 698–707.
14. Wang, S., Lv, W., & Song, W. (2015). Behavior of ants escaping from a single-exit room. *Plos One*.
15. Jelić, A., Appert-Rolland, C., Lemercier, S., & Pettré, J. (2012). Properties of pedestrians walking in line: Fundamental diagrams. *Physical review E*, 036111.
16. Jelić, A., Appert-Rolland, C., Lemercier, S., & Pettré, J. (2012). Properties of pedestrians walking in line. II. Stepping behavior. *Physical Review E*, 046111.
17. Chattaraj, U., Seyfried, A., & Chakroborty, P. (2009 Comparison of pedestrian fundamental diagram across cultures. *Advances in Complex Systems*, 393–405.
18. Sun, J., Lu, S., Lo, S., Ma, J., & Xie, Q. (2018). Moving characteristics of single file passengers considering the effect of ship trim and heeling. *Physica A: Statistical Mechanics and its Applications*, 476–487.
19. Schadschneider, A. (1999). The nagel-schreckenberg model revisited. *The European Physical Journal B-Condensed Matter and Complex Systems*, 573–582.
20. Gazis, D. C., Herman, R., & Rothery, R. W. (1961). Nonlinear follow-the-leader models of traffic flow. *Operations Research*, 545–567.
21. Davis, L. (2003). Modifications of the optimal velocity traffic model to include delay due to driver reaction time. *Physica A: Statistical Mechanics and its Applications*, 557–567.

22. Hall, E. T. (1966). The hidden dimension.
23. Helbing, D., Farkas, I. J., Vicsek, T., (2000). Simulating dynamical features of escape panic. *Nature*, 487–490.
24. Boltes, M., & Seyfried, A. (2013). Collecting pedestrian trajectories, *Neurocomputing*, 127–133.

Study on Pedestrian Flow Prediction of Specific Flow Using Dimensionless Width

Natsuki Fujimoto, Misa Ogidani, Keiya Sakai, Saki Sumida, Yoshifumi Ohmiya, Jun-ichi Yamaguchi, Tomonori Sano, Manabu Tange and Akihide Jo

Abstract In amendment of Building Standards Act of the year 2000, the verification method for evacuation safety was introduced. Knowledge gained in Togawa's study (1955) is frequently used in this verification method; however, depending on the spatial condition, the estimated results differ from the actual crowd walk nature and this remains a challenge. Considering the situation, this study aims to illustrate the relationship between the spatial condition and crowd walk nature and analyze data gained from the Crowd Evacuation Experiment done in 2015 at Tokyo University of Science. When a corridor includes an opening (a bottleneck) or a merging, a pedestrian crowd will be restrained at the opening/merging. Each part of the bottleneck corridor showed a very similar feature as the merging corridor. Therefore, this study analyzed the bottleneck corridor and merging corridor with a uniform model. These analysis results confirmed the relationship between each part's density and the ratio of inflow width to the outflow width and showed that specific flow can be calculated from the margin of two densities, regardless of the spatial condition.

Keywords Evacuation safety · Spatial condition · Crowd flow · Density · Specific flow · Dimensionless width

N. Fujimoto (✉) · M. Ogidani · K. Sakai · S. Sumida · Y. Ohmiya
Tokyo University of Science, 2641 Yamazaki, Noda-City, Chiba 278-8510, Japan
e-mail: nacchan-0517@notmail.com

J. Yamaguchi
Obayashi Corporation Technical Research Institute, 4-640 Shimokiyoto, Kiyose-City, Tokyo 204-8558, Japan

T. Sano
Waseda Univresity, 2-579-15 Mikajima, Tokorozawa-City, Saitama 359-1192, Japan

M. Tange
Shibaura Institute of Technology, 3-7-5 Toyosu, Koto-Ward, Tokyo 135-8548, Japan

A. Jo
Takenaka Corporation, 1-1-1 Shinsuna, Koto-Ward, Tokyo 136-0075, Japan

Nomenclature

B	Bottleneck width (m)
B_m	Merging width in merging corridors (m)
D	Corridor width (m)
D_m	Corridor width in merging corridors (m)
$D*$	Dimensionless width defined by the ratio of inflow width D_m to the outflow width $D_m + B_m$ (−)
N_j	Specific flow of section j (person/m/s)
R_j	Flow rate of section j (person/s)

Greek Symbols

ρ_k	Density of zone k (person/m^2)
γ	The ratio of mainstream specific flow N_{main} and sidestream specific flow N_{side} (m)

Subscripts

after	Of after merging zone
before	Of before merging zone
junction	Of junction zone section
main	Of mainstream section
side	Of sidestream section

1 Background and Aim

In amendment of Japan's Building Standards Act of the year 2000, Fire Prevention Standards were introduced Performance Regulation; more flexible planning is enabled as long as the plan satisfies a certain level of performance. Buildings' safety performance is verified by the evacuation safety verification method prescribed in notice, or advanced methods such as simulations and predictive calculations. However, these methods partially use data on pedestrian crowd gained from Togawa's study [1] and set a uniform standard value, regardless of the spatial condition. This led to an issue of not being able to predict and evaluate the crowd walk nature (and building plans) precisely. Considering the situation, this study analyzes data from the Crowd Evacuation Experiment 2015 [2] to understand how spatial conditions influence the crowd walk nature (density and specific flow) and establish a

calculation model of crowd walk nature [specific flow (person/m/s)] that differs as the spatial condition changes and improves the predictive calculation of evacuation performance.

2 Crowd Evacuation Experiment

2.1 Experimental Overview

Crowd Evacuation Experiment [2] carried out a series of controlled indoor experiments to investigate pedestrian flow through various types of pathway, in Fire Science and Technology Laboratory Center at Tokyo University of Science in October 2015. Experimental layout was set with panels and boxes to control the geometric conditions as shown in Figure 1. Each experimental case basically had three trials (except widened bottleneck corridor IP = 6.0 m), and participant arrangement was shuffled every trial to avoid habituation. This analysis uses the average of the three trials. All 96 participants are undergraduate and graduate students, age of 20–27, who have no walking difficulties. The participants were informed about the goal of the experiments and were asked to walk normally, following the instruction given by experimenters. Participants wore comfortable clothes and caps with color-markers on top. The whole duration of the experiment was recorded by a camera set up at 15.2 m high to capture the pedestrians' cap-markers, and each pedestrian's coordinate is image-proceeded every 1/30 s [3] to gain density, flow rate, and specific flow precisely. Data at the stationary state is used.

Fig. 1 Experimental snapshot

2.2 Experimental Cases

Four experimental cases from the Crowd Evacuation Experiment are analyzed (Table 1). Straight corridor (Case S) is a basic corridor shape and aims to gain basic crowd walk flow that has no disturbance on the way, and its geometric variation is the width of the corridor. Bottleneck corridor (Case B) is a straight corridor with a bottleneck in the middle, and the bottleneck's influence on crowd walk nature can be analyzed. The corridor width D and bottleneck width B are variants. Both Case S and Case B have their initial position set back out of the corridor. Widened bottleneck corridor (Case W) is a widened bottleneck corridor with the initial position placed close to the bottleneck to reproduce high-density crowd walking into the bottleneck. The initial position (=IP) has two types: 1.2 and 6.0 m from the bottleneck, and the influence of initial position is analyzed. Merging corridor (Case M) is a straight corridor with another crowd merging from one side to see the influence of merging phenomena. The mainstream crowd is initially positioned within the main corridor.
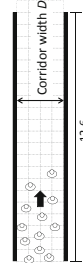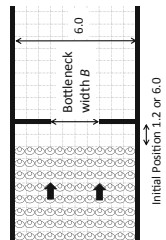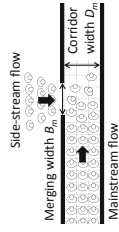
3 Analysis Results

3.1 Trajectories

Before looking into quantitative analysis, trajectories are focused to observe pedestrians' movement within the crowd. Illustrations of crowd trajectories in different cases are shown in Fig. 2.

All cases show a strong tendency of forming lanes at some areas or throughout the corridor. For Case S and Case B, the initial positions are placed far back out of the corridor that the trajectories show naturally formed lanes by the crowd. In corridor width of 1.8 m (Case S), pedestrians seem to split into three lanes, and when a bottleneck of 1.2 m is set on the way (Case B), they still keep the lanes and squeeze through the bottleneck. When the bottleneck width becomes too small for the three lanes to pass through, they reform new lanes that can pass through the bottleneck and keep the lanes till downstream. Case W and Case M are considered to reflect the influence of initial holding arrangement placed within the corridor. Case W's neat arrangement is disturbed when the crowd gathers to the bottleneck and does not reform any lanes at or after the bottleneck except at the bottleneck width of 1.2 m (Fig. 2d). Considering that side streams in Case M (the merging width of 1.2 m) are also forming two lanes when entering the main corridor, pedestrians seem to push themselves through at the two edges of the opening and form two lanes at opening width of 1.2 m. Mainstream of Case M is strongly influenced by the initial arrangement throughout the corridor that even the side stream interrupts the lanes, pedestrians at downstream still keep the initial lanes. The interruption level seems to depend on the corridor width, and it is likely due to the freedom in movement; the wider the corridor is, the more freedom in choice of where to move to.

Table 1 Experimental setup

Sketch of experimental cases (m)	Straight corridor (Case S)	Widened bottleneck corridor (Case W)	Merging corridor (Case M)
	Corridor width D — 12.6	Bottleneck width B — 6.0 — Initial Position 1.2 or 6.0	Side-stream flow; Merging width B_m; Corridor width D_m; Mainstream flow
	Bottleneck corridor (Case B) Bottleneck width B — Corridor width D — 12.6		

Setup condition	Case S	Case B		Case W			Case M	
	Corridor width D	Corridor width D	Bottleneck width B	Corridor width D	Bottleneck width B	Initial position	Corridor width D_m	Merging width B_m
Variation (m)	1.2	1.2	0.8	6.0	0.8 1.2	1.2	1.2	0.8
	1.8	1.8	1.2		1.6 1.8	6.0	1.8	1.2
	2.4	2.4			2.0 2.4			1.6

(a) Case S (Dm=0m, Dm+Bm=1.8m)   (b) Case B (Dm=1.2m, Dm+Bm=1.8m)   (c) Case B (Dm=0.8m, Dm+Bm =1.8m)

(d) Case W (D$_m$=0.8m, IP=1.2m)   (e) Case W (D$_m$=0.8m, IP=1.2m)   (f) Case W (D$_m$=2.0m, IP=6.0m)

(g) Case M (D$_m$=1.8m, B$_m$=1.2m)   (h) Case M (D$_m$=1.2m, B$_m$=1.2m)
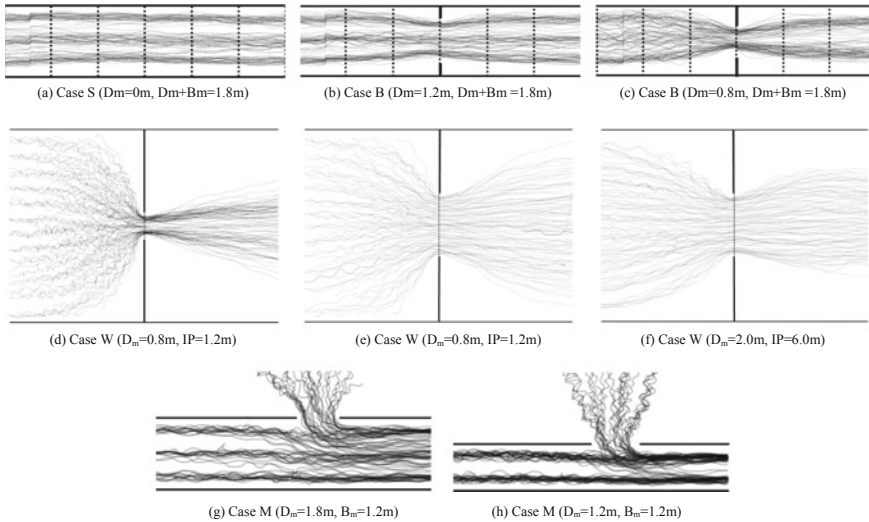
Fig. 2 Trajectories (moving direction: left to right)

When a bottleneck is set on the way of high-density crowd (Case W), the crowd gathers and tries to squeeze through the bottleneck and spread back after. The trajectories show that the narrower the bottleneck is (Fig. 2d, e), the narrower the crowd keeps after passing through the bottleneck. Case B with small bottleneck width (Fig. 2c) shows similar trajectory, and the two reformed lanes do not spread as wide as cases that kept three lanes (Fig. 2b). Furthermore, the farther the initial position is set (Fig. 2f), the narrower the crowd held and more clear spaces are formed on sides of the crowd flow after the bottleneck. It is considered that the longer distance walked to the bottleneck weakens the influence of the initial arrangement and rather strengthens a want to walk straight.

Above discussed clear spaces are considered as inefficient usage of the corridor when considering emergency evacuation. There will be a challenge of how to deal with the clear spaces when the crowd movement data is applied to evacuation prediction, and this issue should be carefully treated when quantitatively analyzing the crowd walk nature.

3.2   Areas and Sections of Analysis

When analyzing the pedestrians' movement, it is necessary to look into the instant movement. Figure 3 shows snapshots and walking vector of Case M and Case W with modeling procedure. When a crowd walks down corridors with merging on the way (Fig. 3a, b), the mainstream crowd is interrupted its way by side stream at junction point as mentioned in Sect. 3.1. In order to avoid the interruption, the mainstream

(a) Merging Corridor Snapshot   (b) Merging Corridor Walking Vector   (c) Merging Corridor Modelling

(b) Bottleneck Corridors Snapshot   (e) Bottleneck Corridors Walking Vector   (f) Bottleneck Corridors Modelling
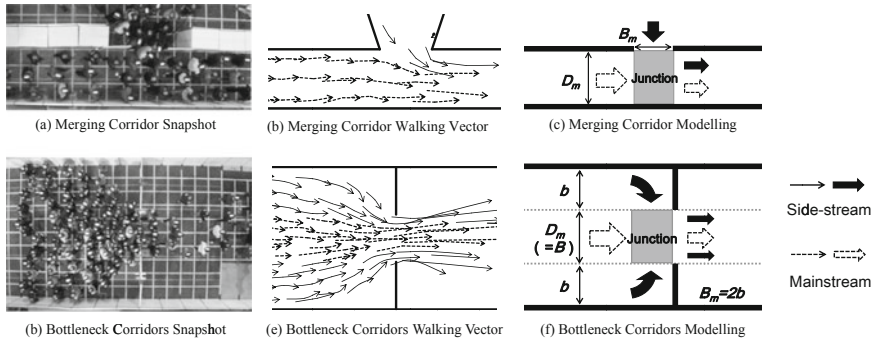
Fig. 3 Modeling procedure

crowd tries to narrow its flow and make space for the side stream to walk through. Similar phenomenon is seen in bottleneck corridors as well (Fig. 3d, e). Pedestrians walking down the center of the corridor face other pedestrians interrupting their way right before the bottleneck and narrow its flow to squeeze and pass through the bottleneck. Considering the similarity at the junction point and just before the bottleneck, the bottleneck corridors are interpreted as merging from both sides of the mainstream; the junction zone set at just before the bottleneck with a merging width of $B_m = 2b$ and the mainstream corridor width of D_m which equals to the bottleneck width B (Fig. 3c, f).

Based on the modeling, each experimental case is given the following analysis zones and sections as shown in Fig. 4. Three zones for density computing are set: the zone before the bottleneck/merging called "before merging," the zone at the bottleneck/merging called "junction," and the zone after the bottleneck/merging called "after merging." Their densities will be presented as ρ_{before}, $\rho_{junction}$, ρ_{after} [person/m^2], respectively. The straight corridor is treated as merging width $B_m = 0$ case, and only one zone was set with its density $\rho_{before} = \rho_{junction} = \rho_{after}$ [person/m^2]. Merging corridor (Case M) is given three sections: mainstream, side stream, and junction to compute specific flow N_{main}, N_{side}, $N_{junction}$, [person/m/s], respectively. Other cases are given only junction section.
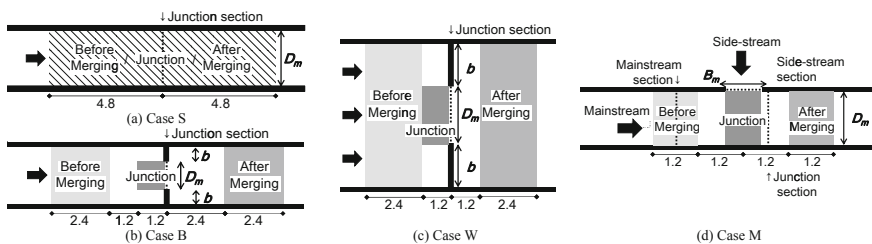
Fig. 4 Analysis zones and sections (unit: m)

Focusing on the junction zone, the geometric parameter is defined as the ratio of inflow width (corridor width D_m + merging width B_m) to the outflow width (corridor width D_m), and it is named as dimensionless width $D*$ [−], as shown in Eq. (1). For bottleneck corridors (Case B and Case W), the inflow width ($D_m + B_m$) equals to the corridor width D; therefore, the dimensionless width $D*$ equals to the ratio of bottleneck width B and corridor width D (B/D).

$$D^* = \frac{D_m}{D_m + B_m} = \frac{B}{D} \tag{1}$$

3.3 Dimensionless Width D* and Density ρ

Considering that the specific flow is the multiplication of crowd density and velocity, this section focuses on area density. The relationship between dimensionless width $D*$ and each zone's density ρ is shown in Fig. 5. In the before merging zone (Fig. 5a), all cases' density ρ_{before} showed a negative correlation to dimensionless width $D*$ and the relation is expressed in Eq. (2). In the junction zone (Fig. 5b), densities $\rho_{junction}$ seem to depend on the $D*$. However, Case W of initial position 1.2 m and Case M show a slightly different tendency. In these cases, the initial position is set within or close to the analysis zone that the density may have included the influence of the initial high-density arrangements. To be realistic and on the safer side, these two cases are excluded to gain Eq. (3).

$$\rho_{before} = -0.37D^* + 2.89 \tag{2}$$

$$\rho_{junction} = 1.61D^{*-0.60} \tag{3}$$

In the after merging zone (Fig. 5c), Case M showed higher density compared to the rest of the cases. Considering that the difference was caused by the corridor width after the bottleneck/merging, adjustment of Case M's density is done using the
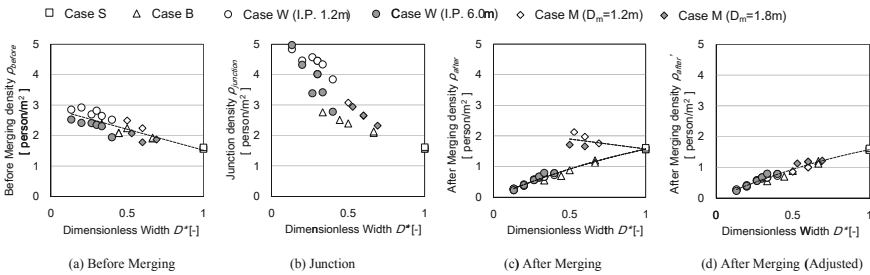
Fig. 5 Dimensionless width $D*$—densities ρ

(a) Bottleneck Corridors (b) Merging Corridors
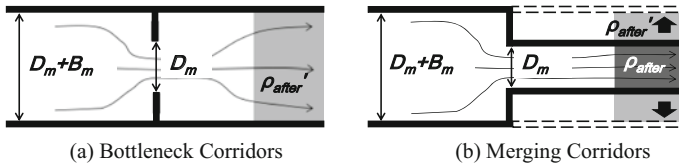
Fig. 6 Adjustment of after merging

process shown in Fig. 6. Assuming that the number of pedestrians passing through the junction section does not depend on the after merging area's width and when the density of the after merging zone width of $D_m + B_m$ is expressed as ρ_{after} and that of width D_m as $\rho_{after'}$, these two relate to each other (Eq. 4). In $D^* - \rho_{after'}$ (Fig. 5d), Case M shows the same tendency as the other cases and Eq. (5) is obtained.

$$\rho'_{after} = \frac{D_m}{D_m + B_m} \cdot \rho_{after} = D^* \cdot \rho_{after} \qquad (4)$$

$$\rho'_{after} = -0.58D^{*2} + 2.16D^* \qquad (5)$$

Considering that the junction section is in between the junction zone and the after merging zone, the margin of those areas' densities $\Delta\rho = \rho_{junction} - \rho_{after}$ is taken into consideration. Figure 7 presents dimensionless width D^*–margin of densities $\Delta\rho$ relation. Yet for Case M, the pre-adjusted value for the after merging density ρ_{after} is used to calculate $\Delta\rho$. As a result, the margin of densities $\Delta\rho$ tends to depend on the dimensionless width D^*, and Eq. (6) is gained.

$$\Delta\rho = 6.43D^{*2} - 12.85D^* + 6.40 \qquad (6)$$

Fig. 7 Dimensionless width D^*–margin of densities $\Delta\rho$
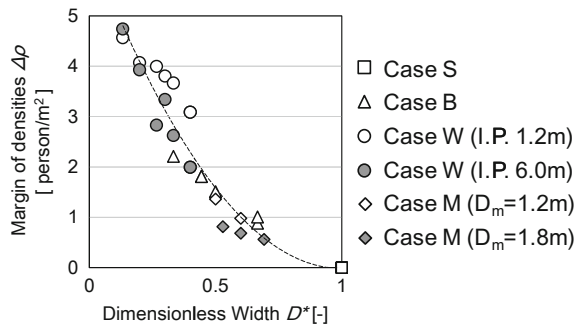
Fig. 8 Dimensionless width
D^*–specific flow N
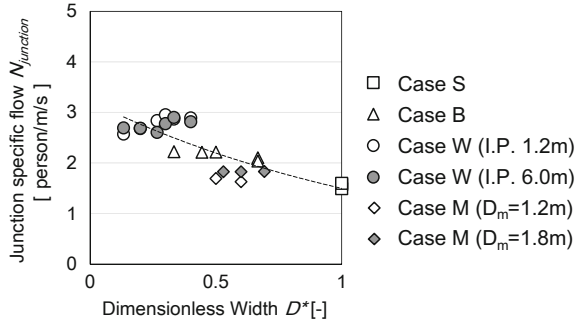
3.4 Dimensionless Width D* and Specific Flow N

It would be easier if the bottleneck's specific flow can be calculated directly from the geometric condition. Looking into the relationship between dimensionless width D^* and junction specific flow N_{junction} (Fig. 8), negative correlation is recognized as overall tendency. Its approximate line is expressed in Eq. (7).

However, looking close into each case, the junction section's specific flow N_{junction} does not seem to depend on and rather keeps a constant value, regardless of dimensionless width D^*. For Case W, both initial positions (1.2 and 6.0 m) show similar tendency that initial position's influence seem do not effect. Case B is partially off the equation, and it is considered that the smallest D^* condition (the bottleneck width B = 0.8 m) reached the smallest limit that crowd flow corresponds to. Case M is almost not on the equation, and its values seem fixed at about 1.8 person/m/s. Therefore, it is difficult to say that specific flow N_{junction} is directly dependent on the dimensionless width D^* and predicting it from D^* is not preferable.

$$N_{\mathrm{junction}} = 3.22\mathrm{e}^{-0.77D^*} \tag{7}$$

3.5 Density ρ and Specific Flow N₃

Figure 9 indicates the relationship between the zone densities ρ and the junction specific flow N_{junction}. In any of the three zones (Fig. 9a–c), the two seem unrelated to each other. Hence, the margin of densities $\Delta\rho$ is once again spotted and shown in Fig. 9d. Overall, junction specific flow N_{junction} increases as $\Delta\rho$ increases. However, each case does not seem to relate and shows a fixed value, regardless of $\Delta\rho$. Cases of which anthropometric dimensions occupy most of the passage width (Case M of D_{m} = 1.2 m and Case B of B = 0.8 m) mentioned in Sect. 3.1 are excluded, to obtain Eq. (8).
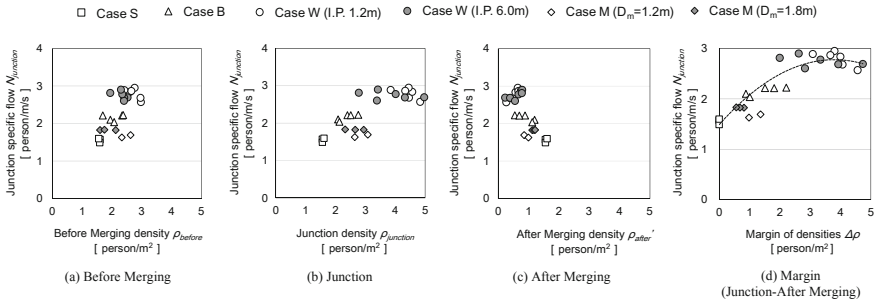
Fig. 9 Density ρ–specific flow N

$$N_{\text{junction}} = -0.09\Delta\rho^2 + 0.68\Delta\rho + 1.49 \tag{8}$$

Case W has the highest around 2.7(person/m/s) at any $\Delta\rho$. It is considered that due to the clear spaces (mentioned in Sect. 3.1) included in the calculation, the ρ_{after} is calculated lower and therefore $\Delta\rho$ became higher. This also applies to Case B, in which N_{junction} stayed around 2–2.2(person/m/s) and two highest $\Delta\rho$ cases are off the equation. For Case M, $D_{\text{m}} = 1.8$ m cases are on the equation, while $D_{\text{m}} = 1.2$ m cases are not. As mentioned in Sect. 3.1, pedestrians strongly kept lanes at downstream in $D_{\text{m}} = 1.2$ m cases and this is considered to lead decrease in density ρ_{after} and therefore increase in the margin of the densities $\Delta\rho$.

4 Calculation of Specific Flow N

4.1 Calculation of Junction Specific Flow $N_{junction}$

In prediction calculation of evacuation, specific flow is often used. Based on equations gained from the quantitative analysis done in Chap. 3, calculation flow for junction specific flow N_{junction} is indicated in Fig. 10. Zone densities ρ_{junction} and ρ_{after} are calculated from the dimensionless width D^* by Eqs. (3) and (5). By subtracting the after merging density ρ_{after} from junction density ρ_{junction}, the margin of densities $\Delta\rho$ is calculated. Lastly, Eq. (8) enables junction specific flow N_{junction} to be calculated from the margin of densities $\Delta\rho$. The calculation result is compared with experimental result in Fig. 11.
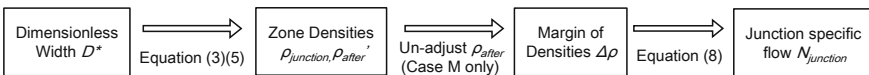
Fig. 10 Calculation flow for specific flow N_{junction}
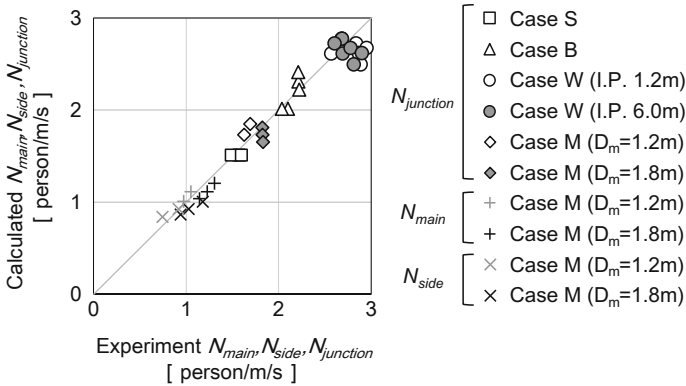
Fig. 11 Comparison of specific flow N

4.2 Calculation of Mainstream and Sidestream Specific Flow N_{main}, N_{side}

In merging corridors (Case M), mainstream and side stream are assumed to merge at a certain ratio. When the ratio is given γ, specific flow N_{main} and N_{side} can be expressed in Eq. (9). The value for γ turned out to be $\gamma = 1.20$ from the experimental result of Case M.

$$N_{\mathrm{main}} = \gamma N_{\mathrm{side}} \tag{9}$$

At a steady state, the inflow to the junction zone (mainstream flow rate R_{main} + sidestream flow rate R_{side}) should be balanced with the outflow of the zone (junction flow rate R_{junction}), and thus, Eq. (10) is approved.

$$R_{\mathrm{main}} + R_{\mathrm{side}} = R_{\mathrm{junction}} \tag{10}$$

Furthermore, each section's flow rate is defined as the multiplication of specific flow with the passage width, as shown in Eqs. (11), (12), and (13).

$$R_{\mathrm{main}} = N_{\mathrm{main}} D_{\mathrm{m}} \tag{11}$$

$$R_{\mathrm{side}} = N_{\mathrm{side}} B_{\mathrm{m}} \tag{12}$$

$$R_{\mathrm{junction}} = N_{\mathrm{junction}} D_{\mathrm{m}} \tag{13}$$

When the dimensionless width D^* is redefined as shown in Eq. (14), the result is substituting Eqs. (9) (11)–(13) into Eq. (10) and the deforming result in Eqs. (15) and (16).

$$D_\gamma^* = \frac{D_{\mathrm{m}}}{\gamma D_{\mathrm{m}} + B_{\mathrm{m}}} \tag{14}$$

$$N_{\mathrm{side}} = N_{\mathrm{junction}} D_\gamma^* \tag{15}$$

$$N_{\mathrm{main}} = \gamma N_{\mathrm{junction}} D_\gamma^* \tag{16}$$

From the above equations, it is theoretically possible to calculate the mainstream and sidestream specific flows N_{main} and N_{side} from the junction specific flow N_{junction} and the ratio of N_{main} and N_{side}, γ.

4.3 Calculation Results and Comparison with Experimental Results

The junction specific flow N_{junction} calculated at 4.1 and the mainstream and sidestream specific flows N_{main} and N_{side} calculated in Sect. 4.2 are compared with the experimental results in Fig. 11. Overall, the calculated specific flow was very close in value to the experimental result and this indicates that uniform prediction calculation is possible beyond the geometric differences.

Case S is successfully calculated at about 1.5 person/m/s, and this supports Togawa's study [1]. For Case B, most of the cases are directly on the proportional line, but two top ones tend to have calculated higher than the experimental result. This may due to the usage of Eq. (8), and the reason for those two cases off the equation is pointed out in Sect. 3.5; pedestrians did not widen its flow after the bottleneck that clear spaces were included in the calculation of density. The same reason can be applied for Case W, in which calculated values are on the proportional line but not settling.

Case M is calculated near the experimental result, but none of them are actually on the proportional line. There are two cases that can be considered: one with process of calculating the junction density and the other with adjustment for the after merging density. For the junction density calculation, Eq. (3) was set excluding Case M and this led to the junction density to be calculated slightly lower than experimental value. Also, Case M had to be adjusted for its after merging density which might have led to decrease in calculation accuracy.

For mainstream and sidestream specific flows N_{main}, N_{side}, they are well calculated; however, due to the junction specific flow N_{junction} being calculated off from the proportional line, the two specific flows are influenced and not directly on the proportional line. However, the calculation accuracy can be said to affirm that mainstream and sidestream specific flows can be calculated from the junction specific flow and the ratio of specific flows N_{main} and N_{side}.

5   Conclusion

This research focused on merging phenomena and attempted to analyze other geometric cases by modeling them into merging. Based on the experimental results of Crowd Evacuation Experiment, it is found that bottleneck corridors have similar features as merging corridors and can be quantitatively analyzed with the same modeling method. Based on the quantitative analysis, prediction calculation model of specific flow which is uniformly applicable to merging corridors as well as bottleneck corridors is established.

This research indicated the possibility of crowd behavior analysis beyond spatial difference, and rather than looking into difference of spatial condition, similarities should be focused and the uniform prediction calculation may be applied to multi-spatial conditions. Calculation method that is easy to use but with high prediction accuracy is strongly required in case of evacuation prediction calculation; therefore, this research hopefully gives clues on pedestrian behavior.

References

1. Togawa, K. (1955). Study of fire escape based on the observation multitude currents. Report of the Building Research Institute, No. 14.
2. Tamura, Y., Sano, T., Tange, M., Yamaguchi, J., Ohmiya, Y., others (2016). Study on pedestrian flow no. 1–10. In Summaries of Technical Papers of Annual Meeting, Architectural Institute of Japan.
3. Tange, M., Imanishi, M., Sano, T., Ohmiya, Y., others (2016). Image processing of pedestrian behavior with multiple color markers and its application to crowd evacuation experiment. *Journal of Architecture and Planning (Transactions of AIJ), 81*(730), 2645–2652 (in Japanese).

Influence of Congestion in Upper Floor on Pedestrian Flow in Staircase Based on Observational Survey of Evacuation Drill in a High-Rise Building

Kosuke Fujii, Masayuki Mizuno, Hiroyuki Kadokura, Tomonori Sano and Ai Sekizawa

Abstract The occupants shall evacuate the building through stairs, in case of fire of high-rise building. A number of evacuees may cause the congestion on stairs. This paper focuses on the characteristics of the non-merging evacuation flow, which is the flow consisting only of evacuees descending on the staircase without merging there under flow conditions on the upper floor, which are generated by the merging of persons going down the staircase and entering there. This study used the data obtained in the observational survey on the real evacuation drills repeated annually for three years in the high-rise building. The flow conditions were classified into three groups based on the congestion and the merging of evacuations in the staircase. As a result of this study, the characteristics of the non-merging evacuation flow in each of the three groups were elucidated.

Keywords Total evacuation · Evacuation drill · Observational survey · Specific flow · Staircase

1   Introduction

In the event that a fire breaks out in a multi-story building, the occupants generally need to evacuate using stairs. High-rise buildings have the long stairs, and the evacuees move into a stairway from the multiple floors. A congestion is caused by

K. Fujii (✉)
National Research Institute of Fire and Disaster, Jindaijihigashimachi, 4-35-3, Chofu, Tokyo 182-8508, Japan
e-mail: fujii@fri.go.jp

M. Mizuno · A. Sekizawa
Graduate School of Science and Technology, Tokyo University of Science, Yamazaki, 2641, Noda, Chiba 278-8510, Japan

H. Kadokura
Faculty of Engineering, Tohoku Gakuin University, Chuo, 1-13-1, Tagajo, Miyagi 985-8537, Japan

T. Sano
Faculty of Human Sciences, Waseda University, Mikajima, 2-579-15, Tokorozawa, Saitama 359-1192, Japan

269

a large number of evacuees. It makes the stairs clogged, there. We have conducted surveys on total evacuation drills in a high-rise building, to clarify the mechanism of the merging flow and the congestion in a staircase of a high-rise building [1]. On the basis of the surveys, the mathematical model for simulating the evacuation flow in the staircase was developed [2]. In addition to our studies, the evacuation behavior on the stairs of multi-story buildings has been researched [3–6], and the theory construction on pedestrian dynamics in evacuation has been worked on [6–12]. These studies have mentioned the characteristics of high-rise building evacuation. The behavior of merging flows on staircases in high-rise buildings has been considered. Hokugo et al. [13] confirmed the density and ratio of flow rate from corridor to total flow rate on the staircase based on the experiments in the three-story staircase. Takeichi et al. [14] proved that the flow rate entering a landing from out of stair hall is influenced by the location of the door to the staircase, through experiments. Galea et al. [15] reported that the location of the door to the staircase affected the occupants merging, their walking speed, and the flow rate entering the landing, using a computer simulation. Boyce et al. [16] and Sano et al. [17, 18] determined the merging ratio of flow rate between entering the landing and going down on the staircase as approximately 50:50 by the research of the evacuation drills. Many findings on the merging evacuation behavior in high-rise buildings were gained by these studies. The situations of the evacuation flow were varied according to simultaneity/phased in total evacuation or merging/non-merging in the stairway. Hoskins [19] showed that data and equations obtained through different assumptions derive the different results.

The data of the various situations is useful for developing and improving the model for simulating the evacuation flow. Little is known about the flow in the downstairs of the floor where the congestion or the merging occurred. This study elucidated the characteristics of the non-merging evacuation flow, which is the flow consisting only of evacuees descending the staircase without merging there, as influenced by the congestion situations in the upper floors. The summary of the evacuation drill, which is carried out in 2011 on the same high-rise building of our study, including the merging flow was analyzed in the study by Sano et al. [17, 18]. Conversely, our study here reports the different perspective in that the non-merging flows in the staircase of the drill conducted from 2012 to 2014 were analyzed in detail. In this study, the data suitable for utilizing as the foundational index for crowd flow was obtained. The data can be expected to be useful for the validation of computer modeling.

2 Purpose

This study aimed to identify the non-merging evacuation flow going down the staircase, under a range of flow conditions on the upper floor, which was caused by the merging of persons going down the staircase and entering there. For a range of the conditions, the flow states were analyzed in detail using the results of the observational surveys on the real evacuation drills.

3   Methods

3.1   Overview of Total Evacuation Drill in High-Rise Building

The observational surveys were conducted from 2012 to 2014, on the total evacuation drill of the 25-story high-rise office building in Japan, repeated annually. Two emergency staircases were at the both ends of the building; whose plan was rectangle. The shapes of staircases were half-turn staircases, and one of them was observed. In each drill, fires were assumed to occur on the 4th floor in 2012, and the 15th floor in 2013 and 2014. The evacuees used either of the staircases and head for the outdoor square on the ground floor in the front of the building. Figure 1 shows the plain figures of the staircase targeted in this study. The width of the staircase shown in Fig. 1 is actual width. Both widths in the height of a handrail and a tread are 1200 mm. The stair tread and riser are 280 and 170 mm, respectively. In the surveys, the movements of the participants going down the staircase in each drill were recorded with video cameras. The total numbers of the participants using the staircase in each drill were 1137 persons in 2012, 816 persons in 2013, and 537 persons in 2014. Most of them were the workers, who were belong to the company, and were familiar with the building. Table 1 shows the number of participants on each floor in the evacuation drills conducted every one year.

This study is not based on an evacuation experiment with subjects but based on an observational survey of the situation of evacuation drill by the video record only from overhead. Therefore, the personal information was not collected, and any individual is not identified at all. Also, the anonymous data and non-invasive method were used. The company conducting the drill and the participants preliminarily received explanation about the survey such as usage of the video recording and consented the survey. The participation in the drill was voluntary, and the method by which informed consent was obtained from the participants was verbal. Further to say, this study was conducted in accordance with the guideline of the Ethics Review Committee on Human Research of Waseda University and was approved by Institutional Approval in the National Research Institute of Fire and Disaster, within the Fire and Disaster Management Agency of the Ministry of Internal Affairs and Communications.
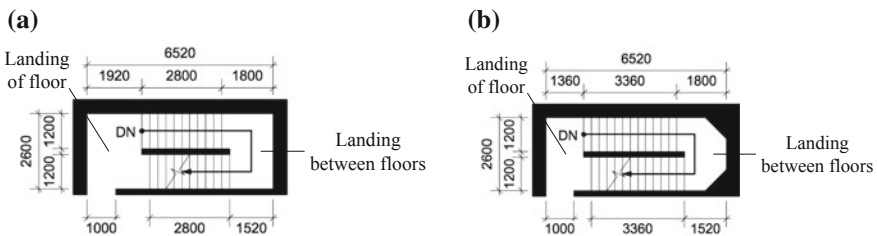
Fig. 1   Plan [mm] of the staircase for (**a**) 4th to 25th floor and (**b**) 1st to 3rd floor

Table 1 Number of evacuees for each floor and drill

Floor	Number of evacuees			Floor	Number of evacuees		
	In 2012	In 2013	In 2014		In 2012	In 2013	In 2014
25th	4	1	5	12th	70	25	30
24th	73	62	50	11th	148	93	59
23rd	46	45	29	10th	97	56	85
22nd	63	44	11	9th	26	15	16
21st	32	6	22	8th	1	4	8
20th	38	10	18	7th	5	2	1
19th	4	27	23	6th	75	64	1
18th	29	34	0	5th	29	15	19
17th	47	16	28	4th	45	27	6
16th	26	24	23	3rd	22	18	11
15th	25	48	47	2nd	4	1	1
14th	106	71	69	1st	–	–	–
13th	122	108	83	Total	1,137	816	537

3.2 Recording Participants' Movement

The participants' movements on every landing with a door of each floor were recorded using video cameras. The numbers of participants who enter the landings from floors and upstairs were counted every one second in each of the stories. These data were used to calculate the flow rates and specific flow, in addition, to derive the merging of the evacuees, who entered the staircase and descended from the upstairs and the flow in the downstairs of the floor where the merging occurred. Each boundary to count the number of people was specified between the vestibule and the landing, and the landing and the steps of stairs from upstairs. The number of evacuees passing through the boundaries per 1 s was counted. Figure 2 shows the example of the evacuation situation in the staircase recorded by video cameras.

3.3 Determination of Evacuation Flow Containing Non-merging Flow

All of the total evacuation drills, which were observed, were phased evacuation plans. There are the times and floors where the merging of evacuation flow going down the staircase and entering there, in the phased evacuation drills. It is possible to confirm the times and the floors where the merging was assumed not to occur in the plans. After that, the times and the floors where the merging occurred in real drills were excluded from above times and floors in the plan based on the movies recorded with

(a)   **(b)**

Entering landing space
from floor

Descending
from upper floor

Descending
to down stair

Descending
from upper floor

Descending
to down stair
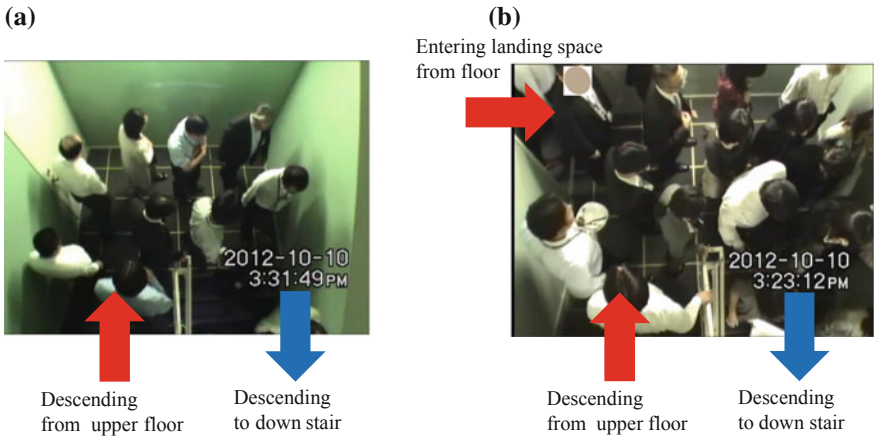
Fig. 2 Example of video recording of evacuation behavior in staircase for (**a**) non-merging and (**b**) merging

Table 2 Time, floor, and year containing non-merging flow in each case

Case	Year	Time and floor	
Case 1	2012	15:15:00–15:20:00	20th floor–15th floor
Case 2	2012	15:20:00–15:29:00	10th floor–4th floor
Case 3	2012	15:29:00–15:38:00	9th floor–4th floor
Case 4	2013	15:13:30–15:21:30	14th floor–10th floor
Case 5	2013	15:27:20–15:30:00	9th floor–2nd floor
Case 6	2014	15:21:00–15:31:00	9th floor–2nd floor

the video cameras. As a result, six cases as the combinations of the times and the floors that contain "non-merging" flows in the real drills to use the following analysis were determined. Non-merging flow is a flow consisting only of evacuees descending from upper floors in a staircase in this study. Table 2 shows the time, floor, and year containing the non-merging flow in each case.

4 Results

4.1 Temporal Change of Specific Flow

The specific flows in each of the six cases every 5 s were calculated. The temporal changes of the specific flows in the six cases were ascertained. In each case, the part of the evacuation flow that was string and did not stop was selected as "non-merging

flow." The steady state of the specific flow in this part was derived, using the temporal change and the movie. Each of the above flows including the steady state from Case l to Case 6 was called Flow 1 to Flow 6, respectively. As examples of the specific flows of "non-merging flow" for time in each case, Figs. 3, 4, and 5 show the temporal change of the specific flows on the part of the floors in Flow 1, Flow 3, and Flow 5, respectively. All steady states in the temporal changes of the specific flows from Flow 1 to Flow 6 on the corresponding floor were extracted such as shown in Figs. 3, 4, and 5.
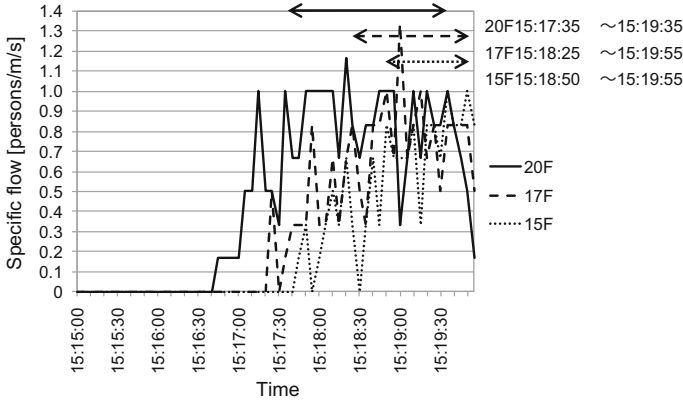
Fig. 3 Specific flows of evacuees descending from upper floor on 20th, 17th, and 15th floors in Flow 1
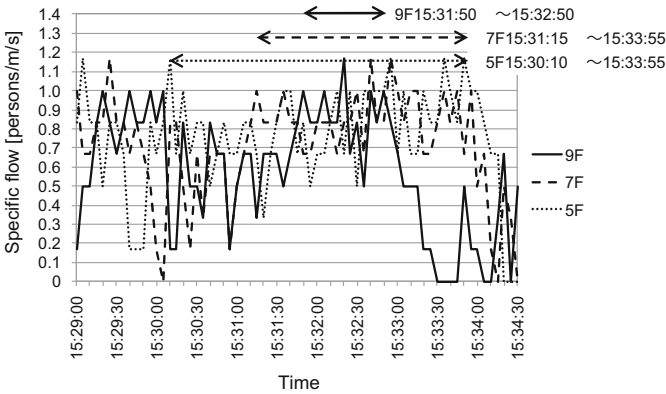
Fig. 4 Specific flows of evacuees descending from upper floor on ninth, seventh, and fifth floors in Flow 3
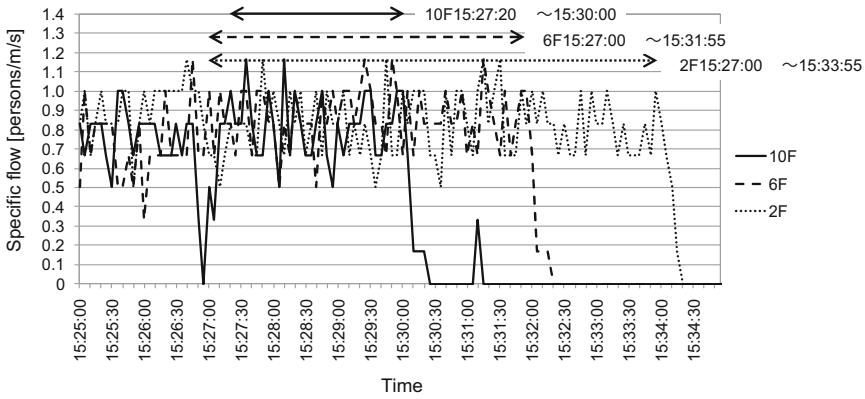
Fig. 5 Specific flows of evacuees descending from upper floor on tenth, sixth, and second floors in Flow 5

4.2 Average Specific Flow of Steady State in Non-merging Flow

Figures 6 and 7 show the average specific flows in the steady-state interval for every combination of the floor and the flow from Flow 1 to Flow 6. All of these flows consisted of evacuees descending from the floors above the measured ones. However, there were some differences between their specific flows. It can be seen that each specific flow of Flow 1, Flow 4, and Flow 6 tends to decrease as the floor is low. In each of Flow 2 and Flow 5, the specific flows on measured floors are approximate value and do not change as the floors increase and decrease. The average specific
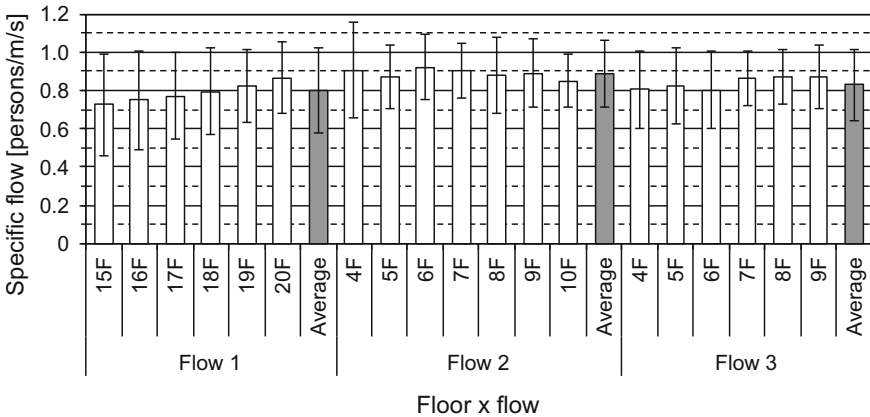
Fig. 6 Average specific flow of steady state for every combination of floor and flow from Flow 1 to Flow 3
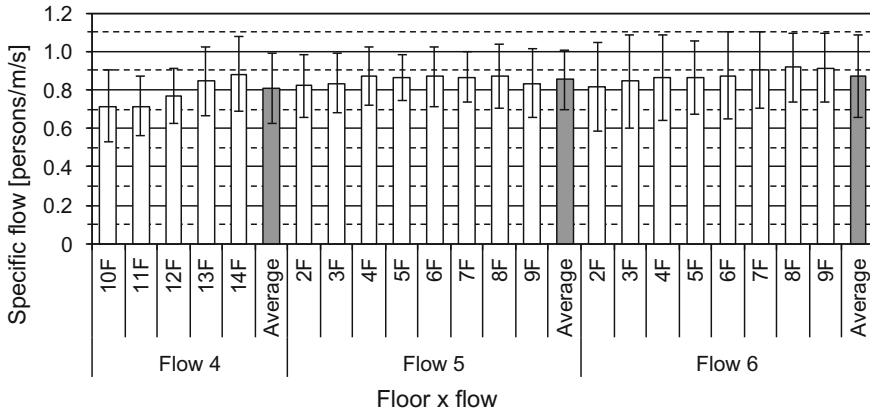
Fig. 7 Average specific flow for every combination of floor and flow from Flow 4 to Flow 6

flows of Flow 3 were close between the floors; however, the specific flows on the seventh through ninth floors were higher than those on the fourth through sixth floors.

The flow conditions in the upper floors of the flows from Flow 1 to Flow 6 were classified according to above three groups. In the higher floors than those of Flow 1, Flow 4, and Flow 6, the merging of the evacuees between different floors occurred; nevertheless, these merging flows did not stop. The merging flow stopped, and the congestion occurred on the upper floors of Flow 2 and Flow 5, unlike Flow 1, Flow 4, and Flow 6. The merging did not occur on the upper floors of Flow 3. The flow stopped on the measured floors and the upper floors before the time interval for the steady states of Flow 3. The relationship between the specific flow of the steady state and the floors was assumed to differ according to the condition of the flow on the upper floor.

4.3 Merging State in Upper Floor of Non-merging Flow

The flow conditions on the upper floors of the flows from Flow 1 to Flow 6, which were non-merging flows, were classified into three kinds of groups, as mentioned in Sect. 4.2. The merging ratio on the landing and the number of the evacuees, who entered the landing from out of the stair hall and descended from the upper story, were determined for disclosing the flow condition on the upper floors. The merging ratio is the ratio of the number of persons descending from the upper floor to the total number of persons entering from the floor and descending from the upstairs to the landing. The number of evacuees was determined every 5 s, and the merging ratio is presented as 0 when both numbers of evacuees are 0. Figures 8, 9, 10, 11 and 12 show the specific flow of the evacuees descending from upper floors or entering from the floor and the merging ratio every 5 s, on the upper floors of the Flow 1, Flow 3, and

(a)

(b)
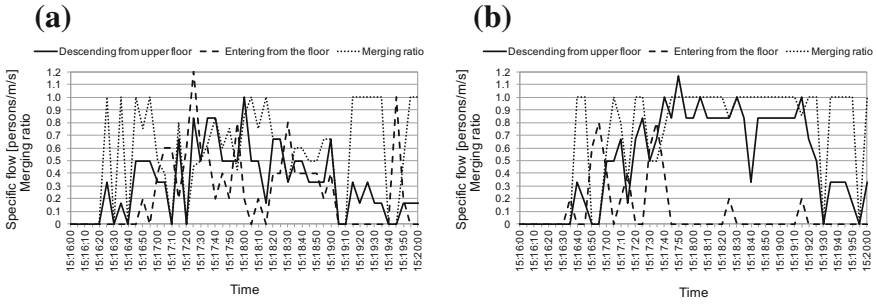
Fig. 8 Specific flow and merging ratio on the upper floors of Flow 1: (**a**) 22nd floor and (**b**) 21st floor
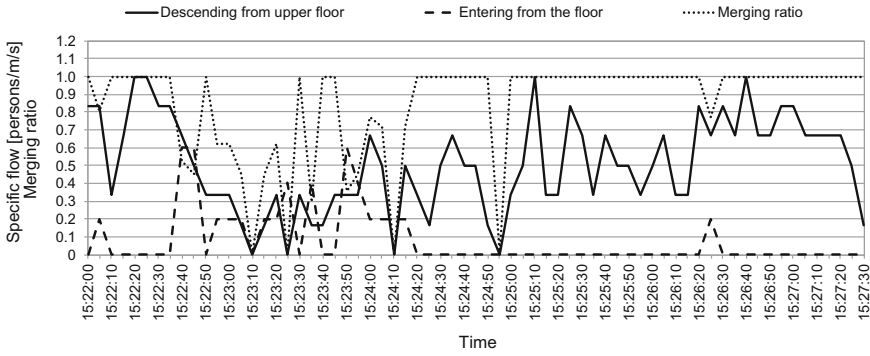
Fig. 9 Specific flow and merging ratio on 12th floor of the upper floor of Flow 5
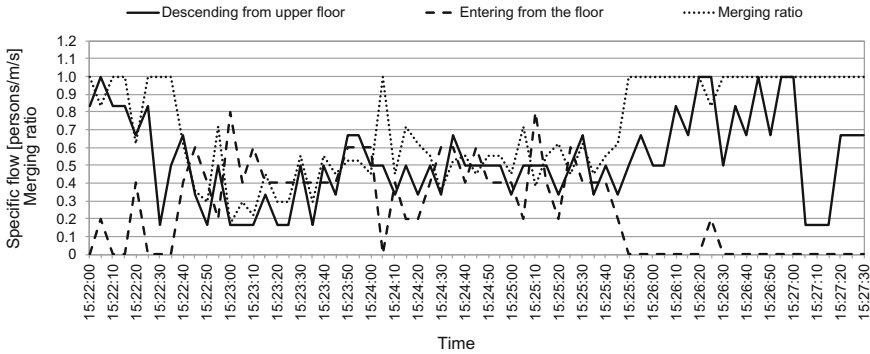
Fig. 10 Specific flow and merging ratio on 11th floor of the upper floor of Flow 5
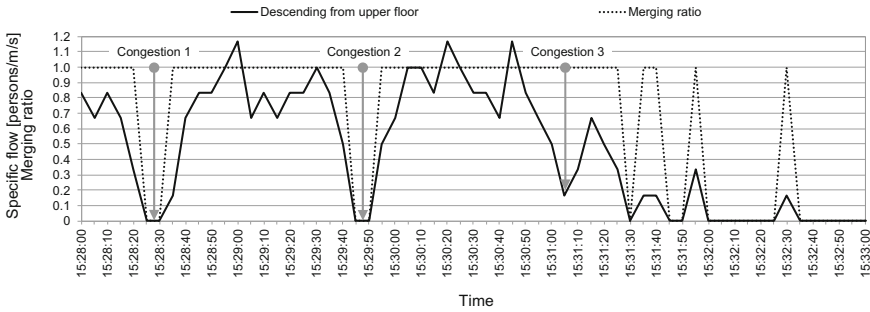
Fig. 11 Specific flow and merging ratio on 12th floor of the upper floor of Flow 3
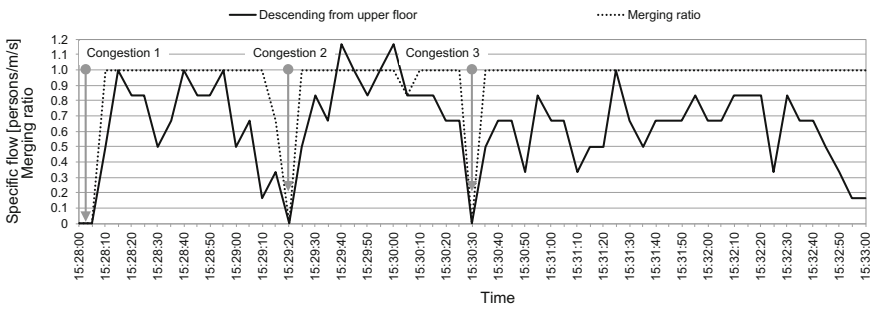
Fig. 12 Specific flow and merging ratio on tenth floor of the upper floor of Flow 3

Flow 5. The figures indicate one flow for each of the three groups as the examples of the flow conditions on the upper floors of the flows from Flow 1 to Flow 6.

Figure 8 shows the specific flows of the evacuees who descended from the upstairs and entered from the floors into the landings, and the merging ratios, on the 22nd and the 21st floor of the upper floors of Flow 1. Each specific flow of the evacuees is descending from the upper floor and entering from the floor on the 22nd floor, or both appeared from earlier than 15:17:35, when the steady state of Flow 1 on the 20th floor started, to 15:19:00. The specific flow after 15:19:00 was due to either of the few persons descending from the upper floor or entering from the floor. The merging flows occurred and did not stop on the landings of the 22nd floor before and during the steady state on 20th floor. The merging ratio of the 22nd floor during this time interval was higher than 0.5 generally. The merging ratio on the 21st floor was 1.0 in most of the time point. Among them, the specific flow of the evacuees descending from the upper floor was approximately constant value between 0.8 and 1.0 persons/m/s, and the merging ratio of 1.0 was also constant, from 17:17:45 to 17:19:15. Almost all of the evacuees walking on the landing of the 21st floor descended from the upper floor and did not stop. It is proved that the merging of the evacuees occurred and did not stop on the upper floor of Flow 1.

Figures 9 and 10 show the specific flows of the evacuees, who descended from the upper floors and entered from the floors into the landings, and the merging ratios, on 12th floor and 11th floor of the upper floors of Flow 5, respectively. Both of the specific flows on these two floors, a few minutes before 15:27:20, when the steady state of Flow 5 on the tenth floor was started, were due to the evacuees descending from the upper floor. Consequently, the corresponding merging ratios were 1.0. On the other hand, the specific flow of the evacuees entering from the floor appeared between 15:22:05 and 15:25:40 on the 11th floor, as indicated in Fig. 10. Among them, the specific flow from 15:22:45 to 15:25:40 went up and down between 0.3 and 0.8 persons/m/s. The evacuees from 11th floor started to enter the landings at 15:22:05, and almost all of them finished to enter there at 15:25:40 in the drill. During this, the specific flow of the evacuees descending from the upper floor on 11th floor appeared continuingly and was approximately between 0.3 and 0.7 persons/m/s. Hence, the merging flow occurred and did not stop on the 11th floor. Both the specific flow and merging ratio on the 12th floor were the values of 0 at some time point such as 15:23:10, 15:24:10, and 15:24:55 during the merging flow occurring on the 11th floor. This shows the merging flow on the 12th floor stopped. The merging of the evacuees on the 11th floor caused the stopping of the evacuees on the 12th floor. Namely, the merging flow stopped, and the congestion occurred on the upper floors of Flow 5.

Figures 11 and 12 show the specific flows of the evacuees, who descended from the upstairs and the merging ratios, on 12th floor and 10th floor of the upper floors of Flow 3, respectively. The specific flows on the 12th and 10th floors were due to the evacuees descending from the upper floors only, and both merging ratios were 1.0. That on the 11th floor was also same. All of the evacuees walking on the landings of the 10th, 11th, and 12th floors descended from the upper floors into the landings of each floor. Both the specific flow and merging ratio on each of the tenth through twelfth floors were the values of 0 at three-time point before the 15:31:50, when the steady state of Flow 3 on the ninth floor was started. This shows the flows stopped at the time points of the 0 values. The flows on the tenth through twelfth floors were string. The congestion occurring on the 10th floor propagates to the reward flow on the 11th and 12th floors. The corresponding congestions between the three floors were named "Congestion 1 through 3," and Congestion 1–3 occurring on the 10th and 12th were illustrated in Figs. 11 and 12, respectively. As mentioned above, these congestions propagated to the upper floors, and also propagated from the lower floors, where Flow 3 descended. It is assumed that the merging did not occur on the upper floors of Flow 3, but the flow stopped there due to the congestion propagating from the floors where Flow 3 was measured, before the time interval for the steady states of Flow 3.

5 Discussion

It is confirmed that the non-merging evacuation flows descending the staircase were classified by the flow conditions in the upper floor, based on the observation data of the evacuation drills. As Flow 1, Flow 4, and Flow 6, the specific flow of the non-merging flow of which no congestion occurred on the upper floor is assumed to tend to decrease as the floor is lower. This is assumed to be because the distances between the evacuees in the non-merging flow descending become narrower as the floor is higher. It is assumed that the crowd density is not so high as the flow stop, and it causes the distances between the evacuees in the non-merging flow on the lower floors to open. After that, the distances are assumed to become narrow in order from behind with time. The specific flow of the non-merging flow of which the congestion occurred on the upper floor is assumed to become constant on regardless of the floors, as Flow 2 and Flow 5. This is assumed to be because the high-density crowd caused by the congestion descends to the lower floors and the distances between the evacuees in the non-merging flow descending on the lower floors are narrow. The average specific flows on each floor of Flow 3 were close to each other, but those on the seventh through ninth floors were larger than those on the fourth through sixth floors. The high density caused intermittently by some congestions occurring temporarily on the floors of Flow 3 and the upper floors. The distances between the evacuees on the higher of the floors of Flow 3, where the congestion occurred later, were assumed to be narrow than those on the lower.

The results obtained will be useful for developing or improving the evacuation model, such as simulating the evacuation flow in more detail and accurately. The results were clarified with the specific flows indicated by the observational data. As the future work, we will reveal the characteristic of the non-merging flow as influenced by the flow conditions on the upper floor, by analyzing the density, speed of evacuees, and relationships between them including the specific flow.

6 Conclusion

This study elucidated the non-merging evacuation flow, which defined as a flow consisting only of evacuees descending on the staircase without merging with the evacuees entering the floor in this study, under various flow conditions on the upper floor, specifically the congestion and the merging of evacuations descending and entering the staircase, with the observational survey on the real evacuation drills repeated annually for three years in the high-rise building. The results were as follows:

(1) The specific flow, under the steady-state condition, of the non-merging flow of which no congestion occurred on the upper floor tends to decrease as the floor is lower.

(2) The specific flow, under the steady-state condition, of the non-merging flow of which the congestion occurred on the upper floor becomes constant on regardless of the height of floors.

(3) The specific flow, under the steady-state condition, of the non-merging flow after the congestion propagating from the lower to higher of the floors, was close between the floors, but those on the higher of the floor were larger than those on the lower.

References

1. Kadokura, H., Sekizawa, A., Sano, T., & Fujii, K. (2015). Study on flow and congestion in staircases during phased evacuation in a high-rise building: Analysis based on the observational data of a real total evacuation drill. *Journal of Environmental Engineering (Transactions of AIJ), 80*(716), 849–856.

2. Mizuno, M., Fujii, K., Kadokura, H., Wang, F., Sano, T., & Sekizawa A. (2017). Development of mathematical model of evacuation flow in a staircase based on a survey result of a real evacuation drill in a high-rise office building. In 12th International Symposium on Fire Safety Science Book of Abstracts Posters (p. 113).

3. Kagawa, M., Kose, S., & Morishita, Y. (1986). Movement of people on stairs during fire evacuation drill–Japanese experience in a highrise office building. *Fire Safety Science*, 553–540.

4. Proulx, G. (1995). Evacuation time and movement in apartment buildings. *Fire Safety Journal, 24*(3), 229–246.

5. Hoskins, B. L., & Milke, J. A. (2012). Differences in measurement methods for travel distance and area for estimates of occupant speed on stairs. *Fire Safety Journal, 48,* 49–57.

6. Peacock, R. D., Hoskins, B. L., & Kuligowski, E. D. (2012). Overall and local movement speeds during fire drill evacuations in buildings up to 31 stories. *Safety Science, 50*(8), 1655–1664.

7. Gwynne, S. M. V., Kuligowski, E. D., Kratchman, J., & Milke, J. A. (2009). Questioning the linear relationship between doorway width and achievable flow rate. *Fire Safety Journal, 44*(1), 80–87.

8. Kuligowski, E. D., Peacock, R. D, & Hoskins, B. L. (2010). *A review of building evacuation models.* 2nd ed. Technical Note 1680, Gaithersburg, MD: National Institute of Standards and Technology.

9. Fruin, J. J. (1987). *Pedestrian planning and design.* Revised Edition 1987, Mobile, AL: Elevator World.

10. Pauls, J. (1987). Calculating evacuation times for tall buildings. *Fire Safety Journal, 12*(3), 213–236.

11. Dinenno, P. J., Drysdale, D., Beyler, C. L., & Walton, W. D. (2008). *SFPE Handbook of fire protection engineering.* 4th ed. Society of Fire Protection Engineers (SFPE)/National Fire Protection Association (NFPA).

12. Kuligowski, E. D, Peacock, R. D, Reneke, P. A., Wiess, E. A., Averill, J. D., Hagwood, R. C., Ronchi, E., Hoskins, B., & Spearpoint, M. (2014). *Movement on stairs during building evacuations* (pp. 1–134). National Institute of Standards and Technology (NIST) Technical Note 1839.

13. Hokugo, A., Kubo, K., & Murozaki, Y. (1985). An experimental study of confluence of two foot traffic flows in staircase. *Journal of Architecture, Planning and Environmental Engineering, 358,* 37–43.

14. Takeichi, N., Yoshida, Y., Sano, T., Kimura, T., Watanabe, H., & Ohmiya, Y. (2005). Characteristics of merging occupants in a staircase. *Fire Safety Science*, 591–598.

15. Galea, E. R., Sharp, G., & Lawrence, P. J. (2008). Investigating the representation of merging behavior at the floor–stair interface in computer simulations of multi-floor building evacuations. *Journal of Fire Protection Engineering, 18*(4), 291–316.
16. Boyce, K. E., Purser, D. A., & Shields, T. J. (2012). Experimental studies to investigate merging behaviour in a staircase. *Fire and Materials, 36*(5–6), 383–398.
17. Sano, T., Yajima, M., Kadokura, H., & Sekizawa, A. (2015). Characteristics of evacuation behavior based on observation of a theater evacuation drill. In *Proceedings of the 6th International Symposium on Human Behaviour 2015*, (pp. 97–108).
18. Sano, T., Yajima, M., Kadokura, H., & Sekizawa, A. (2016). Human behavior in a staircase during a total evacuation drill in a high-rise building. *Fire and Materials, 41*(4), 375–386.
19. Hoskins, Bryan L., & Milke, James A. (2012). Differences in measurement methods for travel distance and area for estimates of occupant speed on stairs. *Fire Safety Journal, 48,* 49–57.

Time Gaps for Passing Through Bus Exits in Tunnel Fires by an Experimental Evacuation and Ordinary Use

Check for updates

Hung-Chieh Chung, Miho Seike, Nobuyoshi Kawabata, Masato Hasegawa, Shen-Wen Chien and Tzu-Sheng Shen

Abstract This study was focused on the time gaps between passengers exiting a bus during an evacuation in the event of a tunnel fire. In a tunnel fire, bus passengers must evacuate irrespective of whether the bus is on fire or not. Hence, considering the tunnel fire situation, we considered two scenarios for evacuation: (1) evacuation in which the passengers do not perceive emergency and (2) evacuation in which the passengers perceive emergency. Based on these scenarios, we carried out experiments and observations to measure the time gaps of able-bodied persons and elders with reduced mobility. The experimental results indicated that the time gaps of able-bodied persons ranged from 0.42 to 4.42 s (mean = 1.40 s) and those of simulated elders ranged from 1.8 to 4.73 s (mean = 2.94 s). The probability distribution of experimental time gap data also demonstrated that the maximum rate of the able-bodied person data corresponds to 1.0–1.5 s, and the maximum rate of the simulated elderly data corresponds to 2.0–2.5 s. Moreover, most time gap data were in the 5 s range in both the evacuation experiment and observations. However, in observations, the

H.-C. Chung (✉)
Kaohsiung City Fire Bureau, No.36, Jingwu Rd., Fengshan Dist., Kaohsiung City 830, Taiwan (R.O.C.)
e-mail: fc751126@gmail.com

Graduate School of Natural Science and Technology, Mechanical Science and Engineering(Doctoral Programs), Kanazawa University, Kakuma-Machi, Kanazawa 920-1164, Japan

M. Seike
Department of Mechanical Systems Engineering, Faculty of Engineering, Toyama Prefectural University, 5180, Kurokawa, Imizu 939-0398, Japan

N. Kawabata
Faculty of Production Systems Engineering and Sciences, Komatsu University, Nu 1-3, Shicho-Machi, Komatsu 923-8511, Japan

M. Hasegawa
Faculty of Mechanical Engineering, Institute of Science and Engineering, Kanazawa University, Kakuma-Machi, Kanazawa 920-1164, Japan

S.-W. Chien · T.-S. Shen
Department of Fire Science, Central Police University, No.56, Shujen Rd., Takang Vil., Kueishan District, Taoyuan City 33304, Taiwan (R.O.C.)

appearance of particular movement characteristics caused relatively longtime gaps which were even larger than the mean value of simulated elders in the experiment.

1 Introduction

Smoke caused by a tunnel fire is initially stratified as it flows through the tunnel. After stratification, smoke is disrupted by heat absorption by the ceiling wall, and it starts to diffuse inside the tunnel, thereby making evacuation activities extremely difficult. The seriousness of Taiwan's Hsuehshan tunnel fire accident on May 7, 2012 (34 injured, two fatalities) [1] demonstrated the requirement for better strategies to prevent tunnel fires and reduced hazards from tunnel fires. In the strategies to prevent disastrous tunnel fires, one important point is to estimate the number of people who will not be able to evacuate a smoke-filled tunnel during a fire incident. When the Hsuehshan tunnel fire accident occurred in 2012, most of the bus passengers were injured after getting off the bus [1].

Seike et al. [2] conducted computational fluid dynamics (CFD) analysis of tunnel smoke behavior and compared evacuation simulation data by one-way coupling. Then, a method for quantitatively evaluating fire safety based on the number of requisite rescuers who are in danger of becoming immovable in the smoke was devised. Mikame et al. [3] used a similar method to conduct a safety assessment by CFD analysis of a semi-lateral flow ventilation system at the time of a tunnel fire and compare evacuation simulation data. The results indicated that most of the bus passengers in the assessment suffered from the danger of smoke and could not evacuate from the bus, even if the exit flow rate of the 50 people on the bus was 0.5 person/s. These results were not based on actual bus exit flow rates; however, the qualitative danger of buses was clarified and indicated that the quantitative danger of buses needed to be clarified.

Ideally, evacuation from a bus should be directed by the driver. However, if the driver does not or cannot instruct the passengers (possibly due to injury or death), passengers must make their own decisions. In SP Fire Technology of bus fire safety [4], it was reported that the time to evacuate a passenger was a maximum of 200–300 s in a particular test; hence, rapid evacuation activity is needed. However, the Hsuehshan tunnel fire accident report [1] mentioned that the initial bus evacuees did not feel directly threatened by the fire in the early stages of the fire incident. The observed behaviors of evacuees were like those in an ordinary condition, which revealed that the passengers seemed not to perceive an emergency. When the fire started to grow and the smoke spread quickly, the bus evacuees seemed aware of the threat of the fire and speed up their movement obviously. These aforementioned phenomena reveal that the actual fire incident is expected to include two scenarios: (1) evacuation in which the passengers do not perceive emergency behave as though it is a non-emergency situation and (2) evacuation in which the passengers perceive emergency. Tunnel fire

evacuation and building fire evacuation have obvious differences. When a tunnel fire occurs, not only do the passengers in a bus which has caught fire need to evacuate, but the passengers in a bus which has not caught fire also need to evacuate for prevention of serious casualties. Hence, to enhance the reliability of bus evacuation evaluation in a tunnel fire, considering these two expected scenarios is necessary.

In recent years, several experimental studies focusing on bus evacuation have been performed and provided fundamental flow rate data for quantitative assessment [5–7] (see Table 1). However, the bus passengers' alighting in tunnel fires was only reported in Chung et al. [5].

Additionally, these experimental studies mainly focused on able-bodied persons because of experimental safety. However, the video record analysis result in Hsuehshan tunnel fire accident report revealed that there were 22 passengers evacuated from the bus. From the door opening to the first 21 able-bodied passengers escaping from bus took about 84s to complete, then the last one elderly people took about 66s to complete evacuation and whom is under the helping of other passengers [1]. This phenomenon reflects that the able-bodied passengers and elderly people have significant differences in evacuation speed. Another serious bus fire incident also revealed the issue in the evacuation of elderly people. On October 13, 2016, a bus fire occurred on the Gyeongbu Expressway. It was reported that a large bus tire blew out and hit the sidewalls and a fire broke out. Many of the passengers were in their 50s and 70s. Because the door of the bus was jammed in by the concrete guard rail, passengers have to broke the bus windows and escaped, but that still results in 10 of the 20 passengers died. [8]. Even though previous experimental bus evacuation results have reported quantified results of the exit flow rates from buses, the flow rate considering the persons with reduced mobility has not been well investigated because they are in minority during flow rate calculation. Hence, in order to investigate the possible delay when passing a bus exit in an evacuation, the persons with reduced mobility (especially elderly) were chosen as a preliminary research subject in the present study.

Table 1 Comparison of bus evacuation experiment

	ECE [6]	Pollard et al. [7]	Chung et al. [5]
Participants	45 adult persons (15 women, 30 men, aged 25–45)	54 adult persons (over 18 years old, able-bodied and uninjured)	16 adult persons (21–63 years old, able-bodied and uninjured)
Scenario setting	Bus evacuation training	Simulating that they were slightly late for work	Assuming a fire accident outside of the bus
Flow rate of exit (person/s)	1.1–1.2 (front door)	0.58–0.62 (front door)	0.66–0.94 (front door)
	0.85 (rear emergency door)		0.57 (emergency door)

The exit flow rate from a bus is defined as the number of people passing the exit per unit time. Consequently, the time gap between two persons would reflect the instantaneous exit flow rate from a bus, and it could reflect the variation in the flow rate. Based on the reason above, when evaluating bus evacuation in response to a tunnel fire, it is important to examine the time gaps between people passing through the exit of the bus. However, the time gap has not been well investigated in past experimental studies.

Therefore, to assess the tunnel fire with high reliability, the primary aim of the present study was to clarify the time gap data when able-bodied persons and persons with reduced mobility pass through the exit of a bus under two scenarios: (1) evacuation in which the passengers do not perceive emergency by observations and (2) evacuation in which the passengers perceive emergency by experiments. Additionally, the results were compared with other studies to investigate the validity and reliability of the time gap data in the present study.

2 Bus Evacuation Experiment

In this section, the place of the experiment, bus type, scenario setting, population of participants and definition of the time gap are explained in detail.

The bus evacuation experiments were conducted in a parking lot in Kaohsiung (Taiwan) in November 2015 and July 2016. A large bus equipped with 43 seats and three exits including one emergency door was chosen for the experiments. The bus type is shown in Fig. 1. For the normal exits (the front and rear doors, which could

Fig. 1 Bus type demonstration

Table 2 Size of different exit types

Exit type	Size (m × m)	Height above ground (m)	Step ladder
Front	2.14 × 0.78	0.34	Yes
Rear	1.89 × 0.78	0.32	Yes
Emergency	1.66 × 0.65	0.52	Yes

Note 'Height' means the height from ground to exit bottom

be used for normal alighting, not just for emergency), the heights of the bottom of the front and rear doors from the ground were 0.32 and 0.36 m, respectively; the height of the bottom of the emergency exit from the ground was 0.52 m (see Table 2). Depending on the experimental cases, the doors were left opened or closed and the chosen doors remained opened during the experiments except emergency exits (because it can be considered that the passengers needed to open these exits by themselves).

A group of 16 people participated in the experiment in November 2015, and a group of 20 people participated in the experiment in July 2016. The majority of the participants was Kaohsiung City Fire Bureau officers. The present study mainly focuses on the time gap data investigation of elderly people. However, letting the elder participants attend the experiment is dangerous; therefore, the aging suit (see Fig. 2) was used to simulate an elderly person's behavior. Younger people wore an aging suit which consisted of a set of separate components, such as special goggles, weight cuffs, knee wraps, crutch and elbow wraps and fixed belts. These components could simulate the mobility and visual impairment of elderly people. For example, special goggles were used to simulate the narrowing of the visual field and opacity of the eye lens caused by cataracts. The joint stiffness, joint mobility restrictions and kyphosis can simulate elderly movement [9].

In the experimental environment, the curtains of the bus were closed and the lights were turned off in order to simulate the environment of a tunnel evacuation in which there is dim lighting but it is still bright enough for the passengers to notice the environmental information from outside the bus. Furthermore, avoiding injury to the participants was the most important aspect of the experiment. Thus, we did not use fire or any other hazardous things, such as flames, high temperatures, smoke or toxic gases. In order to conduct the experiments safely while considering the chaos situation in actual evacuation scenarios, the experimental scenario was that the participants were instructed to behave as though a tunnel fire accident had happened outside of the bus to investigate the human behavior in an emergency situation. Before each experimental case, the participants sat in arranged seats, and the scenario setting was explained in detail.

Six video cameras were arranged inside the bus to ensure that participants' behavior could be recorded completely at each exit.

Based on the above explanation, detailed participant information and experimental conditions in each case are shown in Table 3.

Fig. 2 Aging suit demonstration

Table 3 Experimental cases

Case no.	Participants	Men/women	Age range	Mean (Std. dev.)	Simulated elderly	Used exit number/type
1	16	9/7	22–36	28.2(4.5)	0	2 (front, rear)
2	16	9/7	22–36	28.2(4.5)	0	3 (front, rear, emergency)
3	20	10/10	23–37	29(4.6)	0	1 (rear)
4	20	10/10	23–37	29(4.6)	0	1(front)
5	20	10/10	23–37	29(4.6)	0	1 (emergency)
6	6	3/3	23–37	26.7(4.3)	6	1 (front)
7	6	3/3	23–37	26.7(4.3)	6	1 (emergency)
8	6	3/3	23–37	26.7(4.3)	6	1 (rear)

The time gap in the present study is defined as the time interval between two participants passing through the bus exits, and the unit is in seconds. The analysis of the time gap can clarify variations in the exit flow rate during evacuation more comprehensively. Therefore, the present study primarily focuses on the change in the time gap data. Furthermore, the accuracy of the time gap data is important. In order to calculate the time gap accurately, a recorded video was divided into individual frames to gather time distance between two frames, and therefore the time resolution was 1/30 s. This method enabled us to correctly determine the time when the passenger's foot touched the ground. In this way, the time gap between two passengers was obtained and discussed.

3   Normal Alighting from the Bus by Observation

Based on the incident report of the Hsuehshan tunnel fire incident [1], evacuation in a tunnel fire is expected to be divided into two scenarios: (1) evacuation in which the passengers do not perceive emergency and (2) evacuation in which the passengers perceive emergency. However, since experimental evacuation is known as an expected emergency situation, i.e., all passengers are able-bodied and uninjured, and they were clearly instructed before the experiment. Thus, evacuation is done in an organized, orderly way, and there was no hesitation. However, evacuee needs to perceive the situation of the environment, or must make their own decisions to act, if the driver does not or cannot instruct the passengers in the tunnel fire. At that time, passenger easily feels hesitation or confusion during evacuation. Until the public has perceived danger, evacuees begin to move like under an emergency. Thus, it is difficult to reproduce the aforementioned first evacuation scenario by experiment. Therefore, in order to grasp the behavior in the evacuation scenario when passengers do not feel an emergency, a feasible method is the observation of normal alighting condition which can be considered a similar situation to investigate.

On the other hand, since the moving speed of an elderly person has declined due to the aging of the body, it can be expected that the time gap of the elderly is limited by their movement ability rather than whether they are in an emergency or a non-emergency situation. This reflects that elderly evacuation may not necessarily only be investigated through experiments. Therefore, the present study conducted normal alighting observations which also involve the elderly persons to investigate the time gap data, as well as the movement characteristics related to evacuation delay.

3.1   Places

Most evacuation instructions do not suggest to bring baggage when evacuating. However, based on the analysis of the CCTV footage, evacuees were observed getting off the bus with handheld baggage during the Hsuehshan tunnel fire in 2012. Therefore,

considering the characteristics of passengers carrying luggage in an actual bus incident, the present study selected Kenroku-en, Japan, to observe passengers' behavior when getting off buses.

The reason why Kenroku-en was selected as an observation place is that it is a famous attraction. Many people take buses there for sightseeing and stay for a short time. Thus, it was expected that all the passengers would leave the bus to go outside and a few would have baggage when getting off.

Moreover, because this place is easily accessed by bus, many elderly persons go there. According to the observations, the age of the passengers was mostly in the range between the 50s and the 70s. Thus, the composition of the passengers was close to the condition that the present study aimed to focus on.

3.2 Methodology

In the present study, buses with over ten people were chosen for observations. Five observations were completed. Since the present study was unable to obtain the age of the passengers, their age was roughly described as mostly in the range from 50 to 70 years. For observations, digital cameras were placed in the bus station in advance. The process of normal alighting was recorded when a bus arrived, and the passengers started to get off the bus. Observations were conducted in an unannounced condition to record actual human behavior, so in order to protect the privacy of passengers, all video records mainly focused on the passengers' feet. The time gap calculation method was the same as in the description in Sect. 2. In addition, the whole process did not reveal any information about their personal identity. The total number of passengers observed was $n = 140$.

4   Result and Discussion

4.1 Time Gap Data in Bus Evacuation Experiment and Normal Alighting

The obtained time gap datasets from the bus experiment ($n = 98$) and the normal alighting observation ($n = 140$) are demonstrated in Tables 4 and 5 using statistical description. According to the characteristic of the time gap data in Table 5, the factor of the exit type had no significant influence on the time gap. Hence, the present study merged data from different exit types and compared the results with other studies (after transforming the mean flow rate to the time gap) as shown in Fig. 3.

In 1984, a bus evacuation test was conducted by IKARUS company in Hungary [6, 10] in which the participants included 45 adult persons (15 females, 30 males), aged 25–45 years. The results demonstrated that the flow rate through the front door

Table 4 Statistical description of time gap data in evacuation experiment

Participants	Exit type	Min (s)	Max (s)	Mean (s)
Able-bodied persons	Normal	0.42	3.30	1.34
Able-bodied persons	Emergency	0.77	4.42	1.57
Simulated elderly	Normal	1.90	4.73	2.87
Simulated elderly	Emergency	1.80	4.37	3.07

Table 5 Statistical description of the time gap data during normal alighting

Scenario	Location	Min (s)	Max (s)	Mean (s)
Normal alighting	Kenroku-en	1.06	25.4	3.18
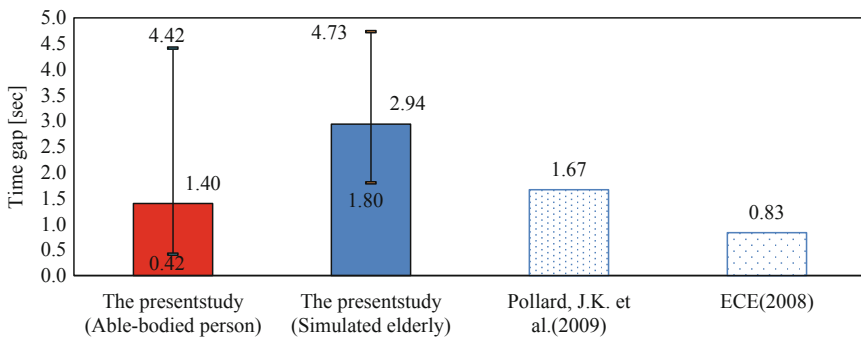
Fig. 3 Time gap data from bus experiment (the present study vs. past experiments)

was 1.1–1.2 persons/s, so the transformed time gap was about 0.83 s. It was obvious that this test attempted to analyze a serious situation, such as a fire incident. In 1996, in Japan, for the purpose of optimizing the design of bus evacuation facilities, a survey on the opening time of the emergency door, a questionnaire about the guide board and an experiment to determine the time of getting off the bus from the start of evacuation were conducted, and the subjects were six elementary school students (8–12 years old), 12 adults (20–28 years old) and six elderly people (66–73 years old). Measurement was made of the evacuation time from standing from the seat to getting off the bus. This study reported that the average evacuation time was 7.7 s for adults escaping from a regular door and 8.5 s for elders escaping from a regular door [11]. In 2008, Pollard et al. [7] conducted a full-scale bus evacuation to measure the exit flow rates through the front door, wheelchair access door, window and roof hatches (in daylight), and the subjects were 54 adults. In this experiment, subjects were asked to simulate that they were slightly late for work and to move directly away from the bus. The results demonstrated that the mean flow rate through the front door was 0.6 person/s, so the transformed time gap was about 1.67 s. These experiments similarly focused on the analysis of the flow rate in evacuation scenarios; hence, an

outline of these experiments is also given in order to make correct comparisons with the results of this experiment.

In Fig. 3, it is obvious that the mean time gap of the able-bodied persons in the present study was similar to the research results of Pollard et al. Moreover, the mean time gap of the simulated elderly persons was greater than that of the able-bodied persons regardless of whether normal exits or emergency exits were used. The main reason can be considered that the aging suit restricted the participants' agility which slowed down their movement. In the study conducted by Shiosaka and Kuboike [11], rather than calculating the flow rate, the evacuation time was measured from standing from the seat to getting off the bus, so it was reasonable that the time gap was greater.

Since the present study aimed to measure general bus alighting data in order to verify the time gap of evacuation in which the passengers do not perceive emergency in an actual tunnel fire, it was important to measure the time gap data in the condition of passengers with fewer luggage.

Therefore, a series of sightseeing bus observation results in Mendenhall Glacier Visitors Center, where passengers were thought to get off without any luggage as much as possible, was also gathered to verify the reliability of the present observation data [12]. In the study conducted by Macheck et al. [12], the flow rate of the front exit was 0.03–0.45 person/s (mean = 0.29 person/s). The results transformed into time gap from the flow rate are shown in Fig. 4.

In Fig. 4, since time gap information from Macheck et al.'s study was transformed from the average flow rate, it is expected that the time gap information cannot well represent the characteristics of the individual time gaps between passengers. Nevertheless, the time gap trend can still be discussed. The time gap from Macheck et al.'s study demonstrated a similar range as 1.06–25.4 s (mean = 3.18 s) in the present research. Although the reason causing the minimum time gap value in Macheck et al.'s study was unknown, the maximum time gap value of this observation result was that there were passengers who got off with a stroller. It seems related to a particular reason which reduced mobility rather than the influence from the elderly.
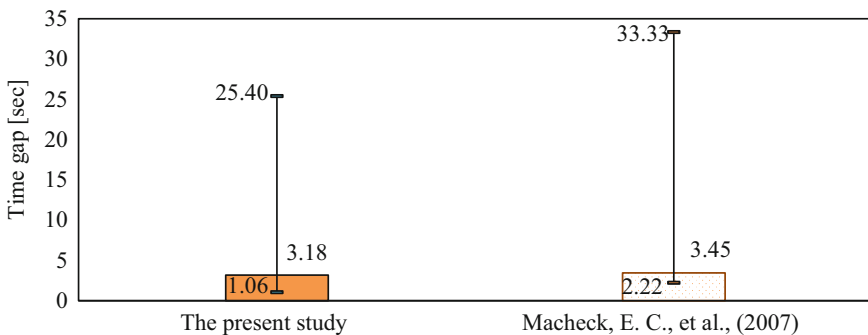
Fig. 4 Time gap data from normal alighting

From the result of normal alighting observation can be inferred that the scenario that evacuation in which the passengers do not perceive emergency, the time gap data possibly demonstrate larger values and wider range.

While comparing the observation data and the experimental data, it can be found that the mean time gap of the normal alighting observation was longer than that of the experimental data of the able-bodied persons but it was similar to the experimental data of the simulated elders.

One reasonable explanation could be that the participants in the experiment were almost all students who were able-bodied, none wore jackets, none carried luggage and every participant followed each other closely. Additionally, all participants of the experiment were told that they needed to evacuate as soon as possible. Thus, it makes sense that the time gap data in the experiments were much shorter than the observation data of normal alighting. Relatively, the proportion of elderly people in observation data is high. For elders or persons with reduced mobility, their movements are mainly limited by their physical agility rather than the situation they perceived, and which would result in they are difficult to speed up their movement during the evacuation, even if dangerous situations are approaching, such as smoke and heat of the fire. Therefore, the experimental data of the simulated elders are similar to the observation data.

4.2 Characteristics of Time Delay

Figure 3 displays the time gap range of the bus experiments from minimum to maximum. Figure 4 demonstrates a much wider range in the individual time gap data of normal alighting observations. This indicates that the time gap data exhibit significant dispersion in individuals, and considerable time gaps appear which affect the variation of the flow rate from the bus.

Thus, in order to enhance the reliability of the bus exit flow rate, this section calculates the probability distribution of different data groups to analyze centralized and decentralized trends of the data. Additionally, the reason as to why considerable time gaps appear will also be discussed. Because the data numbers are different in different categories, the frequencies in each data group were transformed into a histogram of the probability distribution for the purpose of comparison in the same unit. The probability distributions of the able-bodied person data and the simulated elderly data are displayed in Fig. 5; the probability distribution of the observation data is displayed in Fig. 6.

In Fig. 5, the range of the probability distribution of all experimental time gap data corresponds to 0.0–5.0 s. The maximum rate of the able-bodied person data corresponds to 1.0–1.5 s, and the maximum rate of the simulated elderly data corresponds to 2.0–2.5 s.

In Fig. 6, the range of the probability distribution of all observation time gap data corresponds to 0.0–25.5 s. 91% observation data still centralized in the range 0.0–5.0 s, which have similar tendency to time gap data in experiment. Furthermore,
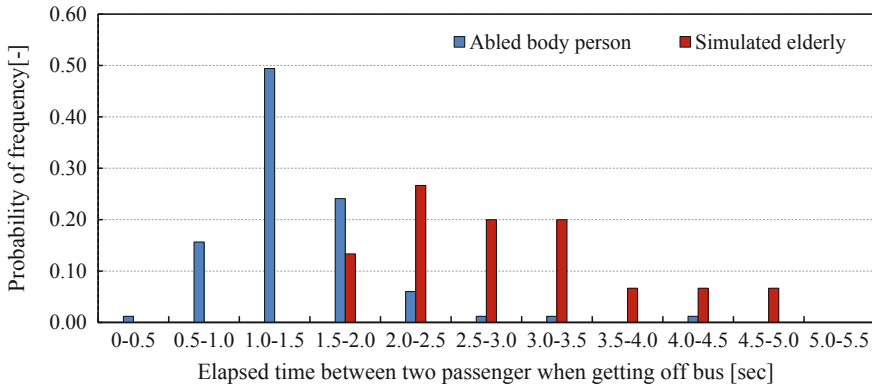
Fig. 5 Probability distributions of gap data in experiment
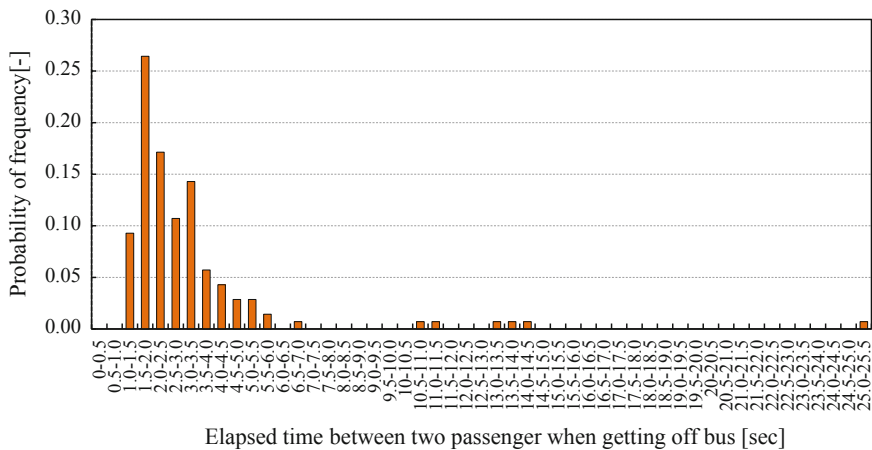
Fig. 6 Probability distributions of the time gap in Kenroku-en

the maximum rate of observation data corresponds to 1.5–2.0 s. However, since passenger composition is unknown, it is difficult to deduce that evacuation which the passengers do not feel emergency also and have the highest probability in the range 1.5–2.0 s.

It is worth noting that there were some time gap data larger than most of the time gap data several times (there seem some outliers) in Fig. 6. Based on the analysis of the video recordings, it was found that the following movement characteristics caused relatively longtime gaps:

(1) When descending the steps of the bus exits, some passengers let two feet touch the same step before moving to the next step. This behavior may be used by elders to avoid injury. Observed passengers who used this method of action

exhibited larger time gaps than the maximum value of the simulated elderly in experiments.

(2) Passengers use a stick to help them get off the bus were observed and which exhibited time gaps are about 13.6 s.

(3) The occurrence of a maximum time gap (25.4 s) is due to an adult holding a children's hands and slowly down the steps while passing through the exit.

In the case of these passenger characteristics during a bus evacuation, it can be expected that the bus flow rate would obviously reduce and the risk of a disaster would be very high.

5 Conclusions

Previous bus evacuation experiments provided fundamental data about the flow rate and guidance to develop the corresponding model which was suitable for bus evacuation safety assessment. Measuring the time gap data of elders with reduced mobility was helpful to enhance the validity and reliability of the flow rate through bus exits when escaping from buses in tunnel fire scenarios. Therefore, the present study investigated the time gap for passing bus exits by evacuation experiments and normal alighting observations, especially when elders are present. The results from this study are summarized as follows:

1. In the present bus experiment, the influence of exit design on the time gap was not obvious because the width of the emergency exit and the height of the emergency exit from the ground in Taiwan are almost the same as the normal exit.

2. According to the evacuation experiment, the time gaps of the able-bodied persons ranged from 0.42 to 4.42 s (mean = 1.40 s), whereas those of the simulated elders ranged from 1.8 to 4.73 s (mean = 2.94 s). The mean of simulated elderly data was larger than that of the able-bodied person data.

3. According to the normal alighting observations, the time gaps ranged from 1.06 to 25.4 s (mean = 3.18 s).

4. Based on the time gap analysis by experiment and observation can be inferred that the scenarios that evacuation in which the passengers do not perceive emergency and evacuation in which the passengers perceive emergency have obviously differences.

5. Regarding the probability distribution of time gap data in evacuation experiment, the maximum rate of the able-bodied person data corresponds to 1.0–1.5 s, and the maximum rate of the simulated elderly data corresponds to 2.0–2.5 s. Regarding the probability distribution of time gap data in normal alighting observation, the maximum rate of observation data corresponds to 1.5–2.0 s.

6. The frequency distribution demonstrated that most time gap data were approximately in the range 5 s in both experiments and observations. However, in normal alighting observations, the appearance of particular movement characteristics would cause relatively longtime gaps.

It should be noted that due to the limited population size, a homogenous group of fit, healthy and young participants were chosen to analyze the time gap data in the experiment. Normal alighting observation was merely provided as an exploratory method for analysis in tunnel fire scenarios. It is recommended that the present study should be validated by more heterogeneous populations and actual bus fire evacuation data in order to thoroughly investigate the time gap data during bus evacuation.

References

1. Taiwan Area National freeway Bureau. (2015). Analysis of fire situation of Hsuehshan Tunnel south 26Kvehicle fire accident and strategy for evacuation and rescue, Final report, (p. 17) (Unpublished).
2. Seike, M., Kawabata, N., & Hasegawa, M. (2017). Quantitative assessment method for road tunnel fire safety: Development of an evacuation simulation method using CFD-derived smoke behavior. *Safety Science, 94,* 116–127.
3. Mikame, Y., Kawabata, N., Seike, M., & Hasegawa, M. (2014). Study for safety at A relatively short tunnel when a tunnel fire occurred. In *7th International Conference Tunnel Safety and Ventilation—New Developments in Tunnel Safety—, Graz*, pp. 133–139.
4. Hammarström, R., Axelsson, J., Försth, M., Johansson, P., Sundström, B., *Bus fire safety*. SP Report 2008:41, (p. 99), SP Fire Technology.
5. Chung, H. C., Kawabata, N., Seike, M, Hasegawa, M., Chien, S. W., & Orito, K. (2016). Experimental analysis of human evacuation from bus fire. In *Fourth International Conference on Fire in Vehicles, Baltimore, USA*.
6. ECE (2008). Inland Transport Committee World Forum for Harmonization of Vehicle Regulations WP 29.
7. Pollard, J. K., Markos, S. H. (2009). *Human factors issues in motorcoach emergency Egress*. National Transportation Safety Board Interim Report.
8. ON.CC (BVI) LTD. (in Chinese, see 2018/1/28) http://orientaldaily.on.cc/cnt/china_world/20160627/00178_001.html.
9. Kobayashi, Y., Takadani, K., Yamagishi, H., & Takizawa, T. (2002). Influence on the gait of wearing equipment for the experience of the aged. *Yamanashi Nursing Journal, 1,* 33–36.
10. Group of Experts on General Safety (GRSG) Regulation 107 (M2 and M3 vehicles). Proposal for amendments concerning emergency windows. Informal Document no. GRSG. 94-02. 94th Session of GRSG (pp. 21–24).
11. Shiosaka, Y., & Kuboike, T. (1996). Research on the evacuation readiness of bus crews and passengers. Investigation of current bus exit performance and effect of easy-to-understand emergency exit display. In *15th ESV Conference, Melbourne* (Vol. 2, pp. 1854–1860).
12. Macheck, E. C., Fisher, F. B., Peirce, S., Ritter, G., & Spiller, G. (2007). *Medenhall Glacier visitor center vehicular and pedestrian traffic congestion study*. Prepared by Volpe Center/USDOT, for U.S. Forest Service, Department of Agriculture. Final report. Part 1: Report no. DOT-VNTSC-USDA-07–01.

Investigation on Residents' Usage for Public Facility of Evacuation at Ordinary Time

Shao Chun-Hao

Abstract The study is an investigation conducted to know the trend of resident's facility usage. Based on the findings of the investigation, we can learn that the most popular location of an indoor facility for residents was "public activity center," and the outdoor facility was "park." Besides, most residents chose "Fellowship" as their usage purpose and 3 times for 1 week was the frequency which most residents chose. When it comes to the problem of facility usage, most problems were focused on hardware problem relating to the inadequacy of equipment for an activity. In order to make residents get familiar with public facilities, the drill of disaster prevention should be designed to get fellowship with residents. Moreover, schools, which are designated shelter in a disaster, should be open to the nearby community.

Keywords Facilities of evacuation · Shelter · Facility usage

1   Purpose of the Study

When a disaster occurs, a designated shelter plays an important role to accommodate evacuee. The behavior of facility usage at an ordinary time will have an influence on refugees' choice of shelters during the period of disaster [2]. In the study, usage of the facility at ordinary day is investigated and shown in statistic data. Based on the data, the trend of facility usage can explain and predict the nearby residents' evacuation behavior during the period of disaster. There are three parts in the study. At the beginning, an introduction of research areas: Fu-Min Village and Fu-Der Village, is given in the first part. Besides, the analysis of the questionnaire conducted in Fu-Min Village and Fu-Der Village in the second part. Finally, a conclusion as well as a suggestion of facility usage was given in the third part. There are several purposes in the study:

S. Chun-Hao (✉)
Central Police University, No.56, Shujen Rd., Takang Vil., Kueishan District, Taoyuan City 33304, Taiwan (R.O.C.)
e-mail: charshao@gmail.com

(1) To understand the different habits of facility usage between disaster prevention community and non-disaster prevention community, when taking a viewpoint of all hazards.
(2) To give the strategies to encourage residents to use a facility positively and this is designated shelter for all hazards in a disaster.
(3) Based on the investigation, a suggestion in views of all hazards viewpoints of designated shelter is given to facility usage in a community.

2   The Background of Research Objects

The information of research areas are Fu-Min Village and Fu-Der Village in Sanchong District of New Taipei City is shown in Table 1. These two villages are located near Danshuei River and near two bridges, Zhongxing Bridge and Zhongxiao Bridge, which link with Taipei City. There are many public facilities, such as five schools and four parks, near the communities. These facilities are also designated shelters during the disaster period.

Though both of two villages have no disaster experience, Fu-Min Village has an experience of building a prevention disaster community in 2016. Both of two villages have no experience of disaster in the past 10 years.

Table 1.   Information of Fu-Min and Fu-Der Village

Village	Fu-Min	Fu-Der
Household	1,364 (Jan. 2017)	1,719 (Jan. 2017)
Population	3,690	4,143
Area (km^2)	0.053	0.081

(From: Goolge Map 2017.1.31)   (From: Goolge Map 2017.1.31)

Cited from "Annual report of statistic for Sanchong District in New Taipei City in 2017 [1]"

3   Process of Investigation on Usage for Facilities of Evacuation at Ordinary Time

Since the residents' habits of usage of the public facility will have an influence on the choice of refuge during the disaster period, we choose two villages of New Taipei City where facilities are concentrated. Besides, we want to know if the villages' experience of disaster prevention community will affect residents' usage of a public facility, so we chose one village with experience of disaster prevention community (Fu-Min Village) and the other with no experience (Fu-Der Village).

A constructed questionnaire of usage of the public facility at ordinary time was conducted from December 1, 2017, to December 31, 2017. Twenty-five samples were chosen randomly for each village, and 50 samples in total. The structure of the questionnaire is listed below.

From Fig. 1, there are four parts in the questionnaire. The first part is a sample background, which includes basic information, such as living district, gender, age, and residence length. The second part is the location choice. The question is designed for residents to choose which facility at an ordinary time for activity. The third part is usage purpose which includes frequency and other factors. The fourth part is usage problems. These problems are classified into hardware and software based on the viewpoint of disaster prevention and fire prevention.
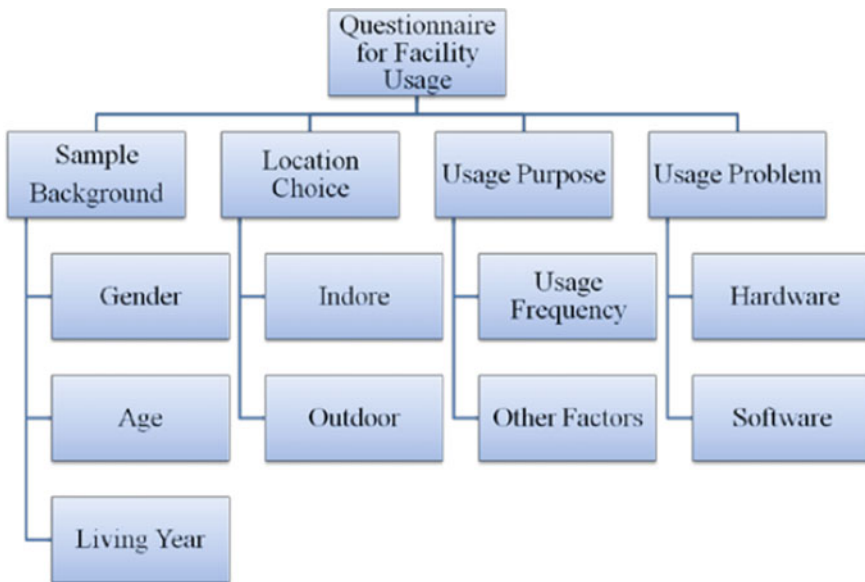
Fig. 1 Structure of questionnaire

4 Analysis of Investigation on Residents' Usage for Public Facility

There are 47 valid questionnaires in the investigation conducted from December 1 to 31, 2016. The analysis of four parts (mentioned in Fig. 1) is listed below to explain the finding from the statistic data which is dealt with by software of SPSS 20.

4.1 Analysis of Sample Background

a. Distribution of Gender

When it comes to gender of subjects, except 6 missing values of subjects, there are 21 male subjects and 20 female subjects (Fig. 2; Table 2).

b. Distribution of Age

When it comes to age of subjects, except 1 missing values of subject, subjects whose age is from 20 to 30 are 6 people, from 31 to 40 is 1 person, from 41 to 50 is 6 people, from 51 to 60 is 26 people, and over 60 years old are 7 people (Fig. 3; Table 3).

c. Distribution of Residence Length

When it comes to residence length of subjects, except 4 missing values of subjects, the longest "Residence Length" is 30 years. In this part, subjects were asked to write
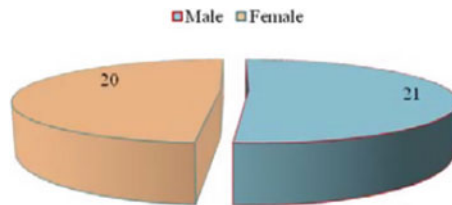
Fig. 2 Pie chart of subject gender

Table 2 Statistics of gender

		Frequency	Proportion	Valid percentage	Accumulated percentage
Valid	Male	21	44.7	51.2	51.2
	Female	20	42.6	48.8	100.0
	Total	41	87.2	100.0	
Missing value	0	6	12.8		
Total		47	100.0		
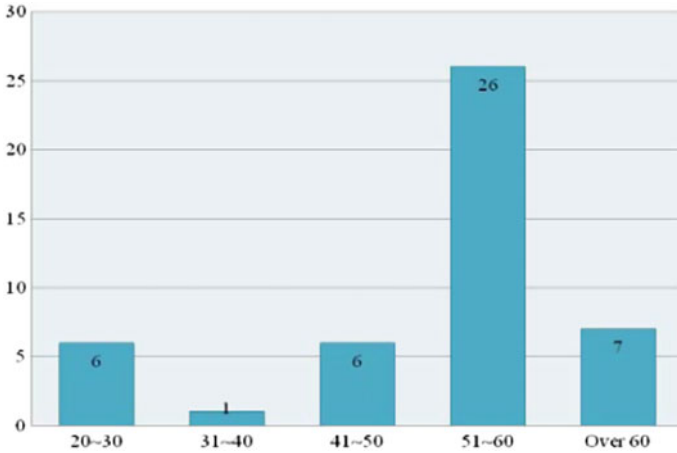
Fig. 3 Histogram of subject age

Table 3 Statistics of age

		Frequency	Percentage	Valid percentage	Accumulated percentage
Valid	20–30	6	12.8	13.0	13.0
	31–40	1	2.1	2.2	15.2
	41–50	6	12.8	13.0	28.3
	51–60	26	55.3	56.5	84.8
	Over 60	7	14.9	15.2	100.0
	Total	46	97.9	100.0	
Missing value	0	1	2.1		
Total		47	100.0		

down the number, rather than let them to choose a range of years. The longest is 30 years written by 7 people. After the arrangement by an interval of the decade, the distribution is shown in Table 4 (Fig. 4).

4.2 Analysis of Location Choice

In this part, we analyze the subjects' "Location Choice." The questions of this part are multiple choices, and subjects can choose at the least 1 answer. There are two classifications of "Indoor" and "Outdoor" in this part.

Table 4 Statistics of living year

		Frequency	Percentage	Valid percentage	Accumulated percentage
Valid	1–10	6	12.7	13.9	13.9
	11–20	8	17.1	18.7	32.6
	21–30	12	25.5	27.9	60.5
	31–40	14	29.8	32.9	93.1
	Over 41 years	3	6.3	6.9	100.0
	Total	43	91.5	100.0	
	Missing value	4	8.5		
		47	100.0		
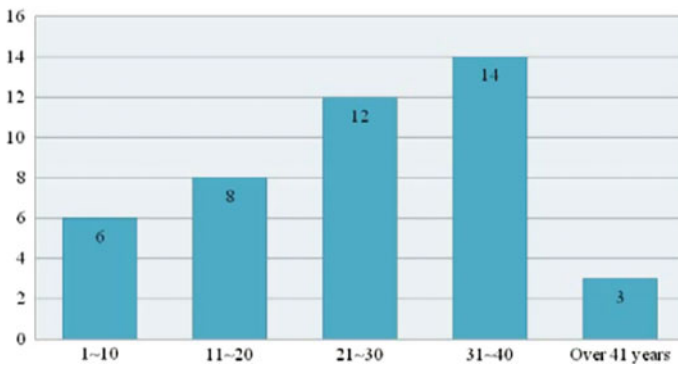
Fig. 4 Histogram of residence length

a.   Indoor Facility

When it comes to "Location Choice" of the indoor facility, missing cases were 10, and valid cases were 37. The most choices selected by subjects was "Public Activity Center (35 counts)," and the least is "Classroom of School (3 counters)." The subjects who select "Others" were 4 people, and "Sports Center" was addressed by 1 person and the rest 3 persons did not use indoor facilities (Fig. 5; Table 5).

b.   Outdoor Facility

When it comes to location choice of the indoor facility, missing cases were 12, and valid cases were 35. The most choices selected by subjects is "Park (27 counts)," the next is "Ground of School (15 counts)," and the least is "Others (3 counters)." The subjects who select "Others" were 3 people, and they did not use any outdoor facility (Fig. 6; Table 6).
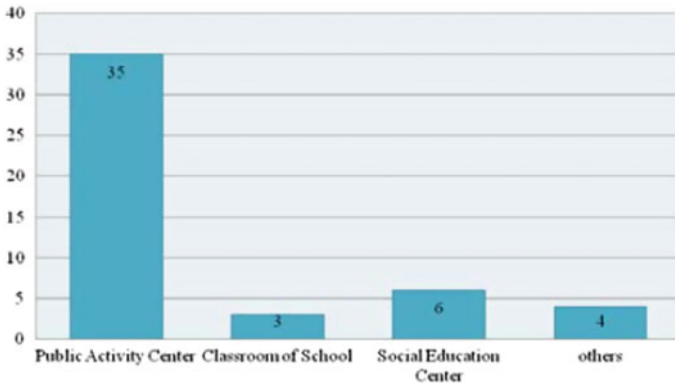
Fig. 5 Histogram of location choice (indoor facility)

Table 5 Statistics of location choice (indoor facility)

Indoor facility	Count	Pct of response	Pct of case
Public Activity Center	35	72.9	94.6
Classroom of School	3	6.3	8.1
Social Education Center	6	12.5	16.2
Others	4	8.3	10.8
Total	48	100.0	129.7
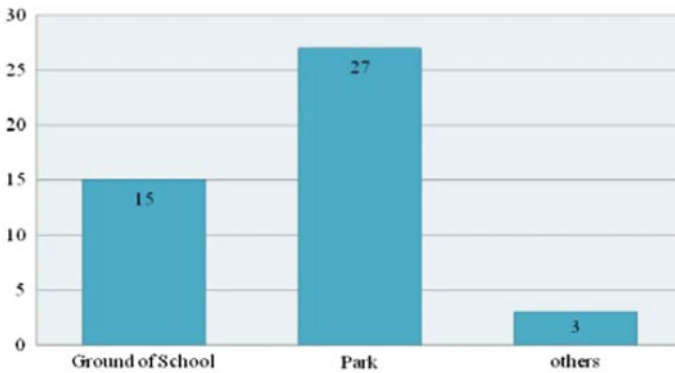
Fig. 6 Histogram of location choice (outdoor facility)

Table 6 Statistics of location choice (outdoor facility)

Outdoor facility	Count	Pct of response	Pct of case
Ground of School	15	33.3	42.9
Park	27	60.0	77.1
Others	3	6.7	8.6
Total	45	100.0	128.6

4.3 Analysis of Usage Purpose

In this part, we analyze the subjects' "Usage Purpose." The questions of this part are still multiple choices, and subjects can choose at least 1 answer. Besides, the other part is "Usage Frequency." Beside the descriptive statistic, the data of frequency was analyzed by t test.

a. Usage Purpose

When it comes to location choice of the indoor facility, missing cases were 6, and valid cases were 41. The most choices selected by subjects were "Fellowship (21 counts)," the next is "Education (10 counts)", and the next is "Meeting (3 counters)." The least is "Garden Party (1 count)." The subjects who selected "Others" were 9 people. One of them is "for Sport," and the rest of 8 people did not write down any purpose (Fig. 7; Table 7).

b. Usage Frequency

In this part, subjects were asked to choose only single answer. From Table 8, if we did not take the frequency of "Others" into a consideration, we can learn that the most choices selected by subjects are "3 times/week (3)," and the next is "1–3 times/week (5)" and "1 time/2 weeks (5)." The least is "Every day (3)." After the interview with 14 people who choose "Others," they told us they did not use the public facilities at an ordinary day, and then chose "Others" (Figs. 8 and 9).

Since the subjects are from Fu-Min Village and Fu-Der Village, one is the disaster prevention community, and the other is not (Table 9). We process a t test to check if the experience of disaster prevention community could have an influence on the frequency of facility usage. The outcome of t test is listed in Table 10.
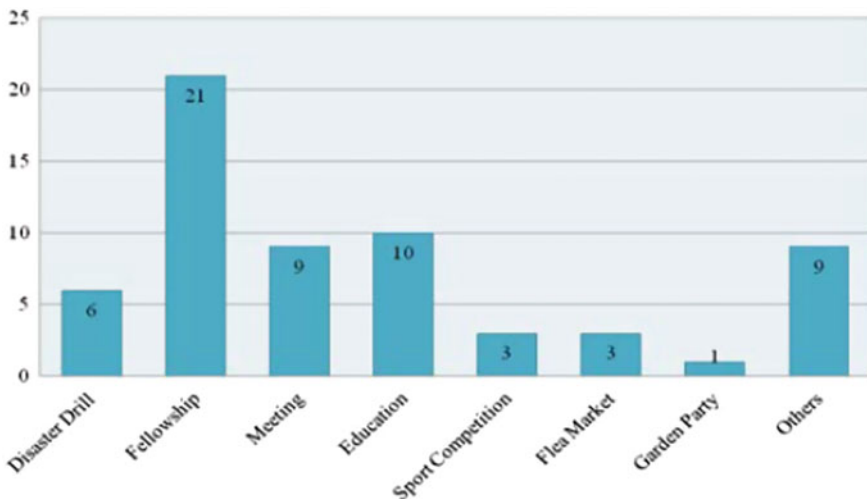
Fig. 7 Histogram of usage purpose

Table 7 Statistics of usage purpose

Usage purpose	Count	Pct of response	Pct of case
Disaster Drill	6	9.7	14.6
Fellowship	21	33.9	51.2
Meeting	9	14.5	22.0
Education	10	16.1	24.4
Sport Competition	3	4.8	7.3
Flea Market	3	4.8	7.3
Garden Party	1	1.6	2.4
Others	9	14.5	22.0
Total	45	100 0	128.6

Table 8 Statistics of usage frequency

Usage frequency		Frequency	Percentage	Valid percentage	Accumulated percentage
Valid	Every day	3	6.4	6.4	6.4
	3 times/week	13	27.7	27.7	34.0
	1–3 times/week	6	12.8	12.8	46.8
	1 time/2 weeks	6	12.8	12.8	59.6
	1 time/month	5	10.6	10.6	70.2
	Others	14	29.8	29.8	100.0
	Total	47	100.0	100.0	
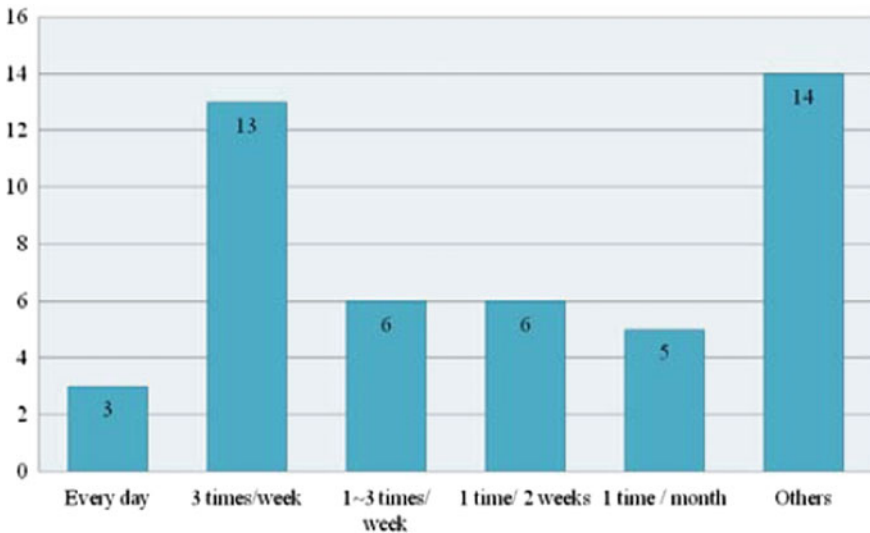
Fig. 8 Histogram of usage frequency
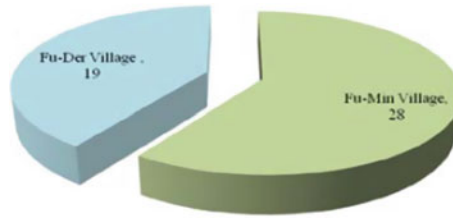
Fig. 9 Pie chart of distribution of subject

Table 9 Descriptive statistic of usage frequency

	Experience of disaster prevention community	Number	Average	Standard deviation	Standard error of average
Usage frequency	Fu-Min Village (disaster prevention community)	28	3.54	1.795	0.339
	Fu-Der Village (non-disaster prevention community)	19	4.26	1.695	0.389

Table 10 *t* test for usage frequency of Fu-Min Village and Fu-Der Village

	Levene's test			*t* test	
	F	Sig.	*t*	Freedom	Sig.
Usage frequency	0.599	0.443	−1.394	45	0.170

α value = 0.05

From Table 10, the *p* value is 0.17, which is larger than 0.05 (α value), and the difference in average value between Fu-Min Village and Fu-Der Village is not significant. In other words, the experience of participation of disaster prevention community did not affect residents' frequency of facility usage.

4.4 Analysis of Usage Problem

In this part, we analyze the subjects' "Usage Problem." The questions of this part are still multiple choices, and subjects can choose at least 1 answer (Fig. 10; Table 11).

When it comes to usage problem, missing cases were 10, and valid cases were 37. The most choices selected by subjects is "Equipment for activity is not enough
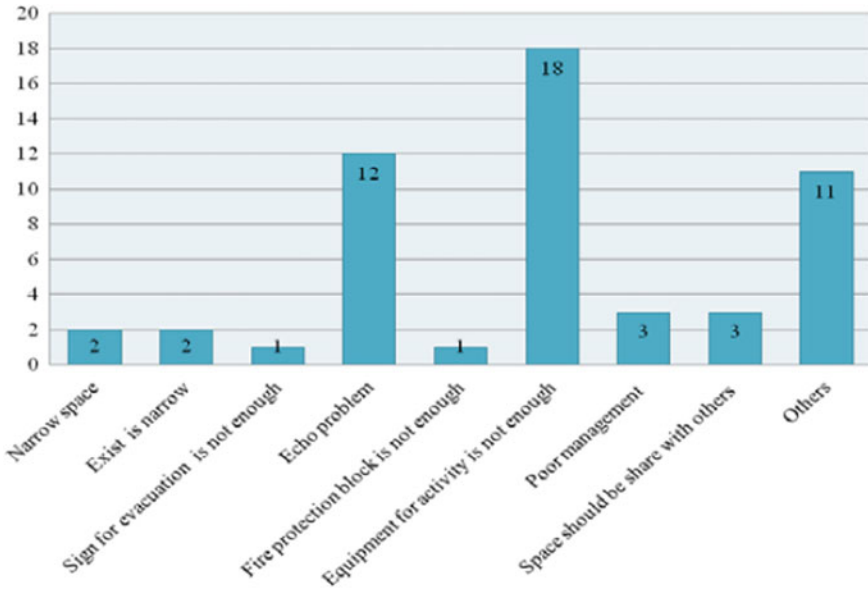
Fig. 10 Histogram of usage problem

Table 11 Statistics of usage problem

Usage problem		Count	Pct of response	Pct of case
Valid	Narrow space	2	3.8	5.4
	Exist is narrow	2	3.8	5.4
	Sign for evacuation is not enough	1	1.9	2.7
	Echo problem	12	22.6	32.4
	Fire protection block is not enough	1	1.9	2.7
	Equipment for activity is riot enough	18	34.0	48.6
	Poor management	3	5.7	8.1
	Space should be share with others	3	5.7	8.1
	Others	11	20.8	29.7
	Total	53	100	143.2

(18 counts)," the next is "Echo problem (12 counts)", and the next is "Others (11 counters)." The least is "Sign for evacuation is not enough (1 count)" and "Fire protection block is not enough (1 count)." After conducting an interview with subjects selecting "Others," the reason is that they did not have experience of public facility usage.

5   Findings and Conclusion

Based on the outcome of investigation, there are several findings stated below.

a. The most popular location of the indoor facility for residents was "public activity center," and the outdoor facility was "park." The finding is a little different from common sense that school is the most popular location at an ordinary time as well as the disaster period.
b. Most residents chose "Fellowship" as their usage purpose. The finding can explain to the residents who are over 40 years old use public facility to make friendship.
c. Three times for 1 week was the most residents' choice to explain the frequency of facility usage. Besides, the experience of disaster prevention community did not influent the frequency of facility usage between Fu-Min Village and Fu-Der Village. The finding goes against the expectation of people who receive the drill to develop disaster prevention community will increase the frequency of facility usage.
d. Most usage problems were focused on hardware problem relating to the inadequacy of equipment for the activity. Equipment of disaster prevention and fire protection showed less attention than normal equipment for the activity. Besides, software problem, such as management, was not regarded by residents frequently, and the count was only a little more than a problem of hardware.

Some findings are against common sense, and the reason could be the number of samples, which are only 47 in the investigation. Besides, based on the findings, to make residents get familiar with public facility can design the drill of disaster prevention to get fellowship with residents and let them use facilities more frequently at ordinary time. Furthermore, usage of school space is not so frequent at an ordinary time on the investigation, but a school usually plays a role of shelter in a disaster. Therefore, schools should be open for residents and hold the activity for the nearby community as more as possible to increase the usage frequency and motivation.

References

1. Annual Report of Statistic for SanChong District in New Taipei City in 2017. (2017, May). SanChong District Office.
2. Kashihara, S., Ueno, J., & Morita, T. (1998). *Study on shelters in great Hanshin Earthquake*. Osaka: Osaka University Press. (In Japanese).

Safety Study on Load-Limiting Device for Rope Rescue

San-Ping Ho, Hue-Pei Chang, Chin-Feng Chen, Steven Chiang, Wei-Chih Fang and W. K. Chow

Abstract This paper provides tests on Tandem Prusik, and two mechanical devices as load-limiting device. The test results on a 3-wrap Prusik demonstrated that it would eventually break when overloaded, which contradicts to popular traditional belief that it will not continuously hold and substantially slip on rope if overloaded. The same tests conducted on mechanical devices show results of a positive maximum static slip of about 600 kg_f, above which the rope will substantially slip to maintain the tension force even with further pulling above this limit. This novel finding is critical as it provides sound indication that the device would automatically make adjustments for the tension to be kept safe in the safe zone in field operations.

Keywords Prusik · Overloaded · Static slip · Substantially slip

1 Introduction

Tensioned rope systems (also called highline or cableway), by definition a rope rescue transportation systems where a track line (s) or runway line (s)/rope (s) is anchored, crosses a span and is pulled tight enough to safely support the weight of a rescuer and subject/patient. A considerable amount of tension is placed in the rope (s) to

S.-P. Ho · H.-P. Chang
Department of Occupational Safety and Health, Chang Jung Christian University, Tainan City 71101, Taiwan, ROC

C.-F. Chen (✉)
Occupational Safety, Health and Medicine Research Center, Chang Jung Christian University, Tainan City 71101, Taiwan, ROC
e-mail: fsl.ccf@mail.cjcu.edu.tw

S. Chiang
TRIS (SAFETY) Pte. Ltd., Singapore 520114, Singapore

W.-C. Fang
Fire Department, New Taipei City Government, New Taipei City 220, Taiwan, ROC

W. K. Chow
Department of Building Services Engineering, The Hong Kong Polytechnic University, Hong Kong, Hong Kong, China

allow it to function as a track or runway. This track or runway then is "ridden" on by a carriage/trolley consisting of pulleys, and pulled side to side with control/tag lines. Tensioning a highline just by pulling "as hard as you can" is dangerous, regardless long or short span. Even systems built out of wire ropes can fail due to slight damage or local fatigue to the ropes, detachment from an anchor drum, or even failure in the system components such as the load limiter [1]. Numerous rescuers have thus discounted and shy away the use of highline citing safety reasons despite this being an ultimate solution in technical rescue for working over water and obstacles, across ravines or buildings, or over collapsed structures, and so on.

Caution is required in determining tensioning limits. When the highline is rigged/setup and pulled with substantial amount of tension, it makes the angle larger (such as θ_1 increasing to θ_2 in Fig. 1), thus causing a higher force multiplication when loaded. Research conducted by Valet et al. [2] shows that wind and water drag might also increase the load on the ropes and cause them to break. In addition, the bouncing movement at the rescue load can result in load variations at the anchor with increased force.

The following rules of thumb are used to help estimate whether the tension on highline is below acceptable limits:

1. One man rule: Tensioning by no more than one person could pull without any mechanical advantage [3].
2. Ten-percent rule: For every 91 kg$_f$ (200 lb$_f$) of load, there should be a sag in the highline/cableway main line (s) equal to 10% of the span of the system, before the system is loaded [4].
3. Fifteen-degree rule: The highline/cableway main line (s) is not loaded and to have a 15° angle when horizontal. For inclined, measure the angles of sag an equal distance from both ends (the sum of the two angles must equal 30°) [5].
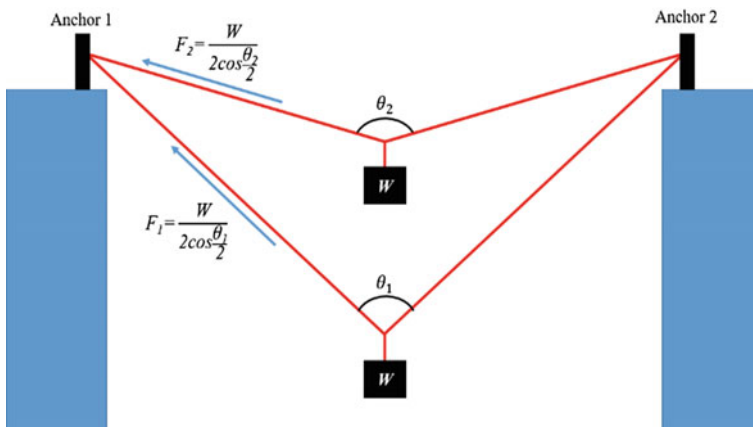
Fig. 1 Load of rope and anchor at different angles

4. Number of persons rule: Number of persons × mechanical advantage system = pre-determined factor for diameter of rope use. Pre-determined factor of 12 for 7/16 inch or 11.1 mm rope [6].
5. Two main lines: Using a pair of 2:1 mechanical advantage systems in series tensioning the two highline/cableway main lines equally [3].

However, these rules of thumb have their limitations of use to achieve the objectives for rescue load in the rescue situation. Such a rescue load consists of two persons simultaneously (rescuer and subject/victim) with a total weight of up to 280 kg$_f$. To achieve the objective for rescue load, it is crucial to tension the highline within acceptable limits and ensure release of undesirable tension in the system to prevent catastrophic failure.

While a dynamometer or other force measurement devices are the only way to determine the exact forces being placed on the system, it would be practical in the field to incorporate a load-limiting device into the system to provide a backup should the system be overloaded. The common practices incorporate the use of load-limiting devices such as the Tandem 3-wrap Ø8 mm Prusik knots/hitches [7, 8] or mechanical devices (e.g., available types of descenders, belay devices, etc.) for determining tensioning limits to act as warning when a specific load has been exceeded. However, the maximum load where the rope slip under specific loads varies, and very much depends on the load rating of the load-limiting device use. Hence, there is a need to identify and test the suitability of the load-limiting device. In this paper, the 2-wrap and 3-wrap Prusiks and mechanical devices (SAR A–B Descender and Petzl I'D S) are selected for the test and comparison of their suitability as load-limiting devices; and we explore further to understand the performance requirements and recognize the contributing factors to consider when selecting a proper load-limiting device.

2 Methods

2.1 Test Samples

The following tests aims to examine the grip and slip occurrence of the standard 2-wrap and 3-wrap Ø8 mm Prusik, SAR A–B Descender, and Petzl I'D S, on sample test ropes of different manufacturers and compare their suitability for use as load-limiting devices, through a series of slow–pull tests. The slow–pull tests were carried out in accordance with the scheme given in Table 1.

2.2 Test Arrangement and Procedure

This research used a tensile strength tester, with the tensile speed set at 300 mm/min. Before testing, the sample test rope was fixed onto the latch of the tester by a single

Table 1 Test conditions and samples

Test number	Load-limiting device	Sample test rope[a]
Test-1–Test-3	Edelrid—Powerloc expert SP/2–wrap Ø8 mm Prusik	Tendon—low stretch rope/Ø11 mm × 16–plait
Test-4–Test-6	Edelrid—Powerloc expert SP/3–wrap Ø8 mm Prusik	Tendon—low stretch rope/Ø11 mm × 16–plait
Test-7–Test-9	SAR A–B Descender[b]	Tendon—low stretch rope/Ø11 mm × 16–plait
Test-10–Test-12	Petzl I'D S[c]	Tendon—low stretch rope/Ø11 mm × 16–plait
Test-13–Test-15	SAR A–B Descender[b]	SAR—low stretch rope/Ø11 mm × 16–plait
Test-16–Test-18	Petzl I'D S[c]	SAR—low stretch rope/Ø11 mm × 16–plait

[a]Sample test rope: conforms to EN 1891 Type A—personal protective equipment for the prevention of falls from a height—low stretch kernmantel ropes
[b]SAR A–B Descender: conforms to EN 341 class C and EN 12841 Type C
[c]Petzl I'D S: conforms to EN 341 class A, EN 12841 Type C, and NFPA 1983 technical use

knot, and then the load-limiting device was connected with the sample test rope and strength tester. Figure 2a–c is test photographs of 3-wrap Ø8 mm Prusik, SAR A–B Descender and Petzl I'D S, respectively, as load-limiting device. After setup, in order for Prusik to firmly hold the rope sample, the system would first be set at a tension of 10 kg$_f$ before stretching began. Furthermore, this research used a thermal imager camera (Argus 4, made by e2v of England, 160 × 120 resolution), or IR camera, during the testing to observe the temperature distribution and heat transfer.
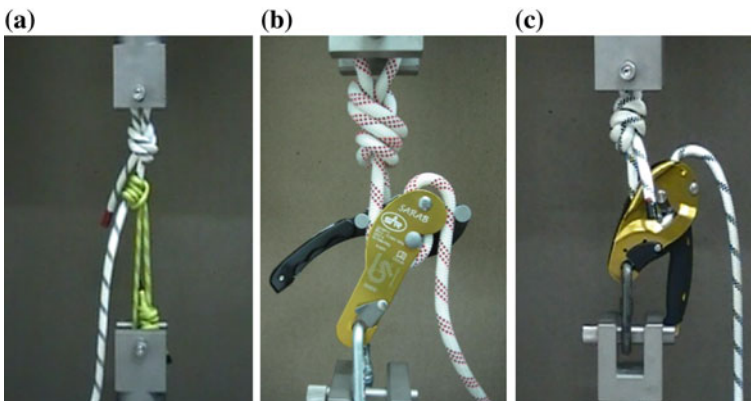
Fig. 2 **a** 3-wrap Ø8 mm Prusik on Tendon Ø11 mm low stretch rope; **b** SAR A–B Descender on SAR Ø11 mm low stretch rope; **c** Petzl I'D S on Tendon Ø11 mm low stretch rope

3   Results and Discussion

3.1   2-wrap and 3-wrap Ø8 mm Prusik on Tendon Ø11 mm Low Stretch Rope

Tests conducted by Long et al. [9] sets 400 kg$_f$ as the static test criteria to determine the force that the Prusik would hold without slipping. Our test results demonstrate that the 2-wrap Ø8 mm Prusik on Ø11 mm low stretch rope slips at average load below 400 kg$_f$. In three test runs, the rope slipped with tensions at 316, 338, and 365 kg$_f$, while the tensions during slipping were 191–275 kg$_f$, 199–284 kg$_f$, and 215–315 kg$_f$, respectively, as shown in Fig. 3a and Table 2. This shows that the 2-wrap Prusik does not produce enough gripping friction and hence justifies the common use of 3-wrap Ø8 mm Prusik on Ø11 mm low stretch rope in field operations. Our test results of 3-wrap Ø8 mm Prusik on Ø11 mm low stretch rope show no significant slippage, and eventual break at average load of 1,701.3 kg$_f$, as shown in Fig. 3b and Table 3. This coincides with the tests conducted by Goulet [10] that showed similar results. This result shows that the Prusik could slip till the system collapse because the rescuer could not observe the scenario to stop the rescue operation.
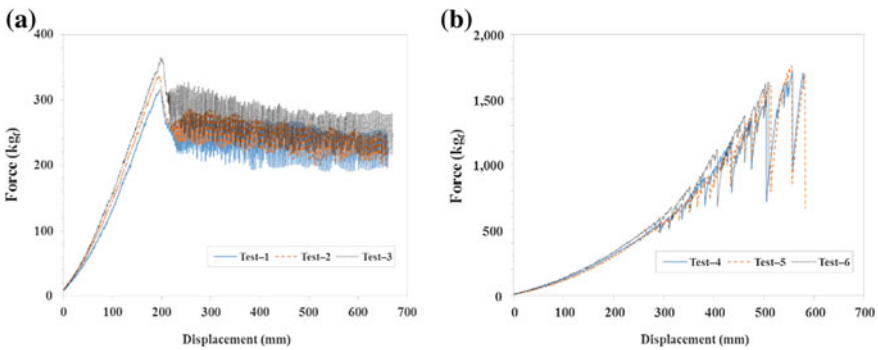
Fig. 3   Ø8 mm Prusik on Tendon Ø11 mm low stretch rope: **a** 2–wrap; **b** 3–wrap

Table 2   Test results of the 2-wrap Ø8 mm Prusik on Tendon Ø11 mm low stretch rope

Test number	Force to initiate sliding under static load (kg$_f$)	Tensions during slipping (kg$_f$)
Test-1	316	191–275
Test-2	338	199–284
Test-3	365	215–315

Table 3 Test results of the 3-wrap Ø8 mm Prusik on Tendon Ø11 mm low stretch rope

Test number	Breaking strength (kg$_f$)	Slipping distance on low stretch rope (cm)
Test-4	1,712	9.0
Test-5	1,759	9.2
Test-6	1,633	14.5

3.2 Mechanical Devices as Load-Limiting Devices

From the test results of using Tendon rope with SAR A–B Descender as the load-limiting device, the minimum static slip ranges from 520 to 621 kg$_f$. When the load surpasses this range, the minimum static slip decreases and drops to 551, 507, and 477 kg$_f$, respectively, unable to keep at a stable value, as shown in Fig. 4a. The stretching distance of tensile strength tester used in this study was not enough for the rope to break, thus the corresponding stable values could not be found. When using Petzl I'D S as load-limiting devices, the minimum static slip of the first test was 755 kg$_f$, significantly higher than the succeeding two tests by 85 and 94 kg$_f$; however, the load for the first test would stabilize between 609 and 651 kg$_f$, while the values for the succeeding two tests were 560–615 kg$_f$ and 600–661 kg$_f$, as shown in Fig. 4b. The results of Test-7 to Test-12 are shown in Table 4.

The tests results have shown that the minimum static slip of SAR Ø11 mm low stretch rope ranges from 535 to 619 kg$_f$, and 537 to 641 kg$_f$ with SAR A–B Descender and Petzl I'D S as load-limiting devices, as shown in Table 5 and Fig. 5. More ideal stable values were obtained when using SAR rope than Tendon rope.

The tests on Tendon rope and SAR rope with Petzl I'D S also show results of average static slip of 618 and 575 kg$_f$, respectively. However, the load of Tendon rope with SAR A–B Descender trended down. In addition, the above-mentioned combinations demonstrated similar grip and slip occurrence during the test and performance test results have similar outcomes as SAR A–B Descender on SAR Ø11 mm low
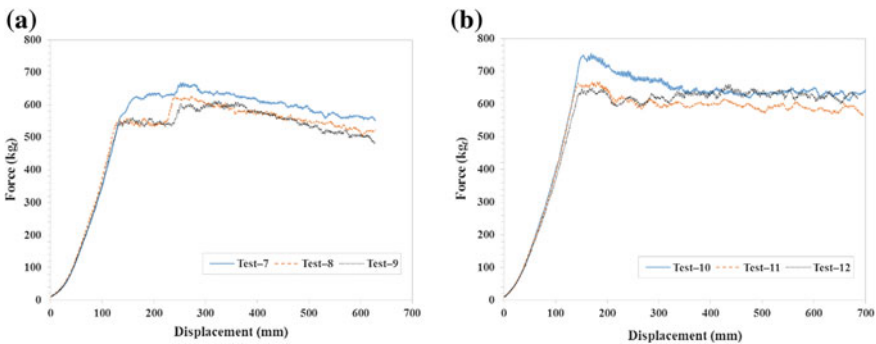
Fig. 4 Mechanical devices on Tendon Ø11 mm low stretch rope: **a** SAR A–B Descender; **b** Petzl I'D S

Table 4 Test results of SAR A–B Descender and Petzl I'D S on Tendon Ø11 mm low stretch rope

Test number	Force to initiate sliding under static load (kg$_f$)	Tensions during slipping (kg$_f$)
Test-7	621	Decreases and drops to 551
Test-8	548	Decreases and drops to 507
Test-9	520	Decreases and drops to 477
Test-10	755	609–651
Test-11	670	560–615
Test-12	661	600–661

Table 5 Test results of SAR A–B Descender and Petzl I'D S on SAR Ø11 mm low stretch rope

Test number	Force to initiate sliding under static load (kg$_f$)	Tensions during slipping (kg$_f$)
Test-13	600	565–614
Test-14	535	512–567
Test-15	619	588–619
Test-16	626	559–641
Test-17	594	541–606
Test-18	575	537–595
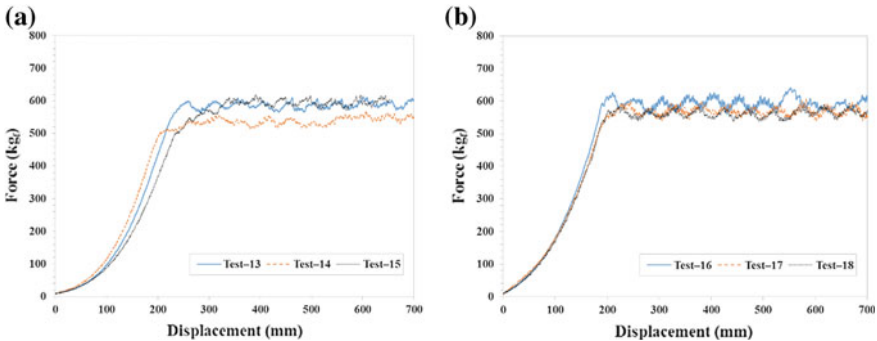
Fig. 5 Mechanical devices on SAR Ø11 mm low stretch rope: **a** SAR A–B Descender; **b** Petzl I'D S

stretch rope. Nevertheless, we strongly do not recommend using these combinations until it has been tested and verified for compatibility by the manufacturer (in this case, SAR). Furthermore, as mentioned earlier, the variables in used ropes (with the each manufacturer's unique design and weaving of the ropes) are much more complex than the tests performed for the purpose of this paper, we recommend further research work on used ropes in relevance to field operations.

3.3 Visual and Tactile Examinations

Visual and tactile examinations performed after each test verified that there were no significant findings from the visual and tactile examinations after each test, except the test on the 3-wrap Ø8 mm Prusik.

During the experiment, cameras and an IR camera were used to monitor the stretching process and heat transfer of the load-limiting device with the sample test rope. A 3-wrap Ø8 mm Prusik provides better grip with the added wrap for more surface friction. During the test, when tensioned, the automatic twisting action of the 3-wrap Ø8 mm Prusik on the sample test rope acts to increase the friction coefficient of the Prusik/rope interface. Figure 6a is the status before stretching, while Fig. 6b shows twisting of the Prusik during stretching. Such friction at the Prusik/rope interface generates heat. When further tensioned, the heat generated is retained at the Prusik/rope contact surface and unable to dissipate, as shown in Fig. 6c. Eventually, the Prusik breaks at its breaking strength. The visual and tactile examinations verified signs of deformation of the sample test rope due to heat transferring from the Prusik. Signs of melting and tearing of the sample test rope were also noted; after removing the sheath, the core was observed to possess ruptures and damage to the fibers, as shown in Fig. 7. As there was no significant slippage observed during the pull test, it can be deduced that the deformation of the sample test rope had led to a tighter grip until the Prusik breaks eventually.

Compared to 3-wrap Prusik, 2-wrap Prusik possesses insufficient grip and friction, therefore when tension surpasses the minimum static slip (or maximum static load), slipping occurs; Fig. 8a, b show that the relative positions of 2-wrap Prusik and sample

(a) **(b)** **(c)**
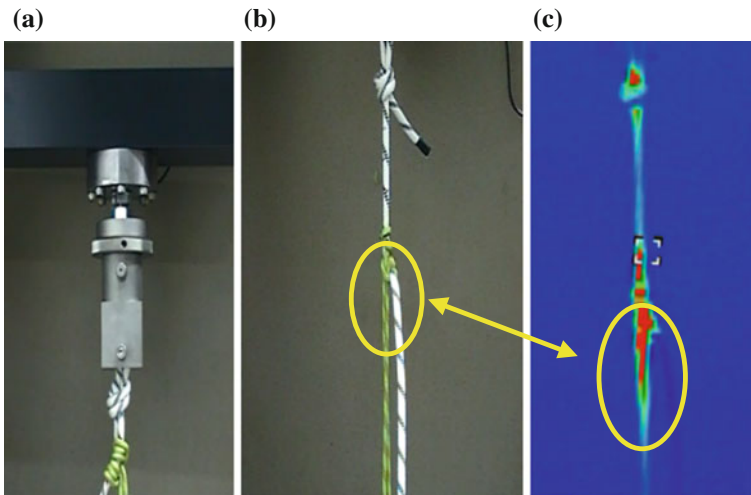
Fig. 6 3-wrap Prusik on Tendon Ø11 mm low stretch rope: **a** before stretching; **b** during stretching; **c** during stretching, with heat centralized at Prusik (IR camera photo)
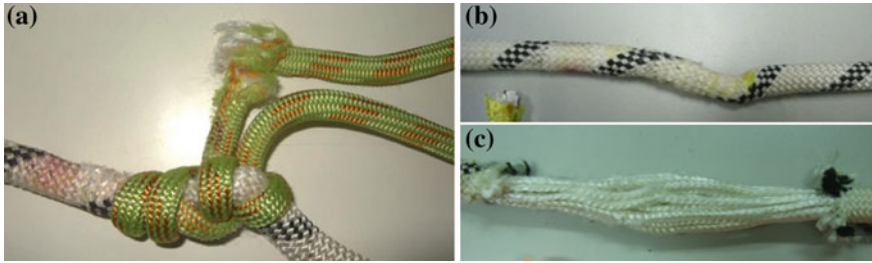
Fig. 7 Test results of 3-wrap Prusik on Ø11 mm low stretch rope: **a** Prusik ruptured; **b** sample test rope deformed, with sheath partially melted and torn; **c** core damage
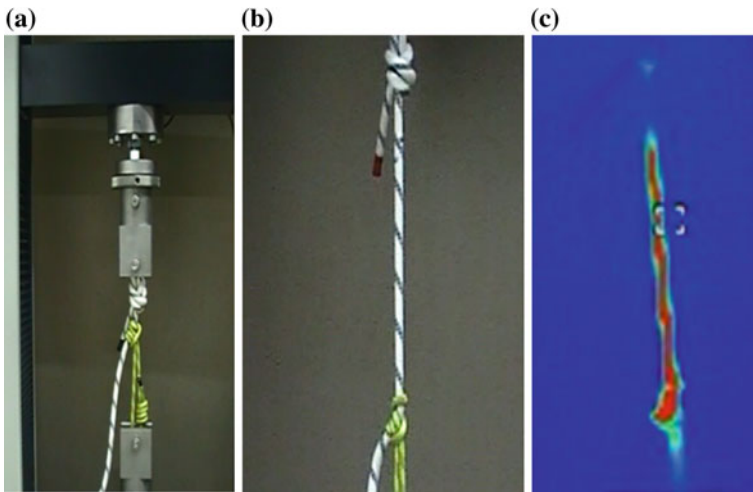
Fig. 8 2-wrap Prusik on Tendon Ø11 mm low stretch rope: **a** before stretching; **b** during stretching; **c** IR camera photograph (during stretching)

test rope did not change during stretching, therefore not possessing the twisting which came with 3-wrap Prusik. In Fig. 8c, the heat produced during stretching of 2-wrap Prusik evenly distributed on the Prusik and Tendon rope, unlike the 3-wrap Prusik in which the heat was concentrated on the Prusik, while the exterior of the sample test rope did not possess any deforms. The core was also intact with no fiber ruptures, as shown in Fig. 9.

In the tests for mechanical devices—SAR A–B Descender and Petzl I'D S, there were no damage to the load-limiting devices, tearing or breaking of sample test ropes, or deformation of the sample test ropes due to even distribution of heat on the sample test ropes (Fig. 10), such as the 2-wrap Prusik test, and heat transferred from the load-limiting devices. The sample test ropes, SAR A–B Descender and Petzl I'D S, can still function as intended.
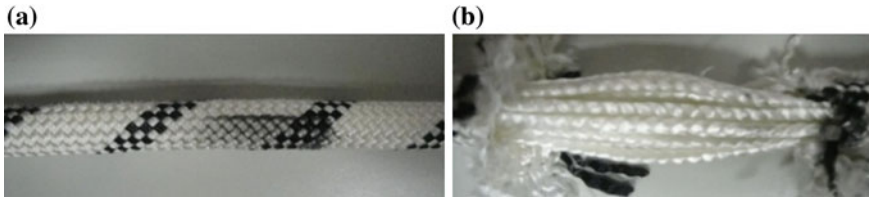
Fig. 9 Test results of 2-wrap Prusik on Ø11 mm low stretch rope: **a** sheath possessed no damage or melting; **b** core status
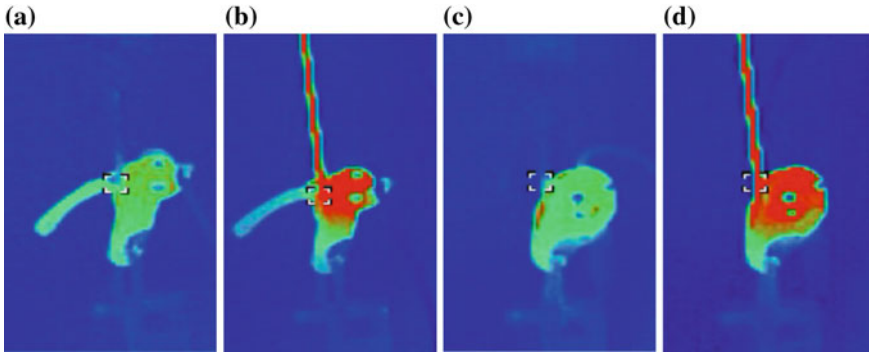
Fig. 10 a SAR A–B Descender before stretching; **b** SAR A–B Descender during stretching; **c** Petzl I'D S before stretching; **d** Petzl I'D S during stretching

3.4 Comparison of Suitability as Load-Limiting Device: Prusik Versus Mechanical Devices

From our study of the two types of load-limiting devices, we draw a comparison of their performances to understand their suitability as load-limiting devices.

Base on the test and the results obtained, we do not recommend the use of 3-wrap Ø8 mm Prusik as compared to mechanical device (SAR A–B Descender and Petzl I'D S) as load-limiting device for highline system. However, being the knot-based and traditional approach, the Prusik is widely and popularly used as a load-limiting device for highline systems. Therefore, there is the need for users to understand the interface dynamics between the Prusik loop and the host rope. Unlike a mechanical device, the interface behavior and the factors that affect the performance are considerably different. Cordage/fiber in all slippage may vary and at best, only approximations about grip versus slippage can be applied. As much concern is raised about melting due to friction when the knot slides under heavy loading, there is much scope for further work on Prusik knots to address such concerns.

The SAR A–B Descender and Petzl I'D S conform to EN 12841 Type C. The grip and slip occurrence during the test and results have shown that it does not cause any permanent deformation or damage to the sample test ropes due to heat

transferring from the devices. EN 12841 Type C has requirement on temperature rise for Descender—the temperature should not rise to a point or develop higher than 48 ØC on uncoated metal and should not have effect on the rope (cause permanent deformation or damage).

As it is important to tension the highline within the recommended acceptable limits and ensure release of undesirable tension in the system to prevent catastrophic failure. Mechanical device is preferred and recommended as a load-limiting device in achieving the objective for rescue load in tensioned rope systems. There are numerous mechanical devices available in the world (such as the use of Petzl GRIGRI by Goulet [10] and the use of descenders by Long et al. [9]) and would perform in a predictable fashion that is very much similar to SAR A–B Descender or Petzl I'D S. These devices may or may not conform to EN 12841 Type C. Nonetheless, for use as load-limiting device, it is recommended that the system (the selected mechanical device and rope together) to be tested and confirmed by the manufacturer for compatibility requirement.

4   Conclusions

In this paper, we have examined the grip and slip occurrence of the standard 2-wrap and 3-wrap Ø8 mm Prusik, SAR A–B Descender, and Petzl I'D S on sample test ropes of different manufacturers and compare their suitability for use as load-limiting devices, through a series of slow–pull tests. Our study has shown that a 2-wrap Ø8 mm Prusik on Ø11 mm low stretch rope slips at average load below 400 kg_f, whereas a 3-wrap Ø8 mm Prusik although provides better grip with the added wrap for more surface friction, showed no significant slippage, and eventually broke at an average load of 1,701 kg_f. It was then deduced that the deformation of the sample test rope had led to a tighter grip until the Prusik breaks eventually. Comparing the performances of the two types of load-limiting devices based on our test results, the use of mechanical devices is recommended and suitable for use as load-limiting devices since it will not cause permanent deformation or damage to the highline main line (s)/trackline (s)/runway line (s) for a rescue load to be transferred. We then recommend and advise that for use as load-limiting device, the system (the selected mechanical device and rope together) has to be tested and confirmed by the specific manufacturer for compatibility requirement. Finally, we also suggest areas that merit further investigation for future research work.

References

1. Piskoty, G., Zgraggen, M., Weisse, B., Affolter, Ch., & Terrasi, G. (2009). Structural failures of rope–based systems. *Engineering Failure Analysis, 16,* 1929–1939.

2. Valet, S., Piskoty, G., Michel, S., Affolter, Ch., & Beer, M. (2013). Accident caused by dynamic overloading of a ship mooring rope. *Engineering Failure Analysis, 35,* 439–453.
3. Frank, J. A. (1998). *CMC rope rescue manual* (3rd ed.). CMC Rescue Inc., CA, USA.
4. Vines, T., & Hudson, S. (1989). *High angle rescue techniques: A student guide for rope rescue classes*. Kendall/Hunt Publishing Company, CA, USA.
5. Padgett, A., & Smith, B. (1987). *On rope* (1st ed.). National Speleological Society, AL, USA.
6. Smith, B., & Padgett, A. (1997). *On rope* (2nd ed.). National Speleological Society, AL, USA.
7. Larson, A. (1990). *New rescue product: The Prusik Minding Pulley* (p. 18). Nylon Highway 30 (as Accessed on http://caves.org/section/vertical/nhback/NH30.pdf).
8. Laidlaw, K. N. (2016). *Considerations for rope rescue in 2016* (as Accessed on http://sarconsiderations.com).
9. Long, A., Lyon, M., & Lyon, G. (2001). *Industrial rope access—Investigation into items of personal protective equipment*. Health and Safety Executive–Contract Research Report, Report No. 364/2001, Health and Safety Executive, UK.
10. Goulet, M. (2001). *Take the load off highline*. 2001 International Technical Rescue Symposium, Golden, CO, USA.

Study on Subway Station Evacuation Performance by the Improved Cellular Automata Evacuation Model

Peihong Zhang and Meng Lan

Abstract By introducing toxicity coefficient to the static force field and pheromone model to the dynamic force field, an improved cellular automata evacuation model (ICAEM) is developed. Evacuation experiments in an 11 m × 8 m classroom are carried out, the time from their initial position to the single exit or double exits of the classroom and the stagnation time near the exits are recorded and compared with the simulation results to validate the ICAEM model, to check the influencing factors of the exit position K_S, the repulsive coefficient K_R, and the pheromone damping coefficient ρ in the model. The results show that when the pheromone damping coefficient $\rho = 0.5$, the self-lining phenomenon is significant. If $K_S = 1$, $K_R = 0.12$, the simulation result is very consistent with the actual evacuation time in the experimental tests. Finally, the ICAEM model is applied in a 118 m × 36 m twenty-first-century subway station platform where there are a total of 2500 persons from two trains waiting for evacuation. The simulation error is reasonable comparing with the calculation results by engineering design code of PRC and the Togawa's formula. It is found that the original layout of EXIT 2 obstructed the evacuation flow of the station platform at a certain degree, resulting in bidirectional counter flow and stagnation near the exit. After improving the layout of the EXIT 2 on the platform based on the simulation results by ICAEM, the RSET of the whole platform is shortened and the stagnation phenomenon is attenuated. The ICAEM model is applicable and meaningful to the crowd evacuation and performance-based safety design in high densely populated public places.

Keywords Crowd evacuation behavior · Cellular automata · Pheromone ·
Following phenomenon · Required safety evacuation time

P. Zhang (✉) · M. Lan
Department of Safety Engineering, Northeastern University, Shenyang, Liaoning 110819, P. R. China
e-mail: zhangpeihong@mail.neu.edu.cn

1   Introduction

Because of the complex space structures, combining with the impact of fire, toxic gases or other similar kind of emergent scenarios, the densely populated people are always in chaos once in emergent hazardous situations, leading to serious consequences of casualties.

Interdisciplinary approaches are widely applied in the field of crowd stampede accident prevention and control field. Pauls suggested that crowd incidents often exhibit a failure of front-to-back communication [1]. Besides the comprehensive effect of inadequate facilities and deficient crowd management, Fruin [2] suggested that four factors increase the probability of crowd accidents, i.e., time, space, information, and energy. Sime [3] argued that a comprehensive crowd accident prevention approach needs to integrate both the psychological aspects and the engineering frames of references. Berlonghi [4] divided the triggering factors into nine types, such as the crowd status and their familiarity degree to the surroundings. Dickie [5] summarized that the common threads to crowd accident are inadequate planning, excited crowd, lack of crowd management and a flaw or hazard in a facility, etc. Based on the analysis of the trample disaster at Mihong bridge in China in 2004, Zhen et al. [6] concluded that the main causes of the crowd disaster are the poor estimation of the tourist population, dereliction of duties, deficient communication, and the design fault of the bridge, etc. Alnabulsia and Drurya [7] survey 1194 pilgrims at the 2012 Hajj and concluded that social identification has a strong effect on the crowd safety of high density.

With the development and popularization of computer technology, scholars have developed continuous and discrete models in the crowd evacuation simulation field. On the basis of goal-directed behavior theory [8], Lee and Hughes [9] developed crowd motion models using Navier–Stokes equations at both high and very high densities of pedestrians and developed a crowd accident prevention strategy. Contrary to the rational psychology theory and the certainty relationship between flow velocity and physical environment, it has been argued that the crowds' behavior is unlikely to be predicted easily because crowds are irrational and erratic. Helbing [10, 11] established social force model for pedestrian dynamics to analyze the attraction and repulsion between pedestrians, as well as pedestrian and constructions. By social force model, it can be deduced that high desired initial velocity can lead to slow flow speed at exit, jam at the bottleneck of evacuation corridor, longer congestion time, etc. Jammed crowd can then crush people to asphyxiation, leading to more panic or excitement emotion of the crowd, which will finally, resulted in fatalities [11]. Cellular automata (CA) model makes the space and time discrete in a certain way, and the automata moves to the neighbor cell at next time step according to the occupied status of neighbor cells, the human behavior rules, the building environment status, etc. The static floor field and the dynamic floor field are applied to describe the affection on automata by the aforesaid parameter. The static floor field only depends on the current status of the building environment and structure, such as the distance between the current cell and the exit. The dynamic floor field is modified according

to the human behavior, evacuees distribution, and some other factors that changing with the time. CA models have been successfully used to describe crowd evacuation dynamics under the impact of obstacles, guides, visibilities, etc., and illustrate significant characteristics of simplicity, flexibility, and efficiency [12–17]. As is well known, fire or accidental situation parameters spread with great randomness and uncertainty resulting in the complex and changeable status of the evacuation corridors and exits, which makes the availability of the route between the current cell and the exit changeable. What is more, the human evacuation behavior shows significant common features with an ant colony's food-searching activities [18–21], such as looking for the shortest distance and Going With the Crowd (GWC). An improved cellular automata model (ICAM) is established to comprehensively express the GWC behavior in the dynamic floor field of the CA model combing with the improvement on the static floor field by the equivalent distance between the current cell and the exit. The ICAM model is verified by the experimental tests in classroom and further applied in the safe evacuation performance evaluation of the Shenyang twenty-first-century subway station.

2 Improved Cellular Automata Model

The classical four Von Neumann neighborhoods are used to quantify the static force field and the dynamic force field of the cellular automata model. The evacuation motion of each cell at the next time step $(t + 1)$ is only determined by the cell status at its present time t and the four neighbor cells. The motion probability $P_{i,j}$ is used to express the results of the various interactions with neighbor cells, obstructions, exits, etc., in the evacuation process as illustrated in Eq. (1).

$$P_{i,j} = K_s P_{S-i,j} + K_D P_{D-i,j} \tag{1}$$

where,

$P_{i,j}$ represents the probability of selecting the cell (i, j) as the next target;
$P_{S-i,j}$ represents the probability that the (i, j) cell is the next target under the static region;
$P_{D-i,j}$ represents the probability that the (i, j) cell is the next target under the dynamic region;
K_S and K_D are the static region influence factor and the dynamic region influence factor, respectively;

2.1 Improved Static Force Field with the Introduction of the Toxicity Coefficient to the Static Force Field

The target probability $P_{S-i,j}$ for selecting the cell (i, j) in the static floor field is expressed as Eq. (2).

$$P_{S-i,j} = \frac{S_{i,j}}{\sum_A S_{i,j}}(1-\alpha_{i,j}) \tag{2}$$

where,

$S_{i,j}$ represents the "static force field" of the cell (i, j);
$\sum_A S_{i,j}$ represents the sum of the "static force field" of the cell (i, j) and the neighborhood cells. A represents the set of cell (i,j) and the four neighbor cells around;

$$\sum_A S_{i,j} = (S_{i,j} + S_{i-1,j} + S_{i+1,j} + S_{i,j-1} + S_{i,j+1}) \tag{3}$$

$\alpha_{i,j}$ is the current occupied status of the cell (i, j). If the cell (i, j) is occupied, $\alpha_{i,j} = 1$, if the cell (i, j) is empty, $\alpha_{i,j} = 0$;

The "static force field" $S_{i,j}$ of the cell (i, j) is calculated by Eq. (4):

$$S_{i,j} = \frac{\varepsilon_{i,j}}{d_{i,j}^2} \tag{4}$$

where

$d_{i,j}$ represents the original geometrical distance from the cell (i, j) to the exit;
$\varepsilon_{i,j}$ is the available coefficient of the route from the cell (i, j) to the exit. For example, if the route has been completely filled by the toxicity smoke or high temperature flame, $\varepsilon_{i,j} = 0$; if the route is completely safe, $\varepsilon_{i,j} = 1$; if the route is partially filled with flame or smoke, $0 < \varepsilon_{i,j} < 1$.

2.2 Improved Dynamic Force Field with the Introduction of Pheromone

The dynamic regional effects of this model include the interaction between automata, as well as automata and the building construction around, etc.

2.2.1 Repulsive Action

Personnel in the evacuation process always do not want close contact with other people or obstructs in the evacuation process, which is called the repulsive action.

The repulsive probability $R_{i,j}$ of the cell (i, j) in the evacuation process is introduced based on the Sigmoid function in the neurology to describe the human evasion response.

$$R_{i,j} = \frac{1}{1 + e^{-\delta V}} \times (1 - \beta_{i,j}) \tag{5}$$

Among which,

$\delta \in [0, +\infty)$ represents the hard coefficient, the hard coefficient between people, between people and the wall are taken as the same value, $\delta = 0.2$;
V represents the relative velocity of the cell (i, j);
$\beta_{i,j}$ represents the repulsive degree by the occupancy state of the cell adjacent to the cell (i, j). $\beta_{i,j} = 1$ if it is occupied, $\beta_{i,j} = 0$ if it is empty.

2.2.2 Attractive Action by the Introduction of Pheromone

It is well known that the GWC phenomenon is common in the emergent evacuation process, which is much similar to the ant in the food searching and carrying. The pheromone concept in ant colony optimization (ACO) algorithm is introduced to simulate the GWC phenomenon in crowd evacuation flow.

With the increase of the pheromone in a certain evacuation route, more persons are attracted to the specified route. The pheromone content of the cell (i, j) at the time step (t + 1) is calculated as follows:

$$C_{i,j}^{t+1} = \rho \sum_{0}^{t} C_{i,j} + 1 \tag{6}$$

$\rho \sum_{0}^{t} C_{i,j}$ represents the total amount of pheromone accumulated in the previous t time steps; when the cells in the grid region are occupied by a person at time t, then the content of pheromone in this cell increases by 1 unit. As the time step advances, the intracellular pheromone content is also updated. The attenuation coefficient ρ is used to prevent from the excessive increase of the pheromone of the cell (i, j). That is to say, if the pheromone of the cell (i, j) increases too much rapidly, pheromone attenuation should be acted to prevent from the congestion of the evacuation route to the cell (i, j).

The generation and attenuation of pheromones are updated at the same time so that each cell has its own pheromone content value. And, the GWC probability $F_{i,j}$ can be calculated by the Eq. (7)

$$F_{i,j} = \frac{C_{i,j}^t}{\sum_A C_{i,j}^t} \tag{7}$$

$\sum_A C_{i,j}^t$ represents the sum of the pheromone content of the cell (i, j) and its surrounding four neighborhood cells at the time step t;

In conclusion, the probability $P_{D-i,j}$ of the cell (i, j) under the dynamic region is calculated as follows:

$$P_{D-i,j} = K_R R_{i,j} + K_F F_{i,j} \tag{8}$$

K_R and K_F represent the repulsive action factor and the attractive action factor, respectively;

3 Model ICAM Validation by Evacuation Test in a Classroom

Two series of evacuation experiments in an 11 m × 8 m classroom in the Dacheng academic building of Northeastern University were conducted to validate the accuracy of the ICAM model. There are originally two 1-m-wide exits and 48 students in the classroom with totally 7 rows of chairs and tables. The initial experimental scenario is shown in Fig. 1.
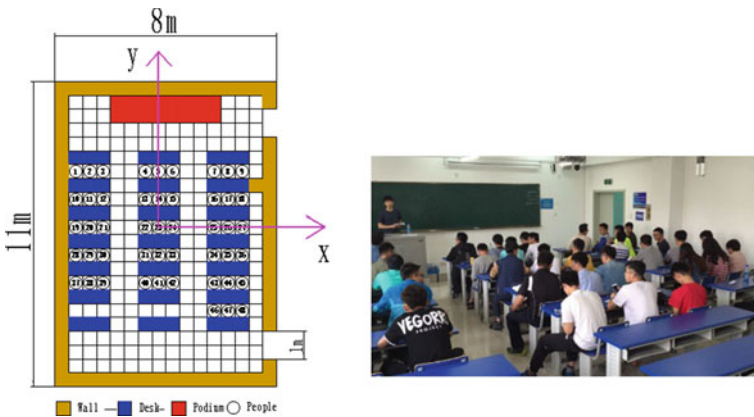
Fig. 1 Initial distribution of experimental classroom

3.1 ICAEM Model Verification by Experimental Tests

3.1.1 Experimental Tests

The exit quantity is changed in the tests and its impact on evacuation time is discussed, as shown in Fig. 2. In the two groups of experimental tests presented in the previous section, it can be seen that the initial pedestrian evacuation velocity decreased with the increase of distance to the exit at both of the two experimental scenarios. The reason can be attributed to the fact that they all know it is a drill and the desire to escape is not significant. Figure 3 illustrates the average evacuation time from their initial position at different rows to the exits, the average stagnation time near the exits, the percentage of the exit stagnation time in the total evacuation process with the change of the row number. In the experimental test with two exits, all of evacuees at No. 4 and No. 5 row select to escape from the nearer EXIT 2 after a small time period of observation and hesitation, so the average evacuation time of No. 5 row is smaller compared to No. 2, 3 and four, which is longer than No. 1 row.

Fig. 2 Tests in classroom with different quantities of exits

(a) Crowd clogged near the single exit

(b) Crowd stagnation attenuated by the availability of two exits

10 time-step   40 time-step   65 time-step

(a) evacuation simulation in classroom with one exit

10 time-step   30 time-step   50 time-step

(b) evacuation simulation in classroom with two exits
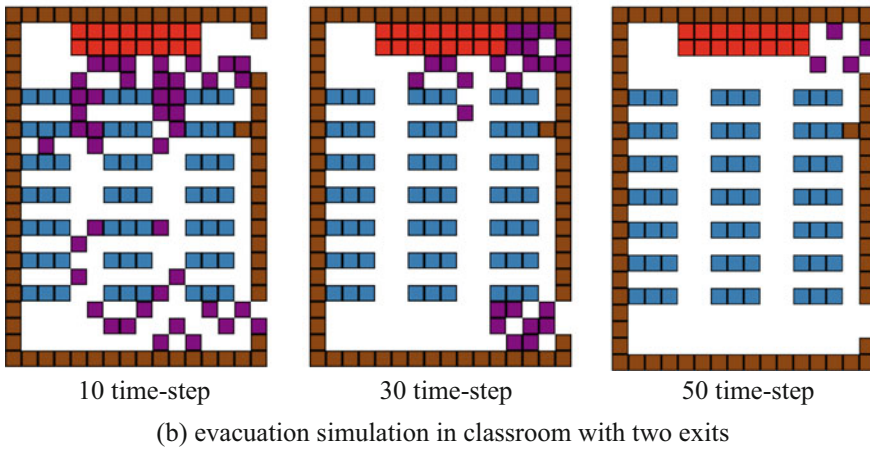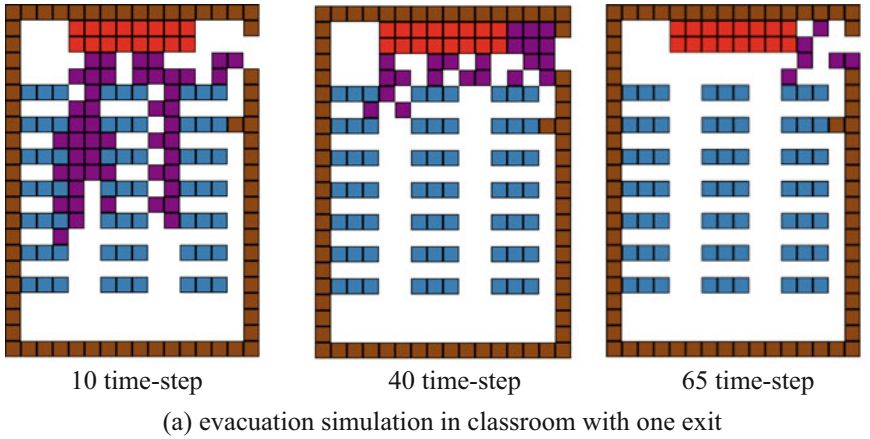
Fig. 3 Classroom evacuation simulation process

3.2 ICAEM Model Verification

The ICAEM model was constructed by using a 0.5 m × 0.5 m cell size in a 11 m × 8 m classroom size with a 2-m-long and 1-m-wide Podium. Each row can accommodate three people to sit down. Exit width is 1 m, two people can go out at the same time.

According to the experimental observations, in the ICAEM simulation process of the scenario with one exit, the initial average speed of people at the No. 1 row is assigned as 1.5 m/s with 0.2 m/s decreasing gradient per row. In the simulation process of the two exits, the initial average speed of the first row is set to 1.7 m/s with the same decreasing amplitude of 0.2 m/s. Because the individual physical quality of some student is very high, so the maximum initial speed is set to 2.0 m/s.

According to the detailed study on the static region and the dynamic region of the impact factor by Kirchner and Schadschneider [13], $K_S = 1.0$ and $K_D = 0.4$ is applied in this model. Based on the study of Yang et al. [14], $K_R = 0.12$ is taken in this model. For the attenuation coefficient ρ, the pheromone content is reduced by half and $\rho = 0.5$. The GWC influence factor is taken as $K_F = 0.12$ in this model. And, the collision hard coefficient $\delta = 0.1$ considering that there is no direct contact between the staff and the wall. The simulation process is shown in Fig. 3 as following.

An ID number is generated for each person at the initial stage of the simulation, and when the automata move out of the exit, the ID number of the cell is automatically traversed. The time step at which it escapes out of the classroom is recorded. The simulation results are compared with the experimental results as shown in Fig. 4.

As can be seen from Fig. 4a, the simulated average evacuation time (AET) is slightly slower than the experimental result for the students at the No. 1, 2, 3 row and faster than the experimental result at the No. 5 row with the error less than 5%.

Fig. 4 Validation of the simulation by experiment results
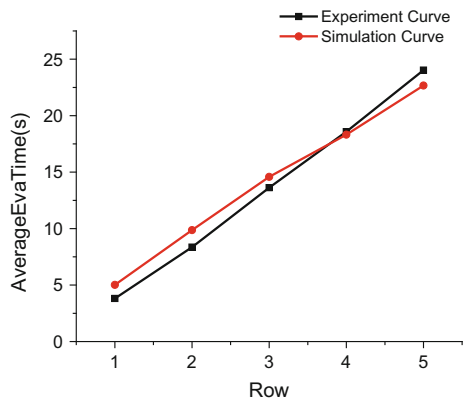
(a) one exit
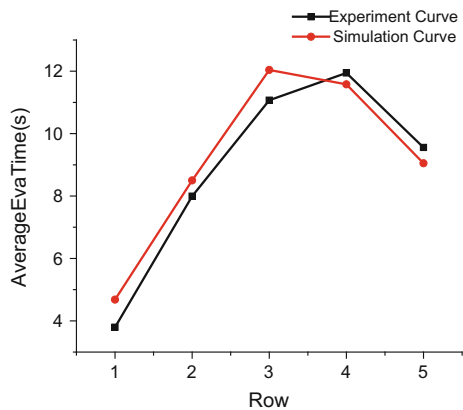
(b) two exits

For the case with two exits, similar simulations can be found that there is 8.4% error to the experimental results. So, the ICAM model is a good description of the human evacuation in classroom with obstacles at a satisfactory consistency and correctness to the experimental tests.

4 Simulation of Crowd Evacuation Behavior

4.1 Crowd Flow Around Obstacles

In order to illustrate the crowd flow phenomenon when encountering obstacle such as the column by ICAM, a population of 345 people was randomly distributed in a 40 m × 10 m corridor. The 345 people were randomly distributed as shown in Fig. 6a at the initial time step. The evacuation flow around obstacles is shown in Fig. 5b–f.

4.2 Self-lining Phenomenon

A total of 320 people are randomly distributed in a 25 m × 25 m room area with a 2-m wide exit at the bottom wall center. The evacuation process at different time steps is shown in Fig. 6.

It can be seen that the crowd moves directly and centrally toward the exit and two self-organized lining flows appear at the 40 time step, where the left row is the most obvious. When the time steps to 60 time step, the two lines are merged together and crowd stagnated at the exit.

5 ICAEM Application in Subway Station Platform

A subway station platform evacuation simulation is conducted based on the ICAEM model, the RSET time T_{sim} is deduced and verified by the subway emergency evacuation formula in China's Subway Design Code and Japan's Togawa evacuation time calculation formula.

The 118 m × 18.5 m Shenyang twenty-first-century subway station is designed for the two-way B-type train with six groups of car with six doors of 2.5-m wide separately. The specific floor plan of the Shenyang Century Subway Station is illustrated in Fig. 7.

According to the daily observations on the crowd density of the subway station, totally 2500 people are assumed to evacuate from two trains stopping at the station. The initial speed of the evacuees is set as 1.3 m/s. Assigning the exits attraction factor $K_S = 1$, the exclusion factor $K_R = 0.2$, the remaining parameters are consistent with

(a) 0 time-step

(b) 20 time-step

(c) 60 time-step

(d) 100 time-step

(e) 200 time-step

(f) 240 time-step
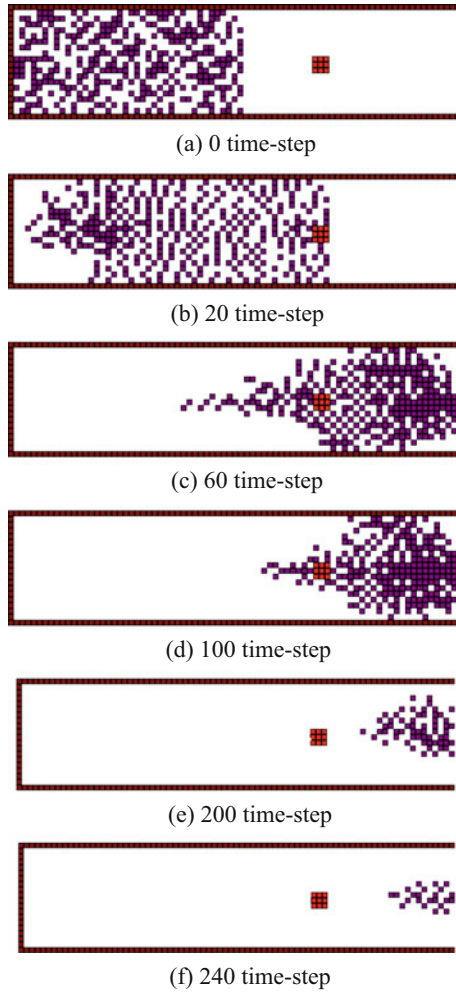
Fig. 5 Crowd flow stagnation phenomenon

(a) 0 time-step   (b) 40 time-step   (c) 60 time-step
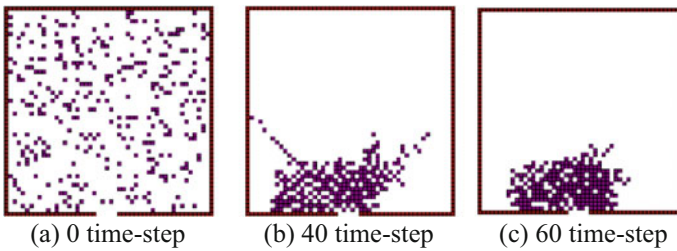
Fig. 6 Self-lining phenomenon in the crowd flow

Fig. 7 Floor plan of the Shenyang twenty-first-century subway station platform

the above discussions, the simulation process at 0, 150, 300, 450, 600, and 700 time step are illustrated in Fig. 8 to illustrate the ICAEM model application at the subway platform.

(a) 0 time-step

(b) 150 time-step

(c) 300 time-step

(d) 450 time-step

(e) 600 time-step
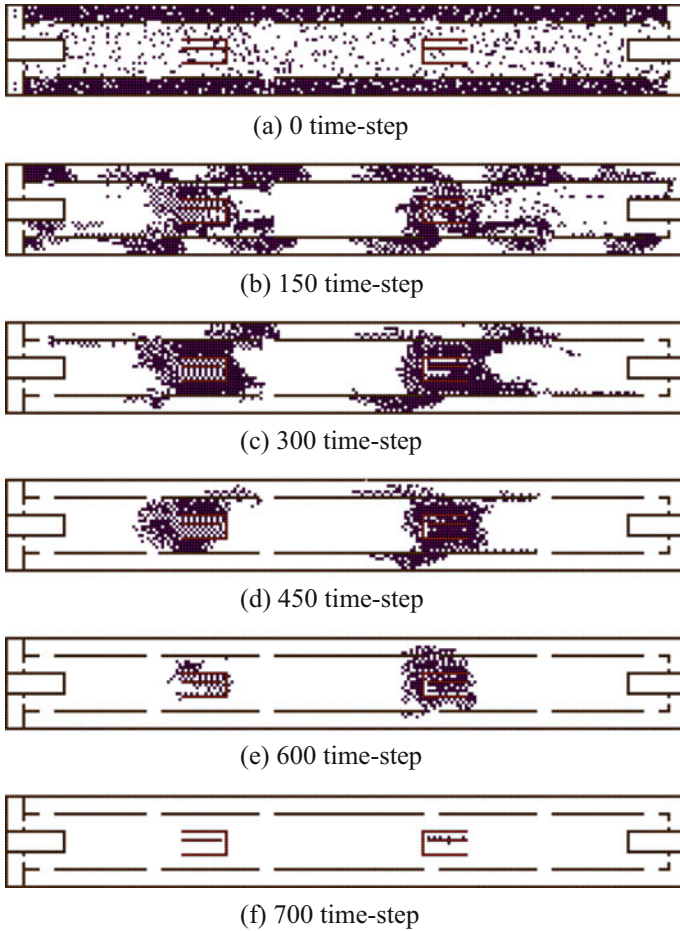
(f) 700 time-step

Fig. 8 Crowd evacuation at the Shenyang twenty-first-century subway station platform

From the simulation process, it can be seen that the whole evacuation process finished at the 700 time step (350 s) and crowd stagnation is serious near the EXIT 2.

The subway station evacuation time T_{spe} can be calculated by the Subway Design Code of China as follows.

$$T_{spe} = 1 + \frac{Q_1 + Q_2}{0.9[A_1(N-1) + A_2B]} = 1 + \frac{2000 + 500}{0.9[160 \times (2-1) + 167 \times 2]} = 337(S)$$

Among which,

T_{spe} is the evacuation time, min;
Q_1 is the number of passengers on the train, persons;
Q_2 is the number of passengers waiting on the platform, persons;
A_1 is the capacity of escalators, persons/(min m);
A_2 is the capacity of pedestrian staircase, persons/(min m);
N is the number of escalators;
B is the total width of the pedestrian staircase, m;

Japanese scholar Togawa proposed the evacuation time approximation formula for personnel-intensive places in 1995:

$$T_{exit} = \frac{N_a}{wC} + \frac{K_s}{V} \tag{9}$$

Among which,

T_{exit} is the evacuation time, S;
N_a is the total number of evacuation (persons);
C is the flow coefficient of the population, person/(m s);
w is the total effective width of the evacuated exits, m;
K_S is the distance from the nearest person to the safe exit, m;
V is the walking speed of the crowd, m/s;

Considering the fact that the evacuees will prefer to choose the exit nearest to their initial position, the evacuation of the twenty-first-century subway station platform can be divided into two parts. The final RSETs calculated by the Togawa formula are as follows:

RSET by exit 1:

$$T_{exit1} = \frac{N_{a1}}{w_1C_1} + \frac{K_{s1}}{V_1} = \frac{1150}{5.45} + \frac{6.8}{1.3} = 216(S)$$

RSET by exit 2:

$$T_{exit2} = \frac{N_{a2}}{w_2C_2} + \frac{K_{s2}}{V_2} = \frac{1350}{5.45} + \frac{6.8}{1.0} = 254(S)$$

It can be seen that the evacuation time of the EXIT 2 T_{move2} is bigger, so the final RSET of the twenty-first-century subway station platform 3.9% bigger than the result by the Subway Design Code of China and 41.3% bigger than the RSET result by Togawa formula.

Considering the fact that the comprehensive human decision behavior is not considered by Togawa equation and the equation by the Subway Design Code of China, we can say that the error between the ICAM model and the engineering calculation equation is reasonable, it can be concluded that the ICAM can simulate the RSET of the subway station platform evacuation at a certain degree of reliability.

5.1 Exit LayOut Improvement by ICAM Model

From Fig. 8, it can see that during the entire evacuation process of subway station platform, the stagnation situation at the EXIT 2 is the most serious, the evacuation at exit 1 finishes at a shorter time, but there are still some passengers stranded at No. 7, No. 8 door at the 600 time step. Why does this happen? The reason is shown in Fig. 9.

Figure 9 is a description of the crowd flow direction of people throughout the evacuation process. As can be seen in Fig. 9, passengers from door 7 and 8 self-organized into two parts, one heading toward exit 2 and the other facing toward the left platform area with less crowd density. Because this part of the flow of people moving toward the exit 2 results in a counter flow with the people from door 9 and 10 in the platform, the crowd flow speed slowed down.

In order to verify the layout effect of exit 2 on the crowd evacuation of the subway station, exit 2 is moved to the right with 18 cells, symmetry with the location of the exit 1 on the center of the platform. The simulation process after the move of the exit 2 is shown in Fig. 10.

Considering the comprehensive and random human behavior in the way-finding decision process in evacuation process such as the way selecting decision behavior, five times of simulation was done to get the total RSET of the subway station platform with different location of EXIT 2. The comparison of the simulation result is shown in Fig. 11.

It can be seen the evacuation simulation time RSET in the original subway station platform with no exit change is about 360 s. After changing the location of the EXIT
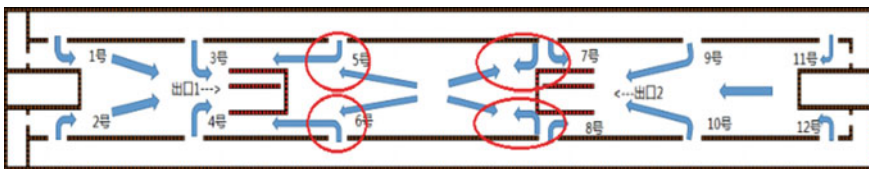
Fig. 9 Flow pattern of station platform layer simulation evacuation

(a) 0 time-step

(b) 100 time-step

(c) 300 time-step

(d) 500 time-step

(e) 600 time-step
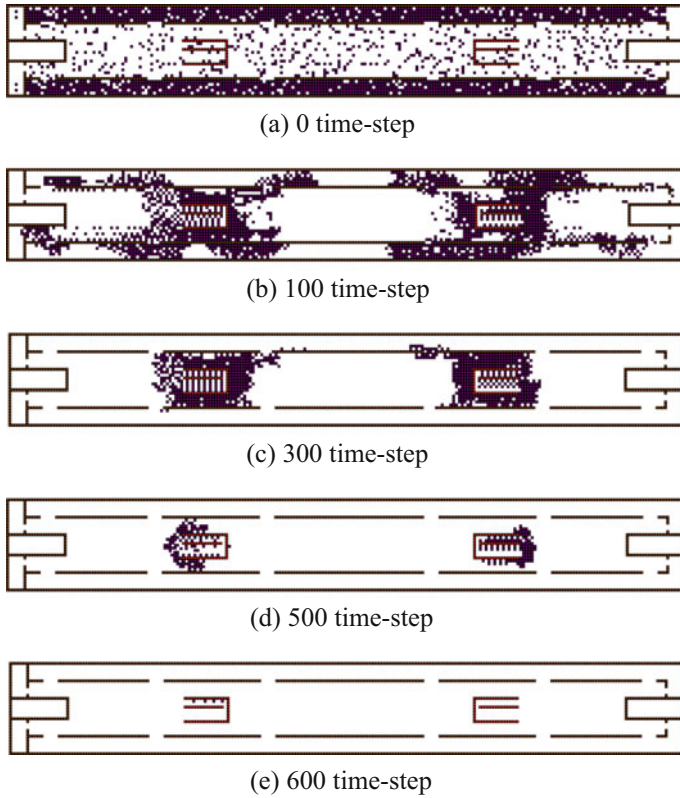
Fig. 10 Evacuation process at the platform with changing of the exit 2 location
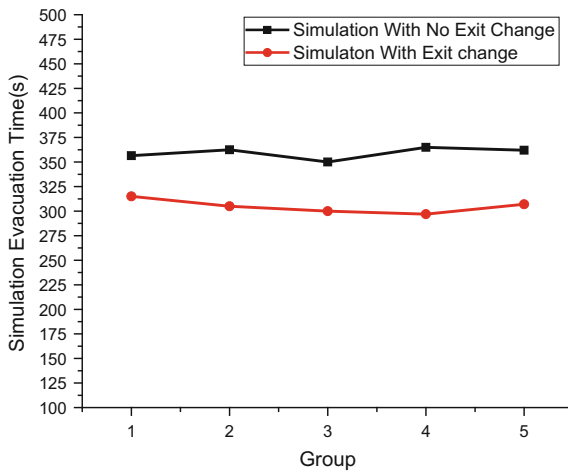
Fig. 11 RSET simulation result of the subway station platform with different layouts of exit 2

2, the evacuation time becomes 303 s, shortened by about 57 s. And, the stagnation status of the exit 2 is greatly mitigated. The optimized layout of the exit will have a great impact on the crowd evacuation in the densely populated subway station platform.

6 Conclusion

(1) Toxicity coefficient is introduced to the static force field and pheromone model to the dynamic force field, as a result, an improved cellular automata evacuation model (ICAEM) is established based on the classical four Von Neumann neighborhoods.

(2) Evacuation experiments in an 11 m × 8 m classroom are carried out, the time from their initial position to the single exit or double exits of the classroom and the stagnation time near the exits are recorded and compared with the simulation results. The ICAEM model is validated, and the influencing factors of the exit position K_S, the repulsive coefficient K_R, and the pheromone damping coefficient ρ in the model are checked. The results show that when the pheromone damping coefficient $\rho = 0.5$, the self-lining phenomenon is significant. If $K_S = 1$, $K_R = 0.12$, the error between the simulation result and the experimental tests is reasonable.

(3) The ICAEM model is applied in a 118 m × 36 m twenty-first-century subway station platform where there are a total of 2500 persons from two trains to evacuate. The simulation errors are reasonable comparing with the calculation results by the equation of the engineering design code of PRC and Togawa's formula.

(4) It is found that the original position of EXIT 2 results in bidirectional counter flow and serious stagnation near the EXIT 2.

(5) After moving the position of the EXIT 2 toward the right side of the platform, the RSET of the whole platform based on the simulation results by ICAEM is shortened and the stagnation phenomenon near the EXIT 2 is attenuated.

(6) In the whole, the ICAEM model is applicable and meaningful to the crowd evacuation and performance-based safety design in high densely populated public places.

References

1. Pauls, J. (1984). The movement of people in buildings and design solutions for means of egress. *Fire Technology, 20*(1), 27–47.
2. Fruin, J. J. (1993). "The causes and prevention of crowd disasters", Originally presented at The First International Conference on Engineering for Crowd Safety, London, England (Revised exclusively for crowdsafe.com, January 2002.) Available at http://www.crowdsafe.com/FruinCauses.pdf. Accessed September 19, 2017.
3. Sime, J. D. (1995). Crowd psychology and engineering. *Safety Science, 21,* 1–14.
4. Berlonghi, A. E. (1995). Understanding and planning for different spectator crowds. *Safety Science, 18*(4), 239–247.
5. Dickie, J. F. (1995). Major crowd catastrophes. *Safety Science, 18*(4), 309–320 (12).
6. Zhen, W., Mao, L., & Yuan, Z. (2008). Analysis of trample disaster and a case study—Mihong bridge fatality in China in 2004. *Safety Science, 46,* 1255–1270.
7. Alnabulsia, H., & Drurya, J. (2014). Social identification moderates the effect of crowd density on safety at the Hajj. *PNAS, 111*(25), 9091–9096.
8. Valach, L., Young, R. A., & Lynam, M. J. (2002). *A primer for applied research in the social sciences*. Westport, Connecticut: Praeger Publishers.
9. Lee, R. S. C., & Hughes, R. L. (2007). Minimisation of the risk of trampling in a crowd. *Mathematics and Computers in Simulation, 74,* 29–37.
10. Helbing, D., & Molnar, P. (1995). Social force model for pedestrian dynamics. *Physical Review E, 51,* 4282–4286.
11. Helbing, D., Farkas, I., & Vicsek, T. (2000). Simulating dynamical features of escape panic. *Nature, 407*(28), 487–490.
12. Burstedde, C., Klauck, K., Schadschneider, A., et al. (2001). Simulation of pedestrian dynamics using a two-dimensional cellular automaton. *Physica A, 295*(3–4), 507–525.
13. Kirchner, A., & Schadschneider, A. (2002). Simulation of evacuation processes using a bionics-inspired cellular automaton model for pedestrian dynamics. *Physica A: Statistical Mechanics and its Applications, 312*(1–2), 260–276.
14. Yang, L. Z., Fang, W. F., & Fan, W. C. (2003). Modeling occupant evacuation using cellular automata-effect of human behavior and building characteristics on evacuation. *Journal of Fire Science, 21*(3), 227–240.
15. Zhao, D. L., Yang, L. Z., & Li, J. (2008). Occupants' behavior of going with the crowd based on cellular automata occupant evacuation model. *Physica A, 387,* 3708–3718.
16. Alizadeh, R. (2011). A dynamic cellular automaton model for evacuation process with obstacles. *Safety Science, 49,* 315–323.
17. Fu, Z., Yang, L., Chen, Y., Zhu, Z., et al. (2013). The effect of individual tendency on crowd evacuation efficiency under inhomogeneous exit attraction using a static field modified FFCA model. *Physica A, 392,* 6090–6099.
18. Dorigo, M., Birattari, M., & Stützle, T. (2006). Ant colony optimization-artificial ants as a computational intelligence technique. *IEEE Computational Intelligence Magazine, 285*(34), 1302–1321.
19. Zhao, B., Li, S., & Jin, J. (2007). Ant colony algorithm based on adaptive selection of paths and pheromone updating. *Computer Engineering and Applications, 43*(3), 12–15.
20. Liu, M., Zhang, F., Ma, Y., et al. (2016). Evacuation path optimization based on quantum ant colony algorithm. *Advanced Engineering Informatics, 30,* 259–267.
21. Forcael, E., Gonzalez, V., Orozco, F., et al. (2014). Ant colony optimization model for tsunamis evacuation routes. *Computer-Aided Civil and Infrastructure Engineering, 29,* 723–737.

Fire Statistics and Risk Assessment

Assessing Probability of Fire in an Administrative District

Check for updates

Ching-An Lee, Yu-Chi Sung, Yuan-Shang Lin and Gary Li-Kai Hsiao

Abstract Building fires have accounted for 74% of all fire disasters in Taiwan. The local government needs a quantitative analysis approach for analyzing the probability of fire. This study adopted the analytic hierarchy process (AHP) to assess probability of fire in 17 villages comprising in an administrative district in New Taipei City, Taiwan. A total of 5 assessment items and 18 assessment indices were comprised for fire probability. The weights were collated into a matrix in order to evaluate fire probability of ratings. The yearly average building fires and the average fire-affected area during 2005–2015 were used to verify the proposed approach. The data of fire were obtained from government databases. The findings obtained can facilitate assessments of fire probability and can also provide reference for building fire-prevention strategies. This study proposes an approach for probability of fire.

Keywords Analytic hierarchy process (AHP) · Probability of fire · Fire safety management · Fire risk

1 Introduction

Fire disasters are the most common anthropogenic hazards to date, the most frequent incidents of which have been building fires. According to statistical data from the National Fire Agency, Ministry of the Interior, Taiwan, the number of fire disasters

C.-A. Lee (✉) · Y.-C. Sung
Department of Civil Engineering, National Taipei University of Technology, Taipei, Taiwan
e-mail: lee.ching.an2@gmail.com

C.-A. Lee · G. L.-K. Hsiao
Fire Department, New Taipei City Government, New Taipei City, Taiwan

Y.-C. Sung
National Center for Research on Earthquake Engineering, Taipei, Taiwan

Y.-S. Lin
Central Police University, Taoyuan City, Taiwan

G. L.-K. Hsiao
Department of Disaster Management, Taiwan Police College, Taipei, Taiwan

Fig. 1 Classification of fire disaster types in New Taipei City

from 2011 to 2015 was 7918, of which 5865 incidents resulted from building hazards (74.1% of all), and 78% (Fig. 1) of the incidents occurred in New Taipei City. Thus, building hazards were the most frequent cause of fire disasters. However, the government has not yet established a quantitative method for conducting assessments on the probability of fire in buildings. In summary, devising a sound and systematic approach for quantitatively analyzing all assessment indices based on the probability of fire is crucial for identifying the most influential factors for fire disaster prevention.

1.1 Research Framework and Procedures

This study adopted the analytic hierarchy process (AHP) to assess the probability of fire in 17 villages in Taishan District, New Taipei City. We initially collected both domestic and foreign papers to consider every factor with a potential influence on the probability of fire. Further, these factors were regarded as major assessment indices that would be subject to on-the-spot analysis for determining the hierarchy standards. Afterward, the assessment standards were categorized in accordance with the AHP results. The weights of the various assessment indices were determined and incorporated into a matrix analysis to identify the probability of fire ratings of each village. The average number of fire disasters as well as the fire-affected area in each village were examined for the 2005–2015 period in order to confirm the results concerning probability of fire, which were then cross-referenced with the assessment findings to confirm assessment accuracy.

1.2   Defining Probability of Fire

Probability of fire is related to fire risk. A number of definitions for probability of fire and fire risk have been proposed.

ASTM International [1] currently defines fire risk as "the combination, probably the product, of the expected frequency of the event, the expected degree of exposure, and the potential for harm," according to its Policy on Fire Standards.

Hansen-Tangen and Baunan [2] indicated that fire risk contains two elements ($R = FQ$): the frequency of fire disasters (probability of fire, F) and the outcome of fires (fire severity, Q).

According to Bukowski and Stiefel [3], in defining fire risk, the potential hazards or impact resulting from a fire must be weighted for their likelihood of occurrence. The value of risk can thus be used to predict the consequences of a fire under all considerations.

In summary, probability of fire and fire severity are both significant elements in determining fire risk. Probability of fire can be used to forecast the probability of a fire disaster, whereas fire severity represents the degree of damage from a disaster.

1.3   Factors as Items of AHP Concerning Probability of Fire

For this study, we analyzed and summarized the impact factor of potential for fire, including land use zoning, population density, building security features, household goods, and the temporal and spatial characteristics of fire incidents.

1.3.1   Land Use Zoning

Kuo conducted an analysis on fire potential based on fire incidents in Kaohsiung City, and found that fires occurred frequently in residential and commercial mixed-use areas as well as in populated areas. In fact, his results revealed that the locations of the fire incidents were highly correlated with the degree of urbanization [4]. Huang examined the correlation between the characteristics of a fire disaster, land use, and the spatial structure. He found that property loss was severe when the fire occurred in industrial and commercial buildings [5].

1.3.2   Population Density

In "Discussion on Fire Safety Factors from Case Studies of Building Fires," Wu reported that the annual number of building fires in the Kaohsiung administrative divisions could be calculated by performing a basic regression analysis of the population [6]. For casualties and property losses resulting from fire incidents in Taiwan,

Tsai and Tao employed empirical estimation models with a Poisson distribution. Their results revealed a positive correlation between fire deaths and population density as well as the population [7].

1.3.3 Building Safety Factor

The Building Technical Regulations of Taiwan focuses on whether building materials can maintain the stability, totality, and heat insulation of a building in case of a fire by considering factors such as the purpose of the building, its height, the area, and the main structure [8].

Huang studied the correlation between fire incidents and the structure and height of buildings, and found a high fire rate for brick- and wood-constructed buildings. In addition, the fire rate of buildings less than five floors was higher than that of their taller counterparts [5].

Kuo and Munson examined the correlation between standard of living and probability of fire, and found that the fire rate of buildings that are old, damaged, and lacking appropriate management was higher compared to those that are new, well-constructed, and properly managed [4].

Lin researched the relationship between fire risk and building safety characteristics. The findings indicated that the materials used for the interior decor, the structural type of the building, its purpose, and the availability of fire equipment may have a substantial impact on the severity of the fire as well as difficulties encountered in escape and rescue efforts [9].

Lathrop investigated emergency escapes and found that civilians have a sufficient amount of time to escape if the building can maintain structural integrity for a longer period, which can also lower the number of fire casualties [10].

After studying the relationship between fire risk and building safety characteristics, Cheng found that the degree of damage, the difficulty of escape, the number of casualties, and property loss in buildings were evidently less severe when a high-safety structure was involved compared with a low-safety structure [11].

1.3.4 Resident Characteristics

In "Socioeconomic Factors and The Incidence of Fire," Lathrop indicated that the characteristics of family members such as their education level, family revenue, and family composition affect their attitudes and level of alertness. For instance, buildings with lower fire rates were occupied by residents with a high education level who lived with their parents and were the homeowners [12].
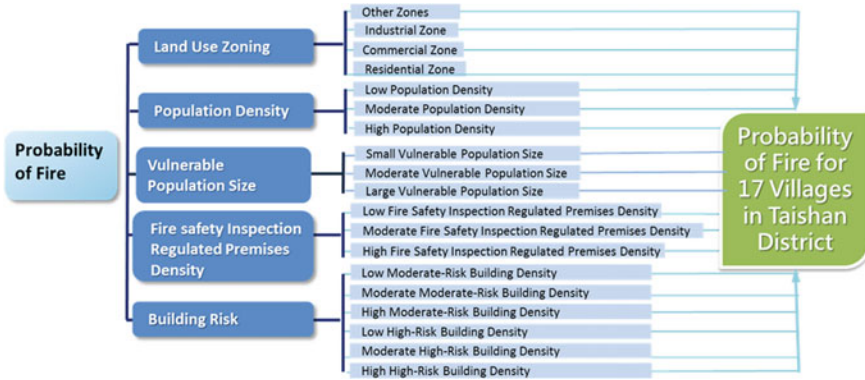
Fig. 2 Framework for the probability of fire assessment system

1.3.5 Timing and Location of Fire Incidents

In their study on fire loss, Stollard and Lin concluded that the probability of fire in resident-occupied buildings was higher compared with non-resident-occupied buildings because residents' responsiveness to fire disasters was relatively lower compared to occupants in buildings for commercial or industrial use [13].

In conclusion, the findings from literature review showed that land use zoning, vulnerable population size, population density, fire safety inspection-regulated premises density, and building risk were factors influencing the probability of a fire. The proposed probability of fire assessment system is composed of the following five assessment items: land use zoning, vulnerable population size, population density, fire safety inspection-regulated premises density, and building risk. The framework for the probability of fire assessment system is shown in Fig. 2.

2 Ratings and Results of the Indices for Assessing Probability of Fire by AHP

2.1 Survey Statistics of the Assessment Indices

We conducted a survey to examine the probability of fire assessment indices across the 17 villages in Taishan District. Our use of an unmanned aerial vehicle was unprecedented in surveying the village locations, building types, and building safety features (material, structure, building age, and number of floors) to generate a 3D model. The model was then combined with tax data collected from the New Taipei City government, along with land data collected from the National Land Surveying and Mapping Center, Ministry of the Interior. Data on population density, vulnerable population size, fire safety inspection-regulated premises density, hazardous materials' place

density, the rescue response time, narrow road density, and water-scarce area density were collected from information systems maintained by various agencies operating under the New Taipei City government. These data are readily available and highly accurate.

2.2 Rating Definitions of the Assessment Indices

The sources of the data, the statistical duration and quantity, the survey results, classification principles, and rating definitions for all of the assessment indices were adopted to assess the probability of fire in the 17 villages in Taishan District, New Taipei City, Taiwan. The employed assessment indices are shown in Fig. 2.

2.3 Rating Classification and Results of the Probability of Fire Indices

In order to establish the assessment indices on probability of fire in the 17 villages in Taishan District, we obtained the average scores for population density, fire safety inspection-regulated premises density, high-risk building density, and moderate-risk building density, which were 14,515 people/km^2, 240 people, 203 (counts), 1119 buildings/km^2, and 1619 buildings/km^2, respectively. The standard deviation values for the four indices were 16,288, 85, 833, and 1625, respectively. Ratings of "high," "moderate," and "low" were defined with a 50% standard deviation margin. Scores that fell between the ratings of "high" and "low" were defined as "moderate."

Based on these criteria and rating definitions, the rating classification results for land use zoning, population density and fire safety inspection-regulated premises density are tabulated in Table 1, and those for high- and moderate-risk building density are listed in Table 2.

3 Analytic Hierarchy Process Results

3.1 Questionnaire Design and Survey

The AHP as modified by Chu [14] was adopted to assess probability of fire from 5 items and 18 indices (Fig. 2).

We distributed 150 questionnaires to six governmental centers, agencies, and bureaus and departments responsible for fire disaster prevention, response, and/or reduction, as displayed in Fig. 3. The response rate was 98%, with 147 questionnaires returned, yielding an effective sample size of 142 questionnaires (96.6%). The

Table 1 Land use zoning, population density, and fire station density ratings for the 17 Villages in Taishan District

No.	Village	Area (km²)	Land use zoning	Population density			Vulnerable population size		Fire safety inspection-regulated premises density	
				Population size	People/km²	Rating classification	Amount	Rating classification	Total	Rating classification
1	Dake Village	6.95	Other	1029	148	Low	63	Low	155	Moderate
2	Liming Village	2.83	Other	3804	1344	Low	224	Moderate	152	Moderate
3	Shanjiao Village	0.53	Other	7144	13,479	Moderate	370	High	111	Moderate
4	Futai Village	0.19	Residential and other	3075	16,184	Moderate	222	Moderate	57	Low
5	Fuxing Village	0.16	Residential Other	3960	24,750	High	195	Low	101	Moderate
6	Fengshu Village	1.32	Industrial and other	4701	3561	Low	246	Moderate	878	High
7	Tongrong Village	1.29	Other	4418	3425	Low	218	Moderate	38	Low
8	Tongxing Village	0.08	Residential	4217	52,713	High	196	Low	79	Low
9	Qianxing Village	0.17	Residential and other	9497	55,865	High	295	High	127	Moderate
10	Yixue Village	0.18	Other	4937	27,428	High	308	High	101	Moderate

(continued)

Table 1 (continued)

No.	Village	Area (km²)	Land use zoning	Population density			Vulnerable population size		Fire safety inspection-regulated premises density	
				Population size	People/km²	Rating classification	Amount	Rating classification	Total	Rating classification
11	Yiren Village	1.5	Industrial and other	8468	5645	Low	459	High	815	High
12	Mingzhi Village	0.54	Other	3931	7280	Moderate	196	Low	36	Low
13	Taiyou Village	0.28	Industrial and other	2379	8496	Moderate	158	Low	114	Moderate
14	Xinming Village	0.96	Other	3668	3821	Low	217	Moderate	57	Low
15	Guizi Village	0.77	Other	4102	5327	Low	227	Moderate	47	Low
16	Guixian Village	0.37	Other	3942	10,654	Moderate	204	Moderate	137	Moderate
17	Guihe Village	0.79	Other	5236	6628	Moderate	297	High	446	High
Total (Average)		18.91		(4618)	(14,515)		4095 (240)		3451 (203)	

Table 2 High- and moderate-risk building density ratings for the 17 villages of Taishan District

No.	Village	Area (km^2)	High-risk buildings			Moderate-risk buildings		
			Total	Density (building/km^2)	Rating classification	Total	Density (building/km^2)	Rating classification
1	Dake Village	6.95	851	122.4	Low	372	53.5	Low
2	Liming Village	2.83	731	258.3	Low	517	182.7	Low
3	Shanjiao Village	0.53	978	1845.3	High	1100	2075.5	Moderate
4	Futai Village	0.19	277	1457.9	Moderate	405	2131.6	Moderate
5	Fuxing Village	0.16	288	1800.0	High	472	2950.0	High
6	Fengshu Village	1.32	1205	912.9	Moderate	623	472.0	Low
7	Tongrong Village	1.29	473	366.7	Low	793	614.7	Low
8	Tongxing Village	0.08	271	3387.5	High	537	6712.5	High
9	Qianxing Village	0.17	419	2464.7	High	647	3805.9	High
10	Yixue Village	0.18	200	1111.1	Moderate	397	2205.6	Moderate
11	Yiren Village	1.5	776	517.3	Low	769	512.7	Low
12	Mingzhi Village	0.54	360	666.7	Low	373	690.7	Low
13	Taiyou Village	0.28	232	828.6	Moderate	274	978.6	Moderate
14	Xinming Village	0.96	327	340.6	Low	260	270.8	Low
15	Guizi Village	0.77	579	751.9	Moderate	1012	1314.3	Moderate
16	Guixian Village	0.37	430	1162.2	Moderate	549	1483.8	Moderate
17	Guihe Village	0.79	839	1062.0	Moderate	838	1060.8	Moderate
Total (Average)		18.91	9244	(1119)		9938	(1619)	
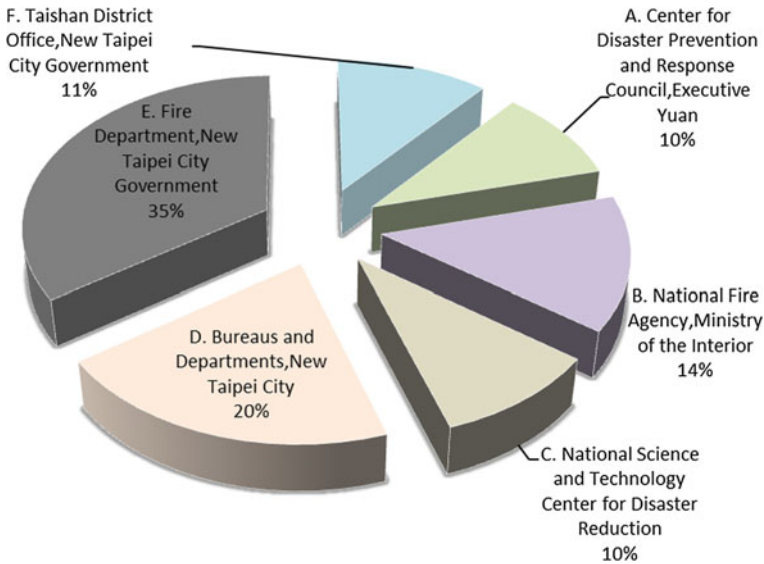
Fig. 3 Questionnaire targets

research has been approved in advance by the Research Ethics Committee of New Taipei City, Taiwan, to conduct questionnaire and the collection of data from questionnaire participants. All participants of the questionnaire have given their informed consent to the collection as well as the publication of their responses.

3.2 Probability of Fire Item and Index Weights

The average weights for land use zoning, population density, vulnerable population size, fire safety inspection-regulated premises density, and building risk were 10.29, 20.78, 16.22, 21.59, and 31.12, respectively (Table 3). The average weight of building risk (31.12) was the highest in this construct, followed by population density (20.78). By contrast, the lowest was land use zoning (10.29).

4 Validation of Probability of Fire Assessment Results

In this study, the verification of probability of fire was based on actual fire disasters, and Taiwan's standards (threshold) for identifying a fire disaster are relatively high. Because it is difficult to research real-life conditions, and because fire disasters were relatively rare in several villages, we relied on fire disaster data obtained from fire

Table 3 Weights of the probability of fire assessment

Probability of fire assessment							
	A	B	C	D	E	F	Average
Land use zoning	12.18	10.22	12.05	10.12	12.08	5.09	10.29
Population density	20.38	18.7	20.62	19.38	22.11	23.47	20.78
Vulnerable population size	20.28	10.99	17.11	16.46	17.2	15.3	16.22
Fire safety inspection-regulated premises density	20.69	25.36	19.00	22.14	11.79	30.57	21.59
Building risk	26.47	34.73	31.22	31.9	36.82	25.57	31.12
1. *Land use zoning*							
Residential zone	4.11	2.91	3.69	2.6	2.51	1.72	2.92
Commercial zone	3.64	2.17	3.4	1.93	3.66	1.5	2.72
Industrial zone	2.69	3.62	4.01	4.37	4.73	1.25	3.45
Other zones	1.74	1.52	0.95	1.22	1.18	0.62	1.21
2. *Popularity density*							
High population density	14.79	10.03	15.42	12.48	15.06	14.09	13.65
Moderate population density	4.46	5.36	3.31	4.78	5.13	6.68	4.95
Low population density	1.13	3.31	1.89	2.12	1.92	2.7	2.18
3. *Vulnerable population size*							
Large vulnerable population size	11.66	6.87	11.27	10.68	12.1	9.54	10.35
Moderate vulnerable population size	5.87	2.47	3.99	4.02	3.65	3.56	3.93
Small vulnerable population size	2.75	1.65	1.85	1.76	1.45	2.2	1.94
4. *Fire safety inspection-regulated premises density*							
High fire safety inspection-regulated premises density	13.06	14.95	11.28	13.46	6.56	17.44	12.79
Moderate fire safety inspection-regulated premises density	4.89	6.11	5.3	5.72	3.55	9.31	5.81
Low fire safety inspection-regulated premises density	2.74	4.3	2.42	2.96	1.68	3.82	2.99
5. *Building risk*							
High high-risk building density	10.85	14.42	11.93	12.1	14.57	9.03	12.15
Moderate high-risk building density	6.21	7.88	7.76	7.32	7.5	5.09	6.96
Low high-risk building density	3.65	4.19	3.23	3.2	4.53	2.55	3.56
High moderate-risk building density	3.13	4.61	4.82	5.32	6.32	4.82	4.84
Moderate moderate-risk building density	1.6	2.15	2.18	2.49	2.49	2.58	2.25
Low moderate-risk building density	1.03	1.48	1.3	1.47	1.41	1.5	1.37

investigations conducted by New Taipei City. The sample size for the number of fire investigations was 160 for the 2005–2015 period.

Based on the rating system proposed in this study, the results of the probability of fire assessment for the 17 villages in Taishan District are as follows (Table 4):

1. Low probability of fire (≤19.99): Guizi Village, Dake Village, Liming Village, Mingzhi Village, Tongrong Village, and Xinming Village (six villages)
2. Moderate probability of fire (20–35.99): Fengshu Village, Yiren Village, Taiyou Village, Guixian Village, and Futai Village (five villages)
3. High probability of fire (≥36): Fuxing Village, Shanjiao Village, Qianxing Village, Tongxing Village, Guihe Village, and Yixue Village (six villages).

In this study, the probability of a fire was based on the yearly average number of fire disasters in each village. Villages with a score of 0.44 or lower were considered to have a low probability of fire. Those with a score between 0.45 and 0.74 were considered to have a moderate probability of fire. Finally, villages that scored 0.75 or higher were considered to have a high probability of fire.

Based on the probability of fire in each village and their yearly average number of fire disasters, the findings showed that the occurrence rate for the low-, moderate-, and high-rated villages was 83, 60, and 50%, respectively. The following are the validation results for the probability of fire assessments for the 17 villages in Taishan District (Table 5):

A. Low probability of fire (≤19.99): The annual probability of 0.44 fire disasters or less is 83%.
B. Moderate probability of fire (20–35.99): The annual probability of 0.45–0.74 fire disasters is 60%.
C. High probability of fire (≥36): The annual probability of 0.75 fire disasters or more is 50%.

Table 4 Scores and ratings for probability of fire in 17 villages of Taishan District

No.	Village	Land use zoning		Population density		Vulnerable population size		Fire safety inspection-regulated premises		Building risk		Total score	Total rating
		Rating	Score	Rating	Score	Rating	Score	Rating	Score	Score			
1	Dake Village	Other	1.21	Low	2.18	Low	1.94	Moderate	5.81	4.93	16.07	Low
2	Liming Village	Other	1.21	Low	2.18	Moderate	3.93	Moderate	5.81	4.93	18.06	Low
3	Shanjiao Village	Other	1.21	Moderate	4.95	High	10.35	Moderate	5.81	14.4	36.72	Moderate
4	Futai Village	Residential/Other	2.07	Moderate	4.95	Moderate	3.93	Low	2.99	9.21	23.15	Moderate
5	Fuxing Village	Residential/Other	2.07	High	13.65	Low	1.94	Moderate	5.81	16.99	40.46	High
6	Fengshu Village	Industrial/Other	2.33	Low	2.18	Moderate	3.93	High	12.79	8.33	29.56	High
7	Tongrong Village	Other	1.21	Low	2.18	Moderate	3.93	Low	2.99	4.93	15.24	Low
8	Tongxing Village	Residential	2.92	High	13.65	Low	1.94	Low	2.99	16.99	38.49	High
9	Qianxing Village	Residential/Other	2.07	High	13.65	High	10.35	Moderate	5.81	16.99	48.87	High
10	Yixue Village	Other	1.21	High	13.65	High	10.35	Moderate	5.81	9.21	40.23	Moderate

(continued)

Table 4 (continued)

No.	Village	Land use zoning		Population density		Vulnerable population size		Fire safety inspection-regulated premises		Building risk	Total score	Total rating
		Rating	Score	Rating	Score	Rating	Score	Rating	Score	Score		
11	Yiren Village	Industrial/Other	2.33	Low	2.18	High	10.35	High	12.79	4.93	32.58	Moderate
12	Mingzhi Village	Other	1.21	Moderate	4.95	Low	1.94	Low	2.99	4.93	16.02	Low
13	Taiyou Village	Industrial/Other	2.33	Moderate	4.95	Low	1.94	Moderate	5.81	9.21	24.24	Moderate
14	Xinming Village	Other	1.21	Low	2.18	Moderate	3.93	Low	2.99	4.93	15.24	Low
15	Guizi Village	Other	1.21	Low	2.18	Moderate	3.93	Low	2.99	9.21	19.52	Low
16	Guixian Village	Other	1.21	Moderate	4.95	Moderate	3.93	Moderate	5.81	9.21	25.11	Moderate
17	Guihe Village	Other	1.21	Moderate	4.95	High	10.35	High	12.79	9.21	38.51	High

Table 5 Results of probability of fire and fire severity assessment and validation for the 17 villages in Taishan District

No.	Village	Probability of fire		
		Annual fire disaster	Annual fire incident rating	Fire probability rating
1	Dake Village	0.27	Low	Low
2	Liming Village	0.36	Low	Low
3	Shanjiao Village	0.73	Moderate	High
4	Futai Village	0.45	Moderate	Moderate
5	Fuxing Village	1.09	High	High
6	Fengshu Village	2.09	High	Moderate
7	Tongrong Village	0.36	Low	Low
8	Tongxing Village	0.27	Low	High
9	Qianxing Village	0.45	Moderate	High
10	Yixue Village	1.18	High	High
11	Yiren Village	2.91	High	Moderate
12	Mingzhi Village	0.09	Low	Low
13	Taiyou Village	0.55	Moderate	Moderate
14	Xinming Village	0.27	Low	Low
15	Guizi Village	0.91	High	Low
16	Guixian Village	0.45	Moderate	Moderate
17	Guihe Village	2.09	High	High

5 Conclusion

A building on fire is a smoky and dark environment both for firefighters and civilians trapped inside [15]. This study adopted a modified version of the AHP to assess probability of fire in 17 villages in Taishan District, New Taipei City. Fire risk was based on the constructs comprising the probability of fire, which was composed of 5 assessment items and 18 assessment indices, the weights of which are listed under Table 3. The probability of fire assessment ratings of the 17 villages is shown in Table 4 and Fig. 4.

This study adopted the yearly average number of actual fire disasters in the 17 villages comprising Taishan District to verify the results of the probability of fire analysis. The results revealed that the correct rates (determined through a rating's comparison between the yearly average number of fires and the probability of fire) corresponding to the high, moderate, and low ratings were 50, 60, and 83%, respectively (Table 6). Thus, our findings showed that the validity of the proposed approach was accurate and reliable for conducting effective quantitative analyses for domestic probability of fire assessments.
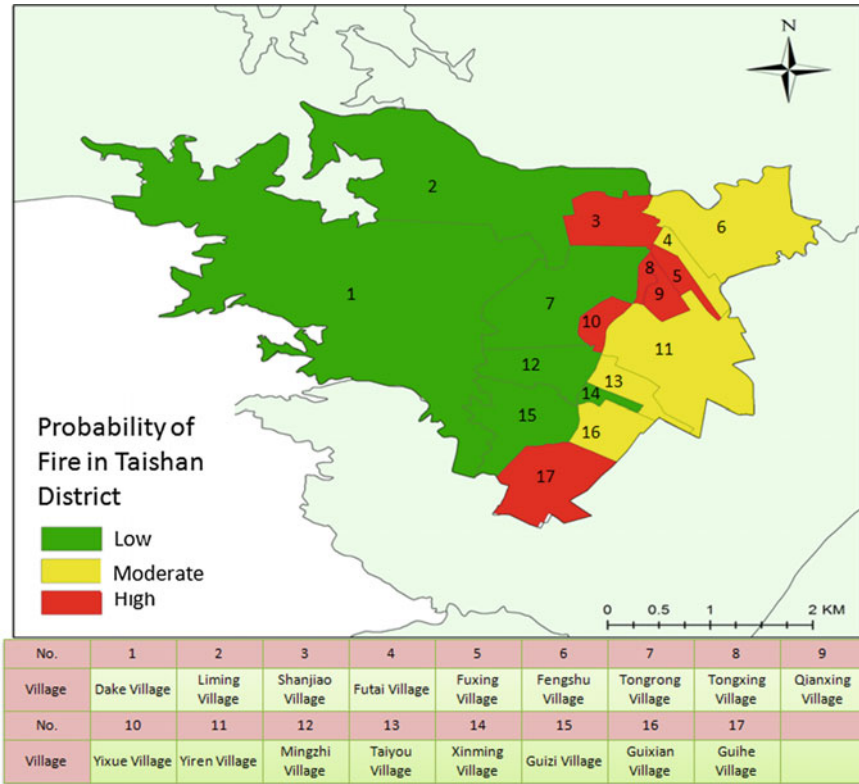
Fig. 4 Probability of fire across the 17 villages in Taishan District

No.	1	2	3	4	5	6	7	8	9
Village	Dake Village	Liming Village	Shanjiao Village	Futai Village	Fuxing Village	Fengshu Village	Tongrong Village	Tongxing Village	Qianxing Village
No.	10	11	12	13	14	15	16	17	
Village	Yixue Village	Yiren Village	Mingzhi Village	Taiyou Village	Xinming Village	Guizi Village	Guixian Village	Guihe Village	

Probability of fire was assessed using the yearly average number of fire disasters and the fire-affected area of the villages. The findings of this paper verified the feasibility of the proposed probability of fire-rating system. The system can thus be used to quantifiably measure probability of fire in Taiwan.

This study is the first to assess probability of fire at the lowest administrative level (village) in Taiwan, and the accuracy of the analysis findings is substantially higher than those conducted at higher administrative levels. Therefore, the referential value is groundbreaking, and the approach is extremely practical. The proposed assessment method can be promoted and taught at all administrative levels for quantitatively analyzing the probability of fire in buildings. Furthermore, our findings can serve as a critical reference for governments seeking more effective building fire-prevention strategies.

Table 6 Assessment and validation of probability of fire and fire severity results

Probability of fire			Annual fire disaster			Relative coincidence results (No. of villages/coincidence rate)
Low	≦19.99	Guizi Village, Dake Village, Liming Village, Mingzhi Village, Tongrong Village, Xinming Village	Low	≦0.44	Dake Village, Liming Village, Tongrong Village, Tongxing Village, Mingzhi Village, Xinming Village	Five villages/83%
Moderate	20–35.99	Yiren Village, Taiyou Village, Guixian Village, Futai Village Fengshu Village	Moderate	0.45–0.74	Shanjiao Village, Futai Village, Qianxing Village, Taiyou Village, Guixian Village	Three villages/60%
High	≥36	Fuxing Village, Qianxing Village, Tongxing Village, Guihe Village, Shanjiao Village, Yixue Village,	High	≥0.75	Fuxing Village, Fengshu Village, Yixue Village, Yiren Village, Guizi Village, Guihe Village	Three villages/50%

References

1. Roux, H. J. (1982). A discussion of fire risk assessment. In G. T. Castino & T. Z. Harmathy (Eds.), *Fire risk assessment* (pp. 16–27). ASTM STP762. https://doi.org/10.1520/stp33486s.
2. Hansen-Tangen, E., & Baunan, T. (1983). Fire risk assessment by simulation-firesim. *Fire Safety Journal, 5*, 205–212.
3. Bukowski, R. W., Stiefel, S. W., Hall, J. R., Jr., Clarke, F. B. (1990). *Fire risk assessment method: Description of methodology*. National Institute of Standards and Technology. NISTIR 90-4242.

4. Kuo, W. T. (2008). Researches on potential analysis of the fire occurred at Kaohsiung City. *Journal of Architecture, 62,* 47–73.
5. Huang, K. T. (1993). *A study on the correlation of character of fire-disaster, land-use and spatial-structure—The cases of fire-disaster of buildings in Taipei City*. Dissertation, National Taiwan University Graduate Institute of Building and Planning.
6. Wu, C. J. (2002). *Discussion on fire safety factors from case studies of building fires*.
7. Tsai, C. F., Tao, H. L. (2003). *A study on the influence factors of fire hazards. An approach to analyze and implement a commercial database*.
8. Building Technical Regulations. Chapter 3: Building Site. Ministry of the Interior, Taiwan. http://www.moi.gov.tw/english/english_law/law_detail.aspx?sn=26. Accessed October 30, 2016.
9. Lin, Y. S. (2003). Research on the relationship between building fire safety characteristics and fire risk. *Academic Journal of Central Police University, 40,* 259–278.
10. Lathrop, J. K. (1997). Concepts of egress design. In: *Fire protection handbook* (18th ed., pp. 35–36). NFPA.
11. Cheng, H., Hadjisophocleous, G. V. (2009). The modeling of fire spread in buildings by Bayesian network. *Fire Safety Journal, 44*.
12. Lathrop, J. K. (1997). *Socioeconomic factors and the incidence of fire* (p. 3). Federal Emergency Management Agency, Washington, D.C., United States Fire Administration, National Fire Data Center.
13. Stollard, P., Abrahams, J. (1995). *Fire from first principles* (pp. 52–53). E & FN SPON, An Imprint of Chapman & Hall.
14. Chu, C. P. (2009). *Analytic hierarchy process theory* (pp. 5–12).
15. Hsiao, G. L. K., Tang, C. H., Huang, T. C., & Lin, C. Y. (2016). Firefighter wayfinding in dark environments monitored by RFID. *Fire Technology, 52,* 273–279. https://doi.org/10.1007/s10694-015-0477-y.

Investigation of Factors and Construction of Statistical Models on Predicting Life Casualties in Building Fires in New Taipei City

Ting-Yu Huang and Yuan-Shang Lin

Abstract The main purpose of this study is to investigate on finding factors significantly affecting life casualties in building fires and constructing explanatory models for prediction. Factors were firstly generalized from literature review, and then an empirical study using data from fire cases during 2015 to June 2017 in New Taipei City was conducted. Chi-square test and t-test were performed later on to screen out factors closely related to life casualties, and those factors were then put into binary logistic regression analysis stepwise subsequently. The statistically significant variables in the three convergent models (human factors group, ignited and building environmental factors group, and built-in fire safety measures, rescue and fire growth factors group) were physical and mental illness, state of consciousness, horizontal fire compartment, narrow alleys, building structure, fire phases, and hydrant separately. By using the proposed binary logistic models, the overall correct classification rates were up to 81.5, 81.6, and 70.4%, respectively. Ultimately, the study provides suggestion in law enforcement, public education, and fire prevention planning.

Keywords Fire risk · Building fires · Life casualties · Chi-square test · T-test · Binary logistic regression

1 Introduction

In the past few decades, types of construction, lifestyles of occupants, and structure of society have changed dramatically. Content in the aspects of fire prevention and rescue under fire safety management system in Taiwan is keeping pace with times. Therefore, the disastrous characteristics of frequencies of fires and losses have altered remarkably. The occurrences of life casualties in fires, however, have

T.-Y. Huang (✉)
Fire Department, New Taipei City, No. 15, Sec. 2, Nanya S. Rd., Banqiao Dist., New Taipei City 220, Taiwan
e-mail: amabel1108@hotmail.com

Y.-S. Lin
Central Police University, No. 56, Shujen Rd., Takang Vil., Kueishan District, Taoyuan City 33304, Taiwan

significant impact on government governance. Considering life is priceless, the acts of government may be challenged. Besides, since interaction between nations and importance of cities are promoted, competition among cities becomes keener and all kinds of comprehensive evaluation index systems of urban governance held by institutes such as International Organization for Standardization, ISO 37120, Common Wealth Magazine, and Global Views Monthly in Taiwan spring up like mushrooms. By examining these various indexes, we found that death toll in fires is all the way included, showing that life safety management when fires break out is indeed an important task the government cannot neglect.

According to statistics of fire cases during 2012 to October 2017 in New Taipei City, 90.2% of all were building fires. Hence, the study set building fires as scope, generalized factors might affect life safety from literature and collected fire cases in New Taipei City for data analyzing, hoping to achieve research purposes listed below:

- Generalized affecting factors of life casualties in building fires.
- Construct explanatory models for predicting life casualties in building fires.
- Integrate life safety measures.

2 Literature Review

The occurrences of fires usually involve anthropic factors [1]. Statistics of residential fires causes in USA, 2007 showed that 40% of cases were cooking and 14% were using heating equipment [2]. Besides, since use of fire was common as well, improper handling and combustible materials nearby might contribute to ignition, spreading or even losses of life and property. Case studies from 2007 to 2011 done by National Fire Protection Association (NFPA) and National Fire Incident Reporting Systems (NFIRS) indicated that mortality rate of the elderly over 65 years old and children under 5 years old was 2.4 times and 1.1 times greater than that of young adults separately. Individuals who were drunk or taking drugs, in the state of soundly sleeping, and physical illness were 15, 34, and 15% of those dying in residential fires, respectively. In conclusion, occupants with characteristics mentioned above are less sensitive in awareness of fire occurrences and have weaker abilities to escape, thus leading to higher risk of deaths in fires [3–6]. The same case studies report also indicated females tended to evacuate immediately, whereas males usually tried to put out fire, resulting in 56% of death tolls and 53% of injuries [7]. Apparently, gender may contribute to different consequences of life casualties in fires. From those mentioned above, factors related to human behavior or distinguishing characteristics can be summarized in uses of fires, age, consciousness, disabilities, and gender.

Whether integrity and stability of buildings will be maintained after fires depend on their materials. In order to ensure safety of evacuees and firefighters, most buildings in Taiwan have to be qualified for being fire resistant in accordance with Building

Technical Regulations, and rooftops, beams, pillars, load-bearing walls, and floors need to meet the requirements of specific fire rates [8]. Regulations also specify that fire compartments should be established when total floor areas are above 1500 m^2, and the divided units will be 1500 m^2 as well. Pipelines and staircases should be divided from floor areas by setting up fire doors or walls proofed with at least 1 h of fire rate [9]. Moreover, considering combustible interior decoration may speed up the process from ignition turning into flashover, which have greater chances of spreading and increase the production of smoke or toxic gases [10]; most buildings, therefore, should use fireproof materials such as fire-retardant plywood and gypsum board for interior decoration [11]. Furthermore, it is necessary to take two way routes into consideration when it comes to the design of evacuation in buildings [12].

It is common to see materials discarded and shoe cabinets placed in front of doors of compartments or in aisles, as well as parking in arcades. However, the more the fire load is, the fiercer the fires are. When motor vehicle fire takes place in arcade, flames can reach to the height of 3.9 m in 100 s because its fire curve belongs to ultra-fast model [13]. Another potential threat will be hoarding, which is defined as collecting or keeping large amounts of various items in home due to having strong urges to save them or feeling distress when discarding them. Hoarding often blocks exits to prevent escape from home. And responding firefighters can be put at risk due to obstructed exits, falling objects, and excessive fire loading that can lead to collapse [14]. From those mentioned above, we can discern that factors affecting occurrences of fires or evacuation in the field of building environment seem to be diverse, and integration can be made to classify them as structure, fire compartment, decoration, emergency exits, and fire load.

According to Fire Services Act, the administrators who have the right to dominate and control a variety of places should provide and maintain the proper fire safety equipment. Besides, periodical service of the fire safety equipment should be conducted [15]. Case studies from 2007 to 2011 done by NFPA indicated that smoke alarm and home fire sprinklers can reduce the risk of dying in fires [16]. What is more, Mattson and Juaas found that if the arrivals of firefighters delay for 5 min, losses of life and property will remarkably increase [17].

Ministry of the Interior in Taiwan regulates the essential space around buildings for firefighting operation based on the function and performance of different types of fire engines. For examples, roadways and the space surrounding apartments under five floors should reserve at least 3.5 m in widths for fire engines passing through and a clear width of 4.1 m for firefighting, respectively [18]. According to those mentioned above, when it comes to factors regarding fire safety and rescue, equipment and firefighting activities can be summed up then.

3 Materials and Methods

3.1 Variables and Database

This study generalized the affecting factors of life casualties in building fires to 26 independent variables under three factor groups (Appendix 1) based on literature review in the previous section. In addition, the categories of every variable were defined in accordance with requirement of laws, regulations, research, and practical experiences. Since the scope was set within New Taipei City, Taiwan, an empirical study was conducted using 138 building fire cases (91 non-casualty cases and 47 casualty cases) during 2015 to June 2017.

3.2 Empirical and Statistical Procedures

The empirical research would refer to fire investigation reports, 119 dispatch information, and fire rescue reports. Then data would be tested to figure out whether there were differences between independent and dependent variables via chi-square test and independent samples via t-test. After that, the study would perform binary logistic regression to construct the explanatory models for predicting life casualties in building fires, and regression coefficients and odds ratios would be demonstrated then.

The study used stepwise forward Wald method to decide whether the independent variables should be included or excluded. First of all, the good fit of the models was tested through log-likelihood ratios, the values of Hosmer-Lemeshow and pseudo R^2. Second, Wald values were applied to survey individually significant differences in order to confirm the predicting effectiveness of independent variables. As Wald values increased, the influences of independent variables on dependent variable would increase accordingly. Third, odds ratios $(\exp(B) = e^B)$ also provided important analytical information. If the value was greater than 1, the probability of occurrence of target group would be higher than that of non-target group. At last, the overall correct classification rate would be demonstrated as well [19].

4 Results

4.1 Chi-Square Test and Independent Samples T-test

The first step in the analysis was to confirm the associations and correlations between 26 independent variables drawn up initially from literature review and dependent variable by using chi-square test and independent samples t-test. The result showed

that there were statistically significant differences between 18 independent variables and dependent variable about whether life casualties would occur when building fires broke out. Those variables were sex, age group, state of consciousness, physical, and mental illness in "human factors" group; source of ignition, building structure, interior decorating, hoarding, horizontal fire compartment, materials in front of door or in corridor, blocked opening on exterior wall, parking in arcade, and narrow alleys in "ignited and building environmental factors" group; hydrant, first response, dispatch of firefighters, dispatch of fire engines, and fire phases in "built-in fire safety measures, rescue and fire growth factors" group(Appendix 1). Those mentioned above would then put into the analysis of binary logistic regression.

4.2 Explanatory Model of Life Casualties in Building Fires (Human Factors)

The following analytical step was to perform binary logistic regression to construct explanatory models with regard to the three factor groups. In terms of human factors, the convergent model of life casualties in building fires contained state of consciousness, physical and mental illness (Appendix 2). The χ^2 values of overall model fit and Hosmer-Lemeshow were $60.472(p = .000 < .05)$ and $.030(p > .5)$, respectively, both indicating the good fit of the model. And the pseudo R^2 values consisting of Cox & Snell R^2 and Nagelkerke R^2 were .372 and .520, showing that independent variables and dependent variable were moderately correlated.

Further, after testing at the .05 level of significance, the Wald values of independent variables were 15.888 and 13.422, performing that there were significant differences between independent and dependent variables, and the two independent variables could effectively predict whether life casualties would occur. In addition, from the implications of odds ratios, occupants with physical and mental illness have 87.577 times greater chance of dying in building fires than physically and mentally healthy ones after controlling the impact of the other. And vice versa, occupants in the state of unconscious (asleep, psychotropic, possibly impaired by alcohol or drugs) have 8.614 times greater chance of dying than the awake.

The explanatory model could be expressed as below:

$$f(x)_{\text{human factors}} = \ln\left(\frac{p_{\text{life asualties}}}{1 - p_{\text{life casualties}}}\right)$$
$$= 3.944 + 4.473(\text{state of consciousness}(1))$$
$$+ 2.153(\text{physical and mental illness}(1)) \qquad (1)$$

Last, there were 87 cases being correctly classified into non-casualties group and only one case being incorrectly classified into casualties group from the original 88 non-casualty observations on the basis of the explanatory model. In the case of the original 42 casualty observations, 23 cases were incorrectly classified into non-

casualties group and 19 cases being correctly classified into casualties group. The overall correct classification rate was 81.5% (Appendix 3).

4.3 Explanatory Model of Life Casualties in Building Fires (Ignited and Building Environmental Factors)

In terms of ignited and building environmental factors, the convergent model of life casualties in building fires contained horizontal fire compartment, narrow alleys, and building structure (Appendix 2). The χ^2 values of overall model fit and Hosmer-Lemeshow were $46.838(p = .000 < .05)$ and $.608(p > .05)$, respectively, both indicating the good fit of the model. And the pseudo R^2 values consisting of Cox & Snell R^2 and Nagelkerke R^2 were .416 and .575, showing that independent variables and dependent variable were moderately correlated.

Moreover, after testing at the .05 level of significance, the Wald values of independent variables were 12.593, 9.191, and 6.140, respectively, performing that there were significant differences between independent and dependent variables, and the three independent variables could effectively predict whether life casualties would occur. In addition, from the implications of odds ratios, buildings without being horizontal compartmentalized (wooden wall or door) have 50.179 times greater chance of having life casualties in building fires than compartmentalized ones (brick, gypsum board, and calcium silicate board) after controlling the impact of the other. And vice versa, the areas surrounding buildings with narrow alleys have 7.615 times greater chance of having life casualties than with broader ones, and non-fireproof structure (sheet metal house, container house, and wooden house) has .047 times greater chance of having life casualties than fireproof structure(reinforced concrete, brick, and brick concrete).

The explanatory model could be expressed as below:

$$
\begin{aligned}
f(x)_{\substack{\text{ignited and building} \\ \text{environmental factors}}} &= \ln\left(\frac{p_{\text{life casualties}}}{1 - p_{\text{life casualties}}}\right) \\
&= -1.426 + 3.916(\text{horizontal fire compartment}(1)) \\
&\quad + 2.030(\text{narrow alleys}(1)) - 3.053(\text{building structure}(1)) \quad (2)
\end{aligned}
$$

Last, there were 53 cases being correctly classified into non-casualties group and 4 cases being incorrectly classified into casualties group from the original 57 non-casualty observations on the basis of the explanatory model. In the case of the original 30 casualty observations, 12 cases were incorrectly classified into non-casualties group and 18 cases being correctly classified into casualties group. The overall correct classification rate was 81.6% (Appendix 3).

4.4 Explanatory Model of Life Casualties in Building Fires (Built-in Fire Safety Measures, Rescue and Fire Growth Factors)

In terms of built-in fire safety measures, rescue and fire growth factors, the convergent model of life casualties in building fires contained fire phases, hydrant (Appendix 2). The χ^2 values of overall model fit and Hosmer-Lemeshow were $29.403(p = .000 < .05)$ and $1.443(p > .05)$, respectively, both indicating the good fit of the model. And the pseudo R^2 values consisting of Cox & Snell R^2 and Nagelkerke R^2 were .196 and .270, showing that independent variables and dependent variable were correlated.

Moreover, after testing at the .05 level of significance, the Wald values of independent variables were 15.833 and 5.618, respectively, performing that there were significant differences between independent and dependent variables, and the two independent variables could effectively predict whether life casualties would occur. In addition, from the implications of odds ratios, the phase of fire turning out to be fully involved or spreading while firefighters arrive have 6.516 times greater chance of having life casualties in building fires than confined state after controlling the impact of the other. And vice versa, buildings without hydrant or hydrant not being functional have 2.747 times greater chance of having life casualties than buildings with the presence of normally operated hydrant.

The explanatory model could be expressed as below:

$$f(x)_{\substack{\text{built in fire safety measures,}\\\text{rescue and fire growth factors}}} = \ln\left(\frac{p_{\text{life casualties}}}{1 - p_{\text{life casualties}}}\right)$$

$$= .345 + 1.847(\text{fire phases}(1)) + 1.010(\text{hydrant}(1)) \quad (3)$$

Last, there were 64 cases being correctly classified into non-casualties group and 24 cases being incorrectly classified into casualties group from the original 88 non-casualty observations on the basis of the explanatory model. In the case of the original 47 casualty observations, 16 cases were incorrectly classified into non-casualties group and 31 cases being correctly classified into casualties group. The overall correct classification rate was 70.4% (Appendix 3).

5 Discussion

5.1 Human Factors

The study performed chi-square test prior to binary logistic regression as a screen test to figure out which independent variables from human factors group would closely relate to life casualties in building fires. After applying stepwise forward Wald method, the convergent model consisting of "state of consciousness" and "physical

and mental illness" was constructed, and both independent variables were statistically significant. By contrast, the former was more significantly associated with contribution to predicting whether occupants would survive when building fires broke out than the latter, indicating that having weak ability to evacuate and being too late to notice that there is fire might be the most important concepts about life safety in fires in view of human factors.

The majority of building fires with life casualties were used for residential purpose, and those places might not be required automatic fire alarms equipment under the standard of MOI-NFA, Taiwan. However, places are encouraged to be provided with residential fire alarms and ensure good function all the time. This type of fire alarms is low cost and easy for operation and maintenance. If there is a fire at home, smoke spreads fast and occupants will need smoke alarms to give them time to get out. So smoke alarms that are properly installed and maintained can help occupants strive for extra time for children, the elderly evacuation, and extinguishment before the arrival of jeopardizing scenario, thus reducing fire deaths and injuries. In addition, evacuation plans should be drawn up in advance and training ought to be held regularly. Only in this way everyone can take appropriate measure to ensure life safety when fires occur.

5.2   Ignited and Building Environmental Factors

The study performed chi-square test prior to binary logistic regression as a screen test to figure out which independent variables from ignited and building environmental factors group would closely relate to life casualties in building fires. After applying stepwise forward Wald method, the convergent model consisting of "horizontal fire compartment," "narrow alleys," and "building structure" was constructed, and all independent variables were statistically significant. By contrast, the significant association and contribution to predicting whether occupants would survive when building fires broke out can be arranged in the order of horizontal fire compartment > narrow alleys > building structure, indicating that confining the development or the spread of fires and maintaining accessibility for rescuing might be the most important concepts about life safety in view of ignited and building environmental factors.

The entrance of a room is the route for air supply, and the supplement of air will affect the development of fire remarkably. Therefore, door unclosed will contribute to brighter and stronger flames, and combustible doors or walls will result in the spread of fire, causing the expansion of burning area or the collapse of the building. For these reasons, keeping doors closed when evacuating and using fire resistant building materials should be propagated.

Moreover, illegal parking in alleys should be forbidden for ensuring accessibility of fire engines, so that the effectiveness of firefighting will be reinforced and elevated notably.

5.3 Built-in Fire Safety Measures, Rescue and Fire Growth Factors

The study performed chi-square test and independent samples t-test prior to binary logistic regression as screen tests to figure out which independent variables from built-in fire safety measures, rescue and fire growth factors would closely relate to life casualties in building fires. After applying stepwise forward Wald method, the convergent model consisting of "fire phases" and "hydrant" was constructed, and both independent variables were statistically significant. By contrast, the former was more significantly associated with contribution to predicting whether occupants would survive when building fires broke out than the latter, indicating that the concept of putting out or suppressing fires instantly is very important when it comes to life safety in view of built-in fire safety measures, rescue and fire growth factors.

Using hydrant to suppress or even put out fire at the beginning of combustion definitely has an absolute benefit to reduce property loss and life casualties. Hence, inspection on places required to provide fire safety equipment to check whether hydrants being installed and periodical service being conducted is a momentous task. Also, regular training for operative accuracy is a must, which cannot be ignored.

6 Limitations

Limitations taken into account in this study are listed below:

- The study set up building fires as research object, whereas wild fires, vehicle fires, ship fires, aircraft fires, and others were excluded.
- Data sources of the empirical study were collected from fire investigation reports, which would present to the local police department to follow up criminal investigation. Therefore, the reports might focus on origins and causes of fires, leading to missing data in some of the variables.
- The definition of life casualties in this study was dying on the spot or injured at first but died in 14 days. Nevertheless, considering self-immolation was someone setting fires deliberately and initiatively, contradicting to the goal of objectively examining the affecting factors about life casualties in building fires of this study. Hence, this type of cases would be excluded likewise.

7 Conclusion

There are various factors affecting whether occupants will survive when building fires break out, and such studies on similar topics are too numerous to mention. However, the key feature of the study is to aim at getting proper results to demonstrate the

characteristics of life casualties in building fires in New Taipei City. In an attempt to achieve the purpose, the framework was constructed and the independent variables were generalized not only on the basis of literature review, but the characteristics of occupants, types of construction, and resources of fire rescue were also all taken into account, hoping to fulfill the research in a more complete way. Moreover, another highlight would be all data in the empirical analysis were collected from government documents which were not easy to obtain. According to the previous sections, independent variables would go through a series of screening tests including chi-square test, independent samples t-test, and binary logistic regression stepwise forward Wald method. Thus, independent variables in the convergent models were the significantly affecting factors on predicting life casualties in building fires in New Taipei City.

The explanatory models in three factor groups displayed the good fit of the model, and the independent and dependent variables were significantly different. The overall correct classification rates were very high. In conclusion, all the three models could provide effective and precise prediction on samples classification between whether life casualties would occur. Consequently, fire department in New Taipei City can combine the analytical results to fire safety propaganda in order to be in connection with the public. In this way, the effectiveness of fire prevention work can be expected and realized.

Appendix 1

See Table 1.

Table 1 Using chi-square test and independent samples *t*-test to analyze the associations and correlations between factor affecting life casualties

Independent variable		Dependent variable		Total (%)	Test
		Non-casualties (%/Mean)	Casualties (%/Mean)		
Human factors					
Sex	Male	58(71.6%)	23(28.4%)	81(100%)	$\chi^2 = 3.073$, df $= 1$, $p = .080$
	Female	32(57.1%)	24(42.9%)	56(100%)	
Age group	Adults (13–64)	81(73.6%)	29(26.4%)	110(100%)	$\chi^2 = 14.291$, df $= 1$, $p = .000$
	Children and the elderly (under 12, over 65)	10(35.7%)	18(64.3%)	28(100%)	
State of consciousness	Awake	56(87.5%)	8(12.5%)	64(100%)	$\chi^2 = 21.982$, df $= 1$, $p = .000$
	Unconscious (asleep, psychotropic, possibly impaired by alcohol or drugs)	33(49.3%)	34(50.7%)	67(100%)	
Physical and mental illness	No	90(77.6%)	26(22.4%)	116(100%)	$\chi^2 = 43.929$, df $= 1$, $p = .000$
	Yes	1(4.5%)	21(95.5%)	22(100%)	
Human involvement in fire using	Not involved	81(66.4%)	41(33.6%)	122(100%)	$\chi^2 = .095$, df $= 1$, $p = .757$
	Involved	10(62.5%)	6(37.5%)	16(100%)	
Ignited and building environmental factors					
Cause of fire	Arson and intentional fires	6(42.9%)	8(57.1%)	14(100%)	$\chi^2 = 7.399$, df $= 4$, $p = .116$
	Electrical	45(69.2%)	20(30.8%)	65(100%)	
	Smoking/candles	16(64.0%)	9(36.0%)	25(100%)	
	Cooking	7(100.0%)	0(0%)	7(100%)	
	Other	17(63.0%)	10(37.0%)	27(100%)	

(continued)

Table 1 (continued)

Independent variable		Dependent variable		Total (%)	Test
		Non-casualties (%/Mean)	Casualties (%/Mean)		
Source of ignition	No	18(94.7%)	1(5.3%)	19(100%)	$\chi^2 = 7.929$, df $= 1$, $p =$ .005
	Yes	73(61.9%)	45(38.1%)	118(100%)	
Building structure	Fireproof structure (reinforced concrete, brick, and brick concrete)	67(61.5%)	42(82.8%)	109(100%)	$\chi^2 = 4.623$, df $= 1$, $p =$ .032
	Non-fireproof structure (sheet metal house, container house, wooden house)	24(38.5%)	5(17.2%)	29(100%)	
Interior decorating	Non-combustible upholstery	40(87.0%)	6(13.0%)	46(100%)	$\chi^2 = 13.092$, df $= 1$, $p =$ .000
	Combustible upholstery	51(56.0%)	40(44.0%)	91(100%)	
Hoarding	No	46(82.1%)	10(17.9%)	56(100%)	$\chi^2 = 11.014$, df $= 1$, $p =$ .001
	Yes	45(54.9%)	37(45.1%)	82(100%)	
Horizontal fire compartment	Compartmentalized (brick, gypsum board, and calcium silicate board)	41(91.1%)	4(8.9%)	45(100%)	$\chi^2 = 18.522$, df $= 1$, $p =$ .000
	Non-compartmentalized (wooden wall or door)	48(53.9%)	41(46.1%)	89(100%)	

(continued)

Table 1 (continued)

Independent variable		Dependent variable		Total (%)	Test
		Non-casualties (%/Mean)	Casualties (%/Mean)		
Vertical fire compartment	Compartmentalized	28(63.6%)	16(36.4%)	44(100%)	$\chi^2 = .057$, df $= 1$, $p = .812$
	Non-compartmentalized (wooden mezzanine, fireproof door uninstalled or unclosed)	50(65.8%)	26(34.2%)	76(100%)	
Materials in front of door or in corridor	No	53(82.8%)	11(17.2%)	64(100%)	$\chi^2 = 15.618$, df $= 1$, $p = .000$
	Yes	37(50.7%)	36(49.3%)	73(100%)	
Blocked opening on exterior wall	No	58(80.6%)	14(19.4%)	72(100%)	$\chi^2 = 14.315$, df $= 1$, $p = .000$
	Yes	33(50.0%)	33(50.0%)	66(100%)	
Parking in arcade	No	40(76.9%)	12(23.1%)	52(100%)	$\chi^2 = 7.614$, df $= 1$, $p = .006$
	Yes	18(48.6%)	19(51.4%)	37(100%)	
Narrow alleys	No	72(80.0%)	18(20.0%)	90(100%)	$\chi^2 = 22.769$, df $= 1$, $p = .000$
	Yes	19(39.6%)	29(60.4%)	48(100%)	
Built-in fire safety measures, rescue and fire growth factors					
Smoke alarm	Properly installed and working	19(61.3%)	12(38.7%)	31(100%)	$\chi^2 = .385$, df $= 1$, $p = .535$
	No smoke alarms or no working smoke alarms	72(67.3%)	35(32.7%)	107(100%)	
Hydrant	Present and operate	44(81.5%)	10(18.5%)	54(100%)	$\chi^2 = 9.539$, df $= 1$, $p = .002$
	No hydrant or did not operate	47(56.0%)	37(44.0%)	84(100%)	

(continued)

Table 1 (continued)

Independent variable		Dependent variable		Total (%)	Test
		Non-casualties (%/Mean)	Casualties (%/Mean)		
First response	Yes	24(92.3%)	2(7.7%)	26(100%)	χ^2 = 9.916, df = 1, p = .002
	No (without putting out fire or failed)	67(59.8%)	45(40.2%)	112(100%)	
Dispatch of fire fighters	Number	89(88.12)	47(126.77)	136	t = −3.136**
Dispatch of fire engines	Number	89(29.12)	47(40.57)	136	t = −2.803**
119 Dispatch	Time	89(76.20)	47(76.85)	136	t = −.125
Attendance	Time	89(62.31)	47(68.53)	136	t = −1.684
Traveling	Time	89(397.81)	47(395.36)	136	t = −.057
Fire rescue	Time	91(1040.79)	47(1391.53)	138	t = −1.054
Fire phases	Confined	52(88.1%)	7(11.9%)	59(100%)	χ^2 = 23.158, df = 1, p = .000
	Fully involved or fire spreading	38 (48.7%)	40(51.3%)	78(100%)	

Note
a. The classification of two categories of age is based on the definition of children and the elderly each from Executive Yuan, Taiwan [20] and World Health Organization [21], respectively
*p < .05. **p < .01. ***p < .001

Appendix 2

See Table 2.

Table 2 Tests of overall model fit and significance of independent variables for three explanatory models of life casualties in building fires

Variables in the equation	Human factors			Ignited and building environmental factors				Built-in fire safety measures, rescue and fire growth factors		
	Physical and mental illness	State of consciousness	Constant	Horizontal fire compartment	Narrow alleys	Building structure	Constant	Fire phases	Hydrant	Constant
B	4.473	2.153	3.944	3.916	2.030	−3.053	−4.319	1.874	1.010	.345
S.E.	1.122	.588	1.133	1.103	.670	1.232	1.115	.471	.444	.263
Wald	15.888***	13.422***	12.119	12.593***	9.191**	6.140***	15.000	15.833***	5.168***	1.712
exp(B)	87.577	8.614	.068	50.179	7.615	.047	.013	6.516	2.747	1.412
Overall model fit	$\chi^2 = 60.472$***			$\chi^2 = 46.838$***				$\chi^2 = 29.403$***		
	Hosmer-Lemeshow $\chi^2 = .030$ n.s.			Hosmer-Lemeshow $\chi^2 = .608$ n.s.				Hosmer-Lemeshow $\chi^2 = 1.443$ n.s.		
	Cox & Snell $R^2 = .372$, Nagelkerke $R^2 = .520$			Cox & Snell $R^2 = .416$, Nagelkerke $R^2 = .575$				Cox & Snell $R^2 = .196$, Nagelkerke $R^2 = .270$		

Note
*$p < .05$. **$p < .01$. ***$p < .001$

Appendix 3

See Table 3.

Table 3 Table of classification of three explanatory models of life casualties in building fires

Human factors				Ignited and building environmental factors				Built-in fire safety measures, rescue, and fire growth factors			
Observed	Predicted			Observed	Predicted			Observed	Predicted		
	Non-casualties	Casualties	Correct classification rate		Non-casualties	Casualties	Correct classification rate		Non-casualties	Casualties	Correct classification rate
Non-casualties	87	1	98.9	Non-casualties	53	4	93	Non-casualties	64	24	72.7
Casualties	23	19	45.2	Casualties	12	18	60	Casualties	16	31	66
Overall correct classification rate			**81.5**	Overall correct classification rate			**81.6**	Overall correct classification rate			**70.4**

References

1. Hall, J. R. Jr., (2008). An overview of the fire problem and fire protection. In *Fire protection handbook* (20th ed., pp. 3–11). National Fire Protection Association, USA.
2. A Profile of Fire in the United States 2003–2007, U.S. Department of Homeland Security (2010) p. 5.
3. Custer, Richard L. P., & Meacham, Brian J. (1997). *Introduction to performance-based fire safety* (pp. 168–174). USA: Society of Fire Protection Engineers.
4. Bryan, J. L. (2002). Behavioral response to fire and smoke. In *SFPE handbook of fire protection engineering* (3rd ed., pp. 3–315–3-317). Society of Fire Protection Engineers, USA.
5. Bryan, J. L. (2008). Human behavior and fire. In *Fire Protection Handbook* (20th ed., pp. 4–6–4-48). National Fire Protection Association, USA.
6. Ahrens, M. (2014). *Characteristics of home fire victims* (pp. 7–9). National Fire Protection Association Fire Analysis and Research Division.
7. Ahrens, M. (2014). *Characteristics of Home Fire Victims* (pp. 6, 8). National Fire Protection Association Fire Analysis and Research Division.
8. Building Technique Regulation. (2013). *Designing rules §69–70*. Taiwan: MOI-CPA.
9. Building Technique Regulation. (2013). *Designing rules §79, 79-2*. Taiwan: MOI-CPA.
10. Yuan-Shang, Lin. (2000). *Building fire risk assessment and empirical study* (p. 176). Taoyuan, Taiwan: Central Police University Publishing Company.
11. Building Technique Regulation. (2013). *Designing rules §88*. Taiwan: MOI-CPA.
12. Chen, H. Y., & Wu, L. S. (2006). *Fire science* (pp. 5–35). Taiwan: Ting Mao Publishing Company.
13. New Taipei City Government Website. Retrieved from http://www.xinzhuang.ntpc.gov.tw/archive/file/01_%E6%B6%88%E9%98%B2%E5%B8%B8%E8%AD%98.pdf.
14. National Fire Protection Association Website. Retrieved from http://www.nfpa.org/safety-information/for-consumers/hoarding-and-fire-safety.
15. Fire Services Act. (2011). *Chapter 2: fire prevention §6, 9*. Taiwan: MOI-NFA.
16. Ahrens, M. (2014). *Characteristics of home fire viztims* (p. 10). USA: National Fire Protection Association Fire Analysis and Research Division.
17. Mattson, B., Juaas, B. (1997). The importance of the time factor in fire and rescue service operations in Sweden. *Fire Safety Journal, 29*.
18. Guidelines for Designating Space for Firefighting Access, MOI, Taiwan, 2013.
19. Wu, Ming Long. (2008). *The application of SPSS-multivariate statistical analysis* (pp. 471–551). Taiwan: Wu Nan Publishing Company.
20. The Protection of Children and Youths Welfare and Rights Act, Chapter 1: General Principles §2, Executive Yuan, Taiwan (2015).
21. World Health Organization Website. (2015). Retrieved from http://www.who.int/healthinfo/survey/ageingdefnolder/en/.

Preliminary Investigation of Critical Separation Distance Between Shacks in Informal Settlements Fire

Yu Wang, Lesley Gibson, Mohamed Beshir and David Rush

Abstract Approximately, one billion people across the globe are currently living in informal shack settlements with a large potential fire risk. Due to the small distance between shacks, a single shack fire may spread and could cause a large area of informal settlement to be burnt in a short period of time. In this work, the critical fire separation distance between shacks is first discussed and determined using a simple physics-based theoretical model. Aerial photography within geographic information systems (GIS) is then employed to verify the calculated results based on a real informal settlement burn scar in Masiphumelele, Cape Town, South Africa. The radiative heat fluxes along the centerline of the shack window, at different distances, are calculated to estimate the ignition potential of combustible materials in adjacent shacks. Meanwhile, the potential fire risks, assuming separation distance as a proxy for risk, pre- and post- a known fire in Masiphumelele are obtained and compared. It was established that the heat flux would decay from around 100 kW/m^2 within 0.5 m to the value smaller than 0.1 kW/m^2 at the distance of 3.5 m away from the shack, which can be considered as a relatively safe distance. The theoretical result agrees well with the minimum effective distance of 3.3 m in real fires occurred in Masiphumelele. However, a GIS analysis of the informal settlement layout in 2015 and 2017 demonstrates that, if the critical fire separation distance is more than 3.0 m, 97% of the settlement could be at risk in a single fire incident. Therefore, more research is required to improve the understanding of fire spread mechanisms in informal settlements.

Keywords Informal settlements · Fire spread · Critical separation distance · GIS

Y. Wang (✉) · L. Gibson · M. Beshir · D. Rush (✉)
School of Engineering, University of Edinburgh, Edinburgh EH9 3JL, UK
e-mail: Yu.Wang@ed.ac.uk

D. Rush
e-mail: D.Rush@ed.ac.uk

1   Introduction

Due to globalization, increasing world populations and urbanization, it is now estimated that approximately one billion people across the globe live in informal shack settlements, and this number is ever increasing (from 650 million to 862 million during 1990–2012) [1]. Many of these informal settlements (i.e. shantytowns, favelas, slums) are at constant risk of lethal, large-scale destructive fires due to flammable construction materials, heating and cooking methods, shack proximity, etc. This potential fire risk is particularly high in the developing regions including Sub-Saharan Africa, Southern Asia and South America [2]. For example, across South Africa, there are an estimated ten shack fires a day, often leaving residents dead and thousands more homeless. In particular, in Cape Town, annually there are around 500 deaths and 15,000 fire-related hospital admissions due to fire, of which a substantial proportion are people from informal settlements [3]. In recent years, this issue is increasing in occurrence in Europe due to the frequent refugee campfires [4, 5]. Some intervention efforts by fire brigades or local governments to improve this fire safety issue have not demonstrated any reduction in fire deaths [6]. Thus, research in the fire safety of informal settlements needs to be conducted [2].

A significant part of these disastrous fire events is the fire spread from dwelling to dwelling. However, with local populations lacking in resources and opportunity to build more robust homes, materials that are easily and cheaply obtainable, including cardboard, paper, wood, galvanized steel sheeting and plastic, are often used in construction of an informal settlement dwelling. In addition, topographical and environmental conditions, including wind speed, building size, building-to-building separation and construction methods, will affect the fire spread rate significantly. All of these factors complicate the fire spread mechanism between the shacks, which includes: direct flame impingement; radiation from walls, openings and general fire plume radiation; and fire branding [7].

As a preliminary investigation, this work primarily focuses on ejected flame impingement and radiation from windows due to its critical role for determination of critical fire separation distance in shack experiments [2]. The heat flux at different distances from the window during the shack fire is estimated by a simple physics-based theoretical model. Since this research is aimed at understanding fire spread, the two large fires in informal settlements were selected using the City of Cape Town Open Data Portal; the two large fires selected both occurred in Masiphumelele in recent years (Fig. 1) as this provided a good comparison within a single settlement. The November 2015 fire, the most recent large structure fire left 2 dead and 4000 homeless and the May 2014 fire left 1000 people homeless. Geographic information systems (GIS) are used to achieve two aims in this paper: (1) to determine the offset distances, of two fires that occurred in Masiphumelele, an informal settlement located south of Cape Town, South Africa; (2) to determine if the settlement as a whole is more or less at risk to multi-dwelling fire post-reconstruction. The theoretical heat flux distances results are compared with the determined offset distances.
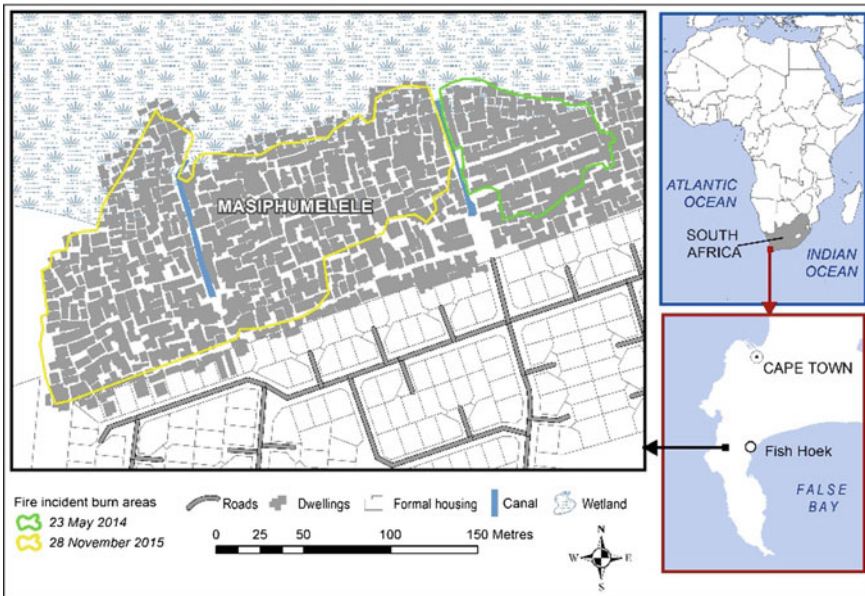
Fig. 1 Location of the Masiphumelele settlement showing the sites of fires in 2014 and 2015

2 Analysis Results

2.1 Theoretical Prediction of Heat Flux Distribution

It is generally recognized that flame ejection from windows and openings is one of the most important contributors to fire spread beyond the room of fire origin [8]. When flashover occurs in one shack, after the fallout of glass (if present), a flame will eject out of the window along with a significant amount of hot gases, either directly impinging and/or radiating on the adjacent shack [9]. To estimate the potential ignition risk of combustibles in adjacent shacks, this work primarily focuses on the heat flux at the locations away from the window. Thus, the flame geometry, particularly the horizontal projection distance, and the radiation received at different locations are calculated. The Law and O'Brien model [10], verified with reasonable accuracy and widely used by fire simulator models [11], is employed to determine the ejected flame horizontal length, which depends on the window dimension, ventilation condition and the presence of vertical and horizontal projects above or beside the window. The window dimension is assumed to be 0.8 (height, h) $\times$ 0.6 (width, w) m^2 according to the shack design schematic from [2]. As there is a short wall above the window of most shacks, and $h > 1.25\,w$, thus with the assumption of no through draft condition, the horizontal length, L (m), along the centerline (axis) of the flame from the window is [10]:

$$L = 2 \times 0.3h(h/w)^{0.54} \tag{1}$$

Therefore, for a 0.8×0.6 window, L is 0.56 m. If the area is kept consistent, and the aspect ratio changes from 4:3 to a relatively large ratio of 3:1 (i.e. a 1.2 m (h) $\times$ 0.4 m (w)), the horizontal flame length increases significantly to 1.3 m, which indicates that the flame length is very sensitive to the window dimension.

In addition, wind is usually present during a fire. In the Kayamandi informal settlement fire on the 15 March 2013, for example, the wind speed was around 20–30 km/h (5.5–8.3 m/s) and influenced the fire spread [2]. If the wind is more than 5 m/s and there are at least two openings for the wind to flow through in the shack, the ventilation condition becomes through draft. With an assumption of sufficient ventilation to give free burning conditions, the flame length will then be [10]:

$$L = 0.605(u^2/h)^{0.22}(z + h) \tag{2}$$

$$z = 23.9u^{-0.43}\dot{m}A^{-0.5} - h \tag{3}$$

where z (m) is the height of flame tip above the top of the window; u (m/s) is the wind speed; A (m^2) is the area of wind; $\dot{m}$ (kg/s) is the rate of burning. If it is assumed that most fires burn out in 20 min [10, 12, 13], the rate of burning can be estimated by the following equation:

$$\dot{m} = M/1200 \tag{4}$$

where M (kg) is the fire load. According to the temperature curve, a fire in shack experiments also experienced approximately 20 min with the fuel load of 25 kg/m^2 on a 3.0×2.4 m^2 floor [2]. Thus, the flame length calculated by the model is considered relatively reasonable, that is 3.3–3.4 m with the above wind speed. In South African informal settlements, woods and other combustible materials are often used as part of facing walls or roofs [11], so it can be assumed that the adjacent shack will be ignited if the projected flame length is beyond the distance between shacks. This assumption has been applied in previous work [7, 13].

In an open space, the radiation, rather than convection, normally dominates more than 90% the heat transfer between the fire and vertical panel [14]. The heteronuclear molecules such as CO, CO_2, H_2O and HCl absorb certain discrete wavelength bands in a volumetric phenomenon. Thus, according to Beer's law, the radiation received by the shack at different distances can be calculated by applying an absorption coefficient [15]:

$$q = I_0 e^{-\kappa L} \tag{5}$$

where q (kW/m^2) is the incident radiation heat flux; κ is the absorption coefficient (m^{-1}) that was estimated as 2–4 m^{-1} according to the heat fluxes measured at different distances in the authors' previous study [16]; L (m) is the distance between flame

tip and adjacent shack; I_0 (kW/m^2) is total radiation from flame and hot gas that is assumed as a constant value. This method has been employed in some glass research [16, 17]. The radiation can be estimated by the following equations [13]:

$$I_0 = (\varepsilon_{\text{flame}} + \varepsilon_{\text{gas}})\sigma T^4 \tag{6}$$

If there is no through draft:

$$\varepsilon_{\text{flame}} = 1 - e^{-0.3 \times \frac{2}{3}h}$$
$$\varepsilon_{\text{gas}} = 1 \tag{7}$$

If there is through draft:

$$\varepsilon_{\text{flame}} = 1 - e^{-0.3L}$$
$$\varepsilon_{\text{gas}} = 1 \tag{8}$$

where σ is Stefan-Boltzmann constant; ε is emissivity; $T(°C)$ is the flame and gas temperature which is assumed as 880 °C according to the maximum ejected flame temperature in authors' recent experiments. Then, we can obtain the original radiation heat flux of the ejected flame and gases of 107 kW/m^2 without through draft and 151 kW/m^2 with through draft. The radiation heat flux decay curve is shown in Fig. 2. The absorption coefficient in Eq. (5) is set as 2.0 for conservative analysis. Within the flame length, the radiation heat flux is assumed to be the same as original heat flux. The condition of no through draft is much more common [13], due to the preference of informal settlement residents preferring a single small window for security and privacy reasons [18], therefore, through draft conditions are not discussed in further detail in this work.

Fig. 2 Radiation heat flux at different locations
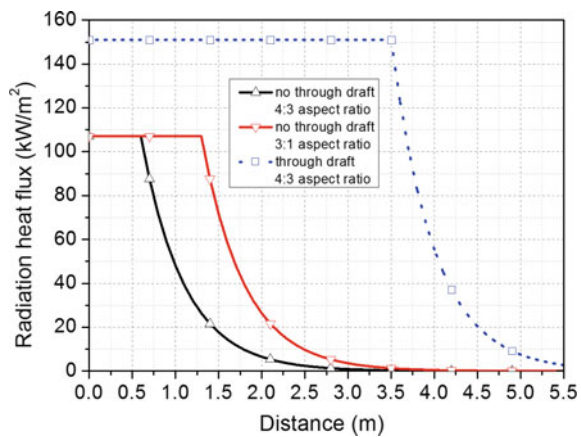
Table 1 Critical separation distance summary

Typical materials	Critical heat flux (kW/m^2) [19, 20]	Separation distance (m)
Wood	5.7	2.1
Rubber	7.5	1.9
Cardboard	5.0	2.2
Newspapers	10.0	1.8
Polyurethane foam	0.5	3.3

In the informal settlement, combustible materials are distributed extensively: newspaper, cardboard, foam or plastic bags are placed into spaces around walls and roofs to prevent drafts and provide insulation; firewood, tyres or polyurethane product is stored in or between shacks [2]. Thus, these materials are discussed separately here without consideration of heating time for conservative results. For wood, the lowest heat flux to cause ignition is approximately 10 kW/m^2 which may be slightly different due to species, grain orientation or moisture content [19]. However, the critical heat flux of Douglas fir may be as low as 5.7 kW/m^2. Based on the critical heat flux of wood and other common materials such as rubber, cardboard, newspapers and polyurethane [20], the conservative critical separation distance is determined and listed in Table 1 according to the black curve in Fig. 2. It can be found that for most materials, the distance of 2.5 m is safe enough to prevent a shack fire spread, while it will increase to at least 3.3 m if polyurethane foam strip exists in the shack. To give a comprehensive analysis, more data will be presented in our future work according to the site survey in South Africa.

2.2 Critical Separation Distance in Real Fire

To investigate the effective critical heat flux distance in real informal settlement fires, an assessment of the separation distance between dwellings was carried out in Masiphumelele. Masiphumelele was established in 1992 and although portions of the settlement have been formalized through the provision of housing and services (through the City of Cape Town), the settlement has expanded northwards into the adjacent wetland where the housing remains informal. Flooding, particularly in the winter months, is a challenge for residents and canals have been constructed as a mitigation measure.

Two big fires occurred in 2014 and 2015 in Masiphumelele, however, both fires did not spread beyond the canal located in the north-eastern portion of the study area, as shown in Fig. 1. In the case of the fire on 23 May 2014, the canal formed the most westerly boundary of the fire and in the 28 November 2015 fire, the same canal formed the most easterly boundary. Although there may be other contributing factors, the possibility of the canal acting as an impassable separation distance, which may have exceeded the critical heat flux distance, should get more attention.

In fulfilment of the first GIS aim of the project, using ArcGIS 10.5.1 software, the width of the canal was measured to be approximately 3.0 m with dwellings being built very close to the edge of the canal. The distance between the dwelling roof edges at different sides was measured along the canal. It should be noted that measurements are approximate as they are obtained from aerial photography (courtesy City of Cape Town) with a ground sampling distance of 0.08 m, and although the images have been geocorrected, the layover effect may be somewhat influencing the measurements. From Fig. 3, it can be seen that, in 2014, the minimum separation distance between dwellings on opposite banks was approximately 3.3 m. In 2015, this minimum distance changed to approximately 4.0 m due to reconstructions after the 2014 fire. Thus, the effective separation distance in these particular fires should be at least 3.3 m which agrees very well with our theoretical predictions. In our future work, more informal settlement fire scenarios will be analysed for a more accurate effective separation distance.
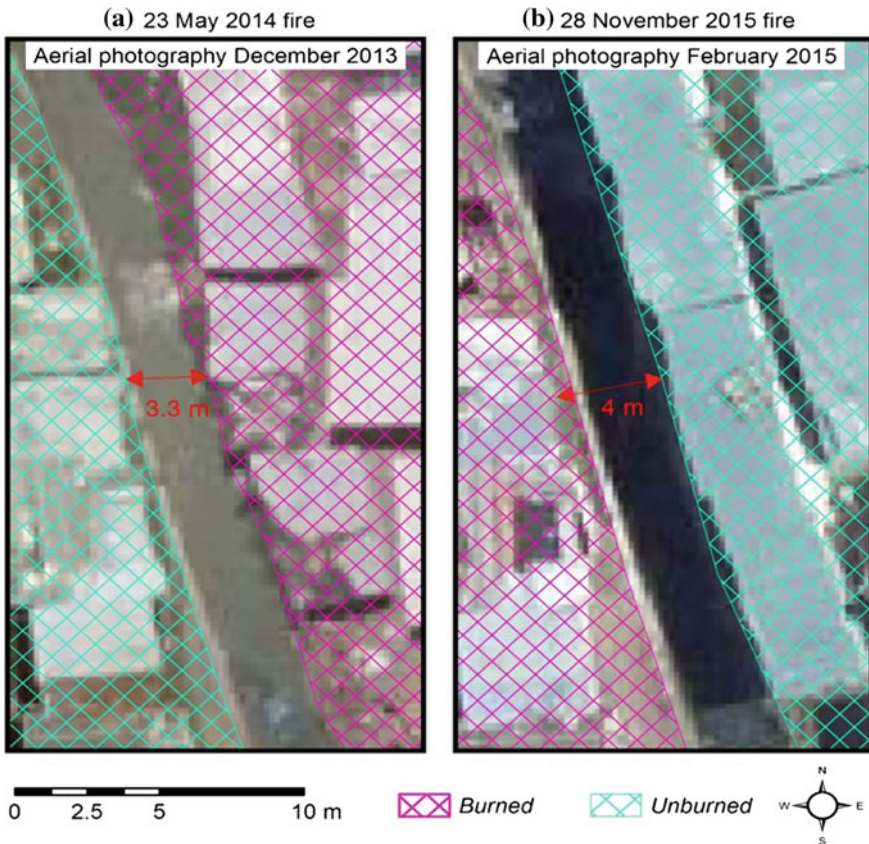
Fig. 3 Eastern canal as a barrier to fire spread: in the fires of 23 May 2014 and 28 November 2015

3 Discussion

Two different methods were employed to estimate the critical fire safety separation distance between shacks. The assumptions made in the analysis are all conservative. From the theoretical and geographic information system analysis, the conservative critical value should be within 3.3–4.0 m. Although each method has its own assumptions and limitations, their results are in good agreement and could be used to provide a valuable reference for the fire safety design of informal settlement planning. It would be difficult to make all the shacks have a distance as large as those suggested due to the competition for habitable space from residents in the informal settlements [2], but it could be a promising option to divide the whole area into several blocks by canals, roadways or fireproof wall as 'fire compartmentalization'. In addition, due to the nature of informal settlement development, firefighting systems in these residential area are very limited. The applicability of smoke detectors is still to be verified. During the firefighting operations, residents have been known to inhibit the strategic efforts of the fire service to protect their immediate concern of protecting their own dwelling. Thus, a permanent method to promote fire safety, i.e. the separation distances, would be a useful way to avoid the fire spread. However, it should be noted that in this work, the fire spread by branding is not considered for the estimation of critical distance as it can spread as great as few kilometres in a real wildland–urban interface (WUI) areas [21].

Since the critical distance may vary significantly when different materials are adopted for shack construction, it is important to know the potential risk in the real informal settlement. Based on the distance between shacks, this section is to assess whether the risk of multi-dwelling fires was increased, decreased or remained unchanged through the reconstruction of the settlement after the fire on 28 November 2015. Pre- and post-fire roof footprints for the area that burned in the 2015 fire were captured from high-resolution aerial photography in a GIS. Using a technique called buffering, the roof footprints were incrementally expanded using separation distances from 0.25 m up to a maximum of 3.0 m. If the critical distance exceeds the real separation distance, it is assumed that all shacks within the separation distance will burn out once a single structure in this area has been ignited.

The size (m^2) of the maximum continuous roof structure at each increment was calculated and expressed as a percentage of the total area. By plotting the separation distance against the largest continuous structure expressed as a percentage of the total area burned (Fig. 4), the layout of the settlement can be assessed to establish the risk of the whole area burning down. With this information, it is possible to combine the concepts of critical distance and separation distance to determine the risk of the settlement to experience large multi-dwelling fires. Using the theoretical continuous roof structure method, it can be found that before the occurrence of the fire, the separation distances of around 90% shacks are smaller than 1.0 m which are significantly smaller than the predicted critical distance of 3.3 m. This could be the primary reason why a large area was burnt very quickly during the fire. In 2017, it is interesting to find that the situation is getting much better. The reason may

Fig. 4 Separation distance as an indication of the risk of the settlement to large multi-dwelling fires
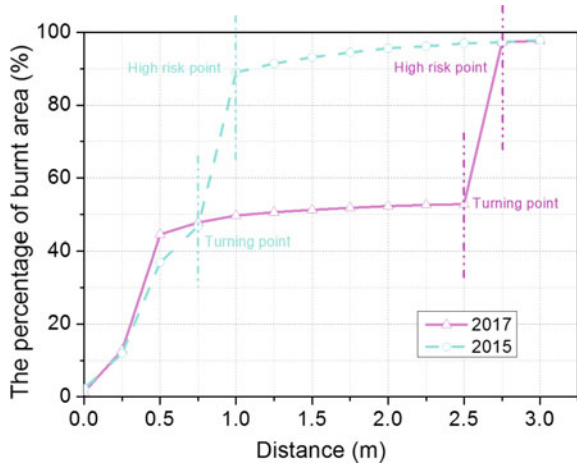
be that the residents learnt from the previous fires or local government, which will be investigated in our future research in social dynamics of informal settlements. However, the risk of the whole area burnt is still larger than 95% if the safety-critical distance is more than 2.75 m. Thus, once there is a fire in one shack, the potential risk of a large area being burnt down is still extremely high.

This is illustrated more clearly in Fig. 5, wherein 2015, a separation of ~1.5 m would result in a single continuous structure covering almost the entire study area. However, in 2017, the critical distance would need to approach 3.0 m to have the same extent. It has been shown that the separation distance between individual dwellings becomes very important when considering critical distance. Improving the fire resistance of construction and improving the fire safety of stored materials could increase the critical safety separation distance and thus decrease the fire risk of the whole area. In particular, if combustible materials similar to polyurethane foam is replaced with less combustible materials in this area, the critical separation distance will reduce from 3.3 m to around 2.2 m, resulting the dramatic risk decrease from 98% to approximately 50% according to the current informal settlement situation in 2017, as shown in Fig. 4.

It should be noted that this work is an initial attempt to understand this influence of separation distances on the fire spread within informal settlements, and more generally, what material and geometric factors within individual dwellings have on potential fire spread. Future investigations will assess more fire cases, consider more robust theoretical and numerical modelling to develop new methods and tools required to evaluate and model fire risks within informal settlements so that situationally appropriate and cost-effective solutions and strategies can be suggested to improve the resilience of South African informal settlement communities against large-scale conflagrations.
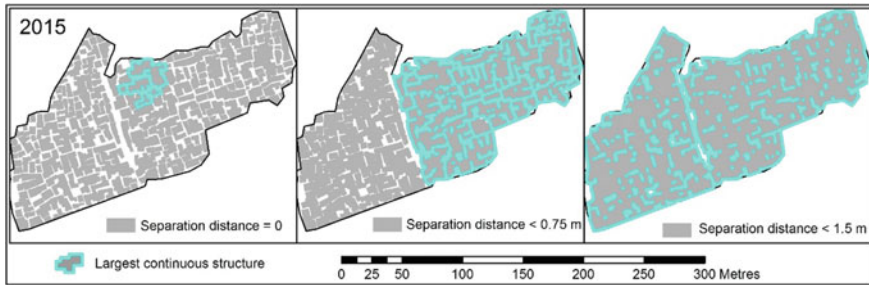
(a) Pre-fire dwelling layout in 2015
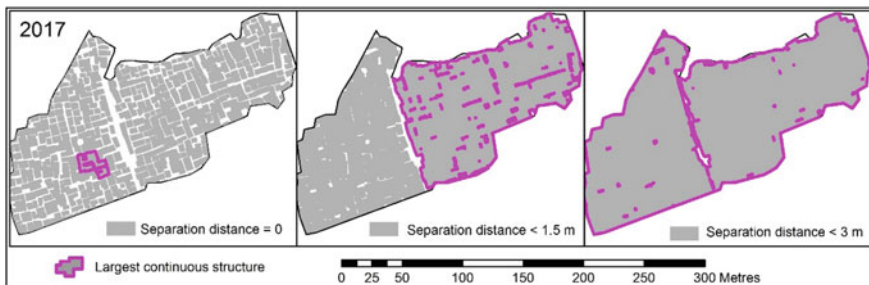
(b) Post-fire dwelling layout in 2017

Fig. 5 Pre- and post-fire dwelling layout showing the extent of a single continuous structure while varying the separation distance

4 Conclusions

This paper demonstrates effective approaches to determine the critical separation distance for fire spread. The risk of multi-dwelling fires is then assessed with respect to the layout of the settlement pre- and post-fire for the 2015 fire. The primary conclusions are as follows:

(1) Theoretical work indicates that the critical separation distance should be at least 3.3 m so as to ensure the fire will not spread between shacks.
(2) The distance was verified by the spatial analysis of the layout of dwellings in the two fires in 2014 and 2015, which shows the critical distance is 3.3 and 4.0 m and provide a proof of concept of the application of GIS to fire safely science in informal settlements.
(3) Separating the informal settlement area into different blocks with this critical distance may be a practical method to avoid or slow down the fire spread.
(4) Although the distance between shacks increased after the fire, according to the risk map determined by separation distance, there still exists very high fire spread risk in the informal settlement.
(5) Increasing the fire resistance of construction materials will substantially and significantly improve the fire safety situation in this area.

(6) More efforts in fire safety engineering and social science are needed to solve the problem, which will be presented in our future work.

References

1. Habitat, U. (2013). State of the world's cities 2012/2013: Prosperity of cities, Routledge.
2. Walls, R., Olivier, G., & Eksteen, R. (2017). Informal settlement fires in South Africa: Fire engineering overview and full-scale tests on "shacks". *Fire Safety Journal, 91,* 997–1006.
3. DMFRS. (2015). Western cape strategic framework for fire and burn injury prevention. In *Western cape disaster management and fire rescue services*.
4. Roberts, E. (2017). Migrants without shelter after fire destroys French refugee camp in CNN.
5. Fire in Germany refugee shelter injures 37 in The Local de (2017).
6. Walls, R., & Zweig, P. (2017). Towards sustainable slums: Understanding fire engineering in informal settlements. In *Advanced technologies for sustainable systems* (pp. 93–98). Springer.
7. Himoto, K., & Tanaka, T. (2008). Development and validation of a physics-based urban fire spread model. *Fire Safety Journal, 43,* 477–494.
8. Himoto, K., Tsuchihashi, T., Tanaka, Y., & Tanaka, T. (2009). Modeling thermal behaviors of window flame ejected from a fire compartment. *Fire Safety Journal, 44,* 230–240.
9. Wang, Y., & Rush, D. (2018). Determination of critical fallout condition of tempered glass in an enclosure fire. *Fire Safety Journal, 101,* 18–24.
10. Law, M., & O'Brien, T. (1989). *Fire safety of bare external structural steel*. Steel Construction Institute.
11. Moradi, A. (2016). *Fire spreading in South African low-cost settlements "A physics-based model"*. Stellenbosch: Stellenbosch University.
12. Drysdale, D. (2011). *An introduction to fire dynamics*. Wiley.
13. Lee, S. W., & Davidson, R. A. (2010). Physics-based simulation model of post-earthquake fire spread. *Journal of Earthquake Engineering, 14,* 670–687.
14. Wang, Y., Wang, Q., Su, Y., Sun, J., He, L., & Liew, K. M. (2015). Fracture behavior of framing coated glass curtain walls under fire conditions. *Fire Safety Journal, 75,* 45–58.
15. Bergman, T. L., Incropera, F. P., & Lavine, A. S. (2011). Fundamentals of heat and mass transfer. Wiley.
16. Wang, Y., Li, K., Su, Y., Lu, W., Wang, Q., Sun, J., et al. (2017). Determination of critical breakage conditions for double glazing in fire. *Applied Thermal Engineering, 111,* 20–29.
17. Cuzzillo, B. R., & Pagni, P. J. (1998). Thermal breakage of double-pane glazing by fire. *Journal of Fire Protection Engineering, 9,* 1–11.
18. Meth, P. (2017). Informal housing, gender, crime and violence: the role of design in Urban South Africa. *The British Journal of Criminology, 57,* 402–421.
19. Spearpoint, M. J., & Quintiere, J. G. (2001). Predicting the piloted ignition of wood in the cone calorimeter using an integral model—effect of species, grain orientation and heat flux. *Fire Safety Journal, 36,* 391–415.
20. Smith, W. K., & King, J. B. (1970). Surface temperatures of materials during radiant heating to ignition. *Journal of Fire and Flammability, 1,* 272–288.
21. Koo, E., Pagni, P. J., Weise, D. R., & Woycheese, J. P. (2010). Firebrands and spotting ignition in large-scale fires. *International Journal of Wildland Fire, 19,* 818–843.

Spectral Characteristic Analysis of Burned Area Based on MODIS Data

Rui Ba, Weiguo Song, Siuming Lo and Zixi Xie

Abstract Wildfires are one of the major serious disasters all over the world. The technology of satellite remote sensing provides useful data for post-fire assessment. This study aimed to investigate the optimal spectral indices for mapping post-fire-burned area. We acquired the post-fire data of Moderate Resolution Imaging Spectroradiometer (MODIS) sensor over several wildfires in boreal forest in western America, 2016. Then, we adopted empirical formula and multi-threshold method to extract the sample sets of five types (burned area, vegetation, cloud, bare soil, and shadow). The separability of spectral indices between burned area and other four types was analyzed by separability index M. Based on the spectral characteristic analysis of burned area, the value of separability index M of the six spectral indices (VI, CSI, MIRBI, NBR, NSEv1, and NSTv1) is larger than 1.0, which indicates that these indices perform well in discriminating burned area and unburned types, and NIR (0.841–0.876 µm), SWIR (2.105–2.155 µm) spectral domain, emissivity of thermal infrared band and land surface temperature are also proved to be sensitive to burned area. The optimal spectral indices obtained in this paper can be integrated into the burned area detection algorithm in further research.

Keywords Remote sensing · MODIS · Burned area · Spectral indices

Nomenclature

ρ_i Reflectance of spectral band i
T_i Bright temperature of spectral band i (K)
E_i Emissivity of spectral band i

R. Ba · W. Song (✉) · Z. Xie
State Key Laboratory of Fire Science, University of Science and Technology of China, Hefei, Anhui 230027, China
e-mail: wgsong@ustc.edu.cn

R. Ba · S. Lo
Department of Civil and Architectural Engineering, City University of Hong Kong, Hong Kong 999077, China

T_s Land surface temperature (°C)

M   Separability index

Greek Symbols

α Slope of empirical formula

β Vertical offset of empirical formula

μ Mean value

σ Standard deviations

Subscripts

i Spectral band

b Burned area

u Unburned type

1 Introduction

During the past few years, wildfires still posed a huge threat to forest ecological system and human lives. Wildfires can ruin the vegetation and buildings on the ground, so it is necessary to evaluate burned area for post-fire assessment.

As a vital part of forest fire research, burned area mapping has been a hot research topic for practical application. In recent years, satellite remote-sensing technology has achieved quite great progress, and satellite can provide valuable information for burned area research. The specifications of satellite sensors determine its applicable ability for burned area research. The major satellite sensors contain the Advanced Very High Resolution Radiometer (AVHRR) [1, 2], VEGETATION (VEG) [3, 4], Moderate Resolution Imaging Spectroradiometer (MODIS) [5–8], Enhanced Thematic Mapper plus (ETM+) [9–12], Advanced Spaceborne Thermal Emission and Reflection Radiometer (ASTER) [13, 14], and Synthetic Aperture Radar (SAR) [9, 15]. MODIS sensor has 36 spectral bands ranging from 0.4 to 14.4 μm as well as global, daily imaging capacity, which can provide abundant data for burned area mapping. On account of complex cover types on the ground, numerous spectral indices were developed to represent the characteristic of different types. A variety of research adopted Normalized Difference Vegetation Index (NDVI) [16] to represent the growing condition of vegetation, and the variations of NDVI were also applied to burned area research, such as Enhanced Vegetation Index (EVI) [17], Global Environment

Monitoring Index (GEMI) [18], Soil Adjusted Vegetation Index (SAVI) [19], Vegetation Index (VI) [5]. In particular, several burned area indices were proposed to reflect the spectral characteristic of burned area. Widely used indices including Burned Area Index (BAI) [20], Char Soil Index (CSI) [21], Mid Infrared Burn Index (MIRBI) [22], Normalized Burn Ratio (NBR) [23]. In addition, S. Veraverbeke et al., developed spectral indices integrating emissivity and land surface temperature to burned area mapping [14].

Numerous studies have carried out to investigate spectral indices over burned area mapping using satellite remote-sensing data. Loboda et al. [7] exploited Normalized Burned Ratio (NBR) to distinguish burned area, while Giglio et al. [5] apply Vegetation Index (VI) to measure the burned. Stroppiana et al. [9, 11, 12, 24] investigated the separability of several spectral indices to distinguish burned area from unburned types based on Landsat TM and ASTER data. Besides, Veraverbeke et al. [14] analyzed the availability of the spectral indices as feature indicators of burned area, which were used to extract the post-fire-burnt extent. However, the applicability of spectral indices derived from spectral bands of MODIS sensor between burned area and other specific cover types have not been deeply investigated. It is necessary to analyze the differences of spectral indices characteristics between burned area and different unburned types.

The purpose of this paper is to assess the separability of spectral indices between burned area and other four unburned types. This paper is mainly focused on several wildfires in boreal forest in America, 2016. We use an empirical formula and multi-threshold method to extract sample sets of five types (burned area, vegetation, bare soil, cloud and shadow). Furthermore, spectral characteristic analysis was carried out to select the optimal spectral indices which can discriminate burned area from unburned types.

2   Study Area

Three large wildfires including Hot Pot Fire, Nevada (July 2, 2016), Range 12 Fire, Washington (July 30, 2016), and Rey Fire, California (August 18, 2016) were selected as our study area. Sample sets of five cover types were extracted from the study area. Major pre-fire plant communities contained brush, long and short grass in Hot Pot Fire, tall grass, brush and short grass in Range 12 Fire, and burned grass, brush, and oak canopy in Rey Fire. The information of fires and vegetation communities are acquired from Incident Information System (InciWeb) (https://inciweb.nwcg.gov/).

The false-color MODIS images generated from band 7-5-6 of the wildfires are shown in Fig. 1. The regions visible as dark purple area are deemed to burned area [8]. Figure 1a shows the burned area of Hot Pot Fire in Nevada, and the MODIS data was acquired on July 7, 2016. Figure 1b shows the burned area of Range 12 Fire in Washington, and the MODIS data was acquired on August 6, 2016. The third case is the burned area of Rey Fire in California, and the MODIS data was acquired on August 24, 2016, which is presented in Fig. 1c.
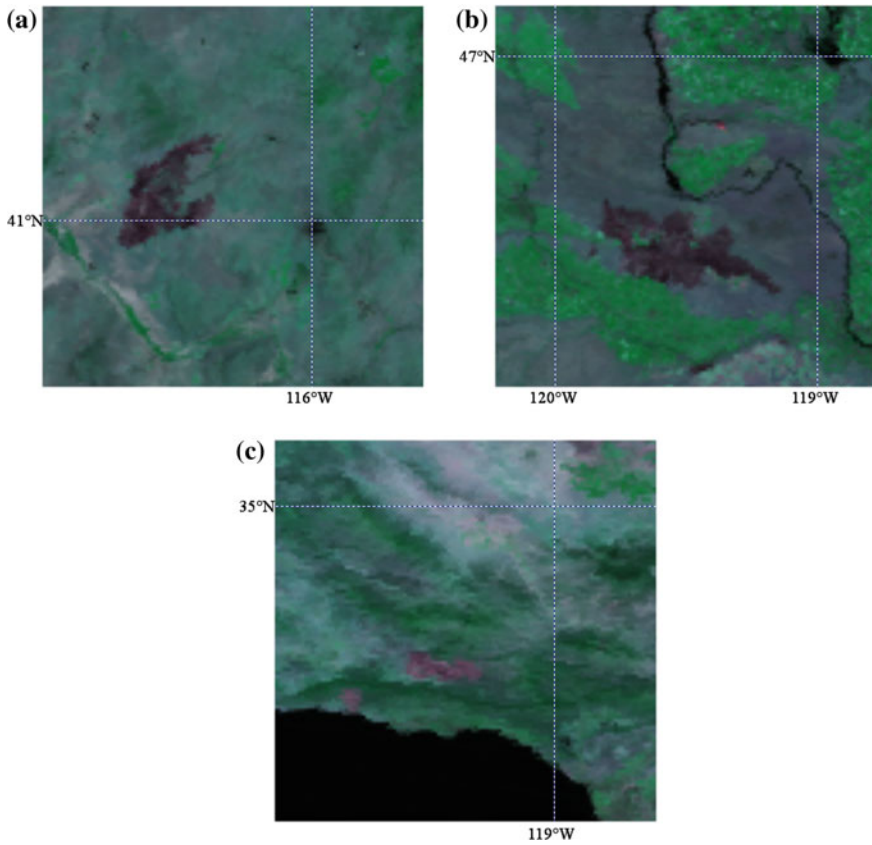
Fig. 1 False-color MODIS images generated from band 7-5-6: **a** burned area of Hot Pot Fire occurred in Nevada; **b** burned area of range 12 fire occurred in Washington; **c** burned area of Rey Fire and several other wildfires occurred in California

3 Methodology

The proposed methodology aims to select the most appropriate spectral indices which can represent the spectral characteristics of burned area. Firstly, a series of data pre-processing steps was applied for original data, and the details are shown in Sect. 3.1. The main procedure of the methodology is composed of two phases. In the first phase, we extracted sample sets of five types by empirical formula, multi-threshold method and visual interpretation on false-color composition image generated by MODIS bands 7, 5, and 6. In the second phase, we carried out the spectral characteristic analysis for different types, which helped us to select the optimal spectral indices to discriminate burned area. The major two phases are presented in Sects. 3.2 and 3.3. The flowchart of the proposed methodology is depicted in Fig. 2.
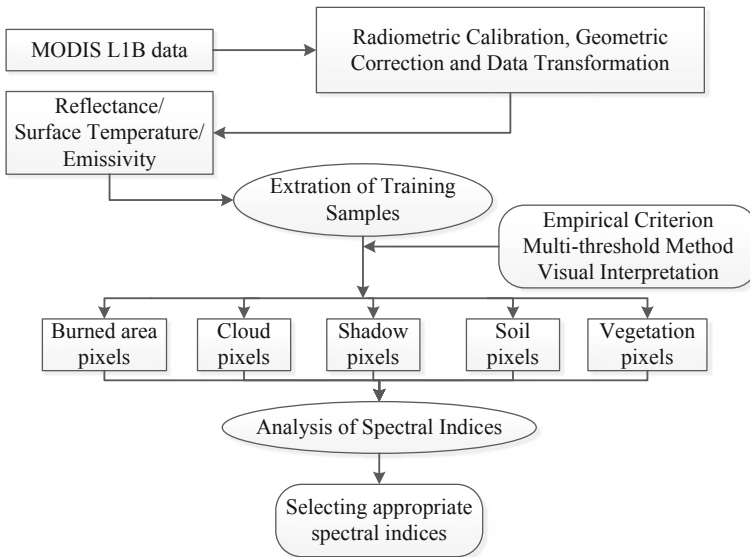
Fig. 2 Flowchart of the proposed methodology for spectral characteristic analysis of burned area

3.1 MODIS Data

The research methodology in this study was developed on MODIS L1B data (MOD02/MYD02) and geolocation data (MOD03/MYD03), which were acquired from the MODIS web (https://modis.gsfc.nasa.gov/) and our remote-sensing laboratory located in Hefei, China. The Terra and Aqua satellite both carry MODIS sensor, and Terra has a 10:30 am equatorial crossing time, while Aqua has a 1:30 pm equatorial crossing time. The width of viewing swath can reach to 2330 km, and it can view the entire surface of the Earth every one to two days, which can provide abundant monitoring data for wildfires. The MODIS sensor has 36 spectral bands in the range of 0.4–14.4 microns which cover from visible to thermal infrared domain. The data of each spectral band are sampled at 1-km meter resolution for subsequent processing.

At the data pre-processing steps, we applied radiometric calibration and geometric correction for original MODIS L1B data. The visible and near-infrared spectral bands were converted to reflectance while thermal infrared band was processed to emissivity, and we can also get the geographic information of the study area. Split-window algorithm [25] was adopted to retrieve land surface temperature. At last, the data of reflectance, emissivity, and surface temperature were combined to derive the spectral indices.

3.2 Extraction of Sample Sets

3.2.1 Empirical Formula of Burned Area Samples

We extracted burned and unburned samples by two rectangular boxes on the false-color RGB 7-5-6 MODIS images by visual interpretation, which is shown in Fig. 3. The pixels we extracted by box 1 contain pixels of burned area and unburned types, while those extracted by box 2 only contain pixels of unburned types. Based on the sample sets, we plotted the scatter plots of reflectance at band 5 versus reflectance at band 7 for the pixels within two boxes. The scatter plot of pixels in box 1 and box 2 is, respectively, shown as Fig. 4a and b, and the integration of the two plots is shown in Fig. 4c, where red symbols represent the pixels in box 1 and black symbols represent the pixels in box 2. We adopted the linear empirical formula Eq. (1), which was proposed in Ref. [8] to discriminate burned area, and the results are drawn in Fig. 4.

After analysis of samples in Hot Pot Fire occurred in Nevada, the coefficient α and β is, respectively, determined as 1.04 and 0.02. The pixels satisfying the condition are classified as burned area pixels. In order to eliminate noisy pixels, we also adopted a series of thresholds (Eq. 2) with the empirical formula Eq. (1) to acquire burned area pixels.

$$\frac{\rho_5 - \beta}{\rho_7} < \alpha \tag{1}$$

$$0.05 < \rho_5 < 0.2 \text{ and } \rho_2 < 0.18 \text{ and } \rho_7 > 0.05 \text{ and } \rho_6 > 0.05 \tag{2}$$

Fig. 3 Extraction of burned and unburned pixels by two boxes: box 1 covers burned area and unburned types, while box 2 only covers unburned types
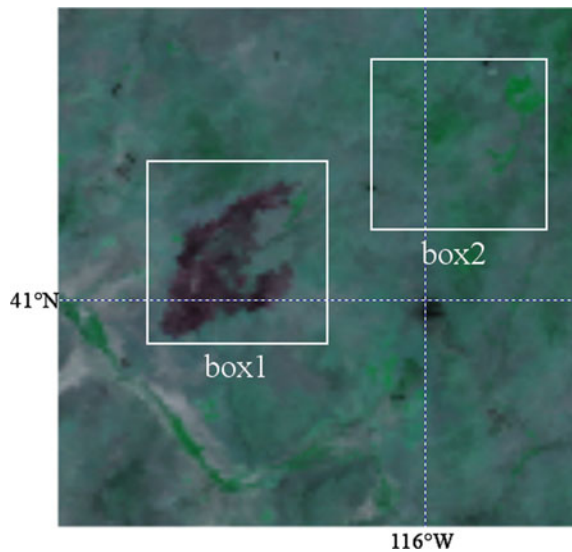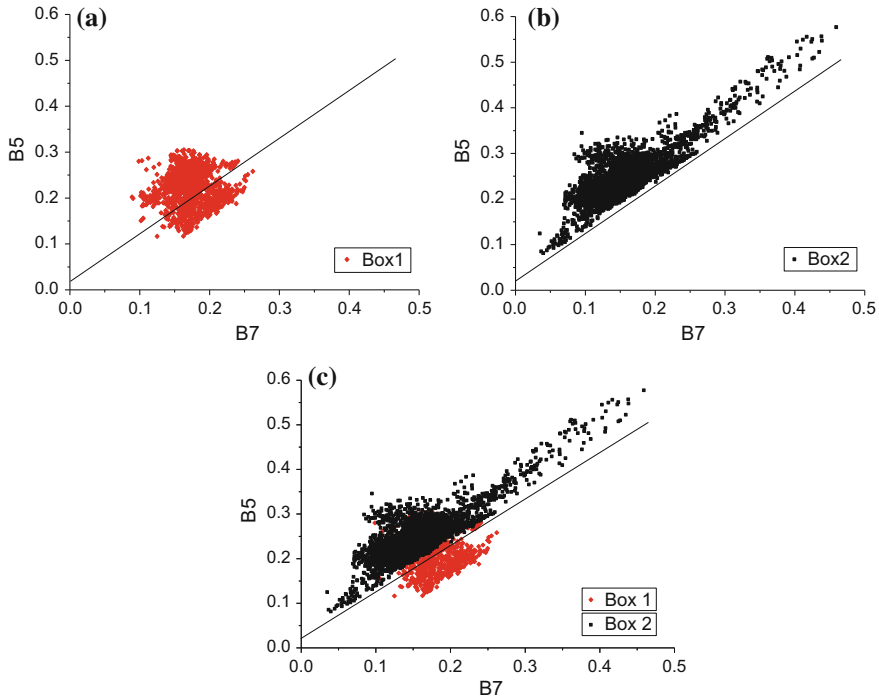
Fig. 4 Scatter plot of reflectance at band 5 versus reflectance at band 7 at Hot Pot Fire, Nevada. **a** scatter plot of pixels in box 1; **b** scatter plot of pixels in box 2; **c** integration of (**a**) and (**b**)

where ρ_i refers to the reflectance of band i, α, and β, respectively, refers to the slope and vertical offset of the empirical formula in Fig. 4.

The method to extract burned pixels was also applied to other wildfire sites. Furthermore, the coefficient α and β of other wildfire samples is, respectively, determined as 0.59, 0.08 in Washington, and 0.75, 0.06 in California. Figure 5a shows the scatter plot of Range 12 fire, Washington, and Fig. 5b shows Rey fire and several other wildfires, California.

3.2.2 Multi-threshold Method of Other Four Types Samples

The Normalized Difference Vegetation Index (NDVI) has a good representation of growth condition of vegetation. As a result, NDVI was adopted to extract vegetation samples, as shown in Eq. (3) [26]. The method to extract cloud samples was based on the cloud detection technique used in the production of the International Geosphere Biosphere Program (IGBP) AVHRR-derived Global Fire Product [27]. The criterions applicable to discriminate larger, cooler cloud pixels [26, 28] are shown as Eq. (4). Samples of cloud shadow pixels were collected by visual interpretation on false-color
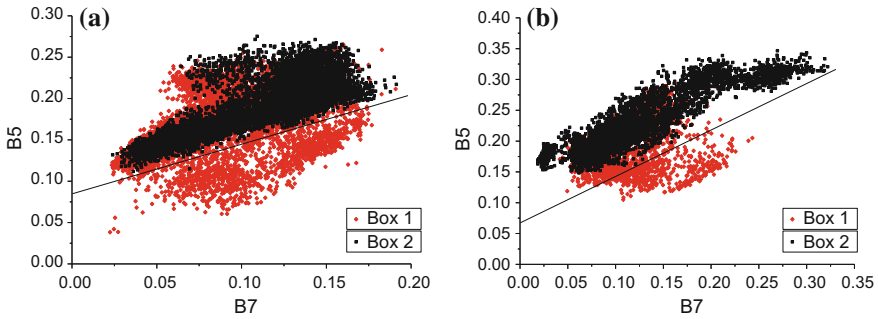
Fig. 5 Integrated scatter plot of pixels in two boxes. **a** integrated scatter plot of Range 12 fire, Washington; **b** integrated scatter plot of Rey fire and several other wildfires, California

RGB 7-5-6 MODIS composition images. Besides, visual interpretation and multi-threshold method (Eq. (5) [29]) were applied to extract the samples of bare soil pixels.

$$\text{NDVI} = (\rho_2 - \rho_1)/(\rho_2 + \rho_1) > 0.3 \tag{3}$$

$$((\rho_1 + \rho_2) > 0.9) \text{ or } (T_{32} < 265\,\text{K}) \text{ or } ((\rho_1 + \rho_2) > 0.7 \text{ and } T_{32} < 265\,\text{K}) \tag{4}$$

$$((\rho_9 - \rho_7)/(\rho_9 + \rho_7) \geq 0.1) \text{ and } (\text{NDVI} = (\rho_2 - \rho_1)/(\rho_2 + \rho_1) < 0.2) \tag{5}$$

where ρ_i refers to the reflectance of band i, and T_i represents the bright temperature of band i.

3.3 Analysis of Spectral Indices

The separability index has been widely used to quantificationally analyze the separation between two cover types [9, 11, 14, 26]. We applied separability index *M* (Eq. 6) to represent the separation degree between burned area and unburned type in different spectral indices. The spectral indices listed in Table 1 incorporated reflectance, emissivity, and land surface temperature were analyzed, including three kinds of spectral indices: vegetation indices (NDVI, EVI, GEMI, SAVI and VI), burned area indices (BAI, CSI, MIRBI, NBR) and new version indices combined by emissivity of thermal infrared band and land surface temperature (NSEv1, NSEv2, NSTv1). The parameters in the formulas of indices are set for specific surface features. For example, the adjustment factor L of EVI is the canopy background adjustment which stresses the nonlinear radiant transfer between NIR and red band through a canopy, while the coefficients C1, C2 are the aerosol resistance terms which aim to correct aerosol influences in red band by blue band [17]. The effect of each parameter can be found in the corresponding reference listed in the last column of Table 2. Based on

Table 1 Spectral indices used to analyze spectral characteristic of burned area in our research

Spectral index	Formula	References
Normalized difference vegetation index	$NDVI = \frac{\rho_2 - \rho_1}{\rho_2 + \rho_1}$	[16]
Enhanced vegetation index	$EVI = G \times \frac{\rho_2 - \rho_1}{\rho_2 + C_1 \times \rho_1 - C_2 \times \rho_3 + L}$ where G = 2.5, L = 1.0, C_1 = 6.0, C_2 = 7.5	[17]
Global environment monitoring index	$GEMI = \eta(1 - 0.25\eta) \times \frac{\rho_5 - 0.125}{1 - \rho_5}$ where, $\eta = \frac{2 \times (\rho_7^2 - \rho_5^2) + 1.5\rho_7 + 0.5\rho_5}{\rho_7 + \rho_5 + 0.5}$	[18]
Soil adjusted vegetation index	$SAVI = \frac{\rho_2 - \rho_1}{\rho_2 + \rho_1 + L}(1 + L)$ where, L = 0.5	[19]
Vegetation index	$VI = \frac{\rho_5 - \rho_7}{\rho_5 + \rho_7}$	[5]
Burned area index	$BAI = \frac{1}{(0.1 - \rho_1)^2 + (0.06 - \rho_2)^2}$	[20]
Char soil index	$CSI = \frac{\rho_2}{\rho_6}$	[21]
Mid infrared burn index	$MIRBI = 10 \times \rho_7 - 9.5\rho_6 + 2$	[22]
Normalized burn ratio	$NBR = \frac{\rho_2 - \rho_7}{\rho_2 + \rho_7}$	[23]
NIR-SWIR-emissivity versions 1	$NSEv1 = \frac{\rho_2 - \rho_7}{\rho_2 + \rho_7} \times E_{32}$	[14]
NIR-SWIR-emissivity versions 2	$NSEv2 = \frac{\rho_2 - (\rho_7 + E_{32})}{\rho_2 + \rho_7 + E_{32}}$	
NIR-SWIR-T_s versions 1	$NSTv1 = \frac{\rho_2 - \rho_7}{\rho_2 + \rho_7} \times T_s$	

ρi and Ei, respectively, is the reflectance and emissivity of band i, and Ts is the land surface temperature

Table 2 Value of separability index M of different spectral index between burned area and unburned types over the three wildfire sites

Spectral index	Hot pot fire, Nevada				Range 12 fire, Washington		Rey fire, etc., California	
	1	2	3	4	3	4	3	4
NDVI	1.491	0.333	0.626	2.467	0.889	4.048	0.334	2.088
EVI	1.956	0.351	1.435	1.913	1.597	3.136	1.333	2.119
GEMI	0.821	1.249	0.711	0.313	1.389	0.283	1.957	0.044
SAVI	0.020	0.423	1.235	2.161	1.561	3.609	0.966	2.275
VI	1.445	2.138	1.326	3.118	1.992	3.421	1.095	2.450
BAI	1.399	0.410	0.909	0.934	2.040	2.596	2.168	1.695
CSI	1.213	1.992	1.338	1.761	1.246	2.357	0.752	1.344
MIRBI	2.125	1.051	1.336	2.516	2.058	1.759	2.286	2.162
NBR	1.696	2.494	1.658	2.835	1.939	3.667	1.20	2.285
NSEv1	1.696	2.497	1.660	2.866	1.938	3.659	1.202	2.282
NSEv2	2.843	0.156	1.196	1.498	1.714	1.637	2.90	1.869
NSTv1	1.565	2.540	1.651	2.815	1.943	3.739	1.081	2.043

The number 1, 2, 3, 4 in the header of the table, respectively, refers to the comparison between burned area and cloud, shadow, bare soil as well as vegetation

the spectral characteristic analysis, we select the optimal spectral indices to represent the spectral characteristic of burned area.

$$M = \frac{\left|\mu_{i,b} - \mu_{i,u}\right|}{\sigma_{i,b} + \sigma_{i,u}} \tag{6}$$

where $\mu_{i,b}$ and $\sigma_{i,b}$, respectively, refers to mean value and standard deviations of burned area, while $\mu_{i,u}$ and $\sigma_{i,u}$, respectively, represents that of unburned type. The higher value of M, the better discrimination between burned area and unburned type.

4   Results and Discussion

We have analyzed three kinds of spectral indices: vegetation indices (NDVI, EVI, GEMI, SAVI and VI), burned area indices (BAI, CSI, MIRBI, NBR) and new version spectral indices added emissivity and land surface temperature (NSEv1, NSEv2, NSTv1). Vegetation indices reflect the growing condition of vegetation. NDVI is commonly used because it is very sensitive to the chlorophyll of vegetation. After the destruction of vegetation, NDVI value decreases as a result of the reflectance of NIR spectral region decreases while that of red band increases [2]. VI has been developed to map burned area because its value obviously decreases after fire [5]. EVI is optimized to be more sensitive to high biomass area, and it can reduce the undesired signal such as canopy background signal and atmosphere influences [17]. As a modification of NDVI, SAVI can modify the influence of soil brightness [19]. GEMI is designed as vegetation index to reduce the undesirable atmospheric effects [18]. In addition, burned area indices are designed specifically to show spectral characteristic of post-fire land. BAI aims to underline the charcoal signal of burned area [20], while CSI and MIRBI incorporate SWIR spectral band which is proved more sensitive to burned area. NBR is widely used because it utilizes the increase of reflectance at SWIR domain and the drop of reflectance at NIR domain. The third type of spectral index is the modification of the NBR. Based on previous study [14], we adopted NSEv1, NSEv2, and NSTv1 to investigate the effect of emissivity and land surface temperature to identify burned area from other types.

Boxplots of each spectral index in burned area, bare soil, cloud, shadow and vegetation in Hot Pot Fire, Nevada are shown in Fig. 6. The separability index M values of spectral indices between burned and unburned types over three wildfire sites are listed in Table 2. The larger value of M is, the better discriminatory capacity of the spectral index to identify burned area. Spectral indices show significant differences in comparison between burned area and other types. It can be found that VI has the best performance among the vegetation indices over all wildfires and its value of burned area is obviously lower than other types. NDVI has weaker discriminatory capacity to identify burned from other shadow and bare soil despite it is good at discriminating burned area from vegetation and cloud. EVI is unfit for identifying
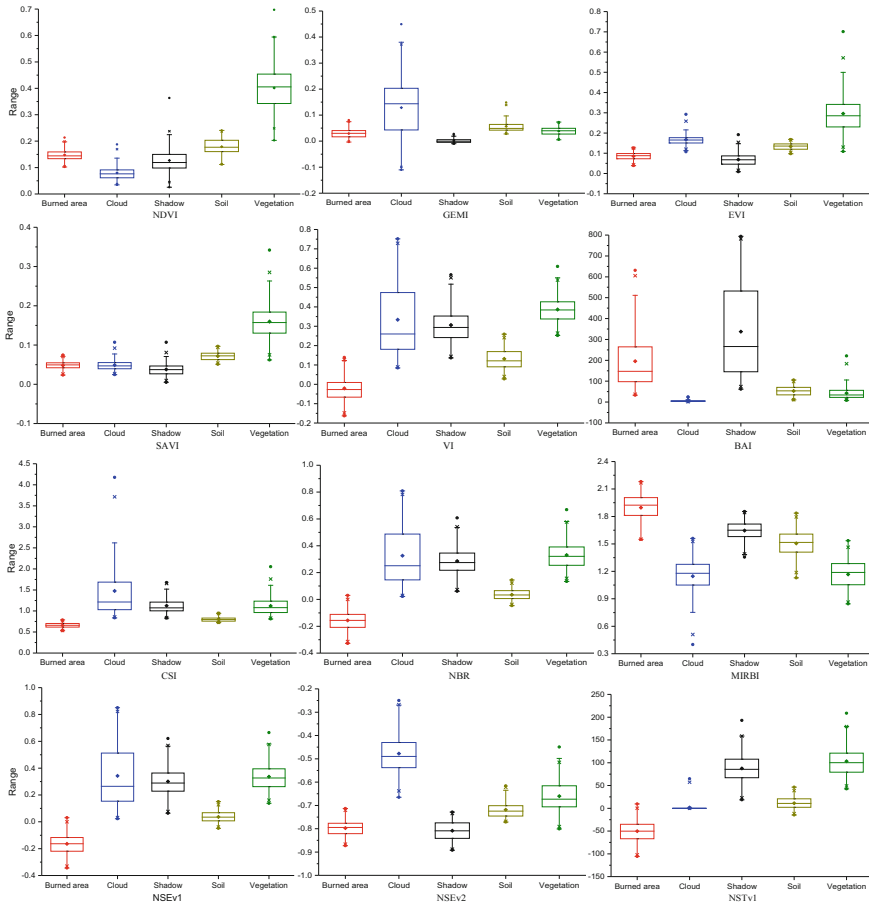
Fig. 6 Boxplots of each spectral index in burned area, bare soil, cloud, shadow and vegetation type over Hot Pot Fire, Nevada

burned area and shadow despite it performs well in other comparisons. Furthermore, GEMI is difficult to discriminate burned area and vegetation, while SAVI has a low value of M in the two comparisons of burned and cloud as well as shadow. The results show that the vegetation indices are good at discriminate burned area and vegetation while its discriminatory capacity is weaker for identifying burned area and other types. According to the statistical results of M, the burned area indices have high value of M besides BAI of which M value between burned and shadow is relatively lower. It indicates that CSI, MIRBI, and NBR which incorporate NIR and SWIR spectral domain are appropriate to be feature indicators of burned area, while NDVI, EVI, SAVI, and BAI which incorporate visible spectral domain have low capacity to identify burned area. Among the third type of spectral indices, NSEv1 and NSTv1 perform better than NSEv2. The results also demonstrate that spectral indices

incorporate NIR and SWIR spectral bands are suitable for burned area discrimination, which further proves that NIR and SWIR spectral domain is sensitive to burned area. In addition, it can be found that the emissivity of thermal infrared band and land surface temperature are effective for burned area identification.

Based on the analysis of spectral indices, six spectral indices including VI, CSI, MIRBI, NBR, NSEv1, and NSTv1 perform well in discriminating burned area and other types, which can be adopted as the feature indicators of burned area.

5   Conclusions

The methodology developed on MODIS data aims to investigate the spectral characteristic of burned area. The methodology applies empirical formula and multi-threshold method to extract sample sets of burned area, vegetation, cloud, shadow, and bare soil. Through the spectral indices analysis of burned area and other types, the results prove that NIR (0.841–0.876 μm) and SWIR (2.105–2.155 μm) spectral domain are more sensitive for burned area, while visible spectral domain including blue (0.459–0.479 μm), green (0.545–0.565 μm), and red (0.62–0.67 μm) spectral domain have low capacity to discriminate burned area with other types. Moreover, the emissivity of thermal infrared band and land surface temperature are effective for burned area detection. In addition, the value of separability index of six spectral indices including VI, CSI, MIRBI, NBR, NSEv1, and NSTv1 between burned area and unburned types over three wildfire sites are larger than 1.0, which indicates that they have high discriminatory capacity for burned area.

The spectral indices investigated by the methodology can be applied to burned area discrimination. It is therefore believed that the methodology is applicable for wildfire assessment. Further research will be devoted to establish training samples and burned area detection algorithm, which can automatically discriminate burned area from other types on MODIS data.

References

1. Pereira, J. M. C. (1999). A comparative evaluation of NOAA/AVHRR vegetation indexes for burned surface detection and mapping. *IEEE Transactions on Geoscience and Remote Sensing, 37*(1), 217–226.

2. Fraser, R. H., Li, Z., & Cihlar, J. (2000). Hotspot and NDVI differencing synergy (HANDS): A new technique for burned area mapping over boreal forest. *Remote Sensing of Environment, 74*(3), 362–376.

3. Stroppiana, D., et al. (2002). Radiometric analysis of SPOT-VEGETATION images for burnt area detection in Northern Australia. *Remote Sensing of Environment, 82*(1), 21–37.

4. Brivio, P., et al. (2003). Mapping burned surfaces in Sub-Saharan Africa based on multi-temporal neural classification. *International Journal of Remote Sensing, 24*(20), 4003–4016.

5. Giglio, L., et al. (2009). An active-fire based burned area mapping algorithm for the MODIS sensor. *Remote Sensing of Environment, 113*(2), 408–420.

6. Cao, X., et al. (2009). An automatic method for burn scar mapping using support vector machines. *International Journal of Remote Sensing, 30*(3), 577–594.

7. Loboda, T., O'Neal, K. J., & Csiszar, I. (2007). Regionally adaptable dNBR-based algorithm for burned area mapping from MODIS data. *Remote Sensing of Environment, 109*(4), 429–442.

8. Li, R. R., et al. (2004). A technique for detecting burn scars using MODIS data. *IEEE Transactions on Geoscience and Remote Sensing, 42*(6), 1300–1308.

9. Stroppiana, D., et al. (2015). Integration of optical and SAR data for burned area mapping in mediterranean regions. *Remote Sensing, 7*(2), 1320–1345.

10. Bastarrika, A., Chuvieco, E., & Martin, M. P. (2011). Mapping burned areas from Landsat TM/ETM plus data with a two-phase algorithm: Balancing omission and commission errors. *Remote Sensing of Environment, 115*(4), 1003–1012.

11. Stroppiana, D., et al. (2012). Positive and negative information for assessing and revising scores of burn evidence. *IEEE Geoscience and Remote Sensing Letters, 9*(3), 363–367.

12. Stroppiana, D., et al. (2012). A method for extracting burned areas from Landsat TM/ETM + images by soft aggregation of multiple Spectral Indices and a region growing algorithm. *ISPRS Journal of Photogrammetry and Remote Sensing, 69,* 88–102.

13. Boschetti, M., Stroppiana, D., & Brivio, P. A. (2010). Mapping burned areas in a Mediterranean environment using soft integration of spectral indices from high-resolution satellite images. *Earth Interactions, 14*.

14. Veraverbeke, S., Harris, S., & Hook, S. (2011). Evaluating spectral indices for burned area discrimination using MODIS/ASTER (MASTER) airborne simulator data. *Remote Sensing of Environment, 115*(10), 2702–2709.

15. Lohberger, S. et al. (2017). Spatial evaluation of Indonesia's 2015 fire affected area and estimated carbon emissions using Sentinel-1. *Global Change Biology*.

16. Tucker, C. J. (1979). Red and photographic infrared linear combinations for monitoring vegetation. *Remote Sensing of Environment, 8*(2), 127–150.

17. Huete, A., et al. (2002). Overview of the radiometric and biophysical performance of the MODIS vegetation indices. *Remote Sensing of Environment, 83*(1), 195–213.

18. Pinty, B., & Verstraete, M. (1992). GEMI: A non-linear index to monitor global vegetation from satellites. *Plant Ecology, 101*(1), 15–20.

19. Huete, A. R. (1988). A soil-adjusted vegetation index (SAVI). *Remote Sensing of Environment, 25*(3), 295–309.

20. Chuvieco, E., Martin, M. P., & Palacios, A. (2002). Assessment of different spectral indices in the red-near-infrared spectral domain for burned land discrimination. *International Journal of Remote Sensing, 23*(23), 5103–5110.

21. Smith, A. M., et al. (2005). Testing the potential of multi-spectral remote sensing for retrospectively estimating fire severity in African Savannahs. *Remote Sensing of Environment, 97*(1), 92–115.

22. Trigg, S., & Flasse, S. (2001). An evaluation of different bi-spectral spaces for discriminating burned shrub-savannah. *International Journal of Remote Sensing, 22*(13), 2641–2647.

23. Key, C. & Benson, N. (1999). Measuring and remote sensing of burn severity. In *Proceedings joint fire science conference and workshop*.

24. Stroppiana, D., et al. (2009). Analysis and interpretation of spectral indices for soft multicriteria burned-area mapping in mediterranean regions. *IEEE Geoscience and Remote Sensing Letters, 6*(3), 499–503.

25. Mao, K., et al. (2005). A practical split-window algorithm for retrieving land-surface temperature from MODIS data. *International Journal of Remote Sensing, 26*(15), 3181–3204.
26. Li, X. L., et al. (2015). Forest fire smoke detection using back-propagation neural network based on MODIS data. *Remote Sensing, 7*(4), 4473–4498.
27. Stroppiana, D., Pinnock, S., & Gregoire, J.-M. (2000). The global fire product: Daily fire occurrence from April 1992 to December 1993 derived from NOAA AVHRR data. *International Journal of Remote Sensing, 21*(6–7), 1279–1288.
28. Giglio, L., et al. (2003). An enhanced contextual fire detection algorithm for MODIS. *Remote Sensing of Environment, 87*(2–3), 273–282.
29. Xie, Y., et al. (2007). Smoke plume detection in the eastern United States using MODIS. *International Journal of Remote Sensing, 28*(10), 2367–2374.

Fire Hazard Assessment of Typical Flammable Liquid Oils in Wind Turbine Nacelle

Wei Sun, Fei You and Ping Li

Abstract To assess fire hazards of gearbox oil and transformer oil applied in the nacelle of a wind turbine, the reaction-to-fire properties prior to combustion should be addressed. Gearbox oil and transformer oil were studied by using cone calorimeter exposed to external radiant heat flux levels of 15, 25, 35, 50, and 75 kW/m^2. Potential fire scenarios in which liquid oils contribute to the fire spread areas and fire intensities were designed and proposed. The reaction-to-fire properties of such oils are researched from two aspects of thermal hazard and nonthermal hazard. And the critical thermal radiant flux (q''_{cr}) and the time of ignition (t_{ig}) were obtained by the conical calorimeter, and the ignition characteristic was analyzed. Results show that based on the analysis of PKHRR and THR, the reaction of fire properties of the transformer oil is higher than gearbox oil, and based on the analysis of PKSEA, PKRSR, and TER, the gearbox oil is higher than transformer oil. In the same radiant heat flux, based on PKHRR and THR to determine the liquid oil fire hazard rankings are: transformer oil > gearbox oil; based on PKSEA and TSR to determine the fire hazard ranking are: gearbox oil > transformer oil. The critical radiant heat flux of gearbox oil and transformer oil is 9.23 and 6.43 kW/m^2 when the radiant heat flux is 15 kW/m^2. The same liquid oils have the least ignition time and the larger fire hazards when the radiant heat flux is 75 kW/m^2.

Keywords Fire hazard assessment · Reaction-to-fire properties · Gearbox oil · Transformer oil · Incident heat flux level · Wind turbine

W. Sun · F. You (✉)
Jiangsu Key Laboratory of Urban and Industrial Safety, Nanjing Tech University, 200 North Zhongshan Rd., Jiangsu, Nanjing 210009, China
e-mail: fyou@njtech.edu.cn

F. You
Institute of Fire Science and Engineering, Nanjing Tech University, 30 South Puzhu Rd., Jiangsu, Nanjing 211800, China

P. Li
Hohai University Wentian College, 333 Horry Mountain Rd., Maanshan, Anhui 243031, China

Nomenclature

q_e'' Radiant heat flux (kW/m^2)
h_{ig} Heat transfer coefficient from the surface at ignition (kW/m^2 K)
q_{cr}'' Critical radiant heat flux (kW/m^2)
$\lambda \rho C$ Thermal inertia (kW^2 s/m^4 K^2)

1 Introduction

Along with the intensification of global atmospheric changes and increasing environmental pressures, the vigorous development of renewable energy has become the consensus of the whole society [1, 2]. Wind power generation has received more and more attention from all over the world due to its technical stability and industrialization development. In the past five years, the world's wind power development has advanced by leaps and bounds, and the installed capacity of wind power has increased rapidly. By 2017, the installed capacity of wind power in the world has reached 539 million kW, and the installed capacity of wind power in China has reached 188 million kW, ranking first in the world [3, 4]. The threat of natural disasters in the large-scale application of wind turbines has attracted more and more attention. The frequency of fire accidents in wind turbines is also increasing every year. Due to the serious and sensitive fan fire accidents, most developers are reluctant to disclose the number of fire accidents, but the fire on the fans is already one of the more prominent wind power accidents in the industry. Moreover, wind farms are generally located in remote areas with sparsely populated areas. It is easy to effectively cover up after a fire accident to avoid causing panic among local personnel. According to the incomplete statistics of the British Wind Energy Organization, on September 30, 2018, there were 337 fire accidents in the world, ranking second in the total number of wind turbine accidents. There have also been many fan fire accidents in China, which will not only cause huge damage to the wind turbine equipment, but also cause a series of casualties and economic losses. It is difficult to extinguish a fire after a wind turbine has a fire accident. In the event of a fire accident, it will cause great economic losses and indirect power loss, and the possibility of external rescue is almost zero. There are many hidden dangers in wind turbines. There are fires in the wind turbine from top to bottom. There are a large number of electrical equipment, flammable liquid and materials inside the cabin. The inside of the tower also has combustible materials and is easy to form air convection. The type of wind turbine fire is very complicated because of the wide variety of combustibles involved, including different types and uses of grease, hydraulic oil, electrical equipment, wire and cable, blades, nacelle covers and their insulation [5]. Therefore, electrical fires, solid fires, and liquid fires can occur. In addition, the wind turbines are often installed

as high as tens of meters or even hundreds of meters from the ground. If a fire occurs, it is almost impossible to effectively control the fire development orientations and situations just on the ground.

The heat release rate (HRR) is the only important parameter used to describe fire intensity size. Quite a few parameters can influence HRR, such as the radiant heat flux levels, ignition locations, fire source materials, fuel loads, fuel phases, and diameters of oil pool fires [6–8]. A higher HRR implies that the higher the temperature and radiant heat flux in the field, the larger the threat to the life and safety of the occupants and surrounding people [9]. Therefore, controlling HRR is an essential measure to prevent the occurrence of fire and reduce the danger of fire. Oil fuels are usually contributing primarily to strong heat release and dense smoke [10]. Hence, it is important to analyze both thermal hazards and nonthermal hazards of liquid oils in wind turbines in combination with reasonable fire scenarios. At present, there are some studies on analysis the performance requirements, monitoring system, and antioxidant properties of the special liquid oils for wind power. Coronado et al. [11] summarized the oil performance sensor to gearbox oil results. Cigno [12] researched the tribological behavior of ionic liquids as additives to gearbox oil. Also, in recent two years, there have occurred some researches aiming at flammability hazards [13, 14], identification of fire issues regarding wind turbines [15], and fire growth simulations [16] in China, UK, and Spain. These pioneer studies provide sound experiences in enriching scientific and engineered fire issues of wind turbines, and also, they point out future directions of improvement to some extent, such as fire properties, thermal decomposition, and potential fire sources selected. However, the reaction-to-fire properties and the fire hazards of real liquid oils utilized in practical fire scenarios have not been discussed. In addition, fire scenarios are required to be elaborately investigated and designed. In consequence, it is necessary to discern possible fire development scenarios including typical oils and carry out a series of experimental characterizations to assess their potential fire hazards.

The aim of this study is to evaluate the thermal hazards and nonthermal hazards of gearbox oil and transformer oil based on the reaction-to-fire properties characterized by cone calorimeter. Afterward, theoretically, the ignition characteristics of the oils were analyzed by calculating the ignition time (t_{ig}) and the critical heat radiation flux (q''). At last, based on the experimental and calculation results, the fire hazards of typical liquid oils in wind turbine nacelle were assessed. Most importantly, this study can determine earlier fire hazards within the special enclosure space wind turbine nacelle with a height of about 70 m, which will provide a theoretical basis and an engineered knowledge for preventing fire in such cases.

2   Materials and Methods

2.1   Sample Preparation and Investigation Methods

The hydraulic oil and transformer oil are selected as typical flammable liquid fuels in wind turbine nacelles. They come from a wind turbine model of G5X-850 kW of the domestic wind farm in Fujian Province of China. Gear oil is mainly based on petroleum lubricating base oil or synthetic lubricating oil and is an important lubricating oil prepared by adding extreme pressure anti-wear agent and oily agent. It is used in various gear transmissions to prevent tooth surface wear, abrasion, sintering, etc., prolong its service life and improve transmission power efficiency. Transformer oil is a fractionated product of petroleum. Its main components are compounds such as alkanes, naphthenic saturated hydrocarbons, and aromatic unsaturated hydrocarbons. Commonly known as square shed oil, light yellow transparent liquid, relative density of 0.895. Freezing point < -45 °C. Transformer oil is a kind of mineral oil obtained by distillation and refining in natural petroleum. It is a liquid natural hydrocarbon which is pure and stable, has low viscosity, good insulation and good cooling a mixture of compounds [12].

According to ISO 5660-1:2002 test method [17], the primary reaction-to-fire properties like heat release rate (HRR), total heat release (THR), specific extinction area (SEA), rate of smoke release (RSR), and total smoke release (TSR) of gearbox oil and transformer oil were measured by cone calorimeter (typed FTT Cone Calorimeter), UK, when the radiant heat flux is 15.0, 25.0, 35.0, 50.0, and 75.0 kW/m^2. The sizes of specimens were 10.0×10.0 cm and held in a retaining frame. The oils were placed into a sample pan with the above sizes and a thickness of 3.0 mm.

3   Results and Discussions

3.1   Identification of Potential Fire Sources in a Wind Turbine Nacelle

None of the aforementioned incidents had detailed reports indicating what is causing the fire. A large number of flammable liquids, flammable materials, and electrical equipment exist in wind turbines, which frequently uses them as shown in Table 1.

Table 1 Combustible material in wind turbine

Component	Material
Impeller	FRP composite, PET, BALTEK
Cabin	Lubricating oil, frequency converter, brake disk, generator, oil stain
Tower	Cable, electrical devices, control cabinet
Blade pitch change mechanism	Hydraulic oil

3.2 Thermal Hazards and Nonthermal Hazards Analysis of Oil Samples

3.2.1 Thermal Hazard Analyses of Individual Oil Samples

The heat release rate and total heat release can reflect the scale of the reaction-to-fire properties [18]. The HRR and THR data and profiles of transformer oil and gearbox oil are shown in Table 2 and Fig. 1. After the ignition, for all oil samples the HRR increases rapidly and appears a peak during the first flaming stage. By HRR curves of transformer oil and gearbox oil and different oils under different external radiant heat fluxes, the peak of HRR (PKHRR) will be increased. The samples were obtained by heating their surface with the radiant heat flux of 15.0, 25.0, 35.0, 50.0, and 75.0 kW/m². The PKHRR values from 385.15 kW/m² (15.0 kW/m²) to 2463.20 kW/m² (75.0 kW/m²), the increase rate is 84.40%, and the synchronous relative rate of change is 4.20 kW/m² s for gearbox oil. The PKHRR of transformer oil increases from 818.74 kW/m² (15.0 kW/m²) to 2480.41 kW/m² (75.0 kW/m²), the increase rate is 66.99%, and the synchronous relative rate of change is 5.36 kW/m² s. However, the opposite is the time of peak HRR (t_{PKHRR}) decreased with the radiant heat flux increased, which is shortened 500 s (gearbox oil) and 310 s (transformer oil). In comparison with several kinds of radiant heat flux, the PKHRR is the largest and the t_{PKHRR} is the least of the transformer oil when the radiant heat flux is 75.0 kW/m².

As can be seen from Fig. 1, after ignited, HRR values of all oils increase rapidly and appear a peak during the flaming stage. With the increase in the external radiant

Table 2 Thermal data of gearbox oil and transformer oil based on cone calorimeter experiments

Radiant heat flux (kW/m²)	Gearbox oil			Transformer oil		
	PKHRR (kW/m²)	THR (MJ/m²)	t_{PKHRR} (s)	PKHRR (kW/m²)	THR (MJ/m²)	t_{PKHRR} (s)
15	385.15	71.01	630	818.74	80.41	415
25	958.74	143.28	320	1584.01	131.07	185
35	1579.17	139.46	235	1941.35	124.56	135
50	1993.37	132.00	145	2212.89	123.09	110
75	2463.20	141.46	130	2480.41	116.58	105
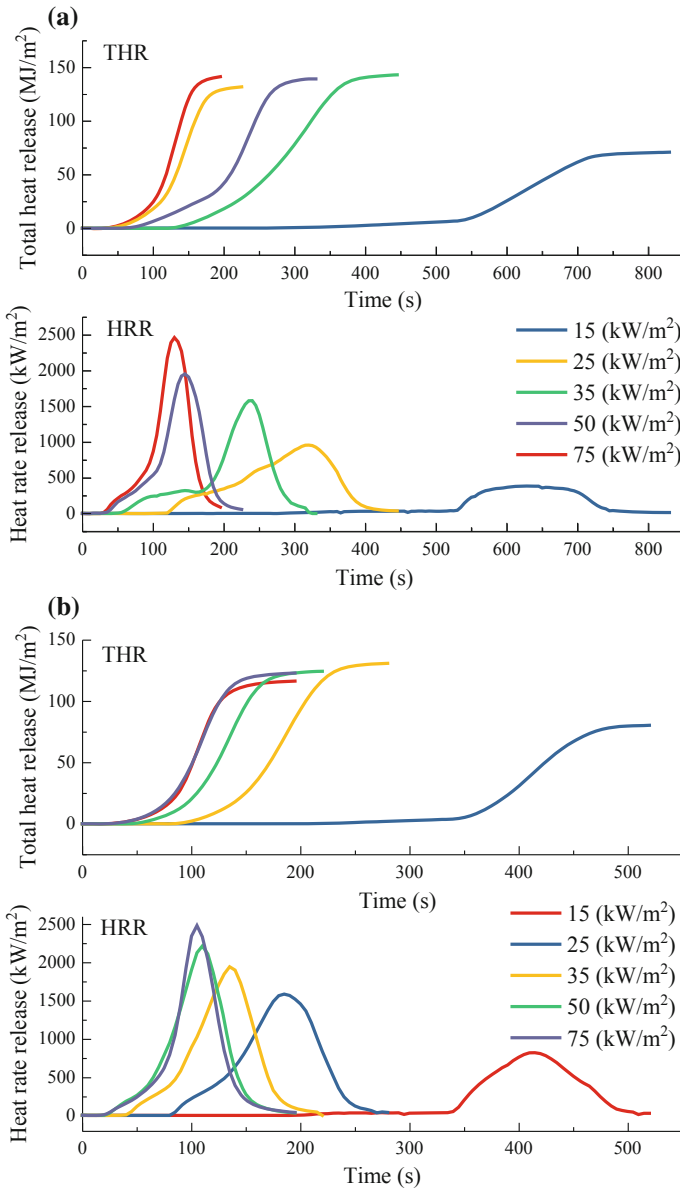
Fig. 1 HRR and THR profiles gearbox oil (**a**) and transformer oil (**b**) from calorimeter experiments

heat fluxes from 15 to 75 kW/m^2, the PKHRR values obviously increase by time. The PKHRR values from 385.15 kW/m^2 (15 kW/m^2) to 2463.20 kW/m^2 (75 kW/m^2), the increase rate is 84.40%, and the synchronous relative rate of change is 4.20 kW/m^2 s^{-1} for gearbox oil. The PKHRR of transformer oil increases from 818.74 kW/m^2 (15 kW/m^2) to 2480.41 kW/m^2 (75 kW/m^2), the increase rate is 66.99%, and the synchronous relative rate of change is 5.36 kW/m^2 s^{-1}. However, the opposite is the time to peak HRR (t_{PKHRR}) decreased with the radiant heat flux increased, which is shortened 500 s (gearbox oil) and 310 s (transformer oil). Comparison of several kinds of radiant heat flux, the PKHRR is the largest and the T_{PKHRR} is the least of the transformer oil when the radiant heat flux 75.0 kW/m^2.

Total heat release (THR) calculated by the total area under the HRR peaks, which is a significant parameter for fire hazards [19]. The THR of gearbox oil is greater than that of transformer oil at the same radiant heat flux as shown in Fig. 1. It can be known through the above analysis, from the perspective of the thermal hazards. Compared with gearbox oil, the THR is less, but the T_{PKHRR} is the fastest of transformer oil. Therefore, the transformer oil can be completely burned within shortened time and correspondingly release more heat (141.46 MJ/m^2) at a higher heat release (75 kW/m^2) when exposed to a fire source, so the transformer oil has a greater thermal hazard.

3.2.2 Nonthermal Hazard Analyses of Two Oil Samples

As for cone calorimeter data, specific extinction area (SEA), rate of smoke release (RSR), and total smoke release (TSR) can all be used to indicate the ability of materials to yield smoke and degree of opacity, generation rate, and total amount of smoke released in the fire as shown in Table 3. In addition, SEA can represent the smoke density and reflect how safe people can escape from a fire situation [20]. Figure 2a showed that with the radiant heat flux increased, the peak of SEA (PKSEA) reduced from 5171.05 to 505.91 m^2/kg and 90.22% reduction for gearbox oil. At the same time, the PKSEA is the largest when the radiant heat flux is 25 kW/m^2 of gearbox oil. To gearbox oil, the time of the peak RSR (PKRSR) is decreased from 375 to 125 s, the PKRSR reaching the maximum when the radiant heat flux is

Table 3 Nonthermal data of gearbox oil and transformer oil based on cone calorimeter experiments

Radiant heat flux (kW/m^2)	Gearbox oil		Transformer oil	
	PKSEA (m^2/kg)	PKRSR (m^2/s)	PKSEA (m^2/kg)	PKRSR (m^2/s)
15	5171.05	9.27	3815.03	7.92
25	5923.63	4.80	486.26	5.21
35	2808.27	8.22	396.59	6.07
50	943.81	9.54	317.29	5.86
75	505.91	11.03	223.72	7.42
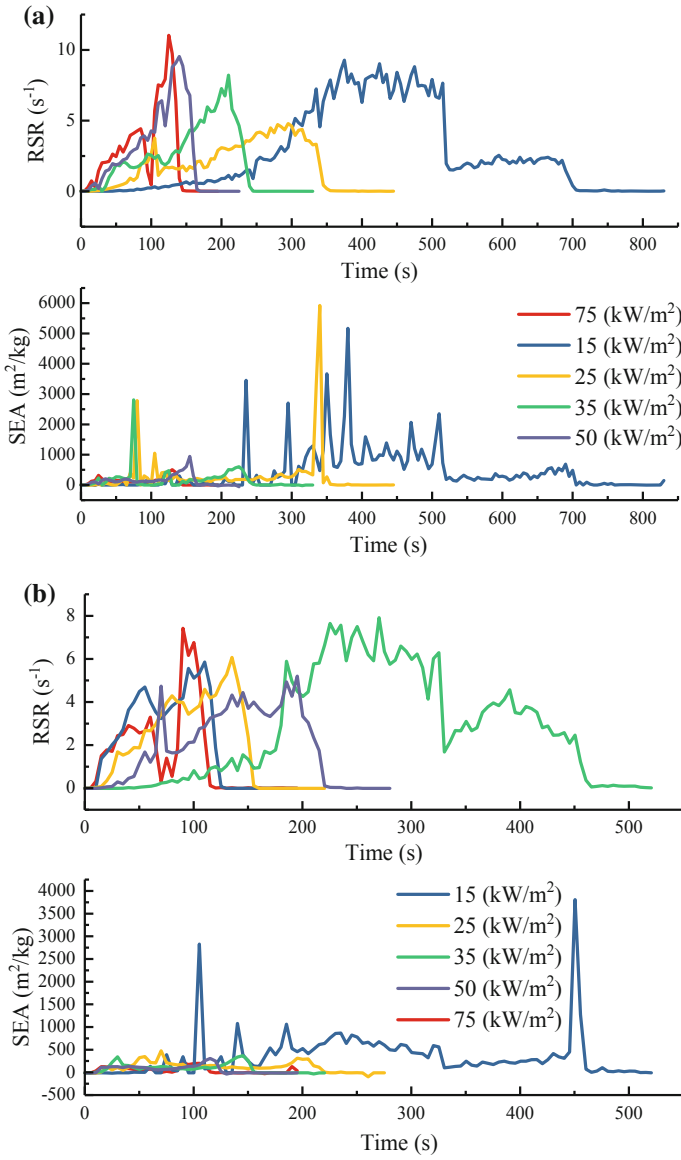
Fig. 2 SEA and RSR curves of gearbox oil (**a**) and transformer oil (**b**)

75 kW/m^2. As shown in Fig. 2b, the PKSEA of transformer oil reduced from 3815.03 to 223.72 m^2/kg, and the time of PKRSR changed from 270 to 90 s.

Figure 3 shows that the total smoke release of the gearbox oil and transformer oil is 2177.79 and 1402.55 m^2/kg, respectively. And the TSR of two liquid oils in five radiant heat fluxes is ranked: TSR (15 kW/m^2) > TSR (25 kW/m^2) > TSR (35 kW/m^2) > TSR (50 kW/m^2) > TSR (75 kW/m^2). From nonthermal hazard, it can be known by the above analysis that the transformer oil can reach the maximum specific extinction area (PKSEA) and the maximum rate of smoke release when it burns under low heat radiant heat flux. It may be making the smoke shade increase rapidly, compared with gearbox oil, the transformer oil has a more nonthermal hazard and has the largest the reaction to fire in wind turbine.

Fig. 3 Total smoke release (TSR) curves of gearbox oil (**a**) and transformer oil (**b**)
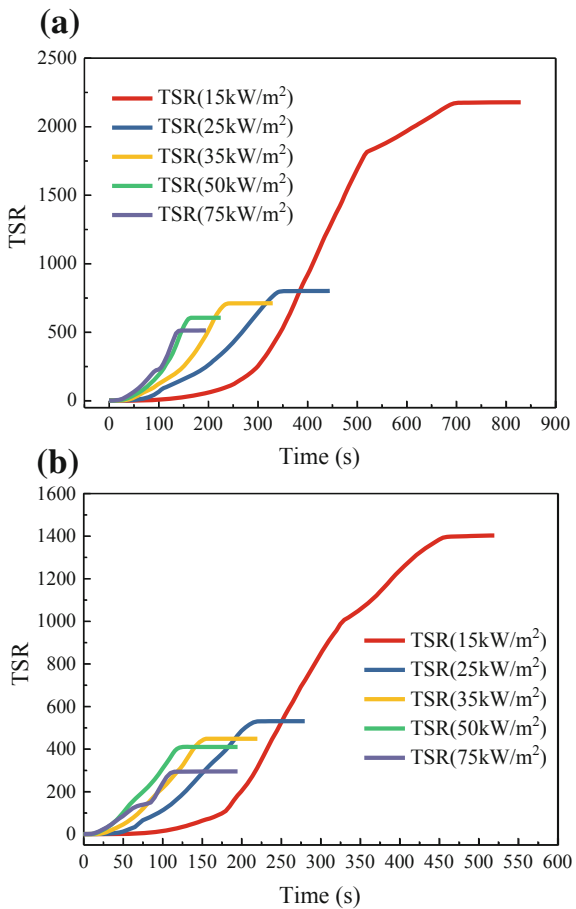
3.3 Theoretical Analyses of Flammability and Ignition Characteristics

3.3.1 Determination of Ignition Time of Individual Oil Samples

Flammability is the ability of a material to be ignited when its surface evaporates under the action of heat [21]. Janssens' method [22] was used to analyze the ignition times of lubricating oils. A good power rule between the ignition time and radiant heat flux is found with a power of 0.55 as shown in Eq. (1).

$$q_e'' = q_{cr}'' \left[1 + 0.73 \left(\frac{\lambda \rho C}{h_{ig}^2 t_{ig}} \right)^{0.55} \right] \tag{1}$$

where t_{ig} is ignition time (s), q_e'' is the radiant heat flux kW/m^2, h_{ig} is the heat transfer coefficient from the surface at ignition (kW/m^2 K), q_{cr}'' critical radiant heat flux (kW/m^2), and $\lambda \rho C$ is the thermal inertia (kW^2 s/m^4 K^2).

This method is proposed to be the best way to analyze ignition data for thermally thick solids by Babrauskas [23, 24], and he also suggested: "for the thick layer liquid, both the theory and the engineering are nearly identical to the case of solid combustibles." In addition, Suzuki et al. [25] maintained that the liquid can be treated as thermally thick material by building an irradiating model in the cone calorimeter to estimate the ignition times of fluids. Thus, fuels in this study are assumed to be thermally thick.

The ignition time of gearbox oil and transformer oil under five radiant heat fluxes was measured by cone calorimeter, the results as shown in Table 4. Curves of ignition time and the radiant heat flux of gearbox oil and transformer oil are shown in Fig. 4.

As can be seen from Table 4 and Fig. 4, the t_{ig} values of gearbox oil and transformer oil decreased with the increase of the radiant heat flux levels, rapid decline from 15 to 35 kW/m^2, then gradually level off. This is because in the case of high radiant heat flux, oils have the possibility of rapid combustion, so the ignition time will be less and less. The ignition time of the gearbox oil and the transformer oil fell by t_{ig}, respectively, 96.32 and 96.97% when the radiant heat flux from 15 to 75 kW/m^2. Obviously, the reduction in t_{ig} of the transformer oil is the largest. Under the radiant heat flux 15 kW/m^2, the transformer oil ignition time is the least, t_{ig} (gearbox oil)/t_{ig}

Table 4 Ignition time values of gearbox oil and transformer oil under different radiant heat flux levels

Sample		Radiant heat flux (kW/m^2)				
		15	25	35	50	75
Gearbox oil	t_{ig} (s)	517	106	31	25	19
Transformer oil		330	72	30	10	10

Fig. 4 Association diagram of ignition time and the radiant heat flux of gearbox oil and transformer oil
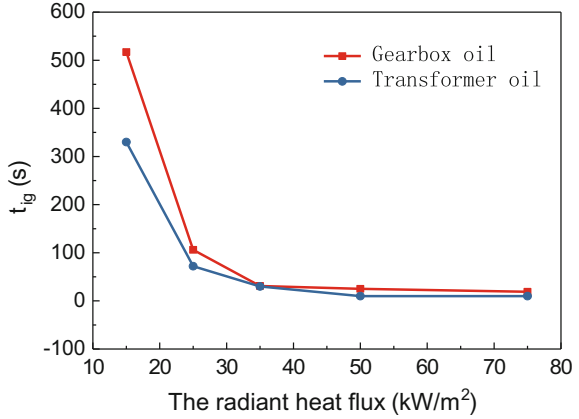
(hydraulic oil) = 1.83, the t_{ig} of gearbox oil is 1.83 times that of transformer oil. Both gearbox oil and transformer oil have the less ignition times when the radiant heat flux is 75 kW/m^2, so liquid oils have the greatest fire hazard in wind turbine.

According to the fire characteristic analysis, the relationship between the t_{ig} and the radiant heat flux of gearbox oil and transformer oil can be obtained, as shown in Fig. 4. It can be found by analyzing the time of ignition when the radiant heat flux exceeds 50 kW/m^2, the ignition time begun to flatten out, down only slightly, this time has been very complete combustion, it is not possible for early fire timely judgments. Because line fitting will result in a positive intercept, the radiant heat flux is selected from 15 to 35 kW/m^2 for the linear fit. By combine with Eq. (1), linear fitting is performed for the ignition time and the heat flux when the heat flux is 15–35 kW/m^2 is shown in Fig. 5. And according to Fig. 5 and Eq. (2) can be

Fig. 5 Relationship of ignition and the radiant heat flux of gearbox oil and transformer oil

$t_{ig}^{-1/2} = 0.00638HF - 0.041$
$R^2 = 0.99987$

$t_{ig}^{-1/2} = 0.00678HF - 0.0626$
$R^2 = 0.98457$
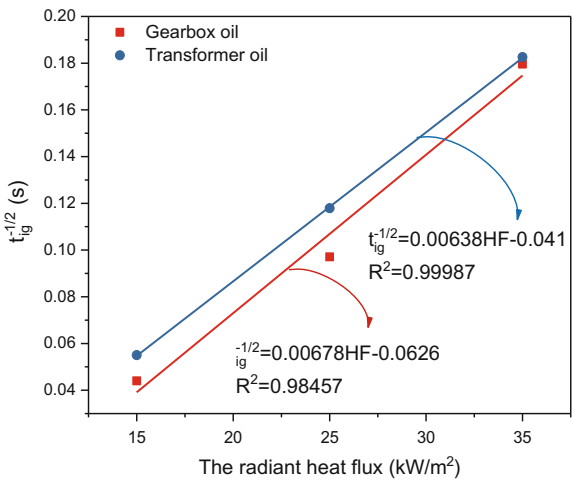
calculated the T_{ig}:

$$T_{ig} = \left(\frac{q''}{\sigma}\right) \cdot \frac{1}{4} \tag{2}$$

The q''_{cr} is 6.43 kW/m^2, and the T_{ig} is 306.16 °C of transformer oil. The q''_{cr} is 9.23 kW/m^2 and the T_{ig} is 352.04 °C of gearbox oil, which is the largest in liquid oils and is nonflammable, it has the minimum fire hazard.

In summary, based on the analysis of the critical radiant heat flux, the transformer oil can be found to be more fire hazard than the gearbox oil. This is the same as the result of fire hazard assessment based on ignition time for liquid oils in wind turbine.

4   Conclusion

In this paper, the fire hazard of gearbox oil and transformer oil in wind turbine was studied by using cone calorimetry experiment, and the fire hazard of liquid oils was compared from several ways. The results are as follows:

The PKHRR, THR, and PKRSR of liquid oils reached their maximum as the radiant heat flux increased, and PKSEA and TSR reached the minimum. In the same radiant heat flux, based on PKHRR and THR to determine the liquid oil fire hazard rankings are: transformer oil > gearbox oil; based on PKSEA and TSR to determine the fire hazard rankings are: gearbox oil > transformer oil.

The same liquid oils have the least ignition time and the larger fire hazards when the radiant heat flux is 75 kW/m^2. The critical radiant heat flux of gearbox oil and transformer oil is 9.23 and 6.43 kW/m^2, the T_{ig} is 352.04 and 306.16 °C. Based on the critical radiant heat flux analysis, the transformer oil has more higher fire hazard compare with gearbox oil.

References

1. Mostafaeipour, A. (2010). Productivity and development issues of global wind turbine industry. *Renewable and Sustainable Energy Reviews, 14*(3), 1048–1058.
2. Lin, Y., Tu, L., Liu, H., & Li, W. (2016). Fault analysis of wind turbines in China. *Renewable and Sustainable Energy Reviews, 55,* 482–490.
3. Wakui, T., Yoshimura, M., & Yokoyama, R. (2017). Multiple-feedback control of power output and platform pitching motion for a floating offshore wind turbine-generator system. *Energy, 141,* 563–578.

4. Wang, X., Yang, X., & Zeng, X. (2017). Seismic centrifuge modelling of suction bucket foundation for offshore wind turbine. *Renewable Energy, 114,* 1013–1022.

5. Rosenbloom, E. (2006, September 05). A problem with wind power [Online]. Available: http://www.aweo.org/problemwithwind.html. [Accessed 2013].

6. Mao, S., & Yang, D. (2016). One-dimensional analysis for optimizing smoke venting in tunnels by combining roof vents and longitudinal ventilation. *Applied Thermal Engineering, 108,* 1288–1297.

7. Li, L. J., Tang, F., Dong, M. S., et al. (2016). Effect of ceiling extraction system on the smoke thermal stratification in the longitudinal ventilation tunnel. *Applied Thermal Engineering, 109,* 312–317.

8. Tang, F., Li, L. J., Dong, M. S., et al. (2017). Characterization of buoyant flow stratification behaviors by Richardson (Froude) number in a tunnel fire with complex combination of longitudinal ventilation and ceiling extraction. *Applied Thermal Engineering, 110,* 1021–1028.

9. Babrauskas, V., & Peacock, R. D. (1992). Heat release rate: The single most important variable in fire hazard. *Fire Safety Journal, 18,* 255–272.

10. Kaplan, H. L., Grand, A. F., & Hartzell, G. E. (1982). *Combustion toxicology: Principles and test methods*. Lancaster, PA: Technomic Publishing Company Inc.

11. Coronado, D., & Kupferschmidt, C. (2014). Assessment and validation of oil sensor systems for on-line oil condition monitoring of wind turbine gearboxes. *Procedia Technology, 15,* 747–754.

12. Cigno, E., Magagnoli, C., Pierce, M. S., & Iglesias, P. (2017). Lubricating ability of two phosphonium-based ionic liquids as additives of a bio-oil for use in wind turbines gearboxes. *Wear, 376,* 756–765.

13. Wang, Z., You, F., Li, P., et al. (2017). Simulation and analysis of the likely fire disasters in the nacelle of certain 850 kW horizontal axis wind turbine. *Journal of Safety and Environment, 17*(1), 133–140. (in Chinese).

14. Zhou, H., You, F., & Li, P. (2017). Fire hazard assessments of combustibles in wind turbines nacelles. *Fire Science and Technology, 36*(4), 547–552. (in Chinese).

15. Uadiale, S., Urban, E., Carvel, R., et al. (2014). Overview of problems and solutions in fire protection engineering of wind turbines. *Fire Safety Science, 11*.

16. Rengel, B., Pastor, E., Hermida, D., et al. (2017). Computational analysis of fire dynamics inside a wind turbine. *Fire Technology, 53*(5), 1933–1942.

17. ISO 5660-1. (2015). Reaction-to-fire tests—Heat release, smoke production and mass loss rate—Part 1: Heat release rate (cone calorimeter method) and smoke production rate (dynamic measurement), International Standard Organization.

18. Leonelli, L., Barboni, T., Santoni, P. A., Quilichini, Y., & Coppalle, A. (2017). Characterization of aerosols emissions from the combustion of dead shrub twigs and leaves using a cone calorimeter. *Fire Safety Journal*.

19. Wang, D. Y., Leuteritz, A., Wang, Y. Z., Wagenknecht, U., & Heinrich, G. (2010). Preparation and burning behaviors of flame retarding biodegradable poly (lactic acid) nanocomposite based on zinc aluminum layered double hydroxide. *Polymer Degradation and Stability, 95*(12), 2474–2480.

20. Gao, L., Zheng, G., Zhou, Y., Hu, L., Feng, G., & Zhang, M. (2014). Synergistic effect of expandable graphite, diethyl ethylphosphonate and organically-modified layered double hydroxide on flame retardancy and fire behavior of polyisocyanurate-polyurethane foam nanocomposite. *Polymer Degradation and Stability, 101,* 92–101.

21. Tewarson, A. (1994). Flammability parameters of materials: Ignition, combustion, and fire propagation. *Journal of Fire & Flammability 12*(4), 329–356.

22. Janssens, M. (1991). Piloted ignition of wood: A review. *Fire and Materials, 15*(4), 151–167.

23. Babrauskas, V. (2003). *Ignition handbook*. Issaquah, WA: Fire Science Publishers.

24. Babrauskas, V. (2002). Ignition of wood: A review of the state of the art. *Journal of Fire Protection Engineering, 12*(3), 163–189.

25. Suzuki, K., Sugawa, O., Yamagishi, A., et al. (2007). Experimental study on ignition and combustion behaviors of insulation fluids for transformer using cone calorimeter. *IEEJ Transactions on Power and Energy, 127*(7), 797–802.

Fire Safety Design and Codes

A Risk-Based Approach to the Performance-Based Fire Safety Design of a Building in Regard to Preventing Building-to-Building Fire Spread

Keisuke Himoto

Abstract Building Standard Law (BSL) of Japan requires a building to maintain certain fire safety performance on preventing building-to-building fire spread in urban area. The level of requirement on a building changes with the site location, total floor area, and number of floors of the building, though in a prescriptive manner. In this study, a prototype of risk assessment method is developed for the performance-based fire safety design of a building in regard to building-to-building fire spread prevention. The fire spread risk of a building is evaluated by an event tree analysis in which occurrence probability of fire spread is considered as the probability of successive occurrence of comprising probabilistic events. The probability of each event is represented as a function of fire-resistive time of building members and fire duration time. For the consideration to maintaining continuity from the existing building regulation to an alternative building regulation, equivalency of the requirement level of the two building regulations is validated by comparing the fire spread risk of a building that can be built under each regulation. A case study was performed with a building located in the fire protection zone (FPZ). The result showed that there are several combinations of design parameters such as the fire-resistive times of exterior wall and opening that satisfy equivalent level of the requirement in terms of the fire spread risk in addition to the ones prescribed in the existing regulation.

Keywords Building-to-building fire spread · Performance-based fire safety design method · Risk-based approach

Nomenclature

A Floor area (m^2)
M Number of fire compartments
N Number of adjacent buildings

K. Himoto (✉)
National Institute for Land and Infrastructure Management, Tachihara, Tsukuba, Ibaraki 305-0802, Japan
e-mail: himoto-k92ta@mlit.go.jp

p   Occurrence probability of event
R   Fire spread risk
s   Setback from the site boundary
t_f Fire duration time of the target building
t_R Fire-resistive time

Greek symbols

τ Fire duration time of the building adjacent to the target building

Superscripts

*   Equivalent without the setback effect
**   Equivalent with the setback effect

Subscripts

fl   Floor
0   Reference

1   Introduction

Historically, cities in Japan frequently suffered from urban conflagrations since they generally comprised wooden houses of low fire safety performance with small separations maintained between each other. Although occurrence of urban conflagration is still concerned in a post-earthquake case, its occurrence for the other cases has been controlled by the end of the 1970s, along with the countrywide improvement of fire services and city structure. The improvement of city structure was driven forward partly by the large-scale redevelopment of densely built urban areas involving land readjustment during the years of high economic growth, and partly by the gradual replacement of old wooden houses with houses of fire-resistive constructions in the fire protection zones (FPZs). The FPZs are designated by the city planning administration of a municipality based on a zoning system, which comprises two categories, i.e., the FPZ and quasi-FPZ requiring a building with fire spread preventive performance of primary and secondary levels, respectively. As displayed in Table 1, FPZ system requires a building in the designated area to be constructed with fire-resistive

Table 1 Requirement for fire-resistive performance of buildings in the fire protection zone and quasi-fire protection zone

	Fire protection zone			Quasi-fire protection zone		
	$A_t <= 50\ m^2$	$50\ m^2 < A_t <= 100\ m^2$	$100\ m^2 < A_t$	$A_t <= 500\ m^2$	$500\ m^2 < A_t <= 1500\ m^2$	$1500\ m^2 < A_t$
$N_{fl} >= 4$	FR	FR	FR	FR	FR	FR
$N_{fl} = 3$	FR	FR	FR	QFR	QFR	FR
$N_{fl} = 2$	QFR	QFR	FR	FP	QFR	FR
$N_{fl} = 1$	FP	QFR	FR	FP	QFR	FR

FR fire resistive, *QFR* quasi-fire resistive, *FP* fire preventive. Requirement of fire resistance *FP* < *QFP* < *FR*

construction categorized either into fire resistive (FR), quasi-fire resistive (QFR), and fire preventive (FP) in association with its size (number of floors N_{fl}, total floor area A_t) by the Building Standard Law (BSL). The FPZ system has been a pillar to achieve the fire safety performance of urban areas of Japan since the middle of the twentieth century. However, the corresponding provisions in the BSL are still not transformed into the performance-based form. Thus, it uniformly requires all the main building members such as columns, beams, walls, and floors with a unique fire-resistive construction in a prescriptive manner as stated in Table 1, which diminishes flexibility of building design leading to the formation of stereotypical cityscape all over the country.

In this study, a prototype of risk assessment method is developed for the performance-based fire safety design of a building in regard to building-to-building fire spread prevention. For the consideration to maintaining continuity from the existing building regulation to an alternative building regulation, equivalency of the requirement level of the two building regulations is validated by comparing the fire spread risk of a building that can be built under each regulation. The risk-based approach which can consider the difference in magnitude of loss among concerning fire scenarios is a reasonable approach for the performance-based fire safety design of a building [1–5]. However, the existing attempts focused mainly on the evacuation safety of occupants inside of a building. Although there are several risk assessment methods that exist for assessing the risk of fire spread in urban area [6, 7], no similar approach exists that presents the performance-based design procedure of a building in regard to the fire safety from building-to-building fire spread.

2 Schematic of the Risk-Based Validation Model

As displayed in Fig. 1, the following scenarios are considered in order to validate the equivalency of the requirement.

Scenario A
Occurrence of fire spread by internal fire

Scenario B
Occurrence of fire spread by external fire
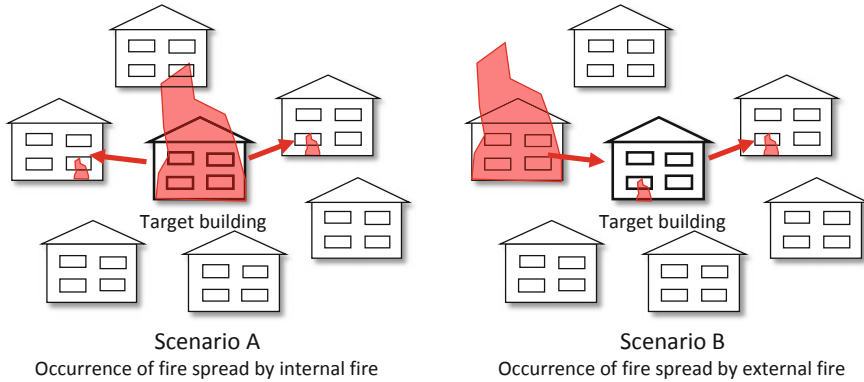
Fig. 1 Fire scenarios assumed in the present analysis

(A) Fire starts from the target building and enlarges and spreads to adjacent build-ings (internal fire source case).
(B) Fire starts from a building adjacent to the target building, spreads to the target building, enlarges inside of the target building, and spreads to adjacent buildings other than the building of fire origin (external fire source case).

The fire safety performance of a building in regard to fire spread prevention can be evaluated by various indices. In the present analysis, the risk of fire spread R is employed as a validation index so as to consider impact of the fire. The equivalency of fire safety performance of a building is validated by guaranteeing the fire spread risk of the target building R does not exceed the reference fire spread risk R_0, which is the maximum acceptable fire spread risk under the present regulation, in both fire spread scenarios, i.e.,

$$\left. \begin{array}{ll} \{(R/R_0)_A \leq 1\} \quad \text{and} \quad \{(R/R_0)_B \leq 1\} \quad \Rightarrow \quad \text{acceptable} \\ \{(R/R_0)_A > 1\} \quad \text{or} \quad \{(R/R_0)_B > 1\} \quad \Rightarrow \quad \text{not acceptable} \end{array} \right\} \tag{1}$$

Occurrence of fire spread to adjacent buildings is analyzed by the event tree as shown in Fig. 2. In the present analysis, fire spread to the adjacent buildings occurs only if the probabilistic events of ignition (event 1), flashover (event 2), burn-through of exterior opening (event 3), and fire spread to adjacent buildings (event 4) occur successively. The fire spread risk R and reference fire spread risk R_0 are evaluated by introducing the following assumptions.

– A building is composed of Mth fire compartments whose conditions including size and fire-resistive time of enclosing materials are uniform. As a consequence, occurrence probability of fire spread becomes uniform for all the consisting fire compartments.
– Fire compartments are aligned in serial. The fire starts from the end of this align-ment, and fire spread between fire compartments occurs successively. Although
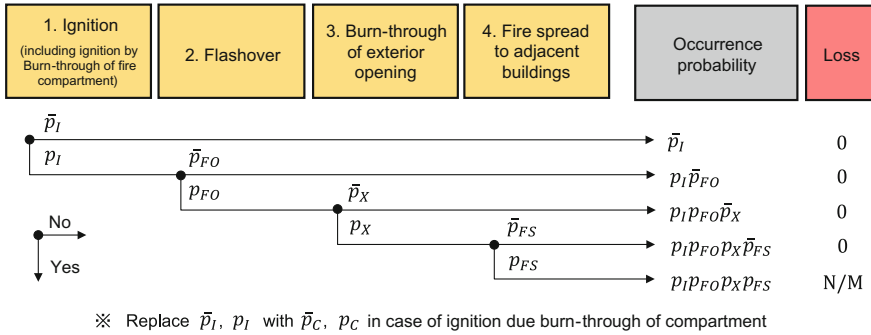
Fig. 2 Event tree of the fire spread from the target building to adjacent buildings

this assumption makes the evaluation procedure simple, it leads to the unsafe evaluation of the fire spread risk at the same time. The difference of connecting direction whether horizontal or vertical is not considered.

– Buildings under the influence of the target building are equally assigned to the consisting fire compartments; i.e., the number of adjacent buildings assigned to a fire compartment is assumed to be *N/M*, with *N* the number of adjacent buildings that get fire from the target building, and *M* the number of fire compartment consisting of the target building. An adjacent building is assigned to one fire compartment, and no overlapped assignment is assumed.

– Fire behavior in each fire compartment is independent from those in other fire compartments.

Since the fire spread risk is calculated per fire compartment, fire spread between fire compartments is also considered in Fig. 2. Under the above assumptions, fire spread risk *R* can be evaluated as the sum of the fire spread risks of consisting fire compartments as follows:

$$
R = p_I p_{FO} p_X p_{FS} \frac{N}{M} + p_I p_{FO} (p_C p_{FO}) p_X p_{FS} \frac{N}{M} + p_I p_{FO} (p_C p_{FO})^2 p_X p_{FS} \frac{N}{M} + \cdots
$$

$$
= p_I p_{FO} \cdot \sum_{i=1}^{M} \left[\frac{(p_C p_{FO})^{i-1}}{M} \right] \cdot p_X p_{FS} N \tag{2}
$$

By substituting Eq. (2) into Eq. (1), the risk ratio of the target building *R* needs to satisfy the following requirement in order to maintain the safety level equivalent to that of the present regulation,

$$
\frac{R}{R_0} = \left(\frac{p_I}{p_{I,0}} \right) \left(\frac{p_{FO}}{p_{FO,0}} \right) \left(\frac{\sum_{i=1}^{M} (p_C p_{FO})^{i-1} / M}{\sum_{i=1}^{M_0} (p_{C,0} p_{FO,0})^{i-1} / M_0} \right) \left(\frac{p_X}{p_{X,0}} \right) \left(\frac{p_{FS}}{p_{FS,0}} \right) \left(\frac{\sqrt{A_{fl}} + 2s}{\sqrt{A_{fl,0}} + 2s_0} \right) \leq 1 \tag{3}
$$

Since each probability in Eq. (3) is based on the fire safety performance of consisting building members including exterior walls, windows, and partitioning members

of fire compartment, the fire spread risk of a building R reflects their combined effects. However, note that the number of adjacent buildings N is considered to be proportional to a side length of the site due to the difficulty of specifying it in urban area.

$$N \propto \sqrt{A_{fl}} + 2s \tag{4}$$

Although Eq. (4) does not provide the exact value for the number of adjacent buildings N, this is enough for the evaluation of the risk ratio R/R_0 in Eq. (3), which is one of the advantages of employing the risk ratio R/R_0 in comparison with the risk difference $R - R_0$ for evaluation of the equivalency.

3 Evaluation of Fire Spread Preventive Performance of Building Members

3.1 Common Expression for Failure Probability of Building Members

In advance of modeling each probabilistic term in Eq. (3), common expression for failure probability of building members is introduced. In the present analysis, failure probability of building members is basically determined based on the magnitude relationship of the fire duration time t_F and the fire-resistive time of corresponding building member t_R. Since the fire load density generally takes a lognormal distribution [8], the fire duration time t_F, which is assumed proportional to the fire load density, also takes a lognormal distribution. As for fire-resistive time of corresponding building member t_R, the actual value is expected to range widely. However, from the viewpoint of imposing regulation, a unique value is set as the lowest level of requirement in the present analysis.

$$p = \text{prob}(t_R < t_F) = 1 - \Phi(\beta) = 1 - \int_{-\infty}^{\beta} \frac{1}{\sqrt{2\pi}} \exp\left(-\frac{z^2}{2}\right) dz \tag{5}$$

where Φ is the cumulative distribution function of the standard normal distribution, $\beta(= (\ln t_R - \lambda_F)/\xi_F)$ is the safety index, $\lambda_F (= \ln\left\{\mu_F/\sqrt{1 + (\sigma_F/\mu_F)^2}\right\})$ and $\xi_F (= \sqrt{\ln\left[1 + (\sigma_F/\mu_F)^2\right]})$ are the parameters for the lognormal distribution, and μ_F and σ_F are the average and standard deviation of the fire load. However, because the relationship between the fire duration time t_F and the fire-resistive time t_R is not that apparent from Eq. (5), the following approximation is introduced [9],

$$\Phi(\beta) \cong 1/\{1 + \exp(-1.7\beta)\} \tag{6}$$

This expression can be further simplified by assuming that σ_F/μ_F is 1/3 based on the existing survey on fire load [8].

$$p \cong 1/\left\{1 + 1.32(t_R/t_F)^{5.24}\right\} \equiv F(t_R/t_F) \tag{7}$$

By introducing the approximation, the failure probability can be modeled as a function of the quotient of the fire-resistive time t_R and the fire duration time t_F. The derived expression is now termed as function $F(t_R/t_F)$ and is commonly used in the subsequent sections.

3.2 Occurrence Probability of Events

Relationship between the fire-resistive time and equivalent fire duration time is depicted in Fig. 3. Note that in the following sections, time corresponding to the target building is represented by t and that to the adjacent buildings is represented by τ. The superscript $()^*$ represents the equivalent time without the setback effect and $()^{**}$ with the setback effect. Equivalent fire duration times are derived in the subsequent section.

In the event 1, different fire sources are considered in two fire scenarios; one is for internal fire source, and the other is for external fire source. The occurrence probability of this event is given by

$$p_I \begin{cases} \propto NA_{fl} & \cdots \text{internal fire source} \\ = F\left(t_{R,X}\big/\tau_F^{**}\right) & \cdots \text{external fire source} \end{cases} \tag{8}$$
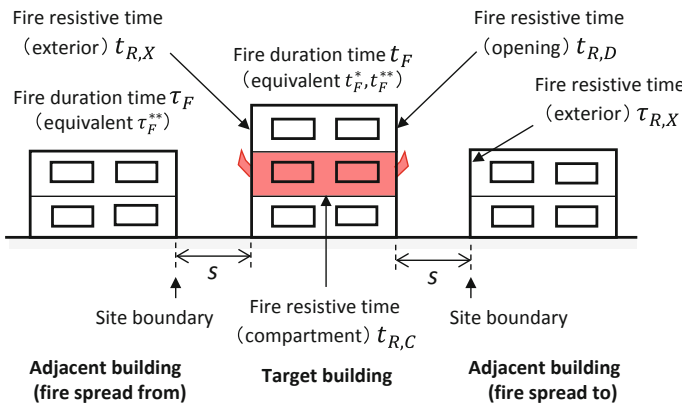
Fig. 3 Relationship between the fire-resistive time and equivalent fire duration time

In the above equation, ignition probability is assumed proportional to the floor area in the internal fire source scenario, while it is expressed as a function of the ratio of the fire-resistive time of exterior $t_{R,X}$ and the equivalent fire duration time of the adjacent fire-involved building considering the setback effect τ_F^{**} using Eq. (7) in the external fire source scenario. However, note that the area of each floor is assumed the same in a building and that the fire-resistive time of exterior $t_{R,X}$ is the area-weighted average of the fire-resistive times of exterior wall $t_{R,W}$ and window $t_{R,D}$.

In the event 2, the occurrence probability of internal fire spread is expressed as a function of probabilities of flashover p_{FO} and burn-through of partitions of fire compartment p_C as formulated in Eq. (3). Although the probability of flashover inside fire compartment p_{FO} is subjected to various factors such as dimension of the fire compartment, interior finishing, and installation of sprinkler system, it is tentatively assumed to take a constant value due to lack of the technical foundation, which is tentatively given by

$$p_{FO} = 1 \tag{9}$$

Probability of burn-through of partitions of fire compartment p_C is expressed as a function of the ratio of the fire-resistive time of partition $t_{R,C}$ and the equivalent fire duration time of the fire-involved compartment t_F^* using Eq. (7) as follows:

$$p_C = F(t_{R,C}/t_F^*) \tag{10}$$

In the event 3, probability of burn-through of exterior opening p_X is expressed as a function of the ratio of the fire-resistive time of opening $t_{R,D}$ and the equivalent fire duration time of the fire-involved compartment t_F^* using Eq. (7) as follows:

$$p_X = F\big(t_{R,D/}t_F^*\big) \tag{11}$$

In the event 4, probability of fire spread to adjacent building p_{FS} is expressed as a function of the ratio of the fire-resistive time of exterior of adjacent building τ_{RX} and the equivalent fire duration time of the fire-involved compartment considering the setback effect t_F^{**} using Eq. (7) as follows:

$$p_{FS} = F\big(\tau_{R,X}\big/t_F^{**}\big) \tag{12}$$

3.3 Equivalent Fire Duration Time

Fire duration time of a fire compartment t_F can be calculated by dividing the fire load $\rho_F A_F$ by the mass loss rate $\dot{m}_B$ as follows:

$$t_F = \rho_F A_F / \dot{m}_B \tag{13}$$

However, the fire-resistive time of materials t_R such as walls, floors, columns, and beams is the time below which the material can maintain its performance under the heating of ISO fire curve. Since actual temperature of fire-involved compartment is different from that of the ISO fire curve in general, the actual fire duration time t_F cannot be directly compared with the fire-resistive time t_R. Thus, it is converted into the equivalent value t_F^* so that the cumulative amount of net incident heat flux from the actual fire is consistent with that from the ISO fire curve, i.e.,

$$\int_0^{t_F} \dot{q}'' dt = \int_0^{t_F} h_k \Delta T dt = \int_0^{t_F^*} \dot{q}''_{\text{ISO}} dt = \int_0^{t_F^*} h_k \Delta T_{\text{ISO}} dt \tag{14}$$

where $\dot{q}''$ is the net incident heat flux from actual fire, $\dot{q}''_{\text{ISO}}$ is that from ISO fire curve, $h_k (= (k\rho c / t)^{1/2}$ for transient phase) is the effective heat transfer coefficient [10], ΔT is the temperature rise of actual fire, and ΔT_{ISO} is the temperature rise of ISO fire curve. Transient temperature rise of actual fire can be obtained by substituting the effective heat transfer coefficient h_k into McCaffrey's fire model [11] which is given by

$$\frac{\Delta T}{T_\infty} = 0.023 \left(\frac{\dot{Q}^2}{A_T A \sqrt{H} \sqrt{k\rho c}} \right)^{1/3} \cdot t^{1/6} \tag{15}$$

where T_∞ is the ambient temperature, $\dot{Q}$ is the heat release rate, A_T is the surface area of the fire compartment, $A\sqrt{H}$ is the ventilation factor, and $\sqrt{k\rho c}$ is the thermal inertia of partitioning material. On the other hand, for the ease of calculation, ISO fire curve is approximated with the following expression [10],

$$\Delta T_{ISO} \cong 230 t^{1/6} \tag{16}$$

The equivalent fire duration time t_F^* can be obtained by substituting Eqs. (15) and (16) into Eq. (14), which is given by

$$t_F^* = \frac{0.005 \dot{Q}}{\left(A_T A \sqrt{H} \sqrt{k\rho c} \right)^{1/2}} \cdot t_F \tag{17}$$

The equivalent fire duration time t_F^* obtained in Eq. (17) is applicable to the events 2 and 3 in which concerning building members are directly exposed to compartment gas as the heat source. However, in the events 1 and 4, concerning building members preventing fire spread are separated from the heat source by the setback from the site boundary, and the building members receive heat mainly by radiation. As depicted in Fig. 4, incident heat flux $\dot{q}''$ of these events is obtained by approximating the view factor as the quotient of projection area of heat source and surface area of the unit
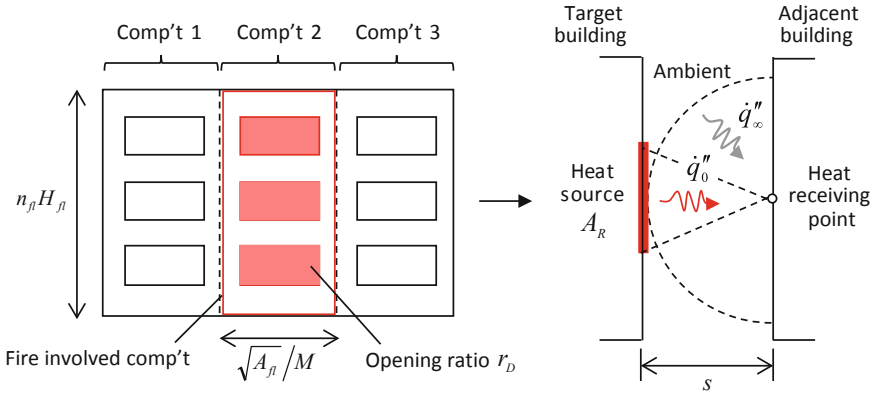
Fig. 4 Calculation of incident heat flux to the adjacent building by thermal radiation

hemisphere, which is given by

$$\dot{q}'' = \left\{ A_R \dot{q}_0'' + (2\pi s^2 - A_R)\dot{q}_\infty'' \right\} / 2\pi s^2 \tag{18}$$

where A_R is the area of the heat source, $\dot{q}_0''$ and $\dot{q}_\infty''$ are the radiant heat fluxes from the heat source and the ambient, respectively, π is the circumference ratio, and s is the setback from the site boundary. Note that in Fig. 4, "comp't" stands for "compartment" inside of the building. By considering the division effect of fire compartments, the area of the heat source A_R is given as follows:

$$A_R = r_D N_{fl} H_{fl} \sqrt{A_{fl}} \Big/ M \tag{19}$$

where r_D is the aerial ratio of the opening to the wall, N_{fl} is the number of floors, H_{fl} is the floor height, and A_{fl} is the area of a floor. By substituting Eq. (18) into Eq. (14), the equivalent time duration of the target building t_F^{**} and that of the adjacent building τ_F^{**} is as follows:

$$t_F^{**} = \left(\frac{(\dot{q}''/\sigma)^{1/4} - T_\infty}{690} \right)^{3/2} t_F^{3/4}, \text{ or } \tau_F^{**} = \left(\frac{(\dot{q}''/\sigma)^{1/4} - T_\infty}{690} \right)^{3/2} \tau_F^{3/4} \tag{20}$$

where σ is the Stefan–Boltzmann constant.

4   Case Study

As a case study of the equivalency validation to the existing level of requirement, the proposed method is used to evaluate the risk ratios for the buildings with conditions

displayed in Table 2 . The target building is a four-story building with total floor area A_t of 3000 m^2 which is located in the FPZ. According to the requirement of the fire-resistive performance of the current building regulation (refer to Table 1), building members of the target building need to be "fire resistive" in association with its size. In this case study, fire-resistive times of exterior walls $t_{R,W}$ and openings $t_{R,D}$ were varied between 10 and 90 min so as to find their combinations under which the required level of fire safety performance is maintained. Note that as the target building needs to be "fire resistive", the reference fire-resistive times which represent the existing level of requirement were set to be 75 min for exterior walls and 20 min for exterior openings. Although the actual requirement for exterior walls is 60 min for "fire-resistive" construction, its performance is presumed equivalent to that of the "quasi-fire-resistive" construction with 20% premium of heating period imposed under the stipulation of the fire-resistive test of building members.

The risk ratios obtained by varying fire-resistive times of exterior walls $t_{R,W}$ and openings $t_{R,D}$ as parameters are displayed in Fig. 5. Note that the judgment condition of the risk ratio for the requirement acceptability described in Eq. (1) is transformed into the following expression for clarification of the differences between the parameters,

$$\left.\begin{array}{ll} \{\log(R/R_0)_A \leq 0\} & \text{and} \quad \{\log(R/R_0)_B \leq 0\} \quad \Rightarrow \quad \text{acceptable} \\ \{\log(R/R_0)_A > 0\} & \text{or} \quad \{\log(R/R_0)_B > 0\} \quad \Rightarrow \quad \text{not acceptable} \end{array}\right\} \quad (21)$$

The result shows that acceptable combinations of the fire-resistive times $t_{R,W}$ and $t_{R,D}$ differ substantially between the two scenarios; i.e., the range of acceptable combinations is wider for the scenario A. However, since the logarithm of the risk ratio $\log(R/R_0)$ needs to be equal to or below zero for both scenarios in order to

Table 2 Calculation conditions of the case study

Items		Parameters of reference building for R_0	Parameters of target building for R
Zoning		Fire protection zone	Fire protection zone
Total floor area A_t (m^2)		3000	3000
Number of floors N_{fl}		4	4
Setback s (m)		0.5	0.5
Maximum size of fire compartment (m^2)		750	750
Fire-resistive time (min)	Compartment walls and floors $t_{R,C}$	75 ($\fallingdotseq$ 60 × 1.2)[a]	75 ($\fallingdotseq$ 60 × 1.2)[a]
	Exterior walls $t_{R,W}$	75 ($\fallingdotseq$ 60 × 1.2)[a]	10–90
	Exterior openings $t_{R,D}$	20	10–90

[a]"Quasi-fire-resistive" performance is presumed equivalent to "fire-resistive" performance with 20% premium of heating period
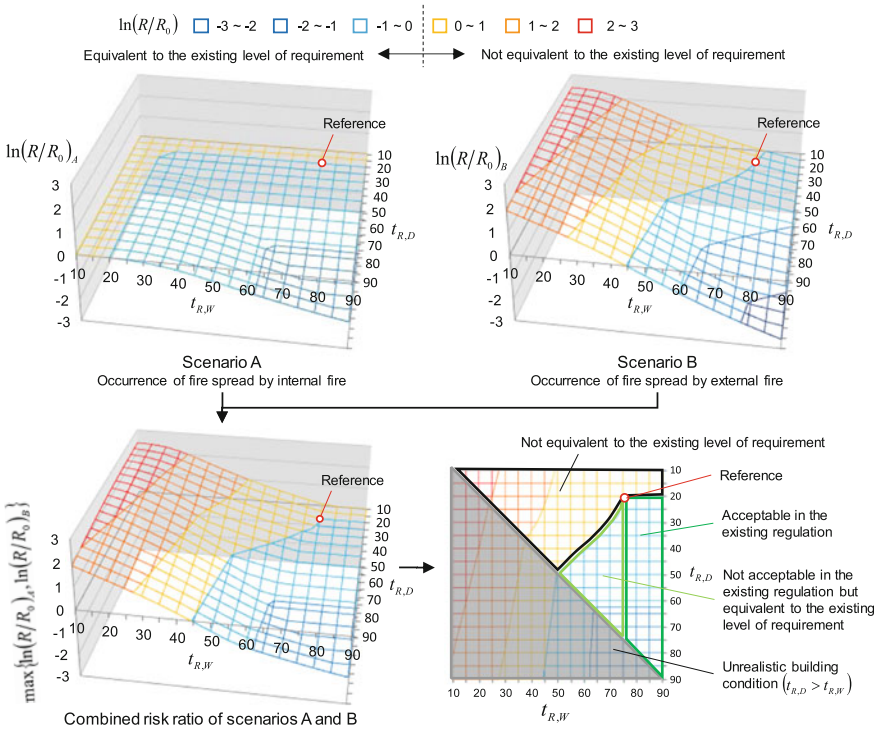
Fig. 5 Risk ratios with varying parameters of fire-resistive times of exterior walls and openings

validate the equivalency to the existing requirement level, the range of acceptable combinations is predominantly controlled by result of the scenario B in this specific calculation conditions. Summary of the result in the bottom-right of Fig. 5 shows that fire-resistive times $t_{R,W}$ and $t_{R,D}$ greater than reference values would automatically be considered acceptable. However, it also demonstrates that there is a certain combination of fire-resistive times $t_{R,W}$ and $t_{R,D}$ that are not acceptable in the existing regulation, but equivalent to the existing level of requirement from the viewpoint of the fire spread risk. Attainability of further design options can be examined with the present risk-based approach, by considering the other parameters such as the total floor area A_t, number of floors N_{fl}, setback s, and size of fire compartment, which are not considered in the present analysis.

5   Conclusions

In this study, a prototype of risk assessment method is developed for the performance-based fire safety design of a building in regard to building-to-building fire spread prevention. Equivalency of the requirement level of an alternative regulation to the

existing prescriptive regulation can be validated by the ratio of their fire spread risks using the proposed method. The result of the case study that tested the effect of fire-resistive times of exterior walls $t_{R,W}$ and openings $t_{R,D}$ demonstrated a possibility of flexibility enhancement of building design in the FPZ. However, the proposed method is still at an exploratory stage and requires several improvements, such as the modification of the simplified assumptions on the uniformity of fire compartment size or on the serial connection of fire compartments that may yield result on the unsafe side.

References

1. Magnusson, S. E., Frantzich, H., & Harada, K. (1996). Fire safety design based on calculations: Uncertainty analysis and safety verification. *Fire Safety Journal*, 305–334.
2. Tanaka, T. (2008). Risk-based selection of design fires to ensure an acceptable level of evacuation safety. *Fire Safety Science—Proceedings of the 9th International Symposium, International Association for Fire Safety Science* (pp. 49–62).
3. Tanaka, T. (2011). Integration of fire risk concept into performance-based evacuation safety design of buildings. *Fire Safety Science—Proceedings of the 10th International Symposium, International Association for Fire Safety Science* (pp. 3–22).
4. Ikehata, Y., Yamaguchi, J., Nii, D., & Tanaka, T. (2014). Required travel distance and exit width for rooms determined by risk-based evacuation safety design method. *Fire Safety Science—Proceedings of the 11th International Symposium* (pp. 49–62). International Association for Fire Safety Science.
5. Kong, D., Lu, S., & Ping, P. (2017). A risk-based method of deriving design fires for evacuation safety of buildings. *Fire Technology, 53,* 771–791.
6. Cousins, J., Heron, D., Mazzoni, S., Thomas, G., & Lloydd, D. (2002). *Estimating risks form fire following earthquake*. Institute of Geological & Nuclear Sciences Report.
7. Himoto, K., Akimoto, Y., Hokugo, A., & Tanaka, T. (2008). Risk and behavior of fire spread in a densely-built urban area. *Fire Safety Science—Proceedings of the 9th International Symposium* (pp. 267–278). International Association for Fire Safety Science.
8. Culver, C. G. (1978). Characteristics of fire loads in office buildings. *Fire Technology, 14*(1), 51–60.
9. Lord, F. M., & Novick, M. R. (1968). *Statistical theories of mental test scores*. Massachusettes, U.S.: Addison-Wesley Educational Publishers Inc.
10. Harada, K., Kogure, R., Matsuyama, K., & Wakamatsu, T. (2000). Equivalent fire duration based on time-heat flux area. *Fire Safety Science—Proceedings of the 4th International Symposium* (pp. 513–524). International Association for Fire Safety Science.
11. McCaffrey, B. J., Quintiere, J. G., & Harkleroad, M. F. (1981). Estimating room temperatures and the likelihood of flashover using fire test data correlations. *Fire Technology, 17*(2), 98–119.

Development of Testing Environment for Thermal Protective Clothing at Critical Conditions

Sungwook Kang, Minjae Kwon, J. Yoon Choi and Sengkwan Choi

Abstract This project examines the thermal protective performance of firefighters' garment. Although this research topic has been rigorously studied to secure the safety of wearers, little information exists on the clothing's behaviour at 'recent' environments created by compartment fires beyond the flashover state; the critical conditions become more severe due to increases in use of synthetic materials in furnishings and construction. As part of the project, this paper discusses particularly (i) the quantification of the current critical fire hazards; (ii) a sequential development of apparatuses capable of generating the heat flux defined, from bench-scale to human adult-scale; and (iii) the establishment of a measurement system incorporating a skin simulant. To represent the up-to-date severity of fires, the upper bound (126 kW/m^2) of the conventional range of flash fires is employed rather than the standard (84 kW/m^2), as the worst-case scenario for fire attack teams. Heaters are systematically advanced and calibrated with respect to the ability to emit, spatial uniformity of irradiance, and its temporal consistency. A measurement plan for testing is established in association with the actual physical damage to wearers (i.e. superficial second-degree burn injury). A skin simulant which exhibits thermo-physical characteristics similar to those of human tissues is also developed to make a sensor which intends to accurately predict burn injuries and thus assess the performance of garments. This work tends to create an advanced testing environment for thermal protective clothing, and therefore will contribute (i) to the full understanding of the garments' behaviours under critical conditions, (ii) to the improvement of the potential shield-like barrier's protective performance, and thereby (iii) to the security of the health and life of firefighters, in due course.

Keywords Thermal protective clothing · Critical fire hazard · Radiant heater · Skin simulant

S. Kang · M. Kwon · J. Y. Choi (✉)
Korea Conformity Laboratories, Fire Safety Centre, Yangcheong3gil, 28115 Cheongju,
Ochangeup, Republic of Korea
e-mail: j.yoon.choi@kcl.re.kr

S. Choi
School of the Built Environment, Ulster University, Newtownabbey, Co. Antrim BT37 0QB, UK

Nomenclature

c_p Specific heat (J/(kgK))
k Thermal conductivity (W/(mK))
I Thermal inertia (J^2/(m^{4}K^{2}s))

Greek Symbols

ρ Density (kg/m^3)
α Thermal diffusivity (m^2/s)

1   Introduction

Over the past decades, there have been significant advances in engineering, technology, and evaluation for thermal protective clothing. This potential shield-like barrier has widely been dressed by firefighting, military, and car racing personnel who are often exposed to hazardous fire environments. Specifically regarding firefighters, although they do not frequently confront critical conditions during extinguishment of fire, such as flashover, backdraught, and fully developed fire, serious burn injuries beyond second degree or tragic fatalities on duty may occur once facing. In particular, fire attack teams or first arrival teams who vigorously strive to control unpredictable developing flames and plumes take much higher risks. In this regard, in the Republic of Korea, the number of firefighter casualties per thousand fire events is still considerable and the ratio of fatality to casualty is even worse, as compared to those of the countries developed in terms of fire safety, as shown in Fig. 1. These statistics indicate that further advanced research on firefighter protective ensemble is needed to protect the life of this group of personnel who devotes to secure the health and safety of our society against fire hazards.

Ministry of Public Safety and Security in South Korea estimates that, from 2006 to 2014, Korea fire brigades had responded to 433,098 fire events, of which 60.9% can be categorised into 'compartment fire', as shown in Fig. 2. It also turned out that 76.4% of 55 'Serious Fire' occurred in compartments. (Serious Fire indicates the fire hazard resulting in more than five fatalities, ten casualties, or five billion damage and loss in South Korea.) The charts indicate that it is reasonable to derive a critical thermal state from compartment fires when quantifying thermal conditions for evaluating the protective performance of firefighter ensemble. In this respect, it was reported by Underwriters Laboratories [1] that compartment fires have recently become more severe due to changes in residence geometries and increases in the use of synthetic construction and furnishing materials. Another research groups [2, 3] noted that the gas temperatures in rooms with modern furnishing increase up to
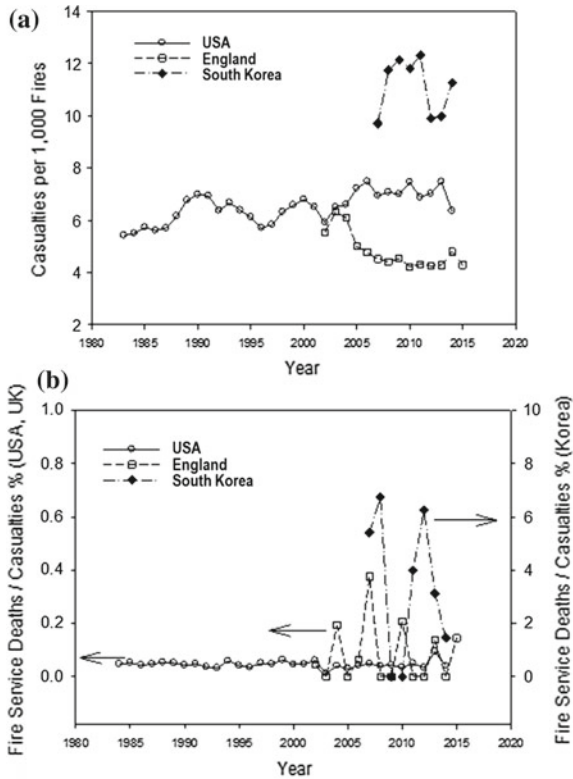
Fig. 1 Statistics for **a** casualties per 1000 fires and **b** the ratio of fire service fatality to casualty in different countries
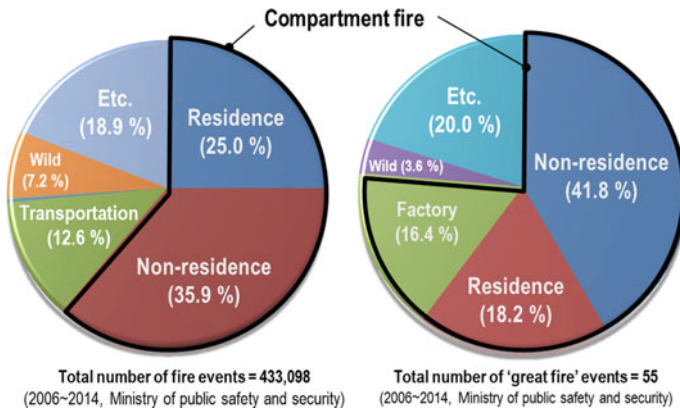
Fig. 2 Statistics for the number of fire events and compositions in the Republic of Korea from 2006 to 2014

approximately 1000 °C; classical theories guide that the criterion of the onset of flashover is the upper gas layer with an average temperature of 500–600 °C [4]. Previous researchers [5–8] are also aware that the standard thermal condition being used in the research field of fire protective ensemble (2 cal/(cm²·s)) could not be indicative of all the recent fire hazards occurring in compartments.

Although the circumstances of more severe recent compartment fire environments, there is a lack of information regarding the performance and behaviours of thermal protective ensemble exposed to more intense thermal conditions than the standard. The standard quantity originates from the work conducted by Behnke [9, 10] who was the first to develop a bench-scale thermal protective performance (TPP) test. It was presented that hazardous flash fires could be quantified as a range of 1–3 cal/(cm²·s), and its average heat flux was used to test the performance of thermal protective fabrics. In this project, the upper limit of the range (3 cal/(cm²·s)) is employed in the assessment of the performance of thermal protective clothing as the worst-case scenario, (i) in order to understand the extent of damage of human skin shielded by garments under critical conditions, and (ii) to contribute to the improvement of thermal protective ensemble with a more advanced performance for fire attack teams in due course. As part of the project, this paper discusses particularly two topics:

- Creation of critical thermal environment—it discusses the origin of the heat flux employed in this work and introduces the process of developing apparatuses capable of emitting the heat flux desired and their calibrations with respect to the ability to emit, spatial uniformity of irradiance, and its temporal consistency;
- Establishment of measurement system—it introduces measurements which could be obtained from the tests designed in this project and associates the measurable data with the actual physical damage to firefighters (i.e. superficial second-degree burn injury) with the development of a skin simulant.

2 Creation of Critical Thermal Environment

2.1 Quantification of Heat Flux Indicative of Critical Fire Hazard

The ability of thermal protective clothing to retard heat transfer to human skin has been conventionally evaluated by the bench-scale TPP test [11] and a full-scale thermal manikin test [12]. In both tests, a standard heat flux of 2 cal/(cm²·s) ($\doteqdot$ 84 kW/m²) is imposed on the exposed surface of fabric samples or that of manikin body. In relation to the existing test methods, it is necessary to review the origin of the standard intensity in order to quantify a heat flux indicative of recent more severe fire hazards.

Behnke was the first to develop the TPP test method for rating protective clothing fabrics and to propose the standard heat flux as a representative intensity of 'flash fire' [9, 10]. Several samples of Nomex III aramid fibre were repeatedly heated

at a constant heat flux of 2 cal/(cm^2·s) for different periods of time by the TPP apparatus. The corresponding response of each of the fabric samples to the total exposure energy imposed (in units of cal/cm^2) was thereby tabulated. Simultaneously, information had been collected for several years, regarding the physical appearances of Nomex garments exposed to several types of real flash fires. Subsequently, the defined fundamental relation between total exposure energy and fabric response was employed to estimate the amount of the total exposure energy needed to duplicate the appearances observed in the collected data. The estimated total heat was then divided by the corresponding exposure time in order to obtain the quantity of heat flux. It was induced from the data that incident heat fluxes from flash fires stay in the range of approximately 1.2–3.2 cal/(cm^2·s). Based on the empirical estimation, it is recommended in the standard TPP test and thermal manikin test that test samples shall be exposed to an average heat flux of 2.0 cal/(cm^2·s) ($\fallingdotseq$83 kW/m^2 ± 4 kW/m^2) [11, 12].

The definition of 'flash fire' originates from the subject of 'hydrocarbon fire' which has three main features [13]: (i) fuel is diffused in air, (ii) once ignited, the flame front moves very rapidly from ignition point to the end of the diffused fuel cloud, and (iii) thus, all the diffused fuel very rapidly burns out in a duration of 3 s or less with the emission of very strong thermal energy. A substantial portion of the flash fire's features is associated with the critical conditions of 'compartment fire', such as flashover, backdraught, and fully developed fire. Previous researchers in several fields have also devoted to quantify such fire risks. A typical hydrocarbon fuel, JP-4, was used in a thermal manikin test to evaluate the performance of thermal protective fabrics in order to protect flight personnel against aircraft crash fires [14]. It was observed that the intensity of radiant thermal load to the manikin increased beyond 84 kW/m^2, up to 272 kW/m^2. In terms of compartment fire, it was stated that the maximum temperature observed during post-flashover room fires was of the order of 1100 °C, of which the thermal environment could be represented by a heat flux of approximately 150 kW/m^2 [15]. It was reported by the National Institute of Standards and Technology (NIST) that the total heat flux measured at the floor level in a room wherein post-flashover fires occur was as high as around 170 kW/m^2 [16]. It was also demonstrated from compartment fire tests [6] that once flashover occurs, heat fluxes higher than 84 kW/m^2 are often observed from room fires. Based on the prior studies, it can be concluded that (i) the standard quantity of heat, indicative of critical fire hazards, originates from the average of empirical estimates; (ii) the present standard heat flux is however not sufficient to cover the risk of recent critical compartment fires taken by fire attack teams; (iii) as the worst-case scenario, this work, therefore, employs the upper limit of the intensity range (i.e. 3 cal/(cm^2·s) $\fallingdotseq$ 126 kW/m^2) in the understanding of the performance of thermal protective ensemble.

2.2   Development of a Series of High-Radiation Emitting Apparatuses

A series of testing apparatuses capable of firmly safely emitting a heat flux of 126 kW/m^2 ($\fallingdotseq$3 cal/(cm^2·s)) were developed systematically from bench-scale through intermediate-scale to full-scale comparable to human body's height. Figure 3 shows the configuration of each of the instruments and schemes for their calibrations. The apparatuses are composed of three main parts: radiant heater, specimen assembly and holder, and trolley rail between the two parts. It is noted that the physical embodiment of the severe thermal environment requires careful scrutiny and consideration on several aspects, such as the configuration of emitter and recipient, type of heating element, type of power source (electricity or gas), way of power supply, and systems of cooling, measuring, recording, and ventilation; the course of developing the laboratory simulation hardware was thoroughly discussed in the authors' previous work [17].

The level of heat flux exposure for test samples is a prerequisite for obtaining the primary datum which is the amount of heat flux (or temperature) transmitted, throughout both fabric layers and air gaps, to the position where human skin is located. The precondition is influenced by two factors: the amount of electric power and the distance of a measuring point from the heating element. As a result, specifically regarding the intermediate-scale instrument (Fig. 3b), the heater was designed to emit the aimed irradiance of 126 kW/m^2 on the exposed surface of a specimen placed at a position around 250 mm distanced in length from the heating panel, with approximately 57% of total electric power to secure mechanical durability of the emitter. The quantity of irradiance was physically measured utilising a calibrated heat flux metre (made by CAPTEC enterprise) in the calibration stage. Figure 4 shows the results of the calibration test conducted for the intermediate-scale apparatus, in terms of the level of heat flux exposure as a function of location in x-, y-, and z-direction (as described in Fig. 3b), the spatial uniformity of heat flux over the exposed surface of specimens, and the temporal consistency of heat emission. The target quantity (126 kW/m^2) was measured at $x = 250$ mm and $y = z = 0$ mm, as shown in Fig. 4a. Less than approximately 2.6% reduction of irradiance from the centre was observed within the 100 mm × 100 mm central area, as described in Fig. 4b, c. It was observed in Fig. 4d that an aimed level of irradiance in the range between 1 and 3 cal/(cm^2·s) was consistently maintained for longer than 60 s. It is noted that such calibrations were individually conducted for each of the apparatuses developed in this project.
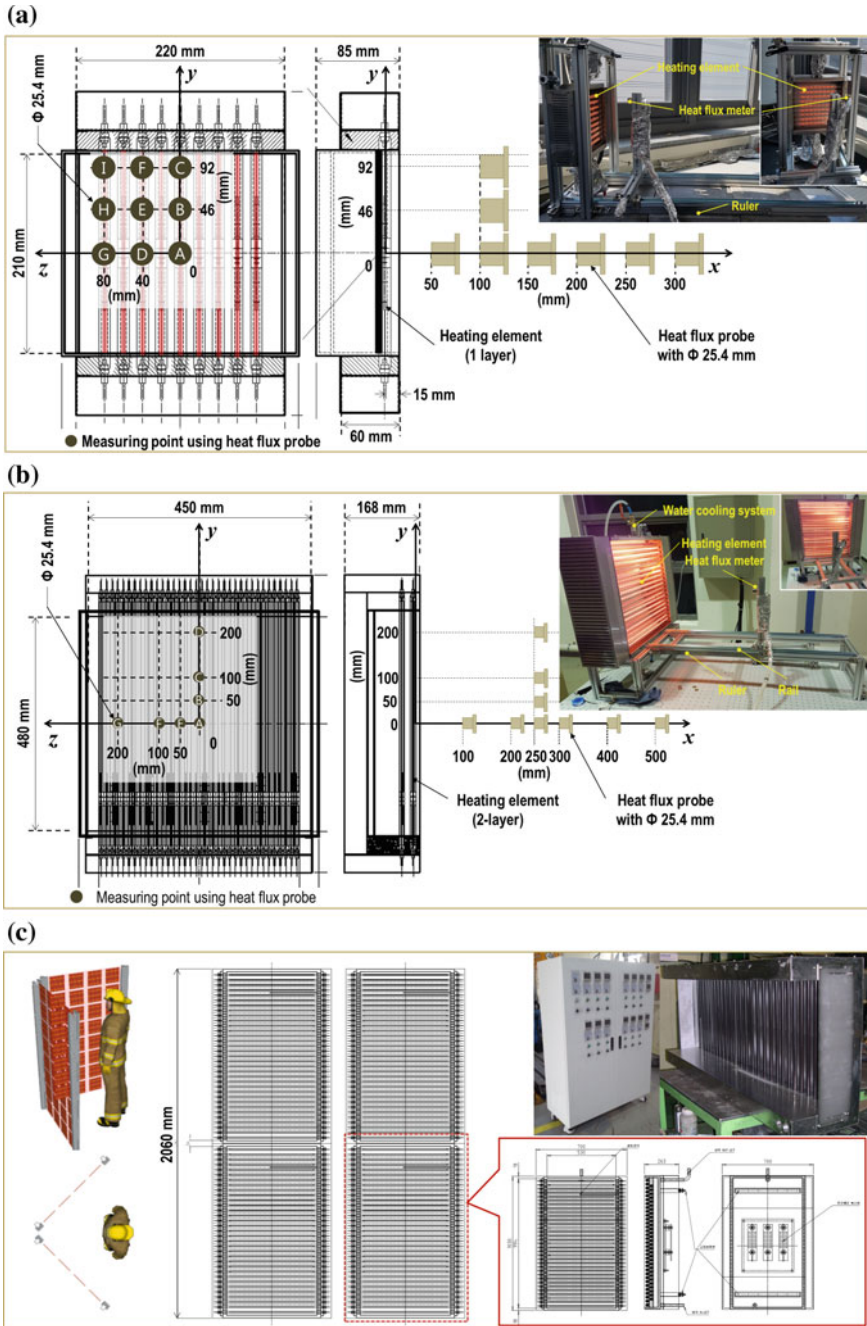
Fig. 3 A sequential development of **a** bench-scale, **b** intermediate-scale, and **c** full-scale apparatuses
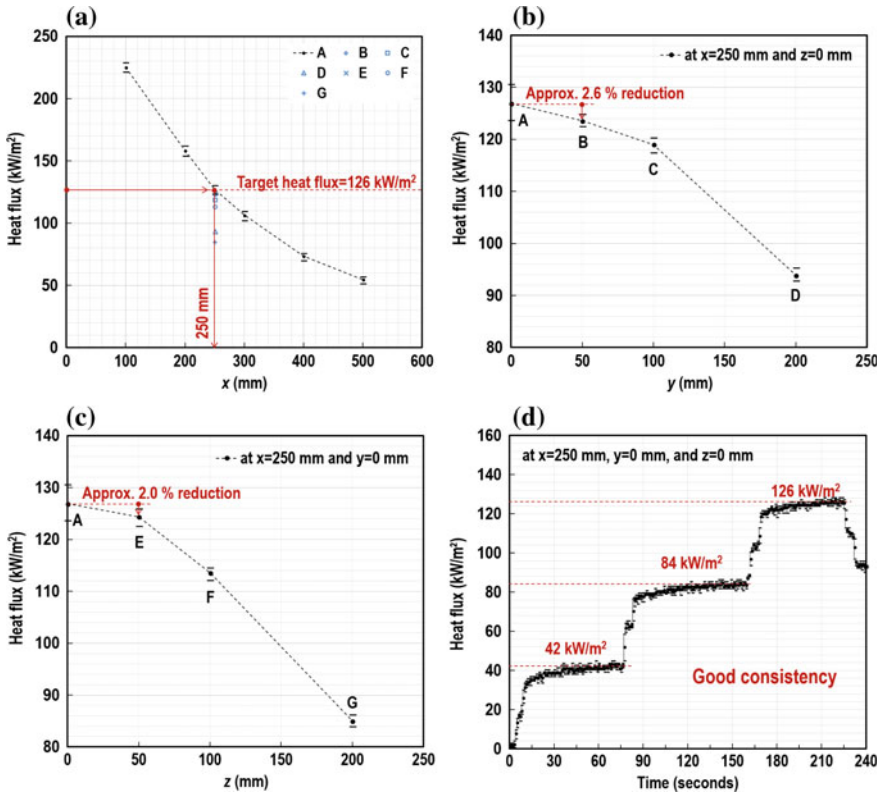
Fig. 4 Results of calibration for intermediate-scale apparatus, regarding irradiance variations with changes **a** in x-coordinate (as described in Fig. 3b), **b** in y-coordinate, **c** in z-coordinate, and temporal consistency

3 Establishment of Measurement System

3.1 Introduction to Measurement Criteria

To understand the performance and behaviour of the thermal protective ensemble exposed to more intense thermal environments, an appropriate measurement plan for testing should be established as well as the process of emitting the adequate amount of heat flux.

Two key measurements could be obtained from the tests designed in this project: (i) the temperature (or the absorbed heat) of the thermometer used and (ii) the time to exposure to the controlled thermal load. For near-to-practice evaluation to be conducted, the data gained need to be subsequently associated with physical damages to garment wearers. In the course of making the connection, the onset of a superficial second-degree burn injury, which is indicative of necrosis of the epidermis and causes

Table 1 Relation between temperature and burn injury (NIST)

Temperature (°C)	Response
48	Human skin receives a first-degree burn injury
55	Human skin receives a second-degree burn injury
62	A phase where burned human tissue becomes numb
72	Human skin is instantly destroyed

oedema and blisters, is conventionally employed as a criterion of damage, since it is the critical bound of wound which can be reversibly recovered without considerable medical assistance. Early studies [18, 19] intensively examined the relationship among the heat absorbed by tissue, pain/tissue damage, and the tolerance time of blistering, with the measurement of skin temperatures in vivo. It was understood from the experimental data that there exists a tissue injury zone in terms of the rate of the incident heat on skin and the exposure duration, and the injury may occur when the temperature of the basal layer of tissue, approximately 80 μm underneath the surface, becomes higher than 44 °C; more specific information on onset temperatures of different degrees of burn injuries were recently presented by NIST, as listed in Table 1. To complete the process of associating measurable data with the near-to-practice point of damage reference, two methods could be used:

- The physical measurement of the time-dependent total thermal energy absorbed (or irradiance) at the position where the exposed surface of the epidermis skin exists, using a thermometer with known thermo-physical characteristics (e.g. copper calorimeter), and the subsequent theoretical calculation of temperature–time profiles at the interfaces of epidermis/dermis and dermis/subcutaneous employing Stoll's criterion [18, 19] or Henrique's burn integral method [20] with thermo-physical properties of tissue [21];
- The direct measurement of temperature–time profiles at each of the interfaces using a skin simulant sensor.

It is noted that although the second method is mainly used to achieve the aim of this project, the first is also conducted to verify the primary approach.

Severity of fire hazard is determined by the quantity of heat flux and the duration of exposure; the first factor is set to 126 kW/m^2 in this work. In terms of the time to exposure, an experienced firefighter discussed the time to escape from compartment fires beyond the stage of flashover and the limit distance [22]. It was presented in his study that approximately 1.5 m is the limit of distance from the exit for survivable escape, based on the background that a firefighter can crawl at approximately 76 cm/s and tolerate extreme thermal environments no more than about 2 s. In this regard, the International Standard [12] suggests that the exposure duration shall be limited to less than 12 s, and the data acquisition period shall be at least 240 s for higher exposure times than 6 s or for multi-layer garments as a considerable amount of heat is still

transmitted from the heated garment and air gaps to the underlying manikin (or human body) in the course of the desperate exit or after the escape from direct fire hazards. In addition to the consideration of exposure time, a criterion of garment performance needs to be established. According to U.S. military medical doctrine, for instance, no greater than a 20% area of human body shall be thermally damaged below the state of the second-degree burn injury to pass the flammability testing for clothing systems [23]. Hence, this project aims to evaluate the thermal protective performance of garment by estimates of the second-degree burn injury (i) resulting from a heat flux of 126 kW/m^2 (ii) during a critical exposure time of 16 s for survival from life threatening-generated fires (such as flashover, backdraught, and fully developed fire) and (iii) during an additional incidental duration of 240 s excluding heating. It therefore strives for contributing to the improvement of its quality (iv) to mitigate the total skin burn injury throughout no more than 20% of the human body's surface area.

3.2 Development of Skin Simulant

A direct measurement of temperature–time profiles at the interface between epidermis and dermis is attempted to assess the protective performance of garment in association with the degree and total area of skin burn injury in this project. To achieve this goal, it would require a skin simulant sensor, which enables to predict an increase in temperature of human skin exposed to heat rather than the conventional copper calorimeter. It was pointed out in a previous study [24] that there exists a considerable difference between the responses of the copper calorimeter and the human skin. In advance of developing a skin simulant sensor, a pilot study was therefore conducted to understand the influence of the type of sensor body, where thermocouples are bonded on measuring temperature–time profiles. Figure 5 describes the three types of specimens, composed of three-layered thermal protective clothing and a substrate representing the sensor body (metal, plastic, or skin simulant). Each of the specimens was subjected to the intermediate-scale apparatus emitting the irradiance

Fig. 5 Configuration of specimens

	Type of substrate
Type 1	Metal
Type 2	Plastic
Type 3	Skin simulant
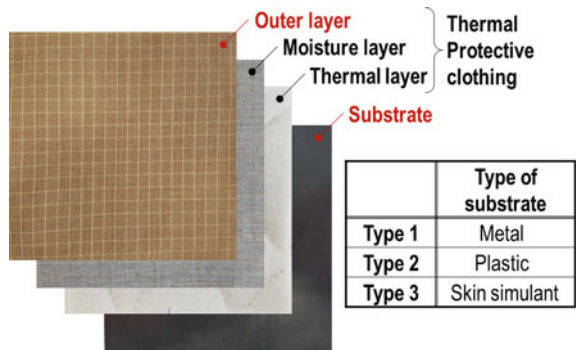
of 126 kW/m^2 at the 100 mm × 100 mm central area of the outer layer's front surface for 16 s and was subsequently left without heating for 240 s. The test was quintuplicated for each of the samples as plotted with the upper and lower bars and the round mark of arithmetic mean value in Fig. 6a. Appreciable differences in temperature developments were observed with respect to the type of cloth backing, which may lead to inaccurate predictions of the total heat absorbed, the time to burn injuries, and thereby the performance of garment. Figure 6b shows the temperature–time profiles of the specimens after the cessation of heating. It was identified that the differences in profiles were even more considerable to monitor skin temperature variations with timelines after the escape from direct fire hazards. It is noted that both the red solid and dotted curves (i.e. TC1 and TC2, respectively) were obtained from the Type 3 specimen, while the thermocouple, TC2, intended not to be firmly contacted on the
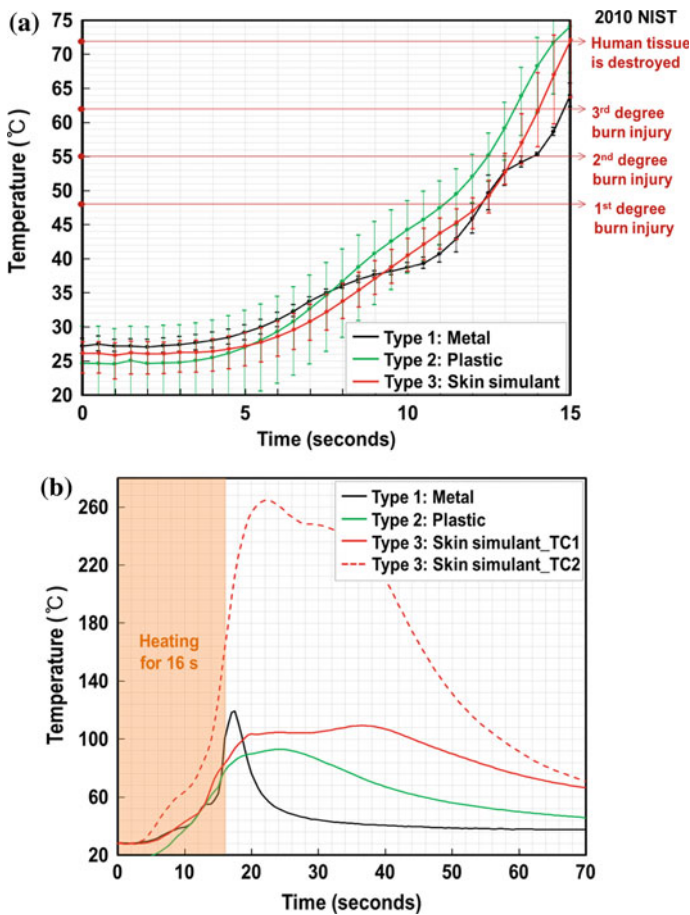
Fig. 6 Results of temperature–time profiles of substrate **a** in the period of heating and **b** in the period of natural cooling

substrate's surface to quantitatively monitor the influence of the thermocouples' contact condition on physical measurements. It can be concluded that the development or use of a skin simulant sensor is required in this project.

Since Maggio's early work [25] in the 1950s, attempts have been made to develop a skin simulant to date [26]. E. I. du Pont de Nemours and Company developed a thin-skin calorimeter for full-scale manikin tests using Thermo-Man®; one T-type thermocouple is embedded in a thermoset polymer resin which exhibits thermal inertia comparable to that of human skin. The University of Alberta [27] developed an inorganic skin simulant composed of calcium, aluminium, silicate with asbestos fibres and a binder, named as Colerceran, which has also thermal inertia similar to that of human skin; one T-type thermocouple was held on the surface of the skin simulant with an epoxy-phenolic adhesive. The existing skin simulants are briefly documented only. In addition, some incorporate asbestos which has desirable physical and fireproofing characteristics but the issue of the health hazards and thereby is heavily systematically restricted since 1975 in the USA, Europe, and Asia countries such as Republic of Korea and Japan.

The difficulties for use or development of skin simulant sensors were overcome through the adoption of silicone as an approachable and non-toxic material. This polymer resin also exhibits resistance to heat, chemical solvent, moisture and mechanical shock, and adequate for testing of thermal protective clothing. The polymer in liquid state was blended with zinc oxide, fillers, and hardener utilising a mechanical stirrer to meet the requirements of thermal inertia and solidification. The mixture was then casted into a glass mould and degassed by vacuum oven to form a skin simulant solid with homogeneous thermo-physical characteristics throughout its volume. The exposed surface of the skin simulant was coated with a thin layer of carbon black paint with an absorptivity of approximately 0.9. Figure 7 shows the comparative data of thermal absorptivity (a square root of thermal inertia) of human skin and skin simulant, provided by the standard [21], Dale's work [27], and the present work. It is noted that the thermal absorptivities of epidermis, dermis, and subcutaneous could be simulated by varying the ratio of silicone to zinc oxide. Based on the developed skin simulant, further studies progress on the formation of sensor and its accuracy.

4   Conclusions

This research project aims at evaluating the performance of thermal protective clothing subjected to recent critical fire conditions, in order to mitigate the total skin burn injury throughout no more than 20% of wearers' body surface area. As part of the project, this paper discussed the development of heating and measuring environments for the achievement of the goal. Firstly, a series of radiant heaters were advanced from bench-scale to human adult-scale in order to embody a critical condition which was defined as 126 kW/m^2 in this work. The calibration for the apparatuses resulted that the developed instruments enable emitting the desired irradiance uniformly on the 100 mm × 100 mm central area of the specimen's exposed surface consistently
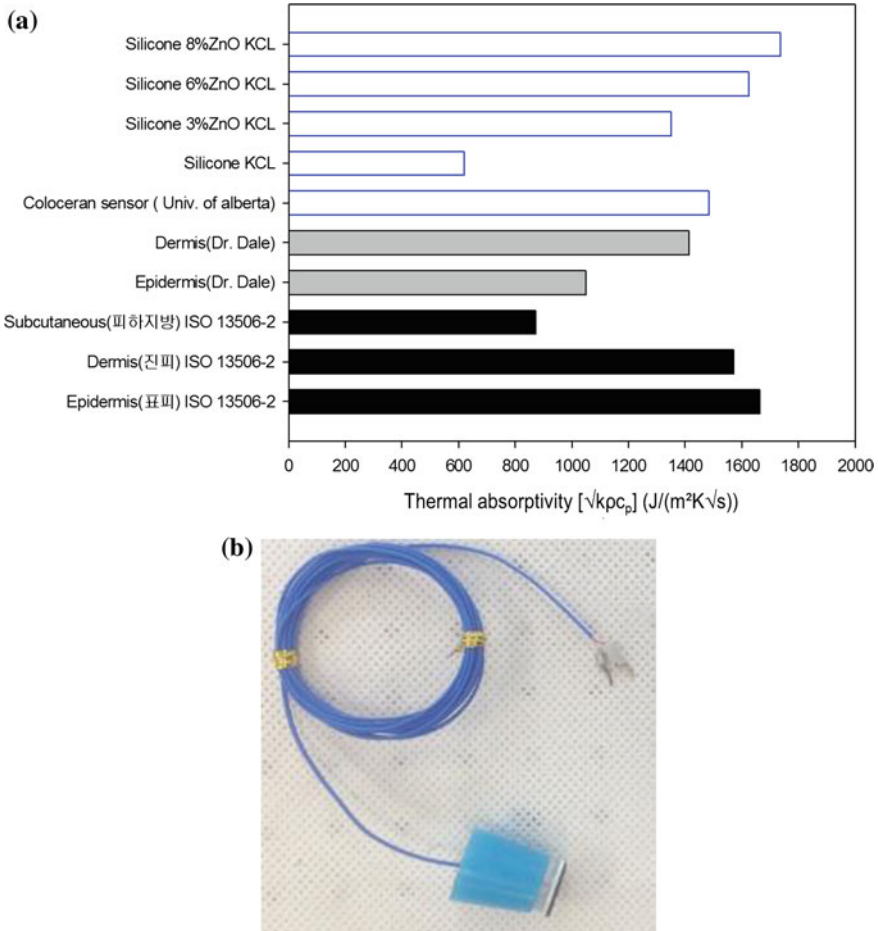
Fig. 7　**a** Comparative results of thermal absorptivity (or thermal inertia) and **b** pilot skin simulant sensor

longer than 60 s. Secondly, a measurement plan for testing was established based on the tissue injury concept: Estimation of the superficial second-degree burn injury resulting from irradiance of 126 kW/m^2 for exposure time of 16 s and additional duration of 240 s excluding heating. To accurately predict burn injuries, a skin simulant composed of silicone, zinc oxide, and additional fillers was developed, albeit with further improvements needed in accuracy. In this regard, the pilot test demonstrated the importance of the type of materials used for sensor body in measuring temperature–time profiles. The advanced testing environment created in this work can contribute to furthering the aims and objectives of the research project.

References

1. Kerber, S. (2012). *Analysis of changing residential fire dynamics and its implications on firefighter operational timeframes*. UL report.
2. Madrzykowski, D., & Kent, J. (2011). *Examination of the thermal conditions of a wood floor assembly above a compartment fire*. NIST TN 1709.
3. Lennon, T., & Moore, D. (2003). The natural fire safety concept—Full-scale tests at Cardington. *Fire Safety Journal, 38,* 623.
4. Drysdale, D. (1999). *An introduction to fire dynamics*. New York: Wiley.
5. Fang, J. B., & Breese, J. N. (1980). *Fire development in residential basement rooms*. National Bureau of Standards, NBSIR 80-2120, Gaithersburg, MD.
6. Krasny, J., Rockett, J. A., & Huang, D. (1988, February). Protecting fire fighters exposed in room fires: Comparison of results of bench scale test for thermal protection and conditions during room flashover. *Fire Technology*, 5.
7. Torvi, D. A. (1997). *Heat transfer in thin fibrous materials under high heat flux conditions*. Ph.D. thesis, University of Alberta.
8. Song, G., Mandal, S., & Rossi, R. M. (2017). *Thermal protective clothing for firefighters*. UK: Woodhead Publishing in association with The Textile Institute.
9. Behnke, W. P. (1977). Thermal protective performance test for clothing. *Fire Technology, 13*(1), 6–12.
10. Behnke, W. P. (1984). Predicting flash fire protection of clothing from laboratory tests using second-degree burn to rate performance. *Fire and Materials, 8*(2), 57–63.
11. NFPA 1971. *Standard on protective ensemble for structural firefighting and proximity firefighting* (2000 ed.). National Fire Protection Association.
12. BS EN ISO 13506-1:2017. Protective clothing against heat and flame. Test method for complete garments. Measurement of transferred energy using an instrumented manikin. British Standards.
13. Margolin, S. (2013, March/April). Flash fire-duration and heat flux. *Well Servicing*, 15–17.
14. Stanton, R. M., Schulman, S., & Ross, J. H. (1973). *The protective characteristics of PBI and NOMEX coveralls in JP-4 fuel fires*. Technical Report AFML-TR-72-253, Air Force Materials Laboratory.
15. Babrauskas, V. (1995). Specimen heat fluxes for bench-scale heat release rate testing. *Fire and Materials, 19*(6), 243–252.
16. Lawson, J. R. (1996). *Fire fighter's protective clothing and thermal environments of structural firefighting*. NISTIR 5804.
17. Kang, S., Kwon, M., Choi, J. Y., & Choi, S. (2018). *Development of high-radiation emitting apparatus for thermal protective clothing*. Submitted to Measurement and Control.
18. Stoll, A. M., & Chianta, M. A. (1969). *Method and rating system for evaluation of thermal protection*. Aerospace Medical Research Department, Department of the NAVY.
19. Stoll, A. M., & Greene, L. C. (1959). Relationship between pain and tissue damage due to thermal radiation. *Journal of Applied Physiology, 14,* 373.
20. Henriques, F. C. (1947). Studies of thermal injury—V. The predictability and the significance of thermally induced rate processes leading to irreversible epidermal injury. *Arch Patho (Chic)*, *43*(5), 489–502.
21. ISO 13506-2:2017. *Protective clothing against heat and flame—Part 2: Skin burn injury prediction—Calculation requirements and test cases*. International Organisation for Standardisation.

22. Dunn, V. (1999). Products of combustion. In *Command and control of fires and emergencies* (p. 246). PennWell Books, USA.
23. Winterhalter, C. A., Lomba, R. A., Tucker, D. W., & Martin, O. D. (2015). Novel approach to soldier flame protection. *Journal of ASTM International, 2*(2), 1–8.
24. Keltner, N. R. (2005). Evaluating thermal protective performance testing. *Journal of ASTM International, 2*(5), 1–14.
25. Maggio, J. M. (1956). *A molded skin simulant material with thermal and optical constants approximation those of human skin*. Technical Report NS 081-001, Naval Material Laboratory.
26. Barker, R. L., Hamouda, H., & Shalev, I. (1999). *Review and evaluation of sensors for use in testing firefighters' protective clothing*. Report, NIST GCR 99-772, USA.
27. Crown, E. M., & Dale, J. D. (1992). *Evaluation of flash fire protective clothing using an instrumented mannequin*. Final Research Project Report.

Effect of Ice Slurry on Suppression and Cooling of Body Temperature in Firefighters

Jongjin Jeong, Tetsuhito Akieda, Masayuki Mizuno, Shinya Yanagita, Shiro Ichimura, Takahiko Yamamoto, Yoshifumi Ohmiya, Tsuguo Genkai, Haruto Mochida, Shun Suzuki and Toshiyuki Kugai

Abstract Firefighters often work in harsh high-temperature and high-humidity environments such as scene of fires. Additionally, the heat and perspiration generated by the human bodies further increase the temperature and humidity inside the fire-protective clothing. The aim of this research is to scientifically evaluate the body load based on vital data from firefighters according to the activities and environment of each firefighter and to further investigate the effect of cooling the human body by fluid intake with the aim of lowering the risk of heatstroke. In a series of experiments, six firefighters took exercise in an environment of 25 and 40 °C as a normal-temperature and a high-temperature condition, respectively. And they took in water or ice slurry before and after exercise. As the experimental result, in case of exercise in the high-temperature environment, intake of ice slurry caused rectal temperature to decrease rapidly compared with intake of water. But in the normal temperature, the cooling effect of rectal temperature by intake of ice slurry showed little difference from ingestion of water. The ear temperature did not show the difference by intake of water and ice slurry both; in addition, after the exercise 1, during rest time with intake of water, the ear temperature decreased to initial temperature at the normal-temperature and high-temperature environment. The trends of cardiac rate looked almost identical between intake of water and ice slurry in each environment for exercise, but after only the exercise 1, intake of ice slurry could decrease cardiac rate to initial condition earlier than intake of water. As a result of this research, ingestion of ice slurry was shown to be effective at reducing the rectal and body surface temperatures during rest after exercise in the high-temperature environment and slowing the heart rate during rest after exercise in both the normal- and the high-temperature environments.

Keywords Firefighter · Vital data · Fluid intake · Temperature increase suppression and decrease effects

J. Jeong · T. Akieda · M. Mizuno · S. Yanagita · S. Ichimura · T. Yamamoto · Y. Ohmiya (✉)
Tokyo University of Science, 2641 Yamazaki, Noda, Chiba 278-8510, Japan
e-mail: ohmiya@rs.noda.tus.ac.jp

T. Genkai · H. Mochida · S. Suzuki · T. Kugai
Operational Safety Section, Fire Technology and Safety Laboratory, Tokyo Fire Department,
1-3-20 Hatagaya, Shibuya-ku, Tokyo 151-0072, Japan

Nomenclature

$T_{surface}$ Body surface temperature [°C]
T_{arm} Body surface temperature of upper arm [°C]
T_{chest} Body surface temperature of breast [°C]
T_{thigh} Body surface temperature of the femoral region [°C]

1 Background of Study

Firefighters often work in harsh high-temperature and high-humidity environments, such as the sites of fires. Although equipment such as fire suits has been improving to offer more safety from fires, the high thermal insulation and airtightness of the fire suit can result in the heat and perspiration generated by the human body increasing the temperature and humidity inside the fire suit. This effect may be one factor in body temperature rise. Since this is expected to increase the risk of heatstroke of firefighters, measures for suppressing rises in body temperature during firefighting activities and cooling the body temperature during rest times should be investigated, taking into account external factors (ambient temperature and humidity, the radiant heat from the fire, high-temperature smoke, sunlight, etc.) and internal factors (such as the heat and perspiration generated by the human body).

Much of the past research has examined the physical load on firefighters, that is, the physiological changes in the human body. However, the discussion has not necessarily extended to measures for preventing heatstroke based on a scientific foundation.

2 Purpose and Outline of Study

In this research, experiments were conducted to measure changes in the vital signs of firefighters attributable to differences in the ambient temperature and humidity and in fluid intake. Current firefighters acted as participants, performing exercise while being measured. In the experiments, participants were asked to perform exercise (stepping on and off a step) to simulate firefighting activities in a constant-temperature, constant-humidity room. The temperature of the test room was set to 25 °C (normal temperature) or 40 °C (high temperature), and the fluid intake was set to water or ice slurry. Vital signs were measured, and the results were analyzed for the different conditions. The aim of this research was to improve the safety and efficiency of firefighting activities by scientifically evaluating the body load on firefighters, according to their activities and the environment. Biological information (vital signs) was considered, and other effects, such as cooling of the body, were investigated.

3 Experimental Overview

3.1 Participants

The experiments were conducted after getting advice and ultimate approval from the Tokyo Fire Department Ethics Review Special Committee. Further, the candidate firefighters were invited to participate after explaining that participating (or not) in the experiment and the results would not have any effect on their personnel evaluations. The six chosen firefighters were all healthy males (age: 34.8 ± 4.5 years, height: 171.3 ± 5.7 cm, weight: 66.1 ± 4.1 kg) from the Tokyo Fire Department Fire Technology and Safety Laboratory. Participants received an explanation of the details of the experiment before the experiment and ultimately agreed to participate, signing written agreements.

3.2 Exercise and Rest Times

The exercise consisted of stepping on and off a step at a rhythm of 100 steps per minute using a step of height 20 cm in the experiment room, as shown in Fig. 1 and described later. The exercise was performed continuously for a maximum of 20 min per trial and was performed two times with a 30-min rest time in between. In this paper, the first exercise is described as exercise 1 (Ex. 1) and the second exercise after 30-min rest is described as exercise 2 (Ex. 2) as shown in Fig. 2. During the experiment, the experimenters constantly observed the participants while periodically checking the rectal temperature and pulse rate and surveying the visual analog scale (VAS) of the participants in the experiment room. Furthermore, during the waiting period before the experiment and during the rest time, participants were in a resting room, where
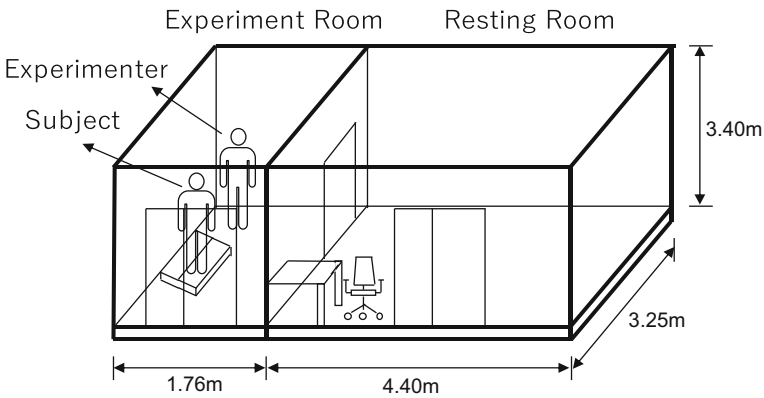
Fig. 1 Schematic of the constant-temperature, constant-humidity room

blood and saliva composition and blood pressure were measured, VAS was checked, and drinks were provided (either water or ice slurry) according to a pre-decided schedule.

3.3 Clothing of Participants

Participants were equipped in the manner usual for activities at a fire site. Specifically, on top of their work clothes, they wore a cooling vest with a total of four frozen cooling packs (approximately dimensions: 20 cm × 13.5 cm; melting point 0 °C; weight: 20 g, volume: 200 ml), with one stored in each of the left and right sides of the chest and back areas, and on top of that they wore an aramid fabric fire suit with separate top and bottom parts. Furthermore, participants wore specialized firefighting boots, gloves, and helmet as well as a face mask connected to respirator equipment worn on the back. The cooling packs in the cooling vest were inserted and replaced immediately before starting exercise 1 and before starting exercise 2. Before starting exercise 1, participants waited in a sitting position while wearing work clothes and began putting on the fire suit and equipment two minutes before the start of exercise 1. In the rest time after exercise 1, the respirator, face mask, and upper part of the fire suit were removed, but the lower part of the fire suit and cooling vest remained worn on top of the work clothes. The test subjects then put on the equipment again before starting exercise 2.

3.4 Exercise Stop Conditions

If any of the following conditions were met during the 20-min exercise, that period of exercise was stopped at that time.

Stop Condition-1: The participant reported that continuing the exercise would be difficult.
Stop Condition-2: The experimenter decided that it would be difficult for the participant to safely continue the exercise (e.g., the participant was becoming unsteady).
Stop Condition-3: The pressure in the respirator air cylinder ran out (cylinders were filled to a volume that is normally enough for 20 min of firefighting activities).
Stop Condition-4: If any two of the vital signs or perceptions of the participant described below were met.
Stop Condition-4-1: Rectal temperature exceeded 38 °C.
Stop Condition-4-2: Pulse rate exceeded 180 bpm.
Stop Condition-4-3: Among the VAS related to body load and perception of heat, anyone exceeded 80 mm, where the full scale of 100 mm represents a critical state.

In addition, the condition where exercise time reaches 20 min is set as below.

Stop Condition-5: The exercise time reached 20 min.

3.5   *Experimental Environment Parameters*

Experiments were conducted in a constant-temperature, constant-humidity room in the Tokyo Fire Department Fire Technology and Safety Laboratory (Fig. 1). The temperature and humidity of the experiment room in which the test subjects performed the exercise were set to either 25 °C and 70% (normal-temperature condition) or 40 °C and 70% (high-temperature condition). The temperature and humidity of the resting room were set to 25 °C and 70%, respectively. The normal temperature of 25 °C was set as the standard temperature at night in tropical climates, and 40 °C was set as the temperature corresponding to the hottest temperature in summer in Tokyo. The humidity of 70% was set as corresponding to the average humidity in summer in Tokyo, and although the humidity is normally lower than 70% when the air temperature is 40 °C, these are thought to be the high-temperature, high-humidity conditions that could occur during firefighting activities inside a burning building (Photograph 1).

Photograph 1 State during exercise
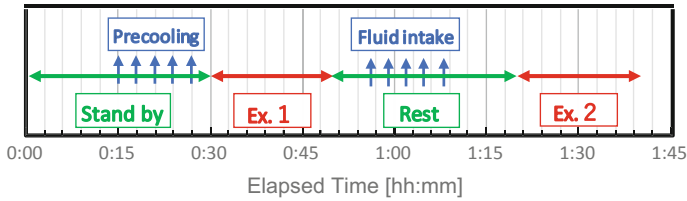
Fig. 2 Experiment schedule

3.6 Methods of Fluid Intake

Fluid intake was of either water (10 °C) or self-made ice slurry (1 °C). The ice slurry was created from only water to limit the number of factors other than temperature. Fluid intake was first performed to reduce the body temperature before starting the exercise, as pre-cooling before exercise 1, and then during the rest time after exercise 1. The method of fluid intake each time was frequent uptake, in which an uptake quantity of 100 g was taken 5 times over a 3-min period, for a total of 1000 g of fluid intake during the series of experiments.

3.7 Time Schedule of Experiments

Figure 2 shows the time schedule for the experiment. The total experimental time was around 1 h 45 min for each participant, which consisted of sitting in the resting room for 15 min from the start of the experiment, taking in fluid from the 15-min to the 30-min mark, performing exercise 1 for 20 min from the 30-min mark, taking in fluid while resting for 30 min from the 50-min mark, then performing exercise 2 for 20 min from the 1 h 20-min mark, ending the experiment at around 1 h 45 min.

During the experiments, participants entered the experiment room singly with one experimenter. The experimenter managed the safety of the experiment, while the participant performed the exercise, recording the rectal temperature and pulse rate every 3 min and asking the participant to fill in the VAS.

4 Measured Items

4.1 Vital Signs

Various sensors were attached at the measurement positions. Vital signs were measured. Additionally, saliva samples were taken, blood pressure was measured, and the blood sugar and lactate levels in the blood were assessed in the standby period

before exercise 1 and in the rest time between exercises 1 and 2. A urine sample was taken, and body weight was measured before and after the experiment. In the following, measurement procedure of the items analyzed in this paper is described.

(1) Rectal temperature

The rectal temperature sensor (model L2-2N-11 by Gram Corporation) was covered in a dedicated rubber cover and coated in medical lubricating gel before insertion of 10 cm into the rectum for measurements.

(2) Ear temperature

The ear temperature was measured by inserting an earplug-type sensor (model L2-2N-13 by Gram Corporation) into the ear. Unlike devices that use the infrared light method to measure tympanic temperature via a pinpoint non-contact state, this device measures the air temperature inside the ear. A seal is ensured by three pleats to make it resistant to external effects.

(3) Body surface temperature

Body surface temperature was measured by covering the temperature-sensitive part of skin temperature sensors (model LT-2N-12 by Gram Corporation) in a thermal insulating cover and attaching them to the front of the chest area, the upper arm area, and the thigh area. The body surface temperature was then found by inputting the temperatures measured at the three locations into the following formula [1].

$$T_{\text{surface}} = 0.43T_{\text{chest}} + 0.25T_{\text{arm}} + 0.32T_{\text{thigh}} \tag{1}$$

(4) Pulse rate

The pulse rate sensor (H7 sensor by Polar Electro) is fixed on the chest using a stretchy back strap. It is also displayed on the wristwatch by the Bluetooth function and recorded on the laptop through the wristwatch.

5 Results of Experiment

Section 5.1 gives an overview of the experimental results, and the remainder of this section reports on the analysis of the effect of ice slurry against water, focusing mainly on changes in rectal temperature, ear temperature, body surface temperature, and pulse rate. Note that the experimental results in the following sections and the graph legends use the test pattern names shown in Table 1.

Table 1 Experimental condition

Experimental parameters		Experimental patterns			
		NW	NI	HW	HI
Exercise room	Temperature (°C)	25		40	
	Humidity (%)	70		70	
Resting room	Temperature (°C)	25			
	Humidity (%)	70			
Fluid intake	Pre-cooling	Water	Ice slurry	Water	Ice slurry
	Cooling during rest	Water	Ice slurry	Water	Ice slurry

NW (25 °C, water), *NI* (25 °C, ice slurry), *HW* (40 °C, water), *HI* (40 °C, ice slurry)

5.1 Exercise Time and Exercise Stop Conditions

Table 2 shows the continuous duration of exercise and reason for ending in exercises 1 and 2 of all six participants under each set of experimental conditions. In exercise 1, all test subjects continued exercising up to the upper limit of 20 min under all conditions. In exercise 2, three of the six participants were not able to continue the exercise for 20 min under the high-temperature condition. Among those, one stopped after 16 min in the NI condition under normal temperature. The reason for stopping the exercise was mostly reaching the upper limit of core body temperature and pulse rate, with one exercise period stopped by decision of the experimenter (the test subject was shaking) and one stopped at the request of the participant.

5.2 Various Vital Data

The results for rectal temperature, ear temperature, body surface temperature, and pulse rate showed some degree of clear variation and trend, and the results are discussed in this paper.

5.2.1 Rectal Temperature, Ear Temperature, and Body Surface Temperature

Figure 4 shows the average value from the five participants for the temperature under each set of experimental conditions. The rectal temperature was measured every 3 min and is shown relative to the initial temperature for comparison. Note that conditions where the experiment failed were excluded.

Table 2 Results of exercise duration for each test subject

Subject no.	Date	Initial tem. (°C)	Exp. conditions[a]	Exercise 1	Exercise 2	Reason for finishing exercise 2
Subject 1	07-03-2017	36.3	NW (25 °C, water)	20 min	20 min	Stop condition-5
	07-28-2017	36.3	NI (25 °C, ice slurry)	20 min	20 min	"
	07-10-2017	36.0	HW (40 °C, water)	20 min	20 min	"
	07-19-2017	36.1	HI (40 °C, ice slurry)	20 min	20 min	"
Subject 2	10-16-2017	36.0	NW (25 °C, water)	20 min	20 min	Stop condition-5
	07-04-2017	36.0	NI (25 °C, ice slurry)	20 min	20 min	"
	07-20-2017	36.1	HW (40 °C, water)	20 min	20 min	"
	07-11-2017	35.9	HI (40 °C, ice slurry)	20 min	20 min	"
Subject 3	08-02-2017	36.4	NW (25 °C, water)	20 min	20 min	Measurement failure (rectal temp., heart rate)
	07-25-2017	36.2	NI (25 °C, ice slurry)	20 min	16 min	Measurement failure (heart rate) Stop condition-4-1 and 4-2
	07-13-2017	35.6	HW (40 °C, water)	20 min	12 min 30 s	Measurement failure (rectal temp.) Stop condition-4-1 and 4-2
	07-05-2017	36.1	HI (40 °C, ice slurry)	20 min	11 min	Stop condition-4-1 and 4-2
Subject 4	07-27-2017	36.3	NW (25 °C, water)	20 min	20 min	Stop condition-5
	07-18-2017	36.0	NI (25 °C, ice slurry)	20 min	20 min	"
	07-21-2017	36.3	HW (40 °C, water)	20 min	20 min	"
	07-06-2017	36.0	HI (40 °C, ice slurry)	20 min	20 min	"

(continued)

Table 2 (continued)

Subject no.	Date	Initial tem. (°C)	Exp. conditions[a]	Exercise 1	Exercise 2	Reason for finishing exercise 2
Subject 5	07-14-2017	35.1	NW (25 °C, water)	20 min	20 min	″
	07-07-2017	35.7	NI (25 °C, ice slurry)	20 min	20 min	Measurement failure (heart rate) ″
	07-26-2017	35.7	HW (40 °C, water)	20 min	12 min	Stop condition-4-1 and 4-2
	08-03-2017	35.8	HI (40 °C, ice slurry)	20 min	13 min 30 s	Finish according to the experimenter's report
Subject 6	08-04-2017	36.5	NW (25 °C, water)	20 min	20 min	Stop condition-5
	07-24-2017	36.5	NI (25 °C, ice slurry)	20 min	16 min	Stop condition-4-1 and 4-2
	07-12-2017	36.3	HW (40 °C, water)	20 min	9 min	″
	10-16-2017	36.3	HI (40 °C, ice slurry)	20 min	9 min	Finish according to the subject's report

[a]The left-side value is the exercise temperature and the right-size item is kind of fluid subject took

(a) Rectal temperature   (b) Ear temperature   (c) Body-surface temperature
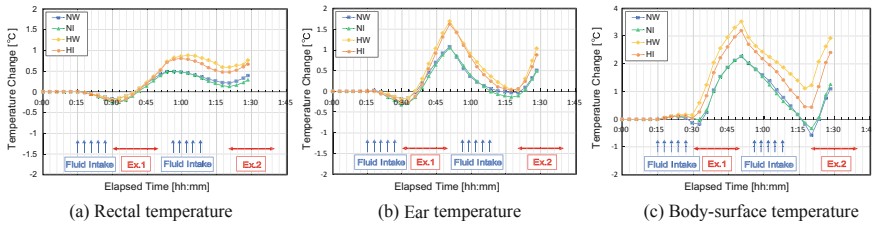
Fig. 3 Change in temperature

(1) Rectal temperature (Fig. 3a)

Looking at the trends in rectal temperature, it is clear that the rectal temperature is ordered as (highest to lowest) HW > HI > NW > NI from the end point of exercise 1. We now discuss the rectal temperature along the flow of the experiment.

Looking at the pre-cooling area, the same trends were observed in the conditions of water intake for water replenishment (NW, HW) as the conditions of ice slurry intake (NI, HI). Ultimately, when compared with the rectal temperature before starting the pre-cooling, the rectal temperature was found to drop by -0.16 °C with NW, -0.25 °C with NI, -0.18 °C with HW, and -0.19 °C with HI. Looking at the exercise 1 area, a trend was observed for the gradient to increase greatly after the start of exercise 1 (for NI, from 3 min after starting exercise), and the normal-temperature conditions and high-temperature conditions diverged from around 3 min before the end of exercise 1. Note that with NI, the temperature was observed to be the lowest among the experimental conditions up to 3 min after starting exercise and resembled the NW condition from 4 min after the exercise finished. Looking at the area during the rest time, the temperature began to decrease from the third fluid intake for HW but began to decrease from the first fluid intake for other conditions. In other words, the timing of the temperature decreasing was faster in the high-temperature environment with intake of ice slurry than with intake of water. Furthermore, comparing NW and NI normal-temperature conditions, the decrease in rectal temperature under the NI condition was larger and was ultimately closer to the initial temperature. Looking at the exercise 2 area, the temperature began to rise as exercise 2 started. Note that the average values of the rectal temperatures are indicated until 9 min after starting exercise 2 because subject 6 stopped the exercise at 9 min after starting exercise 2, due to the experiment stop conditions.

(2) Ear temperature (Fig. 3b)

During pre-cooling, the same trends were observed under all conditions. Ultimately, when compared with the ear temperature before starting the pre-cooling, the values were approximately -0.18 °C for NW, -0.32 °C for NI, -0.19 °C for HW, and -0.27 °C for HI, which confirmed that ice slurry decreased the temperature more than water, by approximately -0.1 °C. During exercise 1, looking at the timing of the temperature rise after the start of exercise 1, the times were 31 min 9 s for NW, 30 min 10 s for NI, 30 min 44 s for HW, and 31 min 16 s for HI, and the

time of temperature increase was slower for water under normal-temperature conditions and ice slurry under high-temperature conditions. Furthermore, after 42 min, the normal-temperature conditions and high-temperature conditions diverged, and a decrease in temperature was observed under all conditions from 1 min after the end of exercise 1. No clear differences were observed in ear temperature between conditions. During the rest time, the overall trend was for the temperature drop to start rapidly and gradually become more gentle up to the start for exercise 2. Looking at the difference between the maximum temperature around the start of the rest time and the minimum temperature at the end of the rest time, the temperatures were -1.15 °C for NW, -1.25 °C for NI, -1.69 °C for HW, and -1.64 °C for HI, and the temperature decrease was largest for the high-temperature conditions. Furthermore, under normal-temperature conditions, the temperature decreased by -0.03°C for NW and -0.14°C for NI over the initial temperature change (0 °C, by definition). In the case of exercise 2, although the normal-temperature conditions and high-temperature conditions diverged and a clear difference was observed, no difference was observed between water and ice slurry. Note that the average values of the rectal temperatures are indicated until 9 min after starting exercise 2 because subject 6 stopped the exercise at 9 min after starting exercise 2, due to the experiment stop conditions.

(3)   Body surface temperature (Fig. 3c)

During pre-cooling, compared with the ultimate body surface temperature before starting pre-cooling, the temperature difference was approximately -0.18 °C for NW, -0.05 °C for NI, 0.15 °C for HW, and 0.02 °C for HI, with the temperature decreasing under normal-temperature conditions and the temperature rising slightly compared with before starting pre-cooling under high-temperature conditions. During exercise 1, the body surface temperature exhibited the same shape as ear temperature, and the temperature was observed to rise and fall at the same time as the start and end of the exercise. Furthermore, comparing the body surface temperature under each condition, it is clear that the normal-temperature conditions NW and NI exhibit the same shapes. Furthermore, comparing the high-temperature conditions HW and HI, the HI condition of taking in ice slurry was observed to have a lower body surface temperature trend. In addition, the body surface temperature increase during exercise 1 was largest under HW conditions where ice slurry was not taken in. During the rest time, comparing the high-temperature conditions HW and HI, HI was observed to have a more sudden decrease in temperature compared. During exercise 2, the high-temperature environment and normal-temperature environment diverged, and although the same trends were observed in NW and NI in the normal-temperature environment, a trend was observed for the temperature to be lower in HI (where ice slurry was taken) than in HW. Note that the average values of the rectal temperatures are indicated until 9 min after starting exercise 2 because subject 6 stopped the exercise at 9 min after starting exercise 2, due to the experiment stop conditions.
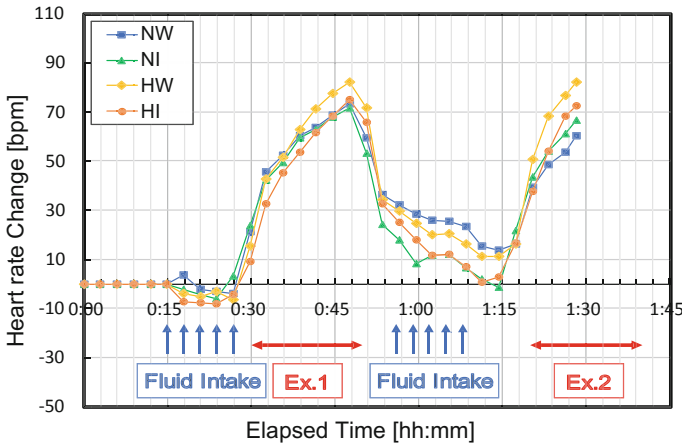
Fig. 4 Heart rate change

5.2.2 Pulse Rate

Figure 4 shows the average values of participants for the pulse rate under each set of experimental conditions. Since the pulse rate exhibits large variation per second, the 10 s average pulse rate was measured every 3 min and is shown relative to the initial temperature for comparison. Note that conditions where the experiment failed were excluded.

The pulse rate was observed to rise gradually with the start of the exercise and fall relatively quickly with the end of the exercise. Focusing on the pulse rate during pre-cooling, it is found that the decrease in the pulse rate is larger, on average, under the high-temperature conditions than under the normal-temperature conditions. During exercise 1, focusing on the maximum value at the end of exercise 1, the value is higher in the high-temperature environment, but lower under HI than under HW. During the rest time, the decrease in pulse rate was larger for conditions NI and HI than NW and HW. During exercise 2, comparing the high-temperature conditions, the rate of increase in the pulse rate was faster under HW than under HI.

6 Controlling Temperature Increases and Analyzing Decreases

6.1 Point of View of Analysis

This section confirms the details of the changes in rectal temperature according to fluid intake. Specifically, this section numerically analyzes the effectiveness of suppressing rise in rectal temperature. For analysis, the highest and lowest temperatures

from each segment were checked (see Fig. 5), with the time split by the following events: The temperature reached the maximum after the start of pre-cooling in segment (1), the temperature reached the minimum from the start of pre-cooling to the end of exercise 1 in segment (2), the temperature reached the maximum from the start of exercise 1 to the end of fluid intake in segment (3), and the temperature reached the minimum from the middle of fluid intake to the middle of exercise 2 in segment (4). Furthermore, the effect of fluid intake, as characterized by the differences between each segment, is compared and analyzed as shown in Table 3 for comparison of the temperatures between segments.
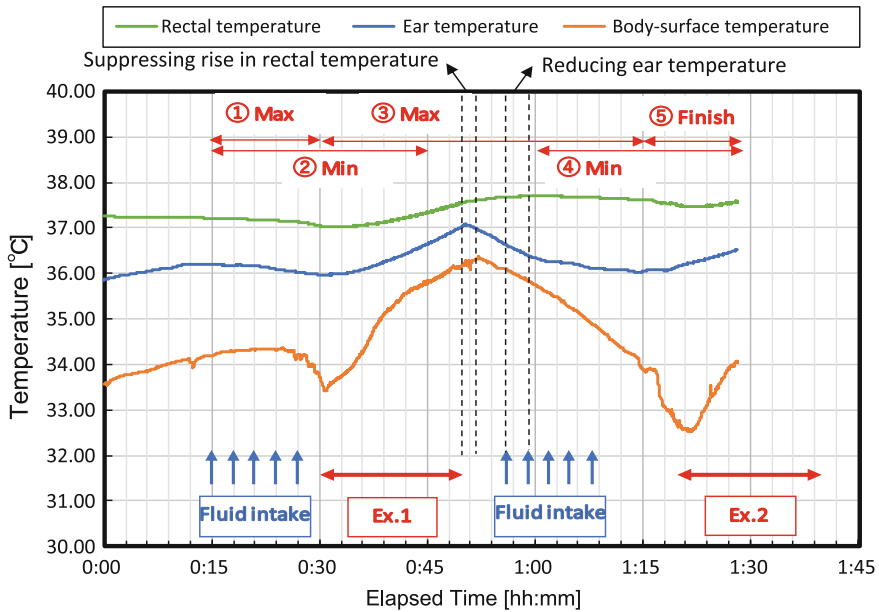
Fig. 5 Example of temperature measurement results (Subject 1 NW)

Table 3 Comparison of temperatures between segments

	Aim of comparison	Effect of environment	Effect of cooling method
(2)–(1)	Effect of pre-cooling	Unconnected	Connected
(3)–(2)	Increase in body temperature due to exercise 1	Connected	A little connected
(4)–(3)	Cooling effect during rest time	Connected	Connected

6.2 Effectiveness of Suppressing Maximum Rectal Temperature

Next, the rectal temperature suppression effect from the temperature was evaluated between the end of exercise 1 and the maximum temperature after exercise 1.

From Fig. 6a, the average value of the decrease in rectal temperature due to pre-cooling before starting exercise was −0.19 °C for liquid intake of water (NW and HW) and −0.28 °C for ice slurry (NI and HI). Thus, ice slurry is highly effective at reducing the rectal temperature in pre-cooling. From Fig. 6b, the increase in ear temperature under the normal-temperature environment was somewhat larger with ice slurry than with water (the average value of ③–② was 0.70 °C for NW and 0.77 °C for NI). However, under the high-temperature environment, these were around the same, nominally higher for ice slurry (1.11 °C for HW and 1.09 °C for HI). Further-more, the rectal temperature rises more readily in the high-temperature environment for exercise 1, and the average value of the rectal temperature rises from after pre-cooling to the maximum temperature after exercise 1. Furthermore, similar values were seen: 0.70 °C for NW, 0.77 °C for NI, 1.11 °C for HW, and 1.09 °C for HI. From Fig. 6c, for the change during the rest time from the maximum temperature after exercise 1, a higher decrease was seen from ice slurry than from water in the normal-temperature environment (the average value of ④–③ was −0.33 °C for NW and −0.39 °C for NI), but under the high-temperature environment the opposite was seen (−0.42 °C for HW and −0.39 °C for HI). Between environments, the decrease in rectal temperature by resting and fluid intake was larger after exercise 1 under the high-temperature environment.

As described above, it is shown that rectal temperature was cooled down by pre-cooling. To see the details of temperature decreasing in average values, intake of 500 g of 10 °C water makes the rectal temperature decrease 0.19 °C, and intake of 500 g of 1 °C ice slurry 0.28 °C. The effect of temperature decreasing by ice slurry intake was 0.09 °C higher than water intake. At both the normal- and the high-temperature environments, there was no much difference in the effects of suppression of the temperature increasing after exercise 1 and decreasing temperature during the
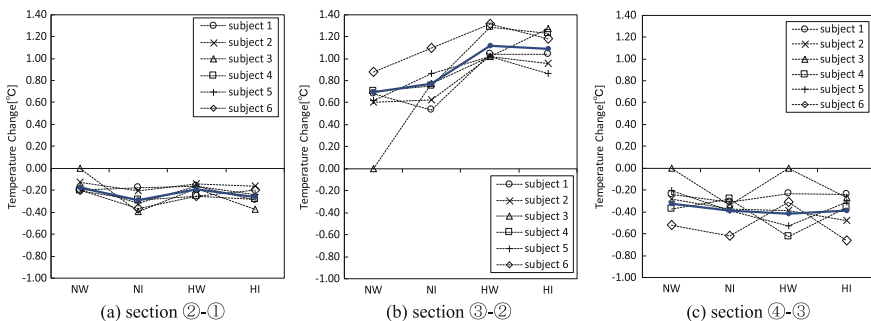
Fig. 6 Rectal temperature comparison of the subject

rest time between intake of water and intake of ice slurry. Note that temperature increasing by exercise 1 at high-temperature environment was larger than at normal-temperature environment.

7 Summary

In Fig. 3a, there is no much difference of rectal temperature changing by intake of water or ice slurry at the normal temperature, but after exercise 1, temperature decreasing was earlier by intake of ice slurry during rest time. On the other hand, at the high-temperature environment, intake of ice slurry causes rapid temperature decreasing more than water, so at the high temperature, ice slurry is more effective to decrease the body temperature than water. In Fig. 3b, the ear temperature did not show the difference by intake of water and ice slurry both; in addition, after the exercise 1, during rest time with intake of water, the ear temperature decreased to initial temperature at the normal-temperature and high-temperature environment both, but not like Fig. 3a, the rectal temperature did not decrease until initial temperature. In Fig. 3c, the body surface temperature did not show the difference between intake of water and intake of ice slurry at the normal-temperature environment, but at the high-temperature environment, intake of ice slurry showed lower temperature from the start of exercise 1 to the end of exercise 2. In Fig. 4, the result of cardiac rate was not clear enough to see the difference, but after the exercise 1, intake of ice slurry could effectively decrease cardiac rate to initial condition more than intake of water. In Fig. 6a, to analyze the pre-cooling, intake of ice slurry was more effective to decrease the rectal temperature than intake of water, and according to Fig. 6b, intake of ice slurry also was more effective suppression of the rectal temperature increasing after exercise 1 than intake of water at the high-temperature environment.

Reference

1. Roberts, M. F., et al. (1977). Skin blood flow and sweating changes following exercise training and heat acclimation, Frontiers in Physiology. *Journal of Applied Physiology, 43*(1).

Experimental Studies of the Effect of Spray Dynamics on Radiation Blockage by Water Curtains

Haobo Wang, Libin Ding, Tian Xie, Jian Wang and Chao Ding

Abstract   As a widely used protection device, the radiation blockage ability of water spray curtain to high temperature heat source is influenced by a number of elements, of which spray dynamics characteristic of nozzles is an important factor. An experimental study on radiation attenuation ability of water sprays has been carried out in laboratory. Droplets diameters and distributions of varied positions have been measured by laser particle sizer at different pressures. The position range varies from 25 to 175 cm and pressure changes from 1 to 3 bars. The attenuated radiation fluxes are measured by radiation heat flux meters to analyze the transmissivity of sprays. The results clearly indicate that the spray dynamic characteristic can severely affect the blockage ability of thermal radiation. The variation tendency of particle mean diameter can directly reflect the change trend of attenuation efficiency. Characteristic of droplets and relative positions of protected objects are two significant factors for affecting attenuation efficiency. These factors should be considered when water spray curtains are to be used in industrial and building fire protection. Furthermore, different nozzles with different characteristics, which should be measured firstly when they are used to discharge the water sprays.

H. Wang · T. Xie · J. Wang (✉) · C. Ding (✉)
State Key Laboratory of Fire Science, University of Science and Technology of China, Hefei 230026, China
e-mail: wangj@ustc.edu.cn

C. Ding
e-mail: dc707@ustc.edu.cn

L. Ding
No. 92493 Unit of PLA, Huludao 125001, China

1 Introduction

In recent years, a protection device, water spray curtain has been given much attention to research the [1–4]. It commonly installed in buildings and industrial facilities to shield the radiation from fires or any other strong heat source because of its availability, simplicity, efficiency, adaptability, and so on [5, 6]. The attenuation mechanisms of water sprays have been known that is the characteristics of water droplets: radiation absorption and scattering (water droplets do not interact with flame directly). In order to improve the attenuation ability, many studies on this issue have been carried out, including theoretical analyses and experimental works. Theoretical analyses can help understanding the key parameters involved in the attenuation ability of radiation. Many calculation models of radiation in water sprays are presented in literatures. Dembélé et al. [3] calculated the absorptance and scattering coefficients of water droplets from the Mie theory. They detailed the radiative characteristics of single water droplet. Collin et al. [7] used the discrete ordinates method to investigate the radiant heat transfer in water sprays. Lechêne et al. [8] presented a numerical method to compare the downward and upward injection situations of water droplets. Forsth and Moller [9] studied the influence of additives on the interaction between radiation from fires and single water droplets. Based on the theoretical researches, the key attenuation controlling parameters have been identified including droplets diameter, size distribution, and concentration of droplets.

In addition, many experimental studies on radiation shielding of water spray have been made. The influence parameters of water curtains such as flow rate, nozzle type, pressure, width and height, and direction have been studied. Parent et al. [10] measured the spectral transmissivity between 1000 and 7000 cm^{-1} by Fourier transform spectrometer and identified mean attenuation levels by water vapor. Experimental studies on the porosity of spray were carried by Chow and Elaine [11] indicated only thermal radiation can be blocked and smoke can still spread through the water curtain. Cheung [12] investigated the parameters involved in mitigation properties of water curtain including shape, working pressures, flow rate as well as nozzles type. Some of the other achievements are available in literatures [13–15]. Overall, most of the researches are focused on the thermal radiation absorption and scattering by droplets. However, the interaction between macro-parameters of curtain and micro-parameters of droplets, that also affect the attenuation ability of thermal radiation. This spray dynamics research on thermal radiation screen is rarely reported in literatures [16]. For maximizing attenuation ability, this paper presents an experimental methodology to investigate the effect of spray dynamics on thermal radiation screen ability.

2 Introduction Experimental Setup

2.1 Experimental Platform

The experiments were carried out in a large-space building (Large-space Fire Testing Hall in State Key Laboratory of Fire Science of USTC) that can eliminate the environmental wind effects. The entire experimental system consisted of pool fire, water sprays curtain system and data acquisition system as shown in Fig. 1. A pool fire of 80 cm diameter was set up by burning alcohol as the heat source of radiation. Water spray nozzles were installed at the midpoint between pool fire and radiation heat flux meters to discharge sprays curtain. The direction of discharging was set downward and upward respectively that can change the relative position between nozzles and installation sites of radiation heat flux meters. The nozzles were set at the height of 200 cm when discharging downward and set ground when discharging upward.

Sprays curtain system was fed with water by the pump, and water pressure can be regulated by regulating valve from 1 to 5 bars as in Fig. 2. Once the nozzles type is fixed that water spray characteristics will change with feeding pressures, as well as the thermal radiation attenuation ability. These variations of attenuation were detected by comparing the measurements of radiation heat flux meters at two sides of curtain.

Main equipments of data acquisition system included a thermocouple tree and three radiation heat flux meters as shown in Fig. 1. The thermocouple tree was
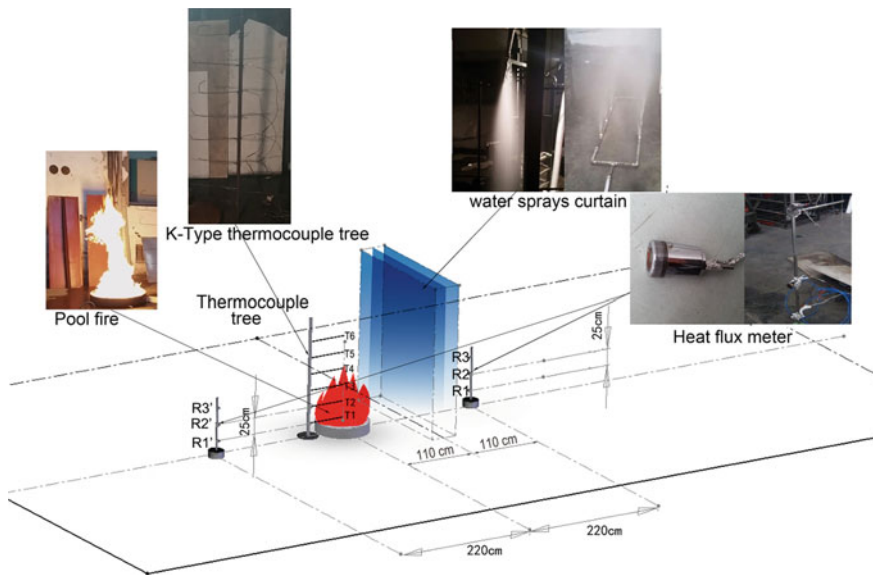
Fig. 1 Schematic view of the experimental setup
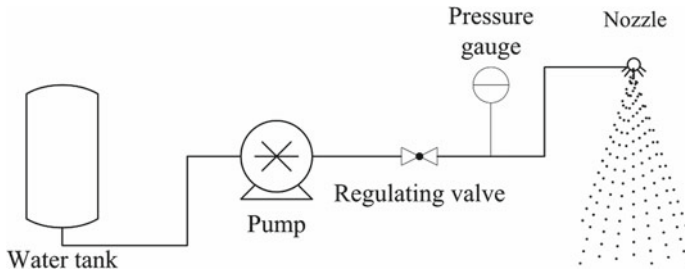
Fig. 2 Sprays curtain system

composed by six *K*-type thermocouples with separation distance 25 cm to measure flame temperature of pool fire, where $T1$–$T6$ represents the thermocouple at different heights. Three radiation heat flux meters ($R1$–$R3$) at the protected side were set with separation distance 25 cm to measure radiant heat flux attenuated by water curtain, and so as the distance of other three radiation heat flux meters ($R1'$–$R3'$) at fireside that to measure the unattenuated radiant heat flux. The sensor measuring range of radiation heat flux meter is ±25 kW/m^2, nominal resolution is 1.5 W/m^2, and the spectral response range is 1–50 μm.

2.2 Nozzle Spray Droplets Measurement

A type of flat-fan nozzle was selected in this spray curtain system. This nozzle is commonly used in building fire protection and industrial decontamination [17]. The variations of nozzle water flow rate with the pressure of feeding water are shown in Fig. 3. The injection angle of this nozzle is 95° and the equivalent aperture is 1.8 mm.

Fig. 3 Water flow rate versus water pressure
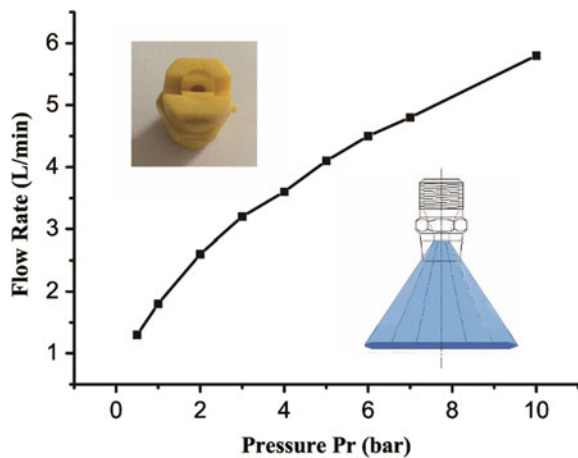
Fig. 4 Laser particle sizer

This nozzle can spray a liquid film with extremely thin edge and droplets in relatively homogeneous distribution. Laser particle sizer manufactured by Shanghai Oriental Magnetic Card Engineering Co., Ltd. as shown in Fig. 4 was used to measure spray dynamics characteristics of this nozzle such as mean diameter, median diameter, size distribution curve, and specific surface [18]. For the selected nozzle, mean droplet diameter and size distribution are different on the condition of varied feeding water pressures and different positions from nozzles.

2.3 Measurement Procedure

Flame temperature distribution of pool fire was measured by thermocouples that determined the height of flame. According to the flame height, the nozzles mounting position can be adjusted, and the installation height was 200 cm when discharging downward in this investigation. Firstly, fixing the water injection direction, then started the feeding water system, regulated the water pressure and lighted the pool fire. Radiant heat fluxes were measured by flux meters at both sides of fire lastly. This process was repeated when water pressure and injection direction changed.

3 Results and Discussion

3.1 Spray Dynamics Analysis

According to the measurements by Laser particle sizer, droplets diameters are varying with positions and pressures. Figure 5 presents variations of Sauter mean diameter (SMD) and mass median diameter (MMD). The absorptance and scattering coefficient of droplets are directly correlated with SMD. And MMD indicates the distribution of water droplets that also affect the attenuation ability of water sprays curtain

(a) Sauter mean diameter

(b) Mass median diameter
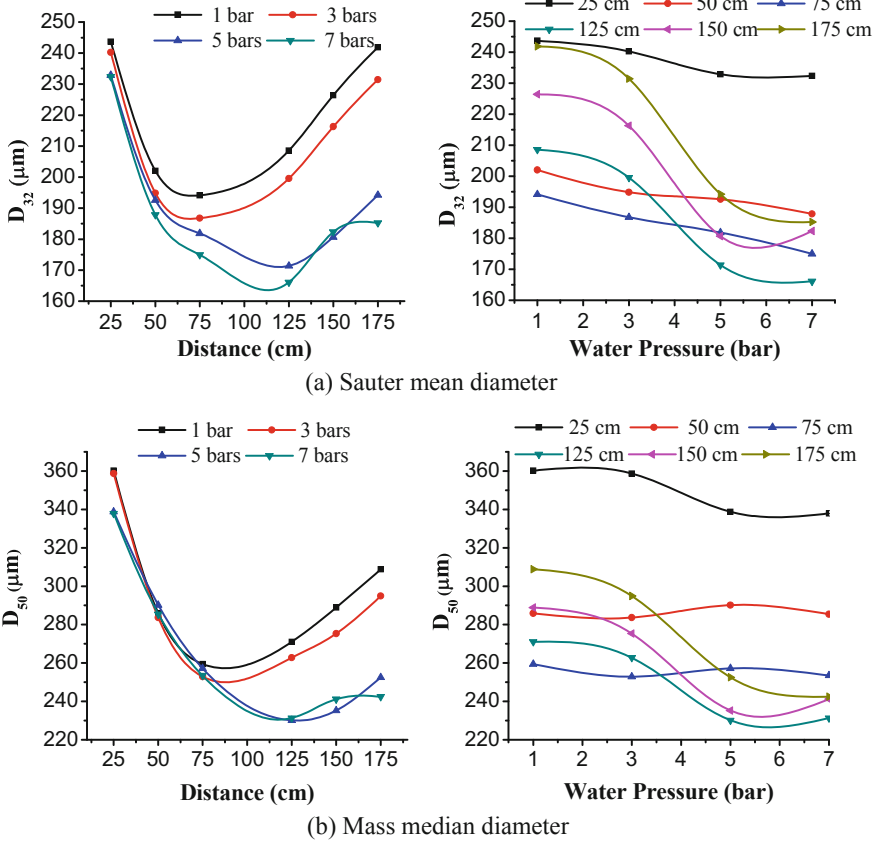
Fig. 5 Variation of water droplets diameter

[19]. It is observed that SMD of droplets first decreases and then increases with the increase of distances as well as MMD. The position of minimum mean diameter varied as water pressure increases, and the higher the pressure, the farther the position away from nozzles. In theory, the site of minimum SMD located should be the position of maximum attenuation. Previous theoretical studies have claimed that maximum attenuation efficiency is afforded by water droplets whose diameter is of the order of the maximum emission wavelength of the heat source, and the droplets of smaller diameter have the stronger attenuation ability in the same spray volume [2]. And previous experiments also indicated that the maximum emission wavelength of alcohol pool fire was between 3.7 and 4.9 μm [20]. The water droplets at the position of minimum SMD or MMD were expected to have the maximum attenuation ability.

3.2 Effect of the Pressure on the Attenuation

Figure 6 presents the flame temperature of pool fire at different heights and the heat flux without attenuation by water sprays curtain. As a result of plume entrainment, $T2$ is fluctuating with time. On the whole, the point at $T2$ height is of the maximum temperature that agrees well with the heat flux distribution, and where $R2$ and $T2$ are in the same height. Received heat fluxes of flux meter at varied heights are varying due to different view factors. As one of the main focuses of this paper, the radiant heat flux at $R3$ position attenuated by water curtain is used to analyze the influence of water pressure on attenuation ability. Figure 7 shows the radiation transmissivity through water curtain of stabilization stage at different water pressures and injection directions. The flow rate of nozzles is increased as water pressure increases, which also leads to finer droplets and greater number of particles per unit volume or concentration. All of these will result in higher attenuation efficiency. In addition, stability of water curtains is improved with pressure increase. The mean droplets diameter (dm) of the upwards direction is less than of the downwards direction at the same pressure as in Table 1, but the attenuation efficiency is more. This phenomenon mainly because the droplets residence time of upwards injection is more than downwards injection direction [21].

Table 1 Summary of characters of spray at the position of R3

Water pressure (bar)	Flow rate (L/min/nozzle)	dm (Upwards) (μm)	dm (Downwards) (μm)
1	1.8	194.13	208.57
2	3.2	186.79	199.58
3	4.1	181.78	1.35
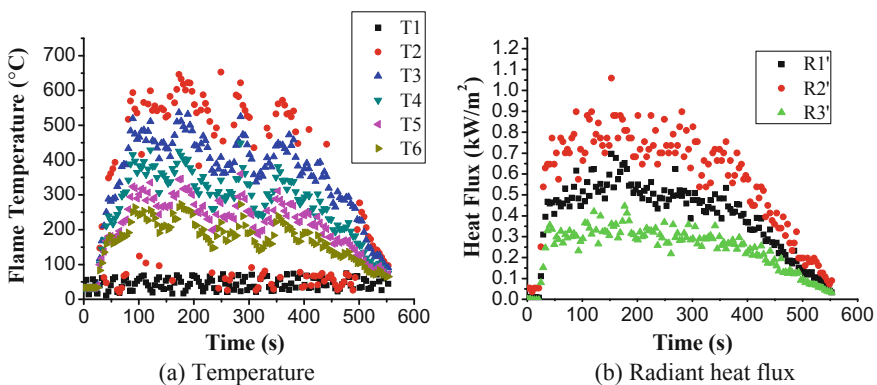
Fig. 6 Typical temperature and radiant heat flux range
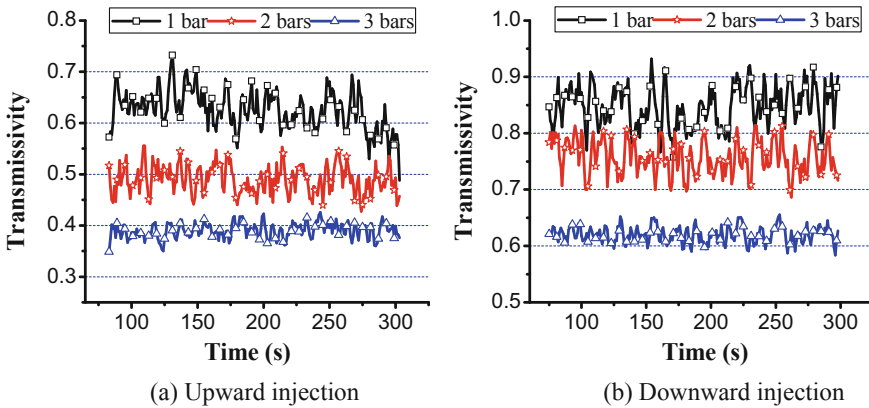
Fig. 7 Variation of transmissivity at the position of *R*3

3.3 *Effect of the Position on the Attenuation*

Though water droplets concentration and spray quality influenced by water pressure that affect the radiation attenuation, the position can also make a difference to it. The transmissivity of different positions at 3 bars is used to analyze the effect of position on attenuation. As illustrated in Fig. 8a, when injecting upwards, the water curtain attenuation ability at 25 and 50 cm is nearly identical, but the radiation blockage efficiency grows significantly. When distance increases from 50 to 75 cm, average transmissivity reduction rate is close to 10.8%. When injection direction is downwards, the whole attenuation ability of water curtain is less than upwards injection, as well as the blockage efficiency growth rate.

It is assumed here that whole attenuation efficiency difference between injection directions is due to the position changing from nozzles, ignoring the residence time alterations caused by injection directions. Changing the directions only alter the dis-
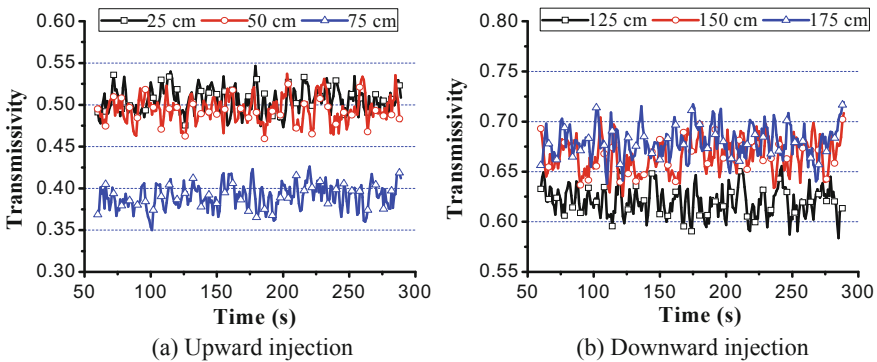
Fig. 8 Variation of transmissivity at the water pressure of 3 bars

tances of measurement points. The average transmissivity is calculated as shown in Fig. 9. On the whole, the average transmissivity decreases as the water pressure increases, and which first decreases to reach a minimum then increases with the distance when injection pressure fixed. Compared with Fig. 5, it is easy to see that average transmissivity has a similar variation trend with mean diameter of droplets. Figure 10 presents the droplets size distributions of different positions at pressure 3 bars. Liquid has not atomized completely near the boundary of liquid-sheet that the mean diameter is larger. The mean diameter diminishes as distance from the nozzle increases and liquid completely atomized. However, the velocity of droplets will decrease dramatically when the distance from nozzles continue to increases, and collision probability of droplets increases at the same time result to more large droplets,
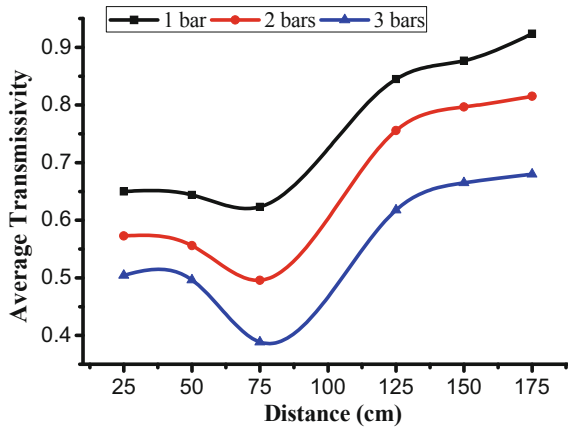
Fig. 9 Average transmissivity versus distance
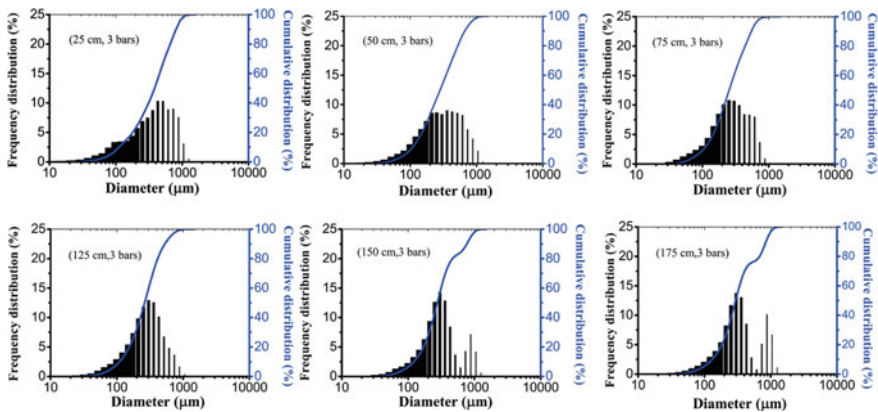
Fig. 10 Water droplets size distribution

which lead to the increase of mean diameter. The mean diameter and distribution of droplets could directly reflect the radiation attenuation ability.

The minimum mean diameter locates between the distance 60 and 90 cm from nozzles when pressure is less than 3 bars. But when pressure is more than 3 bars, the minimum mean diameter is probably on the position of 120 cm as in Fig. 5. With pressure increases, the position of minimum mean diameter will move to the direction of far away the nozzles. The site of minimum transmissivity is expected to move to the same direction as the minimum mean diameter.

4   Conclusions

In order to study the effect of spray dynamics on radiation blockage ability of water curtains, an experimental methodology was adopted. Droplets diameters and distributions at different water pressures and positions were measured by a laser sizer to reflect the characteristic of spray dynamic. Radiation heat flux meters were used to measure the radiant transmittance blocked by water spray curtains. Experimental measurements have clearly shown that sprays dynamic characteristic can strongly affect the attenuation ability of water curtains. The variation tendency of particle mean diameter can directly reflect the change trend of attenuation efficiency. Characteristics of droplets and relative positions of protected objects are two significant factors for affecting attenuation efficiency. These factors should be considered when water spray curtains are to be used in industrial and building fire protection. Furthermore, different nozzles with different characteristics, and which should be measured firstly when they are used to discharge water sprays.

References

1. Ravigururajan, T. E., & Beltrav, M. P. (1989). A model for attenuation of fire radiation through water droplets. *Fire Safety Journal, 15*(2), 171–181.
2. Coppalle, A., Nedelka, D., & Bauer, B. (1993). Fire protection: water curtains. *Fire Safety Journal, 20,* 241–255.
3. Dembélé, S., Delmas, A., & Sacadura, J. F. (1997). A method for modeling the mitigation of hazardous fire thermal radiation by water spray curtains. *Journal of Heat Transfer, 199*(4), 746–753.
4. Hostikka, S., & McGrattan, K. (2006). Numerical modeling of radiative heat transfer in water sprays. *Fire Safety Journal, 41,* 76–86.
5. Ng, Candy M. Y., & Chow, W. K. (2004). Review on the design and scientific aspects for drencher systems in different countries. *Architectural Science Review, 45,* 323–335.

6. Buchlin, J. M. (2003). Water sprays as mitigation means. Invited paper in international workshop on multiphase and complex flow simulation for industry: Physical, mathematical, numerical models and softwares for safety and design improvements. Cargése, Corsica.

7. Collin, A., Boulet, P., Lacroix, D., & Jeandel, A. (2005). On radiative transfer in water curtains using the discrete ordinates method. *Journal of Quantitative Spectroscopy & Radiative Transfer, 92,* 85–110.

8. Lechêne, S., Acem, Z., Parent, G., Jeandel, G., & Boulet, P. (2011). Upward versus downward injection of droplets for the optimization of a radiative shield. *International Journal of Heat and Mass Transfer, 54,* 1689–1697.

9. Forsth, M., & Moller, K. (2013). Enhanced absorption of fire induced heat radiation in liquid droplets. *Fire Safety Journal, 55,* 182–196.

10. Parent, G., Boulet, P., Gauthier, S., Blaise, J., & Collin, A. (2006). Experimental investigation of radiation transmission through a water spray. *Journal of Quantitative Spectroscopy & Radiative Transfer, 97,* 126–141.

11. Chow, W. K., & Elaine, Y. L. (2006). Experimental studies on thermal and smoke blockage by water curtains. In *9th AIAA/ASME Joint Thermophysics and Heat Transfer Conference*, June 5–8, San Francisco, California.

12. Cheung, W. Y. (2009). Radiation blockage of water curtains. *International Journal on Engineering Performance-Based Fire Codes, 1,* 7–13.

13. Viskanta, R., & Tseng, C. C. (2007). Spectral radiation characteristics of water sprays. *Combustion Theory and Modelling, 11,* 113–125.

14. Yang, W., Perry, T., Ladouceur, H. D., & Kee, R. J. (2004). The interaction of thermal radiation and water mist in fire suppression. *Fire Safety Journal, 39,* 41–66.

15. Consalvi, J. L., Porterie, B., & Loraud, J. C. (2003). On the use of gray assumption for modeling thermal radiation through water sprays. *Numerical Heat Transfer Part A, 44*(5), 505–519.

16. Collin, A., Boulet, P., Parent, G., Vetrano, M. R., & Bouchlin, J. M. (2008). Dynamics and thermal behaviour sprays. *International Journal of Thermal Science, 47,* 399–407.

17. Wikipedia. (2014). Spray nozzle. http://en.wikipedia.org/wiki/Spray_nozzle.

18. OMEC. (2014). DP-02 laser particle sizer. http://www.omec-instruments.com/uments.com/productShow.asp?ArtID=557.

19. Boulet, P., Collin, A., & Parent, G. (2006). Heat transfer through a water spray curtain under the effect of a strong radiative source. *Fire Safety Journal, 41*(1), 15–30.

20. Li, Q. Y., & Wang, Y. Y. (2008). Infrared radiation characteristic of flame and detecting wave band. In *CFPA Specialized Committee Electrical Fire Prevention Conference*, Xiamen, China (in Chinese).

21. Lechêne, S., Acem, Z., Parent, G., Jeandel, G., & Boulet, P. (2012). Radiative shielding by water mist: Comparisons between downward, upward and impacting injection of droplets. Eurotherm Conference No. 95: Computational Thermal Radiation in Participating Media IV. *IOP Publishing Journal of Physics: Conference Series, 369*(2012), 012027. https://doi.org/10.1088/1742-6596/369/1/012027.

Structural Behavior in Fire

Small-Scale Tests on Tensile Membrane Action of Reinforced Mortar Slabs at Elevated Temperature

Shiko Fukatsu, Zijing Liu, Toru Yoshida, Kenta Watanabe and Takeo Hirashima

Abstract In case of fire, reinforced concrete floor slabs are heated on the lower surface and are deflected due to the temperature gradient along the thickness direction and the reduction in strength at elevated temperature. In accordance with the deflection of the floor slab, the membrane stress developed and caused the enhancement of load-bearing capacity. This paper discussed, in the basis of the results of high-temperature loading tests of small-scale reinforced mortal slabs, the amount of deflection due to the temperature gradient and the influence of the bottom reinforcement temperature on the maximum strength, and the enhancement factor. The parameters include the support conditions and the steel temperature at the bottom reinforcement. The thermal deflection of the two-way slab due to the temperature gradient approximately agreed with the theoretical value of the one-way slab. The maximum load-bearing capacity in case of the bottom reinforcement temperature of 400 °C was equal to or larger than that at room temperature. The decrease in the maximum strength above 500 °C was lower for the two-way slabs than for the one-way slabs. The enhancement of the maximum strength due to tensile membrane action was confirmed from the test result without punching shear failure.

Keyword Reinforced mortar slabs · Tensile membrane action · Fire resistance · Thermal deflection · High-temperature loading test

Nomenclature

A_s	Cross-sectional area of the bottom reinforcement (mm^2)
d_1	Effective depth of the specimen (mm)
d	Depth of the specimen (mm)
l	Supporting span (mm)
$P_{y,1}$	Collapse load based on the yield line theory for the one-way slab (kN)

S. Fukatsu · Z. Liu · T. Yoshida · K. Watanabe · T. Hirashima (✉)
Division of Architecture and Urban Science, Graduate School of Engineering, Chiba University, 1-33, Yayoicho, Inage-ku, Chiba 263-8522, Japan
e-mail: hirashima@faculty.chiba-u.jp

$P_{y,2}$ Collapse load based on the yield line theory for the two-way slab (kN)
ΔT Difference of surface temperature between upper and lower of the slab (K)

Greek

α The linear coefficient of expansion (K^{-1})
δ The calculated value of thermal deflection at the midspan of the slab (mm)
σ_y Allowable stress for temporary loading of the reinforcement (N/mm^2)

1 Introduction

When a fire breaks out in a building, reinforced concrete floor slabs are heated on the lower surface and are strongly deflected due to the temperature gradient along the thickness direction and the reduction in strength and rigidity at elevated temperature. In the case of a two-way slab, which has restrained vertical displacement at the support part, membrane stress develops due to the deflection and enhances the maximum strength of the slab [1–4].

This phenomenon is called tensile membrane action. Many studies have investigated tensile membrane action for reinforced concrete floor slabs exposed to fire. Cardington tests [5] and other large-scale fire tests [6–8] have indicated the possibility that composite floor slabs could survive because of the effect of tensile membrane action. Small-scale concrete slab tests [9] have also been carried out to clarify the influence of the dimensions of the slab, the load level, the material, and the amount of reinforcement on the deflection behavior at elevated temperatures. However, more fundamental data on tensile membrane action are still needed. For example, it is difficult to estimate the thermal deflection of two-way concrete slabs at maximum strength because the deflection also depends on the load-induced thermal strain in the concrete. Thus, high-temperature loading tests of small-scale reinforced mortal slabs were carried out to obtain the following fundamental data on tensile membrane action.

(1) The amount of deflection due to the temperature gradient along the thickness direction of the mortar floor slab,
(2) The influence of the bottom reinforcement temperature on the maximum strength of the two-way slab,
(3) The enhancement factor of the maximum strength of the two-way slab.

In these loading tests, one-way and two-way specimens were heated under non-loading conditions and were then loaded at the target reinforcement temperature. Mortar was used for the matrix material of the slabs in order to retain homogeneity

in the thin slabs. In this paper, the tensile membrane action of reinforced mortar floor slabs is discussed on the basis of the test results.

2 Test Parameter and Specimen

Table 1 shows the parameters and specimen names for the high-temperature loading tests. The parameters include the support conditions and the steel temperature at the bottom reinforcement. The purpose of the tests was to clarify the influence of these parameters on the thermal deflection and the load–deflection behavior of reinforced mortar slabs at elevated temperatures.

Figure 1a–c shows the specimens and the bar arrangements. For the one-way slap, the length and width were 1600 and 1300 mm, and for the two-way slab 1600 and 1600 mm, respectively. The slab thickness was 60 mm. Top and bottom reinforcements were installed on the specimens. Welded wire meshes (WFP-D in accordance with JIS G-3551) were used for the reinforcements. The bottom reinforcement was

Table 1 Test parameters and specimen names

Support condition	Thickness [mm]	Temperature [°C]			
		Ambient	400	500	600
One-way	60	1-t60-RT	1-t60-400	1-t60-500	1-t60-600
Two-way	60	2-t60-RT	2-t60-400	2-t60-500	2-t60-600

(a) One-way slab   (b) Two-way slab

Temperature measurement point: ● :Bottom reinforcement × :Heating surface ○:non-heating surface

(c) Section of two-way slab
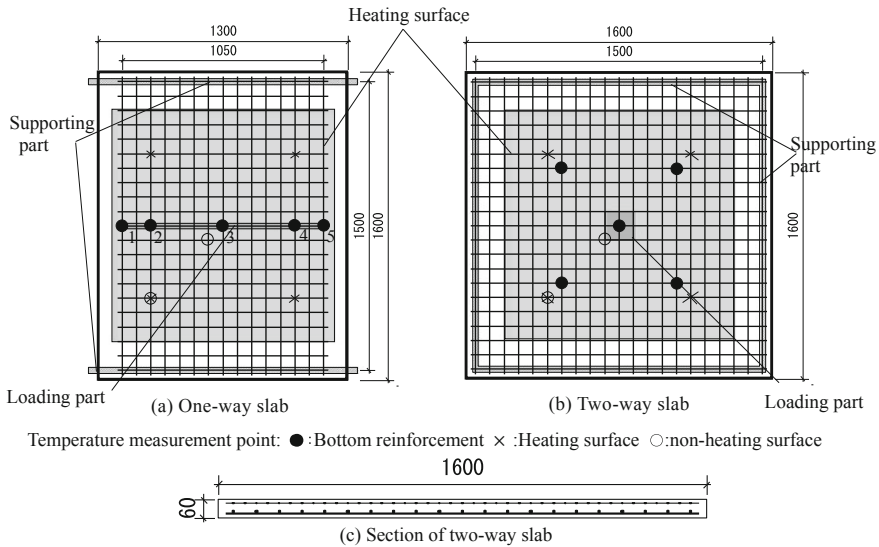
Fig. 1 Specimen

a 75 mm × 75 mm mesh with a wire diameter of 6.0 mm, and the top reinforcement was a 50 mm × 50 mm mesh with a wire diameter of 2.6 mm. The thicknesses of the cover mortar of the bottom and top reinforcements were about 9 and 15 mm, respectively. The tensile strength of the welded wire mesh of nominal diameter 6.0 mm was 581–602 N/mm^2 and 2.6 mm was 627–676 N/mm^2 based on the certified test report. The allowable stress for temporary loading of the welded wire mesh was 295 N/mm^2 and the tensile strength is over 490 N/mm^2 [10]. Table 2 shows the materials used, and Table 3 shows the mix proportions of the mortar. The compressive strength of the mortar obtained by a standard test was 36.1 MPa in 28 days, 42.3 MPa in 77 days (before slab tests), and 48.4 MPa in 135 days (after slab tests). The collapse load $P_{y,1}$ of the one-way slab is given by Eq. (1) with the allowable stress for temporary loading of the welded wire mesh ($\sigma_y = 295$ N/mm^2). The collapse load $P_{y,2}$ of the two-way slab based on yield line theory is given by Eq. (2), which assumes that the concentrated load was applied at the center of the two-way slab.

$$P_{y,1} = \frac{4 \times 0.9 \times d_1 \times A_s \times \sigma_y}{l} \tag{1}$$

$$P_{y,2} = \frac{8 \times 0.9 \times d_1 \times A_s \times \sigma_y}{l} \tag{2}$$

The collapse loads obtained using these equations are shown in Table 4. The values of P_u in Table 4 are the collapse load when substituting the nominal tensile strength of 490 N/mm^2 for σ_y in Eqs. (1) and (2). In addition, the load levels in regard to P_y from the influence of the weight of the slabs were 9.7% (one-way slab), 2.9% (two-way slab). These are the values in the case that the unit weight of mortar was 24 kN/m^3.

With the existing equipment [11], the strain on the mortar under increasing temperature and a constant load was measured. Figure 2 shows the strain–temperature relations for the mortar. In a nonloading test, the thermal expansion strain increased almost linearly from room temperature to 700 °C and the linear coefficient of expansion α was about 10^{-5} (k^{-1}). Figure 3 shows the strength–temperature relations

Table 2 Used materials of the mortar

Cement	Ordinary Portland cement, Density: 3.16 g/cm^3
Fine aggregate	Origin: Kisarazu-shi, Chiba Pref., Land sand Density in saturated surface-dry condition: 2.59 g/cm^3 Water absorption: 2.50%, Maximum size: 5 mm, Percentage of absolute volume: 2.55%

Table 3 Mix proportion of the mortar

Cement (kg/m^3)	Water (kg/m^3)	Fine aggregate (kg/m^3)	Water–cement ratio (%)
607	285	1303	47.0

Table 4 Calculated collapse load of the specimens

Support condition	Width [mm]	Thickness [mm]	Effective depth d_1 [mm]	Cross-sectional area A_s [mm^2]	Collapse load by the allowable stress P_y [kN]	Collapse load by the nominal tensile strength P_u [kN]
One-way	1300	60	48	423.9	14.41	23.93
Two-way	1600	60	45	593.5	37.82	62.81

Fig. 2 Results of the transient temperature tests
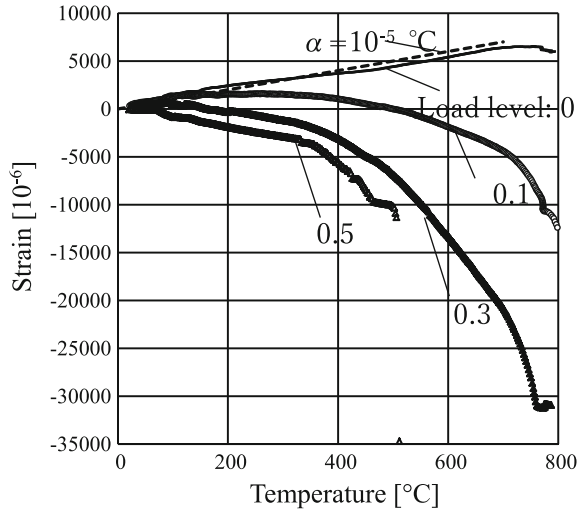
Fig. 3 Compression strength of the mortar at elevated temperature
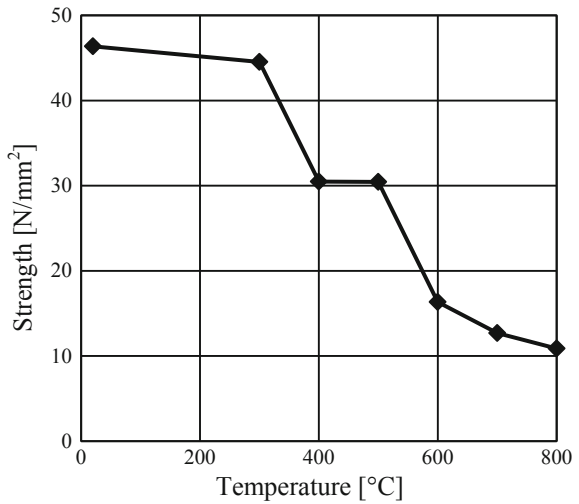
for the compressive strength test at elevated temperatures. The strength decreased slightly up to 300 °C, and then drastically from 300 to 600 °C. In high-temperature loading tests on the slabs, the nonheated surface temperature did not exceed 300 °C in any test, and thus, the decrease in strength on this side of the slabs is expected to be small.

3 Test Setup

Figure 4 shows the equipment used for the high-temperature loading tests on the reinforced mortar slabs. Vertical displacement at the supporting part of the specimen was restrained. The supporting frame and the restraining frame are shown in Fig. 4.
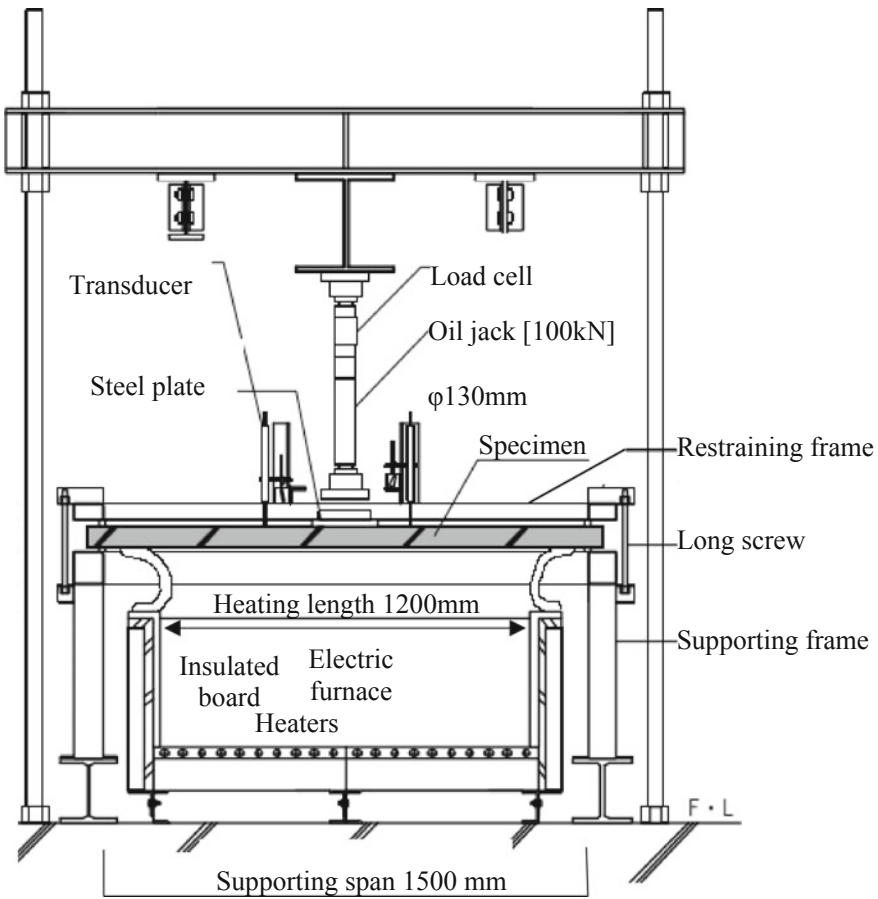
Fig. 4 Equipment of the elevated temperature loading test

The restraining frame was used in order to prevent rising at the corner of the slabs due to loading or heating. The restraining frame was connected to the supporting frame by long screws. The bolts of the connecting screw stick were not tightened hard. The supporting part where the specimen touched the restraining frame and the supporting frame was clamped by steel bars with a diameter of 19 mm, and horizontal displacement of the specimen was not restrained. A pin or roller boundary condition was applied for both ends of the one-way slab. Meanwhile, the boundary at the four corners of the two-way slab did not rotate because the vertical displacement for upper direction was restrained.

The center of the slab was loaded using an oil jack. In the case of the two-way slab, a steel plate (165 mm × 165 mm × 30 mm) was installed between the specimen and the jack. In the case of the one-way slab tests, a cylindrical bar (length: 1000 mm, diameter: 40 mm) was set between the specimen and the jack. While the specimen was heated to the target reinforcement temperature, the specimen was kept at a slight load of 0.3 kN so that the loading position did not move. When the temperature was within 20 °C of the target temperature, the specimen was loaded. The loading rates were 4 kN/min. The heating and loading were stopped when the load-bearing capacity of the entire specimen decreased to 90% of the maximum strength or when the vertical displacement at the center of the slab reached 150 mm.

The specimen was heated using an electric furnace (width: 1200 mm, depth: 1200 mm, height: 550 mm) under the supporting frame. The furnace was composed of four heaters (width: 600 mm, depth: 600 mm, height: 550 mm). The temperature of the specimen was controlled by the heaters in order to reach and maintain the target temperature. To prevent a gap opening due to deflection of the specimen, a ceramic fiber blanket of 1250 mm × 300 mm was set up between the specimen and the electric furnace wall. Figure 1a, b shows the temperature measurement points. The bottom reinforcement temperature was measured at five points. The gas temperature in the furnace and the mortar temperatures at the upper surface and the bottom surface were also measured.

Figure 5 shows the temperature–time relations of 2-t60-600. The bottom reinforcement temperatures shown in Fig. 5 are the average temperatures at four points

Fig. 5 Temperature–time relationships
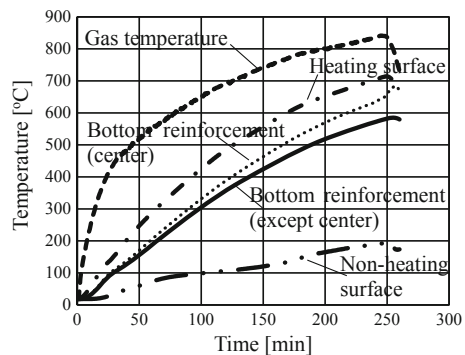
at the center of the four heaters as shown in Fig. 1b. Surface temperatures on the mortar were also mean temperature.

4 Test Results and Discussions

4.1 Thermal Deflection

Figure 6 shows the relations between the reinforcement temperature and the deflection at the midspan of the one-way slabs. The reason why the deflection increased rapidly near 400, 500, and 600 °C is that loading was started at these temperatures. The deflection before loading was thermal deflection due to the temperature gradient through the thickness of the slab. The bottom reinforced temperature was the average temperature at three points around the center (measuring point Nos. 2–4), as shown in Fig. 1a. While the bottom reinforcement temperature was 50–150 °C, the thermal deflection did not increase because the temperature gradient did not increase at around 100 °C due to evaporation of the water content in the mortar. In fact, the difference in surface temperature between the upper and bottom reinforcements did not increase at that time.

Figure 6 shows a comparison of the experimental thermal deflection and the calculated value δ given by Eq. (3).

$$\delta = \frac{\alpha \times \Delta T \times l^2}{8d_1} \tag{3}$$

The linear coefficient of expansion α was determined by the nonloading transient temperature test of the mortar material. The difference in surface temperature ΔT between the upper and lower surface of the slab was determined from the result of the slab tests. The experimental and calculated values were in approximate agree-

Fig. 6 Deflection–temperature relations of the one-way slab
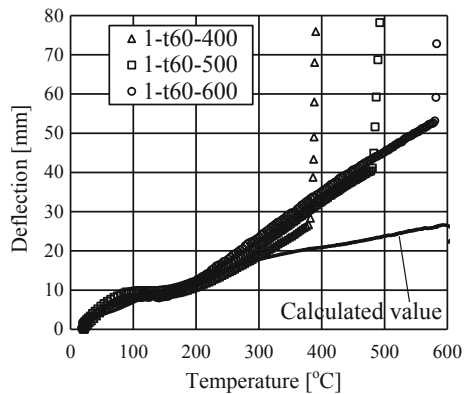
Fig. 7 Deflection–temperature relations of the two-way
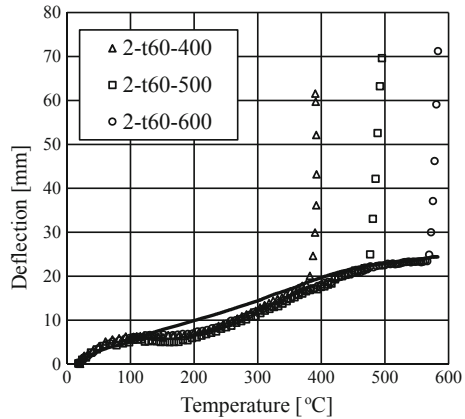
ment up to 250 °C for the slab. Above these temperatures, the calculated thermal deflection was lower than the experimental value. The influence of the weight was not considered in the calculation, although the load level by the weight was about 10% of P_y, as described in Sect. 2. On the other hand, a large contraction strain (i.e., load-induced thermal strain) developed above 200 °C in transient tests of the mortar under 10% of the stress level. The deflection might be influenced by the load-induced thermal strain above 200 °C.

Figure 7 shows the deflection–temperature relations for the two-way slabs. The deflection was vertical displacement of the two-way slab. The reason that the deflection increased rapidly near 400, 500, and 600 °C was the same as that for the one-way slabs. The thermal deflection was lower for the two-way slab than for the one-way slab because the vertical restraint at the supports of the two-way slabs restrained rotation at the supports and reduced the deflection. In the case of the two-way slabs, compression stress at the upper side developed due to the thermal deflection and the weight, and load-induced thermal strain of the mortar also developed. If the influences of the weight and the load-induced thermal strain are ignored, the thermal deflection should be lower than the calculated value. However, the calculated value from Eq. (3) for the thermal deflection of the one-way slabs approximately agreed with the experimental values of the two-way slab tests.

4.2 Load–Deflection Behavior

Figure 8 shows the load–deflection relations for the one-way slabs. The deflection at nonloading was the thermal deflection that occurred before loading. The maximum strength at room temperature considerably exceeded P_y, as shown in Table 4. The yield strength of the welded wire meshes was considerably larger than the allowable stress. The maximum strength at room temperature and at the reinforcement temperature of 400 °C was similar. The yield strength of the mesh at room temperature and

Fig. 8 Load–deflection relations of the one-way slab
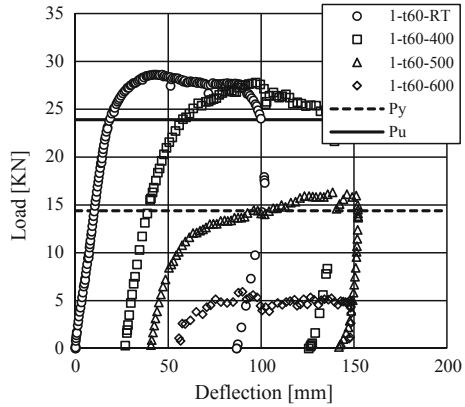
400 °C was also the similar. The strength at 500 °C for the slab was about 55% of that at room temperature. The strength reduction rate at 600 °C was 20% in 1-t60-600. Photo 1a shows the features of the failure of the one-way slabs after the tests. A large crack occurred along the loading part at the midspan of the one-way slab. The failure mode was bending failure due to yielding of the bottom reinforcement at the midspan. Large rotational displacement developed at the supporting parts, as shown in Photo 1b. Meanwhile, the maximum strength at room temperature and 400 °C exceeded the calculated value P_u.

Figure 9 shows load–deflection relations for the two-way slabs. The maximum strength of 2-t60-RT was similar to the Pu. As shown in Photo 2a, in case of 2-t60-RT, concentric large circle cracks on the top surface were not confirmed, and cracks on the diagonal were occurred in the bottom surface. The maximum strength of 2-t60-400 slightly exceeded Pu and this result was similar to the result of the one-way slabs. As shown in Photo 2b, in case of 2-t60-400, punching shear occurred on the center of the slab before enough tensile membrane action appeared. The

Fig. 9 Load–deflection relations of the two-way slab
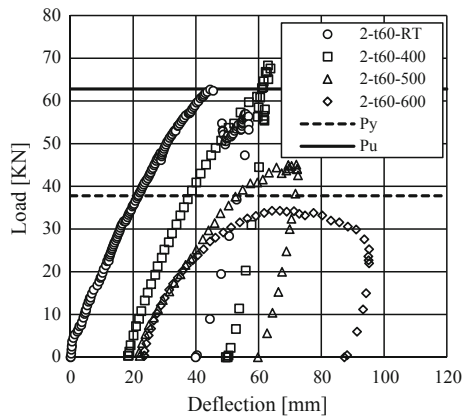
(a) 1-t60-600

(b) 1-t60-400
Rotational displacement at the
supporting part

Photo 1   Global aspect of the one-way slab after the test

maximum strength of 2-t60-500 was 70% of room temperature's maximum strength. The maximum strength of 2-t60-600 was 50% of room temperature's maximum strength. The collapse expression of 2-t60-400 and 2-t60-500 was similar to 2-t60-RT, but as shown in Photo 2d, the concentric circle large cracks were conspicuous on the top surface. In future two-way slab tests, the equipment of the loading part will be improved to be expanded.

4.3   Enhancement Factor of the Maximum Strength

The enhancement factor for the maximum strength was obtained by comparing the experimental results between the one-way slabs and the two-way slabs and by yield line theory. The ratio of the strength based on yield line theory given by Eqs. (1) and (2) was 2.63. In this report, the enhancement factor was defined as the ratio of the maximum strength of the two-way slab divided by the above theoretical ratio (2.63). Table 5 shows the ratio obtained from the test results, the enhancement factor, and the deflection ratio at the maximum loading divided by the effective depth d_1. Bailey indicated that the enhancement factor depends on the deflection and is almost proportional to the deflection ratio at the maximum strength against the effective depth [2]. On the other hand, the enhancement factors were around 1.0 except for the specimens at the reinforcement temperature 600 °C. When the temperature reached 600 °C, the strength of one-way slab was approximately decreased to 80% of maximum strength, and the strength of two-way slab was half of maximum strength at ambient temperature. The strength decrease for the two-way slab was lower than the one-way slab, the enhancement of 2-t60-600 was 2.2, and it was confirmed that this phenomenon
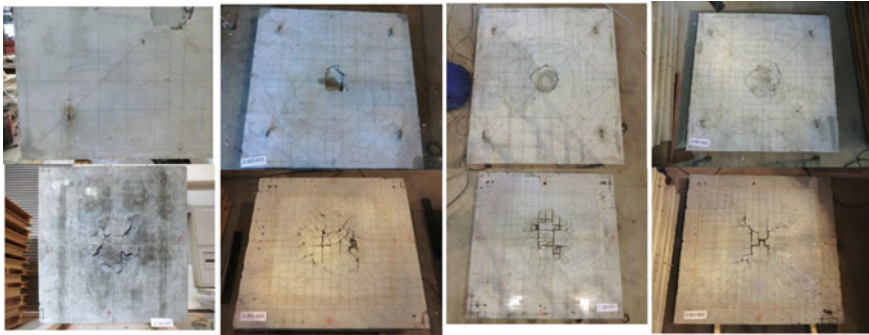
(a) 2-t60-RT   (b) 2-t60-400   (c) 2-t60-500   (d) 2-t60-600

Photo 2 Global aspect of the two-way slab after the test

Table 5 The enhancement factor of the strength

Thickness [mm]	Temperature [°C]	Strength of one-way slab [kN]	Strength of two-way slab [kN]	Ratio of strength by yield line theory	Ratio of strength by the test	Enhancement factor	Deflection /effective depth
60	Ambient	28.6	62.7	2.63	2.22	0.83	0.99
	400	27.8	68.3	2.63	2.5	0.94	1.40
	500	16.3	45.1	2.63	2.8	1.05	1.60
	600	5.9	34.3	2.63	5.8	2.20	1.43

caused by membrane action. The two-way slabs except for 2-t60-600 did not show enough tensile membrane action because punching shear failure occurred before the specimens were deflected enough.

5   Conclusions

The results of the high-temperature loading tests on reinforced mortar slabs were as follows:

(1)   The calculated value from Eq. (3) for the thermal deflection of the one-way slab approximately agreed with the experimental values of the two-way slab tests.
(2)   The reinforcement mortar slab was retained the maximum strength before temperature reaches 400 °C, and the maximum strength was decreased when temperature above 400 °C. The strength decrease of two-way slab was lower than the one-way slab.

(3) In the case of the specimen at reinforcement temperature 600 °C, the enhancement factor of the maximum strength was 2.2. The influence of the membrane action on the strength was found.

In the future, transient temperature tests under constant loads will be carried out with the same type of slabs and the equipment of the loading part will be improved to prevent punching shear failure of the two-way slabs.

References

1. Huang, Z., Burgess, I., & Plank, R. (2001). The influence of tensile membrane action in concrete slabs on the behaviour of composite steel-framed buildings in fire. *Journal of Structural Engineering, ASCE, 126,* 1–14. https://doi.org/10.1061/40558(2001)86.
2. Bailey, C. G., & Moore, D. B. (2006). The structural behaviour of steel frames with composite floorslabs subject to fire: Part 1: Theory. *The Structural Engineer, 78*(11), 19–27.
3. Bailey, C. G. (2001). Membrane action of unrestrained lightly reinforced concrete slabs at large displacements. *Engineering Structures, 23,* 470–483. https://doi.org/10.1016/S0141-0296(00)00064-X.
4. Franssen, J. (2012). Tensile membrane action in composite floors subjected to fire. In *Advances in steel concrete composite and hybrid structures* (pp. 125–154). ISBN: 978-981-07-2613-3. https://doi.org/10.3850/978/-981-07-2613-3_p008.
5. British Steel plc, Swinden Technology Centre, A European Joint Research Programme: The behaviour of multi-storey steel framed buildings in fire, 1999.
6. Zhao, B., Roosefid, M., & Vassart, O. (2008). Full scale test of a steel and concrete composite floor exposed to ISO fire. In *Proceedings of the 5th International Conference on Structures in Fire* (pp. 539–550).
7. Zhang, N. S., Li, G. Q., Lou, G. B., Jiang, S. C., & Hao, K. C. (2009). Experimental study on full scale composite floor slabs under fire condition. In *Proceedings of the Application of Structural Fire Engineering* (pp. 502–511).
8. Stadler, M., & Mensinger, M. (2011). Munich fire tests on membrane action. In *Presentation made at Steel In Fire Forum*. UK: STIFF.
9. Bailey, C. G., & Toh, W. S. (2007). Small-scale concreate slab tests at ambient and elevated temperatures. *Engineering Structures, 29,* 2775–2791. https://doi.org/10.1016/j.engstruct.2007.01.023.
10. Architectural Institute of Japan. (2013). Design recommendations for composite constructions (in Japanese).
11. Tokoyoda, M., Yamashita, H., Toyoda, K., Hirashima, T., & Uesugi, H. (2007). An experimental study of transient strain for a concrete with limestone aggregate. In *Proceedings of the International workshop on Fire Design of Concrete Structures—From Materials Modelling to Structural Performance, fib* (pp. 105–114).

Investigation of Fire Damage in Concrete by Post-peak Control Technique Associated with Acoustic Emission

Li-Hsien Chen, Wei-Chih Chen, Yao-Chung Chen, Chio-Fang Cai, Ming-Yuan Lei and Tien-Chih Wang

Abstract This paper presents a new test method to investigate the influence of fire damage on stiffness, strength, toughness in macro-view and localization of micro-crack in micro-view of concrete by conducting uniaxial compressive test associated with acoustic emission (AE) after specimen subjected to heating with different thermos-conditions such as the rate of heating, maximum temperature, exposure time, as well as cooling condition. During the testing, the extensometer was used as feedback signal control to stabilize crack growth; the complete loading curve including pre- and post-peak stage was then obtained. Therefore, the evolution of AE micro-seismic sources with respect to loading process was also examined. The test results in macro-view show that the stiffness, strength, and toughness decrease with an increase in maximum temperature; the post-peak behavior from snapback (Class II) converts to snap through (Class I) at maximum temperature ranged 200–400 °C, whereas, in micro-view, the AE localization occurred earlier as the maximum temperature increased. When the maximum temperature reached 600 °C, the AE localization cannot be found during the uniaxial compressive test.

Keywords Fire damage · Concrete · Uniaxial compressive test · Acoustic emission

Nomenclature

E_{time} Exposure time (min)
M_{heat} Heating rate (°C/min)

L.-H. Chen
National Taipei University of Technology, 1, Sec. 3, Zhongxiao E. Rd., Taipei City 10608, Taiwan

W.-C. Chen (✉) · Y.-C. Chen
National Taiwan University of Science and Technology, No. 43, Keelung Rd., Sec. 4, Da'an District, Taipei City 10607, Taiwan
e-mail: wezi415@yahoo.com.tw

C.-F. Cai · M.-Y. Lei · T.-C. Wang
Architecture and Building Research Institute, 13F., No. 200, Sec. 3, Beisin Rd., Sindian District, New Taipei City 23143, Taiwan

495

LL   Load level (%)
LL,L   Load level of AE localization (%)
T_{max} Maximum temperature (°C)

1 Introduction

In Taiwan currently, the reinforced concrete (RC) structure is the main system for buildings and constructions, and the quality/quantity evaluation of fire-induced damage in RC structure is important for living safety. Some methods such as color changing identifying of concrete, take core experiment, ultrasonic pulse (UP) measurement and the correlation of concrete strength reducing with temperature were proposed to evaluate the fire-damage degree [1]. However, these methods were not used widely due to its low accuracy [2]. In this study, a uniaxial compressive test coupled with acoustic emission was developed and used to examine the fire-damage characteristics of concrete after heat treatment with different thermal conditions. Furthermore, the extensometer was applied in uniaxial compressive test and used as the feedback signal control to stabilize fracture propagation. The entire loading process was then obtained.

2 Acoustic Emission

The AE phenomenon is defined as transient elastic waves produced by the rapid released energy from localized sources within a material [3]. The rapid released energy generated from micro-cracks formation inside the brittle material which is subjected to outside force (pressure). Kaiser [4] found that when materials are reloaded, the AE signals only growth if the reloading stress is more than the maximum. This so-called Kaiser effect has also been investigated in rocks [5]. The AE signals record the micro-seismic sources and are used as non-destructive measurement technique to examine the micro-crack growth/extension in a material. The AE technique has been widely used to investigate the location of micro-cracks for cement mortar and concrete material [6–8].

3 Fire-Damage Experiment

3.1 Fire-Damage Specimen Preparation

The 50 mm × 45 mm × 120 mm cube concrete specimen with 70 MPa strength produced by Ya Tung Ready Mixed Concrete Corporation was used as the test material
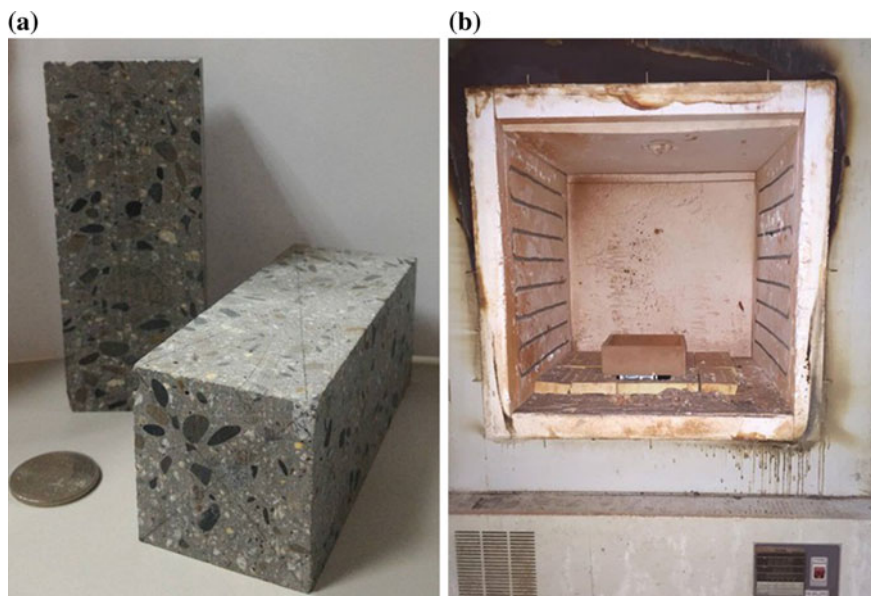
Fig. 1 Fire-damage concrete specimen preparation: **a** concrete specimen, **b** high-temperature oven

as shown in Fig. 1 a. The fire-damage condition with heating rate $M_{heat} = 5$ °C/min, exposure time $E_{time} = 300$ min and maximum temperature $T_{max} = 25, 200, 300, 400, 500, 600, 800$ and 1000 °C was simulate using high-temperature oven as shown in Fig. 1 b. The cube specimens were placed in oven with 105 ± 5 °C and stayed in 24 h to lead void water dissipation. After heat treatment, the specimen was stored by vacuum packaging when the fire-damaged specimen cooling down.

3.2 Uniaxial Compressive Test

After fire-damage treatment, uniaxial compressive test was conducted. In this study, the servo-hydraulic loading system MTS 810, which is multipurpose, accurate and has a high stiffness, was employed as the load system. An axial extensometer (model 632.12F-20, MTS Corp., Eden Prairie, MN, USA) installed with roller chain as shown in Fig. 2 was used to record the circumferential deformation as a feedback signal to automatically control the load output. The crack propagation can thus be stabilized.
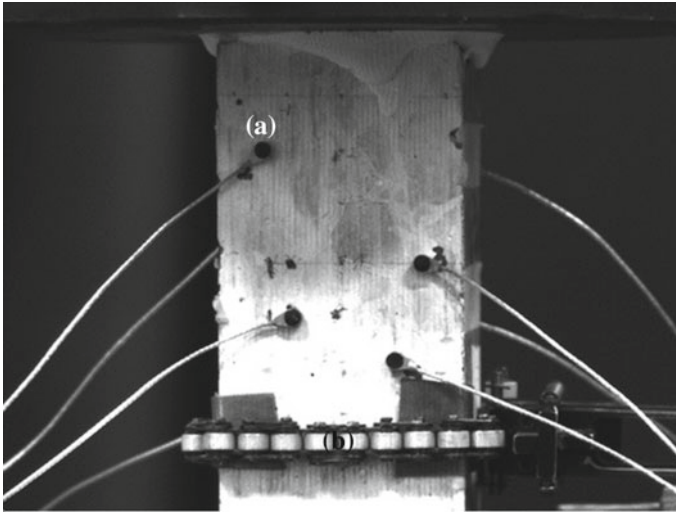
Fig. 2 Uniaxial compressive test coupled with AE for concrete: **a** AE sensor, **b** extensometer

3.3 AE System

The AE signals were captured by using eight piezoelectric transducers (AE sensor) attached to the specimen surface (Fig. 2) and amplified with a gain set to 40 dB before recording. The 8 MHz sampling rate and 7 mv threshold with a sonic rate between 100 and 1200 kHz was used, respectively, to construct a data acquisition system of AE. The signals higher than threshold were recorded in a binary file and used to identify the characteristics of the wave shapes. The arrival time of the P-wave signal at each AE sensor can then be determined.

4 Results and Discussion

4.1 Relation of Loading Behavior and Fire Temperature in Macro-view

The entire loading curve with respect to different maximum temperatures is shown in Fig. 3. Figure 3 shows that the stiffness, strength, and toughness in general decreased with an increase in maximum temperature. However, the stiffness, strength, and pre-peak toughness was not reduced significantly when maximum temperature reached to 200 °C as shown in Fig. 4 a. Until maximum temperature reached to 600 °C, the stiffness, strength, and pre-peak toughness reduced more significantly. In addition, the post-peak toughness increased at $T_{max} = 200 - 500$ °C as shown in Fig. 4 b.
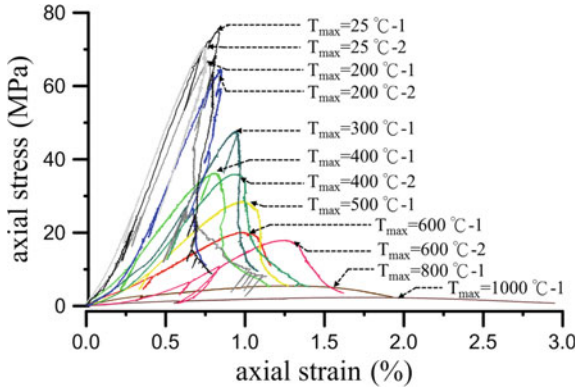
Fig. 3 Completed uniaxial compressive curves of concrete subjected to various temperatures
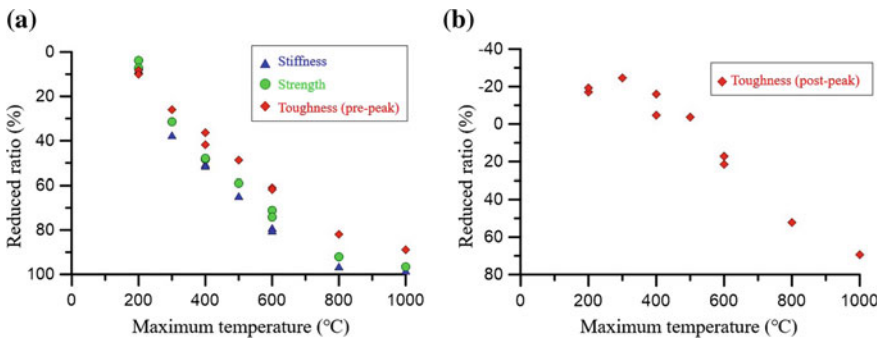
Fig. 4 Effect of fire temperature on stiffness, strength, toughness at pre-peak and toughness at post-peak

This is because that the post-peak behavior from snapback (Class II) converted to snap through (Class I) at maximum temperature ranged 200–400 °C was observed.

4.2 Relation of AE Evolution and Fire Temperature in Micro-view

An AE event represents a microseismic crack occurrence, and the crack evolution is correlated to the loading process. In this study, an entire loading process was obtained; therefore, the whole evolution of the AE activities included occurrence, pause, reoccurrence, localization, and growth could be investigated. Figure 5 illustrates the relation between the loading process and the AE events of concrete subjected to fire damage with $T_{max} = 25$ °C. In Fig. 5, the solid and dotted curves present the macro-view (loading history) and micro-view (AE reactions) behaviors, respectively.

Fig. 5 Identification of
localization by AE
accumulated curve with
respect to loading history
($T_{max} = 25\ °C - 1$)
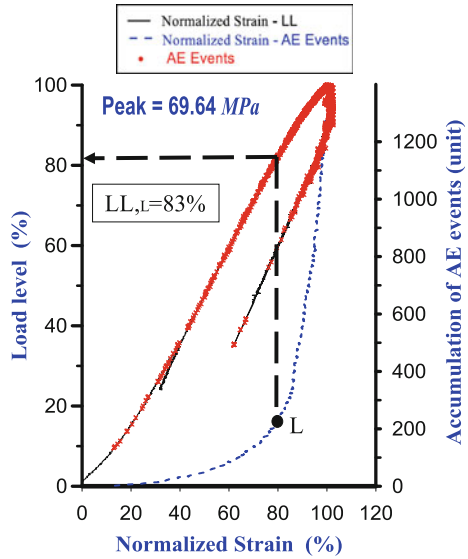
Both curves have the same *x*-coordinate, which indicates normalized strain (defined as strain divided by strain at peak loading stress). The solid curve is the loading curve corresponding to the load level, LL (defined as loading stress divided by peak loading stress) on the left *y*-coordinate. Every point on the solid curve represents the occurrence of an AE event. The dotted line represents the correlation between the accumulated number of AE events and the normalized shear displacement.

In Fig. 5, the accumulated number of AE events increased with the increasing normalized strain. According to the study of Chen [9], localization was defined as the phenomenon of AE events rapidly increasing, as at point L of Fig. 5. The position in which these events occur is correlated to the initial formation and propagation of the macroscopic cracks. Point L in Fig. 5 is the maximum curvature on the curve of the accumulated number of AE events; it shows the localization where LL is approximately 83%. Following the same method, the localization of the concrete subjected to fire damage with different maximum temperature conditions ($T_{max} = 25, 200, 300, 400, 500, 600, 800$ and $1000\ °C$) under uniaxial compressive tests can be found as shown in Table 1. As the maximum temperature increases, the localization of AE occurred earlier (LL_L decrease). However, when maximum temperature reached to $600\ °C$, the AE localization cannot be found. This finding suggested that the AE localization may have occurred before the uniaxial compressive test conducted when the fire temperature is higher than $600\ °C$.

Table 1 Summary LL$_{,L}$ of concrete subjected to fire damage with different maximum temperature conditions under uniaxial compressive tests

Maximum temperature T_{max} (°C)	Test no.	Load level at localization LL$_{,L}$ (%)
25	1	83
	2	–
200	1	80
	2	82
300	1	–
400	1	74
	2	–
500	1	62
600	1	Occurred at heating stage
	2	
800	1	
1000	1	

5 Conclusions

In this study, a uniaxial compressive test in conjunction with the nondestructive AE technique was developed to investigate the fire-damage characteristics of concert. A COD control technique was employed during testing to prevent unstable crack growth; a complete loading process and corresponding AE evolution therefore were obtained. The experimental results can be summarized as follows.

The stiffness, strength, and pre-peak toughness decrease with an increase in maximum temperature. At maximum temperature ranged 200–500 °C, the post-peak toughness increased with an increase in maximum temperature. Furthermore, the micro-crack localization occurred earlier as maximum temperature increased. The AE localization may have occurred before the uniaxial compressive test conducted when the fire temperature is higher than 600 °C.

References

1. Tovey, A. K. (1986). Assessment and repair of fire-damaged concrete structures-an update. *ACI Special Publication, 92,* 47.
2. Luo, B. Y. (2008). *Fire-resistance property of reinforced lightweight aggregate concrete wall.* Master Thesis, National Chung Hsing University, Taiwan.
3. ASTM. (1999). *Standard definitions of terms relating to acoustic emission.* American Society for Testing and Materials.

4. Kaiser, J. (1953). *Undersuchungen Uber Das Aufrterten Geraucchen Beim Zevgersuch*. Ph.D Thesis, Technische Hochschule, Munich.
5. Holcomb, D., & Costin, L. (1986). Detecting damage surfaces in brittle materials using acoustic emissions. *Journal of Applied Mechanics, 53,* 536.
6. Carpinteri, A., Lacidogna, G., Niccolini, G., & Puzzi, S. (2007). Critical defect size distributions in concrete structures detected by the acoustic emission technique. *Meccanica, 43,* 349.
7. Chen, L. H., Chen, W. C., Chen, Y. C., Benyamin, L., & Li, A. J. (2015). Investigation of hydraulic fracture propagation using a post-peak control system coupled with acoustic emission. *Rock Mechanics and Rock Engineering, 48,* 1233.
8. ElBatanouny, M. K., Larosche, A., Mazzoleni, P., Ziehl, P. H., Matta, F., & Zappa, E. (2012). Identification of cracking mechanisms in scaled FRP reinforced concrete beams using acoustic emission. *Experimental Mechanics, 54,* 69.
9. Chen, L. H. (2001). *Failure of rock under normal wedge indentation*. Dissertation, University of Minnesota.

Fire Properties and Testing Methods of Materials

Enhancing the Thermal Stability and Flame Retardancy of Transparent Fire-Retardant Coatings Applied on Wood Substrates by Introducing Multi-walled Carbon Nanotubes

Long Yan, Zhisheng Xu ⬢, Nan Deng, Dingli Liu, Zhiyong Chu and Ye Xu

Abstract Multi-walled carbon nanotubes (CNTs) were introduced into the structure of phosphate ester (PEA) to prepare a series of novel flame retardants named PEA-functionalized CNTs (CPEAs). The chemical structures of CPEAs were carefully characterized by Fourier transform infrared (FTIR) spectroscopy and ^1H nuclear magnetic resonance (^1H NMR) spectroscopy. Then, the obtained PEA and CPEAs were mixed with amino resin to produce five kinds of fire-retardant coatings applied on plywood boards. The optical transparency, fire protection performance, and thermal behavior of the transparent coatings were investigated by various analytical methods. The optical transparency analysis shows that the transparency value of coatings gradually decreases with increasing CNTs contents, and a small amount of CNTs imparts a high degree of transparency to the resulting coatings. The results from the flammability tests indicate that the CPEAs impart lower weight loss, char index, flame spread rating, heat release rate, and total heat release to the resulting coatings than those of PEA. The thermo-gravimetric analysis reveals that the CPEAs possess higher thermal stability and residual weight to the resulting coatings compared to PEA. Char residue analysis indicates that the introduction of CNTs is beneficial to generate more P–N–C and P–O–C cross-linked structures in the condensed phase that form a high-quality intumescent char against heat and mass transfer, thus effectively improving the flame retardancy and thermal stability of the transparent coatings.

Keywords Carbon nanotubes · Transparent fire-retardant coating · Fire protection performance · Thermal behavior

1 Introduction

Wood is the most common raw material being applied in the cultural heritages of the East Asia region. However, the inherent flammability of wood increases the fire risk of cultural heritages, and more efforts need to improve the reaction of wood to

L. Yan · Z. Xu (✉) · N. Deng · D. Liu · Z. Chu · Y. Xu
School of Civil Engineering, Institute of Disaster Prevention Science and Safety Technology,
Central South University, Changsha 410075, China
e-mail: xuzhsh82@163.com

fire performance [1]. The use of transparent intumescent fire-retardant coatings is the most effective method to maintain the original morphology and improve the fire protection performance of wood and wood-based products [2]. Traditionally, intumescent fire-retardant coatings are prepared by physical blending high concentration of additive flame retardants with matrix resins, thus greatly damaging the transparent and decorative properties of coatings [3]. Therefore, the reactive flame retardants are of high interest as they endow a high degree of transparency to intumescent coatings by chemically bonding flame retardants to the backbone of matrix resins [4].

Phosphorus-containing flame retardants are identified as the promising reactive flame retardants and have been widely applied in transparent fire-retardant coatings due to their high flame-retardant efficiency [5]. Further, the cyclic phosphate ester and its derivatives were preferred as a highly effective reactive flame retardant for transparent coatings, which could act as both acid source and carbon source in intumescent system [6]. When heated, the phosphorus-containing compounds can release PO free radicals to interrupt combustion chain reaction in vapor phase, as well as react with matrix resin to form a char layer that inhibits heat and mass transfer in condensed phase [7]. However, when they are used alone, the flame-retardant efficiency and thermal stability are not very high, thus restricting their industrial applications in transparent intumescent coatings [8]. A promising approach to acquire excellent fire protection performance is the incorporation of small amount of nano-fillers in transparent intumescent coatings as synergists. But, the difference in refractive index between nano-filler and matrix resin will sacrifice the optical transparency of coatings, thus limiting the application of nano-filler in transparent fire-retardant coatings [9].

Nowadays, carbon nanotubes (CNTs) are considered to be a promising flame retardant for enhancing the flame retardancy of a large range of polymers due to the formation of a continuous network-like physical barrier to insulate the transport of heat and mass [10]. However, the directly incorporation of CNTs into the intumescent system by physical method is easy to form agglomerates, and the non-uniform dispersion of CNTs will lead to opacity of the coating due to the light scattering of CNTs agglomerates in polymer matrix [11]. To overcome this problem, many efforts have been focused on the uniform dispersion of CNTs in matrix resin by covalent and non-covalent functionalization, leading to the outstanding combination of flame retardancy and transparent properties of coatings [12, 13]. For instance, various flame retardants or polymer chains with functional groups have been introduced on the surface of CNTs to prepare composites with excellent performance and good dispersions [11, 14]. Recently, Wang et al. successfully introduced phosphorus–nitrogen containing polymer [poly(phenylphosphonic-4,4′-diaminodiphenyl-methane)] on the surface of CNTs and obtained good dispersion and synergistic flame-retarded effect [15]. Durkin et al. prepared phosphorus-functionalized CNTs by oxidized CNTs with phosphoric acid, which could improve the flame-retardant effect and dispersion of CNTs efficiently [16]. Fang's group found that grafting of intumescent flame retardant (IFR) on the surface of CNTs could enhance both the dispersion degree of CNTs in polymer matrix and flame retardancy of compounds, but the flame-retardant mixtures of CNTs and IFR will lead to deterioration of flame retardancy [17, 18].

Beheshti et al. also found that the mixtures of CNTs with APP-PER-MEL intumescent flame retardants will decrease the flame retardancy of traditional intumescent coatings for steel structure [19]. Consequently, it is anticipated that the introduction of phosphorus-containing flame retardants on the surface of CNTs can obtain good dispersion of CNTs in the matrix and synergistic flame-retardant effect in the transparent intumescent coatings rather than the physical mixtures of CNTs with the flame retardants. However, relatively few studies have been reported the application and study of CNTs in the transparent fire-retardant coatings as flame retardants.

In this paper, the cyclic phosphate ester was introduced on the surface of CNTs to obtain a series of novel flame retardants named PEA-functionalized CNTs (CPEAs), and the CPEAs were used to prepare transparent intumescent fire-retardant coatings applied on wood substrates. The effect of CNTs on the transparency, thermal behavior and flame retardancy of transparent intumescent fire-retardant coatings by optical transparency test, cabinet method test, tunnel method test, cone calorimeter test and TG analysis. The char residues after cabinet method test were investigated by scanning electron microscope (SEM)-energy dispersive X-ray spectroscopy (EDS) and FTIR, and the synergistic flame-retardant mechanism was also discussed.

2 Experimental

2.1 Materials

Multi-walled carbon nanotubes (CNTs), with an average diameter of 10–20 nm and length of 5–15 μm, were provided by Shenzhen Nanotech Port Co., Ltd. (China). The specific surface area of CNTs is 100–160 m^2/g. Potassium hydroxide (KOH) and phosphoric acid (PA, 85 wt% in water) were supplied by Hunan Huihong Chemical reagent Co., Ltd. (China). Pentaerythritol (PER) was provided by Hangzhou JLS Flame Retardant Co., Ltd. (Hangzhou, China). N-butyl alcohol (n-BA) was supplied by Sinopharm Chemical Reagent Co., Ltd. (Shanghai, China). Melamine formaldehyde resin (MF, model 303-80, 58–62% in n-butyl alcohol) was provided by Jiyang Sanqiang Chemical Reagent Co., Ltd. (Shandong, China). All the materials were used as received.

2.2 Synthesis of PEA and the CPEAs

A cyclic phosphate ester acid (PEA) was synthesized by esterification reaction of PA, n-BA, and PER according to our previously reported [9]. PA (0.8 mol, 92.24 g), PER (0.22 mol, 22.96 g), and n-BA (0.08 mol, 5.93 g) were added into a 500 mL three-neck flask under stirring at 120 °C for 4 h to obtain a yellow transparent liquid product named as PEA. A series of CPEAs flame retardants were prepared by introducing

the cyclic phosphate ester on the surface of CNTs. Firstly, the hydroxylation CNTs (CNT–OH) was prepared according to the literature procedure [20]. About 2 g CNTs were dispersed in 300 ml KOH ethanol solution (2 mol/L) and then added into a 500 mL three-neck flask under stirring at 76 °C for 12 h. After that, the CNTs were separated and washed with deionized water until the PH value reached to 7, and then dried at 80 °C for 12 h to obtain the target product named as CNT–OH. Secondly, different weight of CNT–OH (0.1, 0.3, 0.5 and 0.7 g) was dispersed in 0.8 mol PA (92.24 g) and stirred under refluxing at 100 °C for 4 h, and then 0.22 mol PER (22.96 g) and 0.08 mol *n*-BA (5.93 g) was added into above solution to react at 120 °C for 4 h. After that, the water was removed by distillation to obtain phosphate ester functionalized CNTs (CPEAs). The CPEAs with addition of 0.1, 0.3, 0.5, and 0.7 g CNT–OH were named as CPEA1-CPEA4, respectively.

2.3 Preparation of Transparent Fire-Retardant Coatings

60 g PEA or CPEAs ethanol solution (60 wt%) and 60 g MF *n*-butyl alcohol solution (60 wt%) were thoroughly mixed to produce five kinds of transparent coatings. The resulted coatings were applied on the plywood boards (100 mm × 100 mm × 4 mm and 600 mm × 90 mm × 4 mm) with a wet density of 500 g/m^2, and the coatings cured to 0.4 ± 0.02 mm-thick film at room temperature. The plywood boards with dimensions of $300 \times 150 \times 4$ mm^3 were coated with a wet coating density of 250 g/m^2, and the thickness of dry film was 0.2 mm $\pm$ 0.02 mm. The transparent films obtained from PEA and CPEA1-CPEA4 were marked as CPEA0 and CPEA1-CPEA4, respectively.

2.4 Characterization and Measurements

FTIR spectra of samples were recorded on a Nicolet FTIR IS50 spectrometer (Thermo, USA) over the wavenumber range from 4000 to 500 cm^{-1} using a KBr pellet. ^{1}H NMR spectra of samples were recorded on a Bruker AVANCEIII 400M NMR spectrometer by using D_2O as a solvent.

The optical transparency of the film was measured on a LS116-type light transmittance meter (Shenzhen Linshang Technology Co. Ltd, China). All the tested films were coated on the transparent glass slide with the thickness of 0.2 mm $\pm$ 0.02 mm.

The cabinet method and tunnel method tests were applied to assess the fire protection performance of the fire-retardant coating on wood substrates. The weight loss, char index and intumescent factor of the samples were assessed by a XSF-1-type fire resistant paint tester (small room mode) (Jiangning Analysis Instrument Company, China) according to ASTM D 1360-2011, and the dimension of plywood boards is 300 mm × 150 mm × 4 mm. Flame spread rating (FSR) of the samples was assessed by a SDF-2-type 2-foot flame tunnel instrument (Jiangning Analysis

Instrument Company, China) according to ASTM D3806-2011, and the dimension of plywood boards is 600 mm × 90 mm × 4 mm.

The combustion behavior of the coatings was evaluated by a cone calorimeter (FTT, UK) according to ISO5660-2002 at a heat flux of 50 kW/m². Each plywood board with dimensions of 100 mm × 100 mm × 4 mm coated with the transparent coating was exposed horizontally to the radiator.

Thermo-gravimetric (TG) analysis was performed on a SOTA-851 (Mettler-Toledo, Switzerland) instrument. About 5 mg samples were heated from 25 to 800 °C at a heating rate of 20 °C/min under a nitrogen flow of 20 mL/min.

The morphology of the char residues after the cabinet method test was observed by a MIRA 3 LMU scanning electron microscopy (Tescan, Czech Republic) with a voltage of 20 kV. Energy dispersive X-ray spectrometry (EDS) was used to analyze the element contents of the char residues by an X-Max20 X-ray probe (Oxford instruments, UK) as the component of the SEM.

3 Results and Discussion

3.1 Characterization of PEA and the CPEAs

The mechanism for synthesizing CPEAs is presented in Scheme 1, which can be divided into three steps. The first step is hydroxylation of CNTs by potassium hydroxide ethanol solution, and then grafting H_3PO_4 on the surface of CNT–OH. Subsequently, the CPEAs were synthesized by esterification between P–OH and C–OH in PER and BA.

The FTIR spectra of CNTs and CNT–OH are presented in Fig. 1. Compared to CNTs, CNT–OH sample exhibits strong and broad bands at 3420, 1646, 1558, and 1115 cm^{-1}, which are attributed to the stretching vibration of –OH groups from CNT–OH and absorbed water, –OH group in CNT–OH, C=O groups, and C–O groups, respectively [21, 22]. It reveals that the –OH groups were successfully introduced on the surface of CNTs.

As shown in Fig. 2, PEA and CPEA3 have similar characteristic peaks, and the peaks at 2957, 2895, 2337, 1467, 1130, 988, and 887 cm^{-1} are assigned to –CH$_3$ groups, –CH$_2$ groups, P–OH groups, –CH$_2$ deformation, P=O groups, cyclic P–O–C
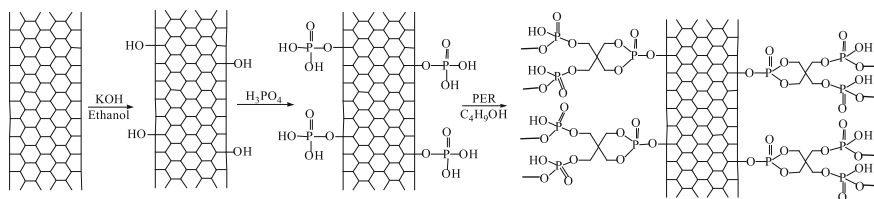
Scheme 1 Synthesis route of the CPEAs
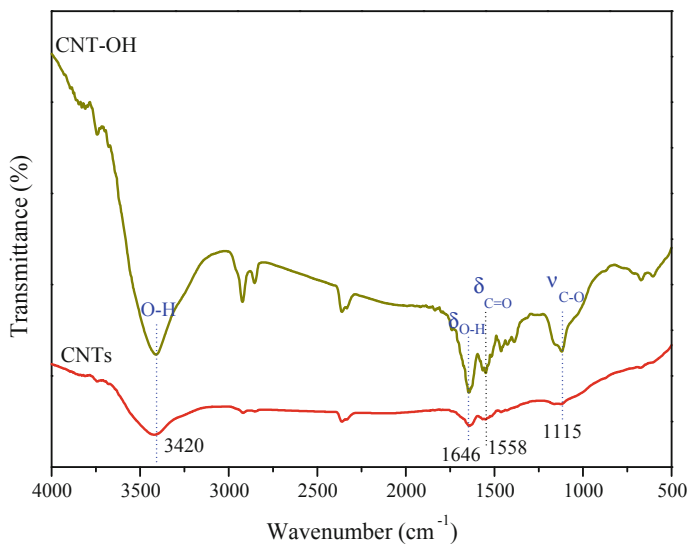
Fig. 1 FTIR spectra of CNT and CNT–OH
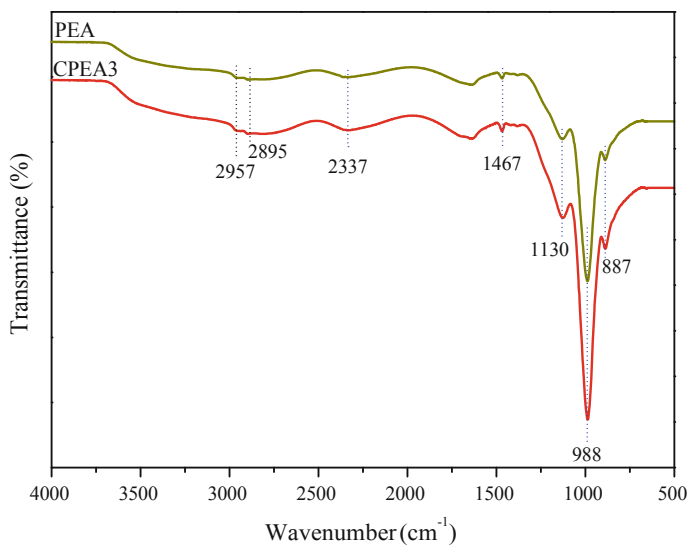
Fig. 2 FTIR spectra of PEA and CPEA3
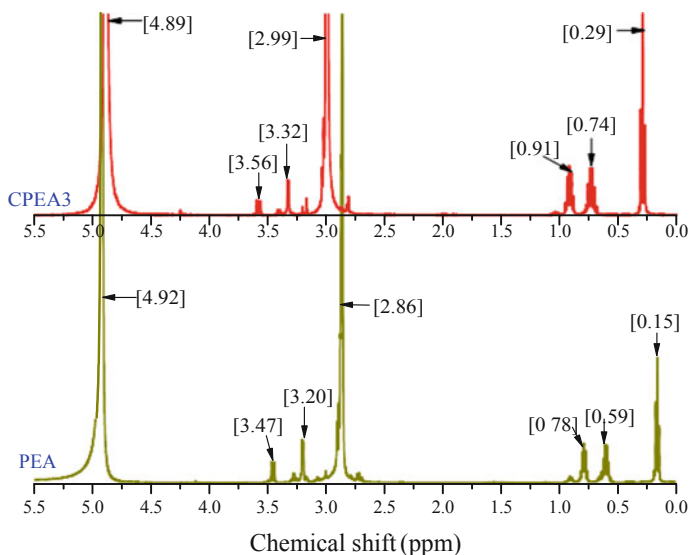
Fig. 3 ^{1}H NMR spectra of PEA and CPEA3

groups and exocyclic P–O–C groups, respectively [9, 19]. Compared to PEA, CPEA3 has a strong peak around 988 cm^{-1}, indicating the occurrence of reaction between CNT–OH with PA and then leaving more P–O–C structures. To further confirm the structure of CPEA3, ^{1}H NMR spectra of PEA and CPEA3 are presented in Fig. 3.

In the ^{1}H NMR spectrum of PEA, the two major peaks at 4.92 and 2.86 ppm are assigned to the cyclic H atoms and exocyclic H atoms, respectively. As for CPEA3, the two major peaks of cyclic H atoms and exocyclic H atoms for CPEA3 move to 4.89 and 2.99 ppm, respectively, indicating that the phosphate ester was successfully introduced on the surface of CNTs. In addition, the peaks of exocyclic H atoms in PER adjacent to cyclic P–O–C groups move to 3.32–3.56 ppm in the spectra of CPEA3 from 3.20 to 3.47 ppm in the spectra of PEA due to the presence of CNTs. The peaks of H atoms in BA move to 0.29–0.91 ppm in the spectra of CPEAs from 0.15 to 0.78 ppm in the spectra of PEA. The above results reveal that the target CPEAs were successfully synthesized by reaction of P–OH groups in PA and –OH groups in CNT–OH, PER, and BA as shown in Scheme 1.

3.2 Fire Protection Performance

The appearance of the fire-retardant coatings applied on plywood boards are shown in Fig. 4, and the optical transparency values of the samples are listed under the images. As shown in Fig. 4, the transparency value of the coatings is gradually decreased with increasing CNTs content, and MCPE4 shows a little black with the

lowest transparency of 70.4% among the samples. Therefore, a moderate content of CNTs is very crucial to maintain the transparency of the fire-retardant coatings, and an excessive amount of CNTs will greatly decrease the transparency of the coatings and limit its application in ancient buildings.

As shown in Fig. 5, the introduction of CNTs decreases the FSR value of the fire-retardant coatings, and the MCPE3 acquires the lowest FSR values of 5.2 among the samples. As for MCPE4, the FSR value is lower than that of MCPE3, indicating excessive CNTs will diminish the fire protection performance of the coatings.

The results of cabinet method test show that the introduction of CNTs decreases the weight loss, char index concomitant with an increase in the intumescent factor during burning. MCPE3 acquires the lowest weight loss (2.7 g) and char index (6.3 cm^3), and MCPE2 shows the highest intumescent factor of 46.3. It indicates that the introduction of CNTs can enhance the fire protection performance of the fire-retardant coatings, but excessive CNTs will inhibit the intumescent process and then decrease the intumescent factor (Table 1).

(a) 88.7%   (b) 87.5%   (c) 83.6%   (d) 78.1%   (e) 70.4%
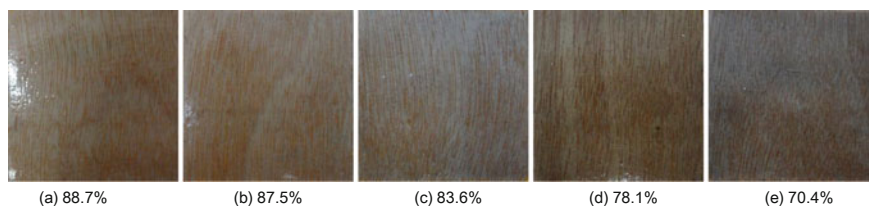
Fig. 4 Digital photographs and transparency values of fire-retardant coatings: **a** MCPE0, **b** MCPE1, **c** MCPE2, **d** MCPE3, and **e** MCPE4
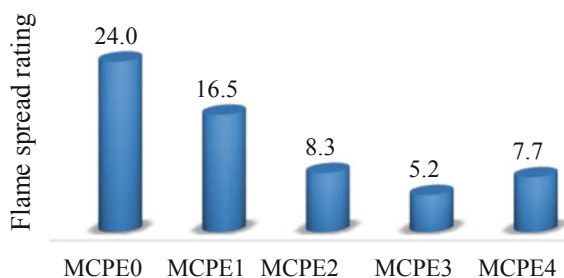
Fig. 5 FSR values of transparent fire-retardant coatings assessed by the tunnel method test

Table 1 Fire protection behavior of transparent coatings assessed by cabinet method test

Sample	MCPE0	MCPE1	MCPE2	MCPE3	MCPE4
Weight loss (g)	4.0 ± 0.3	3.5 ± 0.2	3.0 ± 0.3	2.7 ± 0.2	2.9 ± 0.3
Char index (cm^3)	11.9 ± 0.5	8.6 ± 0.4	7.6 ± 0.3	6.3 ± 0.4	7.1 ± 0.3
Intumescent factor	25.2 ± 3	35.1 ± 4	46.3 ± 3	42.5 ± 3	37.2 ± 4

The char residues of the coatings applied on plywood boards after the cabinet method test are presented in Fig. 6. As for MCPE0, a continuous and fragile residue with some visible cracks is formed after burning, resulting in a poor heat and thermal insulation. With the introduction of CNTs, the coatings trend to generate a more continuous and intumescent char as an effective physical barrier against heat, combustible gases and oxygen transfer, resulting in a better fire protection performance. But, excessive CNTs will suppress the intumescent process of the coatings, which further demonstrated that a moderate content of CNTs is important to intumescent systems.

3.3 Cone Calorimeter Test

The heat release rate (HRR) and total heat release (THR) curves of the fire-retardant coatings applied on plywood boards were investigated by cone calorimeter test, and the results are shown in Figs. 7 and 8, respectively. As shown in Fig. 7, MCPE0 shows an increase in HRR after burning and rapidly reaches maximum of 151.7 kW/m^2 at 25 s. With the introduction of CNTs, the HRR is greatly decreased than that of
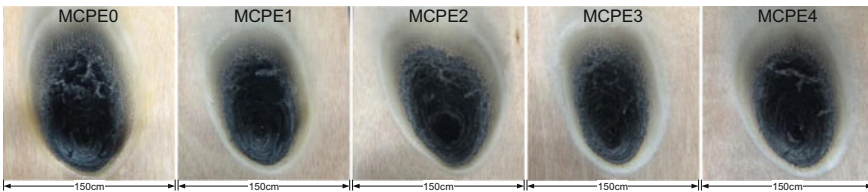
Fig. 6 Digital photographs of char residues for transparent coatings after cabinet method test
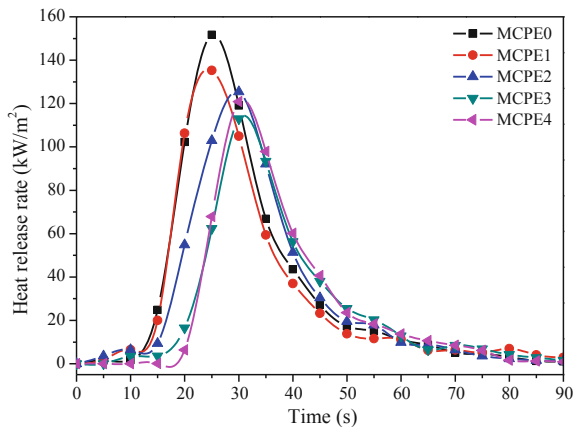
Fig. 7 HRR curves of transparent fire-retardant coatings at a heat flux of 50 kW/m^2

MCPE0, and the peak HRR (PHRR) values from MCPE1 to MCPE4 are 135.3, 125.4, 113.0 and 120.9 kW/m^2, respectively. The effective decrease in HRR can be ascribed to the formation of a more compact and intumescent char residue during burning.

As shown in Fig. 8, the THR decreases with the introduction of CNTs, and the THR values for MCPE0-MCPE4 are 3.0, 2.8, 2.6, 2.3, and 2.4 MJ/m^2, respectively. It is noted that MCPE3 acquires the lowest PHRR and THR among the above samples, which are reduced by 25.5% for PHRR and 23.3% for THR than those of MCPE0. It reveals that the introduction of CNTs performs well in improving the flame retardancy of transparent fire-retardant coatings, and the synergistic flame-retardant effect of CNTs in the transparent coatings depends on the content of CNTs. And, an excessive content of CNTs will diminish the synergistic effect on fire protection performance. This is consistent with the observation of cabinet method and tunnel method tests.

3.4 Thermo-Gravimetric (TG) Analysis

TG test was used to analyze the thermal behavior and char-forming ability of the fire-retardant coatings, and the corresponding data are shown in Fig. 9 and Table 2. As shown in Fig. 9, all the coatings exhibit four decomposition stages in the temperature ranges of 50–160, 160–380, 380–550 and 550–800 °C, respectively. The beginning decomposition stage at 50–160 °C is caused by the weight loss of absorbed water and some small molecules, accompanying with a little mass loss (<7 wt%). The second stage at 160–380 °C is related to the degradation of phosphate ester and amino resin, resulting in the formation of phosphoric acid derivatives and noncombustible gases. The third stage at 380–550 °C is attributed to the thermal oxidative decomposition
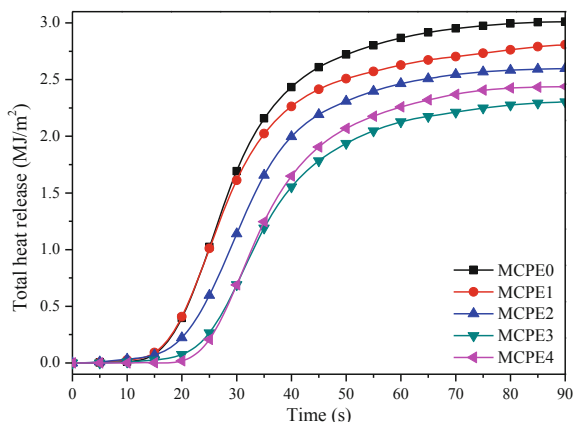
Fig. 8 THR curves of transparent fire-retardant coatings at a heat flux of 50 kW/m^2

(a)

(b)
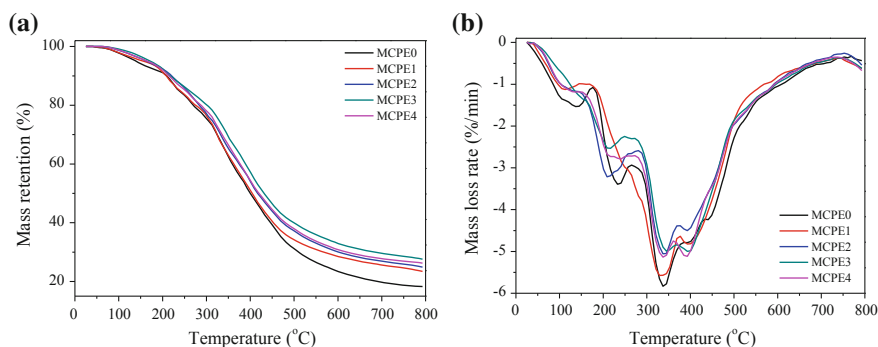
Fig. 9 TG (**a**) and DTG (**b**) curves of transparent fire-retardant coatings under a N_2 atmosphere at a heating rate of 20 °C/min

Table 2 Thermal properties of various fire-retardant coatings under a nitrogen atmosphere

Samples	$T_{5\%}$ (°C)	T_{max} (°C)	PMLR (%/min)	Residue at 800 °C
MCPE0	139.5	337.3	5.9	18.3
MCPE1	155.1	341.3	5.5	23.4
MCPE2	163.5	342.9	5.1	24.9
MCPE3	169.8	345.7	5.0	27.6
MCPE4	164.7	343.4	5.1	26.2

$T_{5\%}$—onset decomposition temperature at 5% mass loss, T_{max}—temperature of peak mass loss rate, and PMLR—mass loss rate at T_{max}

of unstable charred layer, as supported by Shi [23]. The four stages at 550–800 °C are related to the degradation of carbonized backbones at high temperature.

As shown in Table 2, the introduction of CNTs increases the $T_{5\%}$ and T_{max} of the fire-retardant coatings, indicating an enhancement in thermal stability. Besides, the incorporation of CNTs also decreases the mass loss rate of the coatings during the thermal pyrolysis process, thus increasing the residual weight at 800 °C. And, MCPE3 acquires the lowest $T_{5\%}$, T_{max} and *PMLR* among the samples, leaving the highest residual weight at 800 °C. These results indicate that a moderate content of CNT can effectively enhance the thermal stability and residual weight of the fire-retardant coatings, thus improving the fire protection behavior of the coatings.

3.5   Morphology and Chemical Structure of Char Residue

The morphology and chemical structure of the intumescent char plays an important role in clarifying the flame-retardant mechanism of CNTs in intumescent system. Figure 10 presents the SEM images and EDS maps of the char residues after the

cabinet method test. A loose structure with some big cracks and voids is clearly observed in MCPE0, which is difficult to insulate heat and mass during burning. For MCPE3, the char residue is more compact and dense with some smaller voids than that of MCPE0, thus effectively preventing heat and mass transfer between flame and underlying material. EDS analysis shows that MCPE3 has higher carbon content and mass ratio of C/O in char residue than that of MCPE0, indicative that the introduction of CNTs can generate a more thermal stable char [9]. Above results illustrate that the introduction of CNTs can enhance the physical barrier effect of char residue, thus effectively improving the fire protection performance of the coatings.

The FTIR spectra of char residues after the cabinet method test are shown in Fig. 11. The strong bands around $3100 \, \mathrm{cm}^{-1}$ are attributed to the stretching vibrations
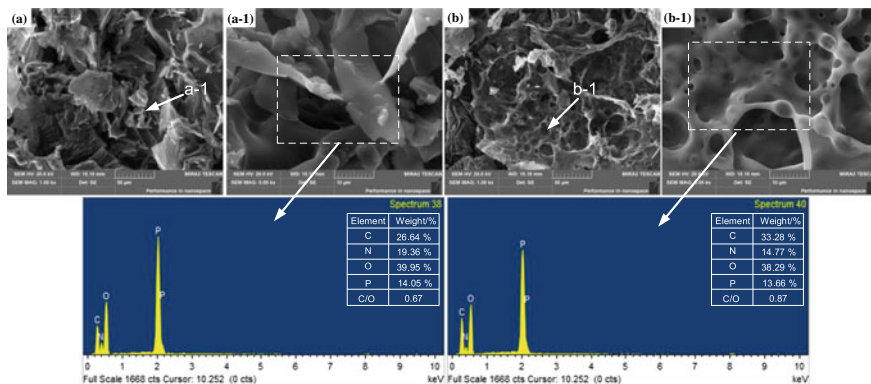
Fig. 10 SEM images and EDS maps of the char residues obtained from the cabinet method test: **a** MCPE0 and **b** MCPE3
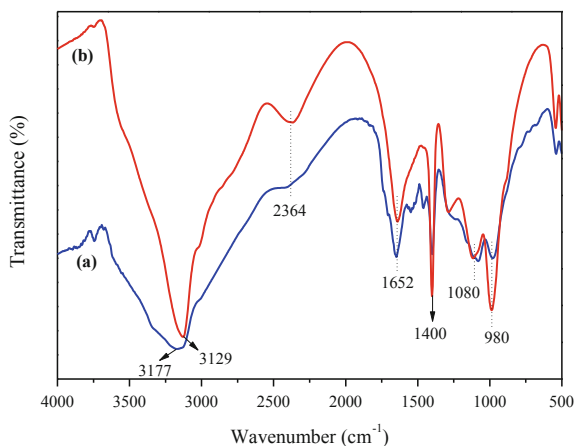
Fig. 11 FTIR spectra of the char residues obtained from the cabinet method test: **a** MCPE0 and **b** MCPE3

of –NH2 and –OH groups. And, the peaks at 2364, 1652, 1400, 1080, and 980 cm^{-1} are assigned to the vibrations of P–OH groups, N–H groups in primary amides, P–N groups, P–O–P groups, and P–O–C groups, respectively [24, 25]. With the introduction of CNTs, the intensities of –NH2 groups, P–OH groups, N–H groups in primary amides, P–N–C groups, and P–O–C groups increase remarkably than that of MCPE0, indicating that more stable cross-linked structures left in the condensed phase, which act as an effective physical barrier to insulate heat and mass transfer, thus greatly enhancing the fire protection performance of the coatings. This is supported by the slowed mass loss rate of the coatings containing CNTs in TG test.

Based on the above results, it can be concluded that the introduction of CNTs contributes to generate a more compact and stable char rich in P–N–C and P–O–C cross-linked structures against the heat and mass transfer between burning zone and underlying material, thus effectively enhancing the fire performances and thermal behaviors of the coatings.

4 Conclusions

In this paper, a series of novel flame retardants named PEA-functionalized CNTs (CPEAs) were successfully synthesized by grafting PEA on the surface of CNTs, and then well characterized by FTIR and ^{1}H NMR spectra. The obtained CPEAs were mixed with amino resin to produce transparent fire-retardant coatings for enhancing the fire safety of wood substrates. The optical transparency analysis indicates that the transparency value of the transparent coatings gradually decreases with increasing CNTs contents, and a small amount of CNTs imparts a high degree of transparency to the resulting coatings. The results from fire protection tests reveal that the coatings containing CNTs possess lower weight loss, char index, and FSR value concomitant with the formation of a more compact and intumescent char compared to the coating without CNTs, revealing the existence synergism between PEA and CNTs. The cone calorimeter test shows that the HRR and THR values of the transparent coatings are reduced with the introduction of CNTs, and MCPE3 acquires the lowest heat release among the samples. TG analysis shows that the thermal stability and residual weight of the transparent fire-retardant coatings are improved after introduction of CNTs, and MCPE3 possesses the highest residual weight of 27.6% at 800 °C. The synergistic effect of CNTs on fire protection performance and thermal behavior of fire-retardant coatings depends on the content of CNTs in the coatings, and an excessive content of CNTs will diminish the synergistic effect. Char residue analysis indicates that the introduction of CNTs contributes to form more P–N–C and P–O–C cross-linked structures in the condensed phase that produce a more compact and intumescent char, thus effectively preventing the underlying material against heat and flame, thereby greatly enhancing the fire protection performance and thermal stability of the coatings.

References

1. Lowden, L. A., & Hull, T. R. (2013). Flammability behaviour of wood and a review of the methods for its reduction. *Fire Science Reviews, 2,* 4.
2. Xu, Z., Chu, Z., & Yan, L. (2018). Enhancing the flame-retardant and smoke suppression properties of transparent intumescent fire-retardant coatings by introducing boric acid as synergistic agent. *Journal of Thermal Analysis and Calorimetry.* https://doi.org/10.1007/s10973-018-7201-3.
3. Xing, W., Song, L., & Jie, G. (2011). Synthesis and thermal behavior of a novel UV-curable transparent flame retardant film and phosphorus-nitrogen synergism of flame retardancy. *Polymers for Advanced Technologies, 22,* 2123.
4. Qian, X., Song, L., & Hu, Y. (2011). Combustion and thermal degradation mechanism of a novel intumescent flame retardant for epoxy acrylate containing phosphorus and nitrogen. *Industrial and Engineering Chemistry Research, 50,* 1881.
5. Zhang, H., Xu, M., & Li, B. (2016). Synthesis of a novel phosphorus-containing curing agent and its effects on the flame retardancy, thermal degradation and moisture resistance of epoxy resins. *Polymers for Advanced Technologies, 27,* 860.
6. Shi, Y., & Wang, G. (2016). An intumescent flame retardant containing caged bicyclic phosphate and oligomer: synthesis, thermal properties and application in intumescent fire resistant coating. *Progress in Organic Coatings, 90,* 83.
7. Tang, S., Qian, L., Qiu, Y., & Dong, Y. (2018). Synergistic flame-retardant effect and mechanisms of boron/phosphorus compounds on epoxy resins. *Polymers for Advanced Technologies, 29,* 641.
8. Xu, M., Li, X., & Li, B. (2016). Synthesis of a novel cross-linked organophosphorus-nitrogen containing polymer and its application in flame retardant epoxy resins. *Fire and Materials, 40,* 848.
9. Yan, L., Xu, Z., & Wang, X. (2017). Influence of nano-silica on the flame retardancy and smoke suppression properties of transparent intumescent fire-retardant coatings. *Progress in Organic Coatings, 112,* 319.
10. Yan, L., Xu, Z., & Zhang, J. (2017). Influence of nanoparticle geometry on the thermal stability and flame retardancy of high-impact polystyrene nanocomposites. *Journal of Thermal Analysis and Calorimetry, 130,* 1987.
11. Yu, H., Liu, J., Wen, X., & Tang, T. (2011). Charing polymer wrapped carbon nanotubes for simultaneously improving the flame retardancy and mechanical properties of epoxy resin. *Polymer, 52,* 4891.
12. Kugler, S., Kowalczyk, K., & Spychaj, T. (2017). Transparent epoxy coatings with improved electrical, barrier and thermal features made of mechanically dispersed carbon nanotubes. *Progress in Organic Coatings, 111,* 196.
13. Rezazadeh, V., Pourhossaini, M. R., & Salimi, A. (2017). Effect of amine-functionalized dispersant on cure and electrical properties of carbon nanotube/epoxy nanocomposites. *Progress in Organic Coatings, 111,* 389.
14. Sun, J., Gu, X., Zhang, S., Coquelle, M., Bourbigot, S., Duquesne, S., et al. (2014). Improving the flame retardancy of polyamide 6 by incorporating hexachlorocyclotriphosphazene modified MWNT. *Polymers for Advanced Technologies, 25,* 1099.
15. Wang, S., Xin, F., & Chen, Y. (2016). Phosphorus-nitrogen containing polymer wrapped carbon nanotubes and their flame-retardant effect on epoxy resin. *Polymer Degradation and Stability, 129,* 133.

16. Durkin, D. P., Gallagher, M. J., & Frank, B. P. (2017). Phosphorus-functionalized multi-wall carbon nanotubes as flame-retardant additives for polystyrene and poly (methyl methacrylate). *Journal of Thermal Analysis and Calorimetry, 130,* 735.
17. Ma, H., Tong, L., Xu, Z., & Fang, Z. (2008). Functionalizing carbon nanotubes by grafting on intumescent flame retardant: nanocomposite synthesis, morphology, rheology, and flammability. *Advanced Functional Materials, 18,* 414.
18. Du, B., & Fang, Z. (2011). Effects of carbon nanotubes on the thermal stability and flame retardancy of intumescent flame-retarded polypropylene. *Polymer Degradation and Stability, 96,* 1725.
19. Beheshti, A., & Heris, S. Z. (2016). Is MWCNT a good synergistic candidate in APP–PER–MEL intumescent coating for steel structure? *Progress in Organic Coatings, 90,* 252.
20. Song, P., Xu, L., & Guo, Z. (2008). Flame-retardant-wrapped carbon nanotubes for simultaneously improving the flame retardancy and mechanical properties of polypropylene. *Journal of Materials Chemistry, 18,* 5083.
21. Song, P., Shen, Y., & Du, B. (2009). Fabrication of fullerene-decorated carbon nanotubes and their application in flame-retarding polypropylene. *Nanoscale, 1,* 118.
22. Yan, L., Xu, Z., & Zhang, J. (2016). Flame retardant and smoke suppression mechanism of multi-walled carbon nanotubes on high-impact polystyrene nanocomposites. *Iranian Polymer Journal, 25,* 623.
23. Shi, Y., & Wang, G. (2016). The novel epoxy/PEPA phosphate flame retardants: synthesis, characterization and application in transparent intumescent fire resistant coatings. *Progress in Organic Coatings, 97,* 1.
24. Wang, G., Huang, Y., & Hu, X. (2013). Synthesis of a novel phosphorus-containing polymer and its application in amino intumescent fire resistant coating. *Progress in Organic Coatings, 76,* 188.
25. Larkin, P. J. (2011). *Infrared and Raman spectroscopy: principles and spectral interpretation.* Amsterdam, The Netherlands, U. K.: Elsevier.

A Method for Translating Compartment Fire Durations to Equivalent Fire Resistance Time at Standard Fire Test Condition

Takeyoshi Tanaka and Tensei Mizukami

Abstract In performance-based structural fire safety design, various calculation models are used to predict the structural behaviors of building elements exposed to fire. Although many of such calculation models require material properties of building elements as input data, it is often difficult, technically and economically, to obtain such material properties. A potential and practicable alternative is to make use a method to translate the fire duration in arbitrary compartment fire conditions to the equivalent fire resistance time of the existing standard fire furnace testing. This paper aims to develop a method for translating the duration of ventilation-controlled compartment fires to equivalent fire resistance time in the standard fire test. The method includes a simple calculation model integrating the radiation heat loss through window openings as well as the heat losses to compartment boundary and fuel and by ventilation. The translation formula is based on the premise that fire-resistant performance is assessed by prescribed temperature criteria. Example calculation results for equivalent fire resistance time are demonstrated. By this translation method, the fire resistance capability of building elements can be assessed without requiring their thermal properties.

Keywords Structural fire safety design · Ventilation-controlled compartment fires · ISO 834 standard fire · MQH formula · Equivalent fire resistance time

Nomenclature

A Area (m^2)
C Constant
c Specific heat of solid (kJ/kg)
c_p Specific heat at constant pressure of air (kJ/kg)

T. Tanaka (✉)
485-14 Iwakura-Hanazono-chow, Sakyo-ku, Kyoto 606-0024, Japan
e-mail: takey.tanaka@gmail.com

T. Mizukami
National Institute for Land and Infrastructure Management, Tachihara 1, Tsukuba 305-0802, Japan

H Height (m)
h Heat transfer coefficient (kW/m^2 K)
I Thermal inertia (kWs$^{1/2}$/m K)
k Thermal conductivity (kW/m K)
m Mass flow rate (kg/s)
m_b Mass burning rate (kg/s)
Q Rate of heat release, transfer (kW)
q Heat flux (kW/m^2)
T Temperature (K)
t Time (s, min)
x Distance from surface into solid (m)

Greek Symbols

α Thermal diffusivity [$=k/c\rho$] (m^2/s)
Φ Factor defined by Eq. 5
ρ Density (kg/m^3)
τ Fire resistance time (s, min)

Subscripts

a   Air
b   Compartment boundary
e   Building element
r   Radiation
T   Total (area) of compartment boundary
w   Window
0   Initial, ambient

1   Introduction

A variety of calculation methods is used in performance-based fire safety designs
(P-B FSD) to predict various behaviors involving in fire. Many of such calculation
methods, which are often called as FSE calculations, are likely to require material
properties as the input data. However, a difficulty is that the suitable data for FSE
calculations are hardly available. The ISO/TC92 has been discussing for years among
the subcommittees (SC) on the coordination for providing the data to be used in FSE
calculations without producing notable outcome yet. One of the reasons is thought to

be that the requirements for the data from FSE side to the testing side tend to be too ideal. Despite that FSE is largely based on fire science, its basic role is not to rigidly follow scientific framework but to promote fire safety practice. It will be necessary for FSE side to reconsider the current FSD procedures and construct a practicable FSD framework so that testing side can provide useful data for FSD.

In the area of structural fire safety as well, many of the current FSE calculations need properties of building materials, e.g., specific heat, density, and thermal conductivity. However, existing fire test apparatuses have been developed basically for rating materials and components based on the measurement of a certain behavior of materials under a certain prescribed condition. Entirely new fire test methods will be necessary to measure such material properties. Furthermore, even if such a test method might be technically possible, its development and running costs can be more than affordable for both testing companies and clients. Obviously, it is beneficial to establish some system that can effectively make use of the existing test methods, e.g., ISO 834, for P-B structural fire safety design. This study explores the possibility to coordinate standard fire resistance test and P-B structural fire safety design.

2 ISO Standard Fire Temperature and MQH Compartment Fire Temperature

Generally, structural fire community consists of two main sectors, i.e., one for fire resistance test and the other for FSD structural fire safety design. The former mostly rates the fire resistance performance of building elements using prescribed standard fire testing, and the latter analyzes various behaviors of compartment fire and the response of building elements exposed to fire using various FSE calculation methods, e.g., analytical formulas and computer models. While the standard fire temperature is uniquely stipulated, the compartment fire temperatures predicted by such FSE calculation methods differ depending on compartment conditions. The first issue is to clarify "what is the relationship between the standard fire and the actual compartment fire?" or "What fire is represented by the standard fire?"

2.1 ISO 834 Standard Fire Temperature

The ISO 834 standard fire curve is approximated by several formulas. For example, a simplest example is as follows [1]:

$$\Delta T = 345 \log(8t + 1) \tag{1}$$

where ΔT is the temperature rise [K] and t is the time [min].

The standard fire temperature curve is based on the pioneering work by Ingberg who compiled the results of various compartment fire tests [2]. This temperature curve may envelope all the temperature data of those experiments that were available at that time, but it is thought influence of different compartment conditions on fire behavior is disregarded. This is one of the very points where people would like to rationalize by P-B structural design.

2.2 MQH Formula for Compartment Fire Temperature

McCaffrey, Quintiere, and Harkleroad developed a formula for compartment fire temperature rise, ΔT, which is now widely known by the nickname of MQH formula [3] as below.

$$\frac{\Delta T}{T_0} = 0.023\left(\frac{Q_f}{A_w\sqrt{H_w}}\right)^{2/3}\left(\frac{A_w\sqrt{H_w}}{A_T}\right)^{1/3}\left(\frac{t}{k_b\rho_b c_b}\right)^{1/6} \tag{2}$$

where Q_f is the heat release rate (HRR) of fire source, $A_w(H_w)^{1/2}$ and A_T are the ventilation factor, total surface area of the compartment boundary, k_b, ρ_b, and c_b are the thermal conductivity, density, and specific heat of the compartment boundary, respectively.

This formula is informative for the factors to determine compartment temperature. If Eq. 2 is applied to ventilation-controlled compartment fire, letting the heat release per fresh air consumption be 3000 kJ/kg (air) [4] and the air inflow rate through window be $0.5 A_w(H_w)^{1/2}$ [5], and the maximum HRR in the compartment is approximated as:

$$Q_f = 1500 A_w\sqrt{H_w} \tag{3}$$

Using Eq. 3 in Eq. 2 yields the formula for ventilation-controlled compartment fire temperature as

$$\frac{\Delta T}{T_0} = C\left(\frac{A_w\sqrt{H_w}}{A_T}\right)^{1/3}\left(\frac{t}{k_b\rho_b c_b}\right)^{1/6} \equiv C\left(\frac{\Phi}{I_b}\right)^{1/3} t^{1/6} \tag{4}$$

where Φ and I_b are defined as

$$\Phi \equiv A_w\sqrt{H_w}/A_T \quad \text{and} \quad I_b \equiv \sqrt{k_b\rho_b c_b} \tag{5}$$

In Eq. 4, C is the coefficient which is $C = 3$ when t is in second and $C = 6$ when t is in minute. Note that Eq. 4 suggests that compartment fire temperature rise with time is governed by Φ, geometrical factor of compartment, and I_b, thermal inertia of compartment boundary. The value of $C(\Phi/I_b)^{1/3}$ in Eq. 4 can be calibrated with

ISO 834 standard fire curve so that Eq. 4 fits well to the standard fire curve. Letting the temperature rise at $t = 60$ min be 925 K as in ISO 834, we obtain

$$C\left(\frac{\Phi}{I_b}\right)^{1/3} = \frac{\Delta T/T_0}{t^{1/6}} \approx \frac{925/300}{60^{1/6}} \approx 1.56 \tag{6}$$

Using this value in Eq. 4, the standard fire temperature curve can be approximated as follows

$$\Delta T \approx 1.56 T_\infty t^{1/6} \approx 460 t^{1/6} \tag{7}$$

The temperature curves of Eq. 1, ISO 834, and Eq. 7, deriving from MQH formula, for 0–180 min (0–3 h), are compared in Fig. 1, to demonstrate very good agreement. Recalling that ventilation-controlled fire was assumed in deriving Eq. 7, ISO 834 standard fire curve is found to be a good representation of a ventilation control fire.

From the viewpoint of the temperature curve for fire-resistant test, the difference of Eqs. 1 and 7 is only trivial. However, from the viewpoint of P-B structural fire safety design, Eq. 4 is superior to Eq. 1 since the parameters to govern compartment fire temperature are explicitly shown in Eq. 4 so can be applied to different compartment conditions.

Although the standard fire curve is not explicitly related to any specific compartment condition, we may consider that it represents the fire in a compartment which has the specific condition as follows

$$\Phi/I_B = (1.56/C)^3 \approx (1.56/6)^3 \approx 0.0175 \tag{8}$$

The compartment fire temperatures calculated by Eq. 4 for different values of Φ/I_b are shown in Fig. 2. The standard fire curve, Eq. 1, is also plotted for reference. As expected from the shape of Eq. 4, the temperatures increase regularly with the increase of the values of Φ/I_b. A problem of Eq. 4 is also seen in this figure. It is that the temperatures for large values of Φ/I_b, which are still reasonable considering the usual conditions of modern buildings, rise to unreasonably high temperature. This is

Fig. 1 Comparison of ISO 834 standard fire curve and Eq. 7
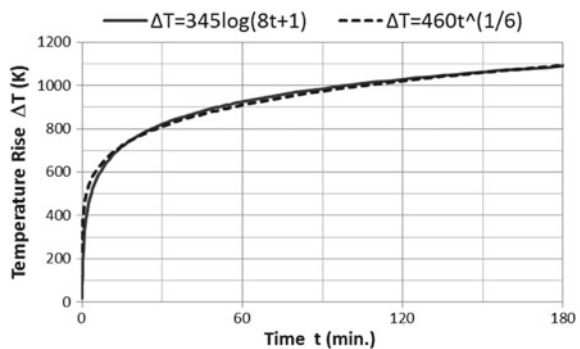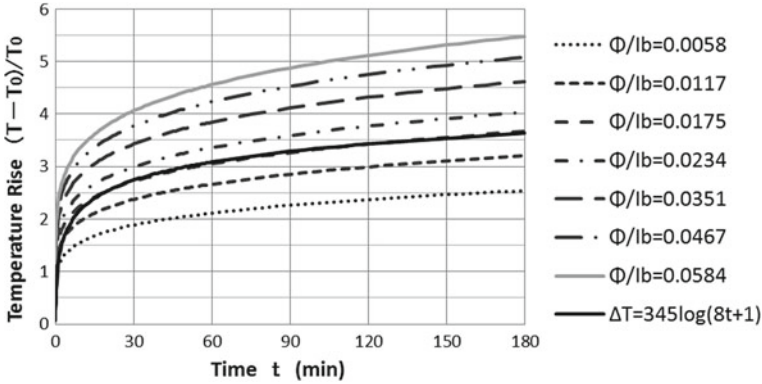
Fig. 2 Temperature–time curve according to the values of Φ/I_b

thought to be because the MQH formula was calibrated by the fire experiments with relatively low temperature, mostly under 600 °C, so that radiation heat loss through window opening is negligible.

3   Compartment Fire Temperature with Radiation Heat Loss Through Window Opening

It is thought that the radiation heat loss through window opening cannot be neglected for ventilation-controlled compartment fire, where very high temperature can be expected depending on the compartment conditions. Below, we consider a simple compartment fire model taking into account the radiation heat loss through window.

3.1   Heat Conservation

The heat conservation of fire for a compartment can be formulated as

$$\frac{d}{dt}\left(c_p \rho T V_R\right) = Q_f - Q_g - c_p m_g (T - T_0) - Q_b - Q_r \tag{9}$$

where T and ρ are the compartment gas temperature and density, V_R is the compartment volume, T_0 is the ambient temperature, Q_f, Q_b, Q_g, and Q_r are the heat release rate (HRR), heat of fuel gasification, heat loss to boundary wall, and radiative heat loss through window opening, respectively, m_g is the mass rate of gas exiting the compartment through window opening, and t is time.

Actually, the LHS of Eq. 9 is zero since $\rho T = $ constant under constant atmospheric pressure. Hence, Eq. 9 is reduced to be

$$Q_f - Q_g = c_p m_g (T - T_0) + Q_b + Q_r \tag{10}$$

3.2 Ventilation Rate and Heat Release Rate

The HRR in a ventilation-controlled compartment fire is the greatest when the oxygen contained in the air entering into a compartment by ventilation is completely consumed for the combustion in the compartment. So, letting m_a be the air inflow rate, the maximum heat release rate is given by

$$Q_f = 3000 m_a \tag{11}$$

The air inflow rate, m_a, is often estimated assuming $m_a = m_g$ and it is well known that $m_a (= m_g) = 0.5 A_w (H_w)^{1/2}$ when compartment fire temperature is over 400 °C [5]. However, the mass burning rate, m_b, i.e., the mass generation rate of fuel gas due to the volatilization of combustible materials, can be too large to be ignored in a fully developed compartment fire. Here, taking this into account, we consider the conservation of mass shown as follows:

$$m_a + m_b = m_g \tag{12}$$

The mass burning rate, m_b, was empirically found to be $m_b = 0.1 A_w (H_w)^{1/2}$ by Kawagoe et al. [6]. Hence,

$$m_g - m_a \approx 0.1 A_w \sqrt{H_w} \tag{13}$$

This equation is thought to be satisfied by the increase of the m_g and the decrease of the m_a from the values in the case of no mass burning rate, i.e., when $m_a = m_g$. Considering the ventilation configuration at the opening in the case without m_b, the neutral plane is formed at the height to make $m_a = m_g$. If m_b is added to this configuration, the compartment pressure rises so the neutral plane becomes lower, which causes the increase of m_g and the decrease of m_a. Although more precise discussions may be made, we employ the approximate estimation of these mass flow rates that meets Eq. 13 as follows

$$m_g = 0.55 A_w \sqrt{H_w}, \quad m_a = 0.45 A_w \sqrt{H_w} \ (\text{kg/s}) \tag{14}$$

Using Eq. 14 in Eq. 11, the HRR inside fire compartment, Q_f, is estimated to be

$$Q_f = 3000 m_a = 3000 \times 0.45 A_w \sqrt{H_w} = 1350 A_w \sqrt{H_w} \tag{15}$$

3.3   Heat of Fuel Gasification

If HRR is estimated based on the heat of combustion, ΔH, and mass burning rate, m_b, of a fuel, i.e., as $\Delta H m_b$, the ΔH may be taken as the effective heat of combustion subtracting the heat of gasification. As the effective ΔH, 10.75 MJ/kg was used in the pioneering studies for compartment fire behavior by Kawagoe and Magnusson, etc. [7], while the heat of combustion of wood volatiles is about 16.4 MJ/kg. This corresponds to a combustion efficiency of $10.75/16.4 = 0.65$ [7].

Here, since the HRR is estimated based on the rate of supply of fresh air, the heat of gasification of fuel has to be separately estimated. Although synthetic materials are increasing in recent years, majority of the fuels in compartment fire are considered to be still cellulosic combustibles. Although the heats of gasification of such combustibles have not been well established, the measurements by Thomas et al., range 100–1200 kcal/kg (about 400–5000 kJ/kg) with the average of 540 kcal/kg (about 2300 kJ/kg) [8, 9]. If we use this average, the LHS of Eq. 10 is calculated as

$$
\begin{aligned}
Q_f - Q_g &= 3000 m_a - 2300 m_b \\
&= 3000 \times 0.45 A_w \sqrt{H_w} - 2300 \times 0.1 A_w \sqrt{H_w} \\
&= 1120 A_w \sqrt{H_w}
\end{aligned}
\tag{16}
$$

This corresponds to the heat of combustion of 11.20 MJ/kg, which is very close to the above effective heat of combustion, 10.75 MJ/kg in the above. Since it does not make much difference, we tentatively adopt here

$$
Q_f - Q_g = 1080 A_w \sqrt{H_w}
\tag{17}
$$

3.4   Heat Loss to Boundary

For estimating the heat loss to compartment boundary wall, we use similar method with that used in MQH formula [3]. That is, assuming that the compartment boundary is a semi-infinite solid whose surface is suddenly raised to fire temperature, T, the well-known formula for the absorbed heat flux into the solid, q is given as [10]

$$
q = \frac{k_e (T - T_0)}{\sqrt{\pi \alpha_e t}} = \sqrt{\frac{k_e \rho_e c_e}{\pi t}} (T - T_0)
\tag{18}
$$

Hence, the rate of heat loss to compartment boundary, Q_b, is given by

$$
Q_b = q A_T = \sqrt{\frac{k_e \rho_e c_e}{\pi t}} (T - T_0) A_T
\tag{19}
$$

Strictly speaking, Eq. 18 holds for constant surface temperature while the compartment boundary surface temperature changes with time. So, we need to tolerate a certain error during transient period, particularly at early stage, but the treatment by Eq. 19 is supposed to be at safer side for the purpose of fire resistance assessment.

3.5 Radiation Heat Loss Through Window Opening

Since fire gases in a fully developed compartment can be regarded to be thermally opaque, the rate of radiation heat loss through window opening, Q_r, is given by

$$Q_r = \sigma\left(T^4 - T_0^4\right)A_w = h_r(T - T_0)A_w \tag{20}$$

where h_r is radiation heat transfer coefficient defined as

$$h_r = \sigma\left(T^4 - T_0^4\right)/(T - T_0) = \sigma\left(T^2 + T_0^2\right)(T + T_0) \tag{21}$$

3.6 Formula for Ventilation-Controlled Fire Temperature Considering Radiative Heat Loss Through Window

Substituting Eqs. 14, 17, 19, and 20 into Eq. 10 yields:

$$1080 A_w\sqrt{H_w} = c_p 0.55 A_w\sqrt{H_w}(T - T_0)$$
$$+ \sqrt{\frac{k_e\rho_e c_e}{\pi t}}(T - T_\infty)A_T + h_r(T - T_0)A_W \tag{22}$$

From Eq. 22, we have an equation for compartment fire temperature as

$$T - T_0 = \frac{1120 A_w\sqrt{H_w}}{c_p 0.55 A_w\sqrt{H_w} + \sqrt{\frac{k\rho c}{\pi t}}A_T + h_r A_w}$$
$$\approx \frac{2036}{1 + \frac{1.8}{\frac{A_w\sqrt{H_w}}{A_T}\sqrt{\frac{\pi t}{k\rho c}}} + h_r\frac{1.8}{\sqrt{H_w}}} \tag{23}$$

Slightly transforming Eq. 23 with the use of the definition of Φ and I_b in Eq. (5) for simplicity, we have

$$\frac{T - T_0}{T_0} \approx \frac{6.6}{1 + \frac{I_b}{\Phi}t^{-1/2} + h_r\frac{1.8}{\sqrt{H_w}}} \tag{24}$$

where a trivial approximation was made of $\sqrt{\pi} = 1.773\ldots \approx 1.8$ for simplicity.

Like MQH formula, Eq. 24 is still a function of Φ/I_b but radiation heat loss through window opening is another factor to govern compartment fire temperature. Since the radiation heat transfer coefficient, h_r, is a function of T as can be seen in Eq. 21, some numerical calculation, using EXCEL spreadsheet, etc., is practical to calculate Eq. 24 for the fire temperature, T.

Letting the window height, H_m, be $H_m = 2$ m, sample calculations of Eq. 24 were carried out for different values of Φ/I_b. The results are shown in Fig. 3. A notable difference between the results in Fig. 3 from Fig. 2 is that the intervals of temperature curves between the values of Φ/I_b are not regular unlike in Fig. 2. In Fig. 3, the larger the value of Φ/I_b, the interval becomes the smaller between the different values of Φ/I_b. Another difference is that the temperature curves are the steeper at the early stage and, on the contrary, the more gentle at the later stage. This tendency is found to be similar with several preceding numerical predictions of compartment fire temperatures [6, 11]. Needless to say, this can be understood from the shape of Eq. 24, i.e., as time, t, becomes large, the term for the heat loss to compartment boundary decays so that the temperature is eventually controlled by the terms for the heat losses by ventilation and radiation through window openings. Incidentally, the temperature curve for $\Phi/I_b = 0.0175$ happens to be closest to ISO 834 standard fire temperature although some difference is seen in the early stage, before 60 min.
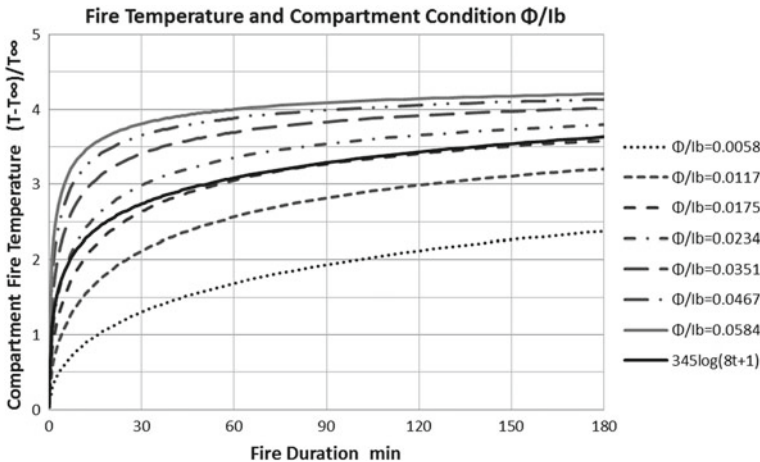
Fig. 3 Compartment fire temperatures for different values of Φ/I_B

4 Translation of Compartment Fire Duration to Fire Resistance Time by Standard Fire Test

As compartment fire temperatures differ depending on the conditions of compartments, the resulting impacts on building elements, e.g., column and beams, differ accordingly. However, we have no fire furnace nor fire test method that can test the fire resistance performance of building elements under various fire temperatures but only have the furnaces that can run a uniquely prescribed standard temperature. Therefore, it is necessary to translate the fire resistance performance under different compartment fire temperatures to those under the standard temperature to experimentally confirm the performance of the building element to endure the compartment fire.

4.1 Temperature Criteria for Fire Resistance

Fire resistance performance consists of three sub-performances, i.e., load-bearing capacity, integrity, and thermal insulation. Of these, the criteria for fulfilling the thermal insulation performance are prescribed in terms of temperature at prescribed locations of the test specimen, e.g., unexposed side surface of a wall. Assuming that the heat conduction theory for semi-infinite solid can be used as a practical means for estimating the temperature in such a case, the temperature at specified location, x_c, is given by

$$\frac{T(x_c, t) - T_0}{T_f - T_0} = \text{erfc}\left(\frac{x_c}{2\sqrt{\alpha_e t}}\right) \tag{25}$$

Consider to apply this equation to materials with same properties but exposed to different fire conditions 1 and 2. Letting the fire temperatures in these conditions be $T_{f,1}$ and $T_{f,2}$, and the times at which the temperatures become the same for both conditions be τ_1 and τ_2, respectively, we have the following relationship:

$$\frac{\tau_1}{\tau_2} = \left\{\frac{\frac{x_c}{2\sqrt{\alpha_e}}}{\text{erfc}^{-1}\left(\frac{T_c - T_0}{T_{f,1} - T_0}\right)}\right\}^2 \bigg/ \left\{\frac{\frac{x_c}{2\sqrt{\alpha_e}}}{\text{erfc}^{-1}\left(\frac{T_c - T_0}{T_{f,2} - T_0}\right)}\right\}^2$$

$$= \left\{\frac{\text{erfc}^{-1}\left(\frac{T_c - T_0}{T_{f,2} - T_0}\right)}{\text{erfc}^{-1}\left(\frac{T_c - T_0}{T_{f,1} - T_0}\right)}\right\}^2 \tag{26}$$

Notice that the properties of the tested building element are not necessary for the translation of fire-resistant time although the properties of compartment boundary, I_b, will be necessary to calculate the fire temperature, $T_f - T_0$. This equation is

seemingly very simple, but the problem is that the $T_f - T_0$ in the RHS is a function of time τ. So, exploring to find an approximate formula, the following formula was found to be a good enough approximation:

$$\frac{1}{\left\{\text{erfc}^{-1}\left(\frac{T_c - T_0}{T_f - T_0}\right)\right\}^2} \approx 6.36\left(\frac{T_c - T_0}{T_f - T_0}\right) \tag{27}$$

Using Eq. 27 in Eq. 26 yields a very simple expression as follows:

$$\frac{\tau_1}{\tau_2} \approx \left(\frac{T_c - T_0}{T_{f,1} - T_0}\right)\bigg/\left(\frac{T_c - T_0}{T_{f,2} - T_0}\right) = \frac{T_{f,2} - T_0}{T_{f,1} - T_0} \tag{28}$$

Since the temperatures, $T_{f,1}$ and $T_{f,2}$, in the RHS of Eq. 29 change with time, we use the average temperature for $0 \le t \le \tau$, i.e.,

$$T_{f,1} - T_0 = \frac{1}{\tau_1}\int_0^{\tau_1}(T_{f,1} - T_0)\mathrm{d}t, \quad T_{f,2} - T_0 = \frac{1}{\tau_2}\int_0^{\tau_2}(T_{f,2} - T_0)\mathrm{d}t \tag{29}$$

Substituting Eq. 29 into Eq. 28 yields;

$$\int_0^{\tau_1}(T_{f,1} - T_0)\mathrm{d}t = \int_0^{\tau_2}(T_{f,2} - T_0)\mathrm{d}t \tag{30}$$

That is, the translation formula turns out to be the equal temperature–time product. For developing a formula to translate the fire duration of an arbitrary compartment fire to the equivalent fire resistance time of standard furnace test, it is convenient to exploit MQH formula, which is very close to ISO 834 standard fire temperature when $\Phi/I_b = 0.0175$. Then, letting condition 1 be the standard fire test condition, the LHS of Eq. 30 becomes as

$$\int_0^{\tau_1}\frac{(T_{f,1} - T_0)}{T_0}\mathrm{d}t \approx 6.0\left(\frac{\Phi}{I_B}\right)^{1/3}\int_0^{\tau_1}t^{1/6}\mathrm{d}t\frac{36}{7}(0.0175)^{1/3}\tau_1^{7/6} = 1.335\tau_1^{7/6} \tag{31}$$

Hence, the equivalent standard fire resistance time, τ_1, is given by Eq. 32 shown below:

$$\tau_1 = 0.78\left\{\int_0^{\tau_2}\frac{(T_{f,2} - T_0)}{T_0}\mathrm{d}t\right\}^{6/7} \tag{32}$$

(a) Translated equivalent fire resistance time: τ_1/τ_2 (b) Increase rate of equivalent fire resistance time: $(\tau_1 - \tau_2)/\tau_2$
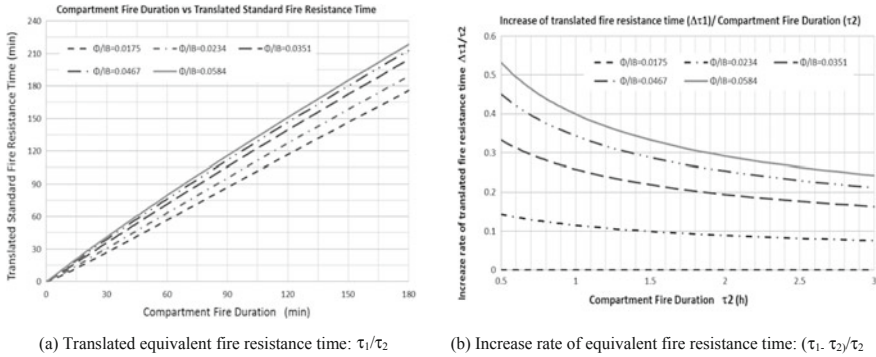
Fig. 4 Example of translated standard fire resistance time

Although the integration in the RHS of Eq. 32 is not possible to be integrated due to the complexity of the equation as shown in Eq. 24, numerical integration of Eq. is easily executed using Excel spreadsheet, etc. The example calculation results of the translated fire-resistant times are shown for several fire compartment conditions in Fig. 4. The left figure (a) shows τ_1/τ_2, i.e., translated equivalent standard fire resistance time/compartment fire duration, and the right figure shows $(\tau_1 - \tau_2)/\tau_2$, i.e., increase in the rate of translated time/compartment fire duration. Needless to mention, the larger the value of Φ/I_b, the longer the time translated for standard fire temperature condition. Also, the shorter the compartment fire duration the larger the increase rate of translated time because of the larger temperature difference of compartment fire at an early stage from the standard temperature curve.

5 Conclusion

It is very useful for P-B structural fire safety design if the duration of compartment fire with various conditions can be translated to the equivalent fire resistance time by standard fire furnace test. The possibility of such a translation method is explored considering ventilation-controlled compartment fire.

The temperature of ventilation-controlled compartment fire is basically governed by the factor Φ/I_b, but the thermal radiation through window plays an important role, particularly when large openings exist in the compartment.

The translation of fire resistance time based on "Equal temperature rise" is proposed. By this, translation of compartment fire duration to equivalent fire resistance time by standard fire furnace test is possible. According to this method, the material property data of test specimens are not required although the thermal inertia of fire compartment is necessary to estimate the compartment fire temperature.

The present method is considering a wall-type building element for which fire resistance performance is assessed by temperature criteria. Further study is necessary for translation methods for other building elements of which the fire resistance performance is assessed by different types of criteria.

References

1. ISO 834. (1999). *Fire resistance tests-elements of building construction*. Geneva, Switzerland: ISO.
2. Ingberg, S. H. (1928). Tests of severity of building fires. *Quarterly of the National Fire Protection Association, 22*(1), 43–61.
3. McCaffrey, B. J., Quintiere, J. Q., & Harkleroad, M. F. (1981). Estimating room temperatures and the likelihood of flashover using fire test data correlations. *Fire Technology, 17,* 98–119. https://doi.org/10.1007/BF02479583.
4. Huggett, C. (1980). Estimation of rate of heat release by means of oxygen consumption method. *Fire and Materials, 4*(20).
5. Nakaya, I., Tanaka, T., & Yoshida, M. (1986). Doorway flow induced by a propane fire. *Fire Safety Journal, 10,* 185–195.
6. Kawagoe, K., & Sekine, T. (1954). Estimation of fire temperature curve in concrete buildings with different thermal conductivity of wall. *Bulletin of Japan Association for Fire Science and Engineering, 3*(2) (in Japanese).
7. Walton, W. D., & Thomas, P. H. (2008) Estimating temperatures in compartment fires. In *SFPE handbook* (4th ed., pp. 3–207).
8. Thomas, P. H., & Nilsson, L. (1973). *Fully developed compartment fires—New correlations of burning rates*. FRN 979. UK: Fire Research Station.
9. Bohm, B. (1977). *Fully developed polyethylene and wood compartment fires with application to structural design*. Technical University of Denmark.
10. *The SFPE handbook of fire protection engineering* (4th ed., Chap. 2, pp. 1–37). SFPE.
11. Sato, M., Tanaka, T., & Wakamatsu, T. (1996–97). Simple formula for ventilation—controlled fire temperatures. *Journal of Applied Fire Science, 6*(3), 269–290.

An Experimental Study on Combustion Characteristics of Printers Depending on Geometrical Type and Kind of Plastics Used

Jaeyoung Lee, Yoshifumi Ohmiya, Kazunori Harada, Ken Matuyama, Yuhsiang Wang, Fumiaki Saito, Seiji Okinaga, Yusuke Shintani, Akihide Jo and Jun Kitahori

Abstract To estimate the fire load of a room, data pertaining to the combustion behavior and other aspects are required. In this study, the fire behavior of diverse printers was observed by conducting a series of combustion experiments. Twelve units of printers were used for the experiments. The weight of the printers ranged between 6.7 and 54.5 kg. The bulk volume was 0.026–0.147 m^3. The projected area was between 0.49 and 1.33 m^2. The ignition source was a propane gas burner using a 10-mm-diameter copper pipe. The supply flow rate of the gas was set to 1 L/min using a mass flow controller. In the burning test, the heat release rate was measured by using the oxygen consumption method, and the weight change was measured by using a set of load cells. The results of the burning test showed that the combustion behavior and the heat of combustion differed significantly according to the type of printers. The heat of combustion of the inkjet printer was 31.7 MJ/kg and that of the laser printer was 24.7 MJ/kg. The fire load was estimated using the measured HRR

J. Lee (✉) · Y. Ohmiya · Y. Wang · F. Saito
Department of Architecture, Faculty of Science and Technology, Tokyo University of Science, 2641 Yamazaki, Noda-shi, Chiba 278-8510, Japan
e-mail: lee_jy@deu.ac.kr

J. Lee
Department of Fire Administration and Disaster Management, Dong-eui University, 176 Eomgwangro Busanjin-gu, Busan 47340, South Korea

K. Harada
Department of Architecture and Architectural Engineering, C1-4, Kyoto University Katsura Campus, Nishikyo, Kyoto 615-8540, Japan

K. Matuyama
Department of Fire Science and Technology, Tokyo University of Science, 2641 Yamazaki, Noda-shi, Chiba 278-8510, Japan

S. Okinaga
The Building Center of Japan, 1-9 Kandanishiki-cho, Chiyoda-ku, Tokyo 101-8986, Japan

Y. Shintani · A. Jo
Takenaka Corporation, 1-1-1 Shinsuna, Koto-ku, Tokyo 136-0075, Japan

J. Kitahori
Akeno Facility Resilience Inc., 2-27-7 Hyakuin-cho, Shinju-ku, Tokyo 169-0073, Japan

and the residual weight after the burning test. The relationship between the initial weight or bulk volume and the fire load is shown. Additionally, the relationships between the surface area and the maximum heat release rate and that between the bulk density and the fire growth rate α are shown. The results of this study revealed that the maximum heat release rate is proportional to the nominal ventilation factor and that the fire growth rate is decreased as the bulk density is increased.

1 Introduction

When considering the fire safety performance of buildings, it is desirable to consider the fire load depending on the type and arrangement of combustibles. In Japan, the fire protection design for large buildings and high-rise buildings is conducted by following the fire resistance performance verification methods and evacuation safety design verification methods. The setting of the fire load is an important issue in all verification processes [1, 2]. A guideline has been published for this purpose [3].

The fire load used for designing fire safety is divided into the initial fire load, which is involved in the initial fire growth immediately after the start of the fire, and the fully developed fire load, which is involved in a fully developed fire in the whole compartment. To estimate the fire load correctly, we must know the combustion characteristics of a single combustible object, the constituent ratio of the combustible materials of it, and the combustion characteristics of it as well as the data on the amount of combustible goods according to the use of the room. The major combustion characteristics are the fire growth rate, the maximum heat release rate [hereinafter, $Q_{\max}$ (kW)], and the total heat release [THR (MJ)] [3, 4] of a combustible object.

Data on combustion characteristics of various objects have been accumulated by many researchers [3–8]. For example, there are many combustion experiments on chairs, sofas, wooden furniture, mattresses, beddings, and vehicles. However, combustion experiments on rigid plastic products are not enough. Recent survey on combustibles in office buildings [9, 10] indicates that a large printer is as one of the major fire source considering its dimensions. However, data are lacking on the constituent ratio of material and combustion characteristics.

The objective of this study is to gather baseline data including fire growth rate, maximum heat release rate, and total heat release of various printers and to observe the combustion characteristics of printers made of rigid plastic.
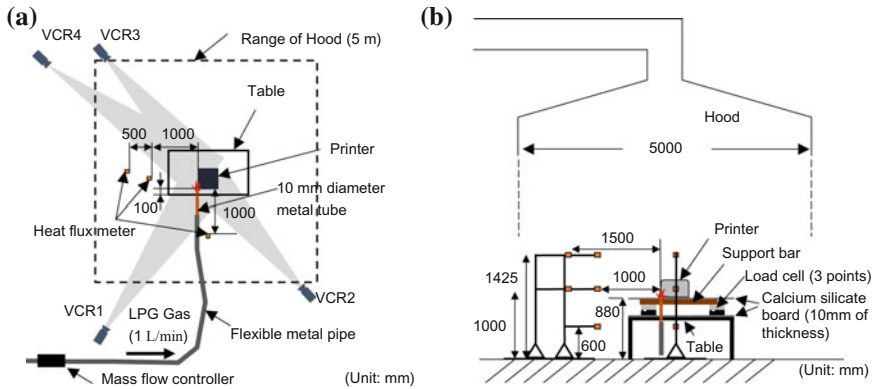
Fig. 1 Burning test method of a printer under a 5-m hood; **a** plan view, **b** cross section

2 Outline of Burning Tests

2.1 Method of Burning Test of a Printer

The (a) plan and (b) cross-sectional view of the burning test setup are shown in Fig. 1. The burning test was conducted under a 5-m square smoke collecting hood. The heat release rate was measured by using an open calorimeter [11]. At the same time, the mass loss was measured by using a set of load cells. Printers were installed on a table, simulating normal daily-use condition. A corner of the printer was ignited by a propane gas burner as an ignition source. The gas burner was continued until the specimen was completely ignited. The gas supply rate was regulated at 1 L/min by a mass flow controller. The heat release rate of the gas burner was 5.71 kW on an average of 20 min. The heat release rate of the gas burner was excluded from the measured heat release rate. The burning behavior was recorded from four sides by using video camera recorders (VCR). The heat flux from a burning printer was measured at 1000 and 1500 mm apart horizontally.

2.2 Measured Items

Table 1 lists the measured items, measurement equipment, and the purpose of the measurement classified by the time of measurement. Before each test, the dimensions and weight of the specimen were measured, and their photo images were recorded. Heat release rate, weight change, heat flux, and observation of combustion behavior (video recording) were measured during burning. After each test, the weight of non-combustible materials was measured in a combustion residue. The fire growth rate and incubation time were estimated from the measured heat release rate.

Table 1 Measured items

Time	Items and measuring devices	Purpose
Before the test	Basic measurements	To obtain the specification of specimen, i.e., weight and size, etc.
	Images taken from five directions/camera (see Appendix 2 for details)	To obtain the surface area of the specimen
During the test	HRR (kW)/open calorimeter	To obtain the heat of combustion ΔH_c, fire growth rate α, incubation time t_0, burning duration, etc.
	Heat flux/heat flux gauge	To obtain the relationship between flame properties and heat flux
	Weight/load cell	To obtain the weight change and calculate the mass loss rate (kW)
	Photo and observation/VCR	To record the burning behavior and flame geometry
After the test	Measurement of weight	To determine the weight ratio of the non-combustible materials

2.3 Specimen Specifications

Table 2 lists the type, production year, dimensions, and weight of 12 printers tested. The printers were divided into four types based on the printing method (laser/inkjet), color (black and white/color), and function (printer/all-in-one). We also investigated

Table 2 Specification of the test specimens

Test no.	Type of printer	Production date (year/month)	Size measured by tapeline			Projected area of five surfaces and volume		Initial weight	Bulk density
			W (m)	L (m)	H (m)	A_s (m^2)	V_{bulk} (m^3)	W_0 (kg)	ρ_{bulk} (kg/m^3)
1	B_Laser	2005/2	0.368	0.250	0.240	0.489	0.026	6.8	261.2
2	B_Laser	2002/11	0.488	0.460	0.288	0.787	0.068	17.1	251.8
3	C_Laser	2007/11	0.538	0.590	0.379	1.242	0.127	54.5	427.9
4	C_Laser	2007/3	0.490	0.620	0.485	1.328	0.147	36.1	246.5
5	C_Laser	2003/10	0.585	0.540	0.325	1.173	0.119	41.6	348.6
6	C_Laser	2004/10	0.490	0.660	0.335	1.028	0.103	31.6	305.2
7	C_Laser	2009/3	0.410	0.490	0.315	0.834	0.072	24.5	341.0
8	C_Inkjet	2006/6	0.597	0.310	0.195	0.730	0.037	9.5	254.5
9	C_Inkjet	2005/10	0.412	0.297	0.158	0.514	0.021	6.7	317.3
10	C_Inkjet	2009/10	0.440	0.400	0.230	0.680	0.045	10.9	241.6
11	A_Inkjet	2007/9	0.485	0.380	0.175	0.680	0.039	10.8	278.1
12	A_Inkjet	2011/9	0.442	0.386	0.114	0.555	0.031	9.2	297.1

B Black and white, *C* Color, and *A* All-in-one type in the table

Fig. 2 Relationship between bulk volume and weight
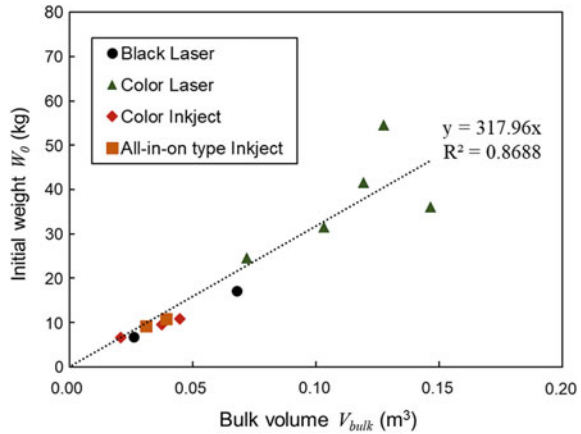
the plastic materials according to the type of printers (three units each), in addition to the printer used for the combustion experiment. The main material of the inkjet printer was "PS-HI (high-impact polystyrene)" and that of the laser printer was "ABS-FP(40)" (Appendix 1). Figure 2 shows the relationship between the bulk volume and weight. The weight of the printer ranged between 6.7 and 54.5 kg. The bulk volume was estimated by photo image as described in Appendix 2. The relationship between the bulk volume and the initial weight can be expressed by Eq. (1):

$$W_0 = 317.96 V_{bulk} \qquad (1)$$

3 Results of the Burning Tests

3.1 Combustion Behavior by Type of Printer

Figure 3 shows the combustion behavior photographed by VCR2. The printers were divided into four types (i.e., black and white laser printer, color laser printer, inkjet printer, and all-in-one printer).

Laser printers (Fig. 3a, b) took a long time to initiate fire growth. The combustion behavior was seen in the following order: (i) the part heated by the burner was melted after a long time and created an opening; (ii) the materials inside of the printer were burnt at the melted opening as similar to a ventilation-controlled compartment fire; (iii) the upper surface gradually melted, and an external flame was ejected from the upper opening; (iv) the flame spread to the whole upper surface; (v) and the burning spread to the side surfaces.

On the other hand, the inkjet printer shown in Fig. 3c had approximately 4 min of incubation time, and the flame spread faster owing to the combustion of the

(a) B_Laser Case of Test 2. Specimen | 4′00″; No change | 14′00″; Start of inside burning | 34′00″; Flame growth and flame from top | 36′00″; Flame from top | 40′00″; Peak burning

(b) C_Laser Case of Test 3. Specimen | 4′00″; No change | 24′00″; Start of inside burning | 36′00″; Continues burning inside | 38′00″; Flame growth and flame from top | 80′00″; Peak burning

(c) C_Inkjet Case of Test 8. Specimen | 4′00″; Melting and burning of the surface | 6′00″; Fire growing and burning of the paper rest | 8′00″; Flame moving along the paper rest | 10′00″; Flame moving to the top surface | 12′00″; Peak burning

(d) A_Inkjet Case of Test 12. Specimen | 4′00″; Melting and burning of the surface | 6′00″; Fire growing | 8′00″; Flame moving to the top surface | 10′00″; Flame moving to the top surface | 28′00″; Peak burning

Fig. 3 Representative examples of combustion behaviors: **a** B_Laser, **b** C_Laser, **c** C_Inkjet, and **d** All_Inkjet recorded by VCR2

paper support (plate supporting the paper). The combustion behavior was seen in the following order: (i) the part heated by the burner was melted and started to burn; (ii) the flame spread to the side of the printer as the paper support was melted down; and (iii) the flame spread to the whole surfaces in a short time as the flame propagated to the upper part of it.

In the case of all-in-one printer shown in Fig. 3d, the flame spread over the surface similar to the combustion behavior of the inkjet printer.

Heat release rate was measured at every 1 s, and the results are shown for the laser printer (Fig. 4a) and the inkjet printer (Fig. 4b). The heat release rates of laser printers varied among specimens. The initial incubation time t_0 was generally 15 min, except for Test 1 with a small laser printer of 6.81 kg. In the cases of Test 4 and Test 6, the location of the ignition source had to be changed by about 1 cm at 13 min 30 s and at
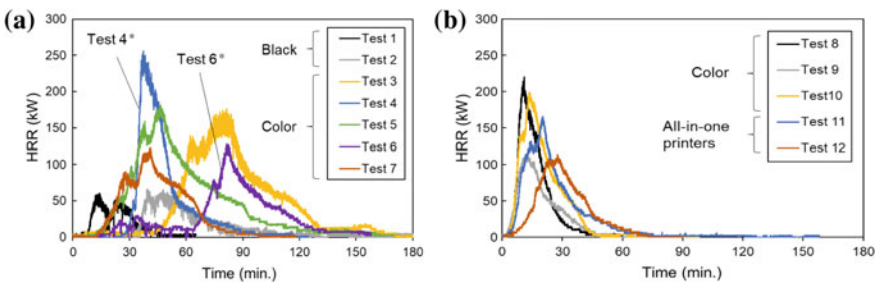
Fig. 4 Measured heat release rates of **a** laser printers and **b** inkjet printers

20 min 23 s, respectively. As the combustible materials around the gas burner were melted away, it was suggested that further heating by gas burner would not reach ignition at the initial position. The heat release rate gradually increased after moving the gas burner. The inkjet printer generally increased the heat release rate around 4–6 min and reached at around 10–30 min. The combustion was almost finished before 60 min.

3.2 Ratio of Combustible Materials

Figure 5 shows the measured results of the weight. Figure 5a shows the initial weight, the weight after the experiments, and the weight of non-combustible materials. The weight of non-combustibles (e.g., metal or glass) was measured by removing the unburnt residual material adhered to the specimen by using a hammer and a steel brush. Figure 5b shows the weight ratio of combustible materials. The ratio of combustible materials is the ratio of the combustible material weight to the initial weight. The weight of the combustible material is obtained by subtracting the weight of non-combustible materials from the initial weight. The weight ratio of combustible materials decreased according to the initial weight; however, the ratio seems to converge to a constant value. Here, when the initial weight of the specimen was 17.1 kg or less, the ratio of the combustible material was about 0.6–0.7. In the specimens with an initial weight of 24.5 kg or more, the ratio of the combustible material was about 0.4–0.5. Previous study on small home appliances showed that the ratio was about 0.4 [7]. The measured results in this study were slightly larger than that of the previous study.
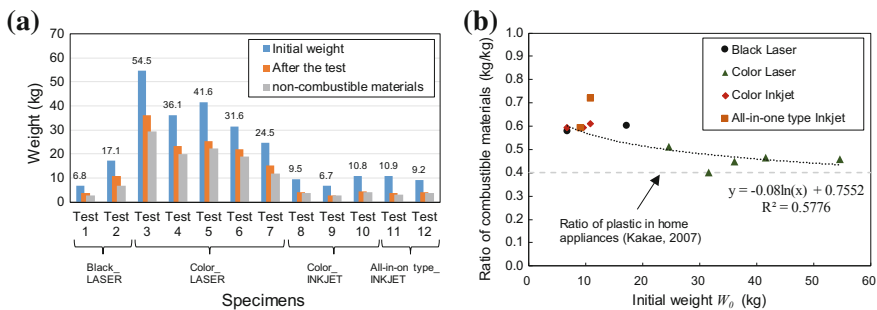
Fig. 5 Measurement results of **a** the initial weight, after the test, and the non-combustible materials and **b** the ratio of combustible materials

4 Relationship Between the Initial Weight and Shape of the Printer and the Combustion Behavior

4.1 Heat of Combustion and Fire Load

The relationship between weight loss and THR is shown in Fig. 6a. The inkjet printer and the laser printer showed different magnitudes of slopes. The slope indicates the heat of combustion ΔH_c of each group of printers. The heat of combustion of the inkjet printers was 31.7 MJ/kg and that of the laser printers was 24.7 MJ/kg. Figure 6b shows the relationship between the initial weight of the printer and the estimation of THR at the time of complete combustion [hereinafter, fire load (G_f)]. Here, the fire load is estimated by Eq. (2), where W_r stands for the weight of the remaining combustible materials (kg), and it is the weight difference between the weight after combustion and the weight of non-combustible materials. In the estimation, the heat of combustion obtained in Fig. 6a was applied to each printer type. The graph also shows the results of the burning test of rigid plastic household appliances in literature [3].

$$G_f = \text{THR}_{\text{measured}} + (W_r \times \Delta H_c) \tag{2}$$

The measurement results in this study were included in the range of the upper and lower limits of the standard deviation of the measurement results of rigid plastic household appliances [3]. The result of the inkjet printer was close to the upper limit and that of the laser printer was smaller than the average. The relationship between the initial weight and the fire load, which was differentiated by the type of printer, is shown in Eq. (3).

$$G_f = 20.0 W_{0,\text{inkjet}}, \quad \left(9.23\,\text{kg} \leq W_{0,\text{inkjet}} \leq 10.92\,\text{kg}\right)$$
$$G_f = 11.3 W_{0,\text{laser}}, \quad \left(6.81\,\text{kg} \leq W_{0,\text{laser}} \leq 54.54\,\text{kg}\right) \tag{3}$$
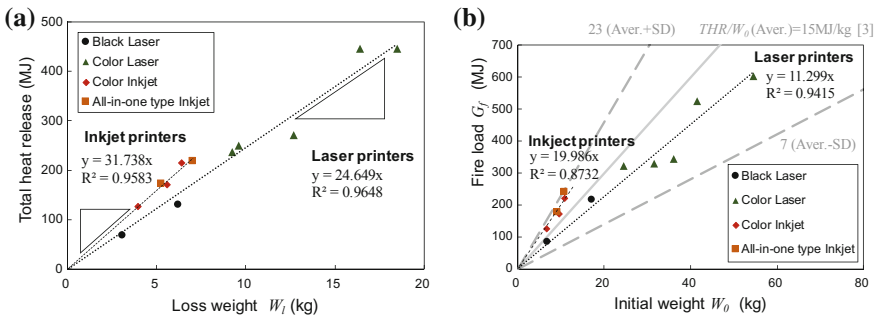
Fig. 6 Relationship **a** between weight loss and total heating rate and **b** between initial weight and fire load of printer G_f
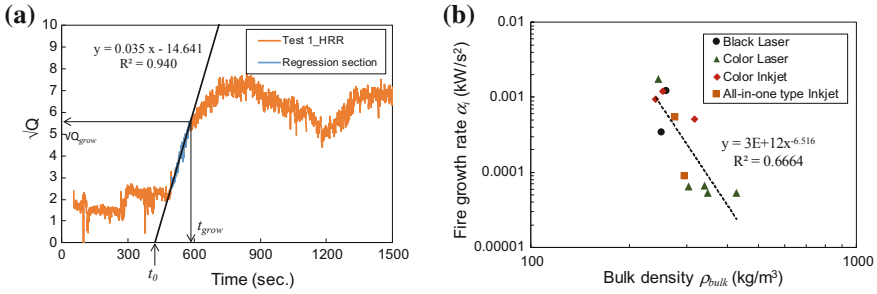
Fig. 7 **a** Relationship between time, $\sqrt{Q}$, and initial fire growth rate α_i on test 1, **b** relationship between bulk density and initial fire growth rate

4.2 Relationship Between Bulk Density and Initial Fire Growth Rate

The heat release rate during initial growth is often expressed by the relationship with the square of time (s) [12]. The correlation coefficient of this relationship is defined as the fire growth rate α_i [kW/s^2] [13]. The fire growth rate is obtained by making the best fit of the square function of time to the measured HRR [13, 14]. In this study, the fire growth rate was obtained by plotting the square root of HRR $Q^{1/2}$ versus time as shown in Fig. 7a. The portion with the largest inclination and the straight line was defined as the regression section. The slope in the regression section was considered as the square root of fire growth rate $\alpha_i^{1/2}$. Here, the initial fire growth rate is expressed by Eq. (4) using Q_{grow}, growth end time t_{grow}, and incubation time t_0. The incubation time t_0 is obtained as the intercept to the horizontal axis.

$$\alpha_i = Q_{\text{grow}}/(t_{\text{grow}} - t_0)^2 \tag{4}$$

Figure 7b shows the relationship between the fire growth rate and bulk density. The fire growth rates of rigid plastic were very small (0.00005–0.00176), and the fire growth rate sharply decreased with increasing bulk density.

4.3 Relationship Between the Shape of Specimens and the Maximum Heat Release Rate

In Fig. 8a, the maximum heat release rates were plotted versus bulk surface area A_s. The guideline equation [3]

$$Q_{\text{max}} = 272A_s \tag{5}$$
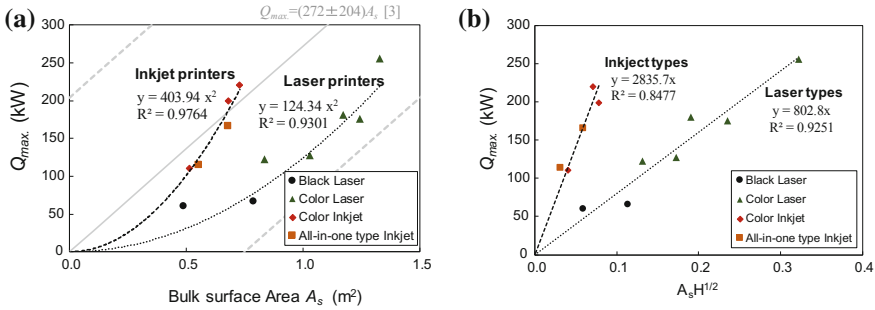
Fig. 8 Relationship **a** between surface area A_s and Q_{max}, **b** and between ventilation factors $A_s H^{1/2}$ and Q_{max}

is also plotted in the graph. However, the relationships were not proportional to the bulk surface area. Square functions fit better to the measured data. The correlation coefficient of the inkjet printer (material: PS-HI) was larger than that of the laser printer. Figure 8b shows the relationship between maximum heat release rates and the nominal ventilation factors $A_s H^{1/2}$. The relationships are fairly linear. As was already shown in Fig. 3, the main route of fire spread was inside of the casing, rather than the side surfaces especially in case of laser printers. Thus, the burning was controlled by ventilation into the casing through holes created over surfaces. Assuming that the holes were created uniformly over the surface, the ventilation factor would be proportional to the nominal ventilation factor $A_s H^{1/2}$. As a result, the maximum heat release rate is proportional to the nominal ventilation factor.

5 Conclusions

A series of burning tests was conducted on a variety of printers with different printing principles, weights, and volumes. The printers used in this experiment weighed between 6.7 and 54.5 kg had a bulk volume of 0.026–0.147 m³ and had a projected surface area of the specimen from 0.49–1.33 m². In the burning test, the HRR was measured by the open calorimeter, and the weight loss was measured by using a load cell. The material analysis showed that the main material of the inkjet printer was "PS-HI (high-impact polystyrene)," and that of the laser printer was "ABS-FP(40) or PC+ABS-FP(40)." The following results were obtained by experiments:

(1) The combustion behavior and the heat of combustion varied by the printer type. As for the inkjet printer, the outer surface material melted in approximately 3–4 min, which was a relatively short period. The internal combustion through the melted hole and the spread of the surface material's combustion occurred at the same time. As for the laser printer, it took a long time to melt the outer casing

material by an ignition source, approximately 15 min or longer. The combustion took place inside of the casing through the holes created by melting.

(2) The heat of combustion of the inkjet printer, mainly composed of PS-HI, was 31.7 MJ/kg, and that of the laser printer, mainly composed of ABS-FP(40), was 24.7 MJ/kg.

(3) The relationship between initial weight and fire load was established by categorizing the printers into inkjet and laser.

(4) The fire growth rate α_i was between 0.00005 and 0.00176 kW/s^2, which was inversely proportional to the bulk density.

(5) The maximum heat release rate of the printers made of rigid plastic was proportional to the nominal ventilation factor $A_s H^{1/2}$, where A_s is the bulk surface area, and H is the height.

Appendix 1: Properties of Plastics

Table 3 shows the physical properties of high-impact polystyrene (PS-HI) and ABS related to the combustion experiment [15, 16].

Appendix 2: Method for Finding the Projected Area and the Bulk Volume of Printer by Image Analysis

Five surfaces of specimens except the bottom surface were recorded as shown in Fig. 9. During the recording, a sticker of 75×75 mm size was attached on the surface of a printer. The number of pixels of the sticker and a printer was calculated by using an image analysis software, and the projected area of each face was calculated by using Eq. (6). The sum of the projected area of five surfaces was set as a bulk surface area A_s. Bulk volume V_{bulk} was calculated by Eq. (7) by using the projected surface

Table 3 Measurement items

Type of plastic	Continuous heat resistance temperature (°C)	Thermal deformation temperature (18.5 kg/cm^2)	Flame rate (flame resistance)
PS-HI	66–77	104 (Maximum)	Slow
ABS	60–110	94–107	Slow
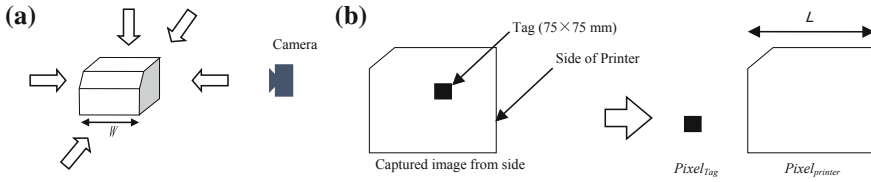
Fig. 9 **a** Take a picture of five surfaces. **b** Using the image analysis software (Image J), obtain the pixel number, respectively

area of a specimen A_{side} and the width of the measured specimen. Bulk density ρ_{bulk} was calculated by Eq. (7).

$$A_s = A_{\text{Tag}}/\text{pixel}_{\text{Tag}} \times \text{pixel}_{\text{ALL}} \tag{6}$$

$$V_{\text{bulk}} = A_{\text{side}} \times W, \quad \rho_{\text{bulk}} = W_0 \times V_{\text{bulk}} \tag{7}$$

References

1. Kaibundo Publishing Corporation. (2001). Nendo hinan anzen kenshō-hō no kaisetsu oyobi keisan rei to sono kaisetsu (in Japanese).
2. Kaibundo Publishing Corporation. (2001). Nendo taika anzen kenshō-hō no kaisetsu oyobi keisan rei to sono kaisetsu (in Japanese).
3. Architectural Institute of Japan. (2013). Recommendation for Design Fire Loads and Fire Actions in Buildings.
4. Architectural Institute of Japan. (2017). Recommendation for Design Fire Resistant Design of Steel Structures.
5. Takahashi, W., & Sugawa, O. (1997). Zairyō no nenshō to sono seisei-mono (in Japanese). *Fire handbook* (No. 13.1).
6. Yoshida, M., & Tomohiro, N. (2006). Kasai anzen sekkei ni mochiiru sekkei hi-gen to shite no shūnō kanen-mono no nenshō seijō (in Japanese), BRI-H18 Lecture text (pp. 109–110).
7. Kakae, N. (2007). Jitsuzai kanen-mono no hatsunetsu sokudo yosoku shuhō no kōchiku (in Japanese). Doctoral thesis of Kyoto University, pp. 108, 208–209.
8. Mizuno, T., & Yamada, H., et al. (1998). Experimental study on burning behaviour of chairs: Part 1–Part 2. Summaries of technical papers of annual meeting Architectural Institute of Japan 1998 (pp. 209–211).
9. Ohmiya, Y., Lee, J., Shintani, Y., Jo, A., & Kitahori, J. (2017). Field survey of fire load using a 3D scanner—Part 2 Outline of the survey, Field survey of fire load using a 3D scanner—Part 3 Data for prediction of local and traveling fire. In *Proceedings of JAFSE Annual Symposium 2017* (pp. 112–115).
10. Lee, J., Jo, A., Kitahori, J., Shintani, Y., Ohmiya, Y., & Harada, K. (2017). Field survey of fire load using a 3D scanner—Part 1 Outline of the survey, Part 2 Comparison of heat release rate with original and using 3D scanner, Part 3 Change over the years of furniture. Summaries of technical papers of annual meeting Architectural Institute of Japan 2017 (pp. 411–416).
11. ISO 24473. (2008). Fire tests—Open calorimetry—Measurement of the rate of production of heat and combustion products for fires of up to 40 MW. International Standardization Organization.

12. Nelson, H. E. (1987). An engineering analysis of the early stages of fire development: The fire at the Dupont Plaza Hotel and Casino on December 31, 1986. NBSIR 87-3560, U.S. Department of Commerce, National Bureau of Standards (NBS), Gaithersburg, Maryland, May 1987.
13. NFPA 72, "National Fire Alarm Code," 1999 Edition. Quincy, Massachusetts: National Fire Protection Association.
14. Natori, A., Kakae, N., Kitahori, J., Tsuchihashi, T., Abe, T., Nagaoka, T., et al. (2006). Development of a simple estimation method of heat release rate based on classification of common combustibles into groups. *Fire Science and Technology, 25*(1), 31–54.
15. Ohe, H., & Matsuura, K. *On heat of combustion of high polyrneric materials and their oxygen indices* (Vol. 23, No. 2, pp. 161–169). Research report of Faculty of Engineering, Fukui University.
16. The Chemical Society of Japan. *Handbook of chemistry: Pure chemistry* (5th ed.).

The Breakage Behavior of Different Types of Glazing in a Fire

Yu Wang

Abstract Different from concrete and steel, window glass or glass façade breaks very easily when subjected to a compartment fire. The new vent created by the glass fallout may cause fire spread out and fresh air entrance which can markedly change the enclosure fire dynamics. Nowadays, different types of glazing, such as clear, coated, ground and multi-pane glazing, are increasingly employed in newly constructed buildings. However, very little is known about their fire risk, especially the comprehensive comparison between them is yet to be investigated. In this paper, the fire resistance comparison of different types of glazing is conducted based on the author's very recent and ongoing experimental results. Literature works of other researchers are also presented for comparison. Additionally, fire safety design and recommendation of glass in buildings are discussed in detail. This research is proposed to provide valuable references for the fire safety performance-based design of glass façades in high-rise buildings.

Keywords Glass type · Fire · Thermal breakage · Fire resistance

1 Introduction

Glass has many advantages, such as high transparency, long-term durability and good esthetics. Therefore, to satisfy the high requirement of building esthetic consideration, glass is extensively used both in envelopes and structures of modern constructions [1, 2]. However, compared with concrete and steel, glass is considerably more prone to breaking due to its brittleness while encountering a huge fire. After the glass breaks, it would fall out with a high probability which may create a new vent in a building fire. This vent could result in a flashover or backdraft that will significantly accelerate the fire development of a compartment [3]. Recently, two fire disasters that, respectively, occurred in China and the UK on June 2017: the Hangzhou residence fire [4] and London Grenfell Tower fire [5]. In both fires, after the glass was broken by a compartment fire, the ejected flame went higher and broke

Y. Wang (✉)
School of Engineering, University of Edinburgh, Edinburgh EH9 3JL, UK
e-mail: Yu.Wang@ed.ac.uk

the window upstairs, causing bigger disaster. This occurred regardless of the existence of combustible cladding. Both fires demonstrate that the glass breakage and fallout caused by fire heating are very important to the fire development in modern high-rise buildings.

This research issue was first highlighted by Emmons [6]: 'there is one structural problem of importance to fire growth and this is the breaking of window glass.' Subsequently, a large number of theoretical, numerical and experimental investigations were conducted. For example, Keski-Rahkonen [7, 8] calculated the critical breakage conditions of a glass panel with circular and square dimensions. Skelly et al. [9] heated the glass panel in a designed compartment model and determined the temperature difference of glass breakage of approximately 90 °C. Pagni et al. [10, 11] developed a software for the time prediction of single and double glazing breakage in a fire. In recent years, more research started to focus on the glass façade other than the four-edge-covered window glass panel. Wang et al. [12, 13] first investigated the fire performance of point-supported glass façade and found that the combination of mechanical and thermal stress is responsible for the crack initiation at fixing points. Through full-scale experiments, Chow et al. [14, 15] studied the effect of smoke movement on the breakage of double skin façade, and the cavity depth was optimized according to the experimental results. Shao et al. [16, 17] conducted full-scale experiments to investigate the efficiency of sprinkler protection for float and toughened glass façades. All previous studies indicate that the glass breakage in fires may be affected by a large number of factors. It is anticipated that the glass type also has a significant influence on the thermal breakage of glass. Considering the increasing number of various types of glazing used in buildings, it is of great importance to study the fire performance of different types of glazing.

However, the comparative study of different kinds of glazing is very limited [1, 18]. In particular, some new types of glazing, such as low-E, coated and multi-pane glazing, are employed extensively, which may cause potential fire risk for buildings. In the present work, the comparison of these glasses is systematically addressed for the fire safety design based on the author's previous and ongoing experimental work. The details and results of experiments are reviewed, and the design recommendations are proposed.

2   Different Types of Single Glazing

A large number of studies have focused on the fire performance of single glazing. The glass types include clear, coated, ground, wired, low-E, etc. In this section, all these glasses are discussed based on our previous experimental work. Toughened glass is also selected to make a comparison.

We select the clear float glass as a reference. In our previous work [19], both clear and low-E glasses with a dimension of $600 \times 600 \times 6 \text{ mm}^3$ were heated under uniform radiation conditions in a well-designed facility. A radiation panel with a maximum power of 90 kW was utilized to provide adequate heat making the glass

break. The experimental results have shown that the critical temperature differences of clear float glass and low-E glass were 95 and 108 °C. The critical breakage condition of clear float glass was very similar to the results obtained by Skelly et al. [9] who established that the edge-protected tests resulted in breakage at an average temperature of 90 °C. In addition, under a pool fire condition, another study [20] highlighted that the clear float glass can withstand the temperature difference that is slightly more than 90 °C (94 °C). Therefore, we estimate the critical temperature difference of clear float glazing is 90 °C, and other kinds of glass are compared to this value. Then, the critical temperature difference of low-E glass is 14% higher than clear ones according to [19].

For coated glass pane, a 500×500 mm^2 heptane pool fire was placed 750 mm away from glass panel with a dimension of $600 \times 600 \times 6$ mm^3 [21] as shown in Fig. 1. A total of sixteen tests were performed. The experimental results indicated that regardless the installation form, the critical breakage condition of coated glass is around 80 °C, which is smaller than that of clear ones.

To clarify the difference in critical breakage condition, quasi-static tensile experiments were conducted using Material Testing System 810 (MTS 810) to explore the strength of clear, coated and ground glass panes [22]. As exceeding tensile stress is the primary cause of the crack initiation of glass in a fire [7, 23, 24], the direct measurement of this parameter can give a very good reference of glass fire resistance. All glass samples were designed in the shape of a 'dog-bone.' Their thicknesses were 6 mm. The overall length and width of each sample were 265 and 20 mm, respectively. The central part of the sample, with a length of 55 mm and width of 10 mm, was the testing section as shown in Fig. 2a. It should be noted that the specimens were cut
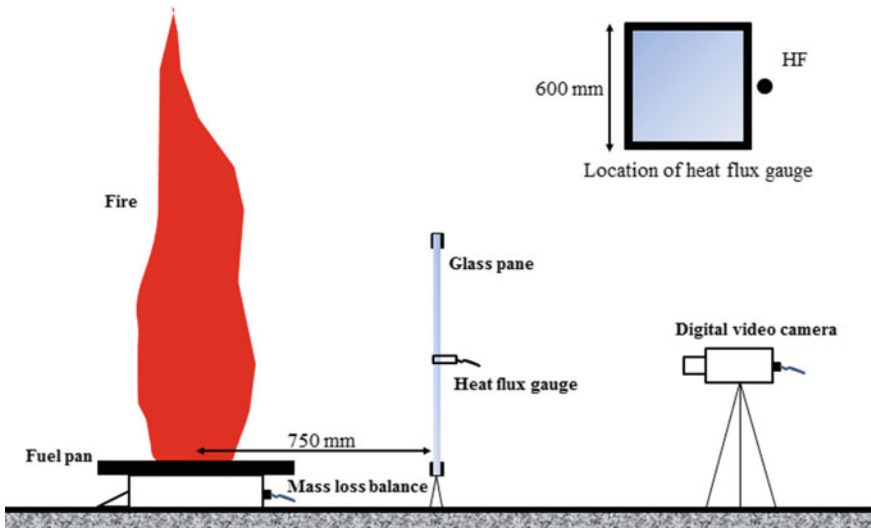
Fig. 1 Schematic of the experimental system with heat flux gauge and thermocouple distributions for coated glazing test [21]

(a) Before and after test, clear glass   (b) Coated (up) and ground glass

(c) The temperature measurement by R type thermocouple and strain measurement by extensometer.
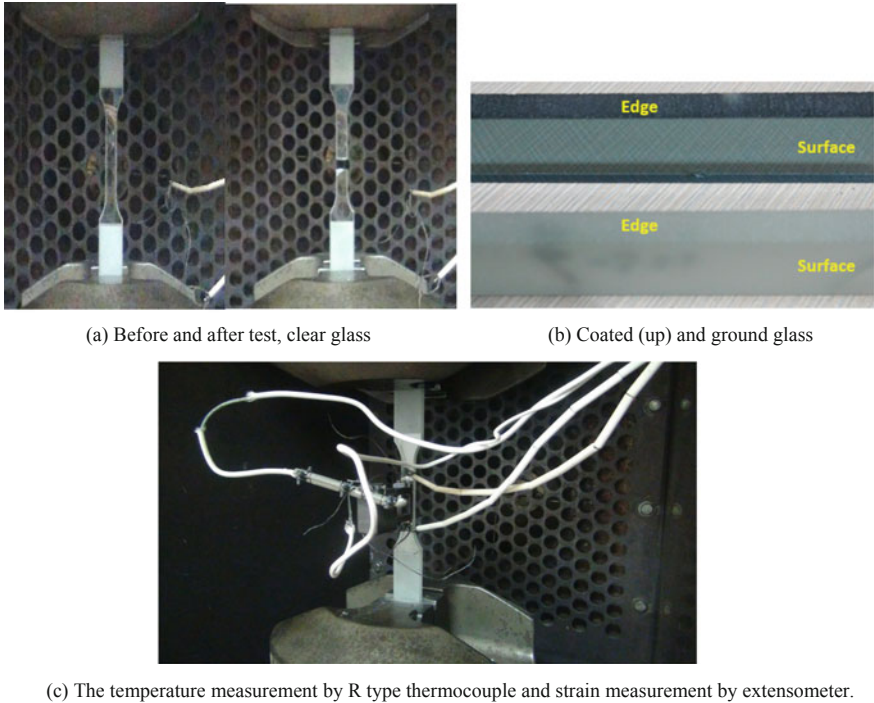
Fig. 2 Specimen in MTS 810, before and after testing [22]

by water knife with a diameter of 1 mm. The cross sections and surface conditions of coated and ground glass are shown in Fig. 2b. For each type of glazing, seven specimens were repeated. For clear, coated and ground glass, the tensile strengths were 35.7, 32.9 and 31.0 MPa [22]; the standard deviations were, respectively, 1.3, 1.0 and 2.0. It was found that the fire resistance order is clear glass, coated glass and ground glass. The relationship between the clear and coated glass is consistent with the full-scale tests in a real fire which confirms the rationality of this tensile tests. For clear glass pane, its tensile strength is 35.7 MPa, while 31.0 for ground one. Thus, from this work, it can be established that the critical tensile strength of clear glass is about 15% higher than the ground one.

Harada et al. studied the wired and float glass panel heated by a propane radiation panel [25]. For wired glass without the lateral restraint, the temperature difference at the initial crack was 22 °C. It should be noted that the thickness of the wired glass was 6.8 mm which was larger than that of 3 mm of float one. Despite the different thicknesses, the average critical temperature difference of float glass without lateral restraint was around 52 °C which was two times more than a wired one. From the comparison, it can be seen that the wired glass pane is the most prone to breakage in a fire. The existing micro crack caused by the wires in glazing may be primarily responsible for the relatively poor fire resistance. The thicker float glass normally has

better fire resistance [26], so the wired glass in this work is considered much weaker than the 6 mm float clear one. Here, it is assumed to ignore the effect of 0.8 mm thickness, and concluded that the wired glass is 58% smaller than that of clear float glass.

All the above-mentioned glasses are float glass, i.e., they are not tempered. However, tempered glass is increasingly used in high-rise buildings instead of ordinary float glass, which has been addressed in the previous work [27–29]. No matter the tempered glass is installed as frame-supported or point-supported glass façades, its fire resistance is significantly better than float one. For example, when the glass was placed 350 mm from the pool fire, no cracks were observed, while the float glass cracked at 89 s under an identical condition during experiments [29]. Figure 3 demonstrates that the tempered glass bent at the final stage but did not break when directly heated by flame radiation. In the authors' ongoing experiments, eleven 6 mm-thick-tempered glass panels were heated in a compartment model with a dimension of $1000 \times 1000 \times 1000$ mm^3. It was concluded that the average critical temperature difference is 357 °C, which is around four times more than that of clear float glazing. This result is similar to the previous studies which indicated the critical temperature difference of tempered glazing was above 300 °C [28, 30]. However, it should be noted that the compartment ventilation condition change caused by glass fallout is a very important issue. The process comparison is shown in Fig. 4, in which the crack initiation time is set as 0 s. It can be found that the tempered glazing fell out completely within 1 s once the first crack was initiated, while float one with much earlier crack initiation may fall out gradually. This difference may markedly affect the compartment fire dynamics.

Based on the reference object of float clear glass, the fire resistance of different kinds of glazing is summarized in Fig. 5, where the fire resistance of clear float glass is set as 1. According to these studies, the order of single glazing is tempered glass, clear glass, coated glass, ground glass and wired glass. The reason for the high thermal resistance of tempered glass is because its manufacture process is markedly different from that in the other types of glass. Tempering puts the outer surfaces into compression and the inner surfaces into tension. The strengths of coated and ground glass are relatively small since the surface treatment during manufacturing results in

(a) Initial stage, straight glass   (b) Final stage, bent glass
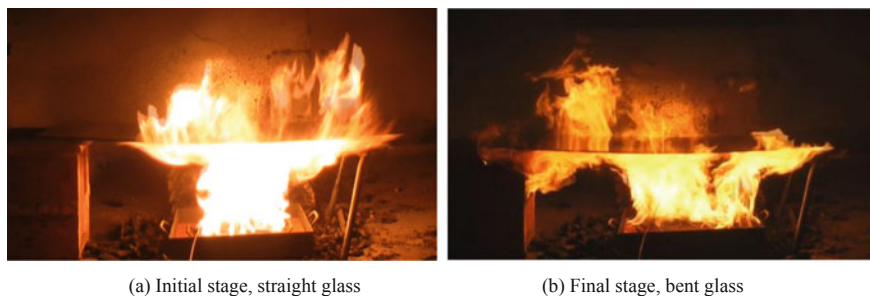
Fig. 3 Tempered glass heated by a 300×300 mm^2 pool fire [29]

0.00s   0.22s   0.44s   0.80s

(a) The fallout of tempered glazing

0s   57s   69s   70s

(b) The fallout of float glazing
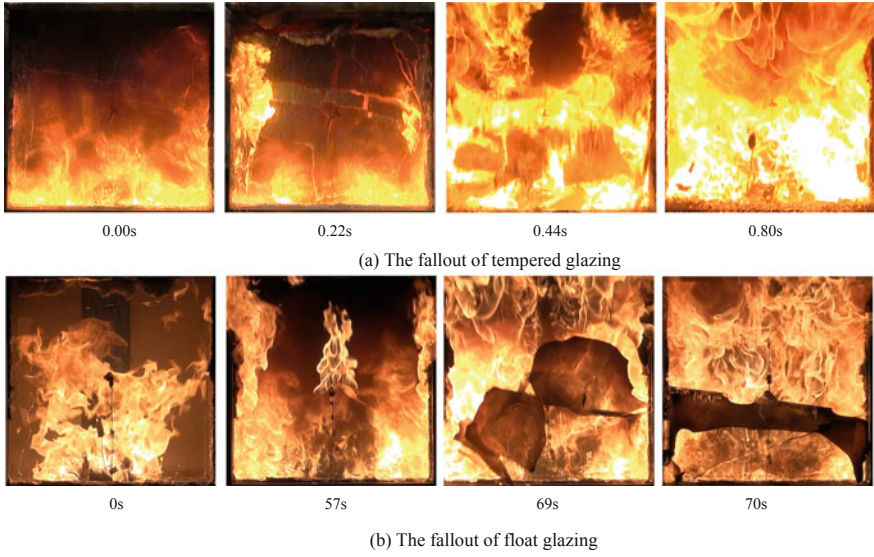
Fig. 4 Fallout process comparison of single tempered and float glazing

Fig. 5 Fire resistance comparison of different types of single glazing
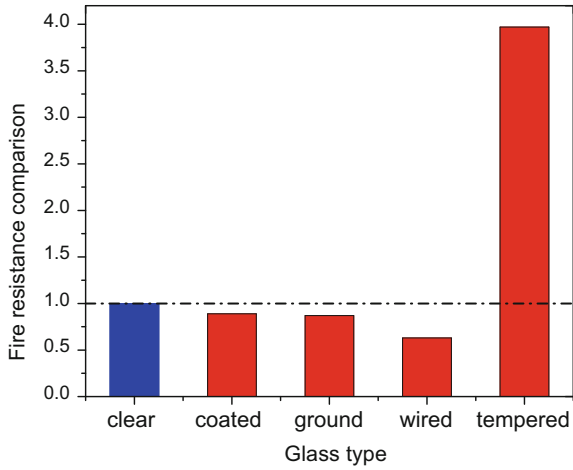
(a) Clear glass   (b) Ground glass
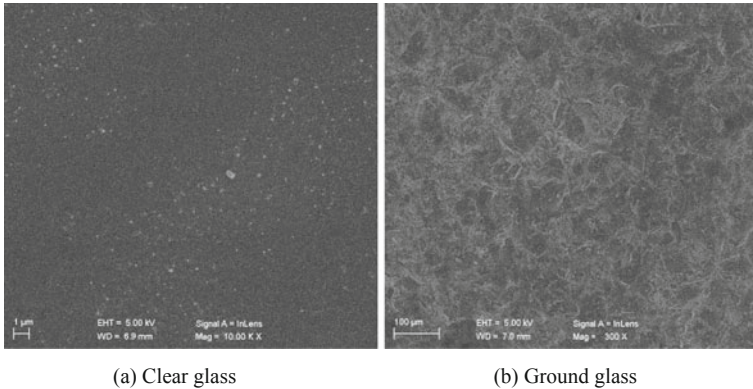
Fig. 6 Surface conditions of clear and ground glasses

more tiny flaws or defects than clear ones [22]. Figure 6 demonstrates the surface conditions of clear and ground glass. Critical breakage condition of wired glass is low because it is difficult to be cut, and many defects would exist at the cutting edge even before heating [25]. The micro cracks around wire may also be the reason for its breakage behavior which needs to be investigated further.

3 Different Types of Multi-pane Glazing

Compared with single glazing, fewer studies have been conducted on the behavior of multi-pane glazing in a fire. In this section, insulated, laminated and triple-pane glazing will be discussed based on the previous work.

Most of the multi-pane glazing work is concerning the installed glazing (IG), more commonly known as double glazing. Cuzzillo and Pagni [10] first developed a theoretical model and calculated the temperature using an in-house software McBreak. Shields et al. [31] installed the double glazing panels in the front wall of the ISO 9705 room and heated them using pool fires. A simple lumped model approach was developed to predict the response of the glazing to thermal insult. In their tests, the double glazing may withstand for more than 23 min in corner fire, while the maximum time of about 11 min for single glazing under similar conditions. The result shows that the double glazed systems consistently perform much better regarding the provision of integrity [31]. It is similar to the conclusion of Mowrer's double glazing window study [32].

These works are primarily about the double glazed window. However, very little is known about the fire performances of insulated glazing in curtain walls and its potential influence on fire dynamics. In our very recent work, the installed glazing with different air gap thickness and installation forms were heated by a 500×500 mm^2 pool fire [33]. It was found that semi-exposed framing glass façades last

longer before breaking than those of fully exposed framing glass, but are more prone
to falling out. The behavior of ambient side panel is related to the fallout of fire side
pane. Figure 7 shows the breakage and fallout of insulated glazing in the experi-
ments. Fallout occurred in the tests of horizontal and vertical hidden glass façades.
To determine the critical breakage condition of insulated glazing, the burner-glazing
distance was changed from 750 to 450 mm, and the fuel mass was increased from
2 to 6 kg [34]. It was found that the critical heat flux of double glazing is more
than 25 kW/m^2, while 6 kW/m^2 for single glazing. From the experimental tests in
which the insulated and single glazing were heated under a similar condition [18], the
installed glazing failure time is 366 s and the average of single glazing breakage time
is 157 s. It should be noted that the single glazing was coated, and the burner-glazing
distance of insulated glazing was smaller than that in single glazing test. Generally,
it can be concluded the fire resistance of insulated glazing is two or three times of
single ones [18, 31].

Very little work has been conducted for laminated glazing in a fire. Manzello et al.
[28] compared the single and laminated tempered glazing in a real compartment fire.
After the fire, all the single glazing fell out, but the unexposed panel of laminated
glazing still kept in place and intact. The results show that the laminated glazing
has a very excellent fire performance even in a real fire situation. In our recent study
[18], under an identical condition (burner-glazing distance of 750 mm and 2 kg fuel),

(a) Exposed framing   (b) Horizontal hidden   (c) Vertical hidden

(c) Thermocouples in double glazing
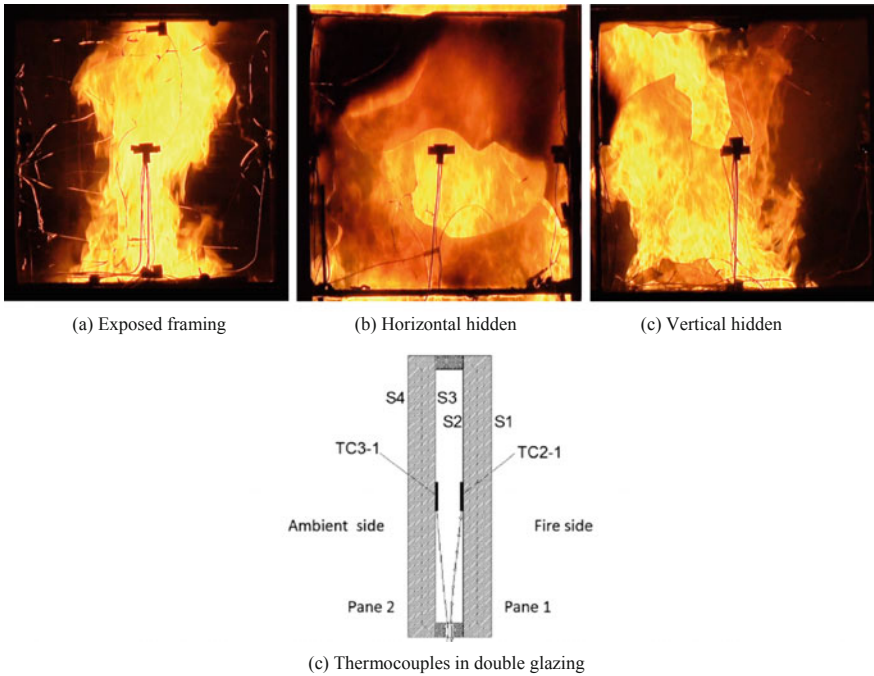
Fig. 7 Behavior of insulated glazing installed in different forms [33]

the average breakage time of single float glazing is 157 s, while 118 and 199 s for the exposed and unexposed side panes of float laminated glazing, respectively. This result is consistent with the study of Manzello et al. [28]. It can be concluded that the fire resistance of laminated glass is about 27% higher than that of clear single glazing. Although the fire resistance of laminated glazing is not as good as insulated glazing, it can keep intact in a fire which still can provide a barrier preventing the fire spreading out.

Therefore, from the above study of the double glazed system, it can be projected that the fire resistance will increase significantly when employing triple-pane glazing specimens. To the author' knowledge, the study by Klassen et al. [35] is the only open literature that addresses this issue. The triple-pane glazing was laminated by interlayer and air gap. For incident heat fluxes 30 kW/m^2 or lower, the triple-pane glazing samples had a total transmittance less than 10% of the incident heat flux, back-side surface temperatures did not exceed 100 °C. For double-pane laminates, the total transmittance was less than 25% of the incident heat flux, the back-side temperature did not exceed 220 °C. However, what is interesting is that the fire exposed pane of triple glazing broke earlier than the double-pane laminated glazing at the given incident heat flux. It is because the exposed panel of the triple-pane glazing samples was isolated from the two inner panes by an air gap; this feature allowed for the more rapid development of thermal stresses in the outer pane and faster breakage times. In most tests, the unexposed panel did not break, which shows its good fire resistance. However, it is difficult to compare the double and triple glazing in this work as no complete failure was reported. Therefore, more tests concerning complicated glass structures need to be conducted in the future, which is believed to be helpful for their fire resistance evaluation. However, as the mechanism of double glazing and laminated glazing is being well understood, the numerical simulation should be more suitable for trip glazing rather than more experimental tests.

According to the above analysis, we select the float clear single glazing as the reference, and the fire resistance comparison of different multi-pane glazing is shown in Fig. 8. The fire resistance is determined by the failure time of the unexposed panel which represents the failure of the whole glazing system. The mechanism of these differences is the heat transfer and thermal stress in glazing [10, 18]. The thermal resistance of air gap is much larger than interlayer material. However, it should be noted that in experiments insulated glazing will fall out more easily due to the weakness in perimeter sealer [33], while laminated glazing can keep intact despite both of panel break. Therefore, before glass type selection, more factors should be considered based on the state of art in this area.

Fig. 8 Fire resistance
comparison of different
types of multi-pane glazing
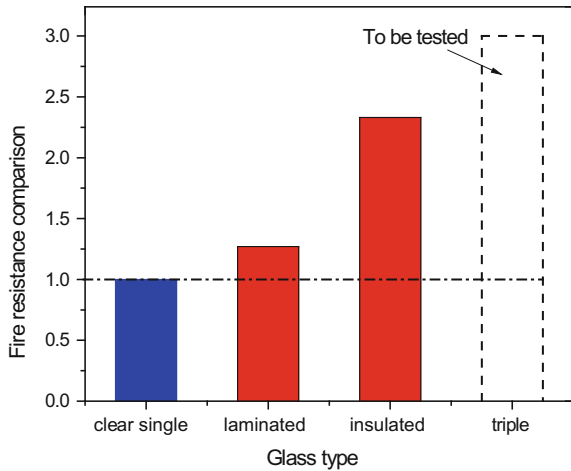
4 Conclusions

Increasing number of different glass types are employed in modern buildings, but
their performance may determine the fire spread way and speed, which will challenge
the whole building safety. A large number of studies have focused on the thermal glass
breakage in a fire. Ten years ago, most of the research in this area was concerning the
ordinary window glass. However, the objective is changing to glass façades in recent
years due to the high-rise building fire safety requirement. Regardless of the research
objective, glass type is always a major issue to be addressed. In particular, glass
products are becoming more diverse and often composited with other construction
materials. Thus, it becomes necessary to know the fire resistance of different types
of glazing.

The paper summarizes and discusses the fire resistance of glazing based on the
author's previous and ongoing studies and some other open literature. Only experi-
mental work is selected to be present so as to make the comparison more reasonable
and reliable. The fire resistance order of different kinds of glazing is provided. Tem-
pered and multi-pane glazings, especially laminated glazing, have much better fire
resistance, which is recommended to be used in engineering. However, these glasses
are considerably more expensive than float single glazing according to the price sur-
vey. What is more, they will inevitably increase the weight of façades. Thus, more
factors should be considered during the selection of glass type.

In the future, more new types of glazing would emerge in the industry, for which
fire resistance should continue to be tested to deepen the understanding of the glazing
thermal behavior. In addition, accurate heat transfer and breakage behavior models
need to be developed to benefit the fire performance prediction and risk evaluation.
Glass fallout in a fire is still a very challenging issue to be studied due to many
influence factors. Different types of glazing have different ways to fall out with
different mechanisms, and despite some island formed, sometimes no pieces fall

out which is very difficult to predict. More research is needed with considering the influence of fire and smoke on its fallout behavior, which is believed to significantly improve the building fire dynamic analysis. In addition, glass fire performance may also be improved by fire resistance coating or property optimization, which may need significantly more efforts in the future.

References

1. Debuyser, M., Sjöström, J., Lange, D., Honfi, D., Sonck, D., & Belis, J. (2017). Behaviour of monolithic and laminated glass exposed to radiant heating. *Construction and Building Materials, 130,* 212–229.
2. Axinte, E. (2011). Glasses as engineering materials: A review. *Materials and Design, 32,* 1717–1732.
3. He, Y., & Poon, L. (1988). Experimental observations and modelling of window glass breakage in building fires. *Fire Safety Science, 3,* 295–306.
4. https://zj.zjol.com.cn/news.html?id=679231.
5. https://en.wikipedia.org/wiki/Grenfell_Tower_fire.
6. Emmons, H. (1986). The needed fire science. In *Fire Safety Science-Proceedings of the First International Symposium* (pp. 33–53). IAFSS.
7. Keski-Rahkonen, O. (1988). Breaking of window glass close to fire. *Fire and Materials, 12,* 61–69.
8. Keski-Rahkonen, O. (1991). Breaking of window glass close to fire, II: circular panes. *Fire and Materials, 15,* 11–16.
9. Skelly, M. J., Roby, R. J., & Beyler, C. L. (1991). An experimental investigation of glass breakage in compartment fires. *Journal of Fire Protection Engineering, 3,* 25–34.
10. Cuzzillo, B. R., & Pagni, P. J. (1998). Thermal breakage of double-pane glazing by fire. *Journal of Fire Protection Engineering, 9,* 1–11.
11. Joshi, A. A., & Pagni, P. J. (1991). *Users' guide to BREAK1, the Berkeley algorithm for breaking window glass in a compartment fire*. National Institute of Standards and Technology, Building and Fire Research Laboratory.
12. Wang, Y., Wang, Q., Shao, G., Chen, H., Su, Y., Sun, J., et al. (2014). Fracture behavior of a four-point fixed glass curtain wall under fire conditions. *Fire Safety Journal, 67,* 24–34.
13. Wang, Y., Wang, Q., Sun, J., He, L., & Liew, K. M. (2014). Effects of fixing point positions on thermal response of four point-supported glass façades. *Construction and Building Materials, 73,* 235–246.
14. Chow, W., Hung, W., Gao, Y., Zou, G., & Dong, H. (2007). Experimental study on smoke movement leading to glass damages in double-skinned façade. *Construction and Building Materials, 21,* 556–566.
15. Chow, W., & Hung, W. (2006). Effect of cavity depth on smoke spreading of double-skin façade. *Building and Environment, 41,* 970–979.
16. Shao, G., Wang, Q., Zhao, H., Wang, Y., Sun, J., & He, L. (2016). Thermal breakage of tempered glass façade with down-flowing water film under different heating rates. *Fire Technology, 52,* 563–580.
17. Shao, G., Wang, Q., Zhao, H., Wang, Y., Chen, H., Su, Y., et al. (2014). Maximum temperature to withstand water film for tempered glass exposed to fire. *Construction and Building Materials, 57,* 15–23.

18. Wang, Y., Wang, Q., Wen, J. X., Sun, J., & Liew, K. M. (2017). Investigation of thermal breakage and heat transfer in single, insulated and laminated glazing under fire conditions. *Applied Thermal Engineering, 125,* 662–672.
19. Wang, Q., Wang, Y., Zhang, Y., Chen, H., Sun, J., & He, L. (2014). A stochastic analysis of glass crack initiation under thermal loading. *Applied Thermal Engineering, 67,* 447–457.
20. Wang, Y., Wang, Q., Sun, J., He, L., & Liew, K. (2016). Thermal performance of exposed framing glass façades in fire. *Materials and Structures, 49,* 2961–2970.
21. Wang, Y., Wang, Q., Su, Y., Sun, J., He, L., & Liew, K. M. (2015). Fracture behavior of framing coated glass curtain walls under fire conditions. *Fire Safety Journal, 75,* 45–58.
22. Wang, Y., Wang, Q., Shao, G., Chen, H., Sun, J., He, L., et al. (2014). Experimental study on critical breaking stress of float glass under elevated temperature. *Materials and Design, 60,* 41–49.
23. Joshi, A. A., & Pagni, P. J. (1994). Fire-induced thermal fields in window glass. 1. Theory. *Fire Safety Journal, 22,* 25–43.
24. Chowdhury, H., & Cortie, M. B. (2007). Thermal stresses and cracking in absorptive solar glazing. *Construction and Building Materials, 21,* 464–468.
25. Harada, K., Enomoto, A., Uede, K., & Wakamatsu, T. (2000). An experimental study on glass cracking and fallout by radiant heat exposure. In *Fire Safety Science—Proceedings of the Sixth International Symposium* (pp. 1063–1074). IAFSS.
26. Zhang, Y., Wang, Q., Zhu, X., Huang, X., & Sun, J. (2011). Experimental study on crack of float glass with different thicknesses exposed to radiant heating. *Procedia Engineering, 11,* 710–718.
27. Li, M., Lu, G., Hu, Z., Mei, X., Li, L., & Wang, L. (2014). Research on fire endurance of tempered glass based on infrared imaging technology. *Procedia Engineering, 84,* 553–557.
28. Manzello, S. L., Gann, R. G., Kukuck, S. R., Prasad, K. R., & Jones, W. W. (2007). An experimental determination of a real fire performance of a non-load bearing glass wall assembly. *Fire Technology, 43,* 77–89.
29. Wang, Y., Wang, Q., Shao, G., Chen, H., Su, Y., Sun, J., et al. (2014). Experimental study on thermal breakage of four-point fixed glass facade. In: *Fire Safety Science—Proceedings of the Eleventh International Symposium* (pp. 666–676). Christchurch, New Zealand: IAFSS.
30. Babrauskas, V. (2011). *Glass breakage in fires.* Fire Science and Technology, Inc. https://www.doctorfire.com/GlassBreak.pdf, 22.
31. Shields, J., Silcock, G. W., & Flood, F. (2005). Behaviour of double glazing in corner fires. *Fire Technology, 41,* 37–65.
32. Mowrer, F. W. (1998). *Window breakage induced by exterior fire.* Gaithersburg, MD: National Institute of Standards and Technology.
33. Wang, Y., Wang, Q., Su, Y., Sun, J., He, L., & Liew, K. M. (2017). Experimental study on fire response of double glazed panels in curtain walls. *Fire Safety Journal, 92,* 53–63.
34. Wang, Y., Li, K., Su, Y., Lu, W., Wang, Q., Sun, J., et al. (2017). Determination of critical breakage conditions for double glazing in fire. *Applied Thermal Engineering, 111,* 20–29.
35. Klassen, M. S., Sutula, J. A., Holton, M. M., Roby, R. J., & Izbicki, T. (2006). Transmission through and breakage of multi-pane glazing due to radiant exposure. *Fire Technology, 42,* 79–107.

The Moisture Evaporation Rate of Walls Revisited and Predicting Temperature Profile of Moisture Containing Walls Exposed to Fire

Tensei Mizukami and Takeyoshi Tanaka

Abstract Most building materials more or less contain moisture. It is often observed at temperature measurements at fire resistance tests and also at numerical calculations of heat conduction in walls containing moisture that the temperature rises stagnate around 100 °C for some time periods. This temperature stagnation significantly contributes to the high fire resistance performance of some types of wall, e.g., gypsum board. In this paper, the existing moisture evaporation rate formula has been revisited and re-examined the heat continuity equation from the standpoint of the existence of heat loss not only for moisture evaporation but also by raising the temperature of the wall. It reduces the number of uncertainties in the heat continuity equation and allows us to skip the step of regression fits to numerical simulation. The new formula is compared to the numerical calculation, and the range of application is validated.

Nomenclature

C_0	Specific heat of wall material (kJ/kg K)
C_w	Specific heat of water (kJ/kg K)
F	Fourier number (–)
F_ϕ	Fourier number corresponding to drying front (–)
C	Proportionality in ISO 834-11 (–)
D	Proportionality constant (–)
D_p	Temperature stagnation time in ISO 834-11 (min)
Δt_v	Temperature stagnation time (s)

T. Mizukami (✉)
National Institute of Land and Infrastructure Management, 1 Tachihara, Tsukuba, Ibaraki 305-0802, Japan
e-mail: mizukami-t92ta@mlit.go.jp

T. Tanaka
Kyoto University, Gokasyo, Uji, Kyoto 611-0011, Japan

L_v Latent heat of water evaporation (kJ/kg)
$\dot{q}''$ Conductive heat flux to drying front (kW/m^2 s)
T Temperature (°C)
ΔT Temperature rise (K)
t Time (s)
d_p Fire protection material thickness in ISO 834 (mm)
x Distance from exposed surface (m)
erfc() Complementary error function

Greek symbols

α Thermal diffusivity of wall material (m^2/s)
ϕ Mass ratio of moisture content to wall material (kg/kg)
λ Thermal conductivity of wall material (kW/m K)
ρ Density of wall material (kg/m^3)

Subscripts

c   Insulation criterion
ϕ At drying front
(x, t) At a given point in time and place
f   Fire
0   Initial
v   Water evaporation

1   Introduction

Most of the building materials more or less contain moisture. It is often observed at temperature measurements in fire resistance tests and also at numerical calculations of heat conduction in walls containing moisture that the temperature rises stagnate at around 100 °C for a certain time period, as shown in Fig. 1.

$$D_\mathrm{p} = C d_\mathrm{p}^3 \tag{1}$$

$$C = \left(\sum_{i=1}^{n} d_\mathrm{p}^3 \times D_\mathrm{p} \right) \bigg/ \sum_{i=1}^{n} d_\mathrm{p}^6 \tag{2}$$
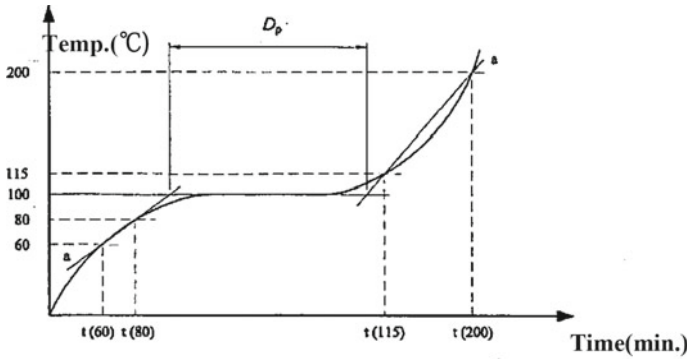
Fig. 1 Evaluation of temperature stagnation period of general moisture containing walls in ISO 834-11

This temperature stagnation significantly contributes to high fire resistance performance. Moreover, some types of wall material, e.g., gypsum board contains crystal water. ISO 834-11 [1] provides a method to estimate the moisture plateau length for the assessment of fire protection to structural steel elements, but it is a method empirically obtained from fire resistance test data, where C is a constant, n is the number of specimens, D_p is the temperature stagnation period for each specimen tested as specified in Fig. 1, and d_p is the fire protection material thickness of each specimen tested. According to Eq. 1, the temperature stagnation period is proportional to the cube of fire protection material thickness.

On the other hand, Mizukami [2], based on theoretical consideration, proposed a simple analytical formula for temperature stagnation period as follows:

$$\Delta t_v \approx \frac{L_v \rho \phi}{\lambda (T_f - T_v)} \cdot x \cdot \Delta x \tag{3}$$

where T_f and T_v are the heating temperature and the water evaporation temperature, respectively, and L_v is the latent heat of water evaporation, ρ is the density of wall material (dry base), ϕ is the mass fraction of moisture to wall mass (dry base), x is the distance from the exposed surface, Δx is the thickness of the slice (Δt_v and x are corresponding to D_p and d_p in Eq. (1), respectively). This formula explains that stagnation period, and Δt_v becomes longer as the distance from exposed surface, x, increases, or more specifically that the Δt_v is proportional to the distance x. Hence, the stagnation period (Δt_v, D_p) is proportional to the cube of the thickness (x, d_p) in ISO 834-11, while it is predicted to be proportional to the thickness in Eq. (3). Also, the moisture content is assumed to be constant, and the correction factor, C, is derived empirically by experimental data set in ISO 834-11, while the stagnation period is predicted to be proportional to the moisture content, ϕ, in Eq. (3).

Also Eq. 3 implies that the stagnation time, Δt_v, should disappear if Δx is taken to be very small, although Δt_v will be observed in reality since thermocouple probes have a certain inspection volume. This was verified by numerical simulations as

shown in Fig. 2, which compared the temperatures between the cases with $\Delta x = 10$ mm and 1.25 mm. This implies that the temperature stagnant region does not actually exist, but there are dried and wet parts and the interface between the two parts proceeds inward continuously. A formula is proposed to predict the time at which the evaporation front to reach an arbitrary depth from the exposed surface is as follows:

$$t_v = \left(\frac{1}{D}\right) \cdot \frac{1}{2} \cdot \left(\frac{L_v \phi}{C_w (T_f - T_v)}\right) \cdot \left(\frac{x}{2\sqrt{\alpha}}\right)^2 \tag{4}$$

where C_w is the specific heat of the wall material, α is the thermal diffusivity of the wall, i.e., $\alpha = \lambda / \rho C_w$.

However, the coefficient, D in Eq. 4 had to be obtained by the regression fits to the results of the numerically computed heat conduction equations under the calculation condition in Table 1. Then, Eq. 4 is rewritten as follows:

$$t_v = \frac{1}{D} \cdot 5.4 \times 10^6 \cdot \phi x^2 \tag{5}$$

Figure 3 shows the numerically calculated dried-up times for different moisture contents, ϕ, and Fig. 4 shows the estimated coefficient number in terms of ϕ to fit

Fig. 2 Comparison of the temperature development with different segment size
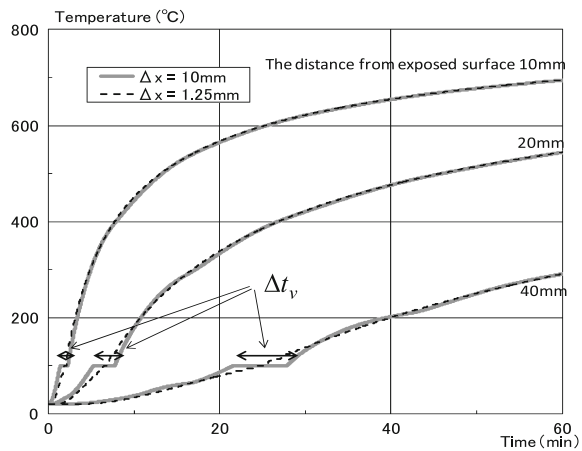
Table 1 Calculation condition

C_w [kJ/kg K]	0.88	T_f [°C]	875
T_v [°C]	100	T_0 [°C]	20
L_v [kJ/kg]	2590	ϕ [−]	0.0375–0.3
α [m²/s]	0.334×10^{-6}	Δx [mm]	1
		Δt [s]	1

Fig. 3 Numerically calculated dried-up times for different moisture contents
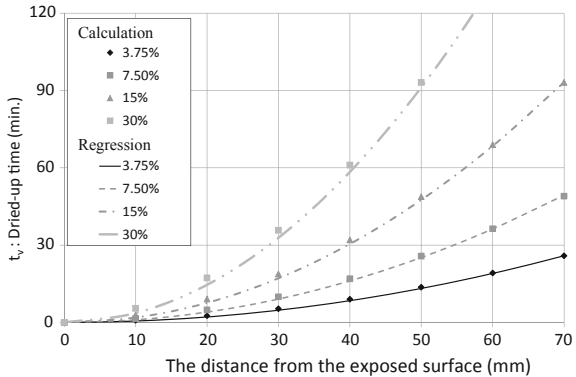
Fig. 4 Estimated coefficient number in terms of moisture contents
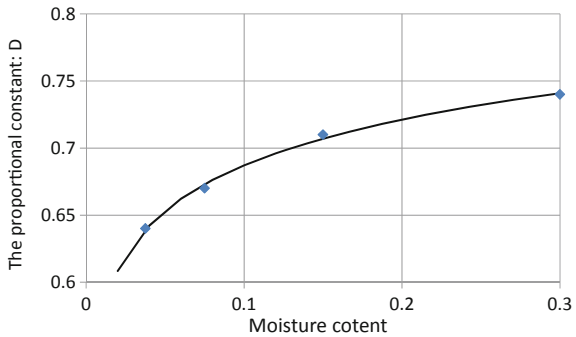
Eq. 5 to the regression lines in Fig. 3, which goes to

$$D = 0.049 \log_e \phi + 0.8 \tag{6}$$

In developing the simple formula, Eq. (4), it was approximated that the temperature gradient from exposed surface to drying front is linear and the conductive heat flux is proportional to the approximated temperature gradient. However, the actual temperature gradient is not linear, but becomes gradually shallower as the distance gets closer to the drying front. This is the reason why the regression by Eq. (6) was introduced.

In this research, instead of introducing the coefficient adjustment, the heat continuity equation is re-examined considering not only the heat for moisture evaporation, but also the heat of raising the temperature of the wall. It reduces the number of uncertainties in the heat continuity equation and allows us to skip the step of regression fits to numerical simulation to estimate the drying front. In the latter part of this research, an extended application method is proposed to estimate the temperature rise of arbitrary distance by using a ratio of Fourier number. The new formula is compared to the numerical calculation, and the range of application is validated.

2   Revised Heat Continuity Equation

The fact that the temperature gradient in the dried region is steep near the exposed surface and shallow near the drying front means that a certain amount of conductive heat is accumulated in the dried region to raise its temperature. Considering a slice element of the wall with an area ΔA and thickness Δx at the boundary of the dried and wet regions, as shown in Fig. 5, and letting the distance of the boundary from the exposed surface be x. When the evaporation front proceeds by Δx, the $\dot{q}''$ needs to provide the heat for evaporating water contained in the slice element and raising the temperature of the wall as shown in Fig. 5. Hence, letting Δt be the time for the evaporation front to take to proceed by Δx, we have the heat continuity equation as follows:

$$\dot{q}'' \Delta A \Delta t = L_v \phi (\rho \Delta A \Delta x) + C_0 \rho (T_f - T_v) \frac{1}{2} \Delta A \Delta x$$
$$+ \{C_0 + C_w \phi\} \rho (T_v - T_0) \frac{1}{2} \Delta A \Delta x \tag{7}$$

where L_v is the latent heat of evaporation of water, C_0 and C_w are the specific heat of the wall material (dry base) and the water liquid phase, respectively, ρ is the density of the wall, and ϕ is the mass fraction of moisture to wall mass (dry base), and the temperature difference profiles between before and after the evaporation of the slice element as shown in Fig. 5, i.e., between t and $t + \Delta t$, is approximated by triangles approximating the conductive heat flux, $\dot{q}''$, as follows:

$$\dot{q}'' \approx \lambda \frac{T_f - T_v}{x} \tag{8}$$

From Eqs. 7 and 8, we have

Fig. 5 Schematic illustration of conservation of energy for moisture containing wall
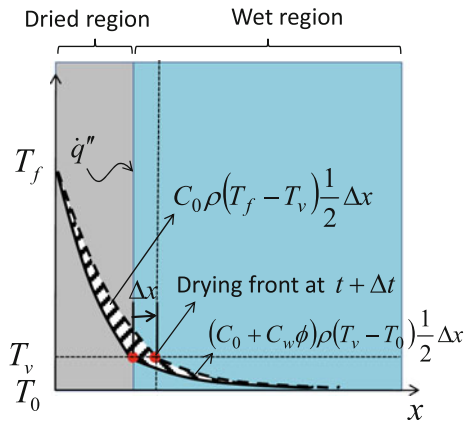
$$\Delta t = \frac{\left\{L_v\phi + \frac{1}{2}C_0(T_f - T_0) + \frac{1}{2}C_w\phi(T_v - T_0)\right\}\rho}{\lambda(T_f - T_v)}x\Delta x \tag{9}$$

Hence, it follows that Δt, which is the time that the drying front makes Δx, is supposed to increase in proportion to the distance x. This appears to be consistent with the observation that the stagnation time at a location in a wall with moisture increases with its distance from the exposed surface, as exemplified in Fig. 2. However, Eq. 9 implies another important fact, i.e., the stagnation time Δt will depend upon, or more specifically in proportion to, the thickness of the slice, Δx, in the numerical calculation as already mentioned by Mizukami [2]. Hence, it is more appropriate to deal with the velocity of the evaporation front than the stagnation period. Rewriting Eq. 9 for the velocity of evaporation front, we have

$$v = \frac{\Delta x}{\Delta t} = \frac{\lambda(T_f - T_v)}{\left\{L_v\phi + \frac{1}{2}C_0(T_f - T_0) + \frac{1}{2}C_w\phi(T_v - T_0)\right\}\rho x} \tag{10}$$

3 Simple Calculation Formula for Drying Front

In the above discussion, it is assumed that temperature stagnation does not exist in the moisture containing wall exposed to fire heating, but the wall is simply dried up from the exposed surface and the drying front, i.e., the boundary between dried and wet layers, moves toward the unexposed surface continuously. The time, t, that the drying front reaches an arbitrary distance, x, can be obtained by changing Eq. 10 to the differential equation shown below

$$dt = \frac{\left\{L_v\phi + \frac{1}{2}C_0(T_f - T_0) + \frac{1}{2}C_w\phi(T_v - T_0)\right\}\rho}{\lambda(T_f - T_v)}x\,dx \tag{11}$$

and integrating Eq. 11 as

$$\begin{aligned} t &= \frac{\rho C_0}{2\lambda}x^2\frac{\left\{L_v\phi + \frac{1}{2}C_0(T_f - T_0) + \frac{1}{2}C_w\phi(T_v - T_0)\right\}}{C_0(T_f - T_v)} \\ &= \frac{x^2}{4\alpha}\left\{\frac{2L_v\phi + C_0(T_f - T_0) + C_w\phi(T_v - T_0)}{C_0(T_f - T_v)}\right\} \end{aligned} \tag{12}$$

Hence the dried-up time, t, that the drying front reaches at a certain distance, x, increases proportionally to the square of the distance, x. Figure 6 shows the results of stagnation time, Δt_v, and the dried-up time, t_v, calculated using numerical predictions under the calculation condition in Table 1. Finite difference method [2] is used to simulate the heat conduction and evaporation in a wall, assuming that the incident heat flux is exhausted by the latent heat of vaporization at the evaporation temperature
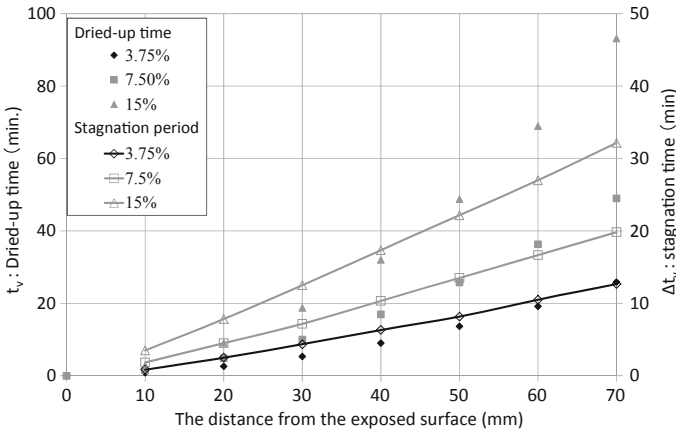
Fig. 6 Dried-up time and stagnation time by numerical calculation

until the mass of water is dried off. Temperature dependence of thermal properties and moisture migration does not take into account. As can be seen in Fig. 6, Δt_v is nearly proportional to x, and t_v is nearly proportional to the square of x that predicted in Eqs. (11) and (12).

3.1 Validation with Numerical Simulation

The time also increases with the increase of moisture fraction. Noting that

$$\frac{2L_v\phi + C_0(T_f - T_0) + C_w\phi(T_v - T_0)}{C_0(T_f - T_v)} = \frac{2L_v\phi + (C_0 + C_w\phi)(T_v - T_0)}{C_0(T_f - T_v)} + 1 \tag{13}$$

It is known that the decrease of fire temperature causes the delay of the drying front to move to a certain distance.

Also, Eq. 12 can be regarded as the formula to obtain the distance of the drying front, x, at an arbitrary time, t. Therefore, it may be convenient to generalize Eq. 13 using Fourier number defined as

$$F_\phi = \frac{x}{2\sqrt{\alpha t}}\bigg|_\phi = \left\{ \frac{C_0(T_f - T_v)}{2L_v\phi + C_0(T_f - T_0) + C_w\phi(T_v - T_0)} \right\}^{1/2} \tag{14}$$

where subscript ϕ denotes the point where moisture fraction, ϕ, becomes zero, i.e., the point of drying front.

The right-hand side of Eq. 14 is a function of fire temperature, T_f, initial temperature, T_0 and moisture content, ϕ, so becomes constant when these values are
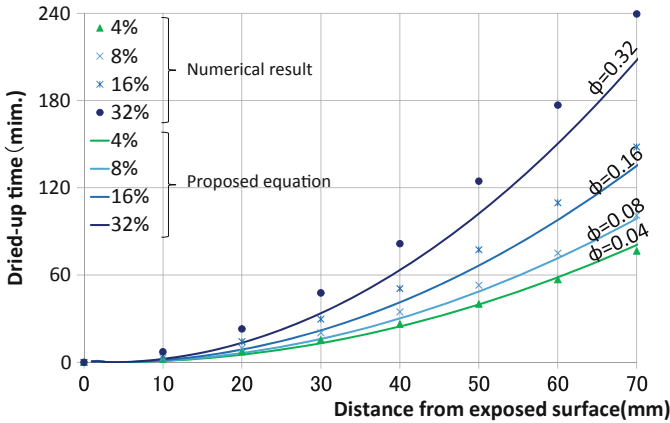
Fig. 7 Comparison of dried-up time with different moisture content

Table 2 Calculation condition

C_w [kJ/kg K]	0.88	T_f [°C]	780
T_v [°C]	100	T_0 [°C]	20
L_v [kJ/kg]	2590	ϕ [⁻]	0–0.32
α [m²/s]	0.334×10^{-6}	Δx [mm]	1
		Δt [s]	1

specified, since the others, i.e., specific heat of wall material, C_w, specific heat of liquid water, $C_0 = 4187$ J/kg K, evaporation temperature of water, T_v, and latent heat of water evaporation, $L_v = 2257$ kJ/kg, are basically constants as material properties.

Figure 7 compares the time of drying front in a wall with different moisture contents to reach different distances from the exposed surface predicted by Eq. 12 and the results of numerical computation of heat conduction equation under the following conditions in Table 2. Equation 12 agrees well with numerical results. The gap seems to be a little larger as the moisture content increases, but it seems to be rather the same taking the ratio of the gap over the dried-up time. If that is the case, the multiple data in Fig. 7 is bundled together by non-dimensioned.

3.2 Error Analysis and Compensation

The dependence of the drying front in terms of the generalized drying front, F_ϕ, on moisture content, ϕ, is calculated by Eq. 14 and compared with numerically calculated results as shown in Fig. 8. It is confirmed by the results in Fig. 8 that the gap between Eq. 14 and the numerical result becomes a little larger as the moisture
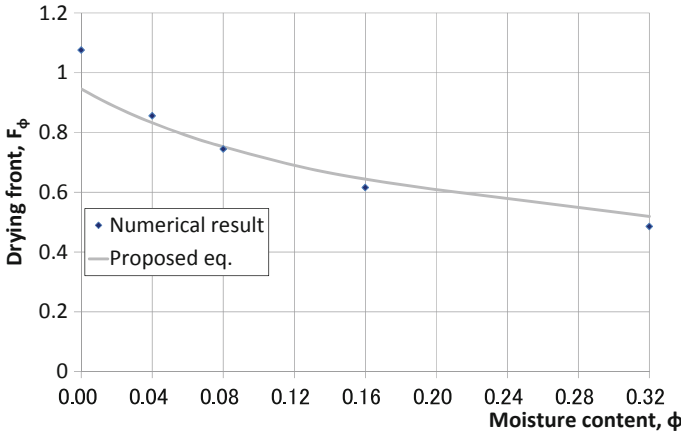
Fig. 8 Relation between drying front and moisture content

content decreases, but that the agreement is fairly good for a significantly wide range. For just checking the extreme case for the simple formula, let us assume $\phi \to 0$, i.e., for dry materials. Then Eq. 14 becomes as

$$F_{\phi=0} = \left.\frac{x}{2\sqrt{\alpha t}}\right|_{\phi=0} = \left(\frac{T_f - T_v}{T_f - T_0}\right)^{1/2} = \left(1 - \frac{\Delta T_v}{\Delta T_f}\right)^{1/2} \tag{15}$$

Equation 15 may be regarded as the simple formula to predict the Fourier number corresponding to ΔT_v for dry wall. On the other hand, the theory of heat conduction of the semi-infinite body in dry materials is well known and available in general heat transfer textbook such as Carslaw [3]. From this, we have

$$F_{\phi=0} = \left.\frac{x}{2\sqrt{\alpha t}}\right|_{\phi=0} = \mathrm{erfc}^{-1}\left(\frac{T_v - T_0}{T_f - T_0}\right)^{1/2} = \mathrm{erfc}^{-1}\left(\frac{\Delta T_v}{\Delta T_f}\right)^{1/2} \tag{16}$$

Therefore, the gap comes from the simplification of the heat conduction in the wall; however, it gives reasonable value over 4% moisture content. And it is safer side treatment to assume materials containing moisture less than 4% as dry material.

4 Temperature in the Dried Region of Materials Containing Moisture

As long as fire-resistant performance is concerned, the building elements containing moisture usually stay sound until the moisture is lost by evaporation. So, it is the dried condition where fire resistance can be issued. Therefore, the target wall is assumed

as a semi-infinite body which has a virtual drying front beyond the back surface of the real wall thickness in this paper.

4.1 Simple Estimation of the Temperature in the Dried Region

In order to obtain the temperature in the dried region, it is necessary to know the temperature profile in the region. However, Eq. 14 only gives the position of drying front, but does not give the temperature profile in the dried region. The simplest method is to assume the linear temperature profile from the surface to the drying front, which is consistent with the assumption for heat conduction in this region by Eq. 8. The advantage of the linear approximation of the temperature profile in the dried region is the simplicity in predicting the time, location or temperature in terms of Fourier number. The schematic of the calculation of the temperature assuming the linear temperature profile in the dried region is shown in Fig. 9.

Although the process of the approximation can be applicable for arbitrary temperatures as well, a temperature with specific interest will be a temperature that has some critical meaning for fire resistance performance. Let T_c be such a critical temperature and F_c be the corresponding Fourier number here. Then, it is easy to find the following relationship:

$$\left(1 - \frac{\Delta T_c}{\Delta T_f}\right) \Big/ \left(1 - \frac{\Delta T_v}{\Delta T_f}\right) = \frac{T_f - T_c}{T_f - T_v} = \frac{F_c}{F_\phi} \tag{17}$$

Hence, the Fourier number, F_c, corresponding to the temperature criterion, T_c, is given by

$$F_c = \left\{\left(1 - \frac{\Delta T_c}{\Delta T_f}\right) \Big/ \left(1 - \frac{\Delta T_v}{\Delta T_f}\right)\right\} \cdot F_\phi \tag{18}$$

Fig. 9 Linear approximation for temperature profile in the dried region
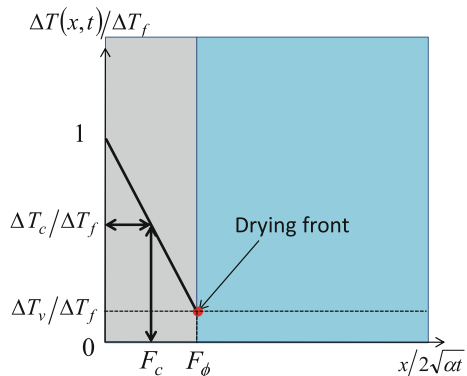
Note that letting t_c and x_c be the time and the distance from the exposed surface, respectively, the above F_c is

$$F_c = \frac{x_c}{2\sqrt{\alpha t_c}} \tag{19}$$

Equation 18 gives the time and the location in the dried region in the wall at which the temperature becomes critical temperature.

Incidentally, if we chose such F_c as $F_c < F_\varphi$, we can predict the temperature, T_c, at arbitrary time and location in the dried region from Eq. 17 as

$$\frac{\Delta T_c}{\Delta T_f} = 1 - \left(1 - \frac{\Delta T_v}{\Delta T_f}\right)\frac{F_c}{F_\phi} \tag{20}$$

4.2   Comparison of the Temperature Between Simple Estimation and Numerical Calculation

Figure 10 compares the linear temperature profiles calculated by Eq. 20 and the results of the numerical computation of the heat conduction equation under the conditions in Table 2 with different moisture contents. The temperature profile by the numerical result in Fig. 10 represents the one at a fixed time, 30 min. Note that the x-axis is non-dimensioned in terms of Fourier number, which consists of the material thickness divided by the square root of the time expressed as Eq. 19.
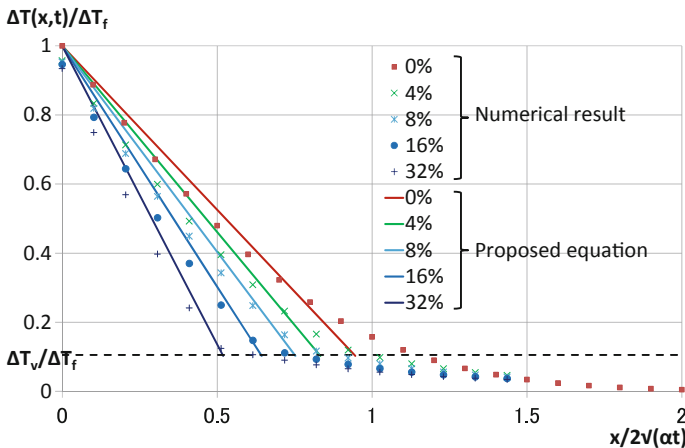
Fig. 10 Comparison of temperature profiles of numerically computed and the linear approximation in the dried region

As can be seen in Fig. 10, while the temperature profile by numerical computation for dry wall starts steeper than the linear profile at low Fourier number, in other words, near the fire exposed surface and becomes gradually gentle, the profiles for high moisture contents are nearly straight in the dried area and matches well with the linear profile. Even in the profiles for low moisture contents, the gap seems to be reduced reasonably for higher temperature, e.g., higher than $0.2\Delta T_f$. In most cases of practical fire safety design, the critical temperature for fire resistance performance is larger than $0.2\Delta T_f$.

4.3 Practical Use of the Simple Temperature Estimation

In practical fire safety design, the relationship between temperature profile and Fourier number can be used for both of the two purposes: (1) To estimate the spatio-temporal position (x, t) in terms of Fourier number when the ratio of critical temperature rise to fire temperature rise, $\Delta T_c/\Delta T_f$ is given, as shown in Fig. 11 and (2) To estimate temperature rise in terms of $\Delta T(x, t)/\Delta T_f$ when the position, (x, t), is given, as shown in Fig. 12. Equations 18 and 20 are available for the first and second purpose, respectively. And its procedures are shown as the arrows in Figs. 11 and 12, respectively. The symbols and lines in Figs. 11 and 12 represent numerical calculations and proposed equations, respectively.

Figure 13 takes the numerical results of Fourier number corresponding to the critical temperature rise in the x-axis and the calculated Fourier number by Eq. 18 on the same condition in y-axis to search the range of application. The symbols represent moisture content. Then, the gap from the diagonal line shows the error, and a safe
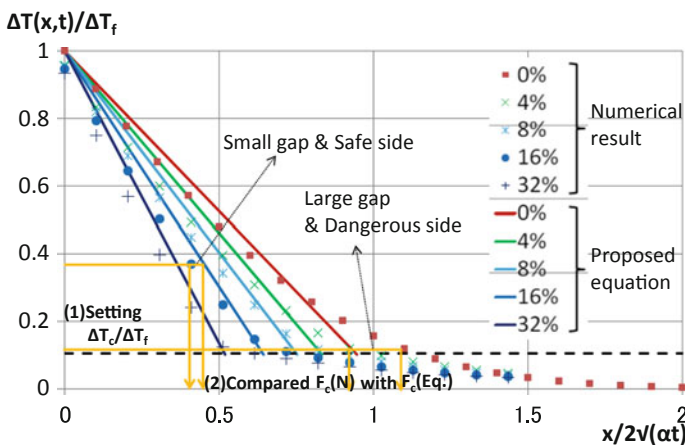
Fig. 11 Flow chart of obtaining the gap of Fourier number between numerical result and proposed Eq. 18
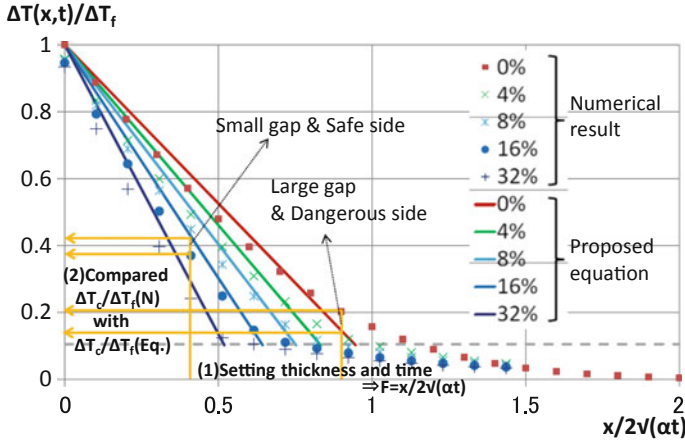
Fig. 12 Flow chart of obtaining the gap of non-dimensional temperature rise between numerical result and proposed Eq. 20
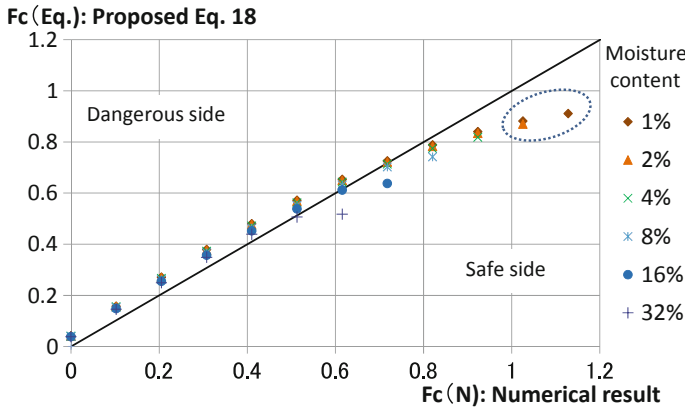
Fig. 13 Comparison of Fourier number between numerical result and proposed Eq. 18 with different moisture content

side is bottom-right-hand side. It is shown that the Fourier number corresponding to the critical temperature rise by Eq. 18 matches well with numerical results in most of the range. As the Fourier number becomes large, Eq. 18 tends to underestimate it. Note that there is an upper limit of the Fourier number, F_ϕ, in each moisture content since the proposed equation is only applied to the dried-up region. And the gap seems to be large close to the upper limit in small moisture content.

In another way, the gap in the non-dimensional temperature rise between proposed Eq. 20 and numerical results is shown in Fig. 14. Note that a safe side is up-left-hand side in this case. It shows that the non-dimensional temperature rise is over-estimated a little in a wide range which is the safe side. However, it becomes underestimated
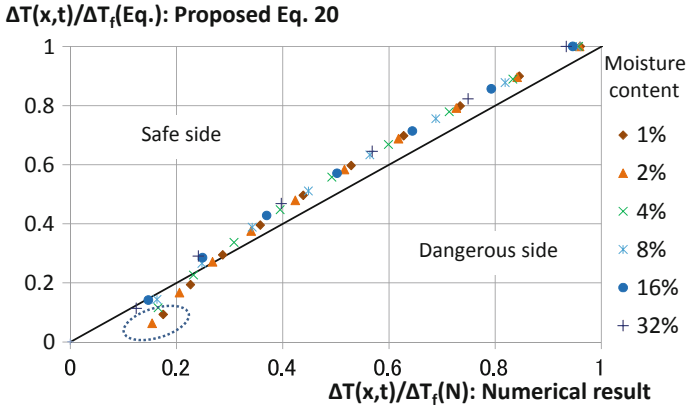
Fig. 14 Comparison of the non-dimensional temperature rise between numerical result and proposed Eq. 20 with different moisture content

and the gap seems to be large with less than 2% moisture content, $\phi \leq 0.02$, and less than 0.1 temperature rise, $\Delta T_c \big/ \Delta T_f < 0.1$. As an example, $\Delta T_c \big/ \Delta T_f$ is about to 0.23 assuming insulation criterion in ISO 834 as $\Delta T_c = 180\,\text{K}$ and assuming the average fire temperature rise at 60 min in ISO 834 as $\Delta T_f = 780\,\text{K}$. The fire exposed temperature and insulation criterion are set arbitrarily in the performance-based fire safety design; however, it seems to be covered by the range of application in practice. And it is safer side treatment to assume the materials containing smaller moisture content than 2% as dry material.

5 Conclusion

The existing moisture evaporation rate formula has been revisited and re-examined considering not only the heat for moisture evaporation, but also the heat of raising the temperature of the wall. It reduces the number of uncertainties in the heat continuity equation and allows us to skip the step of regression fits to numerical simulation to estimate the drying front.

The new formula is further developed to the simple formula for estimating temperature profile in the dried region of materials containing moisture. It compared to the numerical calculation with good agreement in large moisture content. For small moisture content cases, the range of application is presented to be $\phi > 0.02 \cup \Delta T_c \big/ \Delta T_f > 0.1$.

The advantage of this method is that there is no need to employ numerical simulation to estimate the incident heat flux to the drying front. Without it, the location of the drying front and the temperature profile in the dried region are obtained by the simple equation.

References

1. ISO 834. (1999). *Fire resistance tests-elements of building construction*. Geneva, Switzerland: ISO.
2. Mizukami, T., & Tanaka, T. (2012). Simple equations for predicting thermal resistance of mud-plastered wall. In *The 9th Asia-Oceania Symposium on Fire Science and Technology* (pp. 432–442).
3. Carslaw, H. S., & Jeager, J. G. (1959). *Conduction of heat in solid* (2nd ed.). Oxford: Oxford University Press.

Burning of a Polyurethane Slab in Open and in Room Environments

Sho Akao, Kazunori Harada, Daisaku Nii, Sungchan Lee, Junghoon Ji and Tsuneto Tsuchihashi

Abstract To examine the effect of thermal feedback during a fire in a compartment, flexible polyurethane slab was burnt in an open environment and in a model-scale room. The size of the slab was 500×500 mm. The thickness was varied between 50 and 200 mm. The size of model-scale room was 900×1700 mm in plan area. Opening height was changed in the range of 200–800 mm to examine the effect of ventilation and smoke layer thickness. The ceiling height was varied in the range of 400–800 mm to examine the effect of extended flame under ceiling. The polyurethane slab was ignited at the center of top surface. Spread of flame was observed and recorded by video cameras. Mass loss rate, temperature profile, and heat fluxes to ceiling and floor were measured. Experimental results show that the thermal feedback effect is clearly observed even in the case of high ceiling with large openings. As the opening height was reduced, the effect of thermal feedback was increased moderately. At maximum, the heat release rate was increased to 170% of that in open burning. The effect of ceiling height was nonlinear. As the ceiling height was decreased comparable to continuous flame height, heat release rate was greatly increased due to the thermal feedback from extended flame under ceiling. Using the measured data, the effect of thermal feedback was correlated with heat flux to floor. Empirical relationships between ceiling height and fire growth rate, between maximum heat release rate and burning type index were derived.

Keywords Fire source · Thermal feedback · Heat release rate per unit area · Surface flame spread rate

S. Akao · K. Harada (✉) · D. Nii · S. Lee · J. Ji
Department of Architecture and Architectural Engineering, Kyoto University, C1-4 Kyoto University Katsura Campus, Nishikyo, Kyoto 615-8540, Japan
e-mail: harada@archi.kyoto-u.ac.jp

T. Tsuchihashi
General Building Research Corporation of Japan, 5-8-1 Fujishirodai, Suita, Osaka 565-0873, Japan

© Springer Nature Singapore Pte Ltd. 2020

Nomenclature

A_b Burning area (m^2)
A_{fuel} Surface area of specimen (m^2)
A_{op} Opening area (m^2)
q_{max} Maximum HRR per unit area of burning surface (kW/m^2)
q_0 HRR per unit area (kW/m^2)
q_{180} Average HRR per unit area during first 180 s of burning by cone calorimeter (kW/m^2)
Q Heat release rate (kW)
h_{op} Opening height (m)
h_s Height (thickness) of specimen
H Ceiling height (m)
m Mass loss rate per unit area of burning surface [kg/(s m^2)]
r_b Radius of burning area (m)
t Time (s)
t_0 Incubation time (s)
THR   Total heat release (kJ)
v_p Surface flame spread rate (m/s)
w Opening width (m)
W Initial mass of specimen (kg)

Greek symbols

α Fire growth rate (kW/s^2)
χ Burning type index (m$^{1/2}$)
ΔH Heat of combustion (kJ/kg)

Subscripts

max   Maximum

1 Introduction

The heat release rate (HRR) from a fire source is a key parameter in performance-based design of built environments. The HRR is assumed to calculate the consequence of fire in order to judge the appropriateness of fire safety provisions of a built environment under question [1]. The assumption of heat release rate is often based

on measurements by an open calorimeter as determined by ISO 24473 [2]. In such experiments, a package of combustibles is burnt under a smoke-collecting hood. Enough amount of oxygen is entrained so that intrinsic nature of burning will be measured. The method is appropriate to compare and classify the degree of burning of combustible items.

However, in case of a fire in a room, thermal feedback to fire source increases the rate of burning. Hot smoke layer in the upper part of room emits thermal radiation downward. Part of radiation will arrive at surface of combustibles and increase burning rate. Another source of thermal radiation could be flames extended along wall/ceiling surfaces and wall/ceiling surfaces themselves. Therefore, it is *not* recommended to use open calorimeter HRR data as input values of heat release rate to fire models such as two-layer zone models [3].

Attempts were made to extrapolate the open calorimeter HRR data to that in burning in a room. Utiskul et al. proposed a simple model of burning rate of heptane pan fires depending on compartment environment [4]. Mizukami et al. carried out a series of experiments and verified the correlation [5]. Wade et al. applied the set of formulas to a two-layer zone model and predicted the HRRs of upholstered furniture in a compartment [6]. However, the surface flame spread and change of burning area are not explicitly considered by those approaches.

In this study, burning experiments were carried out using flexible polyurethane foam slab in an open environment and in a model-scale box. The HRR and flame spread rates over surface were compared in relation with the occurrence of flame extension under ceiling.

2 Experimental Procedure

2.1 Schematics

Burning experiments were carried out in an open environment and in a mode-scale room. In an open environment, heat release rate and mass loss rate were measured simultaneously. In a model-scale room, mass loss rate was measured together with temperature distribution in the room and heat fluxes to wall, ceiling, and to floor. In both of the experiments, video observations were carried out to measure flame spread rate over horizontal surface of specimen.

2.2 Specimen Material

The specimen was a slab of non-fire retarded flexible polyurethane (PUR) foam. The size was 500×500 mm in plan area. Thickness was varied in 50, 100, 150, and 200 mm. The density was in the range of 15.2–16.3 kg/m^3, 15.6 kg/m^3 in average.

(a)
(b)
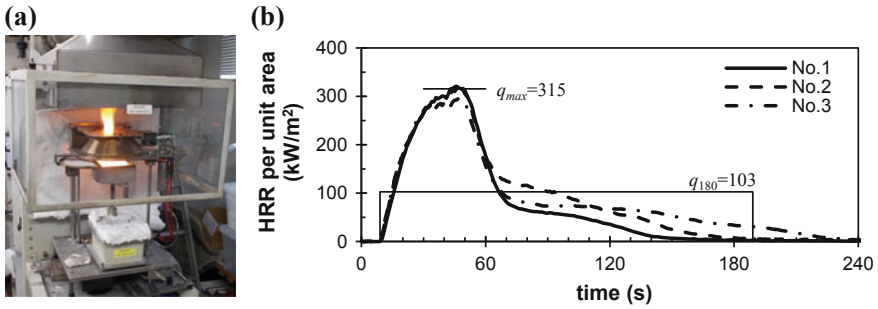
Fig. 1 Cone calorimeter test of material, **a** burning behavior, **b** measured HRR curves

The material was tested by cone calorimeter [7] as shown in Fig. 1a. The material thickness was 50 mm. The irradiance was 20 kW/m^2. As shown in Fig. 1b, the maximum heat release rate was 315 kW/m^2. The average HRR during first 180 s of burning was 103 kW/m^2. Heat of combustion, i.e., total heat release per unit mass, was 30,400 kJ/kg.

3 Burning Experiments in an Open Environment

3.1 Experimental Procedure

Specimen was burnt in an open environment as shown in Fig. 2a. The mass loss rate was measured by a set of load cells. Heat release rate was measured by oxygen consumption calorimetry. The burning behavior was recorded by video cameras in order to measure flame spread rate over horizontal surface. The specimen was ignited at the center of top surface by using a small piece of tissue paper soaked with alcohol as shown in Fig. 2b.

(a)
(b)
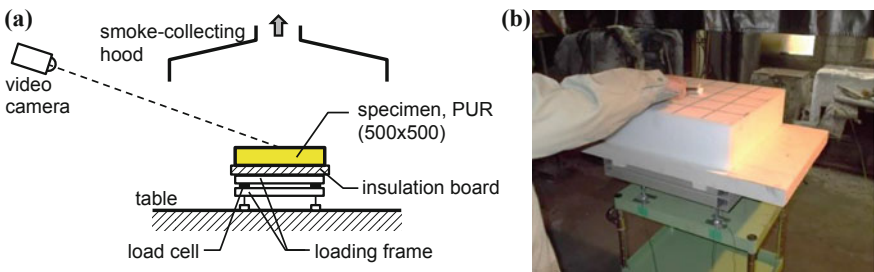
Fig. 2 Schematics of experimental setup in an open environment; **a** experimental arrangement and **b** photographic view at ignition

Table 1 Specifications of specimens for open environment burning

Exp. no.	Thickness (mm)	Specimen mass (g)	Density (kg/m^3)
o4	50	200.8	16.1
o3	100	390.5	15.6
o1	150	586.3	15.6
o2	200	801.8	16.0

0s, ignition	20s	40s	60s, spread to edge	80s
100s, maximum burning	120s	140s	160s, burnt out at center	180s
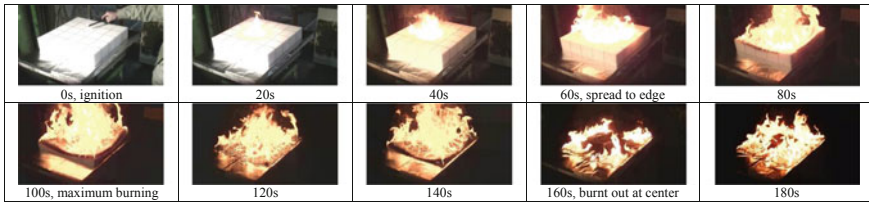
Fig. 3 Burning behavior in experiment o3 (open environment, thickness 100 mm)

Specifications of specimens are shown in Table 1. Specimen size was 500 × 500 mm in plan area. Thickness was varied between 50 and 200 mm. The density was 15.8 kg/m^3 in average but varied slightly between 15.6 and 16.1 kg/m^3.

3.2 Burning Behavior

Burning behavior in experiment o3 (thickness 100 mm) is shown in Fig. 3. After ignition at the top, flame spread over top surface in a circular shape. At about 60 s, flame front arrived at the edge of top surface. After that, flames spread downward. Burning was severe during 80–100 s when the entire top surface is involved with burning. At 140 s and later, center part of the specimen was burnt out. Burnt out portion spread toward perimeter and burning is decreased.

3.3 Heat Release Rates and Heat of Combustion

The heat release rates measured by oxygen consumption are shown in Fig. 4a. The initial growth pattern is independent on specimen thickness. The initial portion of HRR curves were fitted with t^2-growth

$$Q = \alpha(t - t_0)^2 \tag{1}$$

Fig. 4 Heat release rate in open burning **a** by oxygen consumption and **b** by mass loss rate
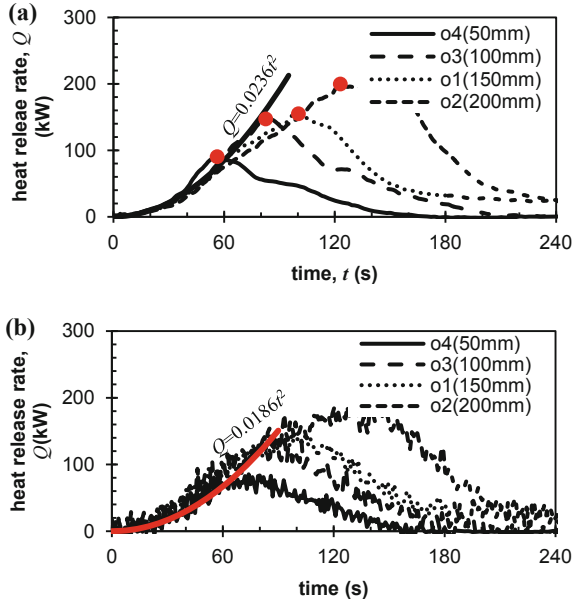
where incubation time, t_0, was introduced to account for delay time to start growth. The fire growth rate, α, resulted in

$$\alpha = 0.0236 \pm 0.0036 \,(\text{kW/s}^2) \tag{2}$$

from the average of the four experiments.

The maximum HRR depended on specimen thickness. In case of experiment o4 (50 mm), maximum heat release rate was small compared with other experiments. This is because the center portion was burnt out before flame spread to entire surface. In cases o3, o1, and o2 (100, 150 and 200 mm), the maximum HRR were largely different because the surface area of specimens differed by the area of vertical surface. The heat of combustion was calculated by dividing total heat release by initial mass of specimen as

$$\Delta H \equiv \text{THR}/W = 29,400 \pm 620 \,(\text{kJ/kg}). \tag{3}$$

Mass loss rates were calculated by differentiating specimen mass measured by the load cell. By multiplying heat of combustion, heat release rates were calculated as shown in Fig. 4b. It was confirmed that oxygen consumption calorimeter and load cell measurement result in similar heat release rates, but the fitted values of fire growth rate by mass loss rate of specimen is slightly different as

$$\alpha = 0.0186 \pm 0.0128 \,(\text{kW/s}^2) \tag{4}$$

The difference is due to the response of load cell measurements and data smoothing. To reduce the effect of fluctuations of cell, measured values of mass loss rate were averaged over an appropriate time interval.

3.4 Surface Flame Spread Rates and Heat Release Rates Per Unit Area of Burning

Surface flame spread rates over the top surface were analyzed. As the flame front spread in a circular way, radius of the burning area was measured by video image. The results are plotted in Fig. 5a. The flame spread rate is fairly constant over time and independent of specimen thickness. The rate resulted in

$$v_p = dr_b/dt = 3.28 \pm 0.42 \text{ (mm/s)}. \tag{5}$$

To obtain the heat release rates per unit area of burning, HRR was correlated with the burning area. The result is shown in Fig. 5b. As an average of data, heat release rate per unit area of burning is

$$q_0 = Q(t)/A_b(t) = 252 \pm 62 \text{ (kW/m}^2). \tag{6}$$

Fig. 5 **a** Radius of burning area over time and **b** HRR versus burning area
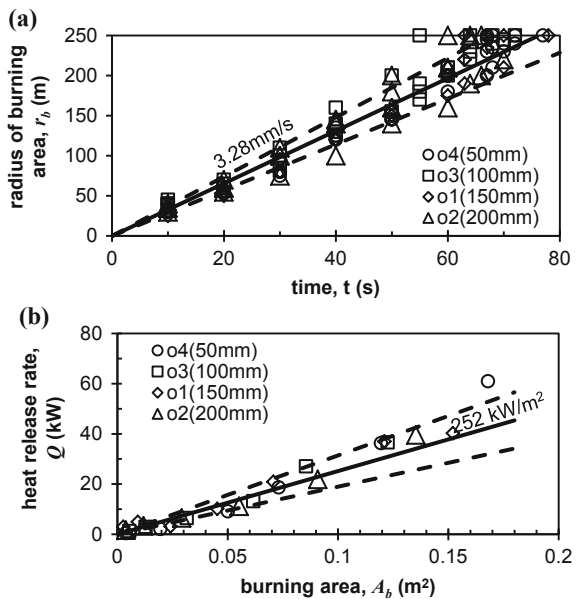
4   Burning Experiments in a Model-Scale Room

4.1   *Experimental Procedure*

In model-scale room experiments, a specimen was put on the center of the floor as shown in Fig. 6. The model-scale room was made of ceramic fiber board (thickness 50 mm, density 250 kg/m^3). The inner dimension was 900×1700 mm in plan area. Two openings were equipped in opposite two sides. The width of each opening was 900 mm. Ceiling height and opening height were varied as experimental parameters.

   The combination of specimen thickness, ceiling, and opening height is shown in Table 2. In the experiments b1–b7, ceiling height was 800 mm. Flame touched the ceiling intermittently as will be shown later. Opening height was varied in the range of 200–800 mm in order to examine the effect of thickness of smoke layer. To examine the effect of extended flame under ceiling, ceiling height was reduced to 620 mm in experiments b8–b10 and to 400 mm in experiments b10 and b11. As
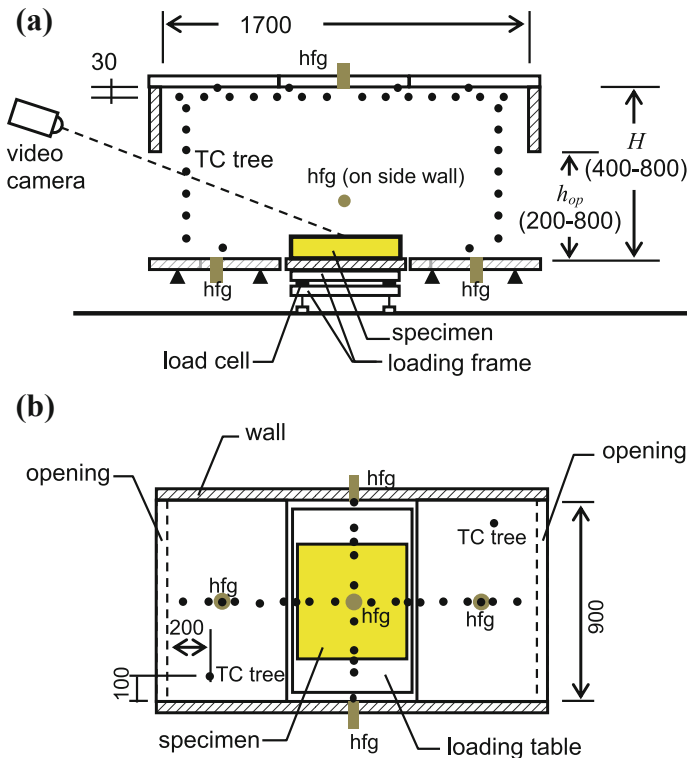
Fig. 6 Schematics of experimental setup in model-scale room, **a** vertical section, **b** horizontal layout

Table 2 Conditions of experiments in a model-scale room

Exp. no.	Ceiling height (mm)	Opening height (mm)	Specimen (PUR foam)		
			Thickness (mm)	Mass (g)	Density (kg/m^3)
b1	800	800	50	203.2	16.3
b2	800	800	100	388.6	15.5
b3	800	800	100	387.8	15.5
b4	800	800	150	601.1	16.0
b5	800	500	100	379.0	15.2
b6	800	500	50	197.7	15.8
b7	800	200	100	405.1	16.2
b8	620	620	100	400.6	16.0
b9	620	320	100	388.3	15.5
b10	620	320	50	197.7	15.8
b11	400	400	50	203.6	16.3
b12	400	200	50	195.9	15.7

the ceiling height was reduced, continuous flame touched the ceiling and extended horizontally.

Specimen's mass loss was continuously measured by a set of load cells. Burning behavior was recorded by two video cameras located at both sides of the model box. Ceiling jet temperature was measured along the centerline of longer and shorter directions at 30 mm below ceiling. Vertical temperature profile was measured by two thermocouple trees located at both ends of the box. Heat flux was measured at center of ceiling, lower part of side walls, and floor.

4.2 Burning Behavior

As an example, burning behavior in experiment b2 is shown in Fig. 7. Ceiling height was 800 mm. Opening height was 800 mm. Similar to burning in open environment shown in Fig. 3, flame spreads in a circular shape over the top surface. During spreading period, smoke layer was developed at the upper part of box. At around 60 s, flame spread front arrived at the edge of top surface. After that, the entire surface was involved with burning. In comparison with the open burning shown in Fig. 3, flame length is increased due to extension along sidewalls and/or under the ceiling. Burnout was earlier than that in experiment o3 even though the specimen is identical.

Measured data in experiment b2 are shown in Fig. 8. HRR was similar to that in Experiment o2, but the maximum HRR was increased as shown in Fig. 8a. As shown in Fig. 8b, the smoke layer is developed by about 200 mm thickness. Smoke layer temperature was 380 °C at maximum. In addition, ceiling jet temperature was
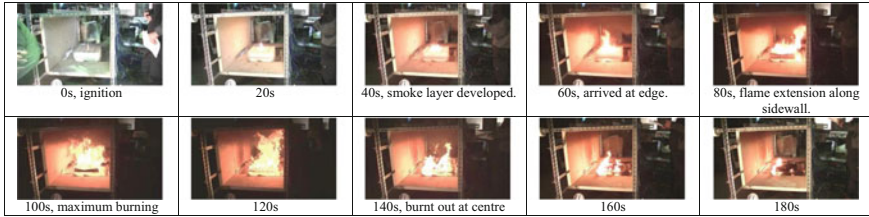
Fig. 7 Burning behavior in experiment b2 (ceiling height 800 mm, opening height 800 mm, and specimen thickness 100 mm)
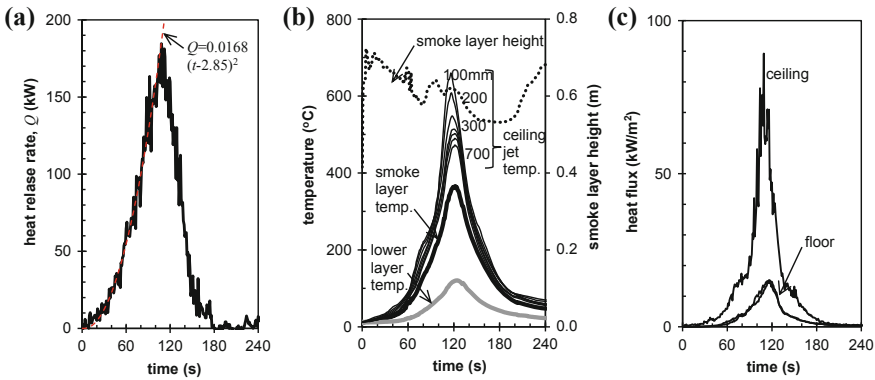
Fig. 8 Measured data in experiment b2 (ceiling height 800 mm, opening height 800 mm, and specimen thickness 100 mm); **a** heat release rate; **b** smoke layer height, temperatures of smoke layer and ceiling jet at 100–700 mm apart from plume axis; and **c** heat flux to ceiling and floor

considerably high due to flame impingement. At 100 mm from plume axis, ceiling jet temperature was 650 °C at maximum, which correspond to intermittent flame extension under the ceiling. As a consequence, heat flux to floor increased up to 15 kW/m^2 at maximum as shown in Fig. 8c. The flux might increase the mass pyrolysis rate of specimen.

4.3 Comparisons of Heat Release Rates

To examine the effect of ceiling and opening height, heat release rates were compared. In Fig. 9a, HRR curves for ceiling height $H = 800$ mm and opening height $h_{op} = 800$ mm were plotted. Thickness of specimen, h_s, was varied in 50, 100, and 150 mm. In comparison with the open burning shown in Fig. 4b, maximum HRR was considerably increased. Especially, in the case of 150 mm thickness, maximum HRR was doubled. Thus, the compartment effect is significant even if the ceiling height is high and openings are large.
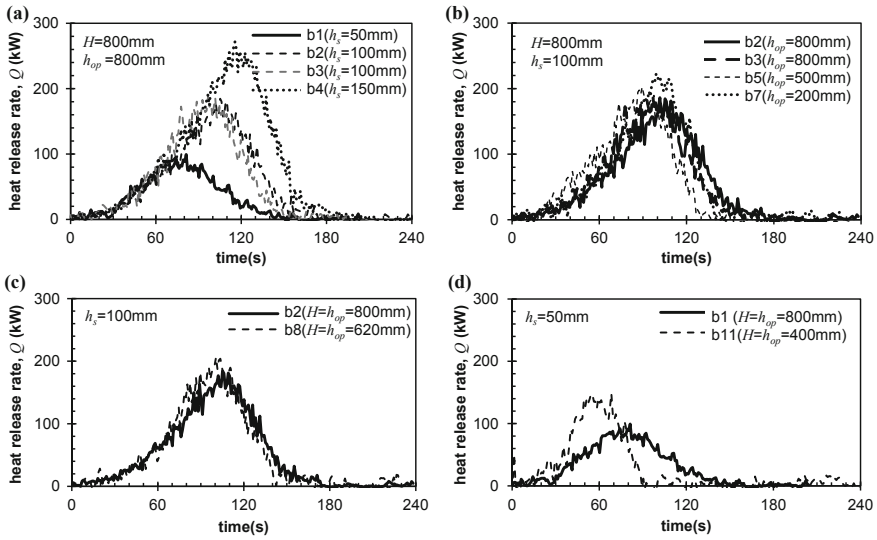
Fig. 9 Comparisons of heat release rates in **a** ceiling height $H = 800$ mm and opening height h_{op} = 800 mm are constant, but specimen thickness varied; **b** ceiling height $H = 800$ mm, specimen thickness $h_s = 100$ mm were constant but opening height was varied; **c** specimen thickness $h_s = 100$ mm, but ceiling and opening heights were varied; and **d** specimen thickness $h_s = 50$ mm, but ceiling and opening heights were varied

The effect of opening height is analyzed in Fig. 9b. The ceiling height and specimen thickness are constant, but the opening height was varied in 800, 500, and 200 mm. As the opening height is reduced, initial fire growth is slightly increased. Maximum HRR is increased by about 20%.

The effect of ceiling height is analyzed in Fig. 9c, d. In all the experiments in these two figures, opening height was set equal to ceiling height in order to minimize the effect of smoke layer. As shown in Fig. 9c, the difference was small if the ceiling height was reduced from 800 to 620 mm. However, considerable differences were observed if the ceiling height was reduced to 400 mm as shown in Fig. 9d. As the flame extended continuously under ceiling, heat feedback from extended flame to specimen was largely increased. As a result, HRR was increased considerably.

4.4 Flame Spread Rate and Heat Release Rate Per Unit Area of Burning

Using the video image, the radius of burning surface was analyzed. Flame spread rate was calculated as the increase rate of burning radius. The calculated results were plotted against heat flux to floor during spreading period, namely 60 s, as shown in Fig. 10a. It is shown that flame spread rate was slightly increased by heat flux to
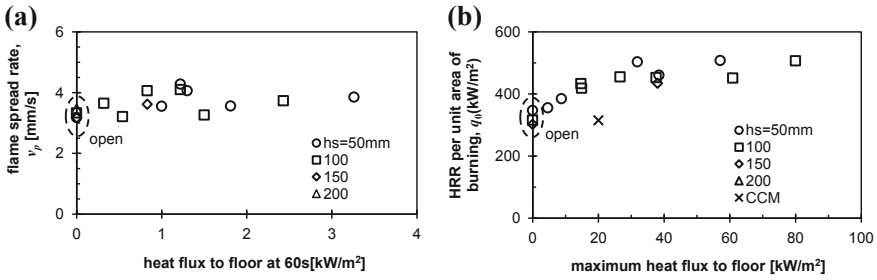
Fig. 10 Correlation of maximum heat flux to floor with **a** flame spread rate over top surface and **b** heat release rate per unit area of burning

floor.

The maximum heat flux to floor is also correlated with HRR per unit area of burning. The result is plotted in Fig. 10b. The HRR per unit area was increased linearly up to 500 kW/m² at 40 kW/m² of heat flux to floor. As the heat flux was increased further, the increase in HRR was saturated. For comparison, cone calorimeter test result is also plotted. The HRR value was close to the values of burning in an open environment.

4.5 Empirical Relationships for Fire Growth Rate and Maximum HRR Per Unit Area

It is beneficial to derive empirical correlations for fire growth and maximum HRR per unit area. For this purpose, simple correlation was examined. As for the fire growth rate, the effect of ceiling height was dominant. Thus, the fire growth rate was plotted against ceiling height as shown in Fig. 11a. As the HRR was less than 100 kW during flame spread period, corresponding mean flame height in open environment was 0.97 m as calculated by Heskestad's formula [8]. Continuous flame height was
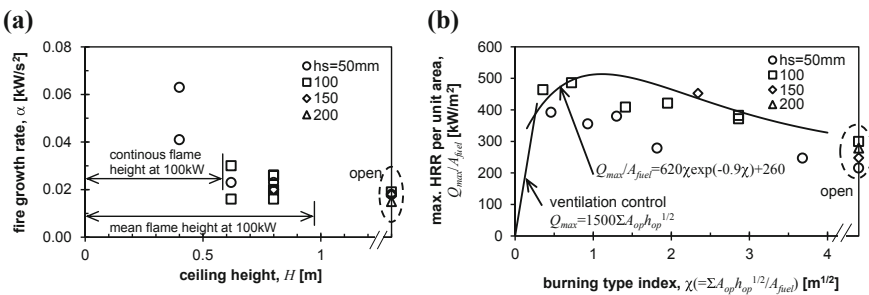
Fig. 11 Empirical correlations of **a** fire growth rate and **b** heat release rate per unit area of burning

$0.97 \times 0.6 = 0.58$ m. Fire growth rate for low ceiling cases were considerably increased especially if the ceiling height was less than continuous flame height. Considering that flame spread rate did not increase as was shown in Fig. 10a, the increase in fire growth rate could be attributed mainly to the increase in heat release rate per unit area.

As to the maximum HRR per unit surface area, maximum HRR was divided by original surface area of specimen, A_{fuel} and plotted against burning type index χ ($=\Sigma A_{op} h_{op}^{1/2}/A_{fuel}$) as shown in Fig. 11b. As a conservative estimate, the data can be included by a function of χ similar to the correlations for other type of fuels [9].

5   Conclusions

To examine the effect of thermal feedback during initial fire in a room, flexible polyurethane foam slab was burnt in an open and in a model-scale room environments. The ceiling and opening heights were varied to examine the effect of extended flame under the ceiling and the effect of smoke layer. Experimental results showed that thermal effect was clearly observed even in the case of high ceiling with large openings. As the opening height was reduced, the effect of thermal feedback was increased. Maximum heat release rate was increased up to 170% of that in open burning. The effect of ceiling height was nonlinear. As the ceiling height was decreased below continuous flame height, heat release rate was greatly increased due to the effect of thermal feedback from extended flame under ceiling. Using the measured data, the effect of feedback was correlated with heat flux to floor. Empirical relationships between ceiling height and fire growth rate, between maximum heat release rate per unit area and burning type index were derived.

References

1. International Organization for Standardization. (2015). ISO 16733-1, Fire safety engineering—Selection of design fire scenarios and design fires—Part 1: Selection of design fire scenarios.
2. International Organization for Standardization. (2008). ISO 24473, Fire tests—Open calorimetry—Measurement of the rate of production of heat and combustion products for fires of up to 40 MW.
3. Tanaka, T., & Yamada, S. (2004). BRI2002: Two layer zone smoke transport model. *Fire Science and Technology, 23,* 1–131.
4. Utiskul, Y., & Quintiere, J. G. (2008). An application of mass loss rate model with fuel response effects in fully-developed compartment fires. In *Proceedings of the 9th International Symposium, International Association for Fire Safety Science* (pp. 827–838).

5. Mizukami, T., Utiskul, Y., & Quintiere, J. G. (2015). A compartment burning rate algorithm for a zone model. *Fire Safety Journal, 79,* 57–68.
6. Wade, C., Fleischmann, C., Spearpoint, M., & Abu, A. (2017). Prediction model for compartment effects on burning upholstered furniture. In *International Conference on Research and Advanced Technology in Fire Safety* (pp. 315–330).
7. International Organization for Standardization. (2015). ISO 5660-1, Reaction-to-fire tests—Heat release, smoke production and mass loss rate—Part 1: Heat release rate (cone calorimeter method) and smoke production rate (dynamic measurement).
8. Heskestad, G. (2016). Fire plumes, flame height, and air entrainment. In *The SFPE handbook of fire protection engineering* (5th ed., Vol. 1, pp. 396–428). Society of Fire Protection Engineers.
9. Ohmiya, Y., Satoh, M., Tanaka, T., & Wakamatsu, T. (1995). Burning rate of fuel in enclosure and generation limit of the external flame. *Journal of Construction Engineering, Transactions of AIJ, 469,* 149–158. (in Japanese).

Diffusion of Carbon Monoxide Through Unpainted and Painted Gypsum Wallboard

Thomas G. Cleary and Jiann C. Yang

Abstract Experiments were conducted to measure effective diffusion coefficients of carbon monoxide through unpainted and painted gypsum wallboard samples. The results show carbon monoxide readily diffusions through gypsum wallboard while application of paint to one surface was shown to have almost no effect, a few percent decreases in the effective diffusion coefficient, to a dramatic reduction in carbon monoxide diffusion, up to 55-fold decrease in the effective diffusion coefficient for samples with two coats of one house paint. All three paints examined were flat-finish, latex-based interior house paints; clearly, the paint chemical formulation affects gas permeability and hence the effective diffusion coefficient for painted surfaces. Two full-scale experiments were conducted in a 11.0 m by 7.3 m by 3.7 m high sealed compartment fabricated with one layer of either unpainted or painted gypsum wallboard on the walls and ceiling. In each experiment, carbon monoxide was released in the compartment, and after the release, the decay of the carbon monoxide concentration was recorded. Over a five-hour period, the painted walls and ceiling experiment's carbon monoxide concentration slightly lagged the unpainted walls and ceiling experiment's measurements which is consistent with the effective diffusion coefficient measurements of the unpainted and painted wallboard samples. The implications for life safety assessment compel one to conservatively assume carbon monoxide diffusion through gypsum wallboard progresses at the higher rate commensurate with an unpainted surface unless specific data is gathered. In full-scale fire experiments with conventional gypsum wallboard construction effects of carbon monoxide diffusion should be considered where carbon monoxide measurements are made.

Keywords Carbon monoxide · Diffusion · Gypsum wallboard

T. G. Cleary (✉) · J. C. Yang
National Institute of Standards and Technology, 100 Bureau Drive, 20899
Gaithersburg, MD, USA
e-mail: thomas.cleary@nist.gov

591

Nomenclature

A Area (m^2)
D Diffusion coefficient (m^2/s)
$\dot{N}$ Total molar flow rate (mols/s)
P Pressure (Pa)
R Universal gas constant (=8.314 J/mol/K)
T Absolute temperature (K)
$\dot{n}$ Molar flowrate of species (mols/s)
y Mole fraction

Greek symbols

δ Gypsum wallboard thickness (m)
φ Porosity (dimensionless)
τ Tortuosity (dimensionless)

Subscripts

co   Carbon monoxide
in   Flowing into chamber
out   Flowing out of chamber
eff   Effective
ij Denotes species i and j
∞ Ambient conditions

1 Introduction

Carbon monoxide poisoning in buildings from combustion appliances, vehicles, stationary power engines, and fire presents a significant life safety hazard. In their Research Letter to the JAMA Editor, Hampson et al. [1] drew attention to the importance of carbon monoxide (CO) diffusion through gypsum wallboard and the role it could play in carbon monoxide poisoning in occupied spaces. Using a plastic dual-chamber with a piece of gypsum wallboard as a partition between the chambers, they demonstrated that CO readily diffused through gypsum wallboard by monitoring the temporal CO concentrations in the two chambers after a CO release in one chamber and that painting one side of the gypsum wallboard decreased the rate of diffusion.

Yang et al. [2] measured the effective diffusion coefficients of helium and hydrogen through gypsum wallboard using a ¼-scale garage. Mean effective diffusion coefficients for helium were 1.4×10^{-5} m^2/s for unpainted (0.0127 m thick) wallboard and 3.4×10^{-6} m^2/s for the same wallboard with one coat of primer and two coats of semi-gloss interior latex paint. Here, painting decreased the effective diffusion coefficient by about a factor of four. Assuming molecular diffusion is the dominant mechanism for gypsum wallboard diffusion; the estimates of CO diffusion for unpainted and painted wallboard can be made. For porous media such as gypsum wallboard, Eq. (1) relates the binary diffusion coefficient (D_{ij}) to the effective diffusion coefficient.

$$D_{\text{eff}} = \frac{\varphi}{\tau} D_{ij} \tag{1}$$

where φ the porosity and τ the tortuosity are properties of the porous media. Thus, at constant temperature and pressure, Eq. (2) can be used to estimate the effective diffusion coefficient for other gas species through porous media.

$$\frac{D_{\text{eff}}}{D_{ij}} = \frac{\varphi}{\tau} = \text{constant} \tag{2}$$

At 20 °C and 101.3 kPa atmospheric pressure, the binary diffusion coefficients for helium/air and CO/air are 5.80×10^{-5} m^2/s and 2.08×10^{-5} m^2/s, respectively, and the computed estimated effective diffusion coefficients for CO through gypsum wallboard samples used in Ref. [2] are 5.0×10^{-6} m^2/s and 1.2×10^{-6} m^2/s for unpainted and painted samples, respectively. These diffusion coefficients are consistent with the experimental results of Hampson et al. [1].

The hazards of CO poisoning and the increase in stand-alone CO alarms and smoke alarms that include CO sensors to detect fire in buildings induced NIST to seek a more complete understanding of CO diffusion through walls and ceilings. This has included measuring the effective diffusion coefficients of two gypsum wallboard types either unpainted or with one or two coats of different types of paints and two full-scale sealed-room experiments where CO was released and allowed to diffuse through painted and unpainted gypsum wallboard walls and ceiling.

2 Experimental Setup

2.1 Measurement of Effective Diffusion Coefficient

Here, a simple method is employed, which was used previously to measure the effective diffusion coefficients of helium and hydrogen through gypsum wallboard using a ¼-scale garage [2]. The method is analogous to a dual-chamber apparatus, except one chamber is the ambient surroundings (an infinite chamber). Figure 1
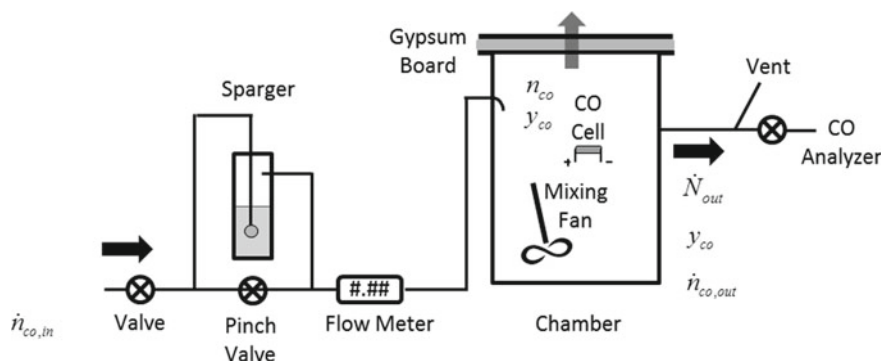
Fig. 1 Schematic of experimental apparatus

shows a schematic of the experimental apparatus. It consists of an open-end stainless steel cylindrical chamber with an internal volume of 8.3 L. The chamber has an inlet and an outlet. A pipe flange was welded to the open end of the chamber. A circular piece of gypsum board with the same outer diameter of the flange was sandwiched between this flange and a removable blank pipe flange with similar dimensions. The edges of the flanges and gypsum board were covered with aluminum tape and secured with four equally spaced clamps to mitigate gas leakage from the gypsum board edges. The inner diameter of the vessel was 0.1900 m $\pm$ 0.0005 m, yielding a surface area for CO transport of 0.02835 m^2 $\pm$ 0.00015 m^2.

An initial set of experiments were conducted using two types of gypsum wallboard, a lightweight wallboard nominally 12.7 mm (½ in.) thick (sample *A*), and type-X wallboard, nominally 15.9 mm (5/8 in.) thick (sample *B*). Both the finished side and backside of the samples had paper exteriors, and when installed the finished side was facing the internal chamber volume. Measurements were made with unpainted and painted boards. The paints were a flat interior latex (latex 1) and a flat interior latex paint and primer product (latex 2). A paint roller applicator was used to apply a uniform layer of paint for one and two coat samples. Painted surfaces were dried for at least one week prior to experimentation.

A compressed gas cylinder of an air/CO mixture with a CO mole fraction of 477.6×10^{-6} mol/mol $\pm 0.1 \times 10^{-6}$ mol/mol was used to continuously supply to the chamber fixed molar (or volumetric) flow rates of nominally 1.0×10^{-3} mol/s (1.5 L/min), 1.4×10^{-3} mol/s (2.2 L/min), or 0.2×10^{-3} mol/s (0.3 L/min). At the highest flow, the pressure difference between the vessel and ambient was about 0.5 Pa, while at the lowest flow the difference was about 0.05 Pa. The CO concentration inside the chamber was made spatially uniform using a small turbo-axial fan. CO concentration was measured using a non-dispersive infrared gas analyzer (expanded relative uncertainty ($k = 2$) of 1%) and/or an electrochemical cell from a residential CO detector, depending on the flow rate. CO was sensed by measuring the voltage drop across a resistor attached to the positive and negative electrodes of the cell. This voltage drop was calibrated against the CO mole fraction of the gas analyzer

over a range from (0 to 477.6×10^{-6}) mol/mol CO in the air with an estimated expanded relative uncertainty ($k = 2$) of 1%. The coverage factor $k = 2$ gives a level of confidence of about 95%. The CO-air mixture was humidified to approximately room air relative humidity by passing a fraction of the incoming flow through a water sparger. Humidity sensors inside and outside the vessel were used to monitor relative humidities. External ambient relative humidity ranged from about 10 to 45% during these experiments and the difference between the external ambient and internal vessel relative humidity at steady-state conditions ranged from -11 to 5% with an average value of 1%. Without humidification of the air mixture from the compressed gas cylinder, the vessel air would become increasingly drier, pulling moisture from both the gypsum board (possibly altering CO diffusion) and the cell (possibly changing the electrolyte concentration and altering the calibration). All experiments were conducted at room temperature (24.5 °C $\pm$ 0.5 °C). Steady-state CO concentrations were typically reached within 2000–10,000 s depending on the flow and the test specimen.

A follow-up set of experiments were conducted using gypsum wallboard from full-scale experiments described below (sample C), an unpainted sample, and samples with one or two coats of a flat interior latex paint (latex 3). Additionally, two samples from the initial experiments and an impermeable steel plate were included in these follow-up experiments.

The main difference between the initial and follow-up experiments was the gas mixture. In the follow-up experiments, a compressed gas cylinder of a nitrogen/CO mixture with a CO mole fraction of 460.0×10^{-6} mol/mol $\pm$ 0.1×10^{-6} mol/mol was used to continuously supply to the chamber a fixed molar (or volumetric) flow rate of nominally 1.4×10^{-3} mol/s (2.2 L/min). The pressure difference between the vessel and ambient was about 0.5 Pa. Again, the CO concentration inside the chamber was made spatially uniform using a small turbo-axial fan and CO concentration was measured using a non-dispersive infrared gas analyzer. The electrochemical cell was not used to record vessel CO concentration here because the CO cell needs oxygen for the necessary chemical reactions, and at steady state, the vessel oxygen concentration is zero. Consequentially, there was no need to humidify the incoming flow. The ambient relative humidity was less than 10% for these experiments.

The following analysis was used to estimate the effective diffusion coefficients from the data. Assuming ideal gas law, a steady-state material balance of CO in the chamber gives

$$\dot{n}_{\text{co,in}} - \dot{n}_{\text{co,out}} - \frac{A D_{\text{eff}}}{\delta}\left(\frac{y_{\text{co}}P}{RT} - \frac{y_{\text{co},\infty}P_{\infty}}{RT_{\infty}}\right) = 0 \tag{3}$$

Assuming ambient mole fraction of CO ($y_{\text{co},\infty}$) is zero, $T \approx T_{\infty}$ (isothermal condition), and $P \approx P_{\infty}$, Eq. (3) becomes

$$y_{\text{co,in}}\dot{N}_{\text{in}} - y_{\text{co,out}}\dot{N}_{\text{out}} - A D_{\text{eff}}\frac{y_{\text{co}}P_{\infty}}{\delta RT_{\infty}} = 0 \tag{4}$$

Since $y_{co,out} = y_{co}$ and the molar flux of air through gypsum is negligible due to very low CO concentration used in the experiments, under these assumptions, a steady-state material balance of air in the chamber results in

$$\dot{N}_{out} = \frac{(1 - y_{co,in})\dot{N}_{in}}{(1 - y_{co})} \tag{5}$$

Substituting Eq. (5) into Eq. (4), we obtain

$$D_{eff} = \frac{\delta R T_\infty \dot{N}_{in}}{A P_\infty}\left[\frac{y_{co,in}}{y_{co}} - \frac{(1 - y_{co,in})}{(1 - y_{co})}\right] \tag{6}$$

Knowing the molar inflow to the chamber and the experimental conditions, an effective CO diffusion coefficient through gypsum can be estimated by measuring the steady-state CO concentration inside the chamber and applying Eq. (6). The molar inflow was computed using the ideal gas law and the measured volumetric inflow. Humidification changes the air/CO inflow mole fraction, so the inflow mole fraction was corrected for water vapor content in the initial set of experiments, but not for the nitrogen/CO inflow experiments which were not humidified.

2.2 Full-Scale Room CO Release and Diffusion Experiments

A room initially constructed inside the National Fire Research Laboratory at NIST for smoke alarm experiments was used to study the diffusion of CO from a large-sealed space with walls and ceilings lined with gypsum wallboard. The internal dimensions of the room were 11.0 m by 7.3 m by 3.7 m high with an internal volume of 294 m^3. Gypsum wallboard 12.7 mm (0.5 in.) thick-lined the walls and ceiling and was finished with paper-taped joints covered with ready-mix lightweight joint compound. The floor was a layer of cement board on top of a layer of plywood. The floor was covered with polyethylene sheeting. Two metal doors and two metal vents were installed in the room and the vents were covered with polyethylene sheeting, so with doors closed, the room was well-sealed with about 210 m^2 of gypsum wallboard surface.

An experiment was conducted with unpainted walls and ceiling and repeated after painting the walls and ceiling with flat interior latex paint (latex 3), in which approximately 28 L of paint was applied with a paint roller in a single uniform coating and allowed to dry for 5 days prior to conducting the experiment.

A high-volume portable fan was placed on the floor in the center of the room to continuously mix the room air contents. CO was released into the room from a small tube running from a compressed gas cylinder located outside the room to the fan. A gas sampling line located in the middle of the room at the mid-floor to ceiling height drew 2.0 L/min of air from the room to a CO gas analyzer to continuously monitor the mixed CO concentration in the room. The entire contents of a 1A compressed gas

cylinder containing a CO/air mixture of approximately 1.5% molar volume fraction of CO were released into the room over a period of about 15 min for each experiment.

A material balance of the room yields the differential equation shown in Eq. (7) for the experimental conditions.

$$\frac{\mathrm{d}y_{co}}{\mathrm{d}t} = \dot{n}_{\mathrm{co,in}}\frac{RT}{PV} - \frac{AD_{\mathrm{eff}}}{V\delta}y_{\mathrm{co}} \tag{7}$$

The concentration decay in the room after the CO release period ($\dot{n}_{\mathrm{co,in}} = 0$) is given by solving the differential equation with the initial condition of $y_{\mathrm{co}} = y_{\mathrm{co,0}}$ (the recorded peak value after the release period) at $t = 0$ (Eq. 8).

$$y_{\mathrm{co}}(t) = y_{\mathrm{co,0}}\mathrm{e}^{-\frac{AD_{\mathrm{eff}}}{V\delta}t} \tag{8}$$

3 Results

3.1 Effective Diffusion Coefficient Measurements

Table 1 summarizes the effective CO diffusion coefficients through the two types of gypsum wallboard and four surface preparations in the initial experiments. The computed means and standard deviations of the effective diffusion coefficient for N repeated trials are tabulated along with the steady-state vessel CO mole fraction and mean inflow. Additionally, the mean values of the flow and CO concentrations (inflow and vessel) were used to compute the combined standard uncertainty, $u_c(D_{\mathrm{eff}})$ (with a $k = 1$ giving a level of confidence of about 68%.), through the propagation of uncertainty of the measured values for comparison [3]. Experiments were conducted with unpainted boards and flow of 1.5 and 2.2 L/min with the vessel exit flow directed to the gas analyzer to compare the resultant diffusion coefficients computed using the gas analyzer and the electrochemical cell concentrations. The mean values computed using the gas analyzer and the electrochemical cell were within 5%. Experiments with unpainted boards conducted at flows of 0.3 L/min using the electrochemical cell yielded mean diffusion coefficients within 5% of the high flow results. All painted-board experiments were conducted at low flow conditions to reduce uncertainties in the computed effective diffusion coefficients.

Table 2 summarizes the estimated effective CO diffusion coefficients through 12.7 mm thick lightweight gypsum wallboard samples (Sample C) used in the two large-scale experiments (unpainted and one coat of latex 3 paint), an additional sample C wallboard with two coats of latex 3 paint, two samples from the initial experiments (for comparison of the two experimental arrangements), and an impermeable steel plate. All experiments were conducted with flows of approximately 2.2 L/min with the outflow directed to the CO analyzer.

Table 1 Effective CO diffusion coefficients and uncertainties for gypsum board samples (air/CO mixture)

Sample	N	Mean y_{co} (mol/mol $\times$ 10^{-6})	Mean inflow (L/min)	Mean D_{eff} (m²/s)	Standard deviation (m²/s)	u_c (D_{eff}) (m²/s)
A—unpainted	4	349.3[a]	1.50	4.06×10^{-6}	6.12×10^{-8}	1.7×10^{-7}
A—unpainted	3	352.4	1.50	3.97×10^{-6}	1.88×10^{-8}	1.7×10^{-7}
A—unpainted	3	382.4[a]	2.20	4.09×10^{-6}	1.31×10^{-8}	2.2×10^{-7}
A—unpainted	3	381.5	2.20	4.13×10^{-6}	6.40×10^{-8}	2.2×10^{-7}
A—unpainted	3	174.6	0.32	4.09×10^{-6}	2.79×10^{-8}	1.0×10^{-7}
A—1 coat latex 1	3	344.4	0.32	9.13×10^{-7}	1.99×10^{-9}	4.0×10^{-8}
A—2 coats latex 1	4	457.4	0.30	9.93×10^{-8}	2.30×10^{-8}	2.4×10^{-8}
A—2 coats latex 2	4	456.0	0.29	8.55×10^{-8}	2.06×10^{-8}	2.3×10^{-8}
B—unpainted	3	388.2[a]	2.20	4.68×10^{-6}	1.06×10^{-7}	2.7×10^{-7}
B—unpainted	3	391.2	2.20	4.48×10^{-6}	1.95×10^{-7}	2.6×10^{-7}
B—unpainted	3	183.8	0.32	4.70×10^{-6}	1.69×10^{-8}	1.2×10^{-7}
B—1 coat latex 1	3	386.5	0.32	6.94×10^{-7}	1.82×10^{-8}	3.9×10^{-8}
B—2 coats latex 1	3	462.0	0.32	1.00×10^{-7}	6.97×10^{-10}	3.1×10^{-8}
B—2 coats latex 2	3	464.8	0.33	8.54×10^{-8}	7.93×10^{-9}	3.2×10^{-8}

[a]CO concentration from gas analyzer

3.2 CO Diffusion from the Full-Scale Room Experiments

The temporal CO concentration measurements for the unpainted and painted gypsum wallboard experiments are shown in Fig. 2. During the CO release period for both experiments, there was a linear increase in CO concentration, peaking at a mole fraction of ~200 $\times$ 10^{-6} mol/mol, followed by exponential decay of the CO concentration. Figure 3 shows the decaying portion of the curves fitted to Eq. (8). The symbols represent the experimental measurements, and the solid lines are the fitted curves. Both curve fits started at a peak CO mole fraction of 184 $\times$ 10^{-6} mol/mol

Table 2 Effective CO diffusion coefficients and uncertainties for gypsum board samples and steel plate (nitrogen/CO mixture)

Sample	N	Mean y_{co} (mol/mol × 10^{-6})	Mean inflow (L/min)	Mean D_{eff} (m^2/s)	Standard deviation (m^2/s)	u_c (D_{eff}) (m^2/s)
Steel plate	2	458.4	2.22	6.42×10^{-8}	2.88×10^{-8}	8.2×10^{-8}
A— unpainted	3	370.7	2.24	4.03×10^{-6}	5.02×10^{-8}	1.3×10^{-7}
A—1 coat latex 1	3	459.2	2.24	3.03×10^{-8}	7.04×10^{-9}	8.2×10^{-8}
C— unpainted	3	367.7	2.24	4.20×10^{-6}	5.47×10^{-8}	1.3×10^{-7}
C—1 coat latex 3	3	369.3	2.24	4.10×10^{-6}	4.72×10^{-8}	1.3×10^{-7}
C—2 coats latex 3	3	372.3	2.25	3.95×10^{-6}	7.08×10^{-8}	1.3×10^{-7}

Fig. 2 Room carbon monoxide concentration during filling period and diffusive loss decay (wallboard sample C and paint latex 3)
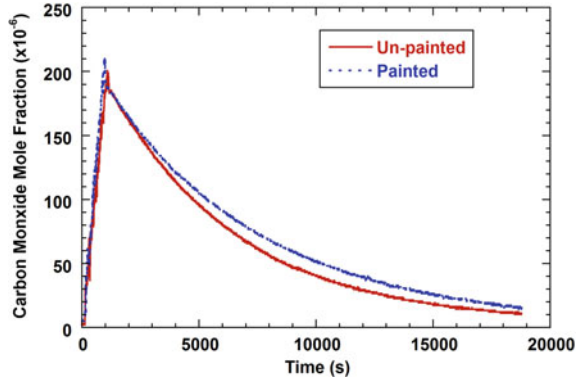
Fig. 3 Fitted room carbon monoxide concentration diffusive loss decay curves (wallboard sample C and paint latex 3)
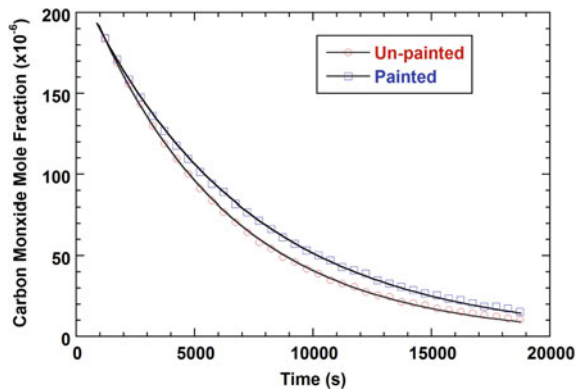
where the concentrations were equal to some 19 min after the beginning of each CO release. Equation (8) provides a good fit to both curves. The fitting parameters $(AD_{eff}/V\delta)$ were 1.713×10^{-4} s^{-1} and 1.447×10^{-4} s^{-1} for the unpainted and painted curves, respectively. Given the room volume of 294 m^3 and the gypsum wallboard thickness and surface area of 0.0127 m and 210 m^2, respectively, effective diffusion coefficients of 3.05×10^{-6} m^2/s and 2.57×10^{-6} m^2/s are estimated for the unpainted and painted wallboard experiments. Here the difference between the sample C unpainted and painted wallboard effective diffusion coefficients is about a 16% reduction, whereas the difference between the measured values in Table 2 was about 2%.

These estimates are somewhat lower than the measured diffusion coefficients, most likely due to an overestimate of the effective area for diffusion. The application of tape and joint compound at seams and joint compound skimmed over nail heads may result in a lower effective area for CO diffusion. Also, the wood or steel studs that the wallboard was attached to may reduce the effective area somewhat. If one uses the measured effective diffusion coefficients and calculates effective areas for diffusion, they are 152 and 129 m^2 or 71 and 60% of the total surface area for unpainted and painted wallboard experiments.

4 Discussion

The initial experiments measuring effective diffusion coefficients demonstrated the technique provides repeatable results with relative standard deviations of repeated measures typically less than 1% for unpainted samples. Through propagation of error, the relative combined standard uncertainty ($k = 1$) for unpainted and one-coat painted samples was typically less than 5%, increasing to between 24 and 37% for samples with two coats of paint. Consistent results were obtained with the CO analyzer and CO electrochemical cell concentration measurements and at the three nominal flow rates examined. Differences between specific wallboard samples could be resolved. The effective diffusion coefficient ratios for unpainted to painted boards (using mean, low flow results) are 4.5, 41, and 48 for the lightweight gypsum board with one or two coats of interior latex paint (latex 1) or 2 coats of the paint/primer product (latex 2), and 6.8, 47, and 55 for type-X gypsum board with one or two coats of interior latex paint (latex 1) or 2 coats of the paint and primer product (latex 2), respectively.

The follow-up experiments identified a wide range of effective diffusion coefficients possible for painted wallboard samples clearly indicating that paint chemical formulation can have wide-ranging effects on the permeability. All paints examined were flat interior house latex-based formulations. The initial assumption was that such paints would be similar to one another and to the experimental results in Refs. [1, 2]. The results for the paint chosen for the full-scale room experiments did not come close to the other paints. This difference was emphasized by comparing the effective diffusion coefficient of a sample with one and two coats of the paint used in

the full-scale experiments (latex 3) to the results from an unpainted sample. One coat provided only a 2.4% reduction in the effective diffusion coefficient and two coats provided only a 6.0% reduction. In contrast, the flat interior latex paint used in the initial experiments (latex 1) showed a decrease in the effective diffusion coefficient by a factor of 4.5 for one coat and a factor of 41 for two coats compared to the unpainted sample.

The technique used in the follow-up experiments provided comparable effective diffusion coefficient measurement to an initial experiment as demonstrated by the values obtained with sample (A—unpainted) where the mean values differ by about 1.5%. Also demonstrated was the inability to resolve the effective diffusion coefficient for painted samples with much lower permeability than unpainted wallboard at the high inflow condition. Both the steel plate and sample (A—1 coat latex 1) measurements yield lower effective diffusion coefficients, but the combined standard uncertainty ($k = 1$) is greater than the measured value in these cases. The steel plate should yield essentially zero diffusion, while the sample (A—1 coat latex 1) is about an order of magnitude lower than the mean value listed in Table 1. These results indicate that the CO concentration resolution and measurement uncertainty are not sufficient here to resolve these diffusion coefficients at the inflow of 2.2 L/min.

The full-scale experiments clearly show the diffusion of CO through gypsum wallboard. While the differences between the painted and unpainted surface experiments do not exactly match the effective diffusion coefficient differences, they still show the results are much closer (perhaps within the experimental uncertainty of the full-scale experiments) than the effective diffusion coefficient measurements with the other paint samples.

Analyses of realistic situations, such as residential conditions detailed by Emmerich et al. [4], are needed to assess the potential hazard of CO diffusion through gypsum wallboard into living spaces and the extent of hazard mitigation by painting wallboard surfaces. With measured effective diffusion coefficients, modeling can be used to assess the movement of CO from, for example, an attached garage space into the living space where CO diffusion is the only significant transport mechanism between spaces. Modeling results could then be used to inform codes and standards development regarding CO hazard mitigation or sensing requirements.

In some fire scenarios, CO transport through gypsum wallboard may significantly affect tenability in remote, enclosed locations. When conducting full-scale compartment fire experiments, CO monitoring in remote rooms should be considered. When modeling compartment fire scenarios, it may be important to assess potential CO diffusion between compartments for a more complete hazard assessment. At present, it is unknown how thermal damage of gypsum wallboard or smoke deposition on wallboard would impact CO diffusion.

5 Conclusions

From these experiments, the following conclusions are drawn.

- The initial experiments show a robust method to measure the effective diffusion coefficients of CO for unpainted and painted samples of gypsum wallboard. The reduction of the flow into the vessel and in situ measurement of the CO concentration by a calibrated electrochemical cell allowed for effective diffusion coefficient measurements of painted wallboard samples.
- Results from the initial experiments and the follow-up experiments showed dramatic differences in effective diffusion coefficients for some painted surfaces. The results show carbon monoxide readily diffuses through gypsum wallboard, while application of paint to one surface was shown to have almost no effect, a few percent decrease in the effective diffusion coefficient, to a dramatic reduction in carbon monoxide diffusion of up to a 55-fold decrease in the effective diffusion coefficient for samples with two coats of one house paint.
- The results from the full-scale room experiments demonstrated CO diffusion through gypsum wallboard in real-scale experiments and that painting gypsum wallboard may only have a small effect on reducing diffusion through the walls and ceiling in a sealed room.
- All three paints examined were flat-finish, latex-based interior house paints; clearly, the paint chemical formulation affects gas permeability and hence the effective diffusion coefficient. To be conservative, one should assume carbon monoxide diffusion through gypsum wallboard progresses at the higher rate commensurate with an unpainted surface unless specific data is gathered.
- In fire experiments such as fire reconstruction experiments in enclosures and standard room detection experiments where CO measurements are made, diffusion of CO through the surfaces should be considered.

References

1. Hampson, N. B., Courtney, T. G., & Holm, J. R. (2013). Diffusion of carbon monoxide through gypsum wallboard. *JAMA, 310*(7), 745–746.
2. Yang, J. C., Pitts, W. M., Fernandez, M., & Prasad, K. (2013). Measurement of effective diffusion coefficients of helium and hydrogen through gypsum. *International Journal of Hydrogen Energy, 38,* 8125–8131.
3. Taylor, B. N., & Kuyatt, C. E. (1994). *Guidelines for evaluating and expressing, the uncertainty of NIST measurement results, NIST Tech. Note 1297*. (1994 ed.). Washington, DC: US Government Printing Office.

4. Emmerich, S., Persily, A. K., & Wang, L. (2013). *Modeling and measuring the effects of portable gasoline powered generator exhaust on indoor carbon monoxide level*. NIST Technical Note 1781, http://dx.doi.org/10.6028/NIST.TN.1781.

Experimental Investigation of Smoldering Combustion of Tropical Peat Layer Under Stratified Moisture Content

Pither Palamba, Mohamad Lutfi Ramadhan, Luthfi Rizki Perdana, Afiri Dianti, Nadhira Gilang Ratnasari, Fahri Ali Imran, Engkos Achmad Kosasih and Yulianto Sulistyo Nugroho

Abstract Considerable amount of experiments regarding smoldering combustion of peat had been conducted through various methods of experiment, modeling, and field study, with factors affecting the smoldering combustion of peatlands include: moisture content, density, porosity, wind speed, etc. However, it can be seen that some researches that focus on the influence of moisture content did not consider the evaporation and drying stages of the smoldering front; thus, the parameters of the test results were determined based on initial moisture content prior to combustion. This experiment was conducted in order to study the smoldering combustion of the peat layer which resembles the real conditions in the field, which involves the stages of preheating, evaporation, drying, pyrolysis, and char oxidation. Varying values of moisture content, increasing with depth, were prepared by drying the raw peat sample (sampling results) at 105 °C for 4, 8, 12, 16, 20, and 24 h. The resulting samples were then placed inside a reactor measuring 10 cm × 10 cm with depth of 20 cm, with each layer of peat with different moisture content at 2.5 cm thick; thus, obtaining a layered peat configuration with the dry peat layer on the surface (MC ~8.5%) and the wet peat layer (raw peat) at the bottom of the reactor. Measurements of smoldering spread, evaporation rate, and mass loss (including evaporation rate) were gathered through instruments of thermocouple, soil moisture sensor, and weight balance, respectively, in real time. The results from the experiment suggested that the evaporation rate, smoldering propagation, and depth of burn depended on the thickness of the burnable dry peat layer, or equivalent to the available amount of heat, which will be partially transferred (converted) for heating, evaporation, pyrolysis, and combustion processes. Therefore, smoldering cannot propagate on the moist peat layer because it will always start with evaporation and drying process. The smoldering front will always be bordered by dry peat layer up to the point where the heat generated is equal or less than the amount needed for evaporation, which is the critical point of extinction.

P. Palamba · M. L. Ramadhan · L. R. Perdana · A. Dianti · N. G. Ratnasari · F. A. Imran · E. A. Kosasih · Y. S. Nugroho (✉)
Fire Safety Engineering Research Group, Department of Mechanical Engineering, Universitas Indonesia Kampus UI, Depok 16424, Indonesia
e-mail: yulianto@eng.ui.ac.id

Nomenclature

MC	Moisture content (% weight)
IC	Inorganic content (%)
HHV	Higher heat value (MJ/kg)
LHV	Lower heat value (MJ/kg)
H	Hydrogen content (%)
Q	Heat (of generation or evaporation) (kW)
$\dot{m}$	Mass consumption rate of peat (kg/h)
$\dot{m}$	Evaporation rate (kg/h)
c_p	Heat capacity of water vapor (kJ/kg·K)

Subscripts

p	Peat
v	Water vapor
g	Generation or release (of heat)
ev	Evaporation

1 Introduction

Wildland fires have risen to global attention in recent years due to environmental
and economic issues, especially after the 1997–1998 El Nino Southern Oscillation
(ENSO) event. Fires are considered a potential threat to sustainable development
because of their direct impact on ecosystems, their contribution to carbon emissions
and their impact on biodiversity. One of the phenomena, and which is the massive
problem in peatland fires is smoldering combustion because it can survive for a long
period of time by propagating along the peat layer to a certain depth [1–3]. In its
natural state, peat has a strong hydrophilicity [4] and a high level of water retention.
Peat can hold a wide range of moisture contents (MC), from 10% under drought
conditions to well in excess of 300% under flooded conditions [5, 6].

Several researchers studied the effects of moisture content toward the smoldering
combustion of peat. Frandsen [7] experimentally found a correlation between criti-
cal MC and IC, recently verified computationally by Huang [8]. The depth of burn
(DOB) and critical MC for extinction at the in-depth spread of peat fires have been

investigated by numerical simulation [9]. McMahon et al. [10] report that peat soils burn at 135% of MC but will not ignite. Wein [11] sampled peat ahead of the smoldering front and found that the smoldering front was spreading into the peat at MC of 100%. Frandsen [7] found that peat moss with less than 10% inorganic content would not smolder when MC was 110% or greater. The results of research conducted by Rein et al. [12] obtained that ignition can be found in the critical moisture content of 125% in dry base with inert fractions of $8 \pm 2\%$. Research with higher moisture content (500%) was conducted by Artsybashev [13]. Rein [14] observed the trend of smoldering combustion, which could spread further and deeper laterally into the ground. Prat [15] obtained the propagation rate of 2.8–6.0 cm/h for numerous moisture content arrangements of burning sphagnum peat. Moisture content is one of the most important factors affecting the ignition, spread, and extinction of smoldering wildfires [6, 7, 12, 16–18]. According to Rein [3], extinction occurs when the vertical spread is quenched by: (i) the presence of the mineral soil layer; (ii) the presence of a thick wet layer; or (iii) the timing of flooding, heavy continuous rains or firefighting.

Several researches on peat samples regarding its moisture content have been conducted, but the majority of the researches were conducted with various moisture content percentages but uniform for the whole depth of the layers. Tests in this study were carried out by burning a layer of 20 cm deep sample with varying moisture content ranging from a dry layer (low MC) on the surface to a very wet sample layer (raw peat) at the bottom, conditioned to resemble the real conditions in the field. With this test, there will be more real information of fire conditions in peatlands, such as the rate of smoldering propagation, mass loss rate, evaporation rate, and depth of burn, as a function of heat generation and moisture content.

2 Materials and Methods

2.1 Sampling and Sample Preparation

The study was conducted on raw peat samples taken from peatland in Tumbang Nusa sub-districts, Pulang Pisau district, Central Kalimantan, Indonesia, at locations with coordinates of S: $-3° 4734''$; E: $113° 55'15''$, with a water table of ± 20 cm. Samples were taken with an undisturbed method, using PVC pipe of 6 in diameter and a height of 65 cm. Based on the soil taxonomy classification method, the peat was categorized as hemic. The sampling location is a peatland that had ever fire in 2015.

For the purpose of this experiment, several numbers of samples (as required) were prepared by drying them in the oven at 105 °C for 4, 8, 12, 16, 20, and 24 h, respectively. Each of the prepared samples was inserted into the reactor with a thickness of 2.5 cm each, starting first from the bottom of the reactor with the raw sample, then on top of that, in the next layer, with the 4 h dried sample until the 24 h dried sample located on the surface. The reactor containing the sample would then be immersed in a water-filled container of 2.5 cm deep and left for 24 h to provide absorption effect
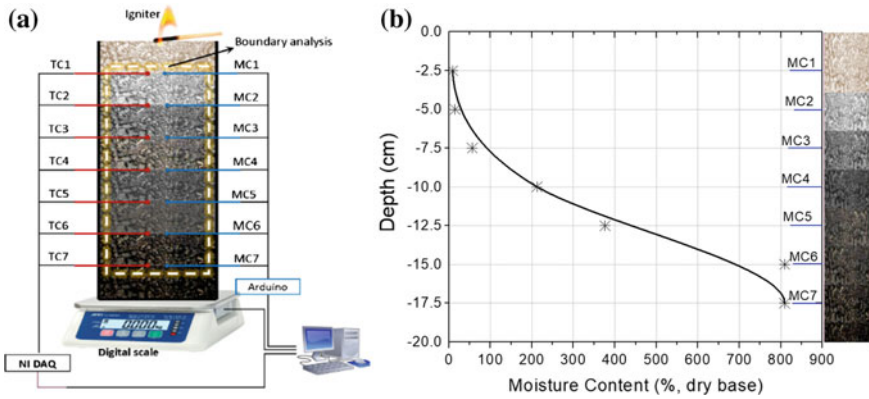
Fig. 1 Experimental setup (**a**) and initial moisture content at a certain depth of peat layer in reactor (**b**). MC stands for moisture content sensor and TC stands for thermocouple

and obtain steady MC distribution to the surface layer. After that, the water on the tray is drained out. From this preparation method, the moisture content percentage on each soil moisture sensor position was measured and acquired as shown in Fig. 1b.

2.2 Experimental Setup

The experiment was conducted using a stainless-steel reactor, and after a 1 cm thick of calci boards placed on each side and base of the reactor, the inside dimension of the reactor was 10×10 cm with 20 cm in height. For every 2.5 cm distance from the surface to the bottom of two sides (left and right wall) of the reactor, a hole is made to implement thermocouples (T1–T7) and soil moisture sensors (MC1–MC7), for each level of peat, respectively, as seen in Fig. 1a. Temperature was acquired with Type *K* thermocouples and data acquisition system (NI DAQ), while moisture content was acquired with soil moisture content sensor and Arduino microcontroller kit. The moisture content reading by Arduino is calibrated with Shimadzu moisture analyzer. After the thermocouples and moisture content sensors were installed in the reactor than placed on a digital scale. Once all measuring devices were ready, the surface of the peat was burned using a burner until sustained combustion was achieved. All the measurement was acquired in real time, from the start of the experiment until the embers in the reactor wore off. In this study, tests were also conducted on dry peat sample (MC 8.5%) with uniform moisture content from its surface all the way through to its base, as a comparison.

3 Results and Discussion

3.1 Temperature Profile, Smoldering Spread Rate and Energy Equilibrium

The smoldering temperature profile during the combustion process of the stratified moisture content can be seen in Fig. 2a compared to the dry layer (Fig. 2b). The curve shows the fuel oxidation at the initial combustion stage, from the surface to sample layer with MC of 21.95%. As pyrolysis reaches the layers with MC 56.25 and 222.58%, the creep rate becomes very slow and char oxidation occurs. In this section, the reaction stage occurs: (1) char oxidation, occurring in the burning layer and consumes the charcoal produced from fuel oxidation of the upper layer, (2) pyrolysis followed by char oxidation on the thin layer below that had become dry, (3) heating and drying of the bottom layer which contains water. The process of char oxidation of the charcoal produced from fuel oxidation above will continue to occur while the char subsidences or collapses. Nevertheless, not all of the peat at the surface was burned to ash due to a large convection heat loss to the air layer. The presence of ash and unburned charcoal at the top layer can serve as heat insulation so that, with the ongoing combustion still occurs, will result in the continuous increase of generated heat.

The sustainability of the downward oxidation reaction to the deeper peat layer is determined by the amount of heat generated during the char oxidation and the heat absorption capacity for moisture content evaporation. The amount of heat generated also depends on the thickness of the dry layer (low moisture content) that can be penetrated by fuel oxidation. In this test, the ability of fuel oxidation can propagate rapidly to a layer thickness of ≤ 7.5 cm within ± 7 h each with an average propagation rate of 2.25, 1.80, and 1.42 cm/h on the layer with an initial moisture content of 8.70, 19.05, and 56.25%.
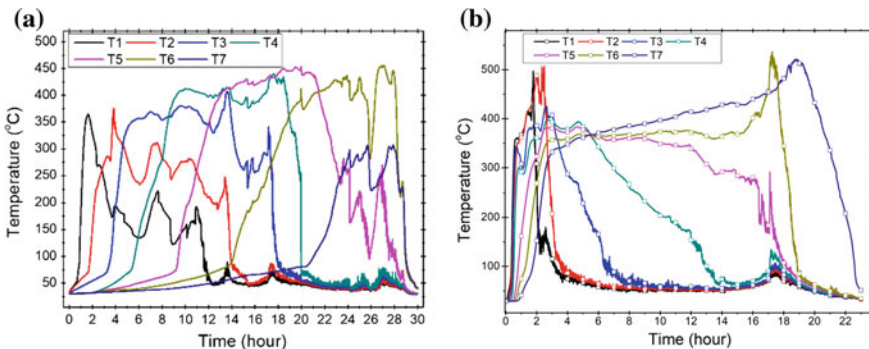
Fig. 2 Temperature profile during smoldering combustion with various MC from top to the bottom (**a**), compared to the dry and uniform MC (**b**)

For comparison, tests were also conducted on a dry sample (uniform moisture content of 9.29%), with a combustion temperature profile as in Fig. 2b, which shows the stages of subtler fuel oxidation and char oxidation. At the bottom of the reactor (where there is no more available fuel to consume), the fuel oxidation stops, and the reaction undergoes char oxidation to the charcoal produced from fuel oxidation above. Along with the char oxidation, the mass and volume of charcoal decrease as it decomposes to ash and smoke. As a result, charcoal that has undergone shrinkage easily subsides and collapses and burn out at the bottom of the reactor. Some other tests [19, 20] are in line with this phenomenon. Similarly, it is in line with the test results on the lateral spread [21], which indicates a tendency for in-depth propagation resulting in overhangs and collapsing.

The average spread rate of smoldering combustion determined based on the time it took when the temperature reaches the ignition temperature at every depth, as the results are shown in Table 1. The deeper the peat layer, the slower the smoldering spread rate, especially, because the combustion inhibited by peat material with high moisture content, so that the heat generated from combustion is partly used for the evaporation and drying process, as discussed in Sect. 3.2.

In the combustion of stratified moisture content peat sample, the smoldering temperature is lower due to the cooling effect of moisture migration from the bottom, and because the heat generated is partly absorbed for the evaporation process. The maximum temperature in this test is ~450 °C with total combustion time of ~29 h, and total average smoldering spread rate of ~0.76 cm/h. In this test, char oxidation can only survive up to about the position of T7, but the layer below the T7 position has partially undergone fuel oxidation and all are in the evaporation phase.

The results of this study indicate conformity with the previous research conducted by Usup et al. [18] in layers I and II of his experimental setup with the appropriate moisture content, which in the study, the spread rate of surface peat fire (at a depth of 0–20 cm) was 1.73–6.49 cm/h for 100–120% moisture content and at a depth of 20–50 cm was 0.5–2.5 cm/h with the moisture content of 120–220%, where the spread rate of deep peat fire was half to a third of that of the surface peat fire. Similarly, there is conformity with the research conducted by Huang and Rein [22] on experiments of downward spread of smoldering peat fires using the 30 cm-high columns of homogeneous peat of 35 and 70% MC. Specifically, the spread rate is found to be in the range of 0.5–2 cm/h. Although both studies were carried out at a depth of 30 and 50 cm, respectively, they were still in low moisture content and did not reveal the stage of the evaporation as part of the phases during the combustion.

3.2 Moisture Content, Evaporation, and Mass Evolution

Figure 3a shows the initial moisture content at various sample depth and its change during the process of combustion evolved. In this case, it should be noted that the recorded data is only at the position of the MC sensor. To better understand this evaporation and drying kinetics, the curve is then merged and arranged with the

Table 1 Average smoldering spread rate at each layer of peat fire tracking by temperature evolution

Layer (depth, cm)	I (0–2.5)	II (2.5–5)	III (5–7.5)	IV (7.5–10)	V (10–12.5)	VI (12.5–15)	VII (15–17.5)	VIII (17.5–20)
Average spread rate (cm/h)	2.25	1.80	1.42	0.94	0.69	0.41	0.22	NA
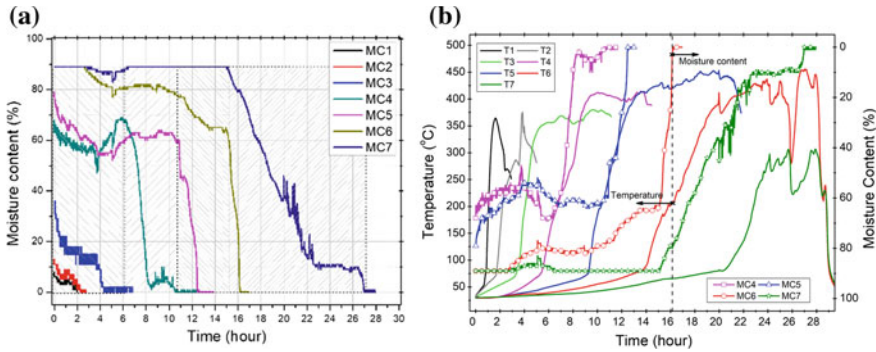
Fig. 3 Moisture content in peat layer exchange during combustion—evaporation—combustion processes (**a**) and compile with the temperature profile during combustion (**b**)

temperature curve based on the depth of layer and the corresponding time, as seen in Fig. 3b. At the beginning of combustion, it appears that high temperatures on the surface (in this case, it was not measured) have had an evaporation effect on moisture content in the lower layers. Despite the low thermal conductivity of peat, but due to the buoyancy effect of smoke and outgoing volatiles, the pressure in the reactor decreases, although it was not measured in this study. At low pressure, saturation temperature also decreases. On the curve, it can be seen that, at temperatures below 100 °C, moisture content up to 12.5 cm deep layer has started to evaporate. Evaporation process below 100 °C can last for 6 and 10 h at 10 and 12.5 cm depth, respectively. At the 4th to about 7th h, it is seen that the moisture content in the peat layer of 10 cm is higher than in the 12.5 cm layer. This is because the process of moisture migration from the layer of 12.5 cm is quite significant and even also has begun on the layer of 15 cm that affected by the vacuum and stronger buoyancy due to an increase in temperature and a thick layer of burning peat. It can also be seen on the curve that at the 5th h, peat at the layer of ~7.5 cm has started char oxidation phase and continue to propagate both downward and upward so that at the 7th h, the embers grow thicker.

The curve in Fig. 3b shows that the preheating process in each layer lasts until the temperature reaches ≤100 °C indicating the pressure in the reactor dropped while evaporation lasts to a temperature of 200–250 °C, where the fuel oxidation starts to take place. The evaporation process is characterized by a fluctuating moisture content curve before falling significantly as a steep curve. The steep curve shows that pyrolysis is taking place down to the peat layer that has become dry. At the ignition temperature where char oxidation begins to occur, samples at MC4 and MC6 are in very dry (MC ~0%), whereas at MC5, the moisture is still relatively high, which is caused by migration of vapor from the underlying layer. Due to the high combustion temperature at the upper layer (± 400 °C) effect the T5s temperature increased and reaches its ignition point. It is also can be seen in the curve that the highest temperature of ~450 °C even occurs in the layer with an initial MC of 89%. This is due to the stagnant smoldering spread and the availability of fuel, i.e., the collapsed of dry samples with a high percentage of carbon content, thus making the

combustion heat greater. As a result of evaporation, the burning condition of the peat samples with initial MC of 89% has changed to ~0%. Thus, it can be concluded that ignition occurs in dry fuel conditions, whereas the initial MC condition changes through the process of preheating, evaporation, and pyrolysis. In the event of fire on the ground, the evaporation reaction is faster because smoldering spread also occurs in 3D where the preheating and evaporation layers are also outside the burning radius. This phenomenon can be seen with the emergence of thick smoke.

At MC7 and T7 position, evaporation is taking place before T7 reaches 100 °C. This is due to the high heating effect with thick smolder on the top layer and a lower pressure due to the discharge of vapor and volatiles. Heat generated from thick smolder of ±7.5 cm lasted from the 7th h until the 23rd h, when T7 reached 100 °C and as a result, the evaporation process occurred significantly below the temperature of 100°. This condition indicates that the pressure in the reactor decreases due to buoyancy from the discharged smoke, and triggered the discharge of the water content. This causes the layer with the most moisture content (MC6 & MC7), i.e. at the bottom, have experienced long periods of heating from the embers layer at the top and result in a significant evaporation rate.

At T5 = 250 °C, MC5 looks high but right afterward the MC decreases drastically because at the transition state the pyrolysis reaction continues to occur with increasing temperature toward char oxidation, causing the value of MC at MC7 layer to quickly drop to dry. In the position of thermocouple T7, char oxidation does not occur despite the presence of pyrolysis; thus, there is a part of the sample that is not burned. In this case, MC7 is mostly influenced by T6 and T5 (Fig. 3b). Thus, sometime after the pyrolysis temperature reaches the maximum, an extinguishing phase occurs because the amount of heat produced is not enough to evaporate the water content while maintaining the combustion itself. At the end of the test, we got the remaining unburned sample and ash, respectively.

In heterogeneous combustion, the drying kinetics is determined by the amount of heat produced and the amount of water content to be dried. Thus, the spread rate also does not run constantly (seamlessly), but there is a time when it looks "as if" it stops where the dominant reaction that occurs is evaporation. To understand this process, the temperature curve and the moisture content curve can be combined as shown in Fig. 4a. In the figure it can be understood that the rising curve (dm/dt increase) indicates that the dominant combustion process is accompanied by evaporation until combustion reaches the condition of which it is unable to burn, followed by evaporation and drying (down curve) until the smoldering front becomes dry and burning process once again occurs. This process continues until the resulting combustion heat is not sufficient to be utilized for evaporation. Drying kinetics of the sample used in this test have been studied [23] where the activation energy is 30.11 kJ/mole.

Figure 4c shows the mass loss curve during the processes. Although the mass evolution curve looks similar to the test of the uniform moisture content sample, this particular graph shows mass loss occurring on each layer due to evaporation as seen with the curve of mass over time (dm/dt). Mass loss curve at the 6th h mark until the 21st h mark looks steeper because, at that time, it burns with maximum temperature, capable of giving maximum evaporation effect so dm/dt becomes substantial. The
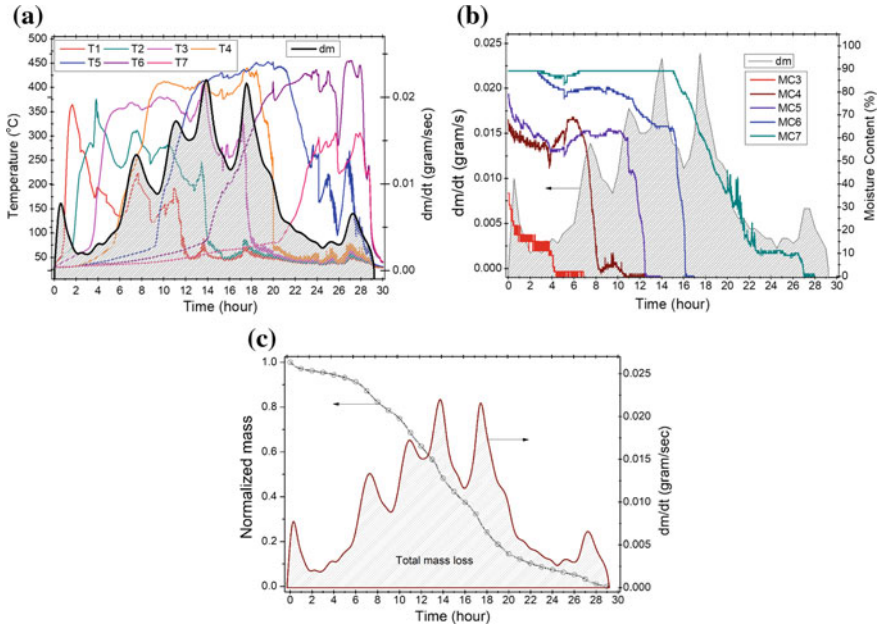
Fig. 4 The relation between smoldering combustion temperature (**a**) and moisture content change (**b**) to the mass loss rate; and differential of mass loss and evaporation at certain time (**c**)

steep curve shows the falling rate period of drying due to the degraded layer of lignin structure. As a reaction at high temperatures above 200 °C, lignin is split into smaller particles and separated from cellulose. This is also because of the shrinkage that formed a lot of voids, resulting in a reduced momentum and increased mass transport of vapor.

Based on Fig. 4a, there is a relationship between the combustion temperature and the rate of evaporation. To know the effectiveness of the absorption of heat of evaporation, energy equilibrium analysis can be conducted. The amount of heat generated (Q_g) based on smoldering spread rate, can be calculated as follows:

$$Q_g = \dot{m}_p \cdot \text{LHV} \tag{1}$$

where:

$\dot{m}_p$ peat consumption mass rate (kg/h)
LHV   low heating value (MJ/kg)
       $HHV - 0.024\,(\text{MC} + 9\text{H})$

For the sample used, it is known the gross calorific value of 20.30 MJ/kg with MC = 12.81% adb and % H = 5.48, so the value of lower caloric, LHV = 20.285 MJ/kg. The amount of heat absorbed in the heating and evaporation process (Q_{ev}) is:

$$Q_{\text{ev}} = \dot{m}_w \cdot c_p \cdot \Delta T + \dot{m}_{\text{ev}} \cdot L_v \tag{2}$$

where:

$\dot{m}_w$ mass flow rate of heating water (kg/h), assumed to be the same of evaporation rate

$\dot{m}_{ev}$ evaporation rate (kg/h)

c_p specific heat of water vapor (=1.996 kJ/kg K)

ΔT difference between evaporation and saturation temperature (K)

L_v latent heat for vaporization (kJ/kg)

By the energy equilibrium between Eqs. (1) and (2), the evaporation rate and heat absorb calculated as the result shown in Fig. 5a. In the figure it can be seen that with the amount of heat generated from the combustion process, although most of it is wasted to the upper part due to buoyancy effect, the buoyancy effect itself creates a reduced pressure and is able to evaporate the water content in the underlying layer with an evaporation rate, which tends to increase with the increase in moisture content and depth. This is because the heat generated to a depth of 12.5 cm is quite large, even though it decreases due to the mass loss and spread rate, but in terms of energy equilibrium, the amount of heat is still capable of evaporating the water content greater than the actual evaporation rate. The energy balance graph is shown in Fig. 5a. shows the energy balance graph, while Fig. 5b shows the relationship between the peat mass loss rate and the carbon emission flux.

The evaporation as part of the mass loss occurs with the process of combustion but at certain times, more heat is used for evaporation process. The higher the temperature and the thicker the smolder, the faster the evaporation rate. At the time the peat begins to dry, shrinkage, and void occurs to facilitate the process of moisture migration out of the surface and heat transfer to the bottom of the sample. Thus, the smoldering spread rate is not only determined by MC but the amount of heat that is available to evaporate and drying the smoldering front. At the end of burning, i.e., when the
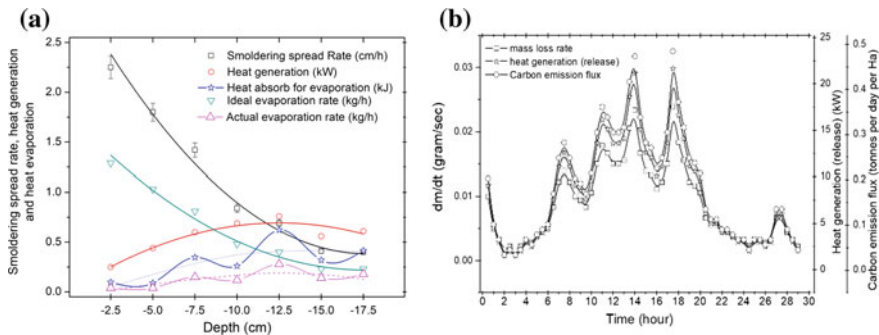
Fig. 5 The relationship between the magnitude of the combustion heat and the smoldering spread rate and the evaporation rate at various depths that represents the moisture content (**a**) and the relationship between the peat mass loss rate and the carbon emission flux (**b**)

smoldering front reaches the lower layer with a high MC (±5 cm from the reactor base), most of the heat is used to evaporate the water content of the wet layer until it reaches a critical point, where the heat is reduced and not sufficient enough to evaporate water.

Based on Fig. 5a, the smoldering spread and heat generation rate decrease as the increases of depth and/or moisture content. However, in Fig. 3 it can be seen that the combustion temperature, actually, increases and lasts until the end of combustion. Similarly, the ideal evaporation rate based on the calculation of energy equilibrium will decrease. In high MC conditions, heat generation is widely used for the evaporation process, which is the endothermic reaction so that the actual evaporation rate tends to increase. This process will last until the heat generation becomes equal or smaller than the heat absorbed. In the heat equilibrium, the larger heat losses are caused by the buoyancy effect of combustion resulting in heat loss by convection. Vapor coming out through the burning layer will also result in heat generation being reduced due to the cooling effect of the vapor migration. From this test can be known as the rate of energy generation and carbon emission flux comparable with the rate of consumption of combustion materials. At a total average mass loss rate yields 18.80 kW with a burning rate (carbon emission flux) equivalent to 7.86 tons per day per ha.

3.3 Depth of Burn (DOB)

To date, no reference has been made to the DOB on peat swamps as a function of moisture content. Through post-fire observation, there are literature reporting the DOB such as Benscoter et al. [5] and Ballhorn et al. [24] who reported observed DOB of 17 cm and 33 ± 18 cm, respectively, although not reported in relation to other parameters such as moisture content. In this test, from the depth of the peat sample with varying moisture content as deep as 20 cm, the combustion can consume samples up to a depth of ±17.5 cm, which can be verified as shown in Figs. 2 and 3, with the ash yield of 12 gs, the charcoal resulted from the fuel oxidation as much as 43.5 gs and unburned samples with MC ± 43% (wet base) as much as 100.5 gs. The total average mass loss rate during the smoldering combustion takes place, in which the evaporation process occurs, obtained by ~0.032 kg/h.

Based on this test, the depth of burned highly depends on the thickness of the dry (low moisture content) peat in the surface layer. Burning a thick dry layer will produce thicker fuel oxidation so that in the further combustion phase, i.e., char oxidation, the combustion will generate a higher-and-longer-lasting of heat; thus, the evaporation and drying process can survive and produce dry layer of the sample to maintain the combustion process viable, as shown in Fig. 3b and illustrated in Fig. 6a. The combustion reaction will stop if the heat generation is not sufficient to vaporize and dry out the moist peat layer below. Thus, DOB is largely determined by MC and the thickness of the dry layer of the peat.
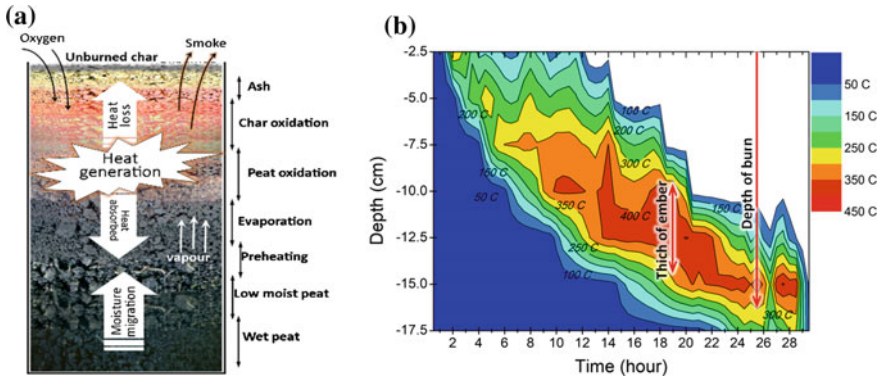
Fig. 6 The illustration of the layer of some substances material in the smoldering combustion process: preheating, evaporation, pyrolysis, char oxidation, and extinction (**a**), and the 2D contour plot of temperature distribution and thickness of smoldering layer among the combustion process (**b**)

Figure 6b shows the profile of the propagation and the thickness of the smoldering ember at a certain time since the combustion started on the surface until extinction on the bottom of the reactor. In figure it can be seen that at the 12th h the thickness of the embers has reached ≥7.5 cm, as measured from the position of the T2–T5s thermocouple. The 7.5 cm thick of ember occurs until the 20th h (for about 7.5 h) where the combustion has reached the position of the T6 thermocouple (5 cm from the bottom of the reactor). After that, the thickness of the embers is reduced to ≥5 cm (measured by the temperature of T5–T7). At the 25th h, it appears that the temperature of T6 and T7 dropped dramatically but increased again at the 26th h and there was a re-burning process that lasted until the 28th h. This is because of large momentary evaporation from the bottom of the sample resulting in a large heat loss from the embers. Measurements in the T7 thermocouple indicate that the fuel oxidation is still last until the 29th h by consuming the sample at the bottom (the layer between the T7 position and the reactor base). The extinguishing and cooling phase lasted until the 30th h.

The results of the study conducted by Usup [18], obtaining the DOB of 50 cm with a spread rate of 0.5–2.5 cm/h at the initial moisture content of 120–220% showed little conformity with the results obtained from this test that at MC ~220 (equivalent at a depth of 10 cm in this study), smoldering combustion may take place with a spread of 0.84 cm/h. However, the stratification of the moisture content of the peat layer in this test differs from that conducted by Usup, where for the moisture content of 50 cm depth was 220%, indicates that the peatland was in a very dry condition caused by the result of drainage channel production and compounded by the El-Nino at that time. In addition, the smoldering combustion in peatland is strongly influenced by wind speed.

4   Conclusion

Drying kinetics becomes an important part during the combustion takes place on peat with high moisture content. The initial MC is not a reference to measure the smoldering spread rate. The stages that take places in the combustion process of moist peat include evaporation and drying, peat oxidation, char oxidation, and extinct. In the dry layer, a fuel oxidation process occurs that precedes the occurrence of char oxidation.

If the heat generated from combustion is sufficient, a certain amount of heat will be absorbed for a rapid evaporation process leading to a condition where the evaporation rate becomes more dominant than the combustion rate. The rate of evaporation depends on the amount of heat released from peat smoldering. The thicker the peat layer is burned, the more heat is released, and the more water content will evaporate; thus, smoldering combustion can propagate deeper into the bottom layer when the layer becomes dry. Under such conditions, the smoldering combustion on the peat layer can survive for a long time. Thus, it can be concluded that embers do not propagate in the wet peat layer but relatively in a dry state (MC ~0%). The moisture content of the peat sample mentioned at the beginning of tests is only the initial condition of samples, which in the combustion process will undergo evaporation and drying.

Smoldering combustion can withstand high MCs when sufficient heat is available to evaporate water content in peat. This can occur when there is a thick layer of dry and/or low moisture content peat in the surface that yields to a thick ember when burned. In this test, the smoldering combustion can produce a total heat release of 18.80 MW (average 643.40 kW/h) and under the same conditions, burning of peat in the field can produce a burning rate of carbon (carbon emission flux) of 7.86 tons per day per ha. In conditions where there is airflow as well as on the ground, combustion will take place more rapidly [21, 22] with higher temperatures, so that the rate of evaporation and combustion will take place more rapidly.

References

1. Page, S. E., et al. (2002). The amount of carbon released from peat and forest fires in Indonesia during 1997. *Nature, 420*(6911), 61–65.
2. Turetsky, M. R., et al. (2015). Global vulnerability of peatlands to fire and carbon loss. *Nature Geosci, 8*(1), 11–14.
3. Rein, G. (2013). *Smouldering fires and natural fuels*, in *fire phenomena and the earth system* (pp. 15–33). Wiley.
4. Perdana, L., et al. (2018). *Hydrophilic and hydrophobic characteristics of dry peat*. In *IOP Conference Series: Earth and Environmental Science*. IOP Publishing.

5. Benscoter, B., et al. (2011). Interactive effects of vegetation, soil moisture and bulk density on depth of burning of thick organic soils. *International Journal of Wildland Fire, 20*(3), 418–429.
6. Watts, A. C. (2013). Organic soil combustion in cypress swamps: Moisture effects and landscape implications for carbon release. *Forest Ecology and Management, 294,* 178–187.
7. Frandsen, W. H. (1987). The influence of moisture and mineral soil on the combustion limits of smoldering forest duff. *Canadian Journal of Forest Research, 17*(12), 1540–1544.
8. Huang, X., Rein, G., & Chen, H. (2015). Computational smoldering combustion: Predicting the roles of moisture and inert contents in peat wildfires. *Proceedings of the Combustion Institute, 35*(3), 2673–2681.
9. Huang, X., & Rein, G. (2015). Computational study of critical moisture and depth of burn in peat fires. *International Journal of Wildland Fire, 24*(6), 798–808.
10. McMahon, C. K., Wade, D. D., & Tsoukalas, S. N. (1980, June 22–27). *Combustion characteristics and emissions from burning organic soils.* In *73rd Annual Meeting of the Air Pollution Control Association. Montreal, Quebec, June 22–27,* pp. 2–16.
11. Wein, R.W., & Maclean, D. (1983). *Fire behaviour and ecological effects in organic terrain.*
12. Rein, G., et al. (2008). The severity of smouldering peat fires and damage to the forest soil. *CATENA, 74*(3), 304–309.
13. Artsybashev, E. (1983). *Forest fires and their control.*
14. Rein, G. (2009). *Smouldering combustion phenomena in science and technology.*
15. Prat-Guitart, N., et al. (2016). *Effects of spatial heterogeneity in moisture content on the horizontal spread of peat fires.* Science of the Total Environment.
16. Frandsen, W. H. (1997). Ignition probability of organic soils. *Canadian Journal of Forest Research, 27*(9), 1471–1477.
17. Garlough, E. C., & Keyes, C. R. (2011). Influences of moisture content, mineral content and bulk density on smouldering combustion of ponderosa pine duff mounds. *International Journal of Wildland Fire, 20*(4), 589–596.
18. Usup, A., et al. (2004). Combustion and thermal characteristics of peat fire in tropical peatland in Central Kalimantan. *Indonesia. Tropics, 14*(1), 1–19.
19. Dianti, A., et al. (2018). *Effect of rewetting on smouldering combustion of a tropical peat.* E3S Web Conference, 67.
20. Nadhira Gilang, R., et al. (2018). Laboratory scale experimental study of foam suppression on smouldering combustion of a tropical peat. *Journal of Physics: Conference Series, 1107*(5), 052003.
21. Huang, X., et al. (2016). Experimental study of the formation and collapse of an overhang in the lateral spread of smouldering peat fires. *Combustion and Flame, 168,* 393–402.
22. Huang, X., & Rein, G. (2017) Downward spread of smouldering peat fire: The role of moisture, density and oxygen supply. International Journal of Wildland Fire.
23. Palamba, P., et al. (2018). Drying Kinetics of Indonesian Peat. *International Journal of Technology, 9*(5), 1006–1014.
24. Ballhorn, U., et al. (2009). Derivation of burn scar depths and estimation of carbon emissions with LIDAR in Indonesian peatlands. *Proceedings of the National Academy of Sciences, 106*(50), 21213–21218.

Pyrolysis Kinetic Analysis of Forest Combustible Material: An Improved Method for Optimization Calculation

Hong Zhu and Naian Liu

Abstract Pyrolysis kinetic analysis of forest combustible material plays an important role in modeling wildland fire. For the kinetic analysis method by using optimization calculations, there is a lack of a reliable method to determine the search ranges of the parameters. This work presents an effort for this problem, for which we propose a comprehensive method by the combined use of the Kissinger method, the model-free methods and a two-point method. For the comprehensive method, the Kissinger method is used to preliminarily evaluate the activation energy of the reaction steps corresponding to the DTG peaks, the model-free methods are used to compare the activation energy values for different pseudo-components, while the two-point method is used to preliminarily evaluate the lower limits of activation energy and pre-exponential factor for the first reaction step. By using this comprehensive method, reasonable search ranges of the activation energy and pre-exponential factor can be determined for optimization calculations. The thermogravimetric experimental data of pine bark at heating rates of 10, 15, 20, and 25 K/min under nitrogen atmosphere are used to check the reliability of the comprehensive method. The genetic algorithm (GA) method is used for optimization calculations. The results show that by the comprehensive method, the GA calculation performs more efficiently than the calculation by using blind range. In addition, if a part of the parameter range is improper, the search range can be further narrowed based on the comprehensive method.

Keywords Kinetic analysis · Kissinger method · Model-free methods · Genetic algorithm

Nomenclature

A Frequency factor (1/min)

H. Zhu · N. Liu (✉)
State Key Laboratory of Fire Science, University of Science and Technology of China, Hefei, Anhui 230027, People's Republic of China
e-mail: liunai@ustc.edu.cn

E	Activation energy (kJ/mol)
$f(\alpha)$	Mechanism function
m	Sample mass (mg)
n	Reaction order
r	Contribution coefficient
R	Gas constant
t	Time (min)
T	Absolute temperature (K)

Greek symbols

α	Conversion fraction
β	Heating rate (K/min)

Subscripts

0	Initial value
∞	Final value
acc	Initially accelerate
i	Number of components
j	Number of experimental runs
k	Number of data points in each run
p	DTG peak

1 Introduction

Pyrolysis of forest combustible material, as the initial stage of the ignition, plays an important role in wildland fires. A substantial amount of research has already been carried out on the pyrolysis of forest combustible material in studies related to fire safety, for which the determination of the kinetic parameters is a major objective [1, 2]. During the past decade, the optimization techniques, especially global search methods, have been widely used to obtain the kinetic parameters for pyrolysis of forest combustible material. Anca-Couce et al. [3] determined the kinetics constants with the least squares method for the reactions of wood pyrolysis, wood oxidation, and char oxidation. Amutio et al. [4] developed a kinetic scheme consisting of six simultaneous reactions for pinewood oxidative pyrolysis, for which the kinetic parameters were calculated with the Levenberg–Marquardt Algorithm. Niu and Liu [5] evaluated kinetic parameters for thermal decomposition of the pine branch by

the combined use of GA and nonlinear fitting algorithm. Ding et al. [6] estimated beech pyrolysis kinetic parameters by shuffled complex evolution. Although there have been many reports [3–6] on optimization techniques, the initial values and the predefined ranges for optimization calculations usually depend on experience and literature data [7]. Wide search ranges are usually used to ensure that the actual kinetic parameter values are covered. However, since many incorrect values are introduced at the same time, it is often difficult to converge the optimal solution. Niu and Liu [5] indicated that although GA is capable of quickly finding promising regions of the search space, it often takes a relatively long time to converge to a localized solution. Li et al. [7] proposed that if the search ranges are too large or misplaced, it takes an even longer time to converge and becomes more difficult to obtain reasonable solutions. Little attention has been paid to the methodology of narrowing the search range. Li et al. [7] chose a range of the peak temperature as ±5 K of a local minimum of the |DDTG| curve. Then, they obtained the ranges of activation energy and pre-exponential factor with the Kissinger method. It is difficult to determine how extent peak temperature shifts for each reaction at different ranges of heating rates. A method to obtain an optimized range depending on the kinetic analysis method has not been reported yet.

With the above problem in mind, the objective of this work is to improve optimization performance by reasonably narrowing the search range for optimization calculations. A comprehensive analysis method, by the combined use of the Kissinger method, the model-free methods and a two-point method, is proposed. The new method is verified by examples of optimization calculations based on experimental data.

2 Experimental

The material used in this work was pine bark of Pinus sylvestris collected in the Great Khingan, northeast of China. The raw samples were dried at 85 °C for 24 h in an electric oven. Prior to thermogravimetric tests, samples were milled to powder (less than 75 µm). The ultimate analysis was conducted by an Elementar vario EL cube, and the results are shown in Table 1.

A Netzsch thermobalance model STA 449F3 was employed for TG experiments. The samples were evenly distributed over the crucible with the initial mass of 6–8 mg. Dynamic experiments were carried out at heating rates of 10, 15, 20, and 25 K/min, from room temperature up to 800 °C. Nitrogen was invoked as the sweeping gas, and

Table 1 Ultimate analysis results of pine bark

Material	N (%)	C (%)	H (%)	O (%)
Pine bark	0.29	50.51	6.34	40.18

the gas flow rate was 100 ml/min. Some runs were repeated to check the repeatability of the tests under the same conditions.

2.1 Reaction Steps of Pyrolysis

The pyrolysis of cellulosic materials consists of reactions of several pseudo-components, characterized by several peaks and shoulders of the DTG curve. If a pseudo-component i goes through an n-order reaction, the decomposition rate can be expressed by

$$\frac{d\alpha_i}{dT} = \frac{A_i}{\beta} \exp\left(-\frac{E_i}{RT}\right)(1 - \alpha_i)^{n_i} \tag{1}$$

where the pre-exponential factor A, the activation energy E and the reaction order n constitute the so-called kinetic triplet, $\beta = dT/dt$ is the heating rate, and R is the gas constant. The conversion fraction α is expressed as

$$\alpha_i = \frac{m_{i0} - m_i}{m_{i0} - m_{i\infty}} \tag{2}$$

where m_0 and m_∞ are, respectively, the initial and final masses of the sample.

The total conversion is thus formulated as

$$\alpha = \sum_i r_i \alpha_i = \sum_i r_i \frac{m_{i0} - m_i}{m_{i0} - m_{i\infty}} \tag{3}$$

where r represents the fraction of component i $\left(\sum r_i = 1\right)$. The first and second derivative of α_i (DTG and DDTG) can be obtained from the TG data. When a major component i approaches the maximum decomposition rate, the DDTG of the pyrolysis of component i will be close to zero. Thus, if no other major reactions exist nearby, the value of the overall |DDTG| may fall rapidly to a local minimum [7]. By this principle, the peak temperatures and the corresponding major reactions could be identified by analysis of the local minimums observed in the |DDTG| curve.

2.2 Comprehensive Method for Preliminary Evaluation of Activation Energy and Pre-exponential Factor

For the pyrolysis of forest combustible material, we propose a comprehensive method by the combined use of the Kissinger method, the model-free method and the two-point method to preliminarily evaluate the initial values and ranges of the activation energy and pre-exponential factor. The method is explained in details as follows.

(1) Kissinger method

The Kissinger method depends on the peak temperatures T_p of DTG curves at multiple heating rates. The derived equation for this method is

$$\ln \frac{\beta}{T_p^2} = -\frac{E}{RT_p} + \ln \frac{AR}{E} \tag{4}$$

The activation energy can be obtained by linear fitting of $\ln(\beta / T_p^2)$ against $-1 / RT_p$ for each stage of pyrolysis. Additionally, based on Eq. (4) we have

$$\ln\left(\frac{\beta_2}{\beta_1}\right) = \ln\left(\frac{T_{p2}^2}{T_{p1}^2}\right) + \frac{E}{R}\left(\frac{1}{T_{p1}} - \frac{1}{T_{p2}}\right) \tag{5}$$

In terms of Eq. (5), if two reactions have the same peak temperature T_{p1} at heating rate β_1 but different T_{p2} at β_2 ($\beta_1 < \beta_2$), the reaction with a smaller T_{p2} has a larger value of E. In our comprehensive method, the Kissinger method is used to preliminarily evaluate the activation energy of the reaction steps corresponding to the DTG peaks.

- Model-free methods

Kissinger–Akahira–Sunose (KAS) method is an integral model-free method expressed as

$$\ln \frac{\beta}{T^2} = \ln \frac{AR}{g(\alpha)E} - \frac{E}{RT} \tag{6}$$

The activation energy can be determined from the slope of the linear fitting curve of $\ln(\beta / T^2)$ against $-1/RT$.

A nonlinear integral model-free method is proposed by Vyazovkin [8]. The activation energy E_α at a specific value of α is determined by searching the value that satisfies

$$\Phi(E_\alpha) = \sum_{i=1}^{n} \sum_{j \neq i}^{n} \frac{I(E_\alpha, T_{\alpha,i})\beta_j}{I(E_\alpha, T_{\alpha,j})\beta_i} = \min \tag{7}$$

$$I(E, T) = \int_{T\alpha-\Delta T}^{T\alpha} \exp\left(-\frac{E}{RT}\right) dT \tag{8}$$

In our comprehensive method, the model-free methods are used to compare the activation energy values for different pseudo-components.

- Two-point method $\left(T_{\text{acc}} \text{ and } T_p\right)$

Based on Eqs. (1) and (4), for a TG curve, when the mass loss starts to accelerate, $\alpha_{acc} \approx 0$, for which we have

$$
\begin{cases}
\ln A = \ln \beta \left(\dfrac{d\alpha}{dT} \right)_{acc} + \dfrac{E}{RT_{acc}} \\[3mm]
\ln A = \ln \left(\dfrac{\beta E}{RT_p^2} \right) + \dfrac{E}{RT_p}
\end{cases}
\tag{9}
$$

We conduct preliminary simulation by setting different values of kinetic triplet. In these simulations, the DTG data are first obtained by using the values of kinetic triplet based on Eq. (1), and then, the temperatures of T_{acc} and T_p are extracted from the DTG data to calculate the values of E and A by Eq. (9). In the calculation $\left(d\alpha / dT \right)_{acc}$ is set to be 10^{-6} K^{-1}. The results show that for $n \leq 10$, when $E > 80$ kJ/mol and lg $A > 8$ [lg (min^{-1})], the relative error of E and A will be less than 10%. For $n \leq 1$, when $E > 40$ kJ/mol and lg $A > 4$ [lg (min^{-1})], the error will be less than 2%. In terms of these simulation results, in our comprehensive method the two-point method is used to preliminarily evaluate the lower limits of E and A for the first reaction step.

2.3 Optimization Calculation

In this work, the DDTG curves of the pine bark samples of Pinus sylvestris are analyzed to locate the peak temperature for each reaction. The above summarized comprehensive method is used to preliminarily evaluate the initial values and ranges of activation energy and pre-exponential factor for optimization calculations. The genetic algorithm (GA) is used for kinetic analysis, for which the optimization calculations are conducted by minimizing the differences between experimental and theoretical mass loss rate curves, i.e., the objective function is expressed by

$$
S_{DTG} = \sum_j S_j = \sum_j \sum_k \left[\left((d\alpha / dT)_{Exp} \right)_{j,k} - \left((d\alpha / dT)_{Simu} \right)_{j,k} \right]^2
\tag{10}
$$

where j is the number of experimental runs, and k is the number of data points in each run. The subscripts Exp and Simu denote the experimental and simulated values, respectively. Experimental data at heating rates of 10, 15, 20, and 25 K/min are simultaneously applied to the optimization calculations in order to overcome the kinetic compensation effects. The GA codes in MATLAB are used to perform the search.

3 Results and Discussion

3.1 Comprehensive Kinetic Analysis

The experimental TG and DTG curves of pyrolysis of pine bark at different heating rates are shown in Fig. 1, for which the data of the dehydration stage have been removed since the focus of our work is on the pyrolysis reaction. Same as many reports on biomass pyrolysis [9, 10], we can observe three apparent reactions in Fig. 1. As mentioned above, the temperature of each local minimum of |DDTG| is in close proximity to the peak temperature for each reaction. The local minimums observed in Fig. 2 are thus judged to correspond to the peak mass loss rates of three pseudo-components of cellulose, hemicellulose, and lignin.

For use of the comprehensive method, we first apply the Kissinger method to the four experimental data sets, and the results are presented in Table 2. The results of the Kissinger method provide a preliminary evaluation on the activation energy and pre-exponential factor for the three pseudo-components as identified in Fig. 1.
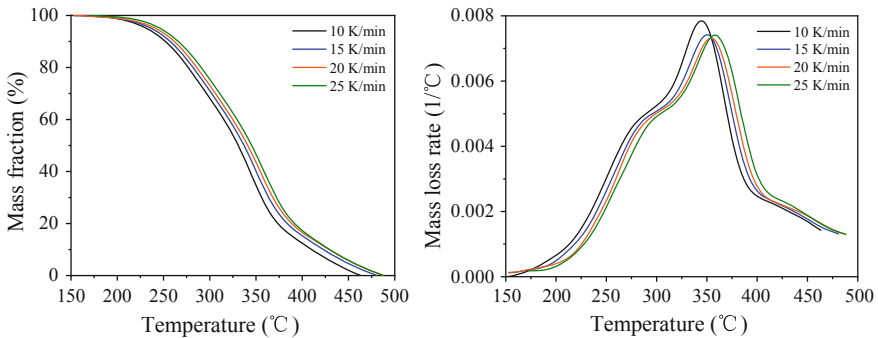
Fig. 1 Experimental TG and DTG curves of pine bark pyrolysis at different heating rates

Fig. 2 Experimental DTG and |DDTG| curves of pine bark pyrolysis at a heating rate of 10 K/min
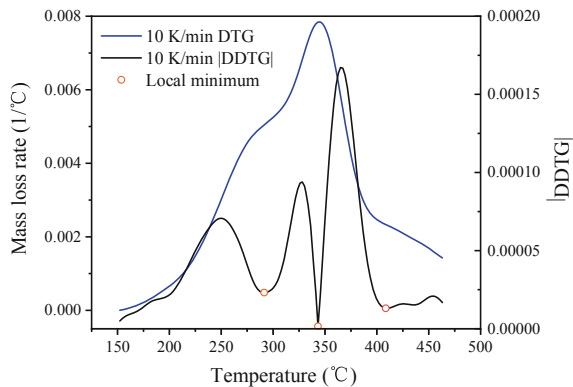
Table 2 Results of the Kissinger method, the KAS method, and the Vyazovkin method

Species	E (kJ/mol)	Kissinger lg A [lg (min^{-1})]	Tp (K) (at 10 K/min)	KAS E (kJ/mol) (at 10 K/min)	Vyazovkin E (kJ/mol) (at 10 K/min)
Hemicellulose	163.52	14.91	564.49	168.95	169.63
Cellulose	220.85	18.55	616.43	187.12	187.73
Lignin	202.77	15.26	681.77	157.13	160.32

Further, the Vyazovkin and KAS model-free methods are used, and the results are shown in Fig. 3a. As shown, the activation energy increases in the conversion range of 10–50% and then decreases in the range of 50–80%. After that, the activation energy has a minor increase and then decreases again. Figure 3b shows the activation energy against temperature at the heating rate of 10 K/min. The results show that the activation energy of hemicellulose is less than that of cellulose: $E_{\text{cellulose}} > E_{\text{hemicellulose}}$. As shown, the activation energy increases within the range between the peak temperatures of hemicellulose and cellulose. Considering that the activation energy obtained by model-free methods corresponds to the whole decomposition of different components, this explains why the effective activation energy calculated by the iso-conversional method is lower than the one obtained by the Kissinger method at the peak temperature of cellulose. For the three major components, the activation energy values can be ranked as $E_{\text{cellulose}} > E_{\text{lignin}} > E_{\text{hemicellulose}}$.

As the third step, we now use the two-point method to evaluate the lower limits of the activation energy and pre-exponential factor for the first reaction step. Such lower limits should be not dependent on the value of the reaction order. Therefore, we first examine the effect of reaction order by using some simulation examples. The parameters for the simulations are $E = 162.60$ kJ/mol, lg $A = 12.78$ [lg (min^{-1})], $n = 0.7$–10 and $\beta = 5$ K/min. As shown in Fig. 4a, a higher n results in a flatter curve with specified E and A. For close observation on the effect of reaction order,
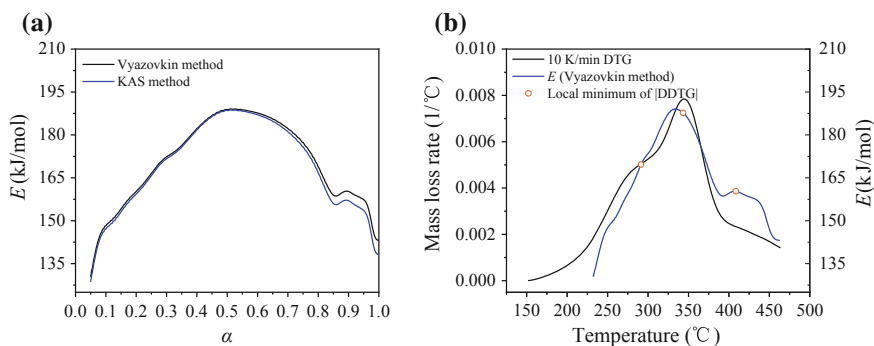
Fig. 3 Activation energy distribution with (**a**) conversion and with (**b**) temperature at a heating rate of 10 K/min

(a)

(b)
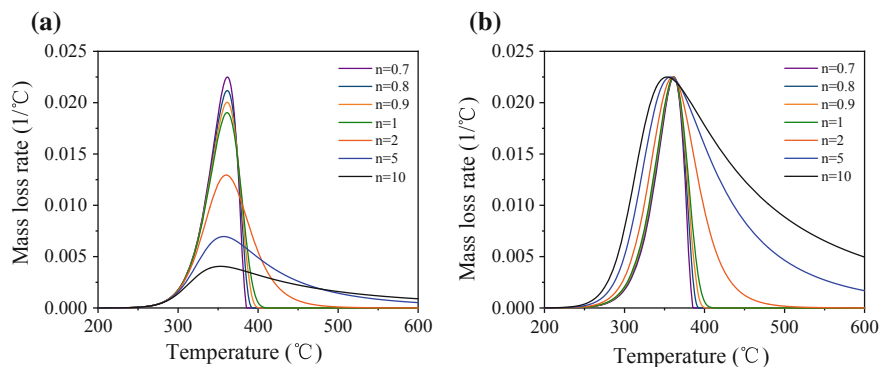
Fig. 4 **a** Effect of the reaction order on the peak shape ($E = 162.60$ kJ/mol, lg $A = 12.78$ [lg (min^{-1})], $n = 0.7$–10 and $\beta = 5$ K/min) and **b** recreated DTG curves enlarged to the same value of peak mass loss rate

we especially amplify the curves in Fig. 4a to the same peak mass loss rate value (Fig. 4b). In terms of Eq. (1), this amplification means that each mass loss rate curve for specified reaction order is multiplied by a coefficient, or in other words, the pre-exponential factor is multiplied by the coefficient, while the activation energy remains the same. A lower reaction order corresponds to a higher peak mass loss rate, and so the coefficient for the amplification is smaller. Therefore, a lower reaction order corresponds to a lower pre-exponential factor after the amplification. As shown, a reaction with a larger reaction order n will start first. While in the range of $n < 1$, reaction curves are close to each other. Therefore, we choose $n = 1$ as a reference value to ensure that if the true $n > 1$, the calculated E and A by the two-point method will be lower than the real values. If the true $n < 1$, the calculated values of E and A will be similar to the actual values.

The early stage of pyrolysis is dominated by hemicellulose. The results of the two-point method at heating rates of 10 and 25 K/min with different initial temperatures are shown in Table 3. In Fig. 5, we first select all the values of the activation energy and pre-exponential factor for the data at 10 K/min from Table 3. Then with different initial temperatures, we use the obtained activation energy and pre-exponential factor to calculate the mass loss rate data of at 10 and 25 K/min by Eq. (1). As shown in Fig. 5, the temperature shifts of calculated curves under the two heating rates are

Table 3 Two-point method results at heating rates of 10 and 25 K/min

Initial temperature (°C)	β (K/min)	E (kJ/mol)	lg A [lg (min^{-1})]	β (K/min)	E (kJ/mol)	lg A [lg (min^{-1})]
60	10	68.69	5.76	25	65.80	5.71
70		74.54	6.34		71.21	6.23
80		80.99	6.97		77.15	6.80

larger than that of experimental curves. This implies that the activation energy by the two-point method is lower than the true activation energy. Thus, there is no need to further discuss the lower values corresponding to the data at 25 K/min in Table 3. If $n = 1$ at a single heating rate, the values of E and A in Table 3 may be close to the actual values. However, according to Eq. (5), since the peak temperature shift ranges of the simulation curves are noticeably larger than those of the experiment curves, the values of E in Table 3 are smaller than the real value. Therefore, setting E = 80.99 kJ/mol as the lower limit of the activation energy for the first reaction step is reasonable.

3.2 Optimization Calculations by Genetic Algorithm (GA)

Based on the above results of the preliminary method, we determine the initial values and ranges of the activation energy and pre-exponential factor, as listed in Table 4. The search range of A is based on the kinetic methods and the compensation effect [11–13]. The mass fractions of three species are selected from the literature: $r_{hemicellulose} = 0.27$, $r_{cellulose} = 0.33$ [14]. To test the reliability of the optimal solution (Table 4), the predicted and experimental DTG curves are plotted in Fig. 6. As shown, they have a good agreement.

Because of the random nature of GA and the interdependencies among parameters, the convergence results of GA alter under repeated runs. The blind search range of Li et al. [7] is employed for comparison. The S_{DTG} values are recorded under the same condition: GA code in MATLAB with default settings, a population composed of 100 individuals [7]. According to the average S_{DTG} values of 10 runs for both search ranges as indicated in Table 4, the comprehensive range performs more efficiently than the blind range.

Table 4 Optimization ranges and optimal solutions for kinetic parameters

Species	Parameter	Initial values	Blind range	Comprehensive range	Optimal solution
Hemicellulose	E (kJ/mol)	163.52	[50, 300]	[80.99, 160.32]	104.90
	lg A [lg (min^{-1})]	14.91	[5, 30]	[5,16]	9.51
	n	2.00	[0.5, 10]	[0.5, 10]	2.49
	r (%)	0.27	[5, 50]	[5, 50]	43.25
Cellulose	E (kJ/mol)	220.85	[50, 300]	[200.85, 240.85]	226.45
	lg A [lg (min^{-1})]	18.55	[5, 30]	[16.55, 20.55]	18.92
	n	2.00	[0.5, 10]	[0.5, 10]	2.76
	r (%)	0.33	[5, 50]	[5, 50]	32.54
Lignin	E (kJ/mol)	202.77	[50, 300]	[80.99, 240.85]	168.06
	lg A [lg (min^{-1})]	15.26	[5, 30]	[5,24]	11.75
	n	2.00	[0.5, 10]	[0.5, 10]	5.97
	r (%)	–	–	–	24.21
S_{DTG} ($\times 10^{-5}$)			11.46 (mean)	6.54 (mean)	2.59
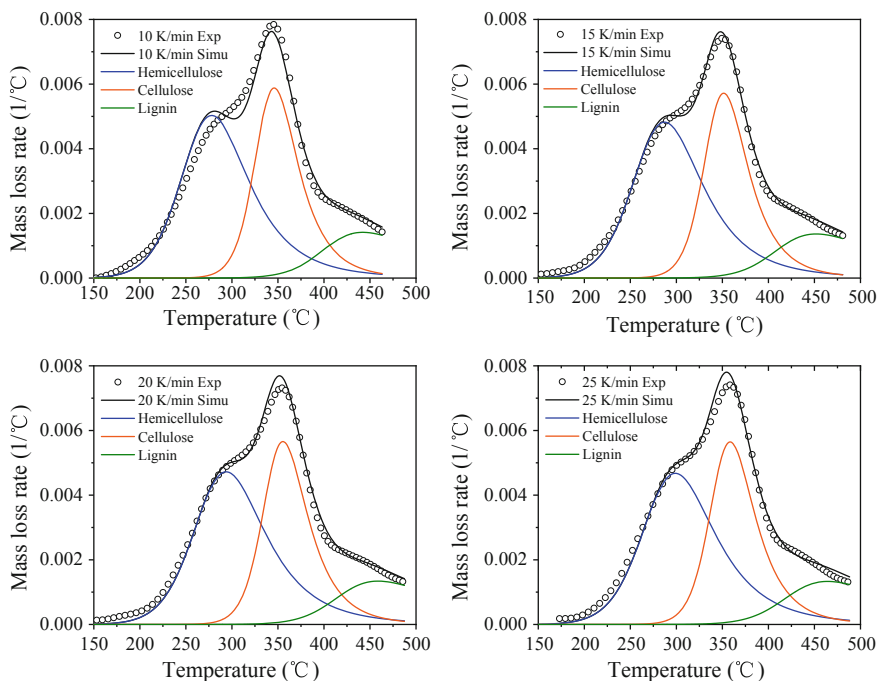
Fig. 6 Comparison between (o) experimental and (-) theoretical DTG curves at 10, 15, 20, and 25 K/min

The reliable comprehensive search range brings other benefits. On the one hand, if a parameter range is improper, the search range can be further narrowed based on the comprehensive range. On the other hand, the comprehensive range helps to identify premature convergence problem by adjusting parameter ranges. For example, in order to verify the rationality of $E_{hemicellulose} = 104.90$ kJ/mol (Table 4), the GA optimization was executed with $E_{hemicellulose} = 130 \sim 160.32$ kJ/mol. The result shows that a larger E will cause a considerable delay in the initial temperature.

4   Conclusion

In this work, we present an effort to improve optimization performance by reasonably narrowing the search range for optimization calculations. A comprehensive analysis method, by the combined use of the Kissinger method, the model-free methods and a two-point method, is proposed. For the comprehensive method, the Kissinger method is used to preliminarily evaluate the activation energy of the reaction steps corresponding to the DTG peaks, the model-free methods are used to compare the activation energy values for different pseudo-components, while the two-point method is used to preliminarily evaluate the lower limits of activation energy and pre-exponential factor. By using this comprehensive method, reasonable initial values and ranges of the activation energy and pre-exponential factor can be determined for optimization calculations. Thermogravimetric experiments of pine bark were conducted at heating rates of 10, 15, 20, and 25 K/min under nitrogen atmosphere. The experimental data are used to check the reliability of the comprehensive method. The results show that by the comprehensive analysis, the GA calculation by using the comprehensive method performs more efficiently than the calculation by using blind range. In addition, if a part of the parameter range is improper, the search range can be further narrowed based on the comprehensive method.

References

1. Moghtaderi, B. (2006). The state-of-the-art in pyrolysis modelling of lignocellulosic solid fuels. *Fire and Materials, 30,* 1.
2. Dollimore, D., Evans, T., Lee, Y., & Wilburn, F. (1991). Calculation of activation energy and pre-exponential factors from rising temperature data and the generation of TG and DTG curves from A and E values. *Thermochimica Acta, 188,* 77.

3. Anca-Couce, A., Zobel, N., Berger, A., & Behrendt, F. (2012). Smouldering of pine wood: Kinetics and reaction heats. *Combustion and Flame, 159,* 1708.
4. Amutio, M., Lopez, G., Aguado, R., Artetxe, M., Bilbao, J., & Olazar, M. (2012). Kinetic study of lignocellulosic biomass oxidative pyrolysis. *Fuel, 95,* 305.
5. Niu, H., & Liu, N. (2015). Thermal decomposition of pine branch: Unified kinetic model on pyrolytic reactions in pyrolysis and combustion. *Fuel, 160,* 339.
6. Ding, Y., Wang, C., Chaos, M., Chen, R., & Lu, S. (2016). Estimation of beech pyrolysis kinetic parameters by shuffled complex evolution. *Bioresource Technology, 200,* 658.
7. Li, K., Huang, X., Fleischmann, C., Rein, G., & Ji, J. (2014). Pyrolysis of medium-density fiberboard: Optimized search for kinetics scheme and parameters via a genetic algorithm driven by Kissinger's method. *Energy & Fuels, 28,* 6130.
8. Vyazovkin, S. (1997). Evaluation of activation energy of thermally stimulated solid-state reactions under arbitrary variation of temperature. *Journal of Computational Chemistry, 18,* 393.
9. Anca-Couce, A., Berger, A., & Zobel, N. (2014). How to determine consistent biomass pyrolysis kinetics in a parallel reaction scheme. *Fuel, 123,* 230.
10. Branca, C., & Di Blasi, C. (2013). A unified mechanism of the combustion reactions of lignocellulosic fuels. *Thermochimica Acta, 565,* 58.
11. Mui, E., Cheung, W., Lee, V., & McKay, G. (2010). Compensation effect during the pyrolysis of tyres and bamboo. *Waste Management, 30,* 821.
12. Galwey, A. (2004). Is the science of thermal analysis kinetics based on solid foundations? A literature appraisal. *Thermochimica Acta, 413,* 139.
13. Narayan, R., & Antal, M. (1996). Thermal lag, fusion, and the compensation effect during biomass pyrolysis. *Industrial and Engineering Chemistry Research, 35,* 1711.
14. Niu, H., & Liu, N. (2014). Effect of particle size on pyrolysis kinetics of forest fuels in nitrogen. *Fire Safety Science, 11,* 1393.

Industrial Fires

Application of Safety Planning Method Based on Quantitative Risk Analysis in Oil Pipeline

Yun Rong, Wen-di Yu and San-ming Wang

Abstract Pipelines are one of the most popular and effective ways of transporting oil, so the safety planning of the oil pipeline is very important. This paper has constructed a set of procedures and indicators for quantitative risk analysis (QRA) of pipelines. The pipeline integrity management method and QRA to construct a theoretical system for pipeline regional safety planning is combined. The system is used to assess the risk of a pipeline in a region, and the calculation results show that the individual risk level of the pipeline in the region is 1.00E–06, which is lower than the standard value 3.00E–06. Therefore, the individual risk of the pipeline's internal and external protection targets is acceptable. The social risk results show that the social risk curve of the pipe section is in an acceptable area and meets the social risk standard. This approach, which is combined with Chinese risk-acceptable criteria, is not only instructive for the safety planning of the protection targets around the oil pipeline, but also has important reference value for the new site selection, reconstruction, and the development of the surrounding land.

Keywords Oil pipeline · Safety planning · Quantitative risk analysis

1 Introduction

The current process of urbanization is accelerating and social wealth is highly concentrated. Scientific construction of new pipelines and regional security planning is particularly important. Safety planning not only affects urban road traffic, construction projects, and the environment, but also affects human life, property, and regional economy. Historically, the root cause of the serious consequences caused by many

Y. Rong · S. Wang (✉)
College of Safety Science and Engineering,
Nanjing Tech University, Nanjing 210009, Jiangsu, China
e-mail: 792323451@qq.com

Jiangsu Key Laboratory of Hazardous Chemicals Safety and Control,
Nanjing 210009, Jiangsu, China

Y. Rong · W. Yu · S. Wang
Graduate Workstation, Safirst Technology Company Limited, Nanjing 210009, Jiangsu, China

pipeline leakage accidents is the lack of a scientific safety plan [1]. Therefore, the common concern of all is how to plan and establish accident prevention and control system scientifically to reduce the loss and impact of accidents [2].

According to domestic and foreign research progress, the specific methods of land safety planning can be mainly divided into three categories: based on the safety distance methods, based on the results of accident methods, and based on risk assessment methods [3]. The characteristics of the three different methods are shown in Table 1.

In this paper, "Safe Net"- Quantitative Risk Assessment software, which was developed by Nanjing Safirst Technology Co., Ltd, is used to make safety plans for oil pipelines. This software contains many complex databases, calculation models, and risk calculation programs, including hazardous substances database, meteorological database, accident model data, risk assessment index database, etc., In this assessment, the risk assessment method and the pipeline integrity management method

Table 1 Comparison of three concrete safety planning methods [4–9]

Methodology	Details	Advantages and disadvantages
Safety distance method	Based on historical experience (such as accident cases and long-term industrial practices) or expert judgment. The impact of the accident was initially judged. The safety distances for different facilities, places, and other important areas are listed	Advantages: Simple and easy to use. Disadvantages: Based on experience. There are few considerations on the detailed design features, safety measures, and facilities of the system
Accident consequence method	Also known as the worst-case scenario, it focuses on assessing the predictable consequences of an accident and does not analyze the likelihood of the incident. The consequence of the accident gives the estimated distance quantified by the extent of the impact of the accident on the person or the environment	Advantages: Decision-making in land use safety planning is convenient. Disadvantages: It is hard to choose the "worst" accident scenario, and the calculation process is complicated
Risk assessment method	Also known as probabilistic risk assessment. Evaluate the severity of the consequences of the accident and the magnitude of its likelihood of occurrence	Advantages: Calculated the severity of the consequences of the accident and the probability of occurrence. Disadvantages: Complicated time-consuming calculation process, and you need to have a multi-faceted database and model

are combined with each other to analyze and research the oil pipeline and provide a reasonable reference for the pipeline scientific planning.

2 Quantitative Risk Analysis (QRA)

QRA is a systematic approach to analyze the probability and consequences of an accident. The assessment results are compared with acceptable risk criteria to determine the degree of risk in the area.

The general formula for risk calculation is shown in Eq. (1)

$$R = \sum_{i=1}^{n} (f_i \times c_i) \tag{1}$$

where n represents the number of accident occurred; f_i is the probability of the i-th accident; and c_i is the consequence of the i-th accident.

QRA indicators include individual risk and social risk [10]. The value of the individual risk is the value that an individual is exposed to at a given place. Social risk refers to the relationship between the consequences of mass death and the frequency of accidents. Social risk, also known as potential loss of life, is mainly used to quantitatively rank the social risks arising from each hazard source. The purpose is to identify the target of risk management and formulate more effective risk management measures.

- Individual risk

Individual risk refers to the probability of individual death of a person caused by a hazard at a fixed location that is individual mortality within a unit of time (one year). Individual risk has nothing to do with the existence of a person, but only with the spatial coordinates of the location. The magnitude of individual risk is related to the distance from the source of danger. To the closer to the hazard, the higher the personal risk value. The individual risk of a pipeline at a fixed location is related to factors such as pipe diameter, pressure, failure probability, and failure mode. In risk decision-making, personal risk is concerned with the point. According to different individual risk allowable standards, risk decisions are made for different functional areas such as industrial areas, commercial areas, residential areas, and hospitals.

Calculated formula for individual risk value is shown in Eq. (2):

$$IR = \sum_{s} \sum_{M} \sum_{K} \sum_{i} f_s P_M P_K P_i v_s \tag{2}$$

where f_s represents the probability of a leakage accident; P_M is the weather rating probability for some time; P_K is the probability of wind direction for some time; P_i is the ignition probability; versus is the accidental death probability of the person; S

Fig. 1 *F-N* curve of social
risk [12]
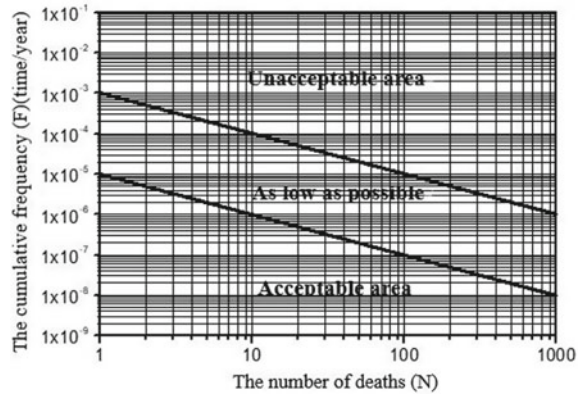
is the number of accidental spill scenarios; *M* is the number of weather classes; *K* is
the number of winds; *i* is the number of ignition sources.

• Social risk

Social risk is the cumulative frequency of accidents where the hazard can cause *N*
death that is the number of deaths per unit time (one year) [11]. Social risk has
nothing to do with spatial location and is only affected by the population density in
the area surrounding the hazard. Social risk is expressed as a relation curve (*F-N*
curve) between the cumulative frequency of accidents (*F*) and the number of deaths
(*N*), as shown in Fig. 1. If there is no personnel in the pipeline risk field, the social
risk value is zero. In risk decision-making, social risk is concerned with the face,
reflecting the size of the risk faced by the public. Pipeline accidents generally tend
to have serious consequences and low probability, so the calculation of social risks
is particularly important.

3   Methodology

The pipeline integrity management method and QRA to construct a theoretical system
for pipeline regional safety planning is combined. The program of quantitative risk
analysis of the oil pipeline is shown in Fig. 2.

• Data collection

The data mainly include information on hazardous substances in the pipeline, distri-
bution of ignition sources around the pipeline, pipeline design parameters, operation
and management information of the pipeline, local weather conditions, population
data, historical data on accidents and equipment, and relevant laws and regulations.

Fig. 2 Program of quantitative risk analysis for oil pipeline
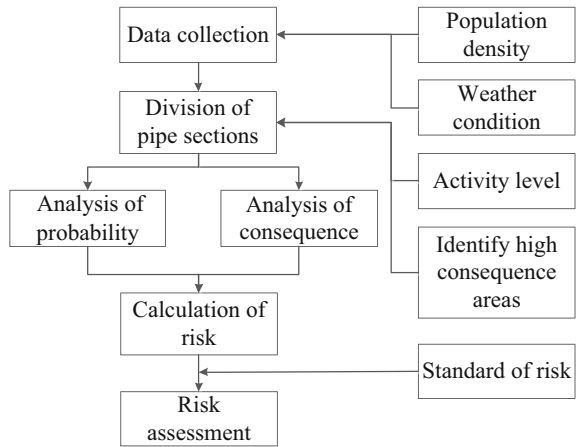
- Division of pipe section

Because of the long distance and wide distribution of pipelines, there are great differences in natural environmental conditions along the pipeline, social and environmental conditions, and pipeline construction. Therefore, the pipeline must be divided and each segment should be considered as a unit of risk analysis. Pipeline segmentation is based on changes in conditions along the pipeline, such as population density, topography, soil conditions, condition of the coating, service life of pipelines, and other risk factors. Referring to the related research results of the pipeline segmentation [13], in the process of risk analysis of natural gas pipelines, the type of population density and topography are taken as the main basis for pipeline segmentation.

This article divides the area into eight categories. The eight categories of areas include: ① Residential areas, commercial centers, parks, etc.; ② Schools, hospitals, theaters, stadiums, and other public facilities; ③ Water source protection areas, etc.; ④ Stations, docks, airports and highways, railways, waterways, etc.; Traffic trunks; ⑤ Farmland protection areas, pastoral areas, etc.; ⑥ Nature reserves; ⑦ Military administrative areas; ⑧ Other areas protected by laws and regulations. Part of the division is shown in Fig. 3.

- The analysis, calculation, and evaluation of risk

Probability analysis is to assess the possibility of fire, explosion, poisoning, and other accidents. Analysis of the consequences is to determine the scope of the consequences of the accident. It is mainly based on the accident consequence damage model, as well as the relationship between the fire heat radiation, the shock wave overpressure, the poison density, other physical quantity and the spatial distance, and compared with the damage criteria (heat flux criterion, overpressure criterion, half lethal quantity and so on).

If the oil and gas pipeline leak, it will cause jet fire and vapor cloud explosion when it meets the ignition source [14]. Once an accident occurs in the pipeline, the conse-
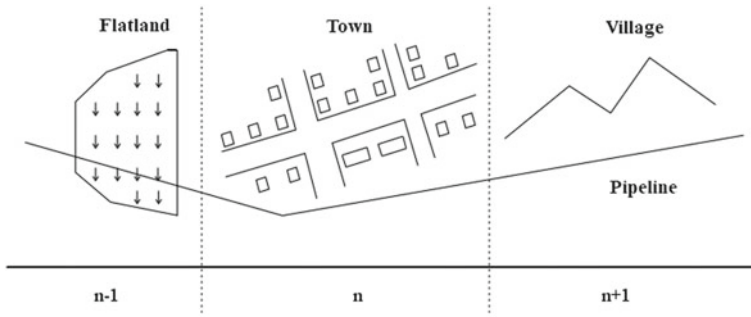
Fig. 3 Basis for pipeline segmentation

quences of fire and explosion accidents will affect the vulnerability targets (persons, buildings, etc.,). It is necessary to consider the degree of damage to the vulnerability target from the consequences of the accident. This article mainly analyzes the fire thermal radiation damage model and the explosion shock wave overpressure damage model.

① Fire thermal radiation damage model

Equations (3–6) are the heat radiation damage probability equation proposed by Petersen [15].

Probability of death when skin is exposed:

$$P_r = -36.38 + 2.56 \ln(tq^{4/3}) \tag{3}$$

Probability of second-degree burn:

$$P_r = -43.14 + 3.0188 \ln(tq^{4/3}) \tag{4}$$

Probability of once burned:

$$P_r = -39.83 + 3.0186 \ln(tq^{4/3}) \tag{5}$$

Under the protection of clothing, the actual radiation intensity received by the body will be reduced:

$$q_c = \beta q \tag{6}$$

where P_r represents the probability of injury; t is the time when the person is exposed to heat radiation; q is the heat flux received by the body; q_c is the actual heat flux received by the body; β is the acceptance rate of heat received by the body, $\beta = 0.4$.

② Explosion shock wave overpressure damage model

Equation (7) proposed by Purdy et al. [16] is used to calculate the explosion death probability.

$$Y = 2.47 + 1.43 \lg \Delta p \tag{7}$$

where Δp represents external pressure received by the body; Y is the probability of injury.

Based on the probabilistic and consequential analysis, individual and social risks are calculated. Risk assessment is a process of determining the level of risk, according to the risk standard, in order to clarify the risk control measures for each object.

This program adopts the principle of ALARP and combines the existing methods such as the pipeline integrity management method and the "Guidelines for Risk Assessment of Oil and Gas Pipelines," and can be universally applied to the quantitative risk assessment of pipelines in an area of China.

4 Case Study: Safety Planning for a Pipeline

Select the transportation pipeline of Shenzhen International Airport depot. Pipeline parameters and the surrounding specific conditions are shown in Table 2. According to the accident cause mechanism analysis, the pipeline runs with pressure, and the leakage in the process can produce two types of accidents, such as jet fire and vapor cloud explosion. According to the analysis of historical cases of pipeline accidents, explosion and fire accidents will occur when the pressurized pipeline fails and encounters fire source. Therefore, this example mainly analyzes the regional risks caused by vapor cloud explosion and jet fire accident in pipeline.

Table 2 Oil pipeline parameters and surrounding conditions

Pipeline	Diameter	Wall thickness (mm)	Pressure (MPa)	Material	Times (year)	Laying way
1	DN[a]300	7.1	0.7	L245[b]	6	Overhead
2	DN300	7.1	0.7	L245	6	Buried
3	DN300	7.1	0.7	L245	6	Overhead
4	DN300	7.1	0.7	L245	6	Buried
5	DN300	7.1	0.7	L245	6	Overhead
6	DN300	7.1	0.7	L245	6	Buried
7	DN300	7.1	0.7	L245	6	Overhead
8	DN300	7.1	0.7	L245	6	Buried

[a]*DN* Nominal diameter
[b]Low pressure fluid coiled steel pipe

Pipelines are divided according to different laying methods. Based on the level of activity of people in the area and HCAs identification rules, the segmented pipe sections are screened and the three most dangerous pipelines are identified. By calculating the probability of failure, the leak point of the three-stage pipeline that is most likely to cause pipeline failure is determined, as shown in Fig. 4. The consequences of these four leak points are then simulated.

Hazardous substances database, meteorological database, accident model data, risk assessment indicator database, etc., as well as corresponding model and risk calculation programs are used. The "Safe Net"—Quantitative Risk Assessment software is used to calculate the individual risk contours and social risk curves, as shown in Figs. 5, 6, 7, and 8.

According to the most adverse principle, we set some parameters according to the actual situation. Leakage patterns can be classified into small holes/cracks, mesopores, and complete ruptures according to the size of the leaky aperture [17]. With reference to the quantitative risk assessment guidelines of chemical companies and the classification of leak aperture recommended by DNV [18], this paper selects the representative apertures as follows: small hole/crack is 20 mm, middle hole is 100 mm, and pipe diameter is completely broken. During the simulation, the typical leakage size of the complete rupture (tube diameter) is mainly considered; Leak time is set to 10 min; Meteorological conditions set for coastal areas in Shenzhen; and the landform is set to the plain area. There is no obstacle around the leakage point, and it is exposed on the ground.

As shown in Fig. 7, the calculation results show that the individual risk level of the pipeline in the region is 1.00E–06 (the probability of death of a single person in the region within one year is 1.00E–06), which is lower than the standard value 3.00E–06.

Fig. 4 Select the leak point

Meteorological condition

Territory :	1
The ground type :	Dense high-rise buildings
Radiation intensity :	Strong (day sunshine)
Atmospheric stability :	D
Ambient pressure(Pa) :	100980
Ambient mean wind speed(Pa) :	2
Ambient air density(kg/m3) :	1.293
Average property density(ten thousand yuan/m2) :	0.1
Ambient temperature(T) :	296
The percentage of buildings occupied :	0.03

Wind direction	Wind frequency
North(N)	2.8
North-North-East(NNE)	5.3
North-East(NE)	7.1
East-North-East(ENE)	5.4
East(E)	10.6
East-South-East(ESE)	8.5
South-East(SE)	5.1
South-South-East(SSE)	2.1
South(S)	2.9
South-South-West(SSW)	4
South-West(SW)	9.4
West-South-West(WSW)	6.3
West(W)	3.5
West-West-North(WWN)	0.9
West-North(WN)	1
West-North-North(WNN)	0.9

Save

Fig. 5 Enter weather conditions information

Fig. 6 Device basic information

Fig. 7 Individual risk contour of pipeline

Fig. 8 Social risk map of pipeline
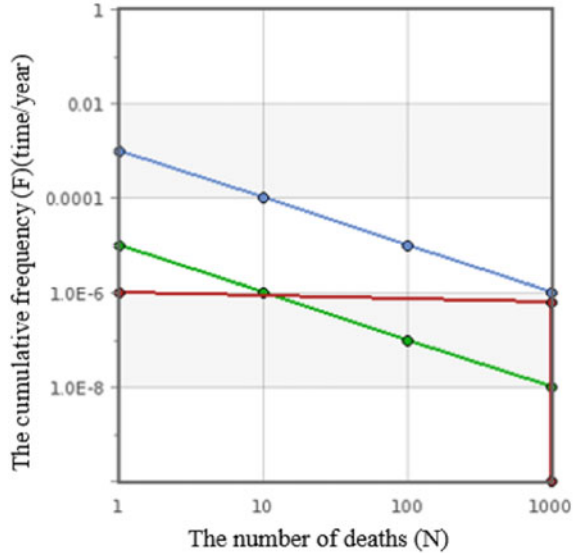
(Individual Acceptable Risk Standards and Socially Acceptable Risk Standards for Hazardous Chemicals Production and Storage [Trial]) [19]. As shown in Fig. 8, according to the SY/T 6859-2012 social risk allowable standard, the cumulative frequency of accidents that caused more than one death is 0.005/year, and the cumulative frequency of accidents that killed more than 1000 people is 1.00E–06/year. The overall social risk curve for oil pipelines in the region is in an acceptable area. It shows that the location of the pipeline is reasonable and the planning of surrounding buildings and facilities is reasonable and there is no sensitive protection target.

5   Conclusion

In this paper, procedures and indicators for pipeline quantitative risk analysis are presented. QRA software is used to calculate the individual risk level and social risk level of the oil pipeline. Under the condition of no protective management measures (management factor correction, safety measures, and accident consequence reduction measures), the individual risk value of the pipeline reaches 1.00E–06, which is lower than the standard value 3.00E–06. The social risk results show that the social risk curve of the pipe section is in an acceptable area and meets the social risk standard. It shows that the location of the pipeline is reasonable and the planning of surrounding buildings and facilities is reasonable and there is no sensitive protection target.

This approach which is combined with Chinese risk-acceptable criteria is not only instructive for the safety planning of the protection targets around the oil pipeline,

but also has important reference value for the new site selection, reconstruction, and the development of the surrounding land.

References

1. Zong-Zhi, W. U. (2004). Study on methods and contents for land use safety planning. *Journal of Safety & Environment*.
2. Wei, L. J., Ying-Quan, D., Li-Jian, Y. U., Liu, J., & Zong-Zhi, W. U. (2007). Probe into the main content of safety planning for chemical industry park. *Journal of Safety Science & Technology*.
3. Ming, X. U., Ying-Quan, D., & Zong-Zhi, W. U. (2008). Review of commonly used approaches for land-use planning vicinity of chemical sites. *Journal of Safety Science & Technology*.
4. Liang, X., Liu, J., Gao, J. M., & Zeng, M. R. (2008). The situation of safety distance on dangerous chemical and its indications. *Journal of Safety Science & Technology*.
5. Christou, M. D., & Mattarelli, M. (2000). Land-use planning in the vicinity of chemical sites: risk-informed decision making at a local community level. *Journal of Hazardous Materials, 78*(1–3), 191.
6. Hauptmanns, U. (2005). A risk-based approach to land-use planning. *Journal of Hazardous Materials, 125*(1–3), 1.
7. Christou, M. D., Amendola, A., & Smeder, M. (1999). The control of major accident hazards: The land-use planning issue. *Journal of Hazardous Materials, 65*(1–2), 151–178.
8. Cozzani, V., Bandini, R., Basta, C., & Christou, M. D. (2006). Application of land-use planning criteria for the control of major accident hazards: A case-study. *Journal of Hazardous Materials, 136*(2), 170–180.
9. Kontić, D., Kontić, B., & Gerbec, M. (2006). How powerful is ARAMIS methodology in solving land-use issues associated with industry based environmental and health risks? *Journal of Hazardous Materials, 130*(3), 271–275.
10. Yang, C.-S. (2014). Study on safety planning method and content of chemical industry park. *Journal of Safety Science and Technology,* 85–89.
11. Lu, C.-J., Yang, G.-L., et al. (2014). Study on device risk ranking based on potential life loss and its application. *Journal of Safety Science and Technology*, 96–99.
12. Wu, Z.-Z., Zhang, S.-Z., et al. (2014). Method of route selection for long-distance oil and gas pipelines based on potential loss of life. *CSSE, 24*(2), 71–76.
13. GB18218-2009. Hazardous chemical major hazard identification.
14. Dziubinski, M., & Fratczak, M. (2006). Aspects of risk analysis associated with major failures of fuel pipelines. *Journal of Loss Prevention in the Process Industries, 19*(5), 399–408.
15. OGP Risk Assessment Data Directory (2010). Vulnerability of plant/structure. Report No. 434–15.
16. Pietersen, C. M. (1990). Consequences of accidental releases of hazardous material. *Journal of Loss Prevention in the Process Industries, 3*(1), 136–141.
17. European Gas Pipeline Incident Data Group (2015). 9th Report of the European Gas Pipeline Incident Group (period 1970–2013).
18. AQ3046-2013, the quantitative risk assessment guidelines of chemical companies.
19. State Administration of Work Safety. Personal acceptable risk standards for hazardous chemicals production and storage devices and socially acceptable risk standards (Trial). State Administration of Work Safety Bulletin 2014 No. 13, 2014-5-7.

Experimental Study on Effectiveness of Water Mist Containing Potassium Salts in Extinguishing Liquid Pool Fire

Hao Liu, Tianwei Zhang, Dengyou Xia and Qiang Liang

Abstract The suppression efficiency of water mist with potassium salts additives on liquid pool fire is experimentally studied in an enclosed space. The penetration pool fire ratio (PPFR) has been utilized to investigate the penetration capability of water mist directly above a pool fire source. The PPFR is generated experimentally by measuring the water mass within the corresponding extinguishing time in the absence of a fire, and a critical PPFR range 40–45% is present, which means more than 45% droplets of water mist arrive at the fuel surface is the essential conditions for additives exerting a chemical effect. The suppression efficiency could be generally sorted in an order of $KNO_3 \approx K_2C_2O_4 > K_3PO_4 \approx$ pure water. The chemical mechanism of potassium additives is due to the active substances KOH and K_xO_y formed at high temperature, and the enhancement effect of CO generated by $K_2C_2O_4$ thermal decomposition under the volume of enclosed space is far greater than fire source can be ignored. All of the results indicate that the addition of potassium salts can improve the extinguishing efficiency of water mist on liquid fire, and the suppression mechanism is considered due to the combination of physical and chemical action.

Keywords Pool fire · Water mist · Potassium salts · Suppression efficiency · Liquid fuel

Nomenclature

U Velocity (m/s)
Q_c Heat release rate (kJ/s)
L Distance from nozzle to oil pan (m)
D_v Droplet diameter (m)
P Pressure (Pa)

H. Liu · T. Zhang (✉) · D. Xia · Q. Liang
The Chinese People's Armed Police Forces Academy, No. 220 Xi'chang Road, Langfang 065000, China
e-mail: cpcbit3120130147@163.com

Greek symbols

ρ   Density (kg/m^3)
Δ   Variable

Subscripts

f   Fuel
g   Air
w   Water
0   Initial state

1 Introduction

Due to its characteristics of no environmental pollution, low water consumption, rapid-fire extinguishing, suitable to many types of fires and little damage to the affected subjects, the water mist fire extinguishing technology is regarded as the major substitute for Halon [1]. The fire extinguishing efficiency can be improved by adding some additives into the water, and the common additives include anti-freezing agents, surfactants, and chemically active additives. However, anti-freezing agents and surfactants which are essentially physical additives can only change the physical properties of water [2].

Chemically active additives can capture the free radicals produced during combustion of the fuel, disrupt the chain reaction during combustion, or decompose to produce inert substances at the flame temperature, so the fire can be extinguished by cooling and asphyxiation [3]. The overall fire extinguishing efficiency of the water mist has been greatly improved by the synergistic effect of the physical and chemical actions of water in the fire extinguishing process.

The additives with higher chemical extinguishing efficiency are soluble compounds containing iron [4], phosphorus [5], and alkali metals [6]. However, the toxicity of iron and phosphorus compounds limits their application, so most of the alkali metal salts become the best choice for the additives of water mist due to its advantages of high fire extinguishing efficiency, relatively small toxicity, irritants, and easy solution. Lask and Wagner [7] reported the high efficiency of potassium salts for fire extinguishing firstly. Shilling [8] compared the suppression efficiency of several alkali metal chlorides by cup-burner and showed a superior efficiency of KCl. The KOH, NaCl, and NaOH with the same molar concentration were obtained by Chelliah [9] through counterflow diffusion flame experiment, and the fire extinguishing efficiency was ranked as KOH > NaCl > NaOH. The CHEMKIN dynamic simulations were performed by Babushok [10] on water mist containing KHCO$_3$

and NaHCO$_3$ additives as well as on CF$_3$Br; the mechanism for calculating was originated from Williams and Fleming [11]. The results showed that water mist containing KHCO$_3$ additive had the best fire extinguishing efficiency. The effectiveness of water mist containing KHCO$_3$, NaCl, and KCl additives to extinguish a pool fire within a confined space was compared by Joseph [12], finding that KHCO$_3$ solution at a mass fraction of 10% had the best fire extinguishing effect. Obviously, the fire extinguishing efficiency of potassium salt additive was superior to that of the sodium salt, so more attention was paid to potassium salt as an additive for water mist.

The minimum extinguishing concentration for water mist containing additives (such as K$_2$CO$_3$, K$_2$C$_2$O$_4$, CH$_3$COOK, KNO$_3$, KCl, and KH$_2$PO$_4$) to inhibit the methane flame was tested by Zhang [13] through cup-burner experiment, and the fire extinguishing efficiency was ranked as K$_2$CO$_3$ > K$_2$C$_2$O$_4$ > CH$_3$COOK > KNO$_3$ > KCl > KH$_2$PO$_4$. The effectiveness of water mist containing K$_2$C$_2$O$_4$, CH$_3$COOK, KCl, KHCO$_3$, and K$_3$PO$_4$ additives was tested by Feng [14] through counterflow flame burner, and the fire extinguishing efficiency was ranked as K$_2$C$_2$O$_4$ > CH$_3$COOK > KCl > KHCO$_3$ > K$_3$PO$_4$.

However, there was inconsistency in the findings of the researchers. On the one hand, the particle size of water mist containing additive in the fire extinguishing experiments was different, causing difference in the extent of the role played by chemically active additives. On the other hand, in the experiment of combustor and oil pool fire, there was a large difference in the flame structure and the application manner of water mist, so the conclusions were inconsistent.

The study on the extinguishing effectiveness of water mist containing potassium salt additive was mainly performed on the small-scale experiment platforms, such as premixed flame, counterflow diffusion flame, and cup-burner buoyancy diffusion flame, minimizing the impact of water mist momentum on the effectiveness assessment, but little research was done on the fire extinguishing effectiveness of water mist containing potassium salt additive in the pool fire model. However, due to the complexity of actual fire scenarios and many factors affecting fire extinguishing efficiency of water mist, the type of fire model and the momentum of the water mist were hard to be considered or not considered in the mechanism experiment, but they probably dominated the fire extinguishing process of water mist in the actual engineering application, and the pool fire model was closer to the actual fire, so experimental conclusions had a certain reference value for the promotion and application of the water mist containing additives.

In the pool fire experiment, in addition to the types and the concentrations of additives, the research mainly focused on the impact of the characteristic parameters on the effectiveness. However, the characteristic parameters only reflected the spatiotemporal distribution of the water mist flow field and did not consider the interaction between the water mist and the flow field, so the research on the quantitative description of the interaction between the water mist and the flame was also insufficient. Nam [15] assessed the ability of droplets to penetrate fire plume through measuring the actual delivered density(ADD) by the water spray to the flame. Subsequently, in order to enhance the interaction between the droplets and the flame, Nam [16] proposed to assess the penetration ability through the penetration ratio(PR)

and obtained the relationship between the droplets' penetration ability and the water flow rate, the droplet size, the water mist momentum, and the spray height. Nam's conclusion, however, was based on water spray systems with larger droplets and did not consider the fire extinguishing technology of water mist or water mist containing additives. The fire model so selected was a fuel spray model for shelf fire, whose dominant mechanism was different from that in extinguishing a typical oil pool fire. In addition, Nam experimental study focused on ADD, so the fuel was always in the combustion state in the experimental process, and fire extinguishing case was not considered.

In summary, the interaction between water mist containing potassium salt and the diffusion flame under the condition of oil pool fire within an enclosed space was focused in this paper. The n-heptane, ethanol, gasoline, diesel, and cooking oil fires were served as pool fire models, and $K_2C_2O_4$, KNO_3, and K_3PO_4 were selected as potassium salt additives. Such potassium salts were selected: which were commonly used and had high fire extinguishing efficiency, or whose fire extinguishing effectiveness under pool fire had less research. Different from the spray fire model of Nam, a pool fire model was used in this study, which quantitatively described the interaction between the water mist and the flame by testing the penetration pool fire ratio (PPFR). The conclusions can be used to further understand the fire extinguishing mechanism of water mist containing potassium salt additive and the factors affecting fire extinguishing efficiency, providing an important reference for the design, construction, and assessment of water mist containing potassium salt additives.

2   Experimental Equipment and Methods

The experiment was carried out in an enclosed space of 3 m × 2.1 m × 2.8 m with a fire door size was 1.9 m × 0.7 m, which kept closed during the experiment. A 1.0 m × 0.6 m observation window was installed on the door for the observation. At the top of the enclosed space was equipped with a centrifugal fan with an air volume of 10 m^3/min, which was used at the end of each experiment to return the compartment to pretest conditions.

The water mist fire extinguishing system consisted of an aqueous solution tank, a nitrogen gas cylinder, an electronic balance, a pressure-reducing valve, a water mist nozzle, and a connecting pipe, as shown in Fig. 1.

The thermal radiation effect should be considered without considering the heat conduction and heat convection in the combustion process when the diameter of the oil pan is ≥20 cm [17]. Therefore, the diameter of oil pan which is made of stainless steel used in the experiment was 20 cm with 5 cm depth. According to NFPA [18], the oil pan was placed just below the nozzle at 1 m and the distance kept unchanged for the optimum state of the nozzle. Four Ni–Cr alloy thermocouples with the diameter of the probe was 1 mm placed vertically. One was below the level of the oil surface with the distance of 0.3 cm from the oil pan bottom which recorded the temperature of the fuel, while the others were placed above the oil with the distance of 18.3,
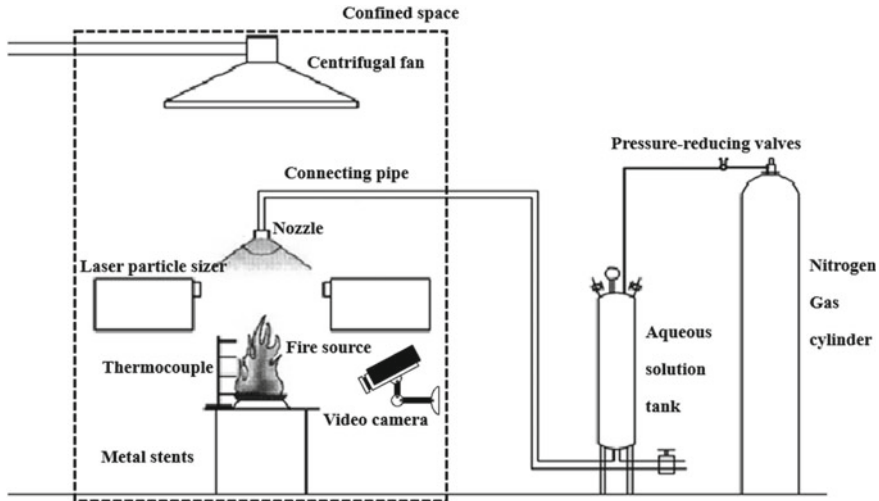
Fig. 1   Water mist fire extinguishing system

12.3, and 6.3 cm separately from the oil pan bottom which were used to record the temperature at different flame heights. An electronic balance connecting with computer was placed under the oil pan, which measured the change of fuel quality.

The low-pressure standard angle solid cone water mist nozzle(BB1/8-SS3) is adopted which can produce the solid conical spray shape, and the characteristic parameters of B3 nozzle are shown in Table 1.

The Winner 318C split-type laser particle size analyzer was used in the experiment to dynamically measure the particle size of water mist. The measurement range was 1–2000 μm, and both accuracy error and repeatability error were less than 3%. The particle size test was performed under no-fire conditions. Regulated the reducing valve on the cylinder to the specified pressure, then opened the value of the water mist. When the water mist particles passed through the test area, the scattering spectrum was generated from the particle group to be tested under the laser radiation, and the parameters of size and distribution of particle size group to be measured under the specified pressure conditions were given.

For PPFR, the influence of the plume thrust on the droplet trajectories was negligible and the spray angle of each aqueous solutions assumed constant, and the method of PPFR measurement was:

Table 1   Characteristic parameter of nozzle

Nozzle	Rated nozzle diameter (mm)	Maximum unblocked aperture (mm)	Volume flow rate (L/min)				Spray cone angle(°)		
			0.2 MPa	0.4 MPa	0.6 MPa	1.0 MPa	0.05 MPa	0.15 MPa	6 MPa
B3	1.5	1.0	1.9	2.5	3.1	3.9	52	65	59

(1) the oil pan was placed on the electronic balance which filled with 100 mL water, the fuel was joined in after the electronic balance reading returned to zero, and the extinguishing experiments were started. When the experiments were over, the remaining water/aqueous solution with the mass $M_1(g)$ in the oil pan was separated through the separator funnel;

(2) the oil pan full of 100 mL water was placed on the electronic balance; the fuel was joined in after the electronic balance reading returned to zero. The fuel was ignited, and the quality loss $M_2(g)$ of the water in the pan during the pre-burn time was recorded;

(3) the oil pan was placed on the electronic balance which filled with 100 mL water, returned the electronic balance reading to zero. The water mist with/without additives was applied, and the applied time was relied on the corresponding extinguishing time from (1), the liquid mass in the oil pan after the discharging was $M_3(g)$, then the PPFR = $(M_1 + M_2)/M_3$.

The 100 mL liquid fuel was added in the oil pan at the beginning of the experiment, and the fuel should be ignited after adjusting the pressure regulating device to the required working pressure. The pre-combustion times which were determined by temperature recorded through thermocouples for heptane, ethanol, and gasoline were 120s, while for that of diesel and cooking oil were 220s. The water mist discharged after a period of steady combustion and stopped when the extinguishing appeared, and the extinguishing time was recorded by a stopwatch and videos. The extinguishing experiment was a failure when the water mist continued for 30s and the flame is not burnt out.

Peanut oil was used as fuel for cooking oil in the text, which was purchased from Golden dragon fish® with the flash point 282 °C. The diesel and cooking oil could not be ignited directly by ignitor due to the high ignition temperature. The method of the induced ignition by placing a big oil pan below the experimental oil pan with adding proper heptane was adopted, and the extinguishing test began when the heptane was burned out and after a period of steady combustion of the diesel and cooking oil fire. The water in the ignition pan evaporated completely before the next set of experiments. Each experiment was repeated for at least five times, and the mean was calculated.

3 Results and Discussion

3.1 Analysis of the Leading Mechanism of Water Mist for Fire Extinguishing

The fire extinguishing by water mist was mainly performed through the physical effects of cooling and diluting oxygen concentration. The volume of enclosed space in this study was much larger than that of fuel, so it can be approximately deemed that the diluting oxygen concentration by water mist played a little role in extinguishing.

During the extinguishing, a part of the water mist stayed in the flame and the other part passed through the fire plume to reach the fuel surface. The combined action of cooling the fuel and the flame by water mist was probably the separate action of each mechanism. The critical water volume flow rate results of extinguishing by pure water mist were calculated through equation given by Liu [19] where it was assumed that the flame had a uniform temperature, and the thermal capacities of the fuel, air, and water were not changed with temperature. The burning rates of five fuels obtained from the experiment was shown in Fig. 2. The fitting degree of mass burning rate curve R^2 measured experimentally for heptane, ethanol, gasoline, diesel, and cooking oil was 0.92595, 0.9426, 0.96295, 0.99781, and 0.99858, respectively, and the results in Fig. 2 were proved to be highly reliable.

As can be seen from Fig. 2, as for the five fuels (except ethanol) selected in the experiment, the amount of water required to cool the flame was greater than the amount of water required to cool the fuel surface, namely cooling fuel surface was the dominant mechanism for water mist to extinguish the liquid pool fuels, which was consistent with the conclusion of Rasbash [20]. Zhang [21] also showed that the unstability of flame root was the fundamental extinguishing reason for the buoyancy diffusion flame. Therefore, the reduction of the amount of water used in the fire extinguishing process depended on whether the water mist droplets could penetrate the fire plume to reach the fuel surface, and only when the downward movement velocity of the water mist droplets was greater than the flame velocity, droplets were theoretically possible to penetrate fire plumes. Mccaffrey [22] divided the buoyancy diffusion flame into three parts by height and pointed out that the velocity of the intermittent flame zone represented the maximum velocity of the flame. The expression of $U_{f\max}$ was:

$$U_{f}\max = 1.9Q_C^{0.2} \tag{1}$$

The flame velocity calculated from Eq. (1) for five fire sources was shown in Table 2.

Fig. 2 Critical volume flow rate for extinguishing fire by pure water mist
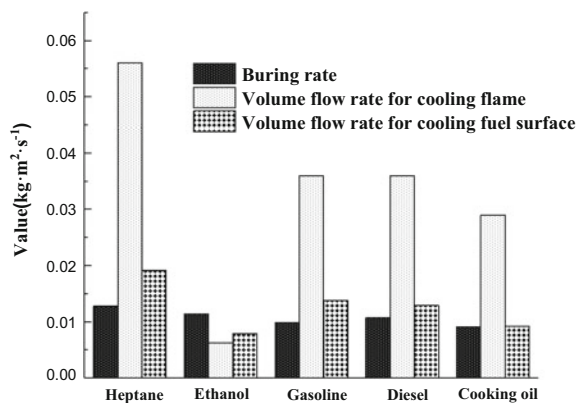
Table 2 Flame velocity of fire source

Fuel	Q_C (kJ s^{-1})	$U_{f\max}$ (m s^{-1})	Fuel	Q_C (kJ s^{-1})	$U_{f\max}$ (m s^{-1})
Heptane	13.54	3.20	Gasoline	9.52	2.98
Ethanol	7.14	2.81	Diesel	10.09	3.02
Cooking oil	7.83	2.87	–	–	–

Assuming that the droplet was a rigid sphere, the evaporation of the droplets was a quasi-steady-state process and the physical parameters of the droplet remained unchanged. The distance from the nozzle to fuel surface was short, so the evaporation of the water within the distance from the nozzle to the fuel surface can be neglected. Therefore, the Williams [23] model was used to calculate the droplet velocity:

$$U_w = U_{w_0} / \exp\left(0.33 \rho_g L / D_v \rho_w\right) \tag{2}$$

where the initial velocity of droplets was expressed as:

$$U_{w_0} = \sqrt{2^{\Delta P} / \rho_w} \tag{3}$$

The droplet velocity calculated from Eqs. (2) and (3) under different pressures was shown in Fig. 3.

The critical conditions for the droplets of water mist to penetrate the fire plume and reach the fuel surface were:

$$U_w \geq U_f \max \tag{4}$$

Fig. 3 Relationship between droplet size and velocity with different pressure
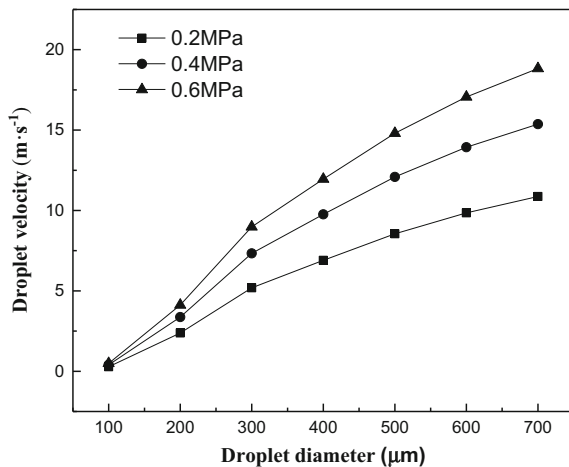
As shown in Table 2 and Fig. 3, the droplet velocity was improved with the increase of pressure and particle size. When the particle size was more than 200 µm and the pressure was more than or equal to 0.4 MPa, the droplet velocity of any of five fire sources was greater than the flame velocity, and theoretically, more water mist can penetrate the fire plume to reach the fuel surface, and the fire extinguishing was performed under the dominant mechanism of cooling the fuel.

3.2 The Effect of PPFR on the Effectiveness of Fire Extinguishing

Under the conditions of 0.4 MPa, the fire extinguishing effectiveness experiments were performed on the five pool fire models by different water mist solution at mass fraction of 5%, and the results were shown in Table 3.

Table 3 showed that different potassium additives had different effects on the fire extinguishing effectiveness for pure water mist. In general, the fire extinguishing efficiency was enhanced, and the chemical fire extinguishing efficacy of the potassium additives at the same concentration was ranked as $KNO_3 \approx K_2C_2O_4 > K_3PO_4 \approx$ pure water. The enhancement by K_3PO_4 additives on the chemical fire extinguishing role for pure water was less than that of the other types of potassium, due to the thermal decomposition products of K_3PO_4 had white and stable glassy substance [14]; however, such substance only played a role in covering and the cooling effect was poor; therefore, its fire extinguishing efficiency was even less than that of pure water mist for diesel fire.

Under 0.4 MPa, the water mist containing additives was unable to extinguish the ethanol fire, indicating that there was a certain limitation on the chemical inhibition role played by water mist, namely when physically fire extinguishing role was unable to be fully played, the chemical inhibition could not play a decisive role.

In summary, the ethanol fire was difficult to be extinguished under the conditions of low-pressure water mist system; while the diesel and cooking oil had a higher flash point and an uneasy ignition, and a lot of black smoke would be generated after combustion, which was not favorable to the observation on experimental phenomena.

Table 3 Average extinguishing time of water mist under 0.4 MPa

Additives	Extinguishing time (s)				
	Heptane	Gasoline	Diesel	Ethanol	Cooking oil
None	17.6	4.8	7.1	Unextinguished	17.85
KNO_3	11.6	3.8	4.2	Unextinguished	<1
$K_2C_2O_4$	11.9	3.7	4.6	Unextinguished	<1
K_3PO_4	16	5.1	9.7	Unextinguished	6.1

Therefore, the *n*-heptane was selected as the representative of the fuel model in the follow-up study.

The experimental results of extinguishing *n*-heptane fire by water mist containing 5% additive were shown in Table 4.

It can be seen from Table 4 that as pressure increased, the fire extinguishing time was obviously shortened regardless of water mist containing additive or not. The PPFR was increased obviously and the effects of different additives on PPFR were different, because the particle size of water was changed due to the existence of additives. Under the same pressure conditions, the particle size of water containing KNO_3 and K_3PO_4 solutions at mass fraction of 5% was obviously larger than that of pure water, because these two solutes increased the surface tension of water, which was not favorable to the atomization effect of water [13]. The particle size of the water containing KNO_3 additive was the largest, indicating that the water mist containing the KNO_3 additive had the lowest atomization effect. The particle size of water containing $K_2C_2O_4$ solution at mass fraction of 5% was smaller than or almost the same as that of pure water; this was because the presence of organic acids would reduce the surface tension of pure water [24], which was favorable to the water atomization effect, while $K_2C_2O_4$ contained two COO-groups which would obviously optimize the atomization effect of pure water, and its particle size was smaller than that of pure water.

Under 0.2 MPa, although the particle size of water mist containing additive was larger than the critical fire extinguishing particle size, the fire extinguishing was failed. According to Table 4, the PPFR during the extinguishing process was below 40%, namely the droplets actually reaching at fuel surface were less, so the fire was unable to be extinguished. However, under 0.4 and 0.6 MPa, the particle size of some fire extinguishing agents was smaller than the critical particle size, but fire extinguishing effect can be achieved by them in the experiment, and their PPFR was all more than 40%. Therefore, taking into account the accidental factors in extinguishing experiments, a critical range between 40 and 45% for PPFR should exist in the fire extinguishing process for the water mist containing additive. If PPFR was below the lower limit of this range, the extinguishing effect was unable to be achieved, and this was because that the particle size of water mist in the actual fire extinguishing process was not uniform. In the extinguishing process, the heat release rate of fuel was decreased, and the critical particle size also became smaller accordingly, as a result, the actual fire extinguishing particle size was less than the theoretical calculation value; therefore, there was some practical significance for the application of PPFR to determine whether the fire extinguishing can be achieved.

Based on mean-standard deviation, in Table 3, the margin of error for extinguishing time was 5.42–14.19%. In Table 4, the margin of error for extinguishing time under 0.4 and 0.6 MPa was 7.11–11.88% and 0.23–1.26%, the margin of error for PPFR from 0.2 to 0.6 MPa was 2.70–5.09%, 1.43–3.75%, and 1.69–2.67%, respectively, the margin of error for droplet size from 0.2 to 0.6 MPa was 0.28–0.66%, 0.45–1.08%, and 0.63–1.68%, respectively. The analysis showed that the maximum error of the experimental data was not more than 15%, which was acceptable in engineering application.

Table 4 Relationship between extinguishing time, PPFR, droplet size, and pressure

Additives	0.2 MPa			0.4 MPa			0.6 MPa		
	Extinguishing time (s)	PPFR (%)	Droplet size (μm)	Extinguishing time (s)	PPFR (%)	Droplet size (μm)	Extinguishing time (s)	PPFR (%)	Droplet size (μm)
None	Unextinguished	36.5	219.9	17.6	51.5	182.2	8.5	57.5	142.2
KNO_3	Unextinguished	37.1	366.3	11.6	54.3	321.5	2.3	59.4	296.0
$K_2C_2O_4$	Unextinguished	39.7	212.4	11.9	42.9	192.6	3.1	49.9	165.4
K_3PO_4	Unextinguished	33.4	339.8	16.0	45.2	279.2	8.2	51.7	222.8

Note The droplet size is Sauter median diameter D_{v32}

3.3   Analysis of Chemical Mechanism of Potassium Additives

Previous analysis showed that the precondition to maximize the chemical effect of water mist containing additives was to apply the droplet to the flame root, while under 0.6 MPa conditions, the PPFR of water mist was all greater than the upper limit of the critical range, which satisfies the conditions. Therefore, the 0.6 MPa was selected as experimental conditions for the analysis of chemical effect of the additives. The experiments were performed on the *n*-heptane fire under 0.6 MPa with water mist containing KNO_3, $K_2C_2O_4$, and K_3PO_4 solutions at mass fraction of 1%, 2%, 5%, 10%, 15%, and 20%, respectively, and experimental results were shown in Fig. 4. The improvement percentages by different potassium salt additives on the chemical efficiency for pure water were shown in Fig. 5.

As shown in Fig. 4, when the mass fraction of additive was less than 5%, the $K_2C_2O_4$ and KNO_3 (except K_3PO_4) could improve the extinguishing efficiency of

Fig. 4 Relationship between mass fraction of potassium additives and extinguishing time and PPFR
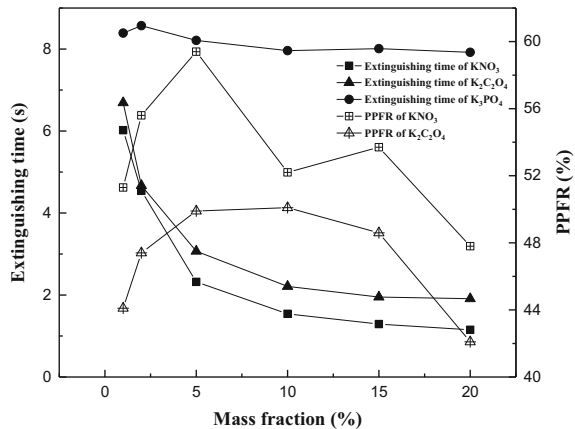
Fig. 5 Promotion of suppression efficiency of water mist by different potassium additives
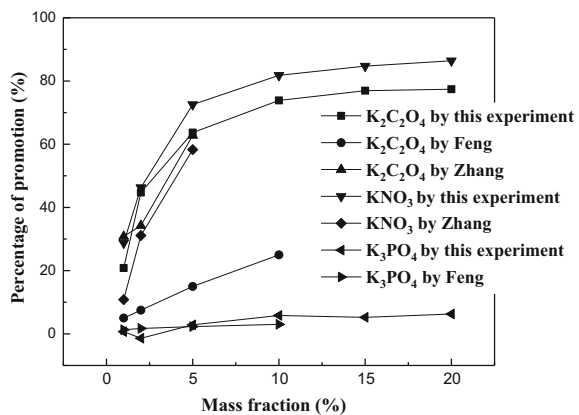
pure water. In case of low concentration, the extinguishing efficiency of water mist containing K_3PO_4 depended on the competitive relationship between the increased chemical effect and the weakened physical effect. The margin of error for extinguishing time by water mist with potassium in different mass fraction was 2.74–4.53%, while the error of average extinguishing time of water mist with K_3PO_4 under different mass fraction conditions was 2.92%. The data showed when the concentration was greater than 5%, $K_2C_2O_4$ and KNO_3 all could improve the extinguishing efficiency of the water, and as the additive concentration was increased, the extinguishing efficiency of the solution mist was improved, while little effect on the effectiveness increasing by K_3PO_4 for fire extinguishing. However, the chemical effect would be a limit which was impacted by the saturated vapor pressure of solute. When the concentration of the solution reached such limit, continuously increasing the concentration played a minor role in improving chemical efficiency. Different potassium salts had different effects on the evaporation rate of water, resulting in a different droplet size in the same position at high temperature. Therefore, the potassium salt solution containing the same mass fraction showed a different PPFR, as shown in Fig. 4.

Figure 5 showed the promotion of suppression efficiency by some potassium-containing substances, which referred to the increasing rate of extinguishing time or the dosage of extinguishants compared with pure water under the same experimental conditions. As shown in Fig. 5, the increasing trend of efficiency by KNO_3 with the mass fraction less than 5% and K_3PO_4 with the mass fraction less than 10% under enclosed space was consistent with the results obtained in Zhang's cup-burner experiment [13] and Feng's counterflow experiment [14], indicating that the chemical effect of the additive with the particle size in this experiment could be realized, and the KNO_3 additive can promote the chemical effect of pure water in extinguishing the buoyancy diffusion flame. Previous studies showed that KOH was the active substance in the fire extinguishing process for the water mist containing potassium salt additives [25], and the thermal decomposition process of KNO_3 was as follows [26]:

$$KNO_3 \xrightarrow[300.14-342.16\,°C]{\text{melt}} KNO_3(1) \xrightarrow[602.44-740.82\,°C]{-O_2-N_xO_y} K_2O \qquad (5)$$
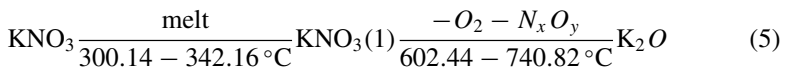
The key substance for KNO_3 to play its chemical effect under water vapor conditions was KOH due to the K_2O could react with water as follows: $K_2O + H_2O$ = KOH. However, Du [27] showed a good effect for extinguishing Class B fire by KNO_3 dry powders with suitable particle size, while there was no water (water vapor) in the experimental environment, indicating that potassium oxide K_xO_y should be the active substance of some potassium salt additives to exert chemical effect during the extinguishing process, which through a series of catalytic cycle reaction of KOH at high temperatures, and finally, K_xO_y was obtained and participated in blocking chain reaction until the fire was extinguished. However, after the drying of aqueous KNO_3 solution on porous combustible materials, such as paper, textile, and wood, a

solid KNO_3 was formed as an oxidizing agent to support the smoldering combustion of these materials.

As shown in Fig. 5, the efficiency of water mist containing K_3PO_4 in extinguishing pool fire and counterflow flame was similar to that of pure water. Shmakov [28] also showed that water mist containing K_3PO_4 was unable to extinguish the *n*-heptane flame in the cup-burner, indicating the promotion effect of K_3PO_4 additives on the chemical effect for pure water was not obvious. After the experiment, a large amount of white glassy substance were found in the oil pan, which was similar to the white dense oxide layer observed in Feng [14]. The melting point of K_3PO_4 was 1340 °C [29], and the thermal stability was strong which was difficult to release K^+ by breaking a chemical bond under the flame temperature [29], leading to a poor chemical effect of K_3PO_4.

As shown in Fig. 5, the efficiency trend of $K_2C_2O_4$ additive on Feng's counterflow flame was different from that of the pool fire tests and Zhang's cup-burner. However, the trend for the improvement role of $K_2C_2O_4$ on the chemical effect for pure water was consistent, the differences of which were mainly caused by the flame structure. Pool fire and cup-burner flame were all diffusion buoyant flames. In the cup-burner test, the droplet produced by ultrasonic atomization enters the flame base through entrainment. For the liquid fuel, the chemical substance could simultaneously play both fuel-phase and gas-phase extinguishing at the base and trailing regions because of the smaller particle size [30]. In this pool fire tests, due to the larger particle size, the fuel-phase extinguishing was more obvious than gas-phase extinguishing, leading to a lower efficiency compared to the cup-burner tests by $K_2C_2O_4$. Therefore, as the mass fraction of $K_2C_2O_4$ increased, the promotion effect was not obvious. The structure of the counterflow diffusion flame determined that it could only play gas-phase extinguishing; however, the flame temperature was higher compared to that of diffusion buoyant flame, which was propitious to the evaporation of water and the decomposition of potassium salts. Therefore, with the increase of dissolved mass in the solution, the fire suppression efficiency increased linearly.

The way for $K_2C_2O_4$ additive to play the chemical effect in the flame was as follows:

$$K_2C_2O_4 \xrightarrow[510.92 - 613.34\,°C]{\text{decomposition}(-CO)} K_2CO_3 \xrightarrow{H_2O(g)} KOH \qquad (6)$$
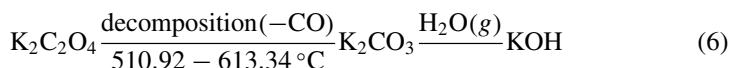
The $K_2C_2O_4$ would release CO during thermal decomposition [13], which would promote combustion. Based on the open space, the fire extinguishing effect due to the oxygen concentration dilution can be neglected in both Feng's counterflow flame and Zhang's cup-burner flame, and the gas-phase combustion of CO can also be ignored accordingly. For the confined spaces, the fire extinguishing effectiveness of $KHCO_3$ and KCl additives which obtained by Joseph was inconsistent with that of Feng, the main reason was that the fire extinguishing effect of inert gas CO_2 and H_2O produced by the thermal decomposition of $KHCO_3$ was different in a confined space and in an open space. Although space was enclosed in this paper, the space volume was much larger than that of Joseph's experimental space, the promoting effect of CO
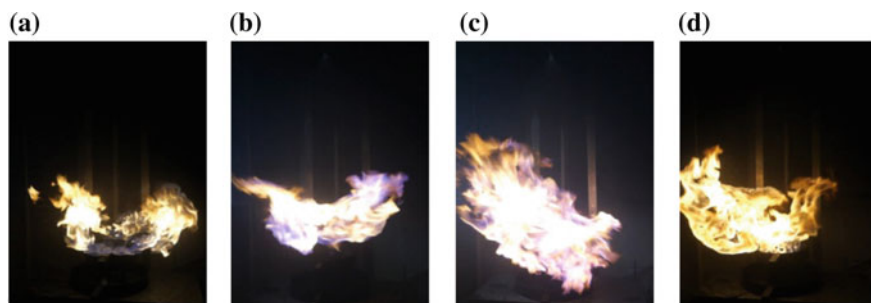
Fig. 6 Instant of water mist and fire for (**a**) without additive, (**b**) water mist with 5% KNO_3, (**c**) water mist with 5% $K_2C_2O_4$, and (**d**) water mist with 5% K_3PO_4

produced by thermal decomposition of $K_2C_2O_4$ on the combustion can be neglected. However, typical snapshots from the fire suppression process of the tests showed that, as compared to other additives, the instantaneous flame enhancement trend in the interaction between the water mist containing $K_2C_2O_4$ and the flame was larger, as shown in Fig. 6.

As shown in Fig. 6, obvious flame reaction was presented in the interaction between the water mist containing potassium salt additives and the *n*-heptane flame, indicating that K^+ in the solution was fully contacted with the flame radicals and played a role of chemical inhibition. The purple flame was more obvious under the action of $K_2C_2O_4$ solution and KNO_3 solution, followed by K_3PO_4 solution. From the view of the brightness of the flame, the flame was bright when K_3PO_4 solution was used in fire extinguishing, but the flame was faint when KNO_3 and $K_2C_2O_4$ solutions were used, indicating that the K_3PO_4 solution had a weak chemical inhibition ability, while the KNO_3 and $K_2C_2O_4$ solutions played a very good role in blocking the combustion chain reaction and had strong chemical inhibition ability.

4 Conclusion

The self-designed low-pressure water mist fire extinguishing system was used in this paper to carry out the experiment for water mist containing additives to extinguish oil pool fire. Five different types of pool fire models were set up, and the interaction between the water mist containing additives and the flames was quantitatively described through PPFR. The fire extinguishing effectiveness of three potassium salt additives $K_2C_2O_4$, KNO_3, and K_3PO_4 was obtained, and the possible chemical fire extinguishing mechanism was speculated. The major conclusions obtained in this paper were as follows:

(1) PPFR was an important parameter to assess the ability of water mist to penetrate the fire plume to reach fuel surface as well as to describe the interaction between the water mist and the oil pool fire where the mist nozzle was directly over the

fire. PPFR was related to the droplet size and the volume flow rate of the water mist, and the critical range of PPFR in inhibiting and extinguishing oil pool fire by water mist was 40–45%. It was more practical for PPFR to be used in measuring the fire extinguishing effectiveness of water mist containing additives in the actual application.

(2) The precondition for additives to play chemical effect to inhibit the buoyancy diffusion flame was that the droplets of water mist can penetrate the fire plume to reach the fuel surface. If the physical fire extinguishing role of water mist was not fully played, the chemical inhibition was unable to play a decisive role.

(3) Different potassium salt additives had different impact on the fire extinguishing effectiveness for pure water mist. In general, the fire extinguishing efficiency was enhanced, and the chemical fire extinguishing efficiency of the potassium salt additives at the same concentration was ranked as $KNO_3 \approx K_2C_2O_4 > K_3PO_4 \approx$ pure water. The chemical mechanism of potassium additives was that the fire was mainly extinguished by the chemically active substances KOH and K_xO_y formed at high temperature. The volume of enclosed space was much larger than that of fire sources, and the enhancement effect of CO produced by thermal decomposition of $K_2C_2O_4$ on the flame was negligible.

References

1. Zhang, T., Liu, H., & Han, Z. (2017). Numerical model for the chemical kinetics of potassium species in methane/ air cup-burner flames. *Energy & Fuels, 31,* 4520.
2. Lan, M., Yuan, L., & Wang, X. (2013). Drop impact onto charring surface of heated Betula costata wood. *Ciesc Journal, 64,* 2807.
3. Yang, L., & Zhao, J. (2011). Fire extinct experiments with water mist by adding additives. *Journal of Thermal Science, 20,* 563.
4. Liu, J., & Cong, B. (2013). Experimental evaluation of water mist with metal chloride additives for suppressing CH_4/air cup-burner flames. *Journal of Thermal Science, 22,* 269.
5. Korobeinichev, O., Shmakov, A., & Shvartsberg, V. (2012). Fire suppression by low-volatile chemically active fire suppressants using aerosol technology. *Fire Safety Journal, 51,* 102.
6. Kuang, K., Chow, W., & Ni, X. (2011). Fire suppressing performance of superfine potassium bicarbonate powder. *Fire and Materials, 35,* 353.
7. Lask, G., & Wagner, H. (1961). Influence of additives on the velocity of laminar flames. *Symposium on Combustion, 8,* 432.
8. Shilling, H., Dlugogorski, B., & Kennedy, E. (1996). In E. Leonardi, C.V. Madhusudana (Eds.). *Proceedings of the Sixth Australasian Heat and Mass Transfer Conference*, (p. 275). New York: Begell House.
9. Chelliah, H., Lazzarini, A., & Wanigarathne, P. (2002). Inhibition of premixed and non-premixed flames with fine droplets of water and solutions. *Proceedings of the Combustion Institute, 29,* 369.
10. Babushok, V., Linteris, G., & Hoorelbeke, P. (2017). Flame inhibition by potassium-containing compounds. *Combustion Science & Technology*.
11. Williams, B., & Fleming, J., 1999. Suppression mechanisms of alkali metal compounds. In *Halon options technical working conference*, p. 27.
12. Joseph, P., Nichols, E., & Novozhilov, V. (2013). A Comparative study of the effects of chemical additives on the suppression efficiency of water mist. *Fire Safety Journal, 58,* 1131.

13. Zhang, T., Liu, H., & Han, Z. (2017). Active substances study in fire extinguishing by water mist with potassium salt additives based on thermoanalysis and thermodynamics. *Applied Thermal Engineering, 122,* 429.
14. Feng, M., Tao, J., & Qin, J. (2016). Extinguishment of counter-flow diffusion flame by water mist derived from aqueous solutions containing chemical additives. *Journal of Fire Sciences, 34,* 121.
15. Nam, S. (1996). Development of a computational model simulating the interaction between a fire plume and a sprinkler spray. *Fire Safety Journal, 26,* 1.
16. Nam, S. (1999). Numerical simulation of the penetration capability of sprinkler sprays. *Fire Safety Journal, 32,* 307.
17. Niu, G., Yu, M., & Liu, Z. (2007). Analysis of dominant mechanism of extinguishment of pool fires with water mist in confined space. *Fire Science and Technology, 26,* 286.
18. NFPA 750. (1996). *Standard for the Installation of Water Mist Fire Protection Systems*. Quincy, USA: National Fire Protection Association.
19. Liu, Z., Andrew, K., & Cartenper, D. (2007). A study of portable water mist fire extinguishers used for extinguishment of multiple fire types. *Fire Safety Journal, 42,* 25.
20. Rasbash, D., & Rogowski, Z. (1957). Extinction of fires in liquids by cooling with water sprays. *Combustion and Flame, 1,* 453.
21. Zhang, T., Han, Z., & Du, Z. (2016). Application of thermal mechanism to evaluate the effectiveness of the extinguishment of CH4/air cup-burner flame by water mist with additives. *International Journal of Hydrogen Energy, 41,* 15078.
22. Mccaffrey, B. (1979). Purely buoyant diffusion flames: Some experimental results. National Bureau of Standards.
23. Williams, A. (1976). *Combustion of sprays of liquid fuels*. U.K.: Unwin Brothers Limited.
24. Liang, T. (2012, May). *Project: Doctoral Dissertation for 2012*. University of Science and Technology of China.
25. Friedman, R., & Levy, J. (1963). Inhibition of opposed jet methane-air diffusion flames. The effects of alkali metal vapours and organic halides. *Combustion & Flame, 7,* 195.
26. Du, X., Du, Z., & Zhao, L. (2013). Study on the feasibility of common potassium salts applied to superfine powder fire-extinguishing agent. *Industrial Safety and Environmental Protection, 39,* 61.
27. Du, X. (2013). *Project: Master Degree Thesis for 2012*. Beijing Institute of Technology.
28. Shmakov, A., Korobeinichev, O., & Shvartsberg, V. (2006). Testing Ogranophosphorus. *Organofluorine and metal-containing compounds and solid-propellant gas-generating compositions doped with phosphorus-containing additives as effective fire suppressants, combustion explosion & shock waves, 42,* 678.
29. Speight, J. (1999). physical properties In *Lange's handbook of chemistry,* (15th ed., p. 5.8). New York: McGRAW-HILL.
30. Katta, V., Takahashi, F., & Linteris, G. (2006). Fire-suppression characteristics of CF3H in a cup burner. *Combustion and Flame, 144,* 645.

Characteristics of Thermal Runaway Propagation of Lithium Ion Battery Module Induced by Thermal Abuses in Enclosure Space

Caixing Chen, Linsheng Guo, Niu Huichang, Zhao Li, Shanjun Mo, Peiyi Sun and Xinyan Huang

Abstract Fire and explosion risks of electric vehicles caused by thermal runaway (TR) of battery have become the main obstacle that delaying the popularization of electric vehicles. Usually, the whole battery pack is completely burned down and destroyed, firstly caused by TR of a single battery, and then by the propagation over the whole battery pack with an extremely rapid rate. In this work, thermal runaway propagation characteristics of lithium ion battery module induced by thermal abuses in enclosure space were experimentally investigated. The results indicated that a temperature rise of 72 °C on the nearby battery was found when overheating one cell in the module with an initial temperature of 25 °C; however, no TR occurred. While for the case of overheating the whole battery module, cells were found to TR in 85 s and thus giving rise to a high temperature of 956 °C, as soon as TR firstly happened in the battery module. Violent explosion and high heat releasing rate were observed and eventually caused the damage of battery module. Therefore, the methods of mitigation of TR propagation when TR occurred in modules will become the focus of future research on the safety of lithium ion battery.

Keywords Lithium ion battery module · Thermal abuse · Thermal runaway propagation

C. Chen · L. Guo · N. Huichang (✉) · Z. Li
Institute of Industry Technology & Chinese Academy of Sciences, Guangzhou, Guangdong 511458, China
e-mail: niuhuichang@gziit.ac.cn

S. Mo
School of Engineering, Sun Yat-Sen University, Guangdong, Guangzhou 510006, China

P. Sun · X. Huang
Department of Building Services Engineering, The Hong Kong Polytechnic University, Kowloon, Hong Kong, Hong Kong

1   Introduction

Thermal runaway (TR) of battery caused violent fire and explosion, which is one of the greatest threat to the safety of passengers, has become the main obstacle that delaying the popularization of electric vehicles [1]. Paying more efforts to study the mechanism of TR and its propagation process is extremely urgent and of significant importance [2]. Among the factors that may trigger TR of a lithium ion battery, thermal abuse is the most direct one that giving rise to a fast runaway propagation and a large-scale fire and explosion.

There are two main thermal abuse conditions of battery in a pack. One is that only a single cell is under overheat or even TR state, which may be caused by mechanical/electrical abuse, thus providing the nearby batteries with a thermal abuse environment. Adiabatic calorimetry experiments conducted by Chen [3] indicated that for a fully charged Li-ion cell with a 100% state of charge (SoC), an exothermic reaction occurred at a temperature exceeding 122 °C, and cells at a SoC of greater than 50% were subject to thermal explosion at the elevated temperatures. Lamb et al. [4] performed a TR propagation test by constructing a triangle battery module with 10 cylinder battery held together, and creating a hard shorting failure within the central cell using mechanical nail penetration. Results showed that 10S1P cylindrical cell module did not involve failure propagation through the module because of the limited contact between neighboring cells, while the 1S10P module had an energetic thermal runaway minutes after the failure initiation due to electrical connectivity. Feng et al. [5] also applied penetration to induce TR of a large prismatic lithium ion battery and found that 12% of the total heat released in TR of a battery is enough to trigger the adjacent battery to TR, and the caused fire had little influence on the TR propagation. Spinner et al. [6] constructed a $LiCoO_2$ chemistry 18650 lithium-ion battery module with six batteries in a hexagonal arrangement and triggered the center battery to TR by overheating with a cartridge heater, which was attached to the battery surface. Video recordings before, during, and after energetic failure events revealed a high degree of heterogeneity; some batteries exhibited short burst of sparks while others experienced a longer and sustained flame during failure. Lopez et al. [7] investigated the cell-to-cell TR propagation behavior by triggering a single cell in a module into TR and strongly recommended a cell spacing of at least 2 mm to minimize the chance of TR propagation and module damage. The above-mentioned works are meaningful in the safety design of a battery module; however, battery pack is usually an enclosure space, and nature convention of the air in the open space may present effects on the results.

Another case is that the whole battery module or pack is under an extremely high temperature, which may be caused by a fire (External fire test has been listed as the international abuse testing standard for lithium ion batteries in vehicles [8].) Compared to the first cases, TR caused by heating the whole battery module or park is more fiercely and TR propagation is faster. Thermal behavior and flame propagation over seven large-format batteries arranged in rhombus and parallel layouts were investigated by Huang et al. [9] by directly heating one of the battery units. It was

found that fire-impingement led to an elevated temperature in the vicinity battery, a rapid temperature rise within the battery module, and even explosions after 20 min of a smoldering period. Effect of battery arrangements on lithium-ion battery fire behaviors was studied by Chen et al. [10], and the results indicated the arrangements could affect the ignition time, heat release rate, and released heat. For the purpose of cutting off the TR propagation, more researches of battery module or pack under a high temperature or a fire should be made.

In this wok, battery modules with 5 * 5 arrangement of cylinder batteries were constructed to analyze the TR propagation properties in enclosure space. Thermal abuse by electric heating was utilized to trigger TR of the center battery to study the case that only a battery was overheated or TR. Thermal abuse provided by thermostat at 155 °C was used to reproduce the condition that the whole battery module was under an extremely high temperature.

2 Experimental Methods

Commercial 18650 lithium ion battery (cathode: $Li(Ni_{1/3}Co_{1/3}Mn_{1/3})O_2$, anode: graphite) with a nominal capacity of 2150 mAh was used in this work. The test modules (102 * 102 * 65 mm) were constructed with 25 cells at the arrangement of 5 * 5, as shown in Figs. 1a, and 2a and b. Flame-resistant ABS frame was used to support the cylinder batteries. Al box (124 * 124 * 124 mm) was applied to provide the enclosure space. Space between batteries was set as 2 mm. Thermal couples were attached to the surface of cells as shown in Fig. 1b on the plane A shown in Fig. 1a. Open circuit voltages (OCV) of cell 1, 2, 3, 7, 8, and 13 were monitored.

Pre-tests of single battery were performed under adiabatic condition maintained by the extended volume accelerating rate calorimeter (EV-ARC) and also under isothermal conditions at 140 °C provided by a thermostat. For the case of triggering
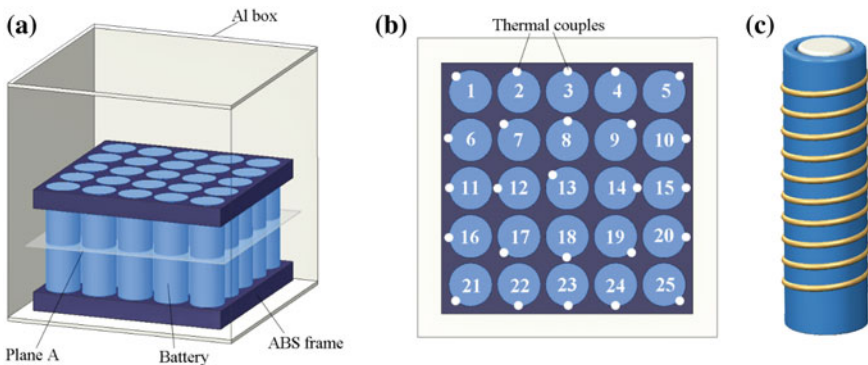
Fig. 1 Diagrams of test battery module: **a** battery module; **b** location of thermal couples; **c** battery heated by resistance heating wire
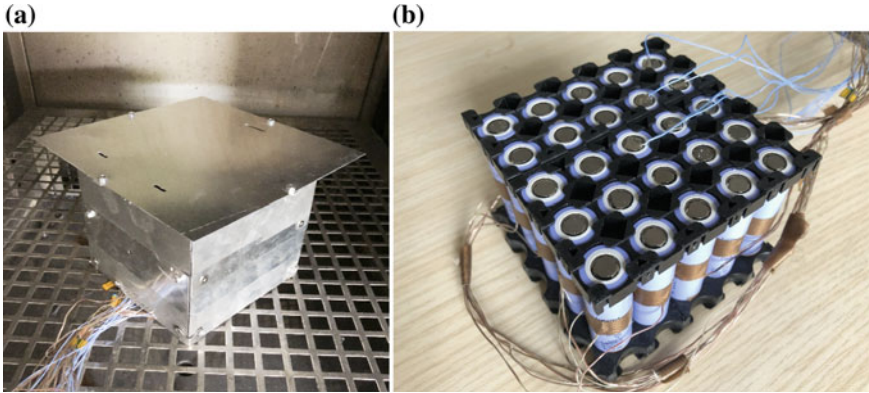
Fig. 2 Diagram of the test unit: **a** battery module in Al enclosure space; **b** The 5 * 5 battery module

the center battery (No.13 shown in Fig. 1b), resistance heating wire (Cr20Ni80) was used and wrapped spirally around the center battery as shown in Fig. 1c. Heating power of the battery was set at 20 W and controlled by a regulated DC power, which was shut off once the battery went into TR. For the case overheating the battery module, the whole battery module was placed in a thermostat whose temperature was controlled at 155 °C. Temperatures of all battery before the tests were the ambient temperature 25 °C.

3 Results and Discussion

3.1 Characterization of Thermal Runaway of a Single Cell

Figure 3 presents the heat abuse test results of a single battery. As shown in Fig. 3a; under adiabatic condition, exothermic reaction (temperature increasing rate is over
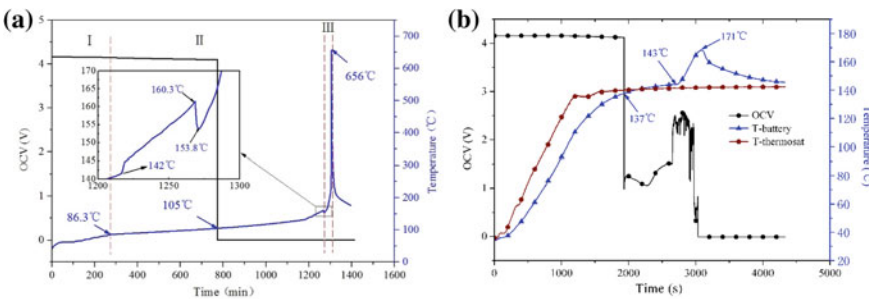
Fig. 3 Heat abuse test of a single battery: **a** tested in ARC; **b** tested in thermostat

0.02 °C/min) was observed at 86.3 °C because of the decomposition of the SEI layer on the surface of anode. Battery OCV dropped to zero at 105 °C caused by the inner short circuit due to the melt of separator. After the complete breakdown of separator at 142 °C, exothermic reactions accelerated and temperature increased faster until 160.3 °C, when the safety valve of battery was removed, and then extensive amount of heat released thus driving the battery to TR. Teat abuse test at 142 °C presented in Fig. 3b indicated exothermic reactions heat the battery to a temperature of 143 °C, which was higher than that of the thermostat. Then, the temperature increased to 171 °C rapidly and leads to the opening of safety valve. However, no TR occurred as a consequence of fast heat dissipation to the ambient. The battery failure temperature was 137 °C, which was much higher than that under adiabatic test. This is because of the nonuniform temperature of battery when heat dissipation existed.

3.2 Characterization of Thermal Runaway Propagation When a Single Battery Was Heated

Figure 4 illustrates temperature variations of 25 batteries during the test by triggering only one battery (No. 13) to TR. The highest temperature of the triggered battery reached to 740 °C. Due to heat radiation and convention, the nearest battery (battery No. 8, 12, 14, 18) got only to 120 °C with a temperate rise of 66 °C, which was smaller than 142 °C tested for a single battery before. The second nearest battery (battery No. 7, 9, 17, 19) achieved the highest temperature of 72 °C with a temperature rise of 18 °C, while the temperatures of the others were much lower. Therefore,
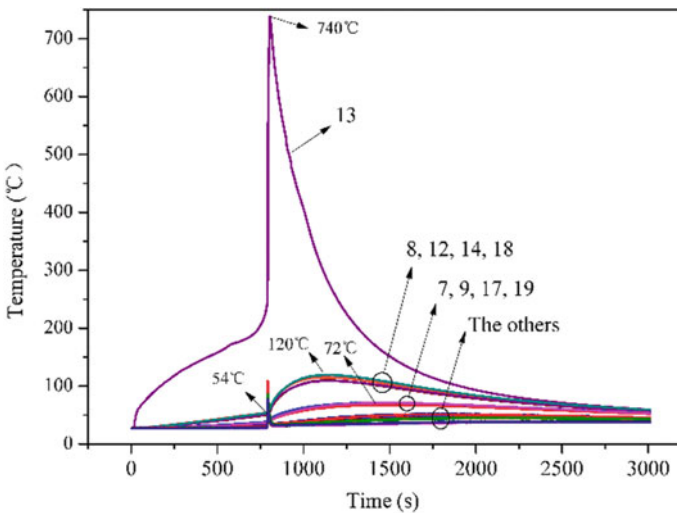
Fig. 4 Temperature variations of batteries
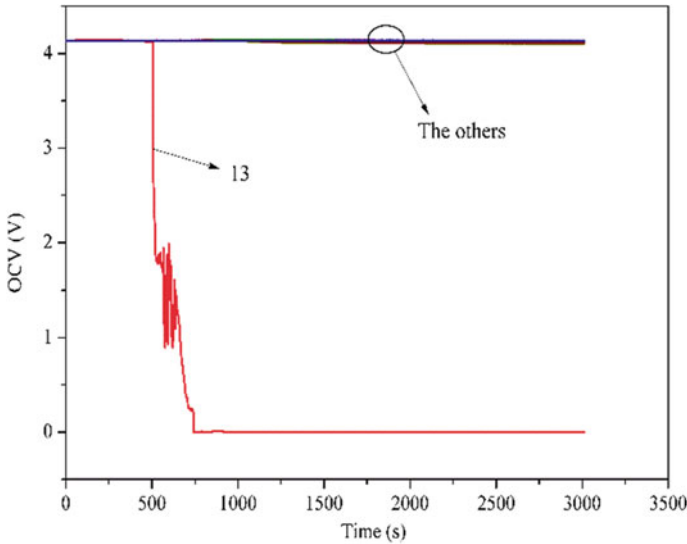
Fig. 5 OCV variations of batteries

no battery failure propagation occurred as presented in Fig. 4, let alone TR propagation. Image of battery module after the test is shown in Fig. 6. Except the battery No. 13, all other batteries are kept undamaged. More researches with higher initial temperatures over 25 °C should be done to determine the critical initial temperature of batteries that will lead to TR propagations during the one battery TR triggering test (Figs. 5 and 6).

3.3 Characterization of Thermal Runaway Propagation When Whole Battery Module Was Heated

Post-test image of the battery module after the whole battery module overheat test is shown in Fig. 7. Batteries and the Al box are all destroyed because of the violent combustion and explosion. Figure 8 presents the OCV variations of the six monitoring batteries. Battery failure sequence was 1-2-3-7-8-13, which meant failure took place from the outside to the inside of the battery module, because of the existed temperature gradient. Temperature variations before TR are displayed in Fig. 9. As shown, the temperature of battery 1 at the corner of the module firstly started to increase quickly from 145 to170 °C, until the safety valve opened. However, temperature decline occurred and no immediate TR happened, on account of heat dissipation, which consequently heated the nearby battery (No. 2) to 183 °C. Temperature increasing rate of battery 2 slowed down slightly, and then sharply increased to TR, followed by the fierce temperature increase of battery 7 nearby battery 2. Temperature variations
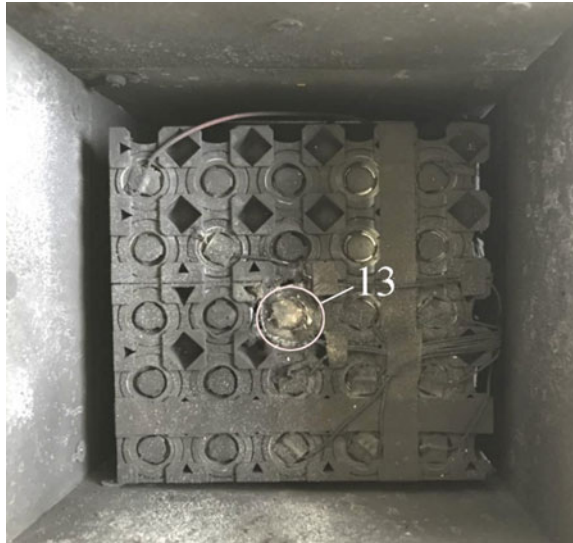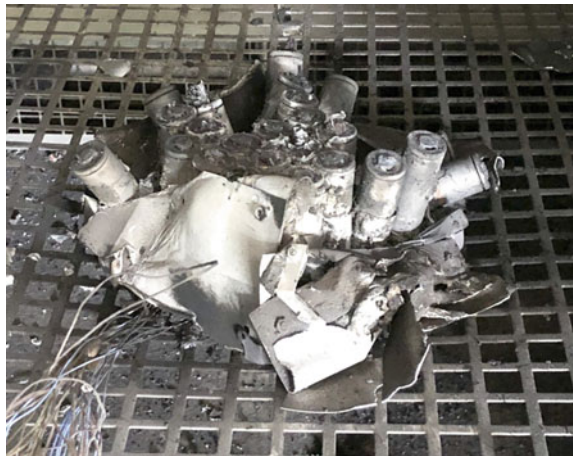
of batteries during thermal runaway process are shown in Fig. 10. Battery 2 firstly came to TR and then reached its highest temperature of 675 from 240 °C in around 18 s. A time interval of 38 s after the TR of battery 2, TR happened on battery 7, followed by battery 3 in 2 s, and battery 1, 6, 8, 12 in 37 s. Temperature of all batteries came over 450 °C and then to TR in 10 s after the TR of battery 12. Violent explosion happened and massive heat released, thus heating the batteries to a highest temperature of 956 °C, which was enough to destroy the battery module and melt the Al box. From the time TR happened, all batteries came to TR in 85 s. Therefore, trying to cut off the TR propagation after TR happened in modules will no longer
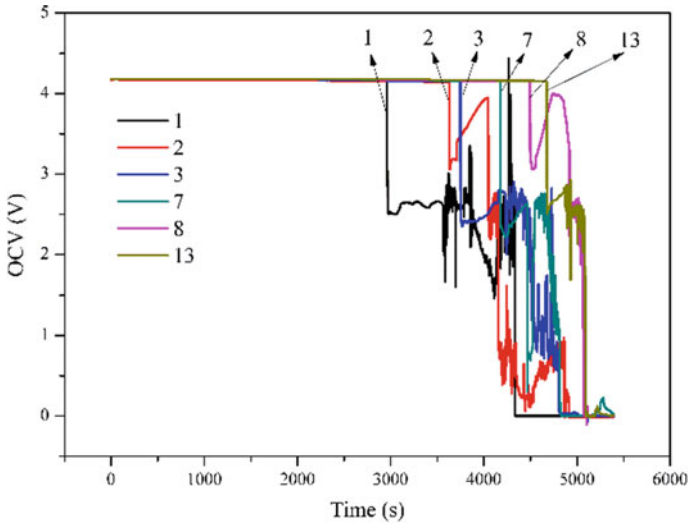
Fig. 8 OCV variations of batteries
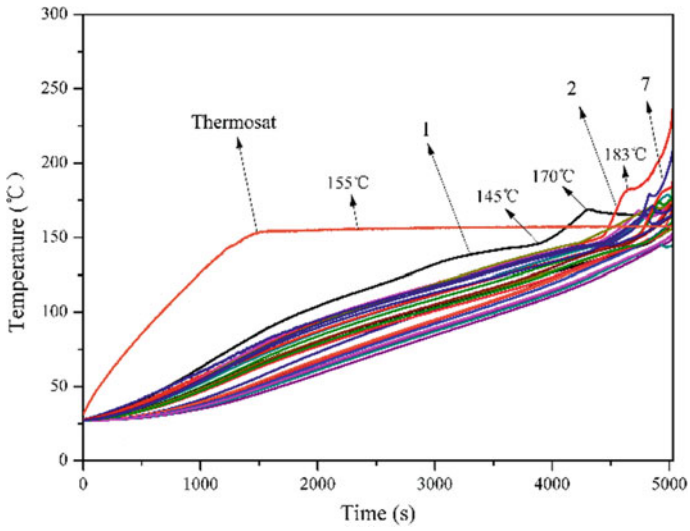
Fig. 9 Temperature variations of batteries before thermal runaway
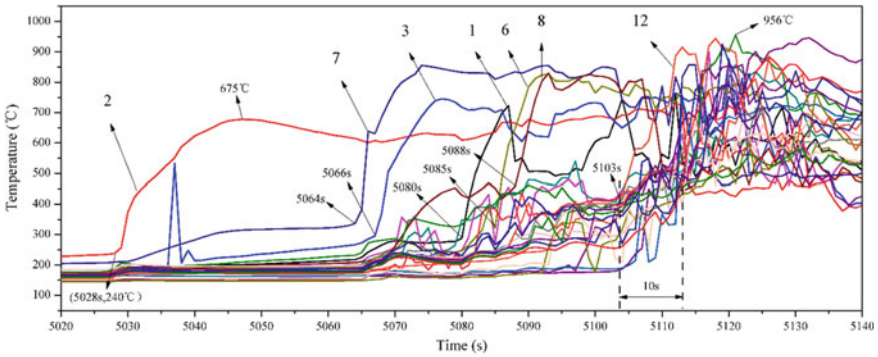
Fig. 10 Temperature variations of batteries during thermal runaway process

be in time. And fast cooling is strongly recommended urgently after the temperature reached around 140 °C, as the last protection of battery module or pack before fire happens.

4   Conclusion

Thermal runaway propagation characteristics of lithium ion battery module induced by thermal abuses in enclosure space were experimentally investigated in this work. For the thermal abuse of overheating one cell at an initial temperature of 25 °C, a temperature rise of 72 °C on the nearby battery was found; however, no TR occurred. Researches with increased initial temperatures should be further considered to determine the critical initial temperature that will lead to TR propagations. For the case of overheating the whole battery, all batteries were found come to TR in 85 s and thus giving rise to a temperature high up to 956 °C, as soon as TR firstly happened in the battery module. Violent explosion occurred and massive heat released and consequently totally destroyed the battery module and melt the Al box. Therefore, trying to cut off the TR propagation after TR happened in modules will no longer be in time. Fast cooling measures are strongly recommended urgently after the temperature reached around 140 °C.

References

1. Wang, Q., Ping, P., & Zhao, X. (2012). Thermal runaway caused fire and explosion of lithium ion battery. *Journal of Power Sources, 208,* 210–224.
2. Feng, X., Ouyang, M., & Liu, X. (2018). Thermal runaway mechanism of lithium ion battery for electric vehicles: A review. *Energy Storage Materials, 10,* 246–267.
3. Chen, W. C., Wang, Y. W., & SHU, C. M. (2016). Adiabatic calorimetry test of the reaction kinetics and self-heating model for 18650 Li-ion cells in various states of charge. *Journal of Power Sources, 318,* 200–209.
4. Lamb, J., Orendorff, C. J., & Steele, L. A. M. (2015). Failure propagation in multi-cell lithium ion batteries. *Journal of Power Sources, 283,* 517–523.
5. Feng, X., Sun, J., & Ouyang, M. (2015). Characterization of penetration induced thermal runaway propagation process within a large format lithium ion battery module. *Journal of Power Sources, 275,* 261–273.
6. Spinner, N. S., Field, C. R., & Hammond, M. H. (2015). Physical and chemical analysis of lithium-ion battery cell-to-cell failure events inside custom fire chamber. *Journal of Power Sources, 279,* 713–721.
7. Lopez, C. F., Jeevarajan, J. A., & Mukherjee, P. P. (2015). Experimental analysis of thermal runaway and propagation in lithium-ion battery modules. *Journal of the Electrochemical Society, 162*(9), A1905–A1915.
8. Ruiz, V., Pfrang, A., & Kriston, A. (2018). A review of international abuse testing standards and regulations for lithium ion batteries in electric and hybrid electric vehicles. *Renewable and Sustainable Energy Reviews, 81,* 1427–1452.
9. Huang, P., Ping, P., & Li, K. (2016). Experimental and modeling analysis of thermal runaway propagation over the large format energy storage battery module with Li 4 Ti 5 O 12 anode. *Applied Energy, 183,* 659–673.
10. Chen, M., Yuen, R., & Wang, J. (2017). An experimental study about the effect of arrangement on the fire behaviors of lithium-ion batteries. *Journal of Thermal Analysis & Calorimetry*, 1–8.

Full-Scale Experimental Study of Boilover Suppression by Floating Perlites

Tzu-Yan Tseng and Kuang-Chung Tsai

Abstract Boilover is the most dangerous occurrence in oil tank fires because it expands the burning field and may hurt firefighters by flame or severe radiant exposure. Because of the low density and cost of perlites, this study uses floating perlites on the surface of burning oil to study whether they can delay the occurrence of large-scale boilover and consequently prevent the flame enlargement. The experiment is performed in a round stainless steel pan with a diameter of 1 m and depth of 0.2 m, containing a 0.08 m layer of thick crude oil was used as fuel, above 0.07 m water. Zero, 1, and 2 layers of perlites are placed above the fuel to investigate their effects. Experimental results show that boilover does not occur after using the perlites, while it does occur in the experiment without perlites test. The use of the perlites can reduce the heat flux of radiation and the flame enlargement when boilover occurs, thus enhancing the fire safety of oil tanks and decreasing the risk of firefighting.

Keywords Boilover · Perlites · Oil tank fire · Large scale

1 Introduction

Boilover is well known to be the most dangerous scenario in oil tank fires. For example, an earthquake in 1964 Japan [1] resulted in oil tank fires with severe boilover. Although no casualties occurred, this fire lasted 10 days. Another boilover accident happened in 1982, in Venezuela, when fuel was spilled over 3 km with a fire the lasted 20 days. This accident caused 150 deaths and at least 500 injured. The uncertainty and danger of boilover phenomenon increased the difficulty of firefighting.

Boilover is caused by the vaporization of water from the bottom of an oil tank when the water is heated by heat transfer from the oil tank fire. The water temperature rises at increasing speed after because the thickness of the fuel layer gradually decreases with time. Once the temperature of water reaches the boiling temperature of water, water vaporizes immediately and the burnt oil is ejected or spilled out of the oil tank. The fire from the spilled fuel injures firefighters, ignites other fuels, forms fireballs,

T.-Y. Tseng · K.-C. Tsai (✉)
National Kaohsiung University of Science and Technology, Kaohsiung, Taiwan
e-mail: tsaikc@nkust.edu.tw
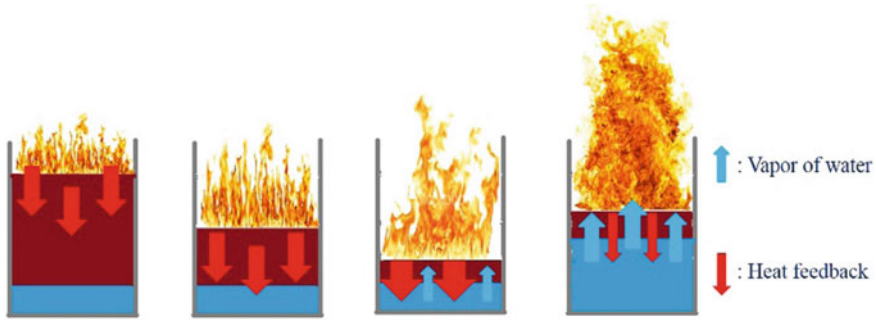
Fig. 1 Mechanism of boilover occurrence

and consequently enlarges the burning field. Figure 1 illustrates the mechanism of boilover.

Hall [2] proposed that the occurrence of boilover had to follow three conditions: the presence of water in the oil; heat wave moved down into the oil well in advance of the burning surface; and the viscosity of oil in nature. Additionally, boilover can be divided into two types, namely hot-zone boilover and thin-layer boilover, which differ mainly in the fuel thickness above the water sub-layer. This study only investigated hot-zone boilover. Hasegawa [3] examined the hot-zone mechanism by using different round pan sizes and different fuels, namely diesel, gasoline, and diesel mixed with gasoline. The experimental results showed that the range of fuel boiling point affected the hot-zone formation. Furthermore, the tank material influenced the formation of hot-zone when the scale of the oil pan was less than 0.8 m. Conversely, the formation of the hot zone was affected by the characteristic of fuel when the scale of the oil pan was more than 0.9 m. Koseki [4] performed experiments using crude oil of different layer thickness and kerosene to compare the boilover mechanisms. The results showed the hot zone appeared in the crude oil test but not in the kerosene test and that the time to boil over and the intensity of boilover rose with the increasing initial fuel layer thickness.

Those studies focused on the physical understanding and major effective parameters of the hot-zone boilover. However, little research has discussed preventing or delaying hot-zone boilover. Foam systems are usually adopted nowadays to extinguish pool fires, but these do not work very well in oil tank fire and performed poorly in preventing boilover. Moreover, the agents of a foam system may not be cleaned up easily after extinguishing the oil tank fire and consequently cause water pollution of the entire environment. Therefore, Tsai et al. [5] proposed the use of vapor suppression spheres, to delay and prevent thin-layer boilover by small-scale tests. Their experimental results revealed that the vapor suppression spheres help to prevent thin-layer boilover. However, vapor suppression spheres have a high cost. Therefore, Tseng and Tsai [6] conducted an experiment for delaying and preventing thin-layer boilover with small-scale tests by using perlites. Their experimental results showed that the floating perlites can prevent thin-layer boilover effectively. However, small-

scale experiments are difficult to match with practical tank fires, and the resulting boilover may also differ from practical boilover phenomenon. Therefore, this study investigates the effect of using floating perlites to delay the occurrence of hot-zone boilover and prevent flame enlargement by undertaking large-scale tests.

2 Experimental Design

2.1 Experiment Field

The experiment was conducted outdoors. The outdoor experiment field was surrounded by hills from three sides, so wind effect occurred only from one side. The ambient temperature and humidity were measured in all experiments before ignition. The ambient wind velocity was measured every 5 min. The average ambient temperature and humidity were 30.15 °C ± 0.96 °C and 58.44% ± 4.05%, respectively. The ambient wind velocity was from 0.4 to 1.5 m/s.

2.2 Fuel

Basra light crude oil that was supplied by CPC Corporation, Taiwan, was used in the experiment. Table 1 shows the characteristics of Basra light crude oil, and Fig. 2 depicts the distillation curve of Basra light crude oil.

2.3 Perlite

Perlite, which is produced by volcanic eruptions and rapid cooling, is an amorphous, porous, light, white particulate substance. Perlite has steady physical and chemical performance and does not react with other chemicals. Moreover, perlite is non-toxic and has good thermal insulation performance (thermal conductivity 0.045–0.047 W/(m k)) and fire performance (temperature is 1300–1380 °C), and

Table 1 Characteristic of Basra light crude oil

Density at 15 °C (kg/L)	0.8775
Flash point (°C)	<0
Viscosity at 30 °C (cSt)	14.5
Total sulfur (% wt)	2.85
Total nitrogen (ppm wt)	1400

Fig. 2 Distillation curve of Basra light crude oil
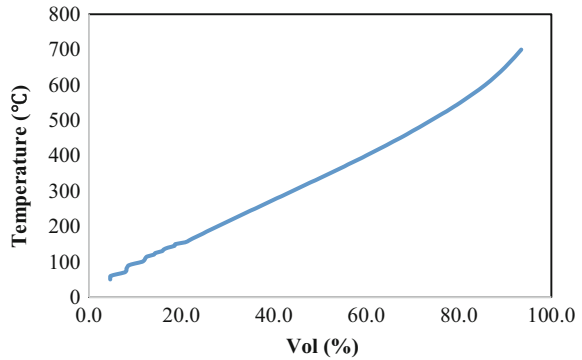
is a commonly used insulation building material. This work adopts perlite with an effective diameter of 3.85 mm $\pm$ 1.4 mm and a density of 0.17–0.25 g/cm^3.

2.4 Experimental Setup

Figure 3a, b display the experimental setup. The experiments adopted a round stainless steel pan with a diameter of 1 m, depth of 0.2 m, and thickness 6 mm. The depths of the fuel and water layers were 0.08 m and 0.07 m, respectively. To determine the effects of perlites, experiments were performed with 0, 1, and 2 layers of perlites placed above the fuel. The weight of one layer of perlites for the fuel pan was 291 g. Because of the same diameter and surface area, the weight of perlites, which was used in the test of 2 layers, was a factor of two of the weight of 1 layer. Figure 4 shows a sectional view of the K-type thermocouples. To measure the temperature inside the
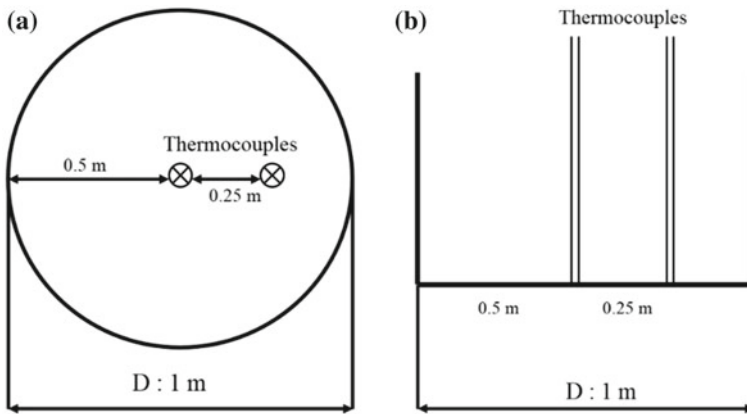
Fig. 3 Experimental setup **a** above view and **b** sectional view (drawing not to scale)

Fig. 4 Sectional view of
K-type thermocouples setup
(drawing not to scale)
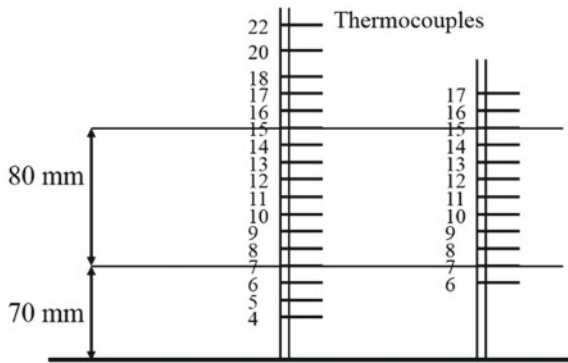
fuel and water, one thermocouple, called the center pole, was set at the center of the
oil pan, while another, called side pole, was set 0.25 m away from the center. Point 4
was set at height 0.04 m from the bottom of the fuel pan and every thermocouple was
set apart from 0.01 m. Furthermore, point 4–6 were in the water layer, point 8–14 in
the oil layer, and point 16–22 above the liquid in the air. In addition, point 7 and 15
were in the interface of oil and water and on the oil surface, respectively. Heat flux
meters were set to determine the effect of firefighting from flames. The horizontal
distance between the pan center and the heat flux meter was set to $L/D = 5$, where
D represents the pan diameter and L represents the distance from the pan center to
the heat flux meter, and the vertical distance was set 1.8 m above the floor. Video
record was set in all experiments to observe the occurrence of hot-zone boilover and
the difference between the test without and with perlites.

3   Results and Discussion

3.1   Experimental Observations

Figures 5 and 6 show the observations of explosive burning without and with perlites,
respectively. The explosive burning with none layer perlites is depicted as hot-zone
boilover because the burnt oil with flame was ejected and spilled out of the fuel
pan. Thus, the flame was enlarged. However, the test with perlites did not perform
hot-zone boilover. This observation might be caused by the existence of the perlites
layer, which formed an insulation layer of heat to decrease the radiation from flame
to water. Furthermore, the decreased radiation lowered the rate of temperature rise
of water. Tests with perlites showed lower levels of vaporizing water and milder
hot-zone boilover than those without perlites. Thus, the experimental observations
indicate that using floating perlites suppresses hot-zone boilover and prevents flame
enlargement. Furthermore, suppressing the hot-zone boilover phenomenon might
decrease the risk of firefighting.

Fig. 5 Observations of explosive burning without perlites

Fig. 6 Observations of explosive burning with perlites

3.2 *Temperature History of Fuel and Water*

Figures 7 and 8 show the fuel and water temperature history for the tests without and with perlites, respectively. A uniform temperature zone, called hot-zone, formed inside the fuel then descended with time in the test without perlites. Furthermore, the temperature without perlites decreased rapidly and then increased to 885 s. Experimental observations show that hot-zone boilover is characterized by rapidly changing
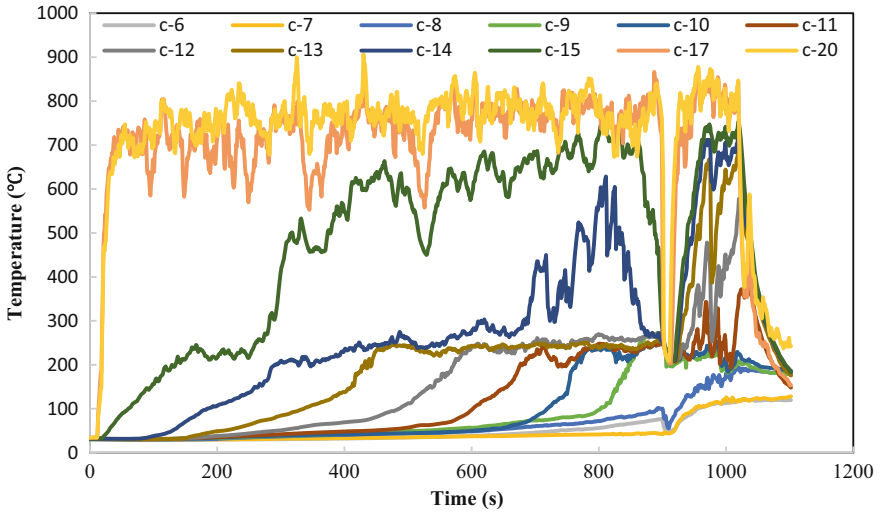
Fig. 7 Temperature history of fuel and water without perlites
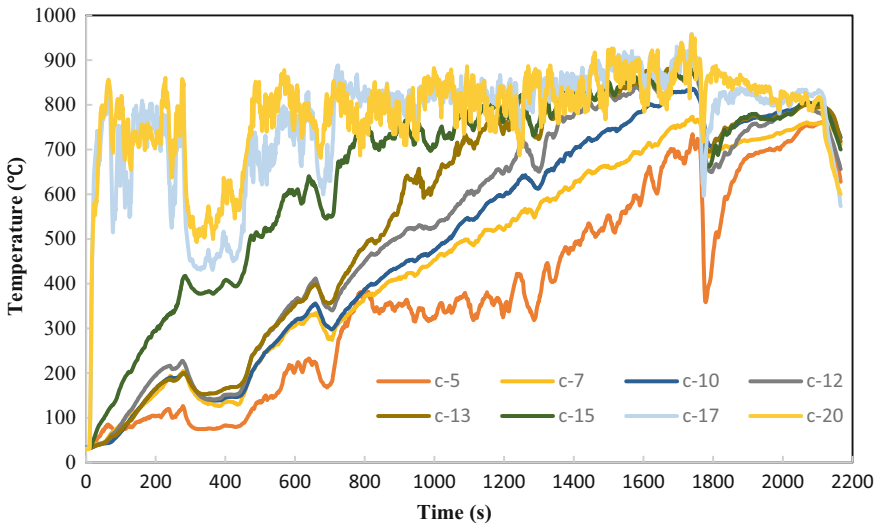
Fig. 8 Temperature history of fuel and water with perlites

Fig. 9 Thermocouples were
stuck by perlites

temperatures. Water vapor causes flame and fuel to be ejected from the oil pan, thus
reducing the fuel temperature measured. The data in this work followed the same
trend as Koseki [7] who conducted a boilover test with a 5-m pan. A uniform tem-
perature zone did not form inside the fuel after perlites were added since the perlites
formed an insulation layer reducing the radiation from the flame to fuel. Thus, the
decreased radiation lowered the rate of temperature rise. The unusual temperature
history after 400 s is shown in Fig. 8. Since the thermocouples were stuck by burned
perlites, as Fig. 9, and the burned perlites maintained a high temperature. Therefore,
the temperature might be the burned perlites.

3.3 Radiation Heat Flux

Figure 10 shows the effect of a number of perlites layer on the heat flux. The radiation
heat flux without perlites shows rapid increase at 885 s and then decrease. Addition-
ally, the phenomenon was illustrated as the occurrence of a hot-zone boilover by the
observation of the experiment. The radiation heat flux with perlites was the same
as that without perlites during the steady burning, but the radiation heat flux with

Fig. 10 Effect of layer number of perlites on the heat flux
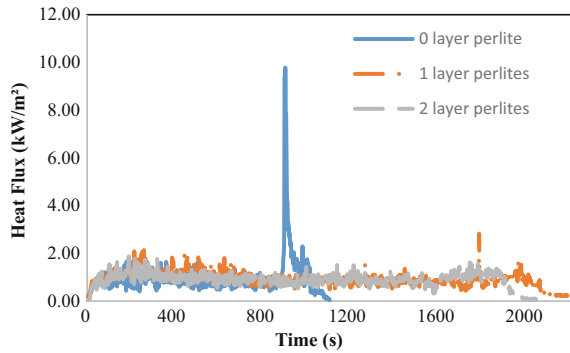
perlites was much lower than that without perlites during the occurrence of hot-zone boilover. Since hot-zone boilover did not occur in the test with perlites, the flame shape and length did not change, either. Thus, adding perlites could effectively decrease the radiation heat flux during hot-zone boilover and increase the safety for firefighting by preventing hot-zone boilover.

4 Conclusion

This study conducted a large-scale boilover test to investigate the effect of floating perlites on preventing hot-zone boilover. The test data show that hot-zone boilover occurred without perlites, but did not occur when perlites were added. The use of floating perlites could prevent the formation of hot-zone and also suppress hot-zone boilover. Furthermore, the use of floating perlites could also decrease the radiation heat flux from flames and the risk for firefighting by preventing the occurrence of hot-zone boilover. Further research is needed to study the mechanism of floating perlites on the occurrence of hot-zone boilover.

References

1. Koseki, H., Dusserre, G., & Iwata, Y. (2014). *Boilover: occurrence and current research* (pp. 1–18). Report of National Research Institute of Fire and Disaster, No. 117, NRIFD.
2. Hall, H. (1925). Oil tank fire boilovers. *Mechanical Engineering, 47*(7), 540–544.
3. Hasegawa, K. (1989). Experimental study on the mechanism of hot zone formation in open tank fires. In: *Fire Safety Science—Proceedings of the 2nd International Symposium* (pp. 221–230). International Association for Fire Safety Science.

4. Koseki, H., Kokkala, M., & Mulholland, G. W. (1991). Experimental study of boilover in crude oil fires. In: *Fire Safety Science—Proceedings of the 3rd International Symposium* (pp. 865–874). International Association for Fire Safety Science.
5. Tsai, K. C., Koseki, H., Tseng, T. Y., Kelly R. (2016). Effects of floating beads on the flash/fire temperatures and occurrence of boilover. In: *Annual International Symposium* (pp. 279–289), Texas.
6. Tseng, T. Y., & Tsai, K. C. (2017). Effect of floating perlites on the occurrence of thin-layer boilover. In: *11th Asia-Pacific Conference on Combustion*.
7. Koseki, H., Natsumeb, Y., Iwataa, Y., & Takahashic, T., Hirano T. (2006). Large-scale boilover experiments using crude oil. *Fire Safety Journal*, 529–535.

Urban, Wildland/Urban Interface and Forest Fires

Influence of Base Sheathing Material on Wind-Driven Firebrand Production During Real-Scale Building Component Combustion

Samuel L. Manzello, Sayaka Suzuki and Tomohiro Naruse

Abstract The production of firebrands during large outdoor fires remains unresolved in spite of many advances in the fire safety science discipline. To better grasp this complex problem, multiple experiments were undertaken using full-scale re-entrant corner assemblies exposed to wind in order to sample firebrands. In prior work, an ignition methodology was developed to generate firebrands from re-entrant corner assemblies constructed of wood studs and oriented strand board (OSB) as the base sheathing material. The objective of this study was to apply this same ignition methodology to examine if the base sheathing material, namely plywood as compared to OSB, greatly impacted the firebrand generation from re-entrant corner assembly combustion. It was interesting to observe that plywood generally produced far greater numbers of smaller firebrands (within size class up to 0.9 cm^2), whereas OSB produced a great number of firebrands in the size class from 3.61 to 14.4 cm^2. It is believed that these differences may be related to the different nature of the production process of these materials. Plywood firebrands clearly showed the presence of veneers, whereas the OSB firebrands show the wood strands still compressed together, suggesting a potential useful inspection methodology for post-fire damage assessment to identify the source of firebrands.

S. L. Manzello (✉)
National Institute of Standards and Technology (NIST), Gaithersburg, MD, USA
e-mail: samuelm@nist.gov

S. Suzuki
National Research Institute of Fire and Disaster (NRIFD), Chofu, Tokyo, Japan

T. Naruse
Building Research Institute (BRI), Tsukuba, Ibaraki, Japan

Present Address:
National Institute for Land and Infrastructure Management (NILIM), Tsukuba, Ibaraki, Japan

1   Introduction

Large outdoor fires, including urban fires, wildland–urban interface (WUI) fires, and informal settlement fires, are becoming a significant fire safety science research topic [1]. 2018 WUI fires in the state of California in the USA destroyed more than 18,500 buildings and left scores of fatalities. Japan does not have a large WUI fire problem but rather is prone to urban or city fires. Japanese urban fires may or may not be produced after the occurrence of strong earthquakes. In Niigata, Japan, the Itoigawa-City fire (2016) was a significant urban fire that developed even though no earthquake was reported.

In both Japan and the USA, after fire disaster studies have demonstrated the importance of firebrands as a leading culprit for fire spread processes and structure ignition [2, 3]. Firebrand research may be divided into generation, transport, deposition, and ignitions by firebrands. In the context of fire safety science, nearly all the prior studies have been directed on firebrand transport [see 4–10; as a brief sample], with scarce research conducted on firebrand generation and ignitions processes caused by firebrands [11]. Recent invention of the firebrand generators (Dragons) by the National Institute of Standards and Technology (NIST) has advanced knowledge of vulnerabilities of structures to firebrand showers [12]. Much less advancement has been made determining firebrand generation from structure combustion.

In historical literature studies of experimental firebrand generation, several actual buildings were ignited, and firebrands were sampled [13, 14]. The size of firebrands was determined by measuring holes produced in polyurethane sheets. In experiments conducted many years later, a wooden house burn in a wind tunnel was undertaken, and firebrands were sampled by pans filled with water or without water [15]. In another study, firebrands collected after a three-story wooden school burn experiment reported the lengths of most of the firebrands were between 10 and 30 mm [16]. In a recent after fire investigation of an urban fire, firebrands were collected [17]. While all these data are quite valuable, firebrand collection methodologies varied, making direct comparisons tenuous. It is important to develop *consistent* experimental methods for firebrand generation research.

A basic approach is to attempt to develop test methods to evaluate building components propensity for firebrand production. In this manner, it may be possible to design structures that produce a reduced number of firebrands. Yet, conducting many full-scale experiments of structure firebrand production is costly and not easy to undertake. As a result, the authors have embarked on an experimental program to determine if smaller-scale experiments may produce useful insight into the firebrand production process. To do this requires firebrand generation data over various scales and complexities using building materials and components typically found in construction to be able to adequately ascertain the efficacy of future test methods.

For completeness, a terse overview of the comprehensive database the authors are developing related to firebrand production from structures is provided. During training exercises for local fire services, an actual residential building in the state of California was burned and firebrands were sampled [18]. As a next step, an exper-

imental burn under similar wind speed was performed with a simplified building constructed from oriented strand board (OSB) and wooden studs [19]. Firebrands sampled from the simplified building had similar masses and sizes to those sampled from the actual residential building. To go even simpler in design and scale, a repeatable experimental ignition methodology using full-scale wall assemblies were developed and demonstrated the capability to predict characteristics of firebrands from all these more complex studies described above [20]. In addition, the effect of cedar siding treatments on wall assembly combustion was investigated using the same ignition methods albeit with OSB *once again* as the base sheathing material [21].

In this paper, the efforts to investigate firebrand production from full-scale re-entrant corner assemblies are presented. As the wind is an important factor in firebrand generation, the experiments were conducted under a range of wind speeds. In prior work [21], a unique ignition methodology was developed to generate firebrands from re-entrant corner assemblies constructed of wood studs and OSB. The objective of this study was to use this same ignition methodology to examine if the base sheathing material, using plywood as compared to OSB, greatly impacted firebrand generation from re-entrant corner assembly combustion.

2 Experimental Description

Experiments were performed in the Building Research Institute's (BRI) Fire Research Wind Tunnel Facility (FRWTF). In this facility, it is simple to vary the wind speed. The re-entrant assemblies used in the experiments were 122 cm wide on each side and 244 cm high. Wood studs (38 mm by 89 mm) spaced 0.40 m on center were used as framing, and plywood (thickness—11.9 mm) was used as the base sheathing material (see Fig. 1). Plywood was selected as it is a common base sheathing material used in the USA and Japan. The assemblies were placed inside the test section of the facility.

The FRWTF was equipped with a 4.0-m-diameter axial fan to provide a wind field up to a 10 m/s. The wind velocity distribution was verified using hot-wire anemometers ($\pm10\%$). The wind speed was measured upstream of the re-entrant corner assemblies. A detailed array of water pans was placed downstream of the assemblies to collect the firebrands produced from the combustion process.

The ignition method used in this study was based on prior work [21]. While the description follows prior work closely, the reader must grasp that this ignition methodology had to be re-verified as the base sheathing used in the construction of the wall assemblies in the present study was totally different. This method provides repeatable conditions to collect firebrands during combustion of the wall assemblies. The effect of wind speed on firebrand production from wall assembly configurations is an important parameter to study, as large outdoor fires occur under windy conditions. Each re-entrant corner assembly was ignited using a propane gas (commercial grade) T-shaped burner with a heat release rate of 26 kW positioned adjacent to the
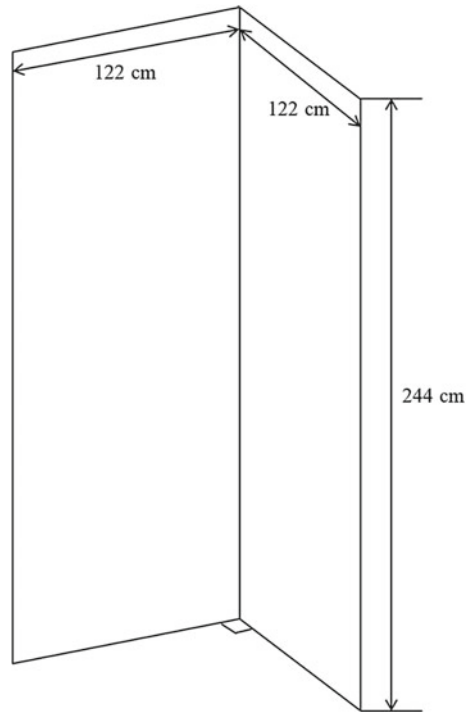
assemblies for 10 min under conditions of no wind. If the burner was placed next to
the re-entrant corner assembly with the wind tunnel flow on, flaming combustion of
the assembly was difficult to achieve due to convective heat loss from the wind. Igni-
tion without wind (with the burner applied for the same duration for each assembly)
resulted in repeatable initial conditions for the experiments. In particular, the area
exposed to direct flame contact was similar for a given assembly. If igniting with the
wind, in addition to the large convective heat loss, the contact area of the flame onto
the plywood surface of the assembly became unsteady.

The total ignition time of 10 min was critical and carefully selected during ignition
in the absence of wind. When trying to ignite for a time shorter than 10 min, once the
wind was added, insignificant firebrand collection was possible from the re-entrant
corner as a result of the lack of combustion. On the contrary, for burner application
greater than 10 min, the re-entrant assembly was observed to be consumed to such a
degree as to make it unstable for firebrand collection, that is, large holes were formed
due to long ignition combustion process compromising the structural integrity.

With the application of the T-shaped burner to the assembly under no wind for
10 min duration, flaming combustion was observed on the exterior of a re-entrant
corner assembly. Once the burner was switched off, the wind tunnel was switched on
(stable wind in 60 s). Firebrands were collected until the assemblies were consumed
to such a degree that they could no longer support themselves (loss of structural

Fig. 2 Full-scale re-entrant corner ignited and 8 m/s wind has been applied. The water pan array is used to collect the firebrands produced

integrity). Figure 2 displays an image after the ignition of the re-entrant corner assembly, with an 8 m/s wind applied. Firebrands were collected using multiple water pans placed behind the re-entrant corner assembly. Water was necessary to stop the combustion of the generated firebrands. After deposition into the water pans, firebrands were filtered from the water using a series of fine mesh filters. Firebrands were dried in an oven at 104 °C for an entire day (to remove moisture). The total drying time required was determined by measuring the firebrand mass loss as a function of time.

3 Results and Discussion

Experimental findings are presented for two different wind tunnel speeds (6 and 8 m/s). Commercially available image analysis software was used to determine the projected area of collected firebrands. Prior to conducting the image analysis, a digital image of each firebrand was taken to ensure that the maximum projected area could

be measured. At the same time, the mass of each firebrand was also determined. Since the authors have used this same analysis methodology in several of our prior papers, the interested reader is referred elsewhere for more details on the technique and associated experimental uncertainties [21].

Figure 3 demonstrates the relationship of firebrand projected area plotted as a function of firebrand mass (log–log scale). It may be seen that only four (four) firebrands had a mass greater than 2500 mg. The combustion of plywood and wood stud combustion was responsible for firebrand production.

The data presented in this paper is compared and contrasted to other studies that used wall assemblies constructed with different sheathing materials [21]. In those experiments, re-entrant corners (walls) were constructed using the same construction methodologies but the main, critical difference was that OSB sheathing was fitted to the framing as opposed to plywood used in this study. The thickness of the OSB sheathing in [21] was 11.0 mm.

Figure 4 is plotted using a log–log scale. A direct comparison of using plywood as compared to OSB as the base sheathing material may be seen. Figure 5 provides a close-up photograph of the firebrand generation process for a wind speed of 8 m/s. The combustion of the wood studs and plywood may be observed.

Figure 6 is a histogram that affords a more detailed comparison of the differing size classes generated for plywood as opposed to OSB base sheathing. It is interesting to observe that plywood generally produced far greater numbers of smaller firebrands (within size class up to $0.9 \, cm^2$), whereas OSB produced a great number of firebrands in the size class from 3.61 to $14.4 \, cm^2$.

It is postulated that these differences may be related to the different nature of the production process of these materials. In the case of plywood, it is constructed using thin sheets of wood veneers that are glued together, often at 90° degree cross-

Fig. 3 Size and mass distribution of collected firebrands from re-entrant corner assembly combustion. The assembly was constructed from wood studs and plywood
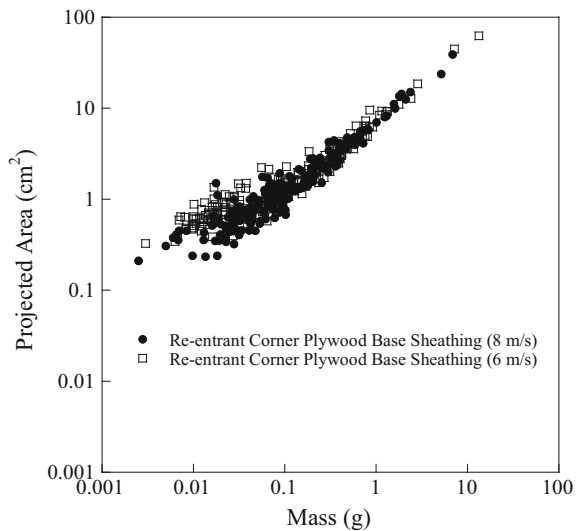
Fig. 4 Size and mass distribution of collected firebrands from re-entrant corner assembly (OSB/wood studs) combustion [21] directly compared to re-entrant corner assembly (plywood/wood studs) data in Fig. 3. In all cases, the wall dimensions were 1.22 m wide on each side, with a height of 2.44 m
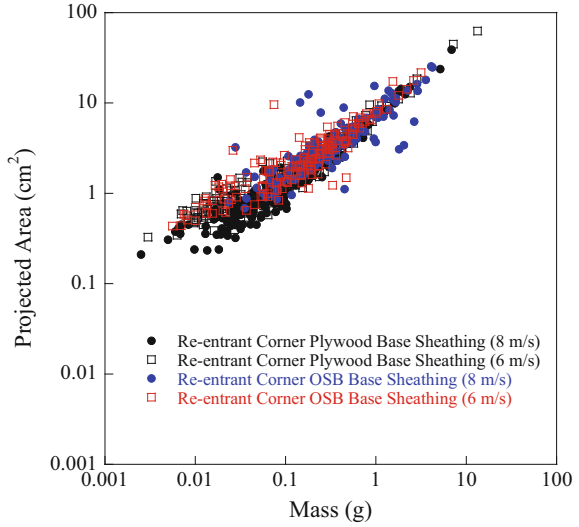
Fig. 5 Picture of firebrand generation process for a wind speed of 8 m/s. The combustion of plywood and wood studs may be observed
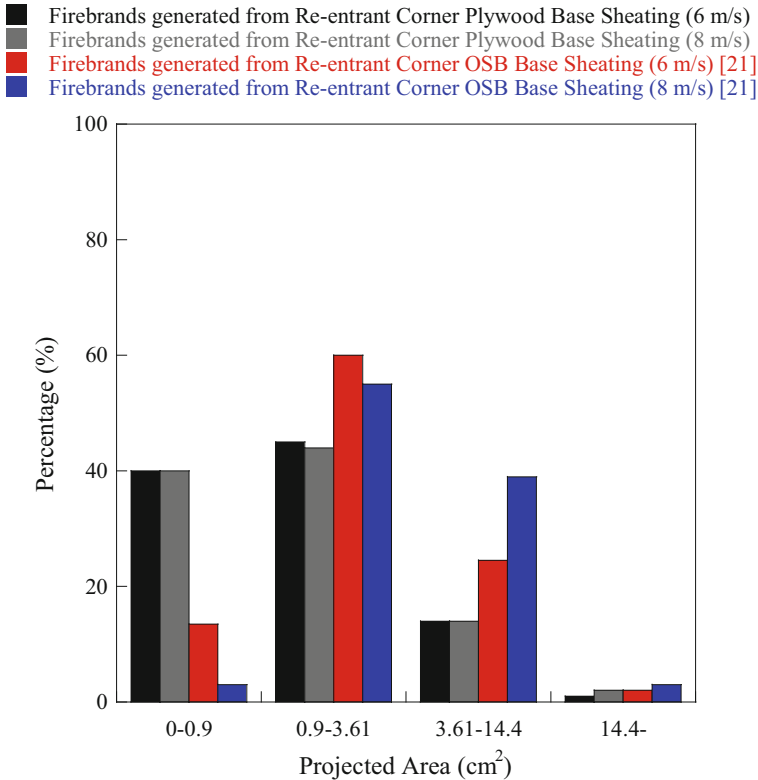
Fig. 6 Comparison of the size distribution for re-entrant corner combustion using plywood or OSB [21] as the base sheathing material. Two wind speeds are shown

angles, to fabricate the entire board. In the case of OSB, layers of wood strands are compressed and glued together. It may be that during the initial combustion stages, the thin wood veneers of plywood result in the production of very small firebrands. Yet, in the case of OSB, the larger wood strands are ultimately liberated during combustion, resulting in the possible explanation for the greater number of firebrands in the medium size class of 3.61–14.4 cm^2. Close inspection of firebrands generated from plywood indicates that the outer thin layer of wood veneer appears degraded due to combustion (see Fig. 7). Another noteworthy item is that plywood firebrands clearly show the presence of veneers, whereas the OSB firebrands (see Fig. 8) show the wood strands still compressed together, suggesting a potential useful inspection methodology for post-fire damage assessment to identify the source of firebrands.

Fig. 7 Photograph of firebrand produced from plywood combustion. Well-defined vertical structure indicating the wood veneer

0.58 g

1 cm

Fig. 8 Photograph of firebrand produced from OSB combustion. Note the presence of the wood strands

1.4 g

1 cm
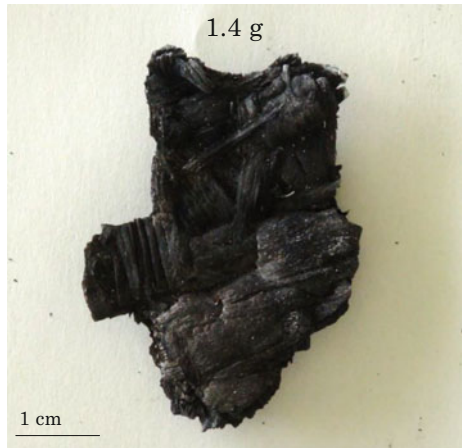
4 Summary

In spite of many advances in the fire safety science discipline, the production of firebrands during large outdoor fires remains unresolved. The objective of this study was to examine if the base sheathing material, namely plywood as compared to OSB, greatly impacted the firebrand generation from re-entrant corner assembly combustion.

It was interesting to observe that plywood generally produced far greater numbers of smaller firebrands (within size class up to $0.9 \, \text{cm}^2$), whereas OSB produced a great number of firebrands in the size class from 3.61 to $14.4 \, \text{cm}^2$. It is postulated that these differences may be related to the different nature of the production process of

these materials. Plywood firebrands clearly showed the presence of veneers, whereas the OSB firebrands show the wood strands still compressed together, suggesting a potential useful inspection methodology for post-fire damage assessment to identify the source of firebrands.

The joint BRI/NIST/NRIFD investigations are providing the scientific basis for developing test methods that afford the ability to compare and evaluate (screen) a material's propensity to produce firebrands, suggesting a mitigation strategy may be possible by simply limiting a building's propensity for firebrand production.

References

1. Manzello, S. L., Blanchi, R., Gollner, M., McAllister, S., Planas, E., Rein, G., Reszka, P., & Suzuki, S. (2017). *Summary of workshop large outdoor fires and the built environment*. NIST SP 1213.
2. Maranghides, A., McNamara, D., Vihnanek, R., Restiano, J., & Leland, C. (2015). *A case study of a community affected by the Waldo fire—Event timeline and defensive actions*. NIST TN1910.
3. National Research Institute of Fire and Disaster. (1977). *Fire spread behaviors of the Sakata Fire*. Technical Report of National Research Institute of Fire and Disaster, No. 11. (In Japanese).
4. Albini, F. (1983). Transport of firebrands by line thermals. *Combustion Science and Technology, 32,* 277–288.
5. Muraszew, A., & Fedele, J. F. (1976). *Statistical model for spot fire spread*. The Aerospace Corporation Report No. ATR-77758801, Los Angeles, CA.
6. Tarifa, C. S., del Notario, P. P., & Moreno, F. G. (1965). On the flight paths and lifetimes of burning particles of wood. *Proceedings of the Combustion Institute, 10,* 1021–1037.
7. Anthenian, R., Tse, S. D., & Fernandez-Pello, A. C. (2006). On the trajectories of embers initially elevated or lofted by small scale ground fire plumes in high winds. *Fire Safety Journal, 41,* 349–363.
8. Woycheese, J. P. (2000). *Brand lofting and propagation for large-scale fires*. Ph.D. Thesis, University of California, Berkeley.
9. Knight, I. K. (2007). The design and construction of a vertical wind tunnel for the study of untethered firebrands in flight. *Fire Technology, 37,* 87–100.
10. Wang, H. H. (2011). Analysis on downwind distribution of firebrands sourced from a wildland fire. *Fire Technology, 47,* 321–340.
11. Fernandez-Pello, A. C. (2017). Wildland fire spot ignition by sparks and firebrands. *Fire Safety Journal, 91,* 2–10.
12. Manzello, S. L. (2014). Enabling the investigation of structure vulnerabilities to wind-driven firebrand showers in wildland-urban interface (WUI) fires. *Fire Safety Science, 11,* 83–96.
13. Vodvarka, F. J. (1969). *Firebrand field studies—Final report*. IIT Research Institute, Chicago, IL.
14. Vodvarka, F. J. (1970). *Urban burns-full-scale field studies– Final report*. IIT Research Institute, Chicago, IL.
15. Yoshioka, H., Hayashi, Y., Masuda, H., & Noguchi, T. (2004). Real-scale fire wind tunnel experiment on generation of firebrands from a house on fire. *Fire Science and Technology, 23,* 142–150.

16. Hayashi, Y., Jaishi, T., Izumi, J., Naruse, T., Itagaki, N., Hashimoto, R., et al. (2014). Firebrands deposition and measurements of collected firebrands generated and transported from a full-scale burn test using a large wooden building. *AIJ Journal of Technology and Design, 20*, 605–610 (in Japanese).
17. Suzuki, S., Fujisaki, S., & Manzello, S. L. (2017). Characteristics of firebrands collected from urban fire—Niigata Fire, December 22nd 2016, 12th IAFSS Poster Session, Lund, Sweden.
18. Suzuki, S., Manzello, S. L., Lage, M., & Laing, G. (2012). Firebrand generation data obtained from a full-scale structure burn. *International Journal of Wildland Fire, 21,* 961–968.
19. Suzuki, S., Brown, A., Manzello, S. L., Suzuki, J., & Hayashi, Y. (2014). Firebrands generated from a full-scale structure burning under well-controlled laboratory conditions. *Fire Safety Journal, 63,* 43–51.
20. Suzuki, S., Hayashi, Y., & Manzello, S. L. (2013). The size and mass distribution of firebrands collected from ignited building components exposed to wind. *Proceedings of the Combustion Institute, 34,* 2479–2485.
21. Suzuki, S., & Manzello, S. L. (2016). Firebrand production from building components fitted with siding treatments. *Fire Safety Journal, 80,* 64–70.

Behavior of Downslope Fire Spread Through a Pine Needle Fuel Bed

Zhuo Yang, Hongmin Zhang, Linhe Zhang and Haixiang Chen

Abstract The downslope fire spread is one of the typical wildfire spread phenomena but has attracted less attention during the past wildfire research. In our prior work (*Fire Technology*, 2018, https://doi.org/10.1007/s10694-018-0740-0), downslope fire spread over thermally thin fuel bed was investigated. However, if the fuel bed was thermally thick, the combustion interface inside the fuel bed would be different and therefore could affect the heat transfer process. This work investigated the downslope fire spread over thermally thick fuel bed. The experiments were conducted by using pine needle fuel beds with 1.2 kg/m² fuel load and the slopes of −30°, −20°, −10°, 0°, and 10°. The combustion interface shape was identified from the temperature profiles of five vertical thermocouples inside the fuel bed and found to tilt backward from the vertical direction of the fuel bed for all slopes, indicating the fuel bed was thermally thick. Experimental results showed that the rate of spread (ROS) decreased firstly and then increased from 10° to −30°, same as that reported in the literature and in our prior work for thermally thin fuel bed. Based on experimental observations, a two-dimensional model of energy balance valid for thermally thick fuel bed was developed. The prediction revealed that the fuel is heated mainly by flame radiation throughout the whole process but the combustion zone radiation plays more important role in the near flame region, which is similar with that reported for thermally thin fuel bed in our prior work.

Keywords Downslope fire · Rate of spread · Thermally thick · Fuel bed

Z. Yang · H. Zhang · L. Zhang · H. Chen (✉)
State Key Laboratory of Fire Science, University of Science and Technology of China, Hefei, Anhui 230026, People's Republic of China
e-mail: hxchen@ustc.edu.cn

Nomenclature

Letters

D	Flame thickness (m)
K_v	Extinction coefficient (m^{-1})
T	Temperature (K)
R	Rate of spread (m/s)
ρ_f	Fuel particle density (kg/m^3)
h_s	Enthalpy of fuel particle (kJ/kg)
B	Stefan–Boltzmann constant (W/m^2 K^4)
X	Distance between the flame and the fuel element (m)
V	View factor (-)
h	Heat transfer coefficient (W/m^3 K)
α	Flame angle (°)
α_c	Combustion interface tilt angle (°)
W	Fuel particle density (kg/m^3)

Greek Symbols

σ	Surface-area-to-volume ratio (m^{-1})
β	Packing ratio of fuel bed (-)
δ	Fuel bed depth (m)
ε	Emissivity

Subscripts

s	Surface fuel element
f	Flame
c	Combustion interface
a	Ambient air

1 Introduction

Wildfire is one of the largest natural disasters over the world and could cause the loss of properties and casualties. The prediction of wildfire behavior is of importance for controlling fire and reducing the losses. Terrain slope is an important factor affecting

wildfire behavior [1–5]. The effect of positive slope (upslope) on wildfire spread has been studied in the most previous work. However, the effect of negative slope (downslope) on wildfire spread is of little concern. Since the rate of spread (ROS) of downslope fire is close to that of flat surface fire [1, 2, 6, 7], Behave [8] simply uses ROS of flat surface fire to represent that of downslope fire for all negative slopes. According to the previous studies [1, 2, 6, 7], ROS of downslope fire decreases firstly and then increases with the slope increasing, presenting a parabolic shape. It seems that there is some unidentified behavior or mechanism behind downslope fire spread.

The parabolic pattern of ROS of downslope fire is not well explained. The first decrease of ROS was deemed because the flame tilted backward gradually with the increase of slope and the radiation from the flame to the unburned surface fuels decreased [6]. For the second increase of ROS, there are many explanations. It could be caused by the combustion zone radiation variation [9], the change of combustion interface tilt angle [10], the enhanced flame emissivity [6], even due to the flaming material that sliding downslope in the situation of steep negative slope [1]. For the entire parabolic shape of ROS, Rossa et al. [7] tried to explain it by a parameter that estimated the radiation of flame to the fuel element. Generally speaking, confusion still exists and it needs more studies on the process and heat transfer mechanism of downslope fire.

In the recent work of the authors [11], downslope fire over thermally thin fuel bed was investigated experimentally and a heat transfer model was proposed. The results indicated that the second increase of ROS was mostly affected by flame emissivity and the the relative importance of flame radiation and combustion zone radiation were compared. This explanation needs more experimental studies to support for different fuel beds. In this paper, we studied downslope fire over thermally thick fuel bed and the heat transfer process was discussed. This new study could be helpful to understand downslope fire behavior deeper.

2 Experimental Setup

A series of 15 experiments for five slopes ($-30°$, $-20°$, $-10°$ (downslope), $0°$ and $10°$ (upslope)) were conducted in an experimental platform. The details of the experimental platform and the fuel can be referred to [11]. Here, we only give the specific experimental conditions in this work. The average measured moisture of the fuel was 11.9% (Sartorius MA145). The fuel loads for the experiments in this work were 1.2 kg/m^2 (dry basis), and the depth of fuel beds was approximately 10 cm. In our previous work [11], the fuel loads were 0.4 and 0.8 kg/m^2. The fire was also initiated along the width of fuel bed simultaneously, as reported before [11]. The tests for each slope were repeated triple. The ambient air was still with the average temperature and humidity of 11 °C and 61% during the experiments. The details of experimental conditions can be found in Appendix 1.

Figure 1 presents the experimental setup with the temperature measurement locations. A total of 13 thermocouples (K-type 1 mm external diameter, 0.178 mm wire

Fig. 1 Schematic of the experimental setup. Nine thermocouples (red dots) were placed at the top surface of the fuel bed horizontally. The small subfigure presented four thermocouples inside the fuel bed vertically with the fifth horizontal thermocouple at the surface
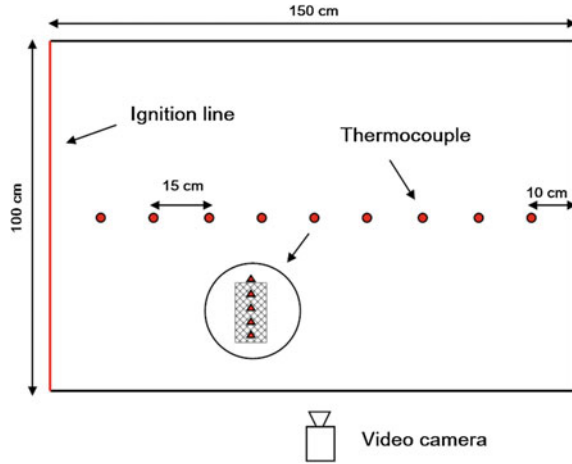
diameter) were used in the experiments, among which nine ones were placed in the central line of the fuel bed top surface with 15 cm intervals. Another four thermocouples were inserted into the fuel bed vertically with 2 cm intervals below the fifth horizontal thermocouple (see Fig. 1), and the lowest one was 2 cm above the fuel bed base. The flame front position was determined by identifying the moment when the temperature measured by the horizontal thermocouples firstly reached 300 °C [12]. The ROS was calculated from the derivative of the curve of 'flame front position versus time' [11]. The combustion interface shape was identified from the temperature data of five vertical thermocouples (four inside thermocouples and the fifth horizontal one). The thermocouple readings were recorded by a NI SCXI-1600 data logger every 1/10 s. The side view of flame was videotaped by a camera (Sony DSR-SR 300, 25 fps) fixed on the experimental bench, and the geometric scale was calibrated by a metallic grid (6 × 6-cm mesh) placed at the side of fuel bed.

3   Result and Discussion

3.1   *Flame Geometry and Emissivity*

Figure 2 shows some typical pictures during fire spread which was captured by the side-view camera. For the no-slope and downslope fires, the fire front exhibited a nearly linear shape. For the 10° upslope fire, the fire front was curved. The flame was nearly vertical for the no-slope fire and almost attached to the burned surface for the −30° slope fire. Twelve sequential side-view images were averaged to determine the flame length and flame angle for each test when fire spread across the center of the fuel bed. The definition of the flame length and flame angle can be seen in our prior work [11]. The average values of flame length and flame angle for each test are listed

Fig. 2 Flame geometry for tests with variable slope from $-30°$ to $10°$. Note that the camera was bound to the bench

in Table 1. It is found that the flame angle for each slope with fuel load of 1.2 kg/m^2 is close to the corresponding values with fuel loads of 0.4 and 0.8 kg/m^2 [11].

Flame emissivity is necessary for the calculation of the radiation heat flux during the process of wildfire spread. In the literature, various values of flame emissivity were used in different wildfire spread models. However, it is commonly recognized that flame emissivity is related to flame thickness and can be correlated by an empirical expression as Eq. (1).

$$\varepsilon_f = 1 - \exp(-K_v D) \tag{1}$$

Agueda et al. [13] measured flame emissivity of fire generated by a pine needle fuel burner, and the extinction coefficient was 0.72. This value is used in Eq. (1) in this work.

The flame thickness was calculated by using the residence time multiplies the ROS. The residence time is defined as the time interval that a fixed point of the fuel bed remains in the interior of flame front [14]. In this work, the residence time was determined by the time interval when the temperatures of the thermocouples were above 300 °C, same as that in [11]. The flame thickness and calculated flame emissivity for the slopes from $-30°$ to $10°$ are presented in Fig. 3. It is shown that both the flame thickness and flame emissivity increase with the negative slope increasing. It is also found that flame thickness (0.2–0.6 m) for 1.2 kg/m^2 fuel load in the present work is much higher than the corresponding values (0.1–0.4 m) for 0.4 and 0.8 kg/m^2 [11] for all negative slopes.

Table 1 Flame geometry parameters for different slope fires with the fuel load of 1.2 kg/m^2

Slope angle (°)	Flame length (m)	Flame angle (°)	Flame thickness (m)
−30	0.811	164	0.621
−20	0.834	155	0.377
−10	0.911	126	0.347
0	0.952	90	0.242
10	1.018	77	0.173
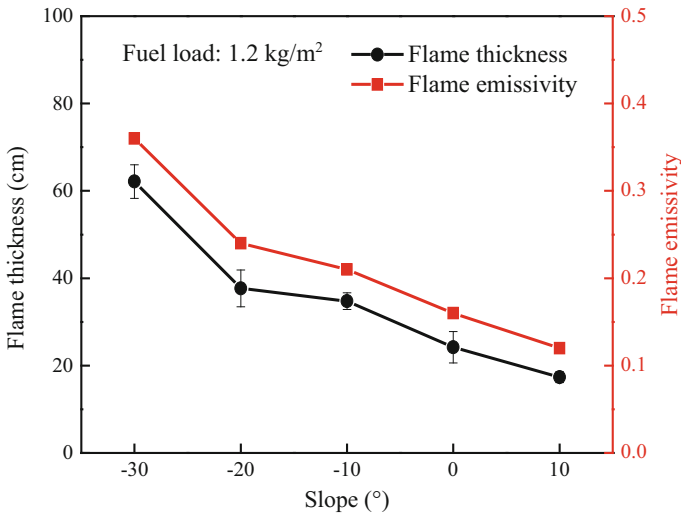
Fig. 3 Flame thickness and calculated flame emissivity for fuel load of 1.2 kg/m^2

3.2   Combustion Interface Shape

The combustion interface shape affects the radiation from the combustion zone of fuel bed. Koo et al. considered that the combustion interface was perpendicular to the fuel bed surface for all slopes [15]. Thomas assumed the combustion interface tilt angle was the same as the flame angle [16]. Dupuy thought that the combustion interface tilted forward with the tilt angle same as the slope angle [10]. However, the experimental evidence on the combustion interface shape for downslope fire spread is very rare. In our prior work [11], the combustion interfaces of fuel beds with fuel loads of 0.4 and 0.8 kg/m^2 for downslope fire were measured and we found that they were perpendicular to the thermally thin fuel bed. This observation is in accordance with the assumption of Koo et al. [15].

This work tried to measure the combustion interface shape of thermally thick fuel bed. Five vertical thermocouples with 2 cm interval were placed inside the fuel bed to reconstruct the combustion interface shape from the temperature profiles. When the fire spread across every thermocouple (please refer to Fig. 1), the time was recorded and the interval time for combustion interface reached each thermocouple was used to calculate the horizontal distance. Figure 4 shows the profile of the combustion interface shape for different slope fuel beds with fuel load of 1.2 kg/m^2. The longitudinal axis means the horizontal distance, and the vertical axis means the distance above the fuel bed base. For the comparison of combustion interface shape for the downslope fire and the upslope fire, an additional experiment for the 10° upslope fire was conducted. It is shown that the combustion interface tilts backward from the vertical direction of the fuel bed for all tests and the combustion interface angle increases with slope. This measured result is different from the previous assumptions

Fig. 4 Profiles of the combustion interface shape for different slope fuel beds with the fuel load of 1.2 kg/m^2. The error bars were obtained through triple repeated experimental runs
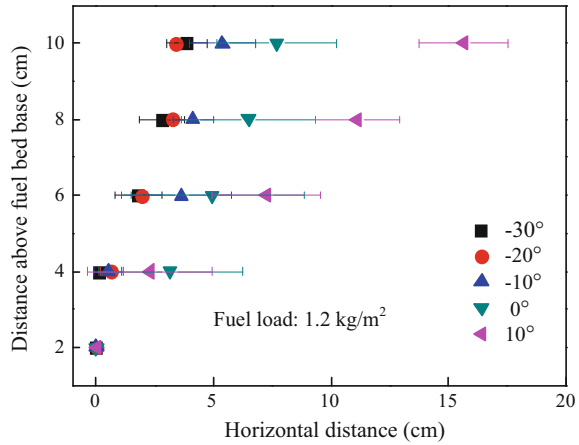
Fig. 5 Illustration of the heat exchanged for the surface fuel element
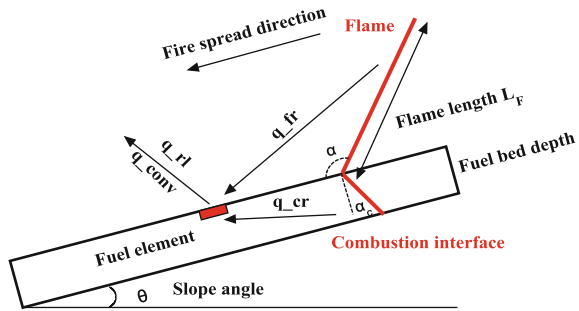
[10, 15, 16] and the observation for thermally thin fuel bed [11]. In the following theoretical calculation (please refer to Fig. 5), the combustion zone interface of fuel bed is seen as a planar surface with a tilt angle for model development and the emissivity is set to be 1 [17].

3.3 A Simplified Physical Model for Downslope Fire Over Thermally Thick Fuel Bed

Figure 5 presents the simplified model for downslope fire spread over thermally thick fuel bed. The combustion shape angle is set as the observation value. The control fuel element is located at the surface of fuel bed since there is temperature gradient inside the thermally thick fuel bed. It is noted that the combustion shape angle was zero and fuel element crossed the top surface and base of the fuel bed since the bed was thermally thin in our prior work [11]. Therefore, the calculation of the radiation from the combustion zone and the energy balance of fuel element are different.

In Fig. 5, the fuel element ahead of the fire front receives the radiation from the flame outside the fuel bed and the radiation from the combustion interface inside the fuel bed. At the same time, it loses energy through its own radiation and natural cooling. The conductive heat transfer inside the fuel bed is ignored. The flame is assumed to be a two-dimensional sheet.

The energy conservation equation for the downslope fire is expressed as Eq. (2).

$$-R\rho_f\beta\frac{\partial h_s}{\partial x} = \frac{\sigma\beta}{4}\varepsilon_f B V_f(X)T_f^4 + \frac{\sigma\beta}{4}\varepsilon_c B V_c(X)T_c^4 - \frac{\sigma\beta}{2}B(T_s^4 - T_a^4)$$
$$- \sigma\beta h(T_s - T_a) \tag{2}$$

The left term in Eq. (2) is the enthalpy change rate of the fuel element. The calculation of this term could be referring to Eq. (4) of our prior work [11] and is not presented here for simplicity. The definition of the symbols can be seen in Nomenclature.

The right first term in Eq. (2) describes the radiation from flame. In the calculation, the flame temperature was taken as the measured maximum temperatures of the flame (1103 K in this study). The view factor between the flame and the surface fuel element can be calculated by Eq. (6) in [11].

The right second term in Eq. (2) represents the combustion zone radiation. The combustion interface emissivity ε_c is set to be 1 as stated above [17]. The combustion zone temperature T_c is set to be 1100 K in this model which was used by Albini and Stocks [17]. $V_c(X)$ is the view factor between the combustion interface and the surface fuel element, which was calculated by the method of De Mestre et al. [18], as shown in Eq. (3). Note that this view factor only appears for the thermally thick fuel bed. The calculation of combustion zone radiation for the thermally thin fuel bed does not involve this view factor [15] because the geometry configuration of fuel element and combustion interface is very simple [11].

$$V_c(X) = \frac{2X\,\cos\alpha_c}{\pi}\int_{z=0}^{W/2}\int_{y=0}^{\delta} r^{-3}e^{-\sigma\beta r/4}\mathrm{d}y\mathrm{d}z$$
$$r = \sqrt{(X+y\,\tan\alpha_c)^2 + y^2 + z^2} \tag{3}$$

The right third term in Eq. (2) represents the radiation heat loss. The last term is the natural convection cooling. The convection coefficient for the natural convective cooling is a function of the Rayleigh number, which depends on parameters such as the thermal expansion coefficient, the characteristic length of the fuel element, and temperature of the fuel.

The ignition temperature of the fuel particle in this model is set to be constant (561 K). The method to calculate ROS by using this model is the same as that in our prior work [11]. Briefly speaking, the value of ROS is preset with a step-changing number and the numerical simulation runs for every preset ROS, until this condition
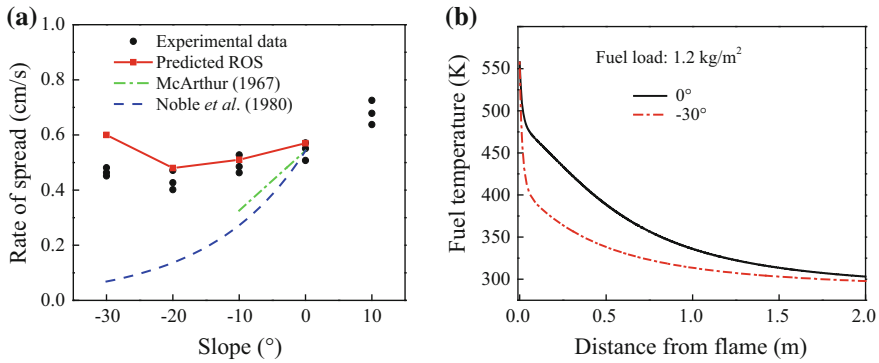
Fig. 6 **a** Experimental and predicted rates of spread for fuel beds with various slopes. **b** Calculated temperature curves of fuel element for 0° and −30° slopes

meets: The fuel element temperature reaches the ignition temperature just at the moment that the flame front arrives the fuel element.

Figure 6a compares the experimental ROS data in this work and the predicted values by the present model. The predictions by the empirical formula proposed by McArthur [19] and Noble et al. [20] are also presented. The experimental ROS for the 10° upslope fire is also measured, but the model is not suitable for prediction, because that the flame front for the 10° upslope fire becomes convex and the view factor is not suitable for the calculation by the present model. It is seen that the experimental ROS data of downslope fire are predicted well by the present model, but not well by the predictions of empirical expressions [19, 20]. Figure 6b shows the calculated temperature profiles for the 0° and −30° downslope fires. It is shown that the temperature for the no-slope fire is higher than the −30° downslope fire in a long range and the temperature rise mainly occurs in the near flame region for the −30° downslope fire. It is indicated that for the steep downslope fire, the fuel is heated very slightly when fire is away and heated intensively when fire is approaching very closely.

Figure 7 shows the predicted instantaneous heat flux contribution of each term in the right side of Eq (2). Both subfigures show that the flame radiation increases gradually when the fire approaches the fuel element, but the combustion zone radiation increases sharply in very near flame region and the value is much higher than that of flame radiation. Comparing Fig. 7a, b, it is found that for the −30° downslope fire, the combustion zone radiation is much higher, but the flame radiation is slightly lower than the corresponding values in the very near flame region for the no-slope fire. It is indicated that combustion zone radiation plays more important role in the near flame region, which should not be neglected in downslope fire models. We also integrated the instantaneous heat flux over time and obtained the total heat contribution of each term. The total flame radiation is 6.32×10^4 kJ/m^3 for the no-slope fire and 3.27×10^4 kJ/m^3 for the −30° slope fire, respectively. And the total combustion zone radiation is 2.20×10^3 kJ/m^3 for the no-slope fire and 4.34×10^3 kJ/m^3 for

(a)

(b)
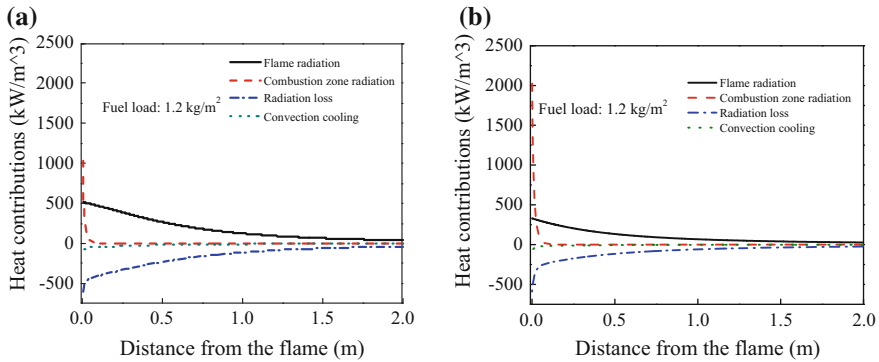
Fig. 7 Heat flux contributions for **a** no-slope fire and **b** $-30°$ downslope fire with the fuel load of 1.2 kg/m^2

the -30° slope fire, respectively. It is seen that the fuel is heated mainly by flame radiation throughout the whole process, but the combustion zone radiation plays more important role in the near flame region, which is also observed for thermally thin fuel bed in our prior work [11]. This means that the roles of flame radiation and combustion zone radiation are valid for both thermally thin and thermally thick fuel beds in downslope fire spread.

4   Conclusion

This paper presents an experimental study on downslope fire over a thermally thick pine needle fuel bed. Flame geometry parameters, such as flame length and flame angle, were investigated to understand the effect of slope on downslope fire behavior. A physical model valid for thermally thick fuel bed was developed to reveal the heat transfer mechanism of downslope fire. The major conclusions are summarized as follows.

(1) The spread rate of downslope fire over a thermally thick fuel bed decreases firstly and increases with the increasing slope. This trend is coincidence with the previous studies and that for thermally thin fuel bed.

(2) The combustion interface was constructed by five vertical thermocouples inside the fuel bed and found to tilt backward from the vertical direction of the fuel bed for all slopes, different from the assumptions in the literature and the measured results for the thermally thin fuel bed.

(3) A simplified model for downslope fire spread over the thermally thick fuel bed was proposed based on the experimental observations. The predicted ROS agrees well with the experimental values. From the heat contribution results, it is concluded that for thermally thick fuel bed, the fuel is heated mainly by flame radiation throughout the whole process but the combustion zone radiation

plays more important role in the near flame region, similar as that reported for thermally thin fuel bed in our prior work. The roles of flame radiation and combustion zone radiation are valid for both thermally thin and thermally thick fuel beds in downslope fire spread.

Appendix 1: Experimental Data Under the Fuel Load of 1.2 kg/m^2

Fuel load (kg/m^2)	Slope angle (°)	Temperature (°C)	Relative humidity (%)	Moisture (%)	ROS (cm/s)
1.2	−30	12.1	57	11.9	0.481
1.2	−30	11.9	59	10.3	0.451
1.2	−30	12.1	61	12.8	0.463
1.2	−20	11.7	66	13.8	0.402
1.2	−20	12.4	58	11.3	0.427
1.2	−20	11.2	54	11.3	0.472
1.2	−10	9.8	66	11.0	0.463
1.2	−10	10.3	62	12.9	0.528
1.2	−10	8.7	62	11.9	0.485
1.2	0	9.5	64	9.6	0.571
1.2	0	8.9	62	13.5	0.507
1.2	0	11.2	66	11.8	0.551
1.2	10	12.2	63	12.5	0.725
1.2	10	11.8	67	11.7	0.638
1.2	10	10.6	59	11.6	0.679

References

1. Butler, B., Anderson, W., & Catchpole, E. (2007). Influence of slope on fire spread rate. In *Proceedings RMRS-P-46CD*.
2. Dupuy, J. L. (1995). Slope and fuel load effects on fire behavior: laboratory experiments in pine needles fuel beds. *International Journal of Wildland Fire, 5*(3), 153.

3. Dupuy, J. L., & Maréchal, J. (2011). Slope effect on laboratory fire spread: contribution of radiation and convection to fuel bed preheating. *International Journal of Wildland Fire, 20*(2), 289.

4. Dupuy, J. L., et al. (2011). The effects of slope and fuel bed width on laboratory fire behaviour. *International Journal of Wildland Fire, 20*(2), 272.

5. Liu, N., et al. (2014). Effect of slope on spread of a linear flame front over a pine needle fuel bed: experiments and modelling. *International Journal of Wildland Fire, 23*(8), 1087.

6. Van Wagner, C. (1988). Effect of slope on fires spreading downhill. *Canadian Journal of Forest Research, 18*(6), 818.

7. Rossa, C. G., Davim, D. A., & Viegas, D. X. (2015). Behaviour of slope and wind backing fires. *International Journal of Wildland Fire, 24*(8), 1085.

8. Andrews, P. L., Bevins, C. D., Seli, R. C. (2003). *BehavePlus fire modeling system, version 2.0: User's guide*. USDA Forest Service Gen. Techn. Rep. RMRS GTR- 106WWW. Ogden.

9. Mendes-Lopes, J. M., Ventura, J. M., & Amaral, J. M. (2003). Flame characteristics, temperature–time curves, and rate of spread in fires propagating in a bed of Pinus pinaster needles. *International Journal of Wildland Fire, 12*(1), 67.

10. Dupuy, J. L. (2000). Testing two radiative physical models for fire spread through porous forest fuel beds. *Combustion Science and Technology, 155*(1), 149.

11. Yang, Z., Zhang, H., Zhang, L. et al. (2018). Experimental study on downslope fire spread over a pine needle fuel bed. *Fire Technology*. https://doi.org/10.1007/s10694-018-0740-0.

12. Xie, X., et al. (2017). Upslope fire spread over a pine needle fuel bed in a trench associated with eruptive fire. *Proceedings of the Combustion Institute, 36*(2), 3037.

13. Àgueda, A., et al. (2010). Experimental study of the emissivity of flames resulting from the combustion of forest fuels. *International Journal of Thermal Sciences, 49*(3), 543.

14. Vaz, G., André, J., Viegas, D. (1998). Predicting the residence time of the fire front of surface forest fires. In *Proceedings of III International Conference on Forest Fire Research/14th Conference on Fire and Forest Meteorology* (vol I, p 547).

15. Koo, E., et al. (2005). A simple physical model for forest fire spread rate. *Fire Safety Science, 8,* 851.

16. Thomas, P. H. (1967). Some aspects of the growth and spread of fire in the open, forestry. *An International Journal of Forest Research, 40*(2), 139.

17. Albini, F. A., & Stocks, B. J. (1986). Predicted and observed rates of spread of crown fires in immature jack pine. *Combustion Science and Technology, 48*(1–2), 65.

18. De Mestre, N., et al. (1989). Uniform propagation of a planar fire front without wind. *Combustion Science and Technology, 65*(4–6), 231.

19. McArthur, A. G. (1967). *Fire behaviour in eucalypt forests*. Canberra: Forestry and Timber Bureau.

20. Noble, I., Gill, A., & Bary, G. (1980). McArthur's fire-danger meters expressed as equations. *Australian Journal of Ecology, 5*(2), 201.

EnKF-Based Real-Time Prediction of Wildfire Propagation

Tengjiao Zhou, Jie Ji, Yong Jiang and Long Ding

Abstract Wildfires are very often difficult to prevent and represent a grave risk; real-time prediction of fire propagation has a vital significance for setting up preventive measures and formulating emergency response plans. However, due to the limitation of computer computation capability, changing of the fire environment and model errors caused by the deficiency of the existed fire simulation tool, current fire models lack the ability to provide considered the accurate prediction of wildfire propagation faster than real-time. Moreover, in the case of the hindrance of heavy smoke, the satellite-based remote sensing or unmanned aerial vehicle (UAV) is incapable of acquiring precise flame front observation data within a certain level of uncertainties. Data assimilation (DA) is extensively functioned in complex predicting problems. And the Ensemble Kalman Filter (EnKF) is one of the best ways of solving large-scale and nonlinear problems, while the computational time is comparatively less than other DA methods. In the present study, real-time prediction of wildfire propagation method is presented by connecting EnKF method and the FARSITE fire area simulator, for updating the dynamically evolving fireline position of a spreading wildfire. The results show that the wildfires forecast are improved with the proposed data-driven methodology than with the stand-alone FARSITE model and successively responsible for an adjusted prediction of the wildfire spread.

Keywords Real-time prediction · Wildfire · Fireline position · Ensemble Kalman filter · State estimation

1 Introduction

Wildfires—unintended wildland fires—may give rise to noteworthy, long-term effects to biological, community, and financial systems. The 2017 California wildfire season has scorched about 6 thousand square kilometers, according to the Department of Forestry and Fire Protection in California. In October 2017, wildfires ruined

T. Zhou · J. Ji (✉) · Y. Jiang · L. Ding
State Key Laboratory of Fire Science, University of Science and Technology of China, Hefei 230026, People's Republic of China
e-mail: jijie232@ustc.edu.cn

approximately 9 thousand structures and killed at least 40 people. It will demand from several months to years to entirely recover from the destroying wildfires that torn through Northern California. While in December 2017, wildland fires made more than 0.2 million people to evacuate and damaged over 1 thousand structures. AccuWeather calculated that the total amount of pecuniary loss of the 2017 California wildfire season may be able to fetch up to about 200 billion dollars.

Wildfire spread and growth depend on three primary physical parameters: wind, topography, and fuel characteristics. For a certain period of time, topography and fuel load at a specific location are measurable and static. Wind, however, may change at every second. And wind promotes a wildfire's progress which could activate the fire to move faster. It can make the work of fire extinguishing even more difficult correspondingly. Uncontrolled wildfires precipitously spread and rage wildland fires boosted with wind action and can devastate a massive meadow or forest land area. Wildfires can even spread to adjacent bushes, farmlands, orchards, and homes. Wildfires are especially hazardous, and therefore, it is necessary to accurate predictions of propagating wildfires and to subsequently develop cost-effective mitigation strategies.

Real-time predictions of the propagation of an ongoing wildfire have been recognized as a worthy investigation point with applied to wildland fire risk assessment [1–4]. Despite the fact that a lot of progress has been made in the last several decades both in our fundamental comprehending of wildfire dynamics and in our skill to mathematically frame and numerically model wildfire spread, the simulation of wildfires is still not an easy job for the reason that the underlying dynamics occur at multiple scales and perform complex multi-physics processes. Wildfires normally characterize a front-like geometry and can be depicted at regional scales (i.e., approximately at several kilometers) as a thin flame zone that self-propagates perpendicular to itself into unburnt plants. The wildfires dynamics behavior is governed by complex interactions between combustion, pyrolysis, flow dynamics, convection heat transfer, radiation, and atmospheric dynamics.

By the level of spatial detail, wildfire models can be categorized as research-level or operational-level models [5]. Research-level models (i.e., FIRETEC, WRFFire and WFDS) integrate developed physical modeling with modern methods of computational fluid dynamics (CFD) to truthfully illustrate the combustion-related processes that dominate the fire dynamic behavior (e.g., thermal degradation of biomass fuel, conduction of heat, buoyancy-induced flow, convection heat transfer, and radiation). Generally, research-level models have a high-computational cost. They are very slow—it is not unusual to require hours or days of supercomputer time to simulate seconds of real time, even for physically small domains.

In contrast, operational-level models (i.e., FARSITE, PROMETHEUS, FORE-FIRE and PHOENIX RapidFire) can be many orders of magnitude faster than research-level models, which can execute in real-time, or better, on affordable desktop computers. It should be noted that the operational-level models have limitations on the scope of the problems which can be modeled, the ease with which they can be modeled and the accuracy of the results. The deficiencies are as follows: without consideration of the interaction between the flame and the atmosphere; moreover,

due to the experimental calibration process, so they have a limited effective domain; furthermore, the considerable uncertainties related to lots of the input parameters to wildfire modeling; In addition, varying fire scenario environment and firefighting factors also lead to significant errors in predictions.

So as to overcome some of the above-mentioned limitations of operational-level wildfire modeling, in the present study, we consider an approach that is based on data assimilation (DA), DA is initially exploited in weather forecast applications that combine device measurements and computational models, considers of observation and model prediction errors, and by this means presents revised estimation of poorly known variables and improves forecasting capabilities. The Ensemble Kalman Filter (EnKF) is one of the best ways of solving large-scale and nonlinear problems while the computational time is comparatively less than other DA techniques. In the field of wildland fire forecasts, the idea of DA is especially appealing given the considerable uncertainties on the parameters for the operational-level model. Ensemble-based DA approach was originally developed for nonlinear dynamic and large state-space problem and has already been employed in the domain of wildfire modeling [1–4]. Using the EnKF methodology, researchers have been able to successfully and accurately predict the movement of wildfires on a 4 m by 4 m scale [6].

In the present study, a new application of ensemble-based DA to forecast wildfires of spatially varying terrain and characteristics of vegetation and temporally varying meteorological conditions is presented by connecting the FARSITE fire area simulator. The proposed method is valid by investigating a larger scale (4 km by 5 km) wildland fire propagation simulation capability that is incorporated into real-time measurements of the fireline position. The proposed method applies an EnKF technique to correct the time-evolving position of the fire perimeter used in the fire propagation simulations. The proposed methodology is presented in Sect. 2. A sensitivity study is presented and the performance of the proposed methodology on wildfire modeling is tested compared with the stand-alone FARSITE model in Sect. 3. In Sect. 4, the conclusions are presented.

2 Methodology

The real-time prediction of wildfires in this study is presented by combining observations and FARSITE operational-level fire model using EnKF. The fundamental principle and application of the FARSITE model can be found in [7, 8], instead of replicating the mathematics of these theories, this paper will have focal point study for how the methodology of EnKF is used to wildland fire prediction.

The EnKF is a Monte Carlo (MC) implementation of the iteratively updating method, EnKF, just as its name implies is ensemble-based DA method using the Kalman filter equations to balance observed and modeled data to generate an ensemble of analyses. Also, an ensemble of model states is applied to represent the error statistics of the model estimate, and the EnKF analyzes the error statistics advance
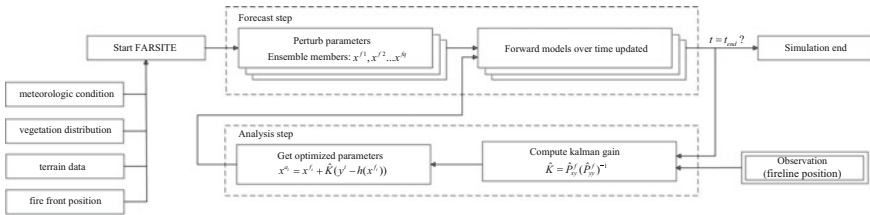
Fig. 1 Framework of real-time wildland fire prediction using EnKF

in time by ensemble integrations. The iteratively updating process is integrated with forwarding the model in time, absorbing new data from time to time.

Based on the MC method, assuming that at time k, we generate an ensemble of q primary state input parameters according to the probability density distribution of prior information. Then performing q parallel FARSITE modeling, at time $k + 1$, we can obtain q forecasted state estimates with random sample errors. Since the true state is not known, we approximate it by using the ensemble members. Thus, we take the prediction ensemble mean as the best prediction estimate of the state. To obtain the analysis estimates of the state, we need to incorporate the measurement data at time $k + 1$, since the EnKF performs an ensemble of parallel DA cycles. Based on the framework proposed in literature [9] for building fire prediction, a framework of real-time wildland fire prediction using EnKF has been proposed in the present study as shown in Fig. 1, when a wildfire is detected, the simulation model is initiated. The model starts to generate a set of ensemble members by perturbing model input parameters of Gaussian distribution. The model then advances over time within the circle of the forecast step. After a certain time interval, when the sensor observations are obtained, the model turns to the circle of the analysis step to revise model parameters by applying Kalman filter equations. And the system can keep the real-time prediction accuracy in a longer time window using the circle of the forecast step. We can start a new cycle and propagate the DA to next time step until the simulation stops. And finally, the numerical experiment is given to illustrate the feasibility of the proposed algorithm. For more details about EnKF, the readers can find it in the literature [10, 11].

3 Application of EnKF to Wildfires

The numerical experiment fire scenario location corresponds to Ouachita National Forest, the oldest National Forest in Southern USA. For illustrative purposes, the region (34°44.48 N to 34°46.59 N, 93°39.25 W to 93°42.06 W) was selected, the size of the forest land investigated approximate to 4 km × 5 km. LANDFIRE (Landscape Fire and Resource Management Planning Tools) is a shared work between the USDA Forest Service, the US Department of the Interior, and The Nature Conservancy. It provides the Landscape (LCP) File in a multi-band raster format utilized by wildfire
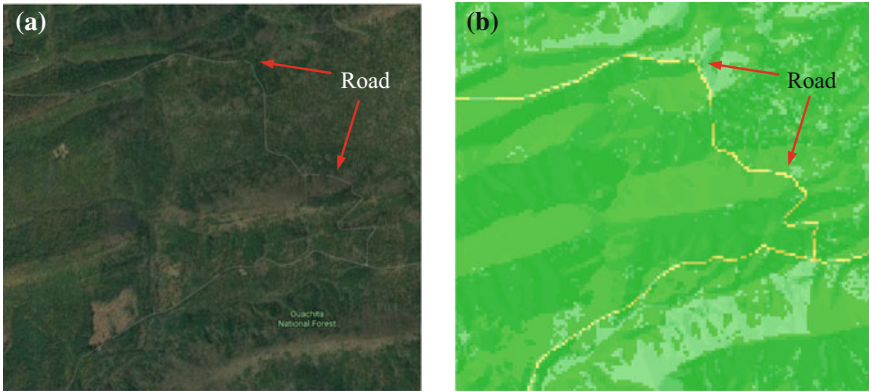
Fig. 2 Illustration of the region investigated **a** Google Map and **b** landscape

behavior and effect simulation models such as FARSITE. Five bands are concluded in a LCP file (.lcp): Fuel Model, Slope, Aspect, Elevation and Canopy Cover. We downloaded the LCP File from https://www.landfire.gov/. The area of interest on Google Map is shown in Fig. 2a and the corresponding graphical style of LCP File is presented in Fig. 2b.

3.1 Sensitivity Analysis

3.1.1 Number of Ensemble Members

The time update step accounts for the main calculation cost. As a result, the computationally time demanded for the EnKF is roughly N model simulations. As expected, both the accuracy of the EnKF and computation time increase as the number of ensemble member grows. This is the trade-off between accuracy and computational time. The number of ensemble members plays a significant role in balancing the accurateness of the EnKF and computation time. Therefore, a sensitivity analysis of a number of ensemble members is required to choose an optimal number of ensemble member.

We trace the position of an object point on a wildland fire front and conduct 50 steps of assimilation. The standard deviation (STD) of the observation data is 10 m and the STD of the forecast data is 1 m. A number of ensemble members with n = 5, 10, 20, 50 are compared, and the results are shown in Fig. 3. The longitudinal axis indicates the distance from the reference point, while the cross axis represents assimilation steps.

As shown in Fig. 3, the model states, i.e., the object point position, the difference between the model prediction and observations get smaller when the number of ensemble number N increases from 5 to 50. When N equals 5 (see Fig. 3a), the
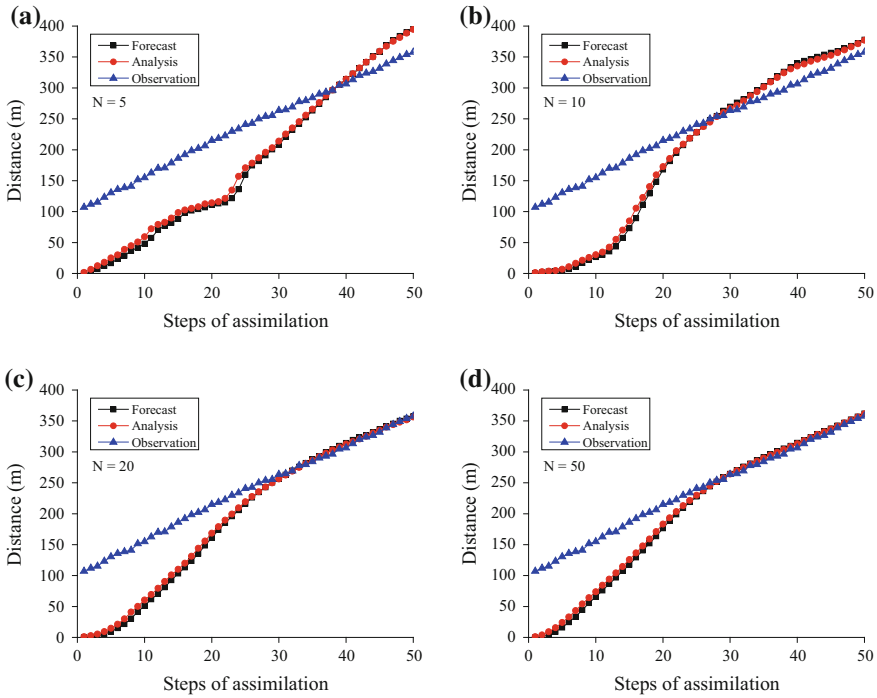
Fig. 3 Test using different number of ensemble numbers **a** $N = 5$, **b** $N = 10$, **c** $N = 20$, **d** $N = 50$

difference between the model prediction and observations is still large after 50 steps of assimilation. While it is smaller when N increases to 10. When N increased to 20, the better prediction accuracy obtained. However, as N increases from 20 to 50, the change of accuracy is not obvious, but computation time consumption increased due to most of the computation time is taken to generate ensemble members in the forecast step in each EnKF calculation circle.

Therefore, 20 ensemble members are applied in the following studies, which mean the proposed method EnKF generates 20 ensemble members following a Gaussian distribution based on MC method, in other words, 20 FARSITE simulation runs are generated by perturbing the influential parameters, i.e., fire front position.

3.1.2　Weight Assignation of Forecast and Observation

In the context of DA method, the analysis should be closer to the data we trust more, whereas suspicious data will be given little weight [12]. DA weights the forecasts and observation (measurement) data according to STD. That is, the results of DA take account uncertainties of both the modeled fire perimeter and the observed fire perimeter. Kalman gains will be larger the more precise the measurement, giving
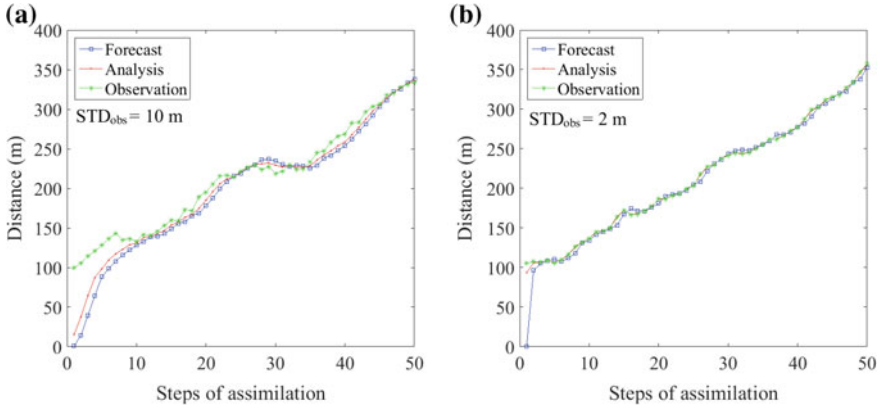
Fig. 4 Weight assignation of forecast and observation **a** forecast with less STD, **b** observation with less STD

measurement data more weight in the update, and smaller the less precise the measurement, giving measurement data less weight. Conversely, Kalman gains will be smaller if the forecast is more precise and larger otherwise. Hence if the forecast is already good, the measurement receives little weight; if it is poor, the measurement receives more weight.

We test our algorithm on the analysis of two distinct cases in the wildfire modeling through twenty steps of assimilation. The STD of forecast data is 5 m, and the STD of observation data is given as follows:

- Case 1: STD of observation data is 10 m;
- Case 2: STD of observation data is 2 m.

The results show the analysis gives more weight to data with the less STD. As shown in Fig. 4a, the DA process gives more weight to forecast which have less STD in case 1 compared to observation data, the analysis is closer to the forecast. While in case 2, the assimilation result gives less weight to forecast, and the analysis is farther to the forecast as seen in Fig. 4b.

3.2 Numerical Experiment Without EnKF

Winds are generally variable in time and large-scale space. However, FARSITE assumes wind conditions to be constant in space for a given wind stream. In other words, there are no topographic influences on wind conditions. The fire propagation model FARSITE is first used without DA.

We first use a simulation to represent the actual fire scene. And make the assumption here that temporal variability in wind speed and direction that changed every four hours. For details, see the second column of Table 1.

Table 1 Comparison of wind conditions

Time stream (h)	Actual	Free run
0	20 m/s, 70°	5 m/s, 0°
4	10 m/s, 90°	5 m/s, 0°
8	15 m/s, 180°	5 m/s, 0°
12	20 m/s, 90°	5 m/s, 0°

In the free run case, the wildfire propagation is occurring under wind conditions that are unknown. But primary flame front positions are assumed to be given. Thus, the wind speed and direction are assumed 5 m/s and 0° (wind direction is stated in degrees, clockwise from north, 0°–360°), respectively according to historical statistics. And winds are assumed to be uniform and unchanging, as can be seen from the third column of Table 1.

The fire spread position is recorded four times in an interval of four hours. The fire propagation model is then used with real wind conditions data (see Fig. 5a) and historical wind conditions data (see Fig. 5b). It is shown that although we know exactly the initial position of the fire line, the process of fire spread is obviously different in different wind fields. This means that wind exerts a significant impact on the wildland flame propagation. Theodori argued that any of the input physical parameters for wildland fire spread, the most interest and consequence are the wind variations [5]. However, the wind is changing that is inevitable and independent of man's will. Thus, the fire simulation model usually feels quite helpless in the face of these problems.

The FARSITE wildfire spread model has become one of the most extensively employed in the worldwide and is the model used by many land management agen-
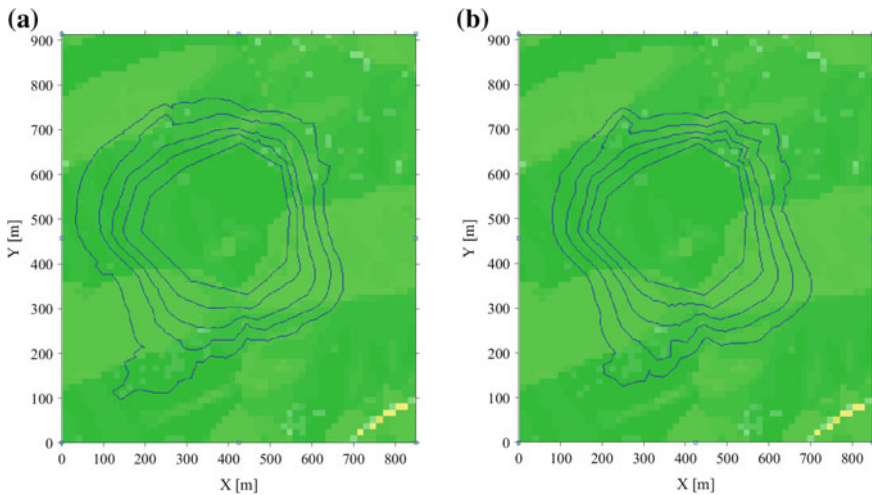
Fig. 5 Wildland fire spread modeling for **a** actual and **b** free run

cies, including the US Forest Service and other federal and state agencies. However, due largely to the result of the assumptions the model makes when creating models, the FARSITE modeling program contains several limitations:

- The wind data incorporated into the model is considered as spatially unvarying. Nevertheless, these values can vary in both direction and speed in temporal dimension. Similarly, daily precipitation values are assumed to be identical on the whole landscape [13].
- The model suggests maximum temperature and minimum humidity are synchronized. Even if it is possible to correct for most situations, it is unlikely true when it's raining [13].
- The pattern of wildfire propagation is assumed as an elliptical wave. Rothermel [14] suggests that FARSITE over forecasts the propagation of wildfire. The problem may result from inaccuracies within fuel witnesses and fuel categories.
- Fuel models are assumed homogenous and ignore potential variations, whose accuracy is extremely reliant on the correctness of the fuel maps. When fuel maps are not accurate, i.e., the landscape may change gradually due to erosion, drought, wildlife habitation; etc., or it may change very rapidly due to a fire, man-made deconstruction, or construction, there is a big error in the result. [5].
- FARSITE considers structures as "non-burnable area", which is not the case in real life [5].

It is worthwhile pointing out that the temporal and spatial distribution of wind conditions show the characteristics of periodicity and randomness. In addition, large wildfires have the ability to generate their own wind field, which further affects the dynamics of fire spread and growth. It brings great difficulties to the modeling of wildfires. To overcome the above shortcomings, the following section explains the proposed data-driven methodology how to overcome the adversity and optimize the modeling results in detail.

3.3 Numerical Experiment with EnKF

Compared to the previous section, uncertainties not only come from the unknown wind condition. In this section, we consider more realistic situation, and the initial location of the fire source is unknown. Thus, we have a rough prediction and processed by the ensemble-based method. The initial input for EnKF and measurement are illustrated in Fig. 6. The blue line is an ensemble of prediction input values. The green lines are observed values with standard deviation respond to 20 m. The initial input for free run we take the mean value of initial input for EnKF.

Measurements do not necessarily on a regular interval, and for the sake of readability, we incorporate the actual fire line position into the simulation model every four hours. Wind conditions in the third column of Table 1 are used for free run and EnKF, while wind conditions in the second column of Table 1 are used for observation run.
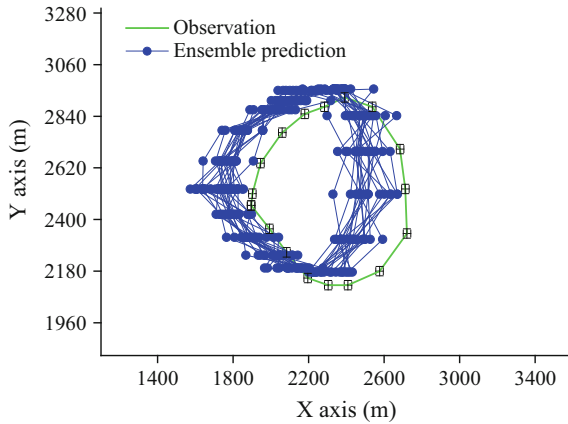
Fig. 6   Initial input of fire line position for EnKF and measurement

The result is presented and once every four hours. Figure 7 gives a comparison of different times of the wildfire front location at time $t = 4$ h and $t = 16$ h, using the FARSITE model, with EnKF technique. The data in Fig. 7 also contain uncertainty is in the form of probability distribution, and all we take are the mean value. It can be seen from Fig. 7a, this is the first time; that is, we view the output of fire spread modeling after four hours of running. There was a vast distance between the free run and observed values. But the assimilation values (analysis) are closer to the observed value. Obviously, although the initial input is an incorrect fire line position, after a step of assimilation, a great correction for the fire line position in the data-driven run.

After four steps of assimilation, as seen in Fig. 7b, the assimilation values (analysis) closer to observed values obviously. In light of this, adopting multiple steps of DA can make predicted values and observed values more closely. While can be seen from Fig. 7b, after the fourth step forecast assimilation, the assimilation values (analysis) have been very consistent with observations. The result of executing DA
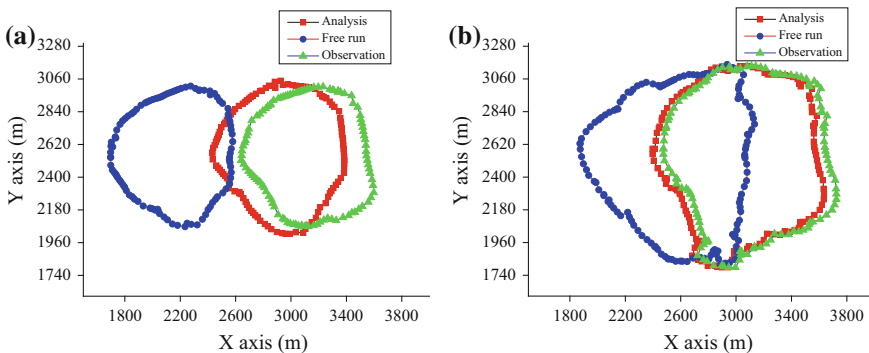
Fig. 7   Effect of assimilation of fire perimeter for time step k **a** $k = 1$, **b** $k = 4$

multiple times (four times, see Fig. 7b) is significantly improved the forecast values as that of executing them once (see Fig. 7a). If there has a big change in the field of fire (e.g. the intervention of firefighters), several more steps of DA process are needed.

4 Conclusions

This paper extends wildfire modeling and simulation to incorporate observations within error using DA methods. The data-driven methodology that uses an EnKF technique to include observation data in FARSITE. The results show that the wildfires forecast are improved with the proposed data-driven methodology than with the stand-alone FARSITE model (free run) and consequently granting an optimized prediction of wildfire spread.

Traditionally, in the context of wildfire computer simulation, we usually take the mean of the distribution of the input parameters by their prior knowledge. That is, we apply one set of input parameters to predict future model states. In this paper, the proposed method is based on a certain number of ensemble members based on MC Method. Moreover, the fire model states are revised when observations are incorporated into the model. The approach is demonstrated on a large wildfire simulation and poses comparison results for multiple step DA results. The results show that after four steps 16 h assimilation, the wildfire spread model was more consistent with that of the observation one than without revising flame front. The data-driven simulation methods can be used in real time to provide a next time step prediction of the wildfire front position. The proposed methodology of wildfire modeling demonstrates an improvement in fireline prediction as compared with the stand-alone FARSITE model.

Real-time prediction of wildfire propagation can allow firefighters to effectively and safely suppress the flames, housing developers to understand the risks of building in certain areas, and governmental agencies to timely preplan an evacuation strategy. While real-time prediction of wildfire propagation is still at an early stage of development, it is foreseen that our power to predict the evolution of wildland fires will rely on the multiple step of assimilation of measurement data into the variable environment of wildland fire modeling. The fire perimeter is focal point in the present study, and future work will extend this to other input parameters (i.e., wind conditions, moisture content, and fuel bed depth) which produce an effect on wildfire propagation.

References

1. Rochoux, M. C., Delmotte, B., Cuenot, B., Ricci, S., & Trouvé, A. (2013). Regional-scale simulations of wildland fire spread informed by real-time flame front observations. *Proceedings of the Combustion Institute, 34*, 2641.
2. Rochoux, M. C., Cuenot, B., Ricci, S., Trouvé, A., Delmotte, B., Massart, S., et al. (2013). Data assimilation applied to combustion. *Comptes Rendus Mécanique, 241*, 266.
3. Rochoux, M. C., Ricci, S., Lucor, D., Cuenot, B., Trouvé, A., & Bart, J. M. (2012). Towards predictive simulations of wildfire spread using a reduced-cost Ensemble Kalman filter based on Polynomial Chaos approximations. In *Proceedings of the Summer Program* (p. 199), Center for Turbulence Research, NASA AMES, Stanford University, USA.
4. Rochoux, M. C., Emery, C., Ricci, S., Cuenot, B., & Trouvé, A. (2014). Towards predictive simulation of wildfire spread at regional scale using ensemble-based data assimilation to correct the fire front position. *Fire Safety Science, 11*, 1443.
5. Theodori, M. F. (2016). *Data-driven wildfire propagation modeling with FARSITE-EnKF*. Master dissertation.
6. Rochoux, M. C., Ricci, S., Lucor, D., Cuenot, B., & Trouvé, A. (2014). Towards predictive data-driven simulations of wildfire spread—Part I: Reduced-cost ensemble Kalman filter based on a Polynomial Chaos Surrogate model for parameter estimation. *Natural Hazards and Earth System Sciences, 14,* 2951.
7. Finney, M. A. (1996). FARSITE-fire area simulator version 2.0. User's guide and technical documentation, Systems for Environmental Management. U. S.
8. Finney, M. A. (1998). *FARSITE: Fire area simulator-model development and evaluation*. U. S.: USDA Forest Service—Research Papers RMRS.
9. Lin, C.-C., & Wang, L. L. (2017). Real-time forecasting of building fire growth and smoke transport via ensemble kalman filter. *Fire Technology, 53*(3), 1101–1121.
10. Evensen, G. (2009). *Data assimilation: The ensemble Kalman filter*. Norway: Springer Science & Business Media.
11. Gillijns, S., Mendoza, O. B., Chandrasekar, J., De Moor, B. L. R., Bernstein, D. S., & Ridley, A. (2006). What is the ensemble Kalman filter and how well does it work? In *American Control Conference,* (pp. 4448–4453), IEEE.
12. Bouttier, F., & Courtier, P. (2002). *Data assimilation concepts and methods*. ECMWF: Meteorological training course lecture series.
13. Brakeall, J. (2013). Wildfire assessment using FARSITE fire modeling: A Case study in the Chihuahua Desert of Mexico, Florida International University Electronic Theses and Dissertations.
14. Rothermel, R. C. (1972). *A mathematical model for predicting fire spread in wildland fuels*. Report No. RP INT–115. Ogden, UT: United States Forest Service.

Fire Detection and Suppression

Experimental Studies of Roll-Paper Storage Burning Behavior with Water Application

Xiangyang Zhou, Dong Zeng and Sergey Dorofeev

Abstract Roll-paper storage is one of the most challenging hazards for fire protection. This work studies the fire behavior of hard surface roll paper with different paper basis weights (i.e., area density) and inert content. Intermediate-scale tests were conducted including both free-burn tests and water suppression tests using the water application apparatus (WAA). The measured heat release rates (HRRs) and applied water fluxes were analyzed to calculate the critical delivered flux (CDF) for the selected papers. The test results showed that roll paper with a larger area density or a higher inert content generally has a lower fire growth rate and a lower CDF. A roll paper density parameter is proposed to reflect the impact of both the paper basis weight and inert content. This parameter shows consistent correlations with fire growth and suppression and thus can be recommended as a means of roll paper classification for fire protection.

1 Introduction

Roll paper fire has been shown to a source of concern in the forest products industry, and roll paper storage has been identified as one of the most severe fire hazards [1]. Such a hazard is aggravated by material handling and economic pressures that lead to increased storage heights, ceiling heights, and ceiling clearance. In addition, roll paper characteristics such as the basis weight (mass per unit area), inert content, and roll paper storage configuration also significantly affect fire hazard levels.

Full-scale fire tests are generally used to evaluate the fire hazard and provide protection guidelines for high storage of roll paper [2, 3]. Numerical modeling is also being developed to predict the fire behavior for different roll-paper storage configurations and gain insight into the underlying physics controlling roll-paper fire suppression [4]. A key phenomenon in roll-paper burning is paper delamination [5], which differentiates roll paper from many other condensed fuels, such as wood,

X. Zhou (✉) · D. Zeng · S. Dorofeev
FM Global, Research Division, 1151 Boston-Providence Turnpike, Norwood, MA 02062, USA
e-mail: xiangyang.zhou@fmglobal.com

corrugated cardboard, or plastics. Paper delamination refers to the detachment of a paper sheet from the bulk roll. After delamination, the paper sheet behaves as a thermally thin material and can be heated up easily, resulting in a higher burning rate and increased fire spread rate.

The complex dependence of roll-paper fire hazard on different parameters makes the protection classification a challenging task. Currently, the National Fire Protection Association (NFPA) provides loss prevention guidelines for roll paper under various storage scenarios. In the NFPA 231F [3] standard for the storage of roll paper, the fire hazard of roll paper is classified mainly based on the paper basis weight, or area density, as lightweight (<50 g/m^2), medium weight (≥ 50 and ≤ 100 g/m^2), and heavyweight (>100 g/m^2). Other parameters such as the storage configuration also affect protection guidelines in NFPA231F [3].

Although the existing fire hazard classification scheme based on the paper basis weight is supported by multiple full-scale fire tests [1], an understanding of the fundamental mechanism for such behavior is still lacking. Furthermore, with the development of paper manufacturing technology, the fire hazard of new types of paper, especially heavily coated paper, suggests that the classification scheme should include the inert content in the paper coating as a parameter. Therefore, a comprehensive study is needed to examine the fire behavior of roll paper with a broad range of parameters and with emphasis on the paper basis weight and inert content.

The main objective of this study is to provide a rationale for the classification of hard surface (non-tissue) roll papers based on their fire growth and suppression behavior. Tissue papers present a class of their own due to their high water absorptivity and low bulk density. The fire behavior of tissue paper is addressed in a separate study. An additional objective of this work is to provide data and physical insights on roll paper flame spread and water suppression phenomena for the development and validation of numerical fire models [4]. These objectives are achieved by conducting carefully designed intermediate-scale experiments with a 6.3-m storage height. It is noted that this height is still relatively low when compared to actual roll paper storage where stacks can be higher than 18 m.

2   Experimental Setup

The experimental studies in the present work included five types of roll paper. The properties of these paper types are summarized in Table 1. The basis weight is defined as the mass per unit area of a single paper sheet; it is obtained from vendor specification and verified by independent measurements. The bulk density of paper rolls was calculated based on the measurements of the roll mass and nominal dimensions. The heat of combustion, elemental, and ash analyses were obtained from a commercial laboratory using ASTM standard test methods [6–8]. Based on existing fire protection standards [2, 3], the 44-g/m^2 paper would be classified as a lightweight paper, the 59- and 83-g/m^2 papers as medium-weight papers, and the remaining two papers

Table 1 Analyses of five roll paper samples

Basis weight (g/m²)	Bulk density (kg/m³)	Heat of combustion (kJ/g, dry)	Elemental analysis C–H–O (wt%, dry)	Ash analysis (wt%, dry)	Coating or filler (wt%)
44	580	15.7	45.5–6.1–44.5	3.6	5
59	660	18.3	41.7–5.3–42.4	11.1	13
83	800	14.8	39.0–5.7–47.8	8.6	20
127	690	16.6	45.1–6.2–43.7	1.4	1.4
180	800	14.5	38.8–5.5–46.8	8.5	15

as heavyweight papers. The ash content of these papers ranges from 1.4 to 11.1 wt% on a dry basis. For convenience, the papers are referred to by their basis weight.

It should be noted that the ash contents reported in Table 1 are not equivalent to the coating or filler content often reported by the paper manufacturer. The ash content is measured according to ASTM standard D3174-12 [8] in which virgin samples are dried and oxidized in a flowing air environment at a temperature of 950 °C. The yielded inorganic residue is treated as the ash content, which may contain metals and minerals in their oxidized form. On the other hand, the paper coatings or fillers are complex mixtures. The most common coating material includes ground/precipitated calcium carbonate (GCC/PCC) and clay, which contain calcium carbonate and hydrated aluminum silicate, respectively. These materials undergo different chemical reactions during pyrolysis or combustion processes; therefore, they may affect the combustion behavior of coated papers. As a result, the coatings or fillers, although non-combustible, cannot be considered as completely "inactive." In this work, the coatings or fillers that include ash are all lumped as inert content (f_{in}), which reduces the specific heat of combustion of coated papers in the analyses presented below.

All the roll-paper fire tests were carried out on 2×3, 3-tier standard arrays. Figure 1 shows elevation and plan views of the test setup of a roll-paper storage under the water application apparatus (WAA) [9]. The nominal diameter of each roll is 1.2 m and the height is 2.1 m. Each roll was not banded or wrapped by other materials. The 18 paper rolls were stacked on end in the standard array configuration [2] with a nominal 6.3-m storage height. Rolls were butted in the north–south direction and were separated by 0.15 m in the east–west direction. Two igniters were placed at the flue center against the base of the middle rolls (see plan view). Each igniter is a 7.6-cm diameter and 7.6-cm long cellucotton roll soaked with 118 ml of gasoline and wrapped in a plastic bag. A torch flame was applied to the igniter to start the fire.

The fire suppression tests were carried out under the WAA. The WAA is designed to deliver a uniform water flux on the top surface of the fuel storage using a set of pipes and nozzles located 0.2 m above the top of the rolls. The timing of the water discharge of the WAA was determined by calculating the response time of a hypothetical sprinkler located 3 m above the top surface and along the centerline of
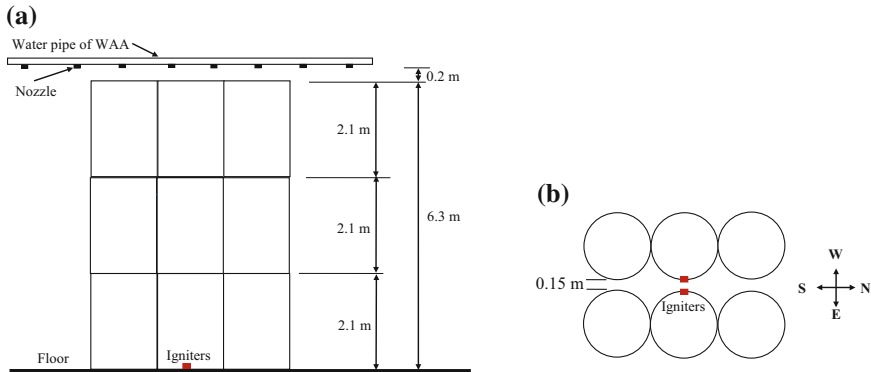
Fig. 1 Elevation view (**a**) and plan view (**b**) of a roll paper storage (2 × 3 × 3) under the WAA

the fuel array. In this work, the link temperature of the sprinkler was assumed to be 141 °C and the response time index (RTI) value was set at 276 (m s)$^{1/2}$. When the free-burn tests were conducted, the WAA was removed from the test site.

All the intermediate-scale tests were conducted under the 20-MW calorimeter in the Large Burn Laboratory (LBL) at the FM Global Research Campus. The LBL is an indoor testing facility of approximately 43-m wide (east–west direction) and 73-m long (north–south direction) and 20-m high. The 20-MW calorimeter is suspended at the center of the LBL. At its base, the 10.7 m diameter calorimeter hood is 11.3 m above the floor. An exhaust gas flow rate of 94 m^3/s was used in this work. The combustion products collected by the calorimeter are transported through a 3-m diameter duct to an instrument station where gas species concentrations, temperature, and flow rate are measured. The chemical and convective HRRs were calculated based on the measured temperature, pressure, and combustion product concentrations of the exhaust gases in the calorimeter duct using the same principle as described in [10, 11]. The chemical HRR (CHRR) was calculated in this work based on oxygen consumption calorimetry. Two video cameras were used to record the fire development from the north and east sides of the array. To improve test repeatability, the fuel and the laboratory were conditioned to control the moisture content (dry basis) of the fuel at 6 ± 2% before the test.

Five free-burn tests and fifteen with water application were conducted using the five papers listed in Table 1. Water discharge fluxes ranging from 4.1 to 24 mm/min were applied to determine the value required to control the fire. To reduce the test cost, some rolls were reused by peeling off the damaged paper sheets from the previous test and reconditioning to control the moisture content. As a result of paper reuse, the average roll diameters varied in the range from 1.2 to 1.0 m.

3 Results and Discussion

3.1 Roll Paper Free-Burn Behavior

The free-burn HRR measurements provide baseline data for characterizing fire behavior. For example, Fig. 2 shows a fire image and the HRR data of the free-burn test using 127-g/m^2 paper. The image was captured at 132 s after ignition. Figure 2a shows that the fire growth has passed the vertical and lateral fire spread stages (S2 and S3 in Fig. 2b) within the central flue and started to propagate toward the outer surfaces of the fuel array. The fire was finally extinguished by firefighters at 190 s when the calorimeter limit was reached.

Figure 2b shows that several distinct fire growth stages exist in both HRR curves. During the first stage (S1) ranging from 0 to ~50 s, a small area at the base of the paper roll is preheated by the flames from the igniter. The second stage (S2, ~50–70 s) is dominated by a drastic vertical and horizontal flame spread along the rolls of the central area around the igniters. In this stage, fire spread is supported by efficient heat transfer within the rolls in the flue. Following this stage, a plateau can be observed in the third stage (S3, ~70–100 s) for both chemical and convective HRRs, in which the fire spreads relatively slowly outwards from the flue space. The slow spread of fire is attributed to a lower radiative heat flux on the outer areas of the array compared to that present in the central area. Since the surface involved in fire continues to increase in this stage, the HRR plateau indicates that the averaged HRR per unit area is reduced, probably due to the thermal insulation effect from char buildup. After the fire spreads out of the central flue area, Fig. 2a shows that a large paper sheet is detaching from the right side of the storage. Because of the delamination of large pieces of paper and resulting in more intense burning, Fig. 2b shows that the fire growth rate quickly increases again in the fourth stage (S4, ~100–190 s). The
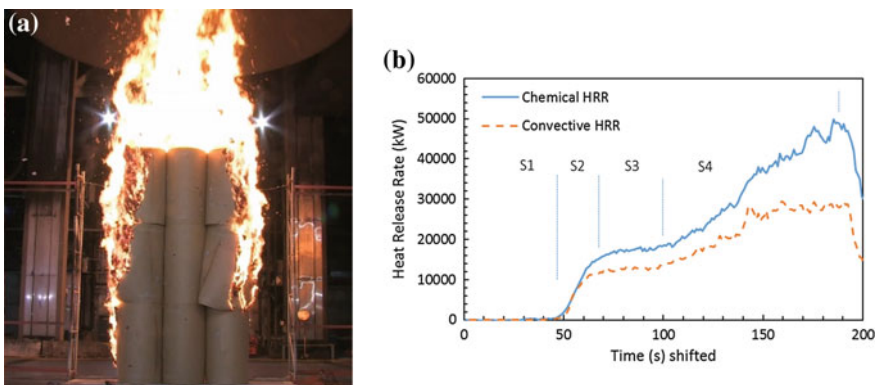
Fig. 2 **a** Fire image at 132 s after ignition and **b** chemical and convective HRRs of the free-burn test using 127-g/m^2 paper

Fig. 3 Fire growth rates of
different papers during the
vertical fire growth stage
after ignition
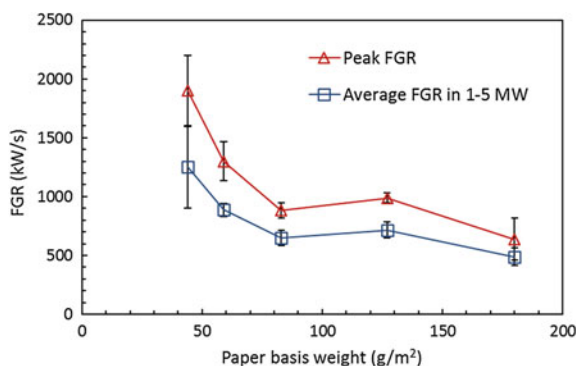
dominating fire spreading mechanism is changed from flame spreading along the
paper surface to flame "jumping" due to delamination.

The fire behavior of the other four paper types undergoes the same fire growth
stages as those shown in Fig. 2. To compare the fire behavior of different papers,
Fig. 3 plots the fire growth rates (FGRs) calculated from the CHRR data within
the period of the second stage. The free-burn tests, as well as the free-burn stage
of the WAA tests, are used to calculate the FGR. For each paper, Fig. 3 shows the
mean value of the peak FGR during the vertical fire growth stage and the average
FGR calculated for CHRRs ranging from 1 to 5 MW. The error bars of Fig. 3 show
the deviation of the FGRs between tests for the same paper. The main source of
uncertainty in this work comes from the varied roll sizes as some rolls were reused.
Although the damaged paper sheets were peeled off and the rolls reconditioned to
control the moisture content, the total burning surface area could have varied due to
the use of rolls of reduced diameter.

Figure 3 shows the same trend of $FGR_{44-} > FGR_{59-} > FGR_{127-} > FGR_{83-}$
$> FGR_{180-g/m}^{2}$ for both the peak and the average FGRs. Generally, the light paper
has the fastest fire growth, with decreasing values as the basis weight increases,
although non-monotonically. It is noted that the FGR of the 83-g/m^2 paper is lower
than that of the 127-g/m^2 paper. As listed in Table 1, the ash content of the 83-g/m^2
paper is 8.6 wt%, higher than that of 127-g/m^2 paper (1.4 wt%). Also, the filler con-
tent reported by the manufacturer of the 83-g/m^2 paper is 20–22 wt%, whereas the
127-g/m^2 paper has no filler. Notwithstanding the other differences between these
two papers, the inert content may potentially change the fire behavior between the
83- and 127-g/m^2 papers.

3.2 Water Application Tests

The differences in free-burn fire behavior of the five paper types could result in differ-
ences in the water suppression effectiveness. To quantify the suppression response,

the critical delivered flux (CDF) was proposed in [9] as the minimum water flux applied on the top of the commodity that is necessary to control the fire. Although it is nearly impossible to realize this critical condition experimentally, the CDF can be approximately determined by interpolating between two test conditions: uncontrolled and controlled fire. For the roll paper arrangement shown in Fig. 1, an uncontrolled fire is defined herein as a fire that spreads to either end of the fuel array; under this condition, adjacent rolls (if present) would be ignited, supporting further fire spread. Otherwise, the fire is deemed controlled.

A controlled fire is illustrated in Fig. 4 with a sequence of images captured at three instances during a test with rolls of 59-g/m^2 paper in standard array (2 × 3 × 3). The applied water flux was 24.4 mm/min. At $t = 42$ s after ignition, the WAA started to deliver water on the fire. Half a minute following water delivery, at $t = 72$ s, the fire size decreased. Finally, the flame was not visible and the fire was controlled, as shown at $t = 162$ s. For a similar roll paper storage scenario, but employing a lower water flux of 4.1 mm/min, Fig. 5 shows images of an uncontrolled fire. At $t =$
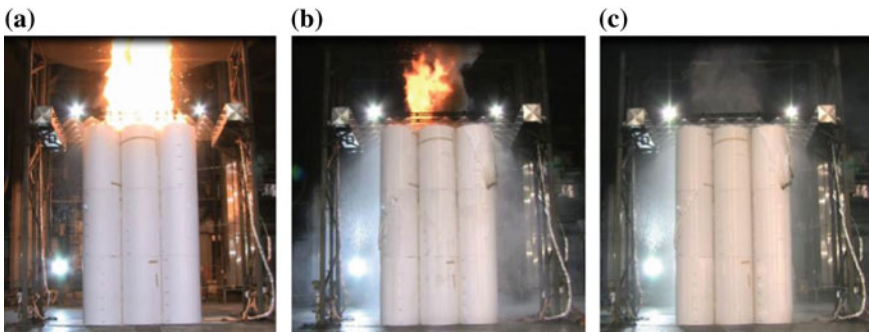
Fig. 4 A controlled fire illustrated at **a** 42 s, **b** 72 s, and **c** 162 s for the 59-g/m^2 paper at a water flux of 24.4 mm/min
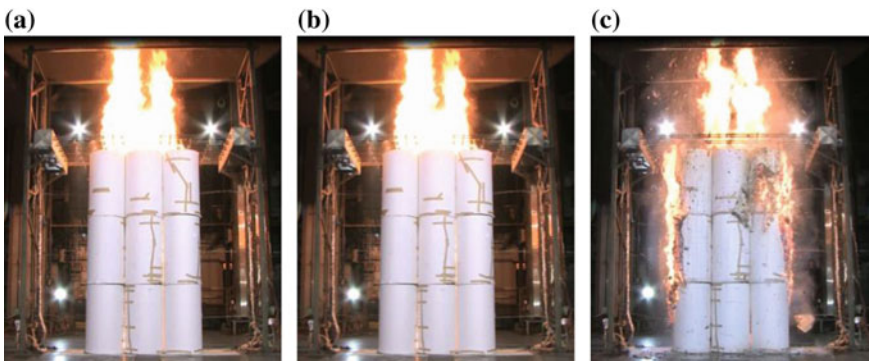
Fig. 5 An uncontrolled fire illustrated at **a** 39 s, **b** 69 s, and **c** 159 s for the 59-g/m^2 paper at a water flux of 4.1 mm/min

39 s after ignition, the WAA started to deliver water. At $t = 69$ s, the fire was still relatively strong. At $t = 159$ s, two minutes after water application, the fire spread to both longitudinal ends of the fuel array. Figure 5 also shows that large pieces of paper delaminated from the bulk rolls and continued intermittent burning outside of the rolls at 159 s. After the detachment of a surface paper sheet, the inner dry paper could be heated up easily by fire, resulting in a continued high burning rate.

The fire suppression effect of water applied on the top of the roll-paper array was quantified by measuring the CHRR. Figure 6 shows the impact of three water fluxes on the CHRR for the 59-g/m^2 paper as an example. The curves in Fig. 6 have been time-shifted to overlap their respective fire growth portions. Each curve is labeled either controlled or uncontrolled with the applied water flux. As shown in Figs. 4 and 5, the fire was controlled at a water flux of 24.2 mm/min and uncontrolled at 4.1 mm/min. After the initial decrease of CHRR with water deliver as shown in Fig. 6, the fire size at 4.1 mm/min increased again, whereas the fire size at 24.4 mm/min continued to decrease. Only the fire at 8.2 mm/min reached a quasi-steady state in the period from 160 to 340 s. This fire is still defined as uncontrolled because the fire reached the ends of the fuel array. The quasi-steady state of CHRR indicates that the fire at 8.2 mm/min was approaching a critical condition, under which the fire would have been controlled if more water had been delivered.

The CDF calculation was interpolated, to first-order approximation, from an uncontrolled fire and a controlled fire using integrated heat release in a period after the beginning of water delivery as:

$$\dot{m}''_{CDF} = \dot{m}''_u - \left(\dot{m}''_u - \dot{m}''_c\right)\frac{\Delta Q_u - \Delta Q_{CDF}}{\Delta Q_u - \Delta Q_c}, \tag{1}$$

where the CDF or the critical water flux $\dot{m}''_{CDF}$ corresponds to the integrated normalized heat release ΔQ_{CDF}. In the CDF calculation, the CHRR data shown in Fig. 6
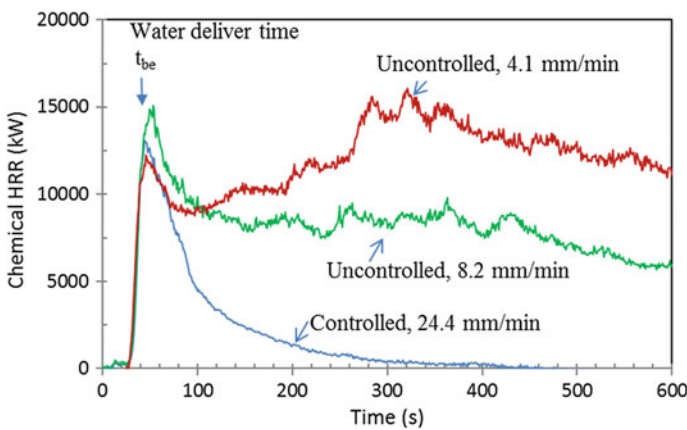
Fig. 6 Chemical HRRs measured for the 59-g/m^2 paper at three water fluxes

are all normalized as $\eta = \dot{q}/\dot{q}_{be}$, where $\dot{q}_{be}$ is the CHRR at the beginning (t_{be}) of extinguishment and the corresponding normalized value is $\eta_{be} = 1$. The normalized heat release ΔQ_u is obtained from the integration of η_u for the uncontrolled fire in the suppression period Δt at a water flux $\dot{m}_u''$, and ΔQ_c is similarly calculated for the controlled fire at a water flux $\dot{m}_c''$. The time t_{be} is determined by the hypothetical sprinkler activation condition discussed early, while the period Δt can be determined as a time interval sufficiently long to differentiate the two fire conditions. Although the integration calculation is affected by the selection of Δt due to the relative change between ΔQ_u and ΔQ_c, further examination of the test data shows that the sensitivity of CDF values to the Δt selection is relatively small if the selected suppression time Δt is sufficiently long.

Based on the results obtained for the 15 WAA tests, the critical heat release condition was selected to correspond to $\Delta Q_{CDF} = 0.5$, which is half of the normalized heat release that would be calculated if the normalized CHRR remained constant and equal to η_{be}. Because of the limited fuel array size (3 rolls in N–S direction, Fig. 1), the critical value of $\Delta Q_{CDF} = 0.5$ is lower than that (=1) used previously [9] and should only be used to separate the controlled from the uncontrolled fires in the current set of 15 WAA tests. For the 59-g/m^2 paper test shown in Fig. 7, the uncontrolled fire yields $\Delta Q_u = 0.637$ at $\dot{m}_u'' = 8.2$ mm/min whereas the controlled fire yields $\Delta Q_c = 0.135$ at $\dot{m}_c'' = 24.4$ mm/min for $\Delta t = 500$ s. Using Eq. (1) and $\Delta Q_{CDF} = 0.5$, the CDF is calculated to be $\dot{m}_{CDF}'' = 12.6$ mm/min.

For the five papers stored in the same standard array and storage height, Fig. 7 shows a plot of the CDF values versus the paper basis weight. The maximum CDF is 15.9 ± 1.6 mm/min for the 44-g/m^2 paper and the minimum CDF is 8.1 ± 0.4 mm/min for the 180-g/m^2 paper. The other three papers have a CDF of 12.6 ± 1.6 mm/min for the 59-g/m^2 paper, 10.6 ± 0.4 mm/min for the 83-g/m^2 paper, and 11.8 ± 0.4 mm/min for the 127-g/m^2 paper. The uncertainty on the CDF calculation includes the effects of the integration time and the selected ΔQ_{CDF} value. The effect of the integration
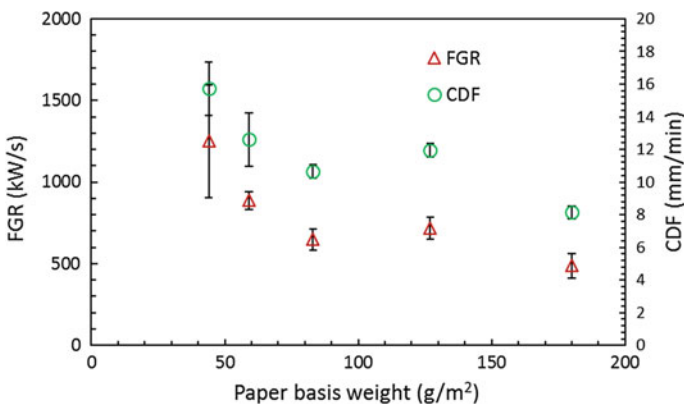
Fig. 7 Dependence of FGR and CDF on paper basis weight
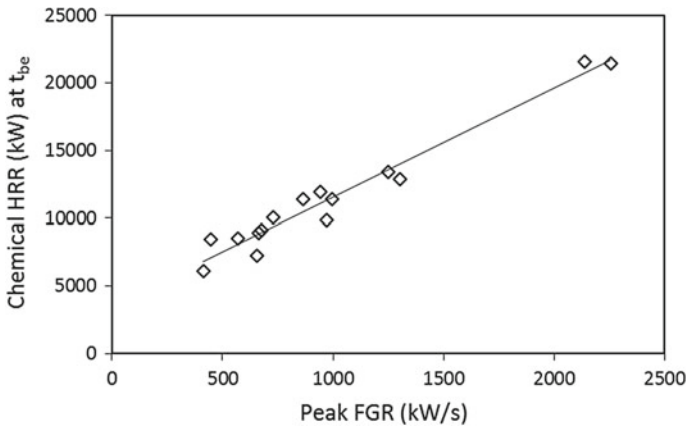
Fig. 8 Scatter plot of peak FGR and $\dot{q}_{be}$ of chemical HRR at the water delivery time t_{be}

time on the uncertainty is relatively small (less than ~3%); however, the selection of the ΔQ_{CDF} and the interpolation method is more sensitive (~10%).

Figure 7 also shows the average FGR data calculated for CHRR 1–5 MW. The general trends of FGR and CDF with increasing paper basis weight are similar. It is reasonable to assume that a roll-paper fire with a higher growth rate in the free-burn stage needs more water to be suppressed.

Figure 7 shows that both FGR and CDF of the 83-g/m^2 paper are lower than those of the 127-g/m^2 paper. As discussed in the free-burn test section, the importance of inert content is also supported by the difference in suppression behavior (CDF) between the 83- and 127-g/m^2 papers.

The observed consistency between FGR and CDF data is fundamentally based on the relationship between FGR and $\dot{q}_{be}$ for all the standard array tests, as shown in Fig. 8. Furthermore, considering that all five types of paper have hard surfaces, high bulk densities, and low water absorption rates, such a consistency is expected. Therefore, these observations indicate that a potential classification scheme for roll paper can be developed in relation to both the fire hazard (burning rate) and the suppression effectiveness (CDF).

3.3 Roll-Paper Fire Hazard Classification

The above discussion shows that roll paper fire hazard can be classified based on both FGR and CDF data. To provide a foundation for the description of the effects of the paperweight and inert content on the paper fire hazard, the following analysis considers an energy balance during roll paper fire growth. The CHRR of roll-paper fire can be expressed as:

$$\dot{Q} = \dot{m}''_{sc} \Delta H_{cc} A \tag{2}$$

where $\dot{m}''_{sc}$ (g/m^{2}s) is specific mass loss rate of cellulose, ΔH_{cc} (kJ/g) is the heat of combustion of cellulose, and A (m^2) is the surface area involved in fire. The specific mass loss rate can be defined as:

$$\frac{\dot{m}''_{sc}}{1 - f_{in}} = \frac{\dot{q}''}{C_p \Delta T}, \tag{3}$$

where $\dot{q}''$ (kW/m^2) is the characteristic heat flux applied on the paper surface and f_{in} is the mass fraction of inert content on a dry basis. The effective heat of gasification is given by the denominator of the right-hand side of Eq. (3), where ΔT (K) is the temperature difference between the pyrolysis temperature and ambient temperature, which is nearly constant for different papers (all are cellulosic materials) and C_p (kJ/kg/K) is the specific heat of paper, which can be considered constant for different papers. Substituting Eq. (3) into Eq. (2), one obtains:

$$\frac{\dot{Q}}{(1 - f_{in})} = \frac{\dot{q}''}{C_p \Delta T} \Delta H_{cc} A. \tag{4}$$

The characteristic heat flux is determined by flue space and radiant fraction considerations and can be approximated to be the same for the papers tested in the same array configuration. Therefore, the term $\left(\dot{q}''/C_p \Delta T\right) \Delta H_{cc}$ is constant, and Eq. (4) can be differentiated with respect to time to yield:

$$\frac{dA}{dt} = \frac{\text{FGR}}{(1 - f_{in})c}, \tag{5}$$

where c represents the term $\left(\dot{q}''/C_p \Delta T\right) \Delta H_{cc}$ with unit of (kW/m^2). Physically, the left-hand side of Eq. (5) represents the growth rate of the burning area with units of (m^2/s). The average FGR (kW/s) values shown in Fig. 7 were used in Eq. (5) to obtain nominal burning area rates for each paper using a c value of unity. These values, in turn, were correlated with paper basis weight as shown in Fig. 9a. The following power correlation provides an R-square value of 0.95 as:

$$\frac{dA}{dt} = a_0 \rho_A^{-0.5}, \tag{6}$$

where a_0 (=7600, g$^{0.5}$m/s) is a fitting coefficient. Substituting Eq. (6) into Eq. (5) yields:

$$\text{FGR} = a_0 c \frac{1 - f_{in}}{\rho_A^{0.5}}, \tag{7}$$
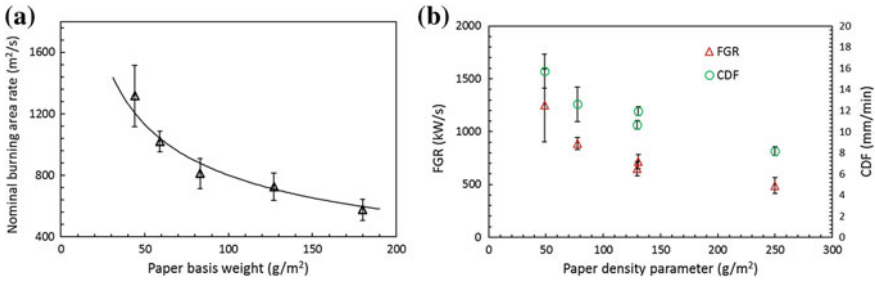
Fig. 9 **a** Growth rate of burning area with paper basis weight (ρ_A) and **b** dependence of FGR and CDF on paper density parameter (ρ_{AI})

Based on Eq. (7), a roll paper density parameter (ρ_{AI}) is proposed, which is proportional to the square of FGR:

$$\rho_{AI} = \frac{\rho_A}{(1 - f_{in})^2},$$ (8)

where f_{in} is the mass fraction of inert content specified by the paper manufacturer.

Using the ρ_{AI} defined above, the 83- and 127-g/m² papers have the same value of $\rho_{AI} = 130$ g/m². Figure 9b shows the dependence of the CDF and FGR on the ρ_{AI} values for five papers. Compared to the data shown in Fig. 7, the parameter ρ_{AI} considers both the paper basis weight and the inert content and appears to better correlate with the intermediate-scale data including both the FGR and CDF.

4 Summary and Conclusions

To evaluate the roll paper classification for sprinkler protection, and assist the development of numerical models for roll paper storage, intermediate-scale free-burn and water suppression tests were conducted under the 20-MW calorimeter and the water application apparatus (WAA). Representative hard surface paper types were included to reflect different area densities and varied inert content. The measured HRRs and applied water fluxes were used to calculate the CDFs for selected papers.

The test results show that the fire growth rates (FGR) and CDF values exhibit similar trends with paper types and confirm that both the paper density and the inert content affect the fire hazard and suppression behavior of roll paper. This allowed for considering a paper classification approach that addresses both fire hazard and suppression performance. A roll paper density parameter, which accounts for both area density and inert content, has been found to correlate well with both FGRs and CDFs. This parameter is therefore recommended for classifying the roll papers fire hazard.

References

1. Xin, Y., & Troup, J. M. A. (2007). *Proceedings of the 5th International Seminar on Fire and Explosion Hazards* (pp. 532–540), Edinburgh.
2. FM Global Data Sheets 8-21. (2014). FM Global property loss prevention data sheets—Roll paper storage.
3. NFPA 231F. (1996). *Standard for the storage of roll paper*.
4. Ren, N., Zeng, D., Meredith, K., Chaos, M., & Wang, Y. (2015). CFD modeling of fire growth between vertical paper rolls. In *9th U. S. National Combustion Meeting*, May 17–20, Cincinnati, Ohio.
5. Zeng, D., Chaos, M., Wang, Y., & Dorofeev, S. B. (2015). *Proceedings of the 14th International Conference on Fire and Materials* (pp. 285–299), San Francisco.
6. ASTM D5865-11a. (2011). *Standard test method for gross calorific value of coal and coke*. West Conshohocken, PA: ASTM International.
7. ASTM D5291-01. (2001). *Standard test methods for instrumental determination of carbon, hydrogen, and nitrogen in petroleum products and lubricants*. West Conshohocken, PA: ASTM International.
8. ASTM D3174-12. (2007). *Standard test method for ash in the analysis sample of coal and coke from coal*. West Conshohocken, PA: ASTM International.
9. Xin, Y., & Tamanini, F. (2008). *Fire Safety Science—Proceedings of the Ninth International Symposium, International Association for Fire Safety Science* (pp. 527–538).
10. ASTM E 2058. (2009). *Standard test methods for measurement of synthetic polymer material flammability using a fire propagation apparatus (FPA)*. West Conshohocken, PA: ASTM.
11. ISO 12136. (2011). *Reaction to fire tests—Measurement of material properties using a fire propagation apparatus*. Geneva, Switzerland: International Organization for Standardization.

A Study on Actual Delivered Density of Water Application Under the Effects of Fire Sources

Chia-Hsin Chen, Masaki Noaki, Yoshifumi Ohmiya, Yuya Miyazawa, Kei Aoki, Kouki Yuki and Tetsuhito Akieda

Abstract Water application has been used widely and considered as one of the most reliable fire extinguisher systems. Although Actual Delivered Density (ADD) is a vital property to evaluate its performance that fire can be suppressed when the value of ADD is higher than that of Required Delivered Density (RDD). It is still unclear how to accurately estimate the amount of water penetrated through flames, which is essential to calculate ADD. The purpose of this study is to assess the influential factors of ADD and to establish proper evaluation criteria of water application. To this end, a series of experiments were conducted to measure the effects of a fire source on the amount of spraying water delivered by water application. The variable parameters include the type of head, the height between head and fire source (later, spraying height), the dimensions of the fire source, and the heat release rate. The experimental results show that the spraying height and the nozzle characteristics can dramatically influence the water penetration ratio. Furthermore, when JJXP060 was within 0.5 m spraying height, the ADDs were significantly affected by the scale of the fire source. Large-scale fire source scenarios were also simulated using Fire Dynamics Simulator (FDS). It shows that the ratio of the ADD with a fire source to the ADD without a fire source, directly below a nozzle at 3 m height, is within 10%, and its value does not decrease as the scale of fire increases. Lastly, a simple predictive model was calibrated experimentally, which can serve as a tool to estimate the amount of water penetrated through flames.

C.-H. Chen (✉) · T. Akieda
Graduate School of Global Fire Science and Technology, Tokyo University of Science, Shinjuku-Ku, Tokyo 162-8601, Japan
e-mail: carriemialy@gmail.com

M. Noaki
Department of Fire Engineering, Building Research Institute, Tsukuba City, Ibaraki Prefecture 305-0802, Japan

Y. Ohmiya
Department of Architecture and Building Engineering, Faculty of Science and Technology, Tokyo University of Science, Noda City Chiba Prefecture, 278-8510, Japan

Y. Miyazawa · K. Aoki · K. Yuki
Department of Architecture, Tokyo University of Science, Noda City Chiba Prefecture, 278-8510, Japan

Nomenclature

D^* Dimensionless of heat release rate $(-)$
Q Heat release rate (kW)
ρ_∞ Air density (kg/m^3)
C_p Specific heat capacity of air (kJ/kg K)
T_∞ Ambient temperature (K)
g Gravitation (9.8 g/m^2)
δx The nominal size of a mesh cell (m)
β Water penetration ratio $(-)$
A Spraying angle (°)
F Water flow rate (kg/s)
W Diameter of water particle (mm)
H Spraying height (m)
Qr Heat release rate (MW)

1 Introduce

Water application is a common extinguishment method. With an automatic system, water can flow through pipes and then convert into water droplets spraying from the head to extinguish burning. Because water droplets can reduce burning rates, decrease radiation heats, it has been considered as one of the most reliable fire extinguisher systems and widely adopted around the world for more than one hundred years. Currently, the minimal sprinkling radius, spraying height, and flow rate of water application are regulated in the present Japanese laws. However, these criteria may not truly reflect the effectiveness of water application. In practice, not all water droplets are useful for extinguishing burning; some of them may be blown away by thermal buoyancy. To advance future water application systems, an approach to evaluate the exact Actual Delivered Density (ADD) is important.

ADD is an essential factor to characterize the effectiveness of fire extinguishment. The concept of ADD was first introduced by Yao [12] as the density of the water that penetrates through fire plumes and arrives on the top of a burning array. Chan et al. [3] identified several influential factors of ADD, including plume characteristics, heat release rate, ignition location, ceiling clearance, water discharge rate, spray pattern, and drop size distribution. It is widely believed that fire can be suppressed or even put off when the value of ADD is higher than that of Required Delivered Density (RDD) (shown in Fig. 1). Such effect can be summarized into a dimensionless factor, water

Fig. 1 Conceptual diagram
of ADD and RDD
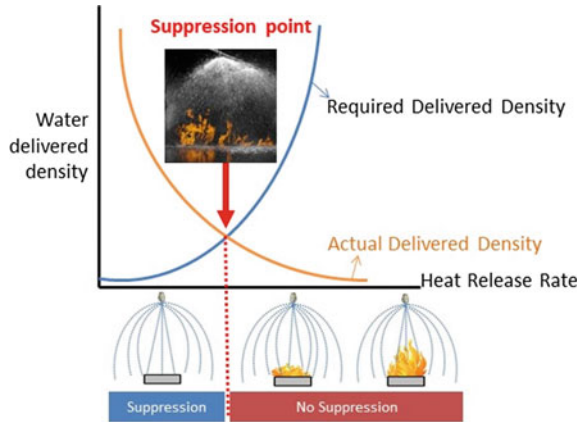
penetration ratio (WPR), which is defined as the ratio of the ADD with a fire source
to the ADD without a fire source [3]. Recently, Noaki et al. [8] provided an in-depth
analysis of the equation of water penetration of Chan et al. [3], showing a relationship
between WPR and the exponents of the influenced parameters. Shimizu et al. [11]
further confirmed the relationship with experiments and found that increasing the
heat release rate and sprinkling height of water application can decrease WPR.

While WPR is essential to predict the performance of water application, little is
known about its influential factors. Asami [1, 2] conducted a series of experiments
to measure WPRs for propane gas flame and confirmed that the small water particles
may be blown away by flame plume and be hard to extinguish the flame. He also
found out some influential parameters such as Sauter mean diameter (SMD), droplet
velocity, distribution of particle, and spraying density. Heskestad [5] identified two
different regimes of water particles. In the gravitational regime, droplets can enter
and penetrate the fire flame if the force of gravity is greater than the drag force created
by the flame buoyancy, whereas in the momentum regime, the penetration of water
particles is determined mainly by water density and pressure.

Since an accurate ADD from a head to a fire source is not available, the objective
of this study is to assess the influential factors and to establish the evaluation method.
We conducted a series of experiments with nozzles and then simulated with large-
scale fire source scenarios in FDS. In addition, we used these data to calibrate a
predictive model for fast safety evaluation.

2 Experiments

2.1 Experimental Equipment

All the experiments were conducted in the Fire Research and Test Laboratory at Noda Campus of Tokyo University of Science. Four kinds of full cone spray nozzles made by Ikeuchi Corporation were used. Nozzle is a type of spraying head, which is similar to a sprinkler. Because of the smaller flow rate of nozzles, we built the spraying system, which used tap water as the water source and connected water pipes to a pump to supply the nozzle. The pump was made by Terada Pump Corporation (model number CMP1-50.2F). The caliber was 25 mm; the supplying pressure was 0.135 MPa. The nozzle characteristics are shown in Table 1.

In each experiment, a single nozzle was set in the center, positioned vertically 0.5 m to 1.5 m above the upper edge of the fire source pan in which heptane and water were poured. Others pans (316 mm × 316 mm × 150 mm) were arranged in L-shape to collect and trace the distribution of dropping water particles (shown in Fig. 2a, b). The calorimetry hood which set above this equipment was used to collect the smoke and gas to analyze the heat release rate. In addition, three thermocouples

Table 1 Characteristics of nozzles

Product Model	Sauter mean diameter (μm)	Spraying angle (°)	Flow rate (L/min)	Initial velocity (m/s)	
				Under 0.1 MPa	Under 0.2 MPa
JJXP010	290	55	0.81	11.3	15.5
JJXP060	520	75	4.57	8.8	12.1
JJXP10	560	80	7.6	10.7	14.7
BBXP060	430	120	4.55	10.6	14.6
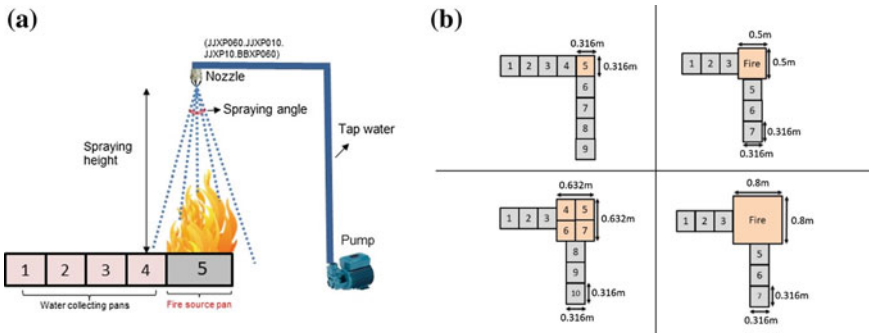
Fig. 2 **a** Elevation of experimental equipment and **b** the arrangement of fire source pan and water collecting pans

were set under the fire source pan, at the medial side of fire pan, and near the nozzle to record the mutative temperatures.

2.2 Heat Source

The fire source pans are square which with different width diameters (0.316, 0.5, 0.632, and 0.8 m) to simulate various heat release rates. A fixed amount of *n*-heptane and water were poured into the central pan which directly below the spraying nozzle as the heat source. The amount of fuel was decided so that the fire load density of *n*-heptane was around 400 MJ/m^2 which is the one of residential. The capacity of *n*-heptane was estimated by platform balance, as the density of *n*-heptane is 0.684 kg/l. Water was added to provide a situation in which *n*-heptane could burn continuously under steady combustion.

These blank experiments were used to confirm the ratio of evaporated water under these four types of fire sources without sprinkling and to measure its actual HRR during burning. The process of blank experiments was to pour the fixed quantity of heptane and water into the fire source pan and ignite it. After fire extinguished, we measured the left water and calculated the evaporated density from the flame. According to Table 2, we found that the density of evaporation was less than 2.37 g/m^2/s, which means that the influence of evaporation is much less than the ADD with water spraying (shown in session 2). To preclude the influence of evaporation and to improve the accuracy of WPR estimation, the following experimental results will consider the amount of evaporated water when calculating ADD.

The reasons for adopting *n*-heptane as the heat source are the following. First, *n*-heptane is not miscible with water, and therefore, the layer of fuel can be separated from water. Second, because its density is smaller than that of water, the fuel layer could be kept on the top of the pan to evaporate and burned completely. Third, its boiling point is lower than that of water, so *n*-heptane can be vaporized faster than water and evaporated comprehensively. As a result, *n*-heptane could provide a constant heat source in the series of experiments. Figure 3 shows that spraying water did not affect the burning behavior of *n*-heptane and the patterns of releasing heat release rate were quite similar. In the stage of fully developed, HRRs were decreased slightly with spraying water. Also, the total heat release rates during the burning with and without spraying were not changed significantly which means that *n*-heptane can be thought of as a stable and suitable fuel in our study.

2.3 Experimental Process

In this study, we considered four variable parameters: the nozzle type, the spraying height, the size of the fire source pan, and the heat release rate (shown in Table 3). The process of experiments was shown in the following. Firstly, the weight of the

Table 2 Result of blank experiments

Width of pan (m)	Average HRR from experiments (kW)	Burning duration (s)	Net water weight before burning (g)	Net water weight after burning (g)	Reducing amount (g)	HRR/Area (kW/m^2)	Evaporated density (g/m^2/s)
0.316	72.4	466	1300	1270	30	725.04	0.65
0.5	217.1	344	3300	3210	90	868.4	1.05
0.632	381.93	315	4000	3845	155	956.2	1.23
0.8	695.6	221	12,600	12,245	335	1086.875	2.37

Fig. 3 Patterns of heat release rate with varied spraying heights under 0.5*0.5 m² fire source
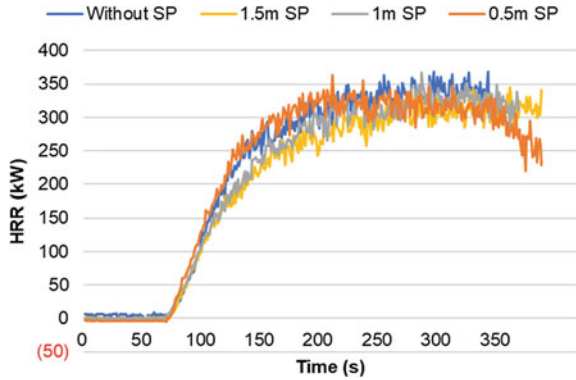
Table 3 Conditions of experiments

No.	Product model	Amount of n-heptane (L)	Assumed total heat release (MJ)	Spraying height (m)	Width of fire source (m)
1	JJXP060	1.3	40	1.5	0.316
2	JJXP060	1.3	40	1.0	0.316
3	JJXP060	1.3	40	0.5	0.316
4	BBXP060	1.3	40	1.5	0.316
5	BBXP060	1.3	40	1.0	0.316
6	JJXP010	1.3	40	1.5	0.316
7	JJXP010	1.3	40	1.0	0.316
8	JJXP10	1.3	40	1.5	0.316
9	JJXP10	1.3	40	1.0	0.316
10	JJXP060	3.3	100	0.5	0.5
11	JJXP060	3.3	100	1.0	0.5
12	JJXP060	3.3	100	1.5	0.5
13	JJXP060	5.2	160	0.5	0.632
14	JJXP060	5.2	160	1.0	0.632
15	JJXP060	5.2	160	1.5	0.632
16	JJXP060	8.4	256	0.5	0.8
17	JJXP060	8.4	256	1.0	0.8
18	JJXP060	8.4	256	1.5	0.8

spraying water delivered into the central pan without a fire source in 180 s was measured. Then, the specific amount of heptane and water was poured into the fire source pan. As the heptane was ignited by fire flames, the nozzle would start to spray water. The end of burning duration was marked when the nozzle stopped sprinkling. In these experiments, we recorded the burning duration, the heat release rate, and the weight of water left in the pans to calculate their ADDs ($g/m^2/s$). Each condition was conducted twice; a total of 36 trials were recorded.

2.4 Experimental Results

The results are presented in Fig. 4. As shown in Fig. 4a, there is a tendency that, under the same scale of the fire source, the water penetration ratio becomes lower as the vertical distance from fire source to the nozzle increases. It is also clear from Fig. 4b that the ADD decreases slightly as width of pan increases. Furthermore, when JJXP060 was within 0.5 m above the pan, the Actual Delivered Densities were significantly higher than the other heights. As the spraying angle of JJXP060 was about 75° and the spraying height was at 0.5 m, the diameter of sprinkling zone will be about 0.768 m. This sprinkling zone can cover with 0.316, 0.5, and 0.632 width meters pans and collect most of the sprinkling water, so their Actual Delivered Densities were higher than 0.8 width meters pan.

The results of this finding show that the height can dramatically influence water penetration ratio corresponding to nozzle type. However, at 1.0 and 1.5 m height, water penetration ratios only weakly depend on the higher heat release rate.
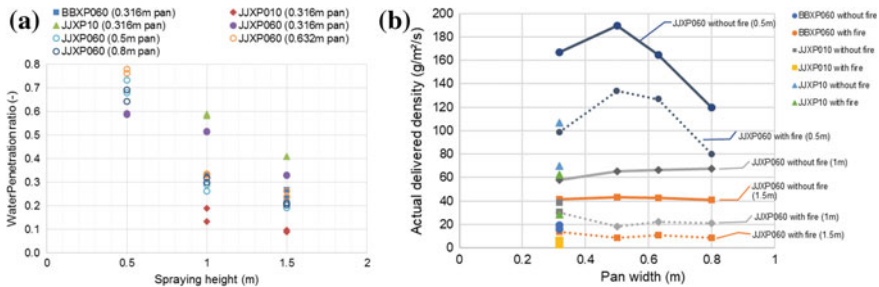
Fig. 4 **a** Relationship between spraying height and water penetration ratio and **b** the relationship between heat release rate and Actual Delivered Density of JJXP060

3 Simulations Using FDS

3.1 Introduction to FDS

Fire Dynamics Simulator (FDS) is a software of computational fluid dynamics (CFD) models of fire-driven fluid flows developed by the National Institute of Standards and Technology (NIST) of the US Department of Commerce. It is commonly used to solve practical fire problems such as fire protection engineering and fire performance design in many countries. The latest version 6.6.0 was released on November 1, 2017.

FDS can reproduce most fire scenes and set the types of observation according to user preferences. Free from costs and restrictions due to conducting real experiments in laboratories, we can study a variety of factors and analyze the trend of the results. Furthermore, FDS can output a file to provide a three-dimensions imaging to certify the spraying distribution. Therefore, we can more clearly observe the phenomena of the flame plume and the pattern of water droplets.

3.2 Mesh Sensitivity Study

One critical factor in using FDS is the mesh setup. Typically, a computational domain must be meshed into multiple cells and each cell is assigned with its own process. According to *Fire Dynamics Simulator User's Guide* [6], a measure of how the flow field is resolved smoothly is given by the non-dimensional expression $D*/\delta x$, where

$$D^* = \left(\frac{\dot{Q}}{\rho_\infty C_p \, T_\infty \, \sqrt{g}} \right)^{2/5} \tag{1}$$

is the characteristic fire diameter and δx is the nominal size of a mesh cell. The quantity $D*/\delta x$ can be thought of as the number of computational cells dividing the characteristic diameter of the fire. With more cells spanning through the fire, the better the results of the simulation.

As *Fire Dynamics Simulator User's Guide* suggests that the range of $D*/\delta x$ is from 4 to 16, we conducted the experimental scenarios with JJXP10 to find out a suitable value of the non-dimensional expression for our study. In the experiment, a nozzle was set at 1.5 meters height to extinguish a 93 kW fire source. We simulated this scenario with different mesh sizes in FDS and imitated the full cone spray distribution in reality (shown in Table 4).

To examine the reliability of using FDS to reproduce the experimental situations, we conducted the experiments with the same situation twice and got the results named experiment 1 and 2. After we input the experimental values to examine the accuracy of simulations in FDS, we found out the results in Fig. 5 that with 0.05-m mesh and 0.1-m mesh have a water distribution similar to the experimental results. Because the

Table 4 Conducted scenarios of mesh sensitivity study in FDS

Type of nozzle	Height (m)	Heat release rate from real situation (kW)	Mesh size (m)	D^* value	$D^*/\delta x$
JJXP10	1.5	93	0.025	0.371	14.832
			0.04	0.371	9.270
			0.05	0.371	7.416
			0.075	0.371	4.944
			0.10	0.371	3.708
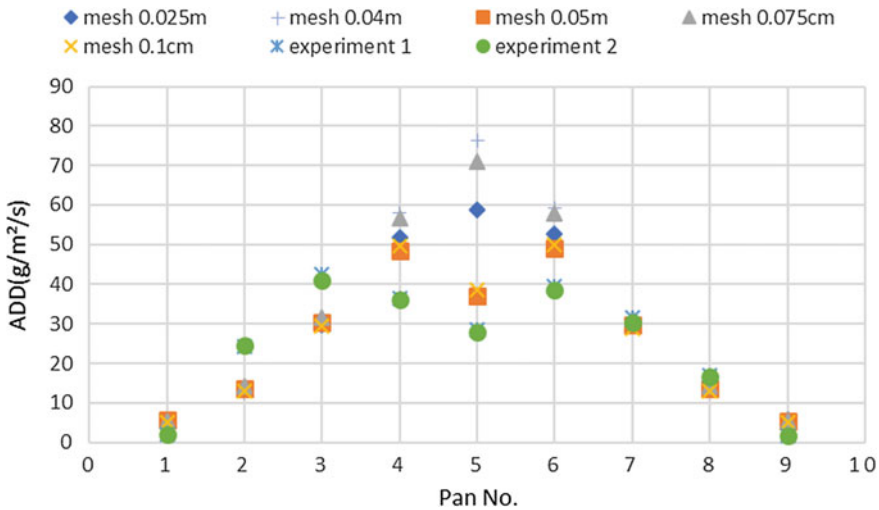
Fig. 5 Mesh sensitivity study with JJXP10 at 1.5 m height

value of non-dimensional expression of the 0.1-m mesh was out of suggested range, we used cubic cells of 0.05 m³ as the mesh in the following analysis, in which the value of non-dimensional expression $D^*/\delta x$ was near 7. With 0.05-m mesh, the fire field can be calculated more accurate than 0.1-m mesh and output the more precise imaging of three dimensions.

3.3 Simulation with Large-Scale Fire Sources

FDS provides us a chance to conduct some scenarios, of which experiments are hard to perform due to space and cost. In the presented experiments shown in session 3.2, we only conducted the situations, in which the HRR was less than 1 MW. In reality,

fire load might be much higher than what we had implemented in the laboratory; hence, simulations with large-scale fire source have to be conducted.

After inputting the experimental values into FDS to examine its reliability, we conducted many simulations, in which the nozzle was set from 1.0 to 3.0 m in height to spray water to extinguish the fire source, and the fire scale was set from 1 to 3 MW, in 400 s with JJXP10 (shown in Fig. 6). As the value of non-dimensional expression $D*/\delta x$ was determined around 7, we used a 0.2-m^3 mesh with 2 and 3 MW fire sources and a 0.15-m^3 mesh with a 1 MW fire source, respectively (shown in Table 5). In the study, we configured several devices to detect the temperature, the heat release rate, and the accumulated mass in the specific pan areas (shown in Fig. 6a). At the end of each burning duration, we used the output values of the fire pan to calculate the simulated ADD (g/m^2/s).

The simulation results using FDS shows that the ADD directly below the nozzle with JJXP010 at 1 m height has a water penetration ratio around 40%, whereas that at 4 meters height has water penetration ratio less than 10%. Furthermore, the decreased rate was not influenced by the heat release rate significantly (shown in Fig. 6b).
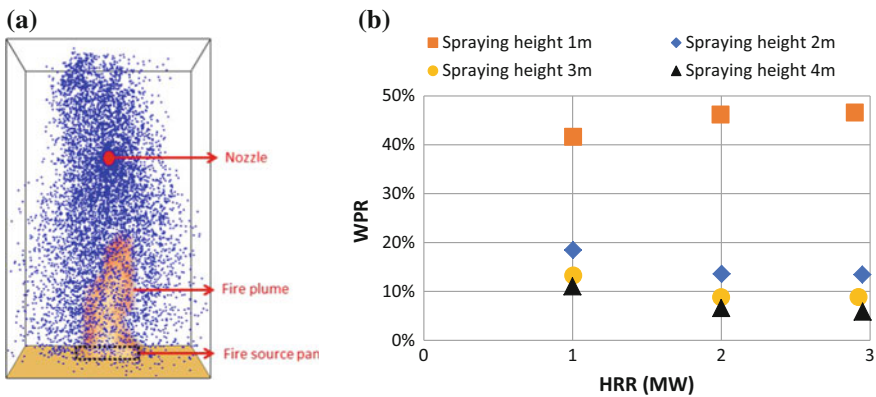
Fig. 6 a Simulation with large-scale fire in FDS and **b** the relationship between Actual Delivered Density and heat release rate with JJXP10

Table 5 Checking the suitable mesh size with different large-scale sources

Type of nozzle	Heat release rate (MW)	Mesh size (m)	$D*$ value	$D*/\delta x$
JJXP10	1	0.15	0.96	6.4
	2	0.2	1.265	6.33
	3	0.2	1.488	7.44

4   Developing a Simple Predictive Model

4.1   Introduction to Multiple Regression Analysis

A simple predictive model provides a fast method for fire engineers to verify the reliability of equipment. Although FDS is widely used in the field of fire engineering, it might cost a long time to run depending on the scale of the simulation. Alternatively, multiple regression analysis is a tool to understand the relationship between independent variables and predictor variables. To deal with numerous data, Microsoft Excel can be used to identify how these independent variables affect a dependent variable.

We analyze the data and identify the coefficients in the nonlinear model. Through the regression line, we can make a prediction of the dependent variable (Y), given the independent variables (X). The performance of a model can be verified, for example, by the R-squared of the predictive residual. When the residual error is small relative to the overall variability, the predictions of the model can be considered reliable.

4.2   Results of Multiple Regression Analysis

A total of 53 sets of experimental results and 13 sets of simulated results were used in the multiple regression analysis. The data included 17 sets of former data from Akieda's and Shimizu's (2015) studies and another 36 sets of results collected in this year. Independent variables include flow rate, diameter of water droplets, spraying height, spraying angle, and heat release rate. We used an exponential function to describe their relationship and let the equation become this form,

$$\beta = \exp(-K \cdot X_1^a \cdot X_2^b \cdot X_3^c \cdot X_4^d \cdot X_5^e) \tag{2}$$

where K is the constant, and X_1, X_2, X_3, X_4, and X_5 are independent variables. This form can explain the interaction of these parameters, as the value of HRR is equal to zero, the water penetration ratio will become 1. On the other hand, if the value of spraying height is extremely high, the predictive WPR will become zero. Using multiple regression analysis, the following model is identified with the R-squared equal to 0.894.

$$\beta = \exp(-0.39 \cdot A^{0.34} \cdot F^{-0.33} \cdot W^{-0.56} \cdot H^{0.94} \cdot Qr^{0.09}) \tag{3}$$

Figure 7 shows the water penetration ratio of the experimental and the predicted results using Eq. (3). This scatter plot shows that the predicted results follow the tendency approximately.
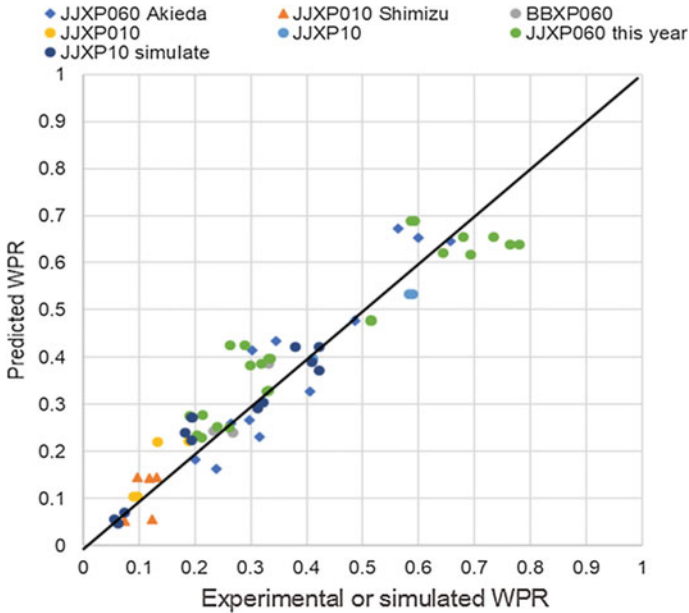
Fig. 7 Scatter plot is made from experimental or simulated WPR

5 Conclusion

In this study, Actual Delivered Density (ADD) was investigated by both experiments and simulations in FDS. We show the amount of water penetrating through flames is a critical index. The empirical results in this research support the idea of Chan et al. [3] that the spraying height and the characteristics of the head can dramatically influence water penetration ratio. As we simulated several large-scale fire source situations using FDS, the results show that the ratio of the ADD with a fire source to that without a fire source is less than 10%, when the nozzle is placed at 3 meters height above the fire source, and its values do not decrease as the scale of fire increases. Furthermore, the decrease rate is not influenced by the heat release rate significantly, and its results are similar to the experimental results. This finding implies that a simple predictive model can be developed, especially for full cone spray nozzles, to identify how the heat release rate affects the water penetration ratio. Considerably more work is required to determine the spraying pattern of different nozzles using more data.

References

1. Asami, T. (1997). Required delivery density (RDD) and the actual delivery density (ADD) of crib fire. In *Annual Conference of JAFSE*.
2. Asami, T. (1998). Measurement of actual delivery density (ADD) for propane gas flame. In *Annual Conference of JAFSE*.
3. Chan, T. S., Kung, H. C., Yu, H. Z., & Brown, W. R. (1994). Experimental study of Actual Delivered Density for rack-storage fires. *Fire Safety Science, 4,* 913–924.
4. Chan, T. S., & Kung, H. C. (2003). Comparison of Actual Delivered Density and fire suppression effectiveness of standard and conventional sprinklers in rack-storage fires. *Fire Safety Science, 7,* 445–456.
5. Heskestad, G. (1979). *Sprinkler performance as related to size and design* (Vol. 1). Laboratory Investigation, FMRC Technical Report, No. 22437.
6. McGrattan, K., Hostikka, S., McDermott, R., Floyd, J., Vanella, M., Weinschenk, C., et al. (2017). *Fire dynamics simulator user's guide* (6th ed.). USA: National Institute of Standards and Technology.
7. Noaki, M., Saito, A., Sato, T., Akieda, T., Hayashi, S., Ohmiya, Y., et al. (2016). Delay of wood ignition owing to attenuation of radiation water. In *Proceedings of 14th International Fire Science & Engineering Conference* (Vol. 1, pp. 571–576).
8. Noaki, M., Shimizu, T., Ohmiya, Y., & Yamaguchi, J. (2015). Study on water delivered density in consideration of penetration through fire—Part 2: Documentary searching and discussion on scattering of water droplets by fire plume. In *Annual Conference of JAFSE* (pp. 96–97).
9. Ohmiya, Y. (2002). Building fire safety design taking consideration of sprinkler system. *Journal of JAFSE, 52*(3), 9–13.
10. Schwille, J. A., Kung, H. C., Hjohlman, M., Laverick, G. E., & Gardell, G. W. (2005). Actual Delivered Density fire test apparatus for sprinklers protecting high commodity storage. *Fire Safety Science, 8,* 823–833.
11. Shimizu, T., Naoki, M., Ohmiya, Y., & Yamaguchi, J. (2015). Study on water delivered density in consideration of penetration through fire—Part 1: Measurement of Actual Delivered Density by using *n*-heptane as fire source. In *Annual Conference of JAFSE* (pp. 94–95).
12. Yao, C. (1988). The development of the ESFR sprinkler system. *Fire Safety Journal, 14*(1–2), 65–73.

Application of Common-Use Temperature Sensors to Early Fire Detection

Daisaku Nii, Mai Namba, Kazunori Harada, Ken Matsuyama and Takeyoshi Tanaka

Abstract Experimental study was conducted to examine the possibility of common-use temperature sensors to apply to early fire detection. In the series of experiments, the velocity of air-conditioning flow and the HRR of a fire source were varied to investigate the ceiling jet behavior and temperature sensor response which is relatively slow compared with ordinary heat detectors. As a result, it was found that a small fire can be detected by common-use temperature sensors by considering the arrangement. Also, the estimation method of sensor response was discussed. The sensor response can be estimated for even a very small fire in the early stage of fire by combining the prediction formulae for ceiling jet flow and for the thermal response of sensors. The influence of air-conditioning airflow was also investigated by the experiments and CFD simulations. It was confirmed that weak ceiling jet induced by a small fire cannot approach to the airflow outlet due to the obstruction by air-conditioning flow. When considering the arrangement of temperature sensors, the sensors should be located at least 1.0 m away from the air-conditioning outlets.

Keywords Fire detection · Common-use sensor · Ceiling jet · Response characteristics · Air-conditioning flow

Nomenclature

C Parameter of heat conduction loss (1/s)
H Vertical distance from a fire source to ceiling surface (m)

D. Nii (✉) · M. Namba · K. Harada
Department of Architecture and Architectural Engineering, Kyoto University, C1-4 Kyoto University Katsura-Campas, Nishikyo, Kyoto 615-8540, Japan
e-mail: nii@archi.kyoto-u.ac.jp

K. Matsuyama
Graduate School of Global Fire Science and Technology, Tokyo University of Science, Yamasaki 2641, Noda, Chiba 278-8510, Japan

T. Tanaka
Emeritus, Kyoto University, Kyoto, Japan

Q Heat release rate (kW)
r Horizontal distance from a fire source to a temperature sensor (m)
RTI   Response time index ($m^{1/2}s^{1/2}$)
T Temperature (°C)
z Height of smoke layer interface from a fire source (m)

Subscripts

a Air
cj Ceiling jet
cj,s Ceiling jet in smoke layer
d Detector or sensor
s Smoke layer

1 Introduction

To promote early evacuation and firefighting, the installation of fire detectors is mandated in wide types of rooms by Fire Service Law in Japan, which has consequently prevented many catastrophic incidents. However, in the aspect of the prevention of false alarms and of the extension of installation conditions to various type of rooms, the specifications of heat detectors are determined in order not to respond to normal activities such as cooking, heating, and so on. For example, the nominal activation temperature of fixed-temperature heat detectors is set more than at 60 °C, which indicates that fire may grow to a certain degree before detection. The delay of detection might cause many casualties, especially in a building such as a hospital or a nursing house with many occupants who need assistance for evacuation.

Meanwhile, various temperature sensors for instrumentation are widely used in controlling the HVAC system, etc. Daily temperature fluctuations in a room can be monitored by such temperature sensors. If an unusual temperature rise could be distinguished from dairy temperature fluctuations, fire detection in the very early stage of a fire may be possible. In order to apply temperature sensors to actual fire detection, there are some problems to be solved. These problems arise from the fact that ceiling jet induced by a fire in the very early stage is very weak. Generally, the response characteristics of common-use sensors are slower than that of normative heat detectors satisfying regulatory specifications. Therefore, it may take a longer time to detect a fire than expected. In addition, weak ceiling jet would be obstructed by airflows caused by daily use instruments such as air conditioner and/or ventilators.

On the ceiling jet behavior under the unconfined ceiling, several estimation models of temperature and velocity were proposed, e.g., [1, 2]. Watanabe et al. proposed the estimation model on ceiling jet temperature under confined ceiling [3]. Similarly,

Yamauchi et al. proposed the estimation model on velocity in addition to temperature [4]. On the response of fire detectors, RTI-C model was proposed by Heskestad et al. [5], and expanded model, 2-RTI model was also proposed by Yamauchi et al. [4].

In this study, to clarify the application range of fire detection by common-use temperature sensors, an experimental investigation was carried out in a real-scale compartment with a small fire source. Temperature measured by common-use sensors and thermocouples were compared with the estimation models in previous studies above. The influence of airflow from the air conditioner was also investigated in the experiments. The horizontal distance that the ceiling jet can reach opposing air-conditioning flow was compared between experiments and CFD simulations.

2 Experimental Setup and Procedures

2.1 Experimental Setup

Experiments were carried out in a real-scale compartment as shown in Fig. 1. The inner size of the compartment is 6500×6500 mm. The ceiling height is 2700 mm. This compartment has a single opening of $^W 2900 \times {}^H 2100$ mm. Although the opening of the actual typical room was relatively narrow compared with this compartment, it was assumed that the weak flow through the opening would give no influence on the burning behavior and rising plume.

To reproduce airflow by an air conditioner, an air blowing equipment was attached on the ceiling at the center of the compartment as shown in Fig. 2. The equipment was composed of an air outlet model and an axial fan connected by a flexible duct.
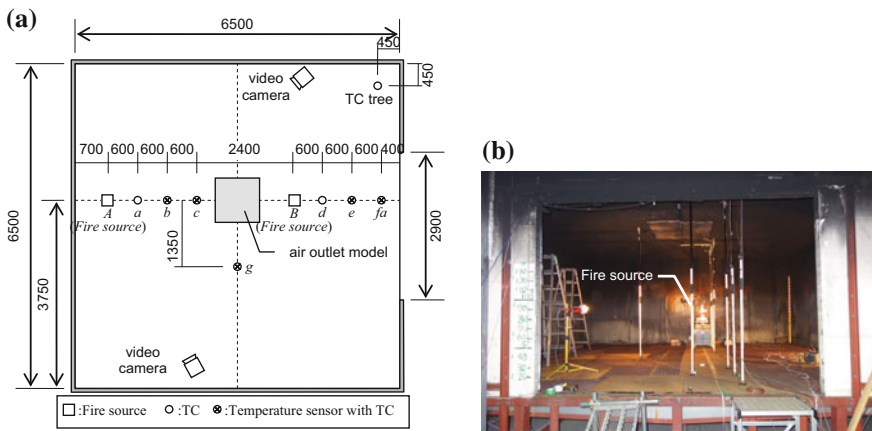
Fig. 1 Experimental compartment and arrangement of measuring points: **a** plan and **b** photographic view from outside

(a)

(b)
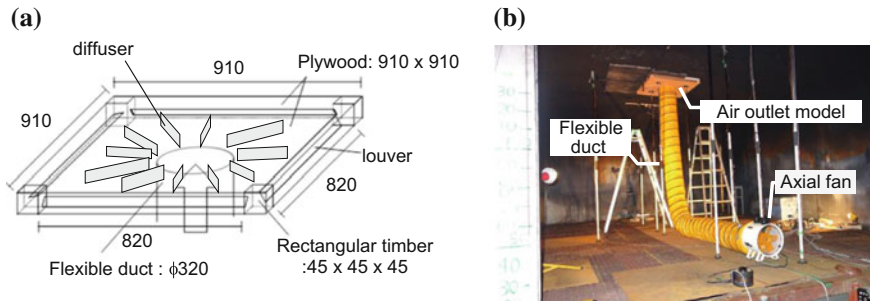
Fig. 2 Air blowing equipment: **a** dimensions of air outlet model and **b** photographic view

Outlet velocity was able to change by controlling the rotational speed of the axial fan. The airflow pumped by an axial fan blows out from four slits of 45 × 820 mm on all the sides of the model. Several diffusers were put inside the air outlet model so as that outlet velocity from side slits was approximately uniform.

Ceiling jet temperatures under 10 mm and 30 mm from ceiling surface at each measuring points, *a–g* in Fig. 1, were measured by T-type thermocouples (φ0.1 mm). Temperature sensors (LR5001, Hioki E.E. Corp.) were also located under 30 mm from ceiling surface at each measuring points except position *a* and *d*. The response characteristics, RTI and C, of this sensor were previously measured as 70 $m^{1/2}s^{1/2}$ and 0.0003 s^{-1}, respectively [6]. At the corner of the compartment, a thermocouple tree was located to measure smoke layer height and temperature by N % method.

2.2 Experimental Procedures

In the experiments, the combinations of combustibles, the height and position of a fire source, and air outlet velocity were varied as shown in Table 1. For the experiments E1 to E6, 360 ml of ethanol poured into a pan with a diameter of 150 mm was burned. For the experiment U1, the flexible polyurethane foam whose size was 450 × 450 × ^{H}150 mm was ignited at the center of the top surface. The heat release rate (HRR) of fire source was obtained by converting the mass loss rate measured by a set of load cells. The heat of combustion is 27.8 MJ/kg for ethanol and 24.8 MJ/kg for polyurethane foam, respectively.

Flow from an air conditioner was simulated in experiments E3 to E6. Among them, the velocity of ceiling jet at measurement point *b* and *e* was measured by hot-wire anemometers in experiment E5 and E6. Ceiling jet behavior was visually observed in experiments E1 to E6 by supplying white smoke at 900 s after ignition.

Table 1 Experimental conditions

Exp. no.	Fire source			Air blowing equipment	
		Height from floor level (mm)	Position of fire source		Outlet velocity (m/s)
E1	Ethanol	720	A	*Not installed*	–
E2		190	A	*Not installed*	–
E3		190	A	Installed	3.0
E4		190	A	Installed	7.8
E5		190	B	Installed	3.0
E6		190	B	Installed	0.0
U1	Polyurethane foam	330	A	*Not installed*	–

3 Experimental Results

3.1 Ceiling Jet Behavior and Sensor Response in Case Without Air-Conditioning Flow

In experiment E2, the HRR was approximately steady at 7 kW as shown in Fig. 3a. Comparing with observation records, N% value was determined as thirty to estimate
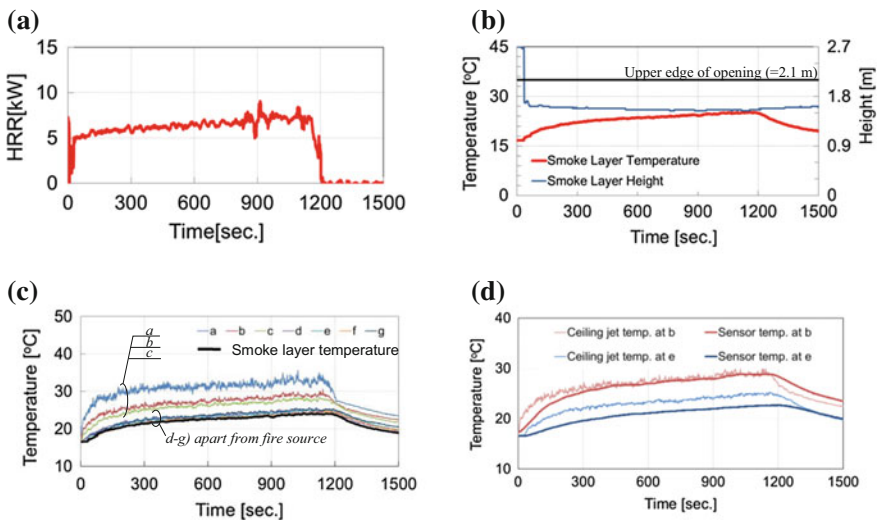
Fig. 3 Measurement results in Exp. E2: **a** heat release rate, **b** smoke layer temperature and height, **c** ceiling jet temperature, and **d** temperature measured by sensors compared with ceiling jet temperature

smoke layer height. Smoke layer was filled shortly after ignition and then became steady at about 1.6 m above floor. Smoke layer temperature was gradually increased until the end of burning as shown in Fig. 3b.

Figure 3c shows the temperatures measured by thermocouples at 30 mm below from ceiling at each measuring point. At measuring points *a–c*, which is close to fire source, temperatures were obviously higher than that of smoke layer. On the other hand, temperatures at measuring points *d–g*, which is relatively far from fire source, were almost close to that of smoke layer.

Figure 3d shows the temperature measured by temperature sensors at measuring point *b* and *e*. Ceiling jet temperature measured by a thermocouple at the corresponding points was additionally shown for comparison. At the measurement point *b*, close to the fire source, the sensor temperature rose at about 60 s later than the rise of a ceiling jet temperature. The sensor temperature became approximately equal to the ceiling jet temperature after around 300 s after ignition. On the other hand, at measuring point *e*, the sensor temperature gradually increased as the ceiling jet temperature increased. However, the sensor temperature was always lower than the ceiling jet temperature throughout the experiment. It is presumed that the convective heat transfer from the ceiling jet to sensing spot inside the sensor was decreased because the velocity of ceiling jet was very small at that position.

This result indicates that a small fire can be detected by a common-use temperature sensor even though there is a large delay of temperature rise when the sensor is apart from a fire source. The arrangement and interval of sensing points should be considered to prevent the delay of detection.

In other experiments without air-conditioning airflow, E1, E6, and U1, similar results were obtained.

3.2   Ceiling Jet Behavior and Sensor Response in Case with Air-Conditioning Flow

The influence of air-conditioning flow was examined in experiment E3 and E4 by comparing with experiment E2. Among these experiments, the velocity of air-conditioning flow was varied, but the other conditions were the same.

In Fig. 4, the pictures of smoke flow around measuring points *a–c* where air-conditioning flow collided with ceiling jet were shown for experiment E2, E3, and E4, respectively. In experiment E3, the outlet velocity of air-conditioning flow was 3.0 m/s. Air-conditioning flow spread out between the ceiling surface and visualized smoke as shown in Fig. 4b. Then, air-conditioning flow was observed to diffuse in the direction of perpendicular to the photograph and mixed with the smoke layer. In experiment E4, the velocity of air-conditioning flow was 7.8 m/s since the air-conditioning flow was discharged strongly. Visualized ceiling jet could not spread concentrically and became considerably faint as shown in Fig. 4c.
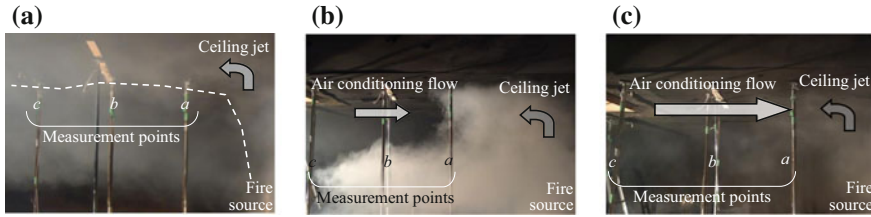
Fig. 4 Photographic view of ceiling jet in case with air-conditioning flow in **a** Exp. E2, **b** Exp. E3, and **c** Exp. E4. *Note* Because the picture shown in Fig. 4 b was taken just after the end of burning, and the momentum of ceiling jet would become weaker
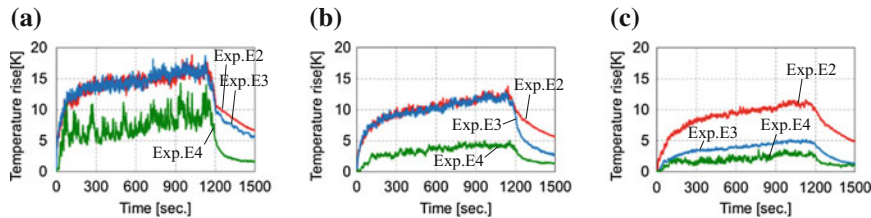
Fig. 5 Temperatures near the ceiling in case with air-conditioning flow at **a** point *a,* **b** point *b,* and **c** point *c*

Temperature rise in experiments E2, E3, and E4 at each measurement point, *a–c*, is shown in Fig. 5. At measuring points *a* and *b*, temperature rise in E3 was almost the same with the value in experiment E2 in which there was no air-conditioning flow. At measuring point *c*, temperature rise in E3 was fairly small compared with that in E2. The temperature fluctuation was also small. Therefore, air-conditioning flow was considered to impinge to ceiling jet and mix with smoke layer at between measuring points *b* and *c*. As seen by the large fluctuation in temperature rise in experiment E4 at measurement point *a*, it was found that air-conditioning flow and ceiling jet were intensely mixed at around point *a*.

4 Discussions

4.1 Estimation of Ceiling Jet Behavior and Sensor Response

To discuss the appropriate arrangement of temperature sensors for fire detection, it is necessary to understand how the temperature sensor responds to ceiling jet. In this section, a method of estimating the temperature sensor response is described.

The correlation formulae of the temperature T_{cj} [°C] and the ceiling jet velocity, u_{cj} (m/s), of ceiling jet to the HRR Q (kW) of a point heat source under unconfined

ceiling were proposed by Alpert [1] as follows,

$$
T_{cj} - T_a = \begin{cases} 16.9\big(Q/H^{5/2}\big)^{2/3} & [r/H \le 0.18] \\ 5.38\big(Q/H^{5/2}\big)^{2/3}(r/H)^{-2/3} & [r/H > 0.18] \end{cases} \tag{1}
$$

$$
u_{cj} = \begin{cases} 0.96(Q/H)^{1/3} & [r/H \le 0.15] \\ 0.195(Q/H)^{1/3}(r/H)^{-5/6} & [r/H > 0.15] \end{cases} \tag{2}
$$

where H is the vertical distance from ceiling surface to a fire source (m), and r is the horizontal distance from temperature sensor to a heat source (m).

In case of the stratified smoke layer under confined ceiling, the temperature of ceiling jet becomes higher than that given by Eq. (1) because the fire plume rising from fire source entrains not only ambient air but also upper hot smoke. In this study, to predict the temperature of ceiling jet in smoke layer $T_{cj,s}$, the formula proposed by Watanabe et al. [3] was applied. The formula is

$$
T_{cj,s} = \left\{1 - (z/H)^{5/3}\right\}(T_s - T_a) + T_{cj} \tag{3}
$$

where z is the interface height of smoke layer above a point heat source (m). The first term of the right-hand side denotes the increase of temperature by entraining hot smoke.

As shown in Fig. (6), though it has been verified only under a few conditions, it was confirmed that Alpert's formula can be applied to the prediction of ceiling jet velocity in smoke layer $u_{cj,s}$. Thus,

$$
u_{cj,s} = u_{cj} \tag{4}
$$

To predict sensor temperature T_d (°C) considering the thermal capacity and conduction loss of the sensor, RTI-C model proposed by Heskestad et al. [5] was applied.

$$
\frac{dT_d}{dt} = \frac{\sqrt{u_{cj,s}}}{RTI}\big(T_{cj,s} - T_d\big) - C(T_d - T_a) \tag{5}
$$
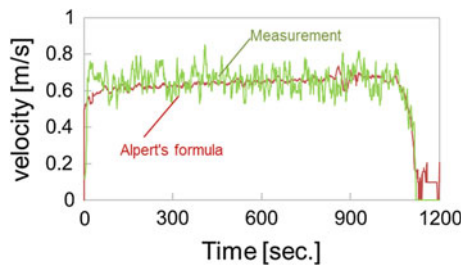
Fig. 6 Comparison of ceiling jet velocity between Alpert's formula and measured results in Exp. E6
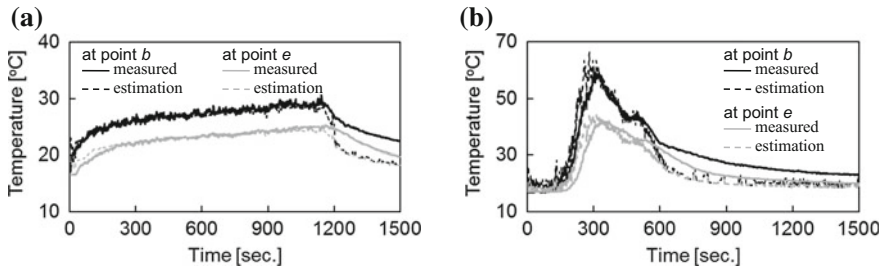
Fig. 7 Comparison of ceiling jet temperature between measurement and estimation in **a** Exp. E2 and **b** Exp. U1
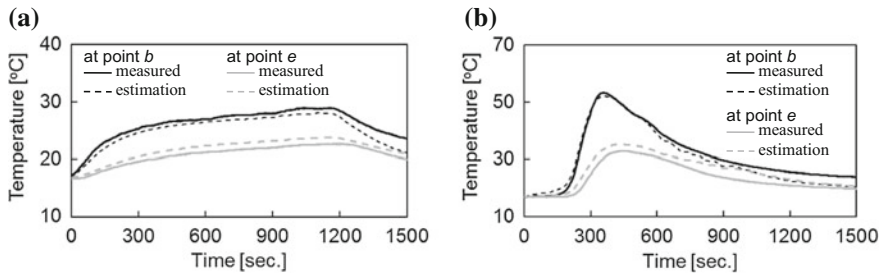
Fig. 8 Comparison of sensor temperature between measurement and estimation in **a** Exp. E2 and **b** Exp. U1

Substituting the HRR, the smoke layer temperature and smoke layer height measured in the experiment into Eq. (1)–(3), ceiling jet temperature could be predicted. In Fig. 7, the results are shown in comparison with the temperature measured at point b and e in Exp. E2 and U1, respectively. For both experiments, the prediction values agree well with the measured results.

Sensor temperatures were also predicted by Eq. (5) as shown in Fig. 8. It was found that the accuracy of the prediction is sufficient for use in practical fire detection. From the above, by combining Watanabe's formula with the RTI-C model, it was confirmed that the sensor temperature can be estimated for either a small steady fire source or for a growing fire source.

4.2 Influence of Air-Conditioning Flow

To investigate the influence of air-conditioning flow against ceiling jet, CFD simulations were carried out for various velocity of air outlet flow. The ceiling jet flow with air-conditioning equipment was reproduced. A standard k-ε turbulence model software (Flow Designer, ver.2017, Advanced Knowledge Laboratory, Inc.) was used for prediction. Calculation domain was divided into about 720,000 cells.

Figure 9 shows isothermal contours of the results of simulating the experiments E2 to E4 at the vertical cross section including the array of measuring points. It was shown that ceiling jet was disturbed by air-conditioning flow, especially in case of large outlet velocity of 7.8 m/s. As the velocity is so large, smoke layer cannot be developed.

The temperature distribution under the ceiling was plotted as shown in Fig. 10. In each condition, the simulation result agrees very well with experimental measurement. In case with air-conditioning flow, the temperature distribution has a steep change at a certain point between fire source and airflow outlet. Such a point was deemed to be the impinging point of two flows. For various outlet velocity of air-conditioning, impinging points in case that the HRR of fire source is 7 kW were plotted as shown in Fig. 11. This figure shows that the distance from fire source to the impinging point is almost proportional to the outlet velocity, but the simulation results of the impinging point underestimate the distance to the impinging point. One of the reasons may be that the tip of the ceiling jet slipped beneath air-conditioning flow in video observations. However, the slope of the plots is similar between experiments and calculations, so the simulation results are correct at least qualitatively. Generally, the outlet velocity of air-conditioning flow is below 3.0 m/s, and the heat release rate generated by home electric devices and/or gas appliances in daily life is less than 7 kW. Therefore, it can be concluded that even a small fire can be detected by common-use temperature sensor installed 1.0 m or more away from the air-conditioning outlet.
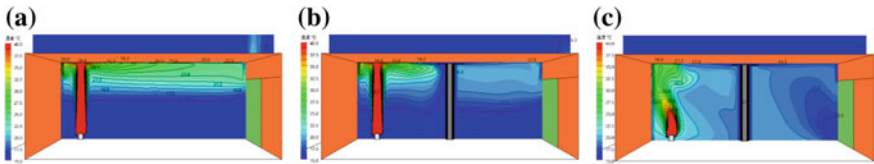
Fig. 9 Isothermal contour of simulating **a** Exp. E2, **b** Exp. E3, and **c** Exp. E4
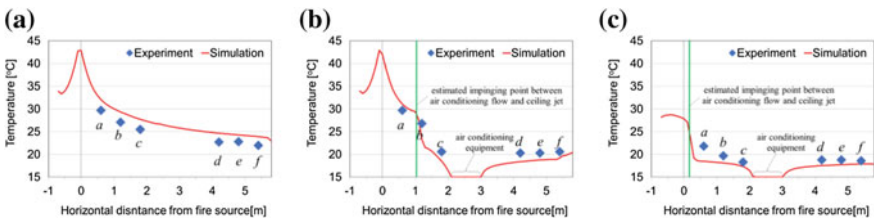
Fig. 10 Temperature distribution at 30 mm under the ceiling surface: **a** Exp. E2, **b** Exp. E3, and **c** Exp. E4
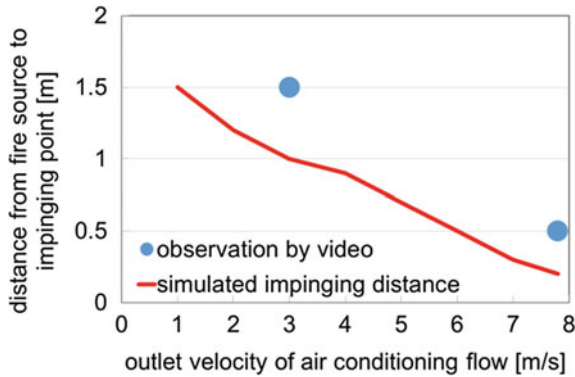
Fig. 11 Simulated impinging points for various outlet velocity of air-conditioning compared with observation

5 Conclusions

To examine the possibility of applying common-use temperature sensors to early fire detection, an experimental study was conducted. In the series of experiments, the ceiling jet behavior and temperature sensor response were investigated under some combinations of the sensor locations and the HRR of a fire source. RTI and C-values of sensors used in experiments were 70 $m^{1/2}s^{1/2}$ and 0.0003 s^{-1}, respectively. As a result, it was found that a small fire can be detected by common-use temperature sensors. The estimation method of sensor response was verified by combining the RTI-C model with prediction formula of ceiling jet temperature through hot smoke layer in the upper part of a compartment.

The influence of air-conditioning flow was also investigated by experiments and CFD simulations. It was confirmed that weak ceiling jet induced by a small fire was obstructed by the air-conditioning flow. It was found that sensors should be located at least 1.0 m apart from air conditioner's outlet in order to catch the temperature rise of ceiling jet in the early stage.

References

1. Alpert, R. L. (1972). Calculation of response time of ceiling-mounted fire detectors. *Fire Technology, 8,* 181–195.
2. Sugawa, O. (2001). Simple estimation model on ceiling temperature and velocity of fire induced flow under ceiling. *Fire Science & Technology, 21,* 57–67.

3. Watanabe, J., Shimomura, S., Aoyama, Y., & Tanaka, T. (2002). A formula for prediction of ceiling jet temperature in two layer environment. In *Fire Safety Science—Proceedings of the 7th International Symposium, International Association for Fire Safety Science* (pp. 431–442).
4. Yamauchi, Y., Mammoto, A., Dohi, M., Ebata, H., & Morita, M. (2005). A calculation method for predicting heat and smoke detector's response. *Fire Science & Technology, 21,* 179–210.
5. Heskestad, G., & Bill, R. G. (1988). Quantification of thermal responsiveness of automatic sprinklers including conduction effects. *Fire Safety Journal, 14,* 113–125.
6. Makikawa, M., Nii, D., & Harada, H. (2016). Response characteristics of common-use temperature sensor to hot air flow. In *Proceedings of 2016 JAFSE Annual Symposium* (pp. 100–101). (In Japanese).

Water Mist Fire Suppression Modeling of Rack Storage Fires in Open Space

N. Ren, K. V. Meredith, H. Z. Yu, Xiangyang Zhou, Y. Wang and S. B. Dorofeev

Abstract   This study presents the modeling progress for water mist suppression of deep-seated solid fuel fires in a rack-storage configuration. The solid fuel consists of 16 pallet loads arranged in a two-tier high, two-pallet load-wide and four-pallet load-long array. Each pallet load is a corrugated cardboard box sitting on a hardwood pallet. The simulations are performed using FireFOAM, with several key sub-models developed for water-based suppression, such as spray dispersion, surface film flow for cooling/wetting solid surfaces, gas-phase flame extinction/re-ignition, spray radiation attenuation, and soot emission reduction due to spray cooling. The simulation results are discussed in comparison with the test data.

Keywords FireFOAM · Water mist · Fire suppression · Flame extinction

1   Introduction

Water-based suppression systems have many advantages, such as high efficiency, low costs, non-toxic, and environmental friendly, and have been widely applied for fire protection. In fire suppression applications, two types of water sprays are used: sprinkler spray and water mist spray, which are mainly differentiated by the overall drop size (e.g., volume median diameter, d_{v50}). The water mist spray is loosely defined as the spray d_{v99} less than 1 mm [1], and the sprinkler spray refers to large droplet sprays with d_{v99} larger than 1 mm. Compared to a sprinkler spray, a water mist spray has smaller droplets, lower flow rate, weaker flame penetration capability, and higher vaporization rate. Consequently, the main applications of water mist suppression are different from sprinkler-based suppression.

Sprinkler sprays have been widely used to protect solid commodities with different flammability and storage configurations (e.g., rack storage, roll paper storage, offices). Water mist sprays have been traditionally used in confined space (e.g., machinery in enclosure) and for situations where sprinkler sprays have certain limitations (e.g., ignitable liquid, indoor transformers, computer rooms) [2]. In recent

N. Ren (✉) · K. V. Meredith · H. Z. Yu · X. Zhou · Y. Wang · S. B. Dorofeev
Research Division, FM Global, 1151 Boston-Providence Turnpike, Norwood, MA 02062, USA
e-mail: ning.ren@fmglobal.com

years, water mist application has been extended to solid combustible fires in open (or large) space. Several fire tests [3–5] have been conducted to investigate the water mist suppression performance with comparison to the sprinkler sprays.

For solid commodity fires using sprinkler sprays, it has been commonly recognized that the primary suppression mechanism is the cooling/wetting of the fuel surfaces. However, for water mist sprays, the primary suppression mechanism has not been well understood. Many suppression mechanisms are potentially important, such as flame cooling, surface wetting, oxygen displacement, and radiation reduction.

To gain insight into the water mist suppression mechanisms, this study performs a series of numerical simulations for deep-seated solid fuel fires in a rack storage configuration in open space, which is the same configuration as in Ref. [5]. Water mist suppression of solid fuel fires involves many suppression physics. Some of the suppression models are in the developing stage. This study presents the preliminary simulation results and the comparison with the test results of Ref. [5].

2 Test Configuration

The test configuration of Ref. [5] uses 16 pallet loads arranged in a two-tier high, two-pallet load-wide and four-pallet load-long array. Each pallet load is a corrugated cardboard box sitting on a hardwood pallet. Figure 1 illustrates the experimental setup. This study chooses two types of water mist nozzle used in Ref. [5]. A summary of the nozzle and the water mist characteristics is given in Table 1. In the fire test,
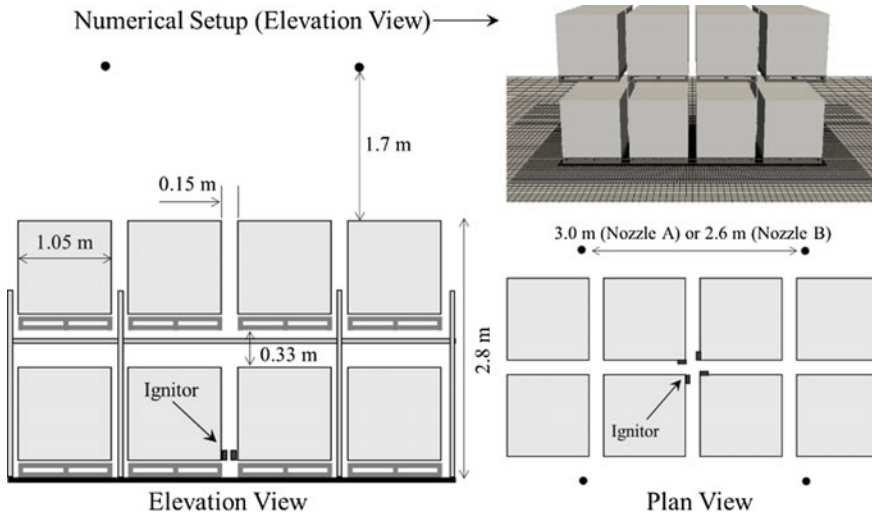
Fig. 1 Illustration of test and numerical configuration of the two-tier high rack storage array

Table 1 Summary of the water mist nozzle, spray characteristics, and suppression results

Cases	K-factor (lpm/bar$^{1/2}$)	Pressure (bar)	d_{v50} (µm)	Nozzle spacing (m)	Water density (mm/min)	Test result
Nozzle-A	8.4	44.8	177	3.0	6.1	Controlled
Nozzle-A	8.4	20	211	3.0	4.1	Un-controlled[*]
Nozzle-B	4	100	70	2.6	6.1	Un-controlled

[*]Fire spreads to one or both ends of the rack storage array

four water mist nozzles are arranged in a square array 1.7 m above the top of the rack. The spacing of the nozzle is 3 m for Nozzle-A and 2.6 m for Nozzle-B.

In the fire tests, the four water mist nozzles are manually activated when the measured convective heat release rate reaches the designed value of 1 MW. Due to the smearing effect of the data acquisition system and the delay of manual activation, the actual convective heat release rate at nozzle activation is larger than 1 MW. The estimated chemical heat release rate is about 1.7–2 MW. In the simulation, spray injection starts when the chemical heat release rate reaches 1.7 MW.

3 Modeling Approach

The current study targets modeling water mist suppression of solid fires based on the first principle physics, which include turbulence, combustion (with flame extinction and re-ignition), radiation, solid-phase pyrolysis, spray dispersion (drag and vaporization), and surface film flows. This study uses FireFOAM [6], a large-eddy-simulation (LES) fire modeling tool based on the OpenFOAM [7] toolbox. Most of the suppression physics models have been developed, implemented in FireFOAM, and validated. Details are presented in Refs. [6, 8–13]. This section highlights some of the key sub-models.

3.1 Fire Growth Model

In the gas phase, FireFOAM solves filtered transport equations for sensible enthalpy, species mass fractions, and the fully compressible Navier–Stokes equations [6]. The k-equation turbulent model [14] is used to model the transport of sub-grid kinetic energy, k_{sgs}. The combustion model uses the Eddy dissipation concept (EDC) [15]. The reaction rate is determined by the sub-grid turbulent mixing rate given by

$$\dot{W}'''_{\text{EDC}} = C_{\text{EDC}} \frac{\rho \epsilon_{\text{sgs}}}{k_{\text{sgs}}} \min\left(Y_{\text{Fuel}}, \frac{Y_{O_2}}{r_s}\right) \tag{1}$$

where ρ is the density, ϵ_{sgs} is the energy dissipation rate given by the turbulence model, $C_{\text{EDC}} = 4$ is a model constant, r_s is the oxygen–fuel stoichiometric ratio, Y_{Fuel}, and Y_{O_2} are the fuel and oxygen mass fractions. The combustion model also accounts for flame extinction/re-ignition and is presented in the following section.

The thermal decomposition of solid fuels and the fire growth is driven by the heat feedback from the flames. The pyrolysis of the solid fuel is treated via a one-dimensional heat transfer model with a single-step Arrhenius reaction. The pyrolysate from the corrugated cardboard and hardwood has complex composition. In the simulations, the pyrolysate (fuel) is converted to CH_4 based on the heat of combustion. The details of the pyrolysis model and the material properties of corrugated cardboard and hardwood are presented in Ref. [9].

3.2 Flame Extinction/Re-ignition Model

The flame extinction/re-ignition model uses the reactive volume fraction (RVF) model [10], which is based on the energy balance between the heat loss rate and heat release rate of the fuel–oxidizer premixture (mixed eddy) at the flame extinction limits. Compared to other flame extinction models available in the literature (e.g., Damköhler number-based model [16]), the RVF model considers not only the interplay of the chemical and flow temporal scales, but also the flow spatial scales (e.g., eddy sizes). Recently, the RVF model has been implemented into FireFOAM and evaluated against experiments for different fuels in oxygen-reduced environments [11].

The RVF model can be simply illustrated using the flammability map shown in Fig. 2 for the lower branch of the S-curve at two oxygen volume fractions. The critical burning condition is formulated using the ratio of flame thickness to eddy size ($x = \delta/\Delta$) and the turbulent Karlovitz number ($\text{Ka} = C_{\text{Ka}} \delta^2 \epsilon^{1/2} \nu^{-3/2}$, where

Fig. 2 Critical burning conditions for mixed eddies (CH_4 flames at two oxygen volume fractions)
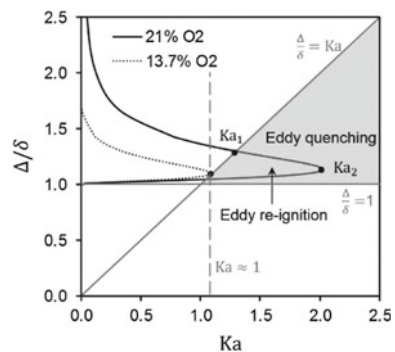
C_{Ka} is a model constant of 0.2, and ν is the viscosity). The flammability range of the mixed eddy sizes is shown by the light gray area between the two solid gray lines ($1 < \Delta/\delta < Ka$). More discussions of the eddy flammability regime are available in Ref. [10].

Figure 2 illustrates the two quenching limits of the mixed eddies. When the eddy adiabatic flame temperature decreases (e.g., dilution by inert or cooling by water mist), the eddy re-ignition region reduces. There is a critical condition where the S-curve becomes tangent to the solid gray line (Ka ≈ 1). Below this point, the reaction cannot be maintained regardless of the level of turbulence. Another quenching limit is related to the increase of the turbulence intensity. If the Karlovitz number is larger than the critical value Ka_2, then all mixed eddies are quenched (the reactive volume fraction, F_{RV}, is 0). The mixed eddies are partially reactive and $0 < F_{RV} < 1$ for $Ka_1 < Ka < Ka_2$.

The reaction rate accounting for flame extinction is modeled by combining the reactive volume fraction with the EDC combustion model (using CH_4 to represent the gaseous fuel) given by:

$$GR1: CH_4 + 2(O_2 + 3.76N_2) \rightarrow CO_2 + 2H_2O + 7.52N_2;$$
$$\dot{W}'''_{GR1} = F_E \dot{W}'''_{EDC} \tag{2}$$
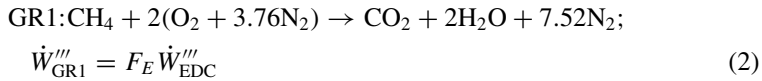
When flame extinction occurs, the original fuel is mixed with oxidizer and quenched, generating a 'mixed-quenched' fuel:

$$GR2: CH_4 + 2(O_2 + 3.76N_2) \rightarrow CH_4^* + 2(O_2 + 3.67N_2);$$
$$\dot{W}''_{GR2} = (1 - F_{RV}) \dot{W}''_{EDC} \tag{3}$$
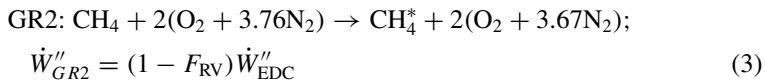
The mixed-quenched fuel does not automatically react (unless certain criteria are satisfied), and its ignition (pilot ignition) is considered as a delayed re-ignition given by:

$$GR3: CH_4^* + 2(O_2 + 3.76N_2) \rightarrow CO_2 + 2H_2O + 7.52N_2;$$
$$\dot{W}''_{GR3} = F_{ig} F_{RV} \frac{\rho}{\Delta_c/S_L} \min\left(Y_{CH_4^*}, \frac{Y_{O2^*}}{r_s} \right) \tag{4}$$
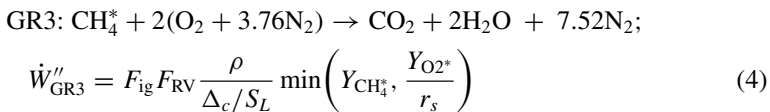
where F_{RV} in GR3 represents the pilot flame, and F_{ig} is a re-ignition factor also given by the FRV model. Assuming the mixed-quenched fuel has been sufficiently mixed with the surrounding air within the computational cell, the reaction timescale is represented by the laminar flame burning velocity S_L of the mixed-quenched fuel and the cell size Δ_c. The available oxygen for the mixed-quenched fuel is simply modeled as the remaining oxygen from GR1, given by $Y_{O2^*} = \max(0, Y_{O2} - Y_F r_s)$.

3.3   Radiation Model

Water mist sprays have strong radiation reduction effects to the flames, such as radiation attenuation, radiation scattering, and flame emission reduction due to spray cooling. Except for the radiation scattering, the radiation attenuation and the flame emission are modeled in this study.

The radiative heat transfer equation is solved by a finite-volume implementation of the discrete ordinate method. Assuming flame is optically thin and neglecting the radiation absorption by water vapor, the radiative heat transfer equation is given by

$$\frac{dI}{ds} = \frac{X_{rf}\dot{Q}_f'''}{4\pi} - \kappa_{\text{spray}}I \tag{5}$$

where I is the radiation intensity at a given solid angle, $\dot{Q}_f'''$ is the local heat release rate, X_{rf} is the local flame radiant fraction, and κ_{spray} is the spray attenuation coefficient given by the spray attenuation model [12]. This study uses the gray simplification of the attenuation model.

For X_{rf}, the current study takes advantage of the description of the radiant loss from flames in the RVF model [10]. It is evaluated there for a given flame thickness using the mean Plank absorption coefficient of gas species. In typical fire scenarios, soot emission contributes most of the flame radiation. This study uses a simple phenomenological model for soot emission by assuming the effective soot volume fraction, $f_{V,eff}$, and decreases linearly with the adiabatic flame temperature, given by

$$f_{V,\text{eff}} = \max\left(0, f_{V0}\frac{T_b - T_{b,\text{crit}}}{T_{b0} - T_{b,\text{crit}}}\right) \tag{6}$$

where f_{V0} and T_{b0} are the effective soot volume fraction and the adiabatic flame temperature at normal air conditions, and $T_{b,\text{crit}}$ is the adiabatic flame temperature at the critical oxygen volume fraction when soot vanishes.

In the RVF model, the radiative loss term $\alpha = 16\delta^2\sigma_R k_R T_0^3/3\rho c_p \chi$ (where σ_R is the Stefan–Boltzmann constant, $\kappa_R = \kappa_{\text{gas}} + C_{\text{soot}} f_{V,\text{eff}} T_0$ is the radiation absorption coefficient with $C_{\text{soot}} = 1808\,(\text{m K})^{-1}$, T_0 is the flame temperature accounting for heat losses, and χ is thermal diffusivity evaluated at T_0) represents the ratio between the radiative and conductive heat transfer rates. Therefore, the local flame radiant fraction is $X_{rf} = \alpha/(1 + \alpha)$. The global radiant fraction is used to quantify the overall flame emission reduction caused by spray cooling, which is calculated as

$$X_r = \frac{\iiint X_{rf}\dot{Q}'''dV}{\iiint \dot{Q}'''dV} \tag{7}$$

This simple radiant fraction model has been studied in Ref. [11] and showed promising agreement with radiation measurement for different fuels and oxygen volume fractions.

3.4 Spray and Water Film

The initial spray profiles, such as drop size, water flux, and velocity distributions, are obtained from spray characterization measurements using the same approach as in Ref. [17]. A discrete-phase, particle-tracking model is used for the spray transport and coupling of the mass, momentum, and energy transfer with the gas phase. Momentum drag, convective heat transfer, and vaporization are treated by the model.

When droplets reach solid surfaces, they can either splash, accumulate into a thin liquid film, or bounce back to gas phase. The small droplets of a water mist spray tend to follow more closely with the gas stream. The conformity of a droplet's movement to the gas flow can be evaluated by the Stoke number given by

$$\text{St} = \left(\frac{\rho_w d^2}{18\mu} \right) \left(\frac{\mathrm{d}u}{\mathrm{d}z} \right)_{\text{air}} \tag{8}$$

where ρ_w is the water density, μ is the air viscosity, d is the drop size, and $(\mathrm{d}u/\mathrm{d}z)_{\text{air}}$ is the airflow velocity gradient magnitude near the solid surfaces. For Nozzle-B, which has very fine droplets, the estimated velocity gradient of the induced airflow near the top array surfaces is about 23^{-1}. When St $\ll$ 1, droplets tend to follow the gas flow instead of depositing on a solid surface. In this study, a simple sub-grid model for spray deposition is used. In the near-wall computational cell, when the droplet size is less than 70 μm (estimated Stoke number is about 0.3), the droplet will be carried away by the airflow. Otherwise, droplets can deposit on the solid surfaces.

The water film model, as described in Ref. [8], is handled through the thin-film formulation of mass, momentum, and energy transport. This formulation results in a two-dimensional, surface tangential equation set to resolve the film thickness, velocity, and enthalpy. Interfacial convective and radiative heat transfer between the gas-phase, liquid-film, and solid-phase pyrolysis regions are included in the model. A partially wetted, contact-angle-based sub-model allows the film to form rivulets or completely flood regions depending on the local film thickness. A film separation model handles reinjection of droplets (e.g., dripping from the underside of the commodity). The combination of predicted surface wetness coupled with heat transfer between gas, film, and pyrolysis regions ultimately determines whether a fire continues to propagate or gets suppressed.
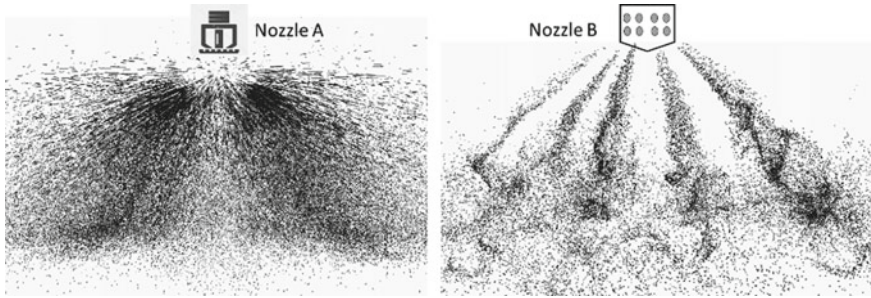
Fig. 3 Illustration of simulated water mist spray

4 Numerical Configuration

The numerical setup is shown in Fig. 1. The simulation domain is about 13 m long, 13 m wide, and 10 m high. A 2.54 cm grid is used in the center of the domain in all x-, y-, z-directions. There are six cells across the 15-cm flue space. Fire is ignited in the center of the array at the bottom tier. In the fire tests, flame is slightly tilted toward the south array. In the simulation, a larger ignitor is used in the south center flue space to initiate the flame tilting.

Figure 3 shows the photographic view of the two nozzles and the simulated water mist spray from a single nozzle in a quiescent space. The spray pattern of Nozzle-A is similar to a typical sprinkler spray. Nozzle-B consists of 10 pairs of small orifices arranged evenly in the azimuthal direction with a 36° spacing. Each pair of the orifices points to the same direction with either an elevation angle of 35° or 55°.

5 Results and Discussion

Figure 4 shows the modeled chemical heat release rates for Nozzle-A at two injection pressures with comparison to the fire tests. In the initial free-burn stage, the modeled heat release rates grow slower than the measurements, which are partially caused by the smearing effect of the data acquisition system in the fire tests. More studies will be given in the follow-up research to reduce the discrepancies with the tests.

In the simulation, spray injection starts at 60 s, when the chemical heat release rate is about 1.7 MW. The fire can be quickly controlled at 44.8 bar, which provides a designed theoretical water density of 6.1 mm/min. The fire cannot be controlled at the lower injection pressure of 20 bar, where the designed water density reduces to 4.1 mm/min. The simulations show good agreement with the fire tests in predicting the general suppression effectiveness at the two injection pressures. Quantitatively, the simulation predicts lower fire growth rate for the 20-bar injection pressure. One possible cause of the lower modeled fire growth rate is the underprediction of the
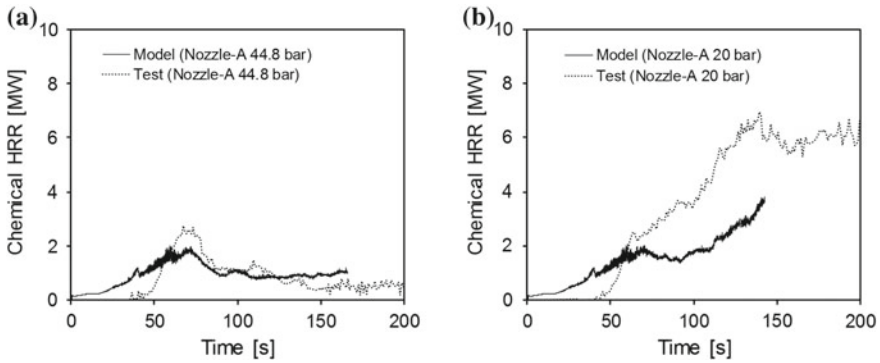
Fig. 4 Comparison of simulated and measured chemical heat release rates using Nozzle-A: **a** at 44.8 bar; **b** at 20 bar

lateral flame spread rate at the first tier. The modeled flame width is slightly narrower than the visible flame width of the suppression test at bottom.

Figure 5 shows the modeled chemical heat release rates for Nozzle-B at 100 bar with comparison to the fire test. Both test and simulation show that heat release continuously increases and fire cannot be controlled by Nozzle-B given a designed water density of 6.1 mm/min. Compared to the Nozzle-A at the same designed water density, the Nozzle-B is less effective for the current rack storage fire.

It is noted that the measured HRR of Nozzle-B shows a sharp decrease upon spray injection, which is attributed to the high spray downward momentum. In the fire test, products (e.g., CO_2, CO) are collected at the downstream (about 11 m) above the rack to calculate the chemical heat release rate. Nozzle-B generates a strong downward spray and spray-induced airflow, which may temporally reduce the product collection

Fig. 5 Comparison of simulated and measured chemical heat release rates using Nozzle-B at 100 bar
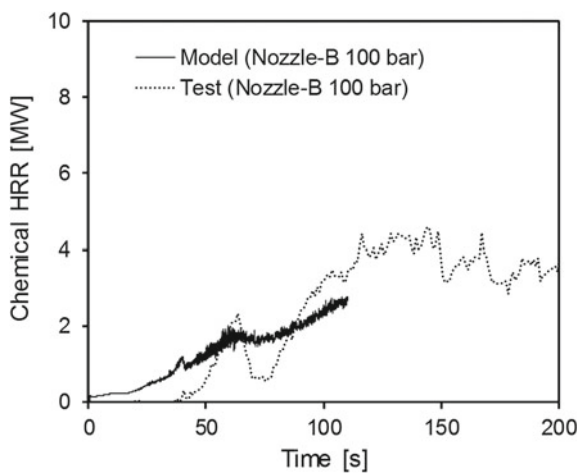
rate at downstream and cause the artificial reduction of HRR. The flame envelope observed in the fire test does not have a noticeable decay after spray injection.

Figure 6 shows the modeled instantaneous flame and water film contours. The flame contour before spray injection is also presented. At 60 s, the flame height is about 5.0 m, which is slightly higher than the elevation location of the nozzles. The three suppression cases are plotted at 110 s, which is 50 s after spray injection. Although Nozzle-B at 100 bar has the same designed water density with Nozzle-A at 44.8 bar, there is less water covering the corrugated boxes, which indicates that Nozzle-B has less actual water delivered density on the commodity. This is mainly attributed to the very fine droplets of Nozzle-B, which have weaker fire penetration capability and lower droplet deposition rate due to small droplet Stoke number. Consequently, Nozzle-B has a weaker capability of wetting and cooling the solid surfaces.

In the current configuration, the second tier of the rack acts as a shield and blocks the direct impinging of droplets to the lower burning surfaces. In this case, surface film flow can be an effective way of delivering water to the deep-seated flames/burning surfaces. For Nozzle-A, when the injection pressure increases from 20 to 44.8 bar, more water is delivered to the fuel array and helps to control the fire.

To better understand the effect of separate physics, Figs. 7 and 8 show the sim-
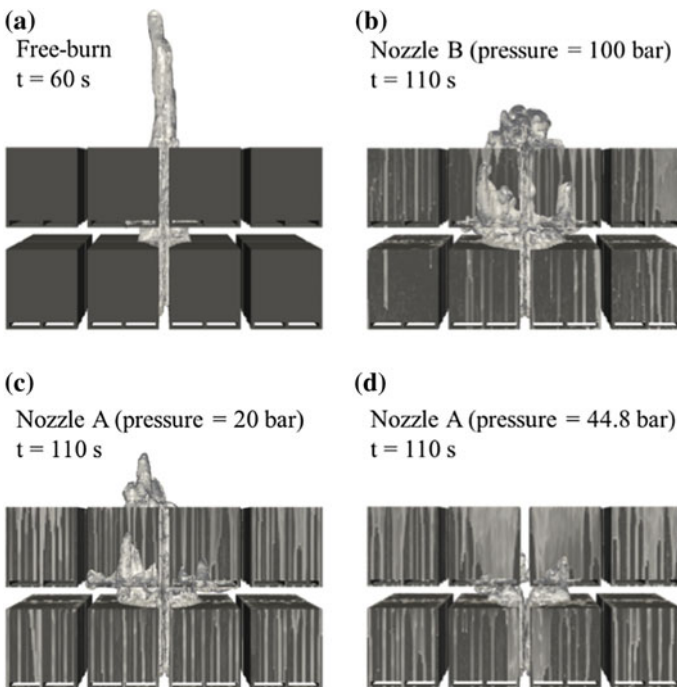
Fig. 6 Illustration of flame contour and surface water film flow on the commodity: **a** flame at spray injection; **b** Nozzle-B at 100 bar; **c** Nozzle-A at 20 bar; **d** Nozzle-A at 44.8 bar
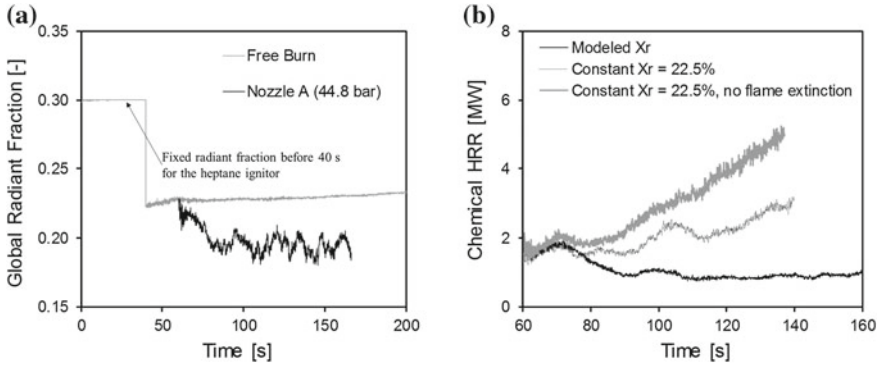
Fig. 7 a Modeled global radiant fraction; **b** modeled chemical heat release rate for Nozzle-A at 44.8 bar
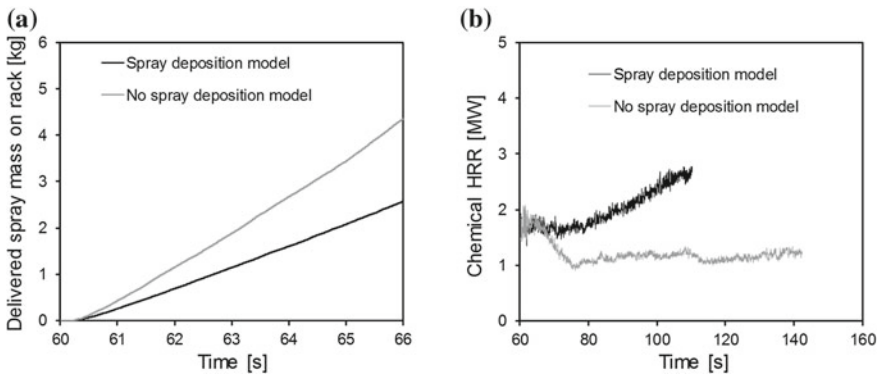
Fig. 8 a Total mass of water deposited on the commodity; **b** sensitivity study of spray deposition model for Nozzle-B at 100 bar

ulations with different model configurations. Figure 7a shows the modeled global radiant fraction with comparison to a free-burn fire. In the initial 40 s, the radiant fraction is prescribed by a constant value of 30%, to mimic the combustion of heptane from the ignitor, which has a higher radiant fraction. After 40 s, the fire size of the ignitor is relatively small, and the radiant fraction is calculated using Eq. 7. The free-burn case shows almost a constant global radiant fraction at about 22.5%. For the suppression case, the radiant fraction decreases approximately to 19%. With a lower radiant fraction, the radiative heat flux on the commodity will decrease, which helps to reduce the fire growth.

Figure 7b compares the modeled HRR using a constant radiant fraction. For the current configuration, the suppression effectiveness is very sensitive to the change of radiant fraction. When a fixed radiant fraction of 22.5% is used, the spray is not able to control the fire growth, which indicates that the reduction of flame emitting power is an important suppression mechanism for a water mist spray. Figure 7b also

shows a simulation when flame extinction is switched off. Without modeling flame extinction, the fire grows even faster, which confirms that flame extinction is a key component for water suppression modeling.

Figure 8 compares the simulations for Nozzle-B with/without a sub-gird spray deposition model, which uses the critical drop size of 70 μm as a criterion. Figure 8a shows the accumulative mass of water on top of the rack for a time interval of 6 s, during which the fire size has not dramatically changed. When the simple spray deposition model is used in the near-wall computational cell, the water delivery rate on top of the rack reduces from 0.8 kg/s to about 0.45 kg/s. Consequently, there are more droplets surrounding the rack and enhances the direct spray cooling effect. On the other hand, there will be less water on the rack for surface cooling/wetting. The simulated HRR is shown in Fig. 8b. When no water deposition model is used, the fire can be controlled, which indicates that for the current deep-seated solid fuel fire, water film cooling is very effective and is an important factor to consider.

6   Conclusion

This paper presents the modeling progress of water mist fire suppression of deep-seated solid fuel fires in open space. A rack storage configuration is used, consisting of 16 pallet loads arranged in a two-tier high, two-pallet load-wide and four-pallet load-long array. Two water mist nozzles are compared, with a designed baseline water density of 6.1 mm/min. Major fire suppression physics specific for water mist is included in the model, such as spray dispersion, spray–fire plume interaction, gas-phase flame extinction/re-ignition, radiation attenuation by water spray, flame radiative emission reduction due to spray cooling, and surface film flow for cooling/wetting solid surfaces. Separate effect studies are performed in the simulations to gain insight into the role of separate physical mechanisms in fire suppression by water mist.

The simulations show good agreement with the fire tests in predicting the overall suppression performance and clearly differentiate the controlled and out-of-controlled configurations. The separate effect studies show that flame extinction in the gas phase is an important mechanism in water mist suppression. The reduction of flame radiation due to gas-phase cooling by spray is also an important suppression mechanism for the studied solid fuel fires. The predicted suppression effectiveness reduces when the fine droplets are carried away by the airflow instead of depositing on the surfaces, which indicates the importance of water film cooling for the solid fuel fires. Future work will focus on improving the model performance in the free-burn stage, completing/improving the model development for radiation scattering, soot/gas-phase emission and spray deposition.

References

1. Mawhinney, J. R. (1997). *Fire protection water mist suppression systems* (18th Ed.). NFPA Handbook.
2. FM Global Data Sheet 4-2, 2013, Water Mist Systems.
3. Arvidson, M. (2014). Large-scale water spray and water mist fire suppression system tests for the protection of Ro–Ro cargo decks on ships. *Fire Technology, 50,* 589.
4. Hjohlman, M. (2012). HI-FOG water mist nozzle receives first UL listing for Ordinary Group 1 applications. *Brandposten, 46.*
5. Yu, H. Z. (2016, September 21–22). Factors affecting efficiency of water mist suppression of solid combustible fires in open space. In: *16th IWMC*, Vienna.
6. Wang, Y., Chatterjee, P., & de Ris, J. L. (2011). Large eddy simulation of fire plumes. In *Proceedings of the Combustion Institute* (p. 2473).
7. OpenFOAM. Available at http://www.openfoam.org/.
8. Meredith, K. V., Heather, A., Xin, Y., & de Vries, J. (2011). A numerical model for partially-wetted flow of thin liquid films. *Computational Methods in Multiphase Flow, VI*, 239.
9. Ren, N., de Vries, J., Zhou, X., Chaos, M., Meredith, K. V., & Wang, Yi. (2017). Large-scale fire suppression modeling of corrugated cardboard boxes on wood pallets in rack-storage configurations. *Fire Safety Journal, 91,* 695.
10. Dorofeev, S. B. (2017). Thermal quenching of mixed eddies in non-premixed flames. *Proceedings of the Combustion Institute* (Vol. 36, pp. 2947).
11. Ren, N., Zeng, D., Meredith, K. V., Wang, Y., & Dorofeev, S. B. Modeling of flame extinction/re-ignition in oxygen-reduced environments. In *Submitted to the 37th Combustion Symposium*, (under review).
12. Gupta, A., Meredith, K. V., & Wang, Y. (2017, April 23–26). Models for absorption and scattering of radiation by water droplets in fire suppression environments. In: *The 10th U. S. National Combustion Meeting*, Maryland.
13. Chatterjee, P., de Ris, J. L., Wang, Y., & Dorofeev, S. B. (2011). A model for soot radiation in buoyant diffusion flames. In *Proceedings of the Combustion Institute* (p. 2719).
14. Yoshizawa, A., & Horiuti, K. (1985). A statistically-derived subgrid-scale kinetic energy model for the large-eddy simulation of turbulent flows. *Journal of the Physical Society of Japan, 54,* 2834.
15. Magnussen, B., & Hjertager, B. (1977). On mathematical modeling of turbulent combustion with special emphasis on soot formation and combustion. In *Proceedings of the Combustion Institute* (pp. 719).
16. Vilfayeau, S., White, J., Sunderland, P. B., Marshall, A. W., & Trouvé, A. (2016). Large eddy simulation of flame extinction in a turbulent line fire exposed to air-nitrogen co-flow. *Fire Safety Journal, 86,* 16.
17. Zhou, X., D'Aniello, S. P., & Yu, H.-Z. (2012). Spray characterization measurements of a pendent fire sprinkler. *Fire Safety Journal, 54,* 36.

The Experimental Studies of the Cooking Oil Fire by Water-Mist Fire-Extinguishing System with Additive

Kee-Chiang Chung, Yu-Chia Chen, Wei-Cheng Han and Ming-Yuan Lei

Abstract An experimental program is conducted to investigate the parameters for extinguishing cooking oil fire by water-mist system with additive. The design parameters are dispatch flow rate and charge pressure. Also adding an additive to increase the ability of extinguishing cooking oil fire is validated in the test program. Two different agent percentage water-mist systems are investigated experimentally as well. Finally, the complete quantitative analysis is provided using data from experimental work.

Keywords Cooking oil fire · Water-mist system · Additive

1 Introduction

Cooking oil fires in kitchens are recognized as a difficult to extinguish fire because they are easy to re-ignite. Such kind of fire is different from the conventional flammable liquid fuel fires and has been classified into a new fire class, i.e., Class K. A statistical analysis of fire loss data, as well as the characteristics of cooking oil fires, was presented by Wijayasinghe and Makey [1]. In the paper, prevention and suppression to minimize the incidence of cooking oil fire in Alberta Canada were included. Obviously, to maintain oil temperature below their flash point and thermostatically controlled deep-fat fryers are the best available solution to the cooking oil fires. One interesting paper of comparison of cooking oil with fuel and lubricating oils was proposed by Koseki et al. [2]. It was found that the flame height and flame radiation and burning rate of cooking oil were larger than those that were expected

K.-C. Chung (✉)
Department of Mechanical Engineering, National Yunlin University of Science and Technology, 640 Touliu City, Yunlin, Taiwan
e-mail: chungkc@yuntech.edu.tw

Y.-C. Chen · W.-C. Han
Graduate School of Engineering Science and Technology, National Yunlin University of Science and Technology, 640 Touliu City, Yunlin, Taiwan

M.-Y. Lei
Architecture & Building Research Institute, Ministry of the Interior, 231 New Taipei City, Taiwan

781

from their flash points. Consequently, it was also found that once a fire occurs, the danger of propagation of cooking oil was similar to that of some lubricating oils and fuel oil.

Qin et al. [3] used cone calorimeter on suppressing cooking oil fires with water mist in a small-scale experiment. It is found that an appropriate water mist system may suppress peanut oil fire effectively. However, for the improper design parameters of water mist system may result in producing more carbon monoxide and dark smoke in a kitchen fire. An experimental study of false alarm of fire detectors by cooking fumes is reported by Xie et al. [4]. Four real fire smokes were carried out for comparison with the nuisance cooking fume. Two cooking fumes and four real fire smokes were used to test both photoelectric and ionization detectors. According to the test results, the ionization detector is easier to give nuisance alarms than the photoelectric detector due to the cooking fumes. Also, the humidity may be an important parameter to avoid nuisance alarms in the kitchen fire.

Water has become the most widely used firefighting agent because of its excellent fire suppression performance. The thermal characteristics of water make it suitable as an extinguishing agent for most types of fire. Water can extract heat directly from the flames or from the surface of the fuel to reduce the hot combustion very quickly. During a burning process, water may absorb a significant quantity of heat from flames and fuels due to its high heat capacity and high latent heat of vaporization [5]. In an enclosure fire, the phase change of water may produce large quantities of water vapor and reduce the oxygen concentration of the surrounding atmosphere. Water and water vapor are effective in extracting thermal energy and extinguishing fire [6]. Liu et al. [7] conducted a series of experiments in a full-scale commercial cooking area to understand extinguishing mechanisms and effectiveness of water-mist against cooking oil fires. The water-mist system design parameters for suppression cooking oil fire were investigated, such as spray angle, droplet size, flow rate, discharge pressure, and type of nozzle.

Hsieh et al. [8] undertook a full-scale single water-mist nozzle test to evaluate the fire suppression effectiveness quantitatively. Different water-mist droplet sizes, opening areas, and fire locations were examined using two constant water supply rates in this study. Test results exhibit that water mist was able to quickly control the fires and cool the enclosure, particularly where the fire is confined. An experiment was conducted by Hsu and Chung [9] to study quantitatively the effect of water mist on fire suppression and extinction with additive.

A revolutionary fire-extinguishing foam has been developed and tested in the experimental program. New additive herb formula not only will not corrode metal and is non-toxic to human body. The herb fire-extinguishing agent is an organic and plant-based fire suppression foam that passed PFOS, chlorine, fluorine, and 46 other safety regulation tests, such as LC_{50} and LD_{50} [10]. The indexes of the herb agent used in the tests for LC_{50} and LD_{50} are greater than 100 mg/L and 5000 mg/kg, respectively. In order to study the fire-extinguishing efficiency provided by different water droplet sizes under the same water supply rates, different characteristics of water-mist nozzles were designed and fabricated in their experimental program. In addition to the effects of water droplet size, another important parameter, the

distance of nozzle-to-fuel surface was also used to investigate the fire-extinguishing parameters for a water-mist spray system with additive. However, no reports are found using additive water-mist system to control the cooking oil fire.

2 Cooking Oil Fire Test Program

In order to understand the fire-extinguishing effects and the temperature distribution during the extinguishing process, a complete fire test program is conducted. The fire test program includes temperature data recording at different water-mist pressures and nozzle heights with and without additive. An important evaluation index fire extinguished time is also included in the test. In addition, one innovation is to determine an appropriate fusible links control temperature for the activating mechanism of water-mist system by experimentally.

2.1 Data Logger System

A 120 measured-point data acquisition system was used to record the temperatures from thermocouples. The output micro-voltage needed to be amplified 1000 times in the range of 0.1–1.0 V. Also, one video camera was located on the east wall viewing the fire inside the test room as well as the fire suppression by the water-mist system.

2.2 Fire Source

The design fire depends on the cooking oil purchased from the market. The soybean oil was chosen for the experimental program and the auto-ignition temperature is about 360–380 °C. Five liters of soybean oil was used at each test. These kinds of fires are regarded as a difficult to extinguish K fire.

2.3 Temperature Measurement

The temperature will include the surface oil temperature as well as the temperature in the oil using thermocouples. Thermocouple trees were located above the fire source. The 0.3 mm diameter K-type thermocouples were used to measure the temperature at some specified measured locations T1, T2, T3, and T4. Three measured points (T2, T3, and T4) located at 15 cm, 30 cm, and 45 cm above the test plate and T1 install inside the cooking oil. The K-type thermocouple can measure temperature ranged from 0 to 1450 °C and the uncertainty is ±0.75%.
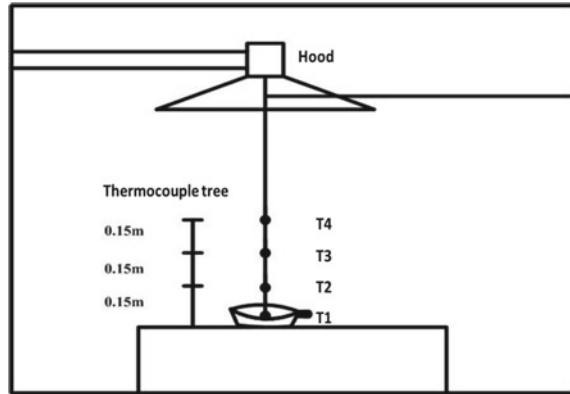
In order to minimize the cooling of the thermocouple by the water mist, allowing the temperature of smoke to be measured, a thin reverse horseshoe-shaped metal shield was installed above thermocouples on T2, T3, and T4 thermocouple measuring point. These metal shields may minimize water from sprinkler reaching the thermocouples directly. All the K-type thermocouples used in the test were wrapped with insulation materials to avoid the damage caused by high temperature. The detailed schematic diagram of the temperature measurement system is illustrated in Fig. 1.

During the test, the nozzle is set at the center of the pan, and the water agent covers all of the area of the fire in the pan. The temperatures are recorded by data logger every second. The 0.7 m is the distance between nozzle and fire source. Three different water discharge pressures (5, 8 and 10 kgw) and three different percentages of additives (0, 10 and 30%) are examined in the experimental program.

3 Results and Discussion

An experimental program is conducted to extinguish cooking oil fire with additive under different control parameters. The different nozzle height, discharge pressure, and percentage of additive are adopted to undertake the tests. Every test uses 5 L of cooking oil purchased from the market. In order to quantitative analysis, the recording temperature data, the water-mist system activates by manual within 15 s after the auto-ignition of cooking oil. Even under the same testing conditions, the times for auto-ignition of cooking oil are not identical to each test. In order to examine cooking oil fire suppression performance by water-mist system, the temperatures above oil pan and fire extinguished time are collected and analyzed.

3.1 Temperature Distribution of Cases with and Without Additive

In order to compare fire-extinguishing ability, the pure water-mist system (0% additive) is tested first. Figure 2 exhibits the temperature distribution for nozzle height
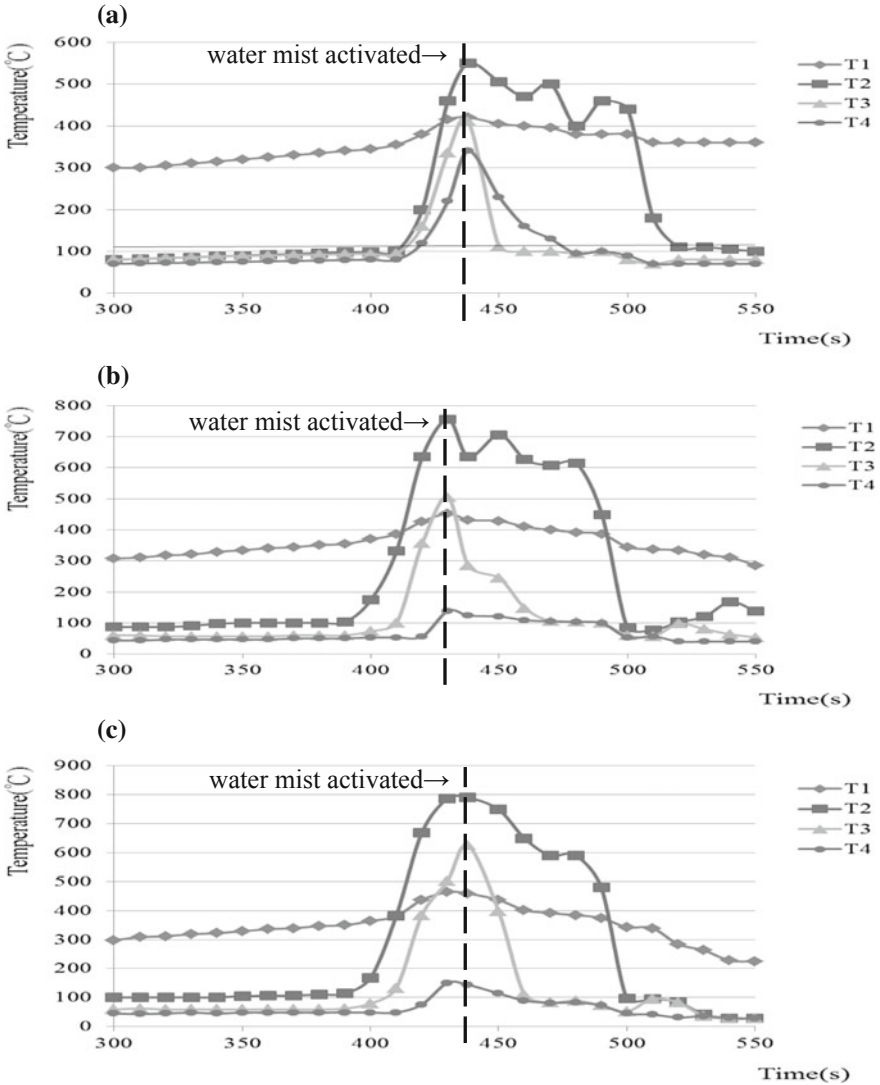
Fig. 2 **a** Temperature distribution of 5 kgw discharge pressure at 0.7 m nozzle height. **b** Temperature distribution for 8 kgw discharge pressure at 0.7 m nozzle height. **c** Temperature distribution of 10 kgw discharge pressure at 0.7 m nozzle height

at 0.7 m without additive cases. Generally, the higher discharge water pressure the lower temperature distribution may be found in Fig. 2. The oil temperature (T1) remains a stable temperature value above 250 °C during the water-mist suppression process. It means that the cooking oil temperature did not decrease even no flame was observed. The air temperature nearest the oil surface T2 will keep in a range of 400–500 °C during the suppression process. The T2 temperature will decrease dramatically when the oil source burns out. Referred to the design conditions and experimental data, pure water-mist system is not able to extinguish the cooking oil fire.

The T2, T3, and T4 temperatures reflect the hot air above the oil surface. T2 has the highest temperature and is over 500 °C, and the temperature may remain relative high temperature during the water-mist activation. However, T3 and T4 temperature will decrease very quickly, as shown in Fig. 2.

An environmental-friendly additive is adopted in the experiments. The non-toxic herbal foam formula will not contaminate the environment as well as human body. Figure 3 shows the temperature distribution using 10% additive in the 0.7 m nozzle height test case. It is found that there are great temperature fluctuations and slower temperature decline at lower discharge pressure value. The temperature measurement points T2, T3, and T4 still has a high temperature when the water mist activated. The lower discharge pressure causes a smaller flow rate and a bigger spray particle in the flame. The smaller spray particles have lower convection and conduction heat transfer in the fire environment, thus, not all of the evaporating droplets absorb heat and part of the water mist is wasted. However, by continuously spraying mist, the flame is extinguished at the end due to low oxygen concentration levels. In the whole process, the temperature curve is divided into three stages. From ignition to water mist activated is the first stage, system discharge water mist is the second stage, and the fire approach to extinguish is the third stage. The highest air temperature is T2. Basically, T2 temperature is greater than T3 and T4.

The temperature profile of T2 in Figs. 2 and 3 demonstrates the significant difference suppression effects with or without additive in water-mist system. The air temperature above oil surface T2 remains a relative high temperature a period of time after cooking oil auto-ignition, as shown in Fig. 2. Conversely, the T2 temperature value decreases quickly after the spray activated as shown in Fig. 3. The test data support that the water-mist system has more efficient fire suppression results with additive.

3.2 Fire Extinguished Time

By increasing the discharge pressure, the ability of water mist to extinguish cooking oil fire significantly enhanced. Additionally, the cooling effect on cooking oil is also significantly improved by water mist. At high discharge pressure, water-mist particles have enough momentum to overcome the flow resistance of the flame and reach the flame zone. At the same time, large droplet evaporation rate causes the
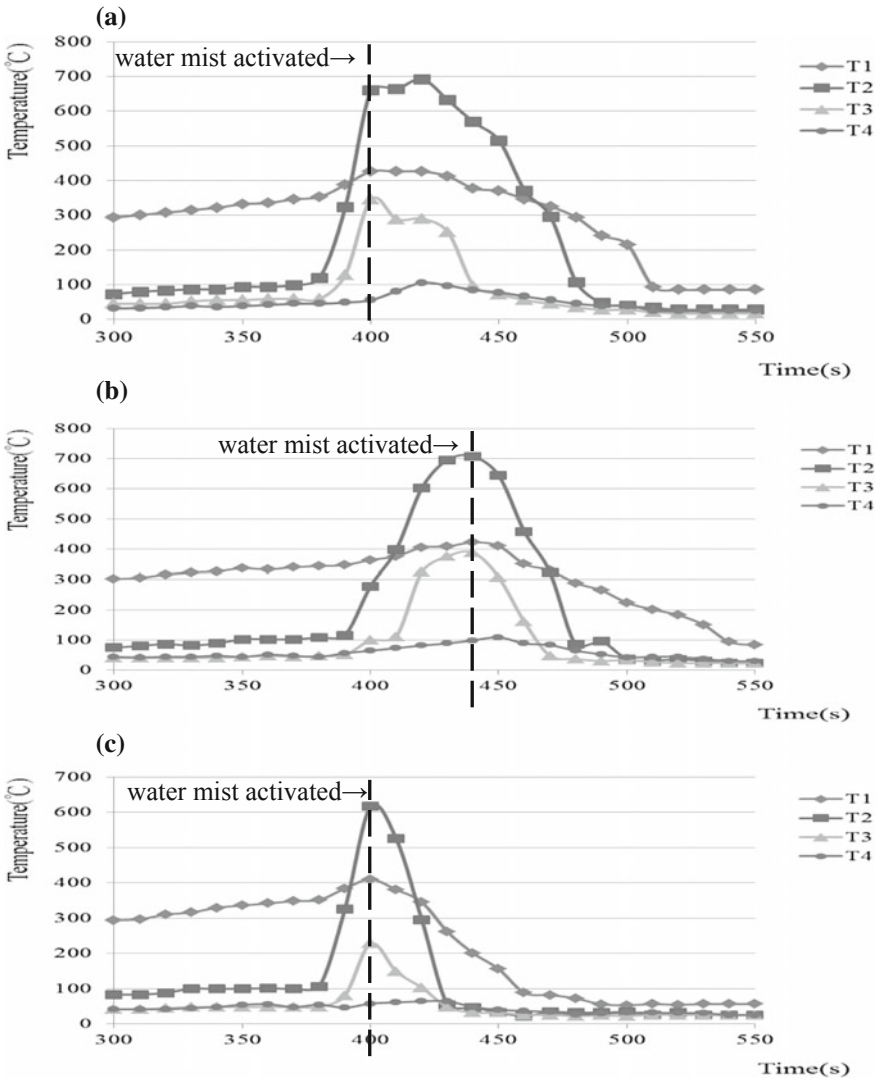
Fig. 3 **a** Temperature distribution for 5 kgw discharge pressure at 0.7 m nozzle height with 10% additive. **b** Temperature distribution for 8 kgw discharge pressure at 0.7 m nozzle height with 10% additive. **c** Temperature distribution for 10 kgw discharge pressure at 0.7 m nozzle height with 10% additive

flame temperature to drop quickly. When the heat from the flame is not sufficient to continue to contribute to the combustion, the flame will be gradually reduced until it goes out.

When the discharge pressure is low, the initial droplet momentum on its own cannot overcome the resistance of the flame and go directly into the flame zone. In the initial stage of water mist, the temperature drop is small at the flame flow area and a strong increase in the absorption capacity. Spray particles in the combustion zone are substantially taken away along with a flame region of the flame; therefore, it cannot play an effective role in extinguishing the flame by cooling the fire.

Water coverage area, water flow rate, and water-mist momentum are three characteristics parameters for extinguishing K class fires. Water mist shall provide enough coverage area to extinguish all flames; otherwise, burning cooking oil flame will continue to supplement the heat to flame. When water-mist system maintains sufficient fluxes, it is easy to cool the temperature of the flame and cooking oil. Eventually, the oil temperature will drop below the point of resurgence. Water-mist droplets have enough momentum to ensure that the droplets penetrate the flame and reaching the surface of the cooking oil flow.

In order to extinguish a cooking oil fire, it is necessary to reduce the size of the fire source and restrict heat from the cooking oil that contributes to the lowest limit of ignition. At the same time, it also needs to use water mist to cool the temperature of the cooking oil to prevent the fire from burning. Unlike other types of fires, during the extinguishing process, the internal temperature of the cooking oil beneath the surface is still much higher than the surface temperature. Although cooking oil itself cannot store energy, it can be treated as heat and energy supplier resulting in the continual of the surface flame. In summary, the use of more cooking oil will result in a more difficult to extinguish fire.

The fire extinguished times for different test cases are listed in Table 1. Three different water-mist discharge pressures and two different additive percentages are compared in the test. Eventually, the greater discharge pressure provides a shorter fire extinguished time. It is an almost 50% time decrease for discharge pressure increased from 5 to 10 kgw/cm^2. Also, the percentage of additive can influence the extinguished time. Thicker additive spray may have better fire-extinguishing effects. However, more verification tests with various additive percentages are needed to be undertaken in order to fully verify the results.

Table 1 Extinguishing time for cooking oil fire tests

	Discharge pressure 5 kgw/cm^2	Discharge pressure 8 kgw/cm^2	Discharge pressure 10 kgw/cm^2
Additive percentage	Nozzle height at 0.7 m		
10%	63 s	45 s	29 s
30%	39 s	23 s	14 s

4 Conclusions

Using water mist to control cooking oil fire is examined experimentally for different parameters. Two important parameters, discharge pressure and percentage of additive, are combined to find appropriate design parameters. As a result, the diameter of the nozzle and water supply pressure are found to have an impact on the water flux. Evidently, the larger diameter nozzle and higher water supply pressure can result in a higher water flux. In fact, it was determined that the water flow rate is proportional to the square root of the water supply pressure as well as to the square of the diameter of the nozzle.

As the pressure increases significantly, shorter cooking oil fire extinguished time by water mist system is needed. The effect is mainly through the cooling surface of the water-mist to extinguish K class fire, but the impact of water mist to destroy the stability roots of combustion is also a major factor. In the process of water, a mist can reduce the flame and quickly drop the temperature of the cooking oil. The lowered temperature of oil surface effectively prevents re-ignition.

Observation of the test results shows that when the cooking oil temperature descends to 250 °C, the flame will be extinguished. The vertical momentum of water particle is greater than the vertical momentum of flame that is a necessary condition for a flame to be extinguished.

Both chemical and physical characteristics affect the cooking oil fire-extinguishing effect and the flame suppression effect significantly. Also, additives viscosity and active ingredients changed the role of the particle size distribution of the water mist and that increased the fire-extinguishing capability quite substantially.

References

1. Wijayasinghe, M. S., & Makey, T. B. (1997). Cooking oil: A home fire hazard in Alberta, Canada. *Fire Technology, 33*(2), 140–166.
2. Koseki, H., et al. (2001). Evaluation of the burning characteristics of vegetable oils in comparison with fuel and lubricating oils. *Journal of Fire Sciences, 19*(1), 31–44.
3. Qin, J., et al. (2004). Experimental study of suppressing cooking oil fire with water mist using a cone calorimeter. *International Journal of Hospitality Management, 23*(5), 545–556.
4. Xie, Q. Y., et al. (2004). Experimental analysis on false alarms of fire detectors by cooking fumes. *Journal of Fire Sciences, 22*(4), 325–337.
5. Voelkert, C. (1998). Out of the frying pan. *Fire Prevention, 314,* 24–26.
6. Grant, G., et al. (2000). Fire suppression by water mists. *Progress in Energy and Combustion Science, 26*(2), 79–130.
7. Liu, Z. G., et al. (2004). Extinguishment of cooking oil fires by water mist fire suppression systems. *Fire Technology, 40*(4), 309–333.
8. Hsieh, T. L., et al. (2006). Characterization of water mist on fire suppression. *JSME International Journal, 49*(2), 490–497.
9. Hsu, S. P., & Chung, K. C. (2005). The effect of additive on the fire extinguishing improvement of water mist spray. *Journal of Applied Fire Sciences, 14*(1), 1–11.
10. Wintime Corporation, Herb fire extinguishing foam, https://www.wintimecorp.com.

Characterization of Typical Fire and Non-fire Aerosols by Polarized Light Scattering for Reliable Optical Smoke Detection

Qixing Zhang, Jia Liu, Jie Luo, Feng Wang, Jinjun Wang and Yongming Zhang

Abstract Optical smoke detector suffers from significantly high false alarm rate caused by nuisance particles. A better knowledge of the optical properties of fire and non-fire aerosols will help to improve the performance of existing detectors. Scattering matrix analysis is a powerful methodology used in polarized light scattering. In this paper, we focused on the extraction of an indicator for discrimination between fire and non-fire aerosols. Numerical simulation of the angular distribution of single scattering matrix element by Lorenz–Mie theory and T-matrix method for smoldering fire smoke and flaming fire smoke, respectively, are presented for comparison with that of typical non-fire aerosols. The sensitivity of normalized scattering matrix element, F_{33}/F_{11}, to particle size distribution is investigated. The value of F_{33}/F_{11} at 160° is proposed as an indicator for discrimination between typical fire and non-fire aerosols. Experimental measurement results for four aerosols, smoldering cotton fire smoke, flaming toluene fire smoke, dust and water droplets, demonstrated the effectiveness of this indicator.

Keywords Fire detection · Smoke detection · Optical properties · Polarized light scattering

Nomenclature

I	Stokes vector
F	Scattering matrix
F	Scattering matrix element
N	Number of primary particles in a fractal aggregate
d	Geometric mean diameter for a lognormal size distribution

Yongming Zhang: deceased

Q. Zhang (✉) · J. Liu · J. Luo · F. Wang · J. Wang
State Key Laboratory of Fire Science, University of Science and Technology of China, 230026 Hefei, China
e-mail: qixing@ustc.edu.cn

Greek symbols

θ Scattering angle
λ Wavelength of incident light
σ Geometric mean standard deviation for a lognormal size distribution

Subscripts

inc   Incident light
sca   Scattered light
i, j Row and column indices in scattering matrix

1   Introduction

Fire detection is important for the protection of life and property when fire occurs. Among various types of fire detectors, photoelectric smoke detector, or namely optical smoke detector, is the most widely used one in state-of-the-art fire protection engineering. As illustrated in Fig. 1, this kind of smoke detector senses the light scattered by the smoke entered into the chamber for fire alarm. The optical smoke detector is widely accepted for its features such as compact, long life, high sensitivity, and low cost. However, it suffers from the high false alarm rate caused by non-fire aerosols, such as dust, steam (water vapor), and cook-generated aerosol, [1].

Many efforts have made to improve the performance of optical smoke detector by academic and industrial researchers. Loepfe et al. [2] built a simple instrument to continuously monitor the polarized scattering cross sections of aerosols from test fires and nuisance. Keller et al. [3] used the diesel particle scatterometer to measure the angular distribution of Mueller scattering matrix elements F_{11}, F_{12}, and F_{34} of particles produced by test fires. They concluded that the simultaneous measurement of several scattering matrix elements can serve a good discrimination
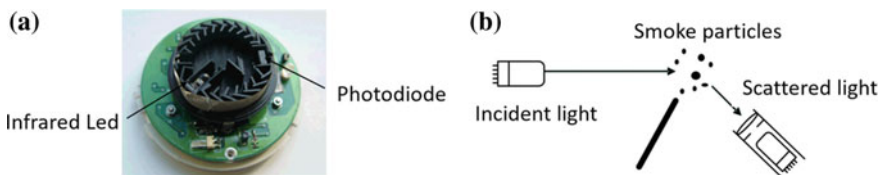
Fig. 1 Illustration of principle of optical smoke detector. **a** Real image of the chamber of a typical commercial optical smoke detector; **b** the illustration to show the interaction of light with smoke particles

criterion for different types of fire (flaming and smoldering fire). Cole [4] used the dual-wavelength light, blue and infrared, to characterize aerosols so as to provide high sensitivity of smoke, while avoiding nuisance alarms from dust and steam. Cleary et al. [5] measured the light-scattering properties of fire smoke and cooking aerosols to assess the performance of currently available smoke alarms. Schultze et al. [6] proposed a polarimetric approach for the distinction between smoke and typical nuisance aerosols. They suggested that a high degree of separation and an accurate estimation of the amount of dust in an aerosol mix of dust and smoke can be achieved.

Aiming to investigate the feasibility and the practicability of polarized light scattering applied in optical smoke detection, our group performed the experimental measurement and numerical simulation study of full scattering matrix elements of typical fire and non-fire aerosols [7]. In this paper, we focused on the extraction of a new polarization indictor, F_{33}/F_{11} at 160°, and its specificity to differentiate fire aerosols from non-fire aerosols. In Sect. 2, the theoretical background of the scattering matrix will be introduced. In Sect. 3, the numerical simulation method and results will be described. The experimental design and results will be presented in Sect. 4. The last section is the conclusion.

2 Theoretical Background

The intensity and polarization state of any beam of quasi-monochromatic light can be fully described by the four parameters of the Stokes vector $\mathbf{I} = [I, Q, U, V]^{\mathrm{T}}$, where the superscript T stands for transpose. Briefly, the Stokes parameters I are the total intensity of the beam. The Stokes parameters Q and U describe the state of linear polarization, while V describes the state of circular polarization of the light. For a collection of randomly oriented particles and in the absence of multiple scattering, light scattering is theoretically described by the transformation of the 4×1 Stokes vector and a 4×4 scattering matrix, as follows [8]:

$$\mathbf{I}_{\mathrm{sca}} = \frac{\lambda^2}{4\pi^2 D^2} \begin{bmatrix} F_{11} & F_{12} & F_{13} & F_{14} \\ F_{12} & F_{22} & F_{23} & F_{24} \\ -F_{13} & -F_{23} & F_{33} & F_{34} \\ F_{14} & F_{24} & -F_{34} & F_{44} \end{bmatrix} \mathbf{I}_{\mathrm{inc}} \tag{1}$$

Here $\mathbf{I}_{\mathrm{inc}}$ and $\mathbf{I}_{\mathrm{sca}}$ is the Stokes vector of the incident and scattered light, respectively. Furthermore, λ is the wavelength of the incident light, and D is the distance between the collection of particles and the detection. The matrix $\mathbf{F}$ with an ensemble of 16 elements $\mathbf{F}_{i,j}$ ($i, j = 1 - 4$) is the scattering matrix. The elements of scattering matrix are functions of scattering angle θ, i.e., the angle between the directions of propagation of the incident and the scattered light. These angle-resolved elements depend on the characteristics of the scattering system, including the number and

physical properties of particles, such as size, structure, and refractive index of the particles.

For the ensemble of randomly oriented particles having a plane of symmetry or having mirror particles in equal numbers, the scattering matrix has the form with six independent parameters [8]:

$$\mathbf{F} = \begin{pmatrix} F_{11}(\theta) & F_{12}(\theta) & 0 & 0 \\ F_{12}(\theta) & F_{22}(\theta) & 0 & 0 \\ 0 & 0 & F_{33}(\theta) & F_{34}(\theta) \\ 0 & 0 & -F_{34}(\theta) & F_{44}(\theta) \end{pmatrix} \tag{2}$$

Among these elements, $F_{11}(\theta)$ is proportional to the flux of the scattered light and is called the phase function. Usually, all elements of the scattering matrix are normalized to $F_{11}(\theta)$, except for $F_{11}(\theta)$ itself. The normalized scattering matrix is irrelevant to the absolute intensity of the scattering light. It depends on the physical and chemical properties of particles excluding concentration of particles after the procedure of normalization.

It is noted that most kinds of environmental aerosol particles can be regarded as an ensemble of randomly oriented particles having mirror particles in equal numbers, so Eq. (2) can be applied, such as dust and smoke particles in this study [3, 9, 10]. $F_{12}(\theta)/F_{11}(\theta)$ and $F_{22}(\theta)/F_{11}(\theta)$ are commonly used in polarized light scattering in previous studies [2, 3, 11]. In this paper, we focused on $F_{33}(\theta)/F_{11}(\theta)$ of typical aerosols for discrimination.

3 Numerical Simulation

3.1 Particle Morphology and Light-Scattering Model

The light-scattering characteristics of particles are generally influenced by morphology, size, and refractive index. Particle morphology is important for light-scattering model selection when the particles size is comparable to the incident wavelength. For optical smoke detection, the wavelength of incident light is usually in the range of near-infrared or visible spectrum. Similarly, most particle diameters are several hundred nanometers to several micrometers. Therefore, the morphology is a key parameter when choosing a light-scattering model for simulation.

Lorenz–Mie theory gives an ideal solution for homogenous spherical particles. Obviously, it is suitable for water droplets. Our previous investigation showed that the smoldering fire smoke particles are spherical, and the light-scattering characteristics can be described well by Lorenz–Mie theory [7]. It is well known that the black

smoke generated by flaming fires are composed of grapy-like aggregates [12]. Fractal aggregate model is developed to describe the morphology of flaming fire smoke [13] (Fig. 2).

From SEM (scanning electron microscopy) image, the dust particles are seemed to be random in morphology with a bigger size than that of smoke particles [10]. Volten et al. [10] measured and modeled the angular distribution of the scattering matrix at two visible wavelengths for representative mineral dust samples in the Earth's atmosphere. Liu et al. [14] measured the complete scattering matrix for cement dust and water droplets as a function of scattering angle from 5° to 160° at a wavelength of 532 nm. The scattering matrix for cement dust and typical natural mineral dusts was found to be similar in trends and angular behaviors. Accordingly, we don't repeat the work for dust and water droplet, and the results presented in literatures [10, 14] are directly used here for comparison.
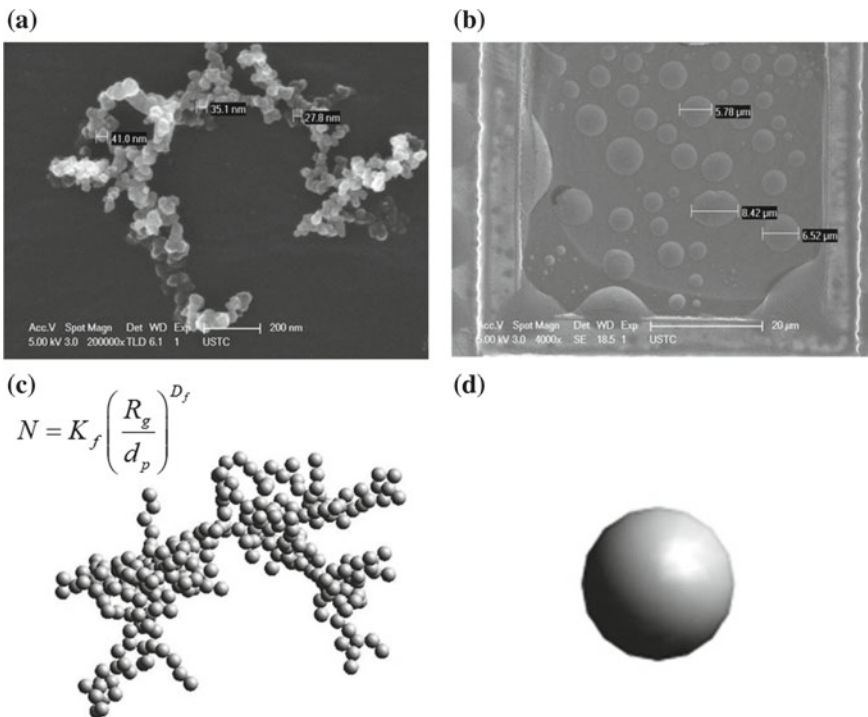
Fig. 2 Illustration of morphology of smoke particles. **a** SEM image of a soot aggregate from flaming n-heptane fire; **b** SEM image of particles from smoldering cotton fire; **c** fractal aggregate model to describe the morphology of particles from flaming fire; **d** spherical model to describe the morphology of particles from smoldering fire

3.2   Simulation Results

Lorenz–Mie calculation results of $F_{33}(\theta)/F_{11}(\theta)$ at 532 nm for smoldering fire smoke particles with a lognormal size distribution is shown in Fig. 3a. The values of geometric mean diameter d, and geometric standard deviation σ, are set according to SMPS measurement results in the literature [3]. Furthermore, sensitivity of $F_{33}(\theta)/F_{11}(\theta)$ to size distribution parameters is also investigated and presented in Fig. 3a. It is shown that the value of $F_{33}(\theta)/F_{11}(\theta)$ at forward and backward scattering angles keep constant when the size distribution parameters vary.

T-matrix method is applied to calculate the light-scattering characteristics of flaming fire smoke. Due to the relatively huge computational cost of T-matrix calculation for fractal aggregate, we only calculate the light scattering of a single particle, not ensembles of particles with polydispersed size distribution. The morphological parameters are set according to SEM measurement results in the literature [12]. The effect of size distribution on the $F_{33}(\theta)/F_{11}(\theta)$ is investigated by variation of N, the number of primary particles, representing the different size of aggregates. It can be observed from Fig. 3b that the size of flaming fire smoke particles has a negligible influence on the $F_{33}(\theta)/F_{11}(\theta)$ at full scattering angles.

As mentioned in Sect. 3.1, the work of Volten et al. [10] and Liu [14] has studied the scattering matrix elements of water droplets and dust particles. We reprint the experimental measurement results of $F_{33}(\theta)/F_{11}(\theta)$ for these two aerosols in Fig. 4. Combined with Figs. 3 and 4, the F_{33}/F_{11} at 160° is extracted as an indicator for differentiation of the four candidate aerosols. We will verify this indicator by experimental measurement in the next section.
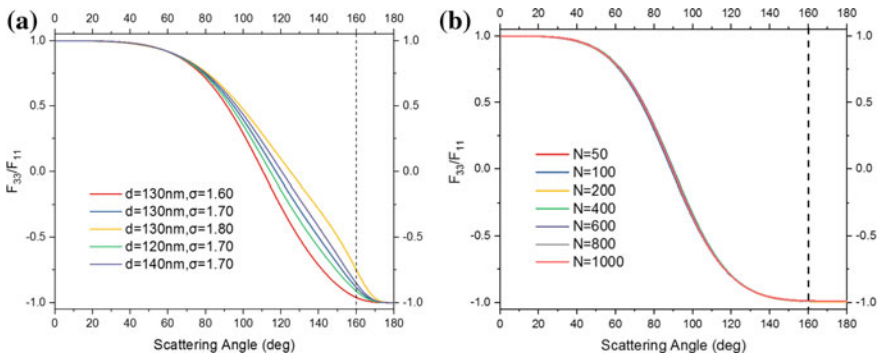
Fig. 3 Simulation results of **a** Lorenz–Mie calculation for different collections of spherical particles obeying lognormal distribution representing smoldering fire aerosol, refractive index $n_s = 1.49 + 0.01i$, incident wavelength $\lambda = 532$ nm; **b** T-matrix calculation for single fractal aggregate representing flaming fire aerosol, fractal dimension $D_f = 1.85$, fractal prefactor $k_f = 1.2$, diameter of monomer sphere $d_p = 30$ nm, refractive index $n_f = 1.57 + 0.56i$, incident wavelength $\lambda = 532$ nm
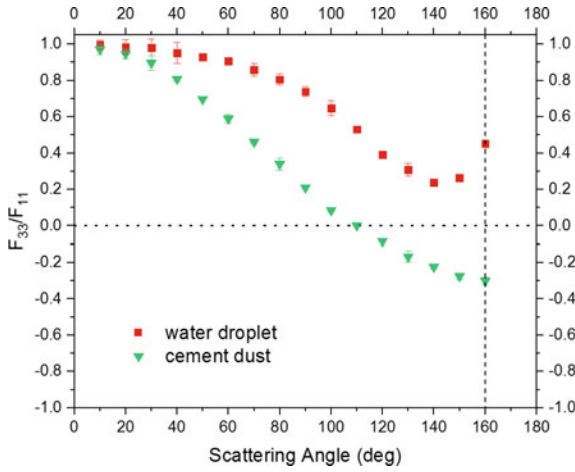
Fig. 4 Reprint of experimental measurement results of water droplet and cement dust given in Ref. [14] for illustration of F_{33}/F_{11} at 160° as an indicator

4 Experimental Measurement

4.1 Scattering Matrix Measurement Setup

The basis of our technique to determine the scattering matrix is the modulation of polarization of the incident light. A schematic illustration of the experimental setup is depicted in Fig. 5. A diode laser with a wavelength of 532 nm was used as a
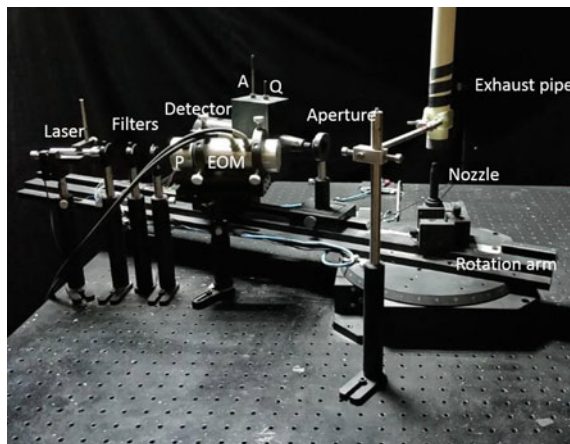
Fig. 5 Schematic diagram of scattering matrix measurement setup, the detector on the scan arm is fixed at 160°

light source. Light from the laser passed through a Glan-Thompson polarizer firstly, and then through an electro-optic modulator before illuminating the smoke particles contained in a jet streaming out from a nozzle.

A photomultiplier tubes (PMTs) mounted at the rotation arm was used as the detector. The dc component, first harmonic, and second harmonic components of the detector output were related to scattering matrix elements with configurations of the quarter-wave plate and the polarizer. A more detailed description of the setup and measurement principle is referred to [9].

In normal operation mode, the detectors scan from $10°$ to $160°$ to measure the angular distribution of scattering matrix elements. Usually, it needs several minutes to complete one scan. The size distribution of particle flow should keep steady during one scan, only the variation of concentration can be normalized by normalization to $F_{11}(\theta)$. However, the size distribution of smoke particles produced by test fires varied quickly, the time resolution of scanning mode is inadequate for time-induced fluctuations. Therefore, the detector is fixed at $160°$ to measure the normalized matrix element, F_{33}/F_{11}, of four kinds of aerosols.

4.2 Generation of Fire and Non-fire Aerosols

Smoldering cotton fire smoke, flaming toluene fire smoke, water droplet, and cement dust are selected to represent the typical fire and non-fire aerosols (Fig. 6). Water droplets stream is produced by an atomizer aerosol generator (ATM-226, Topas GmbH) using pure water. Cement dust stream is generated by a commercial particle disperser (RBG 1000, Palas). Portland cement standard samples, obtained from the National Quality Supervision and Testing Center for Cement, are loaded into the powder reservoir with an inner diameter of 14 mm. A piston pushes dust onto a
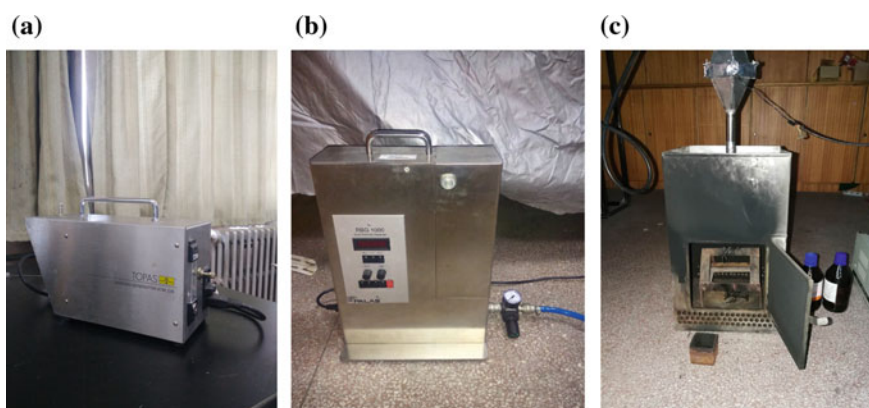
Fig. 6 Real image of apparatus for generation of **a** water droplet, ATM-226; **b** cement dust, RBG 1000; **c** fire smoke, homemade combustion chamber

rotating brush at a certain speed of 65 mm/h, and then cement dust particles are carried out of the generator by the pressurized particle-free air stream. Aerosols are transported through an antistatic hose to reduce the loss of samples, before streaming out from the nozzle with a 3 mm inner diameter. After interacting with the beam of the incident light, test aerosols are discharged through the exhaust pipe.

Smoldering cotton fire is a test fire specified in EN54 [15]. The small-scale setup is used in this study; two cotton wicks are ignited and smolder in a cubic chamber with length 30 cm. The toluene was burned in a 5 cm square pan with edge height 4 cm in the same chamber used for smoldering cotton fire. The toluene is used for the high emission rate of smoke; therefore, a small pan fire can produce enough smoke for measurement.

4.3 Experimental Results and Discussion

Considering the generation method of test samples, the flow of water droplets and cement dust is believed to be stable. We only check the time-dependent variation of aerosols generated by test fire. The fire ignited at zero second; it costs several seconds to transport the smoke to the nozzle. Before 60 s, the variation of the value is mostly due to the small signal caused by limited amount of smoke at the beginning. Therefore, it is reasonable to neglect the measurement results before 60 s until the amount of smoke is enough for efficient data processing. It can be observed from Fig. 7a that the value of F_{33}/F_{11} at 160° is varied around 0.8 due to the fluctuation of smoke flow. It is to be noted that the fluctuation of normalized scattering matrix element, F_{33}/F_{11}, is due to the variation of size distribution, not the concentration. It is also shown in Fig. 7a that the curve of flaming toluene fire smoke is more stable than that of smoldering cotton fire smoke. This is consistent with the prediction of simulation results. The value of F_{33}/F_{11} at 160° is more sensitive to size distribution
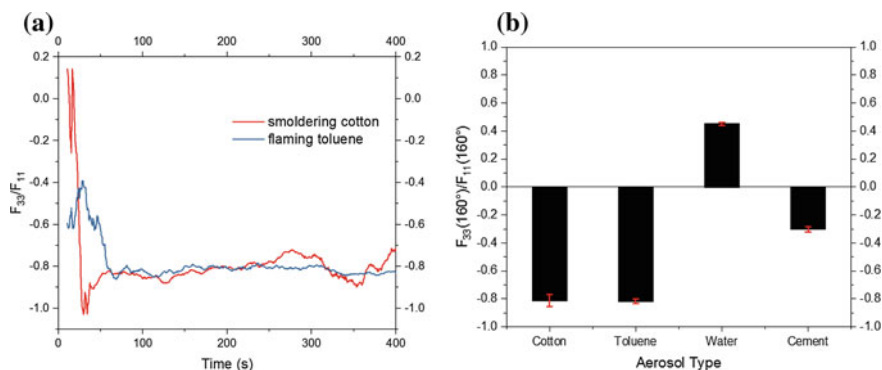
Fig. 7 **a** Time dependent of the value of F_{33}/F_{11} at 160° for smoldering cotton and flaming toluene fire smoke; **b** the average value of F_{33}/F_{11} at 160° for four typical fire and non-fire aerosols

of smoldering fire smoke than that of flaming fire smoke. Nevertheless, the maximum value of F_{33}/F_{11} at 160° of smoldering cotton fire smoke is below -0.7. In contrast, the typical value of F_{33}/F_{11} at 160° for water droplet and dust are 0.45 and -0.3, respectively. As shown in Fig. 7b, it is easy to distinguish the two non-fire aerosols from two fire aerosols by the value of F_{33}/F_{11} at 160°. Moreover, the calculation is succeeded to guide the extraction of this indicator and helps to explain the measurement results. Toward the application in optical smoke detector design, more real fire smoke tests should be conducted further to verify the reliability of this indicator.

5 Conclusion

A better knowledge of the properties of the aerosol particles originating from fires and non-fire sources will help to improve the performance of existing detectors, reduce the amount of false alarms, and serve as a guideline in the development of new measuring techniques. Here, we present a study of single scattering matrix element for four typical fire and non-fire aerosols combined with numerical simulation and experimental measurement. The value of F_{33}/F_{11} at 160° is proposed as an indicator for discrimination between typical fire and non-fire aerosols by numerical simulation. Experimental measurement results for four aerosols, smoldering cotton fire smoke, flaming toluene fire smoke, and dust and water droplets demonstrated the effectiveness of this indicator. The focus here has been on the method for the extraction of indicator combined with numerical simulation and experimental measurement. More real fire and nuisance tests are needed before application in optical smoke design by the indicator proposed here, and this will be done in a latter study.

References

1. Festag, S. (2016). False alarm ratio of fire detection and fire alarm systems in Germany—A meta analysis. *Fire Safety Journal, 79,* 119.
2. Loepfe, M., Ryser, P., Tompkin, C., & Wieser, D. (1997). Optical properties of fire and non-fire aerosols. *Fire Safety Journal, 29,* 185.
3. Keller, A., Loepfe, M., Nebiker, P., Pleisch, R., & Burtscher, H. (2006). On-line determination of the optical properties of particles produced by test fires. *Fire Safety Journal, 41,* 266.
4. Cole, M. (2009). *Aerosol characterization for reliable ASD operation*. In *AUBE'09*. Duisburg, Germany, paper #S04P01.
5. Cleary, T., & Mensch, A. (2017). Polarized light scattering of smoke sources and cooking aerosols. In *AUBE'17*. Maryland, USA, paper #S04P01.

6. Schultze, T., Marcius, L., Krull, W., & Willms, I. (2017). Polarized light scattering analyses for aerosol classification. In *AUBE'17*. Maryland, USA, paper #S04P02.

7. Zhang, Q., Li, Y., Deng, X., & Zhang, Y. (2011). Experimental determination of scattering matrix of fire smoke particles at 532 nm. *Acta Physica Sinica, 60,* 84216.

8. Mishchenko, M., Hovenier, J., & Travis, L. (2000). *Light scattering by nonspherical particles: Theory, measurements, and applications*. San Diego, USA: Academic Press.

9. Zhang, Q., Qiao, L., Wang, J., Fang, J., & Zhang Y. (2009). A polarization-modulated multi-channel Mueller-matrix scatterometer for smoke particle characterization. In: *Proceedings of SPIE* (pp. 75110M).

10. Volten, H., Munoz, O., Rol, E., Haan, J., Vassen, W., & Hovenier, J. (2001). Scattering matrices of mineral aerosol particles at 441.6 nm and 632.8 nm. *Journal of Geophysical Research, 106*, 17375.

11. Hull, P., Shepherd, I., & Hunt, A. (2004). Modelling light scattering from diesel soot particles. *Applied Optics, 43,* 3433.

12. Zhang, Q., Qiao, L., Wang, J., Fang, J., & Zhang, Y. (2009). Characteristics of light scattering by smoke particles produced in test fires based on fractal aggregate shape model. In *AUBE'09*. Duisburg, Germany, paper #S04P03.

13. Koylu, U., & Faeth, G. (1992). Structure of overfire Soot in Buoyant Turbulent diffusion flames at long residence times. *Combustion and Flame, 89,* 140.

14. Liu, J., Zhang, Y., Zhang, Q., & Wang, J. (2018). Scattering matrix of typical urban anthropogenic origin cement dust and the discrimination of representative atmospheric particulates. *Journal of Geophysical Research: Atmospheres, 27,* 3159.

15. European Committee for Standardization. (2003). *Fire detection and alarm systems-Part 7*. London: HIS Press.

A Study on the Application of Automatic Sprinkler Systems in AS/RS Warehouses in Taiwan

Pin-Ping Hsieh, Tzu-Sheng Shen, San-Ping Ho, Yu-Jen Chen, Hue-Pei Chang and Ming-Yuan Lei

Abstract The development of the logistics industry in Taiwan will continue to prosper nowadays and beyond. In order to save more human power while improving transportation effectiveness, the introduction of AS/RS to the storage warehouse has become a trend. It is wildly known that AS/RS warehouse has the characteristic of high risk on fire occurrence. Merely general specifications were presented in Taiwan's code for the design of fire protection systems—the Standards for Installation of Fire Safety Systems Based on Use and Occupancy. Through literature review and fire scenario analyses in warehouse, we can realize that although the automatic sprinkler system activated confidently during a fire, the damage still happened. In this paper, sprinkler design situations of four typical AS/RS storage warehouses in Taiwan were investigated. Finally, compared to the literature review from each warehouse, the analysis of rack sprinkler configuration pros and cons were made. Meanwhile, some conclusions of sprinkler design were also provided for AHJ.

Keywords Automated storage and retrieval System (AS/RS) · Automatic Sprinkler Systems · Warehouse storages

P.-P. Hsieh (✉) · T.-S. Shen
Graduate School of Fire Science and Technology, Central Police University,
Taoyuan City 33304, Taiwan (ROC)
e-mail: apple001423@gmail.com

S.-P. Ho · H.-P. Chang
Department of Occupational Safety and Health, Chang Jung Christian University,
Tainan 71101, Taiwan (ROC)

Y.-J. Chen
Graduate School of Engineering Science and Technology, National Yunlin University of Science and Technology (YunTech), Douliou 64002, Yunlin, Taiwan

M.-Y. Lei
Department of Architecture and Building Research Institute,
New Taipei City 23143, Taiwan (ROC)

1 Preface

The logistic industry has become more and more popular in accordance with the speeding development of domestic economic industry, and the diversity to the demand of daily supports. In order to satisfy the substantial demand of commodity provision, to save the cost of human power, and to establish a smooth and safety distribution method, the factories tend to enlarge their storage space by extending the rack storage configuration deeper and higher. Recently, the introduction of automatic system and retrieval system (ASRS) to store and distribute commodities leads to the convenience with regard to the simple operation from the remote computers. Commodities stored with the high density represent potential fire hazards when there is no competent fire protection system of correspondence.

In article 17 of Standards for Installation of Fire Safety Equipment Based on Use and Occupancy in Taiwan, a warehouse should install automatic sprinkler system where its story height is more than 10 m and its floor area is more than 700 m square. However, there are no technical details or specifications mentioned anywhere on the above regulation, but merely general information. For example, neither storage type categories nor commodity characteristic classifications are present in the regulation. This research relies on the experience of site investigation among the four representative AS/RS storage warehouses in Taiwan. The tremendous divergence of operation process discovers from each AS/RS warehouse result in different form and scale of rack storage configuration with different features of commodities. With regard to the combustion process and literature review, the critical factor of affecting fire growth and the spread of flame derives from the classification of commodities stored in the racks. Instead of comprehensive commodity classification specified in NFPA 13, the Standard for Installation of Fire Safety Equipment Based on Use and Occupancy stipulates merely two categories of commodity classifications, which are inflammable materials (cotton, plastic, wood, and textile material) and other materials. The great deficiency on commodity classification results in the ignorance of the potential fire hazards, which would eventually evolve into a severe fire consequence, not to mention the necessity of competent fire suppression system installed. An attempt to conclude by regulation phases and on-site investigation review, the obedience to comply with rack storage configuration regulations leads to the incapability of competing the variety and complicated up-to-date industrial development. This study will integrate both domestic and foreign regulations with on-site investigation outcomes, which would finally behave as a blueprint for the future design of the rack storage warehouses configurations.

2   Literature Review

2.1   *Characteristic of the Warehouse Fire Behavior*

The definition describes "rack storage" in s Handbook published by NFPA refers to any combination of vertical, horizontal, and diagonal that supports stored materials. Examples of the types of racks covered in this standard are as follows:

- Double-Row racks. Pallets rest on two beams parallel to the aisle. Any number of pallets can be supported by one pair of beams.
- Automatic Storage Type Rack. The pallet is supported by two rails running perpendicular to the aisle.
- Multiple Row Racks. These racks include drive-in racks, drive-through racks, portable racks arranged in the same manner, and conventional or automatic racks with aisles less than 42 in. (1.1 m) wide.
- Movable Racks. Movable racks are racks on fixed rails or guides, and they can be moved back and forth only in a horizontal, two-dimensional plane. A moving aisle is created as abutting racks which is either loaded or unloaded, then moved across the aisle to abut other racks.
- Cantilever Racks. The load is supported on arms that extend horizontally from columns. The load can rest on the arms or on shelves supported by the arms.

Different rack type layout leads to different rack height, row depth, and the amount to store the commodities in. Once a fire happened, it will definitely result in various fire scenarios, requiring different capacity of fire-fighting force. Besides, the hose demand and the water supply duration used to suppress the fire are judged from the warehouse fire potential hazards, which can be inferred from the commodity density, ignition temperature, burning rate, and heat release rate. Therefore, in order to completely protect the rack storage from a fire, the understanding of rack storage fire characteristic is regarded as a fundamental task.

Followings are some reviews from fire science and fire case studies, analyzing the factors that could potentially cause rack storage fire.

- Commodities are stored vertically which present the same direction with fire growth, accelerating the spreading of flame.
- The spaces between rows of the storages (longitudinal/transverse flue space) provide the oxygen necessary for the burning, meanwhile, for the sake of fire detection. It is also the position to install fire suppression system.
- Some of the tin houses were used as warehouse storages whose exterior walls do not have enough time-rating, at the same time, with insufficient compartment areas inside the warehouse storages.
- The warehouses retain only single exit and lack of ventilation systems. When breaking out of fire, the interaction between smoke accumulation and the visibility decline can lead to frustration in the fire-fighting operation.

- A typical rack storage arrangement is its tier height and row depth not accessible for hose station connections, fire-fighting operations, or periodical maintenance.
- Some of the commodities in logistics warehouses had to be stored with confidentially agreements. Therefore, the custodian will not be able to know the material of commodities and their potential fire risks.
- Even though the commodities were non-combustible materials, yet encapsulated with plastic packages or loaded on plastic pallets were still regarded as equivalent hazard approved.
- During the operation to trays and storage container by carousel or conveyer through computer instructions, the potential overheated motor, lubricating oil at flash point and overloaded electrical facilities, should all take into considerations.

With the above warehouse features analysis, they might potentially have higher fire risks compared with other general areas. Once they burst into flames, both fire suppression systems and fire brigade fire-fighting operations are difficult to control the fires. Followings are case studies of some major fire accidents, which cannot only correspond to the rack storage fire behavior mentioned above, but also understand the different reasons of fire ignition, fire spreading process, and the activation of automatic sprinkler systems during the fire. In addition, the case studies also sum up the key criteria of our future work for on-site investigation. Finally, by comparing the domestic regulation, Standard for Installation of Fire Safety Equipment Based on Use and Occupancy, with the National Fire Protection Association (NFPA) codes and standards from the USA, we can have a complete and comprehensive understanding to determine the potential automatic sprinkler protection options for the given AS/RS storage arrangements.

2.2 Case Studies of Major Fire Accidents in Storage Warehouses

There are 10 case studies of major fire accidents shown in Table 1, including domestic and foreign fire cases.

2.3 General Information of Fire Safety Prevention in Storage Warehouse

According to the fire cases mentioned above, sprinkler conditions can be classified into four categories: operated and effective, operated ineffectively, failed to operate, and no sprinkler presence. Those can be expressed as follows:

Table 1 Ten case studies of major fire accidents

Date and location	Caused	Sprinkler presence
1995.11.18 Saitama ken, Japan	Canned factory logistics warehouse fire kills 3	Y
2016.12.2 California, USA 2017.2.16 Saitama ken, Japan 2017.4.1 New Taipei city, ROC 2017.5.22 New Taipei city, ROC	Oakland's ghost ship warehouse fire kills 36 ASKUL stationery warehouse fire damages 45,000 m^2 Plastic canvas warehouse factory fire, no injury reported An industrial dye factory fire, no one injured	N Y Y N
2017.6.8 Kowloon, Hong Kong 2017.6.9 Changhua, ROC 2017.7.5 Pintung, ROC 2017.7.22 Washington, USA 2017.7.25 Texas, USA	Restaurant storage building damaged after a fire A Styrofoam factory fire damaged 662 m^2 Plastic pallets factory fire damaged 9916 m^2 Granite Falls warehouse fire, no injury reported Fire was contained to a storage room in Irving mall	Y N N Y (failed to operate) Y

- Informed by foreign warehouses fire cases, which often took sprinkler's operation effectiveness into the consideration of the fire service efficiency. The implementation of sprinklers in foreign countries is regarded as a common practice for the reasons such as the owner has higher fire prevention awareness, an insurance issue, the extended jurisdiction takes longer time for the arriving of fire service, law enforcement by the authorities…etc.
- Most domestic warehouse fire cases do not refer to the role of sprinklers in fire attack situations. Case studies show half of the structures destroyed by fire were tin houses. It means that the owner has to lease the warehouse from the landlord by a temporary contract, which leads to the unwilling of both sides to install the fire protection systems.
- Moreover, the existence of illegal warehouses (not noticed by the government) results in a potential fire risk. Those building material, which they often apply for construction, is unlikely to retain enough fire resistance.
- In addition, the statistics from National Fire Agency show the average time of fire force to arrive fire scene takes only 5 min in Taiwan. On the other hand, a well-trained employee could be able to extinguish the initial fire before the actuation of automatic sprinkler systems and prevent from fire spreading.
- For the sake of clarifying the reason why buildings installed automatic sprinkler systems activated confidently during the fire, but they still have great damages in their properties, this study integrates the on-site investigation information into comparison and makes code suggestions, expecting to reinforce the protective capability of automatic sprinkler systems as a future work.

3   Site Investigation and Questions Discussions of AS/RS in Taiwan

3.1   Site Investigation Comparison Results of AS/RS in Taiwan

In order to clarify the mechanism of sprinkler operated ineffectively in the automatic storage retrieval system (AS/RS) in this paper, sprinkler design situations of four typical AS/RS storage warehouses in Taiwan were investigated and evaluated. Comparing the differences within sprinkler installation parameters concludes that the severity of fire hazard depends on the properties of commodities stored in the warehouses. Table 2 shows the on-site conditions from different factories installing the AS/RS (Fig. 1).

Table 2 On-site conditions from different factories installing the AS/RS

Object	Column A (t)	Column B (T)	Column B (T)	Column B (T)
Location	Taoyuan	Taoyuan	Kaohsiung	Kaohsiung
Visit time	106.5.12	106.5.2	106.5.5	106.5.27
AS/RS supplier	DEMATIC	TECH-A-WISE GROUP	TECH-A-WISE GROUP	FORMOSA HEAVY INDUSTRIES CORP.
Rack size ($L * W * H$)	54.2 * 14.2 * 37	54 * 7 * 20	97.32 * 13.5 * 30.6	125 * 46 * 29
Rack component	2 single-row, 1 double-row	2 single-row, 1 double-row	2 single-row, 1 double-row	2 double-row, 5 multiple row
Aisle width	1.74 m	1.5 m	1.4 m	1.8 m
Commodities	Class 1–4 commodities (corrugated packaging)	Class 1 commodities (corrugated packaging)	Group A plastic (corrugated/plastic packaging)	Group A plastic (plastic packaging)
Commodities height	1.5 m	1.5 m	2.1 m	2.55 m
In-rack sprinkler specification	Wet pipe sprinkler system (heat collector)	Wet pipe sprinkler system (heat collector)	Wet pipe sprinkler system (heat collector)	Wet pipe sprinkler system (heat collector)
In-rack sprinkler spacing	Vertical spacing: 3 m, horizontal spacing: 2.5 m	Vertical spacing: 3.5 m, horizontal spacing: 2.5 m	Vertical spacing: 3.2 m, horizontal spacing: 2.5 m	Vertical spacing: 2.4 m, horizontal spacing: 2.5 m

Table 2 (continued)

Object	Column A (t)	Column B (T)	Column B (T)	Column B (T)
In-rack sprinkler actuation/K-factor	70°C/K = 114 (quick-response type sprinklers)	70°C/K = 114 (quick-response type sprinklers)	70°C/K = 114 (quick-response type sprinklers)	70°C/K = 114 (quick-response type sprinklers)
Ceiling sprinkler specification	Wet pipe sprinkler system (heat collector)	Wet pipe sprinkler system (heat collector)	Wet pipe sprinkler system (heat collector)	Wet pipe sprinkler system (heat collector)
Ceiling sprinkler spacing	Horizontal spacing: 2.1 m	Horizontal spacing: 2.1 m	Horizontal spacing: 2.1 m	Horizontal spacing: 2.1 m
Ceiling sprinkler actuation/K-factor	70°C/K = 114 (quick-response type sprinklers)	70°C/K = 114 (quick-response type sprinklers)	70°C/K = 114 (quick-response type sprinklers)	70°C/K = 114 (quick-response type sprinklers)
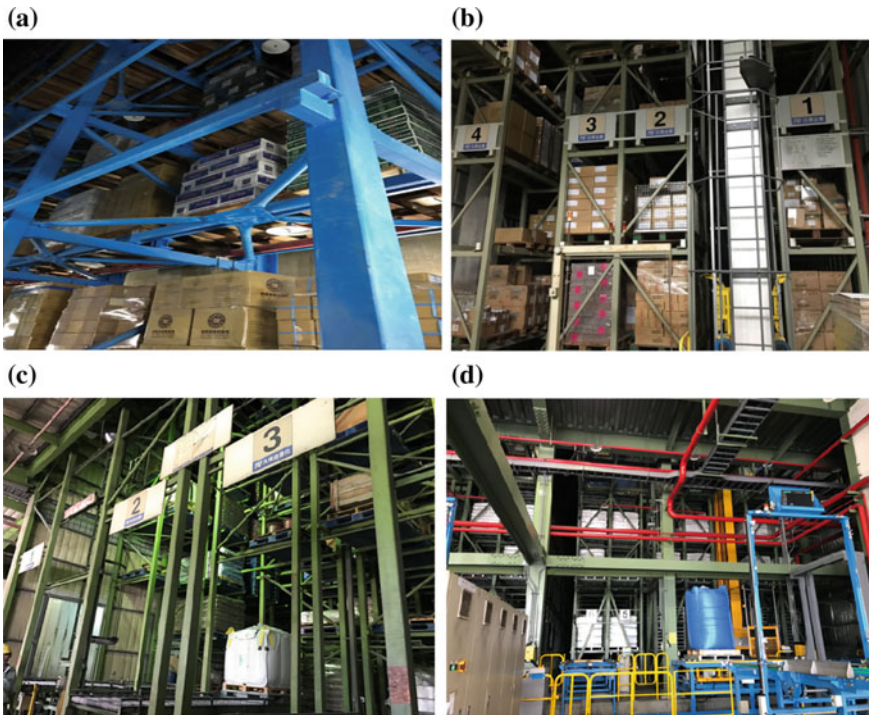
Fig. 1 Site investigation of AS/RS facilities: **a** CP Catering service. **b** C Logistics. **c** CC Group. **d** AP Corporation

3.2 Discussions and Conclusions for AS/RS on-Site Investigation in Taiwan

There are three main AS/RS suppliers in Taiwan: DEMATIC (Germany), TECH-A-WISE GROUP (Japan), and FORMOSA HEAVY INDUSTRIES CORP. (Taiwan). The TECH-A-WISE GROUP produces mostly small-scale AS/RS facilities while FORMOSA HEAVY INDUSTRIES CORP. can be associated with large-scale AS/RS facilities. Table 4 shows the on-site AS/RS investigation results.

4 Discrepancy Comparison Between Standard for Installation of Fire Safety Equipment Based on Use and Occupancy and NFPA Codes

Domestic legislation-Standard for Installation of Fire Safety Equipment Based on Use and Occupancy inclines to have simpler and more general installation requirement when compared with NFPA codes. First, the categories of different rack storage arrangements were not provided in the regulation. When it burst into flames, the flue spaces between rack storages provide the air to entrain while accelerating the spread of flame. Second, the sprinkler installation position should be within longitudinal and transverse flue spaces so as to initial-stage detection and suppression. Third, the discovery of literature review and warehouse fire cases can demonstrate the divergence of manufacture process and logistic characteristic that affect the warehouse fire scenarios tremendously. In addition, the fire scale and fire spreading derived from commodity categories, commodity heat release rates, and fire loads. To study precisely from NFPA codes, it shows the flammability rating of package material is one of the primary factors to affect fire scenarios in storage warehouses. In the conclusion, all the potential conditions mentioned above shall be taken into consideration as the references to analyze the fire risks in storage warehouses. Table 3 shows the sprinkler installation discrepancy between Standard for Installation of Fire Safety Equipment Based on Use and Occupancy and NFPA codes (Table 4).

5 Conclusions and Future Work

5.1 On-Site AS/RS Investigation Discoveries as Follows

- Commodities classification should consider pallet types, since different types of pallets have significant influence on fire scenarios.
- The commodities have not been encapsulated or wrapped in plastic. That may lead to the free-flowing plastic material to create a smothering effect on the fire.

Table 3 On-site AS/RS investigation results

Rack size, component, aisle width	• According to the regulation: Standard for the Installation of Fire Safety Equipment Based on Use and Occupancy, which reveals the storage area over 700 m^2 and higher than 10 m shall install automatic sprinkler system • The ratio of area to height of the on-site AS/RS are as follows (area/height): CP (769.64/37), C (378/20), CC (1313.82/30.6), and AP (5750/29) • The AS/RS in C has not achieved the standard requirements to install the automatic sprinkler system (total area below 700 m^2), but still install automatic sprinkler system to protect their properties • The heights of AS/RS in CP and CC are far higher than 10 m of the criteria stipulated in the regulation • We can summarize that a simple specification requirement of automatic sprinkler system installation criteria is not able to cope with the diversity of AS/RS configuration due to the huge geometry discrepancies
Commodities	• The Standard for the Installation of Fire Safety Equipment Based on Use and Occupancy has defined the commodities into two categories: "combustibles" and "the others" • Both CC and AP stored combustible material (PE, EVA), while CP and C stored other standard commodities (food, glasses) • The feature of the burning commodities depending on the materials and packaging of the objects shall be taken into consideration
Pallets types	• There are three types of pallets: wood, plastic, and metal, which are constructed by various reinforced and non-reinforced material • Commodities stored in CP are loaded on wood pallets, while C utilized two types of pallet depending on the weight of commodities. CC has each of their commodities loaded on double-pallets bundled for stabilization. AP tends to palletize with metal pallet for AS/RS, while wood pallets are for outside temporarily loading • The effect on the commodity classification of various type pallets exhibiting different fire characteristics requires consideration • As a result, the type of pallets shall be assumed in the classification of commodities
In-rack sprinklers specification, spacing, actuation temperature, and K-factor	• By the investigation of the 4 AS/RS, all installed wet pipe pendent sprinklers with heat collectors • The ratio toward vertical and horizontal spacing of the 4 AS/RS are listed, respectively, as follows: CP (3/2.5), C (3.5/2.5), CC (3.2/2.5), AP (2.4/2.5), corresponding to the criteria of standard for the installation of fire safety equipment based on use and occupancy • Actuation temperature is 70 °C and K-factor is 114 for the 4 AS/RS
Ceiling sprinklers specification, spacing, actuation temperature, and K-factor	• AS/RS ceiling sprinkler spacing 2.1 m is identical to the regulation of Standard for the Installation of Fire Safety Equipment Based on Use and Occupancy • Wet pipe pendent sprinkler is adopted by the four AS/RS
Heat collectors	• All AS/RS installed heat collectors • Whether the heat collector can exert its function during a fire shall be demonstrated by simulations and experiments

Table 4 Installation discrepancy of automatic sprinkler system between Standard for Installation of Fire Safety Equipment Based on Use and Occupancy and NFPA codes

Item	Standard for Installation of Fire Safety Equipment Based on Use and Occupancy	NFPA codes
Scope	• The story height is more than 10 m • The total floor area is more than 700 m^2	• NFPA 13 is an installation standard and does not specify the buildings or structures that require sprinkler systems • The administrative authority for requiring sprinklers within buildings rests with any of the following: the local building code, NFPA 5000®, NFPA 101®, International Building Code, or insurance regulations that typically specify the buildings and structures that require sprinkler systems
Commodity (occupancy) classification	N/A	• The classification of commodity is the first major decision that is made in the design of sprinkler system • The proper occupancy hazard classification for a given building operation is determined by evaluating the quantity, combustibility, and heat release rates of the associated contents • The final determination on the acceptability of the occupancy classification is the responsibility of the authority having jurisdiction (AHJ) • Using the following subsections for each commodity classification: Class I, Class II, Class III, Class IV, Group A plastic, Group B plastic, and Group C plastic

(continued)

Table 4 (continued)

Item	Standard for Installation of Fire Safety Equipment Based on Use and Occupancy	NFPA codes
Commodity material	N/A	• The commodity classifications are determined as follows: (1) Materials used in the makeup of the product. (2) Types of container. (3) Whether a plastic material will be used to protect the product. (4) Whether a plastic pallet will be used • The materials used to construct products: Non-combustible product, wood, paper, natural fiber, Group A plastics, Group B plastics, and Group C plastics
Storage height	N/A	• Over 12 ft (3.7 m) up to and including 20 ft (6.1 m) • Over 20 ft (6.1 m) up to and including 22 ft (6.7 m) • Over 22 ft (6.7 m) up to and including 25 ft (7.6 m)
Rack storage arrangements	N/A	Single-row racks, double-row racks, multiple row racks, movable racks, and automatic storage–type racks
Pallet types	N/A	• When loads are palletized, the use of wood or metal pallets, or listed pallets equivalent to wood, shall be assumed in the classification of commodities • For Class I through Class IV commodities, when unreinforced plastic pallets are used, the classification of the commodity unit shall be increased one class
Fire-fighting facilities	Fire hose station, automatic sprinkler system, fire extinguisher	Automatic sprinkler system

Table 4 (continued)

Item	Standard for Installation of Fire Safety Equipment Based on Use and Occupancy	NFPA codes
Ceiling sprinklers	The horizontal distance from any point to the nozzle shall be less than 2.1 m	• Proper positioning and spacing of sprinklers are important to ensure that sprinklers operate promptly and that obstructions to sprinkler distribution patterns do not adversely affect the performance of the sprinkler • The protection area of the sprinkler coverage shall be established by multiplying the S-dimension (distance between sprinklers) by the L-dimension (perpendicular distance to the sprinkler on the adjacent branch line), as follows: $A_S = S * L$ • The maximum distance permitted between sprinklers shall comply with the value indicated in the applicable section for each type of sprinkler • A minimum distance shall be maintained between sprinklers to prevent operating sprinklers from wetting adjacent sprinklers and to prevent skipping of sprinklers • The clearance between the deflector and the top of storage or contents of the room shall be 18 in. (450 mm) or greater

Table 4 (continued)

Item	Standard for Installation of Fire Safety Equipment Based on Use and Occupancy	NFPA codes
In-rack sprinklers	The horizontal distance from any point to the nozzle shall be less than 2.5 m	• The area protected by a single system of sprinklers in racks shall not exceed 40,000 ft2 (3720m2) of floor area occupied by racks, including aisles, regardless of the number of levels of in-rack sprinklers • Sprinklers in racks shall be ordinary-temperature standard-response or quick-response classification with a nominal K-factor of K-5.6 (80), K-8.0(115), or K-11.2(160), pendent or upright • In-rack sprinklers shall be permitted to be placed less than 6 ft (1.8 m) on center • In-rack sprinklers usually operate because they are located within the developing fire plume. Obstructions to the sprinkler discharge patterns are much less critical, and, therefore, the general requirements for obstructions do not apply to in-rack sprinklers
Face sprinklers	N/A	• Standard sprinklers that are located in transverse flue spaces along the aisle or in the rack • Face sprinklers are located within 18 in. (450 mm) of the aisle face of storage, and are used to oppose vertical development of fire on the external face of storage

Table 4 (continued)

Item	Standard for Installation of Fire Safety Equipment Based on Use and Occupancy	NFPA codes
Spray sprinklers (intended for storage applications)	At least one spray sprinkler shall be provided to the places which stored cotton, plastic, wooden and paper products, fiber goods, and other flammable materials for every 4 m height, and one at least installed for every 6 m height if the places store other materials	• Design density greater than 0.34 gpm/ft • Having a nominal K-factor of 11.2 or larger • Capable of producing characteristic large water droplets • Installed in accordance with the occupancy hazard density/area curves • Includes control mode density/area (CMDA) sprinkler, large-drop sprinkler, control mode specific application (CMSA) sprinkler, and early suppression fast-response (ESFR) sprinkler
Horizontal barrier	N/A	A solid barrier in the horizontal position covering the entire rack, including all flue spaces at certain height increments, to prevent vertical fire spread

- AS/RS in logistic facilities, unlike the factories often stored identical commodities, tends to load miscellaneous commodities leading to unpredictable fire risk.

5.2 Future Work for the Amendment of Standard for the Installation of Fire Safety Equipment Based on Use and Occupancy

- Determine the necessity of heat collectors: According to Automatic Sprinkler Systems Handbook: Heat collectors shall not be used as a means to assist the activation of sprinklers. There is evidence that objects above a sprinkler will delay the activation of the sprinkler where fires are not directly below the sprinkler. As a result, installing a heat collector will not help improve the protection of the properties.
- Regulate the classifications of commodities: Recent researches from FM Global and NFPA show that the commodity classification provides a convenient means

of categorizing a relationship between the chemical heat of combustion of various materials and their heat release rates so that the appropriate sprinkler system design can be identified.

- Clarify the configuration layout categorization of rack storages: The quantity and arrangement of materials stored in buildings, such as plastic, flammable liquids, aerosols, and automobile tires, have changed dramatically. These kinds of facilities often create fire hazards that exceed the hazards characterized by the occupancy itself. Consequently, appropriate categorization of configuration layouts can help identify relevant sprinkler system criteria with regard to occupancy hazard descriptions.
- Confirming by the case studies that rules for sprinkler positions, techniques for hydraulic calculations, selection of appropriate pipe materials, and requirements for determining the coverage area for a sprinkler shall conduct further simulation and experiments to verify the achievement of fire control or fire suppression.

References

1. Cai, C. F., et al. (2017). *A study on the fire behavior and fire suppression system installation regulation of AS/RS Logistic Industry Building*. Architecture and Building Research Institute.
2. Chan, T. S., & Kung, H. C. (2003). Comparison of actual delivered density and fire suppression effectiveness of standard and conventional sprinklers in rack-storage fires. *Fire Safety Science*, 445–456.
3. Chen, M. C. (2007). *Sprinkler performance design in warehouse*. CJCU Department of Occupational Safety and Health.
4. Chen, W. L., et al. (1997). The installation and comparison of automatic Sprinkler System in rack storage warehouses. *Journal of Fire Technology and Information*.
5. Chen, J. Z., et al. (2004). A research on fire safety evaluation and optimal design of building. *Architecture and Building Research Institute*.
6. Chen, J. Z., et al. (2014). Obstruction below the sprinkler how to affect extinguishing performance. *Journal of Architecture*.
7. Chien, S. W., et al. (2003). The performance equivalent alternative design for Automatic Sprinkler System and Building Fire Prevention. *Journal of Fire & Safety*.
8. Feng, J. Y. (2002). Fire safety design for high rack storage-the Automatic Sprinkler System. *Department of Civil Engineering of National Taipei University of Technology*.
9. Gary, K. (2015). Warehouse fires & pre-fire planning. *FM Global*.
10. Heskestad, G. (2003). Extinction of gas and liquid pool fires with water spray. *Fire Safety Journal*.
11. Ingason, H. (1997). *In-rack fire plumes*. Melbourne, Australia: IAFSS.
12. Kung, H.-C., Lee, S., Ballard, R. J., & Moseley, M. W. (2011). *Early suppression of rack storage fires with K363 standard response sprinkler*. Factory Mutual.
13. Yu, H.-Z., Lee, J. L., & Kung, H.-C. (1994). *Suppression of rack-storage fires by water*. Factory Mutual Research Corporation.
14. Ho, X. C. (2009). National fire code design standard. *Journal of Electrical Engineering*.

15. Li, Y. S., et al. (2009). *A study for the AS/RS warehouses fire prevention*. Architecture and Building Research Institute.
16. Klaus, M. J. (2016). *Automatic Sprinkler Systems handbook* (13th Ed.). NFPA.
17. Arvidson, M. (2014). Experience from fire sprinklers in a shuttle storage system. *SP Technical Research Institute of Sweden*.
18. NFPA. (2013). *Standard for the Installation of Sprinkler Systems*. NFPA.
19. Qiu, W. F., et al. (1999). *A study on the design regulation of fire safety equipment in rack-storage warehouses*. China Engineering Consultants *Corporation*.
20. Ye, S.W., et al. (2006). *A study on fire safety evaluation standard of logistic warehouse buildings*. Architecture and Building Research Institute.
21. Li, Y. Z., & Ingason, H. (2017). Scaling of wood pallet fires. *Fire Safety Journal*.
22. Yang, Q. (1998). *The design of Automatic Sprinkler Systems in rack storage warehouses*. Fire Protection Technology and Product Information.

Fire Investigation/Fire Services

Chinese Firefighter Fatalities 2007–2016

Ye Hu and Jian-zhang Shao

Abstract This study analyzes the types of duty associated with firefighter deaths, the age and rank of firefighters, and the cause of fatal injuries to firefighters who died 2007 through 2016. There were 193 Chinese firefighters died in line of duty in recent decade, excluding the firefighter deaths in 2015 Tianjing Port explosion. Twenty-one firefighters died for every million fire averagely and 51% fatalities occurred at the scene of emergency response. The firefighters died in 2007–2016 ranged in age from 18 to 51, with a median age of 26 years. The highest death rates were for firefighters between 18 and 25, accounting for about 60% of all. The first three largest shares of deaths were vehicle crash, stress or overexertion, and being caught or trapped, accounting for about 60% of all. The active service system seemed to be an economical institutional arrangement, but it caused the fire brigades always in a situation lacking of readiness. Efforts should be taken to perform genuine changes in the system, improve training, emergency scene operations, firefighter health and safety, and reduce the number of firefighter fatalities in the future.

Keywords Firefighter · Fatalities · Injury · Emergency response

1 Introduction

China government is confronting the challenge of disasters and accidents which increase rapidly with the development in economy and society, while Chinese firefighters are facing rigid situation of fire fighting and other emergency response which result in high fatalities in line of duty.

"Firefighter" in China mainly refers to members of military fire brigades in regional fire departments, which is an agency of the Public Security Bureau. As a branch of the People's Armed Police(PAP), military firefighters perform assigned fire suppression, emergency rescue activities, including vehicle accident rescue, structural collapse and earthquake rescue, water rescue, mountain rescue, etc., and other

Y. Hu (✉) · J. Shao
Department of Fire Command, Chinese People's Armed Police Force Academy, Langfang 065000, CO, China
e-mail: adiliahy@hotmail.com

non-emergency missions. There are totally up to 170 thousands of military firefighters around the nation, and almost all the firefighter fatalities occurred in military fire brigades.

2   General Situation

China Fire Administration issues Annual of Fire Service, where firefighters died in operation at the scene of fireground and emergency rescue will be counted. Fatality reports will be submitted by local fire departments when firefighters died in non-emergency response, training, maintenance, responding to and return from alarms, being on call, under orders or on standby duty, and other activities by accident.

Based on the data of the annuals and fatality reports recent decade, Fig. 1 shows firefighter fatalities in the years 2007 through 2016. There are one hundred and ninety three firefighters died in line of duty, excluding the one hundred and forty four firefighter deaths in 2015 Tianjin Port Explosion, and nineteen firefighters were killed every year averagely [1–10].

Figure 2 shows the firefighter deaths on duty for every million fires. There were

Fig. 1 Firefighter fatalities 2007–2016. *Note* The 144 firefighters died in Tianjin Explosion are excluded
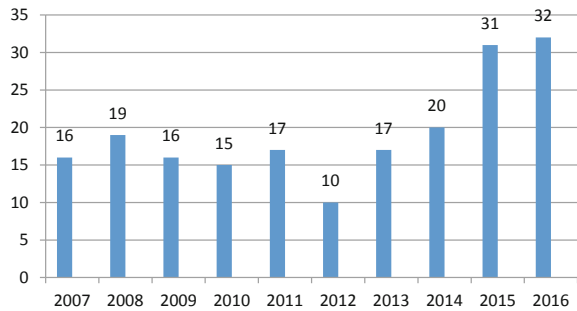
Fig. 2 Firefighters fatalities per million fires 2007–2016
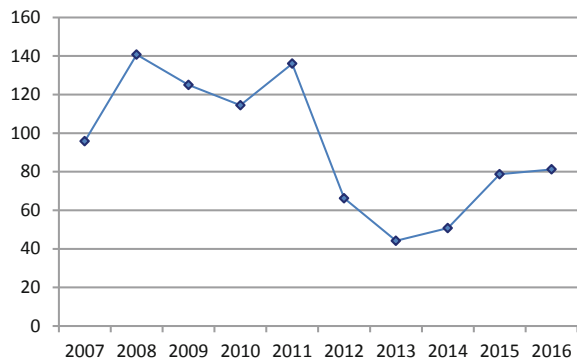
twenty firefighters died for every million fires averagely, whereas the member was three over the same period in the USA [11].

3   Firefighter Deaths by Type of Duty

3.1   Fireground

Figure 3 shows the distribution of the one hundred and ninety-three firefighter deaths by type of duty. Sixty-two firefighters were killed during fireground operations from 2007 to 2016. Of these fatalities, fifty-five died at the scene of structure fires, three were at the scene of vehicle fires, three were at the scene of wildland fires, and one was at the scene of oil fire. The average age of the firefighters killed during fireground operations was 25, with the youngest being 18 years old and the oldest being 37 years old.

Table 1 shows the types of fireground activities in which firefighters were engaged when they sustained their fatal injuries. There are forty-seven firefighters died during interior firefighting operations, where there are policies the Chinese Fire Administration insists on for years [12].

Fig. 3 Firefighter fatalities by type of duty 2007–2016
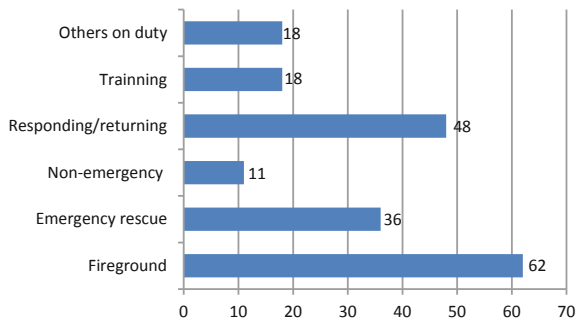
Table 1 Firefighter fatalities by type of fireground activity

Activity	Fatality	Proportion (%)
Advance hose lines	31	50
Search and rescue	16	27
Water supply	3	4
Overhaul	3	4
Forcible entry	2	3
Support	2	3
Command	2	3
Others	3	6

Table 2 Firefighter fatalities by type of emergency rescue activity

Activity	Fatality	Proportion (%)
Water rescue	16	45
Confined space rescue	7	20
Vehicle rescue	5	14
Structural collapse rescue	3	8
HAZMAT response	2	3
Others	3	8

3.2 Emergency Rescue

Thirty-six firefighters were killed while operating at the scene of emergency rescue. Table 2 shows the types of emergency rescue activities which resulted in firefighter's fatal injuries. Sixteen firefighters were absorbed into the flood while trying to save the drowning victims. Seven firefighters died as a result of asphyxiation in confined space rescue. Five firefighters died while operating in vehicle rescue. Three firefighters were buried into the rubble while operating in a structural collapse rescue. Two firefighters died due to LGP tank truck explosion caused by vehicle crash on highway. Three firefighters were stung to death while they were removing hornet nests.

3.3 Responding or Returning

Forty-eight firefighters died en route. Forty-five firefighters were killed as a result of vehicle crash while responding to or returning from emergency calls, non-emergency duties, or on way leaving for fire station [13]. Two firefighters died from heart attacks. One firefighter was struck down and killed by an electric line pole while returning from an accident.

3.4 Training

Eighteen deaths occurred while engaged in training activities: Seven died while involved in physical fitness activities, four died while involved in trainings at heights, four died while involved in equipment maintenances, and three died while participating in full-scale exercises.

Fig. 4 Firefighter deaths by age and rank 2007–2016
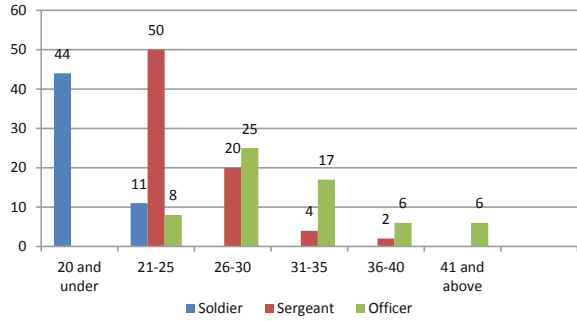
3.5 Others

The remaining twenty-nine firefighters died while involved in a variety of non-emergency response or other related on-duty activities. Eleven firefighters died while responding to non-emergency, including security guard and fire safety inspection. Eighteen firefighters died on other duties in fire station as a result of heart attack, cerebral hemorrhage, fall, or accidents.

4 Firefighter Deaths by Age and Rank

Figure 4 shows the percentage distribution of firefighter deaths by age and rank at the time of injury. The firefighters who died in 2007–2016 ranged in age from 18 to 51, with a median age of 26 years, and had served in fire departments for 6 years averagely. The highest death rates were for firefighters between 18 and 25, accounting for nearly 60% of all. That is also the main reason why young citizens are impressed by the firefighters' activities but hesitate to be drafted, especially after the 2015 Tianjin Port Explosion [14].

There are fifty-five soldiers died on duty and 80% of the soldiers are no more than 20. Seventy-six sergeants (also call Non-Commissioned Officer, NCO) were killed, accounting for 39% of all fatalities. Sixty-two officers died while operating at the scene of emergency response or fire supervision and inspection, ranking from Second Lieutenant to Superior Colonel, with a median age of 26 years.

5 Firefighter Deaths by Cause of Injury

5.1 Vehicle Crash

Figure 5 shows the distribution of deaths by cause of fatal injury. Vehicle crash

accounted for by far the largest share of deaths. Of the fifty-five deaths in this category, ten happened during emergency and non-emergency operations, and forty-five occurred en route while responding to or returning from emergency or non-emergency calls, driving to the training centers or leaving for fire station.

5.2 Stress or Overexertion

Twenty-eight firefighters died as a result of stress or overexertion, which is proved to be the second leading cause of fatal injury. Thirteen firefighters died due to heart attacks, in which the youngest was 22 years old only. Five firefighters died due to cerebral hemorrhage. The remaining ten firefighters died due to pulmonary embolism or other acute diseases [15].

5.3 Caught or Trapped

Twenty-five firefighters were killed when they became caught or trapped. Fifteen firefighters were engulfed by flood when trying to save the drowning victims. Six firefighters were poisoned by poisonous gas in confined space due to lack of proper respiratory protection. Four firefighters were caught by rapid spread fire: one by warehouse fire, two by wildland fire, and one by vehicle fire.

Fig. 5 Firefighter deaths by age and rank 2007–2016
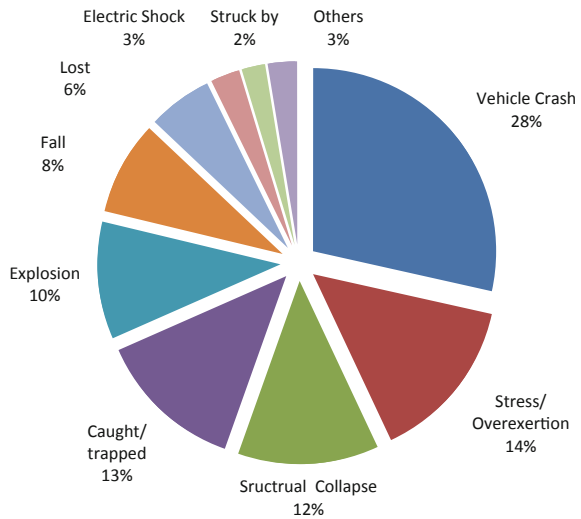
5.4   Structural Collapse

Twenty-four firefighters died as a result of structural collapse. Among them, eighteen were killed on the fireground of commercial buildings, three on the fireground of residential buildings, and three on the fireground of buildings under construction.

5.5   Explosion

Explosion claimed twenty firefighter lives. Twelve firefighters were killed by the explosion at the scene of industrial fire, including ten firefighters died in explosion originated in firecrackers storehouse. Three firefighters died in the explosion at the scene of vehicle crash: Two firefighters died in the explosion of LPG tank truck and one firefighter was sent out of a 40-m bridge by the explosion of petrol tank. Two firefighters died as a result of backdraft while making a forcible entry on the door of a residential house. Two firefighters were killed by the explosion at the scene of commercial structure fire: one by gas containers explosion in a restaurant and the other by air fresheners in a convenience store. One firefighter died in explosion of boiler pipe in a citizen community.

5.6   Fall

Sixteen firefighters died in fatal falls. Nine firefighters died while involved in trainings or maintenances at heights. Three firefighters fell and died when searching for trapped victims on fireground: Two firefighters fell into elevator shaft and one firefighter fell down from stairs. Two firefighters fell from the rescue rope while they were appalling down and trying to entry storied residential houses from outside due to destroyed rope or exposure to smoke separately. One firefighter fell into high-temperature liquid paraffin pool while making salvage. One firefighter fell down onto the ground when trying get into a three-story room along the out walls to fetch keys in fire house.

5.7   Lost

Eleven firefighters died by becoming lost or disoriented inside a burning structure. Six firefighters died as searching team in two separate fire alarms. The other five firefighters were killed due to failure after separating from his team during interior firefighting operations.

5.8   Electric Shock

Five firefighters died due to electric shock. Three firefighters were shocked by the falling electric cable on fireground, one was shocked by the vehicle battery at the scene of vehicle crash and one was killed by high voltage while hanging out hose lines in fire station.

5.9   Struck by

Four firefighters were struck and killed by falling objects: One at the scene of structure fire was struck by a falling tree while operating an fire engine to provide water supply, one at the scene of water rescue was struck by falling stones, one at the scene of wildland fire were struck by falling trees, and one was struck by a failure carabiner while involved in a full-scale training exercise.

5.10   Others

Three firefighters died as a result of hornet stings. The firefighters, while responding to calls of removing hornet's nests, were stung and killed due to anaphylactic shock—two firefighters died without body protection and one firefighter died because the mask of anti-hornet clothing was slashed by the branch.

Two firefighters were killed by their fellowman unintentionally while on duty at fire station.

6   Conclusion

Firefighting, rescue, and other types of emergency operations are essential activities in an inherently dangerous profession, and unfortunate tragedies do occur. These are the risks that all firefighters accept every time they respond to an emergency incident. Furthermore, Chinese fire departments have their own problems caused by the so-called Active Service System which should be focused on especially.

As the firefighters in regional fire department is a part of military force, soldiers, sergeants, and officers serve limited years according to their rank, few of them could regard firefighter as their Whole Life Career and stay in their positions until retirement. Young men are drafted as soldiers through political, psychological, and medical test. After three-month training in the provincial fire academy, soldiers are dispatched and serve two years in fire brigades, where they are on duty twenty-four hours a day and seven days a week, and half of them could reach to the rank of

Sergeant two years later. Sergeant serves 3–9 years with some allowance, and just two-third of the sergeants could be promoted to higher level. Officers serve as chief or staff at different level until the maximum age according to their rank.

Consequently, a worrying circumstance can be seen: On one side, thousands of recruits without any professional knowledge of firefighting are trained in fire academies every year; on the other side, thousand skilled soldiers and sergeants quit form fire bridges to find a new job. The fire brigades are always in a situation lacking of readiness, including essential knowledge, technical skills, and appropriate decision. Encouraged by the conviction to be a hero, young firefighters are brave enough to rush into dangerous heavens to save victims without essential knowledge of firefighter survival, some even having no awareness on how to initiate emergency procedure, find safety heavens and seek for help when they are trapped or lost.

Although the Active Service System seemed to be an economical institutional arrangement at beginning of the implementation of the reform and opening-up policy, the limitation of military brigades gradually appeared recent years, where the tendency of firefighter fatalities is just a demonstration. It is time that the administration focus on specific problems and direct efforts to perform genuine changes in the system, improve training, emergency scene operations, firefighter health and safety, and reduce the number of firefighter fatalities in the future.

References

1. China Fire Administration. (2008). *Annual of fire service* (pp. 403–404). Beijing: China Personnel Publishing House.
2. China Fire Administration. (2009). *Annual of fire service* (pp. 391–392). Beijing: China Personnel Publishing House.
3. China Fire Administration. (2010). *Annual of fire service* (pp. 382–383). Beijing: China Personnel Publishing House.
4. China Fire Administration. (2011). *Annual of fire service* (pp. 367–368). Beijing: China Personnel Publishing House.
5. China Fire Administration. (2012). *Annual of fire service* (pp. 412–413). Beijing: China Personnel Publishing House.
6. China Fire Administration. (2013). *Annual of fire service* (pp. 378–379). Beijing: China Personnel Publishing House.
7. China Fire Administration. (2014). *Annual of fire service* (pp. 371–372). Beijing: China Personnel Publishing House.
8. China Fire Administration. (2015). *Annual of fire service* (pp. 431–432). Beijing: China Personnel Publishing House.
9. China Fire Administration. (2016). *Annual of fire service* (pp. 413–414). Beijing: China Personnel Publishing House.

10. China Fire Administration. (2017). *Annual of fire service* (pp. 415–416). Beijing: China Personnel Publishing House.
11. U.S. Fire Administration and FEMA. (2016). *Federal Emergency Management Agency. Firefighter fatalities in the United States in 2015*. Washington, D.C.: FEMA.
12. China Fire Administration. (2015). *Fireground operations regulations for fire troops*. Beijing: China Fire Administration.
13. Fahy, R. F., LeBlanc, P. R., & Molis, J. L. (2017). Firefighter fatalities in the United States-2016. In *National Fire Protection Association*.
14. Kang, R., Fu, G., Fu, Z., & Gao, P. (2017). Comparative study on death causes of firefighters in China and USA. *Journal of Safety Science and Technology, 13*(4), 181–184.
15. Dong, N. (2017). Safety management for fire force in emergency response. *Journal of Safety Science and Technology, 2,* 164–167.

Planning of Intermediate Refuge Floors as a Comprehensive Measure for Business Continuity Planning of After Large Earthquakes and Mitigation of Fire Damage on Super High-Rise Buildings

Yoshikazu Minegishi, Daisuke Matsuda, Ryosuke Shinozuka and Yuji Hasemi

Abstract Many super high-rise buildings are rapidly constructed in the urban area of Japan and Asia. The population and business activities of super high-rise office buildings are almost the same scale that of a city. If those businesses cannot continue after a big earthquake, huge economic loss and decrease of city function are expected. Therefore, the planning for business continuity after earthquake is strongly required. In addition, super high-rise buildings also have problems fire safety, and it becomes a large problem, especially after earthquake fire safety. To solve both problems, we proposed a comprehensive measure using intermediate refuge floors and its effect of vertical zoning. For business continuity, intermediate refuge floors are used as temporary refuge space for the occupants who cannot stay at their office area because of scattering of fixture, falling of ceilings and water leakage, and business facilities such as electricity and information facilities are divided by the intermediate refuge floors to limit the earthquake damage. As for fire safety, fire prevention equipment such as sprinklers, fire doors, fire shutters, and smoke exhaustion may be damaged by heavy shakiness. Therefore, we expect an intermediate refuge floor as a stable fire and smoke spread prevention measure. Through probabilistic analysis of 100 story model office building, we proposed effective installation measures that intermediate refuge floors are installed primary considering the fire and smoke spread control, and necessary business continuity performance is reinforced by earthquake damage management policy like reinforcing structure, steadily fixing office fixtures, and using flexible sprinkler pipes.

Keywords High-rise building · Earthquake · Business continuity · Fire safety · Refuge floor

Y. Minegishi (✉)
Takenaka Corporation, 1-1-1 Shinsuna, Koto, Tokyo 136-0075, Japan
e-mail: minegishi.yoshikazu@takenaka.co.jp

Y. Minegishi · D. Matsuda · R. Shinozuka · Y. Hasemi
Waseda University, 55-N702, 3-4-1, Okubo, Shinjuku, Tokyo 169-8555, Japan

1 Introduction: Comprehensive Measure for Business Continuity and Fire Safety After Big Earthquake

Recent years, many super high-rise buildings have been constructed in the urban area of Japan and Asia. It is not rare that super high-rise buildings are constructed densely located. Population and business activities of such super high-rise office buildings are almost the same scale that of a city. If those businesses cannot continue after a large disaster, such as big earthquake, huge economic loss and decrease in city function are expected. Therefore, the planning for business continuity after earthquake is strongly required. In the area where many high-rise buildings are located, traditional evacuation planning which requires all the occupants to evacuate to the ground cannot be simply applicable, because of the business continuity, long travel distance and travel time, and for excessive congestion on the ground.

On the other hand, considering fire safety, traditional fire safety planning cannot be also simply applied because not only the size of the building and population, but also fire and smoke spread vertically through the voids driven by buoyancy, and huge number of occupants has no other choice but to evacuate to the ground with a long time through limited number of stairs. As the countermeasure, vertical zoning using buffer floors and intermediate refuge floors can be applied to control vertical fire and smoke spread and to provide evacuees temporary rest space. Those approaches using machine room floors as refuge floors have been taken in the early days of super high-rise buildings in Japan [1]. Recently, a super high-rise building utilized the intermediate roof garden created by the setback of the volume of different usage as temporary rest space and fire buffer [2]. And now in many countries and cities, especially in Asia, provision of refuge floors is required by law [3].

This fire safety approach to limit fire damage and provide evacuees temporary rest space in the super high-rise buildings can be also applied for the planning of business continuity after big earthquakes. Specifically, it is the approach to zoning the electrical and information/communication facilities which are indispensable for business continuity and limit the failure of those facilities. It is also the approach to hold the occupants in the building, i.e., at the intermediate refuge floor, who cannot remain in the office area because of the earthquake damage. If not all occupants cannot remain safely, designed business continuity cannot be accomplished (See Fig. 1).

In addition, intermediate refuge floors are usually limited to be maintained as "safe area," for example, not to use as lent space and not to settle combustible materials. Therefore, it usually becomes negative for construction cost and flexibility of usage. However refuge floors can contribute for both business continuity after earthquake and fire safety, momentum for installing refuge floors by both own judgment of private business owners and political promotion would be rolling.

Considering those aspects, we propose a comprehensive measure for business continuity and fire safety after a big earthquake using intermediate refuge floor and examine its effective design policy through a probabilistic case study.

Fig. 1 Conceptual diagram of comprehensive measures for business continuity and fire safety after big earthquake using intermediate refuge floors

2 Concept of Business Continuity and Fire Safety After Big Earthquake

2.1 Business Continuity After Big Earthquake

After an earthquake, many occupants are forced to refuge to safe space because of the scatter of fixtures, falling of ceilings and partition, and/or water leakage caused by breakage of sprinkler heads and pipes. In this circumstance, we propose to evacuate to intermediate refuge floor considering the difficulty to long-time evacuation to the ground and congestion on the ground (Fig. 1a, b). As provision for fire, we divide into several zones by intermediate refuge floors using them as buffers for fire and smoke spread, and in an analogous way, as provision for business continuity of after earthquake, we use the zones as the unit of facilities which are indispensable for

business such as electricity, information/communication facility, air conditioning, and sanitary facility and limit their damage in a zone. Based on this concept, we define two conditions which are the main function to maintain business activity in safe.

(A) To prepare enough area to temporary refuge in the building.
(B) Safety in the office area and running of facilities.

Condition (A) means to prepare enough temporary refuge area to hold the occupants who cannot remain their office area because of the earthquake damage such as scatter of fixture, ceiling and partition collapse, and water damage. This is the concept that to maintain business activity in a planned way in the case when there are a lot of occupants who have to refuge, enough space of refuge area needs to hold all of them.

Condition (B) means the situation of no earthquake damage; not only occupants can remain their business area but also business facilities such as PCs, electricity, and information/communication facilities are active.

2.2   Fire Safety After Big Earthquake

For fire safety, installing intermediate refuge floors as buffer zone can be a promising measure to mitigate fire damage. This can limit the number of occupants who must evacuate immediately by limiting vertical fire and smoke spread, and this also provides a safe temporary area of near location compared to evacuate to the ground (Fig. 1c).

This kind of measure is effective not only for the usual fire scenario but also, and especially, for after earthquake fire. Considering after earthquake situation, the possibility of fire occurrence increased because of electric leakage, damage of facilities and fixtures, and failure of turning off the equipment using fire due to the heavy shakiness. Moreover, fire prevention equipment such as sprinklers, fire doors, fire shutters, and smoke exhaustion may also be damaged, and therefore, the possibility of failure of maintaining adequate fire and smoke control function may be increased (Fig. 1d).

From this viewpoint, we use intermediate refuge floors not only for the safety measure for usual fire case but also as high reliable fire and smoke control measures for after earthquake fire case (Fig. 1c).

3   Model Building

We configured a model building which has intermediate refuge floors shown in Figs. 2, 3, and Table 1. We assume that both ground and intermediate refuge floors can be used as temporary refuge space for after earthquake and in case of fire. In this

IRF: Intermediate refuge floor
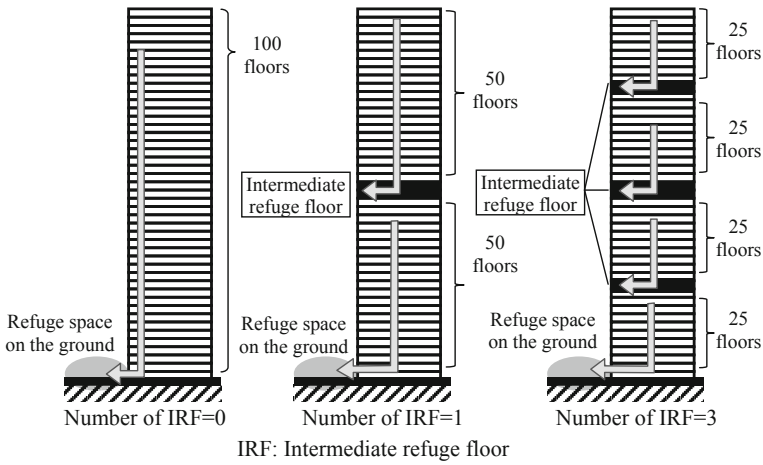
Fig. 2 Conceptual diagram of model building and intermediate refuge floors (section)

(a) Standard floor plan (office floor)   (b) Intermediate refuge floor   (c) Detail around staircase at intermediate refuge floor
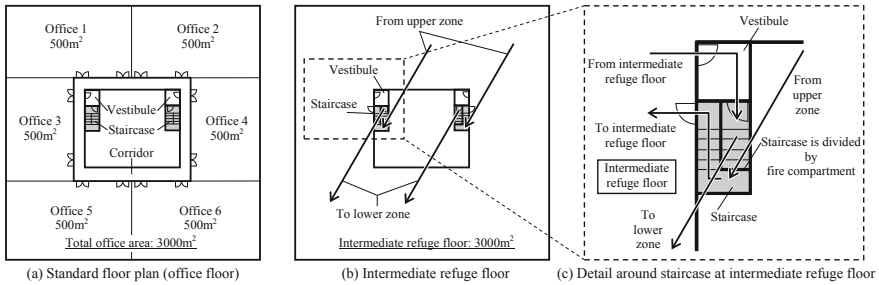
Fig. 3 Conceptual diagram of model building and intermediate refuge floors (plan)

Table 1 Outline of the model building

Building height/number of floors	500 m/100 floors
Proprietary area (office area)/ Area of intermediate refuge floor/ Area of refuge on the ground	3000 m^2/ 3000 m^2/ 3000 m^2
Population density	0.125 persons/m^2 [5]
Number of occupants at each floor	375 persons
Capacity of intermediate refuge floors and refuge on the ground	1830 persons (0.61 persons/m^2) [4]
(Parameter) Number of intermediate refuge floor	0–9 (Install same interval)

research, we install intermediate refuge floors in the same interval of floors and we call those intervals as "zone." These refuge floors are designed as a buffer area to prevent vertical fire and smoke spread.

We defined density in the intermediate refuge floors as 0.61 persons/m^2 based on the standard density which is defined in the guideline for people who are difficult to return their home after big earthquake [4] in consideration that it needs a long time to recover transportation facilities and the comfort of the refuge people. To make the study simple, we assumed all of the area (same area of the office area of general floors; exclude floor core such as elevator (EV), EV hall, stairs, mechanical shaft, WC) of intermediate refuge floor as refuge space. The ground is also the same to that of intermediate refuge floors. And when we install several intermediate refuge floors, we add those floor (Total number of standard floors and intermediate refuge floors will be increased). We assume office floors are divided into six tenants (Fig. 3b).

4　Model of Business Continuity and Fire Safety Controlled by Intermediate Refuge Floors and Zoning

4.1　Fire Safety After Big Earthquake

There are many kinds of earthquake damages concerning to business continuity. In this research, we classified those damages into three damages: (1) scatter of fixtures, (2) falling of ceilings and partition, and (3) water leakage. Data of occurrence probability of those damages are very few. However, we aim to gain target value of structural, architectural, and equipmental seismic adequacy; how many intermediate refuge floors and zonings and how much reliability of equipment are needed to achieve certain business continuity, to estimate the level of safety relatively.

4.2　Definition of Earthquake Damage

(1)　Scatter of fixtures

This classification not only includes scatter of fixtures, but also includes scatter of documents, turnover of PCs, and other office appliances. This damages may be recovered by occupants themselves, but we assume that business activities are disrupted and occupants have to refuge to safe area immediately after earthquake (Consideration of recovery process by occupant themselves is our future work).

(2)　Falling of ceilings

This classification not only includes falling ceilings but also includes the turnover of partitions and collapse of non-structural members. We call them "falling of ceilings"

all together for simplicity. Recovery of them is difficult especially by occupants themselves, and we assume that both business activities and remaining there are impossible.

(3)   Water leakage

This classification means water leakage caused by damage of sprinkler head and pipes. In the area where water leaked, we assume that both business activities and remaining there are impossible. In addition, water leakage at one floor will also leak to lower floors and if water leak into EPS, etc., it will also impair electricity and information/communication function of all floors in the zone. This means water leakage into EPS will cause business disruption of all floors of the zone.

4.3   Definition of Business Continuity and Its Calculation Method

We express the condition of business continuity of (A) and (B) mathematically and we define "expected value of business continuity" P_{BC}. Condition (A) means that all occupants in a zone who cannot remain in their office space after earthquake can be held at the intermediate refuge floor immediately below the zone. To simplify examination, we assume scatter of texture, ceiling falling, and water leakage will occur on one whole floor as a unit. Under this assumption, there is the maximum number of damaged floors based on the capacity of holding occupants who cannot remain their office space. Assume the probability of inability to remain is equal among every floor p_{es}, probability when the condition (A) is satisfied P_A and the expected value of the floors which satisfy the condition (A) is expressed as follows;

$$P_A = \sum_{k=0}^{k_{\max}} p_A(k) = \sum_{k=0}^{k_{\max}} {}_N C_k P_{\text{es}}^k (1 - p_{\text{es}})^{N-k} \tag{1}$$

$$E_A = \sum_{k=0}^{k_{\max}} p_A(k)(N - k) \tag{2}$$

E_A Expected value of the floors which satisfy the condition (A) [floors]
k Valuable of floor number where occupants are needed to refuge [-]
$k_{\max}$ Maximum number of floor where occupants are needed to evacuate, and they can be accommodated at the intermediate refuge floor [floors]
N Number of floors in a zone [floors]
P_A Probability when the condition (A) is satisfied [-]
$p_A(k)$ Probability when the number of floors where occupants are needed to refuge is k [-]
p_{es} Probability of occupant have to evacuate from the floor[-].

Usually, shakiness by earthquake is larger at higher floors than lower floors, and therefore, the assumption that p_{es} of all floors are equal have possibility to improvement. And we expressed the condition in "expected value," but this expression includes cases that occupants who are needed to evacuate cannot be held in intermediate refuge floors. In this aspect, considering "exceedance probability" like 95 percentile will be preferable. There are our future works.

Assume that probability of scatter of fixtures, falling of ceilings, and water damage are independent, p_{es} is calculated by the multiplication of them:s

$$p_{es} = 1 - (1 - p_s)(1 - p_c)(1 - p_w) \tag{3}$$

p_s Probability of scatter of fixtures [-]
p_c Probability of falling of ceilings [-]
p_w Probability of water damage [-].

As for condition (B), we assume that even a floor is not affected by scatter of fixtures, falling of ceilings, and water leakage, if water leaks into EPS, electricity, and information/communication facility will fail and business will be interrupted. Define p_{eps} as the probability of water damage on EPS and assume that p_{eps} is equal among all floors, probability of no water damage on EPS in the zone P_B is expressed as follows;

$$P_B = \left(1 - p_{eps}\right)^N \tag{4}$$

P_B Probability of no water damage on EPS in the zone [-]
p_{eps} Probability of water damage on EPS [-].

We only consider the water leakage of EPS as the factor that interrupts the business of all floors in the zone. But other factors such as air conditioning and plumbing will also be interruption factors. Those modeling will be also our future work.

Last step, we define the expected value of business continuity P_{BC}. To simplify the modeling, we assume that p_{es} and p_{eps} are independent, P_{BC} is defined as the rate of expected floor number which satisfies the condition (A) and (B) to all floors in the zone (Fig. 4).

$$P_{BC} = E_A P_B / N \tag{5}$$

P_{BC} Expected value of business continuity [-].
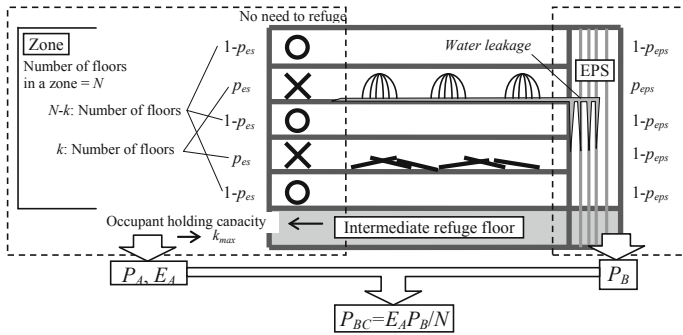
Fig. 4 Definition of expected value of business continuity P_{BC}

4.4 Definition of Fire and Smoke Damage and Its Calculation Method

When a fire occurs in an office room, smoke will propagate to the corridor, vestibule, staircase, and above floors (Fig. 1d). To prevent this kind of smoke spread, fire and smoke management equipment such as sprinkler, fire doors, and mechanical smoke exhaust are installed. But considering after earthquake fire, not only the probability of fire occurrence increases but also the probability of inoperative of those equipments also increases. Therefore, fire and smoke damage of after earthquake fire will be larger than usual.

To limit this damage, we use intermediate refuge floors and zoning concept (Fig. 1c). Dividing staircase at the intermediate refuge floors, even smoke propagate into the staircase, the smoke spread will limit to the fire occurred zone and this ensures that occupants at the non-fire zones do not necessarily evacuate immediately. If intermediate refuge floors are designed as buffer floor to prevent vertical fire spread, the fire spread from façade will also be limited in the fire occurred zone even considering the failure of sprinkler. Both fire and smoke damage should be controlled, but from the viewpoint of evacuation, smoke spreads rapidly and occupants are required quick evacuation. Therefore, we model the smoke spread and its effect to the occupants.

We evaluate the smoke damage in consideration of earthquake damage by event tree analysis. Figure 5 shows the event tree about smoke control equipment constructed based on the assumption shown in Fig. 1d. Actually, success and failure of smoke control are analyzed by simulation and its criteria should be clearly defined, but to simplify the examination of the effect of the combination of smoke control equipment and effect of earthquake, success and failure of smoke control are given just the condition of smoke control equipment. And there may be some other smoke control equipment such as smoke exhaust on office rooms and corridors, but we omitted them because those effects are basically limited to those rooms.
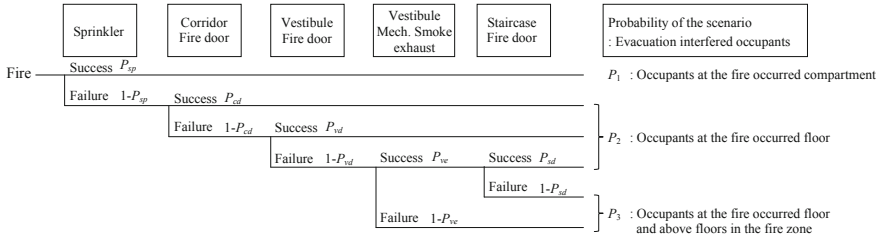
Fig. 5 Settings of event tree about smoke control equipment and evacuation interfered occupants

And we also define "evacuation interfered occupants" based on the location of smoke damage. We evaluate smoke control ability by the expected value of the product of the probability of smoke propagation and the number of evacuation interfered occupants. Expected value of evacuation interfered occupants per one fire E is defined as follows;

$$E = \sum_{k=1}^{N}\left(\sum_{m=1}^{3} p_m Q_{m,k}\right) \tag{6}$$

E Expected value of evacuation interfered occupants [persons]

p_m Probability of smoke propagation scenario of m [-] (Fig. 5)

Q_m Number of evacuation interfered occupants of each propagation scenario m [persons] (Fig. 5)

m Variable which represent smoke propagation scenario [-] (Fig. 5).

5 Parametric Study

5.1 Business Continuity

5.1.1 Settings of Parameter

Default value of the probability of water damage p_w is defined as 1%. It may be a rough assumption, but this concept is as follows: According to a research conducted after the Great East Japan Earthquake [6], 26.3% of investigated buildings of more than 100,000 m^2 of total building area have experienced sprinkler damage. It may be expedient, we suppose the building with 3000 m^2 per floor, 33 stories, i.e., 100,000 m^2 of total building and probability of water damage occurred at least one floor is 26.3%. This is described as $0.263 = 1 - (1 - p_w)^{33}$. Therefore, $p_w = 0.00925$, about 0.01 (1%).

It may also be expedient, other default values are defined as $p_c = 0.1$, $p_s = 0.2$, and $p_{eps} = 0.002$ (defined as 1/5 of the p_w). In this case, p_{es} is acquired as about 0.2872 from the Eq. (3) as a default value. We examined the effect of those values by changing them as parameters.

5.1.2 Result

Figure 6a shows that the expected value of business continuity P_{BC} by changing the value of p_{eps} as a parameter, comparing the value of P_A. We can see that P_{BC} increases as the increase in number of intermediate refuge floors. But its tendency is similar to that of P_A, this means P_{BC} is strongly governed by P_A. About p_{eps}, when p_{eps} is smaller than 0.01, the P_{BC} is almost the same. And changing tendency of P_{BC} by the number of intermediate refuge floors is similar. This reason is that when the effect of p_{eps} is large, the number of intermediate refuge floors is small, but when the number of intermediate refuge floors is small, P_{BC} itself is small. From the curve of P_{BC} on the graph, the number of intermediate refuge floors of about 5–7 (number of floors in a zone is from 12 to 17) is reasonable.

Figure 6b shows the P_{BC} by changing the value of p_{es} and number of intermediate refuge floors as parameters. We can see that when p_{es} is small (ex. 15%), P_{BC} is relatively large regardless of the number of intermediate refuge floors, and when p_{es} becomes large (ex. 45 and 60%), P_{BC} converges to 0% also regardless of the number of intermediate refuge floors. And the larger the number of intermediate refuge floors (the smaller the number of floors in a zone), the smaller the decrease in P_{BC} according to the increase in p_{es}. Increasing in intermediate refuge floor is the most effective when p_{es} is about 30%.

(a) Parameter: the number of intermediate refuge floors

(b) Parameter: Probability of occupant have to evacuate P_{es}
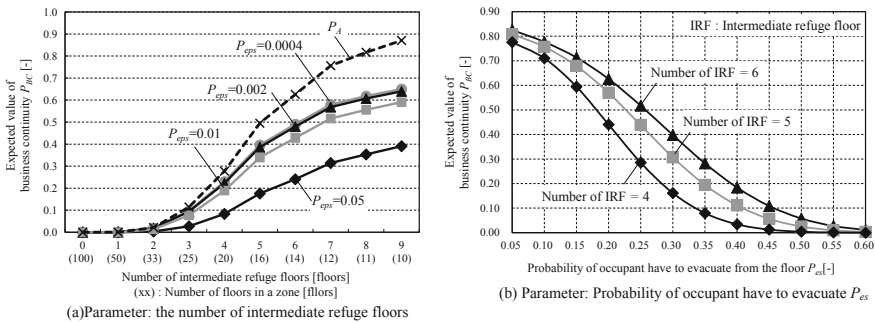
Fig. 6 Expected value of business continuity P_{BC}

Table 2 Settings of success rate of fire safety equipment at after earthquake scenario

	Success rate at ordinary fire scenario	Rate of damage by earthquake (%)	Success rate at after earthquake fire scenario
Fire suppression by sprinkler at the fire room	$p_{sp} = 0.90$	50	$P'_{sp} = 0.450$
Smoke insulation by the fire doors between fire room and corridor	$p_{cd} = 0.90$	29	$P'_{cd} = 0.639$
Smoke insulation by the fire doors between corridor and vestibule	$p_{vd} = 0.90$	29	$P'_{cd} = 0.639$
Mechanical smoke exhaust at the vestibule	$p_{ve} = 0.90$	11	$P'_{ve} = 0.801$
Smoke insulation by the fire doors between vestibule and stairs	$P_{sd} = 0.90$	29	$P'_{sd} = 0.639$

5.2 Smoke Control After Fire Safety

5.2.1 Settings of Parameter

Success rate of fire safety equipment is thought to be differ among buildings and its maintenance attitude, but to simplify the examination, we set the success rate of fire safety equipment in ordinary fire condition as 0.90. Success rate of fire safety equipment in after earthquake is calculated multiplying the rate of damage by earthquake acquired from the research on the Great East Japan Earthquake [6]. These values are shown in Table 2.

5.2.2 Result

Figure 7 shows the expected value of evacuation interfered occupants E in ordinary fire scenario and after earthquake fire scenario. In an ordinary fire scenario, E is almost the same with the number of intermediate refuge floors. This reason is that the smoke spread to upper floors will well controlled by, sprinkler, fire door, and smoke exhaust, and only occupants in the fire room are interfered evacuation. On the other hand, E of the after fire scenario with no intermediate refuge floor case is nine times as large as that of ordinary scenario. But E becomes smaller according
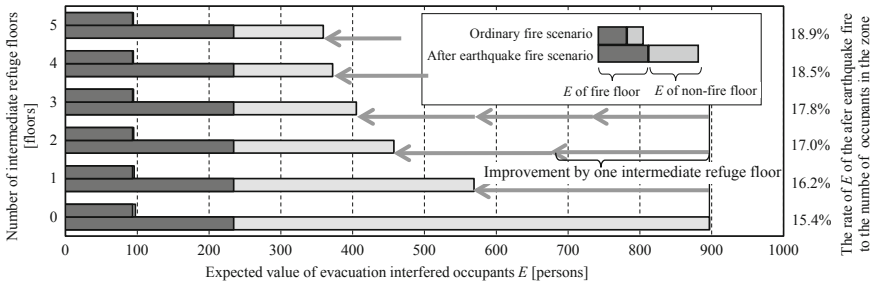
Fig. 7 Expected value of evacuation interfered occupants *E* of ordinary fire scenario and after earthquake fire scenario

to the increase in the number of intermediate refuge floors because smoke spread is limited by the division of the staircases at the intermediate refuge floors.

Improvement effect of *E* by one intermediate refuge floor is larger in the case with a smaller number of intermediate refuge floors. From the viewpoint of cost and space effectiveness, installing one or two intermediate refuge floor is effective.

6 Discussion: Optimal de Sign of Intermediate Refuge Floors Both for Business Continuity and Fire Safety

We have acquired the improvement characteristics of business continuity and fire smoke spread control by intermediate refuge floor. For both, the more intermediate refuge floors are installed, the more business continuity and smoke spread control are improved. But for business continuity, installing five intermediate refuge floors (in this case, number of usual floors in a zone is 16) is effective, and for smoke spread control, installing 1 or 2 intermediate floors is effective from the viewpoint of improvement effect of per intermediate refuge floor. Therefore, both conditions do not necessarily coincide. However, considering both characteristics, the following approach would be good to optimally minimize both disaster damages;

(1) Installing intermediate refuge floors mainly considering after earthquake fire smoke control
(2) In this condition, the performance of business continuity is insufficient. To compensate it, improve the mitigation of earthquake damage; improving resistance of the main structure and secondary members such as ceilings and partitions, using flexible pipe for sprinklers, stably fixing the office fixtures, and mounding up around EPS, etc.

At present, our study only covers the 100 stories simple office building. If the building has more floors like 200 stories, the effect of fire and smoke will become more dominant and more intermediate refuge floors may be required.

7 Conclusion

To solve the problem of business continuity and fire safety after a big earthquake on super high-rise buildings, we proposed a comprehensive measure using the intermediate refuge floor and its effect of vertical zoning. Through probabilistic analysis of 100 stories model office building, we grasped the characteristics of the effectiveness of intermediate refuge floors. For business continuity, installing five intermediate refuge floors is effective and for fire and smoke control, one or two is effective. Therefore, optimal design policy is installing intermediate refuge floor primary considering the fire and smoke spread control and reinforcing necessary business continuity performance by earthquake damage management measures like reinforcing structure, steadily fixing office fixtures, and using flexible sprinkler pipes.

We have acquired major knowledge about comprehensive usage of intermediate refuge floors. However, the source of parameters is limited, and much complicated higher buildings are not studied. We would like to continue further research.

References

1. Shinjuku Center Building. (1985, July). *Collection of actual example of fire safety design 1985 edition* (pp. 26–31). Building Center of Japan. (In Japanese).
2. Takeichi, N., & Minegishi, Y. (2016). Performance-based fire safety design for a skyscraper: A case in Japan. *Fire Science and Technology, 2015,* 235–244.
3. Barber, D., & Johnson, P. (2015). Refuge floors—History, implementation and methods for improvement. In: *Proceedings of 6th international symposium on human behavior in fire 2015* (pp. 245–256).
4. Cabinet Office for Disaster Management (Japan). (2015). *Guideline for people who are difficult to return their home after big earthquake*. http://www.bousai.go.jp/jishin/kitakukonnan/pdf/kitakukonnan_guideline.pdf (last visit 11/17/2018). (In Japanese).
5. Notification No. 1441/1442 of the Ministry of Construction (Japan). (2000). *Establishment of calculation method etc. for the verification method for floor/building evacuation safety*. (In Japanese).
6. Working Group on fire safety measure for large scales fire prevention property, Fire and Disaster Management Agency. (2012). *Report on current condition of disaster management and self-organization of disaster management*. http://www.fdma.go.jp/neuter/about/shingi_kento/h23_daikibo_bouka/bouka/higashinihon_houkoku_01.pdf (last visit 11/17/2018). (In Japanese).

Risk Analysis of Helicopter Search and Rescue Hoist Operation Accident

Fang-Chieh Sen and Yu-Hsiang Huang

Abstract Helicopters are commonly used in search and rescue operations, and hoist operation accidents have occurred during helicopter search and rescue (HSAR) missions. The purposes of this study were to investigate whether the HSAR team to carry out the task of the hoist, may cause casualties accident risk factor. Through the Aviation Safety Council (ASC) database, we collected the statistical analysis of the major accidents of HSAR during 2000–2017, carried out case studies on the investigation report of the HSAR hoist operation casualties in the rear cabin, and semi-structured interviews were conducted with personnel involved in the implementation of the mission. Ensure the completeness through literature reviews and expert meeting discussions. A total of 12 HSAR accidents were identified during the study. Of these, 42% involved were related to hoist operation. The study indicates that there are four essential evaluation dimensions and some risk factors in HSAR missions.

Keywords Risk analysis · Helicopter search and rescue · Hoist accident

1 Introduction

According to the World Bank's report in the Natural Disaster Hotspots: A Global Risk Analysis, Taiwan is the most vulnerable to multiple hazards and ranks first in the world in terms of percentage of the total population [1]. In response to a major disaster, HSAR has become an indispensable part of Taiwan in order to be able to face disasters and complex rescue missions. On March 11, 2016, National Airborne Service Corps (NASC), Ministry of the Interior, AS365N3 helicopter, crashed into the water during hoisting a rescuer to a vessel about the north from Shimen seashore. This mission carried two pilots, one mechanic, and two rescuers. Two were killed, and

F.-C. Sen (✉) · Y.-H. Huang

College of Police Science and Technology, Fire Science, Central Police University, No.56, Shujen Rd., Takang Vil, Kueishan District, Taoyuan City 33304, Taiwan
e-mail: sevenstarlucky7@gmail.com

Y.-H. Huang
e-mail: una459@mail.cpu.edu.tw

the other three were seriously injured. The helicopter was hull loss. The helicopter is assisting in rescue operations involving a cargo ship belonging to the TS Lines, which lost power in the raging sea and ran aground on a shallow reef at an altitude of 300 m. There are 21 people on board [2]. NASC started to receive UH-60M Blackhawks in 2015 to improve air rescue capability. However, on June 30, 2017, one UH-60M Black Hawk helicopter, registration number NA-703, conducted a search and rescue joint training at offshore of Taichung Harbor. There were three pilots, three crew chiefs, and three rescuers, total of nine people aboard, and two rescuers fell into the ocean due to the hook was separated from the hoist system. Two rescuers sustained minor and severe injuries [3]. So, identifying the risk factors associated with hoisting accidents is our main objective.

Identifying hazards and associated risk is the key point to preventing risk and accidents if a pilot fails to search for risk, it is likely that rescuer will neither see it nor appreciate it for what it represents. Unfortunately, the pilots and rescuer rarely have the opportunity to learn from their errors in judgment because even small mistakes in aviation are often fatal [4]. Estimates suggest that more than six thousand patient transports by helicopter have occurred since set up NASC began in the early 2004s through the most recent data in 2016, and the annual volume of these flights has steadily increased since 2010 with more than a quarter hundred transports in 2017 alone [5].

According to ASC's statistics, from 2000 to 2017, a total of 12 HSAR-related accidents occurred, of which five were related to hoisting operations, accounting for about 43% are shown in Fig. 1.
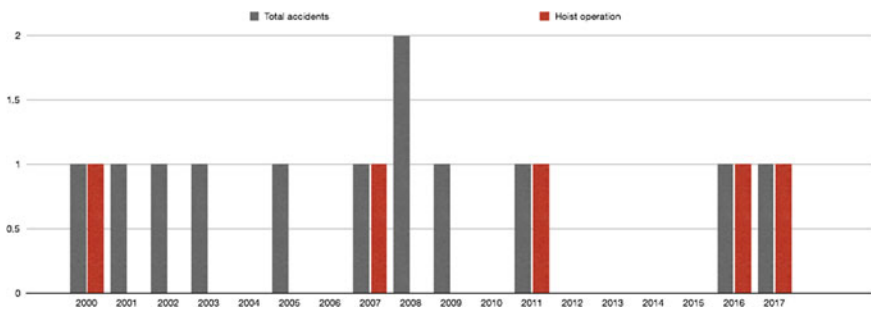
Fig. 1 HSAR total accidents and hoist operation accidents by year

2 Methodology

2.1 Statistical Data

The National Transportation Safety Board (NTSB) often uses three categories to establish multiple causes or factors for aviation accidents: personnel, environment, and aircraft-related [6]. Based on the results of the ASC survey and referring to the NTSB's cause/factor classification, there is at least one reason why the event may occur in each event, and some may have two or more causes and factors. Major data sources include the statistics of the Aviation Safety Council (ASC) aviation occurrences investigation reports and the data from the NASC. Personnel were cited as causes/factors in 56.5% (26% were pilot related, 30% were other personnel such as maintenance personnel and rescuer related), followed by 30.4% of aircraft-related causes/factors and by 13% of environment-related causes/factors. Broad causes and/or factors for an airplane of transport category occurrences over the last seventeen years are shown in Fig. 2. GSIE has developed a unified accident rate since 2011. This is achieved through close cooperation between the International Civil Aviation Organization (ICAO) and the International Air Transport Association (IATA) to align accident definitions criteria and analysis methods used to calculate the harmonized rate, which is considered a key safety indicator for commercial aviation operations worldwide [7]. The accident categories are shown in Table 1, and HSAR accidents 2000–2017 are shown in Fig. 3.

2.2 Case Analysis

The European Helicopter Safety Analysis Team (EHSAT) analyzed the helicopter accident investigation report and identified safety enhancement recommendations called Intervention Recommendations (IRs) [8]. As previously described, a total of

Fig. 2 Broad causes/factors for HSAR category, 2000–2017
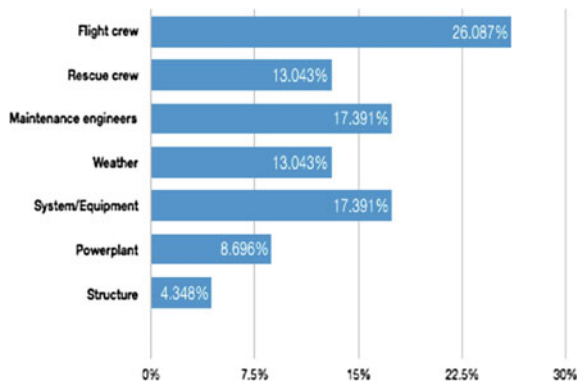
Table 1 Accident categories

GSIE harmonized accident categories	
Category	Description
Controlled flight into terrain (CFIT)	This includes all situations in which the aircraft enters the terrain in a controlled manner, regardless of the crew's situational awareness. Does not include undershoot, overshoot, or collision of takeoff and landing obstacles included in runway safety
Loss of control in-flight (LOC-I)	Loss of control in-flight that is unrecoverable
Runway safety (RS)	These include runway excursions and incursions, undershoot/overshoot, tail impact, and hard landing events
Ground safety (GS)	Includes ramp safety, ground collisions, all ground maintenance, headlights, engine start/go, and arrival events. Taxi and trailer activities are also included
Operational damage (OD)	Damage caused by the aircraft operating under its own power. This includes light damage, foreign object debris (FOD), and all system or component failures, including gear landings and gear collapse
Injuries to and/or incapacitation of persons (MED)	All injuries or incapacitations sustained by anyone in direct contact with the aircraft. Includes turbulence-related injuries, injuries to the ground staff coming into contact with the aircraft and onboard incapacitations and fatalities not related to unlawful external interference
Other (OTH)	Any event that does not fall into the above categories
Unknown (UNK)	The exact cause of any event route cannot be reasonably determined by information or reasoning, or when the facts are not sufficient to make a decisive decision about the classification

five HSAR hoist operation accidents occurred during 2000–2017 (refer to Appendix A). A brief description of the incidents shown in the table is reported through the ASC incident investigation report, and many report descriptions describe the risk factors at the time of the accident. It is worth noting that the findings relate to risk factors that may reduce aviation safety. Some of the findings in this category identify unsafe behavior, unsafe conditions, and security deficiencies, including organizational and systemic risks, making this situation more likely to occur; however, they do not clearly show that they only operate when they occur.

Fig. 3 Occurrences distribution of HSAR 2000–2017 by ICAO occurrence category
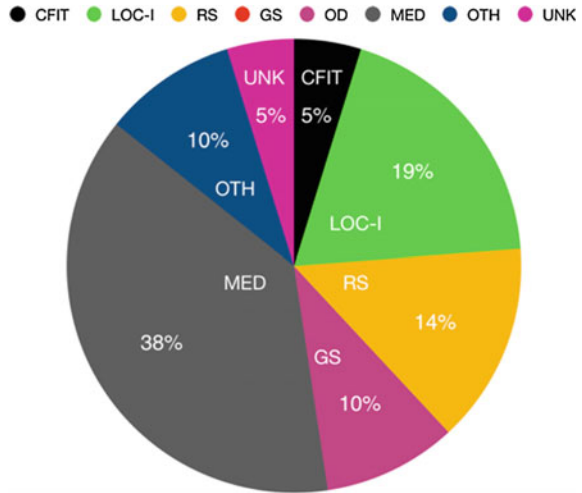
2.2.1 Risk Factor Analysis

From the past 18 years in the hoist accident investigation report case analysis, and sort out the above including possible causes and risk factors [3, 9–12]. The accident report is summarized as follows:

Findings Related to Probable Causes

- Mechanical part maintenance human factors.
- Flight crew members did not follow emergency procedures.
- During the overhaul, the hoist device had a wrong measurement for the axial gap value.
- The aircraft should conduct OGE hovering under irregular tumbling air environment.
- During the hoist operation, displacement appeared to the aircraft, causing a fleet angle to exceed the defined limitations.
- Unusual component abnormalities.

Findings Related to the Risks

- Did not provide the complete standard operating procedures which covered all common service units.
- Hoist line operation and limitations were not included in the education and training manuals.
- Did not integrate for joint implementation from different unit operations including communication and coordination.
- Did not meet the regular inspection period control standard and fleet maintenance management.
- Maintenance personnel does not meet the maintenance quality standards.

- Pilots lacked flight simulator training.
- Insufficient training due to limited training budget.
- Flight crew not wearing the standard PPE in the NASC procedures.
- Maintenance did not meet the standard of the manufacturer's overhaul manual during the hoist device overhaul.
- Maintenance technician used a nonstandard tool.
- Maintenance technician training was not completely implemented.
- Did not integrate for joint implementation from different common service operations, overlapping operations, and items decided after joint evaluations and establish standards of common operating norms, responsibilities, and procedures.

2.3   Semi-structured Interviews

Through data collection via ASC database, we found that the past case data showed fewer cases. In order to approach further even find out the risk factors associated with HSAR hoist operation one step closer, this study aims to interview the personnel related to these tasks (e.g., helicopter pilot and HSAR crew member and chief, maintenance engineers). Huang [13] used the Delphi method to construct open questionnaires and to realize the key factors of helicopter operation risk. Qualitative research methods are considered appropriate when investigators investigate new areas of research or intend to identify and theoretically highlight issues [14, 15]. Semi-structured interviews are a framework in which not only practices and standards are documented, but challenges and enhancements are also realized [16]. Use semi-structured interviews to find relevant risk factors through recording.

2.3.1   Interviewees

The HSAR mission members are composed of four units, respectively, by NASC, NFA-SSART (National Fire Agency Special Search and Rescue Team), CGA-SSC (Coast Guard Administration Special Services Company) organized by the three official departments, and commissioned private helicopter with system maintenance company for maintenance. There are some types of interviewees including in NASC: pilots and crew chiefs, NFA-SSART members, CGA-SSC members, and maintenance engineers. A total of 25 interview content were recorded, corresponding to various parts of four pilots, six crew chiefs, ten rescuers, and five maintenance engineers, from four different units. In particular, the interviewees included two pilots, two crew chiefs, and four SAR as participants in the case incident mentioned above.

2.4 Ensuring the Completeness

Through discussions in the literature and expert meetings, HSAR enhances operational risk factors to assess and supplement the research work in this article and ensure that it is exhaustive. This comment is important because it corrects any bias in the case analysis and interview results methods, including the tasks of search and rescue execution in the previous steps. This section also reviews related risk and accident models. Therefore, the risk and accident model usually refers to a preconceived system structure [18].

2.4.1 Human Error Models Systems Approach

After investigating several major disasters, James Reason presented the cause of the accident called the Swiss cheese model [19]. Reason divided the error into two types: latent error and active error. Reason [20] emphasizes that we are in the age of organizing accidents and due to potential errors triggered by frontline staff (usually organizational or regulatory issues). In other words, the accident is caused by a series of mistakes. Errors are hard to detect or lack of information. It is very difficult for personnel to detect and correct potential mistakes in advance, and the more complicated system leads to more mistakes happened.

The theory provides a general principle of opinion, enable event analysts to follow the principles of overall organizational factors, and conduct a rough analysis of the incident. However, the theory is still somewhat weak. Therefore, Wiegmann and Shappell [21] proposed the Human Factors Analysis and Classification System (HFACS). HFACS was also developed from the Swiss cheese model to build the concept of potential and active failure, divided human error into four levels shown in Fig. 4.
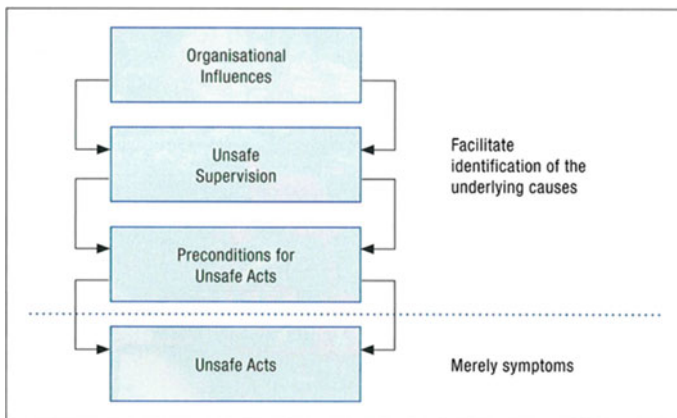
Fig. 4 HFACS model structure (Wiegmann and Shappell [21])

2.4.2 Crew Resource Management (CRM)

Chute and Wiener [22] described that CRM plays an important role in flight safety, and several dramatic incidents have highlighted some of the deficiencies in crew coordination and communication. CRM directly solves the mistakes caused by bad group decisions, ineffective communication, and poor management of tasks or resources [23]. In recent years, all airlines have also actively promoted the training and management of CRM. They hope to improve their flight training through CRM between team members to reduce the damage caused by human factors.

2.4.3 Operational Risk Management (ORM)

In 1996, the US Coast Guard developed a risk management model for performing operations, called operational risk management (ORM) [24]. ORM identifies and controls risks across all activities through management strategies and assessment processes, including assessment tools and the following principles [25]:

- **Accept No Unnecessary Risk**: Search and rescue operations mean risk. Unnecessary risks convey disproportionate benefits for mission security. Effectively complete tasks and be logical while minimizing the exposure of personnel and resources to risk.
- **Accept Necessary Risk When Benefits Outweigh Costs**: Compare all identified benefits to all identified costs. The process of weighing risks and opportunities and benefits helps maximize unit capacity. Even when a high-risk effort can be made when the decision maker explicitly acknowledges that the sum of the proceeds exceeds the sum of the costs. Balancing costs and benefits can be a subjective process that can be explained.
- **Make Risk Decisions at the Appropriate Level**: Appropriate risk decision-making levels must meet this requirement: the most effective way to allocate resources to reduce risk, eliminate hazards, and implement controls. This includes ground rescuers scrutinizing their helicopter rescue plans and whether it is really appropriate. Events that make an action plan must ensure that their subordinates understand their limitations and when they will submit decisions to a higher level.
- **ORM is Just as Critical in Executing as in Planning All Activities**: While ORM is critical in the operational planning phase, the risks in actual missions can change dramatically. Therefore, supervisors and senior leaders should remain flexible and integrate ORM into their execution tasks as much as possible in order to plan for them.

3 Result

Through the Aviation Safety Council (ASC) database, we collected the statistical analysis of the major accidents of HSAR during 2000–2017, carrying out case studies
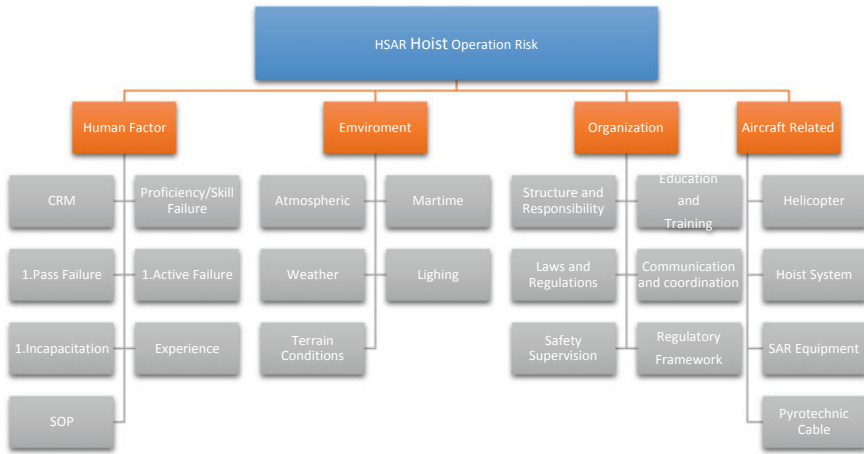
Fig. 5 HSAR hoist operation risk factors

on the investigation reports of the HSAR hoist operation casualties in the rear cabin, and semi-structured interviews were conducted with personnel involved in the implementation of the mission, literature review, and interview results divided into four essential evaluation dimensions and 22 risk factors shown in Fig. 5.

4 Conclusion

Helicopters have become a common tool in search and rescue (SAR) operations in Taiwan and elsewhere in the world. This study collects related data. The first step in this study was to collect data on HSAR-related task cases through the ASC database, and we organize statistics based on documented accidents and their categorization. The outcome shows: 56.5% *Human Factors*, the highest of all; 30.4% *Technical Issues*, helicopter machinery and/or equipment malfunctions; and 13% *Environmental Factors*. Additionally, MED (injuries to and/or incapacitation of persons) is accounted for the highest proportion in cases, according to GSIE Harmonized Accident Categories. This study then further addressed the HSAR accident investigations on five specific cases of hoist operation accidents. Next, the risk factors needed to be accounted for, evaluating them from two perspectives: related to probable causes and related to the risks. Then, semi-structured interviews were exercised to collect valuable information from SAR team members that have previously experienced unexpected difficulties during hoist-related missions. Finally, after careful organization, the study established four major risk prospects, with their respective risk factors listed under each of them. Hopefully, this information will be useful even promote all those operating hoist-related missions, with the reduction in incident probability in mind.

5   Limitation

For this specific application in HSAR, the sample size (absolute number of HSAR accidents) was significantly smaller compared with other types of aviation (e.g., general aviation, commuter operations, or major airlines), and this study is limited by the scope and quality of archived data. Another limitation is that the study is mainly about the hoist operation, and phases of helicopter flights are mainly in the helicopter to reach the rescue target area and SAR Hoisting out of the implementation of the operation begins, then SAR completes the rescue into the cabin phase.

Appendix A

HSAR hoist operation accident 2000–2017		
Year	Description	Injury level
2017	UH-60 Black Hawk helicopter conducted a search and rescue joint training at offshore of Taichung Harbor. There were three pilots, three crew chiefs and three rescuers, total of nine people aboard. Two rescuers fell into the ocean due to the hook was separated from the hoist system. Two rescuers sustained minor and severe injuries	Two rescuers sustained minor and severe injuries
2016	AS365N3 helicopter crashed into the water during hoisting a rescuer to a vessel about 0.3 nm north from Shimen seashore. NA-107 carried two pilots, one mechanic, and two rescuers	Copilot and one rescuer were killed, and the other three were seriously injured. The helicopter was hull loss
2011	UH-1H helicopter had the captain and copilot, one flight engineer, and three rescuers. The aircraft during its third training operations at Longxiang Riverside Park, Flight engineer released the wire rope and started to retrieve the rope to hoist personnel after seeing the end of the rope was hooked well with the trainee. Then the helicopter started moving forward slowly, and at the same time, the flight engineer kept on retrieving the wire rope. At 30 ft from the ground, the flight engineer felt the rope retrieving process was stopped and the rope started to slip down. After inspection flight engineer found that the pulling device could not be controlled, which led the rope to slip downwards and saw the hoisted personnel falling off to the ground	Rescuer sustained severe injuries

(continued)

(continued)

HSAR hoist operation accident 2000–2017		
2007	UH-1H helicopter departed from RCSS airport for a Search and Rescue mission. The aircraft dispatched with two pilots, one engineer, and two rescue members. During the rescue operation, both rescuer and individual under rescue were serious injuries caused by the broken rescue wire rope	Rescuer and individual sustained severe injuries
2000	AS365N3 helicopter performed disaster search and rescue exercises. The aircraft dispatched with two pilots, one engineer, and two rescue members. During the hoist operation, the power plant was failed, then the helicopter crashed into the river	Two pilots were killed and rescuer sustained minor

References

1. The World Bank Hazard Management Unit. (2005). *Natural disaster hotspots a global risk analysis*. The International Bank for Reconstruction and Development/The World Bank and Columbia University.
2. Taipei Times News. (2016). Available at http://www.taipeitimes.com/News/front/archives/2016/03/12/2003641375.
3. NASC NA-703 Occurrence: Preliminary Report. Aviation Safety Council, June 2017.
4. Veillette, P. (2009). *FAA risk management handbook* (p. 28). U.S. Department of Transportation.
5. National Airborne Service Corps database. Available at: http://www.nasc.gov.tw/Nasc/jobStats. Accessed December 10, 2017.
6. Aviation Safety Council. *Injury facts: 2010 edition*.
7. ICAO Safety Report: Annual Report for 2015. Published in Montreal, Canada International Civil Aviation Organization.
8. Stevens, J. (2012). Helicopter safety: Everybody's concern. *The Official Publication of THE UK FLIGHT SAFETY COMMITTEE* (pp. 9–13). ISSN: 1355-1523.
9. NASC NA-107 Occurrence: Investigation Report. Aviation Safety Council, March (2016).
10. NASC NA-511 Occurrence: Investigation Report. Aviation Safety Council, May 2011.
11. NASC NA-520 Occurrence: Investigation Report. Aviation Safety Council, Dec 2007.
12. NASC AP-018 Occurrence: Investigation Report. Aviation Safety Council, Sept 2000.
13. Huang, P. (2011). *A study on the major risk identification of the airborne operation of the special search and rescue team, fire science*. Central Police University, paper.
14. Corbin, J. (2008). *Basics of qualitative research: Techniques and procedures for developing grounded theory* (A. Strauss, Ed., 3rd ed.). California: Sage Publications.
15. Creswell, J. W. (2007). *Qualitative inquiry and research design: Choosing among five approaches: International student edition*. California: Sage Publications.
16. Oakley, A. (1998). *Methodology and people's ways of knowing: Some problems with feminism and the paradigm debate in social science*.
17. Mason, J. (1994). Linking qualitative and quantitative data analysis. In *Analysing qualitative data* (pp. 89–110). UK.
18. Hollnagel, E. (2012). *FRAM: The functional resonance analysis method—Modelling complex socio-technical systems*. Farnham, UK: Ashgate.
19. Reason, J. (1997). *Managing the risks of organisational accidents*.
20. Reason, J. (2008). *The human contribution: Unsafe acts, accidents and heroic recoveries*.

21. Shappell, S., & Wiegmann, D. (2000). *The human factors analysis and classification system (HFACS)*. DOT/FAA/AM-00.
22. Chute, R., & Wiener, E. L. (1995). Cockpit-cabin communication: I. A tale of two cultures. *The International Journal of Aviation Psychology, 5*(3), 257–76.
23. CAA. (2014). *Flight-crew human factors handbook*. UK: Civil Aviation Authority.
24. National SAR Academy. (2013). *Helicopter rescue techniques: Civilian public safety and military helicopter rescue operations* (p. 16).
25. U.S. Coast Guard. (1999). *Operational Risk Management*. Commandant Instruction.

Investigation Report of Bei-Men Hospital Fire in Taiwan on October 23, 2012

Teng-Yi Wang and Kuang-Chung Tsai

Abstract A fire occurred at Bei-Men Hospital, a branch of Sinying General Hospital, on October 23, 2012. This fire caused 13 deaths and 59 injuries, and is regarded as the most severe hospital fire in history in Taiwan. This study adopted on-site investigation on October 30, 2012, one week after this fire, when the fire scene has not been changed much. The fire growth, smoke behavior, and the capacity of fire safety equipment in this fire were investigated particularly. After this survey, the failing of fire and smoke compartmentation on ceiling was found to be the primary cause for this severe fire. Some suggestions were made in the fire safety design for hospitals and ordinary buildings.

Keywords Forensic science · Fire investigation · Hospital fire · Fire compartmentation · Flashover · Arson

1 Introduction

1.1 Fire Safety Issues in Hospitals

Fire safety in hospitals has not been paid sufficient attention because of its complex function. The fire safety design in hospitals needs professions in fire safety, medical act, and hospital management. Flammable liquids [1, 2] or gases [3, 4] are commonly used. Additionally, most people who appear in hospital are patients, and some of them may not move conveniently. Some patients are even with mental disorders and may not always be managed. A report from National Fire Agency, Taiwan, showed that most of the hospital fires were caused by electrical failures.

Hospitals themselves have characteristics of large numbers of poor mobility patients. Once a fire has occurred, smoke and toxic gases [5] will not only make people choke or expose poison, but also reduce the visibility for evacuees [6]. This

fire problem is more severe to those patients with restricted mobility, such as those who use breathing apparatus and are confined to bed [7–10].

1.2 Fire Safety Regulations in Hospitals in Taiwan

A severe fire at the Welcome Restaurant in Taichung caused 64 deaths and 14 injuries on February 15, 1995. After this severe fire, Taiwanese government reviewed related fire codes to strengthen fire safety designs for all kinds building (including hospitals) at different stages of fire growth. Figure 1 shows the strategies for each corresponding fire growth stages. All these strategies were practiced in the fire codes in Taiwan, i.e., "Standard for Installation of Fire Safety Equipments Based on Use and Occupancy" [11]. The installation of fire safety equipment in hospitals in Taiwan stands on the contents of this standard.

Because of some severe fires in hospitals and long-term caring organizations, the National Fire Agency, Ministry of the Interior, amended the national fire codes on May 1, 2012, to improve the fire safety of hospitals and long-term caring organizations (long-term care, nursing, and caring for the dementia), welfare institutions for the handicapped (limited to vegetable, dementia, bedridden, or patient with degraded physical and mental function), and nursing home institutions. The content is that these former places should be installed automatic sprinkler system and automatic fire alarm equipment in the lower floor area so as to improve self-defense capability, early fire detection, immediate evacuation and shorten emergency response time.

The installation of fire refuge facilities in hospitals in Taiwan stands on the contents of "Building Technical Regulations" [12]. Construction and Planning Agency, Ministry of the Interior, amended the former regulations on November 30, 2012, and temporary refuge spaces are necessary for new constructions or additions used for welfare institutions for the handicapped, special schools for the mentally, nursing home institutions, postpartum nursing care centers, elderly welfare and rehabilita-
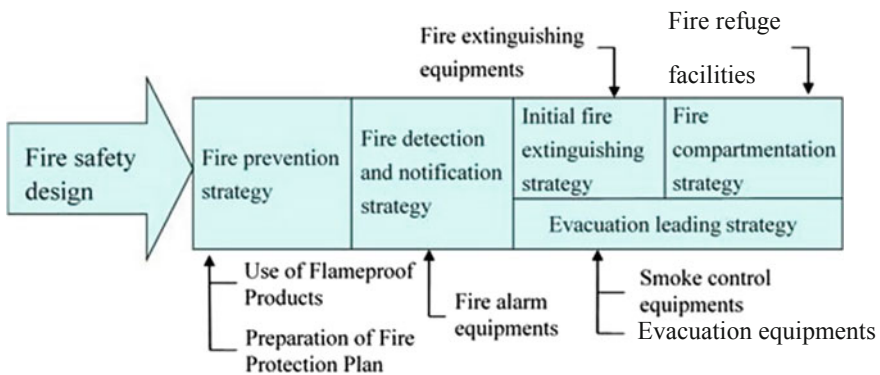
Fig. 1 Strategies for each fire growth stage

tion homes (accommodation type psychiatric rehabilitation agency), and other similar purposes. Therefore, every floor of these places should be divided into at least two sub-compartments [13] by fire compartmentation walls or metal rolling gates for certain duration for fire resistance to prevent the spread of fire and smoke and ensure safety of accommodated people.

In addition to above standard or regulations, fire safety design conformed that specific criteria can be relaxed or dispensed:

(1) When the floor area in a hospital is more than 1500 m^2, the floor should be divided into two sub-compartments by minimum one-hour fire-resistant rating walls, fire doors, etc. If effective automatic fire extinguishing equipment is installed, the maximum floor area for one fire compartmentation, 1500 m^2, can be expanded to 3000 m^2.

(2) The operation rooms, delivery rooms, X-ray rooms, intensive care units, anesthetic rooms, or other similar places in hospitals are not required to install automatic sprinkler systems due to medical use and surgical operations.

2　On-site Surveys of the Fire Scene

2.1　Basic Information of the Building

The building is located in Beimen Dist., Tainan City, Taiwan, and made of reinforced concrete with four floors and flat roof. Each floor area is about 2000 m^2, and the age of building is about 20 years. The first floor is the outpatient area. The northern side of the second floor about 1000 m^2 is outsourced for operations of a nursing home institution, and the southern side of the second floor about 1000 m^2 is used for obstetrics and gynecology clinic, delivery room, labor room, nursing station, ward, and so on. But the southern side of the second floor has been idle for years. The third floor is a negative pressure isolation area, and there are no patients at the time. The fourth floor is for mental ward. All internal compartments of the building are mainly solid brick walls or fire boards.

The fire investigation report of this fire indicates that the fire safety equipment and fire-prevention refuge facilities in the hospital were in compliance with the provisions of fire codes and regulations. Unfortunately, the fire caused 13 deaths and over 59 injuries. Obviously, this hospital is legal, but not safe. It is worthy to further explore the reason for the case. Therefore, this study adopted on-site surveys of smoke flow, disaster damage, the action status of fire safety equipment, and the set circumstances of fire-prevention refuge facilities in the fire scene, and proposed improved suggestions for current fire safety design.

2.2   Fire Investigation

Tainan City Government Fire Bureau received fire notice from Sinying Hospital's Bei-Men Branch at 3:29 am on October 23, 2012. The Bei-Men fire brigade was dispatched immediately and arrived at the fire scene at 3:38 am. No burning trace was appeared on the front facade of the building when the fire brigade arrived. Fires appeared from two windows on the delivery room on the second floor on the southwest side of the building. The aluminum window frames were melted, and some soot stayed on the exterior wall for approximately 10 m², as shown in Fig. 2.

Figure 3 shows the second floor plan. This fire started at the delivery room on the second floor, the southwest side of the building. The northern side of the second floor was used for nursing home.

Figure 4 presents the picture of the delivery room after this fire. A large amount of sheets, quilts, clothes, chairs, hospital beds, cardboard, paper, books, brooms, buckets, and other items were stacked in the fire room; however, those were not necessary facilities for the delivery room. Actually, this room has not been used for a long time, and the nursing home institution treated it as a temporary storage space. On October 23, 2012, a patient with mental disorder used a lighter to ignite some tissue, and threw the tissue inside the fire room and some other places outside the fire room. The tissue fire inside the fire room then spread to all the combustibles, and the entire room was completely destroyed, with an area of about 40 m². The light-gauge steel frame of ceiling was burned down, and calcium silicate boards of

Fig. 2 Fires appeared from two windows on the delivery room on the second floor, on the southwest side of the building

Fig. 3 Second floor plan of Sinying Hospital's Bei-Men Branch

Fig. 4 High fire loads in the fire room

ceiling scattered on the ground. Note that the automatic sprinkler equipment was not necessarily installed in the delivery room according to Taiwanese fire codes.

Figure 5 shows the picture of the ceiling of this fire room. The ceiling made of light frame and cement boards were penetrated by the flame, and the fire reached the concrete ceiling. However, the partition walls between the fire room and this adjacent room still existed after the fire. The partition walls were built to a height of the light-framed ceiling. The space above the light-framed ceiling of all rooms formed a large space without partitions, and smoke can move to other rooms through this "corridor."

Fig. 5 Ceiling of the fire room

No smoke mark on the bottom of inside door of the fire room. It can be considered that the door of the fire room was not closed when this fire occurred. Additionally, a large hole was formed on the outside wall of the fire room. The hole was not penetrated by this fire but damaged by firefighters just for the convenience of their firefighting action.

The ceiling of the nursing station and dentistry department did not collapse, and the walls were generally clean. Only some sooty traces were present along the junction between the ceiling and the partition walls. This phenomenon should be caused by the descent of smoke layers above the light-framed ceiling. Besides the second floor of the building, the internal spaces of other floors were not affected by the fire and smoke.

From the fire investigation report of Sinying Hospital's Bei-Men Branch [14], only four employees were responsible for the evacuation of 72 patients on fire floor in the hospital at that time. Clearly, insufficient capability of staff for emergency responses is another cause for large amount of victim. The report of Massachusetts Hyannis hospital fire indicates that automatic sprinkler system allows medical staff to have more time to carry out the patient in hospital [15]. From the concept of performance-based fire design, the installation of automatic sprinkler system benefits the evacuation of resident. However, the emergency response system is not discussed herein.

3 Discussions

This severe fire can be discussed from the following three items.

3.1 The Change of Use in the Fire Room

The automatic sprinkler equipment was not requested to be installed due to the special condition of medical use and surgical operations. However, the hospital in this case illegally allowed the delivery room to be used as a storage room without the permission of governmental authority. Therefore, when existing space is remodeled or changed to other conditions of use, the fire safety design needs to be reviewed.

3.2 The Management of Storage Room

The spaces which stack plenty of goods in hospitals should be locked. Additionally, some storage spaces are far from those with people and are appropriate places for arson.

3.3 The Failing of Fire and Smoke Compartmentation

From the interview with firefighters and fire investigation, the smoke flow penetrated the light-framed ceiling and entered the space between the light-framed ceiling and concrete ceiling. This space between the light-framed ceiling and concrete ceiling formed a corridor for smoke to move horizontally, and the damage of smoke was consequently enlarged. The sooty trace near the junction between the light-framed ceiling and the partition walls displayed that the smoke descended downwards and entered other spaces. The patient staying in other rooms outside the fire room were threatened. Additionally, there actually existed smoke exhaust equipment and automatic sprinkler system in some rooms and corridors. However, these equipments were located below the light-framed ceiling. The smoke between the light-framed ceiling and concrete ceiling cannot be exhausted by the smoke exhaust equipment. Furthermore, the auto-sprinkler system delayed to detect smoke because it took a long time for the smoke to descend, reach the system, and then activate. Figure 6 shows the schematic of all equipments in this hospital. Therefore, two lessons were taught by this fire: (1) Fire and smoke compartmentation should be build up to the concrete ceiling, rather than just the light-framed ceiling to prevent smoke move horizontally. (2) Fire safety engineers need to consider the positions to install the smoke exhaust equipment and automatic sprinkler system. Otherwise, they may not operate properly.

Fig. 6 Failure of fire
equipment installed below
ceiling
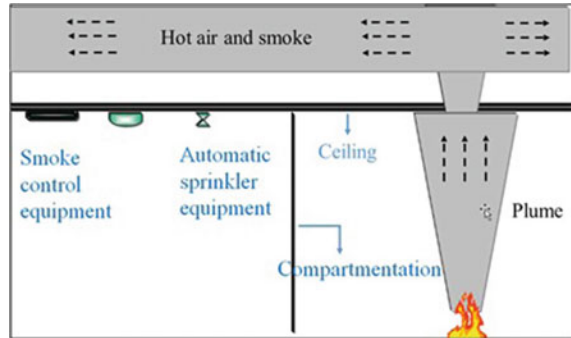
4 Conclusions

The Bei-Men hospital fire caused many victims and was investigated in detail. From
the on-site investigation, the change of use in the fire room, inadequate management
of storage room, and failing of fire and smoke compartmentation were the primary
causes for this severe fire. Several items for improvement were provided.

References

1. Batra, S., & Gupta, R. (2008). *Alcohol based surgical prep solution and the risk of fire in the operating room: A case report* (pp. 2–10).
2. Prasad, R., Quezado, Z., Andre, A. S., & O'Grady, N. P. (2006). Fires in the operating room and intensive care unit: Awareness is the key to prevention. *Anesthesia & Analgesia*, 172–174.
3. Roy, S., & Smith, L. P. (2011). *What does it take to start an oropharyngeal fire? Oxygen requirements to start fires in the operating room* (pp. 227–230).
4. Ahrens, M. (2008). *Fires and burns involving home medical oxygen*. National Fire Protection Association.
5. Stefanidou, M., Athanaselis, S., & Spiliopoulou, C. (2008). Health impacts of fire smoke inhalation. *Inhalation Toxicology*, 761–766.
6. Clarke, F. B. (1997). Physiological effects of smoke: Managing escape. *ASHRAE Transactions*, 411–417.
7. Schultz, C. H., Koenig, L. K., & Lewis, R. J. (2003). Implications of hospital evacuation after the Northridge, California, earthquake. *New England Journal of Medicine*, 1349–1355.
8. Huang, D. C., Chien, S. W., Lin, C. H., Huang, P. T., Song, Y. T., & Sie, H. R. (2011). A study for the evacuation of hospital on fire during construction. *Procedia Engineering, 2011,* 139–146.
9. Mckerracher, D. W., & Dacre, A. J. I. (1966). A study of Arsonists in a special security hospital. *The British Journal of Psychiatry*, 1151–1154.
10. Geller, J. L., Fisher, W. H., & Bertsch, G. (1992, Jun). A follow-up study of state hospital patients' firesetting behavior. *Psychiatric Quarterly*, 143–157.

11. Standard for Installation of Fire Safety Equipments Based on Use and Occupancy, Laws & Regulations Database of The Republic of China, 2016.
12. Building Technical Regulations, Laws & Regulations Database of The Republic of China, 2016.
13. Tseng, W. W., Pan, K. H., & Hsu, C. M. (2011). Performance-based fire safety design for existing small-scale hospitals. *Procedia Engineering*, 514–521.
14. Fire Investigation Report of Sinying Hospital's Bei-Men Branch, Tainan City Government, 2013.
15. Michael, S. I. (1996, October 16). *Fire investigation report: Hospital fire*. Hyannis, Massachusetts: NFPA.

FDS Model Simulates and Reconstructs the Ammonia Fire Accident Scene

San-Ping Ho, Hue-Pei Chang, Chin-Feng Chen and W. K. Chow

Abstract We investigated a fire accident which was caused by an ammonia coolant pipes' removal operation. Fire investigation at the scene of the accident determined that the corridor was adequately ventilated, with the fastest wind speed at approx. 1.62 m/s near the corridor area of storage room R8, but the ventilation of the top area within storage room R8 was extremely inadequate, measuring a wind speed of nearly 0.0 m/s. The use of natural ventilation was incapable of removing the ammonia gas accumulated near the ceiling of the storage room, thus resulting in a fire and casualties among the personnel. Fire dynamics simulator (FDS) was used to simulate the corridor and ceiling wind speed as 1.7 and 0.0 m/s in the same scene. The results proved that FDS is proper tool to reconstruct the ammonia fire accident.

Keywords Fire accident · Coolant pipes removal operation · Fire investigation · Ventilation · Ammonia gas · Fire dynamics simulator (FDS)

1 Introduction

The definition of a confined space, regardless whether it is by the regulations of ANSI, NIOSH, or IOSH of Taiwan [1, 2], is an environment where there are limited openings and poor natural ventilation, which may lead to danger, and even be life threatening. Yet, numerous environments, which seem to be well ventilated, could still be poorly ventilated in some places due to the building structure or machine placements.

S.-P. Ho · H.-P. Chang (✉)
Department of Occupational Safety and Health, Chang Jung Christian University, Tainan City, Taiwan 71101, Republic of China
e-mail: peipei@mail.cjcu.edu.tw

C.-F. Chen
Occupational Safety, Health and Medicine Research Center, Chang Jung Christian University, Tainan City, Taiwan 71101, Republic of China

W. K. Chow
Department of Building Services Engineering, The Hong Kong Polytechnic University, Hong Kong, China

We used computational fluid dynamics (CFD) model to simulate the ventilation and ammonia gas accumulation according to the scene of the accident. At the scene, the wall between the cold storage room and the corridor had already been taken down, as shown in Fig. 1. There were still beams surrounding the top of the storage room. The valve had been opened to remove the ammonia gas within the coolant pipes by means of natural ventilation. From comments of the employees on the scene, there seemed to be a strong smell of ammonia before deconstruction. Although water was sprayed on the floor to reduce the smell, the effectiveness of doing so was very poor.

Before the removal project began, the valves of the coolant pipes were opened to release the ammonia gas within them. However, the molecular weight of the ammonia gas released from the freezing pipe was lighter than air (ammonia: 17.0 g/mol, air: ca. 28.8 g/mol); thus, the ammonia gas floated upward; also there were beams still surrounding the upper portion of the room, creating a partially confined space as shown in Fig. 2, which allowed the ammonia gas to be stagnant near the ceiling.

After measuring the wind speeds of the scene, we found that the wind speed near the ceiling of storage room R8 was nearly 0.0 m/s, while the corridor outside it had a wind speed of 1.62 m/s from a distance of 2.0 m from the ground. Measurements showed that the corridor was adequately ventilated, while the upper part of the storage room was not, which resulted in an ineffective removal of the ammonia gas. Once the fire ignited the ammonia, which had reached its normal explosive limit (16–25%), the fire immediately spread to the other areas and set the thermal insulation material

Fig. 1 Accident scene of the storage room

Fig. 2 Upper portion of the storage room

on fire as well, thus resulting in large amounts of dense smoke, preventing employees from escaping safely.

CFD model had already used to simulate and reconstruct the fire scenes, such as van Wingerden [3] using femtosecond laser-assisted cataract surgery (FLACS) to simulate Buncefield explosion and prove the dense cherry woods accelerating the flame burning and blast wave. Chi et al. [4] and Chi et al. [5] also used FDS for fire investigation and successfully reconstructing the fire scene.

FDS has not only been used as a fire scenario analysis tool, but it also can show good results in ventilation evaluation. For example, Wu [6] applied FDS to conduct research on the ventilation of the recycling processing plant. The wind speed of the simulation model and the actual processing plant were identical, and it was discovered that the inner part of the storage tank area and the dosing motor area would become dead ends for the ventilation. The processing plant then focused on the results created by FDS and attempted to make adjustments. Chen [7] adopted FDS to simulate a confined space under natural ventilation and forced ventilation with different opening sizes and ambient wind speeds. The concentrations of O_2, CO, and CO_2 were measured with a gas detector, and the results were identical to the full-scale experiment of Lu et al. [8].

In this particular case, although the bottom half had adequate ventilation, the area near the ceiling had walls or beams blocking the way, thus prohibiting the refreshing

of the air inside, and also becoming a partially confined space. Under these circumstances, although not possessing potential suffocating dangers like normal confined spaces, the possibility of having combustible gases accumulation is nonetheless dangerous.

2 Simulation Methods

We used the computer simulation program FDS version 5.5.3 to draw a blueprint of the building and the conditions of the associated environment and also to simulate the wind speed at the scene of the fire. Smokeview 5.6 was used to observe the flow of the air within the construction site and top portions of the storage rooms.

FDS was used to simulate the scene of the fire, with the domain set at 64.0 m × 18.0 m × 4.8 m (L × W×H), and grid size at 0.1 m. There were 5,529,600 grids in all. A building with the dimensions of 54.0 m × 18.0 m × 4.8 m (L × W × H) was placed in the set domain. Inside the building, there were 16 rooms and a central corridor about 3.0 m wide. Some of the walls between storage rooms R3–R8 and to the right of R8 were taken down, so we placed openings of 3.0 m × 3.6 m (W × H) in those areas. On the far left end side of the building was an opening of 3.2 m × 3.8 m, while on the right end there were two openings of 4.6 m × 2.8 m and 3.0 m × 3.8 m, respectively. Furthermore, two open areas were placed on the outside area of the building to provide the inlet and outlet of the wind, one on the left and one on the right, with dimensions of 4.0 m × 18.0 m × 4.8 m, as indicated in Fig. 3.

During the scene of the accident, there was wind blowing in through the left opening of the domain, thus a wind speed of 3.0 m/s blowing from the left was set for the simulation, as shown in Fig. 3. Starting from left side of the building, two wind speed measuring trees were set 1.8 and 5.4 m from the wall inside rooms R3–R8; another measuring tree was set in the center of the corridor outside every room, with measuring heights at 1.0, 2.0, 3.0, 3.6, 3.8, 4.0, 4.2, and 4.4 m, respectively (Fig. 4). Ammonia release rate with 0.01 kg/s was set near the ceiling in R3–R8, and ammonia measuring points were also set at 1.0, 2.0, 3.0, 3.6, 3.7, 3.8, 3.9, 4.0, 4.1, 4.2, and 4.4 m high in every room to simulate and observe the profile ammonia gas ventilation.
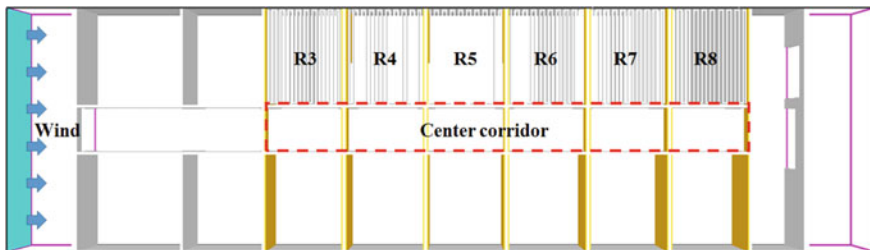
Fig. 3 Layout of the fire accident scene
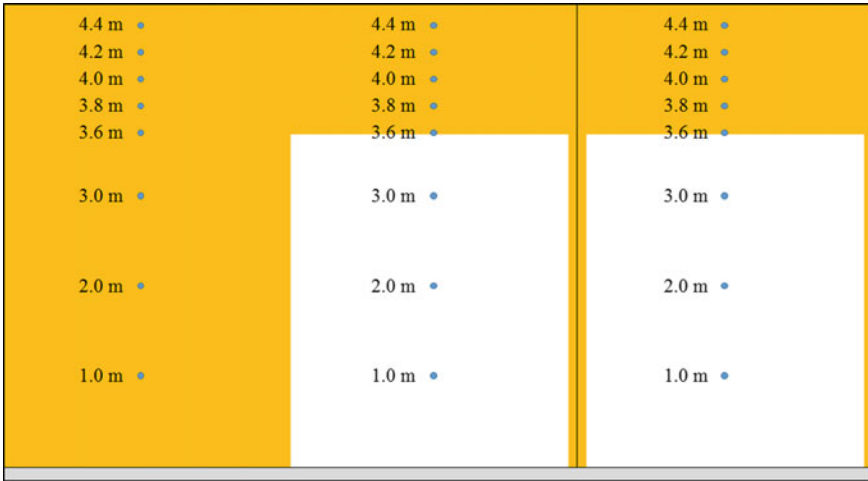
Fig. 4 Side view of the ammonia storage rooms and corridor, along with the places where the measuring points were set

3 Results and Discussion

3.1 FDS Simulation Reconstruct the Ventilation of Scene

From the results of FDS simulation, only at a distance of 2.0 m from the ground of the central corridor was there a wind speed of 1.7 m/s. When using the set wind speed for simulation at 3.0 m/s blowing into the left of the domain, the ceilings at 4.4 m from the ground and inside the storage room had extremely low wind speeds, from 0.04 to 0.05 m/s, as illustrated in Fig. 5. Figure 6 shows that the corridor had numerous beams which prevented the air from flowing, and it is the reason for the slow wind speed around 0.3 m/s in the ceiling area. Moreover, the openings in the walls caused the flow of the air passing through them to have a fan-shaped distribution at 2.0 m high plan view, as shown in Fig. 7. However, the wind could only reach as far as near the opening, whereas it was difficult for it to blow into the inner part of the room, which was why the wind speeds within the rooms were extremely low.

From Fig. 8, the plan view at the height of 4.2 m shows that the ceiling areas of every storage room, because of the blockage caused by the walls, made it difficult for it to ventilate; therefore, the wind speeds in the storage rooms were extremely low. And from Fig. 9, although the corridor was adequately ventilated, the inner portion and ceiling area of storage room R3 was poorly ventilated.
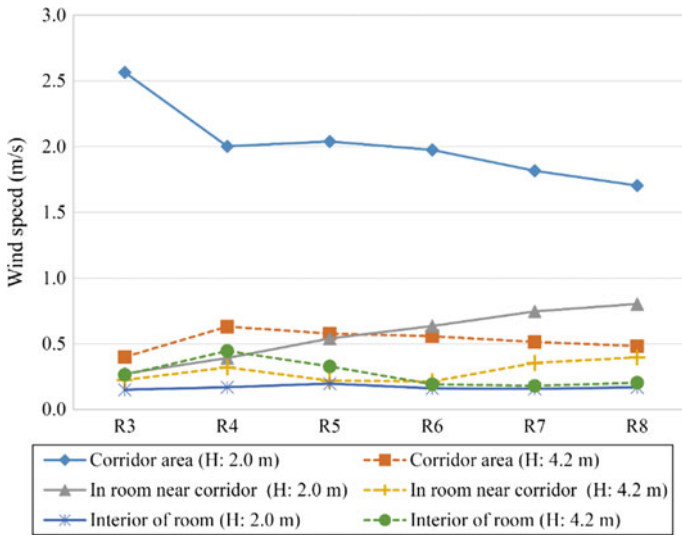
Fig. 5 Wind speeds in different areas
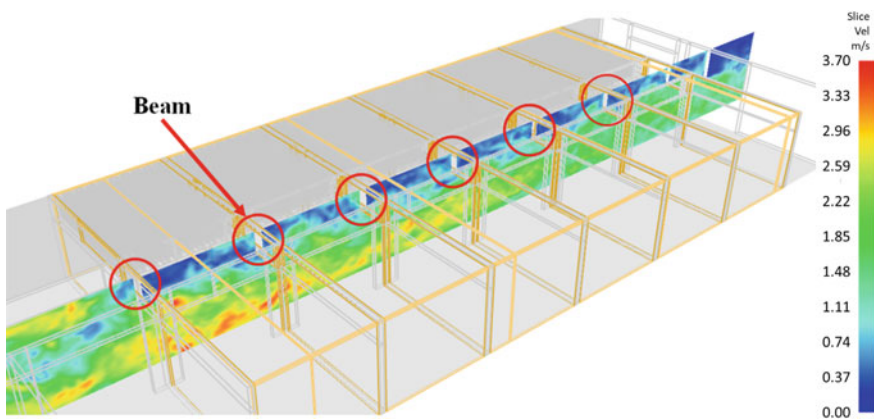
Fig. 6 Beams on the ceiling of the corridor prevented air from flowing through

3.2 Concentration Analysis of Ammonia Gas Inside the Building

After being released, ammonia gas accumulated on the ceiling and the concentration gradually increased until steady state based on FDS simulation. The ammonia concentration reached its normal explosive limit between 16 and 25% near the ceiling of the storage room, and it could be blown away at the lower portion of the room as shown in Fig. 10. When the deconstruction work was started at that day, the ignition
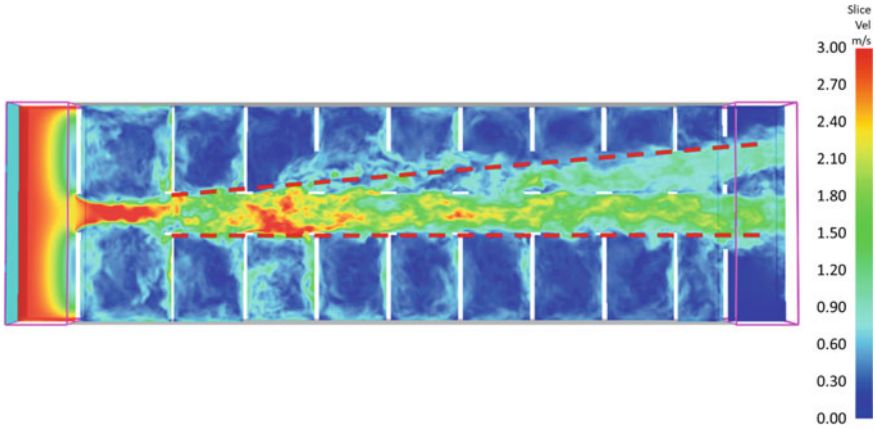
Fig. 7 Plan view of wind speed distribution from 2.0 m off the floor
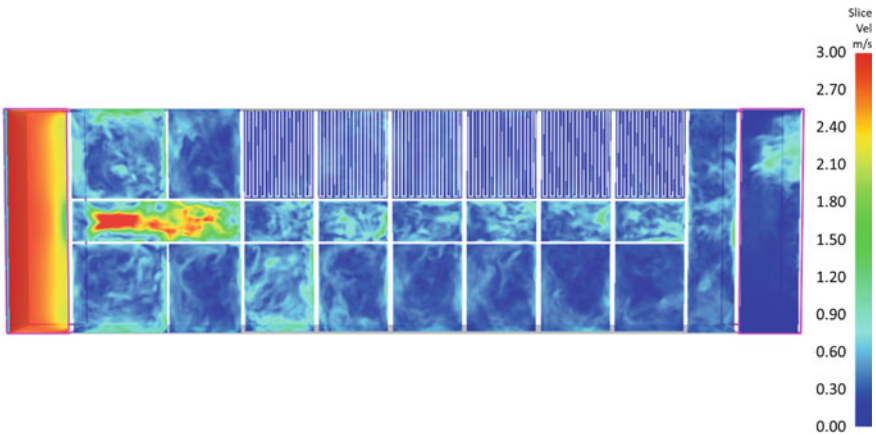
Fig. 8 Plan view of wind speed distribution from 4.2 m off the floor

source of friction ignited the ammonia to cause the fire and the deconstruction worker was killed in this accident.

The results of the simulation showed that by using FDS to simulate an ambient wind speed of 3.0 m/s, the corridor outside R8 had a wind speed of 1.7 m/s when 2.0 m off the floor, which was very similar to the wind speed of 1.62 m/s that was measured at the fire scene. Accordingly, the results show that the FDS simulation was consistent with the actual fire scene. When using an ambient wind speed of 3.0 m/s to simulate, it was found that the corridor areas were all adequately ventilated and the interiors of the storage rooms all had very low wind speeds. It proves that the ventilation conditions at the fire scene were unable to remove the ammonia gas accumulated near the ceiling, which resulted in a tragedy.
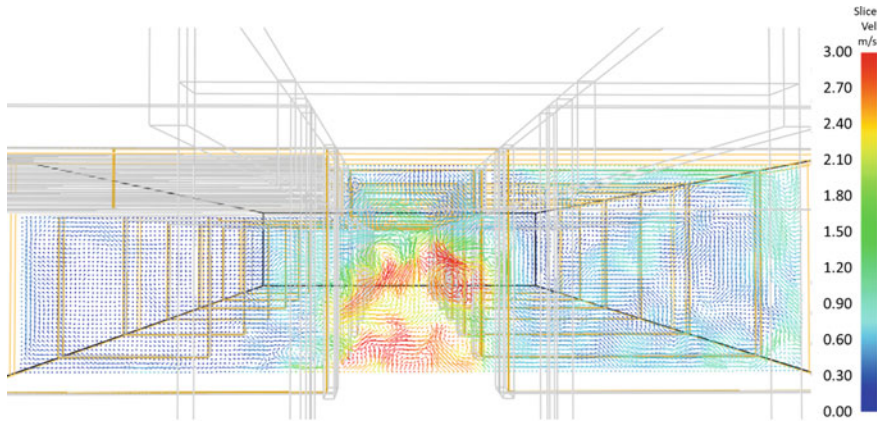
Fig. 9 Cross-sectional view of storage room R3 and its corridor
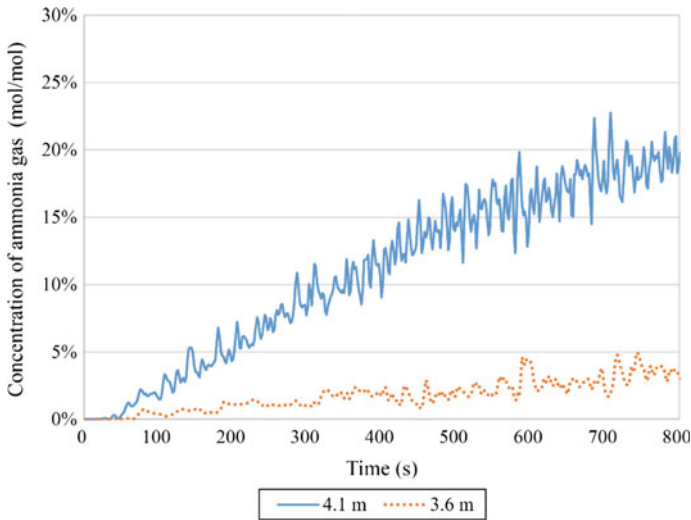
Fig. 10 Concentration of ammonia gas on different height in R3

4 Conclusions

From this case study and other references, it is possible that numerous environments which seem to be well ventilated could still be poorly ventilated in some places due to the building structure or machine placements. We used FDS to simulate the ventilation in the fire scene. The simulated results were very close to the measured wind speeds at the actual scene. This not only proves that the low wind speeds near the roof of the storage rooms resulted in the poor ventilation of ammonia gas, but it

also validates that FDS can be used to assist in fire investigation and the confirming of air ventilation within a working space.

Numerous accidents can be prevented. If the workers had performed risk analysis on the work site beforehand, learned more about toxic and flammable gas hazards, and made good use of anemometers and gas detectors, or used FDS to discover the areas where hazardous gases were stored, then this accident would never have happened. FDS can be an excellent tool to simulate the gas concentration in the work environment and to obtain a sound evaluation of the hazard before starting the work for preventing such accident.

References

1. Chia, T. P., & Chen, Y. J. (2002). A study of confined space safety program. *Journal of Occupational Safety and Health, 10,* 241–251.
2. Fu, H. R., & Peng, F. M. (2002). Analysis on incidents in confined spaces. *Industrial Safety and Hygiene Monthly, 160,* 22–39.
3. Van Wingerden, K. (2009). *Investigations of the Buncefield accident.* (As accessed on http://www.gexcon.com/article/buncefield-explosion).
4. Chi, J. H., Wu, S. H., & Shu, C. M. (2011). Using Fire Dynamics Simulator to reconstruct a hydroelectric power plant fire accident. *Journal of Forensic Sciences, 56,* 1639–1644.
5. Chi, J. H. (2013). Reconstruction of an inn fire scene using the Fire Dynamics Simulator (FDS) program. *Journal of Forensic Sciences, 58,* 227–234.
6. Wu, W. Z. (2012). *The performance on foam extinguishment and ventilation improvement in recycling processing plant.* Master Thesis, Chang Jung Christian University, Taiwan.
7. Chen, C. H. (2012). *A study on carbon monoxide simulation analysis and poisoning control of household gas water heater.* Master Thesis, National Chiao Tung University, Taiwan.
8. Lu, B. H., Chen, C. W., & Zhang, Z. P. (2006). Accumulation of CO from gas water heater on balconies. *Journal of Occupational Safety and Health, 14,* 299–307.

Fire Protection of Cultural Heritages

Fire Protection and Fire Safety Design of New Zealand Heritage Building

Dennis Pau, Christine Duncan and Charles Fleischmann

Abstract The application of performance-based fire safety engineering has enabled the conservation of a heritage building in New Zealand. McDougall House is a two-story heritage building which suffered extensive damages during the Canterbury earthquakes in 2010 and 2011. The scope of repair work carried out included the preservation and restoration of the building external façade, the restoration of the ornamental plasterwork ceiling within the Ballroom, the reconstruction of all damaged internal wall linings, the adaptation of the fireplace, and the reconstruction of the damaged chimney. The fire safety design adopted is the Verification Method C/VM2 with As Nearly As is Reasonably Practicable consideration for the heritage fabrics of the building. The combination of quantitative and qualitative analyses, including smoke and egress modelling, assessment of allowable unprotected areas in external wall for horizontal fire spread, and benefit versus sacrifice analysis on the heritage fabrics have demonstrated compliance with the ten design scenarios of C/VM2, retaining the majority of the cultural heritage values, and also improving the level of fire safety of the building.

Keywords Cultural heritage · Performance-based fire safety design · Fire protection design

1 Introduction

Heritage buildings are an intrinsic fabric of a society that amass historical values over time to provide the present and future communities with invaluable information regarding their past. The construction of these buildings can be unconventional

D. Pau (✉) · C. Fleischmann
Department of Civil and Natural Resources Engineering, University of Canterbury, Christchurch 8140, New Zealand
e-mail: dennis.pau@canterbury.ac.nz

D. Pau
Cosgroves Ltd., Christchurch 8140, New Zealand

C. Duncan
Ministry of Business, Innovation and Employment, Wellington 6140, New Zealand

when compared to the current standard of practice, and the ongoing use of these heritage building and associated conservation process often require the buildings to be assessed to meet the current building regulatory requirements. Despite this, it is vital to ensure that the cultural heritage values which intertwine the past, present, and future are not lost during the process as these values provide the very identity of the society in relation to the ancestors and also a measure of the achievement of the current community [1].

In New Zealand, the Building Act 2004 [2] is the mandatory framework for the building control system within the country, which governs the building design and construction process by improving the control of the building design and construction practice, providing regulations to ensure the health and safety of the building occupants and promoting sustainable development. With specific relevance to the fire safety design of a building, a few sections provide clarity on the minimum requirements, depending on the status of the building and its use. For heritage buildings which are existing, Section 112 covering "alterations to existing buildings" essentially requires the building, after alterations to comply As Nearly As is Reasonably Practicable (ANARP) with New Zealand Building Code (NZBC) in terms of means of escape from fire. The ANARP provision requires the altered building to continue to comply with NZBC as before or if it did not comply originally, the alterations will continue to comply at least with the same extent as before, i.e., level of fire safety of the building should not diminish following the alterations. Therefore, reasonable deviations from the minimum NZBC requirements are allowed for the conservation of existing heritage buildings.

This paper presents a case study on the incorporation of performance-based fire protection and fire safety design to the conservation of a two-storey heritage building in New Zealand, the McDougall House following the Canterbury earthquakes in 2010 and 2011 [3]. McDougall House is the office and business administration center for Nurse Maude, a health care association that provides nursing, homecare, and health support to patients. The International Council on Monuments and Sites (ICOMOS), New Zealand charter outlines the conservation principles of heritage places, including buildings and landscape [1]. According to the surveys and site investigations carried out by the design team, the earthquake repair strategy required significant consideration to the building's cultural heritage value. In accordance with ICOMOS guidance, the conservation approach comprises preservation, restoration, reconstruction, and adaptation of the heritage fabrics to maintain the authenticity and integrity of McDougall House. Not undergoing a change of use, McDougall House as an existing building was assessed in accordance with the requirements of Section 112 for means of escape from fire, with the additional newly constructed sections also assessed for the protection of other property and fire rating performance.

2 Background of McDougall House and Fire Safety Design Solutions

McDougall House is a two-storey, Arts and Crafts, Queen Anne and classical architecture styled building located at 24 McDougall Avenue, in the suburb of Merivale, Christchurch, New Zealand [4]. The building, originally named Fitzroy, was designed by Christchurch architects, the England Brothers, and constructed in 1898. Since then, the building has undergone a number of prominent changes, including the replacement of the original turret with gable, the enclosing of external verandas with bay windows, the addition of southern Ballroom, and the addition of eastern gable. Figure 1 shows the exterior alterations to McDougall House from 1898 to the completion of its recent refurbishment in 2015. The current building essentially retains the same layout as pre-earthquake, with minor alterations which include a few ground and first floor offices adopting a revised layout, restored veranda decking on northern elevation, new exterior paving and landscape along the eastern elevation, new southern entry and restored western entry for the Ballroom, and adapted new Ballroom fireplace with associated chimney shaft.

The ground floor contains a number of partitioned offices, meeting spaces, and miscellaneous spaces such as stores, kitchen, toilets interconnected by a partitioned corridor, which leads to the two stairs serving the first floor. The stairs are located at opposite ends of the corridor comprising an open feature stair which is smoke separated at first floor and a fire-rated safe path stair. The first floor contains additional office spaces with a kitchen and toilets. The building is timber-framed construction with timber weatherboard as external wall cladding, and timber shingles as roofing. Internally, the wall construction is either plasterboard on existing lath substrate or on a new timber frame, or a composite wall of timber panels on lath and plaster with mineral wool in cavity on one side and new plasterboard wall on the other. The ceiling system comprises plasterboard on timber joist floor. According to the heritage survey [4], a number of exterior and interior building elements were classified as having significant cultural heritage values. Externally, as seen in Fig. 1, these include the

Fig. 1 Exterior appearance of McDougall House, **a** original construction showing western elevation in 1898, and **b** western elevations upon the completion of recent refurbishment in 2015

original feature windows, gables and associated pediments, eave and ornate brackets, veranda columns and balustrades, balcony details, shingled roofs, and timber weatherboard and timber tile cladding with original exterior trims. Internally, these are the timber featured skirting, paneling, trims, post and beam structure, arch, doors and stairs, the ornamental plasterwork ceiling with coved cornice in the Ballroom and a number of ornate ceiling roses.

The earthquake assessment report [5] identified the extent of damages occurred as a result of Canterbury 2010 and 2011 earthquakes, a number of building code compliance issues and a few intrusive fire protection features which detract the cultural heritage values of the building. Figure 2 shows a few examples of the damages and intrusive fire protection features throughout the building. The primary damage to the building is the extensive cracking of the original lath and plaster wall system after the 2011 earthquake, whereby its inherently inferior bracing capacity has been reduced by the previous 2010 earthquake. The damage was more severe toward the west end of the building due to the presence of two original chimney shafts which contributed additional mass during the shakes, and also the lack of bracing walls at that part of the building. Other damages comprised cracked chimneys and first floor, including the ornamental plasterwork ceiling of the Ballroom as seen in Fig. 2, and the minor misalignment of ground floor level. The building's ventilation, hydraulics, and electrical systems were found to be requiring upgrade to meet the current NZBC requirements. The existing exposed fire protection systems were found to be detracting from the inherent heritage value of the building, and an indelicate example was the exposed sprinkler pipework located under the ornamental plasterwork ceiling within the Ballroom. Lastly, the earthquake assessment report noted that the damage to the exterior of the building was cosmetic and not of severe nature.

To meet the requirements of the Building Act, the building's fire safety design needs to comply with NZBC C1-C6 clauses, Protection from Fire [6]. The objectives of C clauses are to safeguard the people from unacceptable risk of injury or illness caused by fire, protect neighboring property from damage caused by fire, and

Fig. 2 Examples of the earthquake damages of McDougall House, including **a** the extensive cracking of the original lath and plaster wall system throughout the building, and **b** the cracking of the ornamental plasterwork ceiling within the Ballroom, with an exposed sprinkler pipework which detracts the value of this particular heritage fabric

facilitate firefighting and rescue operation. These objectives are satisfied by achieving the various performance criteria specific to each C clause, which contains a few functional requirements in general, such as reducing the likelihood of fire occurring via control of common building appliances, reducing the likelihood for internal and external fire spread, providing effective means of escape to facilitate evacuation during fire, providing adequate firefighting provisions to facilitate fire service operation, and providing structural systems with adequate performance during fire. To demonstrate that the functional requirements and specific performance criteria are met, there are two types of design solutions, the prescriptive Acceptable Solutions [7] and the performance-based fire safety design.

The prescriptive Acceptable Solutions, C/AS1-C/AS7 have some limitations when applied to existing heritage buildings which predate many of the current design and construction practices. For McDougall House, the size of the first floor exceeds the maximum allowable floor area of an intermediate floor in the Acceptable Solution. The first floor is considered as an intermediate floor due to the open feature stair connecting to ground floor and enclosing this stair would diminish the cultural heritage value of the building, which is not acceptable for the conservation plan adopted. A performance-based fire safety design approach offers more design flexibility to meet the requirements of NZBC C1-C6 and the available options include C/VM2 Verification Method: Framework for Fire Safety Design [8] and Alternative Solution.

C/VM2 is a fire safety design framework which prescribes a number of design inputs and specifies the minimum performance outcomes required for various fire safety aspects. While the design inputs and performance outcomes have been specified, this approach still requires the application of appropriate modeling tools and knowledge to simulate smoke spread, occupant evacuation and radiation to boundary or target which differentiates C/VM2 from a prescriptive design solution. Alternative Solution is a specific fire engineering design approach that requires agreement between the designer and relevant stakeholders, including building control authority, peer reviewer, and fire service on the design inputs, minimum performance criteria and design tools for the fire safety design. For McDougall House, C/VM2 was chosen over Alternative Solution as this potentially simplifies the building consent process due to the inherently accepted design inputs and minimum performance outcomes. The fire safety design comprises quantitative assessment utilizing conventional engineering tools and also qualitative assessment involving benefit versus sacrifice analysis.

3 Performance-Based Fire Safety Design of McDougall House

Figure 3 shows the ground and first-floor plans of McDougall House, indicating the location of exits on each floor, the demarcation of fire and smoke separations and the location of design fires for smoke and egress modelling. The ground floor of
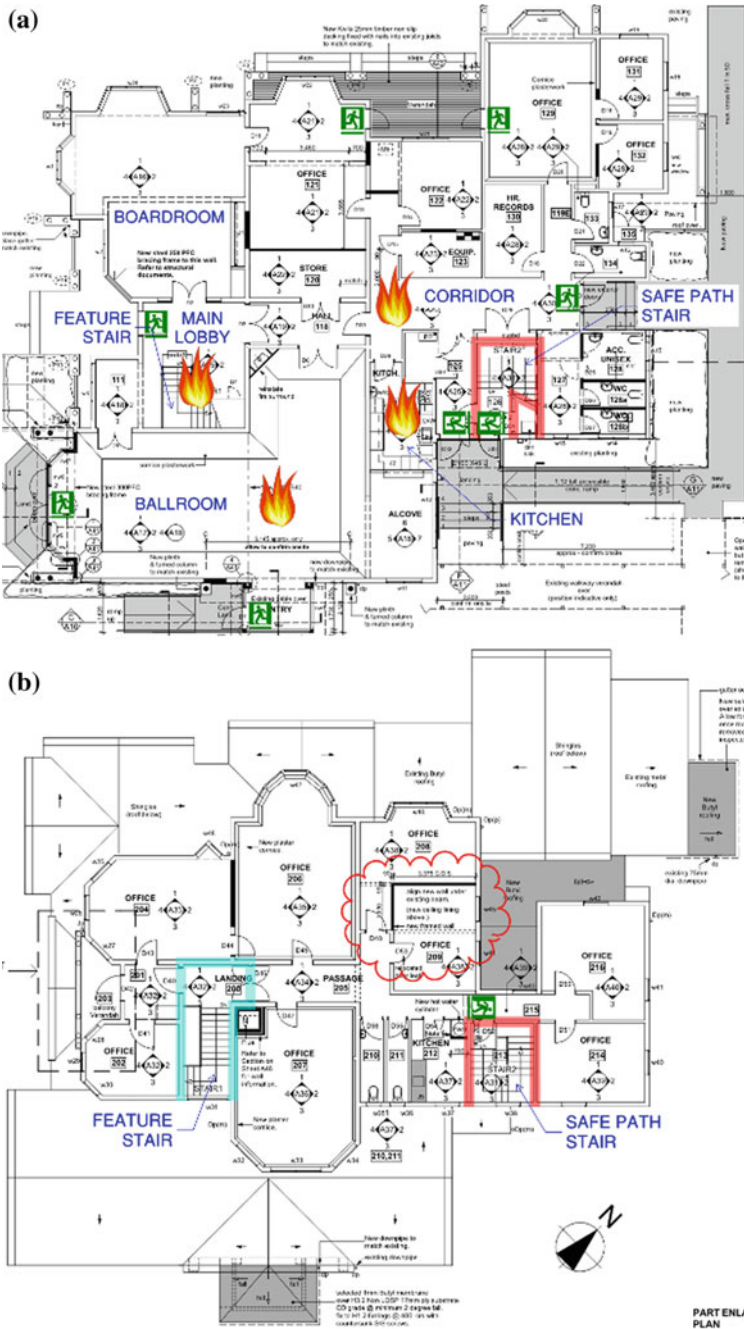
Fig. 3 Floor plans of McDougall House, **a** ground floor layout, and **b** first floor layout showing the location of exits, the demarcation of fire and smoke separations and the location of design fires

McDougall House is served by a number of final exits, indicated by the exit sign which leads directly to the outside car park and linkway. A few spaces of interest such as the Ballroom with ornamental plasterwork ceiling, boardroom, main lobby have been identified in Fig. 3. The first floor of McDougall House is served by a single means of escape via the safe path stair, with convenience access only for the feature stair. The fire rating of the safe path stair and its storage cupboard is 30 min, indicated by the red lines. The feature stair is open to the ground floor but smoke separated at the first floor, indicated by the cyan lines. Based on the floor area and the occupant density for various spaces specified in C/VM2 [8], the occupant load of the building is 95, with ground floor containing 79 occupants and first floor containing 16 occupants.

The fire safety and fire protection systems of McDougall House were surveyed to identify the condition of these systems and to determine the extent of upgrade required, in order to achieve the fire safety requirements of NZBC via C/VM2. The systems include the automatic fire sprinkler, smoke detection and alarm system, the fire-and smoke-rated construction, including the fire and smoke control doors, and the emergency lighting and exit signage. The systems existing condition and upgrades implemented are summarized in Table 1.

3.1 Design Scenarios of C/VM2

C/VM2 [8] presents ten design scenarios that address various fire safety aspects of a building and assess the fire safety design for the adequacy of means of escape, the performance of active and passive fire protection systems, the ability to limit internal and external fire spread, the provisions to facilitate firefighting and rescue operation, and the redundancy of fire protection systems. The description, performance outcome, and compliance method of each design scenario applicable to the fire safety design of McDougall House are summarized in Table 2. A number of design scenarios are satisfied based on the upgrade to the fire safety and fire protection systems of the building described in Table 1.

3.2 Quantitative Analysis: Design Scenario (HS) and (CF)

The maximum allowable unprotected area of Design Scenario (HS) was assessed for the new southern entry of the Ballroom which comprises the new entry at 1.3 m from the notional boundary of the adjacent building, and a portion of the reconstructed original weatherboard external wall at 2 m set back from the entry. According to C/VM2 [8], the fire load energy density for the Ballroom is 800 MJ/m^2, and using the tabulated values of C/VM2 commentary [11], the enclosing rectangle height and width for the reconstructed wall and the new entry are 3 m × 10 m and 3 m × 3 m, respectively. Based on the distance to boundary, the maximum allowable unprotected

Table 1 Upgrade to the fire safety and fire protection systems of McDougall House

Fire safety/protection systems	Existing condition	Upgrade
Automatic fire sprinkler system	Exposed sprinkler pipework under the ceiling	Concealed sprinkler pipework above the ceiling, particularly for the ornamental plasterwork ceiling of Ballroom
	Combination of outdated brass pendant sprinkler head and standard response sprinkler head	Combination of standard and quick response sprinkler heads with concealed type installed within the Ballroom, main lobby, and boardroom
	Exposed fire hose reel mounted on wall	Fire hose reel located within recessed cabinet on the wall
Fire alarm system	Manual alarm system with supplementary smoke detection	Automatic analog addressable smoke detection system with manual call points
	Outdated bell-type sounder	Electronic sounder with compliant alarm signature
Fire and smoke control door	Absence of fire and smoke control doors within the designated fire and smoke separations of the fire-rated safe path stair	Fire and smoke control doors -/30/30 sm rating leading into the fire-rated safe path stair at ground and first floors
	Absence of smoke control doors within the designated smoke separations at first floor of the feature stair	Smoke control doors -/-/- sm rating within the first-floor smoke separation of the feature stair
	Absence of smoke seals, door closers, electromagnetic hold-open devices and certified door tags for the fire and smoke control doors	Fire and smoke control doors equipped with smoke seals, door closers, electromagnetic hold-open devices and certified door tags
Fire-and smoke-rated construction	No fire rating to the first floor and its load-bearing walls and structural steel elements due to earthquake damage to the floor and wall linings	Fire-rated plasterboard timber joist floor and ceiling system, achieving 1-way 30 min fire rating
		Fire-rated plasterboard wall system utilizing existing lath substrate or new timber frame, or the aforementioned composite wall in Sect. 2, achieving 30 min fire rating with fire exposure from all sides

(continued)

Table 1 (continued)

Fire safety/protection systems	Existing condition	Upgrade
		Fire-rated plasterboard timber-framed system encapsulating structural steel elements, achieving 30 min fire rating with fire exposure from all sides
	No fire rating to the fire-rated safe path stair and storage cupboard under stair due to earthquake damage to its wall linings	Fire-rated plasterboard timber-framed ceiling system to underside of stair, achieving 1-way 30 min fire rating
		Fire-rated plasterboard wall system utilizing existing lath substrate, achieving a two-way 30 min fire rating
	No fire rating to the existing chimney voids due to the removal of chimneys following earthquake damage	Fire-rated plasterboard timber-framed shaft system, achieving 2-way 30 min fire rating
	No fire stopping to services penetrations through fire-rated floor and walls	Proprietary fire stopping products, including fire-rated collars and wraps, fire-rated intumescent mastic, fire-rated mineral batts, etc., installed to maintain the fire rating of the floor and walls
Emergency lighting and exit signage	Outdated emergency lighting model with limited coverage (no coverage where there is a change in level, e.g., feature stair and external ramps), not complying with NZBC requirements	Emergency lighting coverage, design and construction details meeting NZBC requirements
	Combination of illuminated exit signage and outdated non-illuminated exit signage, not complying with NZBC requirements	Illuminated exit signage coverage, design and construction details meeting NZBC requirements

areas are 51 and 45%, respectively, and these values are doubled to 100 and 90% due to the presence of sprinkler protection. Hence, the reconstructed weatherboard external wall can remain fully unprotected. The maximum allowable unprotected area of the new entry is 90% of 3 m × 3 m, 8.1 m^2, and the actual unprotected area of the entry is 7.4 m^2 (2.5 m × 3.0 m) which is less than 8.1 m^2, and thus, it can remain fully unprotected. McDougall House satisfies Design Scenario (HS).

For Design Scenario (CF), four design fires were simulated throughout the ground floor. CF1 in the main lobby challenged the smoke separated feature stair and retained the openness at ground level due to the presence of heritage door. CF2 in the Ballroom assessed the impact on the adjacent main lobby and feature stair. CF3 in the corridor

Table 2 C/VM2 design scenarios applicable to the fire safety design of McDougall House

Design scenario	Description/performance outcome	Compliance method
BE: fire blocks exit	This applies to escape routes serving more than 50 people or with a single direction of travel where an escape route may be blocked due to the proximity of the fire source. Single means of escape serves no more than 50 people, with a maximum length of 50 m if the occupants are familiar with the building. Two means of escape to be separated by at least 8 m apart	79 ground floor occupants have multiple escape routes which are separated by at least 8 m. 16 first floor occupants have a single means of escape with a travel distance of less than 50 m. McDougall House satisfies Design Scenario (BE)
UT: fire in normally unoccupied room threatening occupants of other rooms	This applies to spaces containing more than 150 occupants that could be threatened by a fire occurring in another normally unoccupied space (plant, store, etc.) protected by an automatic detection and alarm system where the fire can grow to a significant size undetected, spreading to areas with a large occupant load	McDougall House contains less than 150 occupants, and is protected by automatic smoke detection and alarm system installed to NZS 4512:2010 [9]. McDougall House satisfies Design Scenario (UT)
CS: Fire starts in a concealed space	This applies to spaces containing more than 50 occupants with concealed spaces (roof/ceiling, subfloor, etc.,) which can develop undetected, spreading to areas with large occupant load. Utilizing fire rated construction or suppression to confine the fire to the concealed space. Utilizing automatic detection of heat or smoke to provide early warning	McDougall House is protected by automatic fire sprinkler system which provides the detection of heat and suppression, installed to NZS 4541:2013 [10], including roof and ceiling spaces. McDougall House satisfies Design Scenario (CS)
SF: smouldering fire	This considers slow smouldering fire causing a threat to sleeping occupants	McDougall House does not contain sleeping use, and satisfies Design Scenario (SF)
HS: horizontal fire spread	This considers a fully developed fire in the building resulting in high levels of radiation across a relevant boundary. Allowable unprotected areas in the external wall to be assessed by the tabulated values in C/VM2 commentary [11]. External wall cladding systems to meet specific peak heat release rate and total heat released requirements	Refer to Sect. 3.2 for the assessment of allowable unprotected areas in the external wall. McDougall House building height is ≥7 m and <25 m, and sprinkler protected to NZS 4541:2013, so there are no requirements for the external wall cladding systems

Table 2 (continued)

Design scenario	Description/performance outcome	Compliance method
VS: external vertical fire spread	This considers external vertical fire spread over façade materials, via openings and unprotected areas, and via unprotected lower roof. External wall cladding systems to meet specific peak heat release rate and total heat released requirements. Utilizing apron and spandrel or suppression to limit the external vertical fire spread via openings and unprotected areas. Utilizing fire-rated construction to the lower roof or to the adjacent higher external wall or installing suppression to limit the external vertical fire spread via unprotected lower roof	McDougall House building height is ≤10 m so there are no requirements for the external wall cladding systems. McDougall House is protected by automatic fire sprinkler system installed to NZS 4541:2013 which limits the external vertical fire spread via openings and unprotected areas, and unprotected lower roof. McDougall House satisfies Design Scenario (VS)
IS: rapid fire spread involving internal surface linings	This requires the interior surface finishes such as wall and ceiling linings, flooring, and suspended flexible fabrics to meet the specific performance requirements attained via specific test standards	The new plasterboard linings on wall and ceiling and the new carpet tiles meets the specific performance requirements. Refer to Sect. 3.3 for the benefit versus sacrifice analysis of the existing heritage surface finishes, including the ornamental plasterwork ceiling and numerous timber linings
FO: firefighting operations	This requires adequate provisions for firefighting and rescue operation, including the fire service vehicular access, means of delivering water for firefighting, fire-rated floor and safe path to provide safe access for firefighters, and clear information to identify the fire location, fire safety systems of the building and hazardous activities within the building. Fire service hose run distance of no more than 75 m or provide building fire hydrant system in accordance with NZS 4510:2008 [12]. For escape height of ≤10 m, intermediate floors >40% of firecell floor area and its supporting structure to achieve minimum 30 min structural adequacy, integrity, and insulation rating	McDougall House external car park satisfies the fire service vehicular access requirements. The fire service hose run distance is no more than 75 m. The fire-rated floor and relevant supporting walls, and the safe path stair achieve 30 min fire rating. The fire alarm panel interfaces with the analog addressable smoke detection system and sprinkler system to provide a general location of the fire. McDougall House satisfies Design Scenario (FO)

Table 2 (continued)

Design scenario	Description/performance outcome	Compliance method
CF: challenging fire	This requires the analysis of Available Safe Egress Time (ASET) and Required Safe Egress Time (RSET) for the credible worst-case design fires located in various locations within the building, challenging the fire protection features of the building. RSET < ASET for fractional effective dose of carbon monoxide (FED_{CO}) no greater than 0.3	Refer to Sect. 3.2 for the smoke and egress modeling of the design fires
RC: robustness check	This considers the failure of key fire safety system such as smoke control system, fire and smoke control door, which could expose more than 150 occupants to untenable conditions	McDougall House contains less than 150 occupants and is protected by automatic fire sprinkler system installed to NZS 4541:2013. The fire and smoke control doors are equipped with electromagnetic hold-open device installed to recognized standard which are considered to be sufficiently reliable. McDougall House satisfies Design Scenario (RC)

assessed the impact on the safe path stair via the inherent leakage of the fire and smoke control door. CF4 in the kitchen assessed the impact on the adjacent corridor which is shared by the occupants from the offices. No design fire was specified on the first floor as a fire on first floor will not challenge the occupants on ground floor with multiple exits to outside. B-RISK Version 2013.15 [13], which is a two-layer zone model was used for smoke modelling, with the inherent assumption that the hot upper layer and cool lower layer of the compartment is spatially uniform throughout. The validity of this assumption was assessed for each Challenging Fire based on the dimensionless heat release rate and shape factor of the room of fire origin [14]. The design fire characteristics specified by C/VM2 were fast t-squared, sprinkler controlled with an effective heat of combustion of 20 MJ/kg and a radiative fraction of 0.35. The species yields were 1.5 kg/kg for CO_2, 0.04 kg/kg for CO, 0.07 kg/kg for soot, 0.82 kg/kg for H_2O, and the fuel composition was $C_1H_2O_{0.5}$. Standard response sprinkler characteristics were modelled to control the fire at activation, with Response Time Index of 135 $m^{1/2}s^{1/2}$, C-factor of 0.85 $m^{1/2}s^{1/2}$, activation temperature of 68 °C, and radial distance of 3.25 m. Smoke detector was modelled with optical density of 0.097 m^{-1} outside the chamber and radial distance of 7 m. Both sprinkler and smoke detector were located 25 mm below the ceiling. Egress modelling was based on first order hydraulic calculation [15], which adopts the longest between the travelling time to the furthest exit and the cumulative queuing time at constriction points. Travelling time is governed by the occupant density, with maximum 1.2 m/s for horizontal

travel and 0.85 m/s for vertical travel. Queuing time is governed by the width of the constriction with a maximum flow of 50 person/minute/door leaf. C/VM2 prescribes the notification and pre-movement times, 30 s and 60 s, respectively.

For CF1, the main lobby containing the feature stair was the room of fire origin, the adjacent Ballroom, and two spaces on the first floor preceding the feature stair, the passage and the small lobby were modelled as separate compartments. The tenability monitoring point was 2 m above the floor level. The smoke separation of the feature stair was modelled to fail at an upper layer temperature of 200 °C which will allow the smoke flow into the first floor spaces. The smoke detector activates at 48 s, and the sprinkler activates at 183 s to cap the heat release rate to 1.6 MW. The time to FED_{CO} of 0.3 or ASET is 374 s within the main lobby and 561 s within the Ballroom. On the first floor, this is 439 s within the small lobby and 465 s within the passage. Due to the fire in the main lobby, the occupants are not expected to use the main lobby final exit as there are multiple exits available from the ground floor. The travelling time of 23 s was found to govern the egress from Ballroom, and the queuing time of 85 s at various constrictions within the corridor and stair was found to govern the egress from first floor. Based on the detection time from B-RISK, and the notification and pre-movement times specified in C/VM2, RSET is 161 s for the Ballroom and 223 s for the first floor. This demonstrated that RSET < ASET for CF1, and this was similarly proven for the other design fires. McDougall House satisfies Design Scenario (CF).

3.3 Qualitative Analysis: ANARP Consideration with Benefit Versus Sacrifice Analysis

In order to retain the cultural heritage values of McDougall House, a few aspects of the fire safety design deviate from the minimum of NZBC requirements on ANARP basis. Using benefit versus sacrifice analysis, majority of the heritage fabrics have been retained to maintain the authenticity and integrity of the heritage building. On the exterior, with exception to the unprotected areas assessment on the new southern entry of the Ballroom, the façade of the building has been restored with new paintwork and replacement of damaged weatherboard. The complete reassessment of the entire building was not deemed necessary as the level of risk in terms of boundary fire spread has not changed following the refurbishment.

Internally, the ornamental plasterwork ceiling within the Ballroom has been restored with repair to the cracks and installation of concealed sprinkler pipework and heads above the ceiling. The ceiling was slightly lowered to allow for the installation of the 30 min fire-rated plasterboard floor system above. While the plasterwork did not meet the surface finishes requirements of C/VM2, the design fire simulated in the Ballroom, CF2 is considered to be of similar severity to a fire starting on this surface finish, and the results show the Ballroom occupants have adequate time to escape before untenable condition $FED_{CO} > 0.3$ is breached. This is due to the addi-

tion of smoke detection system to the building which provides early warning to the occupants; thus, the ornamental plasterwork ceiling can be retained.

The damaged lath and plaster internal wall linings of the building have been replaced by a new plasterboard wall system utilizing either the existing lath substrate or new timber frame, or the aforementioned composite wall in Sect. 2. Based on an equivalency assessment with standard plasterboard systems available, the manufacturer advised that these constructions would achieve the required 30 min fire rating. The heritage timber skirting, paneling, trims, etc., have been restored onto the reconstructed walls without further fire-retardant treatment. With reference to the design fires simulated, these are believed to have similar severity to a fire starting on the surface finish, and RSET < ASET were demonstrated for the spaces remote from the fire, satisfying the requirements of C/VM2 allowing the heritage timbers to be retained. Lastly, heritage windows by the Ballroom alcove front onto the external escape route, and quick response sprinkler heads have been installed locally by the alcove to protect these windows. In accordance with C/VM2, the safety of the occupants egressing externally was demonstrated by the Ballroom maintaining a tenable condition, $FED_{CO} < 0.3$ until the completion of egress.

4   Conclusions

The application of C/VM2, coupled with ANARP considerations for the heritage fabrics has enabled the refurbishment of McDougall House, both externally and internally to be carried out according to the conservation plan, retaining majority of the cultural heritage values such as the exterior architectural design and the interior ornamental timber and plasterwork linings. This performance-based fire safety design also improves the level of fire safety of the building with new smoke detection system, heritage sympathetic fire protection systems, e.g., concealed sprinkler heads and pipework, and new fire-rated floor and walls with compatible fire stopping products. Both qualitative and quantitative fire engineering analyses are required to ensure that the fire safety design is compliant with NZBC, and also satisfies the heritage conservation requirements.

References

1. ICOMOS New Zealand Charter for the Conservation of Places of Cultural Heritage Value, ICOMOS New Zealand, 2010.
2. Building Act 2004, Ministry of Business, Innovation and Employment, May 2017.
3. McDougall House Fire Strategy Report, Cosgroves Ltd., April 2014.
4. McDougall House Heritage Report, Fulton Ross Team Architects, 2013.
5. McDougall House Earthquake Assessment, Lewis & Barrow Ltd., March 2012.
6. Extract from the New Zealand Building Code: Clauses C1-C6 Protection from Fire, Clause A3 Building Importance Levels, Ministry of Business, Innovation and Employment, April 2012.
7. C/AS5 Acceptable Solution for Buildings used for Business, Commercial and Low Level Storage (Risk Group WB), Ministry of Business, Innovation and Employment, January 2017.
8. C/VM2 Verification Method: Framework for Fire Safety Design, Ministry of Business, Innovation and Employment, November 2017.
9. NZS 4512:2010 Fire detection and alarm systems in buildings, Standards New Zealand, 2010.
10. NZS 4541:2013 Automatic fire sprinkler systems, Standards New Zealand, 2013.
11. Commentary for Building Code Clauses C1-C6 and Verification Method C/VM2, Ministry of Business, Innovation and Employment, December 2013.
12. NZS 4510:2008 Fire hydrant systems for buildings, Standards New Zealand, 2008.
13. BRANZ Study Report 282, B-RISK User Guide and Technical Manual, BRANZ Ltd., 2013.
14. BRANZ Technical Recommendation 17, Room size limits when using a fire zone model for smoke-filling calculations, BRANZ Ltd., 2013.
15. Gwynne, S., & Rosenbaum, E. (2016). Employing the hydraulic model in assessing emergency movement. In M. Hurley (Ed.), *SFPE handbook of fire protection engineering* (p. 2115). New York: Springer.

Fire Protection of High-Rise Buildings

Sensitivity Analysis of Smoke Flow in New Zealand High-Rise Stairwells

Charles Fleischmann, Dennis Pau, Jack Montgomery and Logan Evans

Abstract The objective of this research was to investigate performance-based fire safety design in satisfying the tenability criteria of high-rise buildings with an occupancy load of greater than 1000 people per stairwell. This was completed through a sensitivity analysis of a 20-story high-rise building model using the Fire Dynamics Simulator for modeling a range of fire scenario. A total of 16 simulations were analyzed, with varying building parameters such as room geometry, sprinkler type, detection devices, and egress door configuration. The building was designed to comply with the New Zealand Verification Method (C/VM2). The acceptance criteria for visibility, toxicity, and thermal effects, were taken from the New Zealand Building Code (NZBC). The results for all simulations showed that the visibility requirements in the stairwell were the controlling tenability criteria when compared to the carbon monoxide and thermal effects. The results demonstrate the need for smoke detectors in conjunction with sprinklers in high-rise buildings.

Keywords Stairwell · Smoke flow · High-rise · Fire dynamics simulator · Sensitivity analysis

1 Introduction

Designing high-rise buildings to perform safely in the event of fire requires a complicated fire safety strategy. The fire safety design of the building must allow all occupants to evacuate via a vertical safe path (typically a stairwell) without being exposed to untenable conditions. The design becomes more challenging when the occupant load increases due to increased height or floor area of the building. The total evacuation time depends upon many variables including: escape height, number of occupants, detection time, and number of stairwells. Another significant factor is

---

C. Fleischmann (✉) · D. Pau · J. Montgomery · L. Evans
Department of Civil and Natural Resources Engineering, University of Canterbury, Christchurch 8140, New Zealand
e-mail: charles.fleischmann@canterbury.ac.nz

the type of evacuation strategy adopted for the building: simultaneous or phased. Simultaneous evacuation alerts all occupants within the building to a fire at the same time, whereas phased evacuation prioritizes occupants on the fire floor and adjacent floors.

Although stairwells are defined as vertical safe paths, smoke infiltration into the stairwell can still occur; primarily during evacuation of the fire floor when the door to the fire floor is open, and to a lesser extent, via leakage through the gaps around doors and other penetrations in the construction. If enough smoke enters the stairwell, the movement of the occupants may be reduced or even completely inhibited due to reduced visibility, as occurred in the MGM Grand fire [1]. It is therefore imperative for a fire engineer to be able to accurately model the smoke flow into a stairwell and understand the sensitivity of the modeling results to minor changes in the model inputs involved.

In New Zealand, most simple buildings are designed using one of the deemed to satisfy documents, *Acceptable Solutions, C/AS1 to C/AS7* [2]. When the design cannot be shown to comply with the deemed to satisfy documents, *C/VM2 Verification Method: Framework for Fire Safety Design* [3] (C/VM2) is used. C/VM2 defines the minimum analysis required by designers to demonstrate that the building satisfies *C-Protection for Fire* clauses of the *New Zealand Building Code* [4] (NZBC). Although C/VM2 is not directly applicable to high-rise buildings, the design fires and modeling rules can be applied in this analysis and have been adopted here without prejudice. The design fire and modeling rules are intended to provide a consistent level of rigor when fire modeling is used to demonstrate that a building complies with the code. The NZBC, *C4: Movement to a place of safety*, defines the acceptance criteria for fire engineering analysis such that the occupants are <u>not</u> exposed to:

1. Visibility at 2 m above the floor of <10 m except in rooms of <100 m^2 where visibility may fall to 5 m,
2. Fractional effective dose of carbon monoxide (FED$_{CO}$) of greater than 0.3,
3. Fractional effective dose of thermal effects (FED$_{therm}$) of greater than 0.3.

For a building that includes a fully compliant sprinklers system and <1000 people in a firecell, the fire safety design does not have to consider the visibility or the thermal FED requirements.

The purpose of this research was to conduct a sensitivity analysis of the Available Safe Egress Time (ASET) versus Required Safe Egress Time (RSET) analysis to building parameters that affect the tenability requirements in the stairwells of a high-rise building.

2   Modeling Setup

The building was modeled using computational fluid dynamics (CFD) software, Fire Dynamics Simulator [5] (FDS6). FDS6 (Version 6.5.3) solves the low-mach number version of the Navier–Stokes equations within a user-defined three-dimensional

domain. The building was modeled as a 20-story high-rise with two stairwells and each floor was sized for 100 occupants. Occupant load was based on one person per 10 m², giving a floor dimension of 32 m by 32 m. Therefore, 50 people on each floor flow into each stairwell and a total of 1000 occupants egress down each stairwell. The fire was modeled on the 10th floor to provide a range of applicability of results. To reduce the size of the computational domain and thus the run time, only the fire floor and the two stairwells were included in the simulations, as shown in Fig. 1.

Within C/VM2, there are a number of modeling rules that specify the inputs for fire engineering analysis. Where possible, these rules were applied in this analysis. C/VM2 specifies a fast αt^2 growth rate with a capped heat release rate (HRR) at the time of sprinkler activation to simulate sprinkler control, not extinguishment, of the fire. In one case of the sensitivity analysis, the fire was allowed to grow to 20 MW to observe the impact of an uncontrolled fire. The combustion properties are also taken from C/VM2 and are given in Table 1.

Fig. 1 Simulation domain representing a 20 story building
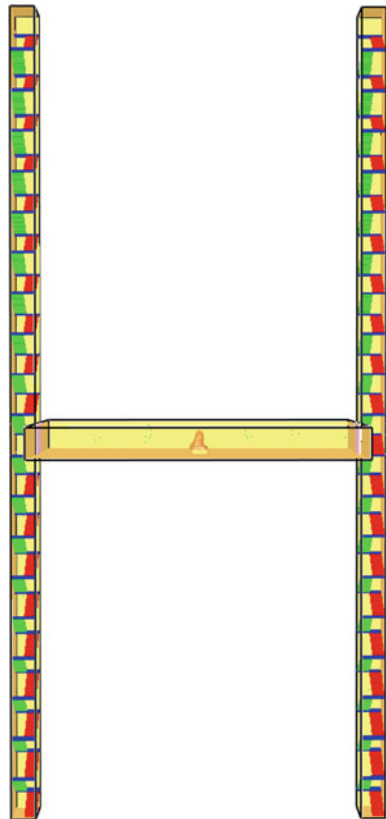
Table 1 Design fire
characteristics

Parameter	Quantity
HRR per unit area	500–1000 (kW/m^2)
Design fire growth rate	0.0469 t^2 (kW)
ΔH_c (Heat of combustion)	20 MJ/kg
Y_{soot} (Soot yield)	0.07 kg/kg
Y_{CO} (Carbon monoxide yield)	0.04 kg/kg
Fuel composition	$CH_2O_{0.5}$

The main model inputs that were investigated included:

- Sprinklers—standard and quick response
- Fire detection system—smoke detection, heat detection, and sprinkler activation
- Ceiling height—3 and 2.6 m
- Stairwell configuration—20-story height, reduced height of stairwell, and shaft only
- Tenability monitoring level in stairwell—multiple levels in stairwell.

C/VM2 also defines the leakage area to be used in the analysis. For modern construction, the leakage area is taken as 0.001 m^2/m^2 of the wall area. In this analysis, the external leakage from the fire floor was modeled as two vents 0.4 m wide and 0.6 m high at the floor and ceiling levels. Fire and smoke-stop doors are commonly required for stairwell doors and include a brush seal to reduce the leakage of smoke around the perimeter of the door. C/VM2 stipulates that fire and smoke-stop doors are modeled with a 10 mm gap along the bottom of the door or as nearly as possible to conform to the smallest computational mesh size. In this analysis, the leakage of the fire and smoke-stop doors in the building was modeled as a 200 mm by 200 mm vent at the lowest mesh in the door. This simulated vent is four times the required leakage area for a typical fire and smoke-stop door. To model the leakage of other egress doors on the floors above and below the fire floor, the individual door leakage areas were lumped together for every four floors, represented by four vents of 200 mm by 200 mm each, evenly distributed throughout the stairwell.

Table 2 summarizes the 16 runs used in this analysis. Column 1 presents the run # used to label the individual runs. Column 2 presents the type of sprinklers used to control the fire, either standard response sprinklers (SRSP) with an RTI = 135 m$^{1/2}$s$^{1/2}$ and $C = 0.85$ m$^{1/2}$s$^{1/2}$ or quick response sprinklers (QRSP) with an RTI = 50 m$^{1/2}$s$^{1/2}$ and $C = 0.65$ m$^{1/2}$s$^{1/2}$. Both sprinklers had activation temperature of 68 °C. Column 3 presents the detection type used to initiate the evacuation which included smoke detectors (SD), heat detectors (HD), and sprinklers. The time of sprinkler activation dictated the peak HRR and in absence of any fire detection, the evacuation was triggered by sprinkler activation. Column 4 presents the detector activation time, and column 5 presents the time that the stairwell door was opened for the evacuation. For office occupancy, C/VM2 stipulates that the evacuation is assumed to start 60 s after the detector activates, allowing 30 s for alarm polling time and 30 s for pretravel activity time. Column 6 presents the peak HRR for the fire

Table 2 Summary of cases and results. Gray shading shows the variable that deviated from the base case (Run 1)

Run #	Fire control	Detector type	Detection time (s)	Door opening time (s)	Peak HRR (kW)	Geometry	D^*/δ_x	Stairwell 1				
								38 m	40 m	42 m	44 m	46 m
1	SRSP	SRSP	182	242	1552	Standard	5.73	272	277	302	328	382
2	SRSP	SD	40	100	1552	Standard	5.73	Visibility >5 m throughout simulation				
3	SRSP	HD	132	192	1552	Standard	5.73	a	251	303	a	a
4	SRSP	SRSP	177	237	1470	2.6 m ceiling	5.6	257	259	292	306	331
5	SRSP	SD	40	100	1470	2.6 m ceiling	5.6	Visibility >5 m throughout simulation				
6	SRSP	SRSP	182	242	1552	Short stairwell	5.73	291	275	303	314	345
7	SRSP	SRSP	182	242	1552	No stairs	5.73	299	b	292	b	308
8	SRSP	SRSP	156	216	1143	100 mm mesh	10.14	Visibility >5 m throughout simulation				
9	SRSP	SRSP	182	242	1552	Door left open	5.73	296	250	283	304	343
10	QRSP	QRSP	148	208	1027	Standard	4.86	a	265	a	a	a
11	QRSP	SD	40	100	1027	Standard	5.73	Visibility >5 m throughout simulation				
12	QRSP	QRSP	143	203	959	2.6 m ceiling	4.72	a	248	289	326	a
13	QRSP	HD	130	190	959	2.6 m ceiling	4.72	248	233	a	a	a
14	QRSP	SD	40	100	959	2.6 m ceiling	4.72	Visibility >5 m throughout simulation				
15	QRSP	QRSP	148	208	1027	Door left open	4.86	392	269	321	364	404
16	None	SD	54	114	20,000	Standard	15.92	359	375	397	426	442

[a] Visibility did not drop below 5 m at this location
[b] Intermediate landing not included in this simulation of the shaft only

that is capped at sprinkler activation. Column 7 summarizes the changes in geometry for each run: (Standard) indicates the building geometry and ventilation which is as described above for Fig. 1, (2.6 m ceiling) indicates that the ceiling on the fire floor was lowered to 2.6 m, (Short stairwell) indicates that the stairwells were truncated to 3 floors above and 1 floor below the fire floor, (No stairs) indicate that stairwell was modeled as a shaft to simplify the geometry, and (Door left open) indicates that the door in the fire floor remained open after the occupants had evacuated the fire floor. In two cases, the stairwell geometry was modified to investigate if simplified setups could appropriately capture the same results as the base case. In the first alteration, the stair was truncated to floors 9 and 14 only and left fully open to the infinite ambient boundary condition. The second simplification was to completely remove the treads, risers, and landings within the stairwell, creating an open shaft from ground to 20th floor. In Table 2, these are Runs 6 and 7 with the geometry labeled as short stairwell and no stairs, respectively. During the evacuation, the door to the stairwell remained open for 60 s while 50 occupants exited the fire floor. In Runs 9 and 15, the stairwell doors on the fire floor were left open after all the occupants exited the fire floor to simulate the scenario where the stair door has failed to close. Having the door on the fire floor open for the entire simulation was the most severe condition which also represents the simultaneous evacuation of all occupants within the building. This scenario results in long queuing times on the fire floor due to the reduced travel speed in the stair caused by the congestion, as opposed to phased evacuation where the fire floor is given priority to evacuate first over other levels. Column 8 presents the D^*/δ_x which varies depending on the peak HRR and the mesh size. For all simulations except Run 8, the mesh size was 200 mm (0.008 m^3) which dictates that the objects and vents must be in increments of 200 mm thus the stairs were modeled with a 200 mm riser and 400 mm tread. In Run 8, the mesh size was reduced to 100 mm (0.001 m^3) to verify that the results were not overly sensitive to the 200 mm mesh size. For simulations involving buoyant plumes, the accuracy of the flow field resolution is derived using the following nondimensional expression:

$$D^*/\delta_x = \left(\frac{\dot{Q}}{\rho_\infty C_p T_\infty \sqrt{g}} \right)^{2/5} \qquad (1)$$

where $\dot{Q}$ is the maximum HRR, ρ_∞ is density of air and T_∞ is the ambient temperature. These values were chosen to represent the attributes of the given fire scenario. Previous research [6] has shown that for plume flows and smoke filling problems D^*/δ_x should be between 4 and 16. Values closer to four indicate a coarser mesh resolution while values closer to 16 represent a finer mesh resolution.

For the analysis of results, there were five primary points of interest within the stairwells:

- Fire floor landing (38 m),
- First intermediate landing (40 m),
- Landing above fire floor (42 m),
- Second intermediate landing (44 m), and
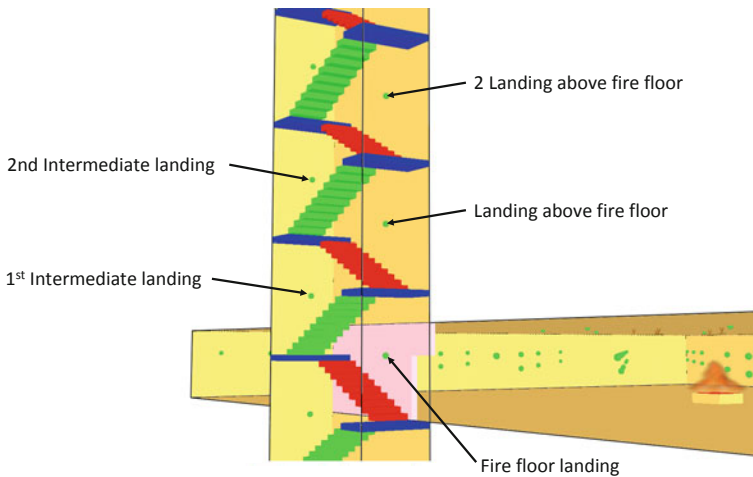
Fig. 2 Stairwell perspective view showing the location of monitoring points (green spheres) in the stairwell including the labels used in graphical results

- Landing two floors above the fire floor (46 m).

These monitoring points of the tenability analysis were in the center of each landing and 2 m above each landing level as shown in Fig. 2 as green spheres. In Table 2, columns 9–13 present the times when the visibility <5 m (limiting tenability criteria) at each of these respective locations is within stairwell 1. The results in stairwell 2 were not significantly different from stairwell 1.

In total, 16 unique cases were created and then simulated for a total 1800 s. The base case was created comprising geometry and ventilation arrangement deemed to be the most general. The base case (Run 1) had no smoke detectors or heat detectors and had only standard response sprinklers. Using the base case as a template, the 15 other cases were developed, manipulating at least one building variable of interest in each run. Each case was then run in FDS6, taking approximately three to seven days to complete. In all cases, the tenability conditions were measured throughout the stairwells and fire floor.

3 Results

3.1 Smoke Flow Behavior and Tenability of Fire Floor

As an exemplary case, the results from Run 1 are described here in detail. Deviation from the base case is summarized in the result presented in Table 2. In all cases, the fire was placed in the center of the open-plan office floor and allowed to grow as stipulated in C/VM2. The fire is ignited at $t = 0$, and the fire develops at the growth
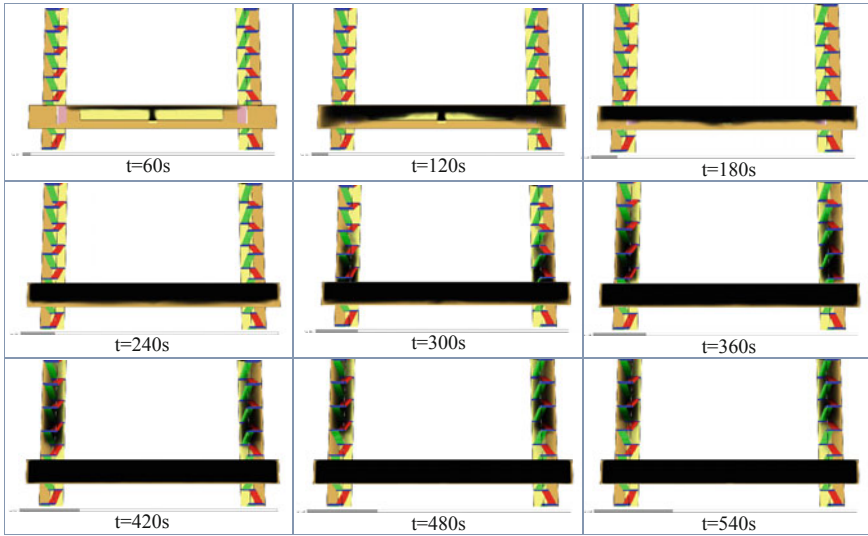
Fig. 3 Series of Smokeview images showing smoke spread throughout fire floor and stairwells

rate of fast t^2. Figure 3 shows a series of Smokeview images at 60 s intervals. In this case, the sprinklers activate at $t = 182$ s. Sixty seconds after the detection device (sprinklers in this case) activates, the stairwell door is open at $t = 242$ s and smoke flows into the stairwell. The door to the stairwell closes at $t = 302$ s (allowing 60 s for the 50 occupants to egress the floor). In the images $t > 240$ s, the smoke can be seen flowing up the stairwell. In the images $t > 360$ s, the smoke is seen moving up the stairwell as a "plug" of smoke as a result of the doors closing and only minor amounts of smoke leaking into the stairwell through the small leakage vent at the bottom of the fire and smoke-stop door.

The tenability on the fire floor was monitored at 24 points spaced 5 m apart, with 6 m offset from the walls. Visibility dropped to <10 m at the first monitoring point at $t = 118$ s. The average time to loss visibility (<10 m) was $t = 133$ s and the last point loses visibility at $t = 149$ s. However, according to C/VM2, in a sprinkler firecell with <1000 people, the only tenability criteria are $FED_{CO} < 0.3$. On the fire floor, the average time to $FED_{CO} < 0.3$ is 800 s. Therefore, the floor is considered to be untenable after 800 s. However, for all of the simulations except Runs 9 and 15, all of the occupants are assumed to have evacuated the fire floor and close the door long before this time. The maximum time assumed for the evacuation of the fire floor is 302 s.

3.2 Simulations Which Maintained Stairwell Tenability

Tenability is maintained in 5 of 16 simulations summarized in Table 2 (Runs 2, 5, 8, 11, and 14). Although the tenability criteria for 1000 people in a firecell include visibility, FED_{therm}, and FED_{CO}, the visibility typically governs the analysis. Simulations that include both sprinklers and smoke detectors all meet the tenability criteria within the stairwell. This is true for both 3 and 2.6 m ceiling heights. With the smoke detectors present, occupants are alerted to the fire earlier than with sprinklers alone, as shown in Table 2, allowing the stairwell doors on the fire floor to close much earlier in the timeline and reduce the overall amount of smoke that enters the stairwell. Having smoke detectors and sprinklers, the quantity of smoke that enters the stairwell was low enough to not compromise tenability. In contrast to this, for the cases where only sprinklers are installed, smoke accumulates behind the fire door prior to it being open, subsequently causing failure when the smoke flows into the stairwells.

The unexpected results were from the 100 mm mesh resolution (Run 8). The equivalent simulation with the 200 mm mesh resolution (Run 1) failed due to the visibility in the stairwell dropping to <5 m, as shown in Table 2. Both fires were controlled by the SRSP; however, the finer mesh provided a more refined ceiling jet with higher temperatures resolved near the sprinklers resulting in earlier activation. The faster sprinkler activation time leads to the fire having a peak HRR of 1140 kW as opposed to 1550 kW for the 200 mm resolution. Figure 4 is a plot of the visibility versus time 2 m above the landing levels at various heights of the stairwell for the 200 mm (a) and 100 mm mesh (b), respectively. For the 200 mm mesh (Run 1), the visibility dropped to <5 m, and therefore, tenability is not maintained. For the 100 mm mesh (Run 8), the visibility dropped to 6 m at 290 s before rising to >10 m after 450 s, therefore, tenability is considered to have been maintained. As seen in Fig. 4, the results from two cases are very similar yet the 200 mm case is considered to have not met the tenability criteria and the 100 mm case does. This is a reflection of the sensitive of the single-point failure criteria more so than the sensitivity of the numerical results.

3.3 Simulations Which Failed Stairwell Tenability

The critical tenability criteria in all simulations were visibility. Carbon monoxide and thermal effects were typically minor or did not breach the design limits until long after the visibility was lost at multiple levels in the stairwell. In all of the simulations, except Run 16, tenability on the fire floor was always maintained until after the occupants had entered the stairwells. In the remaining 11 scenarios, where the tenability was not maintained in the stairwells, the visibility dropped below 5 m at one or more locations in the stairwell. The simulations that failed due to visibility dropping below 5 m are identified in Table 2, columns 9–13 which present the time

Fig. 4 Visibility within one stairwell for standard response sprinkler case with **a** 200 mm mesh (Run 1) and **b** 100 mm mesh (Run 8)
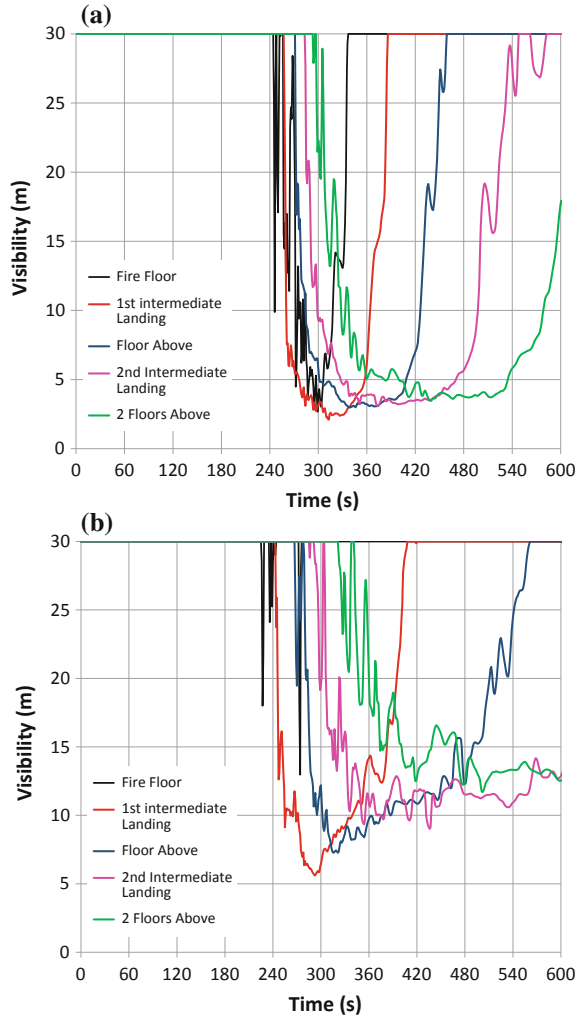
and location where the visibility first dropped to <5 m on the fire floor landing and the next four landings in stairwell 1 as shown in Fig. 2. The loss in visibility was due to smoke infiltration during the period when the door was open while the occupants of the fire floor were evacuating. Figure 4 shows the visibility versus time at the five locations within stairwell 1 that have been identified in Fig. 2. The visibility rapidly increases outside the fire floor once the door has closed, as seen in Fig. 4a. The improvement in visibility in the stairwell after the fire floor door is closed demonstrates how the smoke quickly rises in the stairwell and that there was only minor smoke flow subsequently into the stairwell through the 200 mm by 200 mm leakage vent at the bottom of the fire floor door. In the simulations where the door remains open after the last occupant has evacuated the floor (Runs 9 and

15), the visibility did not improve since the sprinklers only controlled the fire and the smoke continued to flow into the stairwell for the remainder of the simulation.

The most common first failure location, i.e., visibility <5 m, was the first landing above the fire floor (40 m). When results were viewed for these simulations in Smokeview, it was clear that smoke accumulated behind the fire floor door in the seconds before the door was opened. Once the door was opened, the hot buoyant smoke flowed through the door and quickly rose as a door plume to the first landing, causing the visibility to drop below 5 m at this point, often before the visibility was lost on the fire floor landing.

4 Discussion of Results Sensitivity

The results presented here show the importance of smoke detectors in conjunction with automatic sprinklers in a high-rise building. Even with QRSP or heat detectors only, the evacuation was not triggered early enough to prevent smoke flowing into the stairwell which reduces the visibility for the egressing occupants. With QRSP, visibility was reduced to <5 m in only one location within the stairwell in Run 10 which shows that the fire safety design was very close to satisfy the performance criteria of the NZBC.

Lowering the ceiling height from 3 to 2.6 m caused the untenable conditions to be reached earlier in the timeline. When SRSP were modeled (Run 4), the lower ceiling height caused failure to occur 15 s earlier. Additionally, for the QRSP cases with varied ceiling height (Runs 10 and 12), failure occurred only 17 s earlier for the lower ceiling. However, when QRSP were present, the reduced ceiling resulted in the visibility <5 m in three locations instead of only one for the 3 m ceiling height. This behavior is likely due to the lower and hotter smoke layer formed beneath the 2.6 m ceiling compared to the 3 m ceiling resulting in greater smoke flow through the door into the stairwell. This behavior supports the need to accurately model the finished suspended ceiling height and not rely on the unfinished floor slab to unfinished ceiling heights in the analysis.

The case with the stairs truncated to three floors above and one floor below the fire floor (Run 6), showed only minor variation to the base case (Run 1). The order and time at which each device failed varied by only a few seconds except on the fire floor and two floors above. The time to failure on the fire floor often lagged behind the first intermediate landing due to the buoyancy of the smoke as it enters the stairway. Simulation shows the Smokeview image 10 s after the stairwell door is open (a) and 57 s after the door was open (b) when the visibility on the first intermediate landing became <5 m. All of the other devices in the stairwell had visibility >5 m throughout the entire simulation.

Completely removing the stair treads, risers, and landings (Run 7) resulted in times to visibility <5 m similar to the base case at the locations directly above the stairwell door but not on the intermediate landing locations. This is a result of the smoke flow significantly changing compared to the smoke flow patterned observed
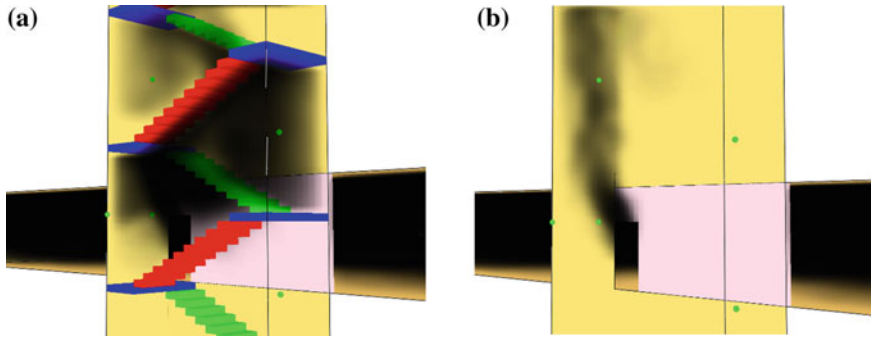
Fig. 5 Smokeview images showing the smoke flow around the monitoring point immediately in front of the door to the fire floor

when the stairs were present. Without the stairs, the smoke flow resembled flow of an attached window plume rather than a well-mixed mass as seen in Fig. 5b.

Reducing the mesh size to 100 mm reduced the max HRR of the fire, as the sprinklers were shown to activate earlier than for the 200 mm mesh size. This is because the ceiling jet is modeled over a smaller depth, closer to the ceiling, decreasing the time at which the sprinklers reaches 68 °C and activates. This also meant that occupants were alerted after 156 s rather than 182 s.

The size of the fire depended on the sprinkler response time and was typically 1027 kW for a QRSP controlled fire and 1552 kW for a SRSP controlled fire. Looking at Runs 1 and 10, which were identical except for SRSP and QRSP controlled fires, respectively, the difference was significant. The QRSP controlled case came very close to passing the acceptance criteria where only the device on the first intermediate landing failed (in both stairwells). Since the SRSP simulation (Run 8) achieved the performance criteria for the 100 mm mesh, it is almost certain that the QRSP simulation (Run 10) would also achieve the performance criteria with a 100 mm mesh.

For all simulations apart from the uncontrolled fire case (Run 16), there was little to no smoke flow into the stairwell through the 200 mm by 200 mm vent at the bottom of the door. This was also observed visually in the Smokeview images. This would indicate that the external leakage vents from the fire floor representing 0.1% leakage, were sufficient to reduce the pressure on the fire floor such that the driving force of the smoke into the stairwell was due primarily to the buoyancy of the smoke. The 200 mm by 200 mm opening at the bottom of the door is four times the door leakage area required in C/VM2 thus any leakage into the stairwell should arguably be greater than expected. This is only the case for small fire such as a sprinkler controlled fire. The results from the simulation with the uncontrolled fire case did not fail due to the smoke that entered while the door was open for occupant evacuation, but instead due to smoke flow through the 200 mm by 200 mm vent at the bottom of the door. This indicates that the gap at the bottom of the door is a necessary feature to be included in the modeling.

Modeling the door open for the duration of the fire, instead of being triggered by sprinklers or other detection devices, produced mixed results between SRSP and QRSP. With SRSP, modeling the door open led to an earlier time to the first failure. This was the opposite for QRSP, where the first failure occurred slightly later. This is a result of the failure occurring very quickly after the door is open and the impact of the door being left open is not demonstrated on the floors near the fire floor. Ultimately, when the door to the fire floor is left open, the visibility in the stairwell is <5 m above the fire floor. With QRSP, the stairwell failed everywhere with the door open, as opposed to only one failure location when the door was closed after evacuation. The analysis of the open door scenario demonstrates the importance of having the door on the fire floor closed as quickly as possible which emphasizes the crucial need for phased evacuation where the fire floor is alerted prior to the other floors so that the stairwell doors on the fire floor function as intended to prevent the uncontrolled of flow of smoke into the stairwell. If the door on the fire floor remains open for any reason, these results show how quickly visibility can be reduced and hinder evacuation even when sprinklers are installed.

5 Conclusions

The results demonstrate that there was a significant sensitivity to the resolution of the mesh. The 200 mm mesh results showed that SD coupled with SRSP were necessary to meet the NZBC performance criteria in the stairwell whereas the 100 mm mesh results showed that only SRSP were necessary. The variation in performance is in the preferred direction, as the coarser mesh results required more fire engineering features (SD), effectively resulting in a restrictive result as the model resolution becomes less precise. However, the visibility in the 100 mm case did drop to <6 m and was close to the <5 m threshold in the NZBC. It is therefore recommended that additional grid sensitivity studies be conducted with multiple meshes to better understand the sensitivity of the visibility results to the size of the mesh.

For the building to meet the NZBC acceptance criteria, automatic sprinklers coupled with smoke detectors were required. The smoke detectors were required to initiate evacuation earlier than sprinkler activation which resulted in less smoke accumulating on the fire floor prior to the stairwell door being opened. In previous research [7], it was shown that adopting a phased evacuation procedure within a high-rise building holds significant performance advantages over a simultaneous evacuation procedure. Results from this analysis strongly support the need for phased evacuation within high-rise buildings with high occupant load. If the building is to meet the NZBC, the occupants on the fire floor need to exit the floor quickly to allow the door to close early in the fire scenario timeline, in order to minimize the quantity of smoke that enters the stairwell.

The results from the uncontrolled fire simulation showed that for the building to satisfy the performance criteria, it is essential to have automatic sprinklers. Without sprinklers, the smoke from the uncontrolled fire became so severe that thick smoke

was flowing through the vent simulating the gap under the fire and smoke-stop door to the stairwell. In New Zealand, modern high-rise buildings are expected to be designed with sprinklers and smoke detectors. Overall, performance of the building is reliant upon the fire doors functioning as intended, meaning they are open during the egress stage and closed after the last person has left. If the door from the fire floor into the stairwell remains open, tenability is compromised regardless of the detection time or sprinkler control, as shown by the simulations where the door was left open after evacuation of the fire floor. This result demonstrates the need for self-closers on stairwell doors and regular inspection of doors and the associated door hardware to increase the likelihood that the door will function as intended.

References

1. Bryan, J. L. (1982). Human behavior in the MGM grand hotel fire. *Fire Safety Journal, 76*, 37–48.
2. Ministry of Business, Innovation & Employment. (2016). *C/AS2-7 acceptable solutions for buildings, For New Zealand building code clauses C1-C6 protection from fire*. Wellington: New Zealand Government.
3. Ministry of Business, Innovation & Employment .(2017). *Verification method: Framework for fire safety design*. Wellington: New Zealand Government.
4. Ministry of Business, Innovation & Employment. (2014). *The New Zealand building code handbook*. Wellington: New Zealand Government.
5. McGrattan, K., Hostikka, S., McDermott, R., Floyd, J., Weinschenk, C., & Overholt, K. (2015). *NIST special publication 1019 fire dynamics simulator user's guide version 6*. National Institute of Standards and Technology.
6. Hill, K., et al. (2007). *Verification and validation of selected fire models for nuclear power plant applications*. Washington, DC: NUREG 1824, United States Nuclear Regulatory Commission.
7. Pau, D. (2015). *Tenability in stairwell of highrise office buildings.* Masters of Fire Engineering Thesis, University of Canterbury, Christchurch.

Tall Building Evacuation Strategy—The Refuge Floor Concept Revisited

S. L. Poon

Abstract As buildings get taller, the issue of safe egress from these buildings becomes an increasing concern. The provision of dedicated refuge floors is a recent design measure that has arisen in an attempt to address the concern of increased hazards associated with egress from tall buildings. Although there have been studies on the perceived benefits in the provisions of refuge floors, little has been studied in depth on its actual performance in terms of achieving the expected safety for egress from tall buildings. This paper attempts to provide a deeper insight into the impact of refuge floor provisions and to assess the extent of the benefits toward achieving a safer outcome for occupants during a fire emergency egress from tall buildings. The general conclusion is that dedicated refuge floors may not necessarily deliver a safer or cost-effective solution.

Keywords Refuge floors · Tall buildings · Evacuation

1 Introduction

Prior to the concept of refuge floors, a number of egress strategies are available to move occupants out of the fire-affected area. For large low-rise buildings where there are a greater number of exits available, and destination to a point of safety on the street can be reached quickly, a simultaneous evacuation strategy to evacuate all the people at the same time is the simplest and the most effective strategy to implement.

For high-rise buildings, a simultaneous evacuation approach should not be implemented as it will choke the stairs since occupants from every floor will be trying to get into the stairs at the same time. Occupants that are most at risk on the floor of fire origin can therefore take an excessively long time to clear. A more effective strategy is to adopt a phased evacuation approach which is implemented on a timed sequence. This approach is based on keeping a large number of occupants in place and moving those directly impacted by the fire first. It allows occupants on the fire floor and the most likely to be affected adjacent floors to evacuate first, while the

S. L. Poon (✉)
Leong Poon & Assoc. Pte. Ltd., Po Box 501, Bukit Merah Central 911531, Singapore
e-mail: lp@leongpoon.com

rest of the building could either exit later or stay, provided that the fire is kept under control. It, however, strongly relies on the efficacy of the operation of the evacuation sequence. There will be initial delays in identifying the fire location and confirmation of its severity before issuing the signal at the correct floors to initiate evacuation. Additional wardens may also be required to manage the phasing of the evacuation to ensure that the floors are evacuated in the correct sequence.

Other strategies include relocation to a protected area of refuge, often adopted in healthcare facilities and hospitals, and also the 'defend-in-place' concept typical for residential buildings which rely on the active and passive fire protection measures to ensure that the effects of fire are controlled and contained within the compartment in which it occurred.

A more recent addition for high-rise buildings is the refuge floor concept, which is an extension of the relocation approach. Conventionally, an area of refuge is an area where people, whose abilities or impairments might cause their evacuation to be delayed, can wait for assistance. In high-rise buildings, concern has been given to occupants being unable to traverse the entire building height and fatigue may set in such that the reduced speed may create bottlenecks for occupants before them.

While it is perceived that the provision of refuge floors adds to the level of building safety for occupants evacuating during a fire, the basis for its implementation has not been well studied. This paper provides a more in-depth study of the impact of refuge floors and proposes a more cost-effective alternative.

2   Relevant Case Incidents of Major Building Fires

New code provisions are often driven by major fire incidents, and the refuge floor provisions are no exception. Amendments for the provision of refuge floors in high-rise buildings have already been implemented in a number of countries as a result.

2.1   Hong Kong

Hong Kong appears to have taken the lead in the provision of refuge floors, and it would appear to have been influenced by some of the significant fires that occurred in the few years prior to its introduction.

The five worst fatal incidents in recent years are briefly described below [1], in which causes, outcome, and damage are illustrated in chronological order.

1. Residential estate, seven fatalities (1997); caused by a careless smoker disposed cigarette end in an illegal store room changed its usage from residential apartment, fire door kept open and smoke spread to other floors throughout stairwell. 7 dead and 38 injured.

2. Karaoke box, 15 fatalities (1997); the karaoke box was divided into many rooms (61 partitions); the suspects threw Molotov cocktail, thinner, and flammable liquid at the ground floor staircase. Fire rapidly travelled to the second and the third floor through vent ducts. Victims drank too much before the blast decreased their alertness. 15 dead and 15 injured.
3. Garley Building, 40 fatalities (1996); the fire was believed to have been started by welding work while building's lift being replaced; quickly filled with smoke and flame soon engulfed the top three floors. 40 dead and 81 injured (renovations which removed fire doors allowed smoke to spread to stairs and prevented escape [2].
4. Hongkong Bank, 13 fatalities (1991); the offender lit up thinner splashed on the floor and bank staff trapped and killed in choking inferno; the staff wrongly assessed the threat and unreasonably hid under the office area. Ventilation had no auto-shutdown function, no detector, no emergency lighting, and no sprinkler system in the bank. Electricity had been cut off so that electric locked doors could not be opened.
5. Bed space apartment, seven fatalities (1990). Staircases on both ends of the floor were closed; the roof exit door was locked so the hot air and dense smoke could not dissipate. The fire intensified because of combustible bedding, wooden partition between cubicles. Hot smoke further ignited discarded items, flame spread to adjoining bed space apartment. Firemen's snorkel cage toppled in carrying double load recommended by regulation. 7 dead and 49 injured.

The Garley Building fire, in particular, was considered the worst building fire in Hong Kong during peacetime [2]. The fire, which occurred when undergoing renovation, damaged the bottom two floors and spread to the top three floors of the building, while the middle floors remained relatively intact. Poorly managed welding activity was blamed for the cause and the rapid spread was via the elevator shaft which was being installed with new elevators and had the fire doors removed. Smoke spread into the stairs and prevented escape.

2.2 Singapore

Although fire incidents are relatively frequent, major fire incidents (involving more than three fatalities per incident) are rare in Singapore. A relatively recent fire in 2014 involving a high-rise apartment is the Marina Bay Suites fire which incurred two fatalities.

It was reported that the fire involved renovation materials, such as paint, at the service lift lobby area. The 65th-floor apartment that caught fire was unsold and unoccupied.

A security guard believed it was a false alarm and went with a co-worker to investigate using a fireman's lift to the 65th floor. There they were overcome by the

smoke and flames soon as the lift door opened and exposed them. Apparently, the lift doors were jammed by the heat and could not be closed.

2.3   USA

The USA had a number of significant building fires in the last few decades. Nonetheless, the requirement for dedicated refuge floors had not been implemented in their major building codes. Some of these building fire disasters include.

2.3.1   MGM Grand Hotel (1980) [3]

The fire started in the electrical wiring over a delicatessen at the east end of the casino. Materials burned near the fountains in the front entrance. Following full involvement of the Deli restaurant, the fire spread rapidly throughout the high-rise complex. Smoke also rose through the high-rise via stairways, seismic joints, elevators, and ventilation systems. During the fire, the heating, ventilation, and air-conditioning (HVAC) system continued operating. Meanwhile, the vertical openings were provided with inadequate protection. The casino and some of the guest rooms were directly infected by fire. Any means of egress from the high-rise tower were impaired because of smoke, and most deaths were caused by smoke. A number of guests had trouble in finding the exits to get downstairs. But when they found the exits, some of the fire doors were locked automatically. Thus, although people can enter the stairwell, they were trapped inside these smoke-filled areas. In addition, the high-rise tower evacuation alarm system did not sound. The fire resulted in 85 deaths and more than 700 injuries.

Many occupants in the high-rise tower, however, were able to exit the building unassisted down stairways. Others were turned back by smoke and sought refuge in rooms. Apart from egress by stairs, helicopter pilots evacuated 300 people from the roof of the high-rise tower.

2.3.2   Las Vegas Hilton Fire (1980)

90 days after the devastating MGM Grand fire [3], an arson fire started at the Las Vegas Hilton. At the time, it was being retrofitted with modern fire safety equipment. The fire department used the knowledge they had learned from the MGM Grand fire, and applied local television networks to notify people to stay in their rooms and not go out to the halls and stairwells. After the incident, many hotels in Las Vegas installed updated fire safety system. Because of the previous lessons learned, only eight people died in this incident.

2.3.3 World Trade Center (2001) [4]

On Tuesday, September 11, 2001, an aircraft departed from Boston crashed into the northern facade of the WTC tower 1. There were 5,000–7,000 occupants in each tower at the time the first attack, around 8:45 in the morning. At 9:03 a.m., another hijacked flight crashed into the south side of the south tower of the World Trade Center.

In the north tower, the aircraft penetrated the core and destroyed all three stair shafts at the floors of impact. There was no vertical route for them to egress. None of the occupants located above the attack in tower 1 survived. But 99% of those located below the impact point were able to escape. Many occupants remained in place and waited for the fire department to initiate an evacuation. The second aircraft destroyed two stair shafts. Fortunately, elevators were successful in evacuating from tower 2. Each tower has three enclosed stairways located in the core. Two stairways discharge on to the mezzanine level in the atrium/lobby area of the respective tower.

3 Refuge Floor Provisions

Conventionally, an area of refuge is normally dedicated to occupants whose abilities or impairments require them to wait for assistance to be rescued. Because the number of occupants requiring assisted evacuation is usually quite low, the areas of refuge dedicated to them are correspondingly small. However, in healthcare facilities, where a larger proportion of occupants have limited mobility, provisions are increased to provide for a larger area of refuge to accommodate the transfer of these occupants to a safer area, usually to a horizontally adjacent protected space. The above is generally the extent to which the conventional provision of areas of refuge is required in building codes.

In high-rise buildings, the phased evacuation approach described earlier is often used, where occupants are moved to adjacent floors which are considered safer but are not dedicated refuge areas.

The requirements for a dedicated refuge floor concept are much more onerous, requiring allocation of 'sterile' spaces at various floor intervals with sufficient space to accommodate all occupants, both abled and disabled, within each interval. In addition, the allocated refuge areas are required to not be habitable. Countries which currently contain provisions for dedicated refuge floor requirements are Hong Kong, Singapore, China, and India. The refuge floor concept is also incorporated in some of the design of high-rise buildings in other countries, but these may be on a case-by-case basis, often associated with the design of very tall buildings.

3.1 Hong Kong

Hong Kong was among the first authority to require provisions of refuge floors in high-rise buildings. This requirement was implemented in the 1996 revision of the Hong Kong Code of Practice on Means of Escape [5].

The concerns expressed were that office, commercial, and private residential buildings are commonly over 40 stories and with about half the population of Hong Kong living in public housing estates and almost all the housing blocks constructed recently are over 35 stories (Lo and Will [6]). This implies that a large number of people in Hong Kong live and work in high-rise buildings. The reasons cited for its implementation as described by Lo and Will were as follows:

1. It acts as a safe place for a short rest before people continue to escape downwards as it is difficult for most people to walk down a tall building without pausing.
2. It also acts as a safe passage for people using one staircase, when encountering smoke, fire or obstruction in that staircase and enables them to proceed to an alternative staircase.
3. Additionally, it acts as a place of assembly for people to wait for rescue in case none of the staircases can be used due to smoke, fire, or obstruction.

Lo and Will also referenced a 10-story building fire in 1995 whereby the stairs were blocked by smoke forcing the occupants to escape to the roof which acted as a refuge space.

One of the criteria for the provision on which the regulations were based was taken from a 1986 study [7] on which fatigue sets in after 5 min descending the stairs. Hence based on an estimated descent rate of 16 s per floor, fatigue is considered to have set in after 18 floors.

3.2 Singapore

A 2007 update to the Singapore Fire Code [8] required that residential buildings higher than 40 storeys must have fire-resistant refuge floors for every 20 storeys. Although there were no significant fire tragedies such as those experienced in Hong Kong, the move to provide refuge floors seemed to be the rational approach to address egress issues associated with high-rise buildings. However, an important difference is that, unlike Hong Kong, refuge floors are only required for residential buildings. This may be a compensatory action to address the increased risk for not requiring high-rise residential buildings to be sprinkler protected.

3.3 China

The Chinese code of fire protection for the building is GB GB 50016-2014. The code requires that all buildings (e.g., multi-function, residential, and office) higher than 100 m should be provided with refuge floors, and the distance between two refuge floors should be less than 50 m. The code also stipulates a number of detailed requirements on the design of refuge floor, similar to those of Hong Kong and Singapore.

3.4 India

In India, new guidelines [9] were introduced in 2012 stipulating that a refuge area will have to be provided at every 7th habitable floor after the first 24 m of the high-rise building. The refuge area shall be provided within the building line at floor level. In case of high-rise buildings having height more than 30 m, the first refuge area shall be provided at 24 m or 1st habitable floor, whichever is higher. Thereafter, the refuge area shall be provided at every 7th habitable floor.

3.5 NFPA 101/5000 [10]

The NFPA 101/5000 recognizes a floor in a sprinkler protected building with at least two smoke separated spaces to be eligible areas of refuge.

Unlike the other codes above, the NFPA provision does not require the area of refuge to be dedicated, i.e., can be habitable provided that the building is sprinkler protected. In addition, stair doors are required to provide reentry back into the building to either seek refuge or an alternative stair.

4 Evaluation

4.1 The Issues

While the provision of refuge floors would appear to add to the level of safety for occupants evacuating during a fire from a high-rise building, the basis for its implementation still appears circumstantial as may often be the case with building code provisions. Many of the significant fires with high fatalities showed that the causes were due to either failure or non-provision of some of the critical building fire protection systems such as sprinklers or fire separation, and in many cases, rendering the stairs unusable. Hence, it may be construed that if access to the stairs cannot be achieved, then access to the refuge floors is also lost, thus rendering the provision

of dedicated refuge space as futile. Alternatively, if refuge floors had been provided in the buildings involved in the above fire incidents, it is not clear that it would had made an appreciable difference in those outcomes.

4.2   The Existing Alternative

The 'existing alternative' is simply the distributed approach based on the NFPA provisions which allow other floors that are sprinkler protected to serve as refuge floors. As many high rises are equipped with sprinkler protection, this provision is readily adaptable, especially with the phased evacuation strategy currently being employed in many high rises where occupants only need to travel up or down 2–3 stories away from the fire floor.

If occupants are most vulnerable to smoke exposure in stairs, then reducing their time spent in stairs would be beneficial.

4.3   The Fatigue Factor

Perhaps the most perceivable benefit with refuge floors may be attributed to a reduction in egress time as a result of alleviating the fatigue of evacuees by providing a temporary area of rest (refuge) and to not slow or block other evacuees in the stairs that are less fatigued. In fact, fatigue appeared to be one of the main basis for the determination of the interval at which to provide a refuge floor as explained in Lo and Will's paper [5].

While issues of fatigue would be alleviated with the provision of refuge floors, would provision of dedicated refuge floors be unnecessarily excessive? The NFPA Code requires that every door assembly in a stair enclosure serving more than four stories has reentry from the stair enclosure to the interior of the building. This arrangement makes it possible to leave the stairway at such floor if the fire renders the lower part of the stair unusable during egress or if the occupants seek refuge on another floor. The advantages this has over dedicated refuge floors are that:

- Seeking refuge or rest can be done at every floor instead of every 15 or 20 floors.
- Refuge floors need not be unusably dedicated.

5   Case Study

To further evaluate the impact of dedicated refuge floors on egress time, the simulation of occupant egress shall be undertaken for a 50-story building with the following variations:

1. No refuge floor,
2. One refuge floor at level 25,
3. Two refuge floors at levels 16 and 32.

For the purpose of simulating the usage of the refuge floor, a total rest time of 15 min will be allocated to occupants in Case 2 with 1 refuge floor and 10 min in each refuge floor in Case 3 with 2 refuge floors. As precise data on the effect of fatigue during stair egress is still lacking, its effects on the changes in travel speed are not modeled in all cases. The results of the scenario runs in terms of the total evacuation time is shown in Table 1.

Also shown in Table 1 are the evacuation time, less the total rest time to minimize the effects of resting on the results. Although one would expect all the results less the rest time to then be fairly similar, the results show quite significant departures from the base case with no refuge floor. Further examination of the egress simulations revealed that this phenomenon was due to occupants being pushed inwards (Fig. 1) as they arrive at the refuge floor. After completing their designated rest period, the initial occupants leaving are those in the interior who now have to weave their way out through the crowd and against the incoming flow of occupants in order to reach the exit and resume their travel down the stairs. The increased delay, as a result, seems significant.

Table 1 Summary of scenario results for total building evacuation time

Scenario	Scheme	Rest time in each refuge space (s)	Evacuation time in secs (mins)	Evacuation time less resting time secs (mins)	%change
1	No refuge floor	0	1,939 (32.3)	1,939 (32.3)	NA
2	One refuge floor	900	3,308 (55.1)	2,408 (40.1)	24%
3	Two refuge floors	$2 \times 600 = 1200$	4,643 (77.4)	3,443 (57.4)	78%
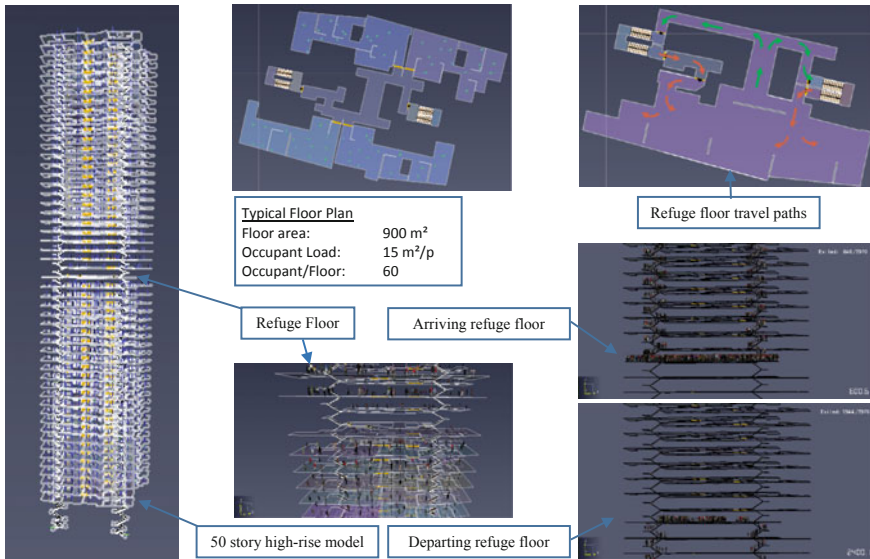
Fig. 1 Egress simulation model of a 50-story building illustrating congestion in the dedicated refuge floor using PathFinder

6 Conclusion

Dedicated refuge floors are a recent design provision to address occupant safety in high-rise buildings. Its requirements appear to be initiated in Hong Kong due to its high density of tall buildings and have been similarly adopted in other Asian countries such as Singapore and China which also have a high density of high rises.

The two main benefits that dedicated refuge floors are considered to provide are: (a) alleviating the effects of fatigue to avoid blockages in the stairs and (b) safeguard occupants within a protected space from the effects of fire. The main disadvantage is clearly the loss of usable space.

However, the current conventional refuge floor provisions as per NFPA 100/5000 would be able to provide the similar, if not improved benefits without the loss of usable space. It has the following advantages over the dedicated approach as follows:

1. Occupants are able to seek refuge or escape from the stairs at any floor quicker without having to the traverse the full height of the refuge floor spacing interval.
2. Holding a large group of evacuees within a single space at a high density can itself cause significant congestion due to crossflows between incoming and outgoing occupants within the refuge floor space. Providing refuge access at each floor would avoid this problem.

Existing experimental studies on high-rise evacuations are based on limited evacuee numbers and are unable to reproduce the congestion effects observed in the

evacuation simulations results. Hence, in a real situation, the perceived benefits of providing dedicated refuge floors may not be satisfactorily realized.

References

1. Fong, N. K., & Wong, K. C. (1988). Statistical data for fires in Hong Kong and preliminary views on building fire risk analysis.
2. https://en.wikipedia.org/wiki/Garley_Building_fire.
3. https://en.wikipedia.org/wiki/MGM_Grand_fire.
4. Shyam Sunder, S. (2004). Building and fire safety: Responding to the world trade center disaster, Chicago Committee on High-Rise Buildings, September 9, 2004. Building and Fire Research Laboratory, National Institute of Standards and Technology.
5. Hong Kong Building Department. (1996). Code of practice for provisions of means of escape in case of fire and allied requirement.
6. Ming Lo, S., & Will, B. F. (1997). A view to the requirement of designated refuge floors in high-rise buildings in Hong Kong. *Fire Safety Science, 5,* 737–745.
7. Egan, M. D. (1986). Concepts in building fire safety. Robert Krieger Publishing Co.
8. Singapore Fire Code (7th ed.). Singapore Civil Defense Force (2013).
9. https://timesofindia.indiatimes.com/city/mumbai/State-lays-down-new-norms-for-refuge-areas/articleshow/11406799.cms.
10. NFPA 5000. (2015). National Fire Protection Association.

Tunnel Fires

The Analysis of the Effects of Critical Velocity in Tunnel Fires with Water Spray System

Guan-Yuan Wu and Shang-Chin Hsu

Abstract In this study, the water spray system of sidewall type in the tunnel fire is simulated by Fire Dynamics Simulation (FDS) where the effect of critical velocity with water spray systems in tunnel fires, the critical velocity variations with various heat release rates, droplet sizes, and water flow rates in tunnel fires have also been investigated. In the tunnel fire model, the heat release rates are from 1 to 10 MW, the performances of the water spray system adopt the same regulation of Nohmi Bosai Ltd. Japan. A metal sheet, with 3 m in length and 2 m in width, is set in 3 m above the fire source. The results of various critical velocities obtained from this tunnel model without water spray system are good agreement with other references. The result shows that the critical velocity is lower after using the water spray system. In the same water flow rate, when the droplet size is smaller, critical velocity is lower simultaneously. In the same droplet size, when the value of water density is bigger, the critical velocity is consequently lower. This study also investigates the vertical temperature distributions in tunnels from various parameters of water spray systems.

Keywords Critical velocity · Water spray system · Tunnel fire · FDS simulation

Nomenclature

c_P	Air specific heat (kJ/kg-K)
D^*	Characteristic fire diameter (m)
g	The acceleration of gravity (m/s^2)
$\dot{Q}$	Heat release rate (kW)
T_∞	Environmental temperature (k)
ρ_∞	Air density (kg/m^3)

G.-Y. Wu (✉) · S.-C. Hsu
Department and Graduate School of Fire Science, Central Police University, Kwei-San, Ta-Kang, Taoyuan, Taiwan
e-mail: una210@mail.cpu.edu.tw

1 Introduction

From 1995 to the present, there have been at least 14 major fire cases of the long road tunnel in the world which caused heavy casualties, transport disruptions and economic losses [1, 2]. The famous tunnel fire cases are as follows: the Tauern Tunnel fire in Austria in 1999, the Mont Blanc Tunnel fire in France in 1999, and the St. Gotthard Tunnel fire in 2001. In addition, a tunnel fire occurred due to vehicle crashes in the Burnley Tunnel in Australia in 2007. In Taiwan on May 7, 2012, the first deadly tunnel fire incident occurred in Hsuehshan Tunnel causing 2 dead, 25 seriously injured, and nearly 150 people were evacuated.

In order to avoid the evacuation difficulties caused by heavy smoke, the smoke control design in a tunnel fire became extremely important. The main strategy was to make the smoke travel through the downstream and to prevent the smoke backlayering in the upstream. As a result, the upstream became a main safety path to avoid the difficulties of people evacuation or fire rescue. Therefore, when a tunnel fire occurs, the longitudinal ventilation velocity should be greater than the critical value of the smoke to prevent backlayering. The smallest longitudinal velocity, which stops the heavy smoke and the toxic gases spreading to the upstream, is called Critical Velocity.

Regarding the studies of the critical velocity, numerous theories and models have been developed and tested to predict the critical velocity and to investigate widely about the impact factors and variations of the heat release rate [3–6]. Moreover, the critical velocity is affected by tunnel slopes [7], vehicle congestion [8], and aspect ratios in tunnels [9, 10], etc.

However, the effects of ventilation will increase the heat release rate, fire growth rate, flame length and fire spreading [11–16]. In addition, the effects of fixed fire-extinguishing system have been widely discussed, many researchers considered that the water spray system is of great benefit to prevent fire spreading, raise fire safety, and reduce the damage in tunnel fires [17, 18]. However, when ventilation system and fixed fire-extinguishing system are both set in a tunnel, the interaction effect will produce definitely. Carvel et al. claimed that the ventilation system and the fixed fire-extinguishing system did not belong to independent set, both of them should be considered as two parts of the fire safety system [12].

In the past, the studies of the ventilation system focused on the critical velocity and the individual impact factor, such as the release rate, tunnel slop, vehicle congestion, fire location, and aspect ratios in tunnels. These studies of fixed fire-extinguishing systems in tunnels emphasized with the discussions about effects of water spray, results for fire suppression, temperature variations and smoke flow directions.

In this study, we mainly focus on tunnel fire simulations about the critical velocities coming from different water spray parameters and base on references and experiment results from all over the world to build up an appropriate FDS tunnel fire model regarding the critical velocity and the water spray system. The values of critical velocity value without water discharge obtained by FDS have been compared the results with various theories and references to validate the tunnel model. Bases on a small fire source, the results show that the discharge conditions of water spray system

under different heat release rates, the water densities, and the droplet sizes. The temperate variations regarding different water spray parameters in vertical heights of tunnel are also investigated and analyzed.

2 Numerical Simulation

In this study, the bi-directional tunnel is built by FDS version 5.5.3 to investigate the effects of critical velocities with water spray systems in tunnel fires and to observe the variations of smoke layers and critical velocities. Based on the same structure of Hu et al. [19], the configuration and dimension of tunnel model with 10.8 m in width, 7.2 m in height, and 100 m in length are shown as in Fig. 1.

2.1 Grid System

Referred to Ma and Quintiere [20], the grid configuration was obtained as the formula of D^* grid size as shown in Eq. (1):

$$D^* = (\dot{Q}/\rho_\infty c_P T_\infty \sqrt{g})^{2/5} \tag{1}$$

where D^* is the characteristic fire diameter (m), $\dot{Q}$ is the total heat release rate (kW), ρ_∞ is the air density (kg/m^3), c_P is the air specific heat (kJ/kg-K), T_∞ is
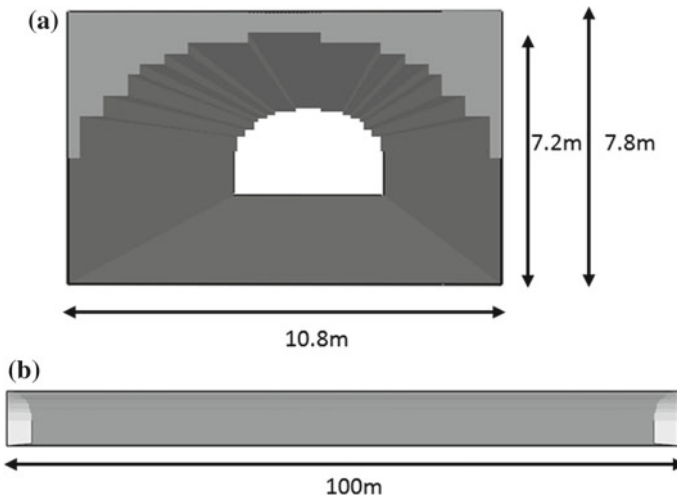
Fig. 1 The configuration and dimension of tunnel model for **a** the cross-section and **b** the total length
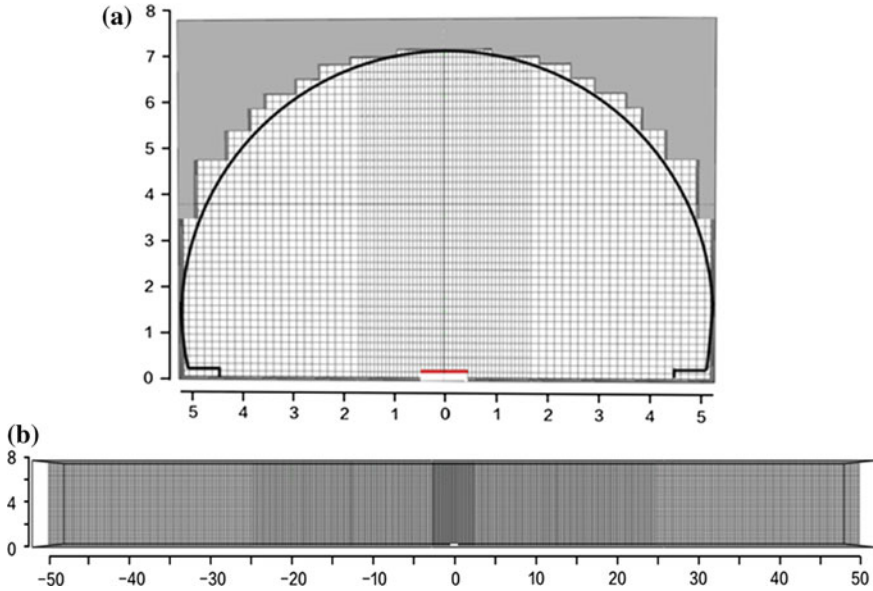
Fig. 2 Grid system diagram of tunnel model on **a** $X–Z$ axis and **b** $Y–Z$ axis

the environmental temperature (k), and g is the acceleration of gravity (m/s^2). The smallest length scale in the fire zone is characteristic fire diameter 0.1 D^*.

According to the grid resolution in the experimental test, when the grid size is 0.1 D^*, the speed and temperate of the average time axis met the regression model of McCaffery's experiment in the Large Eddy Simulation (LES). In order to improve the accuracy of the simulation, this study adopted less than 0.1 D^* as the grid setting of the simulated space, the smallest heat release rate is 1 MW and the value is 9.59 cm.

Moreover, in order to overcome the excessive grid problems of computer calculations, reduce the computer performance load, and avoid the termination of FDS program owing to complicated calculations. Therefore, regarding the grid setting, the grid size around the fire source is 8 cm × 8 cm × 8 cm (grid number 1.47 × 10^5), the water discharge area is 16 cm × 16 cm × 16 cm (grid number 9.98 × 10^5), and other areas are bigger, 32 cm × 32 cm × 32 cm (grid number 1.17 × 10^5). The total grid numbers are 1.262 × 10^6 in this model, the results are as shown in Fig. 2.

2.2 Fire Source

The fire source setting in this study is gasoline fuel. The selected shape of the fuel distributor is a rectangle, the average heat release rate of the fuel distributor fire is 2.2 MW/m^2. The heat release rates in this study are selected in the following 7 types: 1, 1.8, 3.2, 4, 5, 8, and 10 MW.

In addition, the setting of the fire growth curves is according to the study of Hu et al. [19], reached the maximum heat release rate in 60 s, followed by stable combustion lasting for 600 s. All tunnel fires caused due to vehicles catching fire, most of the cars design with roofs in order to avoid the direct effects of the heat release rate of the pool fire by water spray system. Referring to the study of Ko and Hadjisophocleous [21], at the 3 m above, a metal sheet with 3 m in length and 2 m in width is set as the car roof. Therefore, owing to with the car roof metal sheet in the study, its assumption is reasonable regarding the heat release rate of stable combustion.

2.3 Ventilation System Design

The ventilation system design in this study is adopted the longitudinal ventilation system. According to the design of smoke management systems in the Hsuehshan Tunnel, when the tunnel fire occurred, the wind machines in 250 m at the upstream and 500 m at the downstream is stopped operating to avoid the evacuation difficulties of the occupants caused by smoke chaos. In this study, the length of tunnel model is merely 100 m, and the ventilation condition considered as the uniform and stable for the whole tunnel section from the tunnel entrance instead.

2.4 Water Spray System

In this study, the design of water spray system based on the parameters of Japan design regulation, the descriptions of discharge areas, nozzle configurations, discharge time, and water density are as followings.

According to the regulation of water systems in operating tunnels from Japan Ministry of Land Infrastructure and Transport, the principle of the discharge range is at least 50 m, the discharge density is 6 l/min/m^2, and the water quantity should constantly supply for 40 min at least. Therefore, this study referred to the Japan regulation regarding the water discharge area, the total simulation range is 50 m on the effects of the whole discharge in the tunnel.

Based on the Japanese Road Tunnels Final Report with the design of Japan installation regulation and the design sample of the sidewall sprinkler system from Nohmi Bosai Ltd., Japan, the sidewall sprinkler system is with a row of main pipelines of 5.7 m in height, the distance of every sprinkler nozzle is 5 m. There are total 10 composed sprinkler nozzles in the protection area. NFPA 502 [17] indicated that the operating time of the fixed fire-extinguishing system is no more than 3 min. West Nippon Expressway Company Limited suggests that the water spray system operate automatically in 10 min of fire detection in the single-tube two-way road tunnel. According to the domestic regulation of "Design Principles of Water Spray Systems in Road Tunnels" in Taiwan, the staff of the traffic control center checked the on-site

Table 1 Scenario cases

Scenario number	Water density (l/min/m²)	Water droplet (µm)	Heat release rate (MW)
No. 1–7	6	800	1.0, 1.8, 3.0, 4.0, 5.0, 8.0, 10.0
No. 8–14	6	1000	
No. 15–21	6	1200	
No. 22–28	8	1000	
No. 29–35	10	1000	

condition through CCTV, and watched if road users left the fire area. The water spray system should operate within 3 min (for one-way tunnel) and 5 min (for two-way tunnel). Therefore, in this study the discharge time is set in 180 s.

In this study, based on to the nozzles provided form Nohmi Bosai Ltd. Japan, the water destiny is 6 l/min/m², which met the Japan regulation. In order to compare the differences between water density and the critical velocity, the water densities are assumed as 6, 8, 10 l/min/m².

In addition, in order to figure out the tunnel temperature variations caused by different droplet sizes and then to change the critical velocity, the droplet sizes are set as 800, 1000, and 1200 µm for the parameters of the water spray system.

2.5   Scenario Cases

Based on the sizes of heat release rate, water densities, and water droplets, there are 35 scenario cases in this study (as shown in Table 1), to analyze the effects on the critical velocity with water spray systems. From Scenario 1–21, the water spray density is 6 (l/min/m²) and the water droplets were 800, 1000, and 1200 µm to check out the influences on the variations of critical velocities. From Scenario 8–14, and Scenario 22–35, the water droplet is 1000 µm, and the water densities are 6, 8, and 10 l/min/m² to check out the influences on the variations of critical velocities.

3   Results and Discussion

3.1   Comparison of Critical Velocities

In this study, the length of the tunnel model is 100 m, the critical velocity without water discharge should be taken firstly in order to compare with the differences between the before and after activation of water discharge simulation. Based on the heat release rates of 1, 1.8, 3.2, 4, 5, 8, and 10 MW on the design of the fire source, the critical velocities obtained by this model without water spray system are compared
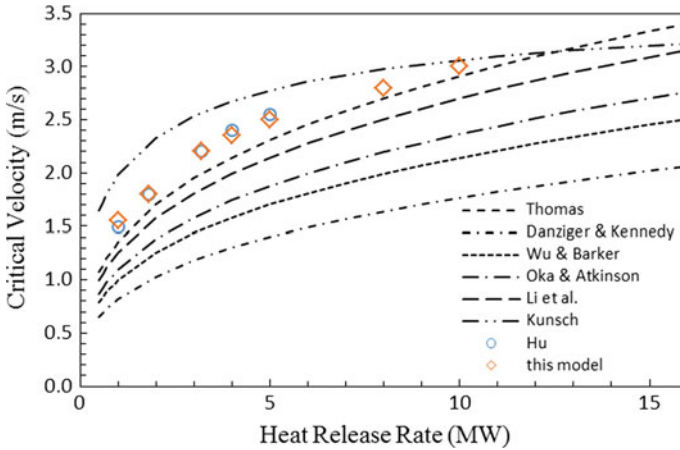
Fig. 3 The critical velocity of fires under different heat release rates

with those by the other researches (as shown in Fig. 3). The result of this model shows that the good agreement with Hu's [19], and the growth curve tendency is similar to other's theories model.

3.2 Effects of Water Spray Systems on Tunnel Fires

When the water spray system activates, the water is able to absorb the heat and lower the temperature, then reduce the thermal buoyancy and decrease the critical velocity accordingly. In this study, on example of the heat release rate of 3.2 MW, the critical velocity without water discharge is 2.2 m/s, the water spray system activates in 180 s, and the longitudinal velocity is 1.6 m/s, the results of smoke layer variations are shown as in Fig. 4, it could be seen that 1.6 m/s is the critical velocity. As a result,
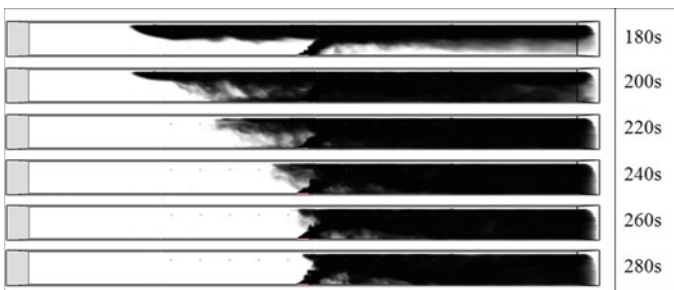
Fig. 4 Smoke layer variations with water spray system in a 3.2 MW fire

in the same heat release rate, the critical velocity with water spray is lower than that of without water discharge.

3.3 Influence of Water Density on Critical Velocity

In this study, the three settings of the water density are as follows: 6, 8 and 10 l/min/m^2, to discuss the variations of the critical velocity in droplet size of 1000 μm under different heat release rates. Figure 5 shows the curve diagram of the heat release rate and the critical velocity under different water densities when the droplet size was 1000 μm. From the diagram, it can find that the water spray system decreases the critical velocity no matter what the discharge water density is. However, the critical velocity increases due to the increasing heat release rate. It should be noted that when the water density is 6 l/min/m^2, the greater the heat release rate, the lower differences of the critical velocity comparing to without discharge. The results show that the greater the water density results the better effect to reduce the critical velocity.

Figure 6 shows the vertical temperature distribution of without water discharge and different discharge water densities at the 5 m upstream, longitudinal velocity of 2.25 m/s, and the heat release rate of 10 MW. It should be noted that the critical velocity of 10 MW with water density of 10 l/min/m^2 is 2.25 m/s. Without discharge, the temperature is much higher than water spray system on the top of the tunnel. The smoke backlayering is affected when the water spray system is activated, and then the temperature of the smoke backlayering decreased by the cooling effect. However, following the increase of water densities, the result of the cooling effect became obviously. Therefore, the effect of cooling the environment temperature in the tunnel with water density of 10 l/min/m^2 is better than the other two discharge densities.
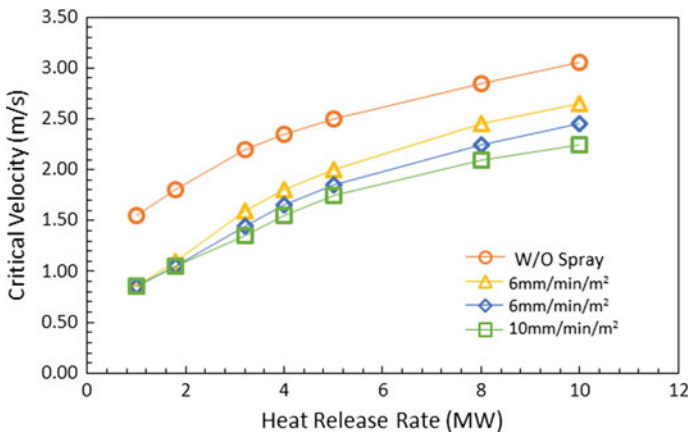
Fig. 5 The critical velocity in different discharge water densities
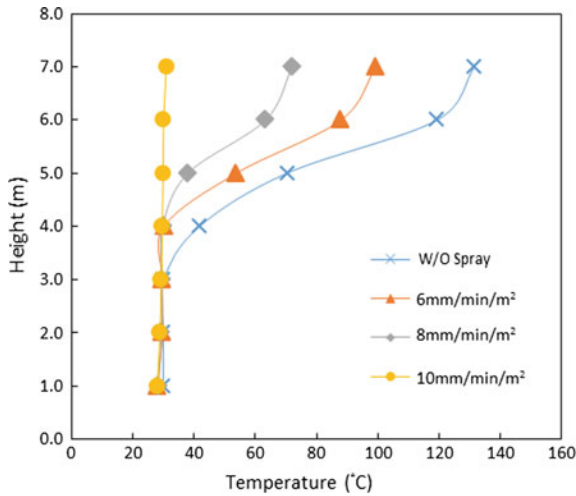
Fig. 6 Vertical temperature distribution of different discharge water densities

3.4 Effect of Droplet Size on Critical Velocity

Figure 7 shows the curve diagram of the heat release rate versus the critical velocity with different droplet sizes when water density is 6 l/min/m^2. It can find that the smaller the droplet size causes the smaller the critical velocity. Moreover, comparing with the condition of without the water spray system, using the water spray system always decreases the critical velocity. When the heat release rate is 1 MW, the difference between the three droplet sizes and critical velocity without discharge is
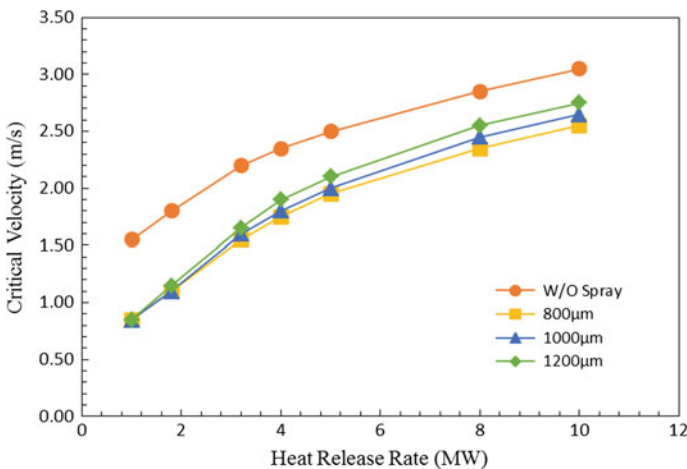
Fig. 7 The critical velocity with different droplet sizes
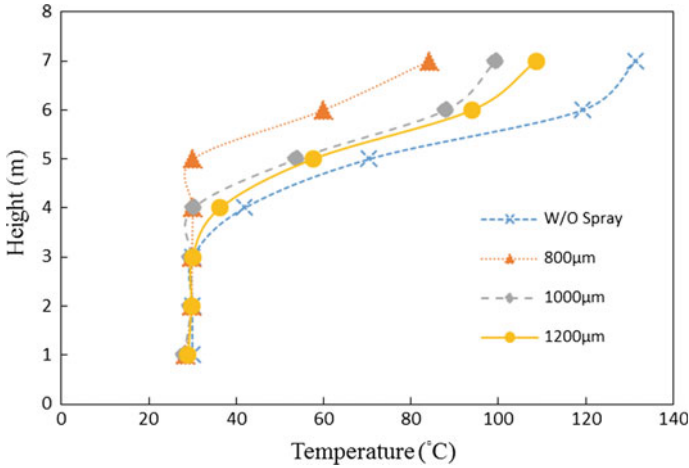
Fig. 8 Vertical temperature distribution with different droplet sizes

0.8 m/s. When the heat release rate is 10 MW without water discharge, the differences among the critical velocities of 800, 1000, and 1200 µm are 0.5, 0.4, and 0.3 m/s respectively. As a result, greater the droplet size causes the greater critical velocity. The greater the heat release rate causes more effects of the droplet size on the critical velocity.

Figure 8 shows the vertical temperature distribution at the 5 m upstream with different droplet sizes, the heat release rate is 10 MW, water density is 6 l/min/m², and the velocity of 2.25 m/s with different droplet size. Without water discharge, the smoke temperature on the top of the tunnel is much high than that when the water spray system activates. When the droplet size reduces, the effect of the cooling effect becomes obviously. The main reason is at the same water density, when the droplet size of 800 µm, the total surface area of the droplet in the air was bigger than 1000 µm or 1200 µm, and the effect of heat absorbing is better. Therefore, its effect of the cooling the temperature in the tunnel is better that the other two droplet sizes.

3.5 Vertical Temperature Variations

Figure 9 shows the distributions of vertical temperatures at the downstream of 5 and 10 m from the fire source with different water densities and reaching the critical velocity at the heat release rate of 10 MW. It should be noted that there is no backlayering in this case whether the water spray system is activated or not. The distribution of vertical temperature at 5 m downstream without water discharge is shown as in Fig. 9a. The highest temperature (138 °C) at the 5 m downstream is the same as at 4 m ground height. The temperature at the top of the tunnel is 104 °C, and the temperature at the 1.8 m ground height is 68 °C.
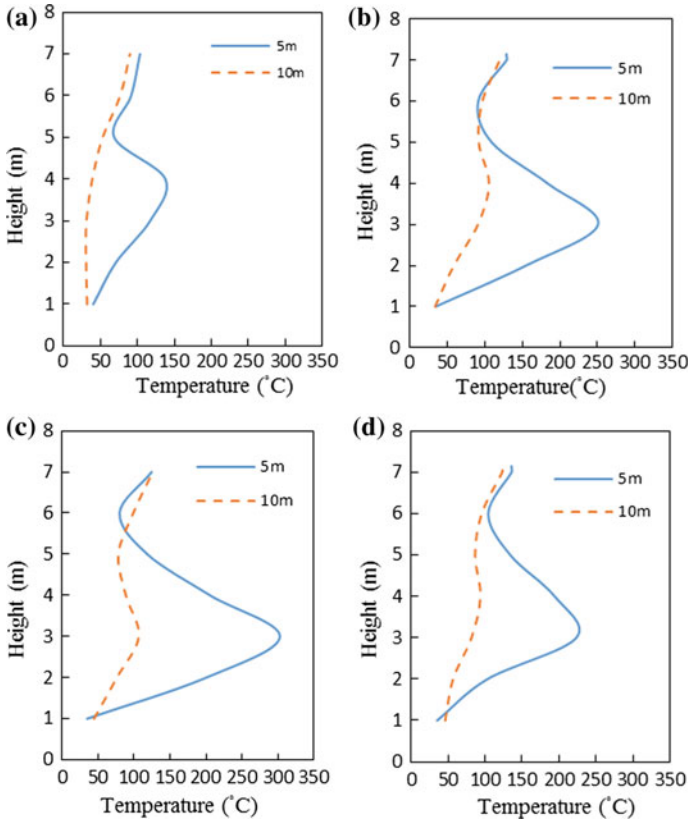
Fig. 9 The distributions of vertical temperatures with different water densities, **a** without water discharge, **b** 6 l/min/m^2, **c** 8 l/min/m^2, and **d** 10 l/min/m^2

In this cases, the highest temperature locates down to 3 m ground height, and the temperature also raises (8 l/min/m2 reaching to 302 °C, as shown in Fig. 9c), the temperature on the top of the tunnel is no difference comparing to without discharge. At the 10 m, comparing before and after for water discharge regarding the distribution vertical temperature distributions, in the middle of the tunnel (at 3.5 m ground height), temperature after water discharge is higher than before.

The reasons for the above situations viewed in this study are as follows: the burning flame and the intermittent flame became sloped after blowing by the wind and which also suppressed by the droplets, wind and pressure owing to water discharge. Although the length of the fire plume had shortened, the heavy smoke and the heat were unable to rise on the top of the tunnel and cause the raise of the temperature in the middle of the tunnel. In addition, different water densities cause the highest temperature change in the middle of the tunnel, the lowest temperature (224 °C) is at 10 l/min/m^2.

4 Conclusions

In order to understand the influence of the water spray system and the ventilation system, this study focuses on the droplet size of the water spray system and the variations of the critical velocity on the discharge water density. The settings of droplet sizes are 800, 1000, 1200 µm and discharge water densities are 6, 8, 10 l/min/m². The result of computer simulation shows that when the water spray system activated, under the same heat release rate, the critical velocity reduced accordingly. However, different water densities cause different reduced results of critical velocities. The greater discharge water densities cause better cooling effects of the smoke layers and the lower critical velocities. The smaller droplet sizes cause better effects of heat absorbing and reduced critical velocities. When the spray droplets are between 800 and 1200 µm, the effects of discharge water densities on temperature are greater than that of the droplet sizes. When the heat release rates were greater, the differences became more obvious. The effects of water spray systems on critical velocities focused on discharge water densities.

With the water spray system, its activation largely affected smoke backlayering, especially at the downstream in the tunnel. The water spray system affects the distribution of the vertical temperature and makes the highest temperature shifted to the ground. Regarding the water spray system, the variation of the critical velocity, the influences of the reducing temperature for emergency response, and the effect of the critical velocity on the water mist system, it is expected that more discussions will be found in the future studies.

References

1. Ingason, H., Li, Y. Z., & Lönnermark, A. (2015). *Tunnel fire dynamics*. New York, USA: Springer.
2. Ejrup, A. M. (2011). *Analysis of design options and trade-offs for road tunnels incorporating suppression systems*. Report 5305, ISSN: 1402-3504.
3. Thomas, P. H. (1968). *The movement of smoke in horizontal passages against an air flow*. Fire Research Note, No. 723. Fire Research Station.
4. Danziger, N. H., & Kennedy, W. D. (1982). Longitudinal ventilation analysis for the Glenwood Canyon tunnels. In *Proceedings of the Fourth International Symposium Aerodynamics and Ventilation of Vehicle Tunnels*, pp. 169–186.
5. Wu, Y., & Bakar, M. Z. A. (2000). Control of smoke flow in tunnel fires using longitudinal ventilation systems-A study of the critical velocity. *Fire Safety Journal, 35*(4), 363.
6. Li, Y. Z., Lei, B., & Ingason, H. (2010). Study of critical velocity and back layering length in longitudinally ventilated tunnel fires. *Fire Safety Journal, 45*(6), 361.
7. Yi, L., Xu, Q., Xu, Z., & Wu, D. (2014). An experimental study on critical velocity in sloping tunnel with longitudinal ventilation under fire. *Tunnelling and Underground Space Technology, 43,* 198.

8. Li, L., Cheng, X., Cui, Y., Li, S., & Zhang, H. (2012). Effect of blockage ratio on critical velocity in tunnel fires. *Journal of Fire Sciences, 30*(5), 413.
9. Lee, S. R., & Ryou, H. S. (2005). An experimental study of the effect of the aspect ratio on the critical velocity in longitudinal ventilation tunnel fires. *Journal of Fire Sciences, 23*(2), 119.
10. Liu, C., Lu S., Zhang, R., Yang, H., Cheng, X., & Zhang, H. (2015). The effect of aspect ratios on critical velocity in tunnel fires. In *Proceedings of the 10th Asia-Oceania Symposium on Fire Science and Technology*, Tsukuba, Japan.
11. Carvel, R. O. (2009). Ventilation and suppression systems in road tunnels: Some issues regarding their appropriate use in a fire emergency. In *2nd International Tunnel safety Form for Road and Rail*, pp. 375–382.
12. Carvel, R. O., Beard, A. N., & Jowitt, P. W. (2001). The influence of longitudinal ventilation systems on Fires in Tunnels. *Tunnelling and Underground Space Technology, 16*(1), 3.
13. Carvel, R. O., Beard A. N., Jowitt, P. W., & Drysdale, D. D. (2001), Variation of heat release rate with forced longitudinal ventilation for vehicle fires in tunnels. *Fire Safety Journal, 36*(6), 569.
14. Li, Y. Z., Vylund, L., Ingason, H., & Appel, G. (2015). *Influence of fire suppression on combustion products in tunnel fires*. SP Report: SP Technical Research Institute of Sweden.
15. Lemaire, T., & Kenyon, Y. (2006). Large scale fire tests in the second Benelux tunnel. *Fire Technology, 42*(4), 329.
16. Ingason, H., & Li, Y. Z. (2010). Model scale tunnel fire tests with longitudinal ventilation. *Fire Safety Journal, 45*(6), 371.
17. NFPA 502. (2014). Standard for road tunnels, bridges and other limited—Access highways. National Fire Protection Association, Quincy, MA, USA.
18. PIARC (2007) Systems and equipment for fire and smoke control in road tunnels,pp. 175–189. PIARC Publications. ISBN 2-84060-189-3.
19. Hu, L. H., Huo, R., & Chow, W. K. (2008). Studies on buoyancy-driven back-layering flow in tunnel fires. *Experimental Thermal and Fluid Science, 32*(8), 1468.
20. Ma, T. G., & Quintiere, J. G. (2003). Numerical simulation of axi-symmetric fire plumes: accuracy and limitations. *Fire Safety Journal, 38*(5), 467.
21. Ko, Y. J., & Hadjisophocleous, G. V. (2016). Study of smoke backlayering during suppression in tunnels. *Fire Safety Journal, Fire Safety Journal, 58,* 240.

Research on Evacuation of Train Fire in Extra-Long Channel Tunnel

Jie Kong, Zhisheng Xu and Wenjiao You

Abstract The Qiongzhou Channel tunnel, which is under construction in China, is taken as an example to study the evacuation of a train in a tunnel. Fire Dynamics Simulator (FDS) and Pathfinder software are utilized to simulate the fire spreading and personnel evacuation. When a fire broke out in the tunnel, the process can be divided into three stages according to the development of fire, which are carriage fire period, fire spread period, and tunnel fire period. The safety of people evacuation in different stages was studied. It has been found that when a fire occurs at the carriage center, people can evacuate to the adjacent carriages safely. In the event of a fire happens at the carriage end, high temperature and smoke would threaten the safety of passengers. If the fire train could drive to the emergency rescue station, it has been proved 200 s ahead to protect passengers than driving outside, and people can evacuate to safety area within the available safety evacuation time. The results show that it is necessary to have an emergency rescue station in the extra-long channel tunnel, and cooling equipment and fire-extinguishing installations should be equipped in carriages to ensure passengers safety.

Keywords Channel tunnel · Emergency rescue station · Train fire · Evacuation

1 Introduction

With the development of world tunnels and the progress of modern technology, deeply embedded and extra-long railway tunnels appear increasingly common underwater worldwide. The increased length of extra-long channel tunnels poses new challenges to fire safety. In the event of the fire in the tunnel, there will be a large number of poison gas and heat generated in the semi-closed structure and could not be quickly discharged, which would cause the temperature rise, even cause the impact on the tunnel structure [12]. If the fire out of control, the tunnel would face the risk of tunnel instability, water seepage, collapse and other devastating accidents and would

J. Kong · Z. Xu (✉) · W. You
Institute of Disaster Prevention Science and Safety Technology, Central South University, Changsha, Hunan 410075, China
e-mail: xuzhsh82@163.com

quickly become a place with low visibility, high temperature, gathered a large number of poison gas. Passengers will be in danger if they expose to a dangerous environment for a long time.

To reduce the impact of fire on passengers, it is necessary to reduce the time for exposing to a dangerous environment and limit the fire development as soon as possible. The time from ignition to threatening passengers' safety is called available safety evacuation time (ASET, for short), while, the time from ignition to safety evacuation is called required safe evacuation time (RSET, for short) [13, 17]. When ASET is longer than RSET, it is considered safe for passengers. Therefore, increasing ASET and reducing RSET can improve the safety of passengers effectively.

In theory, the setting of an emergency rescue station in the extra-long channel tunnel can shorten the travel distance of the train, make passengers evacuate quickly, and reduce the evacuation time. In addition, the layout of automatic fire-extinguishing equipment and facilities in an emergency rescue station could effectively reduce the temperature of tunnel, control the fire spreading, and increase the available safety evacuation time. A large amount of researches have been carried out to study the necessity of the emergency rescue station, scholars fully compared the ASET and the RSET when the train stopped at the rescue station and considered it as the criterion for personal safety [2, 3]. However, from ignition to train stop, several running plans need to be discussed, which is decided by a variety of complex factors, such as train performance, tunnel environment. Furthermore, the plan for train running and personal evacuation should be changed accordingly with the development of fire. To discuss the problems above, in this paper, it has been divided into three periods to study train running mode and personnel evacuation after tunnel fire. Setting up emergency rescue stations, which is discussed as key construction of extra-long tunnel, has been studied from the perspective of safety evacuation.

2 Model Description

2.1 Mathematical Description

In recent years, many numerical simulation studies have confirmed the consistency with experiment; the numerical simulation is used to study the development of train fire. It is possible to determine the law of train fire development and can reduce the cost of research [4, 10, 19].

Fire Dynamics Simulator (FDS, for short) will be used in the research of smoke spreading in trains and tunnels, and the ASET will be received. RSET is closely related to personnel evacuation in trains and tunnels, which can be studied by pathfinder software.
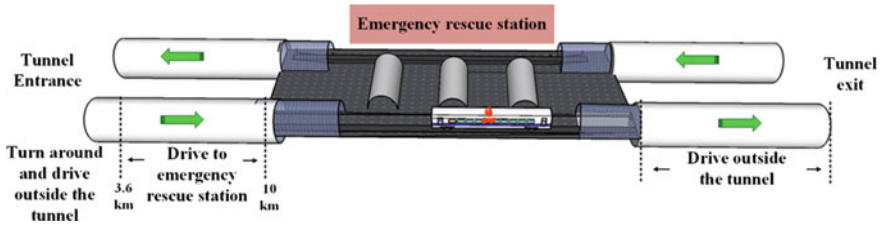
Fig. 1 Scheme of train emergency braking

2.2 Physical Model

Qiongzhou channel is a double-track single tunnel, which measures 21 km in length. As the tunnel is very long and underwater, it will take more time for trains to evacuate in case of fire, and it is also difficult for external rescue workers to reach the tunnel. To improve passenger escape conditions, an emergency rescue station of 500 m has been set 10.5 km away from the entrance of the tunnel, which is shown in Fig. 1.

A model of train carriage is designed with CRH6 by use of FDS software, which is shown in Fig. 3. The size of carriage for numerical simulation is 25,000 m * 3,200 m * 2,600 m (length * width * height). The train is 201.4 m long, which contains eight carriages. The fire heat release rate is 15 MW, and the growth mode is t^2 fire. Three parameters have been detected in the numerical simulation, which are temperature, visibility, and CO concentration. The simulation time is 1800 s. A 1:1 scale model of the tunnel is designed based on the emergency rescue station of Qiongzhou channel tunnel. 600 m is selected as the length of the tunnel model for calculation efficiency. The tunnel is a shield tunnel, the inner diameter is 9.4 m, and the internal clearance area is 58 m^2. The rescue station is 500 m long, 11 cross-passages have been set along the length of rescue station at intervals of 50 m, which is shown in Fig. 2.

Different personal ratios will affect the time of evacuation. According to the designed parameters of CRH6 train as well as common passenger ratios, the evacuation parameters for numerical simulation are shown in Table 1. Carriage evacuation model is built by pathfinder software (see Fig. 4) as well as the model of emergency rescue station evacuation (see Fig. 5).

2.3 Grid Sensitivity

The gird size will affect the calculation accuracy and calculation time. In recent researches, sensitivity tests are available for gird selection. In the simulation, two fire scenarios are chosen for sensitivity tests, which are central carriage fire and tunnel fire. D^*/dx criterion has been widely used for assessing the grid resolution, where dx is the grid size and the characteristic length is calculated by D^*.
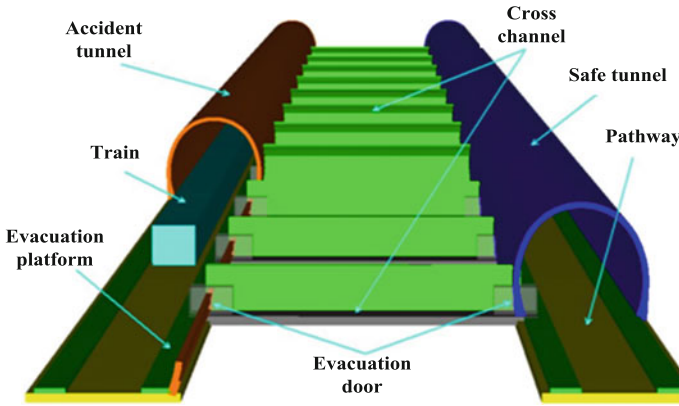
Fig. 2 Model of emergency rescue station
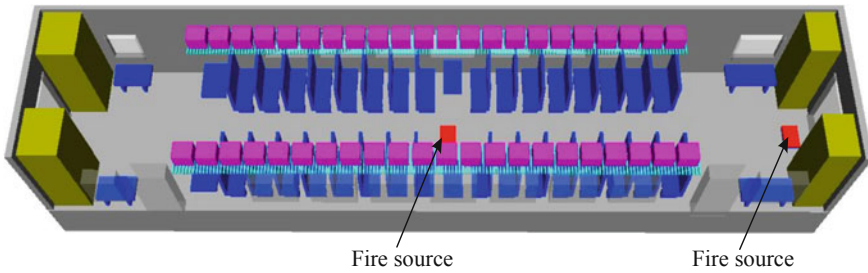
Fig. 3 Model of carriage fire

Table 1 Passenger ratios of evacuation crowds

	Fixed number	Exceed seating capacity		Man (%)	Woman (%)	Elder (%)	Children (%)
Single carriage	78	138	Passenger ratios	45	38	7	10
CRH6 train	557	1024		45	38	7	10

$$D^* = \left(\frac{\dot{Q}}{\rho_\infty C_p T_\infty \sqrt{g}} \right)^{\frac{2}{5}} \tag{1}$$

It was recommended by Mc Grattan that the value of D^*/dx should be in the range of 4–16. Three grid sizes are selected for each fire scenario according to the calculation results of dx. According to the result of numerical simulation, the change low of temperature and visibility at the height of 2 m are measured, which is useful
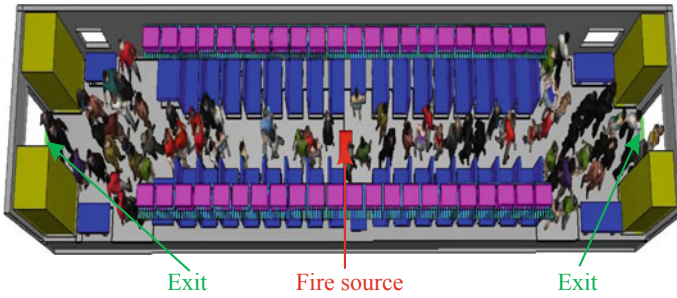
Fig. 4 Model of carriage evacuation
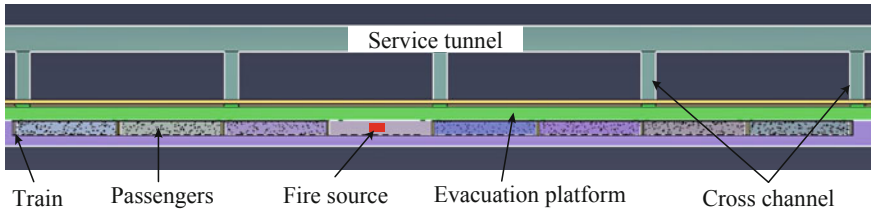
Fig. 5 Model of emergency rescue station evacuation

for gird selection. As a result, Figs. 6 and 7 show that when the grid density reaches a certain value, the variation trend of characteristic parameters will not be influenced
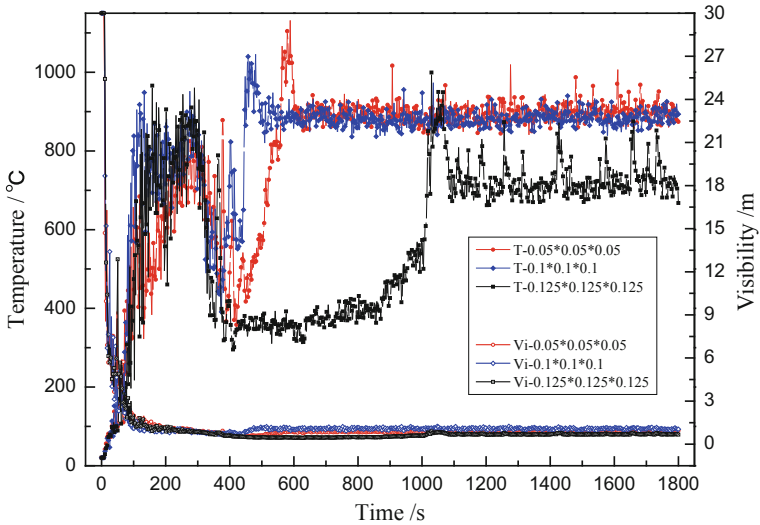
Fig. 6 Variation of visibility and temperature of central carriage fire with different grid densities
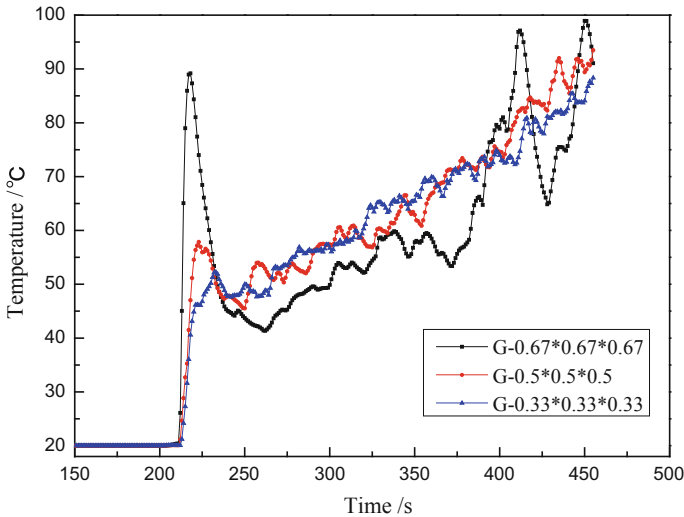
Fig. 7 Variation of temperature of tunnel fire with different grid densities

by grid density. Therefore, we chose the grid size of 0.1 m * 0.1 m * 0.1 m for central carriage fire and 0.5 m * 0.5 m * 0.5 m for tunnel fire.

2.4 Calculation Conditions

Carriage simulation model and train simulation model are shown in Table 3. An important parameter, available safety evacuation time, needs to be determined under the two fire models. When the fire happened in the front or end of the train, the smoke can be controlled by one side, and passengers escaped safely. When the fire happened in the middle of the train, longitudinal ventilation will cause danger to personal security, so it is not suggested in this scenario (Table 2).

As we know, different fire locations will also cause different modes of personnel evacuation. If the fire happens at the end of the carriage, the contact door is unavailable, and passengers need to evacuate to the other exit. If the fire is in the middle of the carriage, two exits can be used for passengers to evacuate. Working conditions for personnel evacuation are shown in Table 3.

Table 2 Working conditions of carriage fire and tunnel fire

The working condition number	Fire source	Fire size (MW)	Method of fire growth	Calculation time (s)	Time of windows breakage (s)
Carriage fire 1	Carriage center	15	t^2	1800	200
Carriage fire 2	Carriage end	15	t^2	1800	200
Tunnel fire 3	The third carriage of the train	15	t^2	1000	200

Table 3 Working conditions for personnel evacuation

The working condition number	Simulation situation	Fire position	The number of people in different working conditions
No. 1	One carriage	Carriage center	78 (fixed number)
No. 2	One carriage	Carriage end	78 (fixed number)
No. 3	One carriage	Carriage center	138 (exceed seating capacity)
No. 4	One carriage	Carriage end	138 (exceed seating capacity)
No. 5	Full train	Middle carriage	557 (fixed number)
No. 6	Full train	Middle carriage	1024 (exceed seating capacity)

3 Emergency Response to Fire Trains and Safe Evacuation Criteria

3.1 Emergency Response to Fire Trains

When a fire starts in the tunnel, a large amount of smoke with poisonous and high temperature will be produced, and it is dangerous for passengers to evaluate. Therefore, most countries in the world have stipulated that the train should be pulled out of the tunnel or stopped the emergency rescue station [5, 14]. There are three emergency measures for trains on fire: (1) continue to run along the tunnel; (2) stop at the emergency rescue station; and (3) emergency brake and turn out of the tunnel [7].

According to the fire locations and running capacities of the train, the evacuation mode has been targeted designed as follows. The double holes single-line channel tunnel is 21.0 km long, and an emergency rescue station should be set 10.5 km away from the entrance of the tunnel. CRH6A intercity EMU has been chosen on this railway line. Parameters of train brake are shown in Table 4 [16]. Carriages of the

Table 4 Emergency braking parameters of train CRH6A

CRH6A	Train speed	Emergency braking acceleration	Deceleration	Train operation acceleration from 0 to 40 km/h	Average acceleration from 0 to 200 km/h
	200 km/h	1.12 m/s^2	$\geq$0.9 m/s^2	0.65 m/s^2	0.34 m/s^2

high-speed train consist of power car and trailer body. Once the power car is on fire, it may lose 25% of the power. Meanwhile, the running speed would reduce from 200 to 100 km/h. The event that the fire happened on two different power cars at the same time is with low probability, so it can be ignored.

When the train catches fire at the entrance of the tunnel, if it can immediately brake and turn out from the entrance, it needs 128 s. If the train continues to travel for 128 s at the speed of 100 km/h, it can run 3558 m, but still cannot arrive at the emergency rescue station. So, if the fire breaks out at the tunnel entrance, turning away from the tunnel takes a shorter time.

According to the calculation, if the fire breaks out within 3.6 km away from the entrance of the tunnel, turning away from the tunnel takes 257 s, which is the best choice in the three emergency measures. Another situation is when the train catches fire from 3.6 km away from the entrance of the tunnel to 0.4 km in front of the rescue station, the train should first run in the uniform speed and then takes emergency braking to stay at the rescue station. In the third situation, theoretically speaking, when fire happens behind the rescue station within 3.4 km, it takes less time for the train to turn back to the rescue station than pulling out of tunnel; however, the manual operation of the train reverse driving is more complex, time-consuming, so the choice to drive out of the tunnel can avoid the uncertainty of artificial operation. The scheme of train emergency braking is shown in Fig. 1.

3.2 Safe Evacuation Criteria

Once the train catches fire, fire development and personnel evacuation have become a parallel development and irreversible process. Fire is a very complex process which includes ignition, growth, fully developed fire, and decay [8]. Personnel evacuation would experience carriage evacuation and tunnel evacuation. Only ensuring the safety of passengers from ignition to final evacuation can be regarded safe.

Available safety evacuation time: Three factors which are considered dangerous to humans are toxic gases, high temperature, and visibility. The shortest time for the three factors to reach the dangerous level is called ASET. In this paper, we take the height of 2 m as a study dimension, which is close to human height. The safety standard is that the temperature at the height of 2 m should no more than 60 °C, visibility should greater than 10 m, and the concentration of CO should below 500 ppm [18].
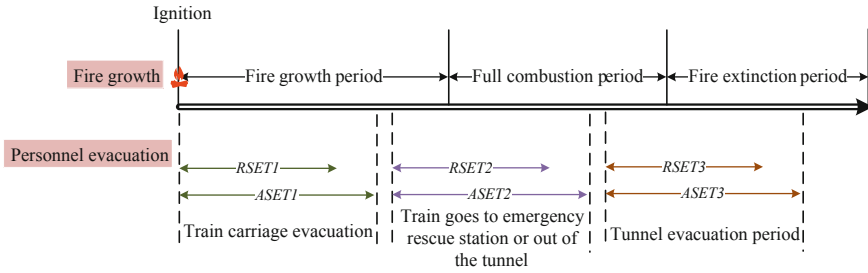
Fig. 8 ASET and RSET in different periods during fire development process

Required safe evacuation time: RSET means the time from ignition to personal safety evacuation, which contains the fire-alarming time, evacuation action time, and evacuation time. We assume that when people discover a fire, they will immediately evacuate to the adjacent carriages, so the time for fire alarming is not considered here.

In our definition of evacuation safety, ASET should be longer than RSET in each stage. The diagram of the safety evacuation criterion is shown in Fig. 8.

4 Analysis on Personnel Safety of Carriage Fire

The determination of typical scenarios has a great influence on personnel safety in carriages. The choice of fire scenarios mainly depends on fire locations. When fire happened in the middle carriage of the train, which is exactly the power carriage is the most dangerous. We mainly consider that fire happens in the middle of the carriage and at the end of the carriage based on the dangerous situation. No matter which scenario, passengers should evacuate to adjacent carriages immediately, but they cannot cross over the fire.

4.1 Fire Happened in the Middle of Carriage

When the fire happens in the middle of the carriage, toxic and harmful gases that produced by fire will be concentrated in the ceiling of carriage and then gradually spread to the surroundings along the roof. From Fig. 9, we can see that carbon monoxide concentration at a height of 2 m reaches the dangerous concentration at 140 s. The temperature exceeds 60 °C that the human body can withstand within 90 s. As the fire produces dark smoke, the visibility near fire source quickly reduces to 10 m. Within 60 s, the majority of the carriage is in danger. So the passengers need to immediately escape from fire and quickly evacuate to adjacent carriages in 60 s.
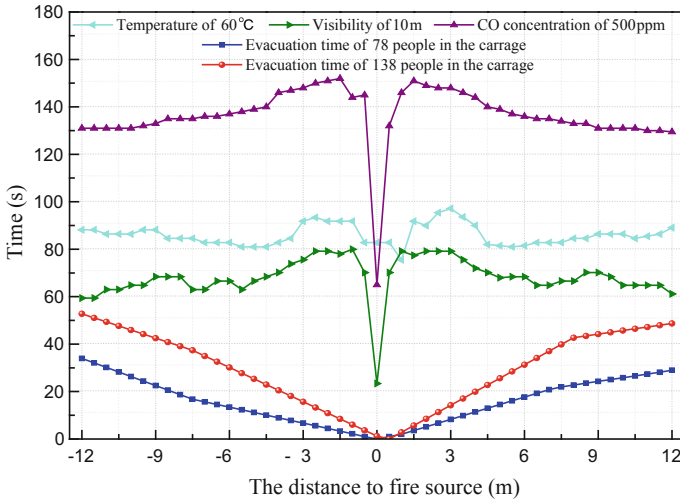
Fig. 9 Safety analysis of personnel evacuation when fire in the middle of the carriage

The simulation results of No. 1 and No. 3 working condition are demonstrated in Fig. 9. We find that the time for personnel evacuation is shorter than 60 s, so people can evacuate to the adjacent carriages securely, no matter there are 78 or 138 people in the fire carriage.

4.2 Fire Happened at the End of Carriage

It can be seen from Fig. 10 that when the fire happens at the end of the carriage, carbon monoxide concentration near the fire source exceeds 500 ppm in 100 s, which can cause harm to the human body. So immediately running away from the fire source and evacuating to the negative direction is necessary. The whole carriage is in danger of carbon monoxide in 140 s. Temperature curve in Fig. 10 shows a rapid growth near the fire source; it exceeds the limit temperature of 60 °C that the human body can withstand in just 30 s. The damaged area spreads to the whole carriage in 100 s. Viewed from visibility curve, the visibility near the fire source rapidly reduces to 10 m. Majority of the carriage has an acceptable visibility in just one minute, and the visibility reaches a danger level 20 s later. To ensure personnel safety, the time for the last passenger's evacuation should shorter than 70 s, in other word, the ASET is 70 s.

RSET is closely associated with personal evacuation time. In Fig. 10, obvious differences exist in the evacuation time of No. 2 and No. 4 conditions, which will directly impact the carriage safety. In No. 2 condition, there are 78 people in the carriage; the evacuation time is shorter than the time for substance reaching to dangerous levels. In No. 4 condition, the time for personnel evacuation is shorter than
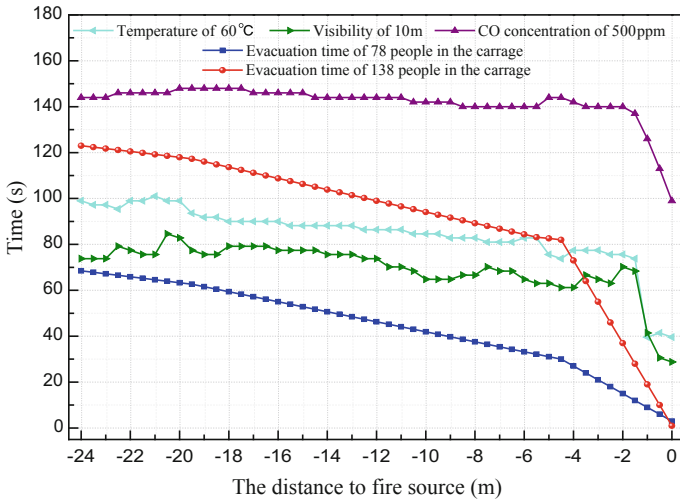
Fig. 10 Safety analysis of personnel evacuation when fire in the end of the carriage

the time for carbon monoxide at dangerous concentration. But, as the fire happens at the end of the carriage, people need to evacuate for a long distance to the other door. With the fire develops rapidly in the closed space, the temperature in the evacuation channel has exceeded 60 °C and visibility has dropped below 10 m, which will affect the evacuation safety.

4.3 Fire Spreads to the Adjacent Carriages

The current design of high-speed train focus more on the fire safety of the carriage, CRH6A intercity EMU train is also a typical one. CRH6A train complies with the standard of TB/T3237-2010s for combustibility flammability, smokiness, and toxicity. Environmental performance of interior decoration materials complies with the requirements of TB/T3139-2006 as well as other relevant laws and regulations. According to "technical conditions on CRH6-type intercity EMU", high-speed train should meet the performance requirements of fire prevention, such as the walls (door) between the CRH6A carriages needs to have a certain fire resistance, when the train catches fire, it is able to ensure that "the fire will not spread between the train coaches within 15 min." Through a serious test about smoke density, toxicity and flame propagation, it is considered that the CRH6 EMU train has fire resistance for 15 min; that is, the available safety evacuation time is 15 min during the process of the fire spreading to the adjacent carriage.

5 Analysis on Personnel Safety of Tunnel Fire

5.1 ASET for the Train in the Emergency Rescue Station

Temperature high enough can cause a rupture of carriage windows. After the windows break, toxic smoke will float into the tunnel and pose a threat to personal safety. Windows breakage due to fires has been studied by many researchers [1, 6]; however, there is no uniform conclusion on the exact time or temperature that can cause windows rupture. Duckhee Lee believes the carriage window will burst at 600 °C [10], and Ying Zhen Li emphasizes the failure of a modern tempered glass used in a train carriage could be expected to occur after exposure to a gas temperature over 600 °C, or an incident heat flux over 40 kw/m^2 [11]. Given the above, 400–600 °C is generally considered as the temperature of window breakage. Contrast with the fire simulation results, the highest temperature interior is 300 °C, which could not reach the minimum temperature of windows rupture. However, to study the effect of tunnel fire on personnel evacuation, the extreme situation would be considered here, that is, when the train stops at the emergency rescue station, the windows break, fire develops quickly in the tunnel and soon reached to 15 MW. If the extreme situation assumed here can meet the requirement of evacuation, it is reason enough to ensure personnel security in the tunnel. The simulation results of the dangerous parameters in the tunnel are shown in Figs. 11, 12 and 13.

In the condition of tunnel fire, fire source is in carriage interior, smoke and heat are limited to spread into the tunnel through carriage windows. Therefore, carbon
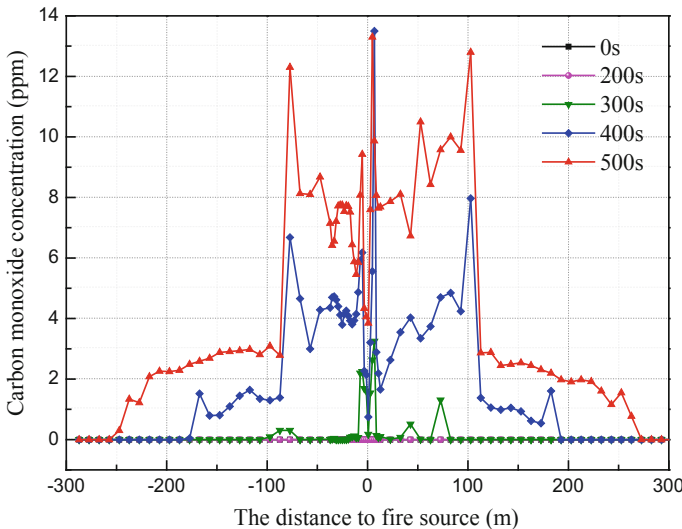
Fig. 11 Distribution of CO concentration at a height of 2 m in the tunnel
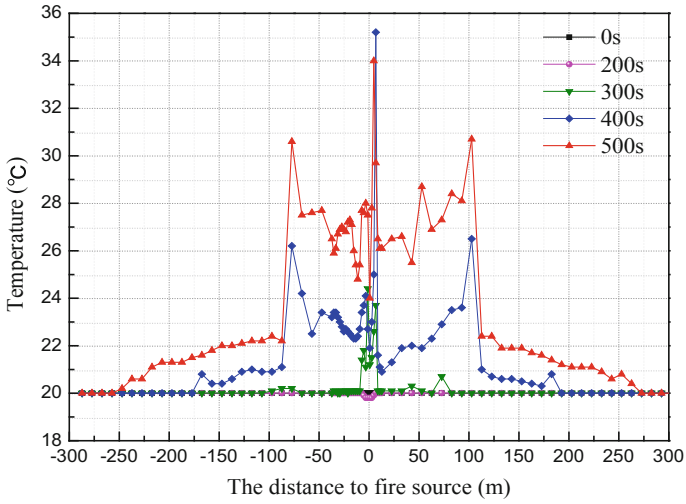
Fig. 12 Distribution of temperature at a height of 2 m in the tunnel
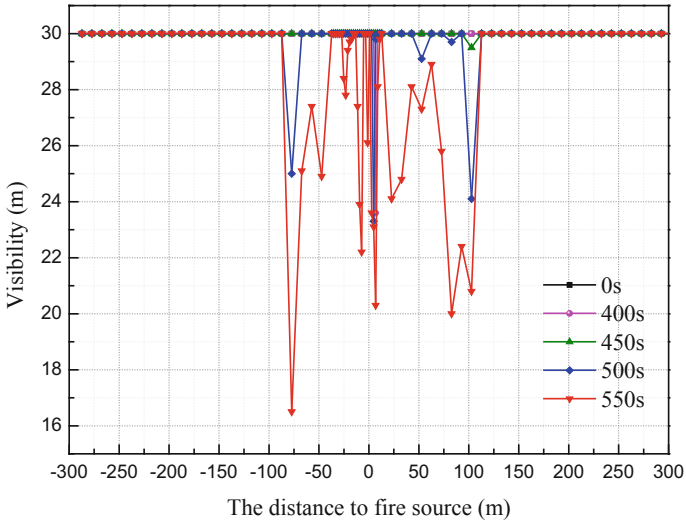
Fig. 13 Distribution of visibility at a height of 2 m in the tunnel

monoxide, temperature, and visibility in the tunnel are in safe level for a long time, the ASET for tunnel evacuation is longer than 500 s.
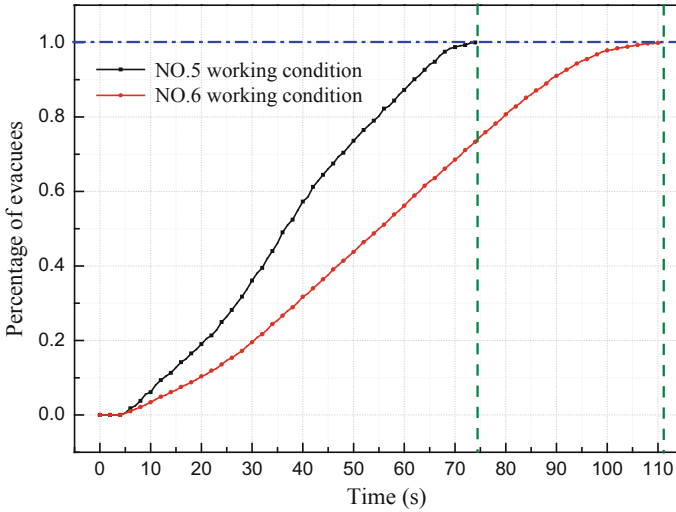
Fig. 14 Personnel evacuation in the tunnel

5.2 Safety Analysis of Train in the Emergency Rescue Station

The personnel evacuation simulation results of No. 5 and No. 6 are demonstrated in Fig. 14. In this section, we consider the two working conditions with fixed number passengers and exceed seating capacity. RSER here refers to the time that people evacuate from train to cross-channels. ASET has been proved longer than 500 s above.

Figure 14 shows the analysis of personnel evacuation time when the train stops at the rescue station under different working conditions, the time for evacuation of fixed number passengers and exceed seating capacity is 74 and 111 s, respectively, which is acceptable for safe evacuation. According to the simulation, we believe the passengers have sufficient time to evacuate to safe area.

5.3 The Impact of the Emergency Rescue Station on Personnel Safety in the Tunnel

When train catches fire in the tunnel, reducing running time will be beneficial for passengers and also be conducive to controlling fire. According to the train emergency braking mode, when train catches fire from 3.6 km away from the entrance of the tunnel to the front of the rescue station, the time for pulling out of the tunnel requires for 258–488 s. While stopping at the emergency rescue station needs 49–256 s. It shows that the fire train stops at the emergency rescue station is the optimum, which can not only short the train running time, but also improve the personnel security.

6 Conclusions and Suggestions

In this paper, we chose the extra-long tunnel as a research object and analyze the fire emergency treatment when fire happens in different locations in the tunnel. The characteristic of fire spreading and personnel evacuation is studied when the fire happens in carriage, spreads between carriages, and burned in the tunnel. By comparing ASET and RSET during the evacuation process in the various stages, we gain the following conclusions:

(1) When a fire breaks out within 3.6 km away from the entrance of the tunnel, turning away from the tunnel is relatively superior. When the train catches fire from 3.6 km away from the entrance of the tunnel to 0.4 km in front of rescue station, stopping at the rescue station is the best choice.

(2) People can successfully evacuate if the fire happens in carriage center. When the fire happens at the end of carriage, under the seat capacity of 78 people, passengers can evacuate to the adjacent carriage before the environment reaching to a dangerous state. If overcrowding, people will be exposed to the high temperature for a long time, and visibility is adverse to fire evacuation. In this case, carriages should be equipped with fire extinguisher equipment for initial-stage firefighting.

(3) If the train has good dynamic performance, pulling out of the tunnel or staying in rescue station is considered safe. Considering the passengers' anxiety, people should leave the dangerous area as soon as possible. It is recommended to set up emergency rescue stations for tunnels more than 20 km.

References

1. Chen, H. D., Zhao, H., Wang, Y., Wang, Q. S., & Sun, J. H. (2017). The breakage of float glass with four-edge shading under the combined effect of wind loading and thermal loading. *Fire Technology, 53,* 1233.
2. Fridolf, K., Ronchi, E., Nilsson, D., & Frantzich, H. (2013). Movement speed and exit choice in smoke-filled rail tunnels. *Fire Safety Journal, 59,* 8.
3. Gong, Y. F. (2014). Research on design of the emergency rescue station of Qingyunshan tunnel in Xiangtang—Putian railway. *Journal of railway engineering society*, 83.
4. Grattan, K. M., & Hamins, A. (2006). Numerical simulation of the Howard street tunnel fire. *Fire Technology, 42,* 273.
5. Guo, C., Wang, M. N., & Zhao, H. D. (2007). Research on the emergency rescue of fire in super long railway tunnel. *China Safety Science Journal, 17,* 153.
6. Harada, K., Enomoto, A., Uede, K., & Wakamatsu, T. (2000). An experimental study on glass cracking and fallout by radiant heat exposure. *Astrophysical Journal, 794,* 210.
7. He, D. L., Liang, J. M., & Ding, C. C. (2014). Development of CRH6 intercity multiple units. *Rolling Stock, 52,* 14.

8. Hu, L. H., Peng, W., & Yang, R. X. (2014). *Fundamentals of tunnel fire dynamics and prevention technology*. Beijing, China: Science Press.
9. Jin, R. G., Mao, L., & Le, Z. (2009). Application of FDS and pathfinder in building fires and evacuation. *Industrial Safety and Environmental Protection, 35,* 44.
10. Lee, D., Park, W., Jung, W., Yang, S. J., Kim, H., George, H., et al. (2013). Estimations of heat release rate curve of railcar fire. *Journal of Mechanical Science and Technology, 26,* 1665.
11. Li, Y. Z., & Ingason, H. (2016). A new methodology of design fires for train carriages based on exponential curve method. *Fire Technology, 52,* 1449.
12. Mo, S. J., Li, Z. R., Liang, D., Li, J. X., & Zhou, N. J. (2013). Analysis of smoke hazard in train compartment fire accidents base on FDS. *Procedia Engineering, 52,* 284.
13. Seike, M., Kawabata, N., & Hasegawa, M. (2016). Experiments of evacuation speed in smoke-filled tunnel. *Tunnelling and Underground Space Technology, 53,* 61.
14. Vuilleumier, F., Weatherill, A., & Crausaz, B. (2002). Safety aspects of railway and road tunnel: example of the lötschberg railway tunnel and mont-blanc road tunnel. *Tunnelling and Underground Space Technology Incorporating Trenchless Technology Research, 17,* 153.
15. Wang, X. L., & Ma, Y. S. (2013) Brief introduction of CRH6 intercity EMU. High speed railway technology, p. 196.
16. Wang, Y. H., Liu, B., & Zhang, Y. G. (2013). Risk assessment on Bohai Bay subsea tunnel in its operational period. *Engineering Sciences, 15,* 107.
17. Xie, B. C., & Xu, Z. S. (2013). Fire evacuation in passenger dedicated line tunnel. *Journal of the China railway society, 35,* 102.
18. Xie, X. Y., Ding, L. P., & Li, Y. S. (2010). CFD Simulation on evacuation of a high-speed train continue-to-roll during long tunnel fires. *Journal of tongji university (natural science), 38,* 1746.
19. Xu, Z. S., Zhou, Q., & Xu, Y. (2004). Fire model experiment and numerical simulation of passenger trains running in tunnels. *Journal of the China Railway Society, 26,* 124.

Experiment on Effects of Sealing Rate on Fire Behaviors in Sealing Tactics Against Tunnel Fire

Changkun Chen, Huang Xiao, Jie Chen, Xiaolong Zhao and Congxiang Zhu

Abstract In the process of sealing tactics against tunnel fire (STATF), sealing rate defined as sealing ratio per unit time, impacts upon sealing firefighting effect via influencing the air flowing, smoke exhaust, etc. A 1/9 small-scale tunnel model was established to study the effects of sealing rate on tunnel fires in this paper. Taken fire size and sealing rate into account, the mass loss rate (MLR), temperature characteristics, and fire overflow were compared and studied. The results show that the MLR starts to drop earlier with the increase of sealing rate. Furthermore, a new parameter, sealing efficiency (denoted by λ), is introduced related to the moment of ceiling temperature in tunnel center turning to drop and the initial sealing time. It is found that the sealing efficiency is improved with the increase of sealing rate. Notably, sealing efficiency minimizes to minus when sealing rate reaches its minimum, indicating that it would have a negative feedback effect on fire extinguishment when sealing rate reduces to a certain degree. In addition, with the decrease of sealing rate, the maximum radiation heat near the tunnel entrance is higher and the existence duration of high-temperature smoke gets longer, which might pose a greater threat to firefighters.

Keywords Tunnel fire · Sealing tactics · Sealing rate · Experiment · Ceiling temperature

1 Introduction

Tunnel fire accidents have occurred over the past decades all around the world. Serious tunnel fire accidents often cause huge casualties and economic losses [1]. In November 2000, for instance, a train traveling in tunnel on Horn Stein hill in Austria Keats was on fire, causing 155 deaths and 18 injuries. In March 2014, a rear-end collision accident between two methanol trains occurred in Yanhou tunnel in China's Shanxi Province, causing 40 deaths, 12 injuries, and 42 burnt-out vehicles,

C. Chen (✉) · H. Xiao · J. Chen · X. Zhao · C. Zhu
Institute of Disaster Prevention Science & Safety Technology, Central South University, Changsha 410075, China
e-mail: cckchen@csu.edu.cn

together with economic losses amounting to tens of millions of dollars. Thus, the development of an effective and reasonable extinguishing method for tunnel fire has aroused widespread concern as it is very important for reducing casualties and property losses.

In recent years, many scholars have studied the temperature field, the law of smoke spread, and the heat release rate for tunnel fires, and have made a lot of research achievements. Ingason and Li and Li et al. [2–4] carried out a series of experiments at small-scale tunnel model, simulating the temperature distribution below the tunnel ceiling, the highest temperature, the heat release rate, and fire growth rate, etc. Based on the Froude model, Kashef et al. and Yuan et al. [5, 6] carried out the reduced-scale tunnel test and studied the distribution and attenuation characteristics of fire smoke temperature under natural ventilation. Ji et al. and Fan et al. [7, 8] conducted a series of experiments to study the transverse smoke distribution of tunnel fire and obtained the temperature prediction formulas at different locations. They also studied the combination behaviors of two pool fires in confined space for different fire size and two fires at different distances [9, 10]. Roh et al. [11] investigated the variation in heat release rate of different ventilation condition in tunnel fire by the small-scale tunnel model, and the results show that the heat release rate increases with the increase of ventilation volume. These academic achievements have a significant reference for us to better understand the development characteristics and influencing factors of tunnel fire.

As for extinguishing tunnel fires, sealing tactics is a useful method by interdicting the supply of combustion supporting in tunnels, and is used among sealing smothering method, foam infusion method, and water injection method to control and eliminate danger of tunnel fires. Moreover, the fire extinguishing work for tunnel fire often adopts the combination of several control methods, so that scientific implementation of the sealing step is of vital importance in tunnel firefighting.

At present, some scholars have studied the sealing as well as the blockage ratio of tunnel fire. Li et al. [12, 13] conducted a series of experiments and numerical simulations to study the effect of tunnel blockage ratio on the maximum temperature under the ceiling. Tang et al. [14] carried out relevant tests for tunnel fire considering the factors of both cross-sectional blockage ratio and blockage-fire distance. Based on CFD modeling, Gannouni and Maad [15] found that the effect of blockage brings about decrease of the critical velocity compared with an empty tunnel, and the decrease is slightly greater when the height between the bottom of obstacle and the tunnel floor increases. Considering three vehicles types in two or three arrays, occupying 5–31% of the tunnel cross section, Lee and Tsai [16] investigated the effects of vehicular blockage on critical ventilation velocity. They found that the critical ventilation velocity decreased due to vehicular obstruction when ventilation flow reached the fires and increased when the vehicle obstructions existed and ventilation flow did not reach the fires. Shafee and Yozgatligil and Meng et al. [17, 18] investigated the effects of blockage and inclination on the tunnel fire behaviors. In our previous researches [19, 20], a series of small-scale model tests have been carried out to investigate the influence of the different sealing ratios and the asymmetric sealing factor on the fire temperature field and the smoke spread law at tunnel ceiling.

When sealing tunnel fires, the sealing tactics needs to be implemented in stages owing to the uncertainty about fire development. The amount of ventilated air flowing into the tunnel will be affected by different sealing rate, and the fire development as well as the extinguishment effect will also be influenced. A question remains to be investigated nonetheless, that is, what effects does sealing rate have on tunnel fire behaviors and the extinguishment efficiency? Hence, a sequence of fire experiments simulating the STATF was conducted in a small-scale model tunnel. Considering different fire source sizes and sealing rates, the fuel mass loss, the temperature variation inside the tunnel and at the entrance, and the thermal radiation near the entrance during the sealing tactics were measured and analyzed.

2 Experiments

2.1 Tunnel Configuration

The experiments were conducted in a 1/9 small-scale model tunnel, and the schematic layout and the three-dimensional sketch are shown in Fig. 1a, b. Froude model is used in this paper to relate the small-scale with full-scale experiments. The Froude number [21] can be expressed as:

$$Fr = \frac{V_m^2}{g L_m} = \frac{V_f^2}{g L_f} \tag{1}$$

where V is velocity, g is the gravitational acceleration, and L is the tunnel length. The subscripts 'f' and 'm' represent the full and model scale parameters, respectively. The scaling relationships are [22]:

$$\frac{Q_m}{Q_f} = \left(\frac{L_m}{L_f}\right)^{5/2}, \ T_m = T_f,$$

$$\frac{t_m}{t_f} = \left(\frac{L_m}{L_f}\right)^{1/2}, \ \frac{M_m}{M_f} = \left(\frac{L_m}{L_f}\right)^{1/2} \tag{2}$$

where Q is the HRR, T is the temperature, t is the time, M is the fuel mass, and L_m/L_f is the similarity ratio.

The tunnel is 8 m (L) × 0.6 m (W). The cross section is an arch with a total height of 0.8 m, and the height of the vertical wall is 0.5 m and that of the semicircular structure is 0.3 m. The sidewall and the bottom of the model tunnel are brick-concrete structure. To improve the tightness of the tunnel, the sidewall was coated with cement mortar. The arch of the tunnel adopted a welded steel frame with a layer of fireproof asbestos on both sides to ensure the solidity and heat insulation simultaneously. Six nonequidistant stone piers were placed near one side of the tunnel entrance to install

(a) A schematic layout of the model tunnel
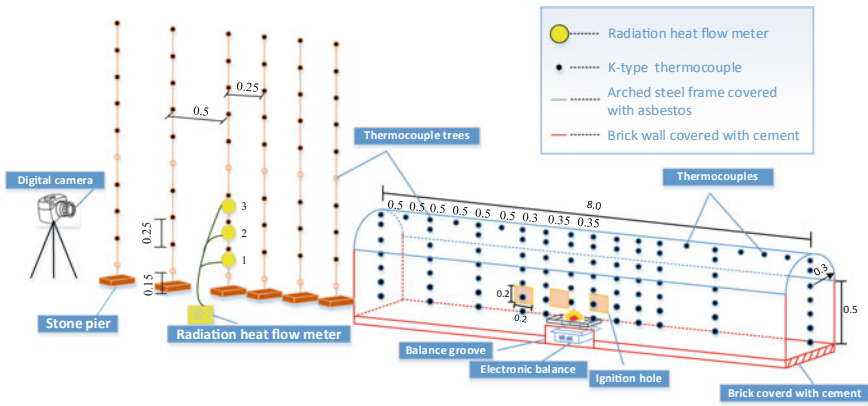
(b) Three-dimensional layout of the model tunnel

Fig. 1 Layout of the model tunnel (Unit: m)

thermocouples matrix. The upper surface of stone piers and the tunnel bottom is of equal height. The ambient temperature during experiments was about 14 °C.

2.2 Measurement Systems

For the temperature measurement system, as seen in Fig. 1b, 12 thermocouple strings with a total of 91 K-type thermocouples (diameter of 0.3 mm) were set inside the tunnel, and each string consists of seven thermocouples. The thermocouples are more intensive near the fire source with seven columns. To measure temperature near the tunnel entrance, six thermocouple strings were arranged appropriately, and each string contains ten thermocouples. Besides, three radiation, heat flow meters were installed 1 m away from the entrance at spacing of 0.25 m in the vertical direction to measure the radiant heat near the tunnel entrance.

Fig. 2 Schematic diagram of the arrangement of different fire size (Unit: m)
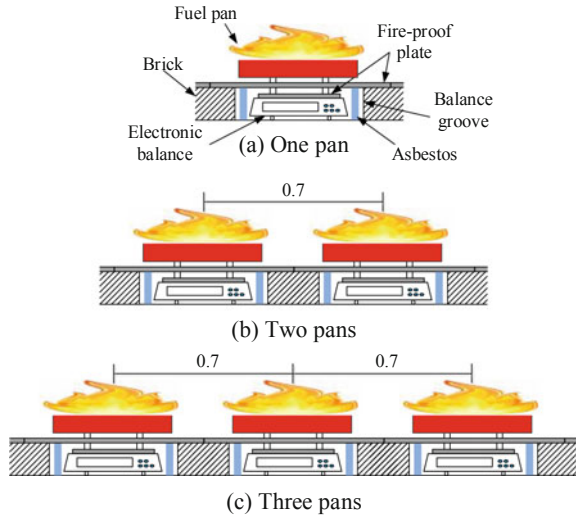
The fuel mass loss was measured by electronic balance placed in the balance groove at the tunnel bottom. The electronic balance was covered with a fireproof plate at the upper part for protection and wrapped with asbestos for heat insulation. Movable bricks were used for balance groove at the tunnel bottom to meet the need of adjustment for electronic balance, so that the fire source could be distributed symmetrically by the tunnel center in all fire scenarios. The arrangement of fuel pans in different fire scenarios can be seen from Fig. 2. The specific dimensions and photos of the experimental apparatus can be found in our previous study [20].

2.3 Sealing Settings

Sealing rate is defined as the sealing ratio per unit time interval, and the height of the tunnel entrance of every sealing phase is as a representative of the sealing ratio in this paper. The sealing rate, denoted by S_u (Unit: m/min), can be expressed as:

$$S_u = \frac{H_e}{\Delta t} \qquad (3)$$

where H_e is the height of the tunnel entrance of every sealing phase, which is 0.2 m in this paper. Δt represents the time interval, which is 1 min (Δt_1), 2 min (Δt_2), and 3 min (Δt_3), respectively. As a result, three kinds of sealing rates are used in the experiment, which are S_{u1} (sealing the tunnel entrance of 0.2 m in height every 1 min), S_{u2} (sealing the tunnel entrance of 0.2 m in height every 2 min), and S_{u3} (sealing the tunnel entrance of 0.2 m in height every 3 min), respectively.

The specific sealing time of every sealing phase under different sealing rates was shown in Table 1, wherein ts_n represents the sealing time. The subscript 'n' represents the phase order of sealing, for instance, ts_1 means the sealing time of the first sealing phase. Each group of the test includes four sealing phases, and the sealing times are different at various sealing rates except ts_1, which is 300 s in the experiment. It usually takes time for the fire brigade to rush to the fire scene. Moreover, the first thing that needs to carry out before the implementation of sealing is evacuation when sealing tactics is taken to extinguish tunnel fire, during which the firefighters use water guns to cool the tunnel entrance and then spray foam to extinguish the oil flow flame around the tunnel entrance, which also needs a certain period of time. It needs to point out that the scenarios simulated in this paper are ideal situations. The fire growth and situation are more complex in real application of sealing tactics so that the sealing steps maybe not such well-organized.

As seen from Fig. 3, asbestos and fireproof board were used to seal the tunnel entrance in the experiment, and the corresponding relationship of sealing time and sealing ratio for different sealing phase has been expressed. According to fuel pan number and sealing rate, a total of 12 cases were set up, as shown in Table 2.

Table 1 Sealing time at different sealing rate and corresponding sealing ratio

Sealing rate	Sealing time			
	ts_1	ts_2	ts_3	ts_4
S_{u1} (s)	300	360	420	480
S_{u2} (s)	300	420	540	660
S_{u3} (s)	300	480	660	840
Sealing ratio (%)	25	50	75	100

Notes: S_{u1} is sealing the tunnel entrance of 0.2 m in height every 1 min, S_{u2} is sealing the tunnel entrance of 0.2 m in height every 2 min, and S_{u3} is sealing the tunnel entrance of 0.2 m in height every 3 min
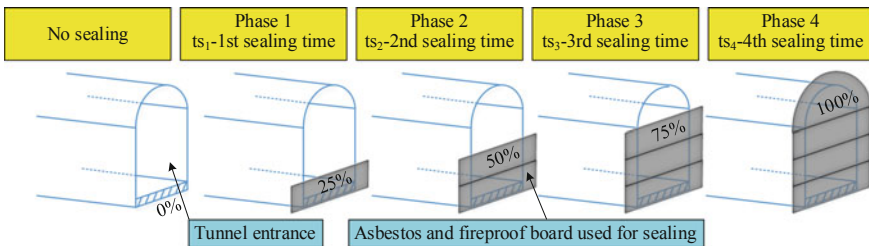
Fig. 3 Schematic diagram of relationship between sealing time and sealing ratio

Table 2 Conditions of the experiments

Group	Condition number	Fuel pan number	Δt (min)	Sealing rate	Fuel mass (kg)
A	A0	1	–	No sealing	4
	A1		1	S_{u1}	
	A2		2	S_{u2}	
	A3		3	S_{u3}	
B	B0	2	–	No sealing	8
	B1		1	S_{u1}	
	B2		2	S_{u2}	
	B3		3	S_{u3}	
C	C0	3	–	No sealing	12
	C1		1	S_{u1}	
	C2		2	S_{u2}	
	C3		3	S_{u3}	

2.4 Fire Source

Industrial methanol was chosen as fuel for pool fires in the experiment with the purity of 99.9% and the calorific value of 19.8 MJ/kg. The design quality of single pan is 4 kg, which is 2916 kg methanol for full scale. The methanol was placed in seamless welded pan, which is of 0.6 m × 0.3 m × 0.1 m in size. Fuel pan is located in the horizontally middle of the tunnel and is distributed symmetrically in longitudinal direction. Three kinds of fire sizes are calculated based on the fuel mass loss measured in the experiments with HRRs of 66.8, 200.5, and 509.2 kW. Using the scaling law of Eq. (2), the corresponding HRRs for full scales are 16.2, 48.7, and 123.7 MW, which are designed for real fire scenarios of a minivan, lorries, and HGVs, separately [23]. It needs to point out that the combustion efficiency is not considered here, which may cause the calculation results to be larger than the actual values, especially for multiple fuel pans. But, the results could still reflect the combustion behaviors of different fire sizes to some degree.

3 Results and Discussion

3.1 Mass Loss Rate

Figure 4 shows the mass loss rates of all cases. For one pan in Fig. 4a, the MLRs firstly increase fast to the maximum value and then maintain a steady burning stage, after which the MLRs start to drop. It is noticeable that the steady stage is obviously longer as the sealing rate decreases, meaning that the MLRs start to drop later. The trends in Fig. 4a can be explained below. The fire growth rate is fast at the early stage as the flame expands to the full surface of the liquid fuel at a very short time.
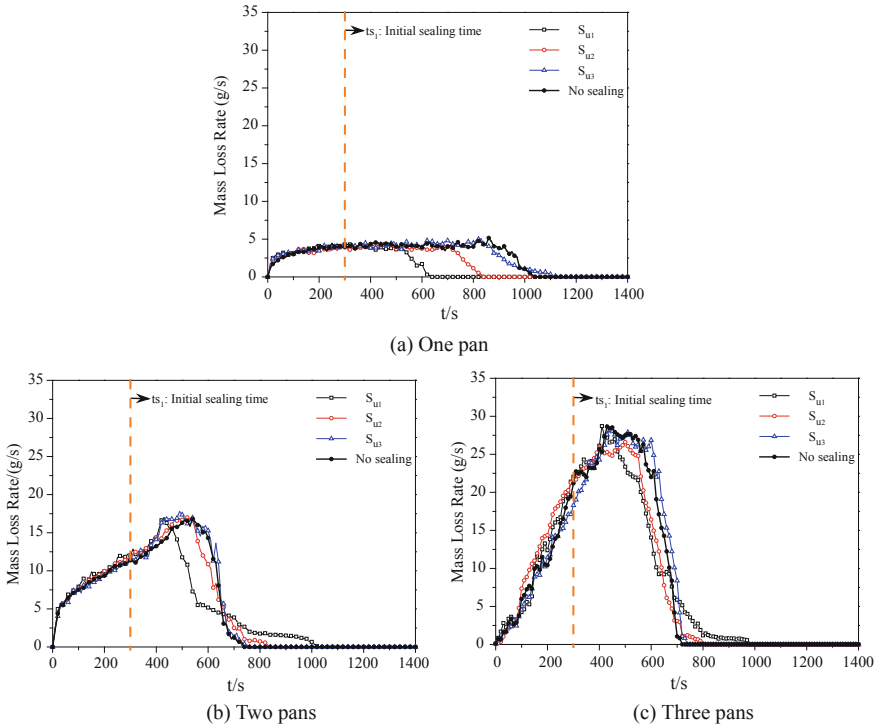
Fig. 4 Mass loss rate versus time

As the temperature rises, the MLRs rise and reach to the maximum, during which the fuel area is considered to be constant. Meanwhile, the oxygen is enough for the fuel burning before the sealing ratio of 100%, thus the MLRs are able to obtain a steady stage. It is found that there is a portion of fuel being unburned at sealing rates of S_{u1} and S_{u2} from the experiment results, indicating that terminates prematurely. This is because the sealing ratios reach 100% faster at sealing rates of S_{u1} and S_{u2}, thus the supply of oxygen is insufficient in combustion, causing the fire in tunnel to be extinguished beforehand. What's more, the time of fire extinction is earlier as the sealing rate increases, and the quality of remaining fuel is larger.

As the fire size enlarges to two and three pans, the MLRs are larger and increase faster compared with the cases of one pan, and there is no apparent stable period as seen from Fig. 4b, c. The reason is that the temperature is higher and the fire growth rate is faster for larger fire size due to higher temperature and more heat feedback from the tunnel walls. It can be observed that the peak MLRs differ very little with the sealing rate for the same fire size. Whereas, the MLRs start to drop earlier as the sealing rate increases, which are similar to the cases of one pan.

3.2   Temperature at Tunnel Ceiling

Figure 5 gives the evolution of the temperature rise at the center of the tunnel ceiling. The average maximum temperature at the tunnel center ceiling is around 700 °C for cases of one pan, 900 °C for cases of two pans, and 930 °C for cases of three pans. It indicates that the average maximum temperature at the tunnel center ceiling increases with the increase of the fire size.

It is noticeable from Fig. 5 that for the same fire size, the time at which the ceiling temperature in tunnel turns to decrease becomes earlier with the increase of sealing rate. Since the combustion inside tunnel will be converted from fuel controlled combustion to ventilated controlled combustion, the sealing ratio grows to a certain extent in the process of STATF. And further sealing will extinct the combustion due to oxygen deficit. The tunnel entrances are sealed more quickly at a faster sealing rate, which reduces the total inflow of fresh air, and the combustion is strongly inhibited. To illustrate with examples of three pans, the time when ceiling temperature at the tunnel center decreases significantly at sealing rate of S_{u1} is at around 420 s, the corresponding sealing ratio is 75%. At sealing rates of S_{u2} and S_{u3}, the corresponding sealing ratios are 50 and 25% at about 420 s. It indicates that a faster sealing rate has
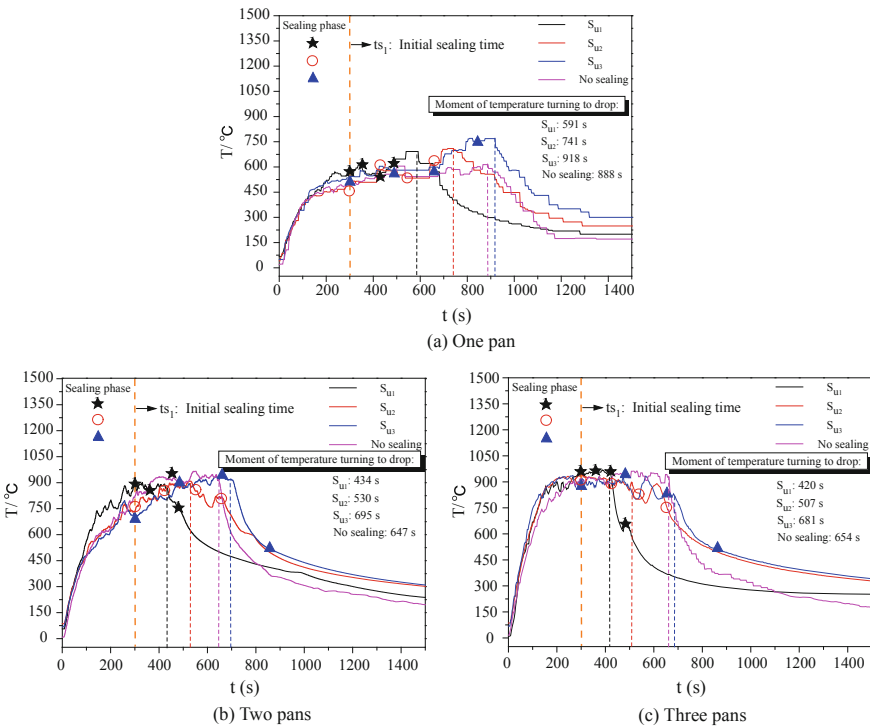
Fig. 5   Ceiling temperature at the center of the tunnel

a stronger inhibitory effect on the combustion by rapidly increasing the sealing ratio, resulting in an earlier decrease in temperature. Nevertheless, at a relatively slower sealing rate, the interval time of sealing becomes longer and the sealing ratio grows slower. Therefore, the combustion is relatively less suppressed and the time of the ceiling temperature turning to drop is delayed. The result shows that a faster sealing rate can effectively expedite the temperature turning to drop inside the tunnel for the same fire size, which plays an important role in raising extinguishment efficiency.

The general temperature rise of the tunnel fire occurred within 2–10 min after the fire. It can be assumed that extinguishing tunnel fires within 10 min after the fire is vital. In other words, it is a significant firefighting strategy purpose for tunnel fires to lower the temperature as soon as possible. For this reason, using the temperature at tunnel center ceiling as a typical representative of the tunnel temperature, the definition of sealing efficiency λ is as below:

$$\lambda = \frac{t_{nd} - t_d}{t_{nd} - ts_1} \tag{4}$$

where t_{nd} (Unit: s) is the time of the ceiling temperature in tunnel center turning to drop on the conditions of no sealing; t_d (Unit: s) represents the time of the ceiling temperature in tunnel center turning to drop on the conditions of sealing for different cases. As mentioned above, ts_1 is 300 s.

Figure 6 shows the relationship between sealing efficiency and sealing rate. It can be observed that the sealing efficiency decreases with the decrease of sealing rate for the same fire size. At sealing rate of S_{u1} and S_{u2}, the sealing efficiency is positive. It indicates that the time of the ceiling temperature in the tunnel center turning to drop is earlier than the condition of no sealing. Furthermore, with the increase of sealing rate, the sealing efficiency reaches to higher. Nevertheless, when the sealing rate decreases to S_{u3}, the sealing efficiency minimizes to minus. That is, the time of the ceiling temperature in the tunnel center turning to drop is later than that of no

Fig. 6 Sealing efficiency versus sealing rate
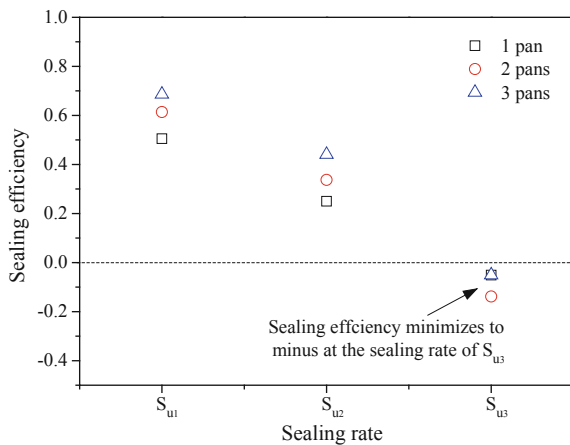
sealing. This result shows that it produces a negative feedback effect on temperature attenuation in the tunnel when the sealing rate decreases to a certain extent. Besides, when the sealing rate decreases to S_{u3}, the sealing efficiency of all the cases has little difference. There may exist the critical sealing rate that makes the sealing efficiency to be zero for each case, which is not obvious in the present experiments and needs to be further studied.

3.3 Temperature Distribution at Tunnel Entrance

In the course of the experiment, the fire overflow appeared symmetrically at two tunnel entrances caused our attention. So the cloud pictures of temperature distribution at one of the tunnel entrance at different sealing rates were made, selecting the temperature field near the tunnel entrance at 10 min after the ignition for the contrast, as shown in Fig. 7.

It can be seen from Fig. 7 that the scale of the high-temperature smoke area (temperature higher than 100 °C) at tunnel entrance increases obviously as the fire size enlarges owing to the increase of the intensity of fire in tunnel. In addition, at 10 min, the area of the high-temperature smoke at the tunnel entrance decreases with the increase of the sealing rate. Particularly, for the conditions of A1 (one pan, the sealing rate of S_{u1}) and B1 (two pans, the sealing rate of S_{u1}), the high-temperature smoke outside tunnel entrance basically disappeared, indicating that the increase in sealing rate can reduce the existence duration of the high-temperature smoke at tunnel entrance. It is helpful for reducing the threat of the high-temperature smoke on the rescuers.

The angle between the edge of high-temperature smoke area and the vertical axis of the tunnel entrance is θ (as shown in B1), which can reflect the threat degree of the high-temperature smoke at a certain extent. The larger the θ is, the greater the range of the high-temperature smoke is, the greater the threat on the rescuers is, and on the contrary, the smaller the threat is. The results have been shown in Fig. 8. It can be seen that θ increases gradually with the increase of fire size at the same sealing rate. Further, θ increases gradually as the sealing rate decreases for the same fire size, indicating that the degree of threat becomes more serious.

3.4 Radiation Heat at Tunnel Entrance

Figure 9 shows the radiation heat measured at three testing points mounted 1 m away from the left opening for cases of two pans and three pans at sealing rates of S_{u1} and S_{u3} selected.

During the burning phase, the radiation heat of measuring point 2 corresponding to about three-quarters height of the tunnel is the largest, while that of the measuring point 3 at the height of tunnel ceiling comes second and the radiation heat of the
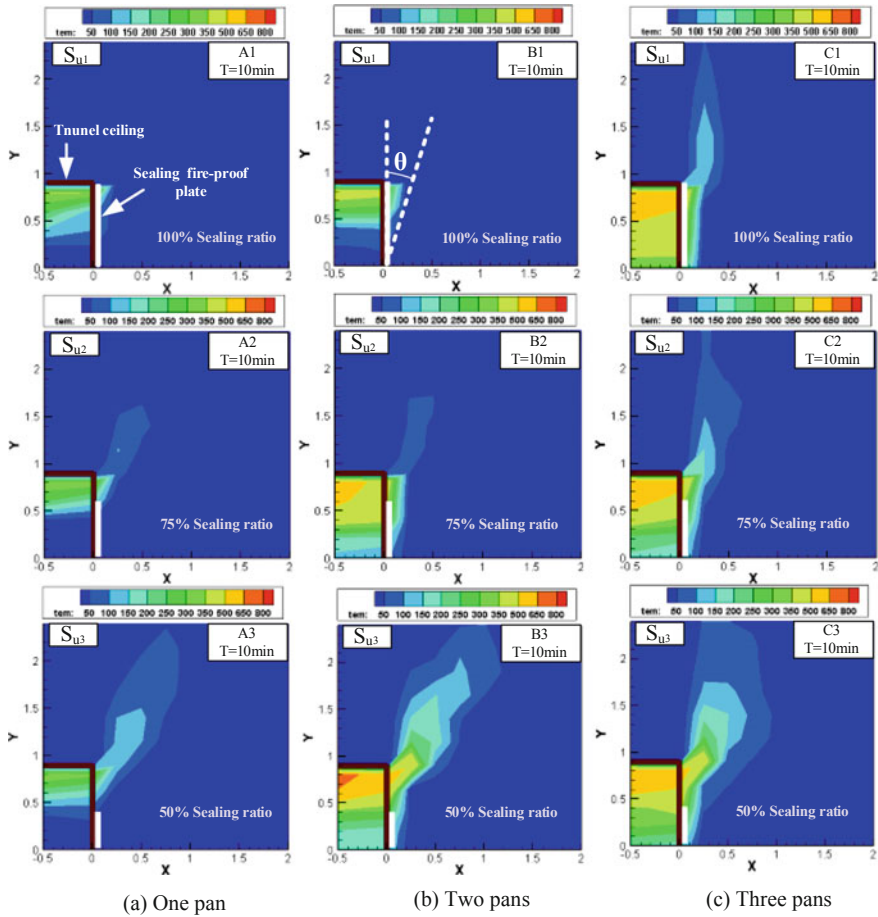
Fig. 7 Cloud chart of temperature distribution near the tunnel entrance (Unit: °C)

measuring point 1 close to the tunnel floor is the smallest in Fig. 9. It indicates that the radiation heat of the tunnel center is higher than that of the upper part while the lower part is relatively lower within a certain distance from the tunnel entrance. In Fig. 9a, b, the maximum radiation heat is about 820, 880, 1790, and 1820 W/m^2, respectively for B1 (two pans, the sealing rate of S_{u1}), B3 (two pans, the sealing rate of S_{u3}), C1 (three pans, the sealing rate of S_{u1}), and C3 (three pans, the sealing rate of S_{u3}). It demonstrates that the maximum radiation heat at sealing rate of S_{u1} is lower than that at sealing rate of S_{u3}. Moreover, the existence time of the radiation heat near the tunnel entrance at sealing rate of S_{u3}, about 15 min (for B3 and C3), which is 1 min after the complete sealing, is obviously longer than that at sealing rate of S_{u1}, about 8 min (for B1 and C1), which is just after the complete sealing. Considering the above two factors of maximum radiation heat and its existence time
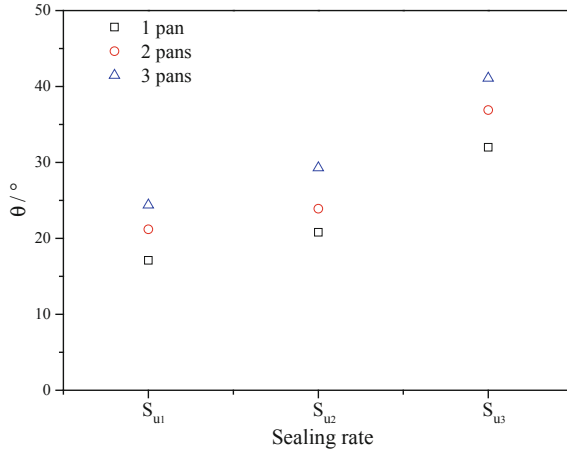
Fig. 8 Angle θ versus sealing rate
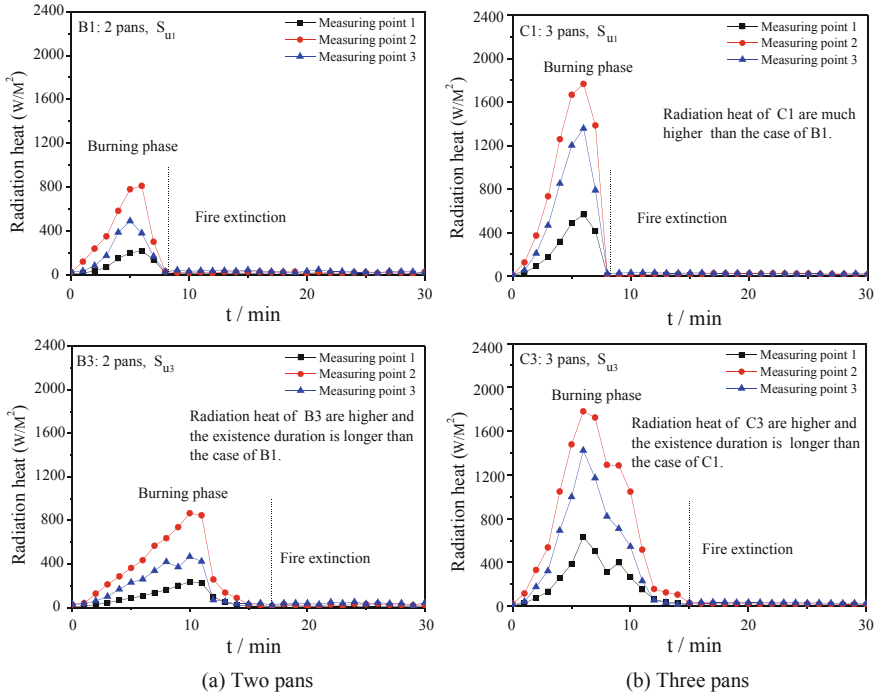
Fig. 9 Radiation heat near tunnel entrance (at sealing rates of S_{u1} and S_{u3})

near the tunnel entrance, the relatively faster sealing rate, which is S_{u1} in the paper, can better reduce the threat of radiation to firefighters.

4   Conclusion

In this paper, the experimental phenomena and results of model tunnel fire have been comparatively analyzed for different fire sizes and sealing rates. And the major conclusions are summarized as follows:

(1) As the sealing rate decreases, the stable period of MLRs stays longer for cases of one pan. While for cases of two and three pans, there is no obvious steady stage. Besides, the moments of MLR turning to drop are gradually earlier with the increase of sealing rate for all cases.

(2) For the same fire size, the time of ceiling temperature turning to drop in tunnel gets earlier with the increase of sealing rate, benefitting the extinguishment efficiency and the tunnel structure. Besides, the sealing efficiency declines with the decrease of sealing rate. Particularly, at sealing rate of S_{u3}, the sealing efficiency minimizes to minus, indicating that it produces a negative feedback effect on temperature attenuation in the tunnel when the sealing rate decreases to a certain extent.

(3) With the decrease of sealing rate, the high-temperature smoke area at the tunnel entrance appears longer; the maximum radiation heat is higher and radiation heat exists longer. Considering the above results, a relatively faster sealing rate is considered to have a better effect of reducing the threat of hot smoke and radiation to firefighters. In addition, the scale of the high-temperature smoke area and maximum radiation heat near the tunnel entrance increase obviously with the enlargement of fire size.

The investigation emphasis of this paper is focused on the variation of temperature field inside the tunnel and near the tunnel entrance. Based on this study, the tunnel fire behaviors appear to be apparently affected by the sealing rate; however, the theoretical analyses of experimental results related to sealing rate are relatively insufficient. The experimental study can be still used to provide some references for optimizing actual tunnel fire extinguishing scheme. Further, detailed study of experimental and numerical settings and theory development is needed.

References

1. Zhou, D., Tian, H. Q., Zheng, J. L., & Yan, X. (2015). Smoke movement in a tunnel of a running metro train on fire. *Journal of Central South University, 22,* 208–213.
2. Ingason, H., & Li, Y. Z. (2010). Model scale tunnel fire tests with longitudinal ventilation. *Fire Safety Journal, 45,* 371–384.
3. Li, Y. Z., & Ingason, H. (2012). The maximum ceiling gas temperature in a large tunnel fire. *Fire Safety Journal, 48,* 38–48.
4. Li, Y. Z., Lei, B., & Ingason, H. (2011). The maximum temperature of buoyancy-driven smoke flow beneath the ceiling in tunnel fires. *Fire Safety Journal, 46,* 204–210.
5. Kashef, A., Yuan, Z. Y., & Lei, B. (2013). Ceiling temperature distribution and smoke diffusion in tunnel fires with natural ventilation. *Fire Safety Journal, 62,* 249–255.
6. Yuan, Z. Y., Lei, B., & Kashef, A. (2013). Experimental and theoretical study for tunnel fires with natural ventilation. *Fire Technology, 51,* 691–706.
7. Ji, J., Fan, C. G., Zhong, W., Shen, X. B., & Sun, J. H. (2012). Experimental investigation on influence of different transverse fire locations on maximum smoke temperature under the tunnel ceiling. *International Journal of Heat and Mass Transfer, 55,* 4817–4826.
8. Fan, C. G., Ji, J., Gao, Z. H., & Sun, J. H. (2013). Experimental study on transverse smoke temperature distribution in road tunnel fires. *Tunnelling and Underground Space Technology, 37,* 89–95.
9. Ji, J., Wan, H. X., Gao, Z. H., Fu, Y. Y., Sun, J. H., Zhang, Y. M., et al. (2016). Experimental study on flame merging behaviors from two pool fires along the longitudinal centerline of model tunnel with natural ventilation. *Combustion and Flame, 173,* 307–318.
10. Wan, H. X., Gao, Z. H., Ji, J., Li, K. Y., Sun, J. H., & Zhang, Y. M. (2017). Experimental study on ceiling gas temperature and flame performances of two buoyancy-controlled propane burners located in a tunnel. *Applied Energy, 185,* 573–581.
11. Roh, J. S., Yang, S. S., Ryou, H. S., Yoon, M. O., & Jeong, Y. T. (2008). An experimental study on the effect of ventilation velocity on burning rate in tunnel fires—heptane pool fire case. *Building and Environment, 43,* 1225–1231.
12. Li, L. M., Cheng, X. D., Cui, Y., Li, S., & Zhang, H. P. (2012). Effect of blockage ratio on critical velocity in tunnel fires. *Journal of Fire Sciences, 30,* 413–427.
13. Li, L. M., Cheng, X. D., Cui, Y., Dong, W. H., & Mei, Z. B. (2013). Effect of blockage ratio on the maximum temperature under the ceiling in tunnel fires. *Journal of Fire Sciences, 31,* 245–257.
14. Tang, W., Hu, L. H., & Chen, L. F. (2013). Effect of blockage-fire distance on buoyancy driven back-layering length and critical velocity in a tunnel: an experimental investigation and global correlations. *Applied Thermal Engineering, 60,* 7–14.
15. Gannouni, S., & Maad, R. B. (2015). Numerical study of the effect of blockage on critical velocity and backlayering length in longitudinally ventilated tunnel fires. *Tunnelling and Underground Space Technology, 48,* 147–155.
16. Lee, Y. P., & Tsai, K. C. (2012). Effect of vehicular blockage on critical ventilation velocity and tunnel fire behavior in longitudinally ventilated tunnels. *Fire Safety Journal, 53,* 35–42.
17. Shafee, S., & Yozgatligil, A. (2018). An analysis of tunnel fire characteristics under the effects of vehicular blockage and tunnel inclination. *Tunnelling and Underground Space Technology, 79,* 274–285.
18. Meng, N., Liu, X. M., Li, X., & Liu, B. B. (2018). Effect of blockage ratio on backlayering length of thermal smoke flow in a longitudinally ventilated tunnel. *Applied Thermal Engineering, 132,* 1–7.
19. Chen, C. K., Zhu, C. X., Liu, X. Y., & Yu, N. H. (2016). Experimental investigation on the effect of asymmetrical sealing on tunnel fire behavior. *International Journal of Heat and Mass Transfer, 92,* 55–65.
20. Chen, C. K., Xiao, H., Wang, N. N., Shi, C. L., Zhu, C. X., & Liu, X. Y. (2017). Experimental investigation of pool fire behavior to different tunnel-end ventilation opening areas by sealing. *Tunnelling and Underground Space Technology, 63,* 106–117.

21. Chow, W. K., Gao, Y., Zhao, J. H., Dang, J. F., Chow, C. L., & Miao, L. (2015). Smoke movement in tilted tunnel fires with longitudinal ventilation. *Fire Safety Journal, 75,* 14–22.
22. Zhong, W., Li, Z. Z., Wang, T., Liang, T. S., & Liu, Z. (2015). Experimental study on the influence of different transverse fire locations on the critical longitudinal ventilation velocity in tunnel fires. *Fire Technology, 51,* 1217–1230.
23. Ingason, H., Li, Y. Z., & Lönnermark, A. (2015). *Tunnel fire dynamics*. New York: Springer.

Potential Risks Assessment Method Using the Model Tunnel Associated with Japanese Expressway Tunnel Fires

Masahiro Yokota, Tetsuya Yamazaki, Nobuyoshi Kawabata and Shiori Imai

Abstract A road tunnel is an enclosed space where backlayering of smoke produced by a fire can extend its damage beyond the part exposed to the fire. To realize a worry-free and safe infrastructure, emergency facilities in tunnels must be improved. Since it is difficult to uniformly apply improvement projects to all tunnels in the face of limited project budgets, it is necessary to prioritize projects to perform improvements systematically. As a method of efficiently conducting these projects, a statistical risk calculation method based on fire accident statistics obtained by defining individual tunnel fire accident risk as "(probability of occurrence of fire in a tunnel) × (loss)," has been proposed. This permits ranking the risk, allowing to set risk improvement project priorities. But to clarify risk improvement effects, medium to long-term observations are necessary. For human loss, which is the loss with the greatest impact on risk, a method of calculating change of potential risk by fire simulation and evacuation simulation has been proposed. But in order to calculate the potential risk of many tunnels, vast computing resources and long periods of time are needed. Therefore, another method was studied, using the results from a model tunnel, and performing evaluations linking fire simulations with evacuation simulations under a variety of conditions as a database. This paper introduces a potential risk calculation method suitable for individual tunnels based on the results of multiple regression analysis performed using these data.

Keywords EU directive · Risk analysis · Statistical risks · Potential risks · Fire simulation · Evacuation simulation · Coupled evaluation · Multiple regression analysis

M. Yokota (✉) · S. Imai
Central Nippon Highway Engineering Tokyo Co., Ltd., 1-23-7 Nishishinjuku, Shinjuku-Ku, Tokyo 160-0023, Japan
e-mail: m.yokota.aa@c-nexco-het.jp

T. Yamazaki
Central Nippon Expressway Co., Ltd., 1-2-14 Ichiikura, Yokkaichi City, Mie Pref 510-0832, Japan

N. Kawabata
Kanazawa University, Kakuma-Cho, Kanazawa City, Ishikawa Pref 920-1192, Japan

Nomenclature

R	Risk
P	Probability
P_t	Probability of tunnel fire (cases/year)
P_f	Probability of tunnel fire due to traffic accident (cases/year)
P_b	Probability of tunnel fire due to vehicle breakdown (cases/year)
L	Tunnel length (m)
H_v	Large vehicle mixing rate (vehicles/day)
E	Portal elevation (m)
S	Difference from the nationwide expressway tunnel average traffic speed(km/h)
F_T	Traffic pattern factor (Two ways: 1, One way: 0)
L_D	Death loss amount (yen/person)
L_d	Injury loss amount (yen/person)
I	Impact (Loss)
HRR	Heat release rate (MW)
T_e	Evacuation start time (s)
D_e	Distance between emergency exits (m)
S_e	Evacuation walking speed (m/s)
i	Inclination (%)
W_s	Wind speed (m/s)
E_x	Number of exits
N	Number of residual evacuees
N_o	Number of residual evacuees for object tunnel
T_o	Traffic volume of object tunnel
T_m	Traffic volume of model tunnel
n_c	Conversion factor for number of residual evacuees

1 Introduction

1.1 Background to the Research

In Europe, beginning with the Mont Blanc Tunnel fire accident of 1999, a series of large fire accidents occurred, and in the European Community which viewed this situation as a serious challenge, industry, governments, and academia in many countries conducted interdisciplinary research and development to improve safety during tunnel fires, resulting in the issuing of EU Directive 2004/54/EC concerning emergency facilities in road tunnels on the major trunk roads of the Trans-European Road Network (TERN). This EU Directive obligates EU member states to carry out
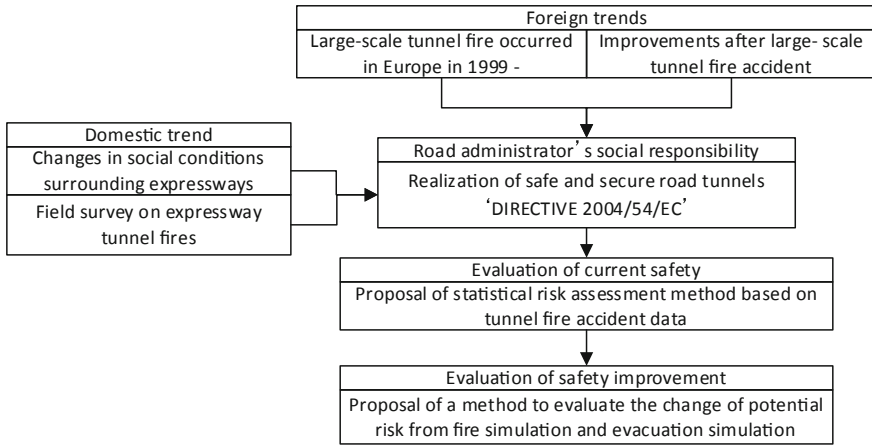
Fig. 1 Expressway tunnel fire risk evaluation framework in Japan

relative safety evaluations, by performing risk analysis of road tunnels on TERN, and to execute improvement projects to enhance safety at regular intervals [1].

In Japan, road tunnel emergency facility installation standards obligate the designation of a tunnel grade based on traffic volume and length, and installation of emergency facilities according to the grade. Fortunately, no large-scale fire accident has occurred since the Nihonzaka Tunnel fire accident of 1979. But the increase in the number of two-way tunnels in outlying regions, and the construction of large cross section tunnels and urban expressway tunnels, has transformed the tunnel environment. Thus, in a previous report, assuming that "relative safety evaluations" must be performed, and effective safety improvement projects with limited budgets must be prioritized in order to guarantee the safety of tunnel users; research was conducted to find a way to perform risk analysis to evaluate and compare the safety of individual tunnels [2]. Figure 1 shows the expressway tunnel fire risk evaluation framework in Japan.

1.2 Risk Evaluation Method

The risk of a road tunnel fire accident is a combination of the general frequency of damage (probability) and the degree of damage (impact). The expressway tunnel fire accident risk considered by this research is obtained by Eq. (1) as shown below [3].

$$R = P \times I = f(P, I) \tag{1}$$

Fig. 2 Tunnel fire accident occurrence frequency procedure
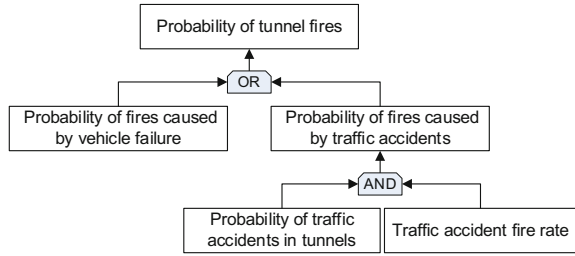
(1) *Statistical risk evaluation: evaluation of current safety*

A previous report proposed a statistical risk evaluation method by statistically analyzing fire accident data for expressway tunnels, and obtaining the probability of a fire accident and the loss accompanying a fire accident in an individual tunnel. Data used for statistical processing was for a total of 283 expressway tunnel fire accidents that occurred nationwide during the 23 year period from 1989 to 2012.

The tunnel fire accident occurrence probability P is, as shown in Fig. 2, broadly categorized as that due to vehicle failure, and that due to traffic accidents. It was proposed to evaluate the degree of impact of tunnel geometric conditions and traffic condition parameters by multiple regression analysis and a limited calculation equation.

For the tunnel fire accident loss I, 283 cases of expressway tunnel fire accident data were analyzed. The human loss incurred by death or injury, material loss caused by fire damage to vehicles and tunnels, and social loss resulting from closure of roads to traffic which results from fire accidents, were classified and converted to monetary values. P in Eq. (1) represents the frequency or fire accidents in road tunnels, and as shown in Fig. 2, it is classified as that due to vehicle failure and that due to traffic accidents. Multiple regression analyses with fires due to accidents as the response variable, and parameters considered to be causes of fire as explanatory variables, were done to obtain a model equation to predict fire occurrence frequency.

$$P_t = P_b + P_f \tag{2}$$

$$P_b = 1.86 \times 10^{-5} \times L + 2.68 \times 10^{-6} \times H_V + 1.62 \times 10^{-4} \times E - 0.00103 \tag{3}$$

$$P_f = \left(1.00 \times 10^{-3} \times L + 6.189 \times 10^{-5} \times T_0 + 2.05 \times 10^{-2} \times S_{-0.7898} \times F_{T-0.845}\right) \times 0.0020 \tag{4}$$

The term on the right-hand side of Eq. (4), 0.0020 is the fire occurrence rate of traffic accidents.

The human loss which has great impact is deaths and injuries, and the tunnel fire accident database was analyzed to obtain the following relational Eq. (5).

$$I_H = I_{Hu} + I_{Hf} \tag{5}$$

$$\text{Fire accident death loss (yen/case)} \, I_{\text{Hu}} = \frac{0.64 \times P_{\text{f}}}{P_{\text{t}}} \times L_{\text{D}} \qquad (6)$$

$$\text{Fire accident injury loss (yen/case)} \, I_{\text{Hf}} = \frac{0.03 \times P_{\text{b}} + 1.01 \times P_{\text{f}}}{P_{\text{t}}} \times L_{\text{d}} \qquad (7)$$

This relationship reveals that for both death loss and injury loss, the frequency of fire accidents P_{f} is dominant. Based on these results, it is now possible to rank the risk based on statistical risk results unique to each tunnel as shown in Fig. 3.

(2) *Potential risk evaluation: Evaluation of safety improvement*

Statistical risk evaluation is the relative risk at the time of evaluation based on fire accident data. Therefore, in a case where a fire has actually occurred in a given tunnel, it is impossible to define the scale of the fire, scale of damage, and how effectively countermeasures would improve safety. Hence, as a trial, a method of evaluating human loss, which has the greatest impact on loss I, it was proposed to consider the results of a fire simulation and evacuation simulation as the potential risk. The fire simulator used was fireless, a three-dimensional LES Smagorinsky model which has been confirmed to provide adequate reproduction capability through quantitative comparison of model tunnel and real road tunnel fire test data, and which has been used as a standard evaluation model for road tunnel fires in Japan [4]. The fire simulation uses fire scale and fire occurrence rate based on type of burning vehicle and combustion time in data for 283 past fire accidents (see Table 1).
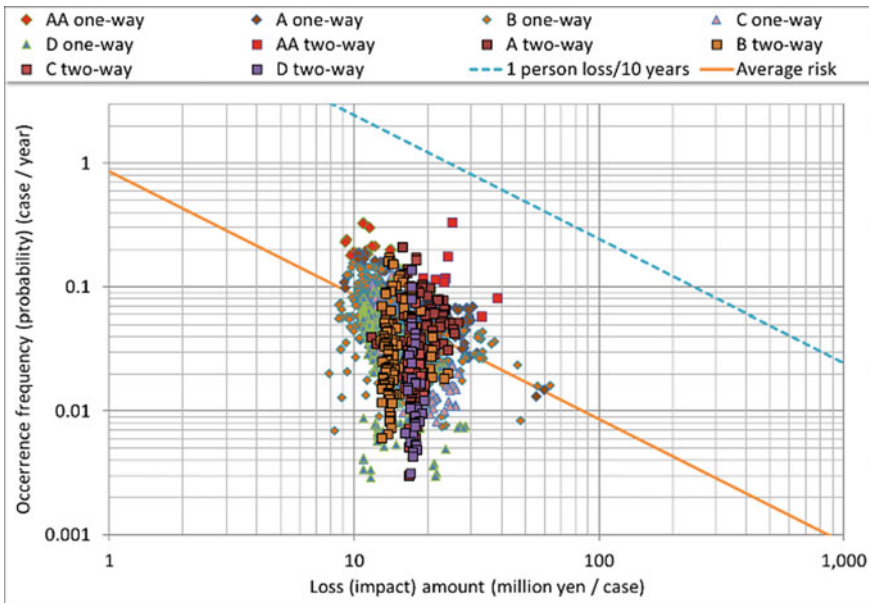
Fig. 3 Statistical risk matrix of expressway tunnels

Table 1 Occurrence rate of estimated fire scale

Fire scale (MW)	Total (%)	1-way traffic (%)	2-way traffic (%)
0	21.3	19.0	36.8
5	54.0	54.2	52.6
10	19.9	21.3	10.5
20	4.1	4.7	0.0
30	0.7	0.8	0.0

A fire simulation reflecting geometric conditions and traffic conditions (stopped vehicles) in the tunnel evaluated for each fire scale was done, obtaining environmental data that changes continually (location and concentration distribution of smoke), and calculating smoke concentration and its spread after fire (degree of risk map). Figure 4 shows the expansion of smoke accompanying a 30 MW class fire in the center of Tunnel A that is 1,000 m long with a longitudinal inclination of 3%.

For the following evacuation simulation, the state of stopped vehicles during a fire (arrangement of victims), evacuation distance (to emergency exit or portal), evacuation walking speed, and the evacuation actions shown in Fig. 5 (trigger that starts action based on type of emergency facility) was set. The evacuation limit of victims was being enveloped in smoke, and the condition for stopping action was assumed to be $Cs \geq 0.4$ m^{-1} at a height of 1.5 m from the road surface.

The evacuation actions of victims found by the evacuation simulation are associated as shown in Figs. 6 and 7 with the environmental change/risk degree map obtained by the fire simulation described above. The horizontal axis in the figure
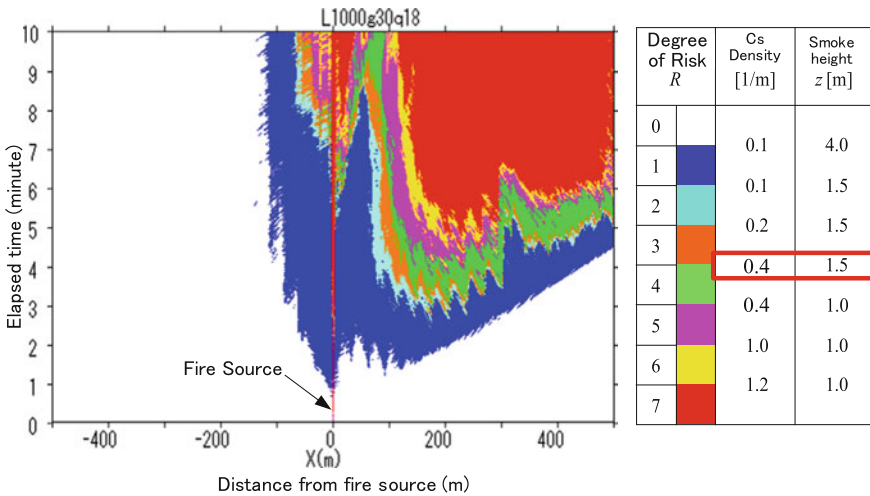
Fig. 4 Example of spread of smoke after a fire (degree of risk map, wind speed: 0 m/s, inclination 3%, 30 MW)
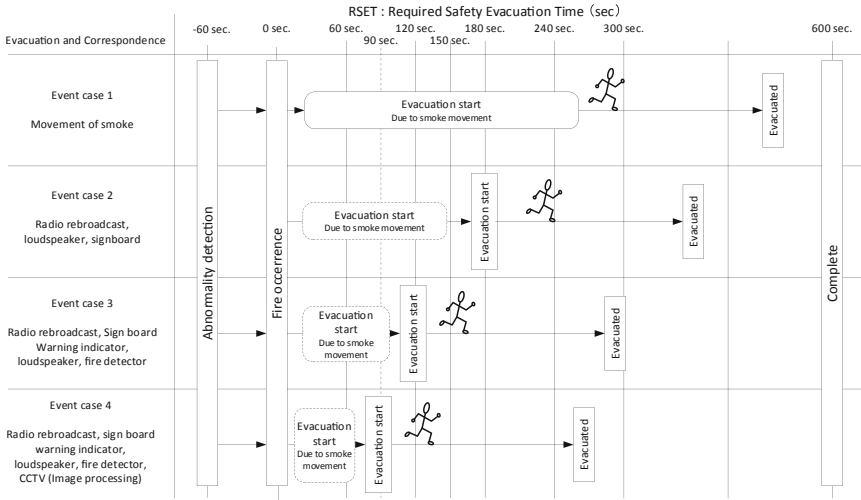
Fig. 5 Fire event change by activity start condition
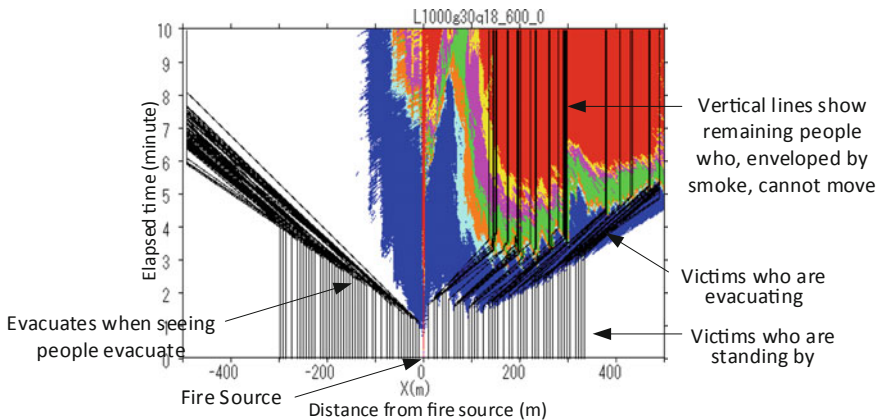
Fig. 6 Coupled evaluation sample cases (see smoke and evacuate)

shows the location inside the tunnel, and the vertical axis shows the passage of time. The dark lines show the locations of the victims, and if evacuation is started by the action start trigger, it changes from a vertical to an inclined line, and people who have reached the evacuation limit (degree of risk 4: green part) stop moving to become residual evacuees (dead or injured people). The number of these people is totaled to calculate the human loss.

Figure 8 shows an example of the change of statistical risk and potential risk (combination of safety improvement measures) in Tunnel A, which does not have
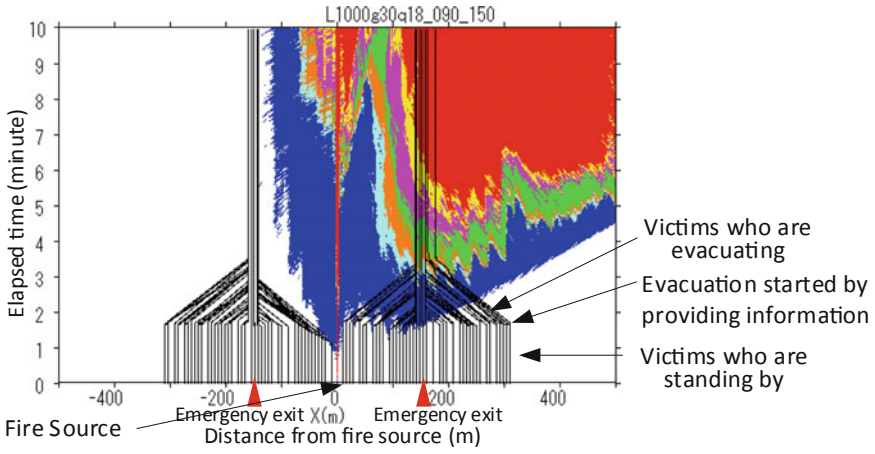
Fig. 7 Coupled evaluation sample case (emergency exits at 350 m intervals)
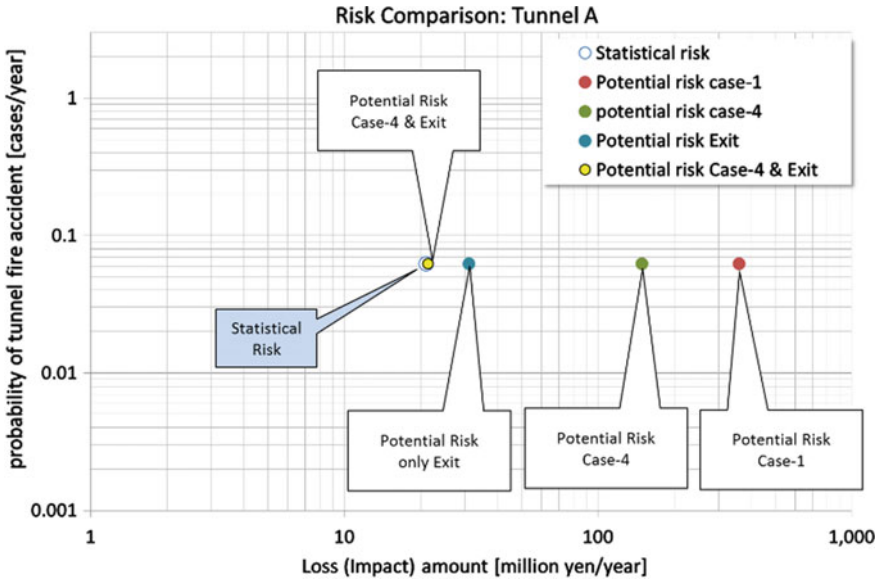
Fig. 8 Tunnel A: safety measures and changes in potential risk

any emergency exits. It reveals that potential risk is higher than statistical risk, but that installing an emergency exit sharply lowers the risk.

1.3 Challenges to Risk Evaluation

As stated above, in a past report, it was possible to clarify the distribution of statistical risk (ranking) for all expressway tunnels in Japan, and of potential risk and change of risk by taking safety improvement measures in "Tunnel A" which was abstracted. But there are about 1,700 tunnels on expressways in Japan, and conditions differ according to geometric conditions, state of traffic, location of fires, scale of fires, and wind speed, etc., so these must be set for each evaluation. Therefore, in order to make a detailed evaluation of the potential risk of an individual tunnel, it is necessary to have vast computing resources and a labor force to process the data.

2 Evaluating Potential Risk Using a Model Tunnel

Tunnel fire safety evaluations are done by setting fire scale, evacuation conditions, etc., for each tunnel. The evaluation parameters are individually set. The results of such evaluations and experiments lead to the following outline of the relationships of the set parameters with evaluation results.

- The in-tunnel atmosphere is proportional to the fire scale (scale of damage also proportional to fire scale)
- Speed of motion of the smoke is inversely proportional to length (the shorter the tunnel, the faster the deterioration of the in-tunnel environment)
- Damage is proportional to vehicles stopped in the tunnel (damage proportional to number of human victims)
- If there are vehicles stopped in the tunnel, smoke descends quickly and near the fire source.
- If wind speed in the tunnel increases, the smoke spreads and descends, harming the environment.
- Damage is proportional to the evacuation distance.
- Damage is proportional to action start time after the fire occurrence.

Based on the above findings, a concept of simplification/generalization of potential risk evaluation is presented below.

- The fire simulation is the result of calculation based on engineering theory, and the parameters which are set and calculation results can be represented by a relational equation (there are accuracy problems, but …)
- The shorter the tunnel, and the more cars stopped, the more rapidly the smoke moves and the sooner the environment deteriorates, so the evacuation risk is on the danger side (direction which overestimates risk).

- The evacuation simulation includes nonlinear elements such as action start time (trigger), walking speed, layout of emergency exits, and so on.

Based on this data, potential risk is evaluated using a model tunnel with the average length and cross-sectional shape of expressway tunnels in Japan. The evaluation obtains fire simulation data which combines fire scale, longitudinal inclination, wind speed in the tunnel and stopped cars, which are presumed to greatly impact the change of environment in the tunnel after the start of a fire. The residual evacuees are obtained based on the results of an evaluation with an evacuation simulation that combines in-tunnel environmental data obtained from the results with safety improvement countermeasures. The combined parameters for the fire and evacuation simulations and the number of residual evacuees thus obtained were stored in a database, and a method of rationalizing the calculation of human loss which should be applied to the tunnel with various traffic volumes was studied.

2.1 Setting the Model Tunnel

Figure 9 shows the model tunnel. It is a two-way traffic tunnel with a length of 1,000 m and cross-sectional area of 61 m^2. Its traffic volume when the fire started was 2,500 vehicles/hour, which is said to be the two-way traffic volume, and its large vehicle rate was the national average of 25%.

(Fixed parameter)
- Traffic method: Two way
- Length: 1,000 meters
- Cross-section area: 61 m^2
- Traffic volume: 2,500 veh./hour
- Large vehicle rate: 25 %
- Fire point: middle of longitudinal direction

(Variable parameter)
- Longitudinal inclination: 0, 0.5, 1.0, 1.5, 2.0, 3.0 %
- Fire scale: 5, 10, 20, 30 MW (50 MW)
- Wind speed: 0 m/s (2.5 m/s)
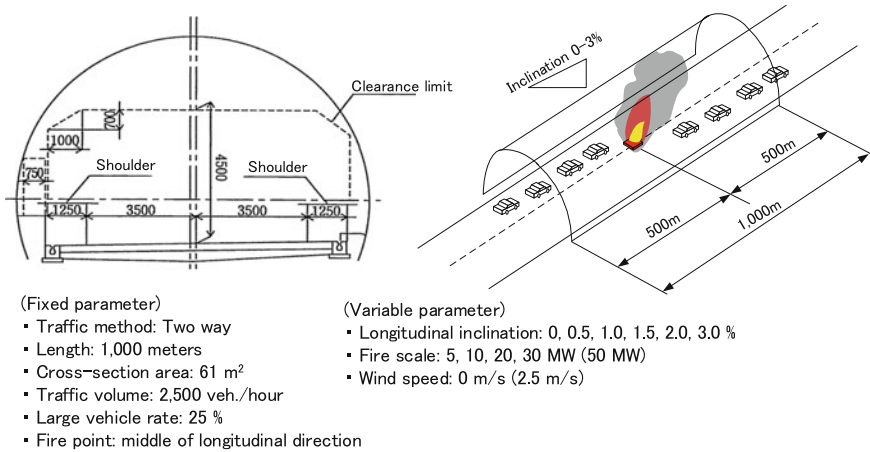
Fig. 9 Model tunnel

2.2   Evaluation Cases

(1) *Fire simulation*

The heat release rate (HRR) change used for this fire simulation was, in this study, the secondary curve (t^2 model) which was used for the fire development model, the maximum HRR was reached 420 s after the fire started, 60% of the total HRR was given as the convection heat release rate, and the evaluation time was 10 min. Table 2 shows the fire simulation cases which were attempted.

The fire simulation is used to create and obtain data concerning the location and concentration of smoke which changes constantly inside the tunnel.

(2) *Evacuation simulation*

Regarding the simulator used to evaluate evacuation, as stated above, the action start time conditions, walking speed, and final location are set as conditions given to the victims in the tunnel, and by coupling the smoke data obtained by the fire simulation described in the previous section, the walking/stopping conditions and the number of victims who could not evacuate during the evacuation period (residual evacuees) are calculated.

Action start time conditions of victims in the tunnel were set as the "basic action conditions" for the stage at which smoke at a concentration Cs of 0.1 m^{-1} was 4.0 m from the road surface, i.e., the state when it reached the height of the lighting fixtures in the tunnel, in other words, a case where "they confirm smoke flowing above their heads and start to evacuate" or "evacuate when they see people evacuating." As shown in Fig. 5, the provision of evacuation facilities and the timing at which evacuation information (action start trigger) is provided, is set. The risk evaluation was done by considering the number of people who, during evacuation, were enveloped by smoke before reaching the final evacuation location and had difficulty in evacuating, which is the human loss. Conditions under which people are enveloped by smoke and stop their action so that they remain in the tunnel was considered to be the stage where the Cs concentration reached 0.4 m^{-1} at a height of 1.5 m from the road surface.

Table 2 Fire simulation cases and parameters which were attempted

Fire scale (MW)	Length (m)	Cross-sectional area (m^2)	Inclination (%)	In-tunnel wind speed (m/s)	Evaluation cases
5	1,000	61 m^2	0, 0.5, 1.0, 1.5, 2.0, 3.0	0	6
10					6
20					6
30					6
30			0, 1.5, 3.0	2.5	3
Total					27

Table 3 Average walking speed during evacuation

Item	Fast	Normal	Slow
Walking speed	1.9 m/s	1.6 m/s	1.3 m/s

Next, the walking speed during fire evacuation was confirmed by a walking speed experiment according to the Cs concentration. This study set the walking speeds shown in Table 3 with reference to the research by Seike et al. [5]. Considering the dispersion of ±0.1 m/s regards the walking speed during evacuation, the number of residual evacuees used was the average number in the results of 1,000 evacuation simulations.

Because it is assumed that the final evacuation locations would be the tunnel portal and emergency exits, the evaluation was performed for two cases: no emergency exit and emergency exits installed at equal intervals.

2.3 Results of Coupled Evaluation

In a total of 1,450 cases, evaluation was performed by coupling the time history data for change of the in-tunnel smoke environment obtained by fire simulation using the model tunnel shown in the previous section with the evacuation simulation that varied the evacuation conditions (see Table 4). The database of simulation results in these cases is called the basic database. Table 5 shows the frameworks of numbers of residual evacuees that were obtained based on the smoke concentration and movement in the tunnel accompanying the fire and the results of coupled evaluation of victims who evacuated.

Table 5, Nos. 1–6 show patterns which fire scale was 10 MW and did not give the action start trigger (evacuation actions start when victims see smoke, or they evacuate when they see other people evacuating), and the number of residual evacuees

Table 4 Evaluation cases and parameters according to the evacuation simulation

Fire simulation parameters			Evacuation simulation parameters			Cases
Fire scale (MW)	Inclination (%)	In-tunnel wind speed (m/s)	Evacuation start time (s)	Distance to emergency exit (m)	Walking speed (m/s)	
5	0, 0.5, 1.0, 1.5, 2.0, 3.0	0	90, 120, 150, 180, 600	100, 200, 300, 400, 500	1.3, 1.6, 1.9	325
10						325
20						325
30						475
	0, 1.5, 3.0	2.5			1.3	
Total						1,450

※ 30 MW also includes irregular evaluation data, and the number of cases increases more than for other cases

Table 5 Basic database (framework)

Case No.	Fire scale (MW)	Evacuation start (s)	Distance to emergency exit (m)	Walking speed (m/s)	Inclination (%)	Wind speed (m/s)	Number of residual evacuees
1	10	600	500	1.3	0	0	0
2	10	600	500	1.3	0.5	0	0
3	10	600	500	1.3	1	0	0.075
4	10	600	500	1.3	1.5	0	3.489
5	10	600	500	1.3	2	0	4.698
6	10	600	500	1.3	3	0	7.421
7	30	600	500	1.3	0	0	0.01
8	30	600	500	1.3	0.5	0	3.002
9	30	600	500	1.3	1	0	23.587
10	30	600	500	1.3	1.5	0	25.035
11	30	600	500	1.3	2	0	48.83
12	30	600	500	1.3	3	0	47.525
13	30	600	500	1.3	0	2.5	57.909
14	30	600	500	1.3	1.5	2.5	57.407
15	30	600	500	1.3	3	2.5	57.77
16	30	600	100	1.3	0	2.5	28.475
17	30	600	100	1.3	1.5	2.5	26.452
18	30	600	100	1.3	3	2.5	26.363
19	30	90	100	1.3	0	2.5	25.057
20	30	90	100	1.3	1.5	2.5	23.214
21	30	90	100	1.3	3	2.5	23.96

increases in proportion to the change of inclination in a case where the distance to the emergency exit (tunnel entrance) and walking speed were constant. No. 7–12 shows the change in the number of residual evacuees in a case where the fire scale was 30 MW based on the same conditions, showing that the number of residual evacuees further increases as the scale of the fire expands.

Next, Nos. 13–15 show cases in which a fire scale of 30 MW and evacuation start trigger are not given, the distance to the emergency exit is 500 m, the walking speed is constant, and the in-tunnel wind speed is 2.5 m/s, showing that the number of residual evacuees is greatest regardless of the change of inclination. In contrast, Nos. 16–18 show cases where the distance to the emergency exit was shortened, revealing that the number of residual evacuees was halved. Nos. 19–21 are cases where the distance to the emergency exit was shortened to 100 m and the action start time was shortened to 90 s, but the decline in the number of residual evacuees is small. Its application to other tunnels is considered based on these databases.

3 Method of Application to Different Types of Tunnels

3.1 Creation of a Regression Equation to Calculate the Number of Residual Evacuees

Many parameters were set to perform the fire simulation and the evacuation simulation using the model tunnel, and a regression calculation method with the number of residual evacuees as the response variable and the parameters which were set as explanatory variables are considered for a case where an attempt is made to similarly calculate the number of residual evacuees obtained as a result for another tunnel. In the case of multiple explanatory variables as here, multiple regression analysis applies a variety of statistical methods, but it is assumed that the relationships between the explanatory variables or the suitability of results which are response variables are also unclear. Hence, this study performed multiple regression analysis using Microsoft Excel, which is a general-purpose linear regression model.

- Response variable: number of residual evacuees in a tunnel fire
- Explanatory variables: Fire scale, evacuation start time, distance to emergency exit, walking speed, tunnel inclination, wind speed, etc.

Table 6 shows the results of the multiple regression analysis. It confirms that the multiple determination coefficient R^2, which is the correlation criterion, is 0.737, and the t value exceeded two at all absolute values, while the p-value is lower than 5% for all items, and its correlation is high.

From the results of this multiple regression analysis, the calculation equation for residual evacuees N is as shown below.

$$N = 0.425 \times \text{HRR} + 0.007 \times T_e + 0.024 \times D_e - 5.139 \times S_e$$
$$+ 2.537 \times i + 11.339 \times W_s - 8.923 \tag{8}$$

Based on this result, the number of residual people which represent a high percentage of potential risk can be calculated by the above Eq. (8), and the calculation can be done according to enlargement of the fire scale, geometric structure applied, and emergency facilities that are installed.

3.2 Application to Other Tunnels

(1) Conversion of number of residual evacuees

Based on Eq. (8) above, the number of residual evacuees can be calculated according to fire scale, hypothetical evacuation start time by layout of emergency equipment, distance to the emergency exit, walking speed during evacuation, longitudinal inclination of the tunnel wind speed, and number of emergency exits. The impact of smoke

Table 6 Results of multiple regression analysis

Summary output					
Regression statistics					
Multiple R		0.858			
R square		0.737			
Adjusted R square		0.735			
Standard error		6.593			
Observations		1.450			

Anova

	df	SS	MS	F	Significance F
Regression	6	174,703	29,117	665	0
Residual	1,443	63,202	44		
Total	1,449	237,906			

	Coefficients	Standard error	t Stat	P-value	Lower 95%	Upper 95%
Intercept	−8.923	1.364	−6.542	0.000	−11.599	−6.247
HRR: Heat release rate (MW)	0.425	0.017	24.681	0.000	0.391	0.459
T_e: Evacuation start time (s)	0.007	0.001	7.452	0.000	0.005	0.009
D_e: Distance to emergency exit (m)	0.024	0.001	18.913	0.000	0.021	0.026
S_e: Walking speed (m/s)	−5.139	0.949	−5.417	0.000	−7.000	−3.278
i: Incline (%)	2.537	0.180	14.081	0.000	2.183	2.890
W_s: Wind speed (m/s)	11.339	0.272	41.665	0.000	10.805	11.873

behavior accompanying change in tunnel length was eliminated from the parameters for regression calculation because the model tunnel was short at 1,000 m, and the results for smoke movement speed or smoke descent location, etc., are on the strict side. But, if the tunnel length changes, the number of stopped cars or in other words the number of victims when the fire starts, also changes. In the model tunnel, the traffic volume was set as 2,500 vehicles/h. This is the traffic volume during two-way traffic. The driving speed inside the tunnel was set as 80 km/h, and the large vehicle rate was set at 25% of the national average value. At this time, when a fire that occurs

Table 7 Number of residual evacuees obtained based on fire scale and occurrence rate

Tunnel length (m)	Traffic volume (Vehicles/h)	Time to stop (s)	Number of stopped vehicles			Number of vehicles		Length of stopped vehicle (m)
			Traffic inside tunnel	Entry after fire occurrence	All vehicles	Large	Small	
1,000 (500)	2,500 (1,250)	120	8	42	50	13	37	440

※ The object is a two-way traffic tunnel, and the length and number of vehicles passing through used are the numerals in ()

at the center of a 1,000 m tunnel has stopped the traffic flow, the number of vehicles stopped in the tunnel, the number of victims, and length of the row of vehicles can be calculated as shown in Table 7. The average headway between vehicles when vehicles are stopped 50 m from the fire source is 11.5 m for large vehicles and 6.5 m for small vehicles, and it is predicted that 2 min must pass from the time the fire starts until the flow of vehicle into a tunnel stops.

This result reveals that in the model tunnel, vehicles are stopped on almost the entire line from the fire source to the entrance. Thus, the number of residual evacuees is converted from the percentage of traffic flow in order to evaluate a different tunnel. The conversion factor n_c Eq. (9) is shown below.

$$n_c = T_o / T_m \tag{9}$$

(2) *Varying the potential risk*

Next, as potential risk trial calculation conditions, considering the evacuation start time, distance to the emergency exit, evacuation speed, inclination, and wind speed conditions inside the tunnel to be equal, and tentatively considering the fire scale and occurrence rate obtained from expressway tunnel fire accident statistics shown above in Table 1 to be Case 1, and the fire scale and occurrence rate which revised estimation conditions with a burning car model and combustion time to be Case 2, the number of residual evacuees was calculated as shown in Table 8. The total of the occurrence rates is one for both Case 1 and Case 2.

In the results of the calculation, the total number of residual evacuees in Case 1 was 3.678, but when the fire scale range and occurrence rate were reviewed, the number of residual evacuees increased to 4.672.

Next, the loss (monetary value) was calculated from the total number N of residual evacuees in the tunnel that is evaluated. The loss was obtained by Eq. (10) according to the death rate and injury rate based on tunnel fire accident statistics from a past report [2], and the loss for death and loss for injury caused by traffic accidents announced by the Cabinet Office [6], and the total of these is considered to be the human loss.

Table 8 Number of residual evacuees obtained based on fire scale and occurrence rate

Case	HRR (MW)	T_e (s)	D_e (m)	S_e (m/s)	i (%)	W_s (m/s)	N	Branch rate	Residual evacuees	Total N
1	0	120	350	1.3	3	0	1.247	0.213	0.266	3.678
	0–5	120	350	1.3	3	0	3.372	0.54	1.821	
	5–10	120	350	1.3	3	0	5.497	0.199	1.094	
	10–20	120	350	1.3	3	0	9.747	0.041	0.400	
	20–30	120	350	1.3	3	0	13.997	0.007	0.098	
2	0–5	120	350	1.3	3	0	3.372	0.794	2.677	4.672
	5–10	120	350	1.3	3	0	5.497	0.100	0.548	
	10–20	120	350	1.3	3	0	9.747	0.069	0.670	
	20–30	120	350	1.3	3	0	13.997	0.007	0.096	
	30–40	120	350	1.3	3	0	18.247	0.017	0.314	
	40–50	120	350	1.3	3	0	22.497	0.010	0.232	
	80–90	120	350	1.3	3	0	39.497	0.003	0.136	

$$\text{Value of human loss} = \text{Total } N \times (\text{death rate} \times \text{loss for a death} + \text{injury rate} \times \text{loss for an injury}) \quad (10)$$

Figure 10 shows the flow of these human loss calculations.

These results are limited, but the potential risk of a two-way tunnel longer than 1,000 m and shorter than 3,000 m based on the fixed frequency of fire occurrence is shown in Figs. 11, 12 and 13, which show the results of a trial calculation of risk for a case without countermeasures, a case where a measure to provide evacuation information was taken, and a case where emergency exits were added. The risks to each tunnel are shown by dots on the figure, and the risk threshold values are, while
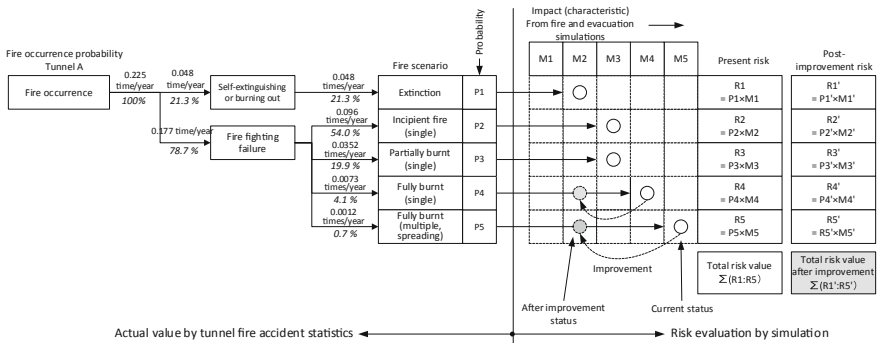
Fig. 10 Image of fire events and of human loss improvement in the evaluated tunnel
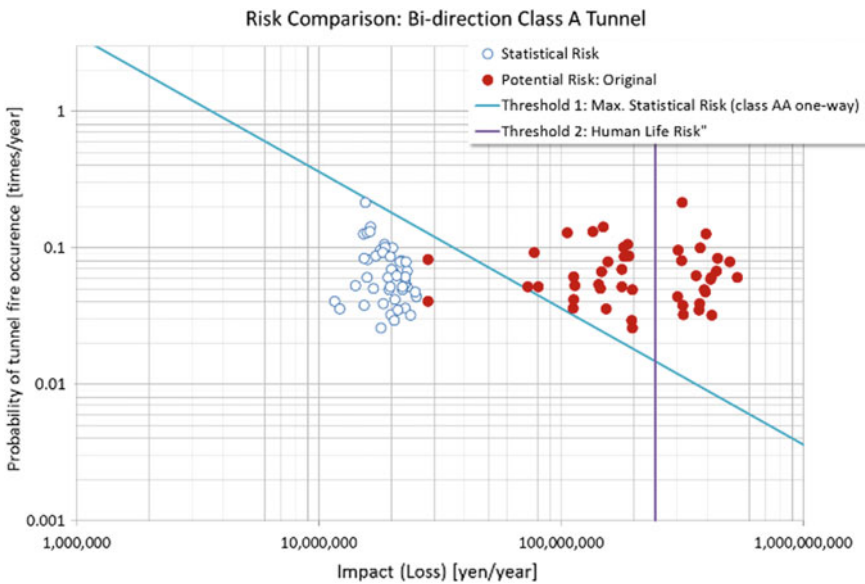
Fig. 11 Present potential risk
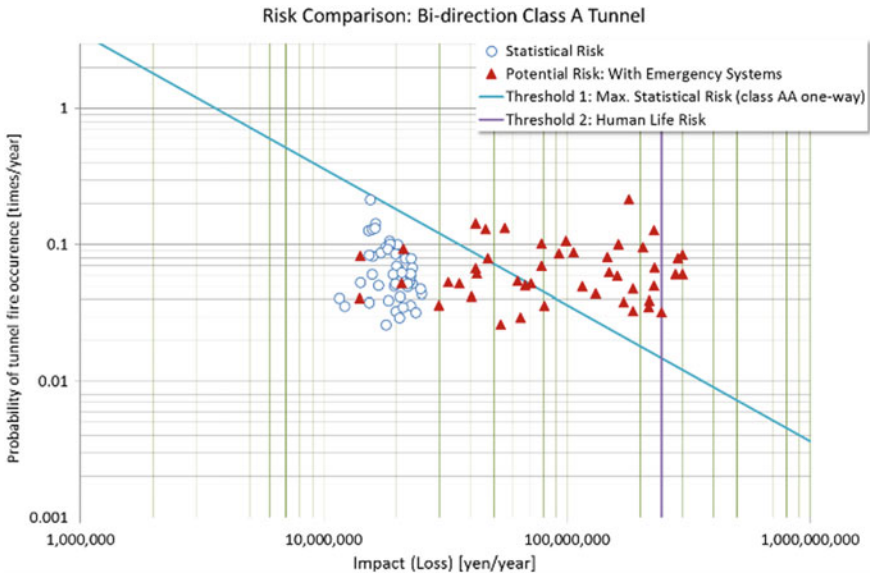
Fig. 12 Case where an evacuation information system is added
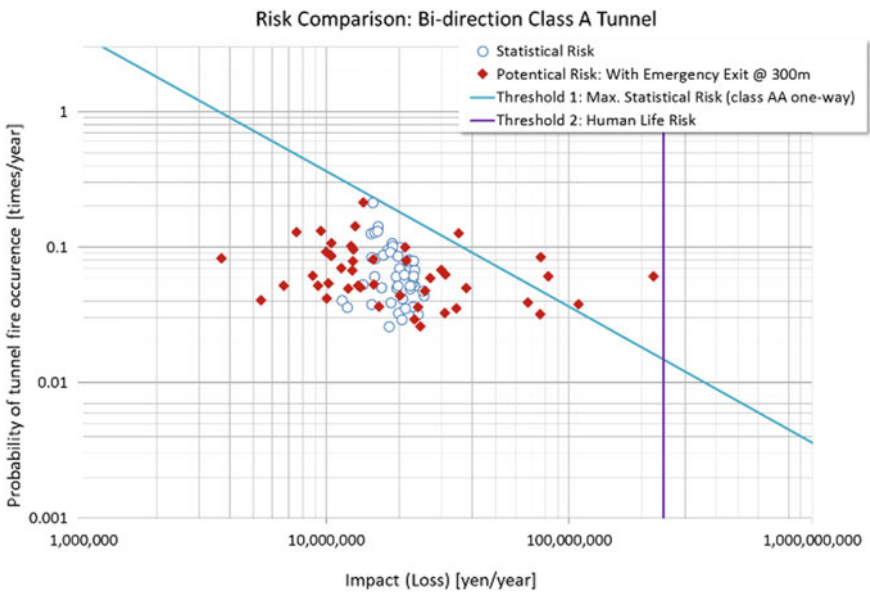
Fig. 13 Case where emergency exits are added

tentative, lower than the value of loss per person (245 million yen) and lower than the maximum statistical risk value of a one-way tunnel in order to prevent deaths. The tunnel shown in the figure is a Class A tunnel with limited installation of emergency facilities (for example, it has no emergency exits). Thus, Fig. 11 shows that there are many tunnels where, when a fire has occurred, the potential risk exceeds the tentative threshold value. But as shown in Fig. 12, although there are tunnels in which the risk is reduced below the threshold by installing an evacuation information system, there are still many tunnels where the threshold is exceeded. It can be said that when more emergency exits are installed, as shown in Fig. 13, the risk falls below the risk threshold in almost every tunnel.

4 Conclusions

It is difficult to clarify the effects of taking measures to improve safety simply by a statistical risk evaluation. Hence, this study created a database with the results of calculations using a model tunnel in order to confirm the effects of measures to improve safety by performing a coupled analysis of a fire simulation and an evacuation simulation, and calculated the number of residual evacuees from variable parameters such as fire scale, to study a method of easily obtaining potential risk, clarifying the following facts.

- A simple method of calculating potential risk was organized.
- To compress calculation resources, a model tunnel simulation was done and the results used to build a database.
- A regression equation to calculate the number of residual evacuees in an optional tunnel under limited conditions was proposed.
- Parameters which greatly contribute to increasing the number of residual evacuees are wind speed, inclination, and fire scale, and parameters that contribute greatly to reducing their number are evacuation speed and evacuation distance.
- Potential risk was visualized by selecting parameters and countermeasures.

However, refining the challenges and increasing the precision of evaluation results shown below are cited as ways to further improve precision.

- Applying parameters that lower fire occurrence frequency.
- Clarifying and expanding the inventory of fire scale and material impacts (impacts of heat in tunnels).
- Calculating risk parameters and setting range, setting the effectiveness of water spray systems, and expanding the basic database.
- Inclusion of soundness of facilities and machinery at risk.
- Setting rational risk management standards (thresholds) (ALARP, etc.).
- Continuous risk monitoring and improvement.
- Expansion of items registered in the fire accident database.

References

1. Directive 2004/54/EC Of European Parlament and of the Council of 29 April, 2004 on minimum safety requirements for tunnels in the trans-European road network. Official Journal of the European Union, L167 of 30 April 2004.
2. Yamazaki, T. et.al. (2015) Study on the potential risks analysis approach for tunnel fires in expressway tunnels. *Journal of JSCE, F2, 71*(1), 31–46 (in Japanese).
3. Kawabata, N., et al. (1999). Numerical simulation of thermal fumes induced by fire accidents in tunnels. *Japan Society of Mechanical Engineers, B65*(634), 1870–1877. (in Japanese).
4. Kikumoto, T., et al. (2007). Characteristic of plume behavior in a small section road tunnel only for passenger cars (A study by numerical simulation). *Journal of JSCE, F, 63*(4), 448–459. (in Japanese).
5. Seike, M. et.al. (2014) Assessment method for road tunnel fire safety by evacuation simulation of smoke behavior from CFD analysis. *Journal of JSCE, F2, 70*(1), 1–12 (in Japanese).
6. Cabinet Office, Government of Japan. (2013). Survey report on economic analysis of damage/loss from traffic accidents, pp. 92 (in Japanese).

Network Flow Modelling for Optimizing Fire Smoke Control in Complex Urban Traffic Link Tunnels: Incorporating Heat Loss and Gas Species Generation Rate Calculation into Models

Dong Yang, Yingli Liu and Tao Du

Abstract We propose the use of network flow analysis for designing and optimizing the smoke control in urban traffic link tunnels (UTLT) with multiple branches. Up-to-date, there have been no specified codes and standards for the application of conventional smoke control measures, such as jet-fan induced longitudinal ventilation and centralized smoke extraction using axial fans, in such tunnels. The use of network flow analysis could avoid the huge computational cost in large and complex tunnels. A self-developed network code incorporated with basic conservation equations was employed in a practical UTLT. The simplification algorithms for calculating the heat transfer rate at the tunnel envelopes and the gas species generation around the fire source were newly presented in this paper. The network analysis results are compared against a three-dimensional numerical simulation, and good agreements were obtained between them. Then, a hybrid mode including a combination of longitudinal ventilation and centralized extraction was simulated using the network code. The benefits and applicability were discussed.

Keywords UTLT · Hybrid ventilation · Smoke control · Network modelling · Flow optimization

Nomenclature

A_t	Cross-sectional area, m^2
c_p	Air specific heat, 1.01 kJ/kg K
d_e	Equivalent diameter of the branch, m
E_f	Convective part of heat release rate of the fire, W
E_w	Heat loss rate through the tunnel walls, W
l_t	Branch length, m
M_j	Mass flow rate of the jth branch, kg/s

D. Yang (✉) · Y. Liu · T. Du
Urban Construction and Environmental Engineering, Chongqing University, Chongqing 400044, People's Republic of China
e-mail: yangdong@cqu.edu.cn

$\Delta P_{r,k}$ Pressure loss resulted from flow resistance in the kth loop
$\Delta P_{r,j}$ Flow resistance of the jth ($j = 1 \sim n$) branch, Pa
$P_{b,k}$ Pressure change caused by buoyancy effect in the kth loop
$P_{b,j}$ Buoyancy force on the jth branch, Pa
$P_{d,k}$ Pressure rise induced by mechanical fan systems in the kth loop
$P_{d,j}$ Pressure rise on the jth branch, Pa
$P_{s,j}$ Pressure rise of the jth branch induced by jet fans, Pa
$P_{z,j}$ Total pressure provided by an axial fan on the jth branch, Pa
Q_j Volumetric flow rate of the jth branch, m^3/s
S_j Flow impedance of the jth branch corresponding to mass flow rate, kg^{-1} m^{-1}
$S_{0,j}$ Flow impedance of the jth branch corresponding to volumetric flow rate, kg/m^7
$t_{sta,j}$ Flow temperature at the start of the jth branch, °C
$t_{end,j}$ Flow temperature at the end of the jth branch, °C
T_0 Ambient air temperature
$T_{f,j}$ Spatially averaged temperature of the jth branch, K
ρ_0 Ambient air density, kg/m^3
ρ_0^* Average flow density in a tunnel branch, kg/m^3
ρ_j Flow density of the jth branch, kg/m^3

Greek Symbols

ξ Local resistance coefficient
λ Friction factor

1   Introduction

In rapidly developing countries such as China, traffic jams have become more and more serious. Urban traffic link tunnels are usually constructed in central commercial districts of cities and it plays the role of relieving the traffic jams [1]. Tunnel fire is a main disaster during the operation of tunnels and it could leads to serious casualties [2]. The tunnel fire, especially the resulting smoke movement process, becomes a hot research issue in the last two decades [3–6]. Note that the previous studies regarding tunnel fire mainly focused on conventional simple tunnels such as the single-hole tunnels. UTLTs are generally consisted of multiple tunnel branches, including main loop tunnels and some ramp exit or entrance tunnel [7–9]. The complex layout of a UTLT is beneficial for fulfilling its function in terms of connecting the underground spaces of the commercial buildings and the ground traffic lines; however, it increases the fire risk and difficulty in fire smoke control and evacuation [1, 8]. In conventional single tunnels, transverse extraction and longitudinal ventilation have been widely

and successfully applied and they show good efficiency [10–12]. The main advantage of transverse extraction is that it can restrict the smoke in a relatively small area [13, 14]. The disadvantage of transverse extraction is that the systems affiliated with transverse extraction such as fan rooms, duct and exhaust shaft could occupy a large area. For a UTLT located in central urban districts, the cost in terms of land occupation could be unaffordable. Although longitudinal ventilation using jet fans can overcome these shortcomings [10, 15], the downstream region of the fire source is occupied by hot smoke, and thus, evacuation in these downstream regions become impossible. In UTLTs, there could be other tunnel braches connected to the tunnel branch where fire occurs. The use of pure longitudinal ventilation could lead to the smoke intruding into these tunnel branches downstream of the fire branch. Therefore, it is crucial for seeking smoke control measures that can not only limit the smoke spreading area, but also save the land occupation. The combination of jet-fan induced longitudinal ventilation in the upstream region and centralized extraction in the downstream may be an alternative strategy for UTLTs. Note that the natural smoke exhaust through roof vents has also been applied in tunnels in recent years [17]. Another option is the use of natural smoke exhaust in the downstream fire region.

The combination of different ventilation or smoke control methods requires a good cooperation between the driving mechanisms provided by multiple systems. This increases the difficulty in design and operation of the smoke control system. Computational fluid dynamics (CFD) has been employed in tunnels [16–19]. However, to obtain a proper design strategy, it is always necessary to implement CFD simulations for several rounds, which could be costly for a complex UTLT with multiple branches. Some network flow codes, e.g., MFIRE [20, 21] and the subway environmental simulation code (SES) [22], have been used to assist in the design of ventilation and smoke control for complex mine tunnels or subway tunnels. However, the codes of the software are not open, and the modification of the algorithms for better applications in UTLTs is difficult. In this paper, we present the combination of different systems for smoke control in UTLTs. A self-developed code is employed to investigate the effectiveness of the hybrid modes. Liu et al. have proposed the use of one-dimensional modelling of fire smoke spread in UTLTs and combined diverse driving force for smoke control [23]. Two important issues related to the fire smoke, the heat transfer occurring at the tunnel envelopes and the pollutant gas species transport, are further considered in this paper. We usually perform adiabatic assumption in previous studies. However, the heat loss rate calculation is necessary for network flow analysis, especially for the tunnels where the buoyancy force is employed for smoke exhaust. Because the magnitude of buoyancy is closely related to the temperature difference between the interior and exterior environment, such a heat loss calculation helps in a better estimation of the magnitude of buoyancy. Pollutant or toxic gas species generation and transport are also very important, especially the carbon monoxide concentration. We incorporate a simple algorithm for gas species calculation in our network models. This is a further improvement for the network analysis codes. The results are discussed and the benefits of such an approach were presented.

2 A Simplified Introduction of Network Modelling

2.1 Mass Conservation of Nodes

The UTLT network is abstracted out as two configurations, branches and nodes, as presented in Fig. 1. The junctions between branches are represented by nodes. Virtual flow branches are artificially linked between the edging nodes. The intervention of these virtual branches leads to the network being entirely divided by loops, and thus, a looped flow algorithm is applicable in UTLT. If there are m nodes and n branches in the network, the flow mass balance equation of the ith node is expressed as

$$\sum_{j=1}^{n} a_{ij} M_j = 0 \tag{1}$$

where a_{ij} is a sign function; $a_{ij} = -1$ means that node i is the ending node of branch j; $a_{ij} = 1$ means that node i is the starting node of branch j; $a_{ij} = 0$ means that node i is not located at branch j.; $M_j (j = 1 - n)$ represents the mass flow rate of the jth branch.

2.2 Thermal Balance of Nodes and Branches

If the heat loss at the nodes is neglected, the heat balance equation of node i is written as

Fig. 1 A presumptive ventilation flow network for a UTLT (the dotted red lines represent virtual branches connecting the edging node of the network)
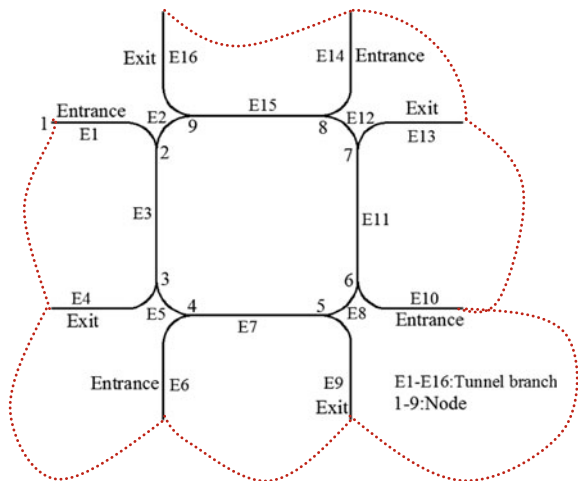
$$\sum_{j=1}^{n} a_{x1,ij} \cdot c_{\mathrm{p}} \cdot |M_j| \cdot t_{\mathrm{sta},j} + \sum_{j=1}^{n} a_{x2,ij} \cdot c_{\mathrm{p}} \cdot |M_j| \cdot t_{\mathrm{end},j} = 0 \qquad (2)$$

where $a_{x1,ij}$ and $a_{x2,ij}$ are sign functions. If the flow of the jth branch comes from node i, $a_{x1,ij} = 1$; otherwise, $a_{x1,ij} = 0$. If the flow of the jth branch enters node i, $a_{x2,ij} = -1$; otherwise, $a_{x2,ij} = 0$.

If the heat loss at the branches is considered, the heat balance equation for the jth branch is written as

$$c_{\mathrm{p}} |M_j| \left(t_{\mathrm{end},j} - t_{\mathrm{sta},j} \right) = E_{\mathrm{f},j} - E_{\mathrm{w},j} \qquad (3)$$

where $E_{\mathrm{f},j}$ is the heat rate released by the fire source. Note that $E_{\mathrm{f},j} = 0$ for the branches without fire source. $E_{\mathrm{w},j}$ is the heat exchange rate at the tunnel envelopes

For the tunnel branches without fire source, the following equation can be used to calculate the difference between the starting node temperature and the ending node temperature:

$$t_{\mathrm{end},j} = t_{\mathrm{air}} + (t_{\mathrm{sta},j} - t_{\mathrm{air}})e^{-hP_j L_j / M_j C_{\mathrm{p}}} \qquad (4)$$

where h is the convective heat transfer coefficient at the tunnel wall surface, and it is suggested to be 20–40 w/(m² k) [2].

Thus, the heat loss rate of the hot smoke at the branch is

$$Q_{\mathrm{w},j} = C_{\mathrm{p}} |M_j| (t_{\mathrm{sta},j} - t_{\mathrm{end},j}) \qquad (5)$$

The heat loss calculation is important because the heat loss accounts for a large proportion of the total heat release rate from the fire source in tunnels. The incorporation of heat loss calculation helps in more accurate estimation of buoyancy.

2.3 Pressure Balance of Flow Loops

For the kth loop, the total pressure rise is equal to the pressure loss resulting from flow resistance. The pressure balance equation of the flow loop is written as

$$\Delta P_{\mathrm{r},k} = P_{\mathrm{d},k} + P_{\mathrm{b},k} \qquad (6)$$

The total pressure loss resulting from flow resistance in the kth loop, $\Delta P_{\mathrm{r},k}$, is composed of the pressure loss of all branches located in the kth loop:

$$\Delta P_{\mathrm{r},k} = \sum \Delta P_{\mathrm{r},j} \qquad (7)$$

The total pressure rise induced by the mechanical fan systems in the kth loop, $\Delta P_{d,k}$, is composed of the pressure rise of all of the branches located in the kth loop:

$$P_{d,k} = \sum P_{d,j} \tag{8}$$

The total pressure change caused by the buoyancy in the kth loop, $\Delta P_{b,k}$, is composed of the buoyancy force generated by all of branches located in the kth loop:

$$P_{b,k} = \sum P_{b,j} \tag{9}$$

The pressure loss in the jth branch is written as

$$\Delta p_{r,j} = S_j M_j^2 \tag{10}$$

where

$$S_j = S_{0,j}/\rho_j^2 \tag{11}$$

$$\rho_j = \rho_0 T_0 / T_{f,j} \tag{12}$$

To obtain the average temperature of the branch, Eq. (4) is used for integral averaging and it gives

$$T_{f,j} = \frac{1}{L_j} \int_0^{L_j} t_l \, dl + 273.15 = t_{air} + (t_{sta,j} - t_{air}) \frac{M_j C_p}{h P_j L_j} (1 - e^{\frac{-h P_j L_j}{M_j C_p}}) + 273.15 \tag{13}$$

The flow impedance coefficient is

$$S_0 = \frac{\left(\lambda \frac{l_t}{d_e} + \sum \xi\right) \rho_0^*}{2 A_t^2} \tag{14}$$

where $\sum \xi$ represents the sum of the local resistance coefficients of a tunnel branch.

The jet fans installed in the jth branch are characterized by a pressure rise, $P_{s,j}$. The performance curve of an axial fan is characterized by a quadratic function:

$$P_{z,j} = a_j Q_j^2 + b_j |Q_j| + c_j \tag{15}$$

$$Q_j = M_j/\rho_j \tag{16}$$

where a_j, b_j, c_j are the characteristic curve coefficients. The pressure rise induced by the mechanical ventilation system in the jth branch includes both the effects of the jet fans and those of the axial fans.

$$P_{d,j} = P_{s,j} + P_{z,j} \tag{17}$$

If there is height difference between the starting point and the ending point of the jth branch and meanwhile it is occupied by hot smoke, thermal buoyancy is generated and is expressed as

$$P_{b,j} = \int_0^L g\Delta\rho_l \sin\theta \, dl = \frac{-\rho_0 g \sin\theta}{k} \ln \frac{T_0 + (t_{sta} - t_{air})e^{-kl_j}}{T_0 + (t_{sta} - t_{air})} \tag{18}$$

$$\sin\theta = \frac{\Delta Z_j}{l_j} \tag{19}$$

where ΔZ_j is the height difference between the actual flow ending and starting nodes of the smoke-occupied jth branch.

It is shown in Eq. (18) that, without the consideration of heat loss at the envelopes, the buoyancy and its resulting smoke exhausting capability would be over-predicted.

2.4 Gas Species Generation and Transport

We consider two typical gas species, carbon monoxide (CO) and carbon dioxide (CO_2). The generation rate of CO_2 is derived from measurement data of fire experiment [24].

$$m_{co_2} = 0.087 E_f \tag{20}$$

where m_{co_2} is the mass generation rate of CO_2. The unit of E_f here is MW.

The volume generation rate of CO is correlated with that of CO_2, and it is provided by Ref. [25]:

$$Q_{co} = 0.05 Q_{co_2} \tag{21}$$

where Q is the volume generation rate.

The species mass concentration at the fire branch is

$$\eta_{co,0} = \frac{m_{co,0}}{|M_0|} \tag{22}$$

The variation of gas species concentration is resulted from dilution. For the tunnel branch downstream of the fire source, if there is no air supply into the branch:

$$\eta_{co,j} = \eta_{co,i} = \eta_{co,0} \tag{23}$$

However, if there is air supply into the downstream branch, the mass concentration of CO is

$$\eta_{co,l} = \frac{m_{co,0}}{|M_l| + |M_k|} \tag{24}$$

where M_k and M_l are the mass flow rates of branch l and k.

3 Comparisons of CFD and Application Cases

3.1 Comparisons of the Network Analysis Result with the CFD Simulation

The selected case was composed of three branches. There is one-way traffic in each tunnel branch. The fire-occupied zone is recommended to be an independent branch, e.g., E5. The layout of the tunnel network is presented in Fig. 2. The dimensions of the cross-section of all the tunnel branches are 8 m (width) × 4.3 m (high), and the length of all the branches are presented in Table 1. The fire occurs in E5, and the total heat release rate is 5 MW, which corresponds to a fire caused by a car [12]. The

Fig. 2 Schematic of an example tunnel
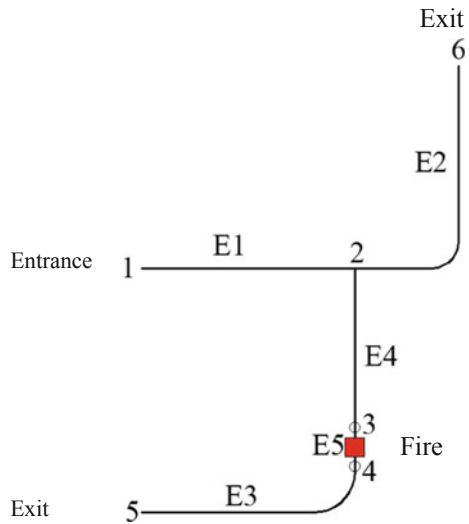
Table 1 Branch lengths and resistance coefficients of the example tunnel

Branch	E1	E2	E3	E4	E5
Length (m)	115	102	143	40	10
Resistance coefficients (kg/m^7)	0.00127	0.00166	0.00083	0.00011	6.7e−7

convective heat release rate accounts for two-thirds of the fire power, i.e., 3.33 MW. Note that there are height differences between the nodes for the ramping tunnels, i.e., E1 and E3. CFD simulations were performed to verify the network flow analysis. The details of the CFD simulation setup were introduced in Ref. [26]. ANSYS Fluent was employed here for CFD simulation. The volumetric heat source has dimensions of 4 m × 2 m × 1.5 m. Four jet fans were used in this case and each one has a pressure rise of 8.4 Pa. Two were installed in E1 and the other two were installed in E2. In this case, the heat transfer at the envelopes was neglected in CFD simulation. Because the hot smoke intrudes in E3, a buoyancy force of 7.84 Pa is generated in the CFD simulation. The buoyancy generated in E3 helps the smoke exhaust through the tunnel exit, e.g., Node 5. There is no back-layering smoke flow in the upstream region of the fire source, indicating the upstream region is safe for rescue or evacuation. The good smoke control effectiveness is resulted from the cooperation between the buoyancy generated in E3 and the driving forces provided by the jet fans. This is a successful example of the combination of two driving forces.

In network modelling, the resistance coefficients of the branches are derived from CFD results and are shown in Table 1. Figure 3 shows the temperature distribution and volume flow rates of the tunnel. Figure 4 shows the corresponding network modelling results. It is shown that they are in good agreement. However, the buoyancy in E3 obtained from network analysis is slightly lower than that of CFD simulation, i.e.,

Fig. 3 CFD results of the example tunnel at a height of 1.8 m
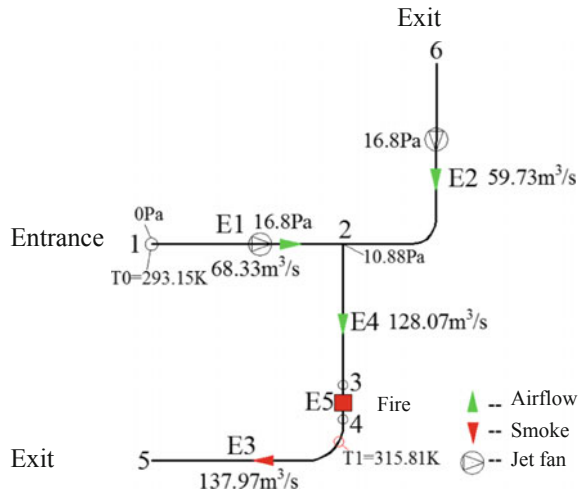
6.78 Pa versus 7.84 Pa. We also noticed that the total pressure of the nodes obtained
from network analysis and CFD is very close.

3.2 Hybrid Mode with Combination of Longitudinal Ventilation and Centralized Smoke Extraction

The schematic of the combination of longitudinal ventilation and centralized smoke
extraction is shown in Fig. 5. The axial fan system is installed in the axial fan room,
which is connected to the fire branch, E19. The fan room and its connecting duct
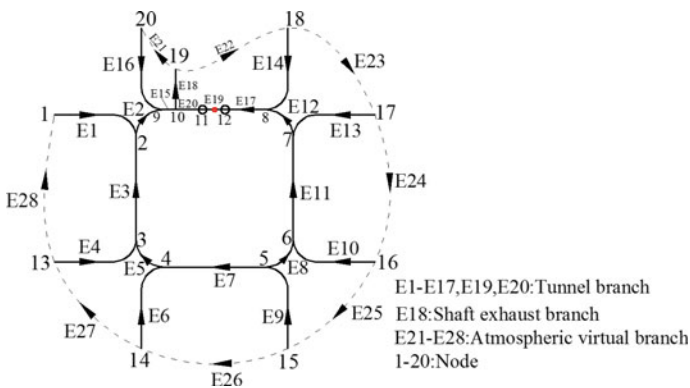
Fig. 5 Ventilation topology structure for the combination of longitudinal ventilation and centralized
smoke extraction

are represented by an additional branch, E18, as presented in Fig. 5. The dimensions of the cross-section of E18 are 3.7 m (length) × 3.7 m (width). The intervention of the axial fan creates new branches, namely, E15, E18, and E20. Their lengths are 20 m, 15 m, and 35 m, respectively. The fire occurs in E19, and the convective heat release rate is 5.33 MW. In this scheme, two parallel axial fans were installed in E18 to exhaust the smoke. The performance curve of the paralleled axial fan system is

$$P = -4.241 \times 10^{-9}Q^2 + 2.567 \times 10^{-3}Q + 544.67 \tag{17}$$

In addition to the axial fans, eight jet fans were employed in the tunnel branches. The pressure rise of each jet fan is 6.86 Pa. Two jet fans were installed in E1, two were installed in E3, two were installed in E16, and the remaining two were installed in E17. Thus, each of the above branches has a pressure rise of 13.72 Pa. Node 5 is identified as the flow separation point in the upstream region. The flow impedance coefficients of E2, E15, E16, E18, and E20 are calculated using Eq. (14), whereas those of the other branches are derived from the CFD simulation results. In this case, the heat loss at the tunnel envelopes is considered. The results are presented in Fig. 6. E15 and E17 have a bulk flow velocity of 2.76 and 2.1 m/s, respectively. Both the air velocity in E17 and that in E15 reach the critical value required to prevent smoke intrusion. Thus, all of the smoke is confined in the downstream fire region of E20 and is exhausted via E18. Except for the downstream fire region of E18 and E20, the
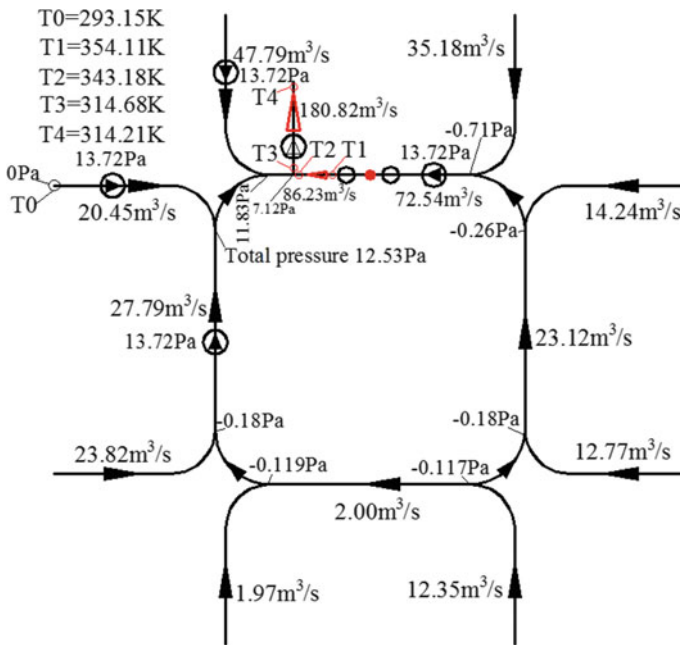
Fig. 6 Longitudinal ventilation and centralized smoke extraction (successful)

temperatures of the UTLT are nearly equal to the ambient temperature. This indicates that most of the branches in the complex tunnel are safe for human evacuation. In addition, the smoke temperature decrease along the flow route is resulted from both air dilutions and heat loss at the envelopes. This is different from the results obtained from adiabatic simulation. It is also shown in Table 2 that the concentrations of CO_2 and CO in E18 and E20 increase, and there is no CO concentration increase in other branches. This means this scheme effectively controls smoke and guarantees human safety.

However, if there are no jet fans in E1 and E3 and meanwhile the pressure rise induced by the jet fans in E16 is decreased to 8.4 Pa and the pressure rise induced by the jet fans in E17 is increased to 41.16 Pa, the network analysis results are shown in Fig. 7. The results indicate that the centralized smoke extraction system cannot expel all of the fire-induced smoke, and a portion of the smoke penetrates E2 and then spreads to the entrance tunnel E1. The smoke controlling objective is not achieved, and thus, the hot smoke transport direction is opposite to the traffic

Table 2 Increase of volume concentration of gas species in tunnel branches for the successful combination style

Branch	E1	…	E17	E18	E19	E20
CO_2 concentration (ppm)	0	…	0	2257	\	5245
CO concentration (ppm)	0	…	0	113	\	262
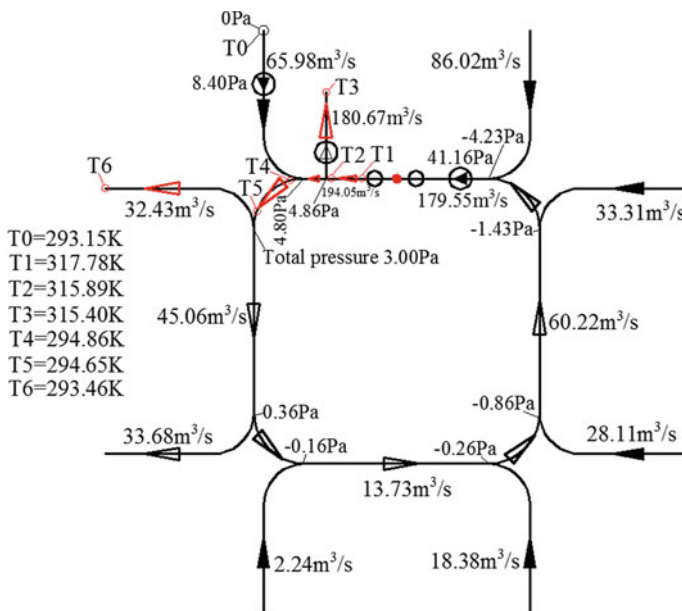
Fig. 7 Longitudinal ventilation and centralized smoke extraction (failed)

Table 3 Increase of volume concentration of gas species in tunnel branches for the failed combination style

Branch	E1	E2	E3	E4	E5	E6	E7	E8	E9	E10
CO concentration (ppm)	16	16	16	16	16	0	13	6	0	0
Branch	E11	E12	E13	E14	E15	E16	E17	E18	E19	E20
CO concentration (ppm)	3	2	0	0	106	0	1	106	\	106

direction in E1. This would cause casualties. The concentrations of CO for this case are shown in Table 3. It is indicated that matching the driving forces is important if different system is employed. Network analysis provides an effective measure to achieve this objective.

4　Conclusions

Urban traffic tunnels usually consist of multiple branches. This paper considers a fire that occurs in the main loop tunnel. The combination of centralized smoke extraction or buoyancy and jet-fan induced longitudinal ventilation are proposed to control the UTLT fire. Network modelling was used to calculate the key flow parameters. We incorporate the sub-models with regard to heat loss rate at the envelopes and gas species generation. The results are compared to that of the 3D CFD simulations. The maximum relative differences in both volumetric flow rate and flow temperature between the network simulation and CFD are small.

For the hybrid ventilation modes, the results demonstrate that the matching of the driving force of different smoke control systems is crucial for smoke control. Excessively large or inadequate driving force is harmful. Multiple rounds of calculations might be necessary to obtain an effective hybrid ventilation mode in UTLTs. The necessity of incorporating heat loss calculation and gas species generation calculation is shown. The network flow modelling only requires a few seconds to reach convergence. Section 2.4 only provides a simple route for incorporating gas species generation and transport into network modelling, which is still an open issue. Other gas species generation rates originated from consolidated literature or experiments can also be incorporated into the modelling.

References

1. Du, T., Yang, D., Peng, S. N., Liu, Y. L., & Xiao, Y. M. (2016). Performance evaluation of longitudinal and transverse ventilation for thermal and smoke control in a looped urban traffic link tunnel. *Applied Thermal Engineering, 96,* 490–500.
2. Beard, A. & Carvel, R. (2011) Handbook of tunnel fire safety. ICE Publishing, 2nd revised edition.
3. Tang, F., Hu, L. H., Yang, L. Z., Qiu, Z. W., & Zhang, X. C. (2014). Longitudinal distributions of CO concentration and temperature in buoyant tunnel fire smoke flow in a reduced pressure atmosphere with lower air entrainment at high altitude. *International Journal of Heat and Mass Transfer, 75,* 130–134.
4. Chow, W. K., Gao, Y., Zhao, J. H., Dang, J. F., & Chow, N. C. L. (2016). A study on tilted tunnel fire under natural ventilation. *Fire Safety Journal, 81,* 44–57.
5. Fan, C. G., Ji, J., Gao, Z. H., Han, J. Y., & Sun, J. H. (2013). Experimental study of air entrainment mode with natural ventilation using shafts in road tunnel fires. *International Journal of Heat and Mass Transfer, 56,* 750–757.
6. Wu, Y., & Bakar, M. Z. A. (2000). Control of smoke flow in tunnel fires using longitudinal ventilation systems—a study of the critical velocity. *Fire Safety Journal, 35,* 363–390.
7. Hua, G. Y., Wang, W., Zhao, Y. H., & Li, L. (2011). A study of an optimal smoke control strategy for an Urban Traffic Link Tunnel fire. *Tunnelling and Underground Space Technology, 26,* 336–344.
8. Du, T., Yang, D., Peng, S. N., & Xiao, Y. M. (2015). A method for design of smoke control of urban traffic link tunnel (UTLT) using longitudinal ventilation. *Tunnelling and Underground Space Technology, 48,* 35–42.
9. Guo, X. J., Yuan, J. P., Fang, Z., & Wang, J. H. (2013). Study on smoke control of Wuhan CBD urban traffic link tunnel. *Procedia Engineering, 52,* 124–130.
10. Li, Y. Z., Lei, B., & Ingason, H. (2010). Study of critical velocity and back-layering length in longitudinally ventilated tunnel fires. *Fire Safety Journal, 45,* 361–370.
11. Yi, L., Wei, R., Peng, J. Z., Ni, T. X., Xu, Z. S., & Wu, D. X. (2015). Experimental study on heat exhaust coefficient of transversal smoke extraction system in tunnel under fire. *Tunnelling and Underground Space Technology, 49,* 268–278.
12. Fire and smoke control in road tunnels. PIARC Committee on Road Tunnels (1999).
13. Mao, S. H., & Yang, D. (2016). One-dimensional analysis for optimizing smoke venting in tunnels by combining roof vents and longitudinal ventilation. *Applied Thermal Engineering, 108,* 1288–1297.
14. Vauquelin, O. (2008). Experimental simulations of fire-induced smoke control in tunnels using an "air–helium reduced scale model": Principle, limitations, results and future. *Tunnelling and Underground Space Technology, 23,* 171–178.
15. Yang, D., Huo, R., Zhang, X. L., Zhu, S., & Zhao, X. Y. (2012). Comparative study on carbon monoxide stratification and thermal stratification in a horizontal channel fire. *Building and Environment, 49,* 1–8.
16. Ang (Edmund), C. D., Rein, G., Peiro, J., Harrison, R. (2016). Simulating longitudinal ventilation flows in long tunnels: Comparison of full CFD and multi-scale modelling approaches in FDS6. *Tunnelling and Underground Space Technology, 52*, 119–126.
17. Ji, J., Gao, Z. H., Fan, C. G., & Sun, J. H. (2013). Large Eddy Simulation of stack effect on natural smoke exhausting effect in urban road tunnel fires. *International Journal of Heat and Mass Transfer, 66,* 531–542.
18. Tilley, N., Rauwoens, P., & Merci, B. (2011). Verification of the accuracy of CFD simulations in small-scale tunnel and atrium fire configurations. *Fire Safety Journal, 46,* 186–193.
19. Colella, F., Rein, G., Verda, V., & Borchiellini, R. (2011). Multiscale modeling of transient flows from fire and ventilation in long tunnels. *Computers & Fluids, 51,* 16–29.
20. US Bureau of Mines (1995) Fire Users Manual Version 2.20. Department of the Interior, Bureau of Mines, Washington, DC.

21. Cheng, L. H., Ueng, T. H., & Liu, C. W. (2011). Simulation of ventilation and fire in the underground facilities. *Fire Safety Journal, 36,* 597–619.
22. Parsons Brinckerhoff Quade & Douglas (1980) Subway environmental design handbook. Volume II: Subway environment simulation (SES) computer program version 3 part 1: user's manual. Draft for US Department of Transportation. Parsons Brinckerhoff Quade & Douglas Inc. Honolulu, HI.
23. Liu, Y., Yang, D., Xiao, Y., Mao, S., & Yang, M. (2018). Combining diverse driving forces for smoke control in complex urban traffic link tunnels (UTLTs) using one-dimensional flow modelling. *Sustainable Cities and Society., 43,* 265–274.
24. Ingason, H., Li, Y. Z., & Lönnermark, A. (2015). Runehamar tunnel fire tests. *Fire Safety Journal, 71,* 134–149.
25. Vega, M. G., Díaz K. M. A., Oro, J. M. F. (2008). Numerical 3D simulation of a longitudinal ventilation system: Memorial tunnel case. *Tunnelling and Underground Space Technology, 23*, 539–551.
26. Yang, D., Liu, Y., et al. (2017). Multiple steady states of fire smoke transport in a multi-branch tunnel: Theoretical and numerical studies. *Tunnelling and Underground Space Technology, 61,* 189–197.

Influence of Stationary Vehicles to Thermal Fume Backlayering Length in Tunnel Fire

Yu Tsung Ho, Nobuyoshi Kawabata, Miho Seike, Masato Hasegawa, Shen-Wen Chien and Tzu-Sheng Shen

Abstract This research is using methods model experiments and numerical simulation in tunnel respectively to discuss what influence that stationary vehicles located in upwind fire source would have on backlayering length L_b of thermal fume. In this experiment, the same scale of the fire source was adapted, and the variables are the obstacles height of upwind fire source. There are two kinds of obstacles: lower obstacles and higher ones; the configuration is divided into two kinds: no stationary vehicles (M0) and both sides of stationary vehicles (M2). This experiment is using 1/5 model of the tunnel, and the model material Biot number and Fourier number is close to the full-scale tunnel. In terms of numerical simulation, a full scale model was built by original code which is self-developed and then calculated the fire source scale and time range of quasi-steady used in numerical simulation with dimensionless formula and Froude scaling methods respectively. Comparing the relation between

Y. T. Ho (✉)
Ding-Hui Project Management Consultants, No. 424, Dannan Road, Taipei 111, Taiwan (R.O.C.)
e-mail: HengBang@hibox.hinet.net

Graduate School of Natural Science & Technology, Kanazawa University, Kakumamachi, Kanazawa 9201164, Japan

N. Kawabata
Faculty of Production Systems Engineering and Sciences, Komatsu University, Komatsu, Japan
e-mail: nobuyoshi.kawabata@komatsu-u.ac.jp

M. Seike
Faculty of Engineering, Department of Mechanical Systems Engineering, Toyama Prefectural University, Imizu, Japan
e-mail: miho.seike@pu-toyama.ac.jp

M. Hasegawa
Faculty of Mechanical Engineering, Institute of Science and Engineering, Kanazawa University, Kakumamachi, Kanazawa, Japan
e-mail: mhase@se.kanazawa-u.ac.jp

S.-W. Chien · T.-S. Shen
Department of Fire Science, Central Police University, Taoyuan, Taiwan (R.O.C.)
e-mail: una179@gmail.com

T.-S. Shen
e-mail: una088@mail.cpu.edu.tw

dimensionless backlayering length L_b/H and $Q^{*1/3}$/Fr with curve fitting equation proposed by Kunikane (11th International Symposium on AVVT, Luzern, Switzerland, pp. 87–101, 2003 [1]), it shows that under the same Froude number circumstance, the L_b with obstacles is shorter than that without obstacles. Also, model experiments and numerical simulation both show similar result. Thus the original code used for numerical simulation in this study is suitable for studying the effect of stationary vehicles on L_b. After analyzing the effect of stationary vehicles on the longitudinal velocity, it is found that in the case of M2, the longitudinal velocity on the upper part of the tunnel is bigger than that of M0. Therefore, the L_b in M2 is shorter than that in M0. Because, in the case of M2, higher obstacles cause the wind speed of the upper part of the tunnel to become faster, which in turn causes the L_b to become shorter and the slope of the fitting curve to become smaller.

Nomenclature

W	Width of tunnel (m)
H	Height of tunnel (m)
H_v	Height of vehicle (m)
h	Heat-transfer coefficient (W/m^2 K)
A	Cross sectional area of tunnel (m^2)
U_m	Longitudinal ventilation velocity (m/s)
U_{mi}	Initial longitudinal ventilation velocity (m/s)
U_{ms}	Average longitudinal ventilation velocity (m/s)
g	Gravitational acceleration (m/s^2)
T_0	Ambient temperature (K)
Q	Theoretical heat release rate (W)
Q_m	Average quasi-steady heat release rate (W)
Q_m*	Dimensionless average quasi-steady heat release rate $Q^* = Q_m/\rho_0 C_p T_0 A\sqrt{gH}$
Q_{mc}	Convection quasi-steady heat release rate (W)
Re	Reynolds number $Re = U_m H/\nu$
L_b	Backlayering length of thermal fume (m)
S_{max}	Maximum smoke generation rate (g/s)
Δt	Temperature rise from initial condition (deg)
t	Elapsed time after ignition in seconds (s)
ρ_0	Air density at ambient temperature (kg/m^3)
C	Specific heat capacity (J/kg K) (use wall = 879 J/kg K)
C_p	Specific heat capacity (J/kg K) (use dry air = 1005 J/kg K)
C_s	Optical density per path length of smoke (m^{-1})

α Thermal diffusivity $\alpha = \lambda/\rho C$ (m^2/s)
λ Thermal conductivity (W/m K)
ν Kinematic viscosity (m^2/s)
Bi Biot number $Bi = hH/\lambda$
Fo Fourier number $Fo = \alpha(H/g)^{1/2}/H^2$
Fr Froude number $Fr = U_m/(gH)^{1/2}$
x Along the tunnel longitudinal axis (east portal direction being positive)
y Along the tunnel transverse axis
z Along the vertical axis ($z = 0$ m is the floor)
u Velocity in the x direction
v Velocity in the y direction
w Velocity in the z direction

1 Introduction

For unidirectional tunnels, when a tunnel fire occurs, the longitudinal ventilation system can prevent the heat and the smoke from moving in the direction of the tunnel entrance, which allows refugees (drivers or passengers) to escape towards the tunnel entrance under safer environmental conditions. If no longitudinal flow velocity, the thermal fume impinges on the ceiling of the tunnel and develops into stratified flows and that spreads from the fire source to the tunnel entrance. The backlayering length L_b is defined as the length of the reversed smoke flow upstream of the fire when the longitudinal flow velocity is lower than the critical velocity U_{cr}. The smoke from the backlayering affects refugees' visibility, and the high temperature may endanger people's life. In terms of controlling backlayering, some researchers think that the L_b should be 0, and some think it is acceptable as long as the backlayering does not jeopardize the refugees' safety. In addition, because backlayering can endanger the safety of evacuees and firefighters, maintaining the stability of the stratification of the backlayering is also a very important issue. In consideration of the height of the smoke layer, it is generally believed that when the height of the smoke layer is less than 1.8 m or a certain height, it may endanger the safety of the personne [2]. No matter what, it is important to understand the characteristics of backlayering in tunnel fire research, and L_b is one of significantly important characteristics of backlayering.

1.1 Pertinent Studies with no Vehicular Blockage

In the past of backlayering research, research methods include theory analysis, full scale or model scale experiments, and computational fluid dynamics simulation, etc. In terms of theory analysis, Thomas [3, 4] built a 90 cm × 90 cm wind tunnel model and proposed a theoretical relational equation about preventing backlayering from

happening, which discusses between U_{cr} and the rate of combustion heat release in a tunnel with longitudinal ventilation system in 1968; Danziger and Kennedy [5] then investigated the impact of tunnel slope and proposed a relevant formula based on Thomas' equation in 1982. In the past two decades, there have been quite a number of published studies on both the backlayering length and the critical velocity related to reducing the backing-line length [6–18]. However, the aforementioned studies are all without any vehicle or obstacle. In spite of learning the factors that influencing L_b includes: fire source, longitudinal flow velocity, tunnel size, tunnel shape, cross-section of tunnel, characteristics of heat absorption in tunnel wall, turbulent flow etc.; however, the research condition is without any vehicle or obstacle. When a fire occurs in a tunnel, vehicles might stop one after another and then cause stationary vehicles. These stationary vehicles will result in a certain extent of impact, thereby affecting the L_b in tunnel fire.

1.2 Studies Pertaining to Vehicular Blockage

In order to further investigate mechanism of vehicular blockage effect, Lee and Tsai [19] conducted small-scale experiments and numerical simulations to investigate longitudinal ventilation in tunnel fire with vehicular blockage on the fire behavior and U_{cr}. They used a 7 m tunnel with cross-section of 0.6 m (height) × 0.6 m (width); and 0.4 m (height) × 0.6 m (width). Three vehicular blockage modes of 2 or 3 rows occupying 5–31% of the cross-sectional area were simulated. When vehicular blockage was upstream of the fire source, the results indicated that when vehicular blockage was placed inside the tunnel model, U_{cr} would reduce, the reduction rate approached the rate of blockage. The fire site and relative positions of vehicles (5, 10, and 15 cm) also affected U_{cr}. However, the focus of the aforementioned study was on U_{cr} to prevent backlayering from happening. As for L_b and vehicular blockage on mechanism of L_b had not been discussed adequately. Some researchers had conducted research and provided opinions of vehicular blockage effect on backlayering. Kunikane et al. [20] investigated the effect of vehicular blockage on L_b with fire simulator using the LES model. Although the study found that the presence of vehicular blockage would result in a shorter L_b, the proportion of large vehicles to the whole traffic density has only a small effect on the L_b. In a study by Gannouni and Maad [21], FDS was used to investigate the effect of blockage on U_{cr} and L_b in longitudinally ventilated tunnel fires. Compared with the empty tunnel, the U_{cr} and the L_b become smaller when the obstacle blockage is used. However, their research is to place an obstacle in front of the fire source, taking the distance from the ground to the obstacle as a research variable, which is different from the full-scale tunnel traffic congestion. When there are some vehicular blockages in the tunnel, the space between vehicles should cause an impact on the airflow. However, the aforementioned 2 papers adopted only numerical simulation to investigate vehicular blockage effects on L_b, and no full scale or model scale experiments was conducted. In addition, they didn't investigate further into the mechanism of vehicular blockage effect

on L_b. Li et al. [22] through model experiments and theoretical analysis conducted research of backlayering fume lengths and critical velocities. They analyzed retained vehicles effects on L_b and U_{cr}. By placing obstruction at the upstream end of a fire source, with blockage occupying 20% of the tunnel cross-section, they proved that U_{cr} decreased with presence of retained vehicles. The decreasing rate was 23%. In other words, the reduction in U_{cr} rate was slightly higher than obstruction to tunnel cross-sectional area ratio. Despite few experimental studies of the effect of obstacles on backlayering, such as Tang et al.'s fire experiment [23] which investigated the impact of blockage-fire distance on L_b and U_{cr} with a 72 m long model scale tunnel, they only took account of one obstacle as variable. However, along with blockage and increasing distance to fire source, L_b and U_{cr} would first decrease, then approach the fixed value in blockage-free scenario. Finally, they derived a global model to predict L_b and U_{cr}; taking into consideration of cross-sectional blockage ratio and blockage-fire distance factors. Although experimental studies purpose is different from ours, but the two studies mentioned previously are both under the condition of one obstacle only, it is still quite different from the reality when there is a traffic jam. In the case of many vehicular blockages, thermal fumes will flow over many vehicular blockages. Therefore, under the condition of many vehicular blockages, the countercurrent smoke length should be different from the above research results.

1.3 The Aims of This Work

In real situation, stationary vehicles may include small vehicles and large buses, hence, in actual tunnel fires, probably many vehicles will stop because of the accident. The longitudinal ventilation velocity will transmit through these stationary vehicles and blow toward fire source. Theoretically, the longitudinal flow will be affected by the ratio of cross-sectional area of the obstructions to the tunnel cross-sectional area, the arrangements of vehicles, or vehicular heights. In addition as there is spacing among the stationary vehicles, the longitudinal flow will flow along top of vehicles and between-vehicles spaces. The longitudinal flow path will not be a smooth surface; and the spacing among vehicles might also affect the stability of smoke layer, even cause phenomena of smoke descent. These still require further study. Therefore, our purposes in the present study are investigating the influence of stationary vehicles to thermal fume L_b in tunnel fire, and stationary vehicles on L_b.

Based on the statement above, Our purposes in the present study are using methods of tunnel model experiments and computational fluid dynamics simulation are respectively adopted to investigate the influence of different stationary vehicles on L_b. The model is a one-way traffic tunnel with longitudinal ventilation system, in which rectangular vehicular blockage were placed to be stationary vehicles. There are two modes of vehicular blockage arrangements and two different heights of vehicular blockage to investigate the influence of different vehicular blockage on backlayering. In addition, to compare and evaluate the results of the model experiments and computer numerical simulation, a numerical simulation of a full-scale tunnel

fire was conducting with computational fluid dynamics that was self-developed with original codes. Aside from the effect of vehicular blockage on the L_b, the accuracy of the original codes in this study was also verified. Finally, the vehicular blockage effects on the mechanism of back-layering fume length are discussed.

2 Experimental and CFD Methods

2.1 Experimental and CFD Models Scheme

The model experiment in this study is a tunnel model that is 1/5 of the actual tunnel size, while computer numerical simulation uses a full-scale tunnel. Figure 1 shows the appearance of the experimental device and the tunnel model. The experimental model has a length of $L = 41.4$ m, a width of $B = 1.93$ m, a height of $H = 1.0$ m, and a tunnel area of 1.93 m^2. The experimental device is larger than all the previous researchers' the tunnel models. Considering the strength and heat resistance of the model tunnel walls, the tunnel model is constructed of ALC (Autoclaved Lightweight Concrete). The material of ALC is close to that of the actual tunnel. When no stationary vehicles in actual tunnel, the wind speed is about 1.53–2.74 m/s; in the experimental condition of model scale tunnel, the wind speed is about 0.68–1.23 m/s. The heat-transfer coefficient of actual tunnel and model scale tunnel are respectively 9.9–13.7 W/m^2 K and 7.3–9.0 W/m^2 K. The Biot number of the model tunnel is 42.7–52.8, which is almost the same with the actual tunnel (44.7–61.8), indicating that the heat transfer between the model tunnel wall and the hot airflow is similar. Thermal diffusivity is derived from thermal conductivity, material density, and specific heat capacity. The concrete generally used in tunnel construction has density and specific heat capacity respectively about 2100 m^3/kg and 879 J/kg K. The autoclaved lightweight concrete used in this study has density and specific heat capacity of respectively 700 m^3/kg and 1210 J/kg K. Hence, the thermal diffusivity, α, of the actual tunnel is 6.01 $\times$
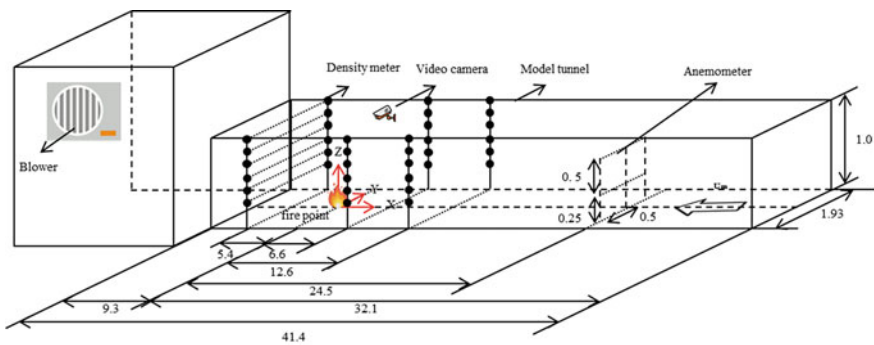

Fig. 1 Model tunnel structure and composition diagram

10^{-7} m^2/s; and the thermal diffusivity α of experimental model is 2.01×10^{-7} m^2/s. Fourier numbers of the model tunnel and that of the actual tunnel are close, which are respectively 6.41×10^{-8} and 1.72×10^{-8}, indicating that the thermal conductivity of the model tunnel approaches that of the actual tunnel walls. The Reynolds number and the heat absorption characteristics of the tunnel walls and ceiling will both affect the measurement results of the L_b. The reason why the wall of experimental model was made of ALC material which is close to the full-scale tunnel is to improve the accuracy of the experimental result. It can be concluded that the endothermic characteristic of the experimental model tunnel and that of the actual tunnel walls were basically the same. To sum up, the model tunnel constructed for the experiment had dimensions, ceiling and wall materials so as to render air flow and heat absorption characteristics similar to those of the actual tunnel. The experimental device is mainly composed of a tunnel part and a cabin part, and a blower is set at the downstream of the fire source to generate a longitudinal flow.

The fire source is regarded as the origin; the tunnel length is x coordinate; the width is y coordinate, and the height is z coordinate. In the study of Vantelon et al. [15] and Saito et al. [16], it is classified to a steady-state with a small Reynolds number. Vantelon et al.'s experimental tunnel model is made of heat-resistant glass, while Saito et al. used ceramic fiberboard as the material of the tunnel wall. If the Fourier number is larger than the other studies, it means the heat absorption of the wall is higher than that of concrete.

The Reynolds number and the heat absorption characteristics of the tunnel wall will both affect the measurement results of the L_b. Lee and Ryou [17] conducted tunnel model experiments with acrylic resin and gypsum board to investigate the effect of aspect ratio on U_{cr}. In the experiment, its Reynolds number belongs to the range of turbulence, but the range of Froude number is too small. And the tunnel is made of acrylic resin material, so the Fourier number is different than that of cement material. Roh et al. [18] used steel material to prevent the model from being warped; however, due to the endothermic nature of steel, the result of the study may be affected. It can be seen from the different experiments in Table 1 that the sectional area of the experimental tunnel is larger than that of other experiments. The reason why the wall of experimental model is made of ALC material which is close to the full-scale tunnel is to improve the accuracy of the experimental result.

The original code used in this study is a original code developed by Japanese in 1998 and is dedicated to the study of tunnel fires [24]. The original code using the large eddy simulation (LES) turbulence model (standard Smagorinsky model), has been validated for the following studies of tunnel fire:

- Estimation of heat release rate [25]
- Estimation of smoke generation rate [26]
- Phenomena of smoke descent [27]
- Transverse ventilation system [28]
- Smoke extraction by natural ventilation [29–31]
- A study of heat absorption effect of water spray [32]
- Critical velocity [11]

Table 1 Comparison of the present experimental and other study conditions

Item	Present study		Vantelon et al. [15]	Saito et al. [16]	Lee [17]	Roh et al. [18]
Type	Experimental model	Actual tunnel (CFD model)	Model tunnel	Model tunnel	Model tunnel	Model tunnel
Section	Rectangular	Rectangular	Semicircular	Rectangular	Rectangular	Horseshoe
Length L (m)	41.4	1000	3	21.6	10.4	10
Width W (m)	1.93	10	0.3	0.3	0.4	0.4
Height H (m)	1	5	0.15	0.3	0.4	0.4
Sectional area A (m^2)	1.93	50	0.0353	0.09	0.16	0.143
Fire source upstream distance	32.1	500	1.5	10.8	7.4	5.3
Re	43,038–77,848	484,177–867,089	1900–2200	5800–8300	10000–15000	21000–27000
Fr	0.07–0.39	0.07–0.39	0.16–0.21	0.175–0.25	0.20–0.29	0.40–0.53
$Q*$	0.072	0.072	0.0218–0.0524	0.13	0.0885	0.175
Material (near the fire source)	ALC	Concrete	Heat-resistant glass	Ceramic fibreboard	Acrylic resin (gypsum board)	Acrylic resin (steel)
Bi ($l = H$)	42.7–52.8	44.7–61.8	0.875–2.73	7.85–64.2	18.7–53.3	18.7–53.3
Fo ($l = H$)	6.41×10^{-8}	1.72×10^{-8}	3.70×10^{-6}–4.03×10^{-6}	2.45×10^{-6}–8.67×10^{-7}	1.16×10^{-7}	1.16×10^{-7}

● Interference between two tunnels [33].

To confirm the accuracy of the original code, the present study was simulated with a full-scale tunnel and compared with the results of the model experiment. Computer numerical simulation adopted the actual tunnel size and used the original code 3D simulator to generate the numerical simulation model. The numerical model of tunnel is length $L = 1000$ m, width $W = 10$ m, height $H = 5.0$ m and tunnel area is 50 m^2. The model is Cartesian coordinate system, x axis is along the tunnel longitudinal direction: from $x = -500$ m to $x = 500$ m; y is the span wise direction, coordinates from $y = -5$ m to $y = 5$ m; coordinates from $z = 0$ m to $z = 5$ m. z is the vertical direction, $z = 0$ m is the floor. The fire source is located at the center of the tunnel, which is also the origin of the system coordinates. The distances from the fire source to the tunnel entrance and to the tunnel exit are both 500 m. The grid sizes in Original code model are 0.333 m in the x direction, 0.286 m in the y direction, and 0.238 m in the z direction. As with model experiments, the tunnel model used for numerical simulation is divided into stationary vehicles and without stationary vehicles.

2.2 The Setting of Experimental and CFD Models

There are two lanes in both experimental and simulated tunnel models. The experimental conditions are divided into two kinds of stationary vehicles (M0) and both side stationary vehicles (M2). In the model experiment, a box made of calcium silicate was used as the stalled vehicles. Obstacles are only placed at upstream of the fire source, and there are lower obstacles and higher ones. In the model experiment, when there are stationary vehicles (M2) on both sides, the distance between the first vehicle and the fire source is 1.0 m, the distance between two fronts of the vehicles is 4.0 m, and the distance between the vehicle and the tunnel wall is 0.2 m. Since the model experiment size is 1/5 of the full-scale tunnel, the numerical simulation tunnel size, the obstacles size, the vehicle pitch, the distance between the first vehicle and the fire source, and the distance between the vehicle and the tunnel wall are approximately 5 times. Experiments and simulations in the present study are based on the variables of vehicle height, as shown in Table 2 and Fig. 2 is the vehicle configuration situation of M0 and M2. In order to present the vehicle configuration situation more clearly, only the plan of the upstream direction of fire source is drawn. The initial value of experimental longitudinal wind speed, U_{mi}, is the average longitudinal wind speed, 30 s before ignition. Being set a total of four anemometers, they were set at $x = 24.5$ m from the fire source, at two altitudes of $z = 0.25$ m and $z = 0.75$ m from the bottom of the tunnel model and $y = 0.5$ m and $y = -0.5$ m. The measured time interval is 1 s and the longitudinal flow velocity is the average of the four anemometers. The wind speed almost maintained a certain value before ignition, but it dropped down due to the impact of hot air flow after ignition. In the experiment, the longitudinal flow velocity is affected by the configuration and the height of the model vehicles. When there is no stationary vehicle (M0), the longitudinal wind speed is

Table 2 Stationary vehicles of experiments and simulations

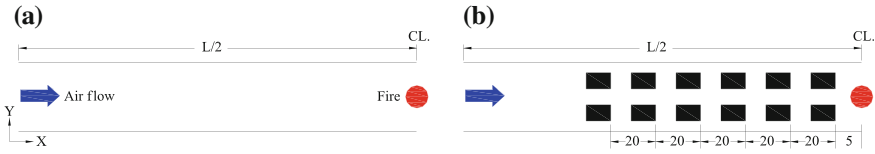| Item	Lower vehicles size (m)			Higher vehicle size (m)			Distance between the front of obstacles (m)	Distance from first vehicle to fire (m)	Distance between obstacles and wall (m)
	L	W	H	L	W	H			
Experimental model	1.26	0.567	0.5	1.26	0.567	0.7	4	1	0.2
Actual tunnel (CFD model)	6.33	2.57	2.62	6.33	2.57	3.57	20	5	1.1

(a)

(b)

Fig. 2 Model configuration of CFD numerical simulation (*unit* m). **a** No vehicle (M0). **b** Both side stationary (M2)

about 0.68–1.23 m/s and 0.23–0.65 m/s for both sides of stationary vehicles (M2). Instead of using the same longitudinal flow velocity, experiments with different vehicle retention conditions are based on the fact that L_b can be measured individually as wind speed condition. Similarly, in numerical simulation, it is also set the range of the longitudinal flow velocity that L_b can be calculated. In the numerical model, the longitudinal wind speed is about 1.53–2.74 m/s for no stationary vehicles (M0) and 0.51–1.46 m/s for both sides of stationary vehicle (M2).

2.3 Heat Release Rate

The fire source for the model experiment was placed at a distance of 9.3 m from the opening of the cabin and 32.1 m from the upstream of the tunnel. Located in the middle of the tunnel horizontally (0.965 m from the tunnel wall), 1500 g of N-heptane and 3000 g of water were placed on a 0.15 m² stainless steel oil pan. In this study, the fuel reduction rate R (g/s) was measured per second with an electronic scale. The fuel reduction rate R (g/s) was multiplied by the fuel unit heat value (N-heptane heat value = 44,560 J/g), and the theoretical heat release rate Q (W) was calculated. In addition, in order to avoid anomalies of the values, another radiometer was placed at 1.5 m from upstream of the fire source and 0.2 m from the tunnel ground. The heat value was measured per 0.2 s. Because the fuel is N-heptane which is low-smoke concentration, and the measuring location is at the windward of the fire source, the smoke will not affect the radiometric measurements. While conducting model experiments, the L_b is measured by thermocouples set every 1 m in the center of the ceiling. In order to measure the temperature distribution inside the tunnel, K-type thermocouples having a diameter of 0.1 mm was used for the measurement. Temperature measurements are sent to the data collector at fixed interval of one second. The thermocouples are used to measure the temperature near the ceiling at a distance of 20 mm. The nine thermocouples are arranged along the y-axis of the tunnel coordinates, and one thermocouple is set at intervals of 2 m, while there is a thermocouple every 1 m along the center of the ceiling. Therefore, there are 169 temperature measurement points on the ceiling. In addition, it is set along the tunnel height with eight locations for temperature measurement in the longitudinal section. A total of 122 measurement points are set every 2 m in x direction. In summary, there are 291 temperature measurement points. The placing of thermocouples is shown in
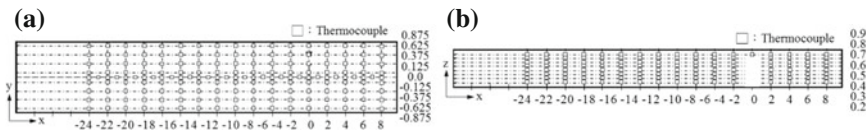
(a)

(b)

Fig. 3 Thermocouples configuration diagram. **a** Configuration of ceiling thermocouples. **b** Configuration of vertical wall section thermocouples

Fig. 4 Initial longitudinal velocity $U_{mi} = 0.71$ m/s, $Q_m = 153$ kW and the time change of longitudinal flow velocity U_m
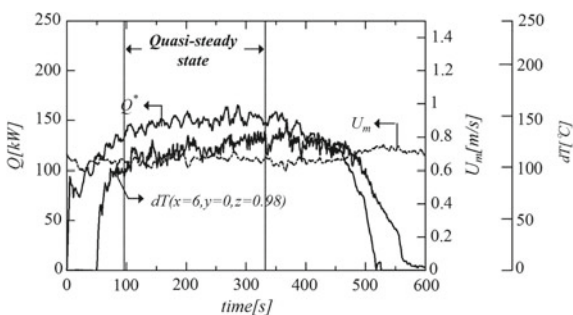
Fig. 3. Figure 4 showing the temporal changes when initial longitudinal flow velocity $U_{mi} = 0.71$ m/s, the theoretical heating rate Q and longitudinal flow velocity U_m.

The average longitudinal flow velocity is obtained by taking the longitudinal flow velocity U_m measured at 30 s intervals and then averaged. The average longitudinal flow velocity $U_{ms} = 0.66$ m/s in Fig. 4. The dT curve shows the temperature result at 6 m from the fire source. It can be seen from the figure that the temperature of the ceiling in the middle of the tunnel starts to rise rapidly in about 50 s after ignition and the theoretical heating rate maintains a steady state after $t = 98$ s. The model experiment sets the time range from $t = 98$ to 330 s as the quasi-constant range. The quasi-constant range of numerical simulation is scaled with the Froude scaling method [34]. The quasi-steady-state time range result of numerical simulation is approximately $t = 220–720$ s. Although the theoretical heating rate Q changes over time, the theoretical heating rate Q varies within $\pm 5\%$ over a 286 ± 15 s of the theoretical maximum heating rate Q. Therefore, in this study, the average of the theoretical heating rate Q which is obtained every 30 s in the quasi-steady state range is taken as the quasi-steady average heating rate Q_m. Taking $t = 286$ s as an example, the average maximum quasi-stationary heating rate Q_{max} can be calculated as 169 kW by taking the average ± 15 s. Compared with other researchers' tunnel model experiments in Table 1, Vantelon et al.'s HRR used in the experiment was 300–800 W [15], Saito et al.'s HRR was 6 kW [16], Lee and Ryou et al.'s HRR was 9.96 kW [17], Roh et al.'s HRR was 3.71–15.6 kW [18]. The average theoretical quasi-steady heat release rate of model experiments is 153 kW, which is equivalent to the fire source scale of full-size tunnel with HRR 8.86 MW can be obtained by dimensionless average quasi-steady heat release rate $Q^* = 0.072$. The maximum average quasi-constant heating rate $Q_{max} = 169$ kW, which is equivalent to the fire

source scale of the full-scale tunnel HRR 9.79 MW. Compared with other researchers' tunnel model experiments, the fire source size in this study is relatively larger. As the same as the model experiment, numerical simulation, whether with or without stationary vehicles, takes the same fire source scale for experiments.

By setting different longitudinal wind speeds, we can investigate the changes of L_b. Due to the tunnel model experiments using relatively low-smoke N-heptane as fuel, convection heat accounts for about 40–60% of total heat in pool fire combustion according to Kunikane et al. [1]. Therefore, in this study, the convection heat release rate $Q = 4.43$ MW is with a numerical simulation of 50% of total heat release rate. The fire source of numerical simulation has length of 1.94 m, x direction with 6 grid points, y direction with 7 grid points, the size of 3.75 m^2, which is 5 times of the model experiments fire source size.

3 Result

3.1 Dimensionless Heat Release Rate and Froude Number

As Vantelon et al. [15] study shown, without longitudinal wind speed, the fire plume develops into stratified flows simultaneously in two opposite directions. Under the effect of ventilation, flames and plumes are deflected. A plume is a substance which moves from a source into its surrounding area, such as a plume of smoke. A thermal plume is a plume that is specific to temperature alone. In general, the thermal plume study focused on Heat Release Rate (e.g. Behavior of Fire Plume in a Large Cross Sectional Tunnel [1]) may include convective heat, radiant heat, and thermal feedback of the tunnel wall. In this study, for both model and numerical simulation, we set the field 5 °C above normal temperature as the thermal fume and the $_b$ as the distance between the front of the smoke and heat flow and the center of the fire source. This study focused on the convection heat caused by the L_b, the Thermal Fume is defined as "due to the combustion of convective heat generated by the 'hot gas', the temperature of 5 °C above normal temperature".

However, when the longitudinal wind speed is smaller, the distance of L_b will be longer, and the distance between the front end of L_b and the fire source is relatively longer. At this moment, the thermocouple measured at the front end of L_b only has convection heat. However, when the longitudinal wind speed is close to the critical wind speed value, since the distance between the front end of the L_b and the fire source is very close, the measured temperature of the thermocouple may include convective heat, radiant heat, and thermal feedback of the tunnel wall. In other words, when the thermocouple's measurement position is very close to the fire source, it is very difficult to measure the convective heat in the combustion heat correctly. The measurement result may be overestimated (including both convection heat, radiant heat and tunnel Thermal feedback of the wall). Therefore, in this study, the values of $L_b/H > 5$ were used to compare the results of the model experiment and numerical

simulation. Using a large tunnel model, Minehiro et al. [35] investigated the L_b and constructed a model that takes into account the similarities of Froude numbers and the endothermy of the tunnel walls. According to the results of equation $L_b/H = a(Q^{*1/3}/Fr)-b$, the length of dimensionless backlayering can be deduced from dimensionless heat release rate and Froude number. When the L_b/H approaches zero, the parameter b is introduced to calculate the L_b by using a finite Froude number or a dimensionless heat release rate. Next, the study has taken Minehiro et al. suggested equation for charting to investigate the relation between L_b/H and $Q^{*1/3}/Fr$. The x-axis in Fig. 5 is $Q^{*1/3}/Fr$, and the y-axis is L_b/H, showing a comparison of the results of this study with those of other tunnel modeling experiments in the past. The longitudinal flow velocity at L_b of zero can be obtained from b/a. It can be seen from Fig. 5 that the range of L_b/H and $Q^{*1/3}/Fr$ in this study is more general than other studies. Saito et al.'s research results vary quite greatly due to little measurement points [16]. The length of the model tunnel is long enough to obtain the complete L_b without being affected by the tunnel exit. In contrast, Lee et al.'s research has smaller range of $Q^{*1/3}/Fr$ or L_b/H than other studies, but the results of Lee et al. are more similar to fitting curve. Roh et al.'s experimental goal is to investigate the U_{cr} [18], so research has smaller range of $Q^{*1/3}/Fr$ and L_b/H. Likewise, Roh's results are similar to fitting curve. Figure 6 shows that the simulation results are close to the experimental results, when the Froude number is the same, the L_b/H with stationary vehicles is shorter than the length of no stationary vehicle. In the case of the same L_b/H, the Froude number without stationary vehicles is larger than the one with stationary vehicles. Both experimental and simulation results show the same trend as previous studies [19–23]. In other words, at the same wind speed, the L_b of the hot-air stream becomes shorter when there is an obstacle at upstream of the fire source (e.g. buses, cars). Table 3 shows the results of the line slope the critical Froude number for different vehicle heights and different vehicle high and other experimental results. The Froude number of numerical simulation is a little smaller than the result of the present model experiments, but it is still close. In addition, the curve slope of M2 is less than the curve slope of M0. In the case of M2, the slope of fitting curve is significantly higher at lower vehicle altitudes. Overall, we can see that the effect

Fig. 5 Compare result of present experiments with other experiments, relation between L_b/H and $Q^{*1/3}/Fr$
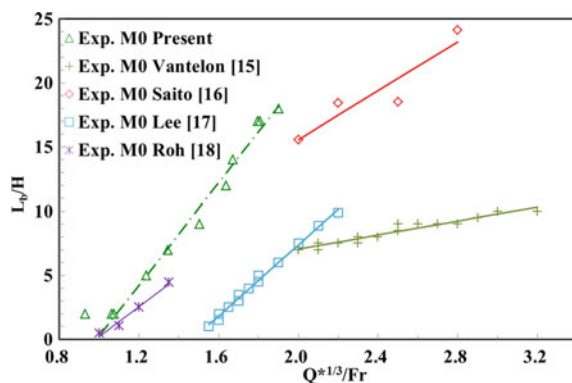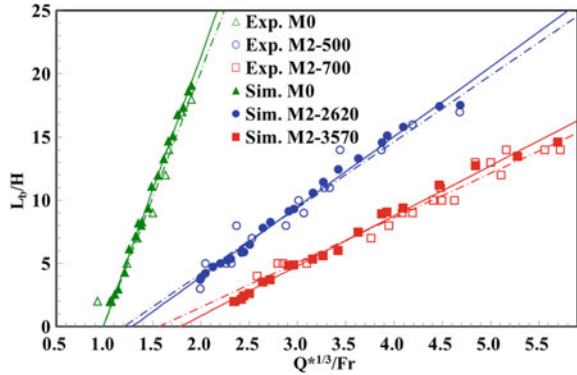
Fig. 6 Comparison between simulation and experiment result, relation between L_b/H and $Q*^{1/3}/Fr$

of stationary vehicles on backlayering, original code numerical simulation results and model experiments show the same distribution, and it also shows the accuracy of original code used in this study as a method of researching the effect of stalled vehicles on L_b. In addition, Table 3 also lists the vehicle blockage ratio in the case of M2. In the numerical simulation, M2 with lower obstacles has the lowest vehicle blockage ratio (27%) and the largest line slope (5.53). In model experiments which M2 has higher obstacles, the vehicle blockage ratio is the largest (41%) and the line slope is the smallest (3.53). From this observation, it was found that when the vehicle blockage ratio is larger, the relationship between L_b/H and $Q*^{1/3}/Fr$ is smaller.

3.2 Effect of Detention Vehicle on Longitudinal Flow Velocity

As the longitudinal velocity is one of the main factors affecting the L_b, the cross-sectional view of the longitudinal velocity in the x-z plane and the y-z plane is shown in Fig. 7 under different vehicle configurations when initial longitudinal ventilation velocity $U_{mi} = 1.65$ m/s. Since the L_b is 69.9 m in the case of no stationary vehicle (M0), it can be seen from the upper part of Fig. 7a x-z sectional view that the longitudinal flow and the hot air flow of fire source combustion offset each other at about 69.9 m from the fire source ($x = -69.9$ m). In the x-z section of Fig. 7b, c, the L_b is 9.5 and 6.9 m.

The longitudinal flow and the hot air flow of fire source combustion offset each other at these locations respectively. After observing the Fig. 6b, c, it is found that the longitudinal velocity of the upper tunnel becomes significantly larger with both side stationary vehicles. Moreover, if the stalled vehicles are higher, the longitudinal velocity of the upper tunnel becomes faster, resulting in a shorter L_b.

Figure 8 shows that there is no thermal fume at $U_{mi} = 1.65$ m/s, $x = -100$ m, $y = 0$ m, $z = 0$–5 m, $t = 720$ s, and the distribution of longitudinal velocity in z direction can be observed. It can be seen from the figure that the distribution of the longitudinal velocity of M2 in z direction is quite different from that of M0. In the

Table 3 Critical Froude number and coefficient a of different vehicle configurations, vehicle high and other experimental results

Coefficient	Configuration						Vantelon et al. [15]	Saito et al. [16]	Lee [17]	Roh et al. [18]
	Model experiments			Numerical simulation			No obstacle			
	M0	M2		M0	M2					
		Lower obstacles	Higher obstacles		Lower obstacles	Higher obstacles				
Line slope a	20.0	5.23	3.53	21.2	5.53	3.96	2.75	9.57	13.9	11.7

(continued)

Table 3 (continued)

Coefficient	Configuration									
	Model experiments			Numerical simulation			Vantelon et al. [15]	Saito et al. [16]	Lee [17]	Roh et al. [18]
	M0	M2		M0	M2		No obstacle			
		Lower obstacles	Higher obstacles		Lower obstacles	Higher obstacles				
Critical Froude number *b/a*	0.987	1.199	1.559	0.988	1.284	1.782	–	0.372	1.468	0.987
Vehicle blockage ratio	–	29%	41%	–	27%	37%	–	–	–	–
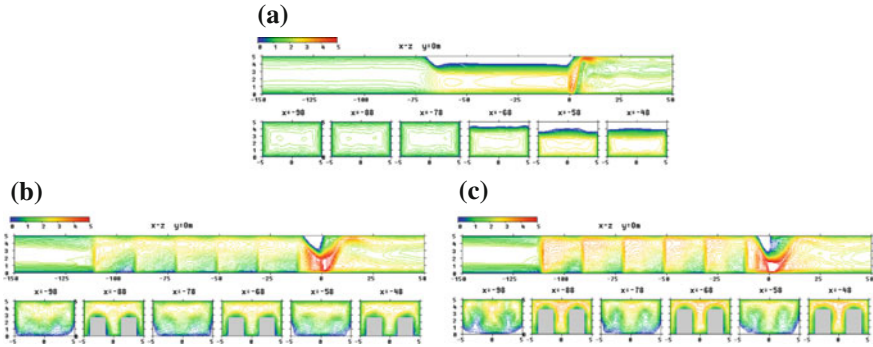
Fig. 7 The section of longitudinal velocity in the x-z plane and the y-z plane, $t = 720$ s. **a** M0-no stationary vehicle. **b** M2 ($H_v = 2620$ mm). **c** M2 ($H_v = 3570$ mm)

Fig. 8 Distribution of longitudinal velocity in z direction
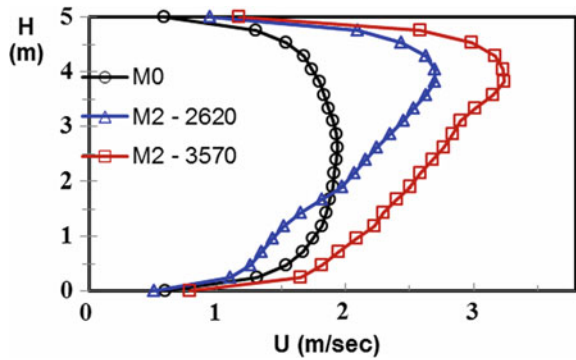
case of M0, the longitudinal velocity at the bottom of the tunnel is larger. In the case of M2, the wind speed above the tunnel is greater than the center and bottom of the tunnel. When the obstacle is higher, it can be seen from the curve that the wind speed the upper part of the tunnel becomes faster. However, in the case of M2, the shape of the longitudinal velocity curve is significantly offset. The longitudinal velocity increases faster with the height, which also shows why M2 cases can significantly reduce the L_b.

4 Conclusions

Through the uses of model experiment and numerical simulation, this study investigates how stationary vehicles in upstream of the fire source influence the L_b. The model scale experimental data and the results of computational fluid dynamics simulation are compared, and both methods show consistent results. About new point of view in this study and conclusions are as follow:

- At the same longitudinal velocity, the L_b becomes shorter when there are stationary vehicles at upstream of the fire source.
- In the case of M2, higher stalled vehicles cause the L_b to become shorter obviously, and the slope a of M2 in a dimensionless approximate curve is smaller than that of M0.
- Whether model experiments or numerical simulation, when the vehicle blockage ratio is larger, the line slope of relationship between L_b/H and $Q^{*1/3}/Fr$ is smaller in case of M2.
- Analysis of the influence of stationary vehicles on the longitudinal velocity shows that higher obstacles will cause the wind speed of the upper part of the tunnel to become faster, which in turn will result in shorter L_b.
- The original code used in this study has accuracy and is helpful for further investigation of the parameters affecting the L_b of stationary vehicles in the future.

References

1. Kunikane, Y., Kawabata, N., Takekuni, K., & Shimoda, A. (2003, July). Behavior of fire plume in a large cross sectional tunnel. In *11th International Symposium on AVVT*, Luzern, Switzerland (pp. 87–101).
2. Wu, B. S., & Shaw, J. J. (2007). *Study of two layer model applied to building fire prevention and human evacuation* (p. 16). ROC (Taiwan): Architecture and Building Research Institute, Ministry of the Interior.
3. Thomas, P. H. (1958). *The movement of Buoyant fluid against a stream and the venting of underground fires*. Fire Research Note, No. 351. Fire Research Station.
4. Thomas, P. H. (1968). *The movement of smoke in horizontal passages against an air flow*. Fire Research Note, No. 723, Fire Research Station.
5. Danziger, N. H., & Kennedy, W. D. (1982). Longitudinal ventilation analysis for the glenwood canyon tunnels. In *Proceedings of the 4th International Symposium on Aerodynamics and Ventilation of Vehicle Tunnels* (pp. 169–186).
6. Oka, Y., & Atkinson, G. T. (1995). Control of smoke flow in tunnel fires. *Fire Safety Journal, 25,* 305–322.
7. Lannermark, A., & Ingason, H. (2006). Fire spread and flame length in large-scale tunnel fires. *Fire Technology, 42*(4), 283–302.
8. Fujita, K., Minehiro, T., Kawabata, N., & Tanaka, F. (2012). Temperature characteristics of backlayering thermal fume in a tunnel fire. *Journal of Fluid Science and Technology, 7*(3), 275–289.
9. Tang, F., Li, L. J., Mei, F. Z., & Dong, M. S. (2016). Thermal smoke backlayering flow length with ceiling extraction at upstream side of fire source in a longitudinal ventilated tunnel. *Applied Thermal Engineering, 106,* 125–130.
10. Wu, Y., & Bakar, M. Z. A. (2000). Control of smoke flow in tunnel fires using longitudinal ventilation systems—A study of the critical velocity. *Fire Safety Journal, 35,* 363–390.
11. Wang, Q., Kawabata, N., & Ishikawa, T. (2000, October). Evaluation of critical velocity employed to prevent the backlayering of thermal fume during tunnel fires. In *Proceedings of International Conference on Asian Computational Fluid Dynamics ACFD* (pp. 404–411).
12. Lee, S. R., & Ryou, S. H. (2006). A numerical study on smoke movement in longitudinal ventilation tunnel fires for different aspect ratio. *Building and Environment, 41,* 719–725.
13. Chow, W. K., Gao, Y., Zhao, J. H., Dang, J. F., Chow, C. L., & Miao, L. (2015). Smoke movement in tilted tunnel fires with longitudinal ventilation. *Fire Safety Journal, 75,* 14–22.

14. Hu, L. H., Huo, R., & Chow, W. K. (2008). Studies on Buoyancy-Driven backlayering flow in tunnel fires. *Experimental Thermal and Fluid Science, 32,* 1468–1483.

15. Vantelon, J. P., Guelzim, A., Quach, D., & Son, D. K. (1991). Investigation of fire-induced smoke movement in tunnels and stations: an application to the Paris metro. In *Proceedings of the Third International Symposium on Fire Safety Science* (pp. 907–918).

16. Saito, N., Sekizawa, A., Yamada, T., Yanai, E., Watanabe, Y., & Miyazaki, S. (1994). Study report on fire performance in special space of use of underground space. *Fire Defence Research Datum, 29.*

17. Lee, S. R., & Ryou, H. S. (2005). An experimental study of the effect of the aspect ratio on the critical velocity in longitudinal ventilation tunnel fires. *Journal of Fire Sciences, 23,* 119–138.

18. Roh, J. S., Seung, H. Y., Hong, S. R., Myong, O. Y., & Youn, T. J. (2008). An experimental study on the effect of ventilation velocity on burning rate in tunnel fires—Heptane pool case. *Building and Environment, 43,* 1225–1231.

19. Lee, Y. P., & Tsai, K. C. (2012). Effect of vehicular blockage on critical ventilation velocity and tunnel fire behavior in longitudinally ventilated tunnels. *Fire Safety Journal, 53,* 35–42.

20. Kunikane, Y., Kawabata, N., Yamada, T., & Shimoda, A. (2006). Influence of stationary vehicles on backlayering characteristics of fire plume in a large cross section tunnel. *JSME International Journal, 49*(3), 594–600.

21. Gannouni, S., & Maad, R. B. (2015). Numerical study of the effect of blockage on critical velocity and backlayering length in longitudinally ventilated tunnel fires. *Tunnelling and Underground Space Technology, 48,* 147–155.

22. Li, Y. Z., Lei, B., & Ingason, H. (2010). Study of critical velocity and backlayering length in longitudinally ventilated tunnel fires. *Fire Safety Journal, 45,* 361–370.

23. Tang, W., Hu, L. H., & Chen, L. F. (2013). Effect of blockage-fire distance on buoyancy driven backlayering length and critical velocity in a tunnel: an experimental investigation and global correlations. *Applied Thermal Engineering, 60,* 7–14.

24. Kawabata, N., Wang, Q., Yagi, H., & Kawakita, M. (1998). Study of ventilating operation during fire accident in road tunnels with large cross section. In *Proceedings of the Fourth KSME-JSME Fluid Engineering Conference* (pp. 53–56). Pusan.

25. Kunikane, Y., Kawabata, N., Takekuni, K., & Shimoda, A. (2003). Heat release rate induced by gasoline pool fire in a large-cross-section tunnel. *Tunnel Management International, 6*(4), 22–29.

26. Seike, M., Ejiri, Y., Kawabata, N., & Hasegawa, M. (2014). Suggestion of estimation method of smoke generation rate by CFD simulation and fire experiments in full-scale tunnels. *Journal of Fluid Science and Technology, 9*(2), 1–11.

27. Kawabata, N., Kunikane, Y., Yamamoto, N., Takekuni, K., & Shimoda, A. (2003). Numerical simulation of smoke descent in a tunnel fire accident. *Tunnel Management International, 6*(4), 357–366.

28. Ejili, Y. (2004). *Simulation of hot gas flow during tunnel fire based on transverse flow ventilation, seminar outlines* (pp. 62–65). Japan Association for Fire Science and Engineering.

29. Sengoku, T. (2005). Heat extraction efficiency of natural ventilation opening during tunnel fire. *Transactions of the Japan Society of Mechanical Engineers, II*, 361–362.

30. Yokota, M., & Kawabata, N. (2012). A study of chimney natural exhaust effect for road tunnel fire -an evaluation using the numerical simulation of the real scale tunnel. In *6th International Conference Tunnel Safety and Ventilation* (pp. 82–89). Graz: New Developments in Tunnel Safety.

31. Ura, F., Kawabata, N., & Tanaka, F. (2014). Characteristics of smoke extraction by natural ventilation during a fire in a shallow urban road tunnel with roof openings. *Fire Safety Journal, 67,* 96–106.

32. Ishikawa, T., & Kawabata, N. (2003, September 3–6). Large eddy simulation of thermal fume under water spray induced by emergency fires in tunnels. In *The 12th International Conference on Fluid Flow Technologies* (pp. 722–727). Budapest, Hungary.

33. Kawabata, N. (2004). Interference of smoke in intermittent tunnels with snow shed during fire. *Transactions of the Society of Heating, Air-Conditioning and Sanitary Engineers of Japan* (94), 61–68.

34. Ingason, H., Li, Y. Z., & Lönnermark, A. (2015). *Tunnel fire dynamics*. New York: Springer.
35. Minehiro, T., Fujita, K., Kawabata, N., Hasegawa, M., & Tanaka, F. (2012). Backlayering length of thermal fume in tunnel fire experiments using a large-scale model. *Journal of Fluid Science and Technology, 7*(3), 389–404.

Model-Scale Fire Experiments and Simulations of a Tunnel with Point-Extraction Ventilation

Ti-Sheng Huang, Nobuyoshi Kawabata, Miho Seike, Masato Hasegawa, Futoshi Tanaka, Shen-Wen Chien and Tzu-Sheng Shen

Abstract In recent years, the application of point-extraction ventilation systems in road tunnels has attracted worldwide attention. Considering the experience of tunnel fire disasters, Taiwan Eastern Highway Project with eight tunnels about to open to traffic has also adopted this type of ventilation system. However, the smoke layers are possibly diffused by the exhaust flow in the vicinity of the extraction vent during emergency ventilation when a tunnel fire and then the smoke could deteriorate the evacuation environment. This study used Froude-scaling methods and dimensionless models to simulate experimental conditions with CFD software (our original code). These simulations of smoke distribution were compared with results from experiments with a 1:5 scale-model tunnel equipped with a point-extraction ventilation system. The predictions of smoke propagation derived by the original code are in good agreement with the scale-model experiment results. Furthermore, through

T.-S. Huang (✉)
Graduate School of Natural Science and Technology, Mechanical Science and Engineering (Doctoral Programs), Kanazawa University, Kakuma-Machi, Kanazawa 920-1164, Japan
e-mail: adison690526@gmail.com

Fire Department of New Taipei City Government, No. 792, Changrong Rd, Luzhou District, New Taipei City 24765, Taiwan (R.O.C.)

N. Kawabata
Faculty of Production Systems Engineering and Sciences, Komatsu University, 4-Nu-1-3, Komatsu 923-8511, Japan

M. Seike
Department of Mechanical Systems Engineering, Faculty of Engineering, Toyama Prefectural University, 5180, Kurokawa, Imizu 939-0398, Japan

M. Hasegawa
Faculty of Mechanical Engineering, Institute of Science and Engineering, Kanazawa University, Kakuma-Machi, Kanazawa 920-1164, Japan

F. Tanaka
Department of Mechanical Engineering, Faculty of Engineering, University of Fukui, 3-9-1, Bunkyo-Ku, Fukui 910-8507, Japan

S.-W. Chien · T.-S. Shen
Department of Fire Science, Central Police University, No. 56, Shujen Rd., Takang Vil., Kueishan District, Taoyuan City 33304, Taiwan (R.O.C.)

© Springer Nature Singapore Pte Ltd. 2020

conformed the CFD cord accuracy, we could have the prediction and understand the smoke behaviour affected by this type of ventilation system, in order to assess the influence on the safety of evacuation environment in full-scale tunnel fire accident.

1 Introduction

Ventilation systems are one of the most important safety systems for road tunnels to control the spread of heat and smoke in case of fire to facilitate a safe evacuation environment. Over the last two decades, several serious fire catastrophes occurred in European bidirectional road tunnels, increasing interest in point-ventilation systems. However, only limited experimental data about the efficiency of these combined systems was available before 2000, including the Memorial Tunnel Fire Ventilation Test Program in 1995 [1]. Over the last decade, several experiments have confirmed that point-extraction ventilation effectively controls smoke flow [2]; however, full-scale experiments remain difficult because they are still time-consuming, logistically complicated and rife with uncertainty. For instance, the wind conditions at portals are difficult to control and the heat-release rate data gathered in the Runehamar tunnel fire tests include 15–20% uncertainty [3, 4].

To reduce cost and accurately control experimental parameters, Froude-scaling is extensively applied to model-scale tunnel fire experiments. Vauquelin et al. tested concentrated exhaust ventilation systems in 1:20 model-scale tunnel in 2005 [5]. Ingason and Werling carried out well-defined tests using a model-scale tunnel with longitudinal ventilation combined with single-point-extraction system in 1999 [6], and Ingason and Li bridged simulations with a 1:23 model-scale tunnel in 2010. By projecting model-scale simulation results to the actual Runehamar tunnel, these tests showed good correspondence between model-scale and full-scale test results [7]. Recently, a series of fire tests has been carried out in 1:10 model-scale tunnel; the heat-release rate, ventilation velocity, fire-source height and tunnel geometry were tested in 2015 [8]. In addition, a series of 1:5 model-scale tunnel fire tests have been performed in Japan, testing natural chimney exhaust [9], longitudinal ventilation [10] and hybrid ventilation strategies [11].

On the other hand, many of fire simulators used as computational capacity have developed rapidly since 2000. Ingason et al. performed numerical simulations of model-scale tunnel fires with the FLUENT CFD software to compare simulation results with experimental data obtained from well-defined model-scale tunnel tests [12]. Other researchers have used the Fire Dynamics Simulator (FDS), which was developed by the US NIST for researching fire accidents in buildings and tunnels; however, smoke descent in tunnel fires has not yet been simulated effectively [13].

In this study, the original code three-dimensional CFD simulator is used. This software tool is capable of predicting smoke-layer propagation and descent distance

over time in a tunnel fire. The simulation results have compared with full-scale or model-scale experimental results in Japan from 2000 [9, 10, 14–18]. However, the point-extraction ventilation system is relatively few investigated. The section discusses the accuracy of the simulator original code for the verification of the point-extraction ventilation system.

2 Simulation Method

We used the original code (large eddy simulation (LES) turbulence model) in this study. The following assumptions are included: (1) the flow is as a compressible and ideal gas. (2) The effect of pressure on density is neglected, so that density is a function of temperature alone. (3) The heat region is modelled as an electric heater, ignoring the effects of chemical reactions, and the influence of radiant heat is also ignored. The governing equations consist of the continuity equation, Navier–Stokes equation, energy equation, a state equation and the smoke-diffusion equation. The simple marker-and-cell (SMAC) method is used to calculate pressure and velocity fields. Heat flux absorption into the tunnel wall is estimated for cells that touch tunnel walls by solving the one-dimensional heat-transfer equations [17].

2.1 Heat-Release Rate

The composition of the simulated mixed fuel is similar to gasoline used in experiments, so 50% of the theoretical total heat-release rate was chosen as the convective heat-release rate (HRR_{conv}) used in the simulation [18]. In these experiments, the time period of 120 from 180 and 300 s after fire ignition was defined as the quasi-steady section marked in Fig. 1. The HRR reaches 82 kW from 40 kW instantly after ignition. However, in order to ensure conditional convergence and avoid divergence, setting the simulated HRR_{conv} to keep increasing and reach to the maximum HRR_{conv} at 50 s after ignition, so the whole process lasts for 400 s, as shown in Fig. 2. With this

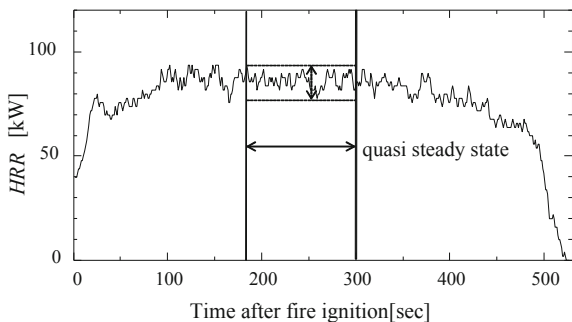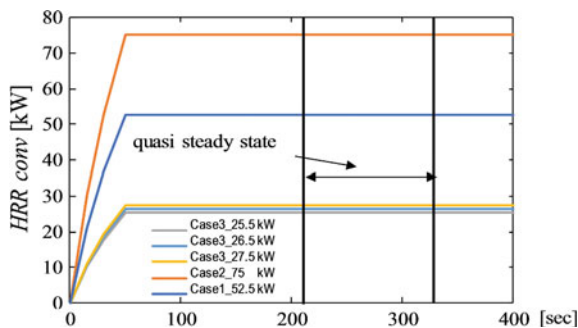**Fig. 1** An example experimental *HRR* curve and quasi-steady section

Fig. 2 Simulated HRR$_{conv}$
curves and quasi-steady
section

adjustment, both the smoke-extraction flow rate and the longitudinal flow velocity reach their set values by 30 s after ignition.

Considering the time lag in smoke propagation between the experiments and simulations for initial combustion, in these simulations, the 120 s time period between 210 and 330 s after ignition is defined as the quasi-steady section in simulations, as shown in Fig. 2.

2.2 Derivation of Smoke Generation Rate

The smoke concentration (Cs) is widely used to indicate the optical smoke density in studies of tunnel fires. In this study, Cs (also called Csy) was averaged based on the model tunnel width and calculated as the extinction coefficient in the Lambert–Beer equation [19]. In the simulation, the mass density of smoke particles m (g/m^3) was calculated using the convective diffusion equation. Therefore, the mass density of smoke particles m (g/m^3) and the optical smoke density Cs (m^{-1}) should agree [20]. In addition, the smoke generation rate (SGR) is proportional to the smoke density, and the shape of the HRR$_{conv}$ curve is applied to that of the SGR curve so that the maximum value of the SGR time curve is normalised to 1.0. Referring to experimental results from an experiment burning *n*-heptane, the value of $\alpha = 10$ (1/m)/(g/m^3) is chosen for the present simulations [21]. Moreover, in combustion experiments with kerosene and light oil as the fuel, the relationship between the mass density of smoke particles and optical smoke density was not substantially linear at high density (above Cs = 2); the Cs growth rate decreased gradually with increasing m in this case [22]. The smoke mass concentration was obtained from the CFD analysis, and the extinction coefficient was calculated using the following equation [13]:

$$
\begin{aligned}
\text{Cs} &= \alpha\, m = 10\, m \quad m \leqq 0.26\, \text{g/m}^3 \\
\text{Cs} &= 1.73 \ln m + 4.94 \quad m > 0.26\, \text{g/m}^3
\end{aligned}
\tag{1}
$$

in which m denotes the mass density of smoke particles.

3 Scale-Model Tunnel Fire Scenarios

3.1 Fluid Physical Properties Comparison of Model/Real Tunnel Ratio

Table 1 shows the specifications of the full-scale tunnel and three scaled models. The longitudinal flow velocity U at each model tunnel is shown by the Froude number similarity rule which assumes that the longitudinal flow velocity in the full-scale tunnel is 2 m/s, Reynolds number $Re = 63,3000$, $Re = 57,000$ for the model tunnel with scale ratio $\gamma = 1/5$ and $Re = 7000$ for $\gamma = 1/20$. The pipe friction coefficient f_0 of the actual tunnel is set between 0.015 and 0.025 [23]. The Moody diagram shows the relationship between pipe friction coefficient f_0 and Re [24], the pipe friction coefficient falls within the range in fully developed turbulent region where f_0 does not depend on Re in the wall surface roughness (ε) divided by the hydraulic diameter (D) in the range of 0.0004–0.002, and Re is in the range of 300,000–1,000,000 or more. Table 1 shows the values of f_0 in full-scale tunnel for $\varepsilon/D = 0.0006$. In this case, $f_0 = 0.018$ for full-scale tunnel (complete turbulence $f_0 = 0.0173$), $f_0 = 0.022$ for Model 1, $f_0 = 0.029$ for Model 2, $f_0 = 0.035$ for Model 3; therefrom, it could be understand that full-scale tunnel is nearly complete turbulence, and the resistance compared with the full-scale is to increase by about 20% in Model 1 and about two times in Model 3. Therefore, Model 1 used in this study seems to be able to reproduce the flow of the real tunnel nearly. Therefore, Model 1 used in this study seems to be able to reproduce the flow of the real tunnel nearly.

Table 1 Relationship between model-scale ratio and Reynolds number

Tunnel item		Full scale	Model 1	Model 2	Model 3
Dimensions	H (m)	5	1	0.5	0.25
	W (m)	10	2	1	0.5
	A (m^2)	50	2	0.5	0.125
Scale ratio	γ	1	1/5	1/10	1/20
U (m/s)	$U_{\text{Model}} = \sqrt{\gamma} U_{\text{Real}}$	2.0 (assumed)	0.90	0.64	0.44
F_r	$U/\sqrt{gH}$	0.1428	0.1428	0.1428	0.1428
Re	UH/ν	63,3000	57,000	20,000	7000
Friction factor f_0	$\Delta p/\left(\frac{L}{D} \cdot \frac{\rho U^2}{2}\right)$	0.018	0.022	0.029	0.035

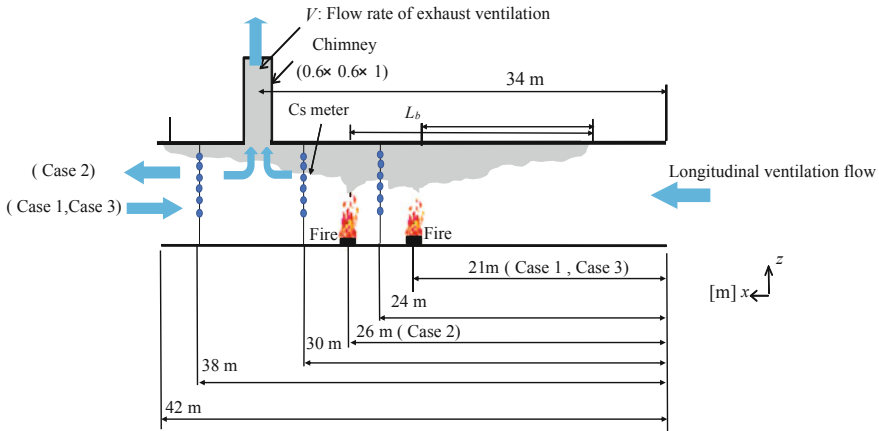*Note* Kinematic viscosity $\nu = 1.58 \times 10^{-5}$ (at 293 K)

Fig. 3 Schematic of the computational model of Exp. 1 and Exp. 2

3.2 Outline of Fire Experiments in the Tunnel Scale Model

The model tunnel is one-fifth scale of the real tunnel, with height 1 m, width 1.96 m and length 43 m. Figure 3 shows a schematic of the experimental set-up. In this experiment, an extraction vent with area 0.36 m^2 is installed 34 m upstream from the tunnel portal. Only the point-extraction ventilation device is activated in Case 1 and Case 3, and Case 2 also has the longitudinal fan activated. The measurement items include the temperature distribution, longitudinal flow velocity, air flow velocity in the exhaust duct, heat-release rate of the fire source and smoke-concentration distribution. There are six smoke densitometers installed at heights 0.3–0.8 m from the tunnel floor at 0.1 m intervals at three longitudinal locations: 24, 30 and 38 m from the right portal of the model tunnel.

3.3 Experimental Conditions

The consideration of similarity in the governing rules is important in scale-model experiments, so the experimental conditions were determined by applying the Froude-scaling law. These experimental conditions are listed in Table 2, with the values for the full-scale tunnel shown in parentheses. Mixed fuel with weight ratio of 80% heptane and 20% toluene was used; toluene was included to adjust the smoke density. In Experiment 1, longitudinal air flow velocity is induced by smoke exhaust from the point-extraction vent, so the longitudinal air flow velocity increases as the extraction flow rate increases. In Experiment 2, the longitudinal ventilation velocity is 2 m/s in the full-scale experiment, which is scaled to 0.89 m/s by the Froude law.

Table 2 Experimental and simulation conditions

	Case 1 Exp. 1	Case 2 Exp. 2	Case 3 Exp. 1
Scale	Model scale (full scale)		
Q_m = HRR$_{total}$ (kW) [(MW)]	105 (5.87)	150 (7.83)	51, 53, 55 (3.3)
Q^* = Dimensionless *HRR*	0.049	0.065	0.025
HRR$_{conv}$ (kW) (HRR$_{total}$ 50%)	52.5	75	25.5, 26.5, 27.5
Fire position x (m)	26(130)	21(105)	26(130)
V = Extraction flow rate (m^3/min)	110 (6149)	50 (2795)	155, 140, 125 (8664, 7826, 6987)
Longitudinal velocity (m/s)	0.46 (1.02)	0.89 (2)	0.65, 0.58, 0.52 (1.45,1.30, 1.16)

Q^*: The ratio of the heat-release rate and the enthalpy flow rate

Table 3 Endothermic characteristics of real tunnel and model tunnel

	Real tunnel	Model tunnel
	Concrete	ALC
H (m)	5.0	1.0
Cp (J/kg K)	8.4×10^2	12.1×10^2
ρ (kg/m^3)	2.3×10^3	7.00×10^2
h (W/m^2 K)	7.0–20.0	7.0–20.0
λ (W/m K)	1.6	0.17
Bi ($l = H$)	21.9–62.5	41.2–117.6
Fo ($l = H$)	2.36×10^{-8}	6.41×10^{-8}

ALC material was used for the tunnel walls. For the physical properties of the wall surface, the simulation temperature boundary was defined as the endothermic conditions for the ceiling and side walls listed in Table 3 and as adiabatic conditions for the road surface.

3.4 Analytical Area

In this study, the numerical simulation analysis proceeds as shown in Fig. 4. Following the previous studies [13], we chose 25 divisions for high accuracy, and the simulation grid dimensions were $\Delta x = 0.05$ m, $\Delta y = 0.05$ m and $\Delta z = 0.04$ m. In order to simulate nonstationary flow phenomena including fine flow fluctuations, 0.25 of the Courant number was chosen as the variable time step for stability and reproduce fluctuations. The boundary conditions were slightly simplified; the tunnel
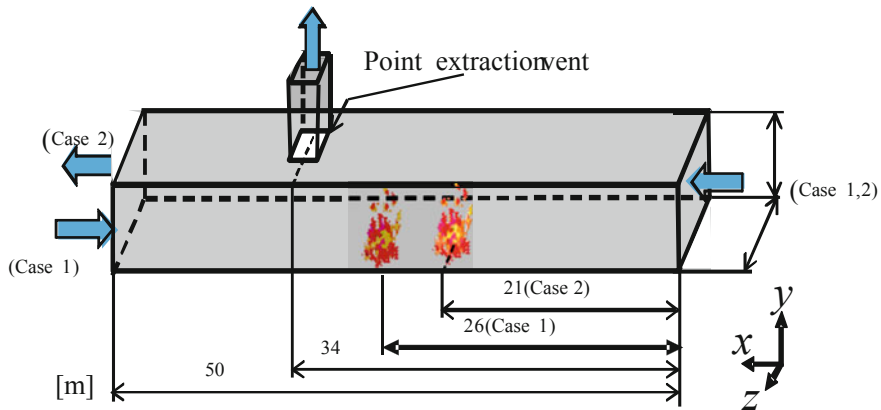
Fig. 4 Schematic of longitudinal flow velocity and point-extraction ventilation

was lengthened to 50 m to allow the flow to develop fully without affecting the heat flow and smoke-concentration distributions at the measurement points. At the inlet boundary, the simulation adopted the average value of the inflow air velocity measured directly in the experiment, and the extraction flow rate (m^3/s) was specified as the boundary condition of the point-extraction vent.

3.5 Dimensionless Analysis Applied to Compare Experimental and Simulated Smoke Concentrations

The comparison of simulation and experiment relies on the conversion of smoke particle mass density to optical smoke density; furthermore, the smoke generation rate of mixed fuels cannot be determined accurately. Some uncertainty arises from the CFD modelling and measurements of these quantities. Since the smoke generation rate (SGR) does not affect the other variables in these simulations, this study paid more attention to the dimensionless ratio of smoke-concentration distribution. Here, dimensionless analysis can be used to compare experimental and simulated smoke concentrations. In this paper, take Cso as a benchmark, which is the average smoke concentration between tunnel height $z = 0.3$–0.8 m at $x = 30$ m, as shown in Fig. 5.
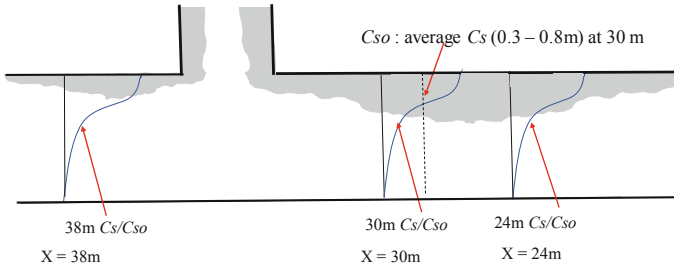
Fig. 5 Dimensionless analysis comparing experimental and simulated Cs (m^{-1}) based on the average smoke concentration between $z = 0.3$ and 0.8 m at $x = 30$ m

4 Experimental and Simulation Results

4.1 Longitudinal Flow Velocity Induced by Operating Extraction (Case 1)

The full-scale fire HRR_{total} is 5.87 MW, which assumed a sedan burning in a real tunnel. This value converted into model-scale HRR_{total} is 105 kW; the fuel pan area is 0.074 m^2. Though there is a longitudinal velocity in the tunnel induced by point-extraction ventilation alone, the longitudinal velocity is not much, which was predicted that the backlayering distance of the smoke will be long, so we installed a fire source at $x = 26$ m, and set the extraction flow rate to 110 m^3/min. Theoretically, the longitudinal flow velocity induced by the extraction ventilation flowing towards the extraction vent from the two tunnel portals should be 0.46 m/s. Figure 6 shows that due to the influence of point-extraction ventilation, the fire plume tilts towards the extraction vent, and there is a little amount of smoke passes over the vent to the downstream side. However, in addition to exhaust smoke, the point-extraction fan sucks much fresh air into the tunnel. The smoke backlayering distance spreads to 25 m upstream (the experimental measurement is 26 m), and the smoke outflow distance downstream of the extraction vent is 4.7 m (the experimental measurement is 3.4 m), at the 5th minute after fire ignition. Even after smoke stops spreading, the smoke layer is still stratified in tunnel. Although the longitudinal air velocities are 0.44 m/s at $x = 6$ and 0.46 m/s at $x = 37.5$ m ($y = \pm 0.5$ m, $z = 0.5$ m, $t = 300$ s), the simulation results correspond well with the experimental measurement results overall. Figure 7 shows that the average horizontal vector of the flow velocity distribution is not the same as the measurement points, as mentioned above. This indicates that the hot flow and cold air flow are induced by combustion, and that the smoke layer and air flow induced by exhaust smoke at the same time. Hence, between the extraction vent and the fire source, the smoke layer is disturbed, and less smoke descends to $z = 0.3$ m, as shown in Figs. 6 and 8a.

Fig. 6 Cs distribution at longitudinal (x-z) section and traverse (y-z) section of the tunnel in Case 1 (simulation)

Through dimensionless analysis, Fig. 8b shows the simulation result at $x = 24$ m, $z = 0.3$–0.7 m is higher than the experimental result. Even so, the simulation results agree well with experimental results overall.

4.2 Smoke Extraction Combined with Forced Longitudinal Flow Velocity (Case 2)

When operating the longitudinal ventilation fan and point-extraction fan in combination, the fire source can be larger than Case 1 because the longitudinal velocity is enough to prevent smoke backlayering. The full-scale fire HRR_{total} is 7.83 MW,

Fig. 7 Horizontal vector of flow velocity in longitudinal (x-z) section and traverse (y-z) section of the tunnel in Case 1 (simulation)
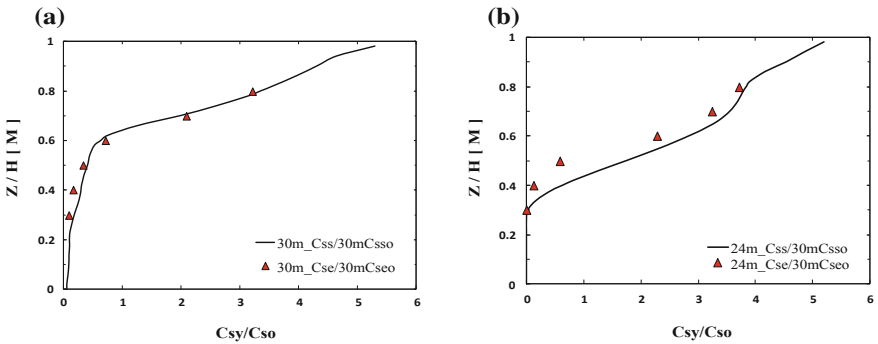
Fig. 8 **a** $Q_m = 105$ kW, 30 m, comparison of the dimensionless Csy/Cso between experiment and simulation. **b** $Q_m = 105$ kW, 24 m, comparison of the dimensionless Csy/Cso between experiment and simulation

assumed a van burning in a real tunnel. The equivalent model-scale HRR_{total} is 140 kW, so the fuel pan area is 0.11 m^2 placed at $x = 21$ m, the extraction flow rate is 50 m^3/min, and the longitudinal flow velocity is 0.89 m/s (2 m/s in the full-scale tunnel).

Figure 9 shows the longitudinal (x-z) and traverse (y-z) section smoke-propagation distributions per minute after ignition in Case 2. The smoke backlayering had spread about 8 m upstream at 5th minute after ignition; then it stops spreading. Resembling the experimental result, a stratified smoke layer remains upstream and downstream of the fire source. In addition, the extraction vent also drew a little fresh air, but performs better than Case 1. Figure 10 shows the horizontal vector of the flow velocity distribution; because of the strong longitudinal flow velocity, the airflow direction points consistently downstream and the flow velocity slows downstream of the vent, due to the influence of exhaust smoke. The dimensionless analysis shown in Fig. 11a, b shows the dimensionless smoke-concentration distribution at 38 m (4 m
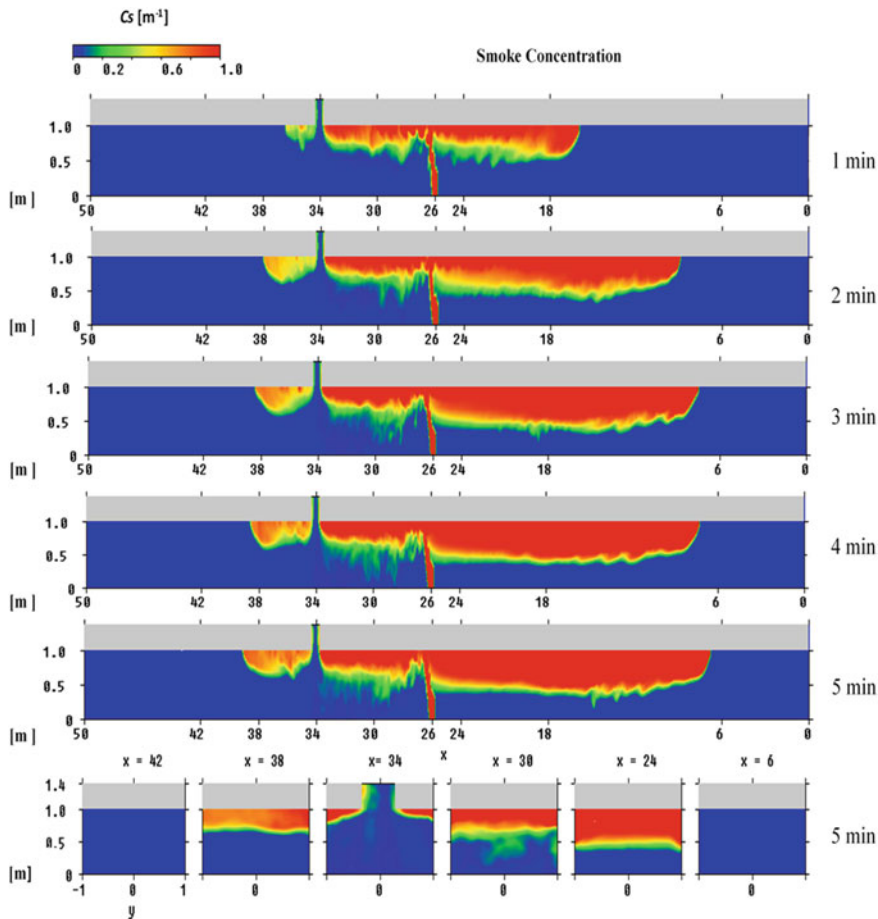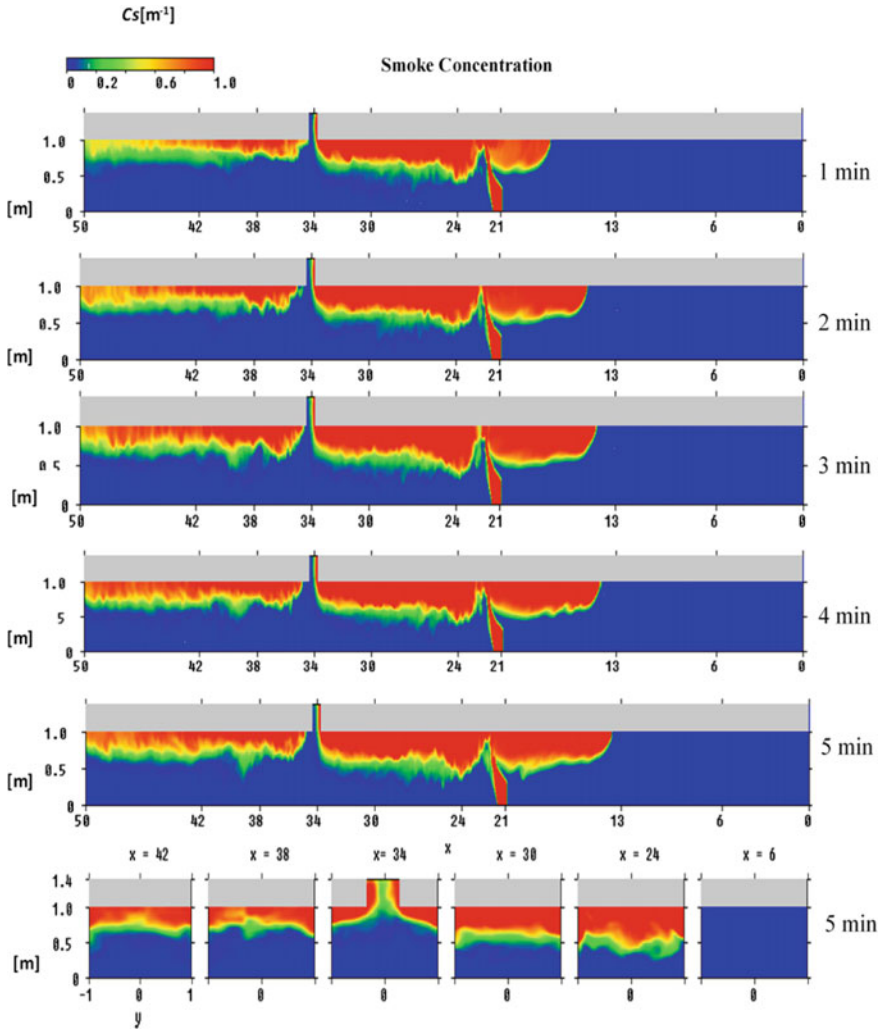
Fig. 9 Cs distribution at longitudinal (*x-z*) section and transverse (*y-z*) section of the tunnel in Case 2 (simulation)

downstream of the vent) and 30 m (4 m upstream of the vent). The simulation results at $z = 0.7$–0.8 m show higher smoke concentration than the experimental results and lower concentration at $z = 0.3$–0.6 m, meaning that the smoke exhaust rate in the model-scale experiment is greater than the simulated value. Figure 11c shows the dimensionless smoke-concentration distribution at 24 m (10 m upstream of the vent and 3 m downstream of the fire source). Since this location is near to the fire source, the effect of the ceiling jet caused by the rising heat plume impacting on the ceiling drives the smoke layer down as the smoke spreads along the longitudinal axis; then
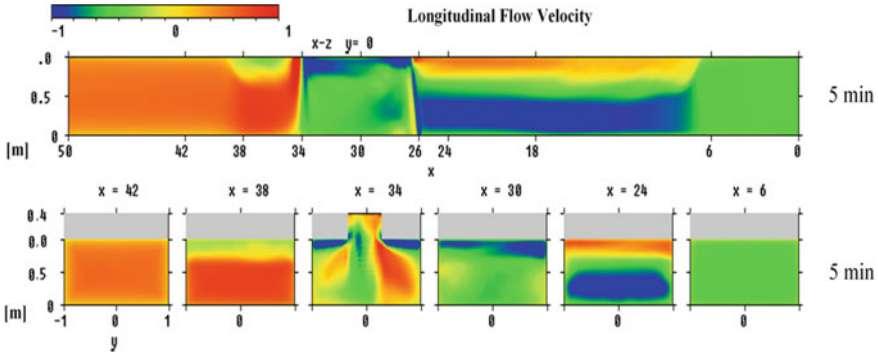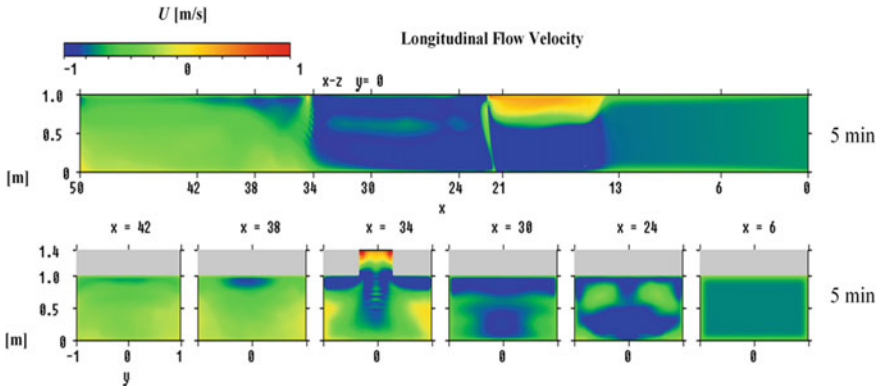
Fig. 10 Horizontal vector of flow velocity at longitudinal (*x-z*) section and traverse (*y-z*) section of the tunnel in Case 2 (simulation)
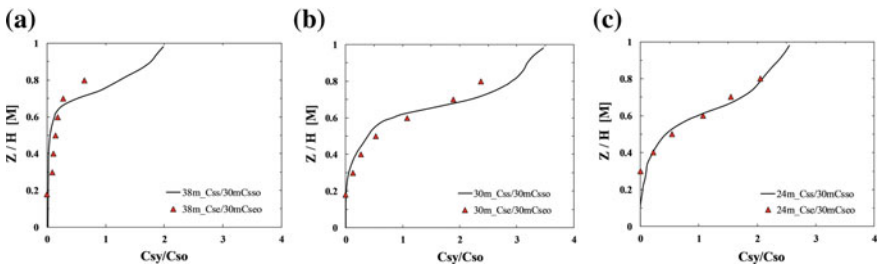

Fig. 11 **a** Qm $= 150$ kW, 38 m Csy/Cso dimensionless comparison. **b** Qm $= 150$ kW, 30 m Csy/Cso dimensionless comparison. **c** Qm $= 150$ kW, 24 m Csy/Cso dimensionless comparison

the smoke rises rapidly due to the effect of heat-flow buoyancy as shown in Fig. 9. The simulation results of $z = 0.4$–0.8 m correspond well to the experimental results.

4.3 Case 3

In Case 3, the longitudinal velocity varies with the smoke-extraction flow rate, and the heat-release rate also fluctuates. When the velocity is slow, *HRR* increases; along with the higher longitudinal velocity, the heat flow moves more easily and *HRR* decreases. In Fig. 12a, at $x = 30$ m, the smoke-extraction flow rate increases. The dimensionless smoke-concentration distribution of experiment Cse/Cseo decreases at the tunnel height of 0.8 m, and it increases at 0.6 m. As the smoke-extraction flow rate increases, the longitudinal ventilation velocity increases accordingly, so the

(a)

(b)
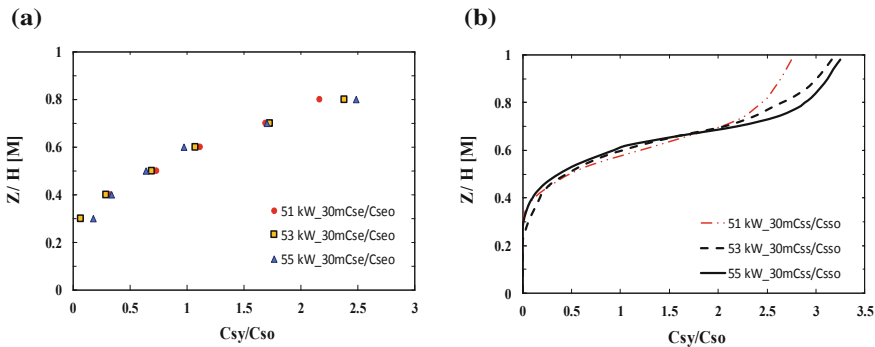
Fig. 12 **a** Qm = 51, 53, 55 kW, 30 m, Cs/Cso dimensionless comparison of experiments. **b** Qm = 51, 53, 55 kW, 30 m Cs/Cso dimensionless comparison of simulations

vortex diffusion at the smoke-layer boundary and the fire-source fluctuation increase simultaneously, causing more smoke to flow at lower heights.

Through dimensionless analysis, although the smoke concentration at tunnel height 0.3–0.4 m is somewhat different from the experimental results, the simulation results also correspond to the experimental results overall, as shown in Fig. 12b. The Cs/Cso very low at the model-scale tunnel height of 0.3 m, corresponding to the height of 1.5 m in full-scale tunnels which is human eye height. This means that smoke would have no influence on the evacuation environment in this case.

4.4 Backlayering Distance (L_b) from Fire Source

From these experiment results, the point-extraction ventilation can reduce the backlayering velocity and the length depending on the size of the fire source, smoke-extraction flow rate and the longitudinal flow velocity. The equation of dimensionless backlayering distance L_b/H and $Q^{*\,1/3}/Fr$, expressed as Eq. (2) [25], is shown in Fig. 13. As in the above analysis, these simulation cases are generally consistent with the experimental results.

$$\frac{L_b}{H} = 20\left(\frac{Q^*}{Fr^3}\right)^{1/3} - 18 \tag{2}$$

Fig. 13 Comparison of the dimensionless *Lb/H* and *Q*¹ᐟ³/Fr* between simulation and experimental results
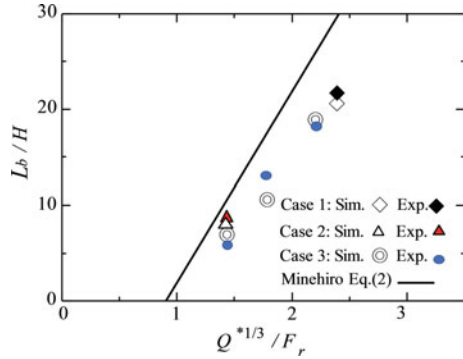
5   Conclusion

The simulated results were compared with results from model-scale fire experiments, and we draw the following conclusions:

1. The smoke-propagation behaviour and the smoke-concentration distribution are generally consistent with experimental results.
2. If the smoke generation rate of the fire source is not clear, a dimensionless approach can be applied, which also yields good agreement with the dimensionless smoke-concentration distribution.
3. For different heat-release rates, the appropriate smoke-extraction rate combined with controlled longitudinal flow velocity can keep the smoke layer away from the downstream side of the extraction vent while keeping the smoke layer from declining rapidly between the fire source and extraction vent. Moreover, point-extraction can reduce the backlayering velocity and concentrate smoke at the extraction vent.
4. The smoke concentration at the model-scale tunnel height of 0.3 m has almost no smoke, and this height corresponds to human eye height at actual scale. This level of smoke concentration would not adversely affect an evacuation. These simulation results demonstrate the reliability of point-extraction ventilation systems, suggesting that such simulations can be used to design smoke-evacuation systems and assess their impact on the evacuation environment.

References

1. FHWA (1995) *Memorial tunnel fire ventilation test program—Test report* (pp. 8–18). USA: Massachusetts Highway Department and Federal Highway Administration.
2. Ingason, H., & Li, Y. Z. (2011). Model scale tunnel fire tests with point extraction ventilation. *Journal of Fire Protection Engineering, 21,* 5–36.
3. Ingason, H., Lönnermark, A., & Li, Y. Z. (2011). *Runehamar tunnel fire tests* (p. 55), SP report. SP Technical Research Institute of Sweden.

4. Khattri, S. K. (2017). From small-scale tunnel fire simulations to predicting fire dynamics in realistic tunnels. *Tunnelling and Underground Space Technology, 61,* 198–204.
5. Vauquelin, O., & Telle, D. (2005). Definition and experimental evaluation of the smoke confinement velocity in tunnel fires. *Fire Safety Journal, 40,* 320–330.
6. Ingason, H., & Werling, P. (1999). *Experimental study of smoke evacuation in a model tunnel.* FOA Defence Research Establishment. FOA-R–99-01267-311-SE. Sweden: Tumba.
7. Ingason, H., & Li, Y. Z. (2010). Model scale tunnel fire tests with longitudinal ventilation. *Journal of Fire Protection Engineering*, *45*, 371–384.
8. Li, Y. Z., & Ingason, H. (2015). *Fire-induced ceiling jet characteristics in tunnels under different ventilation conditions* (pp. 306–131). BRANDFORSK Project, SP Technical Research Institute of Sweden.
9. Yokota, M., & Kawabata, N. (2008). A study of chimney natural exhaust effect of road tunnel fire, "A case of low longitudinal air velocity condition". In *International Congress Smoke Control in Buildings and Tunnels*, Spain (pp. 323–344).
10. Kikumoto, T., Kawabata, N., Maruyama, D., & Yamada, M. (2007). Plume characteristics and surrounding circumstances of refugee in small section road tunnel for passenger cars. *Journal of Japan Society of Civil Engineers, 63*(4), 448–459. (in Japanese).
11. Tanaka, F., Majima, S., Kato, M., & Kawabata, N. (2014). Performance validation of a hybrid ventilation strategy comprising longitudinal and point ventilation by a fire experiment using a model-scale tunnel. *Fire Safety Journal, 71,* 287–298.
12. Ingason, H., & Fredric, S. (2005). *Numerical simulations of a model scale tunnel fire test.* SP Swedish National Testing and Research Institute, SP Report 47. BORÅS, Sweden.
13. Seike, M., Kawabata, N., & Hasegawa, M. (2017). Quantitative assessment method for road tunnel fire safety: Development of an evacuation simulation method using CFD-derived smoke behavior. *Safety Science, 94,* 116–127.
14. Wang, Q., Kawabata, N., & Ishikawa, T. (2000). Evaluation of critical velocity employed to prevent the black-layering of thermal fume during tunnel fires. In: *Proceedings of International Conferences on Applied Computational Fluid Dynamics* (pp. 404–411).
15. Ishikawa, T., Kawabata, N., Tottori, H., & Ishida, M. (2000). Backlayering characteristics of thermal fume during tunnel fires in Hanshin Expressway (pp. 597–614).
16. Ejiri, Y., & Kawabata, N., et al. (2004). Large-eddy-simulation of fire in transverse ventilation tunnels. In *Japan Fire Association Research Presentation Conference* (pp. 62–65).
17. Kawabata, N., Kunikane, Y., Yamamoto, N., Takekuni, K., & Shimoda, A. (2003). Numerical simulation of smoke descent in a tunnel fire accident. *Tunnel Management International, 6*(4), 45–52.
18. Kunikane, Y., Kawabata, N., Takekuni, K., & Shimoda, A. (2003). Heat release rate in a large cross section tunnel. *Tunnel Management International, 6*(3), 22–29.
19. Schlichting, H., & Gersten, K. (2017). Boundary-layer theory (pp. 416–419). Springer-Verlag.
20. Seike, M., Ejiri, Y., Kawabata, N., & Hasegawa, M. (2014). Suggestion of estimation method of smoke generation rate by CFD simulation and fire experiments in full-scale tunnels. *Journal of Fluid Science and Technology (Japan), 9*(2), 1–11.
21. Mulholland, GW., & Croarkin, C. (2000). Specific extinction coefficient of flame generated smoke, National Institute of Standards and Technology, Gaithersburg, MD 20899, USA. *Fire Matererials, 24*, 227–230.
22. Takao, J., Fukuchi, N., & Hu, C. (2004). The characteristics analysis of oil pool fire phenomena for fire safety design in engine room (part 2), A kinetic characteristic of emitting smoke during oil burning. *The Society of Naval Architects of Japan, 194,* 291–301. (in Japanese).
23. Jang, H. M., & Chen, F. (2002). On the determination of the aerodynamic coefficients of highway tunnels. *Journal of Wind Engineering and Industrial Aerodynamics, 90,* 869–896.
24. McGovern, J. (2011). *Technical note: Friction diagrams for pipe flow* (p. 9). Ireland: Dublin Institute of Technology.
25. Minehiro, T., Fujita, K., Kawabata, N., Hasegawa, M., & Tanaka, F. (2012). Backlayering distance of thermal fumes in tunnel fire experiments using a large-scale model. *Journal Fluid Science Technology, 7*(3), 389–404.

Fire Smothering and Post-fire Ventilation Strategy for Cable Compartment in Urban Utility Tunnel

Jian Li, Congling Shi, Changkun Chen, Yingzhe Zhang, Xuan Xu and Jiehong Shi

Abstract To address fire safety of cable compartment in urban utility tunnel, provision of fire separation is necessary, and identifying a fire separation distance that is both safe and practical is thus of great importance. This paper studies the cable compartment fire occurring and development pattern, fire smothering, post-fire ventilation, and smoke exhausting under different fire separation distances by CFD numerical simulation. This paper proposes a general process for fire smothering in cable compartment of urban utility tunnel and comes up with a series of judging criteria for the best fire door opening time. The research discovers that under different fire separation distances, there is not big difference in maximum heat release rate (HRR) as well as the maximum temperature and smoke layer settling rate in the utility tunnel. After fire door is opened, the smoke exhaust time with an 800 m fire separation distance is obviously higher than any other fire separation distance. We believe that the present mainstream 200 m fire separation distance can be properly increased no matter from the perspective of fire spreading control or post-fire ventilation, for example, no excess of 500 m. The research results of this paper can provide theoretical basis for fire safety design and management of urban utility tunnels.

Keywords Urban utility tunnel · Cable compartment · Fire separation distance · Post-fire ventilation strategy

J. Li · C. Shi (✉) · Y. Zhang · X. Xu · J. Shi
Beijing Key Laboratory of Metro Fire and Passenger Transportation Safety, China Academy of Safety Science and Technology, Beijing 100012, People's Republic of China
e-mail: shicl@chinasafety.ac.cn

J. Li
e-mail: lijianaky@chinasafety.ac.cn

J. Li · C. Chen
Institute of Disaster Prevention Science and Safety Technology, Central South University, Changsha, Hunan 410075, People's Republic of China

Nomenclature

t_{REST} Required safe evaluation time (s)
t_b Early warning time (s)
t_c Response time (s)
t_s Evaluation time (s)
t_{close} Fire door closing time (s)
t_{open} Fire door opening time (s)

1 Introduction

Urban utility tunnel is a tunnel space built underground the urban area and is used to house different types of engineering pipelines including electrical, telecommunication, fuel gas, heat supply and water supply, and drainage pipelines. Urban utility tunnel is indeed an important infrastructure and "lifeline" for assured operation of cities. As a "lifeline" project of a city, its safe operation is of great importance to safe operation and guaranteed functioning of the city.

Scholars all over the world have been conducting safety researches on urban utility tunnels from multiple perspectives. Ishii et al. [1] examine a fire detection system for utility tunnels on the basis of the fact that temperature distribution along an optical fiber can be determined through measurement of the Raman backscattering of the Stokes and anti-Stokes lines. Canto-Perello and Curiel-Esparza [2–4] concerned with the risk assessment and indoor atmosphere hazard identification in person entry urban utility tunnels. Chen et al. [5–7] investigated the seismic response of underground utility tunnels through shaking table testing and FEM analysis.

Fire is one of the major sources of danger affecting safe operation of urban utility tunnels. For different compartments of urban utility tunnel, the configuration of fire protection equipment and facilities adopts different standards. However, in general, the fire protection equipment and facility configuration standards are really not very high considering that few people will enter the utility tunnels, as a result of which a fire may not be put under control right after the fire occurs inside the utility tunnels. Sun [8] has conducted a simulation analysis of the occurrence of cable fire in the cable compartment under different ventilation velocities as well as the fire hazards, the result of which shows that a ventilation system may effectively reduce the hazards of cable fire. By building a 1:3.6 model scale utility tunnel model, Du [9] has acquired the cable compartment fire burning pattern as well as the ceiling temperature distribution pattern. Hao [10] has studied the fire development, smoke diffusion, and temperature change during a cable fire inside a cable compartment and has acquired the pattern of influence of the three factors (ventilation velocity, arrangement of ID fan as well as location of vent) on the smoke exhaust effect during post-fire smoke exhausting.

Existing investigations are mainly focused on the occurrence and development of urban utility tunnel fire, but very few scholars have placed their research priority on

extinguishing utility tunnel fire. Considering the narrow and small space inside the utility tunnel, the possibility of manual firefighting will be very low if the fire cannot be put out automatically by the firefighting equipments in case of fire. Under such condition, the most effective method may be fire smothering. Then, this will involve the issue of fire separation distance setup, because if the fire separation distance is too big, the fire smothering effect may be poor, and if the fire separation distance is too small, the arrangement of equipment inside the utility tunnel may be difficult. Currently, the 200 m fire separation distance is generally adopted in Chinese standards. However, actual engineering practices mostly indicate that the 200 m distance is not conducive to pipeline arrangement and routine management. Identifying a fire separation distance that is both safe and practical has been a challenge for relevant engineers and scientists in recent years.

Bearing in mind the setup of fire separation distance for urban utility tunnels, this paper will study the cable compartment fire occurring and development pattern, fire smothering, post-fire ventilation and smoke exhausting under different fire separation distances by setting up different fire separation distances.

2   Fire Smothering Progress in Urban Utility Tunnel

As a measure that can be taken when the automatic fire extinguishing system fails or fire extinguishing cannot be done by people following a fire extinguishing failure in case of fire in the cable compartment of a utility tunnel, use of the fire smothering strategy needs to meet a certain conditions. A general process of fire smothering in urban utility tunnel is proposed in this paper, as shown in Fig. 1.

In the following researches in this paper, worse conditions are taken into account and the following assumptions are made:

(1) Fire detectors can identify the occurrence of a fire in a timely manner;
(2) Ventilation is off or ventilation stops following a fire occurrence is identified by the fire detector;
(3) There is no fire extinguishing system or the fire extinguishing system fails;
(4) The utility tunnel is occupied by maintenance persons and the fire doors located at both ends of the section on fire shall be closed after the persons are successfully evacuated.
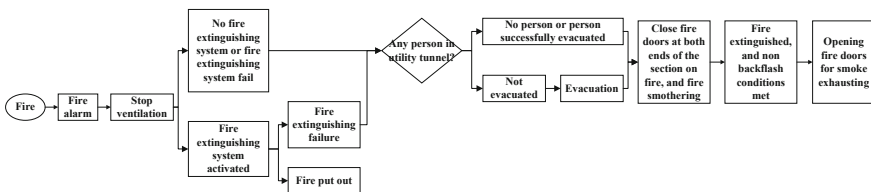
Fig. 1 General process of fire smothering in urban utility tunnel

3 Basic Condition of Utility Tunnel Under Research

The utility tunnel numerically simulated is an urban utility tunnel under construction in China. This utility tunnel is being built by using shielding method. Its upper deck is a cable compartment and the lower deck is a telecommunication and water supply compartment. See Fig. 2a for the specific dimensions. Inner diameter of the utility tunnel is 5.4 m, wherein the upper deck has a headroom of 2.4 m and the lower deck has a headroom of 2.9 m. The intermediate partitioning board is about 0.1 m thick.

In simulation, the model has a width of 5.4 m and a height of 2.4 m. There are 16 cables inside the utility tunnel, and its length equals to the length of the utility tunnel. Its cross section has two dimensions, respectively, Type A with a cross section of 0.4 m × 0.4 m and Type B with a cross section of 0.3 m × 0.3 m. Cross-sectional view of the model built is as shown in Fig. 2b.

The cables utilize cross-linked polyethylene insulated cable, with a decomposition and carbonization temperature of 330 °C, a density of 1500 kg/m^3, a specific heat

(a)   **(b)**

(c)
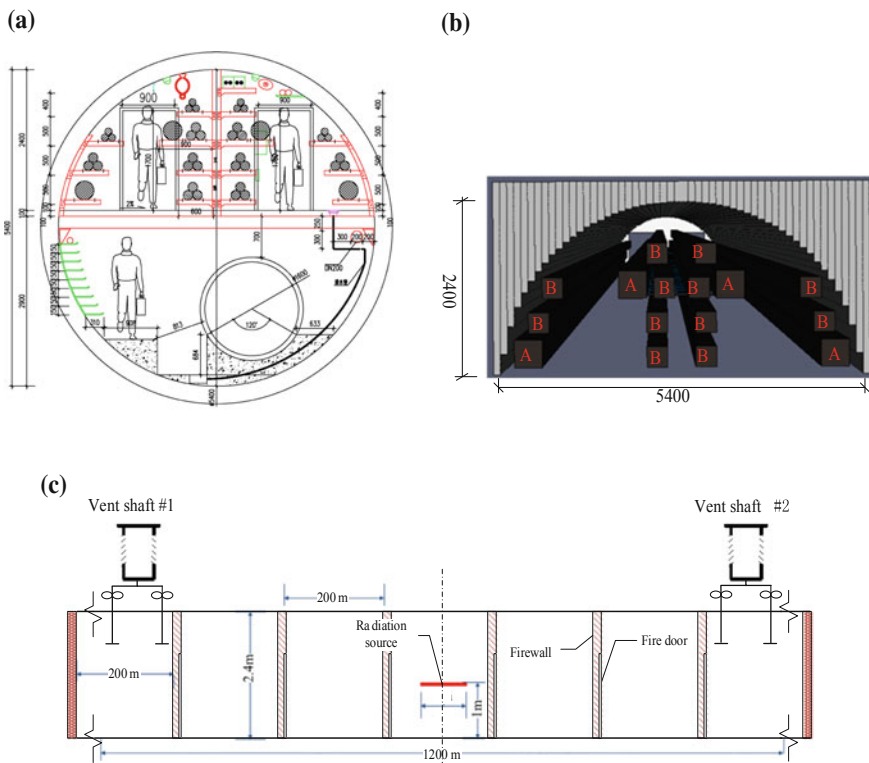
Fig. 2 Cross section of utility tunnel and cross section of numerical simulation model (dimensions in the drawings are in 'mm' except otherwise indicated): **a** cross section of utility tunnel; **b** cross section of numerical simulation model; **c** ventilation, radiation source, and fire separation

capacity of 1.5 kJ/kg K, heat conductivity of 0.2 W/m K, and a combustion heat of 2500 kJ/kg. The initial ambient temperature inside the utility tunnel is set as 20 °C, and the initial pressure is the normal atmospheric pressure. The sidewalls are concrete walls, which have a thickness of 0.2 m. The concrete has a density of 2280 kg/m^3, a specific heat capacity of 1.04 kJ/kg K, and a heat conductivity of 1.8 W/m K.

The cable is ignited by using a high-temperature thermal radiation method. With a radiation source temperature of 3000 °C, spontaneous combustion of cables is enabled.

4   Simulated Scenario and Measuring Points Arrangement

4.1   Setup of Simulated Scenario

To investigate the pattern of fire smothering in the cable compartment under different lengths of fire compartment, four different fire compartment lengths are set up in this research, which are, respectively, 200, 300, 500, and 800 m.

According to the fire smothering process described above, personnel should be first evacuated, that is, the condition of ASET (Available Safe Evacuation Time) > RSET (Required Safe Evacuation Time) must be met in the first place. Required safe evacuation time is calculated by using the following formula:

$$t_{REST} = t_b + t_c + t_s \tag{1}$$

In this research, the detection time is set at 60 s, the personnel responding time is set at 120 s and the personnel walking speed is taken as 1.2 m/s. The required safe evaluation time obtained under the four different fire compartment lengths is, respectively, 347, 430, 597, and 847 s, rounded off to 350, 450, 600, and 850 s, respectively. The four fire scenarios are as shown in Table 1.

According to FDS user guide [11], the recommended mesh size can be quantified by a non-dimensional expression $D^*/\delta x$, where D^* is a characteristic fire diameter.

$$D^* = \left(\frac{\dot{Q}}{\rho_\infty c_p T_\infty \sqrt{g}} \right)^{0.4} \tag{2}$$

Table 1   Setup of scenarios

Fire scenario	Spacing of fire compartments (m)	Fire door closing time (s)
Case 1	200	350
Case 2	300	450
Case 3	500	600
Case 4	800	850

The $D^*/\delta x$ values are recommended ranged from 4 to 16. As a result, the recommended mesh size ranges from 0.11 to 0.44 m. In this paper, the mesh size at y-axis and z-axis set as 0.2 m, and x-axis 0.4 m.

4.2 Measuring Points Arrangement

Arrangement of measuring points is as shown in Fig. 3, where A, B, C refer to the measuring point groups along the central axis of the utility tunnel cross section, which are 2.2, 1.8, and 1.4 m from the bottom surface, respectively; designations 1, 2, 3, ..., 25 standard for the 25 rows of measuring point groups and slice cross sections long length of the utility tunnel (crosswise), with a measuring point spacing of 50 m; a separate slice is provided along the length, which is located at center of the utility tunnel.
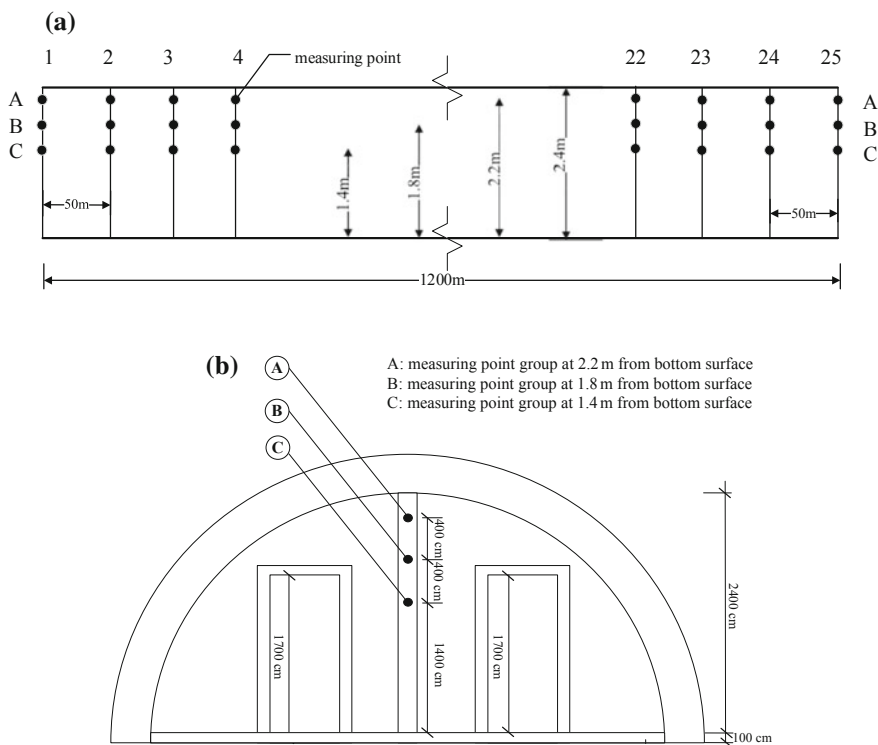

Fig. 3 Measuring point group arrangement (designations 1, 2, 3, ..., 23, 24, 25 crosswise; designations A, B, C lengthwise). **a** Crosswise arrangement of measuring points A, B, and C (spacing 50 m), **b** lengthwise arrangement of measuring point groups

5 Main Results and Analysis

5.1 Fire Development and Fire Smothering

Figure 4 shows the heat release rate curves for cable fire inside the utility tunnel under four different fire separation lengths. It can be seen that under a 200-m fire separation distance, since the oxygen content in the utility tunnel section is fairly high, combustion can still be supported after the fire doors are closed at 350 s, and thus, the heat release rate keeps on increasing until 700 s when it begins to drop. Under a 300-m fire separation distance, the heat release rate keeps on increasing until 800 s after the fire doors are closed at 450 s, before it begins to drop. Under a 500-m and 800 fire separation distances, oxygen content in the gallery section drops to a much lower value after the fire doors are closed at 600 and 850 s, and the peak release rate is reached respectively at 850 and 850 s, and thereafter since the fire doors are closed, the heat release rate gradually drops as the oxygen content becomes too low. In general, under different fire separation lengths, the heat release rate curves for cable fire tend to be basically identical.

Meanwhile, it can also be seen that the heat release rate reaches the highest value of about 5.2 MW (at 700 s) under the 200-m fire separation distance, while the maximum heat release rates under other fire separation distances are, respectively, 5.9, 5.9, and 5.9 MW, and the time used to reach the maximum heat release rates is, respectively, 810, 850, and 850 s. As the fire separation distance increases, the maximum heat release rate and the time used to reach the maximum heat release rate gradually increases, however, the increase trend gradually decreases, wherein the 500 and 800 m fire separation distances do not make any obvious difference. The temperature nephogram shown in Fig. 5 also helps prove the above patterns. Figure 5 shows the temperature nephogram within a 100-m range at the left and right

Fig. 4 Heat release rate curves for cable fire with different fire separation distances
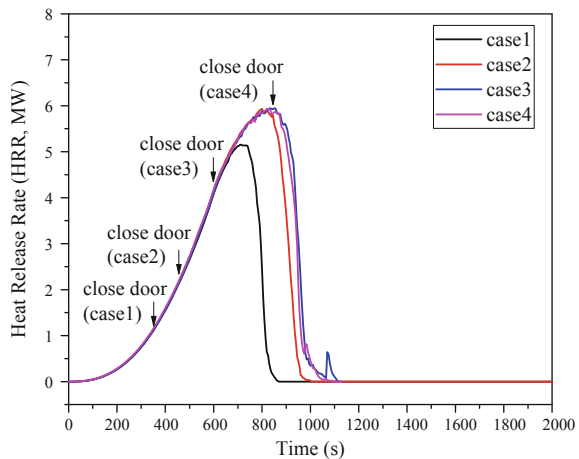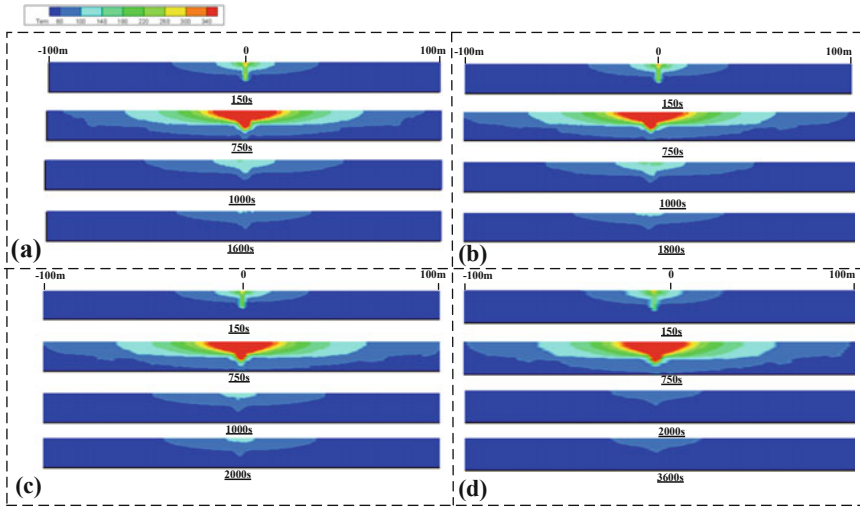
Fig. 5 Smoke temperature inside utility tunnel after ignition: **a** Case 1; **b** Case 2; **c** Case 3; **d** Case 4

Fig. 6 Maximum smoke temperature during fire
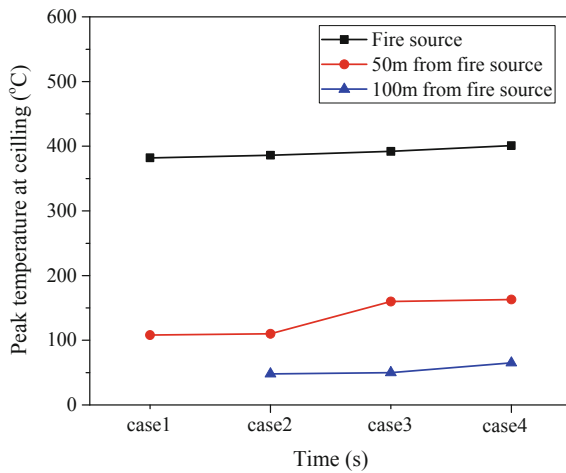
ends of the fire course, respectively, under four different fire separation distances. It can be seen from the figure that as the fire separation distance increases, the high-temperature area increases slightly, which matches the results of heat release rates.

Figure 6 shows the maximum temperature of the ceiling smoke at different distances from the fire source. This is similar to Fig. 5. As the fire separation distance increases, the maximum smoke temperature nearby at 50 and 100 m from the fire source increases slightly, which also matches with the results shown above.
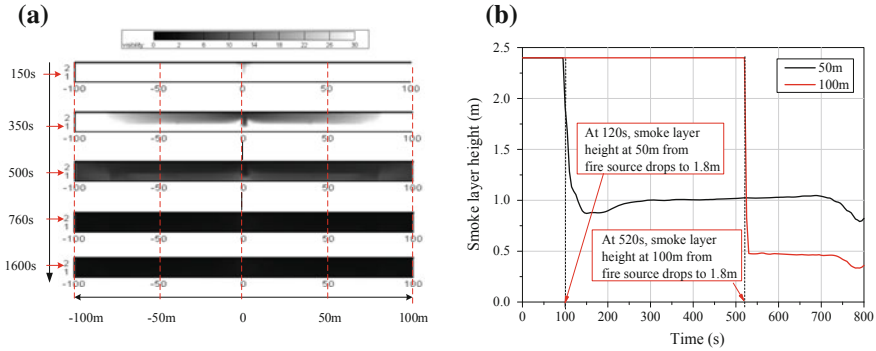
Fig. 7 Smoke layer dropping process after cable on fire (taking Case 1 as example): **a** visibility change; **b** change of smoke layer height at 50 and 100 m from fire source

Table 2 Time for smoke layer dropping to 1.8 m

Time for smoke layer height dropping to 1.8 m	50 m from fire source (s)	100 m from fire source (s)
Case 1	102	520
Case 2	97	435
Case 3	102	440
Case 4	100	430

With the development of the fire, the smoke layer will drop. Figure 7 shows the change of smoke layer inside the utility tunnel after the cable is ignited by taking Case 1 as example. It can be seen that at about 102 s, the smoke layer height at 50 m from the fire source drops to the height of a man (1.8 m), and at 520 s, it drops to the height of a man at 100 m from the fire source. Times used for the smoke layer to drop to 1.8 m height under other conditions are shown in Table 2. Times required for the smoke layer to drop to 1.8 m level at 50 m from the fire source are not quite different under different fire separation distances, and the time required for the smoke layer to drop to 1.8 m level at 100 m from the fire source in Case 1 is longer, but there is no much difference in other cases.

5.2 Post-Fire Ventilation

According to the fire smothering process for urban utility tunnel proposed in this paper (see Fig. 1), it is necessary to open the fire doors for ventilation and smoke exhaust after fire smothering is done for a certain period of time. The following is a proposition of our judging criteria for fire door opening time:

Table 3 Fire door opening time

Spacing of fire compartments (m)	Fire door closing time t_{close} (s)	Fire door opening time t_{open} (s)	$t_{open} - t_{close}$ (s)
200	350	1620	1270
300	450	1810	1360
500	600	2000	1400
800	850	3600	2750
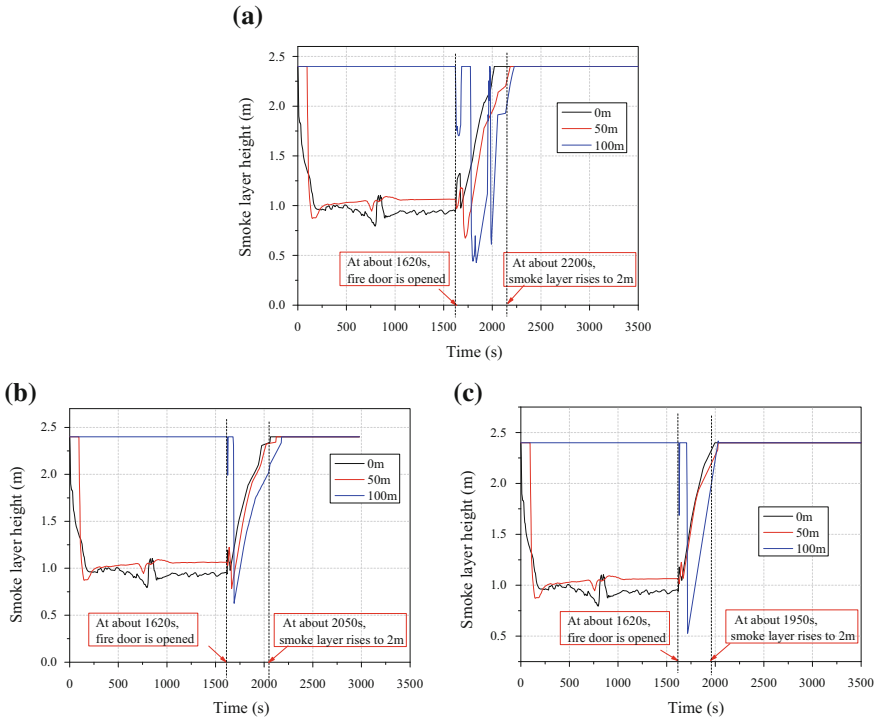
Fig. 8 Rise of smoke layer under different ventilation velocities after opening of fire door (taking Case 1 as an example): **a** 1 m/s; **b** 2 m/s; **c** 3 m/s

(1) HRR is 0;
(2) Temperature at fire source is lower than 100 °C;
(3) Temperature at 50 m from the fire source approaches the design temperature in the utility tunnel.

According to the above-mentioned preliminary judging criteria, a numerical simulation is conducted of the four cases studied in this paper. Times for opening the fire doors are as shown in Table 3.

Table 4 Smoke exhaust time under different ventilation velocities

Spacing of fire compartments (m)	Smoke exhausting time at a ventilation velocity of 1 m/s (min)	Smoke exhausting time at a ventilation velocity of 2 m/s (min)	Smoke exhausting time at a ventilation velocity of 3 m/s (min)	Shortening of smoke exhausting time when ventilation velocity increases from 1 to 2 m/s (%)	Shortening of smoke exhausting time when ventilation velocity increases from 2 to 3 m/s (%)
200	10.2	7.5	6.0	26	20
300	11.5	7.7	6.5	33	16
500	12.7	8.6	8.1	32	6
800	15.8	10.8	8.7	32	19

Figure 8 shows the rises of smoke layer at a ventilation velocity of 1, 2, and 3 m/s after the fire doors are open. It is quite apparent that a faster ventilation velocity means a quicker rising of the smoke layer. Table 4 shows the smoke exhaust time under different ventilation velocities. It can be seen that as the ventilation velocity increases from 1 to 2 m/s, the smoke exhausting time drops by 26–33%, and as the ventilation velocity increases from 2 to 3 m/s, the smoke exhausting time may drop by 6–20%. In addition, it is also discovered that no matter under what ventilation velocity, the ventilation time under 800 m fire separation distance is far longer than 200–500 m fire separation distance.

6   Conclusions

To address the issue of fire separation distance setup for urban utility tunnel, this paper studies the cable compartment fire occurring and development pattern, fire smothering, post-fire ventilation, and smoke exhausting under different fire separation distances by employing CFD numerical simulation.

This study firstly proposes a general technological process for fire smothering in urban utility tunnel according to the operating requirements of urban utility tunnel, and subsequently, all investigations in this study are based on the proposed technological process.

Looking from the results of numerical simulation, the heat release rate curves for cable fire in the compartment show the same trend under four different fire separation distances, namely 200, 300, 500, and 800 m, and the maximum HRR increases as the fire separation distance enlarges. However, the increasing trend is increasingly slow. There is not much difference for the maximum HRRs under different fire separation distances, and nor the maximum temperature inside the utility tunnel and the smoke

layer dropping speed. From the perspective of fire development control, the fire separation distance may be properly increased.

Also studied is the impact of different post-fire ventilation velocities. It is found that the smoke exhausting time under the 800 m fire separation distance is obviously longer than under other fire separation distances. As ventilation velocity increases, the smoke exhausting time shortens. However, the shortening tends to be slow with increase of the ventilation velocity. In terms of post-fire ventilation, a 500 m or shorter fire separation distance may be more suitable.

This paper believes that the present mainstream 200 m fire separation distance can be properly increased no matter from the perspective of fire spreading control or post-fire ventilation, for example, no excess of 500 m. The research results of this paper can provide theoretical basis for fire safety design and management of urban utility tunnels.

The current study mainly focuses on CFD simulations, and the simulation results are expected to be verified by model scale experiments in the near future.

References

1. Ishii, H., Kawamura, K., Ono, T., Megumi, H., et al. (1997). A fire detection system using optical fibres for utility tunnels. *Fire Safety Journal, 29,* 87–98.
2. Curiel-Esparza, J., & Canto-Perello, J. (2005). Indoor atmosphere hazard identification in person entry urban utility tunnels. *Tunnelling and Underground Space Technology, 20,* 426–434.
3. Canto-Perello, J., Curiel-Esparza, J., & Calvo, V. (2013). Criticality and threat analysis on utility tunnels for planning security policies of utilities in urban underground space. *Expert Systems with Applications, 40,* 4707–4714.
4. Canto-Perello, J., & Curiel-Esparza, J. (2015). No access risks and potential hazards in utility tunnels for urban areas. *Proceedings of the Institution of Civil Engineers-Municipal Engineer, 156,* 51–56.
5. Jiang, L., Chen, J., & Li, J. (2010). Seismic response of underground utility tunnels: shaking table testing and FEM analysis. *Earthquake Engineering and Engineering Vibration, 9,* 555–567.
6. Chen, J., Shi, X., & Li, J. (2010). Shaking table test of utility tunnel under non-uniform earthquake wave excitation. *Soil Dynamics and Earthquake Engineering, 30,* 1400–1416.
7. Chen, J., Jiang, L., Li, J., et al. (2012). Numerical simulation of shaking table test on utility tunnel under non-uniform earthquake excitation. *Tunnelling and Underground Space Technology, 30,* 205–216.
8. Sun, D. (2014). A hydraulic power plant cable fire simulations at different ventilation conditions. *Sichuan Electric Power Technology, 37*(03), 91–94.

9. Du, C. (2017). *Analysis of temperature field distribution and smoke flow characteristics of cable fire in underground pipe gallery*. China University of Mining and Technology.
10. Hao, G. (2017). *Simulation study on the fire smoke in the cable compartment*. Xi'an University of Architecture and Technology.
11. Mcgrattan, K. B., Hostikka, S., & Floyd, J. E. (2007). Fire dynamics simulator (version 5): User's guide. *NIST Special Publication, 4*(4), 206–207.

Numerical Studies on the Smoke Control Parameters of Water Mist Screens with Transverse Ventilation System in Tunnel Fires

Qiang Liang, Hui Xu, Youbo Huang and Yanfeng Li

Abstract Emergency ventilation systems are commonly used for smoke control during tunnel fires. Numerical results show that the fire and smoke would be confined effectively by the water mist screen and transverse ventilation system (WMSTV system) system, and the environment inside the confined zone would be suitable for occupants' evacuation and fire fighting. In this paper, the smoke control parameters of WMSTV system are proposed. The visibility distributions and smoke extraction efficiency are analyzed by FDS simulation. The results show that the minimum spacing distance between smoke vents should not be less than 40 m, while the maximum spacing distance should not exceed 60 m for 30 MW of fire. The spacing distance between the screen and vent is suggested to fall in 30–45 m. Two vents are recommended in the control zone with the screen spacing of 120 and 150 m. Four vents are recommended in the control zone with the screen spacing of 180 m.

Keywords Smoke control · Water mist screen transverse ventilation · Tunnel fire · Visibility · Smoke extraction

Nomenclature

D^*	Characteristic fire diameter (–)
H	Heat release rate from fire (kW)
T_0	Temperature of ambient (K)C
σ	Empirical constants (–)
d_m	Median droplet diameter (µm)
η_i	The smoke extraction efficiency of vent i
Q_i	The smoke extraction rate of the single vent i

Q. Liang (✉) · H. Xu
The Chinese People's Armed Police Forces Academy, No. 220 Xi'chang Road, Langfang 065000, China
e-mail: 68714484@qq.com

Y. Huang · Y. Li
Beijing University of Technology, No. 100, Pingleyuan, Chaoyang District, Beijing 100124, China

L_1 Distance of smoke vents (m)
ρ_0 Density of ambient (kg/m^3)
c_p Constant pressure specific heat [kJ/(kg K)]
g Acceleration of gravity (m/s^2)
d Droplet diameter (μm)
η Smoke extraction efficiency
Q The total smoke generation rate (kg/s)
L Distance of water mist screens (m)
L_2 Distance of vent with water mist screen (m)

1 Introduction

According to statistics, more than 80% of the deaths in fires are caused by smoke [1]. Smoke control is an important research content of fire science. The smoke spreading process in different forms of building space is different. As a typical building structure, narrow and long passage is not only the tie of all kinds of building space but also the only way to evacuate the crowd. The consequences cannot be imagined once the smoke gushes into the building. The common narrow and long passages in engineering include highway and railway tunnels, subway tunnels, urban underground traffic tunnels, and corridors inside buildings [2].

Fire researchers have conducted a number of scientific studies on narrow-lane fires, mainly including the migration of toxic components of smoke gas, the transport and control, of smoke and the application of water mist fire extinguishing. Huo [3] used a small-scale model experiment of 120 cm (length) * 16 cm (width) * 20 cm (height) to study the movement characteristics of hot smoke in the vicinity of the upper wall of a rectangular inclined channel under natural convection when a fire occurs in a rectangular inclined channel of finite length. Hu [4] has studied the smoke control effect of the air curtain in narrow and long passages. Yuan [5] used 1/20 small-scale model experiment to study the smoke exhaust characteristics of urban tunnel fire combined ventilation; Dong [6] used large-scale full-scale experiment to study the fire isolation effect of water curtain. The results show that the heat insulation performance of the water curtain is good, but the reason for the poor smoke prevention effect is that the water curtain is not only discontinuous water particles but also large. And the porosity of the water curtain is high. Fernandez [7], Felis [8], and Severino [9] proposed a double-stream-twin-jet (DS-TJ) method to control the longitudinal spread of smoke gas in tunnels. This method improved the air curtain, but the smoke gas was always circulated in the tunnel. If the smoke gas emission was not considered, the smoke control will lose its function. Fang [10] uses 10:1 model test and solid tunnel fire test to prove that water spray can effectively reduce tunnel temperature and prevent smoke and heat from propagating downstream. The experimental water spray pressure is 0.3 and 0.5 MPa. Formaldehyde is used as fuel without carbon black particles, and only changes in temperature parameters
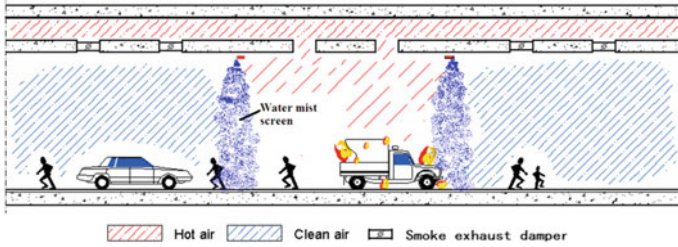
Fig. 1 Cross section of the WMSTV system in operation

are analyzed by him. Water mist, as an efficient, water-saving and environmental protection fire extinguishing method, has also been applied to tunnel fires [11, 12]. Its main function is to extinguish vehicle and solid cargo fires in the tunnel. In the study of water mist fire control, scholars have observed that water mist not only has a good cooling effect but also can improve the visibility of fire field by washing dust particles [10, 13, 14].

According to the previous researches, it can be concluded that most previous studies focused on the smoke compartmentation in tunnels to improve transverse ventilation efficiency. A new smoke control system, which is composed of water mist screens and transverse ventilation system (WMSTV system) as shown in Fig. 1, was proposed by Liang [15]. The system of water mist screens was used to confine the smoke and fire in a restrained zone. The length of the restrained zone will be doubled when a fire directly below the water mist screen. Numerical method with a large eddy simulation model (LES) has been used in this research. The traditional natural ventilation system and transverse ventilation system without water assistance are used for comparison of the effectiveness WMSTV. Based on the previous study by Liang [15], the selection of key parameters for the application of WMSTV system can be optimized by simulation using FDS. Through the analysis of the visibility distribution and the extraction efficiency of every smoke vents, both the control parameters of the transverse ventilation system, including the numbers of vents and the distances between different vents, and of the water mist screen, including the distance between different screens and between the smoke vent and the screen, can be determined. The objective of this paper is to present a data set of simulation for reference when drafting codes or conducting the relative experiments.

2 Numerical Experiments

CFD has been widely used in tunnel fire researches. Fire Dynamics Simulator (FDS, Version 5.0) developed by NIST is selected for numerical simulations of thermal driven flow in this study. Previous studies have shown that FDS is an effective and reliable numerical tool for tunnel fire study.

2.1 FDS

Fire Dynamic Simulation (FDS) software has been regarded as a practical tool for simulating fire-induced environment as it solves numerically a set of the Navier–Stokes equations for thermally driven flow. It includes both direct numerical simulation (DNS) model and large eddy simulation (LES) model [14]. It is used to conduct the numerical simulation validated by an experimental test in Northeastern University, and FDS is used to numerically investigate the different droplet sizes on the fire suppression/extinguishment mechanisms [15, 16]. Lagrangian particles can be used to represent a wide variety of objects that are too small to resolve on the numerical grid. In FDS spray modeling, Lagrangian particles are used to represent water droplets. The spray characteristics are defined at the injection point by a set of parameters including the fluid thermal properties, droplet size distribution, and injection features. The droplet size distribution is denoted by Rosin–Rammler and log-normal distributions.

$$
F(d) = \begin{cases} \frac{1}{\sqrt{2\pi}} \int_0^d \frac{1}{\sigma d'} e^{-\frac{[\ln(d'/d_m)^2]}{2\sigma^2}} dd' & (d \leq d_m) \\ 1 - e^{-0.693 \left(\frac{d}{d_m}\right)^{\gamma}} & (d_m < d) \end{cases}
\tag{1}
$$

2.2 Physical Model and Grid Sizes

The model tunnel has a rectangular cross section of 10 m (W) × 5 m (H) and a length of 600 m, as shown in Fig. 2. The height of the smoke exhaust duct is 2 m, which has the same width with the tunnel.

Grid size sensitivity studies have shown that the accuracy of the model depends on the characteristic fire diameter D^* [16], which is defined as:

$$
D^* = \left(\frac{H}{\rho_0 c_p T_0 \sqrt{g}} \right)^{2/5}
\tag{2}
$$
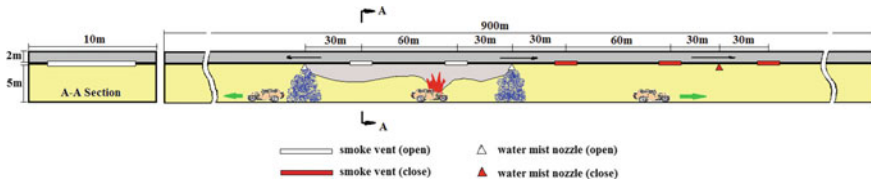
Fig. 2 Schematic diagram of the tunnel and the layout of smoke vents and water mist screens

Table 1 Computation domains and the grid number

	The domain of mesh (m)			Grid size (m)			Grid number
	x	y	z	δx	δy	δz	
Mesh 1	−5 to 5	−300 to −100	0–7.5	0.5	0.5	0.5	20 × 400 × 15
Mesh 2	−5 to 5	−100 to 100	0–7.5	0.25	0.2	0.25	40 × 1000 × 30
Mesh 3	−5 to 5	100 to 300	0–7.5	0.5	0.5	0.5	20 × 400 × 15

It is suggested that the cell size at the near field of the fire source should be 0.05–0.1D* , while the larger grid size can be used in the far field which should not exceed 0.5D* [19]. Mawhinney indicated that refining the grid size consumed more computation time without significantly improving the prediction accuracy [20]. According to NFPA 502 [21], the fire load in this study is set as 30 MW. For a 30 MW fire, D* is 3.74 m, 0.1D* is 0.34 m, and 0.5D* is 1.87 m. The computation zones with different mesh sizes are listed in Table 1.

2.3 Fire Scenarios

To investigate the parameters of WMSTV system, nine fire scenarios with different distance intervals of water mist screens and smoke vents are set. The test matrix of simulations is given in Table 2, and some typical scenarios are shown in Fig. 3. The heat release rate of fire is 30 MW. The exhaust fans are located at both ends of the smoke duct with a flow rate of 120 m³/s. The ends of the tunnel are set as an open boundary in the simulations. Both the ambient temperature is 20.0 °C. The water mist screen consists of 14 nozzles, and the layout is shown in Fig. 4. The flow rate

Table 2 Fire scenarios in numerical simulation

Scenario number	Distance of water mist screens (m)	Water mist screens position	Numbers of smoke vent	Distance of smoke vents (m)	Distance of vent with water mist (m)
1	120	−60 m/60 m	2	60	30
2			3	30	30
3			4	20	30
4	150	−75 m/75 m	2	60	45
5			3	45	30
6			4	30	30
7	180	−90 m/90 m	2	60	60
8			3	60	30
9			4	40	30
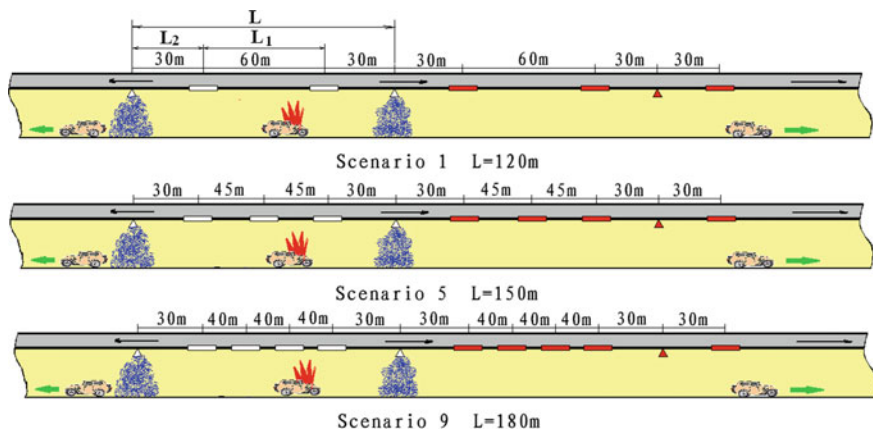
Fig. 3 Schematic diagram of the tunnel and the layout of smoke vents and water mist screens
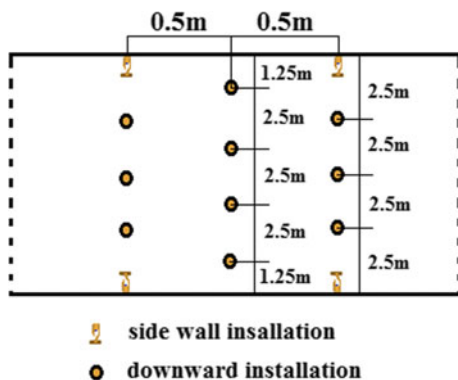
Fig. 4 Schematic diagram of the water mist nozzle arrangement

of each nozzle is 30 L/min. The initial droplet velocity is 10 m/s, and the average particle diameter is 300 μm. The injection pressure is 10 MPa. The mass flux of the water mist droplets is from 0 to 0.75 kg/m^2/s.

2.4 Calculation of Smoke Extraction Efficiency

The smoke extraction efficiency of the WMSTV system is defined as the percentage of the sum of the smoke extraction rate by all the smoke vents and the smoke generation rate [22]. Then, the smoke extraction efficiency for a single vent can be defined as the percentage of its smoke extraction rate by all the smoke vents and the smoke generation rate. By supposed n smoke vents were set in a WMSTV system, the

Table 3 CO_2 generation rate of diesel combustion

Heat release rate of fire source (MW)	Heat of combustion (kJ/kg)	Mass loss rate (kg/s)	CO_2 generation rate (kg/s)
30	46,000	0.652	8.67

smoke extraction efficiency of vent i can be calculated as:

$$\eta_i = \frac{Q_i}{Q} \times 100\% \tag{3}$$

Therefore, the smoke extraction efficiency of the WMSTV system is:

$$\eta = \frac{\sum_i^n Q_i}{Q} \times 100\% \tag{4}$$

where Q_i is the smoke extraction rate of the single vent i (kg/s), and Q is the total smoke generation rate (kg/s).

In FDS simulation, the smoke generation rate can be replaced by the generation rate of CO_2 in the burning process, and specifying a DEVC with a 'VOLUME FRACTION' and a SPEC_ID of CARBON DIOXIDE will output the volume fraction of carbon dioxide in the gas phase. Thus, the smoke extraction rate for a single vent can be represented by its extraction rate of CO_2, and the smoke extraction efficiency can be expressed as:

$$\eta = \frac{\sum_i^n Q_{CO_2,i}}{Q_{CO_2}} \times 100\% \tag{5}$$

where $Q_{CO_2,i}$ is the CO_2 extraction rate of the single vent i (kg/s), and Q_{CO_2} is the total CO_2 generation rate (kg/s).

Kerosene ($C_{14}H_{30}$) is selected as fuel in the simulation, of which the chemical reaction is:

$$C_{14}H_{30} + 20.82O_2 \rightarrow 13.29CO_2 + 0.085CO + 14.97H_2O + 0.693soot \tag{6}$$
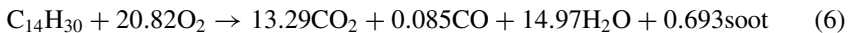
So the CO_2 generation rate with different heat release rate can be calculated, and the results are shown in Table 3.

3 Results and Discussions

In tunnel fire scenarios, the ceiling structure of the tunnel can be easily destructed by the high temperature. And the smoke is harmful to human beings. According to Liang's simulation [15], the decrease in visibility is the most critical factor that makes

the evacuation more difficult in a tunnel fire. For this reason, the design parameters of the WMSTV system are determined through the analysis of the factors, including the visible distance and the smoke extraction efficiency, which significantly affect the evacuation.

3.1 Visibility Distributions

The distributions of visible distance in different scenarios with the same number of smoke vents and the different distances between the water mist screens are shown in Figs. 5, 6, and 7.

As in Fig. 5, the smoke can be limited between the water mist screens in all the three scenarios with two smoke vents in every two screens, where the visible distance below 2 m high can be kept above 10 m. However, with the smoke dragged down by the water mist, the visible distance in the area between the water mist screen and the smoke vent is reduced to an unacceptable level for evacuation. And the range of this area is increased, the distance between the vent and screen also increased. According to experimental observations, the maximum moving distance for human beings is about 20–30 m away in fire smoke, for which the farthest distance from
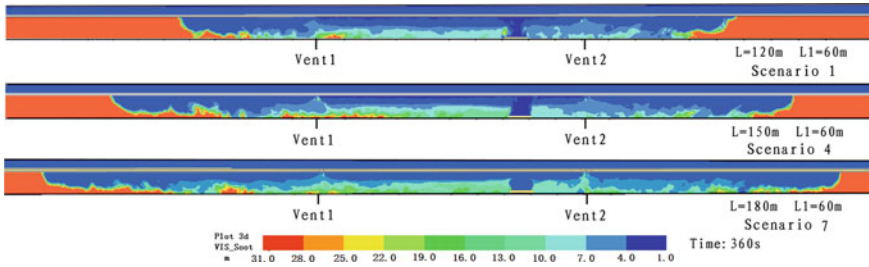

Fig. 5 Visibility distributions of two vents with different water screen distance
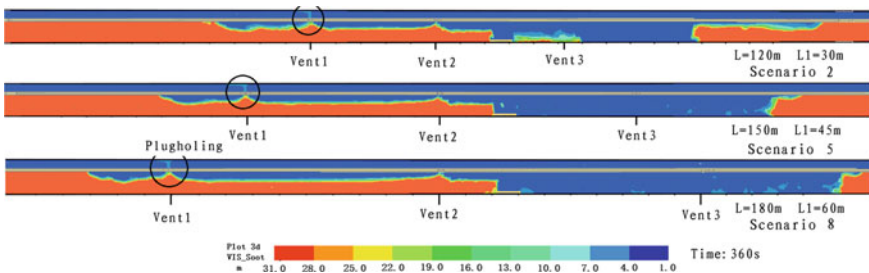

Fig. 6 Visibility distributions of three vents with different water screen distance
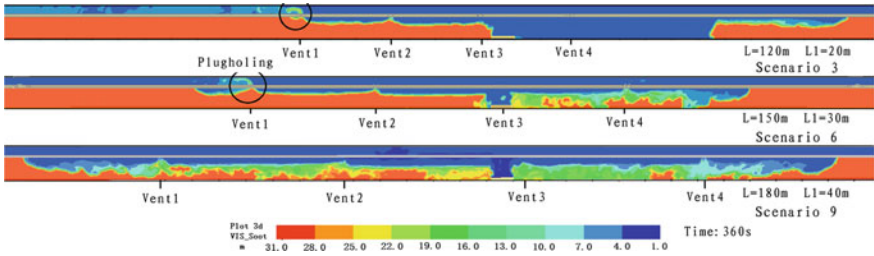
Fig. 7 Visibility distributions of four vents with different water screen distance

any location to the nearest smoke vent in the building is limited in 30 m in the Code for Fire Protection Design of Building in China. So the distance between the water mist screen and smoke vent can reasonably be 30 m.

From Fig. 6, it can be seen that the WMSTV system failed to control the smoke in the condition that three smoke vents are set between every two screens. Although the smoke diffusion distance is also limited, the visibility is reduced severely that the visible distance below 2 m high is decreased to 1 m, which is hard for evacuation and rescue operation. What's more, plugholing can be observed at the smoke vent on the left side of the fire source, which significantly reduces the smoke extraction efficiency that will be illustrated in the analysis of smoke extraction efficiency below. At the same time, the flow rate of smoke to the vent is slowed down by the extraction of fresh air in replace of smoke, which brought smoke control much more difficulty to the water mist screen on the other side.

It can be seen in Fig. 7 that, the shorter distance between smoke vents leads to the worse extraction result when the number of vents between two water mist screens is upgraded to four. In Scenario 3 where the water mist screen spacing is 120 m and the smoke vent spacing is 20 m, smoke is successfully controlled in the left side by the water mist screen throughout the duration of 360 s. But on the right side of the fire source, the smoke vents are installed too close to control the smoke effectively, in which the severe plugholing effect can be obviously observed at Vent 1. For Scenario 6 where the water screen spacing is increased to 150 m and the smoke vent spacing is increased by 10 m, smoke control effect of the WMSTV system is improved with the water mist screen on the left side closed in 360 s, but plugholing has still existed at Vent 1. While the water screen spacing is enlarged to 180 m with the smoke vent spacing increased to 40 m, the water mist screens on both sides are opened, where smoke is completely limited in the 180 m spacing through the vent extraction, and plugholing is successfully eliminated. The visibility below 2 m can be kept above 16 and 7 m, respectively, between water mist screens, which also demonstrate the better smoke extraction effectiveness.

From the analysis of scenarios with different water mist screen spacing above, it can be seen that the smoke control effectiveness is strongly affected by the number of smoke extraction vents and the spacing distance between them. It is suggested that minimum spacing distance between smoke vents should not be less than 40 m, while

the maximum spacing distance should not exceed 60 m. A suitable spacing distance between the water mist screen and smoke extraction vent in the range of 30–45 m is recommended.

3.2   Smoke Extraction Efficiency

In this section, the smoke extraction effect is analyzed in the view of smoke extraction efficiency. The CO_2 extraction rate for single vents and open time of the water mists screen are listed in Table 4. The calculation results for smoke extraction efficiency of both the single vent and the total WMSTV system is shown in Table 5.

From the results of the four scenarios where one smoke vent is set between water mist screens listed below, it is failed to control the smoke with the only single vent. In scenarios with the screen spacing distance of 60, 120, 150, and 180 m, the smoke extraction efficiency is 14.88, 15.69, 16.38, and 16.6%, respectively, which is too inefficient to control the smoke. Large amount of smoke spreading through the water screen on the right side is cooled and dragged down by the water mist which makes the smoke layer disturbed so severely that the tunnel space on the right side of the fire source is quickly filled with the settling smoke. On the left side of the fire source, the violent plugholing effect can be clearly observed and water mist screen on the left-hand side has not opened in 360 s.

In scenarios where two smoke vents are located between the screens, the smoke is successfully limited in the spacing between screens with the screens on both sides opened which guaranteeing the smoke separation. For this reason, the smoke can only be extracted out from the smoke vents, which greatly improved the smoke extraction efficiency that the total efficiency in Scenario 1, Scenario 4, and Scenario 7 have upgraded to 89.85, 81.11, and 82.93%, respectively. The extraction efficiency for a single vent is dependent on its distance to the fire source. The nearer distance corresponds to greater efficiency. For example, in Scenario 1 where the screen spacing is 120 m, the extraction efficiency of Vent 1 with a distance of 45 m is 27.22%, while the extraction efficiency of Vent 2 with a distance of 15 m is 62.63%.

In Scenario 2, 5, and 8, three smoke extraction vents are located in the water mist screen spacing. In Scenario 2 with a 120 m screen distance, the screen on both sides is opened. However, the total smoke extraction rate can only reach 22.45% and the single vent extraction rate is low, for the 30 m smoke vent spacing is so short that plugholing effect can be observed at both the two smoke vents on the left side. On the right side of the fire source, the water mist screen is failed to stop the smoke from spreading through. And in Scenario 5 and 8, only the screen on one side is opened, which cannot control the smoke spreading. In addition, the smoke extraction efficiencies are only 22.28 and 19.33%, respectively, in Scenario 5 and 8, which is too low to accept. Thus, none of the three scenarios should be taken into operation in engineering applications.

When the number of smoke vents is added up to four, different results occur in Scenario 3, 6, and 9. Both in Scenario 3 and 6, with the screen spacing distance, is 120

Table 4 Open time and CO_2 extraction rate at smoke vents

Scenario number	Vent 1		Vent 2		Vent 3		Vent 4		Water mist screens	
	Open time (s)	CO_2 flow rate (kg/s)	Open time (s)	CO_2 flow rate (kg/s)	Open time (s)	CO_2 flow rate (kg/s)	Open time (s)	CO_2 flow rate (kg/s)	Open time (s)	
									1	2
1	16.7	2.36	4.81	5.43					36	27.4
2	20.7	0.29	4.45	0.772	4.81	0.884			120	24.8
3	21.5	0.0813	7.7	0.378	3.34	0.713	4.82	0.757		22.9
4	16.7	2.02	4.81	5.012					56.2	42.2
5	37.4	0.279	4.45	0.806	9.26	0.847				29.2
6	51.4	0.156	11.8	0.259	4.35	1.704	13	0.56		56.6
7	4.8	1.98	16.3	5.21					82.5	62.5
8	61.1	0.165	4.81	0.816	17.8	0.695				38.9
9	42.6	1.357	13.3	2.108	5.57	2.386	23	1.423	107	65.9

Table 5 Smoke extraction efficiency

Scenario number	Smoke extraction efficiency (%)				Overall efficiency (%)
	Vent 1	Vent 2	Vent 3	Vent 4	
1	27.22	62.63			89.85
2	3.35	8.9	10.2		22.45
3	0.94	4.36	8.22	8.73	22.25
4	23.3	57.8			81.11
5	3.22	9.3	9.76		22.28
6	1.8	3	19.65	6.45	30.9
7	22.84	60.09			82.93
8	1.9	9.41	8.02		19.33
9	15.65	24.31	27.52	16.41	83.9

and 150 m, respectively, only the water mist screen on the right side is opened and the total smoke extraction efficiency is 22.25 and 30.90%, respectively, which seems still to be low. It is caused by the excessively short spacing distance, which is only 20 m in Scenario 3 and 30 m in Scenario 6, because not only will the control effect of water screen be decreased but also severe plugholing effect might be resulted if the spacing distance of vents gets too short. While in Scenario 9 the vent spacing distance is added up to 40 m, the smoke is successfully controlled with relatively high efficiency by the WMSTV system. Therefore, it is suggested that the number of smoke vents installed between the water screens should be dependent on the screen spacing, and the minimum distance of 40 m is recommended.

4 Conclusion

Nine scenarios of the application of WMSTV system in tunnel fire smoke control are simulated and analyzed in the view of the effectiveness and efficiency in this chapter. It can be concluded that the water mist screen spacing distance should be determined concerning the total length of the evacuation path or refuge path in tunnels, and the number of smoke vents located between the water mist screens should be determined in accordance with the screen spacing distance. The detailed conclusion can be listed as follows:

1. In the fire scenario with fire source of which heat release rate is 30 MW, the minimum spacing distance between smoke vents should not be less than 40 m, while the maximum spacing distance should not exceed 60 m.
2. The spacing distance between the screen and vent is suggested to fall in 30–45 m. Two vents are recommended in the control zone with the screen spacing of 120 and 150 m. Four vents are recommended in the control zone with the screen spacing of 180 m.

3. All the result is based on the simulation in FDS, which is still needed to be further proved by experiment.

References

1. Tong, Z., Yin, Y., Huang, Q., & Lin, F. (2005). Review of quantitative assessment methods on fire smoke toxicity. *Journal of Safety and Environment*, *5*(40), 101–105.
2. Zhang, J. (2012). *Studies of the generation and distribution of CO in the tunnel model* (pp. 1–2). China: University of Science and Technology of China.
3. Huo, Y., & Zhao, J. (2015). Temperature characteristics near the ceiling of an inclined channel with finite length in case of fire. *Journal of Harbin Engineering University, 36*(4), 461–466.
4. Hu, L. H., Zhou, J. W., Huo, R., Peng, W., & Wang, H. B. (2008). Confinement of fire-induced smoke and carbon monoxide transportation by air curtain in channels. *Journal of Hazardous Materials, 156,* 327–334.
5. Yuan, J., Fang, Z., Tang, Z., & Sun, J. (2010). Study of smoke exhaust of combined ventilation system in urban tunnel fires. *Engineering Journal of Wuhan University*, *43*(6), 738–742.
6. Dong, H., Zou, G., & Gao Y. (2002). Large scale fire experiment system with laser devices checking smoke blockage by water curtain. *Journal of Harbin Engineering University, 23*(5), 80–83.
7. Fernández, J. A., Elicer-Cortés, J. C., Valencia, A., Pavageau, M., & Gupta, S. (2007). Comparison of low-cost two-equation turbulence models for prediction flow dynamics in twin-jets devices. *International Communications in Heat and Mass Transfer, 34,* 570–578.
8. Felis, F., Pavageau, M., Elicer-Cortés, J. C., & Dassonville, T. (2010). Simultaneous measurements of temperature and velocity fluctuations in a double stream-twin jet air curtain for heat confinement in case of tunnel fire. *International Communications in Heat and Mass Transfer, 37,* 1191–1196.
9. Severino, G., Elicer-Cortés, J. C., & Fuentes, A. (2013). Characterization of a diffusion flame inside a scale tunnel using double stream-twin jets air curtains. *Fire Safety Journal, 62,* 264–271.
10. Fang, Z., Luo, K., Sun, J., Wang, J., & Yuan, J. Experimental study of using water mist segment as a fire compartment in tunnels. *48*(5), 673–679.
11. Blanchard, E., Fromy, P., & Carlotti, P. (2014). Experimental and numerical study of the interaction between water mist and fire in an intermediate test tunnel. *Fire Technology, 50,* 565–587.
12. Zhang, P., Li, N., Zhang, X., et al. (2011). Study on fire suppression effects by coupling water mist with smoke exhaust in a highway tunnel. *Journal of Jianzhu University (Natural Science), 27*(1), 106–111.
13. Zhang, X. (2001). Design and experimental study of dusting system by fine water spray. *Industrial Safety and Environmental Protection, 27*(8), 1–4.
14. Pan, L. (2011). *Study on the characteristics of smoke stratified transportation with smoke control in tunnel* (pp. 125–126). University of Science and Technology of China.
15. Liang, Q., Li, Y., Li, J., Xu, H., & Li, K. (2017). Numerical studies on the smoke control by water mist screens with transverse ventilation in tunnel fires. *Tunnelling and Underground Space Technology, 64,* 177–183.
16. McGrattan, K., Hostikka, S., Floyd, J., Baum, H., Rehm, R., Mell, W., et al. (2010). *Fire dynamics simulator (Version 5)-technical reference guide*. NIST Special Publication 1018-5. Gaithersburg, MD: National Institute of Standards and Technology.

17. Ferng, Y.-M., & Liu, C.-H. (2011). Numerically investigating fire suppression mechanisms for the water mist with various droplet sizes through FDS code. *Nuclear Engineering and Design, 241*, 3142–3148.
18. Yang, J., Zhang, Y., & Zhang, P. (2018). Numerical simulation on water mist fire suppression effects and mechanisms in hot and high humidity surroundings. *Procedia Engineering*, *211*, 881–887.
19. Petterson, N. M. (2002). *Assessing the feasibility of reducing the grid resolution in FDS field modelling*. Fire Engineering Research Report. Christchurch, New Zealand: School of Engineering, University of Canterbury.
20. Mawhinney, J. R., & Trelles, J. (2010). Performance testing of fire protection systems in tunnels: Integrating test data with CFD simulations. In *Fourth International Symposium on Tunnel Safety and Security*, Frankfurt am Main, Germany.
21. National Fire Protection Association. (2011). *NFPA 502: Standard for road tunnels, bridges, and other limited access highways*. Quincy, MA: National Fire Protection Association.
22. Yan, S. X., Wu, X. P., & Wang, D. (2011). Study of the performance of smoke control under non-uniform smoke exhaust velocity. *Procedia Engineering, 11,* 385–393.

Effects of Tunnel Length on Combustion Efficiency in Tunnel Fires

Tasuku Ishikawa, Keita Kasumi and Futoshi Tanaka

Abstract Combustion efficiency in tunnel fires was measured using a 1:20 scale model tunnel with a 0.25-m height, H, while varying the length of the model tunnel, L, as the experimental parameter. A series of fire experiments was conducted to confirm whether combustion efficiency was affected by the tunnel length, L. A dimensionless tunnel length defined as $L^* = L/H$ was selected as $L^* = 8$, 16, 24, 32, 40, and 48, corresponding 40–240 m in full scale. The results showed that combustion efficiency was not affected by the dimensionless tunnel length ranging from $L^* = 8$–32, and its average value was 90%. However, when the dimensionless tunnel length was $L^* = 40$ or more, part of the smoke flowing under the ceiling of the model tunnel descended to the floor, and the smoke descent phenomenon dramatically changed the flow dynamics of the smoke. As a result, the flame on the gas burner became unstable, and ultimately the ghosting flame phenomenon was observed close to the fire source. We qualitatively discussed the cause of the ghosting flame phenomenon, in addition to combustion efficiency.

Keywords Combustion efficiency · Model experiment · Oxygen consumption method · Temperature distribution · Ghosting flame

Nomenclature

B	Bias limit
C_p	Specific heat at constant pressure (kJ/kg K)
E'	Net heat of combustion of oxygen consumed ($E' = 17.2$ MJ/m^3)

T. Ishikawa · K. Kasumi
Mechanical Engineering, Graduate School of Engineering, University of Fukui, 3-9-1 Bunkyo, Fukui-shi, Fukui 910-8507, Japan

F. Tanaka (✉)
Mechanical Engineering, Faculty of Engineering, University of Fukui, 3-9-1 Bunkyo, Fukui-shi, Fukui 910-8507, Japan
e-mail: f-tanaka@u-fukui.ac.jp

E'' Net heat of combustion of oxygen consumed in the burning of carbon monoxide ($E'' = 23.1$ MJ/m^3)

f Fraction of depleted oxygen going into the formation of carbon monoxide (–)

g Gravitational acceleration (m/s^2)

H Tunnel height (m)

ΔH_T Lower calorific value of propane gas ($\Delta H_T = 46 \times 10^3$ kJ/kg)

L Tunnel length (m), length (m)

$\dot{m}$ Mass flow rate of the propane gas (kg/s)

Q Heat release rate (kW)

Q_{ch} Chemical heat release rate (kW)

Q_T Heat release rate for complete combustion (kW)

$S\bar{x}$ Precision index of average

t Student's t value (–), time (s)

T Temperature (K)

ΔT Rise in temperature (K)

U Measurement uncertainty with a 95% confidence level

V Velocity (m/s)

V_A Volume flow rate air referred to standard conditions (m^3/s)

x X-coordinate (m)

X_i Volume fraction of gas species i (–)

Greek symbols

χ Combustion efficiency (–)

ϕ Fraction of oxygen-depleted (–)

γ Scale ratio (–)

θ_i Sensitivity coefficient for a chemical heat release rate of a parameter i (e.g. $\theta_T = \partial Q_{ch}/\partial T$)

Superscripts

*   Dimensionless value

Subscripts

0   Ambient condition

1 Introduction

Combustion efficiency is an important parameter in the field of tunnel fire research. Normally, combustion efficiency, χ, is defined as the ratio of the chemical heat of combustion, Q_{ch}, to net heat of complete combustion, Q_T, that is, $\chi = Q_{ch}/Q_T$ [1]. In a number of studies on tunnel fires, the value of combustion efficiency measured by free burning in an open space has been used for estimating the chemical heat release rate from the mass loss rate of fuel burning in tunnel fires [2]. However, it has not yet been clarified whether the value of combustion efficiency estimated by free burning in an open space accurately corresponds to that of combustion efficiency in tunnel fires regardless of the fire scale, type of fuel, tunnel geometry, and so on. For instance, combustion efficiency in tunnel fires may decrease with an increase in tunnel length. If the value of combustion efficiency in tunnel fires can be estimated, the chemical heat release rate can be accurately calculated by multiplying the heat release rate under the assumption of complete combustion estimated based on the mass loss rate for fuel burning by the value of combustion efficiency. As a result, the distribution of the rise in temperature below the ceiling of a tunnel [3], the height of the smoke layer flowing under the tunnel ceiling [4], and the mass flow rate of smoke [5] can be accurately estimated by using the chemical heat release rate.

In this study, the chemical heat release rate, Q_{ch}, was measured by the oxygen consumption method [6], and the heat release rate under the assumption of complete combustion, Q_T, was estimated by multiplying the mass loss rate of fuel burning by the chemical heat of combustion of the fuel [1]. Based on the combustion efficiency measured by a series of fire experiments using 1:20 scale model tunnels with different lengths, we examined the effects of tunnel length on combustion efficiency in a tunnel fire. Furthermore, we found that the smoke descent phenomenon dramatically changed the flow dynamics of smoke in a tunnel, and the ghosting flame phenomenon occurred close to the fire. We qualitatively discussed the reason for the occurrence of ghosting flame in addition to the effect of tunnel length on combustion efficiency.

2 Experimental Apparatus

Table 1 lists the scaling correlations based on Froude's scaling law used for our fire experiments [7]. Figure 1a shows a schematic diagram of the 1:20 scale model tunnel. The tunnel cross section was rectangular with an aspect ratio of unity. The model tunnel was 0.25 m wide (corresponding to 5 m in full scale), 0.25 m high (5 m in full scale), and 2–12 m long (40–240 m in full scale). The length of the model tunnel was chosen as an experimental parameter. Following the suggestion of Vauquelin and Telle [8], a half tunnel (one end closed) was constructed with its plane of symmetry at the position of a fire source, assuming that the smoke produced by a fire would flow in bilateral symmetric directions. The model tunnel was made of autoclaved lightweight aerated concrete (ALC) board. ALC was chosen because its
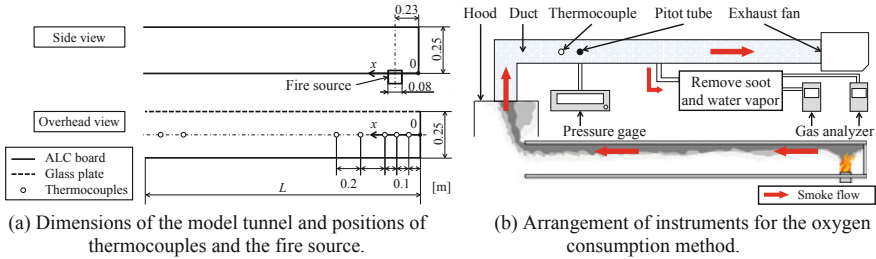
(a) Dimensions of the model tunnel and positions of thermocouples and the fire source.

(b) Arrangement of instruments for the oxygen consumption method.

Fig. 1 Schematic diagram of the experimental apparatus

Table 1 Scaling correlations used for the fire experiment

Type of unit	Scaling
Heat release rate Q (kW)	$Q_f = \gamma^{5/2} Q_m$
Velocity V (m/s)	$V_f = \gamma^{1/2} V_m$
Time t (s)	$t_f = \gamma^{1/2} t_m$
Length L (m)	$L_f = \gamma L_m$
Temperature T (K)	$T_f = T_m$

thermal properties are closest to those of concrete when modeling equivalent thermal characteristics under 1:20 scale conditions to full scale [9]. Part of the bottom and one side wall of the tunnel were made of a heat-resistant glass plate in order to be able to observe the smoke flowing in the tunnel. A propane gas porous bed burner with a diameter of 0.08 m was used as the fire source and installed at a position 0.23 m from the closed wall (a symmetrical plane). The mass flow rate of propane gas consumed by the burner was measured with a mass flow meter (KOFLOC, Model 3760). K-type thermocouples with a diameter of 0.1 mm were installed along the centerline at 0.2-m intervals and 5 mm directly below the ceiling of the tunnel. In addition, in the vicinity of the fire source, thermocouples were installed at 0.1-m intervals.

Figure 1b shows the schematic diagram of the oxygen consumption method [6]. Smoke exhausted from the tunnel portal on the opposite side of the closed end was collected by a hood. The velocity and temperature of the smoke flowing through the duct connected to the hood were measured by a combination of a Pitot tube and a fine differential pressure gage (Setra Systems, Inc., Model 239) and a K-type thermocouple, respectively. The mass flow rate of the smoke flowing in the duct was estimated from the average velocity and temperature considering the temperature and velocity distributions in the duct. Furthermore, part of the smoke collected was used for measuring the gas concentration in the smoke by gas analyzers. A non-dispersive infrared gas analyzer (Shimadzu, CGT-7000) was used for measuring the concentration of carbon dioxide and carbon monoxide. A magnetic wind-type oxygen analyzer (Shimadzu, POT-8000) was used for measuring the concentration of oxygen. The 90% response time of the oxygen analyzer and the carbon dioxide

and carbon monoxide analyzer is 45 and 30 s, respectively. The concentration of water vapor was estimated by the Antoine equation based on the relative humidity measured by a relative humidity sensor. All the data (ceiling temperature, mass flow rate of propane gas, velocity and temperature in the duct, and gas concentrations) were measured by a data logger (KEYENCE, NR-250) at 1-s intervals.

3   Experimental Conditions and Method for Estimating Combustion Efficiency

Table 2 lists 21 items of experimental conditions and primary data measured. The several parameters listed in Table 2 will be explained below. The test number, the dimensionless tunnel length, the heat release rate under the assumption of complete combustion, the chemical heat release rate estimated by the oxygen consumption

Table 2 Experimental conditions and primary data

Number	L^*	$Q_{\mathrm{T}} \pm U$ [kW]	$Q_{\mathrm{ch}} \pm U$ [kW]	$\chi \pm U$	$\chi_{\mathrm{avg.}} \pm U_{\mathrm{avg.}}$
1	0	5.28 ± 0.14	4.76 ± 1.49	0.90 ± 0.28	0.90 ± 0.27
2		5.30 ± 0.14	4.67 ± 1.42	0.88 ± 0.27	
3		5.34 ± 0.14	4.82 ± 1.45	0.90 ± 0.27	
4	8	5.40 ± 0.14	4.79 ± 1.38	0.89 ± 0.26	0.88 ± 0.27
5		5.31 ± 0.14	4.54 ± 1.40	0.86 ± 0.26	
6		5.55 ± 0.14	4.83 ± 1.42	0.87 ± 0.26	
7		5.31 ± 0.14	4.74 ± 1.40	0.89 ± 0.26	
8		5.33 ± 0.14	4.67 ± 1.42	0.88 ± 0.27	
9		5.28 ± 0.14	4.75 ± 1.56	0.90 ± 0.30	
10		5.40 ± 0.14	4.80 ± 1.55	0.89 ± 0.29	
11	16	5.33 ± 0.14	4.60 ± 1.38	0.86 ± 0.26	0.91 ± 0.25
12		5.32 ± 0.14	4.90 ± 1.37	0.92 ± 0.26	
13		5.53 ± 0.14	5.15 ± 1.38	0.93 ± 0.25	
14	24	5.19 ± 0.14	4.59 ± 1.44	0.88 ± 0.28	0.88 ± 0.27
15		5.47 ± 0.14	4.85 ± 1.42	0.89 ± 0.26	
16		5.36 ± 0.14	4.71 ± 1.42	0.88 ± 0.27	
17	32	5.32 ± 0.14	4.72 ± 1.43	0.89 ± 0.27	0.90 ± 0.28
18		5.03 ± 0.14	4.66 ± 1.44	0.93 ± 0.29	
19		5.36 ± 0.14	4.78 ± 1.46	0.89 ± 0.27	
20	40	5.48	–	–	–
21	48	5.07	–	–	–

Note The scale ratio, γ, equals 20 in our model tunnel. The indices "full" and "model" indicate full scale and model scale, respectively

method, combustion efficiency in each case, and average combustion efficiency with measurement uncertainty are shown in Columns 1–6. The tunnel length, L, was selected as the experimental parameter and varied at 0, 2, 4, 6, 8, 10, and 12 m. The experimental condition of the 0-m tunnel length indicates free burning directly under the hood without the model tunnel. All the fire experiments were performed for 25 min, so that the time curves of the gas concentrations measured by gas analyzers and temperature distribution under the ceiling would reach a quasi-steady state. However, in the case of the fire experiment under the condition of a tunnel length of 10 m or more, as the ghosting flame phenomenon occurred, the heat release rate of the fire could not be measured, and the fire experiment where ghosting flame occurred was stopped. Figure 2 indicates the time curves of the heat release rates and temperatures at several positions under the tunnel ceiling in the condition of a dimensionless tunnel length of eight (Case 4 in Table 2). The average heat release rates were evaluated as the mean values over a time range of 600 s between the dashed lines determined by looking at the graphs, under the assumption of quasi-steady combustion. Similarly, the temperature values measured by thermocouples were averaged in the same time range as the average temperature for evaluating the temperature distribution under the tunnel ceiling.

Equation (1) shows the definition of combustion efficiency, where Q_{ch} is the chemical heat release rate estimated by the oxygen consumption method, and Q_T is the heat release rate for complete combustion estimated by the mass loss rate for fuel burning.

$$\chi = \frac{Q_{ch}}{Q_T} \qquad (1)$$

Equation (2) indicates the definition of the chemical heat release rate, Q_{ch}, where E' is the net heat of combustion per unit volume of oxygen consumed referred to standard conditions (25 °C, 1 atm) assuming carbon goes to carbon dioxide ($E' = 17.2$ MJ/m^3), E'' is the net heat of combustion per unit volume of oxygen consumed
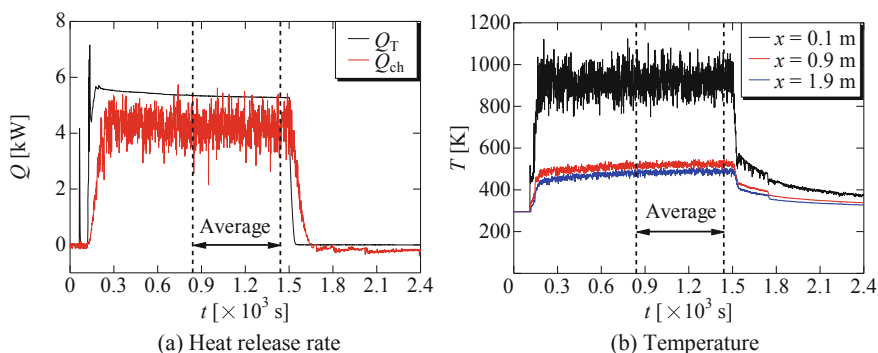

Fig. 2 Time curves of the heat release rate and temperature

referred to standard conditions in the burning of carbon monoxide ($E'' = 23.1 \, \text{MJ/m}^3$), $X^{\circ}_{O_2}$ is the volume fraction of oxygen in ambient air, f is the fraction of depleted oxygen going into the formation of carbon monoxide, ϕ is the fraction of oxygen depleted, and V_A is the volume flow rate air referred to standard conditions [6].

$$Q_{ch} = \left[E' - f(E'' - E') \right] X^{\circ}_{O_2} \phi \, V_A \tag{2}$$

Equation (3) indicates the definition of the heat release rate under the assumption of complete combustion, Q_T, where ΔH_T is the lower calorific value of propane gas ($\Delta H_T = 46 \times 10^3$ kJ/kg) and $\dot{m}$ is the mass flow rate of the propane gas.

$$Q_T = \dot{m} \Delta H_T \tag{3}$$

4   Measurement Uncertainties

In this section, we provide information on measurement uncertainty in our fire experiments. Normally, measurement uncertainty at a 95% confidence level, U, comprises the bias limit, B, the precision index of average, $S\bar{x}$, and Student's t value as follows: [10].

$$U = \left(B^2 \pm (t S\bar{x})^2 \right)^{1/2} \tag{4}$$

The product of the precision index of average, $S\bar{x}$, and Student's t value is the estimated value of the precision error limit. The bias limit, B, is the estimated value of the upper limit of bias error. In the fire experiments, we have measured data at 1-s intervals and evaluated the data as the value averaged for 600 s. As the number of sampling data was 600, we evaluated the Student's t value as two. The chemical heat release rate was calculated using many parameters measured, such as the concentrations of gases and pressure difference measured by the Pitot tube and gas temperature for estimating the mass flow rate in the duct.

$$Q_{ch} = \text{func}\left(X_{O_2}, X_{CO_2}, X_{CO}, T_D, \Delta P, T_A, h_A, T_0, h_0 \right) \tag{5}$$

Estimating the chemical heat release rate based on many parameters, we can represent the bias limit, B, and the precision index of average, $S\bar{x}$, as follows.

$$B = \left(\left(\theta_{X_{O_2}} B_{X_{O_2}} \right)^2 + \left(\theta_{X_{CO_2}} B_{X_{CO_2}} \right)^2 + \left(\theta_{X_{CO}} B_{X_{CO}} \right)^2 + \left(\theta_{T_D} B_{T_D} \right)^2 \right.$$
$$\left. + (\theta_{\Delta P} B_{\Delta P})^2 + \left(\theta_{T_A} B_{T_A} \right)^2 + \left(\theta_{h_A} B_{h_A} \right)^2 + \left(\theta_{T_0} B_{T_0} \right)^2 + \left(\theta_{h_0} B_{h_0} \right)^2 \right)^{1/2} \tag{6}$$

$$S\bar{x} = \left(\left(\theta_{X_{O_2}} S\bar{x}_{X_{O_2}} \right)^2 + \left(\theta_{X_{CO_2}} S\bar{x}_{X_{CO_2}} \right)^2 + \left(\theta_{X_{CO}} S\bar{x}_{X_{CO}} \right)^2 + \left(\theta_{T_D} S\bar{x}_{T_D} \right)^2 \right.$$

$$\left. + (\theta_{\Delta P} S\bar{x}_{\Delta P})^2 + \left(\theta_{T_A} S\bar{x}_{T_A} \right)^2 + \left(\theta_{h_A} S\bar{x}_{h_A} \right)^2 + \left(\theta_{T_0} S\bar{x}_{T_0} \right)^2 + \left(\theta_{h_0} S\bar{x}_{h_0} \right)^2 \right)^{1/2} \tag{7}$$

Table 3 lists the bias limits for all the instruments, the precision indexes of average for all the measurement values, and sensitivity for all the measurement values in Case 17. The bias limits were evaluated as half of the measuring precision for each instrument. Through the fire experiments, we obtain many measurement values: gas concentrations (oxygen, carbon dioxide, and carbon monoxide), temperature and pressure difference measured by Pitot tube in the duct, ambient humidity, ambient temperature, and humidity and temperature of the gas entering the analyzers. As the precision index of average values of the data measured by each instrument was significantly less than the values of the bias limit of the instruments, the measurement uncertainty of the data measured was dominated by the bias limits of the instruments. Using these data, we ascertained that the measurement uncertainties of the chemical heat release rate and the heat release rate for complete combustion were estimated as ±1.43 and ±0.14 kW, respectively. Consequently, the measurement uncertainty of the combustion efficiency of the fire in the model tunnel was ±0.27. The chemical

Table 3 List of all the bias limits and the precision indexes of average

Case	Parameter i	Description	Units	B_i	$S\bar{x}_i$	θ_i	θB_i	$\theta S\bar{x}_i$
17	T_D	Temperature in the duct	K	1	5.5×10^{-2}	7.9×10^{-3}	7.9×10^{-3}	4.3×10^{-4}
	ΔP	Pressure difference	Pa	2.5×10^{-1}	2.7×10^{-2}	6.9×10^{-1}	1.7×10^{-1}	1.9×10^{-2}
	X_{O_2}	O$_2$ volume fraction	–	6.3×10^{-4}	1.7×10^{-6}	2.2×10^{3}	1.4	3.8×10^{-3}
	X_{CO_2}	CO$_2$ volume fraction	–	5.0×10^{-4}	1.1×10^{-6}	4.7×10^{2}	2.3×10^{-1}	5.2×10^{-4}
	X_{CO}	CO volume fraction	–	5.0×10^{-6}	1.1×10^{-8}	7.7×10^{2}	3.9×10^{-3}	8.2×10^{-6}
	T_A	Temperature in the analyzer	K	1.5×10^{-1}	2.9×10^{-3}	5.4×10^{-4}	8.0×10^{-5}	2.4×10^{-5}
	h_A	Humidity in the analyzer	%	2.0×10^{-2}	2.1×10^{-3}	1.8×10^{-3}	3.5×10^{-5}	3.7×10^{-6}
	T_0	Ambient temperature	K	1.5×10^{-1}	5.8×10^{-3}	6.8×10^{-3}	1.0×10^{-3}	4.0×10^{-5}
	h_0	Ambient humidity	%	2.0×10^{-2}	4.4×10^{-2}	1.5×10^{-3}	3.0×10^{-5}	6.6×10^{-5}

heat release rate estimated by the oxygen consumption method was dominated by the bias limit of O_2 volume fraction. The effect of other measurement values except for this parameter on the chemical heat release rate was small.

5   Results and Discussion

5.1   Temperature Distribution

In this study, fire experiments under the same experimental conditions were conducted three times to check repeatability. Figure 3 shows the longitudinal distributions of the rise in temperature under the ceiling in the cases of dimensionless tunnel lengths of 16 and 32. The vertical and horizontal axes are the dimensionless x-coordinate and temperature, i.e., x^* and ΔT^*, which are defined as shown in Eqs. (8) and (9), respectively.

$$x^* = \frac{x}{H} \tag{8}$$

$$\Delta T^* = \frac{\Delta T}{Q^{*2/3} T_0} \tag{9}$$

where Q^* is the dimensionless heat release rate, the definition of which is as follows.

$$Q^* = \frac{Q}{\rho_0 T_0 C_p g^{1/2} H^{5/2}} \tag{10}$$
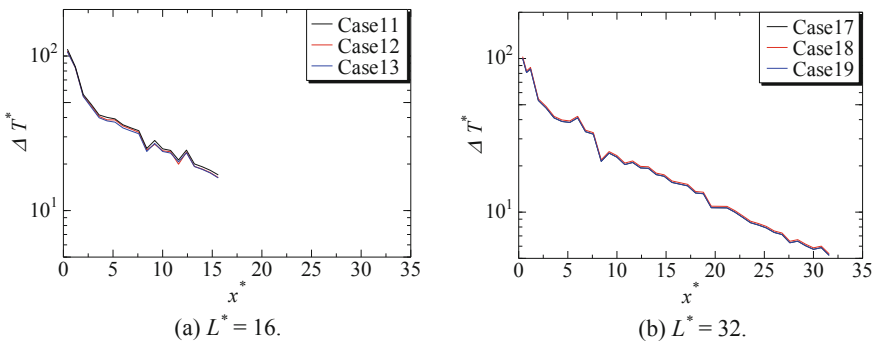

(a) $L^* = 16$.   (b) $L^* = 32$.

Fig. 3   Dimensionless rise in temperature distributions under the ceiling

As shown in Fig. 3a, b, the dimensionless temperature distributions under the same experimental conditions agreed with each other in Cases 11–13 and Cases 17–19. The fire experiments conducted under the same experimental conditions were found to have repeatability.

5.2 Heat Release Rate

Figure 4 shows an example of the time curves of the four gas concentrations, temperature, and pressure difference measured by Pitot tube in the duct under the experimental condition of dimensionless tunnel length $L^* = 24$, which is Case 14 of the fire experiments. The amplitudes of its time variation with respect to the average values of the gas concentrations measured by gas analyzers are small. The rapid time variation cannot be captured by analyzers with a long response time (oxygen, 45 s; carbon dioxide and carbon monoxide, 30 s). As a result, the measurement uncertainties of the gas concentrations are dominated by the bias limits of the analyzers. The mass flow rate of smoke flowing in the duct was determined depending on the pressure difference of the Pitot tube and the average temperature in the duct. The time variation of the temperature inside the duct was small but the time variation of the pressure difference of the Pitot tube was large. As a result, the measurement uncertainty of the mass flow rate of smoke flowing in the duct was dominated by the precision index of average and the bias limit at the velocity measurement by the Pitot tube.

Figure 5 shows the time curves of the heat release rate in the cases of $L^* = 16$ and 32. The red and black lines indicate the chemical heat release rate measured by
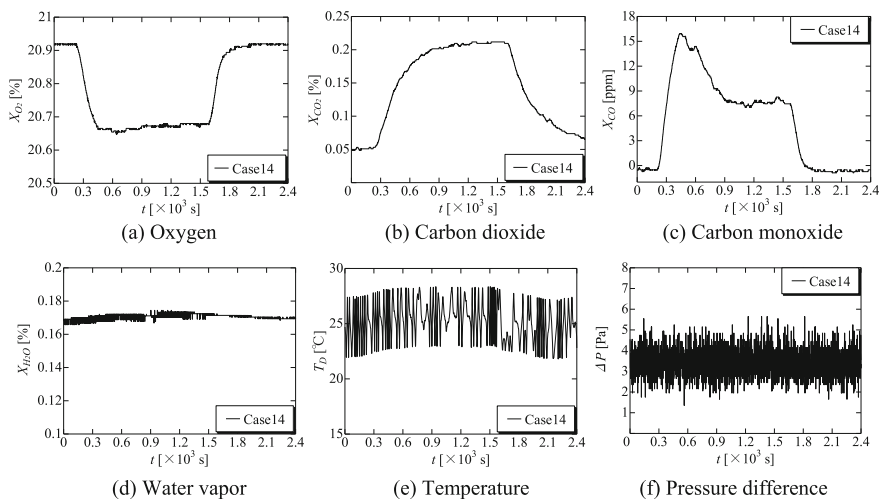

Fig. 4 Time curves of the concentration of gases, temperature, and pressure difference
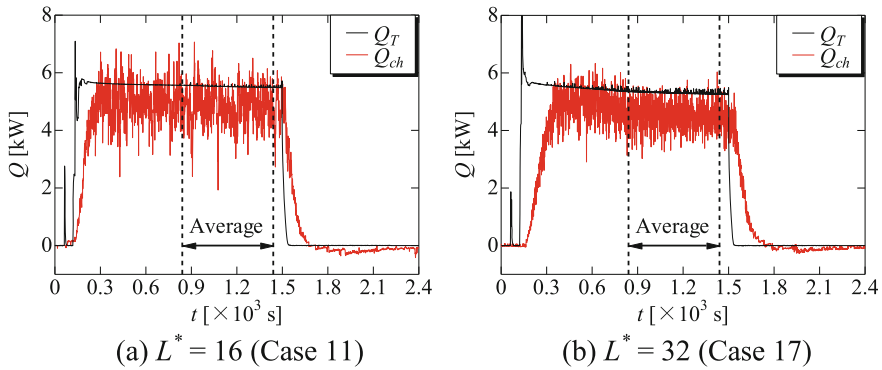
Fig. 5 Time curves of the heat release rates under dimensionless tunnel length $L^* = 16$ and 32

the oxygen consumption method and the heat release rate for complete combustion estimated by the mass loss rate for fuel burning, respectively. The time curves of the chemical heat release rate have rapid time variation compared to those of the heat release rate for complete combustion because the rapid time variation of the mass flow rate in the duct affected the chemical heat release rate. The average chemical heat release rates were evaluated as the mean values over a time range of 600 s between the dashed lines as shown in Fig. 5.

5.3 Combustion Efficiency and the Ghosting Flame Phenomenon

Figure 6 shows the relationship between the length of the model tunnel and combustion efficiency. As shown in Table 2 and Fig. 6, combustion efficiency of the fire in the model scale tunnel with a dimensionless tunnel length ranging from 0 to 32, which corresponds to 0–8 m in model scale and 0–160 m in full scale, was not affected by the tunnel length. In this study, the fire scale of the propane gas burner

Fig. 6 Combustion efficiency under the conditions of dimensionless tunnel length $L^* = 0$–32
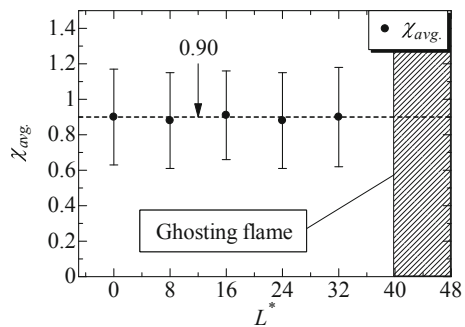
was about 5.7 kW in 1:20 model scale, corresponding to a 10-MW fire in full scale. A 10-MW fire is not a large fire as a tunnel fire. Under the 5.7-kW fire in 1:20 model scale, fresh air supplied by natural ventilation from the tunnel portal contains a sufficient amount of oxygen to maintain the flame, and the combustion mode was in a fuel-controlled state. Therefore, the combustion mode was not influenced by the tunnel length, and combustion efficiency, which became a constant value within the range of measurement uncertainty, was 90%. However, when the dimensionless tunnel length was 40 or more, the flame on the gas burner became ghosting flame [11, 12], causing a dramatic change in the combustion mode.

Figures 7a–d show the state of the flame on the gas burner in the case of $L^* = 48$, corresponding to the times 4 min after ignition, 4 min 35 s later, 5 min 35 s later, and 6 min later, respectively. The fire initially burned above the gas burner (see Fig. 7a), and then moved toward the symmetrical wall slightly (see Fig. 7b). The flame left from the gas burner (see Fig. 7c) and the size of the fire became small with the passage of time (see Fig. 7d). The reason for this phenomenon was an insufficient supply of fresh air and a fuel-rich condition. Since propane gas was supplied from the gas burner regardless of the amount of fresh air supplied from the tunnel portal, the concentration of propane gas near the fire increased with the passage of time. Accordingly, the flame moved toward the symmetrical wall where a low concentration of propane gas was maintained. These phenomena can be explained as ghosting flame [11, 12]. We found that the smoke descent phenomenon occurred in the model tunnel based on the observations of the smoke flow in the dimensionless tunnel length of $L^* = 40$ or more. Ghosting flame was caused by the smoke descent phenomenon.

Figure 8 shows a schematic diagram of the hypothesized air flow. In the dimensionless tunnel length of 40 or more, before all the smoke was exhausted through the tunnel portal, part of the smoke flowing under the ceiling descended to the tunnel floor. The descended smoke was mixed into the fresh air sucked in from the portal of the tunnel due to natural ventilation. The airflow was contaminated with part of the smoke flowed toward the fire. If the smoke descent condition lasted for some time, circulation of airflow contaminated with smoke was formed between the fire and the descent point of the smoke flow. The oxygen concentration of the airflow contaminated with smoke gradually decreased. Consequently, the amount of oxygen supplied to the fire gradually decreased, and ghosting flame occurred in the tunnel

(a) 4 min after ignition   (b) 4 min 35 s later   (c) 5 min 35 s later   (d) 6 min later

Fig. 7 Ghosting flame phenomenon under the condition of dimensionless tunnel length $L^* = 48$
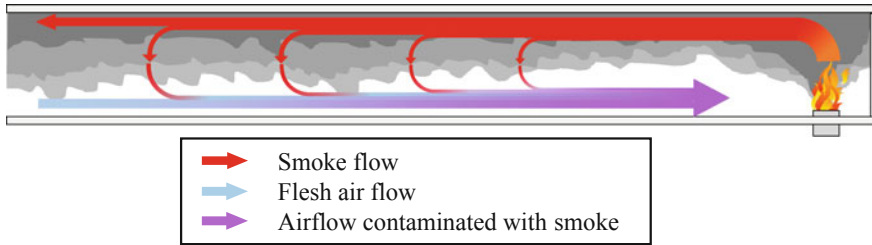
Fig. 8 Schematic diagram of the flow of smoke and fresh air under the ghosting flame condition

with the dimensionless tunnel length of 40 or more, since there was a sufficient supply of propane gas from the gas burner regardless of the amount of oxygen supplied. However, further research is needed to clarify the conditions for the occurrence of the ghosting flame phenomenon when liquid or solid fuel is used as fuel burning in tunnel fire experiments.

6 Conclusion

In this study, we demonstrated that the combustion efficiency of a tunnel fire was not affected by the tunnel length under the condition of no smoke descending to the tunnel floor, and the combustion efficiency was 90% within the range of measurement uncertainty. When part of the smoke descended to the tunnel floor, the ghosting flame phenomenon occurred.

References

1. Tewarson, A. (2002). Generation of heat and chemical compounds in fires. In P. J. DiNenno, et al. (Eds.), *SFPE handbook of fire protection engineering* (3rd ed., Vol. 3, pp. 82–161). Gaithersburg: Society of Fire Protection Engineers.
2. Hu, L. H., Huo, R., Wang, H. B., Li, Y. Z., & Yang, R. X. (2007). Experimental studies on fire-induced buoyant smoke temperature distribution along tunnel ceiling. *Building and Environment, 42,* 3905–3915.
3. Takeuchi, S., Aoki, T., Tanaka, F., & Moinuddin, K. A. M. (2017). Modeling for predicting the temperature distribution of smoke during a fire in an underground road tunnel with vertical shafts. *Fire Safety Journal, 91,* 312–319.
4. Gao, Z. H., Ji, J., Fan, C. G., & Sun, J. H. (2016). Determination of smoke layer interface height of medium scale tunnel fire scenarios. *Tunnelling and Underground Space Technology, 56,* 118–124.

5. Zukoski, E. E., Kubota, T., & Cetegen, B. (1980). Entrainment in fire plumes. *Fire Safety Journal, 3,* 107–121.
6. Parker, W. J. (1982). *Calculations of the heat release rate by oxygen consumption for various applications*, *NBSIR 81-2427-1*. Gaithersburg: National Bureau of Standards (U.S.).
7. Ingason, H., Li, Y. Z., & Lönnermark, A. (2015). *Tunnel fire dynamics* (pp. 485–488). Berlin: Springer.
8. Vauquelin, O., & Telle, D. (2005). Definition and experimental evaluation of the smoke "confinement velocity" in tunnel fires. *Fire Safety Journal, 40,* 320–330.
9. Tanaka, F., Takezawa, K., Hashimoto, Y., & Moinuddin, K. A. M. (2018). Critical velocity and backlayering distance in tunnel fires with longitudinal ventilation taking thermal properties of wall materials into consideration. *Tunnelling and Underground Space Technology, 75,* 36–42.
10. American Society of Mechanical Engineers. (1985). ASME Performance Test Codes, Supplement on Instruments and Apparatus, Part 1, Measurement Uncertainty, PTC19.1-1985.
11. Audouin, L., Such, J. M., Malet, J. C., & Casselman, C. (1997). A real scenario for a ghosting flame. *Fire Safety Science, 5,* 1261–1272.
12. He, Q., Li, C., Lu, S., Wang, C., & Zhang, J. (2015). Pool fires in a corner ceiling vented cabin: ghosting flame and corresponding fire parameters. *Fire Technology, 51,* 537–552.

The Analysis of HGV Fire Scenarios in Tunnel with Point-Extraction Ventilation

Li-Wu Fan and Guan-Yuan Wu

Abstract In this study, the authors numerically simulated heavy goods vehicle (HGV) fire scenarios in order to investigate the tenable conditions of a two-way traffic road tunnel with point-extraction ventilation system consisting of water spray system. A computational fluid dynamics (CFD) model was used to simulate the interaction between the point-extraction ventilation and the water spray system. A total of four cases were carried out in a 600 m tunnel model. Distributions of smoke, temperature, visibility, and CO concentration profiles in tunnels axial-sections for the considered model and point-extraction ventilation system were provided. Results show that the characteristics of tenable conditions for the tunnel fires having water spray are distinctive from those of the tunnel without water spray and ventilation. Tunnel with the point-extraction ventilation and water spray system can provide the relative safety region for occupants at the outside of the water spray zone once HGV fires occur.

Keywords Tunnel fire · Point extraction · Water spray system · Numerical simulation

Nomenclature

C_P Constant pressure specific heat (kJ/kg K)
g Acceleration of gravity (m/s^2)
D^* Characteristic fire diameter (–)
$\dot{Q}$ Heat release rate from fire (kW)
ρ_∞ Density of ambient (kg/m^3)
T_∞ Temperature of ambient (K)

L.-W. Fan · G.-Y. Wu (✉)
Department and Graduate School of Fire Science, Central Police University, Kwei-San, Ta-Kang, Tauyuan 333, Taiwan ROC
e-mail: una210@mail.cpu.edu.tw

1 Introduction

Road tunnels are infrastructure that provides for convenient transport and economic development in worldwide. However, many serious tunnel fires occurred such as the Mont Blanc road tunnel fire in France (1999) [1], St. Gotthard road tunnel fire in Switzerland (2001) [2], and a rear-end collision accident involving two methanol tankers occurred in the Yanhou tunnel in China (2014) [3]. These tunnel fire cases caused loss of lives, injuries, severe property damage, service disruption, and even incalculable economic losses.

It is well known that tunnel fire is a very complex phenomenon because of the mutual interactions between fire dynamic process, suppression system, ventilation system, and tunnel geometry layout. Many studies on tenability conditions have been done in the past, including analytical correlations, experiments, and numerical modeling. A number of different numerical simulations have been proposed. Lin and Chuah [4] studied on smoke extraction strategy of long road tunnel with numerical simulation and investigated the performance of different smoke extraction strategies for a 100 MW fire scenario. Through numerical simulation and theoretical work, Li and Ingason [5] investigated the effect of cross-section on critical velocity of fire smoke in longitudinally ventilated tunnel fires. Using small-scale tunnel model experiments, Jiang et al. [6] analyzed the airflow velocity and smoke back-layering length with different smoke outlet area and heat release rate in the point smoke extraction system. The purpose of these studies is to ensure the safety of occupants, the integrality of tunnel structures in the event of tunnel fire.

Tunnel fire research projects with the water spray system have been studied by several investigators [7–9]. Arvidson summarized a series of large-scale fire suppression tests conducted to simulate a fire in the trailer of a heavy goods freight truck on a ro-ro deck [7]. In this study, fire was fully exposed to the water spray or shielded and analyzed by several parameters such as the water discharge density, the system operating pressure, and the nozzle K-factor. Ingason et al. presented the results of the six large-scale tests with different types of fixed fire fighting system in the Runehamar tunnel in 2016 [8]. In this experiment, 420 standardized wooden pallets and a target of 21 wooden pallets were used as the fire load. Using three different types of side wall nozzle with an interval distance of 5 m, the tests were carried out with a 30 m long deluge zone versus varying water densities. Using numerical simulation, Liang et al. proposed a new system with simultaneous water mist screen and transverse ventilation system (WMSTV system) [9]. In the system, water mist screens are used to confine smoke from spreading widely, which can confine the fire and smoke effects, and be regarded as a feasible smoke control strategy.

In Taiwan, the Su-Hua highway engineering project is in progress, a total of eight tunnels (total 24.6 km) except Ren-shui tunnel is two-way traffic road tunnel (2.9 km), and the others are one-way traffic road tunnel that will be constructed. At the same time, five tunnels will install water spray system and adopt the point-extraction ventilation in engineering construction. Although Lin and Chuah have presented some numerical results for a 100 MW fire scenario in a tunnel, their model

was focused on a road tunnel with single-point extraction (SPE) opening strategy versus multi-point extraction (MPE) opening strategy [4]. Effects of water spray and point-extraction ventilation on the HGV fires in a tunnel cannot be concluded from these studies.

The main purpose of this study is to analyze the HGV fire scenarios in tunnel with point-extraction ventilation and water spray system. Distributions of smoke spread, temperature, CO concentration, and visibility versus different cases were also analyzed. It was found that the point-extraction ventilation and water spray system have a significant effect on the fire suppression by reducing the temperature near the source of fire and confining smoke spread for safe evacuation of the occupant in tunnel.

2   Numerical Analysis

In the past few decades, many researchers used Fire Dynamics Simulator (FDS) to simulate and investigate the complex tunnel fires studies [9–12]. This software package has been validated extensively and the results indicated that FDS has good agreement with the experiments. Liu and Cassady [10] discussed a modified critical velocity for road tunnels with a dedicated smoke extraction system and water-based fire suppression system. To confirm the performance of this modified critical velocity, they also analyzed the design parameters such as fire scenarios, fire sizes, tunnel gradient, fire location, smoke extraction location, and a total number of open smoke extraction dampers. It is well known that the damper configuration, the damper number, and the damper flow rate affect the results of the visibility and temperature distribution in the tunnel fires obviously. Using FDS 5.5, the influence of smoke damper configuration on point-extraction ventilation system of an urban tunnel has been investigated by Yuan et al. [11]. Wang et al. used four different simplified geometrical shapes in FDS6 to simulate a fuel package that represents a large-scale HGV tunnel fire [12]. The results in the study of Wang et al. showed that significant differences are obtained during the fully developed phase while using the different fuel shapes [12]. In this study, Fire Dynamics Simulator (FDS, Version 6.6.0) is used to analyze and investigate the results of HGV tunnel fires with water spray system and the point-extraction ventilation system.

2.1   FDS

FDS software is computational fluid dynamics models (CFD Models). Its core computing equation is the Navier-Stokes equations and analyzes the growth of fire under Low-Mach domain. By dividing the computational domain into many FDS, it is
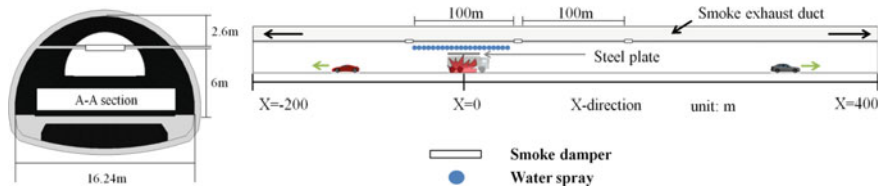
Fig. 1 Schematic diagram of the tunnel and the layout of smoke damper and water spray

modeled on large eddy simulation (LES) and direct numerical simulation (DNS). FDS slice the simulation space into many small grid cells, as the basis for computation, for many phenomena in the fire, such as fire, flame, heat flow, and smoke flow, derived from Navier-Stokes equations, including conservation of mass, conservation of momentum, conservation of energy, and conservation of species [13]. The range of FDS applications is low-Mach number flow domain analysis, which can analyze the fire temperature, smoke concentration, and distribution simulation. After FDS numerical simulation, Smokeview software can be used to obtain the process of dynamic presentation.

2.2 Physical Model

The full-scale physical domain analyzed is shown in Fig. 1. It consists of a two-way road tunnel 600 m long, equipped with water spray system, arranged in point-extraction ventilation system. The cross-section of the tunnel is based on the Ren-shui tunnel (a two-way traffic road tunnel) in Su-Hua Highway Improvement Project Tunnel Plan (Version E) [14]. The height of the smoke exhaust duct is 2.6 m. The fire source is located at central area of cross-section, $Y = 0$ m, and 200 m from the left portal of the tunnel, but with various cross-sectional layouts as shown in Fig. 1.

2.3 Grid Sizes

Referring to Baum et al. [15], Ma and Quintiere [16] used a grid size approach with a grid size of $0.1D^*$. The grid dimension near the fire site was initially determined by using a characteristic fire diameter D^*, which is defined as:

$$D^* = \left(\frac{\dot{Q}}{\rho_\infty C_P T_\infty \sqrt{g}} \right)^{2/5}$$

(1)

If x is the nominal size of a grid cell, the quantity D^*/x can be thought of as the number of computational cells spanning the characteristic diameter of the fire.

Table 1 Computation domains and the grid number

	The domain of mesh (m)			Grid size (m)			Grid number
	X	Y	Z	δx	δy	δz	
Mesh 1	−200 to −45	−8.12 to 8.12	0–6.24	1	0.406	0.780	155 × 40 × 8
Mesh 2	−45 to 55	−8.12 to 8.12	0–6.24	0.50	0.406	0.195	200 × 40 × 32
Mesh 3	55 to 400	−8.12 to 8.12	0–6.24	1	0.406	0.780	345 × 40 × 8
Mesh 4	−200 to 400	−5.887 to 5.887	6.24–8.91	1	0.406	0.534	600 × 9 × 5
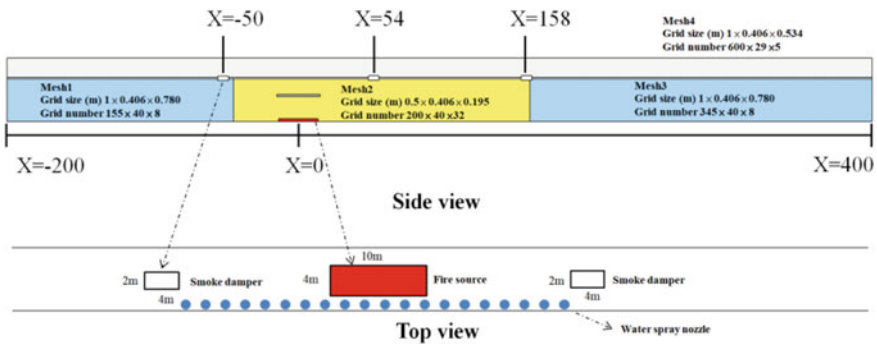
Fig. 2 Fire source, smoke damper, and water spray position layout for fire simulation cases (not to scale)

According to the experimental test grid resolution, when the grid size is 0.1D*, large eddy simulation (LES) simulated time-averaged axial velocity and temperature coincided with the McCaffery experimental regression equation. The fire size $Q =$ 100 MW, D* is about 6 m, then 0.1D* is approximately 0.60 m that can be taken as a reasonable grid size.

Referring to Lin [4], the grid size of this study in the vicinity of the fire within 100 m (Mesh 2) is set as 0.50 m (X) × 0.406 m (Y) × 0.195 m (Z). Mesh uniform grid size in tunnel Y, X, and Z axes is used uneven grid size. Total grids number was 503,000. The computation zones with different mesh sizes are listed in Table 1 and shown in Fig. 2.

2.4 Fire Scenarios

In the event of HGV tunnel fires, many studies have considered a fuel spill triggers ignition of the cargo carried on the vehicle and the heat release rate are often assumed

up to 100 MW. For example, fires with heat release rates ranging from 10–100 MW were produced in Memorial Tunnel Fire Ventilation Test Program [17]. The test results are applicable to the design of new tunnels and the optimal configuration management of ventilation in existing tunnels. The Runehamar tunnel test in 2003 for four different cargoes combustion experiments, the peak heat release rate of the test resulted in Test 4 was about 70 MW, and the other tests were above 100 MW [18].

The simulation results of heat release rate and smoke flow for 100 MW in this study and the results studied in Ref. [4] are shown in Figs. 3 and 4. These results are found to be in good agreement. Therefore, the constructed model and the grid sizes considered in this study are reasonable.

In this study, the steel plate whose size is 11 m $(L) \times 2.5$ m (W) referred Ref. [19] is set at 3 m above the fire source. The steel plate is assumed to simulate the roof of HGV cargo space. It is well known that for the fires where the fire was shielded from direct water application, the simulation systems had a limited effect on the total heat release rate and the associated total energy. There are some studies which show the similar assumption of steel plate for the experiment and simulation [7, 8, 20]. For example, a series of large-scale fire suppression tests conducted to simulate a fire in the trailer of a heavy goods freight truck on a ro-ro deck with/without a roof of the simulated HGV cargo space have been investigated by Arvidson [7]. Ko et al. set the metal sheet above the pool fire to avoid sprinkling affected by the pool fire heat release rate [20].
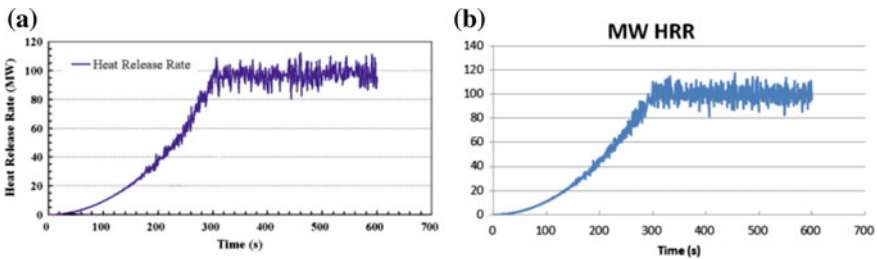

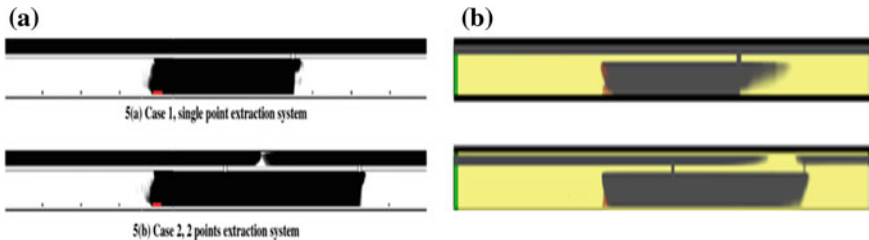**Fig. 3** Heat release rate of 100 MW for **a** Lin and Chuah [4] and **b** This study

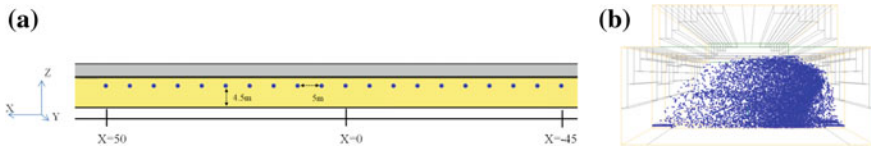**Fig. 4** Smoke flow simulations for **a** Lin and Chuah [4] and **b** This study

Fig. 5 **a** Schematic description of nozzle and **b** Schematic description of water spray

The requirements concerning the nozzle is set by referring to the Japan's regulation which water discharge for each zone is 50 m in length, discharge density is 6 l/m², and the diameter of droplet is 1000 µm [21]. It should be noted that when fire occurs, two zones of water spray systems are activated simultaneously. In this study, the specifications of water spray system refer to "NOHMI BOSAI LTD" side wall design standard [22]. The pipe was placed at the wall on one side of the tunnel, with nozzles discharging water toward the opposite wall and the fuel. Moreover, the height of nozzle is 4.5 m. The interval between two adjacent nozzles is 5 m as shown in Fig. 5a. The result of discharge simulation for the cross-section is shown as in Fig. 5b.

The Su-Hua highway engineering project contains eight tunnels (total 24.6 km) except Ren-shui tunnel is two-way traffic road tunnel (2.9 km), the others are one-way traffic road tunnel. In this project, five tunnels will install water spray system and adopt the point-extraction ventilation in engineering construction. Considering the different traffic road, there are two types of point-extraction ventilation in this project. For Ren-shui tunnel, the size of smoke damper is 2 m × 4 m and the distance for each damper is 100 m. When fire occurs in the tunnel, the dampers will be operated immediately and the flow of smoke exhaust will reach to 324 m³/s at 180 s. The more detailed layout of the instruments used in the Su-Hua highway tunnels are shown as in Table 2.

In this study, a HGV accident fire is assumed and four kinds of fire scenarios are considered as listed in Table 3. It should be noted that the activation time of water spray system is limited to 3 min for one-way traffic road tunnel, and 5 min for two-way traffic road tunnel in Taiwan [23]. For case 1, the smoke flow freely flows in the tunnel with no water spray system and point-extraction ventilation. For case

Table 2 Layout of the instruments used in the Su-Hua highway tunnels

Tunnel	Type	Water spray zone	Smoke exhaust flow (m³/s)	Smoke damper number	Water spray start-up time (s)
Ren-shui tunnel	Two-way traffic road tunnel	2	324	3	300
Other tunnels	One-way traffic road tunnel	2	240–360	1 or 3	180

Table 3 Fire scenarios in numerical simulation

Scenario case	Point extraction system	Water spray system	Water spray activation time (s)	Fire location (m)
Case 1	–	–	–	0
Case 2	Y	Y	180	0
Case 3	Y	Y	300	0
Case 4	Y	–	–	0

2 and 3, the water spray system is activated at 180 and 300 s, respectively. For these two cases, the point extraction system reaches the maximum exhaust flow at 180 s. For case 4, it is assumed that the water spray system is damaged, but point extraction system can be operated normally. The ambient temperature is assumed to be 30.0 °C in this study.

3 Results and Discussions

In the design of fire emergency responses for Su-Hua tunnels, one of the key objectives is to ensure that the occupants have sufficient time to safely evacuate before the egress routes become untenable from the effects of heat and smoke from a fire. In Taiwan, the government provides specific guidance on setting the tenability criteria in tunnel fire with water spray system. Furthermore, the values for tenable criteria are set as follows: temperature <60 °C, visibility >10 m, CO concentration <800 ppm, and radiant heat <2 kW/m^2 at 1.8 m height above the ground [23]. In this study, distributions of smoke, temperature, visibility, and CO concentration profiles in tunnel axial-sections for cases 1–4 are provided and discussed as follows.

3.1 Smoke Spread Process

Figure 6 shows the distributions of smoke spread for cases 1–4 along the tunnel at 200, 300, 400, and 500 s, respectively. Without the water spray system and ventilation, it can be seen that the smoke of case 1 spreads rapidly to both ends of the tunnel and the tunnel fills up smoke directly. It should be noted that the point-extraction ventilation system is activated at 180 s for cases 2–4. At 200 s, the distributions of smoke spread for cases 2, 3, and 4 are very similar due to the effect of ventilation system. At 300 s, the smoke of case 2 can be seen that is confined to the water spray zone well. Though the activation time of water spray for case 3 is at 300 s, the result of smoke spread for case 3 is the same as case 4 at this moment (as shown in Fig. 6b).
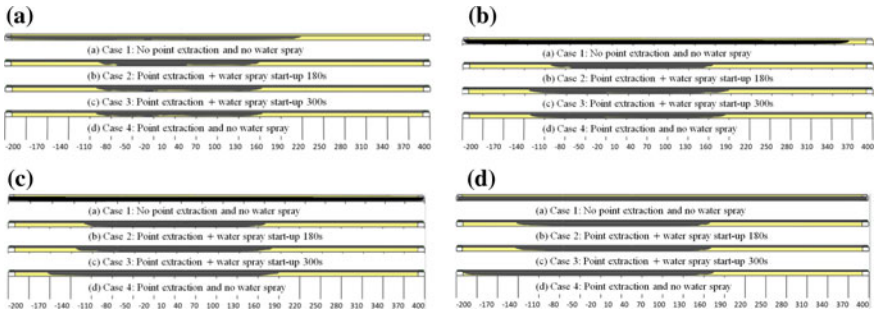
Fig. 6 Simulation results of smoke distribution at **a** 200 s, **b** 300 s, **c** 400 s, **d** 500 s
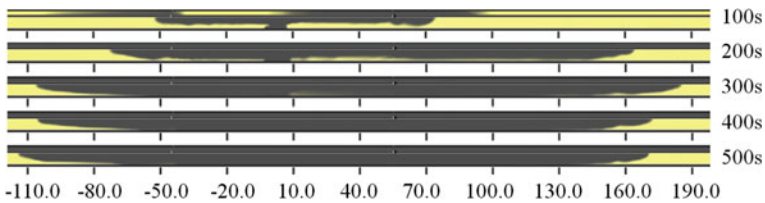

Fig. 7 Smoke spread process for case 3

Figure 6c shows the smoke distributions of cases 1–4 at 400 s. As shown in this graph, the smoke distribution of case 3 is confined well than that of case 4. At 500 s, the smoke distributions of case 2 and 3 are still confined well. It shows that tunnel with the point-extraction ventilation and water spray system can confine the smoke of tunnel fire. Because there is only one smoke damper at $X = -50$ and without water spray system, the smoke of case 4 spreads to left portal of the tunnel. Figure 7 shows the smoke spread process in case 3 where the smoke is confined well so that the smoke does not spread over a wide area due to the combined effects of water spray system and point extraction system.

3.2   Temperature Distributions

The distributions of temperature near fire source for cases 1–4 at time intervals of 200, 300, 400, and 500 s are shown in Fig. 8. These graphs show that case 2 and case 3 can effectively reduce the temperature after water spray system activation. Without water spay system and ventilation system, the temperature of case 1 spreads rapidly to the both portals and then temperature increases vertically. At 400 s, the temperature of case 1 will exceed 60 °C from $X = -110$ to $X = 100$ at 1.8 m height. However, the temperature of the entire tunnel will not exceed 60 °C for cases 2 and 3 except that it is near the fire source. These results of temperature for cases 2 and
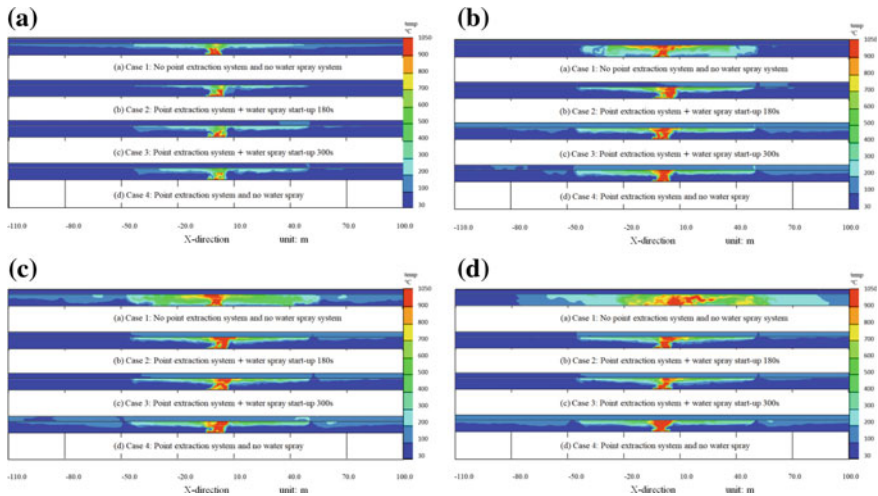
Fig. 8 Temperature distributions along the tunnel at **a** 200 s, **b** 300 s, **c** 400 s, **d** 500 s

3 will comply with the tenable criteria of "The fire-risk parameters index in road tunnels" in Taiwan [23].

3.3 Visibility Distributions

In Taiwan, the tenable criterion of visibility is greater than 10 m for occupants at 1.8 m height. Figure 9 shows the distributions of visibility for cases 1–4 along the tunnel at 200, 400, and 500 s. From these figures, it can be seen that the visibility decreases obviously when water spray system is activated at 400 and 500 s. This phenomenon of visibility is probably caused by the mixture of water vapor and hot smoke. For case 1, the visibility of the entire tunnel is less than 10 m when the time is over 400 s. The results of visibility for case 2, 3, and 4 are greater than 10 m at the outside of water spray zone. In addition, the visibility for case 2, 3 is better than case 4 at 400 and 500 s, respectively. These results show that tunnel without point extraction and water spray could cause a threat to occupant's evacuation.

3.4 CO Concentration Distributions

Figure 10 shows the distributions of CO concentration for cases 1–4 at 200, 400, and 500 s. The tenable criterion of CO concentration is less than 800 ppm for occupants at 1.8 m height for any time. For case 1, it is the worst case, but the CO concentration does not exceed 800 ppm during the fire simulation. For cases 2 and 3, the CO
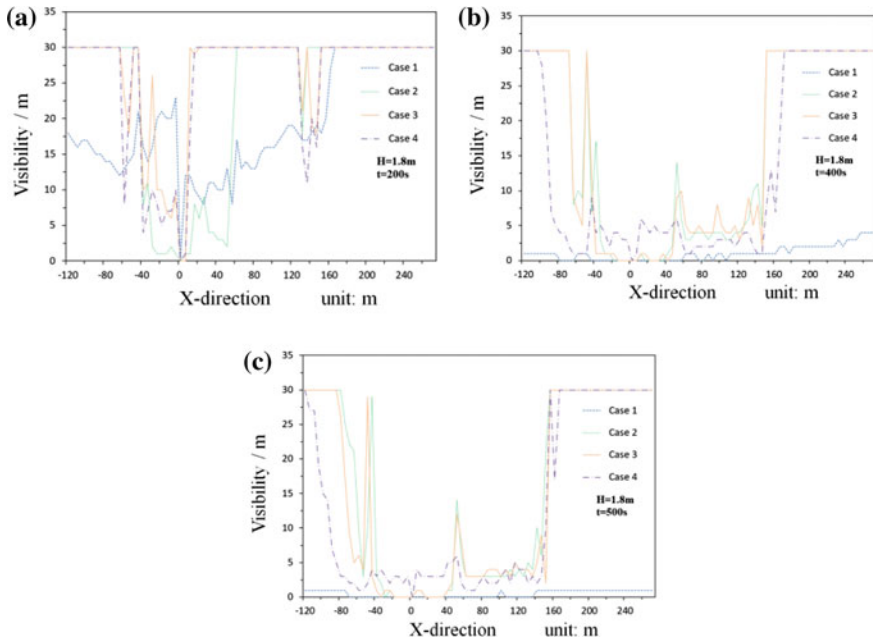
Fig. 9 Numerical visibility distributions at 1.8 m above the floor level at **a** 200 s, **b** 400 s, **c** 500 s
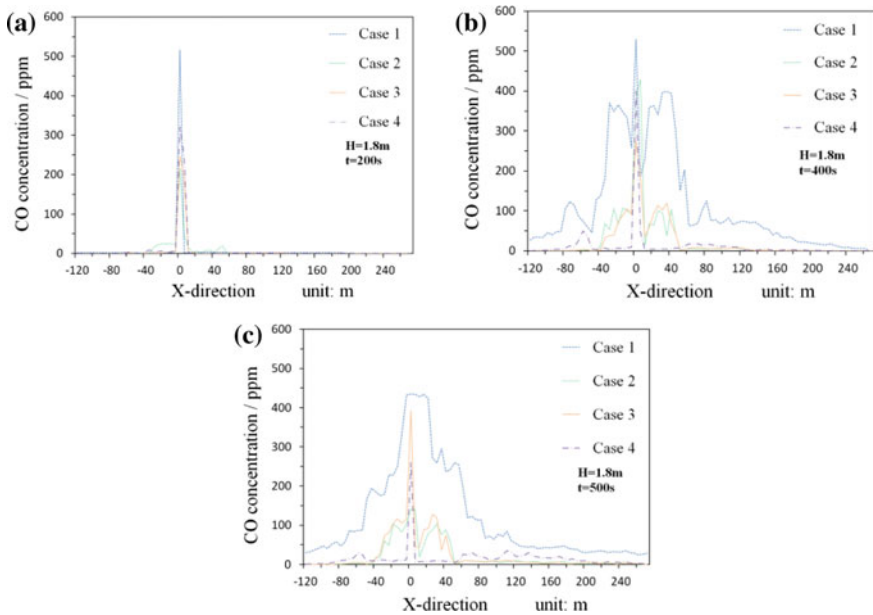

Fig. 10 Numerical CO concentration distributions at 1.8 m above the floor level at **a** 200 s, **b** 400 s, **c** 500 s

concentration decreases to 0 ppm in the outside region of the smoke damper, which indicates that the toxic gas can also be prevented by the point extraction system and water spray system effectively.

4　Conclusions

In this study, computational fluid dynamics (CFD) model was used to simulate the tenable conditions of HGV fire scenarios in tunnel with point-extraction ventilation and water spray. A total of four cases were carried out in a 600 m tunnel model in which the smoke distribution, temperature, visibility, and CO concentration profiles were provided for both the no-spray and the spray conditions. Comparisons of the numerical results with Lin and Chuah [4], in terms of heat release rate and smoke flow, were found to be in a good agreement. Simulation results demonstrate that the water spray system has a significant effect on the fire suppression by reducing the temperature near the source of fire and confining smoke spread. In addition, when the water spray system is activated, the zones within water spray can result in lower visibility and higher CO concentration. However, the flow of smoke can be quickly exhausted from the tunnel because of the activation of point-extraction ventilation. Furthermore, two modes of water spray suppression for case 2 and 3 are found that the tenable conditions are very similar at 500 s when the water pray system stared up at 180 and 300 s, respectively. Through the simulation results, tunnel with the point-extraction ventilation and water spray system can provide the relative safety region for occupants at the outside of the water spray zone once HGV fires occur.

For a two-way traffic road tunnel, both ends of the tunnel are given a certain wind flow to restrict the smoke. Turbulent flow may occur near sources of ignition and fire bed. Therefore, more physical scaling and investigation such as different water spray system, water droplets, heat release rates, emergency operations and full-scale tests are needed in the future to enhance the overall safety of tunnel fires.

References

1. Abraham, O., & Dérobert, X. (2003). Non-destructive testing of fired tunnel walls: The Mont-Blanc tunnel case study. *NDT & E International, 36,* 411–418.
2. Zhu, H., Shen, Y., Yan, Z., Guod, Q., & Guo, Q. (2016). A numerical study on the feasibility and efficiency of point smoke extraction strategies in large cross-section shield tunnel fires using CFD modeling. *Journal of Loss Prevention in the Process Industries, 44,* 158–170.
3. Ingason, H., & Li, Y. Z. (2017). Spilled liquid fires in tunnels. *Fire Safety Journal, 91,* 399–406.
4. Lin, C. J., & Chuah, Y. K. (2008). A study on long tunnel smoke extraction strategies by numerical simulation. *Tunnelling and Underground Space Technology, 23,* 522–530.

5. Li, Y. Z., & Ingason, H. (2017). Effect of cross section on critical velocity in longitudinally ventilated tunnel fires. *Fire Safety Journal, 91,* 303–311.
6. Jiang, X., Liu, M., Wang, J., & Li, Y. (2018). Study on induced airflow velocity of point smoke extraction in road tunnel fires. *Tunnelling and Underground Space Technology, 71,* 637–643.
7. Arvidson, M. (2010). Large-scale water spray and water mist fire suppression system tests. In *Fourth International Symposium on Tunnel Safety and Security*. Germany: Frankfurt am Main.
8. Ingason, H., Li, Y. Z., & Bobert, M. (2016). *Large scale fire tests with different types of fixed fire fighting system in the Runehamar tunnel*. SP Technical Research Institute of Sweden, SP Report 2016:76.
9. Liang, Q., Li, Y., Li, J., Xu, H., & Li, K. (2017). Numerical studies on the smoke control by water mist screens with transverse ventilation in tunnel fires. *Tunnelling and Underground Space Technology, 64,* 177–183.
10. Liu, Y., & Cassady, S. (2014). A modified critical velocity for road tunnel fire smoke management with dedicated smoke extraction configuration. *Case Studies in Fire Safety, 2,* 16–27.
11. Yuan, J. P., Fang, Z., Tang, Z., Li, Q., & Wang, J. H. (2016). Influence of smoke damper configuration on point extraction ventilation system of an urban tunnel. *Procedia Engineering, 135,* 99–106.
12. Wang, X., Fleischmann, C., & Spearpoint, M. (2016). Assessing the influence of fuel geometrical shape on fire dynamics simulator (FDS) predictions for a large-scale heavy goods vehicle tunnel fire experiment. *Case Studies in Fire Safety, 5,* 34–41.
13. McGrattan, K., et al. (2017). *Fire dynamics simulator technical reference guide volume 1: Mathematical model* (6th ed.). Gaithersburg: National Institute of Standers and Technology.
14. Directorate General of Highways. (2016). MOTC, Provincial Highway 9 Su-Hua Highway Mountain Road Improvement Project Tunnel Accident and the Overall Disaster Relief Business Plan (Version E).
15. Baum, H. R., McGrattan, K. B., & Rehm, R. G. (1997). Three dimensional simulations of fire plume, international association for fire safety science. In *Fire Safety Science Proceedings 5th International Symposium* (pp. 511–522).
16. Ma, T. G., & Quintiere, J. G. (2003). Numerical simulation of axi-symmetric fire plumes: Accuracy and limitations. *Fire Safety Journal, 38,* 467–492.
17. Massachusetts Highway Department and Federal Highway Administration. (1995). Memorial Tunnel Fire Ventilation Test Program—Test Report.
18. Runehamar Tunnel Fire Tests. (2008). UPTUN WP2 Fire development and mitigation measures D213.
19. Ministry of Transportation and Communications R.O.C. (2017). Road Traffic Safety Regulations.
20. Ko, Y. J., & Hadjisophocleous, G. V. (2013). Study of smoke backlayering during suppression in tunnels. *Fire Safety Journal, 58,* 240–247.
21. Ministry of Transport, Netherlands. (2001). Sprinklers in Japanese Road Tunnels Final Report.
22. Nohmi Taiwan Limited. (2015). General Description of Water Spray.
23. Chien, S. W. (2013). *The results report-provincial highway 9 Suhua highway mountain road improvement project emergency response project research*. Taiwan: Directorate General of Highways, MOTC and CECI Engineering Consultants, Inc.

Correction to: An Experimental Study on Pressurization Smoke Control System in Staircase

Hyun woo Park, Tomohiro Mitsumura, Yoshifumi Ohmiya, Masashi Kishiue, and Wataru Takahashi

Correction to:

Chapter "An Experimental Study on Pressurization Smoke Control System in Staircase" in: G.-Y. Wu et al. (eds.), The Proceedings of 11th Asia-Oceania Symposium on Fire Science and Technology, https://doi.org/10.1007/978-981-32-9139-3_12

The original version of the book was published with subtitle for this Chapter "An Experimental Study on Pressurization Smoke Control System in Staircase" now subtitle has been updated from "Influence of a Dynamic Pressure Control System Opening Vestibule Doors Confirmation of Differential Pressure Adjustment Damper Performance" to "Influence of a Dynamic Pressure Control System and Opening Vestibule Doors and Confirmation of Differential Pressure Adjustment Damper Performance".. The chapter and book have been updated with the change.

The updated version of this chapter can be found at
https://doi.org/10.1007/978-981-32-9139-3_12